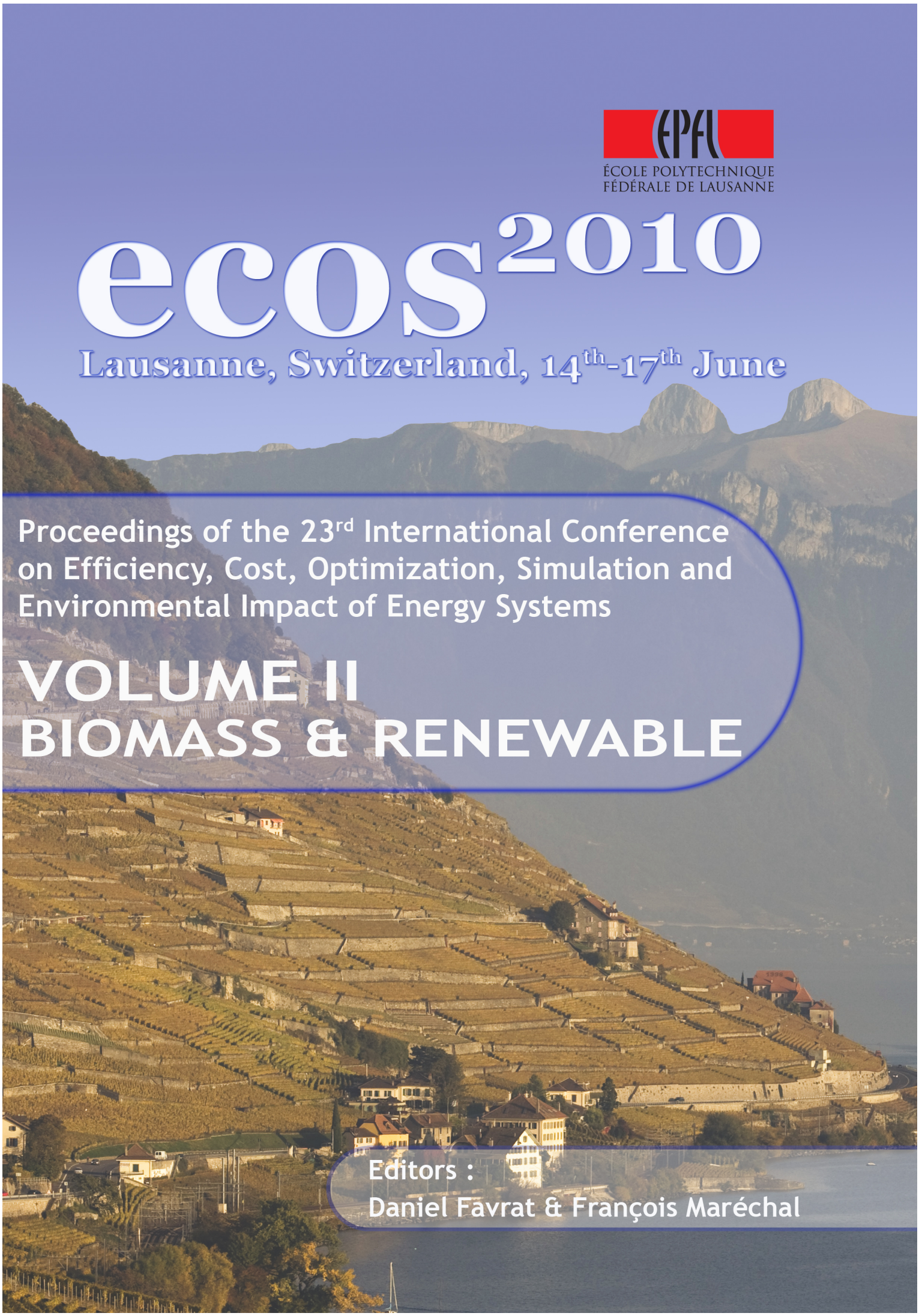
ÉCOLE POLYTECHNIQUE
FÉDÉRALE DE LAUSANNE
ecos2010
Lausanne, Switzerland, 14th-17th June
Proceedings of the 23rd International Conference on Efficiency, Cost, Optimization, Simulation and Environmental Impact of Energy Systems
VOLUME II
BIOMASS & RENEWABLE
Editors :
Daniel Favrat & François Maréchal

ecos2010

Proceedings of the 23rd International Conference on
Efficiency, Cost, Optimization, Simulation,
and Environmental Impact of Energy Systems

Lausanne, Switzerland
June 14-17, 2010

Volume II
Biomass & Renewable

Editors
Daniel Favrat and François Maréchal

Organised by
Laboratoire d'Énergétique Industrielle (LENI)
École Polytechnique Fédérale de Lausanne (EPFL)

Official Website of the conference
www.ecos2010.ch

Corresponding e-mail
ecos2010@epfl.ch

Corresponding address
EPFL / LENI – ISE - STI
Bat. ME A2
Station 9
CH-1015 Lausanne
Switzerland

Book creation
Nicolas BORBOËN, Yannick BRAVO

PREFACE

Energy plays a major role in human societies. The supply of energy services is also a major contributor to the global and, too often, local environmental problems the World is facing. According to the International Energy Agency, actions to target future CO_2 concentrations in atmosphere below either 550ppm, or even below 450ppm, will have to be primarily focused on efficiency. A broader use of renewable, nuclear power and perhaps carbon sequestration will also contribute. To maintain a viable economic development these actions will have to be cost effective while globally reducing all emissions and caring about energy and material resources. A systemic approach is therefore essential to get a holistic vision, design better systems and optimize money and resources utilization.

The ECOS conferences have a long tradition in fostering the key aspects and the scientific knowledge that are essential for the engineers. The organizers of this 23rd edition are proud to acknowledge one of the largest participation ever with many original and high quality papers.

Our thanks go to the authors who accepted to travel from all continents and meet in Lausanne to present and share their scientific contributions. Many thanks also to all reviewers and members of the scientific committee who contributed to the quality of these proceedings. The conference chairmen are also grateful to the local organizing team including in particular, Nicolas Borboën, Stina Zufferey, Brigitte Gabioud, Yannick Bravo, Suzanne Zahnd and Irène Laroche. Many thanks also to the other members of the Industrial Energy Systems Laboratory of EPFL, the MEDIACOM EPFL team and the sponsors who greatly helped the organization of this fruitful event.

Daniel Favrat & François Maréchal

ORGANISING COMMITTEE

Prof. Daniel Favrat (chairman)
François Maréchal (chairman)

Nicolas Borboën, Yannick Bravo, Brigitte Gabioud,
Irène Laroche, Suzanne Zahnd, Stina Zufferey

INTERNATIONAL ADVISORY BOARD

Ozer Arnas, United States
Christos A. Frangopoulos, Greece
George Tsatsaronis, Germany

SCIENTIFIC COMMITTEE

Monika Axel, Sweden
Rangan Banerjee, India
Adrian Bejan, United States
Thore Berntsson, Sweden
Asfaw Beyene, United States
Paolo Bosshard, Italy
Denis Clodic, France
Stephen R. Connors, United States
R.L Cornelissen, Netherlands
Michel Feidt, France
Carl-Johan Fogelholm, Finland
Richard Gaggioli, United States
Yalçın A. Göğüş, Turkey
Gershon Grossman, Israel
Simon Harvey, Sweden
Abel Hernandez-Guerrero, Mexico
Gerard Hirs, Netherlands
Andrew Forbes Alexander Hoadley, Australia
Koichi Ito, Japan
Hervé Jeanmart, Belgium
Signe Kjelstrup, Norway
Jiri Klemes, Hungary
Zygmunt Kolenda, Poland
Andrea Lazzaretto, Italy
Noam Lior, United States

Sylvie Lorente, France
Giampaolo Manfrida, Italy
Philippe Mathieu, Belgium
Alberto Mirandola, Italy
Michael Moran, United States
Zhang Na, China
Silvia Azucena Nebra, Brazil
Eduardo de Oliveira Fernandes, Portugal
Silvio de Oliveira Júnior, Brazil
Ricardo Rivero, Mexico
Marc A. Rosen, Canada
Dominick A. Sama, United States
Peter Schossig, Germany
Enrico Sciubba, Italy
Luis M. Serra, Spain
Samuel Stucki, Switzerland
Pascal Terrien, France
Jules Thibault, Canada
Daniel Tondeur, France
Vittorio Verda, Italy
Laura Vanoli, Italy
Michael R. von Spakovsky, United States
Carl-Jochen Winter, Germany
Li Zheng, China
Andrzej Ziębik, Poland
Ron Zevenhoven, Finland

Exergy Efficiency Analysis of Liquid Biofuels Production Processes

Héctor Iván Velásquez Arredondo[a], *Silvio de Oliveira Júnior*[b], *Pedro Benjumea*[a]

[a] *National University of Colombia, Alternative Fuels Group, Medellín, Colombia*
[b] *Polytechnic School, University of São Paulo, São Paulo, Brazil*

Abstract: In this work, an exergy analysis for liquid biofuels production processes is developed. The processes under analysis were acid hydrolysis to convert lignocellulosic material into glucose, enzymatic hydrolysis to transform amilaceous material into glucose, fermentation to convert sugars into ethanol and transesterification to produce biodiesel and glycerol from palm oil.

Results of process simulation taking into account the effect of several variables on the performance of the exergy efficiency are presented. The main variables considered were energy consumed (heat and work), reaction time, biomass chemical composition, and waste and by-products generation. The results indicate how the biofuels development researchers must be conducted in order to improve the exergy efficiency of biofuels production processes.

Keywords: Exergy analysis, Biomass, Biofuels, Hydrolysis.

1. Introduction

Ethanol and biodiesel produced from different renewable feedstocks constitute the most widely used alternative fuels for internal combustion engines [1-6]. These biofuels are considered biodegradable and are sulfur free. Additionally, as their carbon content has a vegetable origin it can diminish the carbon dioxide content in the atmosphere. Ethanol and biodiesel can be used neat or blended with gasoline and conventional diesel fuel, respectively, and so their use allows decreasing fossil fuel consumption as well as to increase the energy security of a region or country.

In Brazil, sugarcane has been used to produce ethanol for almost 90 years. It has proved to be a key raw material due to its high content of sucrose, which through milling, fermentation and distillation, can be used as a feedstock to produce ethanol. Developments in bioprocesses are being made to allow the use of amilaceous and lignocellulosic materials to produce ethanol through hydrolysis, fermentation and distillation. Vegetable oils or animal fats can be converted into biodiesel by the transesterefication reaction.

A primary tool to analyze the production processes of biofuels from an integrated point of view is offered by exergy analysis. Exergy is defined as the maximum (theoretical) work that can be extracted from a mass or energy stream when it passes from a given thermodynamic state to one in chemical, mechanical and thermal equilibrium with the environment in a reversible way, interacting only with components of the environment. Therefore, any deviation from the environmental reference can be assumed as exergy content [7].

When exergy analysis is performed, the thermodynamic irreversibilities can be quantified as exergy destruction, which is a wasted potential for producing work [8]. In addition, exergy allows comparisons between all inflows and outflows, regardless if they are mass or energy streams, using the same physical basis [9, 10].

Exergy analysis has been used to evaluate biodiesel production from cooking oils [11]. Similar studies have been developed using palm oil as a raw material [12, 13]. The combined production of sugar, ethanol and electricity taking into account different configurations of the cogeneration plant, have been analyzed using exergy-based costs [14, 15].
The aim of this work is to evaluate four liquid biofuels production processes using exergy analysis and to study the effect of several process variables on exergy efficiency. The selected process were: acid hydrolysis of starch obtained from banana fruit, enzymatic hydrolysis of

Corresponding Author: Héctor Velásquez, Email: hivelasq@unal.edu.co

lignocellulosic material obtained from banana plant residues, fermentation of sugars obtained from sugarcane into ethanol, and transesterification of palm oil for biodiesel production. Each process is characterized by mass and exergy balances identifying and quantifying the raw materials, inputs including work and steam, products and co-products, and destroyed exergy.

2. Processes description

The processes studied were hydrolysis of amilaceus and lignocelulósico material, fermentation of sucrose and glucose syrup and transesterification of vegetable oil.

2.1. Hydrolysis

Hydrolysis is a chemical or biochemical process which allows the production of reducing sugars from starch and lignocellulose. It is an indispensable and intermediate step in ethanol production since microorganisms that promote fermentation are not able to directly metabolize the original raw materials.

Hydrolysis can be carried out in two ways: acid (chemical via) or enzymatic (biochemical via) [16-18]. Because of its low cost and availability, sulfuric acid (H_2SO_4) is most often used in the acid hydrolysis. Hydrochloric (HCl) and nitrous (HNO_2) acids are also used. Enzymes commonly used in the enzymatic hydrolysis are α-*amylas and cellulases* [19, 20]. In general, the cellulose is converted in glucose, and hemicellulose in pentose and hexose [21, 22]. The chemical reaction representing hydrolysis is given by [23]:

$$(C_6H_{10}O_5)n + nH_2O \xrightarrow{\text{acid or enzymatic medium}} nC_6H_{12}O_6$$

Figure 1 shows the different stages, going from raw material reception to sugar syrup production, that biomass has to undergo in order to transform its starch content into sugars by acid hydrolysis. When banana fruit is used as a raw material, it is possible to use the entire fruit or only its pulp. In the former case, the fruit is chopped and crushed. In the later case the banana fruit is peeled. In the next step, the material is ground and water is added to it until acquiring a proper consistency for the reaction. This is a critical step since it implies heat and mechanical work consumption.

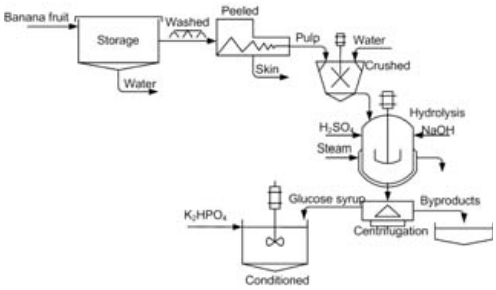

Fig. 1. Scheme of a plant for the acid hydrolysis of starch.

In the acid hydrolysis reaction, diluted sulfuric acid (H_2SO_4) is added and the mixture is stirred and heated by steam during 10 hours at 100 ^{0}C. After that time the syrup obtained is neutralized using NaOH which forms Na_2SO_4. Then, the mixture is filtered by centrifugation, and the syrup and residues are separated. The syrup is conditioned for fermentation with proteins and minerals as K_2HPO_4.

Figure 2 shows the different stages that biomass has to undergo in order to transform its cellulosic material content into sugars by enzymatic hydrolysis. The lignocellulosic material is shattered and crushed before passing through a delignification process which is carried out at ambient temperature using NaOH. Then, the material is hydrolyzed by adding sulfuric acid and the enzyme for 5 hours at 50°C. Finally, the mixture is also neutralized and filtered before fermentation.

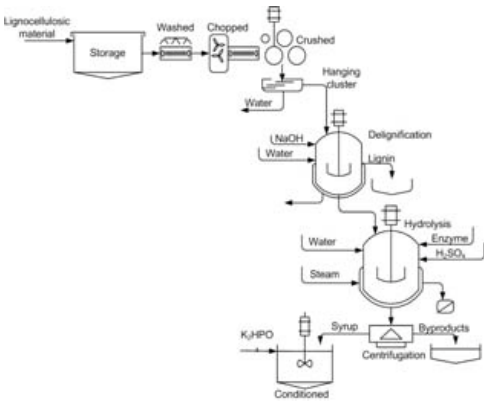

Fig. 2. Scheme of a plant for the enzymatic hydrolysis of lignocellulosic material.

2.2. Fermentation

Fermentation is a process whereby yeast modifies its metabolic route to convert sugars into ethanol as shown in the following chemical irreversible reaction [24]:

$$C_{12}H_{22}O_{11}+H_2O \rightarrow 2C_6H_{12}O_6 \rightarrow 4C_2H_5OH+4CO_2$$

The sucrose in the presence of enzymes absorbs one water molecule and splits into reducing sugars (glucose and fructose) which are finally converted into ethanol releasing CO_2.

As shown in figure 3, the fermentation process is divided in two parts: yeast growing and syrup fermentation. Yeast growing requires an initial syrup supply and a constant oxygenation to guarantee aerobic conditions. Additionally, agitation and refrigeration are required to maintain a constant temperature in the reactor (33°C).

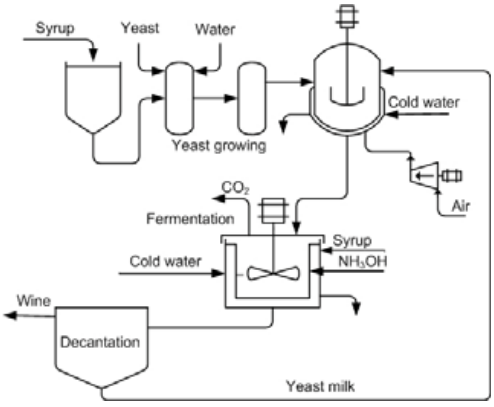

Fig. 3. Scheme of a plant for the fermentation of sugars.

Syrup fermentation is accomplished under anaerobic conditions with constant agitation and maintaining the temperature between 32°C and 35°C. After fermentation, the mixture is decanted, and the separated wine is sent to distillation while the yeast milk is returned to the process.

The nature of the syrup which is fed to the fermentation process depends on the raw material. It is composed of glucose and water when it comes from the hydrolysis of starch, or sucrose and water in the case of sugarcane.

2.3. Transesterification

Figure 4 shows a scheme of a biodiesel or methyl esters (ME) production plant. The data used in this study came from a pilot plant designed to test several raw materials with a capacity to process 1 t of oil per day.

The first step is the mixing of methanol with the selected catalyst (NaOH). For refined palm oil (RBD), composed only by triglycerides (TG), a 6:1 molar ratio of methanol to oil (100% excess alcohol) and a 0.6% by weigh of NaOH are used. In the case of crude palm oils having free fatty acid (FFA) contents in the range 3%-5% by weight, it is necessary to increase the alcohol excess (12:1 molar ratio) and to use an additional quantity of catalyst, required to neutralize the FFA:

$$FFA+NaOH \rightarrow Soapstock+H_2O$$

The second and main step is the transesterification reaction:

$$TG+3CH_3OH \Leftrightarrow 3ME+G$$

The alcohol-catalyst mixture is combined with the palm oil in the reactor and agitated for 1 hour at 60ºC. Once the reaction is complete, the reactor content is separated in two phases, one rich in ME and the other rich in glycerol (G). The separation step can be promoted by gravity using a settling vessel and/or by centrifugation. The lighter ME rich phase can also contain catalyst and free glycerol traces, variable concentrations of bonded glycerol, mono-glicerydes and di-glycerides, depending on the reaction yield, soaps (proportional to the oil FFA content), and a substantial amount of the excess methanol. On the other hand, the denser rich glycerol phase contains most of the catalyst used and soap formed, the rest of the excess methanol and any water formed in the occurring reactions.

The denser phase is only about 50% glycerol and so it has little value and disposal may be difficult. Also, the methanol content requires the glycerol to be treated as hazardous waste. The glycerol refining step begins with the addition of a diluted acid, such as phosphoric or sulfuric one, to split the soaps into FFA and salts. The added acid also neutralizes the present catalyst. This neutralization step requires heating and mixing. The FFA is not soluble in the glycerol and will rise to the top

where it can be removed. The salt precipitates out and can be filtered and dried. The methanol and water in the glycerol are removed by evaporation.

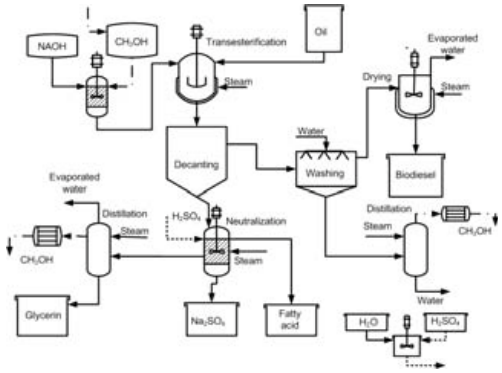

Fig. 4. Scheme of a plant for biodiesel production.

3. Modeling approach and simulation

The developed model aim at simulating the steady state operation of all control volumes studied. It is composed of mass, energy and exergy balances and was implemented and simulated in EES software, using its data base of thermodynamic properties for H_2O, CH_3OH, C_2H_5OH and for ideal gases such as CO_2, H_2O, O_2, CO, N_2, CH_4, etc [25].

The exergy balance for the biofuels production processes considered in this work was represented by the following equation [26]:

$$B_{Bio} + B_{In} + B_V + B_W = B_P + B_{BP} + B_C + B_D \qquad (1)$$

Where B_{Bio}, B_{In}, B_V, B_W, B_P, B_{BP} y B_C are the exergy of biomass, inputs, steam, mechanical work consumed by pumps and stirrers, products, co-products and recovered condensates, respectively. B_D takes into account the exergy destroyed in the system. Table 1 shows the items considered for each process.

The exergy evaluation of the processes was carried out defining the exergy efficiency η_B as shown in Eq. (2) [27, 28]:

$$\eta_B = \frac{B_e - B_W}{B_i} = \frac{B_p}{B_i} \qquad (2)$$

where B_e is the exergy of exit flows, B_w the exergy considered as waste, B_i the flow exergy entrance to the process and B_p the exergy in products. By using this criterion, the exergy destroyed inside the system together with those of the wastes represent the irreversibilities of the processes.

Table 1. Substances considered for the exergy balance of biofuels production processes [26]

Process	Biomass	Inputs	Products	Byproducts
Transesterification	Palm oil	CH_3OH, H_2O, NaOH, H_2SO_4, steam, work	Biodiesel	Glycerol, AG, Na_2SO_4
Acid hydrolysis	Banana fruit and banana pulp	NaOH, H_2SO_4 H_2O, K_2HPO_4, steam, work	Glucose syrup	Na_2SO_4, residual biomasa, H_2O and lost syrup
Enzymatic hydrolysis	Hanging cluster	NaOH, H_2SO_4, H_2O, Enzyme, K_2HPO_4, steam, work	Glucose syrup	Lignin, H_2O, Na_2SO_4, residual biomass, and lost syrup
Fermentation	Glucose syrup and sucrose syrup	NaOH, H_2SO_4, CaO, KH_2PO_4, work	wine	Residual biomass

Thermodynamic properties of sucrose-water solutions were calculated according to the correlations given in [29]. Exergy of ethanol-water solutions were taken from [30]. The elemental composition of different kinds of biomass (banana fruit, banana skin, hanging cluster of banana brunch), higher and lower heating values (HHV and LHV), necessary to develop the exergy analysis, were obtained by experimental analysis and they were analytically corroborated using expressions proposed in literature [31, 32]. The composition of palm oil and biodiesel were obtained by gas chromatographic analysis and its properties were calculated using the Joback method of contribution groups [33, 34]. The thermodynamic properties and chemical exergy of other substances like: NaOH, H_2SO_4, Na_2SO_4,

CaO, CH_3OH and KH_2PO_4, were obtained from differences bibliographic sources [7, 35-37].

4. Results

The exergy efficiency of the biofuels production processes under actual operation conditions is shown in Table 2.

With banana pulp the hydrolysis showed a better exergy efficiency (57.4%) than with hanging cluster (20.3%) especially for the higher content of amilaceous material in banana pulp (80.2%) with relation to cellulosic material in hanging cluster (40.9%) [38, 39].

The fermentation process showed similar performance for all raw materials because the process conditions were similar in all cases. Nevertheless, the exergy efficiency was higher when sugarcane was used since the sugar molecule for fermentation is sucrose. On the other hand, the syrup sent to fermentation in the case of the hydrolysis of the amilaceous and lignocellulosic materials is glucose.

Table 2. Exergy efficiency of biofuels production processes

Process	Raw material	Exergy efficiency (%)
Transesterification	Palm oil	90.0
Hydrolysis	Banana pulp	57.4
	Banana fruit	51.3
	Hanging cluster	20.3
Fermentation	Sucrose syrup	90.0
	Glucose syrup	75.3 – 77.0

The exergy efficiency for biodiesel production was obtained taking into account only biodiesel as product. It is high due to the intrinsic transesterification reaction characteristics. Since the reaction is considered reversible the exergy destruction is low. When glycerol was also taken as a product, the exergy efficiency increased to 96.3%.

The exergy evaluation of the processes allowed identifying the variables susceptible to be optimized.

4.1 Variables affecting hydrolysis

For the hydrolysis case the more representative variables were: the content of starch or cellulose in biomass, the water content of the mixture, the temperature and time of reaction, the mixture pH, and the glucose losses in neutralization.

The water content of the mixture affected inputs consumption and energy requirements for later processes such as distillation. The water/biomass ratio can be reduced by two ways: decreasing biomass moisture and decreasing the dilution level of sulfuric acid.

Figure 5 shows the effect of water/biomass ratio on exergy efficiency and ethanol production when banana pulp was used as raw material. Under actual process conditions that ratio was 4.86 w/w corresponding to an ethanol production of 77.9 kg per t of banana fruit.

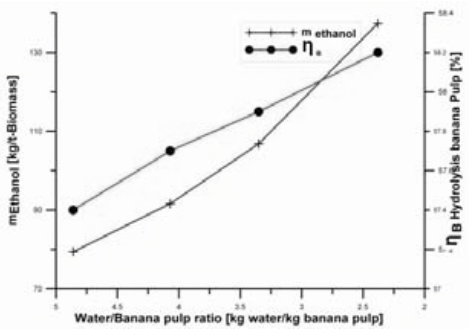

Fig. 5 Effect of water/biomass ratio on ethanol production and exergy efficiency. Banana pulp case.

When the moisture of the banana pulp decreased ethanol production increased, since the space occupied by water inside the reactor would be occupied by biomass susceptible to be transformed into ethanol, and then exergy efficiency also increased.

The water/biomass ratio could be decreased until 3.7. That value corresponded to a glucose concentration of 214 g/L, which was the maximum allowed quantity for fermentation. At higher concentrations the yeast was deactivated by osmotic pressure. In that way it would be possible to increase ethanol production until 106.8 kg-ethanol/t-banana and to increase exergy efficiency until 57.9%.

Figure 6 shows the effect of pH variation on the hydrolysis of the banana fruit. Under actual conditions the hydrolysis was carried out at a pH of 0.8. It was clear that an increase in the pH lead

to a decrease in inputs consumption, increasing slightly the process exergy efficiency.

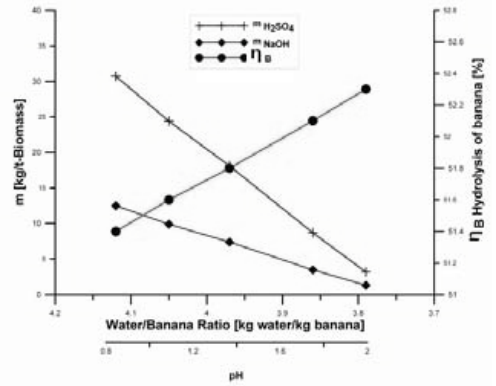

Fig. 6. Effect of pH and water/biomass ratio on inputs mass consumption and hydrolysis exergy efficiency

The relationship between exergy efficiency and inputs consumption was not direct due to several factors. Under actual process conditions, the consumption of H_2SO_4 was 30.7 kg/t-banana and of NaOH was 12.5 kg/t-banana, with an exergy efficiency of 51.4%. For a reduction in the water/biomass ratio (kg water/kg banana) until 3.8, the consumption of H_2SO_4 and NaOH decreased until 3.2 and 1.3 kg/t-banana, respectively, and exergy efficiency only increased until 52.3. In that way it is showed that inputs consumption had a low impact in exergy efficiency. This could be explained according to the low exergy value of the inputs with relation to the raw material and products.

The relationship between the conversion efficiency of biomass into glucose and the process exergy efficiency was analyzed by simulating the efficiency of the hydrolysis of the hanging cluster of banana with relation to exergy efficiency and ethanol production as can be seen in Figure 7. Under actual process conditions the efficiency of conversion of the hanging cluster hydrolysis was 22.5% and the exergy efficiency was only 20.3%. However, it would be possible to increase exergy efficiency to values slightly greater than 40% if the reaction conversion reaches values close to 60%. These results give insights to the researches in order to focus in processes that guarantee greater ethanol yields as a consequence of better biomass conversions.

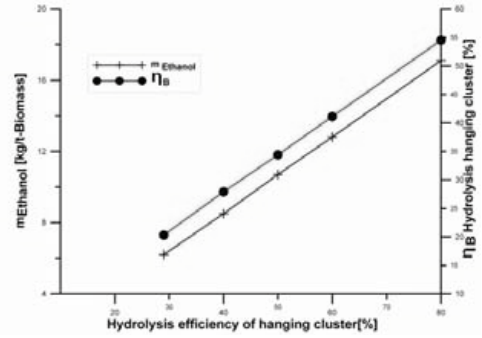

Fig. 7. Relation of the exergy efficiency with the efficiency of the hydrolysis of the hanging cluster of banana fruit

4.2 Variables affecting syrup fermentation

In the case of the fermentation process, the main variable affecting exergy efficiency was the efficiency of the sugars conversion into ethanol. Figure 8 shows a simulation of the effect of glucose conversion (obtained from the banana pulp hydrolysis) on ethanol production and exergy efficiency. Under actual process conditions the fermentation yield was 90% and the exergy efficiency close to 77%. If the fermentation yield could reach 95%, the exergy efficiency would be 81.1% and the ethanol production 83.8 kg de ethanol/t banana, without modifying any other variable.

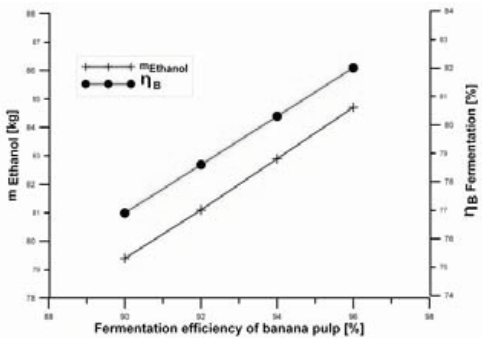

Fig 8. Effect of glucose conversion on ethanol production and fermentation exergy efficiency

Other variables affecting fermentation yield were reaction time and syrup type. Mechanical work for stirring increased with reaction time. The fermentation yield for sucrose was higher than that for glucose.

4.3 Variables affecting syrup fermentation

In the case of biodiesel production, the main variable affecting the transesterification of palm oil was oil quality. Figure 9 shows the variation of the exergy efficiency of the biodiesel production process with oil quality. When only biodiesel was taken into account as transesterification product the exergy efficiency was 90%. When glycerol was also considered, exergy efficiency reached a value of 97.7%.

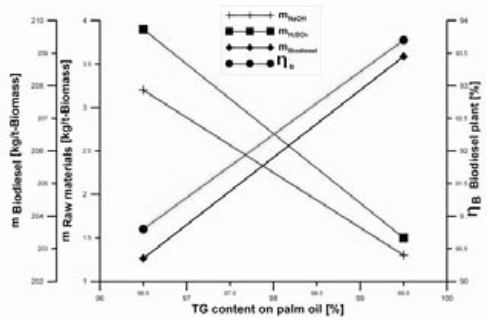

Fig 9. Effect of biodiesel quality on the exergy efficiency of palm oil biodiesel production.

An increase in oil quality expressed as a reduction in the free fatty acid content led to a decrease in catalyst (NaOH) and neutralizing agent (H_2SO_4) consumptions, and some increases in biodiesel production and process exergy efficiency.

Other variables affecting the transesterification reaction were time and reaction temperature. Higher reaction time and temperature increased mechanical work and steam consumption.

5. Conclusions

The proposed methodology for exergy analysis allows simulating the effect of selected variables on exergy efficiency of biofuels production processes and so the developed model constitutes a valuable tool for process optimization.

In the case of hydrolysis, the higher exergy efficiency was reached when banana pulp was used. The analysis showed that exergy efficiency was improved by using biomass with higher starch or lignocellulosic content, decreasing the water/biomass ratio, temperature and stirring time, and increasing pH.

The fermentation of the four types of syrups reaches exergy efficiencies between 75.3% and 79.6%. The main variable affecting exergy efficiency was reaction yield.

The greatest exergy efficiency was obtained in the case of biodiesel production by palm oil transesterification due to the low exergy destruction as a result of reaction reversibility. However the process could be optimized by increasing oil quality and decreasing agitation time and reaction temperature.

Acknowledgments: The authors would like to acknowledge the support of the DIME office, the Crude and Petroleum products laboratory of the National University of Colombia, the Biochemical Laboratory of the National University of Colombia, the Brazilian Research Council (CNPq), AUGURA association, Azucar Manuelita S.A and Aceitesa S.A.

References

[1] Mann, M.K. and P.L. Spath, Life Cycle Assessment of a Biomass Gasification Combined-Cycle System, in Life Cycle Assessment. 1997, National Renewable Energy Laboratory. p. 160.

[2] Wang, M., C. Saricks, and D. Santini, Effects of Fuel Ethanol Use on Fuel-Cycle Energy and Greenhouse Gas Emissions. 1999, Argonne National Laboratory, Center for Transportation Research: Argonne.

[3] Hsieh, W., et al., Engine Performance and Pollutant Emission of an SI Engine Using Ethanol–Gasoline Blended Fuels. Atmospheric Environment 2002. **36**: p. 403-410.

[4] Kadam, K.L., Environmental Benefits on a Life Cycle Basis of Using Bagasse-Derived Ethanol as a Gasoline Oxygenate in India. Energy Policy 2002. **30**: p. 371–384.

[5] Malça, J. and F. Freire, Renewability and Life-cycle Energy Efficiency of Bioethanol and Bio-ethyl tertiary butyl ether (bioETBE): Assessing the Implications of Allocation. Energy, 2006. **31**: p. 3362–3380.

[6] Demirbas, A., Biodiesel Fuels from Vegetable Oils Via Catalytic and Non-

catalytic Supercritical Alcohol Transesterifications and other Methods: a Survey. Energy Conversion and Management, 2003. **44**: p. 2093–2109.

[7] Szargut, J., D.R. Morris, and F.R. Steward, Exergy Analysis of Thermal, Chemical, and Metallurgical Processes. 1988, New York: Hemisphere. 332.

[8] Bejan, A., G. Tsatsaronis, and M. Moran, Thermal Design and Optimization. 3TH ed. 1996, New York: Jhon Wiley & Sons. 542.

[9] Ayres, R.U., Eco-thermodynamics: economics and the second law. Ecological Economics, 1998. **26**: p. 189-209.

[10] Rosen, M.A., Can Exergy help us Understand and Address Environmental Concerns? Exergy, an International Journal, 2002. **2**: p. 214-217.

[11] Talens, L., G. Villalba, and X. Gabarrell, Exergy Analysis Applied to Biodiesel Production. Resources, Conservation and Recycling, 2007. **51**: p. 397-407.

[12] Velásquez, H.I., P. Benjumea, and S. Oliveira. Exergy and Environmental Analysis of the Palm Oil Biodiesel Production Process. in *The 20th Internacional Conference in Efficiency, Cost, Optimization, Simulation and Environmental Impact of Energy Systems*. 2007. Padova, Italy.

[13] Velásquez, H.I., P. Benjumea, and S. Oliveira. Exergy Analysis Of Palm Oil Biodiesel Production By Base Catalyzed Methanolysis. in *19th International Congress of Mechanical Engineering*. 2007. Brasilia, DF.

[14] Pellegrini, L.F., J.C. Burbano, and S. Oliveira. JR. Exergy Analysis of Advanced Cogeneration Plants for Sugarcane Mills: Supercritical Steam Cycles and Biomass Integrated Gasification Combined Cycles. in *19th International Congress of Mechanical Engineering*. 2007. Brasilia.

[15] Pellegrini, L.F. and S. Oliveira. Exergy Efficiency of the Combined Sugar, Ethanol and Electricity Production and Its Dependence of the Exergy Optimization Of the Utilities Plants. in 20 TH Internacional Conference in *Efficiency, Cost, Optimization, Simulation and Environmental Impact of Energy Systems,(ECOS 2007)* 2007. Padova Italy

[16] Spano, L.A., J. Medeiros, and L. Mandels, Enzymatic Hydrolysis of Cellulosic Wastes to Glucose. Resource Recovery and Conservation, 1976. **1**: p. 279-294.

[17] Wykvan. J, P.H., Hydrolysis of Pretreated Paper Materials by Different Concentrations of Cellulase From Penicillium Funiculosum. Bioresource Technology 1999. **69**: p. 269-273.

[18] Movagharnejad, K. and M.A. Sohrabi, Model for the Rate of Enzymatic Hydrolysis of Some Cellulosic Waste Materials in Heterogeneous Solid–Liquid Systems. Biochemical Engineering Journal, 2003. **14**: p. 1-8.

[19] Jennylynd, A. and H. Byong, Glucoamylases: Microbial Sources, Industrial Applications and Molecular Biology-Review. Journal of Food Biochemistry, 1997. **21**: p. 1-52.

[20] Cao, Y. and H. Tan, Effects of Cellulase on the Modification of Cellulose. Carbohydrate Research, 2002. **337**: p. 1291-1226.

[21] Mohamed, A.F., et al., Effect of Peracetic Acid, Sodium Hydroxide and Phosphoric Acid on Cellulosic Materials as a Pretreatment for Enzymatic Hydrolysis. Enzyme and Microbial Technology, 1983. **5**: p. 421-424.

[22] David, C., R. Fornasier, and P. Thiry, Utilization of Waste Cellulose-V Comparative Effects of Different Pretreatments on the Enzymatic Hydrolysis of Cellulose and Ligno-cellulosic Substrates. European Polymer Journal, 1986. **22**: p. 515-519.

[23] Nouri, M., Catálisis ácida VS Hidrólisis Enzimática en la Industria Almidonera. Alimentación Equipos y Tecnología, 1991: p. 141-145.

[24] Camargo, C.A.c., Conservaçao de Energía na Indústria do Açúcar e Àlcool. 1990, São Paulo: Instituto de Pesquisas Tecnológicas.

[25] Klein, S.A. and F.L. Alvarado, EES – Engineering Equation Solver for Microsoft Windows Operating Systems. 12TH ed. 2007: F-Chart Software.

[26] Velásquez, H.I., Avaliação exergética e exergo-ambiental da produção de biocombustíveis in Escola Politécnica da Universidade de São Paulo. Departamento de Engenharia Mecânica. 2009,

Universidade de São Paulo: São Paulo. p. 212.

[27] Tsatsaronis, G. and M. Park, On Avoidable and Unavoidable Exergy Destructions and Investment Costs in Thermal Systems. Energy Conversion & Management, 2002. **43**: p. 1259-1270.

[28] Gong, M. and G. Wall. On Exergetics, Economics And Optimization Of Technical Processes To Meet Environmental Conditions. in TAIES'97. Thermodynamic Analysis and Improvement of Energy Systems. 1997. Beijing, China.

[29] Nebra, S.A. and M.I. Fernández-Parra. The Exergy of Sucrose-water Solution: Pproposal of a Calculation Method. in *Proceedings of the 18th International Conference on Efficiency, Cost, Optimization, Simulation, and Environmental Impact of Energy Systems* 2005. Trondheim, Norway.

[30] Modesto, M. and S.A. Nebra. A Proposal to Calculate the Exergy of Non Ideal Mixtures Ethanol-Water Using Properties of Excess. in *14th European Biomass Conference,*. 2005. Paris.

[31] Channiwala, S.A. and P.P. Parikh, A Unified Correlation for Estimating HHV of Solid, Liquid and Gaseous Fuels. Fuel, 2002. **81**: p. 1051-1063.

[32] Hugot, E., Handbook of Cane Sugar Engineering. 3TH ed. 1986, Neu York: Elsevier Science Publishers.

[33] Poling, B.E., J.M. Prausnitz, and J.P. O'Connell, The Properties of Gases and Lliquids. 5TH ed. 2000: McGraw-Hill.

[34] Reid, R.C., J.M. Prausnitz, and B.E. Poling, The Properties of Gases & Liquids. 5TH ed. 2000: McGraw-Hill.

[35] Moran, M.J. and H.N. Shapiro, Fundamentals of Engineering Thermodynamics. 5TH ed. 2006: Jhon Wiley & Songs.

[36] Smith, J., H.C. Van. N, and M.M. Abbott, Introdução à Termodinâmica da Engenharia Química. 2003, México, D.F: McGraw-Hill. 697.

[37] Ball, D.W., Fisicoquímica. 1ª ed. 2004, México: Thomson.

[38] Montes.V, N. and L. Torrez. C, Hodrólisis del Banano Verde de Rechazo, in Facultad de Minas. 2004, Universidad Nacional de Colombia- Sede Medellín: Medellín. p. 104.

[39] Hoyos, L.M. and Y.M. Pérez, Pretratamiento de Banano de Rechazo de la Zona de Urabá para la Obtención de un Jarabe Azucarado, in Facultad de Minas. 2005, Universidad Nacional de Colombia-sede Medellín: Medellín. p. 156.

[40] Bohórquez, C. and S. Herrera, Determinación de las mejores condiciones de hidrólisis del banano verde de rechazo, in Facultad de Minas. 2005, Universidad Nacional de Colombia, sede Medellín: Medellín. p. 120.

Lignin Extraction Technology Integrated in Kraft Pulp Mill: Implementation Strategy

Zoé Périn-Levasseur[a], Marzouk Benali[a] and Jean Paris[b]

[a] *Natural Resources Canada, CanmetENERGY, Industrial Systems Optimization, Varennes, Canada*
[b] *Ecole Polytechnique de Montréal, Department of Chemical Engineering, Montréal, Canada*

Abstract: Integrating biorefinery technologies in existing Kraft pulping mills could generate new revenues and improve the profitability of the pulp and paper industry by broadening its product mix to new, high value added green products. The actual benefits of such biorefinery technologies will depend largely on product opportunities, technology selection and optimization decisions, as well as on the baseline conditions for operating Kraft pulping mills. The lignin contained in the black liquor has the potential to be a major source of bio-products and bio-fuels. Acid precipitation, ultrafiltration, and electrolysis have been assessed as the key technological alternatives for lignin extraction and treatment. In view of the opportunities to improve energy efficiency, heat recovery through the heat exchanger network, and the combined heat and power generation have to be considered. The energy impacts of integrating lignin extraction technology in a Kraft pulping mill have to be discussed to establish the feasibility of a sustainable biorefinery concept.

Keywords: Biorefinery, Lignin extraction, Energy impacts, Pulp and paper, Kraft pulping,

1. Introduction

Pulp and paper (P&P) products manufacturing is an important and mature industry in Canada. Annual revenue of $36 billions positions this industry in third-place among all Canadian manufacturing industries. Canada is the second worldwide producer after the United-States. However, the emergence of new competitors with large and modern facilities and fast-growing forests, the constant increase in energy costs and the decrease demand for commodity products makes it necessary to elaborate new strategies to maintain the industry's competiveness and even increase its revenue. In this context, converting P&P mills into integrated forest biorefineries (IFBR) [1] could be the solution to restore the financial soundness of the industry and overcome the crisis. A Canadian roadmap [2] outlining the characteristics of potential pathways leading to a Canadian forest biorefinery industry has been launched to analyze and develop the Canadian concept of an IFBR. Diversifying the industry's product mix by producing bio-fuels and bio-materials could be a way to penetrate new markets while maintaining its core production of pulp and paper.

There are different pathways to produce bio-materials from lignocellulosic feedstock (LCF) materials. Figure 1 shows an overview of these pathways.

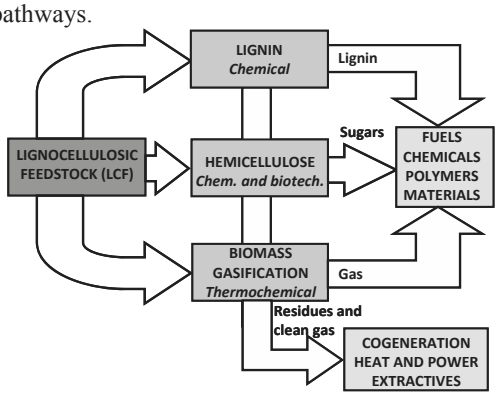

Fig. 1. Lignocellulosic feedstock biorefinery [3]

Identified products and operations can be divided into three categories:

a. Lignin extraction: lignin can be extracted from the residual black liquor from the cooking of the chips and used as a chemical feedstock to produce a variety of already known bio-materials such as adhesives, binders, surfactants or road additives but also to produce advanced chemicals (phenols and others aromatics) and new fiber materials (carbon fibers).

b. Hemicellulose extraction: hemicellulose can be recovered from wood prior to pulping or black liquor and then converted into ethanol, furfural,

xylitol, polymers and other chemical intermediates.

c. Biomass gasification: residual biomass can be gasified to produce syngas that could be further converted to produce chemicals such as methanol, liquid transportation fuel (DME: dimethyl ether) or green diesel. Electricity and steam for the process can also be produced from syngas using high-efficiency gas turbine. All these operations imply energy consumption and waste heat. The energy management should, therefore, be considered together with the biorefinery integration in a P&P mill.

The aim of this work is to explore the feasibility of lignin-based biorefineries in Kraft pulp mills based on an exhaustive literature review. Key technologies for lignin extraction and treatment have been studied. Process integration alternatives are highlighted and their consequences on the process are discussed. The possible energy impacts of integrating lignin extraction technology on a Kraft pulp mill performance are presented. A Canadian initiative evaluating the impacts and the feasibility of the implementation of biorefining technologies in Kraft mills is introduced.

2. Kraft lignin-based biorefinery

As a key component of spent liquor generated in a conventional Kraft mill, lignin offers new opportunities for process debottlenecking and biorefinery business development. Kraft process is therefore an attractive candidate for partial conversion to biorefinery while maintaining the manufacturing of its traditional core products.

2.1. The conventional Kraft process

Kraft pulping is the prevalent chemical pulping process in Canada. A simplified diagram of a conventional Kraft pulp mill with typical mill data is shown in Figure 2. Wood chips are pre-impregnated with white liquor, which is a mixture of sodium hydroxide (NaOH) and sodium sulphide (Na_2S) and enter the digester where lignin and hemicellulose are dissolved. The brown stock pulp exiting the digester is washed, bleached and dried. The remaining spent liquor, namely black liquor, contains lignin soluble fragments, carbohydrates from the breakdown of hemicellulose, sodium carbonate (Na_2CO_3), sodium sulphide and other inorganic salts. It is concentrated in the evaporators and burnt in a recovery boiler to produce steam and a mixture of inorganic salts. The smelt composed of sodium carbonate and sodium sulphide is dissolved and reacts with calcium oxide (CaO) to regenerate white liquor. Calcium oxide (quick lime) is produced by the calcination of calcium carbonate ($CaCO_3$) in the lime kiln, which is an important carbon dioxide emitter: total emission may be as high as one tonne of CO_2 for every tonne of quick lime produced.

2.2 Debottlenecking the recovery boiler

The lignin contained in the black liquor is usually burned in a recovery boiler to generate steam for the process and to recover the cooking chemicals. However, increasing production capacity is often limited by the recovery boiler which cannot easily process the extra amount of black liquor generated and often is one of the main bottlenecks in the expanding processing capacity. The recovery boiler can be upgraded to support the new load, but this is a very expensive option. Furthermore, older recovery boilers have already been upgraded to their maximum limit. A potential alternative to debottleneck the recovery boiler would be to keep the load constant and extract lignin from the surplus of black liquor generated to produce value-added products.

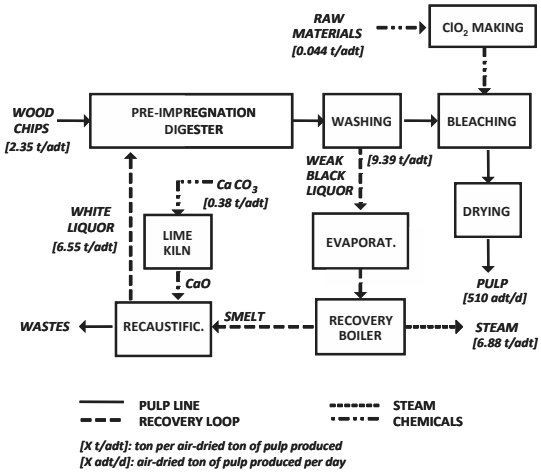

Fig. 2. Conventional Kraft pulp mill simplified process diagram

3. Lignin extraction

Several extraction techniques are described in the literature [4-8] to recover lignin from black liquor. These methods include chemical, electro-chemical and mechanical treatments. Chemical extraction processes are already implemented or at pre-

commercialization step. Electro-chemical methods, which are still in development, could represent an attractive alternative. Mechanical methods are being investigated at the laboratory level. Lignin separation processes, the product obtained, impacts on the process and cost estimates of the various lignin separation methods are described below.

3.1 Lignin separation methods

Acid precipitation (AP) consists in lignin precipitation from partially concentrated black liquor by acidification to lower a pH to about 9 using carbon dioxide. Filtration and washing of the lignin cake are done in acidic aqueous conditions using sulphuric acid (Figure 3). The lignin obtained has a high energy density, low ash content and sulphur content between 1 and 3%w/w. The commercialized version of this technology, the LignoBoost concept, is owned by Metso and has been demonstrated on a scale of 4000 t/y in a pilot plant located in Sweden. Ohman et al [9, 10] in collaboration with Innventia AB have largely documented this technology and also introduced a particularity to avoid plugging of the filter cake. In this variant, the filter cake is redispersed and pH, ionic strength and lignin solubility changes occur in the re-slurry tank rather than in the filter. The advantages of this technique are reduced filter dimensions and increased lignin purity [11].

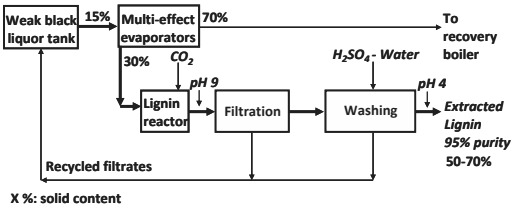

Fig. 3. General layout of the acid precipitation lignin removal process

Precipitation by electrolysis is an electro-chemical alternative to acid precipitation. Lignin reactor is replaced by an electrolytic unit. A fraction of the sodium present in the black liquor is electrolytically converted to caustic soda [7]. Lignin is precipitated and filtered from the treated liquor by acidification with sulphuric acid. The remaining sodium salts can be recycled to the recovery system or discharged as an effluent. An advantage of this process is that the sodium bound to the precipitated lignin is the only loss of reactant.

Other benefits from the electrolysis are that it produces high-quality caustic soda suitable for pulp bleaching, and hydrogen can be recovered from the electrolysis of water and then used possibly as fuel [7,12,13]. Furthermore, oxidation of the black liquor before processing is no longer necessary to prevent H_2S emissions present during CO_2 acid precipitation. Large-scale pilot installation of this process is under development.

A mechanical technique is also potentially interesting for lignin extraction. It consists in cross-flow separation by ultrafiltration and nanofiltration of weak black liquor from the digester through ceramic or polymeric membrane. The main advantage resides in the fact that the withdrawal of the liquor can be done at any location in the process, without pH or temperature adjustment [8]. Furthermore, the liquor concentration is not crucial. To complete lignin separation using ultrafiltration, black liquor is dialyzed using fresh water. The water removes 90% of any membrane-permeable species from lignin [14]. Ultrafiltration is used to obtain lignin with a narrow molecular weight distribution for manufacture of specific products [5].

3.2 Consequences of lignin separation

The main effect of lignin extraction by acid precipitation and electrolysis precipitation is an increase of the load on the black liquor evaporation plant. Lignin washing adds water to the filtrates that are recirculated in the evaporators. The steam demand is increased and the properties of the black liquor are expected to be affected. Moosavifar et al. [15] have observed that the black liquor viscosity is lower when lignin has been extracted than in the regular black liquor at the same temperature and solids content. The boiling point elevation remains sensibly constant. A lower viscosity could lead to lower investment cost since the necessary heat transfer area is smaller due to a high heat transfer coefficient.

Another important effect of lignin extraction is its capability to maintain the sodium and sulphur balance within the process. Hydrogen sulphide (H_2S) emissions need to be carefully controlled. The oxidation of sodium sulphide in the black liquor to sodium thiosulphate ($Na_2S_2O_3$) [5] and the control of the pH at 9 during precipitation can minimize H_2S emissions. The sulphur from

sulphuric acid (H_2SO_4) used for washing has to be removed as Na_2SO_4 in the recovery boiler. To compensate for the loss of sodium, additional NaOH make-up is needed [16]. The final effect to be highlighted is the reduction of steam production in the recovery boiler. The implementation of energy efficiency measures around the mill could compensate for this effect and it is discussed later.

3.3 Cost estimates

A preliminary economic assessment of the three lignin separation methods has been performed based on literature data. The most detailed and recent cost estimates are provided in [17] for the separation of lignin by ultrafiltration and nanofiltration from weak black liquor (WBL) before the evaporators and from strong or evaporated black liquor (SBL) after the evaporators. These estimates include the evaluation of the capital cost of membrane units as well as the operating costs, the membrane replacement and cleaning, and the maintenance and labour costs.

The ultrafiltration of the cooking liquor has a higher cost (88 CAD/t[1] of lignin produced) than the ultrafiltration of the evaporated liquor (49 CAD/t[1] of lignin produced) according to [17]. This is due to a poor retention of lignin and a high volume reduction. To reduce this cost, one can increase the lignin retention using a denser membrane and operate at a reduced volume. However, Cloutier et al. [13] found in laboratory tests that acid precipitation yielded lower costs and better separation than ultrafiltration. The LignoBoost process from Innventia AB gives high quality lignin at interesting investment (15 Millions CAD[1] for a plant producing 50 000 t/y) and operating costs (30-83 CAD/t[1] of lignin produced) [11]. Davy et al. [6] found that the combination of electrolysis and acid precipitation is also profitable, especially if the price of the caustic soda is high. Further investigation is required to evaluate the advantage of this combination in comparison to stand-alone acid precipitation.

The lignin extracted can be used for the production of several value-added chemicals. Berntsson et al. [18] have made a first classification of potential and existing products from lignin extracted from Kraft black liquor. Refining processes, applications and development status for each of the products are shown in Table 1. Potential products need to be evaluated in terms of critical parameters such as the yield of extraction, the evaluation of technical challenges to implement technologies, the availability of technologies for their usage and finally the market value and size. A first estimate of market prices and volumes of those value-added products has been done by [19], and carbon fibers, phenols and other aromatics were found to be the most interesting products (Table 1).

Table 1. Value-added products from lignin: available technologies, market value[1] and size [18,19]

Product (Process)	Use	Status	Market (CAD$/t)/(kt/y)
Phenols (Supercritical oxidation, catalysed hydrogenation)	Phenolic resins	Laboratory	2800 / 10700
Carbon fibres (Spinning, carbonisation, activation)	Construction, sporting goods, adsorbents, catalyst	Laboratory	26000-800000 / 27
Lignin fuel (Purification)	Fuel	Pilot plant	ND
Road additive, binder, battery additive, dispersant, plant nutrition, soil treatment (Purification, sulfonation)	Binder, dispersant, emulsifier	Commercial	470-1100/450 (USA)
Active carbon		Laboratory	ND

4. Opportunities for process integration

The integrated forest biorefinery (IFBR) is based on the existing infrastructure of pulp and paper (P&P) mills. Since biorefinery implementation would be done in a retrofit mode, a careful process system analysis needs to be performed to understand its impact on existing processes. Identifying the most profitable products and applying process integration techniques to evaluate the impact of implementing these products pathways in existing P&P mills can be an effective approach to identify promising biorefinery technologies.

[1] On February 2010 basis

Process integration tools can be applied at two levels: to decrease the chemical demand by the integration of chemical recycling loops, and to perform energy benchmarking and analysis to identify potential heat recovery options, reduce the overall energy consumption and evaluate the impact of lignin extraction on the energy profile of the whole process.

4.1 Chemical recycling loops integration

Acid precipitation technology using carbon dioxide as first precipitating agent has been identified as the most promising route for lignin extraction in terms of yield and cost. The profitability of this technique depends highly on the CO_2 cost and of energy prices. An interesting way to mitigate the CO_2 cost could be its capture from the flue gases of the recovery boilers or the lime kiln (Figure 4). For low pressure and CO_2 concentration in flue gases, the chemical absorption is a relevant separation technique and requires no design modifications of the recovery boiler [20]. Monoethanolamine (MEA) is generally used as an absorbent. The desorption of this solvent for regeneration still represents a high energy demand. The energy impacts on the system should be determined and thermal process integration should eventually be applied to generate low-pressure steam for the desorption unit [20].

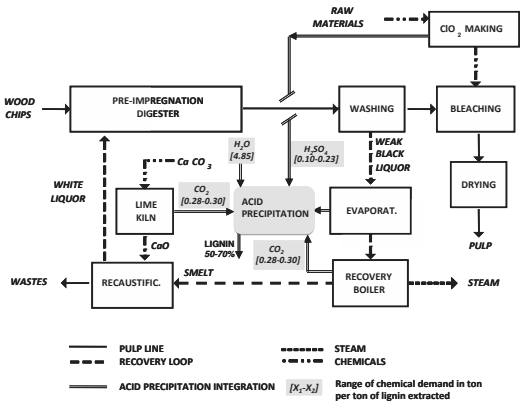

Fig. 4. Opportunities of process integration

Chlorine dioxide generator produces large quantity of waste acid (H_2SO_4). This sulphuric acid could certainly be used for washing the extracted lignin (Figure 4). Though it could also be applied as a precipitating agent instead of CO_2 its use should carefully be monitored and controlled to avoid the production of hydrogen sulphide (H_2S). In both cases, it may be necessary to sewer some Na_2SO_4 produced from the H_2SO_4 to not exceed the maximum sodium-to-sulphur ratio is not to be exceeded and to avoid a significant effect on the mill sulphur balance [6].

Table 2 shows the CO_2 and the H_2SO_4 available for a typical Kraft pulp mill producing 500 adt/d.

Table 2. Chemicals available

Chemicals	Flowrate (t/adt pulp*)
CO_2 from the recovery boiler	2.54
CO_2 from the lime kiln	1 t/t of CaO produced
H_2SO_4 from the ClO_2 generator	0.017 (50% mass)

* adt pulp: air-dried ton of pulp produced

If applied, these two measures would contribute to the abatement of the chemical demand and, in the case of CO_2 capture, reduce the GHG emissions and therefore could diminish the economical and environmental impact of introducing a lignin-based biorefinery route in a pulp and paper mill.

4.2 Potential heat recovery options and energy impact discussion

Extracting lignin from the black liquor has an important impact on the mill energy flows. Process integration tools should be used to evaluate the implementation effect of biorefinery technologies in a P&P process and should contribute to the elaboration of a trade-off between the lignin extraction to produce either value-added products or energy. The heat recovery options, the energy consequences on the system if lignin-based biorefinery is implemented, or the opportunity for cogeneration, are key factors to take into account.

As discussed earlier, the main consequence in lignin precipitation is an increased steam demand in the evaporation section to evaporate the washing water directed from the filtrates to the evaporators. A steam imbalance effect can also be expected since less black liquor is burned in the recovery boiler. Nevertheless, most commonly with an increase of production capacity, the recovery boiler cannot treat the extra amount of black liquor generated so it is often as one of the main bottlenecks of the plant expansion. The conventional approach to debottleneck the recovery boiler is to increase its capacity and produce electricity. Nevertheless, boilers are often operating at full capacity, and upgrading the existing boiler can be quite expensive. The alternative is lignin extraction combined with

internal process heat recovery scenarios. The need to analyze all these possibilities is critical.

Most of the work concerning lignin separation and recovery boiler upgrade has been done by Berntsson and coworkers from the Heat and Power technology group of Chalmers University of Technology [16,18,21,22]. These studies led to two conclusions:

a. Process integration measures for steam saving have to be combined with lignin separation to be economically interesting under specific price conditions.

b. The lignin and electricity prices are the two decision parameters for evaluating the profitability of lignin extraction.

For a lignin price of 21 CAD/MWh [2], lignin extraction was found to be an economically interesting alternative to debottleneck the recovery boiler. For high electricity price (superior to 46 CAD/MWh[2]) and a long-term investment strategy, upgrading the boiler and combined heat and power production would give a higher profitability.

5. Canadian lignin-based biorefinery

A Canadian initiative under the *BioKrEn* project [23] carried out in collaboration with Natural Resources Canada (NRCan) research program on forest biorefinery, evaluates the impacts and the feasibility of the implementation of biorefining technologies in Kraft mills.

The objective of this project is to develop and demonstrate a methodology and criteria to evaluate the feasibility of bioenergy options for Canadian Kraft processes, and to propose optimized process designs that best integrate biorefining into existing mills. The implications of implementing biorefinery technologies in existing Canadian Kraft mills which have been selected as representative of a large spectrum of operating conditions and constraints are listed. The state-of-the-art simulation and systems engineering tools are used to optimize the proposed options in terms of their effect on the mills energy and water balances, on atmospheric emissions, and on the overall process economics as well as to compare them with the optimized base-cases for these mills. The results will be provided into guidelines facilitating better a-priori assessments of future biorefinery proposals.

The implementation of a lignin-based biorefinery is studied within this project. Acid precipitation has been selected in respect to the state of development, the market trends and *BioKrEn* partners interests. A process flowsheet diagram has been developed based on literature data and partners contributions. A simulation is in progress but it faces several challenges:

a. Modelling of non-conventional substances such as black liquor or lignin

b. Elaboration of real thermodynamic reactions models for chemical transformation processes such as electrolysis, acid precipitation or even lignin combustion in the recovery boiler

c. Finding model reactions for the evaluation of the real composition of electrolytes, including pH calculation.

5.1 Chemical reaction model

A method based on stoichiometry to model and analyze the integration of lignin precipitation to a Kraft process has been developed in collaboration with the *Laboratoire des technologies de l'énergie* of Hydro-Québec. Extraction of lignin from black liquor involves non-conventional solids (NCS) characterized by their composition $C_\alpha H_\beta O_\gamma S_\psi Na_\varepsilon$ where α, β, Y, Ψ and ε are known (M fixed at 100 kg/kmole) (Table 3).

Table 3. Non-conventional solids characterization

NCS	Definition	Characterization*	h_o^f**	HHV**
BLS	Black liquor solids	$C_{2.92}H_5O_{2.19}S_{0.16}Na_{0.87}$	-677	14480
BLSO	Black liquor organic solids	$C_{3.91}H_{6.84}O_{2.11}S_{0.08}Na_{0.43}$	-383	21060
BLSO1	BLSO remaining after precipitation	$C_{2.88}H_{11.38}O_{3.2}S_{0.07}Na_{0.02}$	-395	20718
Lignin	Lignin after precipitation step	$C_{5.19}H_{5.5}O_{1.7}S_{0.094}Na_{0.09}$	-205	25305

* Derived from the literature or chemical analysis

** Enthalpy of formation is calculated with Eq (1) in MJ/kmol, higher heating value (HHV) is in kJ/kg

The enthalpy of formation ((ΔH_f) is derived from the heat of combustion (ΔH_c) as shown in (1). The heat of combustion corresponds to the higher heating value (HHV) of each NCS. The HHV can be found in the literature or calculated from its elemental composition using Milne formula[3].

[2] On February 2010 basis

[3] HHV_{Milne} =0.341C+1.322H-0.12H-0.12N+0.0686S-0.0153ash

$$C_\alpha H_\beta O_\gamma S_\psi Na_\varepsilon + xO_2 \rightarrow yCO_2 + \beta/2H_2O + Na_2SO_4 + zNa_2CO_3 \quad (1)$$

$$h_o^f = -\Delta Hc + yh_{o\,CO_2}^f + \beta/2h_{o\,H_2O}^f + \psi h_{o\,Na_2SO_4}^f + zh_{o\,Na_2CO_3}^f$$

For the lignin extraction, the following reactions are considered in the model:

(2) Acid precipitation with CO_2

$$BLSO \rightarrow LIGNIN + BLSO1 + NaOH + H_2O$$
$$Na_2S + 2H_2O \rightarrow 2NaOH + H_2S$$
$$CO_2 + 2NaOH \rightarrow Na_2CO_3 + H_2O$$
$$CO_2 + Na_2CO_3 + H_2O \rightarrow 2NaHCO_3$$

(3) Acid washing

$$LIGNIN + 0.0517H_2SO_4 \rightarrow LIGNIN^* + 0.0412Na_2SO_4 + 0.0490H_2O$$

where LIGNIN*: 95% pure lignin

The reactions for the evaluation of the real composition of electrolytes and pH calculation are also modelled.

5.2 Model of lignin acid precipitation

The lignin-based biorefinery model is simulated with Aspen Plus®. A sensibility analysis is performed to determine the effect of black liquor composition, pH, ionic strengths, lignin molecular mass, and concentration variations on purity of lignin and its throughput. The collected information will be used for modules development and/or existing modules modification of biorefinery units in CADSIM Plus®, a pulp and paper simulation software. The impact of the integration of the biorefinery options, including the lignin-based biorefinery will be also evaluated on the overall mill energy consumption. Energy efficiency enhancement measures and implementation of scenarios will be developed.

Concluding remarks

Converting pulp and paper mills into integrated forest biorefineries is one of the most suitable technology options to overcome the long-term crisis of the pulp and paper industry in industrially mature countries. In order to improve energy efficiency and increase productivity, Kraft pulping mills must optimize their carbon value chain: increasing the production forces the recovery boiler to exceed its full capacity of black liquor burned and create a major bottleneck. The solution consists in keeping the recovery boiler load constant and extracts lignin contained in the black liquor to produce bio-products and bio-fuels. Several alternatives for lignin extraction and treatment have been proposed and evaluated: acid precipitation has been found as an economic and available process for the extraction. However, electrolysis of the black liquor has also economic and technical advantages that should be further studied at large scale. The implementation of lignin extraction has been discussed in terms of system and energy impacts. Implementation strategy measures can be derived and guidelines for efficient integration of lignin-based biorefinery are proposed:

- The integration of the chemical recycling loops could have a significant impact on the process energy and economic balances, and therefore it influences the choice of the biorefinery integration strategies.

- The application of process integration techniques is essential to study the trade-off between conversion of lignocellulosic materials into bio-materials and energy.

- It is important to consider simultaneously the heat recovery through heat exchangers and the combined heat and power production.

- Coupling conversion of bio-material and energy efficiency analysis is essential.

- Selling prices of lignin and power are of primary importance to evaluate the profitability of lignin extraction versus the boiler upgrade solution.

The ultimate goal of NRCan program is to bring the forest products industry to embrace the concept of the biorefinery and to become a producer of bioenergy and biochemicals. This transformation is a paradigm shift in which the market will be the driver and every element of the chain can contribute to the overall value.

References

[1] Van Heiningen, A., 2006, Converting a kraft pulp mill into an integrated forest biorefinery. Pulp and Paper Canada, 107(6), pp.38–43.

[2] Browne, T. et al., 2006, Towards a technology roadmap for Canadian forest biorefineries. Technical report, ISBN 0-662-49344-3, Industry Canada.

[3] Kamm, B., Gruber, P. and Kamm, M., 2007, Biorefineries – Industrial processes and products, in Ullmans Encyclopedia. Wiley-VCH, Weinheim.

[4] Alen, A., Patja, P. and Sjostrom, J., 1979, Carbon dioxide precipitation of lignin for pine kraft black liquor. Tappi Journal, 62(11), pp.108–110.

[5] Loutfi, H., Blackwell, B. and Uloth, V., 1991, Lignin recovery from kraft black liquor: Preliminary process design. Tappi Journal, 74(1), pp.203–210.

[6] Davy, M., Uloth, V. and Cloutier, J., 1998, Economic evaluation of black liquor treatment processes for incremental kraft pulp production. Pulp and Paper Canada, 99(2), pp.35–39.

[7] Cloutier, J. N., Azarniouch, M. K. and Callender, D., 1993, Electrolysis of weak black liquor part I: laboratory study. Journal of Pulp and Paper Science, 19(6), pp.244–248.

[8] Jonsson, A.-S., Nordin, A.-K. and Wallberg, O., 2008, Concentration and purification of lignin in hardwood kraft pulping liquor by ultrafiltration and nanofiltration. Chemical Engineering Research and Design, 86(11), pp.1271–1280.

[9] Ohman, F., 2006, Precipitation and separation of lignin from kraft black liquor. PhD thesis, Departement of Chemical and Biological Engineering, Chalmers University of Technology, Gothenburg, Sweden.

[10] Ohman, F. , Wallmo, H. and Theliander, H., 2007, An improved method for washing lignin precipitated from kraft black liquor - the key to a new biofuel. Filtration, 7(4), pp.309–315.

[11] Tomani, P., 2009, The LignoBoost process. In 2nd Nordic Wood Biorefinery Conference - NWBC2009, Finland.

[12] Cloutier, J. N., Azarniouch, M. K. and Callender, D., 1995, Electrolysis of weak black liquor part II: Effect of process parameters on the energy efficiency of the electrolytic cell. Journal of Applied Electrochemistry, 25(5), pp.472–478.

[13] Cloutier, J. N., Azarniouch, M. K. and Callender, D., 1994, Electrolysis of weak black liquor. part III. continuous operation test and system design considerations. Pulp and Paper Canada, 95(5), pp.68–72.

[14] Uloth, V. and Wearing, T., 1989, Kraft lignin recovery: acid precipitation versus ultrafiltration. part I: Laboratory test results. Pulp and Paper Canada, 90(9), pp.T310–T314.

[15] Moosavifar, A., Sedin, P., and Theliander, H.P, 2006, Viscosity and boiling point elevation of black liquor: consequences when lignin is extracted from the black liquor, Nordic Pulp and Paper Research Journal, (21) 2, pp.180–187.

[16] Olsson, M., Axelsson, E., and Berntsson, T., 2006, Exporting lignin or power from heat integrated kraft pulp mills: A techno-economic comparison using model mills. Nordic Pulp and Paper Research Journal, 21(4), pp.476–484.

[17] Jonsson, A.S., and Wallberg, O., 2009, Cost estimates of kraft lignin recovery by ultrafiltration. Desalination, 237(1-3), pp.254–267.

[18] Berntsson, T., et al., 2006, Lindgren. Swedish Pulp Mill Biorefineries – A vision of future possibilities, Report commissioned by the Swedish Energy Agency.

[19] Lindgren, K., 2009, Potential lignin applications beyond energy. In 2nd Nordic Wood Biorefinery Conference - NWBC2009, Finland.

[20] Hektor, E., and Berntsson, T., 2007, Future CO2 removal from pulp mills – Process integration consequences. Energy conversion and management, 48, pp.3025-3033.

[21] Laaksometsa, C, et al., 2009, Energy savings combined with lignin extraction for production increase: case study at a eucalyptus mill in Portugal. Clean TEchn Environ Policu, 11,pp.77-82.

[22] Axelsson, E., Olsson, M., and Berntsson, T., 2006, Increased capacity in kraft pulp mills: lignin separation and reduced steam demand compared with recovery boiler upgrade. Nordic Pulp and Paper Research Journal, 21(4), pp.108

[23] BioKrEn Project, 2008, Implementation of biorefinering technologies in Kraft mills: impact assessment and feasibility, Collaborative Research and Development Grant, NSERC ID 90335267.

Acknowledgments: The authors acknowledge the financial support provided by the Program on Energy Research and Development of Natural Resources Canada.

Efficient Energy Conversion and Biorefinery Implementation in a Chemical Pulp Mill

Zoé Périn-Levasseur [a], *François Maréchal* [b] *and Jean Paris* [c]

[a] *Natural Resources Canada, CanmetENERGY, Industrial Systems Optimization, Varennes, Canada*
[b] *Ecole Polytechnique Fédérale de Lausanne, Industrial Energy Systems Laboratory, Lausanne, Switzerland*
[c] *Ecole Polytechnique de Montréal, Department of Chemical Engineering, Montréal,Canada*

Abstract: The importance of energy costs is significative on the global economy of a pulp and paper process. From the energy prices rising constantly and the introduction of new environmental restrictions in line with the Kyoto protocol has emerged a growing awareness that there are potentially large energy cost reductions to be obtained by improving the energy efficiency of existing pulp and paper operations. Diversifying the industry's product mix by producing bio-energy and bio-materials could be a way to penetrate new markets while maintaining its core production of pulp and paper. The objective of this work is to illustrate the trade-off between conversion of materials and of energy and shows the importance of considering simultaneously the heat recovery through heat exchangers and the combined heat and power production. Process integration techniques are applied to study a mill which produces pulp and three additional by-products: bioethanol, lignosulfonates and yeast. The process is divided in production sub-systems with flow diagrams and flow rates dependent on the main product being manufactured. Mass balance constraints are introduced in the formulation of the model of the flow distribution between sub-systems and the hot and cold streams are computed for each section and integrated at the mill scale level. The optimal integration of a combined heat and power production unit is determined taking into account the simultaneous maximization of process internal heat recovery. Biorefinery strategies are evaluated in a thermo-economic perspective. Trends for biorefinery strategies in the pulp and paper industry are presented.

Keywords: Energy conversion, Biorefinery, Pulp and paper, Energy efficiency, Energy savings

1. Introduction

Energy cost is a significant factor on the overall economics of a pulp and paper (P&P) process. Increasing energy prices and restrictive environmental regulations have motivated the P&P industry to seek for energy cost reductions improving the energy efficiency of its operations. Another concern of the P&P industry is the competition of the resources utilisation: wood can be used as an energy resource or to produce bio-materials as well as the raw material to produce P&P. The retrofit implementation of biorefining technologies in Kraft P&P mills can be a promising solution to revitalize the industry by producing biofuels and value-added bio-materials while maintaining its core production of pulp and paper [1].

There are different pathways to produce bio-materials from lignocellulosic feedstocks (LCF). Lignin can be extracted from the residual black liquor and burned to produce heat, cleaned to be sold directly or even be gasified to produce gas and electricity. Lignin can also be used as a chemical feedstock to produce a variety of already known bio-materials such as adhesives, binders, surfactants or road additives but also to produce advanced chemicals (phenols and others aromatics) and new fiber materials (carbon fibers). Bioethanol, furfural, xylitol and other chemical intermediates can be produced from the hemicellulose extraction from wood prior to pulping or from black liquor. Residual biomass can be gasified to produce syngas that could be transformed to produce chemicals and green diesel. Producing bio-materials implies energy consumption and production of waste heat. The energy management cannot be dissociated from the biorefinery integration in a P&P mill: both energy and mass integration must be considered. The aim of this work is to present a study that couples an energy efficiency analysis methodology to a biorefinery integration. We propose to demonstrate the application of process integration techniques to

Corresponding author: Zoé Périn-Levasseur, Email: zoe.perin-levasseur@nrcan.gc.ca

study the trade-off between conversion of lignocellulosic materials into bio-materials and energy.

2. Energy enhancement methodology

Reducing energy consumption in the P&P industry can lead to considerable cost savings. The three main points to consider when implementing an energy efficiency program in a mill are the reduction of the energy requirement, the energy recovery and the efficient integration of the energy conversion system. This analysis leads to the definition of an energy efficiency road map with the evaluation of the energy savings and the related investment costs. Due to the high level of integration of a P&P process, no single method can cover the spectrum of tasks to be accomplished; a spectrum of computer-aided process engineering tools must be used. Mill-wide process simulation combined with the application of process integration tools, such as pinch analysis, is the key for reaching the energy savings target. A comprehensive computer-aided methodology to analyse the integration of utility systems and energy conversion technologies has been developed (Figure 1). Its goal is the identification of energy savings options by means of process integration and thermo-economic optimisation techniques.

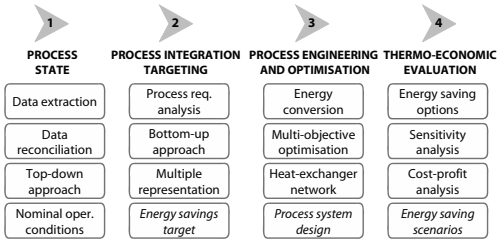

Figure 1: Four-phase method

The methodology starts with the establishment of a reconciled model of a complex pulping facility where utility and process measurements are studied simultaneously. Derived operating nominal conditions are validated through a sensitivity analysis. The resulting base case model is considered to be representative of the original process and constitutes the basis of the process energy integration definition problem.

The core of the methodology consists in the application of two successive approaches: the top-down and the bottom-up approach. The top-down approach allows to identify which sub-systems of the facility consume more energy and could eventually lead to large energy savings. Conversion technologies used to produce utilities and their distribution to the process are also identified.

The bottom-up approach benefits from the results of the top-down approach in order to evaluate the energy saving potentials. Systematic definition of the process heat transfer requirement defined as hot and cold streams is obtained according to different heat-temperature profiles. The exergy concept is employed to explain how using different heat-temperature profiles of the same energy requirement is changing the perspective of the energy use in the facility and therefore make possible the identification of energy saving opportunities with different levels of process modifications. The development of scenarios using systematically all energy requirement definitions is done and allows the elaboration of a decision support tool that point out the critical process modifications necessary to achieve interesting energy savings.

3. Energy savings opportunities

3.1. Process integration for energy optimization

Process integration techniques have been applied widely in the P&P industry. Pinch analysis [2] is a process integration technique used to identify the minimum energy consumption of a process and make the design of heat exchanger network to recover energy by heat exchange, following technical and economical constraints. It is a mature methodology that has been applied in several industries, including the P&P industry [3], [4], [5] and [6]. However, the original method only concerns the reduction of the heat requirement, rather than reducing the energy bill of the whole process [7]. Various additions, such as integration of turbines and heat pumps [8, 9] and systematic optimization algorithms, have enriched the pinch analysis methodology. Furthermore, a method linking the optimization techniques and their corresponding graphic representation was developed [10, 11, 12, 13].

Pinch analysis aims at identifying the heat recovery between hot and cold streams in a system. It is based on the assumption of a minimum approach temperature difference in a counter-current heat exchanger. The pinch analysis starts with an inventory of the hot and cold streams of the process. The streams are then integrated to build hot and cold composite

curves. Performing counter-current heat exchanges allows one to compute the maximum possible heat recovery between hot and cold streams in the process and by energy balance obtain the minimum energy requirement [14].

3.2. Case study

The calcium bisulfite pulp mill considered in the study produces cellulose as a main product. This cellulose is used for pulp making, as chemical intermediate and as plastic moulding. The mill functions also as a biorefinery unit which manufactures yeast, ethanol and lignosulfonates as well as fuel for the main mill boiler. Figure 2 shows a simplified diagram of the mill and illustrates the treatment of the waste liquor from the pulping process which is used to produced bio-materials as discussed later.

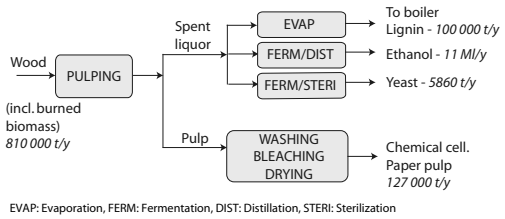

Figure 2: Simplified process diagram

The composite and Grand composite curves of the process are illustrated in Figure 3. Table 1 gives the heating and cooling minimum energy requirement and the pinch point location of the endothermic subsystems of the plant. The pinch point is created by a hot stream corresponding to the condensation of the water evaporated during pulp drying. One can notice another area of low net heat flow around 52 ^oC (created by the condensation until ambient temperature of the water evaporated in multi-effect evaporators). This is called a *near-pinch* and should be taken into account during the design of the heat exchanger network since it represents an additional point where network design is highly constrained and where pinch rules should eventually be applied again [15].

Table 1: Heating and cooling MER requirement and pinch point location

Heating MER (Q^+)	37 953 kW	1 189 490 GJ/y
Cooling MER (Q^-)	37 326 kW	1 160 988 GJ/y
Pinch point	99.6 ^oC	-

The calculation of the minimum energy requirement assumes that the hot and cold utility have the appro-

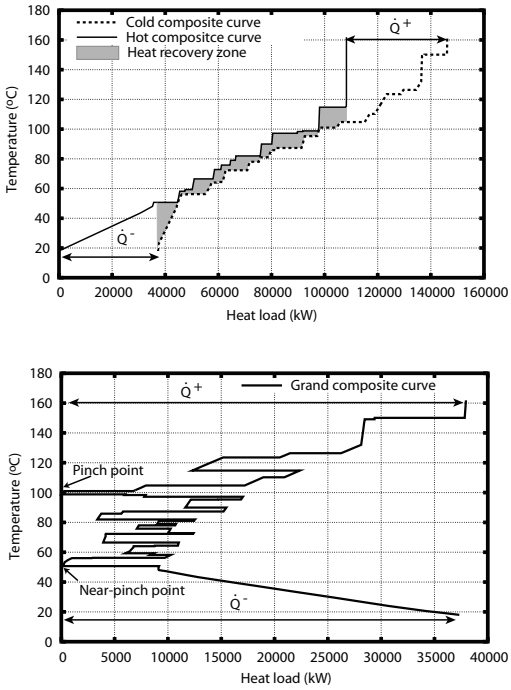

Figure 3: 3(a) Process composite curves, 3(b) Grand composite curve

priate temperature levels to supply the energy of the process. In reality, the energy requirement is satisfied by converting, in energy conversion units, energy resources into useful energy that will be delivered to the process by means of energy distribution system and of heat exchangers [14]. The temperature, pressure and flowrate of utility streams resulting from conversion of resources are chosen in order to minimise the cost to satisfy the process energy requirement. The quantification of the utilities necessary to satisfy the minimum energy requirement computed is done calculating the possible electricity production through cogeneration (combined heat and power options) and the energy consumed (fuel and steam import).

Energy savings cases can been evaluated by key indicators such as the energy consumed, the electricity produced and the total costs. The total costs are evaluated in term of utilities consumption and heat exchanger investment. Four cases can be examined: (a) the actual case, (b) the actual case if sensible heat losses from the flue gases of the boilers are recovered, (c) the improvement of the utility system with limited modifications on the process and (d) the improvement of the process if the real heat transfer de-

mand in each process unit operation is considered. Table 2 summarized all key indicators for the four cases.

Table 2: Key indicators for energy savings opportunities

Cases		**(a)***	**(b)**	**(c)**	**(d)**
Energy	(kW)	87649	77506	50140	37953
Elect.	(kW)	2899	2899	9438	9485
Oper. cost	(CHF/y)	22157	15158	11844	9454
Inv. cost	(CHF/y)	5841	5958	6051	6301
Total cost	(CHF/y)	22157	15158	17895	15755
Benefice**	(%)	-	25	36	44

*(a): Actual case, (b): Actual case if flue gases recovered (c): Utility modifications, (d): Process modifications
** Compared to (a): Actual case

Energy savings potential can be deduced from the present analysis. Sensible heat of the boilers combustion gases can be recovered and lead to a potential energy saving of 10 143 kW. This corresponds to an energy saving of 12% if compared to the actual steam consumption of the facility. The condensate recovery can be increased. The energy saving corresponds to 326 kJ per extra kg of condensate returned to the boiler and additional saving would be obtained from the decrease of the demineralised water production. The implementation in the base case of those good energy practice measures are characterised by minimal changes to equipment and moderate investments. On the other hand, high energy savings imply advanced and maximized energy integration characterized by major process configuration changes, such as heat exchanges between condensates and incoming liquor in evaporators and heat pumping integration in evaporation section.

4. Biorefinery implementation

The implementation of a biorefinery in a mill modifies its energy profile and influences the choice of biorefinery integration strategies. In the present case study, waste liquor can be either evaporated and burned in a recovery boiler to produce steam, sold as lignosulfonates, fermented and distilled to produce ethanol or fermented, evaporated and sterilized to produce yeast. Both energy and mass integration must be considered. For example, when lignosulfonates are produced, less sulfur is recycled with the waste liquor and additional sulfur must be purchased. This has an effect on the cost of the products but also on the energy efficiency.

Table 3 shows the distribution of the waste liquor burned in the recovery boiler and used to produce the by-products and the maximum production capacity of each unit. To determine a trade-off between conversion of material and minimization of energy consumption, five scenarios have been developed.

Table 3: Actual production and maximum production capacity of the waste liquor usage per ton of cellulose produced (tcp)

Usage	**Production** (t/tcp)	**Max capacity** (t/tcp)
Burned	0.959	1.014
Lignosulfonates	0.738	0.937
Ethanol	0.0738	0.103
Yeast	0.0464	0.0546

- The *nominal* scenario (**1**) or the *reference case*
- The *integrated* scenario (**2**) or the reference case after heat recovery and CHP energy integration
- The *net profit maximization* scenario (**3**) gives the optimal use of the waste liquor from an energy point of view to maximize the net profit
- The *ethanol* scenario evaluates the energy recovery and the efficient integration of the energy conversion system with maximum production capacity (**4a**) and without (**4b**) ethanol production.
- The *maximum waste liquor combustion* scenario (**5**) is defined by the maximum waste liquor burning rate achievable in the recovery boiler. The scenario that would completely eliminate the recovery boiler (no waste liquor burned) is discarded since the actual installations cannot support the treatment of the liquor supplement that may result.

A systematic definition of the process heat transfer requirement defined as hot and cold streams in the process has been developed in order to compute the minimum energy requirement for all scenarios. For the steam consumption sections, the process requirements have been defined by means of the multiple representations concept [7]: the energy requirement defined by the heat-temperature profiles of each process unit is systematically analysed at three levels: the *thermodynamic requirement* or the heat transfer required by the process

unit, the *technological requirement* or the way they are satisfied by the technology that implements the operation and finally the *utility requirement* or the way they consume the distributed energy. Defining a given process unit requirement from the different temperature-enthalpy profiles helps to identify possible energy savings with different levels of process modifications. The analysis is completed by identifying the energy that could be recovered from waste streams and by heat exchanged between mill sections.

The scenarios were evaluated using all representations. The utility representation **[U]** with limited modifications of the process units and the thermodynamic representation **[R]** including a detailed analysis of the possible heat exchanges are presented.

4.1. Mass and economic models

Using flowsheeting models, the heat requirements in the different by-product lines were computed as a function of the by-products flowrates. Table 4 shows the by-product distribution for the five scenarios. This was done by taking into account the maximum production capacity of each by-product, as defined in Table 3. The following mass balance constraints were introduced to model the flow distribution of the total waste liquor available ($\dot{m}_{wlt}$) to be burned in the recovery boiler ($\dot{m}_b$), transformed in lignosulfonates ($\dot{m}_l$), ethanol ($\dot{m}_e$) or yeast ($\dot{m}_y$). A second equation gives the amount of sulfur required by the process to produce the cooking acid ($\dot{m}_{rp}$) as a function of the sulfur recovered from burning the waste liquor ($\dot{m}_{sb}$) and of the sulfur entering the sulfur boiler ($\dot{m}_{seb}$). The biorefinery mass balances are added as linear constraints in the process integration model that is solved by MILP [7].

Table 4: By-products repartition per ton of cellulose produced (t/tcp)

Sc.	Burned (t/tcp)	Ligsulf. (t/tcp)	Ethanol (t/tcp)	Yeast (t/tcp)
1*	0.959	0.937	0.0738	0.0464
2	0.959	0.937	0.0738	0.0464
3	0.641	1.011	0.1033	0.0547
4a	0.641	1.011	**0.1033**	0.0547
4b	0.753	1.011	**0**	0.0547
5	**1.107**	0.551	0.1033	0.0547

*Identification code is also used for Table 5 and Figure 4

In order to compare and evaluate the relevance of the proposed scenarios, the operating cost was computed by Equation 3, as a function of the mass flowrate ($\dot{m}$), electricity power ($\dot{E}$) and cost (C) of imported steam (s), purchased fuel (f) and electricity (e) for an operating time (*time*) of 8000 h/y from which the revenue from selling the by-products is deducted.

$$\dot{m}_b + \dot{m}_l + \dot{m}_e + \dot{m}_y = \dot{m}_{wlt} \quad (1)$$

$$\dot{m}_{sb} + \dot{m}_{seb} = \dot{m}_{rp} \quad (2)$$

$$C_{op} = (\dot{m}_s C_s + \dot{m}_f C_f + \dot{E} C_e) * time \quad (3)$$

Three performance indicators were evaluated:

- *Energy* is the savings percentage achievable on the energy bill in comparison to the reference case
- *By-product* is the profit percentage realized if all bio-materials are sold at the market price in comparison to the reference case
- *Net profit* is the difference between the energy and by-product percentages.

4.2. Results

Energy, by-products and net profit percentages have been evaluated and compared to the reference case (**1**) for all scenarios (**2,3,4a,4b,5**) in both energy requirement representations (**[R],[U]**) (Table 5). For example, the integrated scenario in thermodynamic representation (**2[R]**) shows an energy saving of 52% on the energy bill in comparison to the reference case. The net profit percentage is illustrated in Figure 4.

*Table 5: Energy, by-products and net profit difference in comparison to the reference case (**1**)*

Sc.	Energy (%)	By-products (%)	Net profit (%)
1	reference	reference	reference
2[R]	52 +++*	0	29 ++
2[U]	31 ++	0	17 +
3[R]	39 ++	37 ++	80 +++
3[U]	17 +	37 ++	67 +++
4a[R]	39 ++	37 ++	80 +++
4a[U]	17 +	37 ++	67 +++
4b[R]	48 +++	10 +	42 ++
4b[U]	26 +	10 +	30 ++
5[R]	54 +++	-11 -	13 +
5[U]	35 ++	-11 -	2

*Effect: +++ very high, ++ high, + moderate, - negative

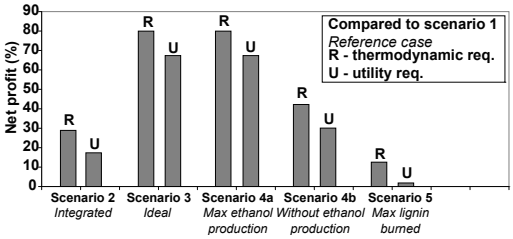

*Figure 4: Net profit difference for each scenario in comparison to the reference case (**1**)*

There is a clear biorefinery integration strategy emerging from the results: the mill should push the ethanol production to its maximum. The *ideal* scenario (**3**) and the *maximum ethanol* production scenario (**4a**) show the best net profit (67% for **[U]** representation, i.e limited modifications of the process units)). The scenario *without ethanol* production (**4b**) is less advantageous (30% for **[U]** representation) but still better than the reference case or the *integrated* scenario (**2**)(17% for **[U]** representation). Finally, burning the maximum waste liquor that the recovery boiler can support (**5**) is not a judicious strategy, since it gives the lowest net profit percentage of all the scenarios (2% for **[U]** representation).

The analysis of the minimum energy requirement of the process computed for the different requirement representations (**[R], [U]**) provides other interesting results. Using heat cascade MILP models, the energy savings through heat recovery within and between sections have been quantified in terms of fuel consumption and optimal combined heat and power production. The energy saving and net profit percentages are always higher in the **[R]** representation than the **[U]** representation for all the scenarios. It should be note that switching from utility to thermodynamic representation requires equipment modifications and investment. Therefore a systematic analysis of the required modifications has been done to identify the configuration that would have the higher impact on the energy requirement.

5. Conclusions

The goal of this work was to couple conversion of bio-materials and energy efficiency analysis. A simple methodology to model the integration of biorefinery concepts in a pulping process has been shown and integrates heat recovery potential of the pulping process as well as heat and mass integration of the biorefining processes. The importance of considering simultaneously the heat recovery in heat exchangers and the combined heat and power production is also shown.

An analysis of the energy/biorefining products trade-off has been done. The implementation of biorefinery has been discussed in terms of system and energy impacts. Trends for biorefinery strategies in the P&P industry are introduced:

- Increased heat recovery potential leads to higher energy savings
- The cost of energy penalty is compensated by the increase income from selling a value-added bio-product, in this case ethanol
- Burning additional liquor reduces bio-products production and therefore net profit despite the reduction of the energy bill
- In the present market conditions, burning waste liquor is less attractive than producing bio-products

This study emphasizes that the efficient energy conversion is crucial for the biorefinery implementation in a chemical pulp mill.

References

[1] A. Van Heiningen. Converting a kraft pulp mill into an integrated forest biorefinery. *Pulp and Paper Canada*, 107(6):38–43, 2006.

[2] B. Linnhoff, D.W. Townsend, and D. Boland. *User guide on process integration for the efficient use of energy*. IChemE, Rugby, UK, 1982.

[3] C. Bengtsson, R. Nordman, and T. Berntsson. Utilization of excess heat in the pulp and paper industry - a case study of technical and economic opportunities. *Applied Thermal Engineering*, 22(9):1069–1081, 2002.

[4] J. Labidi, G. Noel, M. Perrier, and J. Paris. Analyse des procédés et optimisation énergétique - chap. iii dans réduction des coûts énergétiques dans l'industrie des pâtes et papiers. Technical report, 1999.

[5] G. Noel. Pinch technology study at the donohue clermont newsprint mill. *Pulp and Paper Canada*, 96(7):38–41, 1998.

[6] U. Wising, T. Berntsson, and P. Stuart. The potential for energy savings when reducing the water consumption in a kraft pulp mill. *Applied Thermal Engineering*, 25(7 SPEC. ISS.):1057, 2005.

[7] D. Brown, F. Maréchal, and J. Paris. A dual representation for targeting process retrofit, application to a pulp and paper process. *Applied Thermal Engineering*, 25(7 SPEC. ISS.):1067–1082, 2005.

[8] D.W. Townsend and B. Linhoff. Heat and power networks in process design. part 1. criteria for placement of heat engines and heat pumps in the process networks. *AiChE*, 29(5):742–748, 1983.

[9] D.W. Townsend and B. Linhoff. Heat and power networks in process design. part 2. design procedure for equipment selection and process matching. *AiChE*, 29(5):748–771, 1983.

[10] F. Maréchal and B. Kalitventzeff. Identify the optimal pressure levels in steam networks using integrated combined heat and power method. *Chem. Eng. Sci.*, 52(17):2977–2989, 1996.

[11] F. Maréchal and B. Kalitventzeff. Targeting the minimum cost of energy requirements: A new graphical technique for evaluating the integration of utility systems. *Computers and Chemical Engineering*, 20(SUPPL.1), 1996.

[12] F. Maréchal and B. Kalitventzeff. Energy integration of industrial sites: Tools, methodology and application. *Applied Thermal Engineering*, 18(11):921–933, 1998.

[13] F. Maréchal and B. Kalitventzeff. Process integration: Selection of the optimal utility system. *Computers and Chemical Engineering*, 22(SUPPL.1), 1998.

[14] F. Maréchal. *Improving process performances using pinch analysis, chapter 3.19.1.8 - Encyclopedia of Life Support Systems*. Ed. Christos Frangopoulos and Georges Tsatsaronis, EOLSS Publishers Co Ltd., 2008.

[15] Ian.C. Kemp. *Pinch analysis and process integration: a user guide on process integration for the efficient use of energy*. Second Edition, Elsevier, Butterworth-Heinemann, UK, 2007.

Acknowledgments: This work was made possible by a grant from the Swiss Federal Office of Energy (SFOE) which is gratefully acknowledged. The authors acknowledge the support provided by the Program on Energy Research and Development of Natural Ressources Canada.

Optimal Process Design of Hydrothermal SNG Production from Waste Biomass

Martin Gassner [a], *Frédéric Vogel* [b] *and François Maréchal* [a]

[a] *Laboratory for Industrial Energy Systems, Ecole Polytechnique Fédérale de Lausanne, Switzerland*
[b] *Laboratory for Bioenergy and Catalysis, Paul Scherrer Institut, Villigen, Switzerland*

Abstract: Hydrothermal gasification of biomass in supercritical water is one of the rare pathways that potentially allows for a complete conversion of wet waste biomass into Synthetic Natural Gas (SNG). This paper summarises an extensive process design study and discusses some key aspects of the process integration and, in particular, the influence of the feedstock on the optimal process design and its performances. It thereby demonstrates that the process design and performance is not only influenced by available technology, catalyst deactivation issues and scale, but also the characteristics of the processed substrate.

Keywords: biofuels, hydrothermal gasification, process design, process integration, optimisation

1. Introduction

Conventional biomass conversion technologies for the production of fuel and power require relatively dry and clean feedstock and thus suffer from increasing competition for a relatively scarce resource. Hydrothermal gasification of biomass in supercritical water is a promising process alternative to produce synthetic natural gas (SNG) since it relaxes this requirement and grants access to a large range of low quality feedstocks such as wet lignocellulosic biomass and biomass wastes that are difficult to valorise by other means and thus relatively cheap.

Several authors, for example [1–3], have reviewed process fundamentals, chemistry and catalysis for hydrothermal gasification while mainly focussing on the pathway to hydrogen. The production of methane has been experimentally demonstrated in a batch reactor from wood substrate [4, 5], and technology and process development for a continuous process is under way [6, 7]. Most of these studies discuss general process principles, present laboratory and pilot units or focus on detailed experimental investigations. To our knowledge, only Luterbacher et al. [6] has presented a process design model that quantitatively takes energy integration and recovery into account. At the time of their developments, only limited insight into some process steps was yet available. Energy integration has been performed on a scenario basis without optimisation, and the synergies between the reaction and separation subsystems through process integration have been disregarded. For this reason, the conceptual process design of hydrothermal gasification for the cogeneration of SNG and power from wet lignocellulosic biomass and biomass wastes has been systematically investigated in [8]. The model of [6] has been improved with both more general and detailed technology models that are reconciled and validated with data from experimental investigations. A general superstructure for integrated product separation, power recovery and heat supply for the process is developed, and multi-objective optimisation is applied to explore the design alternatives and performances for selected candidate substrates.

This paper summarises some key aspects of the process integration and discusses the influence of the feedstock on the optimal process design and its performances.

2. Process description

2.1. Thermodynamic considerations

The conversion of biomass into methane and carbon dioxide is based on the conceptual overall net reaction, which can be written for a typical composition of lignocellulosic matter:

$$\begin{aligned} &CH_{1.35}O_{0.63} + 0.3475\ H_2O \longrightarrow \\ &0.51125\ CH_4 + 0.48875\ CO_2, \\ &\Delta\tilde{h}_r{}^0 = \text{-}10.5\ \text{kJmol}^{-1}_{CH_{1.35}O_{0.63}} \end{aligned} \quad (1)$$

Corresponding author: Martin Gassner, Email: martin.gassner@epfl.ch

Technically, the conversion requires a heterogeneous catalyst and is thus impossible to perform directly with the solid biomass feed since the big macromolecules cannot access the active sites. The most envisaged conventional route is thus to first decompose the solid feedstock by gasification and then catalytically synthesise the obtained H_2/CO-rich producer gas into CH_4 and CO_2 [9]. The conversion of (1) therefore splits up in an endothermal gasification step above 800°C and an exothermal synthesis step at 350-450°C at which CH_4 is thermodynamically favoured. This limits the product yield since a considerable part of the energy content of the feed is required to form intermediate H_2/CO and is then converted into excess heat in its highly exothermal methanation.

The hydrothermal route omits the endothermal step at high temperature and targets a direct conversion at 350-450°C into CH_4 and CO_2. Instead of forming an intermediate gas, the biomass is hydrolysed and gasified in a supercritical aqueous environment at around 300 bar, which allows for an efficient contact with the catalyst [4]. The thoroughly fluid processing thereby requires a feed in form of a pumpable slurry with a minimum total solid contents of approximately 20%wt depending on the type of substrate [4, 5]. Although this makes the process suitable for wet biomass since the heat requirement up to the gasification temperature is reduced by high pressure and drying is not required, the design must take care of the high amount of water that accompanies the reacting species throughout the process. As this represents the major share of the heat transfer requirements, the overall performance gets sensitive to the energy integration of the plant.

2.2. Technical process layout

Depending on the humidity and type of biomass that is processed, the first step in the block flow diagram of Fig. 1 is to mechanically dry or grind and dilute the feed. The slurry is then compressed to 300 bar and heated close to pseudo-critical conditions, during which hydrolysis and other reactions occurs [4]. When passing the pseudo-critical point, inorganics present in the feedstock will precipitate as salts and risk to plug the equipment and deactivate the catalyst if they are not efficiently removed. To do so, the subcritical slurry is injected through a dip-tube into a heated vessel, in which the salts precipitate at supercritical conditions [7]. The hydrolysate then passes through a fixed bed of nickel- or ruthenium-

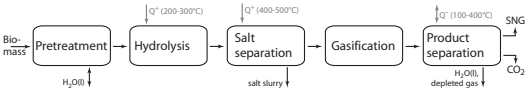

Figure 1: Block flow diagram.

based catalyst, which converts, at ideal conditions, more than 99.9% of the organic matter into CH_4, CO_2, some residual H_2 and only traces of CO [5].

In order to inject the produced methane at the required purity of 96%mol into the natural gas grid, it must be separated from water, carbon dioxide and possibly hydrogen. For a typical lignocellulosic feedstock (1) diluted to 20%wt total solids, the crude product contains approximately 84%mol of H_2O and 8%mol of each CH_4 and CO_2 in a near- or supercritical mixture at 350-450°C and around 300 bar. As indicated in Fig. 1, the process furthermore requires additional heat for the salt separator. The design of the product separation should therefore not only consider the grid quality specifications for SNG, but also the recovery of the exergy potential of the crude and the supply of required heat for the plant. For a similar separation problem in conventional SNG production, it has been shown that the overall process benefits from a tight integration of the reactive and separation systems [10], and similar effects can be expected for a hydrothermal plant.

3. Process design

3.1. Methodology

Following the developed methodology for the conceptual design of thermochemical production of fuels from biomass, a decomposed modelling approach is adopted to develop and evaluate candidate flowsheets [11]. The material conversion in the process units and their energy requirements are computed in energy-flow models, which are assembled in a process superstructure of all relevant technological options. The material flows defined by this superstructure act as constraints in the energy-integration model that is formulated as a mixed integer linear programming problem in which the heat exchanger network is represented by the heat cascade. Considering waste and intermediate product streams as fuel to supply the required heat, the combined SNG and power production is optimised with respect to operating cost. For the so-determined flowsheet, design heuristics and pilot plant data are used for rating and costing the equipment required to meet the thermodynamic design target.

3.2. Combined crude product separation and energy recovery options

While no major technology alternatives for feed pretreatment, hydrolysis, salt separation and gasification exist, several distinct strategies for the separation and expansion of the crude product are conceivable and might influence the process performance markedly. The crude product from gasification contains more than 80% H_2O, approximately equal amounts of CH_4 and CO_2, and some marginal H_2 and CO. Due to the supercritical conditions, its upgrade and expansion to grid conditions potentially allows for recovering mechanical energy, which however competes with the supply of thermal energy required for hydrolysis and salt separation. Another important aspect of the separation system design is the quality of the depleted stream, which may be used to supply the required heat and thus relax the need for a high methane recovery in the separation. The given boundary conditions thereby suggest different strategies for combined product separation and expansion that are outlined in the general superstructure of Fig. 2. Apart from conventional absorptive separation at grid pressure with a dedicated physical solvent followed by a membrane stage to remove residual hydrogen [9], the better solubility of CO_2 compared to CH_4 in water may become technically relevant at the prevailing process pressure. As discussed in [8], a trade-off between selectivity and good absolute solubility might thereby occur with respect to pressure. In any case, the separation is best at low temperature, and additional water is required for absorbing the bulk CO_2 to reach grid quality.

In order to recover mechanical energy from the crude product at high pressure, the separated vapour phase – or the entire supercritical bulk, if no high pressure separation is applied – may be expanded through turbines. It might thereby be advantageous or even necessary to preheat the stream, which increases the thermal efficiency of the recovery and prevents an expansion to far into the two-phase region. Compared to an isenthalpic expansion through valves, this causes less heat to be available from the crude product stream since energy is withdrawn at high temperature. For the liquid phase obtained from the separation at high pressure, the available exergy can be recovered by liquid expanders [12]. As an alternative, the liquid phase could also be reheated and expanded into the the vapour domain, which would allow for extracting more mechanical energy from the available potential, but also requires a considerable amount of heat to be supplied.

If the product is not upgraded to grid quality at high pressure, the liquid vapour and gas separation need to be carried out after the expansion of the crude product and similar technology as in the conventional route applies [9]. For the complete gas separation at grid pressure, a Selexol column seems appropriate. The combination of both high pressure and grid pressure separation is also conceivable. In order to reduce the amount of required additional water and thus pump power, the gas could only be pre-separated at high pressure and a single polymeric membrane stage at grid pressure could be used.

3.3. Minimum energy requirements

Fig. 3 shows the minimum energy requirements (MER) of the principal flowsheeting options for wood at the default operating conditions reported in [8]. The composite curves that identify the contributions of the process sections highlight that the layout of the product separation and expansion section determines the pinch point and influences the energy demand markedly. If no power recovery from the crude product is performed (Fig. 3(a)), the process pinch is situated at the salt separator where 186 kW $MW_{biomass}^{-1}$ are required at 440°C. Below, the specific and latent heat of the crude product is sufficient for preheating and hydrolysis of the feed, and an excess of about 150 kW $MW_{biomass}^{-1}$ can be recovered between 250 and 400°C. Limited power recovery by liquid expansion of the high pressure condensate and/or expansion of the incondensable mixture with previous reheating to the process pinch does not change the MER and only marginally influences the amount of excess heat.

If no separation at high pressure is applied and the crude product including the bulk water vapour is expanded in a turbine, the energy withdrawn as mechanical work is not available anymore at the gasification outlet temperature. As a consequence, the pinch point shifts to the turbine outlet temperature and results in an increased MER at lower temperature (Fig. 3(b)). Reheating the crude might thereby be required to avoid condensation in the final turbine stages and enhances the thermodynamic conversion efficiency, which leads not only to an increased power output but also heat demand.

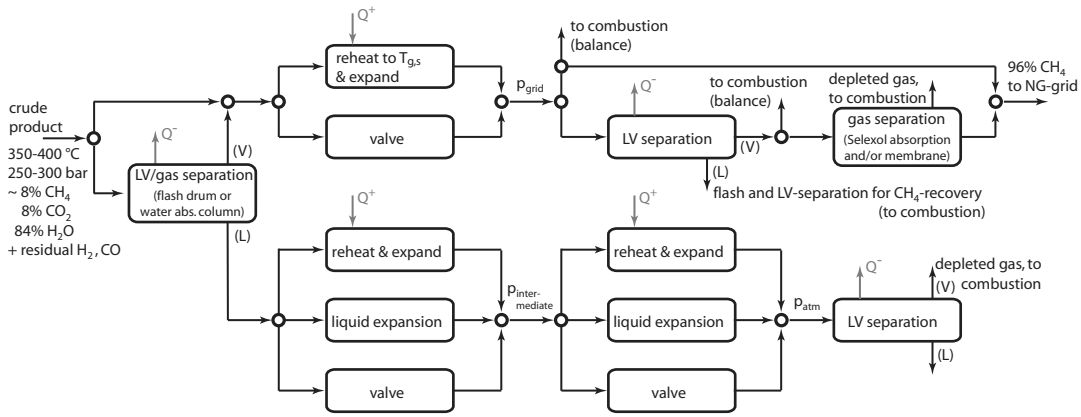

Figure 2: Superstructure including all possibilities for combined crude product separation and expansion.

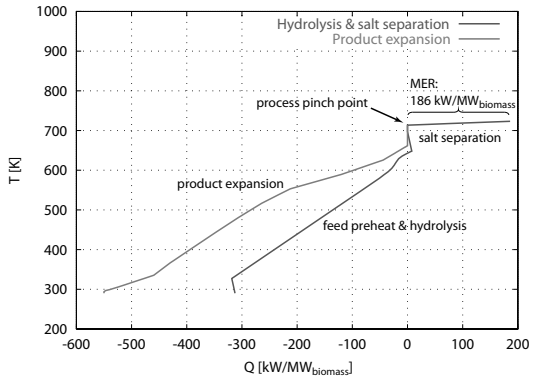

(a) Product expansion without power recovery.

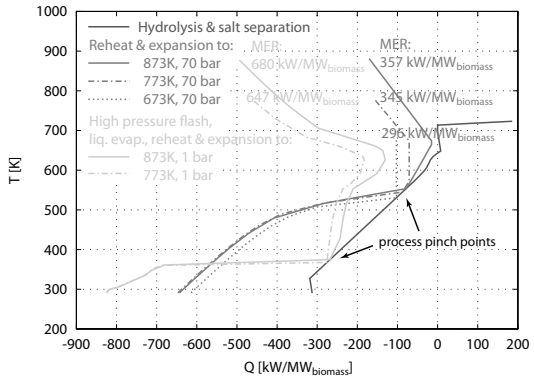

(b) Power recovery by reheating the entire crude product.

Figure 3: Minimum energy requirements.

If the condensable phase from separation at high pressure is evaporated, reheated and expanded to atmospheric pressure, the characteristics of the process integration change drastically. For such a configuration, the pinch point would shift to the saturation temperature of the mixture at atmospheric pressure and the MER increases to 64-68% of the raw material's heating value. This would require to burn a large part of the produced gas and turn the generation of electrical power to the plant's main purpose.

4. Process performance for selected substrates

4.1. Candidate substrates

Tab. 1 provides the relevant properties of a selection of candidate feedstocks for hydrothermal gasification. Among the potential substrates, manure and sewage sludge are abundant biomass wastes with a large potential. Coffee grounds and lignin slurry represent typical energetically exploitable by-products. While the former is a residue from the food industry, large amounts of biomass are retrieved as slurries with high lignin content in the pulp and paper industry or in a future production of fuel ethanol from lignocellulosic biomass. In case of the latter, excess heat from the SNG production might thereby also satisfy the requirement for biomass pretreatment and ethanol distillation, and favourable effects might emerge from process integration [13]. Finally, microalgae are considered as a photosynthetically efficient energy crop that are cultivable in photobioreactors on marginal land [14], from which a reduced environmental impact is expected.

Compared to wood, all these substrates offer a higher hydrogen fraction and thus an increased theoretical methane yield from the dry, ash-free substance according to (1). Except coffee grounds and lignin slurry, they yet suffer from a higher ash con-

		Proximate analysis			Ultimate analysis					St. coeff. in (1)	
		Φ	ash	Δh^0	C	H	O	N	S[a]	CH_4	CO_2
Substrate	Ref.	%wt	$\%wt_{dry}$	MJ kg^{-1}_{daf}			$\%wt_{daf}$			-	-
Wood	[9]	50	0.6	18.6	51.1	5.8	42.9	0.2	n/a	0.51	0.49
Manure (pig)	[4]	97	24.9	21.2	48.0	8.3	36.1	7.0	0.6	0.62	0.38
Sewage sludge[b]	[15, 16]	73	47.8	19.2	49.2	6.0	37.6	7.2	n/a	0.54	0.46
Coffee grounds	[16]	50	0.3	26.0	60.1	8.5	29.6	1.6	0.2	0.62	0.38
Lignin slurry	[13]	75	0.6	23.4	55.8	8.2	36.0	n/a	n/a	0.60	0.40
Microalgae	[14]	87	12.5	25.3	57.7	7.6	25.3	8.1	1.3	0.61	0.39

[a] n/a: not available in database. All substrates yet contain enough sulphur to assume equilibrium concentration in the supercritical phase after salt separation in order to quantify catalyst deactivation [8].

[b] internal data [15] for a mixture of conventionally digested primary and secondary sludges, ash content and humidity from [16]

Table 1: Properties of the candidate feedstock.

tent which reduces the effective biomass content if diluted to the same dry solids content. Among the substrates, manure suffers from a particular low solids content on an as-received basis and is the only substrate for which water purification by reverse osmosis is considered necessary.

4.2. Process optimisation

The process design for hydrothermal conversion is particularly flexible with respect to the co-production of fuel and power. In order to explore this particular trade-off, the cogeneration potential is addressed in a first optimisation step that considers the partial SNG and electric efficiencies defined by the ratios of the SNG and electricity yields to the biomass input, respectively, as objectives. In a second step, thermo-economic optimisations of the process design are carried out with and without considering the catalyst cost to investigate the importance of catalyst deactivation in the design. The chemical efficiency, defined as the equivalent SNG yield if electricity is substituted by the amount of gas consumed for its generation in a combined cycle at an exergy efficiency of 55%, is thereby used as an aggregated thermodynamic objective. As economic objective, the specific investment cost per installed capacity is used, including also the total catalyst cost over the entire plant lifetime if catalyst deactivation is considered. Mathematically detailed definitions of these objectives, economic assumptions, and the process design variables to be optimised are reported in [8].

Fig. 4 provides the Pareto fronts of the overall best configurations for all substrates in the different optimisation steps. The maximum partial efficiencies in (a) assess a nearly equal cogeneration potential for coffee grounds and lignin slurry, which are performing slightly better than wood. Microalgae, manure and sewage sludge are consecutively worse. In comparison with Tab. 1, this order mainly follows the ash content of the substrates. With an equal total solids content of 20%, the net dilution of the reactive biomass in water almost doubles in the worst case of sewage sludge and has a fatal impact on process efficiency since the amount of water to be entrained is doubled as well. In addition to the maximum combined efficiency situated close to the maximum SNG yield, power recovery from the high pressure vapour phase allows for a high marginal efficiency in substituting the SNG by electrical power generation. This leads to a second peak with respect to the combined efficiency at net SNG yields below roughly 50%, which is particularly beneficial for low quality substrates like sewage sludge.

The efficiency considerations have a big impact on the thermo-economic performance of the conversion. Compared to coffee grounds and lignin slurry which are dominating the common Pareto domain of (b) and (c), the conversion of wood is slightly less efficient and more expensive due to the higher CO_2 share in the crude product that requires more effort for separation. It is thus competing with microalgae whose conversion is disfavoured by a slightly higher ash content. The waste substrates are clearly worst. While sewage sludge is seriously penalised by its low thermodynamic performance, manure suffers from high investment cost for dewatering and especially wastewater treatment by reverse osmosis.

Fig. 5 illustrates the evolution of the process configuration on the thermo-economic Pareto fronts and clearly highlights that the optimal choice depends not only on the availability of energy recovery technology, catalyst deactivation and plant scale, but

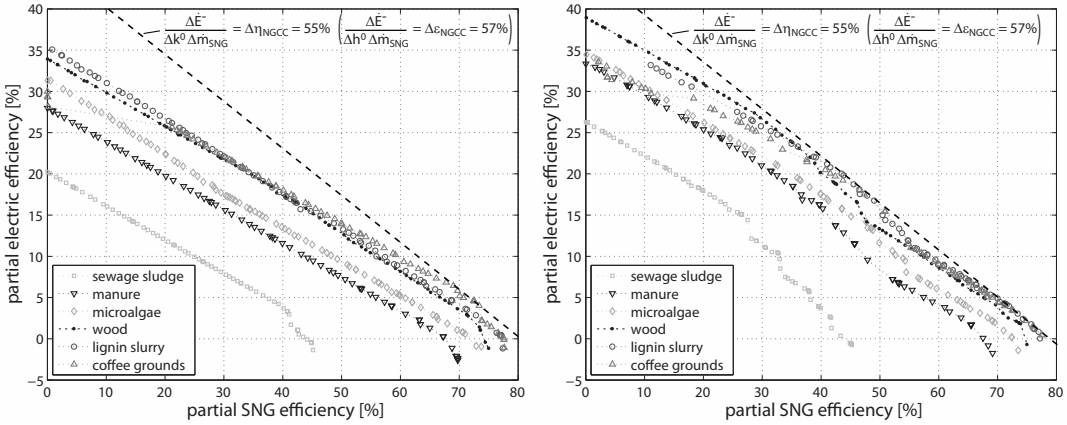

(a) Maximum partial efficiencies.

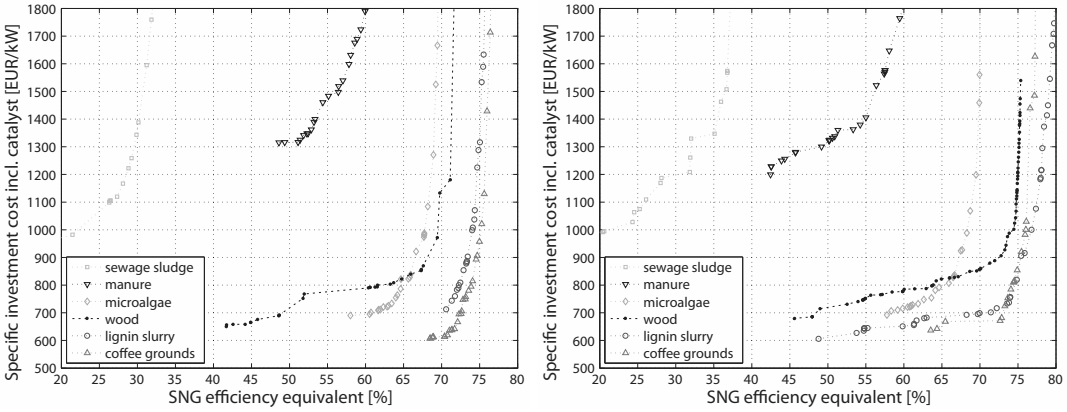

(b) Full consideration of catalyst cost.

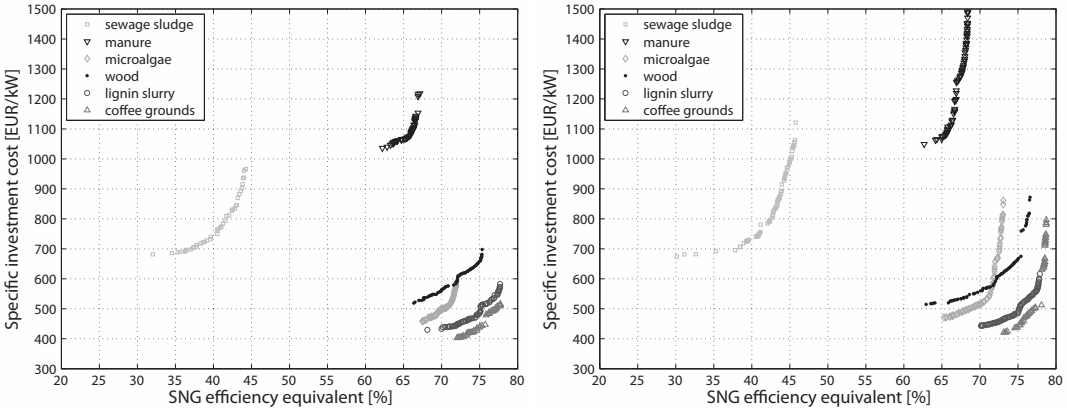

(c) Without catalyst deactivation.

Figure 4: Optimal thermodynamic and thermo-economic trade-off at 20 $MW_{th,biomass}$ without (left) and with power recovery from the high pressure vapour phase.

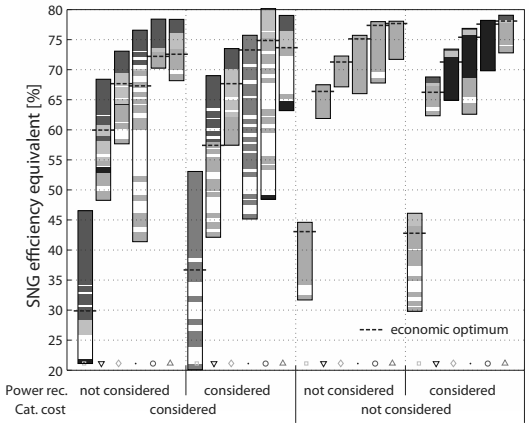

(a) Evolution of the optimal process layout on the Pareto front.

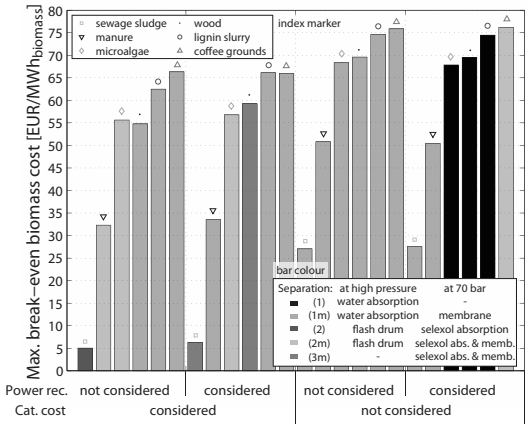

(b) Break-even costs for the most economic solutions.

Figure 5: Optimal process configurations at 20 $MW_{th,biomass}$ depending on substrate.

also on substrate properties. Although the use of a single separation technology is more efficient, its combination with a membrane is less costly since the purification requirement is relaxed. The flowsheets with absorption of CO_2 in water thereby require less investment than Selexol, but are disfavoured at higher efficiency. An exception is observed if power recovery from high pressure vapour is excluded and catalyst cost can be disregarded, for which water absorption is the unconditionally best technology for all substrates. If catalyst cost is considered and power recovery feasible, superheating and expansion of the bulk crude product emerges as an interesting alternative since its efficiency is less sensible to the design constraints imposed to avoid excessive deactivation. For the economically best configurations, an almost neutral power balance at high SNG yield seems best if catalyst deactivation does not need to be considered. Otherwise, a yield distribution in which up to 10% of the biomass input is converted into power is more advantageous. The assessed break-even costs for coffee waste, lignin slurry and microalgae are similar or higher to those of wood, which results in considerably higher plant profitability if lower substrate prices apply. Although manure conversion suffers from high investment cost, such plants might yet be profitable since also low compensations for the feedstock can be expected. The conversion of sewage sludge increases the energy efficiency of wastewater treatment, but economical benefits should principally emerge from avoiding another type of waste treatment.

5. Conclusions

This paper has summarised a systematic analysis of the process design alternatives for hydrothermal production of SNG from wet biomass and biomass waste. Based on a general superstructure for combined product separation and internal energy recovery from the supercritical conditions, the possibilities for an efficient cogeneration of SNG and power have been explored.

Even with conservative hypothesis on practical design limitations, a sound process integration and energy recovery allows for an energetically and economically viable process design. Thermo-economic optimisations have revealed that the hydrothermal conversion should thereby be regarded as a polygeneration system in which SNG and electricity yields are to a large extent on a par. It is demonstrated that the process design and performance is not only influenced by available technology and catalyst deactivation, but also the characteristics of the processed substrate. Wet but energetically valuable industrial by-products with a high hydrogen and low ash content such as lignin slurries or coffee grounds have been identified as a particularly well suited feedstock that allow for greater efficiencies than wood. Biomass wastes with high ash content such as manure and digested sewage sludge are less advantageous since their effective biomass content is severely reduced if processing is limited to slurries containing no more than 20% total solids. From the perspective of waste treatment with disposal as principal objective, also marginal profit from a complete energy recovery from wastes might yet be valuable.

Acknowledgments: The authors acknowledge funding provided by the Competence Centre for Energy and Mobility (CCEM), Erdgas Ostschweiz AG, Gasverbund Mittelland AG and Gaznat SA (all Switzerland).

Nomenclature

$\dot{E}$ Electricity, MW

$\dot{m}$ Mass flow, kg s^{-1}

Greek Letters

Δh^0 Lower heating value, MJ kg_{daf}^{-1}

Δk^0 Exergy value, MJ kg_{daf}^{-1}

ϵ Energy efficiency, %

η Exergy efficiency, %

Φ Biomass humidity, %wt

Subscripts

daf dry, ash free

References

[1] A. Kruse. Supercritical water gasification. *Biofuels, Bioproducts and Biorefining*, 2(5): 415–437, 2008.

[2] D. C. Elliott. Catalytic hydrothermal gasification of biomass. *Biofuels, Bioproducts and Biorefining*, 2(3):254–265, 2008.

[3] A. A. Peterson, F. Vogel, R. P. Lachance, M. Fröling, M. J. Antal Jr., and J. W. Tester. Thermochemical biofuel production in hydrothermal media: A review of sub- and supercritical water technologies. *Energy and Environmental Science*, 1(1):32–65, 2008.

[4] M. H. Waldner and F. Vogel. Renewable production of methane from woody biomass by catalytic hydrothermal gasification. *Industrial and Engineering Chemistry Research*, 44: 4543–4551, 2005.

[5] F. Vogel, M. H. Waldner, A. A. Rouff, and S. Rabe. Synthetic natural gas from biomass by catalytic conversion in supercritical water. *Green Chemistry*, 9(6):616–619, 2007.

[6] J. Luterbacher, M. Fröling, F. Vogel, F. Maréchal, and J. W. Tester. Hydrothermal gasification of waste biomass: Process design and life cycle assessment. *Environmental Science and Technology*, 43:1578–1583, 2009.

[7] M. Schubert, J. W. Regler, and F. Vogel. Continuous salt precipitation and separation from supercritical water. Part 1: Type 1 salts. *Journal of Supercritical Fluids*, 52:99–112, 2010.

[8] M. Gassner. *Process design methodology for thermochemical production of fuels from biomass*. PhD thesis, EPFL, 2010.

[9] M. Gassner and F. Maréchal. Thermo-economic process model for thermochemical production of Synthetic Natural Gas (SNG) from lignocellulosic biomass. *Biomass and Bioenergy*, 33:1587–1604, 2009.

[10] M. Gassner, R. Baciocchi, F. Maréchal, and M. Mazzotti. Integrated design of a gas separation system for the upgrade of crude SNG with membranes. *Chemical Engineering and Processing*, 48:1391–1404, 2009.

[11] M. Gassner and F. Maréchal. Methodology for the optimal thermo-economic, multi-objective design of thermochemical fuel production from biomass. *Computers and Chemical Engineering*, 33:769–781, 2009.

[12] M. J. Perlmutter, H. E. Kimmel, C. Chiu, and H. Paradowski. Economic and environmental benefits of two-phase LNG expanders. pages 1121–1130, 2004.

[13] S. Zhang, F. Maréchal, M. Gassner, Z. Périn-Levasseur, W. Qi, Z. Ren, Y. Yan, and D. Favrat. Process modeling and integration of fuel ethanol production from lignocellulosic biomass based on double acid hydrolysis. *Energy and Fuels*, 23:1759–1765, 2009.

[14] A. G. Haiduc, M. Brandenberger, S. Suquet, F. Vogel, R. Bernier-Latmani, and C. Ludwig. SunCHem: An integrated process for the hydrothermal production of methane from microalgae and CO2 mitigation. *Journal of Applied Phycology*, 21(5):529–541, 2009.

[15] N. Descoins. Internal data for a mixture of digested primary sewage sludges. Laboratory for Industrial Energy Systems, EPFL, 2009.

[16] ECN. Phyllis, database for biomass and waste. www.ecn.nl/phyllis, last visited 06/2009.

Thermo-economic Evaluation of the Thermochemical Production of Liquid Fuels from Biomass

Laurence Tock [a], *Martin Gassner* [a] *and François Maréchal* [a]

[a] *Industrial Energy Systems Laboratory, Ecole Polytechnique Fédérale de Lausanne, Lausanne, Switzerland*

Abstract: Different technological alternatives for the thermochemical production of liquid fuels from lignocellulosic biomass are systematically analyzed and optimized based on thermo-environomic models. The competitiveness of the production of Fischer-Tropsch fuel (FT), methanol (MeOH) and dimethyl ether (DME) is compared with regard to energetic, economic and environmental considerations, and the optimal process configuration and operating conditions are identified. For the conceptual process design a consistent methodology using simultaneously process integration techniques, life cycle assessment (LCA) and a multi-objective optimization strategy is applied. In particular, the influence of the process integration on the overall process efficiency is investigated by studying several possibilities to satisfy the minimum energy requirements, to recover and valorize at most the available heat, and by studying the effect of the operating conditions. The most promising options for the polygeneration of fuel, power and heat will be identified based on multiple criteria. The performance for the different process steps and some exemplary technology scenarios of integrated plants are computed, and overall energy efficiencies in the range of 50-60% are assessed.

Keywords: Biomass, Biofuels, Process design, Process integration, Thermo-economic modeling.

1. Introduction

In the context of global warming and energy security, renewable energy resources are generally accepted as alternative to substitute fossil fuels. Biomass is a widely available and renewable energy source that can contribute to decrease the CO_2 emissions by generating heat, electricity and transportation fuels. Currently, research and development focuses on the conversion of biomass to liquid fuels (BtL). Several studies indicate that the production of biofuels by biomass conversion is technically feasible [1, 2], however some challenges remain for the successful large-scale commercial implementation. Energy efficiencies ranging from 33 to 55% have been assessed by technical and economic evaluation of the Fischer-Tropsch (FT), methanol (MeOH) and dimethyl ether (DME) synthesis by biomass gasification in [3–6], respectively. Flowsheeting models are used in most of these studies for the performance evaluation and capacity based correlations disregarding specific process condition for the economics estimations. No systematic energy integration assessing cogeneration possibilities in detail and life cycle assessment (LCA) have been performed. In [7–9] the performance of the production of synthetic natural gas from biomass is analyzed and optimized by applying a consistent methodology based on the development of thermo-economic models for the energy integration and performance computation, on LCA for environmental impacts assessment and on a multi-objective optimization strategy for the identification of trade-offs between competing performances. By proceeding in a similar way, the competitiveness of different biomass conversion processes will be investigated systematically in this study based on previously developed thermo-economic models for biomass gasification and subsequent producer gas treating [8] and for liquid fuel synthesis [10].

The purpose of the present work is to compare and optimize different technological alternatives for BtL processes by evaluating at the same time several competing criteria like energy efficiency, costs and environmental impacts based on thermo-economic models. It is essentially focused on process integration and highlighted how the performance is influenced by appropriate energy integration considering the polygeneration of fuel, power and heat and by the operating conditions. Promising process configurations are identified by the simultaneous analysis of multiple criteria including LCA [7–9, 11] .

Corresponding author: Laurence Tock, Email: laurence.tock@epfl.ch

2. Methodology

This paper follows a previously developed methodology for optimal thermo-economic process design of fuel production from biomass [7, 8]. After the identification of suitable technologies for the process, all the different options are defined in a superstructure and thermo-economic models are developed. The thermodynamic model consists of an energy-flow model computing the chemical and physical transformations and the associated heat requirements using the commercial flowsheeting software Belsim-Vali [12], and a separate energy integration model representing the heat recovery system. The energy-integration model computes the optimal thermal process integration and defines with the pinch analysis methodology the heat recovery potential from the hot and cold streams and their minimum approach temperature ΔT_{min}. By solving the heat cascade the minimum energy requirement (MER) is computed. Several utilities techniques are proposed to satisfy the process needs such as combustion of waste and producer gas (PG), Rankine cycle for power production, heat pump, gas turbine and cogeneration. The optimal utility integration is defined by maximizing the combined production of fuel, power and heat with regard to minimal operating cost by solving a linear programming problem [7, 13, 14]. The data from the thermodynamic model is used to size the equipment and estimate the grass roots cost with respect to the specific process designs with correlations from the literature [15, 16]. For the LCA model, the cradle-to-gate LCA approach described in [9] is applied with a functional unit of 1 MJ of biomass at the inlet of the installation and the impact assessment method Impact2002+. The multi-objective optimization approach [7, 9, 11] identifies the relationship between competing objectives with regard to environomic (i.e. thermodynamic, economic and environmental) criteria and yields finally an optimal conceptual design of integrated biofuel plants.

3. Process description

The thermochemical process converting biomass into liquid fuels consists of feed conditioning, gasification, steam methane reforming (SMR), gas cleaning and treatment including water-gas shift reaction (WGS), and fuel synthesis and purification. The general process superstructure represented in Fig. 1 summarizes the different technological options for each process step that can be considered and displays the LCI flows within the system limits. For the gasification, the entrained flow gasifier (EF) and the circulating fluidized bed gasifier (CFB) technology, either indirectly heated by an external heat source or directly heated through oxidation is considered. The process layout for the producer gas production is similar to the one described in [8] and for FT, MeOH and DME synthesis the ones in [3, 4, 6], respectively. Detailed information about the different drying, gasification, cleaning and synthesis technologies are given in [1–5, 8, 17].

3.1. Thermo-economic process model

For each process configuration included in the superstructure (Fig.1) thermo-economic process models have been developed in previous work [8, 10]. Energy-flow and energy integration models, and approximate sizing and cost estimation procedures have been set up. The chemical conversion in the circulating fluidized bed gasification, methanol and DME synthesis reactions are modeled by equilibrium relationships with an artificial temperature difference, while for the other reactions equilibrium is assumed as explained in [8]. Table 2 reports the main chemical reactions involved in the different process units. The upgrading section is modeled to reach a purity of 99.8wt% DME and of 99.9wt% MeOH respectively, by flash drum separation and distillation (Appendix Table 6), whereas the FT purification is not modeled in detail. After liquid-liquid separation from water the crude FT fuel is the final product, which can be sent to a refinery for upgrading. An overview of the nominal operating conditions and its feasible range is given in Table 1. More details on the modeling and assumptions can be found essentially in [8] and in [10] (Appendix: modeling parameters and thermodynamic models).

4. Process performance

4.1. Performance Indicators

The thermodynamic, economic and environmental performances of the conversion processes is addressed through several competing indicators computed from the thermo-environomic model. The overall energy efficiency ϵ_{tot} that depends on the chemical conversion and the quality of the process integration is defined by the ratio between the total energy outputs and inputs including electricity. In the chemical efficiency ϵ_{chem} definition the electricity is substituted by a natural gas fuel equivalent

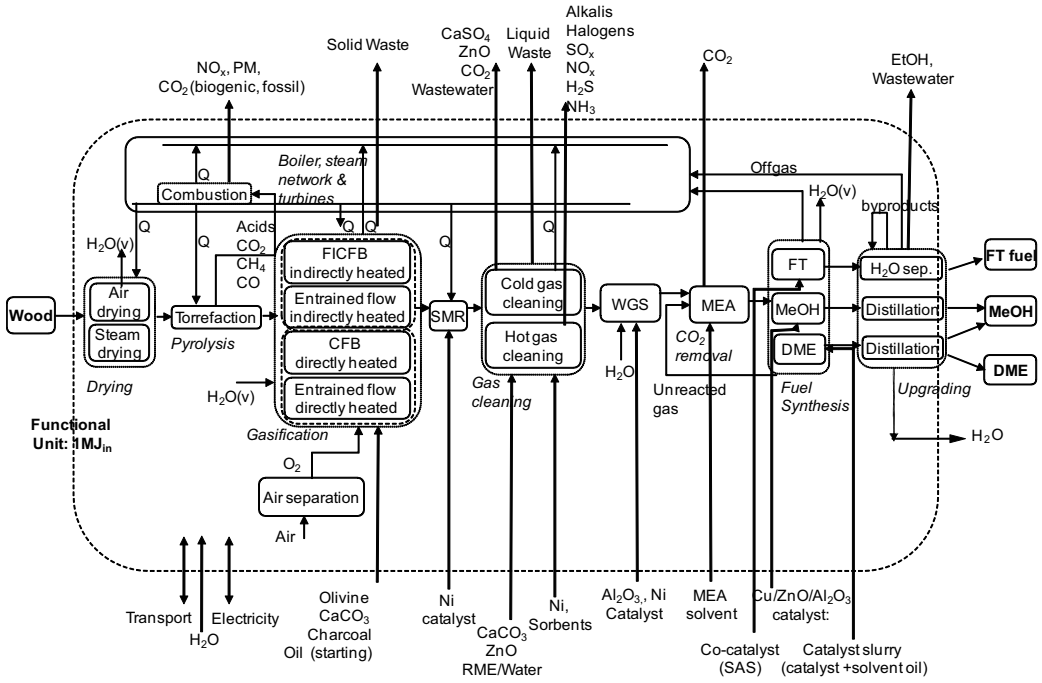

Figure 1: Superstructure of biomass to liquid fuels conversion process with recycling options including thermo-economic and LCA model flows.

Table 2: Chemical reactions occurring in the process.

Name	Reaction	$\Delta\tilde{h}_r^0$	*Reactor*	
Olefins formation	$2nH_2 + nCO \rightarrow C_nH_{2n} + nH_2O$		FT	(1)
Paraffins formation	$(2n+1)H_2 + nCO \rightarrow C_nH_{2n+2} + nH_2O$		FT	(2)
Methanol synthesis	$CO + 2H_2 \rightleftharpoons CH_3OH$	$-90.8\ kJ/mol$	$MeOH, DME$	(3)
	$CO_2 + 3H_2 \rightleftharpoons CH_3OH + H_2O$	$-49.16\ kJ/mol$	$MeOH$	(4)
Ethanol formation	$2CH_3OH \rightleftharpoons C_2H_5OH + H_2O$	$-71.8\ kJ/mol$	$MeOH$	(5)
Methanol dehydration	$2CH_3OH \rightleftharpoons CH_3OCH_3 + H_2O$	$-23.4\ kJ/mol$	$DME, MeOH$	(6)
One-step DME synthesis	$3CO + 3H_2 \rightleftharpoons CH_3OCH_3 + CO_2$	$-246.5\ kJ/mol$	DME	(7)
Steam methane reforming	$CH_4 + H_2O \rightleftharpoons CO + 3H_2$	$206\ kJ/mol$	SMR	(8)
Ethene reforming	$C_2H_4 + 2H_2O \rightleftharpoons 2CO + 4H_2$	$210\ kJ/mol$	SMR	(9)
Water-gas shift equilibrium	$CO + H_2O \rightleftharpoons CO_2 + H_2$	$-41\ kJ/mol$	SMR, WGS	(10)
			$DME, MeOH$	

calculated by considering an exergy efficiency of 55%. These efficiencies are expressed on the lower heating value basis. The grass roots cost and operating cost characterize the economic performance with the same assumptions as stated in [8]. Whereas the environmental performance is defined by different impact categories (i.e. human health, ecosystem quality, climate change and resource) computed by the Impact2002+ method. For the electricity impact contribution the Swiss mix for medium voltage electricity production at grid is considered. All the performance analyses are performed for a plant capacity of 20$MW_{th,biomass}$.

Table 1: Operating conditions of the process units and feasible range for optimization.

Operating parameter	Nominal	Range
Drying		
Temperature (inlet) [K]	473	[433-513]
Wood humidity (outlet) [wt%]	20	[5-35]
FICFB		
Pressure [bar]	1	-
Temperature [K]	1123	[1000-1200]
Steam to biomass ratio [wt%]	50	-
SMR		
Temperature [K]	-	[950-1200]
WGS		
H_2O flow [kg/s/kg PG]		[0.06-0.1]
FT		
Pressure [bar]	25	[20-30]
Temperature [K]	613	[590-660]
CO-conv [%]	85	[82-88]
Growth probability [-]	0.884	-
H_2/CO [-]	2	-
MeOH		
Pressure [bar]	85	[75-90]
Temperature [K]	533	[500-600]
Unreacted gas recycling [%]	90	[80-95]
$\frac{H_2-CO_2}{CO+CO_2}$ [-]	2	-
MeOH synthesis ΔT [K]	3.6	-
DME		
Pressure [bar]	50	[40-60]
Temperature [K]	550	[500-600]
Unreacted gas recycling [%]	80	[70-85]
H_2/CO [-]	2	-
MeOH dehydration ΔT [K]	5	-

4.2. Energy integration

The minimum energy requirement is computed from the hot and cold process streams through the heat cascade method that takes the potential heat recovery into account. For the FT process consisting of air drying, indirectly heated fluidized bed gasification (FICFB) and cold gas cleaning, the characteristic composite curve representing the heat cascade is illustrated in Fig.2. Above the pinch point, heat is required by the endothermic reforming and gasification reaction, while heat is released below the pinch point by the producer gas cooling and the exothermic synthesis reaction.

Since the pinch point is located at the reforming temperature, the excess heat available at high temperature can be valorized in a Rankine cycle to generate electricity. A cycle with two production, two usage and one condensation level is thereby considered with the parameters given in Table 3.

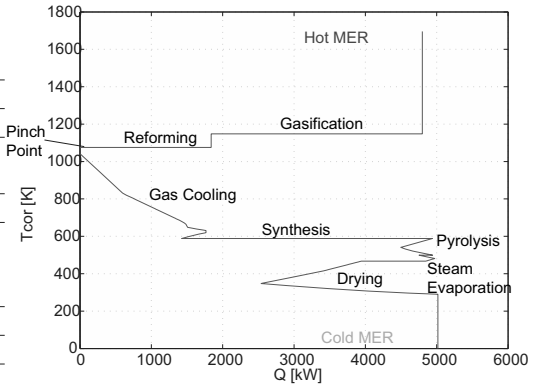

Figure 2: Grand composite curve of FT process with FICFB gasification.

Table 3: Operating conditions of the steam network and feasible range for optimization.

Operating parameter	Unit	Nominal	Range
1st Production level	bar	80	60-90
2nd Production level	bar	120	100-120
Superheating temperature	K	773	623-823
1st Utilization level	K	473	323-523
2nd Utilization level	K	433	-
Condensation level	K	292	-

The heat demand is satisfied by the combustion of waste streams (i.e. unconverted char and gaseous residues of the separation and purification sections) and if necessary additional process streams (i.e. hot or cold producer gas from the gasifier). The excess heat is withdrawn from the process by cooling water. The process integration including a steam network and hot and cold utilities is represented in Fig.3 by the integrated composite curve for the FT process. Typically, the introduction of the steam network increases the chemical efficiency of the FT process from 50.6 to 59.3%, by reducing the net electricity consumption through the electricity generation from the steam turbine.

4.3. Process comparison

The performance of the different synthesis processes is evaluated at identical nominal conditions for the producer gas production which consists in air drying, indirectly heated fluidized bed gasification and cold gas cleaning. The reforming temperature is chosen by sensitivity analysis to adjust the stoichiometry for the synthesis to yield the best conversion efficiency (i.e 1050K for FT, 1223K for DME and MEOH). The steam network with appropriate production and consumption levels is integrated to

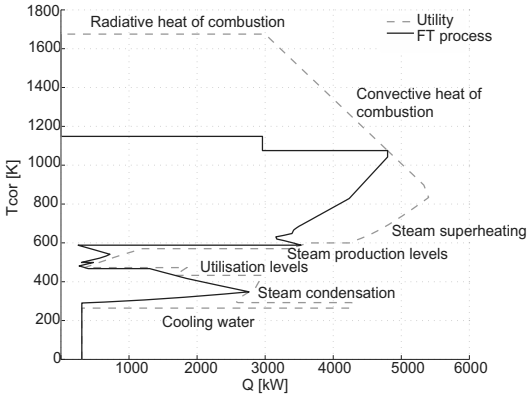

Figure 3: Integrated composite curve of FT process with FICFB gasification including steam network and other utilities.

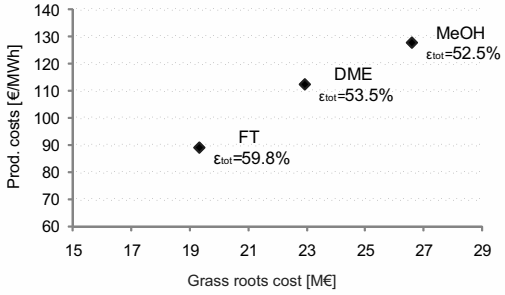

Figure 4: Comparison of the thermodynamic and economic performance of the FT, DME and MeOH processes with FICFB gasification.

valorize the heat excess. The thermo-economic performances presented in Fig.4 highlight that the FT process is best both with respect to grass roots cost, production cost and efficiency.

This is partly explained by the fact that FT-upgrading is not modeled and that no CO_2 removal unit is included. However, the main difference comes from the power demands variation reported in Table 4. Since the methanol process operates at high pressure, a large amount of power is required to compress the producer gas to the synthesis conditions, while the other synthesis reactions operate at lower pressure (Table 1) which requires less mechanical power. In addition a large amount is required for the compression and solvent regeneration in the CO_2 removal process by chemical absorption with monoethanolamine (MEA).

For the analysis of the environmental impacts, the life cycle inventory (LCI) is performed by identifying the LCI flows within the system limits in Fig.1. The comparison of the results presented in Fig.5 highlights the main contributions for each process. The major difference between the three processes is due to the impact of the electricity consumption. The largest impact is attributed to the rape methyl ester (RME) produced from colza cultivated with insecticides and consumed for the cold gas cleaning, consequently alternative colza cultivation methods and the development of alternative cleaning technologies such as hot gas cleaning has to be investigated in detail.

Table 4: Mechanical power balance [kW] for the FT, DME and MeOH process. The net electricity output is negative if the integrated process requires additional electricity.

Power balance	FT	DME	MeOH
Consumption:			
· PG production [kW]	444	448	448
· CO_2 removal [kW]	0	226	545
· Synthesis [kW]	1308	1410	1830
Production:			
· Steam network [kW]	1662	1128	1117
Net electricity [kW]	-90	-956	-1706

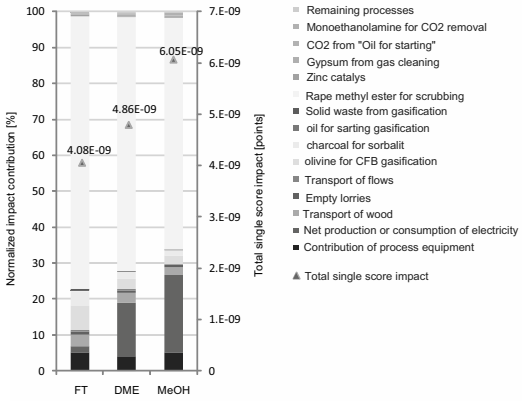

Figure 5: Comparison of the environmental impacts of the FT, DME and MeOH processes evaluated by the Impact2002+ method for single score category for a functional unit of 1 $MJ_{biomass}$.

4.4. Process optimization

In order to address and understand the trade-off between several competing factors defining the process performance multi-objective optimization is performed for the FT process. The chosen objectives are the maximization of the chemical efficiency ϵ_{chem} and the minimization of the grass roots costs.

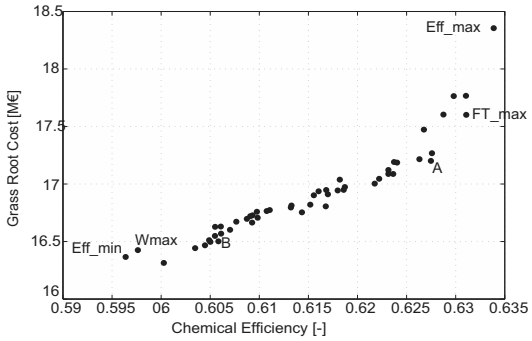

Figure 6: Optimal solutions in the Pareto domain for the FT process.

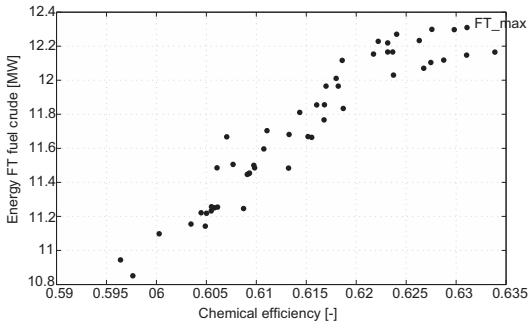

Figure 7: Variation of the energy content of the FT crude fuel with respect to the chemical efficiency for the FT process.

The decision variables and their variation range are chosen according to the key process operating conditions and the steam network characteristics and are identified in Tables 1 and 3. The generated Pareto curve in Fig. 6 represents the optimal trade-off between the objectives.

For the different analyzed configurations the efficiency increase goes in pair with an increase of the grass roots cost. The detailed analysis of several configurations selected from the Pareto plot in Fig.6 is reported in Table 5. The maximal amount of fuel is produced by configuration FT_max, while the maximal mechanical power is generated by the operating conditions of point Wmax. The efficiency increase is essentially related to the increased FT crude fuel production as illustrated in Fig. 7. The conversion into fuel is enhanced by the variation of the operating conditions.

The comparison of the energy integration represented by the integrated composite curves of the configuration with the lowest and highest efficiency in Fig.8 highlights the influence of the process operating conditions on its heat demand, as well as the influence of the steam network characteristics. In the configuration with the highest efficiency, the steam network is well integrated and recovers a large amount of the excess heat for mechanical power production. Even if the grass roots cost increase with the efficiency, the production cost decrease (Table 5). The additional annual fuel production preponderates the annualized investment impact. Around the highest efficiency this trend becomes less pronounced. The lowest production cost are associated to configuration A (ptA). The environmental impact is highly related to process efficiency in terms of power consumption or production. The configuration generating the largest amount of net electricity through the steam turbine has the lowest environmental impact, since essentially the resource impact is reduced by the substitution of nuclear electricity in the Swiss electricity production mix.

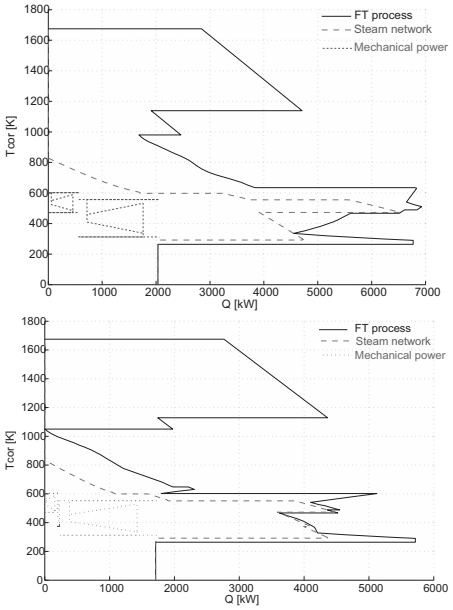

Figure 8: Integrated composite curve of FT process with FICFB gasification including steam network. Top: configuration with lowest ϵ_{chem} (Eff_min), bottom: configuration with highest ϵ_{chem} (Eff_max).

5. Conclusion

A systematic methodology based on thermo-economic and LCA models coupled with a multi-

Table 5: Decision variables, objectives and performance indicators of some selected FT process configurations.

	Eff_max	FT_max	A	B	Wmax	Eff_min
Decision variables						
Synthesis P [bar]	20.3	20.8	20	20	20	20.8
Synthesis T [K]	627.2	641.6	657.1	660	657.1	660
CO-conv [%]	87.8	87.6	87.6	87.7	87.4	86.4
SMR T [K]	1025	993	983.8	958.7	950	954.9
Drying T [K]	513.1	510.5	489.2	509.8	502.8	502.5
Humidity drying outlet [%]	35	32	32.1	15.2	14.6	13.3
Gasification T [K]	1103.8	1152.4	1146	1132.5	1136.5	1114
H_2O flow [kg/s/kg PG]	0.084	0.086	0.094	0.075	0.094	0.094
1st Prod. level [bar]	60.8	65.7	67.5	64.7	64.3	64.9
2nd Prod. level [bar]	119.9	115.2	117.7	118.1	117.7	117.4
Superheating T [K]	823.1	817.7	822.8	823.1	823.1	817.7
1st Utilization level [K]	373.3	323.7	324.9	323.1	330.3	332.3
Power balance						
Fuel Output [MW]	12.2	12.3	12.1	11.2	10.8	10.9
Power consumption [kW]	1485.4	1549.1	1538.3	1518.5	1509.5	1544.7
Power generation [kW]	1800.5	1740.8	1812.1	2060.7	2186.9	2149.4
Net electricity [kW]	-315.1	-191.7	-273.8	-542.2	- 677.4	-604.7
Performance						
ϵ_{chem} [%]	63.4	63.1	62.7	60.5	59.8	59.6
ϵ_{tot} [%]	62.5	62.4	61.9	58.8	57.7	57.6
Grass roots cost [M€]	18.3	17.6	17.2	16.5	16.4	16.3
Production cost [€/MWh]	81.5	80.9	80.6	82.1	82.9	83.1
Single score impact [10^{-9}pts]	3.65	3.74	3.61	3.21	3.03	3.13

objective optimization algorithm has been applied to the conceptual design of integrated plants for liquid biofuel production. The competitiveness of different process options for the production of Fischer-Tropsch fuel, DME and methanol is evaluated consistently with respect to energy efficiency, cost and environmental impacts. In particular, it was pointed out how appropriate energy integration and operating conditions improve the process performance by maximizing the combined production of fuel, heat and power. There is a trade-off between fuel and electricity generation as highlighted by the FT process optimization. This work and the developed thermo-economic models [8] form the basis for multi-objective optimizations of the MeOH and DME processes to reveal optimal configurations with the goal of performing a systematic comparison between liquid and gaseous biofuels produced from biomass.

Nomenclature

Abbreviations

BtL Biomass to Liquid
CFB Circulating Fluidized Bed
DME Dimethyl Ether
EF Entrained Flow
FICFB Fast Internally Circulating Fluidized Bed
FT Fischer-Tropsch
GRC Grass Roots Cost
LCA Life Cycle Assessment
LCI Life Cycle Inventory
MEA Monoethanolamine
MeOH Methanol
MER Minimum Energy Requirement
PG Producer Gas
RME Rape Methyl Ester
SMR Steam Methane Reforming
WGS Water-Gas Shift

Greek letters

$\Delta\tilde{h}_r^0$	Standard heat of reaction	kJ/mol
ϵ_{chem}	Chemical efficiency	%
ϵ_{tot}	Overall energy efficiency	%

Roman letters

$\dot{E}$	Mechanical/electrical power	kW
P	Pressure	bar
$\dot{Q}$	Heat	kW
T	Temperature	^oC or K
T_{cor}	Corrected Temperature	K

wt%	Weight percent	%

Superscripts

$^+$	Material/energy stream entering the system
$^-$	Material/energy stream leaving the system

References

[1] I. Olofsson, A. Nordin, and U. Söderlind. Initial review and evaluation of process technologies and systems suitable for Cost-Efficient Medium-Scale gasification for biomass to liquid fuels. Technical report, Energy Technology & Thermal Process Chemistry, University of Umea, 2005.

[2] P.L. Spath and D.C. Dayton. Preliminary Screening-Technical and economic assessment of synthesis gas to fuels and chemicals with emphasis on the potential for Biomass-Derived syngas. Technical Report NREL/TP-510-34929, National Renewable Energy Laboratory, Colorado, 2003.

[3] C.N. Hamelinck, Faaij A.P.C., H. den Uil, and H. Boerrigter. Production of FT transportation fuels from biomass; technical options, process analysis and optimisation, and development potential. *Energy*, 29(11):1743–1771, September 2004.

[4] C.N. Hamelinck and A.P.C. Faaij. Future prospects for production of methanol and hydrogen from biomass. *Journal of Power Sources*, 111(1):1–22, September 2002.

[5] M.J.A. Tijmensen, A.P.C. Faaij, C.N. Hamelinck, and M.R.M. van Hardeveld. Exploration of the possibilities for production of fischer tropsch liquids and power via biomass gasification. *Biomass and Bioenergy*, 23(2): 129–152, August 2002.

[6] X. Zhang, C. Solli, E.G. Hertwich, X. Tian, and S. Zhang. Exergy analysis of the process for dimethyl ether production through biomass steam gasification. *Industrial & Engineering Chemistry Research*, 48(24):10976–10985, December 2009.

[7] M. Gassner and F. Maréchal. Methodology for the optimal thermo-economic, multi-objective design of thermochemical fuel production from biomass. *Computers & Chemical Engineering*, 33(3):769–781, March 2009.

[8] M. Gassner and F. Maréchal. Thermo-economic process model for the thermochemical production of Synthetic Natural Gas (SNG) from lignocellulosic biomass. *Biomass & Bioenergy*, 33(11):1587–1604, 2009.

[9] L. Gerber, M. Gassner, and F. Maréchal. Integration of lca in a thermo-economic model for multi-objective optimization of sng production from woody biomass. `http://infoscience.epfl.ch/record/131210`, 2009. In Proceedings of the 19th European Symposium on Computer Aided Process Engineering, Cracow, Poland.

[10] L. Tock, M. Gassner, and F. Maréchal. Thermo-economic process model for thermochemical production of liquid fuels from lignocellulosic biomass. `http://infoscience.epfl.ch/record/143638`, submitted to biomass & bioenergy 2009.

[11] F. Maréchal, F. Palazzi, J. Godat, and D. Favrat. Thermo-Economic modelling and optimisation of fuel cell systems. *Fuel Cells*, 5(1):5–24, 2005.

[12] Belsim SA. `http://www.belsim.com`, last visited 01/2010.

[13] F. Maréchal and B. Kalitventzeff. Identification of the optimal pressure levels in steam networks using integrated combined heat and power method. *Chemical Engineering Science*, 52(17):2977–2989, September 1997.

[14] F. Maréchal and B. Kalitventzeff. Process integration: Selection of the optimal utility system. *Computers & Chemical Engineering*, 22: 149–156, May 1998.

[15] R. Turton. *Analysis, Synthesis, and Design of Chemical Processes*. Prentice Hall, Upper Saddle River, N.J, 3rd ed edition, 2009.

[16] G.D. Ulrich and P.T. Vasudevan. *A Guide to Chemical Engineering Process Design and Economics a Practical Guide*. CRC, Boca Raton, Fla, 2nd ed edition, 2003.

[17] T. Kaneko, F. Derbyshire, E. Makino, D. Gray, and M. Tamura. Coal Liquefaction. In *Ullmann's Encyclopedia of Industrial Chemistry*. Wiley-VCH, 2001.

Appendix

A. Thermo-economic model for BtL synthesis [10]

Table 6: Parameters of the DME and MeOH purification models (extracted from [10]).

	DME process			MeOH process	
Parameter	1st dist.	2nd dist.	3rd dist.	1st dist.	2nd dist.
$\epsilon_{murphree}$	85%	85%	85%	85%	85%
N^o plates	8	11	16	22	45
Feed plate	1	5	5	11	20
Reflux	0.7	0.7	2.6	1.3	1.3
Inlet T [^oC]	27	142	87.5	115	85
Inlet P [bar]	32	32	2	8	2

A.1. Thermodynamic Model

In the flowsheet modeling different thermodynamic models are used to calculate the liquid-vapor equilibrium. Ideal behavior is also assumed for the FT process streams because of the presence of hydrocarbons. However, for the synthesis and purification units of the DME and MeOH routes the effects of binary interactions should be considered. The liquid and vapor phase behavior is predicted by the equation of state model Peng-Robinson with the parameters obtained from DECHEMA Chemistry Data Series (http://www.dechema.de/) (Table 7).

The thermodynamic model used to calculate the interaction properties in the purification section is the activity coefficient model UNIQUAC for the methanol process and the NRTL model for the DME process. The parameters for each model are adapted from the DECHEMA Chemistry Data Series (http://www.dechema.de/) (Tables 8, 9 & 10).

Table 7: Interaction parameters for the Peng-Robinson model adapted from DECHEMA Chemistry Data Series.

Peng-Robinson model		
Compound i	Compound j	kij
N_2	MeOH	-0.2141
C_2H_6	MeOH	0.027
H_2O	MeOH	-0.0778
CO	MeOH	-0.2141
CO_2	MeOH	0.0583

Table 8: Binary parameters for the activity at infinite dilution (Ln(gam)=isGAM0+isGAMT/T) in the UNIQUAC model for the MeOH separation (adapted from DECHEMA Chemistry Data Series).

UNIQUAC model			
Compound i	Compound j	isGAM0	isGAMT
CH_4	H_2O	5.41	-0.25
CH_4	MeOH	6.2	0
N_2	H_2O	3.0	0
N_2	MeOH	3.0	0
H_2O	CO	6.96	0
H_2O	CO_2	8.69	-1543.5
H_2O	H_2	7.96	0
CO	MeOH	2.9	0
CO_2	MeOH	0.99	-121.85
H_2	MeOH	4.7	0

Table 9: Coefficients for the UNIQUAC equation for the free energy for the MeOH separation unit (adapted from DECHEMA Chemistry Data Series). The parameters Aij, Bij, Aji, Bji occur in the relationships (Uij - Ujj) / R = Aij + Bij / T and (Uji - Uii) / R = Aji + Bji / T where Uij, Ujj, Uji and Uii are the coefficients from the UNIQUAC equation for free energy and R is the perfect gas constant. Here temperature independency is assumed: Bij=Bji=0.

UNIQUAC model			
Compound i	Compound j	Aij	Aji
H_2O	MeOH	239.67	-153.37
H_2O	EtOH	178.14	-31.03
MeOH	EtOH	-6.039	-1.79
MeOH	DME	-145.46	433.94

Table 10: Coefficients from the NRTL equation for the free energy for the DME separation unit (adapted from DECHEMA Chemistry Data Series). The NRTL parameters ijC0, ijCT, jiC0, jiCT, ijA0, ijAT are involved in the relationships (gij-gjj) / R = ijC0 + ijCT· T, (gji-gii) / R = jiC0+jiCT·T and Aij=ijA0+ijAT·T where gij, gji, gii, gjj and Aij are the coefficients from the NRTL equation for the free energy and R is the perfect gas constant. Here temperature independency is assumed: ijCT=jiCT=ijAT=0.

NRTL model				
Compound i	Compound j	ijC0	jiC0	ijA0
H_2O	DME	567.58	-284.52	0.3
H_2O	MeOH	-86.60	386.75	0.3
DME	MeOH	187.80	-66.27	0.3

Upgrading of Biomass by Hydrothermal Carbonisation: Analysis of an Industrial-scale Plant Design

Berit Erlach, George Tsatsaronis

Technische Universität Berlin, Institute for Energy Engineering, Germany

Abstract: Hydrothermal carbonisation (HTC) is an artificial coalification process which converts wet biomass into a high quality fuel with properties similar to coal. The reaction takes place in water at approximately 200°C and 20 bar with a residence time of three to twelve hours. In order to commercialize the technology, an efficient heat recovery for preheating the biomass feedstock is essential. This paper presents a design for an industrial-scale HTC plant comprising a reactor, biomass pressurizing and preheating, heat recovery and biocoal dewatering and drying. Material and energy balances were modeled with the simulation software Aspen Plus. The influence of degree of carbonisation, feedstock moisture and degree of biocoal mechanical dewatering on overall performance are examined. The HTC process upgrades the biomass by increasing the heating value and decreasing the water content. However, approximately 10% of the feedstock energy is lost both as low-grade thermal energy and through soluble compounds in the waste water. To evaluate the potential benefit of hydrothermal carbonisation, a combined heat and power plant was added to the model and fired variously with biocoal and with wood chips. The resulting conversion chain efficiencies are compared.

Keywords: hydrothermal carbonisation, biocoal, biomass

1. Introduction

In the face of climate change and the need to decarbonize energy systems, biomass is discussed as a substitute fuel for thermal power plants. However, most raw biomass is ill suited for this purpose. Its high moisture content lowers the thermal efficiency of combustion, and its low energy density can result in higher transport costs. Because of the heterogenous nature of biomass, a fuel handling and combustion system tailored to one type of biomass is unlikely to work well with other types. Several upgrading technologies which convert fresh biomass into a uniform and higher quality fuel have been discussed in literature. These include pelletising, torrefaction [1], and the production of an oil/char slurry by pyrolysis [2]. One such technology, which has lately attracted new interest, is hydrothermal carbonisation (HTC) [3].

HTC, also referred to as hydrothermal pre-treatment, wet torrefaction or artificial coalification, is a process which converts organic matter into coal powder in hot pressurized water at approximately 175°C to 250°C. Research into the HTC reaction dates back to 1913 [4]. Much of the early work [4-6] focussed on the understanding of natural coal formation, employing HTC to simulate coalification under laboratory conditions. Early technical applications of HTC include several pilot-scale and commercial peat upgrading plants, in service between 1904 and 1964, and with capacities of 6000 to 50000 tonnes of product per year [7].

HTC can potentially mitigate climate change in two ways. First, biocoal, unlike biomass, can provide a chemically stable carbon sink. This option is widely discussed for biocoal from pyrolysis (biochar) [8] but has also been suggested for biocoal from HTC [3]. Second, biocoal as an upgraded biofuel with properties similar to coal is well suited for use in coal-fired power plants without requiring significant changes to the fuel handling and combustion system. Moreover, in combination with carbon-capture-and storage (CCS), a biocoal-fired power plant offers the potential for net negative carbon dioxide emissions.

This paper focuses on the second point, the application of HTC as an upgrading technology for biomass as a power plant fuel. A process design for an industrial-scale HTC plant is proposed, modeled and analyzed, both separately and in combination with a thermal heat and power plant.

Corresponding Author: Berit Erlach, Email: erlach@iet.tu-berlin.de

2. The HTC reaction

Hydrothermal carbonisation is not a single reaction but a complex network of reactions, including decarboxylation, dehydratisation, condensation and, under certain conditions, aromatization [9]. The reaction pathways have not been fully understood, but attempts to formulate a stoichiometric equation for the net overall reaction can be found in literature [4-5]. Based on experiment, Bergius [4, 10] suggests (1) and (2) for the maximum possible carbonisation of cellulose and lignin, respectively:

$$(C_6H_{10}O_5)_{50} = C_{263}H_{200}O_{26}+37\ CO_2+150\ H_2O \quad (1)$$

$$C_{11}H_{10}O_4 = C_{10}H_8O+CO_2+H_2O \quad (2)$$

A variety of feedstocks, such as wood, peat and moss, as well as model substances like glucose, cellulose and lignin, have been hydrothermally carbonised under a wide range of conditions on laboratory scale [5-7, 10-15].

In addition to the solid biocoal product, the reaction yields carbon dioxide and other gaseous products in small amounts and water with soluble compounds dissolved. The solid phase has been the most thoroughly studied, since most of the early research effort was aimed at natural coal formation. Indeed, complete mass and energy balances for all products were usually not reported.

The byproducts dissolved in water may include organic acids, furfural, phenolic structures and other intermediates and degradation products of (hemi-) cellulose and lignin [16]. Based on an analysis of published experimental data, Funke [9] reports that 5% to 30% of the feedstock resides in the liquid phase, but concludes that in a technical application this loss can probably be limited to 5% of the feedstock.

The gas phase obtained from the hydrothermal carbonisation of cellulose at 225°C was found to contain 91% CO_2, 6.4% CO, 0.8% H_2 and 0.4% hydrocarbons [10]. The quantity of feedstock converted into gaseous products as well as the volume fractions of H_2 and hydrocarbons increase with reaction temperature. For temperatures up to 250°C, between 1 and 7% of the feed stock carbon reacts to CO_2. [5-6]

The ratio r between carbon dioxide and water formed during the reaction defined as

$$r = \frac{mol\ CO_2}{mol\ H_2O} \quad (3)$$

has been reported to be in the range of 0.19 to 0.23 for cellulose and 0.30 to 0.42 for lignin [17]. According to reaction (1), the carbonisation of cellulose at 310°C, r is 0.247.

Figure 1 shows a van Krevelen diagram for raw and carbonized wood, cellulose, and lignin, with lignite and bituminous coal for comparison. H/C and O/C are the atomic ratios of hydrogen to carbon and oxygen to carbon, respectively. The carbonization products were obtained at moderate temperatures (175–230°C), except for the product of maximum carbonization according to (1), which was obtained at 310°C.

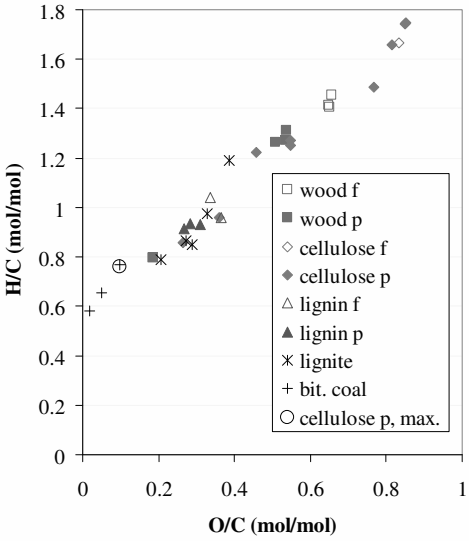

Fig. 1: Van Krevelen diagram for raw and carbonized wood, cellulose, and lignin. Data from [4-6,10,13-14]. f and p denote feedstock and carbonization product, respectively.

During the HTC process, the O/C and H/C ratios decrease, and between 20% and 90% of the feedstock oxygen is removed. For the carbonisation at moderate temperatures, the final product lies mostly in the range of lignite, independent of the feedstock.

The degree of carbonisation and the formation of gaseous and liquid byproducts depend on the reaction conditions, the most important of which appears to be temperature, residence time, pH, and biomass to water ratio.

A higher temperature and a longer residence time both lead to a higher degree of carbonisation. Over 90% of the feedstock hemicellulose was found to be converted at 200°C, while cellulose and lignin needed higher temperatures and were still only partially converted [14]. The higher the temperature, the more gaseous products are formed.

The pressure needs to be at least equal to the vapor pressure at the reaction temperature and does not otherwise seem to have a significant influence on the reaction [16]. The pH-value should be below 7, but decreases automatically during the reaction due to the formation of byproducts [9]. A high biomass to water ratio generally seems to have a positive effect on the biocoal yield, since it promotes the polymerization of dissolved monomers [16].

For technical applications, process efficiency is important. Mass yield γ_m and energy yield γ_e are defined as

$$\gamma_m = \frac{\dot{m}_{biocoal,dry}}{\dot{m}_{biomass,dry}} \quad (4)$$

$$\gamma_e = \frac{\dot{m}_{biocoal,dry} HHV_{biocoal,dry}}{\dot{m}_{biomass,dry} HHV_{biomass,dry}} \quad (5)$$

The mass flow rate $\dot{m}$ and the higher heating value *HHV* are based on dry matter.

If the calorific values of the feedstock and product are not available, the higher heating value on a dry basis in (MJ/kg) can be estimated using

$$HHV_{dry} = 34.91c + 117.83h - 10.34o - 1.51n + 10.05s - 2.11a \quad (6)$$

with *c*, *h*, *o*, *n*, *s*, *a* being mass fractions of carbon, hydrogen, oxygen, nitrogen, sulfur and ash [18].

The overall reaction is exothermic and results in oxygen being removed from the feedstock, thereby increasing its carbon content and calorific value. The stronger the carbonisation, the higher the calorific value of the resulting biocoal, but the lower the mass yield, (because more oxygen is removed), and the lower the energy yield, (because more of the feedstock energy is released as heat of reaction). Figure 2 shows the energy yield versus the higher heating value of the product. The lines depict the reaction according to (1) and (2), and the carbonisation of wood with two values of *r*, assuming that biocoal, carbon dioxide and water are the only reaction products. The filled points represent experimental results from literature.

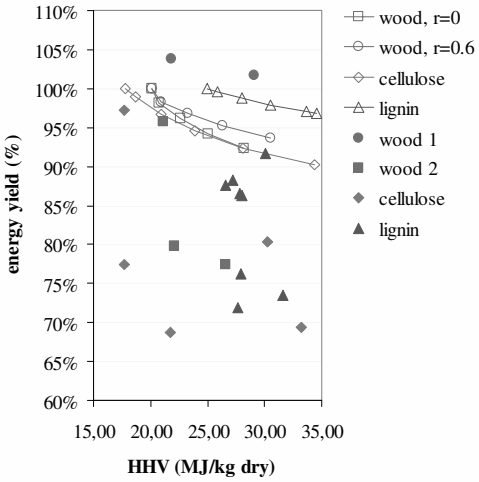

Fig 2: Energy yield versus higher heating value. Data from [4-6,10,13-14].

The four depicted reaction models for wood, cellulose and lignin represent upper bounds, since they do not consider carbon losses to the liquid phase. Compounds dissolved in the liquid phase offer one explanation as to why the energy yield of most measured data from literature is significantly lower than suggested by the reaction models. Some experimental data show energetic yields over 100%. In this case recycled water from previous HTC experiments was used, and organic compounds dissolved in the water may have been recovered with the solid product [13].

With respect to the relatively low mass and energy yields obtained from some reported data, one should recall that most of the early research was not concerned with the development of efficient technical processes. These investigations focused on the properties of the solid phase and little attempt was made to minimize losses in the form of dissolved compounds. For an HTC-process with waste water recycling, the energy yield in an industrial scale plant is estimated to be around 95% [13].

Biomass also contains mineral matter. Some elements remain in the biocoal, while others are dissolved. Experimental results for the HTC of threshed hay indicate that Cl, Br, K and Na are completely dissolved, whereas P, S, Ca and Mg are partly dissolved, and Si, Al and Fe remain almost entirely in the solid product [19].

3. Design considerations for an industrial-scale HTC plant

A crucial parameter for a technical fuel is its water content, since a high water content dramatically decreases the efficiency of combustion. Fresh wood has a water content of 50 to 60% [20]. Due to its structure, mechanical dewatering is not possible to any significant extent. By destroying the colloidal structure and removing oxygen-containing functional groups from the feedstock, HTC makes the product hydrophobic [14] and amenable to mechanical dewatering. Experiments show that biocoal from organic waste can be mechanically dewatered down to 32% to 43% water on a mass basis [21].

Regarding the degree of carbonisation, there is a trade off between the heating value and the energy yield, as shown in Fig 2. This may lead one to the conclusion that a mild carbonisation is probably advantageous. However, less carbonisation also means less reaction heat and, therefore, less heat available for preheating and drying.

The HTC process can be batch or continuous. A continuous process is better suited to efficient heat recovery, but requires feeding biomass against pressure. Since the reaction takes place in water, pumping a biomass slurry seems technically preferable to lock hopper delivery. Slurry pumps have been used in peat upgrading plants, but then biomass is possibly more difficult to turn into a pumpable slurry than peat. The pressurization of the biomass is likely to be one of the technical challenges for a continuous HTC plant [9].

The biomass should be preheated using heat recovery from the reaction products. In the peat upgrading plants, slurry temperatures greater than 100°C caused fouling and clogging within heat exchangers [22]. Direct heat exchange was therefore necessary for preheating at higher temperatures.

For commercial plants, treatment and disposal of waste streams needs consideration. The gaseous products will need to be oxidized since they contain minor amounts of carbon monoxide. The water from the reactor contains organic compounds and minerals and will most likely require treatment. For peat processing plants, the recovery of valuable chemicals from the waste water and methane production via anaerobic fermentation have been suggested [23]. Chlorine and some minerals are also dissolved in the liquid phase. These might require treatment of the waste water, but their removal improves the quality of the biocoal, by decreasing its ash content and reducing problems with corrosion during combustion.

To reduce the amounts of waste water produced and fresh water needed, the water from the reaction products should be recycled [16]. Since the reaction products leave the reactor at a high temperature, this is advantageous for preheating. The low pH of the recovered water makes it well suited for preparing the biomass slurry, since a low pH is favorable for the reaction. The use of recycled process water is also beneficial for the carbon balance of the reaction [13].

4. Process model of a HTC plant

For this work, a design for an industrial-scale HTC plant with a continuous reactor and a capacity of 5000 kg/h as-received biomass was developed. The flow sheet, which is based on the design of a peat upgrading plant [7] is shown in Fig. 3. Mass and energy balances were modeled with the simulation software Aspen Plus. Several simulation cases were created by varying important parameters such as degree of carbonisation, feedstock moisture and degree of mechanical dewatering of the biocoal.

Biomass is mixed with water to create a pumpable slurry. The slurry is pressurized to 0.35 MPa and preheated to 101°C in heat exchangers with 0.1 MPa and 0.6 MPa steam. It is then further preheated by mixing with steam and pressurized to 2.5 MPa in three steps. Before the slurry is fed to the reactor, surplus water is removed. Additional steam is added to the reactor to reach the defined reaction temperature of 210°C in the base case. The biocoal slurry is de-pressurized in four steps to 0.1, 0.6, 0.35 and 0.1 MPa. Steam is recovered in each step. Heat from the reactor off-gas is recovered to produce steam at 0.6 MPa. The biocoal is mechanically dewatered in a filter press, and dried to a final water content of 10%. Water from the filter press is recovered to prepare the biomass slurry, the remainder is discharged as waste water. Waste water treatment is probably required but is not considered in this work. Since the heat recovered from the process is not sufficient to achieve the reactor temperature, additional steam must be produced in a boiler. The boiler and drier are fired with natural gas (and not biocoal) for operational reasons.

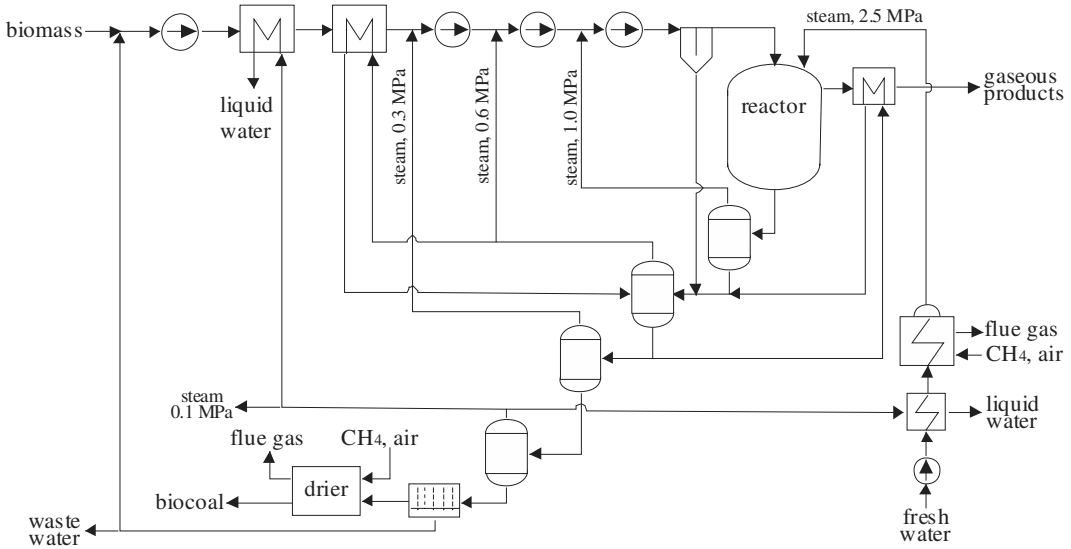

Fig. 3: Flow sheet of the proposed HTC plant design.

4.1. Modeling assumptions

The following assumptions are employed in the base case and for all other simulation cases if not otherwise stated. The feedstock is fresh willow wood with a water content of 60% in the base case. The composition of wood and of mildly and strongly carbonised biocoal is given in Table 1, while operating parameters are listed in Table 2. Note also

- The reactor is modeled as a black box using mass and energy balances. The ratio r is assumed to be 0.23. The percentage of oxygen removed from the feedstock is assumed to be 30% for mild and 60% for strong carbonisation.
- The gaseous products consist of carbon dioxide and water vapor only.
- All mineral matter (ash) remains in the solid product.
- The composition of dissolved organics is the same as the composition of the ash-free biocoal, approximately 5% of the feedstock carbon ends up as soluble organics.
- Ambient air temperature is 15°C, dry air composition is 79% N_2, 21% O_2, and the relative humidity is 60%.
- Natural gas is modeled as pure methane.

The water to biomass ratio at the slurry pump inlet of 1:1 corresponds to a dry matter content of 20%.

Table 1: Composition and heating value of wood and biocoal; mass and energy yield of strong and mild HTC. All values on a dry matter basis.

	wood	biocoal strong HTC	biocoal mild HTC
c	47.5%	65.1%	54.6%
h	6.2%	5.7%	6.0%
n	0.4%	0.6%	0.5%
s	0.0%	0.0%	0.0%
o	44.1%	25.9%	36.7%
a (ash)	1.8%	2.6%	2.1%
HHV (MJ/kg)	19.29	26.75	22.30
mass yield		66.2%	81.4%
energy yield		91.8%	94.2%

Table 2: Operating conditions of the HTC plant.

reactor operating conditions	210°C, 2.3 MPa
water to biomass ratio at slurry pump	1:1
water to biomass ratio at reactor inlet	1:1
biocoal water content after filter press	30%
slurry pump efficiency	45%
reactor heat loss	5 kW
biomass slurry / biocoal slurry heat loss	13 kW / 12 kW
drier and boiler heat losses	3%
boiler excess air fraction	15%
drier exhaust	110°C, 60vol% H_2O

4.2. Results

Table 3 shows the energy balance for the base case (HTC-1). Natural gas for the boiler and for the biocoal drier amount to 4.7% of the total energy input of the plant. 87% of the total energy input is converted to biocoal. Heat losses and waste heat amount to 10% of the total energy input. Around 20% of these losses are surplus steam at 0.1 MPa which cannot be used in the plant since there is no heat demand at this low temperature level. If heat demand exists on-site, for example for space heating, this heat could be utilized. The other waste heat streams are the exhaust streams from the boiler, drier and reactor, and the thermal energy at temperatures below 100°C contained in the biocoal and in the waste water. Organic compounds dissolved in the waste water amount to 2.6% of the total energy input. Around 5% of the biomass energy fed to the reactor is dissolved in water, but about half of this is assumed to be recovered since it remains within the solid product in the drier. 6.6% of the feedstock dry matter is converted to carbon dioxide.

Simulations were conducted using mild and strong carbonisation. The reactor temperature, the biomass to water ratios at pump and reactor inlet, the degree of mechanical dewatering, and the biomass water content were also varied.

Table 4 shows the results of all simulation cases. The energy efficiency of the plant is defined as

$$\eta = \frac{\dot{m}_{biocoal} HHV_{biocoal}}{\dot{m}_{biomass} HHV_{biomass} + \dot{m}_{CH4} HHV_{CH4} + \dot{W}} \quad (7)$$

where $\dot{W}$ is the electric power required for pumps and the filter press.

With mild carbonisation (HTC-2), the biocoal energy is 2.6% higher than with strong carbonisation (HTC-1). However, in the mild carbonisation reaction less heat is released, and consequently more than twice as much steam has to be provided by the gas boiler in order for a reactor temperature of 210°C to be reached. Therefore, the overall energetic efficiency of the HTC plant is actually 0.5 percentage points lower if mild carbonisation is employed, and a higher share of the total energy input is natural gas.

A lower water content of the biomass (HTC-3, HTC-4) reduces the slurry mass flow that needs to be preheated, and therefore also the amount of steam required from the boiler. Plant efficiency increases by 2 to 3 percentage points if biomass with 50% water content is used as a feedstock.

Table 3: Energy balance for the base case HTC-1.

Energy balance	**(kW)**
biomass energy	**10716**
natural gas consumption, total	**528**
drier	314
boiler	215
electricity consumption, total	**22**
slurry pumps	19
filter press	3
biocoal energy	**9837**
compounds in waste water	**296**
heat losses and waste heat, total	**1132**
surplus steam at 0.1 Mpa	223
exhaust gases and vapours	643
other	265

Depending on the type and particle size of the biomass, the water to biomass ratio required for pumping can vary. HTC-6 represents a case with a higher water ratio at the pump inlet, resulting in 8% dry matter. This additional water increases the heat demand for preheating the biomass slurry, resulting in an efficiency decrease of 5.7 percentage points. Natural gas provides more than 10% of the total energy input in this case, due to the additional fuel used by the boiler. In HTC-7, more water is removed before the reactor inlet, after pressurizing the biomass. This has little effect on plant efficiency, since the mass flow that needs to be preheated remains the same. This parameter can therefore be adjusted to the needs of the chemical reaction without considering its effects on the energy balance. In HTC-5, a lower degree of dewatering in the filter press is assumed. The water which is not removed mechanically in the filter press has to be evaporated in the drier, thereby increasing the fuel consumption of the drier and decreasing the plant efficiency by 2.2 percentage points.

Increasing the reactor temperature by 20°C results in 30% more boiler fuel and a decrease in efficiency by 0.4 percentage points, given that the reaction stoichiometry is not affected. Since a higher reaction temperature usually requires a lower residence time to reach the same degree of carbonisation, accepting a lower efficiency in order to speed the process might prove

Table 4: Results for various simulation cases of the HTC-plant. The feed stock energy is 10716 kW in all cases.

	HTC-1	HTC-2	HTC-3	HTC-4	HTC-5 [1)]	HTC-6 [2)]	HTC-7 [3)]	HTC-8 [4)]
HTC reaction	strong	mild	strong	mild	strong	strong	strong	strong
feed stock water content	60%	60%	50%	50%	60%	60%	60%	60%
biocoal energy (kW)	9837	10091	9990	10258	9914	9803	9849	9845
natural gas consumption (kW)	528	883	412	695	907	1265	544	597
electricity consumption (kW)	22	22	20	20	22	48	21	30
steam demand for reactor (kg/h)	263.5	611.6	111.3	368.0	263.7	1171.6	278.3	351.3
energetic efficiency	87.3%	86.8%	89.6%	89.7%	85.1%	81.5%	87.3%	86.8%
energy input as natural gas	4.7%	7.6%	3.7%	6.1%	7.8%	10.5%	4.8%	5.3%

[1)] HTC-5: biocoal water content after filter press = 45% (HTC-1: 30%)

[2)] HTC-6: water to biomass ratio for slurry pump: 4:1 (HTC-1: 1:1)

[3)] HTC-7: water to biomass ratio at reactor inlet: 0.4:1 (HTC-1: 1:1)

[4)] HTC-8: reactor temperature =230°C (HTC-1: 210°C)

worthwhile. The time/temperature correlation, as well as the effects on reaction stoichiometry, needs to be further studied in order to select an optimal reactor temperature.

5. Conversion chain efficiencies of HTC and subsequent combustion

Hydrothermal carbonisation can convert biomass into a higher quality fuel with a much reduced moisture content and a higher heating value of the dry matter similar to lignite. However, in the process about 13% of the energy input is lost as low grade heat and through compounds dissolved in the waste water. To find out if HTC can really contribute to the more efficient use of biomass, HTC and the subsequent combustion of the biocoal need to be compared with the direct combustion of raw biomass. For this purpose, an industrial combined heat and power (CHP) plant was added to the Aspen Plus simulation, and fired alternatively with biocoal and with wood chips. The CHP plant, comprising a simple steam cycle with a back-pressure turbine, is shown in Fig. 4.

Two designs of a wood-fired plant are considered. First, the combustion of fresh wood and second, the combustion of dried wood with on-site drying to a water content of 10%, using a steam extraction for supplying the heat for the drier.

In the base case, it is assumed that biocoal is produced off-site using decentral HTC plants. On the other hand, siting the HTC and the CHP plants together eliminates the need for the natural gas fired boiler for the HTC plant, since steam for the HTC reactor and the biocoal drier can be taken from a turbine extraction. This integrated design is modeled as case HTC-9. All simulation cases are designed to deliver 20 MW of process stream at 5 MPa. The operating parameters and modeling assumptions are listed in Table 5. The main results for the CHP plant and the overall conversion chain are shown in Table 6.

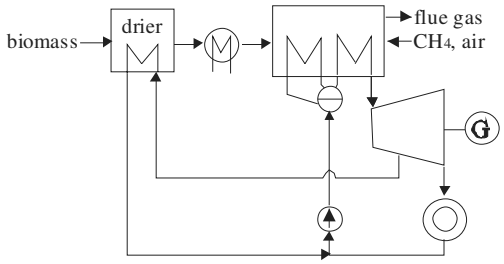

Fig 4: Flow sheet of the cogeneration plant with drier.

Table 5: Operating parameters and modelling assumptions.

turbine inlet conditions	510°C, 7.0 MPa
condensate return	152°C, 5 MPa
extraction pressure (for drier)	1.0 MPa
flue gas exit temperature	162°C
turbine isentropic efficiency	90%
generator efficiency	98.5%
boiler and drier heat loss	3%
boiler water-side pressure loss	10%
boiler excess air fraction	15%
drier exhaust	110°C, 60 vol% H_2O

Table 6: Results for simulation cases of the CHP plant and the overall conversion chain. All cases deliver 20,000 kW of process steam.

HTC	HTC-1 strong	HTC-2 mild	HTC-3 strong	HTC-4 mild	HTC-9 [1)] strong	wood-1	wood-2	wood-3	wood-4
feedstock water content	60%	60%	50%	50%	60%	60%	60%	50%	50%
CHP plant									
CHP plant fuel moisture	10%	10%	10%	10%	10%	60%	10%	50%	10%
CHP plant fuel energy (kW)	30259	30808	30256	30808	32218	41342	45448	37111	39299
electricity production (kW)	5474	5473	5473	5473	5579	5473	7427	5473	6583
heat extraction for drier (kW)					1560		9712		5521
electrical efficiency	18.1%	17.8%	18.1%	17.8%	17.3%	13.2%	16.3%	14.7%	16.8%
energetic efficiency	84.2%	82.7%	84.2%	82.7%	84.2%	61.6%	81.7%	68.6%	81.7%
flue gas volume (m^3/MJ_{th})	0.580	0.599	0.579	0.599	0.580	1.044	0.617	0.863	0.617
overall system									
biomass energy (kW)	32963	32716	32455	32183	35080	41342	45448	37111	39299
natural gas (kW)	1625	2695	1248	2087		0	0	0	0
net electricity production (kW)	5407	5407	5414	5412	5507	5473	7427	5473	6583
electrical efficiency	15.6%	15.3%	16.1%	15.8%	15.7%	13.2%	16.3%	14.7%	16.8%
energetic efficiency	73.5%	71.7%	75.4%	74.2%	72.7%	61.6%	60.3%	68.6%	67.6%
exergetic efficiency	33.0%	32.6%	33.8%	33.6%	32.2%	27.2%	28.8%	30.4%	31.4%

[1)] integrated design of HTC and CHP plant

In cases wood-2 and wood-4 with on-site wood drying, the wood is cooled to 60°C after drying for safety reasons. Complete combustion in the boiler is assumed in all simulation cases.

Pre-drying of the wood and HTC both increase the energetic efficiency of the CHP plant by more than 20 percentage points, and also reduce the boiler exhaust gas volumetric flow by more than 40%, which will reduce costs for duct work and the chimney. The CHP plant efficiency in case HTC-1 (strong carbonization) is about 2.5 percentage points higher than in case wood-2, where pre-dried wood is used as the fuel.

The most interesting results, however, are the efficiencies of the overall conversion chain from raw biomass to heat and electricity. Pre-drying the wood (wood-2) does not actually improve the efficiency of the conversion chain in comparison to the combustion of raw wood (wood-1), since the heat provided to the drier is eventually lost in the exhaust of the drier. HTC, on the other hand, leads to an increase of the conversion chain energetic efficiency of 11.8 percentage points compared to the combustion of the raw wood in the case of strong HTC (HTC-1) and 10.1 percentage points when mild HTC is employed (HTC-2). This is due to the fact that in HTC, a large part of the water is removed from the biocoal mechanically, which consumes much less energy than thermal drying. In Table 7, drying to 10% water content and strong HTC with subsequent drying of the biocoal to 10% water content are contrasted. The energetic efficiency of the HTC is about 5 percentage points higher.

The simulation cases employing raw wood with a water content of 50% show the same tendencies, although less pronounced. The advantage in conversion chain efficiency is 6.8 and 5.5 percentage points for the strong (HTC-3) and mild carbonisation (HTC-4), respectively.

Table 7: Energy balance of HTC and drying.

		HTC-1	wood-2
raw biomass energy	(kW)	32963	45448
upgraded biomass energy	(kW)	30259	45448
steam demand	(kW)		9712
natural gas demand	(kW)	1625	
electricity demand	(kW)	67	
energetic efficiency	(-)	87.3%	82.4%

In the case with pre-drying, the electricity production is 36% higher than in the case of raw wood combustion. This is due to the fact that the drier creates an additional heat demand, resulting in more electricity being produced in cogeneration. The ratio between net electricity production and

heat delivery (heat for the drier not included) is 0.37 in this case, compared to 0.27 for the combustion of raw wood. In the case of HTC, on the other hand, the net electricity production is 1% lower than in the case of raw wood combustion, since some electricity is consumed in the HTC plant. The electrical efficiency for the case with pre-drying is 0.7 percentage points higher than for the case with strong HTC.

Compared with drying, HTC leads to a higher overall energetic efficiency of the conversion chain, but to a lower electricity to heat ratio and a slightly lower electrical efficiency. For a more revealing comparison, the exergetic efficiency should be taken into consideration, which is 4.2 percentage points higher for the HTC case (HTC-1) than for the pre-drying case (wood-2). The exergetic efficiency for the case with pre-drying is 1.6 percentage points higher than for the combustion of raw wood.

It should be pointed out that the advantage in energetic efficiency of HTC over drying shown for the CHP scenario is possibly limited to back-pressure steam cycles, where the entire turbine outlet steam flow is used as process steam. Further work on HTC in combination with other types of power plants is planned.

The integrated design of the HTC-plant with the CHP plant (HTC-9) has no thermodynamic advantage over the stand-alone configurations. The overall energetic efficiency is indeed 0.8 percentage points lower. This is due to the fact that the natural gas used in the stand-alone plant is replaced by additional use of biomass in the integrated process. However, the integrated design might have economic advantages over the stand-alone plant, since it eliminates the need for the boiler at the HTC plant, and it replaces the use of natural gas with the use of more biomass. On the other hand, transport of wood chips to the CHP plant is likely to be more expensive than transport of biocoal from decentral HTC units to a CHP plant. For a conclusive answer, the two arrangements need to be analyzed and compared from an economic perspective.

6. Conclusions

Hydrothermal carbonisation (HTC) converts biomass into a high quality fuel, biocoal, which can be readily used in power plants. By removing oxygen from the biomass feedstock and by destroying its structure, HTC increases the heating value and facilitates mechanical dewatering, both of which markedly increase the efficiency of subsequent combustion.

The suggested design for an industrial-scale HTC plant results in energetic efficiencies of 85 to 90%, based on the higher heating value. Since the exothermic heat from the HTC reaction is not sufficient to preheat the biomass and dry the biocoal, additional natural gas is required. Although a mild (less complete) HTC reaction results in a higher energetic yield for the reaction itself, the overall plant efficiency is higher when strong (more complete) carbonisation is employed. The biomass to water ratio required for pumping the slurry has a large impact on the plant efficiency.

In comparison with direct combustion of fresh and pre-dried wood as a fuel for an industrial CHP plant, pre-treatment of the wood with HTC leads to a 5 to 12 percentage points increase in energetic efficiency for the overall conversion chain. The overall electrical efficiency, however, is slightly higher when the wood is pre-dried rather than hydrothermally carbonised, due to the electricity consumption of the HTC plant.

More research is required on the influence of reaction conditions on the formation of byproducts, especially compounds dissolved in the waste water, and on their remedial treatment and disposal.

References

[1] Bergman, P.C.A. , and Kiel, J.H.A., 2005, Torrefaction for Biomass Upgrading, *Proc. 14th European Biomass Conference & Exhibition*, ETA-Florence, Italy, and WIP-Munich, Germany.

[2] Henrich, E. et al., 2009, Cost estimate for biosynfuel production via biosyncrude gasification, Biofuels, bioproducts & biorefining, 3(1), pp. 28–41.

[3] Titirici, M., et al, 2007, Back in the Black: Hydrothermal Carbonization of Plant Material as an Efficient Chemical Process to Treat the CO2 Problem?, New Journal of Chemistry, 31, 787–789.

[4] Bergius, F., 1913, Die Anwendung hoher Drucke bei chemischen Vorgängen und eine Nachbildung des Entstehungsprozesses der Steinkohle, Willhelm Knapp, Halle (Saale).

[5] Berl, E., and Schmidt, A., 1932, Über die Entstehung der Kohlen II. Die Inkohlung von Cellulose und Lignin in neutralem Medium, Liebigs Ann. Chem. 493, pp. 97−123.
[6] Schuhmacher, J. P., et al, 1960, Chemical Structure and Properties of Coal XXVI – Studies on Artificial Coalification, Fuel, 39, pp. 223−234.
[7] Mensinger, M., 1980, Wet Carbonization of Peat: State-of-the-Art Review, *Symposium Proceedings*: *Peat as an Energy Alternative.* IGT, Chicago, Ill., pp. 249−280.
[8] Lehmann, J., et al., 2006, Bio-char Sequestration in Terrestrial Ecosystems – a Review, Mitigation and Adaptation Strategies for Global Change, 11, pp. 403–427.
[9] Funke, A. and Ziegler, F., 2009, Hydrothermal Carbonization of Biomass: A Literature Survey Focussing on its Technical Application and Prospects, *17th European Biomass Conference & Exhibition*, ETA-Florence, Italy, and WIP-Munich, Germany, pp. 1037−1050.
[10] Bergius, F., 1928, Beiträge zur Theorie der Kohleentstehung, Die Naturissenschaften, 16 (1), pp. 1−10.
[11] Geissler, C., and Belau, L., 1971, Zum Verhalten der stabilen Kohlenstoffisotope bei der Inkohlung, Zeitschrift für angewandte Geologie, 17 (1/2), pp. 13−17.
[12] Titirici, M., et al, 2008, Hydrothermal carbon from biomass: a comparison of the local structure from poly- to monosaccharides and pentose/hexoses, Green Chemistry, 10, pp. 1204−1212.
[13] Kleinert, K., and Wittmann, T., 2009, Carbonisation of Biomass Using a Hydrothermal Approach: State-of-the-Art and Recent Developments, *17th European Biomass Conference & Exhibition*, ETA-Florence, Italy, and WIP-Munich, Germany, pp. 1683−1687.
[14] Yan, W. et al., 2009, Thermal Pretreatment of Lignocellullosic Biomass, Environmental Progress & Sustainable Energy, 28 (3), pp. 435−440.
[15] Berl, E., and Schmidt, A., 1928, Über das Verhalten der Cellulose bei der Druckerhitzung mit Wasser, Liebigs Ann. Chem. 461, pp. 192−220.
[16] Funke, A. and Ziegler, F., Hydrothermal Carbonization of Biomass: A Summary and Discussion of Chemical Mechanisms for Process Engineering, Biofuels, Bioproducts and Biorefining, accepted for publication.
[17] Ruyter, P., 1982, Coalification model, Fuel, 61, pp. 1182−1187.
[18] Channiwala, S. and Parikh, P., 2002, A Unified Correlation for Estimating HHV of Solid, Liquid and Gaseous Fuels, Fuel, 2002, 81, pp. 1051−1063.
[19] Pels, J.R., and Bergman, P.C.A., 2006, TORWASH. Proof of Principle. Phase 1, Technical Report, ECN-E-06-021, Energy research Centre of the Netherlands (ECN), Petten.
[20] Kaltschmitt, M., et al., eds., 2009, Energie aus Biomasse, 2nd ed., Springer, Berlin, Chap. 9, p. 358.
[21] Ramke, H., 2009, Wässrige Phase aus der HTC: Zusammensetzung und Abbaubarkeit, Presentation at HTC-Fachveranstaltung Johann Heinrich von Thünen Institut, Eberswalde, URL: http://www.bmelv.de/cae/servlet/contentblob/429750/publicationFile/23089/HTC-Ramke.pdf.
[22] Hägglund, S. E. (ed.), 1960, Vatkolning av Torv AB, Technical Report, Svensk Torvförädling, Lund, Sweden.
[23] Lau, F.S., et al., Peat Beneficiation by Wet Carbonization, 1987, Int. J. Coal Geology, 8, pp. 111−121.

Acknowledgments: This work was funded by the German Federal Ministry of Education and Research as part of the joint research project 01LS0806B. The authors acknowledge useful discussions with the other project partners.

Gasification of Giant Sensitive Plants in a Fixed Bed Reactor

Thanasit Wongsiriamnuay and Nakorn Tippayawong

Department of Mechanical Engineering, Faculty of Engineering, Chiang Mai University, Chiang Mai, Thailand

Abstract: A giant sensitive plant (Mimosa pigra L.) is a fast growing and spreadable weed. It infests strongly along the rivers, surrounding large reservoirs, wetland reserves and agricultural fields. Its invasion threatens the production and preservation values of wetlands, and poses a major problem in agricultural areas. To avoid food-fuel dilemma, the weed may be utilized as a biorenewable energy source. In this study, it was used as feedstock for generation of producer gas. Mimosa sample were collected, and air dried. They were subsequently milled, sieved and classified into fractions of uniform particle size between 0.3 and 0.6 mm. Fuel characterization was performed using proximate and ultimate analyses. Gasification of giant sensitive plants was carried out at atmospheric pressure in a laboratory-scale fixed bed reactor to investigate the effect of reactor temperature and catalyst biomass ratio on gas yields and product gas composition. The product gas from thermochemical process was found to contain high CO and H2 which was a useful low heating value gaseous fuel. With an increase in temperature, gas yield was found to increase while char and tar were found to decrease. Increasing catalyst to biomass ratio was found to result in an increase in hydrogen, and a decrease in carbon monoxide. It appeared that the weed can be utilized as a useful renewable fuel.

Keywords: Biomass, Gasification, Mimosa, Renewable energy, Fixed bed.

1. Introduction

Mimosa, known in Thai as a giant sensitive plant, is a native plant of Central and South America. It was purposely introduced to Thailand in the late 1940s as a green manure and cover crop in tobacco plantations [1]. It is a leguminous thorny shrub that can grow to a height of six meters. Mimosa is able to form mono-specific stands, replacing the native wet vegetation and thereby reducing the available habitats of native flora and fauna. It is considered to be one of the worst environmental weeds of wetland in Thailand. When faced with an extensive weed infestation, it is natural to find ways to utilize it. Mimosa has been utilized for its ornamental value, medicinal use, green manure and erosion control. It has also been used as animal feed, timber and biomass material [1]. In Thailand, it has been used for firewood, temporary fences, and tested for fiberboard. However, the use is still limited in rather small scale applications. Alternative energy utilization method may offer different options and a mean for the weed management.

Thermochemical processing is recognized as the most important available technology for biomass conversion. Gasification is viewed to be a suitable conversion technology that offers high thermal efficiency and environmental acceptability. Gasification process is favourable for producing low to medium calorific value gas. If the weed is gasified efficiently, it may generate a high yield of clean product gas. Thermal decomposition of mimosa has been investigated [2, 3]. It was viewed to have potential as a bioenergy source via gasification. However, tar can potentially impair the product gas quality. Using of catalysts in the gasification process has been proved to be an effective method to reduce tar and improve gasification efficiency. Dolomite is among the cheapest and most available catalysts used to control tar. Natural dolomite has been shown to reduce tar content in producer gas [4, 5].

In this work, giant sensitive plants were used as a biomass feedstock for the generation of producer gas. A laboratory scale, fixed bed reactor was developed. The thermochemical conversion of mimosa was performed in the fixed bed reactor. The influence of different operation conditions, including reactor temperature and catalyst to biomass ratio on product yields (gas, char, and tar) and the composition of fuel gas in terms of H_2 and

H_2/CO was investigated. Air was used as gasification medium. Natural dolomite was used as an *in situ* catalytic gas conditioning agent.

2. Experimental setup

2.1. Sample characterization

Mimosa samples collected in agricultural zone in Chiang Mai, Thailand were used. The collected stalks were cleaned and air dried naturally in a dry store room at ambient condition. The dried samples were later ground in a high speed rotary mill, screen sieved and used for further analysis. The proximate analysis of the weed was carried out according to standard norms. The determination of moisture, volatile matter and ashes was performed following the standards; ASTM D 3173, ASTM D 3175. ASTM D 1372, ASTM 3177, respectively. The fixed carbon was calculated by difference to 100%. The determination of the ultimate analysis was made using a CHN-932 elemental analyzer (ASTM F 3174). The higher heating value of the weed waste was determined with a Parr calorimeter bomb (ASTM 5865). These parameters are displayed in Table 1. One can see that the weed has a high content of volatile matter and low content of ash, which is very interesting with respect to its applications in gasification and pyrolysis processes. The low N content ensures that thermal NO_x formation during the gasification process is negligible.

2.2. Test apparatus and procedures

Gasification experiments were performed at an atmospheric pressure using air as gasification medium. The experimental setup is shown schematically in Fig. 1. The fixed bed reactor was equipped with electric heaters around its perimeter which was covered with a thick insulation layer.

Table 1. Properties of the air dried mimosa stalk.

Property	Quantity
Proximate analysis (% w/w)	
Moisture	1.6
Volatile	71.1
Fixed carbon	23.6
Ash	3.7
Ultimate analysis (% w/w)	
Carbon	43.9
Hydrogen	6.0
Nitrogen	1.4
Oxygen	48.7
Higher heating value (MJ/kg)	17.5

Its setup consists of the fixed bed reactor, an air compressor and an feed air heater. The reactor was made of 1Cr18Ni9Ti stainless steel tube. The effective height of the reactor was 900 mm, with an internal diameter of 60 mm. Two type K thermocouples were used to measure and control the temperatures in the middle of the gasifier and the biomass in a basket.

A collection module was used as cooling unit for fuel gas cooling and tar capture. It consists of two series of impinger bottles containing a solvent for tar absorption, placed separately in two cold baths. The first three impinger bottles were immersed in a temperature below 5 °C, whereas, the next three impinger bottles were cooled at a temperature under −20 °C which tar and moisture will be completely collected. The tar aerosols were collected by both condensation and absorption in the solvent. Each impinger bottle was filled with approximately 100 ml of isopropanol, which was considered to be the most suitable solvent for tar absorption [5]. The gas flow rate was measured with a volume meter. The cool, dry, clean gas was sampled using gas bags and analyzed on a Shimadzu Model GC-8A gas chromatograph fitted with a ShinCarbon ST Micropacked column and a thermal conductivity detector, for measuring volumetric concentration of H_2, O_2, N_2, CH_4, CO,

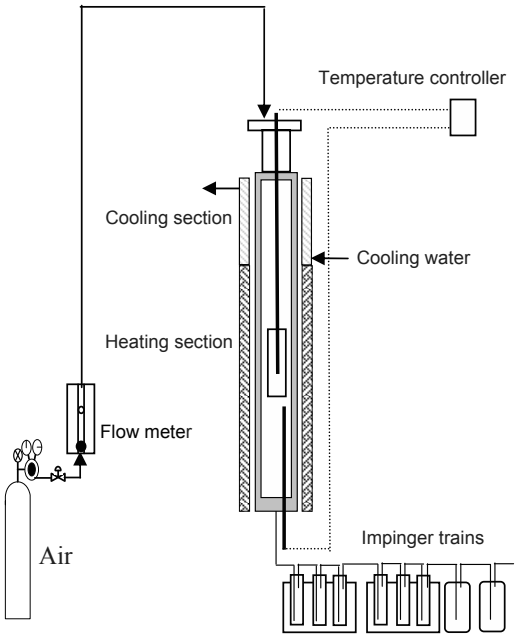

Fig. 1. Gasification experimental setup.

Corresponding Author: Thanasit Wongsiriamnuay, Email: w_thanasit@hotmail.com

CO_2. Standard gas mixtures were used for quantitative calibration.

Initially, the electric heater was switch on to heat the reactor. Once the set point temperature was achieved in the gasification reactor, the biomass was displaced from the cooling section to the heating section. Air was fed from the top of the gasification reactor. When stabilization was reached with respect to the temperatures, gas sampling and analysis were carried out. It was normally completed in about 20 min. Experiments were performed for (i) air gasification at 500 cm^3min^{-1} with varying temperature between 600 – 900°C and (ii) catalytic gasification with natural dolomite at varying proportions (% w/w referred to catalyst and biomass ratio) at 900°C with the same air flow condition. All experiments were carried out isothermally and initial mimosa mass of 10 g was used.

3. Results and discussion

3.1. Product yields

Fig. 2 shows effect of reaction temperature on the product yields from gasification of mimosa without presence of catalyst. The gas yields were found to increase from about 51% to 64% as the reaction temperature was raised from 600°C to 900°C. The char and tar fractions appeared to decrease with increasing temperature. Changes from 700°C to 800°C showed only marginal effect on the yields. Fig. 3 shows the product yields from gasification of mimosa at different catalyst to biomass ratios between 0.5 – 2.0 at a fixed temperature of 900°C. It was observed that while the char yield stayed relatively constant, the gas yield appeared to go through a maximum of 72% at a catalyst to biomass ratio of 1.0.

3.2. H_2 and H_2/CO yields

Figs. 4 and 5 show effects of reaction temperature on the H_2 and H_2/CO yields from non-catalytic gasification. It can be seen from the experimental results that both the hydrogen yields and hydrogen to carbon monoxide ratios were primarily influenced by the operating temperature. Changing the temperature from 600 to 900°C resulted in an increase in the H_2 yields [6, 7], while H_2/CO yields were found to decrease slightly from 0.72 to below 0.60. The increases of the hydrogen fraction with

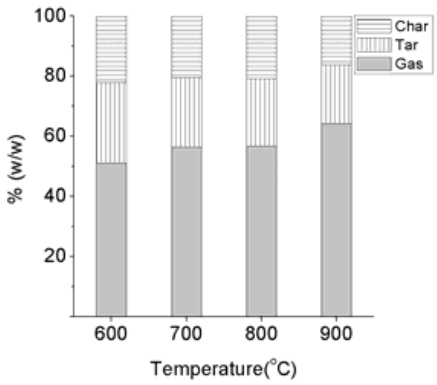

Fig. 2. Effect of reaction temperature on yields of gasification products

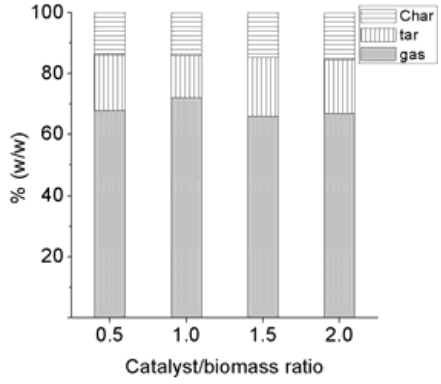

Fig. 3. Effect of catalyst/biomass ratio on yields of gasification products

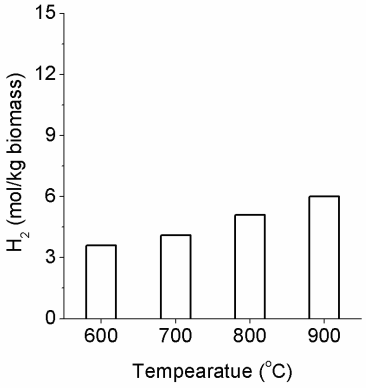

Fig. 4. Effect of reaction temperature on H2 yields.

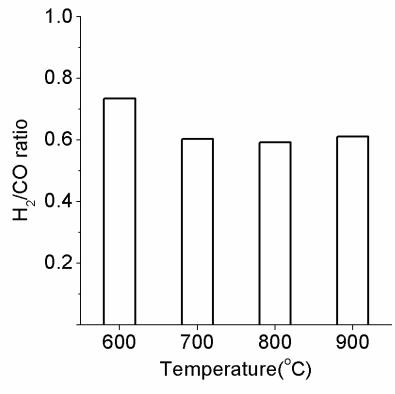

Fig. 5. Effect of reaction temperature on H_2/CO ratio.

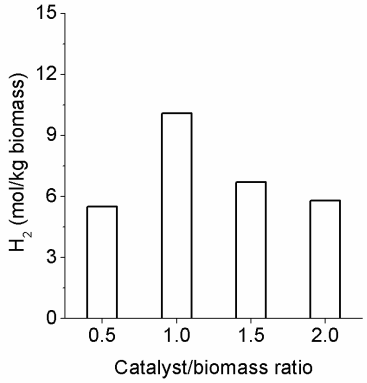

Fig. 6. Effect of catalyst/ biomass ratio on H_2 yields.

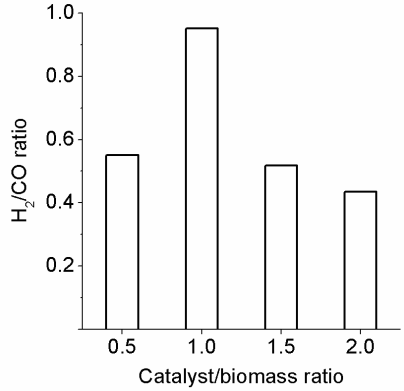

Fig. 7. Effect of catalyst/biomass ratio on H_2/CO ratio.

Table 2. Comparison of H2 yields for different types of biomass without catalyst.

Reference	Biomass	Temp (°C)	H2 yield (%)
This work	Mimosa	900	17
[6]	Sawdust	900	38
[9]	Saw dust	810	10
[9]	Wood	550	8
[10]	Rice straw	800	10
[10]	Rice straw	900	23

Table 3. Comparison of H_2 yields for different types of biomass with dolomite catalyst.

Reference	Biomass	Temp (°C)	H_2 yield (%)
This work	Mimosa	900	26
[10]	Rice straw	900	37
[11]	Sawdust	800	11
[12]	Pine sawdust	850	52
[13]	Pine sawdust	750	51

temperature were due to the greater production of gas in the initial pyrolysis (faster at higher temperatures), and the endothermic reactions of gasification of the char, which increases with temperature. It was clear that temperature has integrated effects on these results.

The effects of catalyst to biomass ratio on H_2 and H_2/CO yields when the reactor temperature was kept constant at 900°C are shown in Figs. 6 and 7. Generally, the H_2 yields were observed to increase with the presence of catalyst. The peak value of H_2 yield appeared at the catalyst to biomass ratio of 1.0 was twice as much as that at similar condition without the catalyst. This may be attributed to an increase in surface reaction area on the dolomite, greater the contact area between the biomass and the dolomite, leading to higher chemical reaction rates and gasification reactions [8]. However, increasing catalyst/biomass ratio did not prove to increase the hydrogen yield further. With respect to H_2/CO ratios, similar pattern to H_2 yields was observed that a maximum ratio of 0.95 was obtained at catalyst to biomass ratio of 1.0. However, at other catalyst to biomass ratios, the H_2/CO yields appeared to be slightly lower than the value at similar condition without the catalyst.

3.3. Comparison with literature

H_2 yields obtained from gasification of mimosa in this study were compared against those obtained from other types of biomass at similar thermal conditions. Results (in % by volume) are shown in Tables 2 and 3 for the cases with and without

catalyst, respectively. It was found that H_2 yields were comparable to other biomass considered.

4. Conclusions

In this work, air gasification of giant sensitive plants under atmospheric pressure in a fixed bed reactor has been carried out with and without dolomite as a catalyst. Effects of reaction temperature and catalyst to biomass ratio have been investigated. Gas yields were found to increase with increasing temperatures. With catalysts, over 60% gas yields were obtained. Increase in temperature resulted in an increase in H_2 yields. The H_2 yields were found to increase further with presence of catalyst. A peak of H_2 yield was observed at catalyst to biomass ratio of 1.0. Producer gas yields and composition obtained from gasification of mimosa were in similar magnitude and comparable to other types of biomass. Mimosa appeared to have potential as a biofuel candidate.

References

[1] Miller, I. L., 2004, Uses for Mimosa pigra, In: *Research and Management of Mimosa pigra*, eds Julien, M., Flanagan, G., Heard, T., Hennecke, B., Paynter, Q, and Wilson, C., pp 63-67, CSIRO Entomology, Canberra, Australia.

[2] Wongsiriamnuay, T., et al., 2008, Renewable Energy from Thermal Gasification of a Giant Sensitive Plant (*Mimosa pigra* L.), *5th International Conference on Combustion, Incineration/ Pyrolysis and Emission Control*, Chiang Mai, Thailand.

[3] Wongsiriamnuay, T., and Tippayawong, N., 2010, Non-isothermal Pyrolysis Characteristics of Giant Sensitive Plants Using Thermogravimetric Analysis, Bioresource Technology, in press.

[4] Sutton, D., et al, 2001, Review of Literature on Catalysts for Biomass Gasification, Fuel Processing Technology, 73(2), pp. 155-173.

[5] Li, C., and Suzuki, K., 2009, Tar Property, Analysis, Reforming Mechanism and Model for Biomass Gasification - An Overview, Renewable and Sustainable Energy Reviews, 13(3), pp. 594-604.

[6] Turn, S., et al., 1998, An Experimental Investigation of Hydrogen Production from Biomass Gasification, International Journal of Hydrogen Energy, 23(8), pp. 641-648.

[7] Lv, P.M., et al., 2004, An Experimental Study on Biomass Air-steam Gasification in a Fluidized Bed. Bioresource Technology, 95(1), pp. 95-101.

[8] Rapagna, S., and Latif, A., 1997, Steam Gasification of Almond Shells in a Fluidised Bed Reactor: the Influence of Temperature and Particle Size on Product Yield and Distribution. Biomass and Bioenergy, 12(4), pp. 281-288.

[9] Ni, M., et al., 2006, An Overview of Hydrogen Production from Biomass. Fuel Processing Technology, 87(5), pp. 461-472.

[10] Xie, Y. R., et al., 2009, Influences of Additives on Steam Gasification of Biomass: 1 Pyrolysis Procedure, Energy and Fuels, 23(10), pp. 5199-5205.

[11] Hanping, C., et al., 2008, Experimental Investigation of Biomass Gasification in a Fluidized Bed Reactor, Energy and Fuels, 22(5), pp. 3493-3498.

[12] Lv, P., et al., 2007, Bio-syngas Production from Biomass Catalytic Gasification, Energy Conversion and Management, 48(4), pp. 1132-1139.

[13] Delgado, J., et al, 1996, Calcined Dolomite, Magnesite, and Calcite for Cleaning Hot Gas from a Fluidized Bed Biomass Gasifier with Steam: Life and Usefulness, Industrial and Engineering Chemistry Research, 35(10), pp. 3637-3643.

Acknowledgements: This research is financially supported by the Thailand Research Fund (no. RSA5080010) and Faculty of Engineering, Chiang Mai University. The Royal Golden Jubilee PhD scholarship (no. PHD/0047/2550) awarded to TW is greatly appreciated. Supports from the Energy Research and Development Institute, Chiang Mai University are also acknowledged.

Technical Economic Optimization of Existing Combustion Plant Utilizing Coal and Biomass

Michal Touš[a], *Martin Pavlas*[a], *Petr Stehlík*[a] *and Pavel Popela*[b]

[a] *Brno University of Technology, Faculty of Mechanical Engineering, Institute of Process and Environmental Engineering, Brno, Czech Republic*
[b] *Brno University of Technology, Faculty of Mechanical Engineering, Institute of Mathematics, Brno, Czech Republic*

Abstract: By 2020 renewable energy should account for 20% of the EU's final energy consumption in order to reduce the effects of climate change. Biomass-based fuels contribute to this effort. The new sophisticated optimization approach introduced in this paper supports sustainable biomass-based fuels integration into the existing energy system. Besides environmental effects, biomass co-firing is also economically beneficial under particular conditions. The plant involved in the case study produces approximately 3400 TJ of heat and 460 GWh of electricity per annum. It secures delivery of heat to residential areas, public institutions and industrial enterprises. First, the conditions for effective biomass utilization are identified using mid-term operation planning (one year, time step of one month) procedure (optimum amount of fuels burned in every boiler with maximum profit with respect to export limitation). Then sensitivity analysis of parameters such as fuel prices, energy prices and government subsidies for renewable energy production is performed in order to find conditions appropriate for biomass utilization. The plant model was built and validated using real operation data which enhances its practical application. A limited resource of various types of biomass over a year represents typical inventory type constraints and makes the problem multi-period. Some of the equalities representing transformation functions (e.g. input-output model of boiler and turbine) and inequalities representing limitations (e.g. biomass availability, boiler capacity) in the model are nonlinear and therefore it is non-linear programming problem (NLP). Even though a phenomenon of increased biomass utilization for energy production is discussed world-wide, effective biomass integration using advanced optimization techniques is rarely solved. The model introduced in this paper is implemented in GAMS (General Algebraic Modeling System). It is high-level modeling system, which provides an environment for mathematical programming and optimization. Excel interface was developed to provide user-friendly and comfortable use of GAMS.

Keywords: Optimization, non-linear programming, biomass co-firing, combustion plant.

1. Introduction

Fossil fuels such as coal still dominate in current energy production plants. However, due to its large carbon footprint, rising prices and unclear availability of fossil fuels, increasing interest in renewable and alternative fuels is observable. By 2020 renewable energy should account for 20% of the EU's final energy consumption in order to reduce CO_2 emission production and other negative impacts on the environment [1]. Co-firing fossil and biomass-based fuels represents a low-cost, short-development-time method (compared to other renewable options) how to achieve this target [2]. As [3] assesses the estimated technical biomass co-firing potential in existing coal-fired power plants in EU is about 520–940 PJ/year which leads to electricity generation from renewable energy sources (RES-E) approximately 52–87 TWh/y. This corresponds to about 1.5-2.5% of the total gross electricity generation.

Another aspect that influences biomass co-firing potential is biomass availability. The technical potential corresponds to only about 10% of the estimated biomass supply potential in the EU27 [3]. But the location of the energy producing system and biomass producer has to be considered. If the technical potential outweighs local biomass availability it should be further researched whether it is still beneficial to transport biomass under certain circumstances (distance, amount of biomass), or not.

However not only technical potential and biomass availability are important. Also economic factors play key role. The economic feasibility of biomass co-firing depends mainly on relative cost of coal and biomass (as well as retrofitting costs), CO_2

emission allowances price [2] and government subsidies for RES-E ("green electricity").

There have been recently published works dealing with minimizing of the environmental impact of biofuels supply chain [4]. This paper contributes to economically effective biomass utilization in existing plants. The impulse for the task development arises from the increasing interest in renewable and alternative fuels as the effort of reducing the negative impact of fossil fuels usage on the environment [5]. The optimization procedure proposed supports development of energy producing systems where fossil fuels are substituted with renewable and alternative fuels. The goal is to provide the plant with valuable information which is helpful for decisions concerning mid-term (one year) operation planning and suggestions of trend in operation. The model and the optimization procedure are designed using real operation data of a heating plant in the Czech Republic. Though the procedure is designed using one particular plant it can easily be adjusted to be suitable for any plant. Many papers deal with optimal operation planning for energy systems, e.g. [6], but only few of them considers biomass co-firing, e.g. [7].

2. Methodology

The mathematical model of the plant is based on real operation data analysis and therefore it provides us with better accuracy than simple or more complex thermodynamic models used by other authors [8,9].

2.1. Data analysis of the heating plant

The heating plant included in the case study satisfies two thirds of the demand for heat and cold in a city of nearly 200 thousand inhabitants. Electricity is produced simultaneously. The plant secures delivery of heat to residential areas, public institutions, and a regional hospital as well as to industrial enterprises (e.g. a brewery). Block diagram of the heating plant with process streams is shown in Fig. 1. An overview of key components of the heating plant (boilers and turbines) is depicted in Table 1. Biomass consisting of wooden chips and bark is introduced in boiler houses II and III.

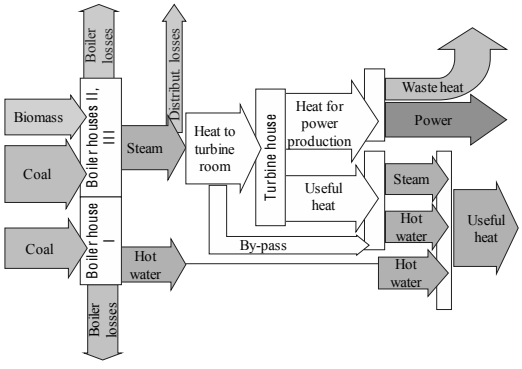

Fig. 1. Block diagram of the heating plant.

Table 1. List of key components

Component	Description
Boiler house I	2 hot-water boilers with capacity 35 MW
Boiler house II	2 granulation powder steam boilers with capacity of 128 MW
Boiler house III	1 fluidized bed steam boiler with capacity of 135 MW
Turbine house	1 back-pressure turbine 70 MW, 1 condensing extraction turbine 67 MW

Data analysis is crucial for mathematical modeling of the system. The objective is to find functions describing the system with sufficient accuracy. The process of steam production and electricity generation is represented by transformation functions.

2.2 Model building

The model is designed to evaluate operation conditions with respect to heat and electricity demand which are set in the form of interval (maximal and minimal value). From the biomass co-firing point of view the most important operation parameter is the amount of fuels introduced into every boiler. The others are heat and electricity production (inside the demand interval) and determination of flows through other key components with respect to their capacity. The following paragraphs describe the model building in more details.

2.2.1. Components

As said in previous text operation of key components (boilers, turbines) is represented by transformation functions. The boiler efficiency represents the transformation functions for boiler houses. There are certainly many factors influencing the boiler efficiency such as average load, amount of biomass co-fired [10], etc. Using available data, these were included in more complex regression models (with more factors). None of them provided us with acceptable accuracy. The boiler efficiency can be assumed as an uncertain parameter in more advanced stochastic model (see Fig. 2). For now, average values are used. The average

efficiency of boilers in boiler house I, II and III is 67 %, 84 % and 89 % respectively.

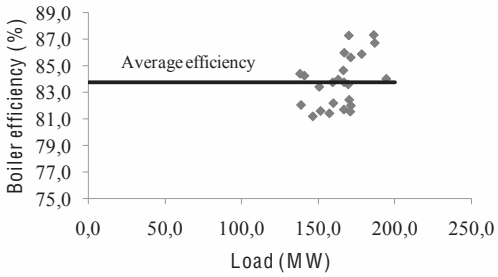

Fig. 2. Stochastic character of historical data of the boiler efficiency in boiler house II

Modeling of each of installed turbines separately is out of the scope of the problem being solved [11]. Furthermore data for this purpose was not provided. So the turbines in the turbine house are considered as one "black box". Transformation functions for turbine house were derived from the correlation between power to heat ratio and specific steam consumption for this heat production (see Fig. 3). This regression model provides us with the best accuracy of all other possible regression models tested. It evaluates the amount of steam led into the turbine and waste heat according to heat and electricity demand (see Fig. 1). Furthermore the reduction station is included to complete the transformation function for turbine house.

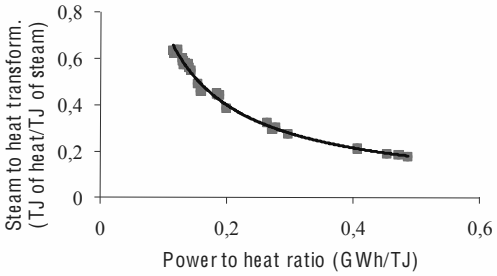

Fig. 3. Transformation function for turbine house

The model of the process includes also functions for internal-consumption of heat and electricity and determination of losses due to steam transport from boiler house to turbine house.

2.2.2. Constraints

The next part of the modeling consists of constraints formulation. The boiler house capacity and technical limitations on biomass co-firing have to be included. These are in the form of maximal ratio of biomass flow mass rate to coal flow mass rate for boiler house II and in form of maximal ratio of heat content in biomass to heat content in coal for boiler house III. The amount of biomass that can be introduced is restricted to 5% by mass flow rate (boiler house II) and 40% by heat content (boiler house III). The turbine house constraint includes overall capacity and limitation of the turbines' operation area. The electricity production can vary for the particular level of heat production inside the area bounded by lower and upper bound as shown in Fig. 4.

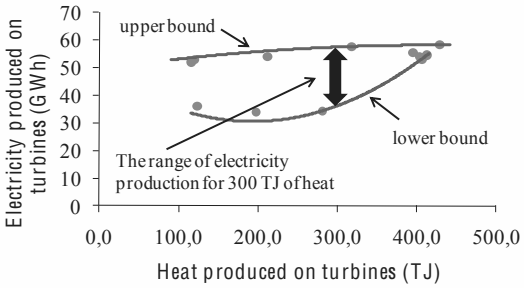

Fig. 4. Operation area of the turbine house

2.3. Optimization

The goal of the optimization is to find an optimal operation plan (fuel feeding rates determined on a monthly basis) providing maximal annual profit. The objective function consists of:

- incomes from:
  - heat and electricity export
  - government subsidies for RES-E
  - CO_2 allowances trading
  - bonus on electricity from cogeneration (CHP)
- costs of:
  - fuels purchasing
  - ash disposal
  - flue gas desulphurization.

The government subsidies for RES-E and cogeneration bonus are governed by national legislation harmonized with EU directives on renewable energy [1] and cogeneration [12].

The decision variables representing operation parameters are:

- amounts of fuels introduced into every boiler
- heat and electricity production

- flows through other key components.

The heating plant model with objective function is implemented in GAMS (General Algebraic Modeling System) which is a high-level modeling system for mathematical programming and optimization. It includes solvers for various types of problems like linear programming, non-linear programming, mixed integer programming, etc. Obviously the model of the heating plant is non-linear (see Fig. 3) and has to be solved using non-linear problem solvers e.g. CONOPT, MINOS. As far as model size is concerned, there are 525 variables and 587 equations.

3. Practical use

3.1. Optimal planning of fuel utilization

The objective of optimization is to find optimum amount of fuels burned in every boiler with maximum profit annually with respect to necessity of heat delivery to consumers connected to the district heating system (heat demand) and opportunity to sell electricity produced (electricity demand). The demand interval corresponds to 5 % scatter around the historical values, which are shown in Fig. 5.

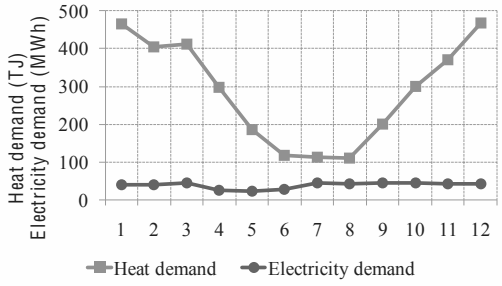

Fig. 5. Heat and electricity demand

The optimization is performed at current prices, which are depicted in Table 2.

The goal of the optimization is to find an optimal operation plan which proposes utilization of the fuels for each month of the year with maximum profit.

Table 2. Prices of fuels, energies and bonuses

Item	Price
Coal	1.8 (€/GJ)
Biomass	4.7 (€/GJ)
Heat	1.7 (€/GJ)
Electricity	81 (€/MWh)
CO_2 allowance	11 (€/t of CO_2)
Subsidies for RES-E	24 (€/MWh)
CHP subsidies	1.7 (€/MWh)

3.1.2. Optimal plan vs. expected plan

Historical data of coal and biomass utilization in the heating plant from recent few years are used to formulate the most probable operation plan applied by the heating plant. This plan, denoted as the expected plan, is compared to the calculated optimal plan.

The optimal plan provides 1.69 % higher profit (about € 0.52 M/y) than the expected plan without optimization. It is important to emphasize that amount of biomass utilized in the optimal plan is the same as in the expected plan. The difference between optimal solution and real operation is shown in Fig. 6.

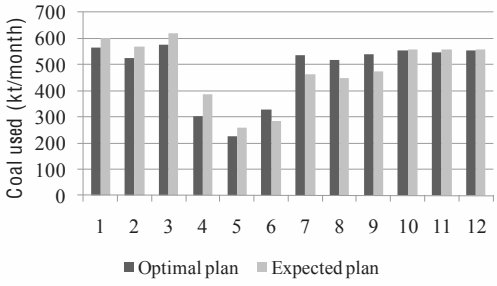

(a)

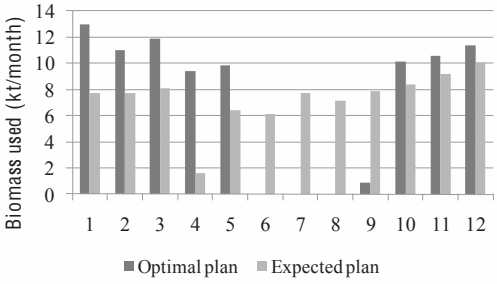

(b)

Fig. 6. Optimal plan vs. expected plan based on historical operation data: a) coal combusted, b) biomass combusted

The optimal solution proposes feeding biomass only in winter months. Different distribution of biomass throughout the whole year is therefore the main reason for the increased profit. It would be expected that using biomass in summer months is preferential, since the highest efficiency of electricity generation is achieved in summer months (see Fig. 7). Due to the mixing of biomass and coal in boilers it is no longer possible to determine how much electricity was produced from biomass

alone. The amount of RES-E is calculated using a formula which includes waste heat. Waste heat affects it negatively; the more waste heat the less amount of RES-E. Looking at Fig. 8, government subsidies for RES-E are the main part of income. Together this results in a preference for biomass utilization in winter instead of summer.

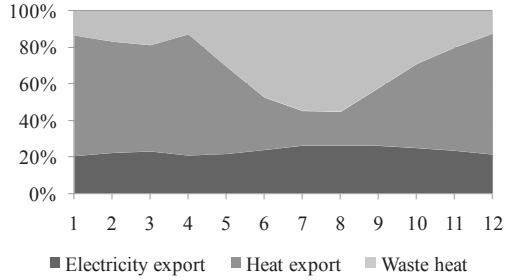

Fig. 7. Structure of energy utilization

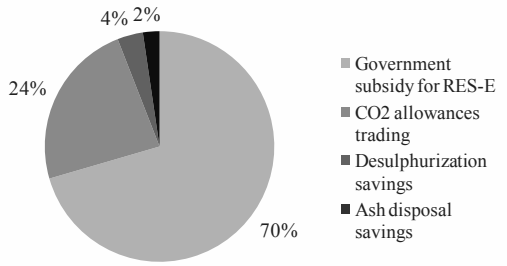

Fig. 8. Structure of income from biomass utilization

But the introduction of the optimal solution into plant operation is closely related to biomass logistics. Biomass producers would not be willing to supply biomass only for a few months a year. Moreover the biomass is probably not available in the demanded amount in winter months. So investment in a store for biomass could be the solution. Considering the fact that the optimal plan increases profits by € 0.52 M/y an acceptable investment could be e.g. € 2.6 million with a return on investments in terms of simple payback within 5 years.

Another difference between the expected plan and the optimal plan is significant reduction of usage of boiler house I. This is logical because the boiler efficiency is low compared to boiler houses II and III and in addition it does not produce steam for electricity generation (see Fig. 1). Heat production by cogeneration is preferred. Turbine by-pass is minimized.

3.1.2. Scenario analysis

Three scenarios in the heating plant are analyzed to show the effect of biomass utilization from a financial point of view:

- scenario 1 – coal utilization only
- scenario 2 – coal and biomass limited by local biomass availability potential
- scenario 3 – coal and biomass utilization limited by technical potential for biomass co-firing.

The local biomass availability is approximately 100 000 tones of biomass per year and the technical potential is about 125 000 tons per year. Considering the composition of the objective function there are two items the value of which is the same for all three scenarios: income from heat and electricity export, and bonus of electricity from cogeneration (the same amount of heat and electricity is produced). The value of the other items differs as shown in Fig. 9.

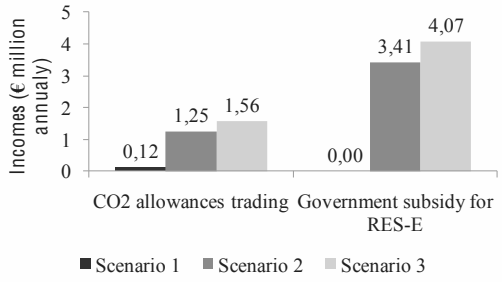

(a)

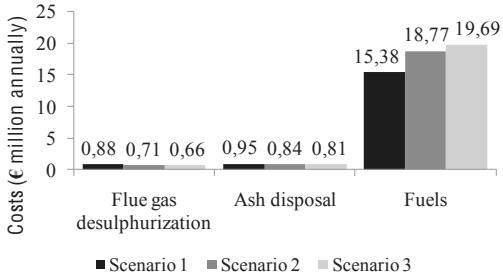

(b)

Fig. 9. Incomes and costs of all three scenarios: a) incomes, b) costs

The biomass utilization considerably increases income from government subsidies for RES-E and from CO2 allowances trading. Looking at Fig. 9 b) costs of flue gas desulphurization and ash disposal are reduced (due to lower sulphur and ash content

in biomass). On the other hand the fuel costs are much higher since biomass is currently 2.67 times more expensive than coal (see Table 2). But thanks mainly to the government subsidies and CO_2 allowances trading (see Fig. 9 a), biomass co-firing is more profitable than introducing coal only; profits for all three scenarios are summarized in Table 3. The difference between scenarios 2 and 3 is not so significant but it shows that the transport costs of extra biomass over the availability limit may be up to € 0.2 million per annum.

Table 3. Profits per annum

Scenario	Value of objective function (annual profit)
Scenario 1	29.79 M€
Scenario 2	31.22 M€
Scenario 3	31,41 M€

3.2. Sensitivity analysis

It was shown previously in this paper that increased biomass utilization is not only economically feasible but may also be profitable. It depends mainly on the amount of the government subsidies for RES-E, CO_2 emission allowances price and biomass price. Therefore sensitivity analysis of these factors on the amount of biomass co-fired was investigated. Analysis is performed using optimization procedure and changing only one factor at a time; the others are of their current value (see Table 2).

3.2.1. Biomass price

At present, the heating plant purchases biomass which is 2.67 times more expensive than coal. The biomass price is expected to increase due to higher interest in biomass fuels and higher transport cost. However the price of coal grows as well so the difference should be partially offset. The influence of biomass price on biomass usage is shown in Fig. 10.

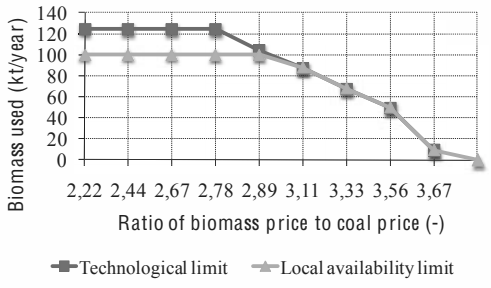

Fig. 10. Influence of biomass price on biomass used

As stated previously, the technical limit is 25 000 t/y higher than local availability limit. This extra amount of biomass can be transported from further resources. If the transport costs increased biomass price up to 2.78 times of coal price the technical potential would be still fully utilized. For increase up to value of 2.89, the extra amount of biomass from further resources is not beneficial anymore. Higher biomass prices result in decrease of biomass utilization under the local availability potential. Biomass is no longer financially beneficial when the price of biomass is higher than 3.78 times that of coal.

3.2.2. Government subsidies for electricity generation from renewable sources

Government subsidies for electricity generation from renewable sources are a method to support biomass utilization. In the Czech Republic, the government subsidies for RES-E decreased from 33 €/MWh down to 24 €/MWh (current value) in last four years. Fig. 11 shows that a slight decrease of subsidies (approximately 14 % of current amount) is acceptable for utilization of technical potential (assuming values of other factors at the value as shown in Table 2). If the subsidies decreased down to about 40 % of current amount the biomass would be no longer economically beneficial.

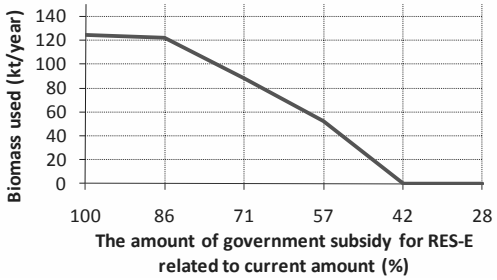

Fig. 11. Influence of the amount of government subsidies for biomass used

3.2.3. CO_2 allowances

The CO_2 allowance price is variable. For example it was fluctuating between € 8 and € 15 per t of CO_2 in 2009. The influence of CO_2 allowances price is shown in Fig. 12.

If the price was less than € 6.9 per t of CO_2 the biomass availability potential would not be fully utilized. It can also be seen that biomass is profitable even if there is no CO_2 allowances market. However this is only due to government subsidies.

The influence of changes in subsidies and in price of CO_2 allowances is shown in Fig. 13. It can be seen what combination of these factors is needed to keep biomass utilization in the heating plant on technical potential or local availability potential.

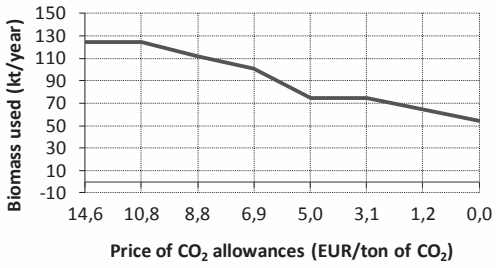

Fig. 12. Influence of CO2 allowances price on biomass used

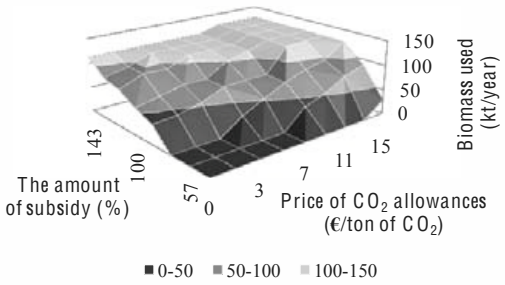

Fig. 13. Influence of CO2 allowances price and the amount of subsidy on biomass used

4. Conclusion

Biomass co-firing contributes to the reduction of CO_2 emissions and other negative environmental impacts. Even though biomass is more expensive than coal, it is the economically beneficial fuel under particular circumstances.

The model of a real heating plant was built and used for finding the optimum amount of fuels introduced in every boiler with maximum annual profit. Biomass co-firing is beneficial due to government subsidies for RES-E and CO_2 allowances trading. The calculation of the amount of RES-E is influenced by waste heat. More waste heat means less RES-E. Therefore the optimal plan shows that it is preferential to use biomass in cold months. To show influence of biomass utilization on annual profit of the plant, scenarios for coal only utilization and biomass co-firing are analyzed. Presently, biomass co-firing is very beneficial.

The amount of biomass utilized depends mainly on relative biomass and coal price, the amount of government subsidies for RES-E and CO_2 allowances price. Therefore sensitivity analysis was performed to investigate the influence of these factors. Three scenarios: technical biomass co-firing potential, local biomass availability potential and coal only utilization were analyzed and their limit points were determined.

The presented model is intended to provide information for mid-term decisions. As far as long-term decisions are concerned government subsidies for RES-E, biomass and coal price, etc. are random in long-term horizon. The current model is planned to be extended to stochastic model which is able to handle with uncertain future [13]. This is important for big investment decisions such as new biomass boiler house.

References

[1] The European Parliament and the Council, 2009, Directive 2009/28/EC of 23 April 2009 on the promotion of the use of energy from renewable sources, Journal of the European Communities, pp. 16-62 (L 140)

[2] Baxter, L., 2005, Biomass-Coal Co-Combustion: Opportunity for Affordable Renewable Energy, Fuel, 84 (10), pp. 1295-1302

[3] Hansson, J., et al., 2009, Co-Firing Biomass with Coal for Electricity Generation – An Assessment of the Potential in EU27, Energy Policy, 37 (4), pp. 1444-1455

[4] Lam, H.L., Varbanov, P.S., and Klemes, J.J., Optimisation of Regional Energy Supply Chains Uitilising Renewable: P-graph Approach, Computers and Chemical Engineering, 34 (5), pp. 782-792

[5] Drápela, T., et al., 2009, Energy Conception of an Integrated System – I. Analysis of Available Data and Its Processing, Chemical Engineering Transactions, Klemeš, AIDIC, Italy, 18, pp. 635-640

[6] Oh, S., et al., 2007, Optimal Planning and Economic Evaluation of Cogeneration System, Energy, 32 (5), pp. 760-771

[7] Ko, A. S., and Chang, N., 2008, Optimal Planning of Co-Firing Alternative Fuels with Coal in a Power Plant by Grey Nonlinear Mixed Integer Programming Model, Journal of Environmental Management, 88 (1), pp. 11-27

[8] Aguilar, O., et al., 2007, Design and Optimization of Flexible Utility Systems Subjects to Variable Conditions, Chemical Engineering Research and Design, 85 (8), pp. 1136-1148

[9] Varbanov, P., et al., 2007, Synthesis of Industrial Utility Systems: Cost-Effective De-Carbonization, Applied Thermal Engineering, 25 (7), pp. 985-1001

[10] De, S., and Assadi, M., 2009, Impact of cofiring Biomass with Coal in Power Plants - A Techno-Economic Assessment, Biomass and Bioenergy, 33 (2), pp. 283-293

[11] Salgado, F., and Pedrero, P., 2008, Short-Term Operation Planning on Cogeneration Systems: A Survey, Electric Power Systems Research, 78 (5), pp. 835-848

[12] The European Parliament and the Council, Directive 2004/8/EC of 11 February 2004 of the promotion of cogeneration based on a useful heat demand in the internal energy market, Journal of the European Communities, pp. 50-60 (L 52)

[13] Ruszczynski, A., 2004, *Handbooks in Operations Research and Management Science: Stochastic Programming*, Elsevier, Amsterdam, Chap. 10

Acknowledgments: We gratefully acknowledge financial support of the Ministry of Education, Youth and Sports of the Czech Republic within the framework of Research Plan No. MSM 0021630502 "Waste and Biomass Utilization focused on Environment Protection and Energy Generation"

Comparative analysis of large biomass & coal co-utilization units

Marcin Liszka[a], *Grzegorz Nowak*[a], *Krzysztof J. Ptasinski*[b]

[a] *Silesian University of Technology, Gliwice, Poland*
[b] *Eindhoven University of Technology, Eindhoven, The Netherlands*

Abstract: The co-utilization of coal and biomass in large power units is considered in many countries (e.g. Poland) as fast and effective way of increasing renewable energy share in the fuel mix. Such a method of biomass use is especially suitable for power systems where solid fuels (hard coal, lignite) are dominating. On the other hand, the admixture of usually wet biomass to the main fuel impacts the steam boiler efficiency and durability. Moreover, the production of electricity generates emission not only by the direct combustion, but also during externally-connected processes, like e.g. preparation and transport of both renewable and fossil fuels. Considering abovementioned aspects, the legitimacy of biomass co-utilization in large, basically coal-fired, power units should be carefully analyzed. The main goal of the presented study is therefore the assessment of energy efficiency and CO_2 emission due to biomass use as a secondary fuel in large, basically coal-fired power units. Two methods of fossil and renewable fuel coupling have been analyzed: direct biomass and coal co-combustion by mixing them before coal mills in classical pulverized-fuel unit, as well as, biomass gasification followed by co-combustion of syngas with coal in the same steam boiler. Both systems have been modeled mathematically to determine the mass and energy fluxes crossing their boundaries. Models were prepared using *Aspen Plus* software. The main assessment factor used for comparison of two biomass utilization methods is cumulative CO_2 emission calculated per unit of produced electricity.

Keywords: Biomass, co-firing, gasification, large power units.

1. Introduction

The co-utilization of coal and biomass in large power units is considered in many countries (e.g. Poland) as fast and effective way of increasing renewable energy share in the fuel mix [1]. Such a method of biomass use is especially suitable for power systems where solid fuels (hard coal, lignite) are dominating. The main advantages of the co-utilization technology are high efficiency of biomass conversion and low capital cost related to the power unit adjustment. The relatively high efficiency of biomass utilization results from the large scale of system-type, basically coal-fired power units. On the other hand, the biomass-to-coal admixture may impact crucial steam boiler parameters like combustion flame temperature, radiative and convective heat transfer coefficients and finally the energy efficiency. Moreover, the production of electricity generates emission not only by the direct combustion, but also during externally-connected processes, like e.g. preparation and transport of both renewable and fossil fuels. Considering abovementioned aspects, the legitimacy of biomass co-utilization in large, basically coal-fired, power units should be carefully analyzed.

In general, there are three main methods of biomass and coal coupling in the same power unit [1,2]:

- direct co – firing,
- indirect co-firing,
- parallel combustion.

The direct co-firing is technologically the simplest solution. Biomass and coal are burned in the same combustion chamber, using the same or separate mills and burners, depending on the properties of biomass. This technology allows for co-firing of up to ca. 10% (by mass) [2,3] of biomass referring to the whole fuel stream supplied to the boiler. Higher biomass contents may cause serious erosion and corrosion problems in the pulveriser and boiler. The investment cost related to the power unit adjustment is however negligible

In the case of indirect co-firing, the biomass is first gasified or fired in separate combustion chamber. The produced syngas or hot flue gas is then supplied to the combustion chamber in the steam

Corresponding Author: Marcin Liszka, Email: marcin.liszka@polsl.pl

boiler. The syngas may be also used as reburning fuel to reduce NO_x emissions [4]. The indirect technology allows for use of wide range of biomass fuels. Serious drawback of this technology is much higher investment costs.

The parallel combustion is used mostly in the paper industry, but applications in large system-type power units are also known [5]. Biomass and coal are burned in separate boilers, combined with a common steam turbine system. Such a configuration ensures high flexibility of both fuel substitution, but the investment costs seems to be much higher than in previous two solutions.

As already mentioned, the main reason for co-firing of biomass with coal in the same large-scale power unit is a high efficiency of biomass utilization resulting from high efficiency of a large-scale power units. In this context, the crucial problem is the potential impact of biomass admixture on boiler and whole power unit efficiency. The decreased efficiency may partially reduce the positive renewable fuel impact as the CO_2 emission from coal combustion increases with decreasing efficiency. The cumulative CO_2 emission should thus also be investigated to check if the overall biomass-related emission effect is positive.

The main purpose of this paper is therefore the assessment of the change of power unit efficiency, as well as, of the cumulative CO_2 emission during production of electricity using two methods of biomass and coal co-utilization – combustion of biomass with coal directly in the boiler and gasification of biomass and then co – firing of syngas with coal in the same boiler. All calculations are made for typical Polish fuel conditions.

Several previous works related to this area have been found in the literature [2,3,6,7,8,9]. In [8] several scenarios of hard coal and biomass co-firing have been analyzed including different coal and biomass types (sawdust, short rotation coppices). The detailed life cycle assessment, accounting among others for toxicity of power unit waste products, has been done for pulverized-coal and circulating fluidized-bed boilers. The results indicates, that the impact of biomass-related background processes on the greenhouse effect is much lower comparing to the foreground ones.

The analysis presented in [7] points out, that the contribution of the construction, maintenance and dismantling phases to the total CO_2 emission is negligible, while the biomass production processes may be of important impact. The study presented in [7] deals however with a biomass-fed IGCC system with deep CO_2 removal which makes the shares of foreground and background emissions quite different comparing to units without the CCS processes.

The measured data on the change of steam boiler efficiency and emissions because of sawdust-to-coal admixture have been presented in [9]. The calculated differences in the individual parameters of the energy balance of the boiler are related to the increase of the stack loss and unburned carbon in slag and fly ash. The decrease of boiler efficiency because of 9.5 % (by weight) biomass to coal admixture has been calculated to 0.3 percentage point.

2. Case studies

The reference plant for both analyzed cases is one of the existing power units located in southern Poland. The reference pulverized fuel boiler is of one-through, sub-critical design. The nominal parameters of the reference boiler island are summarized in Table 1. The boiler is coupled with the steam turbine producing nominally 360 MW of electricity (gross).

Table 1. Nominal parameters of reference steam boiler

Live/reheated steam flow	kg/s	303/275
Live/reheated steam pressure	MPa	17.9/17.9
Liver/reheated steam temperature	°C	535/535
Boiler feed water temperature	°C	250
Flue gas temperature at economizer outlet	°C	324
Flue gas temperature at air preheater outlet	°C	125

As already mentioned two methods of biomass utilization in the reference boiler have been analyzed. The direct combustion concept is presented in Fig. 1. It was assumed that the coal-fired power plant, the coal mining and the coal transport systems are already built and operating.

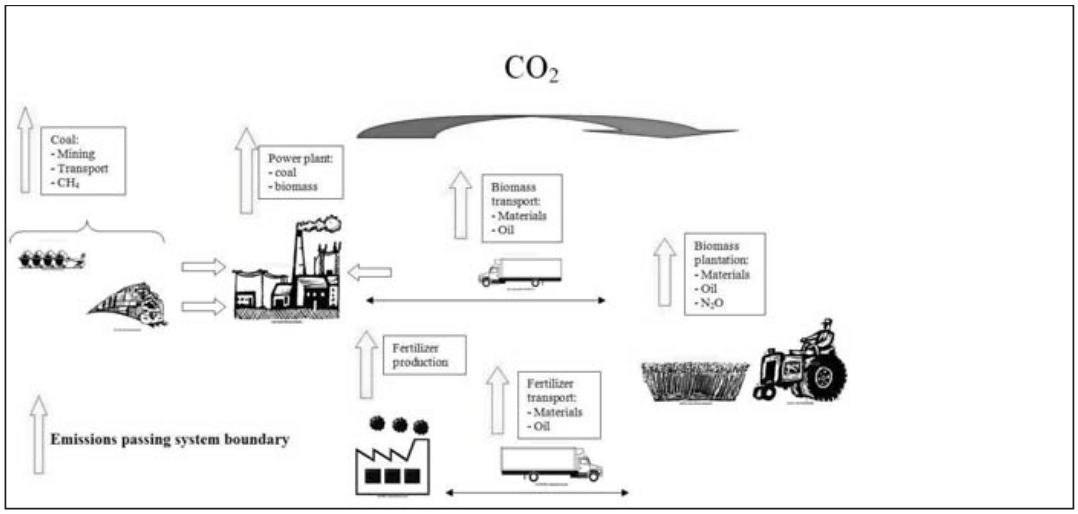

Fig. 1. Analyzed direct co-firing system.

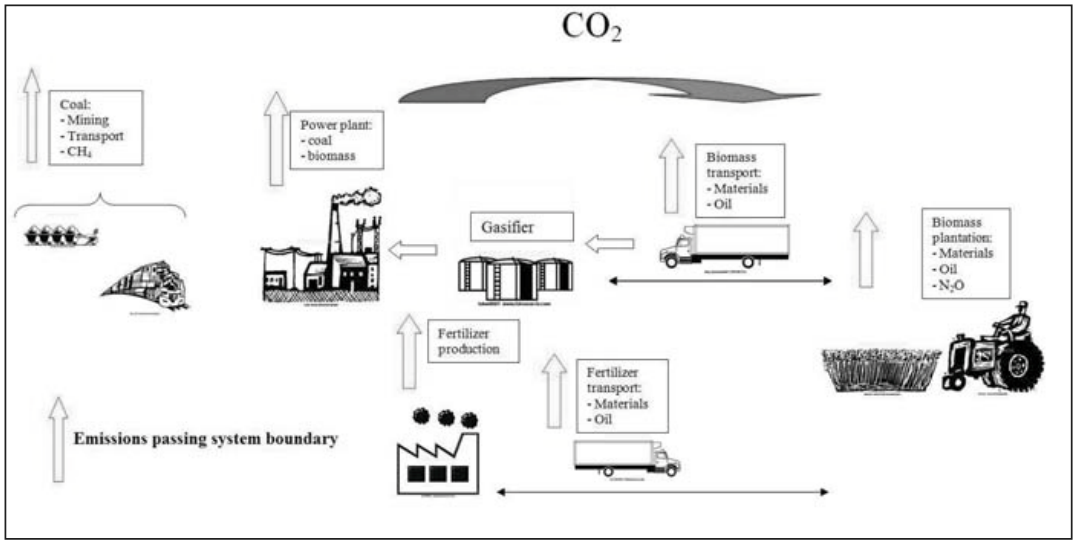

Fig. 2. Analyzed indirect (gasification) co-firing system.

The newly introduced sub-systems are related to biomass transport and cultivation, as well as, biomass storage and internal handling at power plant area. In the second analyzed case (Fig. 2), the biomass gasifier is added as a new device to the system. The syngas is assumed to be co-fired with coal in the boiler.

The cumulative effects of biomass co-utilization are calculated taking into account changes in all strongly connected system branches impacted by biomass-to-coal admixture. The following sources of CO_2 emission are thus considered:

- combustion of coal in the boiler,
- combustion of coal for production of auxiliary electricity used for coal rail transportation and coal mining,
- combustion of diesel fuel used for biomass transport and biomass cultivation,
- production of materials used for building of trucks and other equipment used for biomass transport and cultivation,
- production of fertilizers used for biomass cultivation.

The abovementioned CO_2 sources are schematically notified by red arrows in Figs 1 and 2. The direct emission from biomass combustion (green arrow) is not accounted because of assumed full renewability of biomass fuel.

General assumptions for calculation of particular emissions are listed below:

- biomass is produced at a long-term renewable plantation,
- transportation of biomass to power plant is done by trucks,
- trucks are replaced to new ones three times during the life time of the system (each 10 years),
- 75 % of the materials used for truck production are recycled,
- materials used for production of trucks and other new equipment are composed of steel and cast iron,
- diesel oil is produced from fossil crude oil,
- three different fertilizers N, K_2O and P_2O_5 for biomass cultivation are used,
- gasifier is build of concrete and steel.

3. Assessment factors

The main assessment factor used for evaluation and comparison of the analyzed cases is specific cumulative CO2 emission defined in accordance with Eq. (1).

$$\gamma = \frac{\dot{m}^*_{CO_2}}{N_{elN}} \quad (1)$$

while

$$\dot{m}^*_{CO_2} = \dot{m}_{CO_2,el} + \dot{m}_{CO_2,t,m,c} + \dot{m}_{CO_2,b} + \dot{m}_{CO_2,m} + \dot{m}_{CO_2,o,p} \quad (2)$$

$$N_{elN} = N_{elG} - \left(N_{el_{aux\,1}} + N_{el_{aux\,2}}\right) \quad (3)$$

$$N_{elG} = \dot{Q}_{SB} \cdot \eta_{SC} \quad (4)$$

$$N_{el_{aux\,2}} = N_{elFGF} + N_{elAF} \quad (5)$$

where:

$\dot{m}^*_{CO_2}$ cumulative CO_2 emission related to electricity production, kg/s,

$\dot{m}_{CO_2,el}$ emission of coal combustion, kg/s,

$\dot{m}_{CO_2,t,m,c}$ emission of transport and mining of coal including CH_4 emission recalculated to CO_2 in accordance to [10], kg/s,

$\dot{m}_{CO_2,b}$ emission of biomass cultivation, kg/s,

$\dot{m}_{CO_2,m}$ emission of production of materials used for transportation and production of biomass, kg/s,

$\dot{m}_{CO_2,o,p}$ emission of production of diesel fuel, kg/s,

N_{elN} net power unit electric power, kW,

N_{elG} generator terminal power, kW,

$N_{el_{aux\,1}}$ auxiliary electricity consumption which do not depend on biomass admixture, kW,

$N_{el_{aux\,2}}$ auxiliary electricity consumption which do depend on biomass admixture, kW,

$\dot{Q}_{SB}$ usefull heat produced in the boiler, kW,

η_{SC} energy efficiency of the steam cycle (generator included),

N_{elFGF} electric power of fuel gas fans, kW,

N_{elAF} electric power of combustion air fans, kW.

The total auxiliary electricity consumption within the power unit boundary has been divided into two parts: $N_{el\,aux\,1}$ which is constant – doesn't depend on the biomass-to-coal admixture and $N_{el\,aux\,2}$ which is calculated as sum of electric powers of flue gas and combustion air fans. These fan powers are functions of the biomass admixture.

Values of the parameters describing coal and biomass transport, as well as, biomass cultivation have been assumed on the literature basis [3,6,10,11,12]. They are collected in Table 2.

The values of parameters in Eq. (3-5) which are kept constant during analysis are presented below:

η_{SC}=0,445

$N_{el_{aux\,1}}$=14500 kW

In addition to the cumulative CO_2 emission, the steam boiler efficiency - Eq. (6) and power unit net efficiency – Eq. (7) have been calculated.

$$\eta_{SB} = \frac{\dot{Q}_{SB}}{\dot{E}_{ch_{coal}} + \dot{E}_{ch_{bio}}} \quad (6)$$

Table 2. Parameters for determination of indirect CO2 emissions [3,6,10,11,12]

Crop of biomass	kg/year/ha	13400
Emission from production and preparation of diesel fuel	kg CO2/kg fuel	0.3
Consumption of diesel fuel by one transportation truck	l/100km	30
Use of fertilizers		
N	kgN/ha	100
K2O	kg K_2O /ha	200
P2O5	kg P_2O_5/ha	50
Emission from fertilizers production		
N	kgCO_2/kg N	2.6
K2O	kgCO_2/kg K_2O	0.86
P2O5	kgCO_2/kg P_2O_5	1.48
Distance of biomass transportation	km	100
Distance of fertilizers transportation	km	100
Emissions of steel production	kg CO_2/kg steel	1.76
Emissions of cast iron production	kg CO_2/kg iron	0.0116
Consumption of steel at biomass plantation	kg/m^2	0.181
Consumption of cast iron at biomass plantation	kg/m^2	0.000345
CH_4 emission from coal mining	kg CH_4 /kg coal	0.01348

$$\eta_{elN} = \frac{N_{elN}}{\dot{E}_{ch_{coal}} + \dot{E}_{ch_{bio}}} \quad (7)$$

where:

$\dot{E}_{ch_{coal}}$ flux of the chemical energy of coal (LHV based), kW,

$\dot{E}_{ch_{bio}}$ flux of the chemical energy of biomass (LHV based), kW.

4. Simulation model

The simulation model of a steam boiler has been prepared using the Aspen Plus [13,15] software. First, the *design mode* model has been build taking the physical boiler configuration and required inlet/outlet water and steam parameters as input data. Second, the *off-design* model has been created assuming the heat transfer surface areas and heat transfer coefficients calculated in the *design* mode of simulation. The heat transfer from the flame to the evaporator walls has been modelled basing on relations for heat radiation, taking the Christiansen method [16] and assuming constant flame and evaporator walls emissivities. Such a simplified model of heat radiation seems to be sufficient for analysis of the existing boiler off-design operation. Such an approach is also applied in commercial power plant simulators, e.g. in GateCycle [17]. The relations for radiative heat transfer have been added to the Aspen models as Fortran code using the design space [15] capability. The rest of heat exchange sections in the boiler is treated as convective. The scheme of the simulation model is presented in Fig. 3.

The new equipment referring to the reference (existing) boiler structure are:

- fuel mixer in case of direct co-firing,
- coal dryer, biomass gasifier, syngas cleaner and cooler in case of indirect co-firing.

The additional coal dryer applied in the indirect co-firing case uses the waste heat from the syngas cooler.

The existing boiler structure has been simplified for modeling purposes to the following subsections:

- combined fuel dryer and pulverizer,
- combustion chamber,
- evaporator,
- 4 convective live steam superheaters,
- 2 convective steam reheaters,
- rotary air preheater,
- flue gas and air fans.

For the analysis of indirect co-utilisation of biomass, the gasification island has been modelled. The air-blown gasifier has been modelled using the minimisation of Gibbs free energy method as in other similar studies [13,14]. The gasifier operates at atmospheric pressure while the temperature of the produced syngas is equal to 900 ^oC. The syngas behind the gasifier is cleaned of solid particles and cooled down to optionally 300 or 600 ^oC. Only a part of the syngas physical enthalpy is used for biomass drying - the rest is rejected to the environment. It is not

possible to use the whole waste heat flow rate for biomass drying as the biomass temperature at the dryer outlet is limited. The assumption of no intervention into the existing steam cycle has also been done, so the condensate preheating by hot syngas has not been analysed. The practically applicable value of the syngas temperature at steam boiler inlet should be carefully verified taking the material aspects into consideration.

For all analyzed cases it was assumed that the boiler feed water flow and steam flow for reheating (at boiler inlet) are kept constant. Some slight changes of live and reheated steam flows are caused by water to steam injection for live and reheated steam temperature control. The temperatures and pressures of live and reheated steams, as well as boiler feed water are always kept constant.

The assumed parameters of coal and biomass are presented in Table 3.

Table 3. Parameters of coal and biomass (mass %)

	Coal	Biomass
Moisture	9	50
Ash	22.02	2.38
Carbon	58.56	24.76
Hydrogen	3.72	3.02
Nitrogen	1.17	0.07
Sulphur	0.69	0.04
Oxygen	4.82	19.71
LHV, kJ/kg	22 800	7 550

The impact of biomass admixture on unburned carbon content in slag and fly ash has not been analyzed.

5. Simulation results

The computational analysis has been done for varying mass share of biomass in the total fuel flux supplied to the system. The profiles of calculated boiler efficiency are presented in Fig. 4. In case of indirect co-firing, the boiler efficiency defined by Eq. (6) is calculated at the system boundary including the gasifier island (see. Fig. 3).

The exemplary temperature profiles of flue gas, steam/water and air in the boiler are presented in Fig. 5. They were obtained for reference boiler, fired by coal only.

The composition of syngas supplied to the steam boiler is presented in Table 4. The syngas composition is the same for all indirect co-firing computation while the syngas flow is each time calculated considering actual biomass share in the total fuel flow.

The change of the boiler efficiency as well as the change of auxiliary power consumption Eq. (5) impact the net power unit efficiency as presented in Fig. 6.

The constituents of CO_2 emissions as presented in Eq. (2) are collected in Fig. 7 taking direct co-firing as example. The cumulative emissions are presented in Fig. 8 for all analyzed cases. Finally, the specific cumulative CO_2 emission (see Eq. 1) is visible in Fig. 9.

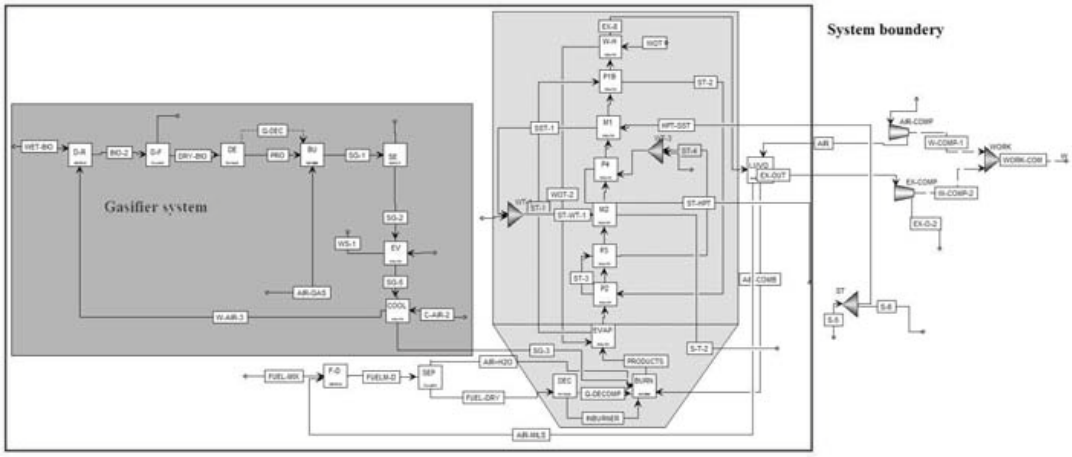

Fig.3 Simulation model of the steam boiler

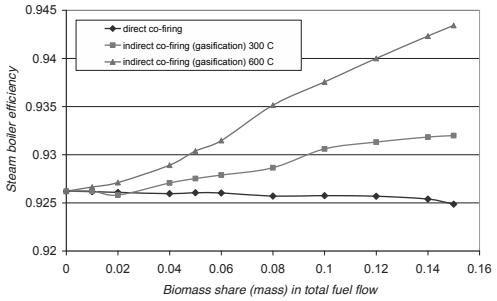

Fig.4 Steam boiler efficiency

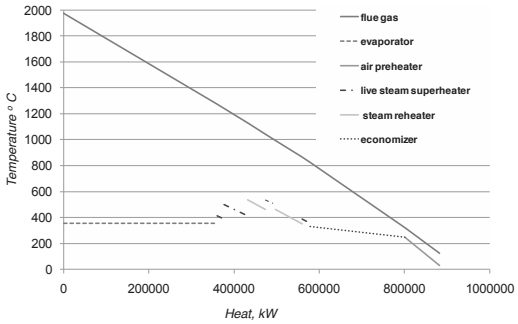

Fig.5 Temperature profiles of boiler streams for coal-only operation (reference plant)

Table 4. Syngas composition (indirect co-firing only)

	Molar fraction
H2O	0.116
N2	0.556
O2	0
H2	0.090
CO	0.116
CO2	0.119

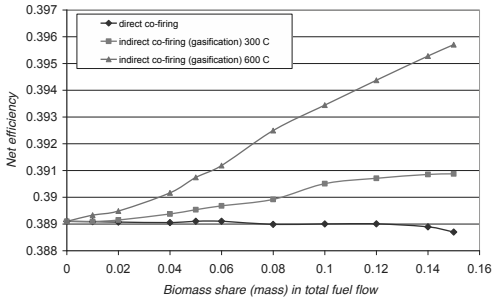

Fig.6 Net power unit efficiency

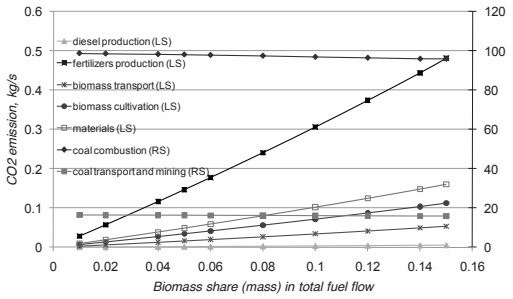

Fig.7 Component CO2 emissions for direct co-firing (LS – left scale; RS – right scale)

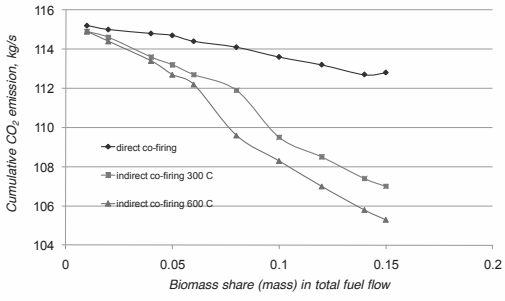

Fig.8. Cumulative CO2 emission

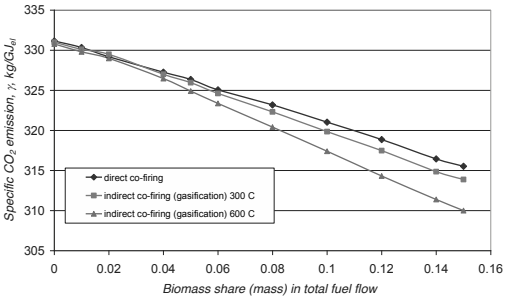

Fig.9. Specific cumulative CO2 emission

6. Conclusions

The biomass-to-coal admixture has a little negative impact on boiler efficiency (Fig. 4) in case of direct co-firing, which is caused by high moisture content in the renewable fuel. The calculated efficiency drop is of the same order of magnitude as published measured data for similar boiler unit [9]. In the case of gasifier application, the increase of boiler efficiency is clearly visible as the biomass has been dried using a part of the syngas physical enthalpy.

The shape of net power unit efficiency (Fig. 6) follows the shape of the boiler efficiency. The change of flue gas and air fan power because of biomass co-utilization is not significant.

As it is visible in Fig. 7, only the emission related to direct coal combustion as well as coal transport and mining is relevant and may be treated as final cumulative emission.

Results presented in Figs 8 and 9 bringing conclusion that the indirect co-firing using gasification is more effective – the absolute and specific CO2 emission is much lower than in the direct co-firing case. The syngas temperature at the steam boiler inlet is a crucial parameter for boiler efficiency and effective emission reduction. It is however limited by the syngas duct and burner material conditions.

References

[1] Al-Mansour F., Zuwala J., 2010, An evaluation of biomass co-firing in Europe, Biomass and Bioenergy (in press), doi: 10.1016/j.biombioe.2010.01.04.

[2] Lechwacka, M., et al., 2008, Co-firing – from research to practice: technology and biomass supply know-how promotion in Central and Eastern Europe example solutions and barriers, COFITECK Newsletter, No 3.

[3] Lewandowski, I., et al., 1995, CO2 balance for the cultivation and combustion of Miscanthus, Biomass and Bioenergy, 8(2), pp. 81-90.

[4] Wu K.T., Lee H.T. et al., 2004, Study of syngas co-firing and reburning in a coal fired boiler, Fuel, 83, pp. 1991-2000.

[5] Hansen, S., and Sørensen, H.D., 2003, Process design and optimization of the Avedore 2 multifuel power plant. Proceedings of ECOS, Copenhagen, Denmark.

[6] Mann, M., and Spath, P., 1997, Life cycle assessment of a Biomass Gasification Combined-cycle System, Midwest Research Institute, USA.

[7] Corti A., Lombardi L., 2004, Biomass integrated gasification combined cycle with reduced CO_2 emissions: Performance analysis and life cycle assessment (LCA), Energy, 29, pp. 2109-2124.

[8] Benetto E., Popovici E.C., et al., Life cycle assessment of fossil CO_2 emissions reduction scenarios in coal-biomass based electricity production, Energy Conversion and Management, 45, pp. 3053-3074.

[9] Zuwala J., Sciazko M., 2010, Full-scale co-firing trial tests of sawdust and bio-waste in pulverized coal-fired 230 t/h steam boiler, Biomass and Bioenergy (in press), doi: 10.1016/j.biombioe.2010.03.003

[10] Pollutants Emissions to the Atmosphere, Jastrzebska Coal Company Inc., www.jsw.pl

[11] Acaroglu, M., and Aksoy, A., 2005, The cultivation and energy balance of miscanthusxgiganteus production in Turkey, Biomass and Bioenergy, 29, pp. 42-48.

[12] Gaines, L., et al., 1998, Life-Cycle Analysis for Heavy Vehicles, Conference paper San Diego, California, USA.

[13] Ruggiero, M., and Manfrida, G., 1999, An equilibrium model for biomass gasification processes, Renewable Energy, 16, pp. 1106-1109.

[14] Ptasinski, K., et al., 2007, Exegetic evaluation of biomass gasification, Energy, 32, pp. 568-574.

[15] Aspen Plus 11.1, 2001, User guide manual, Aspen Technology Inc.

[16] Kostowski, E., 2006, Heat transfer *(in Polish)*, Publishers of The Silesian University of Technology, Gliwice, Poland.

[17] GateCycle Version 5.40, Copyright © 1989 - 2001 GE Enter Software, LLC.

Acknowledgments: The present study was made possible thanks to the Polish Ministry of Science and Higher Education. Their financial support within confines of grant no. PBZ-MEiN-4/2/2006 and help in the organization are gratefully acknowledged.

Modeling study of Tsinghua oxygen staged entrained-flow gasifier

Zhe Wang, Zhiwei Yang, He Fen, Zheng Li, Jiansheng Zhang, Yali Xue

State Key Lab of Power Systems, Dept of Thermal Engineering, Tsinghua University, Beijing 100084, China

Abstract: A full working condition simulation model was established and the results were validated using industrial scale gasifier operation data. Gas phase reaction studies shows that the syngas will reach a quasi-equilibrium state very quickly, making the carbon conversion ratio a critical parameter for the model accuracy. Due to the staged oxygen feed, the temperature showed a special profile, with two temperature peaks, along the height of the gasifier, and the highest temperature inside the gasifier is much lower than that of a GE-Texaco entrained-flow gasifier with the same oxygen and slurry feed rates, explained the reason that the Tsinghua oxygen staged gasifier has a much longer nozzle life time.

Keywords: oxygen staged, gasifier, simulation model, full-working condition

1. Introduction

The past three decades have seen a rapid development of coal gasification technologies due to the increasing demand for clean fuels and chemical products. Virtually all clean energy technologies involving coal will require gasification as an integral part of the process chain. Therefore, as the core component of gasification process, the investigation of gasifier has received more and more attention from both industry and academy. Tsinghua designed entrained-flow gasifier has higher effective syngas composition ($CO+H_2$) and longer nozzle life time compared with GE-texaco gasifiers, Tsinghua designed oxygen staged entrained flow gasifier seems to be very promising to play an important role in future integrated gasification combined cycle (IGCC), poly-generation and pre-combustion carbon capture and storage (CCS).

The oxygen staged entrained flow gasifier is a relatively new technology and there are less operation experience and understanding. A training simulator based on full working-condition modeling work is a powerful tool to obtain a clear and deep understanding of the gasifier as well as for gasifier operator training. Equilibrium models [1-3] used minimum Gibbs free energy to calculate the equilibrium state species concentration. In these models, the reaction rates among the involved species were assumed to be fast enough to reach an equilibrium state before exiting the gasifier. Kinetic models calculated the reaction rate of the heterogeneous and homogenous reactions inside the gasifier to study gasifier performance [4-12]. Li's model [4-5] utilized cell model concept, which divided the Texaco gasifier into a series of cells and calculated the mass and energy balance for each cell. Five heterogeneous and six homogenous reactions were considered in the model. The model results of the syngas composition were very close to real application. More complicated CFD modeling work includes momentum, mass, and energy conservation of the solid and gas phase species together with the turbulence calculations [6-12]. However, these models may concentrate too much on the calculations of flow conditions and concentration distribution inside the gasifier, which affects the accuracy due to simplified reaction mechanism.

Till now, there is very little work on full working condition modeling and simulation. Moreover, Tsinghua designed oxygen staged gasifier is a relatively new gasifier and there is even less work on its modeling. In the present work, a full-working condition gasifier model was established; the model results were compared with real data; the gasifier performance was discussed.

2. Gas phase reaction study

It was assumed that at the end of the gasification process, there is no further gasification or the gasification process can be neglected since there is

Corresponding Author: Zheng Li, Email: lz-dte@tsinghua.edu.cn

little carbon conversion ratio change according to previous studies [5-12], therefore, only homogeneous reactions need to be considered for this stage. Using commercial available Chemkin software with GRI Mech III, the gas phase special dynamic performance inside entrained-flow gasifier environment has been thoroughly studied. The Chemkin calculation results showed that the gas phase reaction reaches equilibrium state very quickly inside typical entrained-flow gasifiers, including Tsinghua oxygen staged gasifier, and the time reaches the equilibrium state is much shorter than the residence time (about 100 times faster). This implies that the final syngas composition can be mainly determined by the gas phase reactions. Further calculations showed that the shift reaction, $CO+H_2O=CO_2+H_2$, mainly determines the major syngas composition (CO, CO_2, H_2, H_2O). This indicates that in the gasifier modeling, the calculation of carbon conversion ratio would be a critical issue for the model results to be coincident with the real value since the relative syngas composition can be calibrated equilibrium state. Details of the gas phase reaction study can be referred to literature [13].

The syngas composition measured downstream was generally used for model validation. However, the syngas composition may change during the cooling process for composition measurement. In the present work, study has been conducted to investigate the composition change during the cooling process using closed-homogenous reactor (CHR) model [14]. Relative error is defined as $R_{error}=([C]_t-[C]_0)/[C]_0\times100\%$, to show the measurement error due to the cool-down process, where $[C]_t$ is the instantaneous species concentration, and $[C]_0$ is the real concentration inside the gasifier. The relative error of the different species was investigated for the syngas temperature to be linearly cooled down from 1588.15 K to 375 K with different temperature drop rates and pressure drop profiles using the same syngas reported in literature [13].

In Fig. 1, the solid line represents the case when the syngas is cooled down linearly within 50 seconds at a pressure of 25.6 bars, and the dotted-line represents the same temperature profile with a pressure drop from 25.6 bar to 1 bar within the first 0.01 seconds. As shown, as the temperature decreases, there are more CO_2 and H_2 produced since the water shift reaction favors lower temperature. Further studies show that there is different syngas composition shift depends on different cooling process (temperature and pressure drop profile). These results show that in model validation, it is not appropriate to simply compare the model results with the measured value and there should be some difference and need to be compensated.

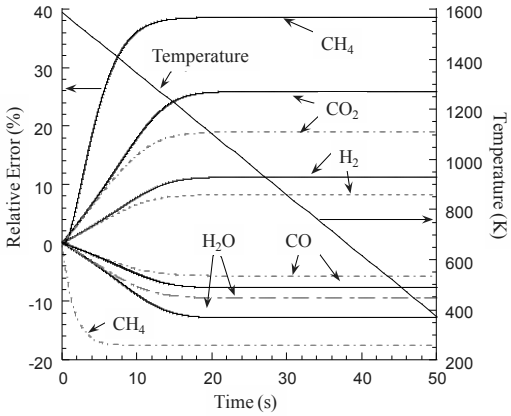

Fig. 1. Measurement error due to the cool-down process (temperature gradually decrease to 373.15 K in 50 seconds)

3. Model description

The model was built up by dividing the gasifier along the height of the gasifier into a series of compartments, as shown in Fig. 2. For each compartment, chemical reactions including heterogeneous and homogeneous reactions, mass transfer processes, and heat transfer processes were considered. The flow structure inside the gasifier was assumed to be a plug flow [15], that is to say, the flow of the coal slurry and oxygen entering the gasifier were assumed to flow through the gasifier along the height without any recirculation or back mixing. By this assumption, the adjacent components can be linked together with simplified solid and gas phase materials passing through as shown in Fig. 3.

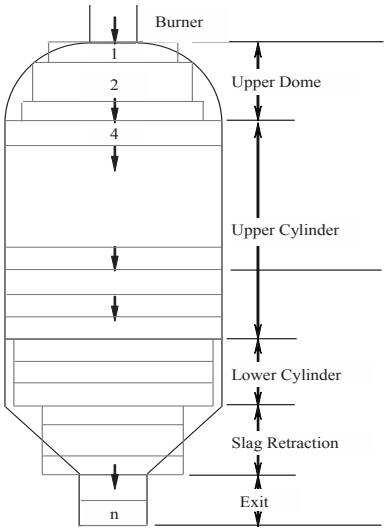

Fig. 2. Schematic diagram of the compartments division along the height of the gasifier

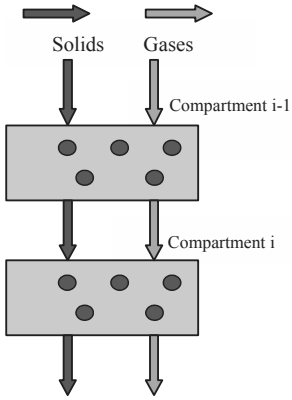

Fig. 3. Mass flow (gas and solid phase) balance between the two adjacent compartments (Note: there is solid-to-gas mass transfer due to gasification)

Based on the simplification made above, a series of governing equations were listed for the energy balance and mass balance of these species concerned.

The energy balance for compartment i can be written as:

$$\frac{dH_i}{d\tau} = H_{f,g,i} + H_{f,s,i} + H_{g,i-1} + H_{s,i-1}, \qquad (1)$$
$$-H_{g,i} - H_{s,i} - Q_i$$

where $H_{f,g,i}$ is the enthalpy flow of gaseous components into compartment i; $H_{f,s,i}$ is the enthalpy flow of the solid into compartment i; $H_{g,i-1}$ is the enthalpy flow of gaseous components from compartment i-1 to compartment i; $H_{s,i-1}$ is the enthalpy flow of the solid from compartment i-1 to compartment i; $H_{g,i}$ is the enthalpy flow of gaseous components from compartment i to compartment i+1; $H_{s,i}$ is the enthalpy flow of the solid from compartment i to compartment i+1; Q_i is the energy loss to the environment from compartment i.

The mass balance of the gaseous components in compartment i can be written as:

$$\frac{d(HU_{j,i})}{d\tau} = W_{g,j,i} + F_{j,i-1} - F_{j,i} + R_{j,i}, \qquad (2)$$

where $HU_{j,i}$ is the mass of the gaseous component j; $W_{g,j,i}$ is the mass flow rate of gaseous component j entering compartment i; $F_{j,i-1}$ is the mass flow rate of gaseous component j flowing from compartment i-1 to compartment I; $F_{j,i}$ is the mass flow rate of gaseous component j leaving compartment i; $R_{j,i}$ is the net mass flow rate of gaseous component j generated or consumed through chemical reactions in compartment i.

The mass balance of solids in compartment i can be written as:

$$\frac{d(HU_i^p)}{d\tau} = W_{S,i} + W_{E,i-1} - W_{E,i} - r_{C,i}, \qquad (3)$$

where HU_i^p is the mass of the solid in compartment i, $W_{s,i}$ is the mass flow rate of solids entering compartment i; $W_{E,i-1}$ and $W_{E,i}$ are flow rates of solid entering compartment i and flowing out of compartment i; $r_{C,i}$ is the carbon conversion rate in compartment i.

For compartment i, the carbon balance can be written as:

$$\frac{d(HU_i^c)}{d\tau} = W_{E,i-1}X_{i-1} - W_{E,i}X_i - r_{C,i}, \qquad (4)$$

where HU_i^c is the mass of the carbon in compartment i; X_i is the mass fraction of carbon in the solid.

For simplicity concern, details of the gasification process are reduced to a minimum set of equations. Among the various compositions of the syngas,

CO, CO_2 H_2, H_2O, CH_4, and H_2S are the products of primary interest. Other trace species, such as HCl, HCN, and NH_3 are excluded from the study scope. It is further assumed that all nitrogen and argon are assumed to be presented as inert N_2. All sulphur is assumed to be irreversibly converted to H_2S. The following reactions were considered, including homogeneous and heterogeneous reactions, as listed in Table 1. The detailed reaction rate of each reaction can be found in literature [4-5].

Table 1. Reaction Mechanism.

Homogenous reactions	Heterogeneous reactions
$CO+0.5O_2 \rightarrow CO_2$	$C + H_2O \rightarrow CO + H_2$
$H_2+0.5O_2 \rightarrow H_2O$	$C+2H_2 \rightarrow CH_4$
$CO + H_2O \rightarrow CO_2 + H_2$	$C + 1/\Phi\ O_2 \rightarrow (2-2/\Phi)CO + (2/\Phi -1)CO_2$
$CO_2 + H_2 \rightarrow CO + H_2O$	$C + CO_2 \rightarrow 2CO$
$CH_4+H_2O \rightarrow CO+3H_2$	$CO + H_2O \rightarrow CO_2 + H_2$
$CH_4+2O_2 \rightarrow CO_2+2H_2O$	

These governing equations were coupled together with the heterogeneous and homogeneous reactions and usually they are solved using Newton-Raphson method [4]. However, the Newton-Raphson method is not applicable to dynamic model for real time calculation. In the present work, it is assumed that the temperature change of each compartment inside the gasifier is slower than the change of the syngas composition and the flow condition, therefore decoupling the calculation of these governing equations is possible. That is, for the calculation of each time interval, firstly, the mass flow rate of the involved species was determined based on the status of last time interval; the species, including gas phase and solid phase species, were calculated then based on the previous temperature profile and species concentration; and the temperature profile will be updated thereafter. As described in the previous section, the water-shift reaction reaches quasi-equilibrium with the gasifier temperature above a certain value, and this means adding an additional equation and accelerating the model solution.

4. Results and discussion

The model presented in this article has been compared to the data from a real industrial scale gasifier, which is a 500 t/d oxygen staged entrained flow gasifier designed by Tsinghua. As shown in Fig. 4, the gasifier has two stages for oxygen supply. One is at the top of the gasifier and the other is on the upper part of the gasifier. The proximate and ultimate analyses of the coal used in this gasifier are given in Table 2.

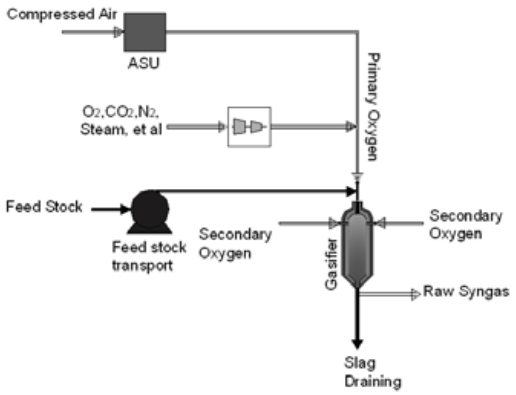

Fig. 4. Schematic diagram of the oxygen staged entrained flow gasifier

Table 2. Proximate analysis and ultimate analysis.

Proximate analysis	wt% wet basis
Moisture	14
Fixed carbon	50.38
VM	29.59
Ash	6.04

Ultimate analysis	wt% dry basis
Ash	7.02
Carbon	75.14
Hydrogen	4.50
Nitrogen	0.96
Sulfur	0.42
Oxygen	11.98

The model presented in this article was validated at the normal working condition of the plant using the inlet parameters shown in Table 3. Table 4 showed that slightly differences have been observed between model results and industrial data based on the syngas composition at the gasifier outlet and the quench chamber outlet. As shown, the results were very close to measured value. According the previous section, the measured CO_2 and H_2 volume percentage at the gasifier outlet

should be a little bit higher than the model result, which is exactly the case as shown in Table 4.

Table 3. Plant inlet parameters at the baseline scenario.

Oxygen		Slurry		Operating target	
Purity (%)	95	Concen-tration	0.6	Gasifier tempe-rature	1240.8
Primary feed rate (kg/s)	4.15	Feed rate (kg/s)	7.28	Gasifier pressure (MPaG)	4.1
Secondary feed rate (kg/s)	0.73	Tempe-rature (degC)	50	Quench chamber pressure (MPaG)	4.0
Tempe-rature (degC)	30	Pressure (MPaG)	5.6	Scrubber pressure (MPaG)	3.9
Pressure (MPaG)	5.6				

Table 4. Model validation (concentration expressed on a wet molar basis).

	Gasifier outlet		Quench outlet	
	model result	Industrial data	model result	Industrial data
CO	36.36%	35.74%	13.94%	13.61%
H_2	30.46%	30.53%	11.67%	11.74%
CO_2	14.17%	14.47%	5.42%	5.51%
CH_4	0.1%	0.09%	0.04%	0.04%
H_2O	17.36%	17.45%	68.32%	68.35%
N_2,AR	1.49%	1.5%	0.57%	0.58%
H_2S	0.11%	0.11%	0.04%	0.04%
Syngas flow rate	72630.09 Nm^3/hr	71637.89 Nm^3/hr	189487.2 Nm^3/hr	188085.57 Nm^3/hr

In order to demonstrate the advantages of the oxygen staged gasifier, a comparison has been made between an oxygen staged gasifier and a one-stage gasifier. As shown in Fig. 5, due to the staged oxygen feed, the temperature in the gasifier showed two temperature peaks along the height of the gasifier, and the highest temperature near the nozzle of the gasifier is much lower than that of a one-stage GE-Texaco gasifier with the same oxygen and slurry feed rates. Because of this, the Tsinghua oxygen staged gasifier has a much longer nozzle life time.

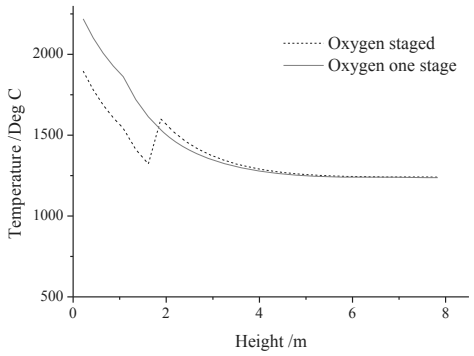

Fig. 5. Temperature along the height of the gasifier in oxygen staged gasifier and one stage GE-Texaco gasifier

In real situation, experimental results also showed that the effective syngas ($CO+H_2$) of a Tsinghua oxygen staged gasifier is a little bit higher than that of a one stage GE-Texaco gasifier under the same working condition. This is because the staged oxygen feed manner intensifies the reduction reactions in the gasifier by changing the structure of the flow field. However, since the complicated flow condition was greatly simplified, the present model can not reflect this phenomenon.

5. Summary

A full working condition simulation model for Tsinghua designed oxygen staged entrained flow gasifier was established and the results were validated. The model was constructed by dividing the gasifier into a series of cells along the height of the gasifier and setting mass, species, and energy conservation equations for each cell. To obtain a deep understanding of the reaction mechanism, Chemkin software (GRI Mech III) was utilized to study the reactions among CO, CO_2, H_2, H_2O, O_2, N_2, CH_4, and H_2S to simulate the transient syngas species concentration change process inside the gasifier after coal-oxygen reactions and during the temperature cooling down process for down-stream syngas composition measurement. Results showed that the shift reaction, $CO+H_2O=CO_2+H_2$, is the dominating reaction step, and it reaches an equilibrium state in a typical entrained-flow gasifier very quickly, therefore determining the main syngas species compositions. This gives an extra equation for the species concentration calculation and enables the model with real time

calculation capability. Results also indicated that there is difference between the real syngas composition inside the gasifier and the measured value after being cooled down, requiring compensation in model validation. These understanding were applied in establishing and validating the simulation model. The model results were compared with the data from a real industrial scale gasifier, it was found that under normal working conditions, they were highly consistent. The model also demonstrated its ability to simulate the whole working conditions including start-up and shut-down process. Steady-state and dynamic performance of the gasifier were studied as well using the simulation model. Due to the staged oxygen feed, the temperature showed a special profile, with two temperature peaks, along the height of the gasifier, and the highest temperature inside the gasifier is lower than that of a GE-Texaco entrained-flow gasifier with the same oxygen and slurry feed rates, explained the reason that the Tsinghua oxygen staged gasifier has a much longer nozzle life time.

Acknowledgement: The work is sponsored by national research project of China under contract 2005CB221207 and 2010CB227006.

References

[1] Ruggiero, M., and Manfrida, G., 1999, An equilibrium model for biomass gasification processes, Renewable Energy, 16(1-4), pp. 1106-1109.

[2] Chern, S.M., et al., 1991, Equilibrium modeling of a downdraft Gasifier. 1. Overall gasifier, Chemical Engineering Communications, 108, pp. 243-265.

[3] Li, X., et al., 2001, Equilibrium modeling of gasification: a free energy minimization approach and its application to a circulating fluidized bed coal gasifier, Fuel, 80(2), pp. 195-207.

[4] Li, Z., et al., 2001, Study of mathematical model for Texaco gasifier (I)-Modeling, Power Engineering, 21(2), pp. 1316-1319.

[5] Li, Z., et al., 2001, Study of mathematical model for Texaco gasifier (II)-Calculation and analysis, Power Engineering, 21(4), pp. 1161-1168.

[6] Ruprecht, P., et al., 1988, A computer model of entrained coal gasification, Fuel, 67(6), pp. 739-742.

[7] Chen, C., et al., 2000, Numerical simulation of entrained flow coal gasifiers, Part I: modeling of coal gasification in an entrained flow gasifier, Chemical Engineering Science, 55, pp. 3861-3874

[8] Chen, C., et al., 2000, Numerical simulation of entrained flow coal gasifiers, Part II: effects of operating conditions on gasifier performance, Chemical Engineering Science, 55, pp. 3875-3883

[9] Chen, C., et al., 2001, Use of numerical modeling in the design and scale-up of entrained flow coal gasifiers, Fuel, 80, pp. 1513-1523

[10] Choi, Y., et al., 2001, Numerical study on the coal gasification characteristics in an entrained flow coal gasifier, Fuel, 80, pp. 2193-2201

[11] Cho, H., 2000, A numerical study on parametric sensitivity of the flow characteristics on pulverized coal gasification, International Journal Energy Research, 24, pp. 511-523

[12] Vicente, W., et al., 2003, An Eulerian model for the simulation of an entrained flow coal gasifier, Applied Thermal Engineering, 23, pp. 1993-2008

[13] Wang, Z., et al., 2009, Syngas Composition Study, Frontiers of Energy and Power Engineering in China, 3(3), pp. 369-372.

[14] Lutz, A., et al., 1988, SENKIN: A Fortran Program for Predicting Homogeneous Gas Phase Chemical Kinetics with Sensitivity Analysis, Sandia National Laboratories Report, 87-8248, Sandia.

[15] Wen, C., and Chaung, T., 1979, Entrainment coal gasification modelling, Industrial and Engineering Chemistry, Process Design and Development, 18(4), pp. 684-694.

Synthetic Natural Gas (SNG) Production at Pulp Mills from a Circulating Fluidized Bed Black Liquor Gasification Process with Direct Causticization

M. Naqvi [a], J. Yan[a, b], E. Dahlquist [b]

[a] *KTH Royal Institute of Technology, Stockholm, Sweden*
[b] *Mälardalen University, Västerås, Sweden*

Abstract: Synthetic natural gas (SNG) production from black liquor gasification (BLG) replacing conventional recovery cycle at chemical pulp mills is an attractive option to reduce CO_2 emissions and replace fossil natural gas. This paper evaluates the potential of SNG production from a circulating fluidized bed BLG process with direct causticization by investigating synthesis gas composition, purity requirements for SNG and process integration with the reference pulp mill producing 1000 air dried tonnes (ADt) of pulp per day. The objective of this study is to estimate the integrated process efficiency from black liquor (BL) conversion to SNG and to quantify the differences in overall process efficiencies of various bio-refinery options. The models include a BLG Island including BL gasifier, synthesis gas cooling and cleaning unit, methanation with SNG upgrading and a power boiler. The result indicates a large potential of SNG production from BL but at a cost of additional biomass import to compensate energy deficit in terms of BL conversion to SNG. In addition, the study shows a significant CO_2 abatement when CO_2 capture is carried out in SNG upgrading and also reducing CO_2 emissions when SNG potentially replaces fossil natural gas.

Keywords: Black Liquor Gasification; Synthetic Natural Gas; Pulp Mill; CO_2 Emissions.

1. Introduction

According to Energy Information Administration (EIA), worldwide energy consumption is increasing and it is projected to expand 50% from 2005 to 2030 causing depletion of known fossil resources [1]. In Europe, about 25% of the total energy comes from natural gas and the demand will increase 2-3% annually in the period till 2020. Natural gas is a primary energy source used for electricity generation, domestic and commercial heating purposes, and more importantly as an automotive fuel i.e. compressed natural gas (CNG). The rapid growth in fossil natural gas utilization leads to increased greenhouse gas emissions. In this perspective, mitigation of climate change and energy security is one of the driving forces for increased biomass energy utilization. A variety of initiatives are under development aiming at reducing natural gas dependency and fossil based greenhouse gas emissions.

Forest-based biomass plays an important role as a raw material for wood-based products and as a renewable for energy uses. The pulp and paper industry consumes a large proportion of forest biomass and is considered a potential candidate to become renewable fuel supplier in future energy system using black liquor (BL). BL is spent cooking liquor that can be gasified at high temperature to produce a synthesis gas containing CO, H_2, and CH_4 as major constituents. The synthesis gas is cooled, cleaned from tars and sulfur containing compounds and further processed to produce renewable energy products e.g. electricity, synthetic natural gas (SNG), methanol, dimethyl ether (DME) etc. Renewable SNG production via black liquor gasification (BLG) is an interesting option to reduce fossil fuel demand and the associated greenhouse gas emissions. The BLG route can be advantageous in terms of fuel security, existing supply infrastructure and natural gas applications in wide range of industries.

During the past couple of decades, a number of studies have been performed to investigate various BLG technologies including SCA-Billerud process, Manufacturing and Technology Conversion International (MTCI) process, Direct Alkali Regeneration System (DARS), BLG with direct causticization, and Chemrec BLG system, to replace conventional BL recovery cycle with the recovery boiler [2-7]. Various options to produce electricity or bio-fuel from BLG is currently being investigated by a number of researchers [8-10].The BLG technologies were developed to eliminate the

Corresponding Author: Muhammad Naqvi, Email: rnaqvi@kth.se

drawbacks associated with the recovery boiler e.g. low electricity generation efficiency, smelt-water explosions and reduced-sulfur gas emissions [11]. The potential electricity or biofuel production have been studied mostly with Chemrec BLG system integrated with modern pulp mills but there is no valuable effort made to estimate the potential electricity or biofuel production from other gasification technologies [3, 12].

The present paper evaluates the potential of SNG production from a circulating fluidized bed BLG process with direct causticization by investigating synthesis gas composition, purity requirements for SNG and process integration with the reference pulp mill producing 1000 air dried tonnes (ADt) of pulp per day. The objective of this study is to estimate potential SNG production, integrated process efficiency from black liquor (BL) conversion to SNG and to quantify the differences in overall process efficiencies of various bio-refinery options. The emphasis is to keep pulping process unchanged and to recover cooking chemicals for re-use in digestion unit. In addition, the potential CO_2 reductions are estimated if SNG is used as an automotive fuel replacing fossil natural gas.

2. Process configurations

In a BLG process, a gasification Island is used to replace the conventional recovery cycle to increase potential energy efficiency and also eliminating the drawbacks associated with the recovery boiler. BL is gasified in the reactor at high temperatures under reducing conditions and synthesis gas is separated from the inorganic content e.g. mainly sodium carbonate and sodium sulfate [13]. SNG production from BL consists of three major process steps, namely a circulating fluidized bed gasification with direct causticization, methane synthesis and gas upgrading. Fig. 1 shows a simplified scheme of BL conversion to SNG. The major steps are discussed in later sub-sections.

2.1. Dry BLG with direct causticization

In dry BLG (DBLG) process with direct causticization, the recovery boiler is replaced by a gasifier but also the conventional recovery cycle is replaced by a titanate cycle. The Titanate cycle in the DBLG system is shown in Fig. 2. BL is introduced into a fluidized bed of titanium dioxide (TiO_2) in a circulating fluidized bed (CFB) gasifier [13]. The organics of BL are gasified by steam reforming due to relatively low temperature (below 870 °C) and relatively high water content (>20% water). The synthesis gas constitutes H_2, CO, CH_4 and CO_2, as main feedstock for SNG production. During the gasification, sulfates in BL are reduced to sulfides and a major part of sulfides are evaporated as hydrogen sulfide (H_2S). The sodium carbonate is evaporated to CO_2 forming $Na_2O.TiO_2$ which means direct caustization in the bed. This leads to elimination of complicated and energy-intensive lime kiln for reburning of $CaCO_3$ as is normally the case in the conventional recovery cycle. The main reactions in the gasifier are [14]:

$$7\ Na_2CO_3 + 5\ (Na_2O.3TiO_2) \rightarrow 3\ (4Na_2O.5TiO_2) + 7\ CO_2 \quad (1)$$

$$Na_2SO_4 + 2\ C \rightarrow Na_2S + 2\ CO_2 \quad (2)$$

$$Na_2S + CO_2 + H_2O \rightarrow Na_2CO_3 + H_2S \quad (3)$$

During leaching with water, the sodium pentatitanate formed in the gasifier is converted to sodium trititanate and sodium hydroxide (white liquor). See reaction 4.

$$13(4Na_2O.5TiO_2) + 7H_2O \rightarrow 5(Na_2O.3TiO_2) + 14NaOH \quad (4)$$

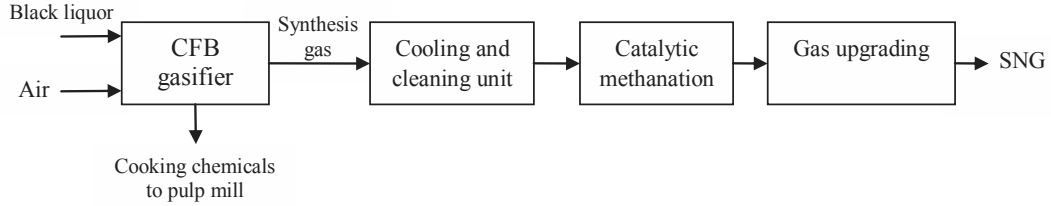

Fig. 1. Simplified flow chart of BL conversion to SNG

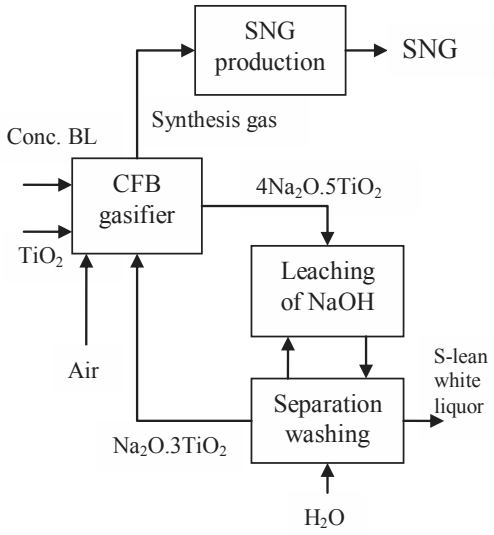

Fig.2. The DBLG system with titanate cycle

The sodium tri-titanate is separated from the white liquor and recycled to the gasifier. The sulfur-lean white liquor is sent back to the pulp mill for reuse in the digestion unit. The H_2S in the synthesis gas is recovered using selective absorption and can be used to produce sulfur-rich aqueous stream.

2.2. Synthesis gas cooling and cleaning

The synthesis gas leaving the CFB gasifier is saturated with water vapours representing a considerable amount of heat energy that can be recovered to generate medium and low pressure steam. The synthesis gas needs to be free of both sulphur compounds and tars. To accomplish both operations, a combined gas cooling and particulate removal unit is used e.g. counter current condenser type of gas cooler [3]. A stream of cold methanol is used as a solvent in an absorption unit that removes condensable tar like benzene, naphthalene and water. The solvent is regenerated by liquid-liquid extraction after dilution with water and final separation by distillation. To remove sulfur components in the synthesis gas, a new type of absorption system is used with sodium carbonate (Na_2CO_3) solution as solvent, developed by Dahlquist and Wallin [13]. H_2S is absorbed in a gas scrubber, reacting immediately with Na_2CO_3 solution in a selective way; while CO_2 reacts very slowly. The designed absorption system provides 20 times more absorption of H_2S than the absorption of CO_2. The sulphur rich stream is then sent back to pulp mill to re-use in the pulping process.

2.3. Catalytic methanation

The H_2/CO ratio prior to methanation is approximately at 3 in the synthesis gas that eliminates need for CO-shift conversion. Methanation is a catalytic process to convert the synthesis gas (mainly carbon monoxide and hydrogen) to methane using a nickel-based catalyst. Methane synthesis occurs with the following strongly exothermic reaction [15]:

$$CO + 3H_2 \leftrightarrow CH_4 + H_2O \qquad \Delta Hr = -217 \text{ kJ/mol} \quad (5)$$

$$CO_2 + 4H_2 \leftrightarrow CH_4 + 2H_2O \qquad \Delta Hr = -178 \text{ kJ/mol} \quad (6)$$

Due to strong exothermicity, the methanation process represents a valuable source of heat to generate steam. This heat must be removed to achieve high conversions and efficient performance of the reactor. This is done by performing methanation in successive adiabatic units with a recycle flow to control the temperature (e.g. Hygas or Lurgi) [16-17]. The methanation process operates at a temperature range of about 250-500 °C. Temperature control is necessary due to carbonyl formation at low temperatures, carbon depositions on the active catalyst surface and catalyst poisoning at higher temperatures.

2.4. SNG Upgrading

SNG upgrading includes CO_2 and N_2 separation from the gas to achieve high purity of SNG as product. See following sections.

2.4.1. CO_2 capture

SNG rich synthesis gas from the methanation unit contains a significant amount of water and CO_2 that must be separated. Initially during SNG upgrading, most of the water is condensed by cooling the gas and remaining water is removed in CH_4-CO_2 separation unit. Various commercial separation technologies for CO_2 removal are available like membrane gas separation, pressure swing adsorption (PSA) or physical absorption (e.g. Selexol process). In the present study, the Selexol process is selected based on CO_2 absorption in a solvent i.e. dimethyl ether of polyethylene glycol (DMPEG). The Selexol

process is ideal for bulk removal of CO_2 e.g. 99% CO_2-CH_4 separation efficiency [18]. The solubility of CO_2 in the solvent is significantly higher than CH_4 that results in a high purity of SNG. The CO_2 rich gas is sequestrated in empty gas fields allowing the overall process to be CO_2-negative. However, the compression energy required is not included in overall efficiency estimation. Note CO_2 capture technologies are still under development and are not implemented yet.

2.4.2. Nitrogen rejection

In air blown BLG process, N_2 is a major contaminant in the synthesis gas (about 39% vol) and is quite difficult to separate from SNG. The heating value of the gas is lowered due to dilution of SNG with N_2 and makes it unacceptable to use as transport fuel. For this reason, a cryogenic nitrogen rejection system is employed to separate N_2 from SNG in this study [24]. The cryogenic process separates SNG and N_2 based on the phase change (from gas to liquid) at different temperatures. Methane is liquefied (temperature ranges between –160 to –165 °C) and collected, as it drops out of the product gas. The remaining gas is re-vaporized which can be either flared or vented to the atmosphere. The process is energy intensive and requires a significant amount of electric power.

3. Methodology

3.1. System boundary

This section presents system boundary with assumptions and methodology adapted to model dry BLG (DBLG) system with direct causticization for SNG production integrated with a reference pulp mill (a detail on reference pulp mill is discussed in next section). To avoid any major impacts on the pulping process, it is assumed that all cooking chemicals must be recovered from the gasifier and sent back to the pulp mill for reuse in digestion unit. The integrated BLG system with the pulp mill for SNG production requires compensating process heat and electricity from BL by additional biomass import and combustion in the power boiler. This is due to BL conversion to SNG instead combustion in the recovery boiler to generate process heat (steam) and electricity. The new energy demand for the integrated reference pulp mill is reduced in DBLG system mainly due to the elimination of energy intensive lime kiln.

3.2. Reference pulp mill system

An Eco-cyclic pulp mill developed within the Swedish research program KAM (Kretslopps Anpassad Massafabrik) is selected as a reference for material and energy balances. KAM mill is a hypothetical and generic mill with commercially best available technologies with better integration under high environmental standards. The nominal scale of the KAM reference pulp mill is 2000 air dry metric tonnes (ADt) per day of pulp production [19]. Base capacity for the reference mill selected for this study is 1000 ADt/day of pulp production that is approximately equivalent to1700 tonnes per day of black liquor solids (BLS, as dry). The reference mill is assumed to produce a surplus of bark and electricity. Table 1 shows key assumption parameters used for modeling of DBLG integrated reference pulp mill.

3.3. Process simulation and energy balances

The process flow charts of SNG production from DBLG system with operational parameters is shown in Fig. 3. The integrated DBLG system comprises all units from BL conversion to SNG production and a power boiler. The process models include BL input to CFB gasifier, gas cooling and cleaning unit, catalytic methanation unit and SNG upgrading.

The key input values used for modeling and energy calculations are listed in Table 2. The DBLG system is modeled from simulations with polynoms (i.e. SIMCA) made from the pilot plant operations and physical relations.

Table 1. Reference pulp mill characteristic

Pulp production	ADt pulp/day	1000
Wood consumption	tonnes/day	2074
BL concentration	% solids	80
BLS per tonne pulp	tonnes/tonne	1.7
BLS flow rate	tonnes BLS/day	1700
BL, heating value	MJ/kg	12.4
BL energy content	MW	243.5
Mill steam use	MW_{th}	125
Mill electricity use	MW_e	29.7
High-pressure steam	°C	545
	bar	140
Medium-pressure	°C	195
	bar	12
Low-pressure	°C	150
	bar	4

Table 2. Key operating parameters for DBLG system modeling

CFB Gasifier		
Pressure	bar	1.01
Temperature	°C	720
BLS to gasifier	%	100
Gas at cooler outlet		
Temperature	°C	30
Methanation unit		
Temperature	°C	300
Pressure	bar	10
Selexol process		
CH_4 loss	%	1
CO_2 removal	%	98
Nitrogen rejection		
Temperature	°C	-165

Table 3. Synthesis gas data at CFB gasifier's outlet

	Vol%	mol/sec	
H_2	14.2	181.1	
CO	3.6	45.9	
CH_4	1.8	22.9	
CO_2	11.2	142.8	
H_2S	0.54	6.9	
H_2O	29.6	377.4	
N_2	39.1	498.5	
Flow rate	Nm^3/sec		28.4
Lower heating value	MJ/ Nm^3		3.3
Energy content, (LHV)	MW		93.7

The composition of synthesis gas from pilot plant data at a relative oxidation of 35% and H_2S removal in newly designed absorption system using sodium carbonate as a solvent for H_2S reported by Dahlquist and Jones (2005) is used [13]. The gas composition in DBLG system was measured by Dahlquist in a pilot plant operated in Vasteras, on-line with respect to CO_2, CO, H_2 and CH_4, while H_2S was measured by extracting gas through a "Draeger tube". See Table 3. The compositions of N_2 and O_2 were obtained from measurements of air flow rate and knowledge about "organic" oxygen content of the black liquor from chemical analysis. H_2O content was calculated from condensate flow and temperature of the synthesis gas.

3.4. Power boiler

The combustion of BL in the recovery boiler is responsible for generating steam and electricity for the pulping processes [20]. However, in case of integrated BLG with the reference pulp mill for SNG production, the total demand of heat and electricity shall be fulfilled by employing a new biomass power boiler. To compensate energy deficit due to BL conversion to SNG, additional biomass is combusted in the power boiler. In addition, the power boiler will use falling bark and part of the synthesis gas.

The assumed design fuel mix for the power boiler is; 80 wt% biomass and falling bark and 20 wt% synthesis gas. The power boiler is dimensioned primarily to generate steam as much as produced by the recovery boiler for mill process use and also to meet internal steam demand of BLG Island. The high pressure steam is used in a back pressure steam turbine for process steam extraction.

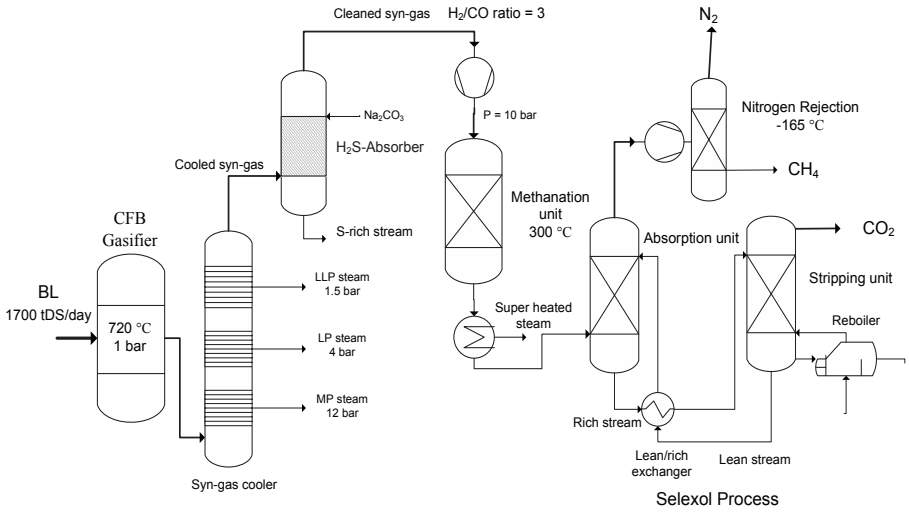

Fig.3. Process flow diagram of SNG production via DBLG system

4. System performance indicators

In present study, the results for feasibility of SNG production from BLG with direct causticization are evaluated using system performance indicators i.e. SNG production potential, BL to SNG conversion efficiency, and comparison with conventional recovery boiler system and also with alternative bio-fuel production routes. Material and energy balances are used to determine the potential electricity, steam and SNG production based on reference pulp mill capacity. The additional biomass import needed to compensate the energy withdrawn from BL in terms of fuel production is also estimated. The results based on system performance indicators are summarized and compared in the following sections.

4.1. Potential SNG production

In order to evaluate the system performance, the integrated BLG system with SNG production is compared in terms of steam and electricity with conventional recovery boiler. The potential SNG production is calculated. A detailed mass and energy balances for important streams in BLG Island integrated with the reference pulp mill are shown in Table 4. Recall that pulp mill's steam demand is met by both BLG Island and additional biomass combustion in the power boiler.

4.2. Comparison of Process efficiency with other bio-refinery routes

The overall process efficiency is defined as the sum of mill process steam, net electricity import or export, and SNG production divided by the sum of energy inputs i.e. black liquor (dry solids), bark to lime kiln and bark to power boiler. The process efficiency is used as a performance indicator to evaluate the competitiveness of integrated BLG system to replace the recovery boiler. Table 5 shows a comparison of different biofuel production routes from various BLG technologies e.g. Chemrec BLG system and Catalytic hydrothermal BLG system. The data from various studies have been scaled up to a pulp production of 1000 ADt/day for justified comparisons.

4.3. Potential CO_2 savings

The potential CO_2 offset is calculated for CO_2 capture in the Selexol process and also CO_2 use replacing natural gas. It is important to mention that CO2 capture technologies are still in research phase and the study only estimates possible CO2 savings. To estimate the potential CO_2 savings, it is assumed that SNG produced from black liquor is CO_2 neutral. There are some fossil fuel CO_2 emissions from upstream processes i.e. additional biomass cultivation and transport to production site. In addition, the electricity import outside the pulp mill facility also contributes CO2 emissions, but these emissions are not included in the scope of this study. About 0.05 kg of CO_2 could be saved for each mega joule of SNG replacing natural gas [21]. The theoretical annual CO_2 savings from SNG replacing natural gas based in black liquor availability in the reference case, Sweden, Europe and World is reported in Table 6.

5. Discussion

The DBLG system differs mainly with conventional black liquor recovery system and also in terms of energy balances. In conventional recovery system, sodium and sulfur as molten sodium sulfide and sodium carbonate, in the form of smelt are recovered at the bottom of the recovery boiler. The smelt is then dissolved in weak wash to produce green liquor. Before it can be reused for delignification, the causticizing of green liquor is performed to produce calcium carbonate and sodium hydroxide. However, in DBLG system direct causticization is performed within the reactor that eliminates the causticizing needs i.e. elimination of the lime kiln.

Table 4. Comparison of heat and mass balances of conventional recovery system with DBLG system

		RB[a]	DBLG
BL, LHV[b]	MW	243.5	243.5
Existing bark, LHV	MW	40.5	40.5
Bark to lime kiln [c]	MW	21.1	-
Bark to power boiler	MW	-	55.1
Net bark available	MW	19.6	-14.6
Electric power			
Mill use	MW	27.6	26.1
BL unit consumption	MW	2.5	5.3
Electricity production	MW	52.2	16.7
Import/Export (-/+)	MW	22.1	-14.7
Steam balance			
Mill use	MW	125	125.6
Net BLG production	MW	-	68.9
Power boiler	MW	-	56.7
SNG Production	tonnes/day	-	110.4
LHV	MW	-	63.8

[a] Conventional recovery boiler system
[b] Lower heating values (LHV)of fuels, e.g. BL (12.3MJ/kg), bark (19.4 MJ/kg), natural gas (50 MJ/kg).
[c] Elimination of lime kiln in BLG with direct caustization.

Table 5. Comparison of process efficiencies of various biofuels

Parameters	Bio-refineries			
Reference system	Ekbom et al. (2003) [3]	Andersson and Harvey (2006) [8]	Naqvi et al. (2010) [10]	DBLG
Product	DME	H_2	CH_4	SNG
Pulp (ADt/day)	1000	1000	1000	1000
BLS, MW	243.5	243.5	243.5	243.5
Steam to mill's process, MW	125	125	125	125
Bark to power boiler, MW	73.4	85.8	117.4	55.1
Bark to lime kiln, MW	24.5	29.7	29.6	-
Electricity, Import/Export (-/+), MW	-27.7	-28.4	1.1	-14.7
Fuel production (LHV), MW	137.5	130.5	240.2	63.8
Process efficiency				
Total energy input, MW	341.4	359	390.5	298.6
Total energy output, MW	234.8	227.1	366.3	174.1
Energy efficiency, %	69	63	93	58

Table 6. Potential CO_2 offset based on BLS availability in 2008

DBLG system		Ref. mill	Sweden	Europe	World
BLS availability [a]	million tonne BLS/year	0.60	14.4	66.8	230
SNG production	million tonnes/year	0.04	0.96	4.5	15.4
CO_2 savings					
SNG upgrading (CO_2 capture)	million tonnes/year	0.18	4.32	20.1	68.9
Natural gas replacement	million tonnes/year	0.098	2.4	11.1	37.7

[a] Based on the Food and Agriculture Organization (FAO) data base 2008 [23]

With the dry BLG process approximately 65% of the sulfur is forming H_2S and goes with the gas phase. It is then recovered with a mixture of NaOH and Na_2CO_3 at pH 10.5, where a selective absorption of H_2S can be achieved in relation to CO_2, and thus a strong NaHS phase formed (1 molar). When the sodium oxide titanate is leached in water we directly get NaOH, and thus a separation is made between NaOH and NaHS, which enables modified cooking [22].

From energy perspectives, DBLG system showed higher process energy efficiency and significant improvements in the overall energy system at the pulp mill compared to the recovery boiler i.e. 60% energy efficiency in DBLG system compared to 55% efficiency in recovery boiler system. About 24.5 MW of bark is required in the lime kiln in conventional recover system but DBLG system eliminates significant bark requirement.

The reference pulp mill system has a better potential in electricity balance. About 22 MW of electricity can be export to grid, after meeting mill process electricity demand. However, the DBLG system of SNG production requires an import of about 12 MW of electricity from the grid.

The DBLG system offers significant incentives in terms of potential CO_2 savings both in the process and replacement of natural gas use. See Table 6. In SNG upgrading step, the Selexol process, part of the biomass carbon is captured as CO_2, which can stored to make system CO_2 negative as CO_2 emissions associated with biomass usage are assumed to be re-absorbed photosynthetically by biomass growth. The compression energy required for CO_2 storage is not included in this study. The study shows CO_2 capture potential in the process much larger than CO_2 savings from natural gas replacement.

6. Conclusions

Bio-refinery operation at the pulp mills for SNG production is an interesting option to reduce CO_2 emissions. SNG is a promising fuel for a large number of efficient and clean applications in transportation and industrial sector. The study shows large SNG production potential in Sweden, Europe and World based on black liquor availability. The process modeling of black liquor gasification with direct causticization shows an attractive energy efficiency of 60% that is competitive with other bio-refinery routes. In addition, potential CO_2 offset from the system is significant.

References

[1] Energy Information Administration, 2009. Independent statistics and analysis, Department of energy, United States. http://www.eia.doe.gov/oiaf/ieo/world.html

[2] Berglin, N., and Berntsson, T., 1998, CHP in the pulp industry using black liquor gasification: thermodynamic analysis, Applied Thermal Engineering 18, pp. 947-961.

[3] Ekbom, T., et al., 2003, Technical and commercial feasibility study of black liquor gasification with Methanol/DME production as motor fuels for automotive uses-BLGMF, European commission, Altener program. Stockholm, Sweden.

[4] Möllersten, K., Yan, J., and Westermark, M., 2003a, Potential and Cost-Effectiveness of CO_2-Reduction in the Swedish Pulp and Paper sector, Energy 28, pp. 691-710.

[5] Möllersten, K., et al., 2004, Efficient energy systems with CO_2 capture and storage from renewable biomass in pulp and paper mills, Renewable Energy, 29, pp 1583-1598.

[6] Harvey, S., and Facchini, B., 2004, Predicting black liquor gasification combined cycle powerhouse performance accounting for off-design gas turbine operation, Applied thermal engineering 24, pp. 111-126.

[7] Yan, J., et al., 2007, Integration of Large Scale Pulp and Paper Mills with CO_2 Mitigation Technologies, the 3rd International Green Energy Conference, Västerås, Sweden.

[8] Andersson, E., and Harvey, S., 2006, System analysis of hydrogen production from gasified black liquor, Energy 31, pp. 3426-3434.

[9] Consonni, S., Katofsky, R., and Larson, E., 2009, A gasification-based biorefinery for the pulp and paper industry, Chemical Engineering Research and Design, in press.

[10] Naqvi, M., Yan, J., and Fröling, M., 2010, Bio-refinery system of DME or CH_4 production from black liquor gasification in pulp mills, Bioresource technology 101, pp. 937-944.

[11] Whitty, K., 2005, Black Liquor Gasification: Development and Commercialization Update. ACERC Annual Conference, Provo Utah.

[12] Larson, E., Kreutz, T., and Consonni, S., 2006, A Cost-Benefit Assessment of Gasification-based biorefining in the Kraft Pulp and Paper Industry, Final report, Volume 1. Princeton University and Politecnico di Milano.

[13] Dahlquist, E., and Jones, A., 2005 Presentation of a dry black liquor gasification process with direct caustization, TAPPI Journal, pp. 15-19.

[14] Nohlgren, I., and Sinquefield, S., 2004, Black liquor gasification with Direct Causticization Using Titanates: Equilibrium Calculations, Ind. Eng. Chem. Res., 43 (19), pp. 5996-6000.

[15] Meijden, C.M., Veringa, H.J., Rabou, L.P., 2009, The production of synthetic natural gas (SNG): A comparison of three wood gasification systems for energy balance and overall efficiency, Biomass and Bioenergy, in press.

[16] Bair, G., Leppin, D., and Lee, A.L., 1975, Design and operation of catalytic methanation in hygas pilot plant. Advances in Chemistry Series, No. 146, pp. 123–137.

[17] Moeller, W., Roberts, H., and Britz, B., 1974, Methanation of coal gas for SNG. Hydrocarbon Processing, 53, No. 4, pp. 69–74.

[18] Ruben, S., et al., 2007, Development and application of optimal design capability for coal gasification systems. Report DE-AC21–92MC29094.

[19] KAM-report A100, 2003, Final report from the ecocyclic pulp mill programme: STFI, 2003, Stockholm, Sweden.

[20] Joelsson, J., and Gustavsson, L., 2008, CO_2 emission and oil use reduction through black liquor gasification and energy efficiency in pulp and paper industry, Resources, Conservation and Recycling 52, pp. 747-763.

[21] Energy Information Administration, 1998, Natural gas issues and Trends, DOE/EIA-0560(98), Department of energy, United States. http://www.eia.doe.gov/pub/oil_gas/natural_gas/analysis_publications/natural_gas_1998_issues_trends/pdf/it98.pdf

[22] Hakanen, A., and Teder, A., 1997, Modified Kraft Cooking with Poiysulfide: Yield, Viscosity, and Physical Properties, TAPPI Journal 80(7), pp. 189-196.

[23] FAOSTAT - Forestry, Food and Agriculture Organization of the United Nations, January 2008.

[24] Lokhandwala, K. et al., 1999, Nitrogen removal from natural gas, Phase II draft final report, U.S. Department of Energy Morgantown, WV.

Acknowledgments: One of authors (Naqvi) would like to acknowledge the HEC/SI Scholarship Programme, which is funded by Higher Education Commission Pakistan and managed by Swedish Institute.

RELIABILITY ANALYSIS OF SUGARCANE ETHANOL PROCESSING PLANT EQUIPMENT

Fernando J. Guevara Carazas [a], Rodolfo Molinari [a] and Gilberto F. Martha de Souza [a]

[a] *Polytechnic School, University of São Paulo, São Paulo, Brazil*

Abstract: The sugarcane ethanol processing plant is a complex facility using typical steps for large production of sugar and ethanol, including milling, refining, fermentation and distillation. Energy for the process facility can be provided through the combustion of bagasse and other available biomass materials to generate power and process steam. Taking in view that the technology for design, construction and operation of high capacity ethanol processing plants is quite recent its reliability should be carefully evaluated in order to foresee the performance – technical and economical – of the plant.

This study presents a reliability evaluation of pieces of equipment installed in ethanol processing plant. The analysis first step consists on the elaboration of the equipment functional aiming at defining the functional links between the equipment subsystems. The next step is the development of the Failure Mode and Effects Analysis (FMEA) for the components of each piece of equipment to define the most critical components for plant operation. This criticality is based on the evaluation of the component failure effect on the plant operational performance. For the critical components a maintenance policy can be proposed considering the Reliability Centered Maintenance (RCM) concepts aiming at reducing the reliability decrease during a specific operational time. The new proposal must be compared with the manufacturer's recommendation to verify any adjustment in the maintenance tasks. The method third involves a reliability analysis based on the 'time to failure data' recorded during the equipment operational time or even values gathered in reliability database. The failures should be classified according to the subsystem definition and the plant reliability is simulated through the use of block diagram. The analysis allows the prediction of possible reliability improvement taking in view the application of new maintenance procedures.

The analysis of an ethanol processing plant with an annual production capacity of more than 100 million liters of ethanol is executed. The reliability of pieces of equipment is simulated based on failure database. Special attention is given to the milling operations once their interruptions not only stop the extraction of sucrose from the cane (that is lately processed to obtain ethanol) but also stop the production of bagasse that is used as boiler fuel, interrupting the electricity generation for the plant. The use of RCM concepts allows the proposal of new maintenance procedures. The new simulation indicates that the implementation of those procedures can improve the plant reliability.

Keywords: Reliability simulation, ethanol, roller mill.

1. Introduction

Over the last 30 years, the Brazilian sugarcane industry has experienced major and continuous technological improvement. Today, Brazilian sugarcane is the basic input for a diverse range of value added products including food, animal feed, biofuel and electricity coming from modern, integrated biorefineries that produce sugar, ethanol and bioelectricity.

Ethanol, can be produced by the fermentation of sugarcane juice and molasses. It has recently emerged as a leading fuel for combustion engines, representing about 45% of all fuel consumed by Brazilian automobiles.

Bioelectricity is produced by burning bagasse, the dry, fibrous waste that is left after sugarcane has been processed. This already happens in all sugarcane mills and ethanol distilleries, and can be used for powering not only the ethanol production plant but can also be sold in the energy market. Recently, G.E. and Brazilian energy company Petrobras have successfully used sugarcane-based ethanol to replace gas in a turbine system. The application at the Juiz de Fora power station, with two G.E. gas turbines, one of whose combustors was modified to allow ethanol to be used on it, making it a dual-fuel system, marks the world's first use of sugarcane ethanol in this scale.

Corresponding Author: Gilberto Francisco Martha de Souza, Email: gfmsouza@usp.br

Taking in view the importance of ethanol for Brazilian energetic matrix, the sugarcane-based ethanol production plants must present high reliability.

To improve the plant reliability and availability, the present paper applies a reliability-based method to propose some improvements in the maintenance policy of the roller mill in order to reduce its failure frequency. That method is adapted from the Reliability Centered Maintenance (RCM) philosophy, and was previously applied by the authors to improve thermal power plants equipment availability [1,2].

In a large enterprise, such as a sugarcane-based ethanol production plant, keeping asset reliability and availability, reducing costs related to asset maintenance, repair, and ultimate replacement are at the top of management concerns. In response to these concerns, the RCM concept was developed. RCM has been formally defined by Moubray [3] as "a process used to determine what must be done to ensure that any physical asset continues to do whatever its users want it to do in its present operating context".

The RCM, as a procedure to identify preventive maintenance requirements of complex systems, has been recognized and accepted in many industrial fields, [4] [5]. The RCM philosophy's main focus is on the identification of the functions of each one of the components of the system. This allows the application of the specified maintenance task for each one of the components considered critical, in order to guarantee the availability to operate, and the cut-back of maintenance costs.

2. Sugarcane-based ethanol production description

Most of the industrial processing of sugarcane in Brazil is done through a very integrated production chain, allowing sugar production, industrial ethanol processing, and electricity generation from byproducts. The typical steps for large scale production of sugar and ethanol include milling, fermentation, distillation of ethanol, and dehydration. Once harvested, sugarcane is transported to the plant. After quality control sugarcane is washed, chopped, and shredded by revolving knives. The feedstock is fed to and extracted by a set of mill combinations to collect a juice, called garapa in Brazil, that contain 10–15% sucrose, and bagasse, the fiber residue. The main objective of the milling process is to extract the largest possible amount of sucrose from the cane, and a secondary but important objective is the production of bagasse with a low moisture content as boiler fuel, which is burned for electricity generation, allowing the plant to be self-sufficient in energy and to generate electricity for the local power grid. The cane juice or garapa is then filtered and treated by chemicals and pasteurized. Before evaporation, the juice is filtered once again, producing vinasse, a fluid rich in organic compounds. The syrup resulting from evaporation is then precipitated by crystallization producing a mixture of clear crystals surrounded by molasses. A centrifuge is used to separate the sugar from molasses, and the crystals are washed by addition of steam, after which the crystals are dried by airflow. Upon cooling, sugar crystallizes out of the syrup. From this point, the sugar refining process continues to produce different types of sugar, and the molasses continue a separate process to produce ethanol. The resulting molasses are treated to become a sterilized molasses free of impurities, ready to be fermented. In the fermentation process sugars are transformed into ethanol by addition of yeast. Fig. 1 presents a schematic flow of ethanol production, [5.6].

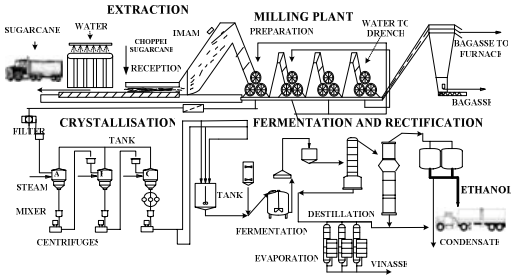

Fig. 1. Ethanol Production Flowchart

Taking in view the importance of ethanol for Brazilian energetic matrix, the ethanol production plants must present high reliability. Typically the plant pieces of equipment are subjected to overhaul maintenance in the month preceding the harvest period aiming at reducing the equipment failure rate during the operational year.

Aiming at improving the plant reliability and availability, the present paper applies a reliability-based method to propose some improvements in the maintenance policy of some pieces of equipment in order to reduce their failure frequency of occurrence.

3. Method description

The method is based on system reliability concepts and adapted from a previous study presented by Carazas e Souza, [2].

The method first step consists in the elaboration of the ethanol production plant functional tree that allows the definition of the functional links between the equipment subsystems. Although all plants use almost the same equipment, such as mills, distillates, heat exchangers, there are differences between the technologies used by the manufacturers; therefore the functional tree must be developed for each specific production plant.

The second step is the elaboration to the block diagram aiming at defining the system configuration as for reliability analysis.

The next step is the development of the Failure Mode and Effects Analysis (usually referred to by the acronym FMEA) of each plant equipment component in order to define the most critical components for plant operation. FMEA provides a lot of valuable qualitative information about the system design and operation, once its goal is to identify, concisely, the failure modes and mechanism of interest. The quantitative treatment of failures will be carried out in the analysis third step, using reliability concepts instead of FMECA approach (where the "C" stands for "criticality").

The analysis is based on the evaluation of the component failure effect on the plant operation, [3]. For the definition of the system degradation, the FMEA analysis uses a numerical code, usually ranking from 1 to 10. The higher the number the higher is the criticality of the component that must be evaluated for each component failure mode. For the present analysis that index is classified in three main severity levels: marginal, critical and catastrophic. Each level is split into other three sub-levels to express some variety of failure effects. A criticality scale between 1 and 9 is proposed. Values between 1 and 3 express minor effects on the plant operation while values between 4 and 6 express significant effects on the plant operation. Finally, failures that cause plant unavailability or environmental degradation are classified by criticality values between 7 and 9 [6].

The method third step involves a reliability analysis based on the 'time to failure' data recorded during the plant operation. The failures should be classified according to the subsystem presented on the functional tree. The reliability of each subsystem is calculated based on the failure data and the plant reliability is simulated through the use of block diagram.

Once the critical components are defined a maintenance policy can be proposed for those components, considering the RCM concepts. This maintenance policy philosophy is focused on the use of predictive or preventive maintenance tasks that aim at the reduction of unexpected failures during the component normal operation, [4]. For complex systems, the occurrence of unexpected components failures highly increases maintenance costs associated with corrective tasks not only for the direct corrective costs (spare parts, labour hours) but also for the system unavailability costs. In Fig. 2 a flowchart is used to illustrate the method main steps.

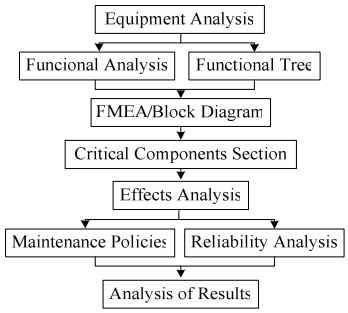

Fig. 2. Flowchart for Complex System Reliability Evaluation.

4.Application

The method is applied on the analysis of ethanol production plant with 24 t daily sugarcane milling capacity, allowing the production of more than 1000 m^3 /day of ethanol and having an energy nominal output of more than 50MW.

4.1. Functional Tree .

As previously presented, the first step in the plant reliability analysis involves the development of the functional tree. That tree is presented in Fig. 3.

The sugar cane based ethanol production system is modeled as for reliability analysis as a series system, once the failure of a given operation interrupts the ethanol production. For the present study the plant performance criterion as for reliability is the production of a given volume of ethanol. Any failure that interrupts that fuel production affects the plant reliability.

For any equipment, the greater the number of moving parts, the greater is the probability of failure. Most of the piece of equipment used in an

ethanol production plants are pressure vessels or heat exchangers, having a small number of moving parts. Furthermore, those pieces of equipment are usually designed according to international standards associated with chemical or petrochemical industries that take into account some reliability concepts in their design.

Other equipment such as pipes and pumps usually are submitted to a maintenance program that intends to reduce their failure probability. The literature usually recommends the use of predictive inspection for those pieces of equipment once they present evidences that a failure mode is under development. The detection of that evidence allows the maintenance planning aiming at avoiding unexpected failure.

The most critical process as for reliability analysis is the milling process once the mills presents great number of mechanical components which are subjected to cumulative damage mechanism. Furthermore, according to the literature, the metallurgical industry also spends a great amount of money to keep the milling system available.

Based on that consideration the present paper focuses on the roller mill reliability analysis, once its failure interrupts not only the production of bagasse but also causing a lack of fuel for co-generation process.

Although the technology for roller mill design and production has been continuously improved due to requirements of the development of rolled-metal production, the mills used in ethanol production plant are submitted to different environmental and loading conditions that cause a great number of failures. The complex mechanization and automation of the production operations introduced into ethanol production also demands greater reliability and longer service life of the equipment, which should take the form of:

a) constant improvement of equipment design; b) manufacture of parts from materials possessing necessary physical-chemical properties; c) manufacture, assembly and adjustment of machinery with high accuracy.

According to the method proposed in section 3, the mill functional tree is detailed in Fig. 3. The mill is basically composed by the following systems: i) The work rolls and their bearings - made of material harder than it is intended to roll. The present study considers a three roller mill; ii) The Mill Foundation - reinforced concrete for every ton of mill weight, iii) Rolling balance system - to ensure that the upper work and back up rolls are maintain in proper position relative to lower rolls; iv) Mill protection devices - to ensure that forces applied to the backup roll chocks are not of such a magnitude to fracture the roll necks or damage the mill housing, v) Gearing - to establish desired rolling speed, dividing power between the three rollers spindles, rotating them at the same speed but in different directions; vi) Drive motors - rolling narrow foil product to thousands of horsepower; vi) Mill Instrumentations - sensors to monitor all important parameter processes; vii) Operating Controls - enable the mill operator to handle rolling process.

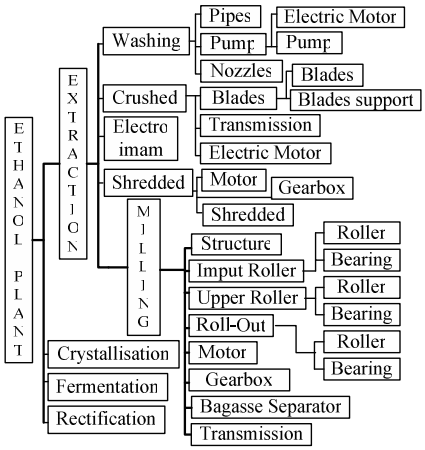

Fig. 3. Ethanol Production Plant Functional Tree

4.2. Failure Modes and Effect Analysis

Although there are many variants of FMEA, it is always based on a table, as shown in Fig. 4. In the left-hand column the component under analysis is listed; then in the next column the physical modes by which the component may fail are provided. This is followed, in the third column, by the possible causes of each of the failure modes.

The fourth column lists the effects of each failure mode that are classified according to the criticality scale, which expresses the degradation degree in the turbine operation.

The FMEA analysis was performed for each component listed in the end of a given branch of the functional tree. In Table 2 the analysis for the electric motor is partially presented as an example.

The failure modes for the components were developed according to manufacturer's information and other failure analysis available in the open literature, [9,10].

The analysis pointed out that the most critical components for the roller mill, which are listed in Table 3.

4.3. Reliability analysis

Reliability can be defined as the probability that equipment will perform properly for a specified period of time under a given set of operating conditions. Implied in this definition is a clear-cut criterion for failure, from which on may judge at what point the equipment is no longer functioning properly.

In order to estimate the ethanol production plant reliability, a block diagram is developed, as shown in Figure 4. The diagram emphasizes the roller mill reliability block diagram that is the main focus of the study.

The roller mill, as for reliability analysis, can be represented as a series system, composed by electric motor, gear box (aiming at reducing the electric motor speed), transmission (composed by three gears, each one coupled to a roller mill and to the pinion at the outer shaft of the gear box), three rollers (each one composed by two bearings and a roller) and bagasse separator.

The rollers are represented in a parallel configuration, once at least two rollers must be operation in order to mill the sugarcane. In a series system the components are connected in a such a manner that if any one of the components fail, the entire system fails.

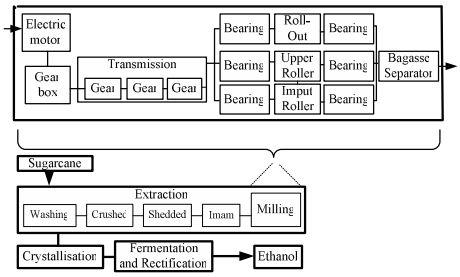

Fig.4. Ethanol plant reliability block diagram

The roller mill reliability is expressed as:

$$R_{Rollermill}(t) = R_{Electricmotor}(t).R_{Gearbox}(t).R_{Transmission}(t).R_{Bearings}(t).R_{Roller}(t).R_{Separator}(t) \quad (1)$$

The reliability data for each block is defined based on literature information and presented in Table 4. Although data presented in literature database can be considered as a first approach for reliability analysis, the estimated reliability can be used for future maintenance policy decision.

According to those data, the reliability of the components can be expressed by Weibull or Exponential reliability distributions.

The two parameter Weibull distribution, typically used to model wear-out of fatigue failures, is represented by the following equation:

$$R(t) = e^{-\left(\frac{t}{\eta}\right)^{\beta}} \quad (2)$$

Table 2. Failure Mode and effects Analysis: Example – Electric motor

Function	Failure Mode	Failure Causes	Failure Effects	Critically
	Sheared armature shaft	Fatigue	Seized	8
	Cracked housing	Fatigue/External shock Vibration	Leakage of dust into motor/Shorted or seized	6/8
	Bearing wear	Poor lubrication / Contamination/ Overloading or high/ temperature	Noisy/Heat build-up/Armature rubbing stator/Seized	4/6/8/8

Table 3. Results of the Application of Failure Mode and Effects Analysis for the Roller Mill

System	Subsystem	Component	Failure Mode	Critically
Ethanol Plant.	Roller Mill	Electric motor	Sheared armature shaft / Cracked rotor laminations / Cracked housing / Bearing were / Worn brushes / Worn sleeve bearing / Open winding / Shorted winding	8/8/8/8/ 7/8/8/9
		Bearing	Fatigue damage – Flaking / Noisy bearing / Bearing seizure / Bearing vibration	8/7/7/8
		Gear Box	Full geared coupling fails- teeth worn	9
		Rollers	Due to failure of key, sprocket is free / Bearing seizure due to wear out, / Roller wear	8/7/7

Table 4. Roller Mill Components Reliability Distribution

Component	Reliability Distribution	Distribution Parameters	Reference
Electric motor	Weibull	η= 100000 β=1,2	[7]]
Motor gearbox	Exponential	λ=1.10^{-5} failures/hour	[7
Transmission	Weibull	η= 75000 β= 2,0	[7]
Bearing	Weibull	η= 50000 β= 1,3	[7]
Roller	Exponential	λ=1.10^{-5} failures/hour	[7]
Separator	Weibull	η= 50000 β=1,2	[7]

The exponential distribution can be used to model failure modes not related to wear-out, named random failures. The reliability curve is expressed by the following equation:

$$R(t) = e^{-\lambda t} \tag{3}$$

The reliability curve for the roller mill is presented on Fig.5. For a operational period of 8760 hours the equipment reliability is equal to 70,9%. That value indicates that a great number of corrective repairs should be executed in the roller mill during the operational and justifies the execution of an overhaul preventive maintenance at the end of a given operational year. The plant maintenance register confirms the necessity of mill corrective repairs during operation.

The equipment reliability is seriously affected by the bearings reliability. Some common characteristics of bearing failures are: wear, fretting, corrosion, indentations, cracking and flaking. Some of the factors that may lead to bearing failure are improper lubrication, impact loading, vibration, excess temperature, contamination, excessive loading, and misalignment. Typically, for the ethanol plant environment it is expected to have bearing flanking caused by heavier external loading than had been anticipated. Those external loading are related to the great amount of cane used in the mill feeding.

According to literature, the typical roller failure mode is fatigue, cause by heavy loadings during sugarcane milling. The gear box and transmission failure modes have been discussed in literature, but are typically caused by gear tooth fatigue or bearing failure.

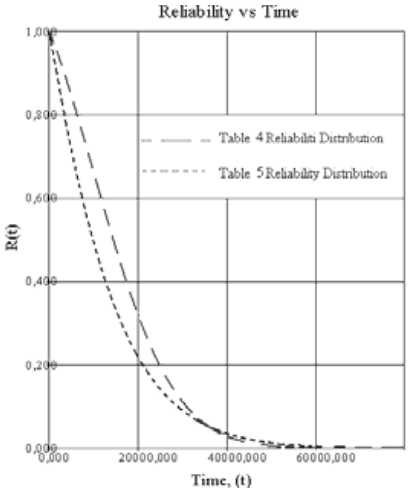

Fig.5. Reliability distribution

To execute a sensitivity analysis of the roller mill reliability estimate, other data from literature can be used to define the components reliability, as shown in Table 5. For that analysis the components, except for the separator, are considered to be modeled by exponential distributions.

For the operational period of 8760 hours, the roller mill reliability, calculated using equation 3, is equal to 54,13%, smaller than the value previously calculated. According to the data presented in Table 3, the bearings are the most critical components for reliability analysis.

The reliability curve for the roller mill, based on the data presented on tables 4 and 5, is presented in Fig. 5. The curve defined by the data presented in table 5 is more conservative, indicating lower reliability for the roller mill. Both curves present a similar behavior and can be used for reliability estimate.

There are two possible manners to improve the roller mill reliability: assigning reliability goals to components within a system in order to achieve the reliability system requirements or improve maintenance plans in order to control the components critical failure modes.

The first possibility implies in some changes in the equipment architecture to substitute some components, being, usually, more expensive. The second possibility uses the maintenance planning to control the development of critical components failure modes through the application of preventive or predictive maintenance tasks as suggested by RCM philosophy.

Table 5. Roller Mill Components Reliability Distribution as for Sensitivity Analysis

Component	Reliability Distribution	Distribution Parameters	Reference
Electric motor	Exponential	λ=28,4.10^{-6} failures/hour	[8]
Motor gearbox	Exponential	λ=1.10^{-5} failures/hour	[8]
Transmission	Exponential	λ=1.10^{-5} failures/hour	[8]
Bearing	Exponential	λ=3.10^{-6} failures/hour	[8]
Roller	Exponential	λ=1.10^{-5} failures/hour	[8]
Separator	Weibull	η= 50000 β=1,2	[7]

4.4. RCM Maintenance planning for roller mill

The plant operators usually intend to operate the plant at maximum possible efficiency. To evaluate the plant performance the OEE (Overall Equipment Effectiveness) is used to facilitate meaningful comparisons of plant performance over time. In the classic sense, it is the product of three measurements: availability, efficiency and rate of quality products.

The availability of a complex system such as an ethanol production plant is strongly associated with the parts reliability and maintenance policy. That policy not only has influence on the parts repair time but also on the parts reliability affecting the system degradation and availability,[2].

The maintenance planning is strictly associated with the plant availability improvement through the reduction of equipment failure rate. In order to control the development of deterioration process an appropriate planning and performing of predictive or preventive maintenance actions are required, according to RCM philosophy.

Initially, in order to reduce the roller mill failure rate, a preventive maintenance plan could be applied. Based on the reliability analysis, if some preventive maintenance tasks are bimonthly applied, aiming at replacing worn components before failure. Considering that after maintenance action the equipment is ‘ as good as new’, the reliability of the roller mill, at 1440 hours (corresponding to two operational months), according to data presented in Table 4, would be 96,2%. So, the application of preventive task, can significantly reduce the failure probability of the mill, increasing its OEE. The use of that maintenance plan can also reduce the number of activities to be executed during the annual overhaul maintenance.

The tasks to be executed in that preventive intervention are suggested in Table 6, based on RCM concepts.

Typically, the manufaturer´s recommendations regarding mill maintenance focus mainly on the roller. For that part, a preventive intervention at each 1000 operational hours is recommended, including teeth inspection and restoration, shaft’s seals substitution and general adjustment, including general bolts tightening.

Table 6. Maintenance Proposed Schedule for Roller Mill

Description	Comments	Maintenance Frequency
Overall visual inspection	Complete overall visual inspection to be sure all equipment is operating and safety systems are in place.	Daily
Check mill structure	Check for loose connections, leaks, etc./ inspect and readjust the unions in case they have lost the adjustment due to vibration. Inspect the presence of cracks or deformations in the structure.	Bimonthly
Electric motor condition	Check the condition of the electric motor through temperature or vibration analysis and compare to baseline values.	Bimonthly
Roller	Check the condition of the roller through vibration analysis and compare to baseline values.	Bimonthly
Motor alignment	Aligning the motor coupling allows for efficient torque transfer.	Bimonthly
Check bearings	Inspect bearings and for wear. Adjust, repair, or replace as necessary.	Bimonthly
Gear Box	Check for lubrication oil leakage, inspection of the vibration pattern.	Bimonthly
General recommendations for predictive and preventive maintenance.		
Vibration	Check for excessive vibration in motors, fans, and pumps	
Check lubrication	Assure that all bearings are lubricated according to the manufacture's recommendation.	
Thermographic Analysis	Check and monitoring motors and bearings	

That proposal does not recommend any inspection of the transmission system, including electric motor and gears box that are identified as critical parts by the FMEA analysis. The present proposal seems more comprehensive than the manufacturer's recommendation, aiming at checking the critical parts as for reduction of mill unavailability due to unexpected failures.

5. Conclusions

The proposed method for reliability analysis seems to be suitable for complex systems, such as the sugarcane based ethanol production plant, since it allows not only the identification of critical components for maintenance planning but also defines quantitatively the system reliability.

The development of the system functional tree is important for the understanding of the functional relation between system components. Based on the functional hierarchy, the FMEA analysis is performed considering the failure modes associated with the components listed in the end of each branch of the functional tree, identifying the effects of component failure on the system under analysis. Once the critical components are identified, based on the failure effects classification, a maintenance policy can be formulated to reduce their occurrence probabilities.

The maintenance policy aims to reduce the system unavailability through the use of predictive or preventive maintenance tasks for critical components. This policy allows the reduction of unexpected failure occurrences that cause the system unavailability and are usually very expensive to repair.

The method applied on the analysis of the roller mill indicates that the use of predictive or preventive tasks seems feasible providing that a complex monitoring system is applied. The use of bimonthly predictive actions can significantly increase the roller mill reliability, reducing the unavailable time due to emergencies corrective actions. Furthermore, the most critical components of the roller mill are the bearings used to support rollers once they are submitted to heavy loadings that can cause failure by flanking. In order to increase bearings maintenance planning the use of vibration monitoring systems is recommended. Any increase in bearing vibration is an indicative of some failure mode development and the maintenance activity can be planned in advance, reducing the roller mill unavailability associated with unexpected corrective actions.

Nomenclature

$R(t)$ reliability at time t
$R_{Rollermill}(t)$ roller mill reliability at time t
$R_{Electricmotor}(t)$ electric motor reliability at time t
$R_{Gerboxl}(t)$ gear box reliability at time t
$R_{Transmission}(t)$ transmission reliability at time t
$R_{Bearings}(t)$ bearing reliability at time t
$R_{Roller}(t)$ roller reliability at time t
$R_{Separator}(t)$ separator reliability at time t
t time period [h]

Greek letters

β Weibull distribution shape parameter
η Weibull distribution characteristic life [h]
λ Exponential distribution failure rate parameter [failures/h].

References

[1] Carazas F. and Souza G.M, 2009, .Availability Analysis Of Gas Turbines Used In Power Plants, International Journal of Thermodynamics, 12 pp28-37.

[2]Carazas F. and Souza G, 2007, Availability Analysis of Gas Turbines used in Thermo Power Plants, Proc *20th ECOS*, Padova, Italy,.pp. 277-285.

[3] Moubray, J. 1999. *Reliability-Centred Maintenance*, Butterworth-Heinemann, New York.

[4] Rausand, M, 1998, Reliability Centered Maintenance, Reliability Engineering and System Safety, pp121-132.

[5] Velasquez et al, 2009, Biofuels Production: Exergo-Enviromental Evaluation, *22th ECOS*, Foz do Iguaçu, Brazil.

[6] Takahashi C, Tuyama I, Figueiredo L, Ishihara P, 2009, *Sis. Produção de Alcool Anidro- Identificação das variveis críticas do processo*. Sao Paulo, Brazil.

[7] Bloch H, 1994, *Practical Machinery Management for Process Plants*, Publishing Company, Houston,TX.

[8] Shith D, 1997, Reliability, *Maintainability and Risk practical Method for Engineers*. Fifth Edition. Butterworth Heinemann. Oxford,US.

[9] Deshpade V. and Modak J.,2002, Maintenance strategy for tilting table rolling mill based on reliability considerations, Reliability Engineering and System Safety 80 pp 1-18.

[10] Carderock div, 2006, Handbook of reliability prediction procedures for mechanical equipment, West Bethesda, Maryland, US.

Primary Energy Efficiency Consideration of Biomass-to-Liquid Systems Yielding Fischer-Tropsch Fuel

Thomas Kohl[a], Cristina Gil de Moya[a], Carl-Johan Fogelholm[a]

[a] *Aalto University, School of Science and Technology, Dept. of Energy Technology, Espoo, Finland*

Abstract: The objective of the paper is to compare the efficiency of three different biomass-to-liquid systems. For this purpose European standards for energy rating of buildings have been successfully modified and applied to biofuel production. The method compares the primary energy consumption - expressed by primary energy factors- and the fossil CO_2 emissions of the analysed systems. For all systems biomass is collected and differently pre-processed in local plants of 50 MW_{th}. Subsequently biomass is transported to a central gasification / synthesis plant. The transport distance is varied and, in connection with the pre-processing, strongly influences the system efficiency. We further show the influence of the initial moisture content on the system efficiency. The results confirm that high conversion efficiency in the actual biomass-to-liquid process is important. However, the system with highest actual biomass-to-liquid conversion efficiency does not perform best concerning relative use of fossil primary energy and CO_2 emissions. In general, the method applied gives clear results and good insight in the actual impact of the conversion systems. Further, saving potentials for primary energy and CO_2 emissions can be easily obtained and application to other systems should be easily possible with basic process data. The main advantage of the method is the clearly defined system boundary that allow objective comparison.

Keywords: Biomass-to-liquid systems, Energy system evaluation, Primary energy efficiency, Primary energy factor, Transport distance influence.

1. Introduction

According to the IEA CO_2 emissions of the OECD countries in 2030 will need to be cut to 40% below the 2006 levels. This would allow the world energy consumption to grow by approximately 22.4% (based on the 2006 level) and would still limit the raise of the global average temperature to 2°C (so-called 450 policy scenario). It is assumed that meeting this target will avoid the most severe and irreversible effects of global warming on our environment, society and economy. The most important measures to reach the required CO_2 mitigation are improved energy efficiency and increased use of renewable energy sources, accounting for approximately 54% and 25%, respectively [1]. Among the renewable energy sources, biomass will play an important role - the estimated technical potential contribution to the world's future energy supply vary from 200-400 EJ in 2050 [2]. World energy consumption in 2004 was 467 EJ. Among many options biomass can be used for the production of liquid transport fuels in so-called biomass-to-liquid (BtL) processes. Thus biomass can directly replace fossil fuel in current transport systems. However, the restricted availability of biomass demands for most efficient use of this source as well. Different BtL processes are currently researched but the question how to compare different systems is not yet answered. It is not defined which parts and sidetracks of the process chain should be included into the consideration. In other words the system boundaries are not generally defined. A suitable approach seems to be defined by European Union's standards EN 15603 [3] and EN 15316-4-5 [4] that apply energy rating of heating systems of buildings based on the total system's primary energy (PE) consumption. In chapter 8.1 of [3] it is stated that "a building generally uses more than one energy carrier". This also accounts for almost all industrial processes since usually different forms of energy carriers (e.g. steam, heat and electricity) are required to produce goods. The standard further suggests "a common expression of all energy carriers […] to aggregate the used amounts […] having various impacts. According to this standard, the aggregation methods are based on the following impacts the use of energy have: - Primary energy; - Carbon dioxide emission;". PE is energy that has not been subjected to any conversion or transformation process [3], it is hence not yet extracted from the source. In the PE

Corresponding Author: Thomas Kohl, Email: thomas.kohl@tkk.fi

approach described in [3] all energy carriers involved in the process are retraced to their sources and all energy needed to deliver the product are aggregated to the PE consumption of the product. This approach allows simple addition of different types of energy (rated as PE) and thus enables comparison of different energy systems utilising different kinds of energy carriers. Thus the PE approach applies the holistic principles of life cycle assessment to an energy rating procedure. By retracing energy consumption to the source the system boundaries automatically include the whole world, and thus depict the real impact of the system concerning energy consumption and CO_2 emissions. However, the PE approach does not consider other often discussed environmental and societal impacts of biomass use such as negative effects on food prices, agriculture and land and water use. In this paper we modify and apply the standards to three BtL processes, yielding Fischer-Tropsch (FT) product, under Finnish conditions. The aim of the study is to create energy performance values as an objective basis for BtL-system comparison in Finland, regarding energy efficiency and CO_2 emissions.

2. Energy rating in standards EN 15603 and EN 15316-4-5

2.1. Primary energy rating

The PE efficiency (PEE) is expressed by means of primary efficiency factors (PEF). PEFs can be calculated for every step of the process and PE consumption is then aggregated considering the whole system. Aggregation includes the PE to extract and to transport the energy carrier as well as all energy (rated with its PEF) used for processing, storage, generation, transmission, distribution, and any other operation necessary for delivery. Further PE required to build transformation units, transport system and for waste disposal **may** be included. The calculation of the systems' PEE requires the use of certain PEFs (based on country specific data) which are not yet existent. In this case, partly factors of Annex E of [3] were used or adequate values were determined by the authors. Although, according to the standard, PEFs shall be based on the higher heating value (HHV), all our calculations are based on the biomass' lower heating value (LHV) on a wet basis. Reasons for that are: it makes calculation more transparent and all relevant process data found is based on LHV and conversion to HHV rated values was not possible due to insufficient data. PE use of a system is described by two different factors.

2.1.1. Total primary energy factor (PEF_{tot})

It is the sum of all PE input to the system divided by the useful energy delivered at the system border (in our case energy bound in the FT product). It thus describes how much PE input is needed in order to obtain one unit of product and can hence be seen as an inverted efficiency.

2.1.2. Resource primary energy factor (PEF_{res})

It is the non-renewable PE divided by the delivered energy. It describes how much non-renewable PE (nuclear and fossil, later simply referred as fossil) input is needed in order to obtain one unit of product.

2.2. CO_2 rating

2.2.1. CO_2 emission coefficient ($ECCO_2$)

The CO_2 rating is done by calculating a CO_2 emission coefficient that quantifies the total amount of fossil fuel derived CO_2 that is emitted to the atmosphere per unit delivered energy, using the same principles as for the calculation of PEF_{tot}. Within the coefficients CO_2-equivalent emissions of other greenhouse gases **can optionally** be included. However this has not been implemented into this study, due to a lack of data.

3. Biomass-to-liquid systems

We compare three different systems yielding for FT product, a precursor that needs some further upgrade to FT diesel. In order to operate economically, FT-fuel refineries are estimated to require plant sizes in the range of 1 GW_{th}. Provision of the required biomass can result in average transport distances as long as 1000 km. This causes undesired environmental impact and costs. Different pre-treatment processes, increasing the energy density of biomass might abate this impact. Three FT-fuel production systems were defined that are suitable to convert either pelletised, pyrolysed or untreated biomass. Pre-treatment will take place in local plants with a capacity of 50 MW_{th}. The systems, as shown in Fig. 1, are similar concerning biomass input, extraction and local transport. Further processing differs depending on the subsequent technologies that are derived from the following BtL concepts:

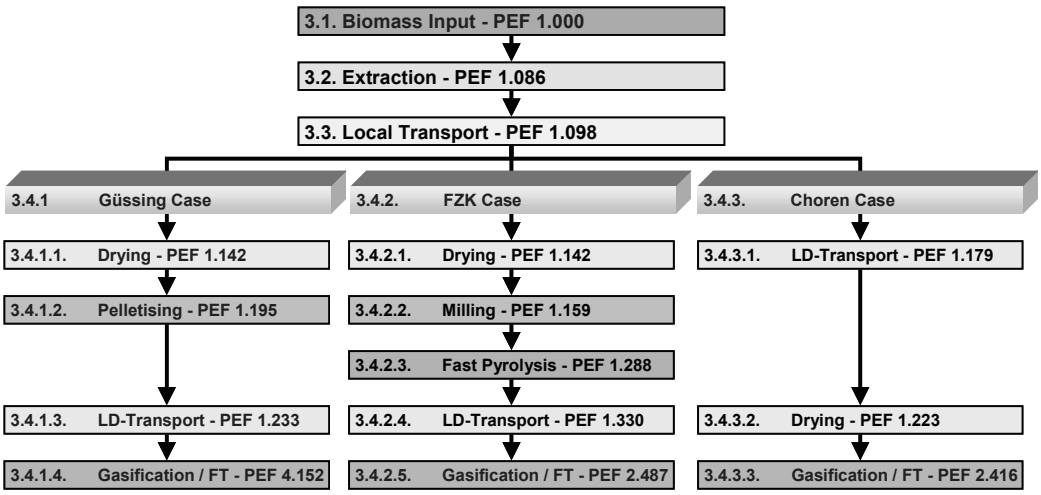

Fig. 1: Overview of the different BtL system with accumulated PEFs for M_1 = 50%, LD-distance is 500 km.

Biomassekraftwerk Güssing: The biomass gasification combined heat and power plant in Güssing, Austria, has been in operation since 2001. It applies fast internal circulating fluidized bed gasification where the cleaned product gas is fired in a gas engine producing power and heat. The product gas is well suited for diesel production via FT synthesis. Integration of fuel synthesis has been analysed in a case study [5]. Based on the gasification technology we consider pellets as a suitable feedstock, although the actual fuel is wood chips. Pelletising is the mechanical densification of milled woody biomass to wood pellets with a bulk density of 600kg/m^3 (LHV: 16.78 MJ/kg wet, moisture M = 0.1). It comprises milling, drying, densification and fan cooling of the product. The concept is later referred to as Güssing case.

Forschungszentrum Karlsruhe (FZK): In the bioliq concept, developed by FZK, biomass is pyrolysed in small local plants and undergoes entrained flow gasification with subsequent FT-synthesis in a central plant. Fast pyrolysis is the thermal degradation of feedstock in absence of an oxidising agent with short residence times and temperatures of approximately 500°C. Product distribution is roughly 70 w-% liquids, 15 w-% char and 15 w-% gases. In the FZK concept char and liquids are mixed to so-called bioslurry with a density of 1250 kg/m^3 [6]. The LHV of slurry was calculated to 15.7 MJ/kg wet (M = 0.2), based on a HHV of 21.6 MJ/kg dry ash free (daf) and water content of 20 w-% [6]. Hydrogen was here estimated to 6.15 w-% (daf). The concept is later referred to as FZK case.

Choren Industries: Choren Industries developed the Carbo-V process which applies entrained flow gasification subsequent to a slow pyrolysis of wood chips. The 45 MW_{th} β-plant is in operation since 2003 producing clean synthesis gas [7]. In April 2008 the construction of the subsequent synthesis plant was finished and is currently in start up [8]. Biomass does not require further milling but must be dried to M = 0.15 [7]. The concept is later referred to as Choren case

3.1. Biomass input

Availability: The unused woody biomass potential in Finland is estimated to V_{tot} = 26 Mm^3 per year [9], mainly residues. This biomass is thought to be evenly distributed over the Finnish forest area which equals 75% of the total land area of A_{land} = 338144 km^2 [10]; further, 12.5% of protected forest areas are considered in the calculation of the local transport distances.

LHV calculation: The size of the local pre-treatment plant was set to 50 MW with 330 operating days per year (t_{op}). This equals a thermal input of E_{BM} = 1.4256·10^9 MJ/year. In order to determine the mass flow, starting from an HHV of 20.295 MJ/kg (daf), $LHVs_{wet}$ for four different M (30, 40, 50, 60 weight-%, reflecting the natural variation of wood moisture) and a hydrogen percentage of 6.15% were calculated according to [11]. The HHV and biomass composition is derived from the database Phyllis [12] (selected

subgroups: untreated wood → birch and fir/pine/spruce).

Density and bulk density calculation: Transport energy is dependent on the biomass' density and bulk density. For calculation of the average dry density ρ_{dry} (411.35 kg/m^3) the density of the prevalent Finnish tree species birch (475 kg/m^3), pine (412.6 kg/m^3) and spruce (385.3 kg/m^3) taken from [13] were rated with their percentage on the whole growing stock [10]; 56% for pine, 32% for spruce and 12% for birch, respectively. Water content was included for the determination of wet biomass' density using the following equation derived from [14]: $\rho_{wet} = \rho_{dry} / (1 - M)$. For the bulk density, the solid volume content of wood chips has been calculated to $v_s = 0.36$ [14], which corresponds well with values found in [15]. Bulk density is then calculated for different M according to: $\rho_{bulk} = \rho_{wet} \cdot v_s$.

3.2. Extraction

Firstly biomass is extracted and collected to the forest roads where it is assumed to be chipped by a mobile device for easier transport by trucks. The PEF for extraction ($PEF_{Extr.}$) has been taken from Annex E of [3] to 1.06 (bark). Energy for extraction ($E_{Extr.}$) is thus calculated according to: $E_{Extr} = E_{BM} \cdot (PEF_{Extr.} - 1)$. This PEF is chosen since no specific value for residues is given and bark was considered as the option most similar. As the standard does not give detailed specification of the energy consumption accounted for, the authors assume based on [16] that the value given covers all energy expenses needed for set-up and maintenance of the plantation (life-time 100-120 years), provision of infrastructure needed for harvesting, all forest processes as well as transport to the nearest forest road. Energy consumption for roadside chipping (E_{RC}) is calculated with a specific energy consumption of e_{RC} = 19.3kJ/MJ [17] (calculated with a density, LHV and PEF of diesel of ρ_f = 0.85kg/l, LHV_f = 43 MJ/kg and PEF_f = 1.35 [3], respectively) to: $E_{RC} = e_{RC} \cdot E_{BM}$.

3.3. Local transport

The chipped wood is transported to the local plant by road trains with an estimated 40 tons net freight and a maximum load volume of 145m^3. The truck capacity corresponds with [15] for special equipped road trains with a maximum length of 25.25 metres in Finland. Due to bulk density change depending on the biomass' moisture, the maximum load is either restricted by volume or by weight, thus determining the number of vehicles (n) needed. The transport energy (E_t) further depends on the following factors: specific fuel consumption per kilometre (f), average one-way transport distance (s) and on PEF_f and is calculated according to: $E_t = n \cdot f \cdot 2s \cdot \rho_f \cdot LHV_f \cdot PEF_f$. Specific fuel consumption f for local transport is 0.64 litres/km [15].The average one-way transport distance s has been adapted from [18] and is a function of average biomass availability $B = (V_{tot} \cdot \rho_{bulk})/(A_{land} \cdot 0.75 \cdot 0.875)$ [t/ha·a], the plant size $P = E_{BM}/(t_{op} \cdot LHV_{wet})$ [t/d], the non-dimensional parameters for average land use (n/Φ) and the accessibility of the harvesting areas (τ) as shown in (1):

$$s = 0.6833\tau\sqrt{\frac{n}{\Phi}}\sqrt{\frac{P}{B}} \quad (1)$$

According to [18] τ varies from 1.27 for a flat terrain to 3 for a complex, hilly terrain constrained by e.g. lakes and swamps. For Finland the value was set to 2 due to its relatively flat terrain along with many lakes and swamps. The parameters n and Φ describe the land area used for foresting (use inverse value) and protected forest, respectively, and are set to 1.33 and 0.875.

3.4. Biomass conversion

3.4.1. Güssing case

3.4.1.1. Drying

Prior to the actual pelletising process the biomass is dried from the initial moisture content M_1 to M_2 = 10%. The wood-fired flue gas dryer (thus reducing the initial amount of biomass) consumes q_{drying} = 3100 kJ/kg water evaporated [19]. Along with the increased LHV_{dried} the dried biomass' energy content E_{dried} can thus be calculated as:

$$E_{dried} = \frac{E_{BM}\dfrac{1-M_1}{1-M_2}}{\dfrac{M_1-M_2}{1-M_2}\cdot q_{drying} + LHV_{wet}} \cdot LHV_{dried} \quad (2)$$

3.4.1.2. Pelletising

The specific electricity consumption for milling, pressing and cooling is estimated to e_{Pellet} = 300 MJ/ton [20], [21]. With a PEF for electricity production in Finland of $PEF_{Electricity}$ = 3.11, derived from [22], the PE consumption for pelletising can then be calculated as:

$$E_{Pelleting} = E_{dried} / LHV_{dried} \cdot e_{Pellet} \cdot PEF_{Electricity} \quad (3)$$

It must be noted that cooling of pellets further decreases moisture by approximately 2 percent points to $M_3 = 0.08$. Thus energy content of pellets is calculated according to:

$$E_{Pellet} = \frac{1 - M_2}{1 - M_3} \cdot \frac{LHV_{Pellet}}{LHV_{dried}} \cdot E_{dried} \quad (4)$$

3.4.1.3. Long-distance (LD) transport

The LD transport energy is calculated according to 3.3. to

$$E_{t,LD} = n \cdot f \cdot 2\bar{s} \cdot \rho_f \cdot LHV_f \cdot PEF_f \quad (5)$$

, where $\bar{s}$ is the average transport distance to the central plant. $\bar{s}$ has been varied from 100 to 1000km in intervals of 100 km. n is calculated with pellets' bulk density according to the truck specification given in 3.3. The diesel consumption for LD transport is reduced to 0.54 litres/km [15].

3.4.1.4. Gasification and FT-synthesis

According to a case study on the integration of FT-fuel production the conversion efficiency from biomass to FT-product is 29.7% corresponding to a $PEF_{Güssing}$ of 3.37 [5]. Hence energy contained in the product was calculated as: $E_{Güssing} = E_{Pellet} / PEF_{Güssing}$. It must be noted that the concept plant would also generate heat and electricity with net-efficiencies of 45.5% and 13.8%, respectively. However, evaluation of by-products has not been considered in this study.

3.4.2. FZK case

3.4.2.1. Drying

Fast pyrolysis requires feedstock with moisture content M_2 of 10% in order to keep the water content of the product as low as possible [23]. The biomass' energy content after drying E_{dried} has been calculated as shown in (2).

3.4.2.2. Milling

In order to provide sufficiently fast heat transfer the biomass must be milled to a particle size of below 2 mm [23]. Specific electricity consumption is estimated to $e_{Milling} = 90$ MJ/ton [20], [21] and PE consumption $E_{Milling}$ is derived according to (3).

3.4.2.3. Fast pyrolysis

The FZK fast pyrolysis process converts 90% of the biomass energy into bioslurry [6], corresponding to a $PEF_{Pyrolysis}$ of 1.11. Thus, energy after pyrolysis can be calculated as $E_{Slurry} = E_{dry} / PEF_{Pyrolyis}$.

3.4.2.4. LD transport

The transport energy is calculated as shown in (5) in consideration of the bioslurry's density.

3.4.2.5. Gasification and FT-synthesis

The conversion efficiency to FT product is given to 53.3% [6]. This corresponds with a PEF_{FZK} of 1.87. FT product's energy was calculated as $E_{FZK} = E_{Slurry} / PEF_{FZK}$.

3.4.3. Choren case

3.4.3.1. LD transport

In order to consider the differences between the local street network and LD transport two modes of transport, local and LD, are considered. LD transport was calculated according (5).

3.4.3.2. Drying

Drying to $M_2 = 15\%$ is calculated as shown in (2) resulting in E_{dried}.

3.4.3.3. Gasification and FT-synthesis

The process conversion efficiency to FT product is given to 50.6% [24], which gives a PEF_{Choren} of 1.98. Thus, product energy can be calculated to $E_{Choren} = E_{dry} / PEF_{Choren}$.

4. Results and discussion

For clearness, results are only displayed for M_1 equal to 0.3 and 0.6, respectively, in Fig. 2a) to 2d). All values for other M are in between the curves displayed, not proportional though. $ECCO_2$ is displayed for M1 equal to 0.5, often used by others for average moisture of biomass.

4.1. Total PEF (PEF_{tot})

The PEF calculation for the Güssing case is exemplary given: $PEF_{tot, Güssing} = (E_{BM} + E_{Extr} + E_{RC} + E_t + E_{Pelleting} + E_{t,LD}) / E_{Güssing}$. Other PEFs are calculated accordingly.

The PEF_{tot} (Fig. 2a) shows clearly the strong influence of the gasification step. In the Güssing case the conversion efficiency to FT fuel is much lower than in the other cases. This results in a PEF_{tot} that is roughly 1.8 times higher than for the two alternatives, thus being 1.8 times less efficient. This can also be seen from the PEFs included in Fig. 1. It can further be seen that the transport distance has a bigger influence on the Choren case (greater gradient), where undensified biomass is transported. This is especially the case

for high moisture contents, where the amount of water transported increases. For high water content and transport distances greater than ca. 600 km the FZK case becomes more efficient.

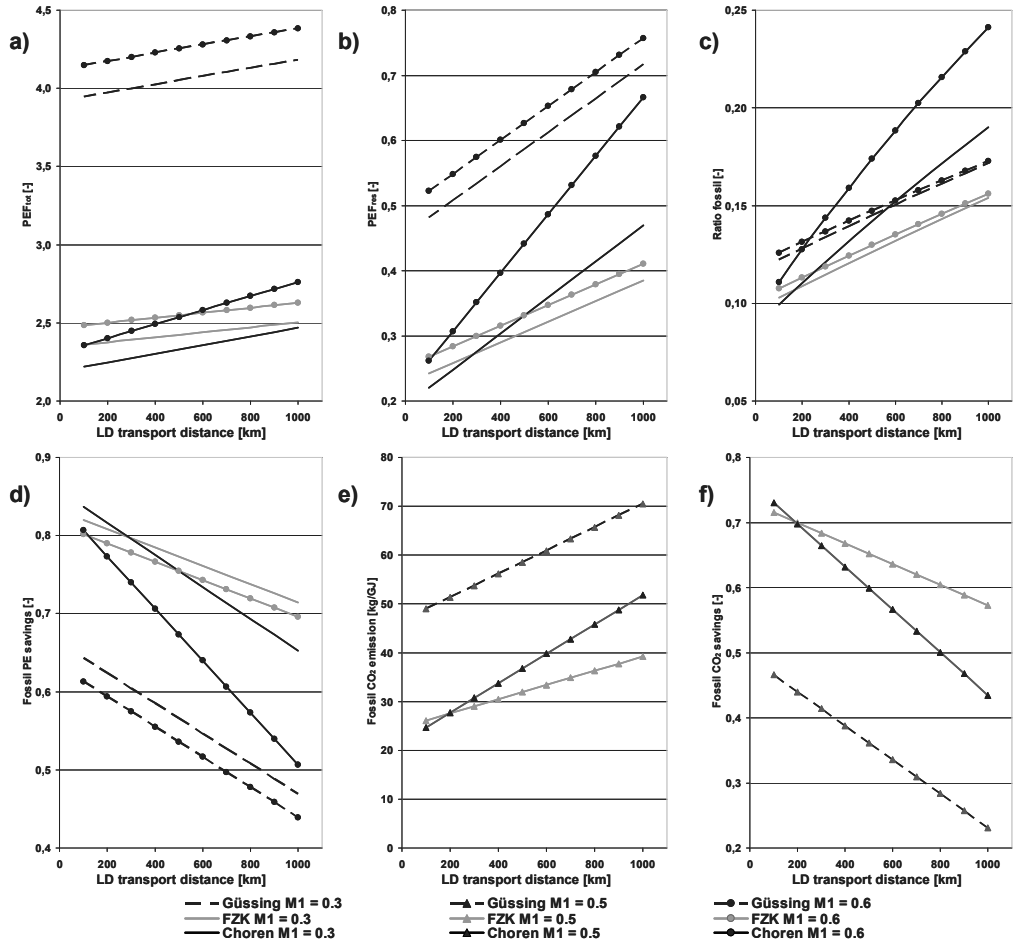

Figure 2: Results of BtL system comparison for different moisture contents (M) and varied LD transport distance
a) Total PEF b) Resource PEF c) Fossil ratio in the product
d) Fossil PE saving potential e) CO_2 emission coefficient f) Fossil CO_2 saving potential

4.2. Resource PEF (PEF_{res})

For calculation, $PEFs_{res}$ for extraction and fuel are taken from [3], $PEF_{Electricity}$ for Finland is 2.13 [22]. The PEF_{res} (Fig. 2b) expresses how much fossil PE is utilized per unit product. Also here the strong influence of the gasification efficiency is evident; this is due to the fact that the factor divides fossil PE consumption through the energy bound in the product. However, concerning resource PEE the FZK case is already superior for transport distances greater than 300 km for lowest moisture contents of 30%. This influence can also be seen in Fig. 2c) where PEF_{res} / PEF_{tot} illustrates the ratio of fossil PE in the product. This shows that for long transport distances up to 24% of the product is "produced" with fossil PE. It must be mentioned that the Güssing case with low conversion efficiency has a lower fossil share in the product than in the Choren case for transport distances greater than 500 km. By relating the PEF_{res} of the system to the PEF_{res} of diesel according to 1 – ($PEF_{res,system}$ / $PEF_{res,f}$) the fossil PE saving potential of the system can be demonstrated, as shown in Fig. 2d). Again there is a strong influence of the transport distance; again the FZK case is superior for distances greater than 300 km. Having in mind that the only fossil PE used in the Choren case is transport fuel it can be said that the

transport distance has a strong influence on the system performance.

4.3. CO2 emission coefficient

The system's $ECCO_2$ has been calculated with the following coefficients: $ECCO_{2,f}$ = 91.7 kg/GJ, $ECCO_{2,Extr.}$ = 1.1 kg/GJ (both derived from [3]) and $ECCO_{2,Electricity}$ = 75 kg/GJ as calculated from [22]. Results are shown for M_1 = 50%. As it can be seen from Fig. 2e), emissions vary from 25 to 70 kg/GJ. CO_2 emissions in the FZK case are lowest. This account for all M. By relating the $ECCO_2$ of the system to $ECCO_{2,f}$ the saving potential of the system for fossil CO_2 can be displayed. It varies from 22 to 72% depending on system and transport distance.

5. Conclusions and remarks

It can be said, that the PEF_{tot} illustrates the results that can be expected regarding the used FT-conversion efficiencies of the three considered FT-systems: It shows the lowest PEFs for the Choren case with a conversion efficiency of η_{conv} = 0.506 and highest values for the Güssing (η_{conv} = 0.297). This shows that the actual conversion step to FT product has the highest influence on the PEE and offers thus the biggest potential for process improvement. However, deeper analysis by means of PEF_{res} reveals that the Choren case is not superior when it comes to fossil PE consumption. The product is meant to replace fossil transport fuel hence its use in the production chain should be as low as possible. Also systems' performance concerning CO_2 emissions was clearly revealed. As mentioned the Güssing case suffers mainly from its poor FT conversion efficiency resulting in a much lower product yield. However, the concept is planned for polygeneration of fuel heat and power. This would need to be considered in a final evaluation. The intermediate products at different stages of the process chain differ in their physical and chemical properties and suitability to be processed with certain technologies. Hence, there is no best pre-treatment concept and no best gasification technology. This makes evaluation of the whole process chain necessary.

Our study clearly shows the influence of transport distance and water content on the conversion efficiency. In general biomass should be allowed for natural drying as long as possible before transport. It must be mentioned that there is evidence for drying causing considerable energy losses due to biological degradation [17]. As it can easily be shown, that assuming pellets to be used in the Choren concept clearly improves its performance, it can be said that for LD transportation of biomass, densification is essential.

Weakest point of the analysis is the data of biomass availability since estimation is difficult and only one source was found. We also do not have proof for our assumptions concerning the local transport distance. However this is common input (which has been considered to fulfil the standards' requirements, see 2.1.) for all systems compared and does not affect the qualitative results. However the quantitative results can easily change with better data.

In general the method applied gives clear results and good insight in the actual impact of the conversion systems. Advantages and disadvantages concerning fossil PE use and CO_2 emissions become evident. Saving potential for PE and CO_2 mitigation potential can be calculated in a simple way. Results are closer to the final user since the method is product oriented ("how much do I need to produce one unit") rather then educt oriented ("how much can I produce with one unit raw material"). This approach also seems to be easier to understand for technical laymen, which might be important when it comes to decision making, whether a technology shall be further developed or not. No economical data has been used which is disadvantageous concerning feasi-bility, but advantageous for potential estimation regarding development of most efficient future biomass conversion systems.

We further think that application to other countries and systems should be easily possible as long as basic process knowledge (pre-treatment options, process alternatives, conversion efficiencies) is available. The method then allows for system comparison on a relatively early stage of development. It should further allow comparison of energy systems producing different products, as e.g. production of ethanol and diesel from woody biomass.

The main advantage of the method is the clearly defined system boundary, which often seems to be the bottleneck when discussing energy efficiency.

References

[1] N.N., 2008, *World Energy Outlook 2008*, OECD/IEA, Paris, pp. 407-450.

[2] N.N., 2007, Potential Contribution of Bioenergy to the World's Future Energy Demand, IEA Bioenergy.

[3] EN 15603:2008, Energy performance of buildings. Overall energy use and definition of energy ratings, European Committee for Standardization, CEN, Brussels.

[4] EN 15316-4-5:2007, Heating systems in buildings. Method for calculation of system energy requirements and system efficiencies. Part 4-5: Space heating systems, the performance and quality of district heating and large volume systems, European Committee for Standardization, CEN, Brussels, 2007

[5] N.N., 2008, Process Optimisation of BtL production, RENEW SP2 Scientific Report 080328, www.renew-fuel.com.

[6] Henrich, E., 2007, The status of the FZK concept of biomass gasification, *2nd European Summer School on Renewable Motor Fuels*, Warsaw.

[7] Rudloff, M., 2005, Biomass-to-Liquid Fuels (BtL) – Made by CHOREN Process, Environmental Impact and Latest Developments, *10th EAEC European Automotive Congress*, Belgrade.

[8] CHOREN website, 2010: www.choren.com.

[9] N.N.,2002, *Energy visions 2030 for Finland*, VTT Energy, Edita Prima Ltd, Helsinki, p.79.

[10] N.N., 2008, *Environment Statistics Yearbook 2008*, Statistics Finland, Helsinki.

[11] Quaak, P., 1999, *Energy from Biomass – A Review of Combustion and Gasification Technologies*, World Bank Technical Paper No. 422, Washington D.C., Annex 1.

[12] http://www.ecn.nl/phyllis: PHYLLIS is a service provided by the Energy Research Center of the Netherlands – ECN, 17.9.2009.

[13] Repola, J., 2006, Models for Vertical Wood Density of Scots Pine, Norway Spruce and Birch Stems, and Their Application to Determine Average Wood Density, Silva Fennica 40(4), pp.673-685.

[14] Gullichsen, J. and Paulapuro, H. (editors), 1999, *Papermaking Science and Technology, Book 6A, Chemical Pulping*, Fapet OY, Helsinki, Chap. 3.

[15] Ranta, T. and Rinne, S., 2006, The profitability of transporting uncomminuted raw materials in Finland, Biomass Bioenergy, 30(3), pp. 231-237.

[16] Werner, F. et al., 2007, Life Cycle Inventories of Wood as Fuel and Construction Material. Final report ecoinvent 2000 No. 9.EMPA Dübendorf, Swiss Centre for Life Cycle Inventories, Dübendorf, CH.

[17] Wihersaari, M., 2005, Aspects on bioenergy as a technical measure to reduce energy related greenhouse gas emissions, Ph.D. Dissertation, Helsinki University of Technology, Espoo, Finland.

[18] Overend, R.P., The average Haul Distance and Transportation Work Factors for Biomass Delivered to a Central Plant, Biomass 2 (1982) 75-79.

[19] Wimmerstedt, R., 1999, Recent advances in biofuel drying, Chem. Eng. Process. 38(4-6), pp. 441-447.

[20] Bloch, L., 2010 personal correspondence, ANDRITZ Feed & Biofuel A/S, Denmark.

[21] Sokhansanj, S., Cost benefit of biomass supply and pre-processing, BIOCAP, Canada, 2006.

[22] Dones, R. et al, 2004, Life Cycle Inventories of Energy Systems: Results for Current Systems in Switzerland and other UCTE Countries, ecoinvent report No. 5, Paul Scherrer Institute Villigen, Swiss Centre for Life Cycle Inventories, Dübendorf, CH.

[23] Bridgwater, A.V., 2000, Fast pyrolysis processes for biomass, Renewable and Sustainable Energy Rev., 4(1), pp. 1-73.

[24] Rudloff, M., 2007, First Commercial BTL Production Facility – The Beta Plant Freiberg, SYNBIOS II, Stockholm, Sweden.

Acknowledgement

This work is part of the Primary Energy Efficiency project of Nordic Energy Research.

The funding of the Graduate School of Energy Science and Technology (EST) is gratefully acknowledged.

The support of ANDRITZ Feed & Biofuel A/S is gratefully acknowledged

STEAM DEMANDS AND WATER CONSUMPTION FOR DIFFERENT PRODUCTION PATTERNS OF SUGAR AND ETHANOL PRODUCTION FROM SUGARCANE

Reynaldo Palacios-Bereche[a], Mauro Francisco Chavez-Rodriguez[b], Silvia A. Nebra de Perez[c]

[a,b] *Mechanical Engineering Faculty (FEM), State University of Campinas(UNICAMP)*
[c] *Interdisciplinary Center of Energy Planning (NIPE), State University of Campinas (UNICAMP)*

Abstract: Ethanol from sugarcane is a biofuel in expansion, especially in Brazil where its production is raising in an average of 12% per year. In a scenario where Sao Paulo legislation restricts withdrawals of water at 1 m^3/t of sugarcane for sugar-ethanol plants, water consumption has become a variable that needs careful management inside the plant. Most of the sugarcane plants in Brazil have been projected to produce both, sugar and ethanol, prioritizing one over other according to prices in the market. Nevertheless, this change in the production pattern affects parameters in their production such as water consumption, steam demands, bagasse surplus and electricity produced. This work presents the results of a simulation of a sugarcane plant at different production patterns: all juice of sugarcane is sent to produce ethanol without sugar production, distribution of 50%/50% of total recoverable sugars in sugar and ethanol production, and all juice is sent to sugar production and only molasses are used for ethanol production. It is concluded that production pattern change dramatically the net effective collecting of water, reporting the case less favorable when ethanol is prioritized, presenting a requirement of 0.704 m^3/t of sugarcane. In the other hand, water content in sugarcane is more than enough to supply water needs in the plant when sugar production is prioritized, reporting a water surplus of 0.049 m^3/t of sugarcane. Steam demands are not affected in a great amount by production pattern changes, being the case of 50%/50% the most efficient in terms of steam demands, resulting in 480 kg of steam per tonne of sugarcane crushed in the simulated plant.

Keywords: Water, Ethanol, Sugar, Steam, Sustainability.

1. Introduction

Over recent years as energy security and environmental concerns have risen up various political agendas, there has been a substantial interest in biofuels and their potential contribution to energy security, mitigation of GHGs in the transport sector and also in delivering rural economic development benefits. Many countries around the world have developed or are developing biofuel mandates that require specific and rising contributions within the transport sector the next years.

Worldwide, fuel ethanol consumption in 2007 was estimated as about 50 billion litres, being the increase of almost 25% [1], regarding the previous year. Since 2006, US is the main world producer; in 2008 its production was estimated as 30 billion litres, while the consumption as fuel was estimated as 30 billion litres and with importations of around 2.2 billions litres. For more than three decades (from mid-1970s to 2006) Brazil was the world's largest producer and consumer of fuel ethanol. In 2008 its production reached 24.5 billion litres, while the domestic consumption as fuel was close to 18 billion litres [2]. In the period 2002-2007, fuel ethanol production in Brazil raised at annual average rates of 12%.

Most of the sugarcane plants in Brazil have been projected to produce both, sugar and ethanol, prioritizing one over other according to prices in the market.

The decisions of producing sugar or ethanol in sugarcane mills are mainly influenced by the market conditions of these products.

For instance, in terms of volume, sugar exportations in Brazil reported an increasing of 25%, summarizing 24.2 millions of tonnes in 2009, this fact is due mainly to the high international prices of sugar caused by the crop failure of big producers, like India.

Additionally, Brazilian ethanol exportation felt in 35% in 2009, summarizing 3.3 billions of litres

exported, due, between other factors, to the falling of international prices of oil, and mainly by the reduction of direct exportations to United States [3]. However, the decisions in distribution of sugarcane sugars in production process, which increment one product over another, will affect the demands of water and steam for the processes, and this could have some impacts in their sustainability, for example in their water consumption or GHG emissions balances.

Another by-product of Brazilian sugarcane plants is electricity generated by their cogeneration systems. Plants with generating capacities exceeding 28 kWh per t of processed sugarcane are usually able to offer surplus energy for sale to the public electricity grid. The operation of these plants under typical conditions in Central-South Brazil, milling 2 million tons of sugarcane annually using conventional cogeneration systems at 6.5 MPa and 480°C, would translate into an installed production capacity of 31 MW [4].

The aim of this work is to assess the steam demands, water needs and potential of water re-use at different production patterns: (i) all sugarcane juice dedicated to ethanol production without sugar production, (ii) sugar and ethanol distributed equally, and (iii) all sugarcane juice dedicated to sugar production and molasses for ethanol. Simulation in Aspen-Plus software of a plant has been done using literature values and data collected in the field. The cogeneration system was also simulated in the same software and integrated to the rest of the plant. Challenges were found for simulation of sugarcane plant due to some sugarcane components are not present in the simulator database. Thus, it was necessary to accomplish a study of properties of sucrose-water solutions, ethanol-water solutions and sugarcane bagasse, in order to compare the accuracy of the simulator for property calculations in relation to literature data.

2. Sustainability impacts due to different production pattern

Nowadays, in Sao Paulo State in Brazil, sugarcane-ethanol sector represents around 7% of superficial water withdrawals in the State, according to [5] it is estimated that currently the sector have an average water withdrawal of $1 m^3/t$ of sugarcane which have been reduced drastically when compared to 5.6 m^3/t of sugarcane in the 1990s. Legislations, approved (Resolution SMA-88, 19/12/2008) establish regional division in the State, and approve new enterprises with a top of $1 m^3/t$ of sugarcane in adequate regions, and only 0.7 m^3/ t of sugarcane in adequate regions with environmental restrictions. In this way, sugarcane plants were forced to improve water management, reducing water losses, closing circuits, and take advantage of water content in the own sugarcane (average of 700 litres of water in a tonne).

Water re-use has become a solution as a means of reducing the total amount of water intake. This, in turn, not only saves upstream treatment of raw water but also reduces wastewater treatment costs. The current drive towards environmental sustainability and the rising costs of fresh water and effluent treatment have encouraged the process industry to find new ways to reduce freshwater consumption and wastewater generation.

Works evaluating the potential for reducing water consumption for a plant that uses sugar from sugarcane distributed 50% for sugar production and 50% for ethanol production has been done, and resulted in a great potential of re-use mainly from vegetal vapours condensates [6]. However, a distillery that produces only ethanol does not have the same sources for re-use [7].

Electricity selling is related with the mitigation of GHG emissions. The bagasse-derived electricity today avoids the dispatch of natural gas thermal plants in the Brazilian National Interconnected System. For example, for distillery plants (ethanol only), electricity selling based in bagasse burning have credits accounted for about 62 $kgCO_2eq/m^3$ of anhydrous ethanol produced avoided, considering the substitution of natural gas-electricity, generated with 40% efficiency [8].

3. Methodology

It was modelled a sugarcane plant with a crushing rate of 490.2 t/h for production of sugar and anhydrous ethanol. Production patterns determine the quantities of sugar and ethanol that will be produced.

Because sugarcane that arrived to the mill contains some amount of field soil that is carried in harvesting operation, dry cleaning was considered in simulation. The most usual cleaning system is wet process, which uses water for cleaning, but dry process is being preferred in modern plants because it does not consume water [6].

After Dry Cleaning Operation cleaned sugarcane goes to the milling sector. The imbibition water rate considered is 300 kg of water/t of sugarcane and the efficiency of sugar extraction is assumed as 97% [9]. Extracted juice goes to the physical-chemical treatment where sugarcane juice passes through phosphatation, heating, liming, flashing and decantation stages in order to eliminate impurities. Filter cake is obtained in an amount of 36.6 kg/t of sugarcane as consequence of the juice treatment process.

In order to obtain a concentration of sugars in the juice adequate to the process fermentation, 39% of the juice clarified with an original Pol of 11.7% is concentrated in an evaporation system until reach a Pol of 55.4%. An evaporation system of five effects is assumed; and also, bleed vapours are used to supply heat duties in the plant. Each one of the evaporation effects produces condensates with slight different properties. But normally they are put together for re-use. For sugar production, concentrated juice goes to crystallization process, which is accomplished in vacuum pans, in order to maintain low temperatures in *massecuite*, which has high content of soluble solids. In this way, problems of sucrose inversion can be avoided. Vapour of first effect is used for heating of vacuum pans and for water evaporation of syrup.

After that, massecuite goes to crystallizer tanks were the crystals formation is completed. The next step is the centrifugal separation where sugar is separated from *molasses*. Molasses and sugar are re-circulated in order to obtain a sugar of higher purity, which is the main product. Residual molasses are redirected to ethanol production. After that, sugar needs to be dried to be stored in appropriate conditions, for this purpose, air is heated at a temperature of 100°C by turbines exhaust steam.

For ethanol production, original clarified juice is mixed with the concentrated one, resulting in *must* with a Pol of 16.9%. The sterilization of must is done using a High Temperature Short Time treatment. In this treatment, must is heated until 130°C, staying in this temperature for approximately 30 minutes. After that, there is a fast cooling until fermentation temperature in the range of 32°C [9]. In the fermentation process, a conversion factor of 89% from sugars to ethanol is considered. Finally Wine passes through the distillation and dehydration (MEG) stages resulting in anhydrous ethanol 99.4 wt%. A diagram of the different stages of the process can be seen in Figure 2 in Appendix section. This diagram shows a plant that produces ethanol and sugar. Exhaust steam streams, water streams and process streams are indicated in this figure.

The different production patterns considered correspond to different distributions of the total recoverable sugars (TRS) in sugarcane. For the "Case I" TRS are destined exclusively for the production of ethanol, in "Case II" sugar and ethanol are produced (considering that 50% of recoverable sugars for sugar and 50% for ethanol production), being the ethanol production carried out with the residual molasses from the sugar production, besides some amount of syrup and treated juice. For "Case III" sugar production is prioritized, all sugarcane juice is dedicated to this, and only residual molasses are sent to fermentation to produce ethanol. In all cases it is assumed to have an electricity demand constant of 12 kWh/t of sugarcane crushed. According to the characteristics of the cogeneration plant, a surplus of electricity was produced, which is sold to the distribution grid. Products and by-products of these different production patterns are showed in Table 1.

Table 1. Products and by-products for different Cases.

Parameter	Case I	Case II	Case III
Cane input (t/h)	490.2	490.2	490.2
Sugar produced (t/h)	0.0	29.6	47.5
Anhydrous Ethanol Produced (m^3/h)	38.7	20.2	9.6
Vinasse (t/h)	485.4	254.3	121.3
Bagasse surplus (t/h)	8.9	15.9	9.2
Electricty surplus (kW)	22825.5	20794.5	23463.5

4. Use of Water Results

The water use in the industrial process was analyzed considering all the process needs. To represent the water requirements [6], the first step was to register the water needs of a mill without any closed circuit. The consumption rates reported were founded in the literature and also collected in real mills [5,10]. Table 2 shows the water needs in each simulated case.

It can be observed from Table 2 that refrigeration and condensing processes such as cooling of fermentation vats, barometric condenser of

evaporation, condenser of distillation and vacuum in the pans are the major water users in the plant. Water needs for these processes changes dramatically according if sugar or ethanol is prioritized. For instance, in Case I, demands for cooling of fermentation vats and condenser of distillation have the highest needs for water, but in Case III water for vacuum in pans and for barometric condenser in evaporation are the highest. Adding all water uses, Case I have the higher water needs; even though it does not have the same water needs as sugar production, like water for vacuum in pans, added for sugar, for dilution of molasses, etc. this fact is explained by the big amounts of cooling needs for fermentation and distillation, supplied by cold water.

Table 2. Water Uses (without considering recycles) in the Sugarcane Plant

Water Uses	Case I (m^3/h)	Case II (m^3/h)	Case III (m^3/h)
Imbibition	147.2	147.2	147.2
Bearings Cooling	24.5	24.5	24.5
Oil of Lubrification Cooling	196.1	196.1	196.1
Sulfitation Cooling	0.0	6.9	9.8
Preparing of milk lime	9.4	9.4	9.4
Filter Cake Washing	34.3	34.3	34.3
Water for centrifugal washing	0.0	9.0	14.4
Water for dilution of poor molasses	0.0	0.7	1.1
Water for dilution of sugar	0.0	2.1	2.9
Water added to pans	0.0	1.2	2.0
Barometric Condenser of Evaporation	653.7	1251.1	1919.7
Barometric Condensers of Filters	92.5	92.5	92.5
Cooling of juice for fermentation	1652.7	822.7	419.8
pans	0.0	919.8	1457.3
Dilution of milk yeast	66.2	33.5	17.6
Cooling of fermentation vats	1975.4	1031.3	489.2
Condenser of Destilation	1228.7	545.0	203.1
Condenser of Rectification	364.1	202.9	210.2
Condenser of Extractive Column	306.8	160.6	76.4
Condenser of Recuperation Column	49.9	52.0	19.9
Cooling of solvent	32.8	32.8	8.2
Washing Scrubbers(boiler)	429.9	403.9	430.8
Boiler feed water	245.7	230.8	246.2
General cleaning	24.5	24.5	24.5
Drinkable uses	14.7	14.7	14.7
Cooling of Turbogenerators	98.0	98.0	98.0
Cooling of Crystallizers	0.0	14.9	23.9
Total (m^3/h)	7647.1	6362.4	6193.6
Ratio (m^3/t of sugar cane)	15.6	13.0	12.6

The second step was to identify and quantify water Sources to re-use such as condensates in sugar plant. Table 3 shows these “water sources”, their flows, temperature and pressures. May be, these currents need to be treated, according their quality.

Table 3. Water Streams for Reuse

Water Sources	Case I (m^3/h)	Case II (m^3/h)	Case III (m^3/h)
Condensate of filtration	1.4	1.4	1.4
Condensate of 1st effect Vegetal Vapor(collected in the output of the 2nd effect calandria)	16.1	31.4	48.8
Condensate of Bleeding 1st effect Vegetal Vapor to heating in treatment of	66.2	66.2	66.2
Condensate of Bleeding 1st effect Vegetal Vapor to heating Pan A	0.0	39.7	62.0
Condensate of Bleeding 1st effect Vegetal Vapor to heating Pan B	0.0	5.8	9.2
Condensate of 2nd effect Vegetal Vapor	17.7	34.3	53.1
Condensate of 3rd effect Vegetal Vapor	19.2	37.1	57.3
Condensate of 4th effect Vegetal Vapor	20.9	40.2	61.9
Condensate of 5th effect Vegetal Vapor in Barometric Condenser	22.8	43.6	66.9
Condensate of Vegetal Vapor of Pan A	0.0	27.1	42.9
Condensate of Vegetal Vapor of Pan B	0.0	4.4	7.0
Boiler Blowdown	12.3	11.5	12.3
Washing scrubber water losses	21.5	20.2	21.5
Vinasse*	485.4	254.3	121.3
Cleaning water collected (50%)	12.3	12.3	12.3
Recovery Water Dehydration Process	1.8	1.0	0.5
Total (m^3/h)	697.4	630.5	644.7
Without Vinasse(m3/h)	212.1	376.2	523.4
Ratio (m^3/t of sugar cane)	0.43	0.77	1.07

Condensates of evaporation section could be re-used without treatment, for example in imbibition, as make-up water in cooling systems, etc.

It can be observed in all cases that Vinasse is the greatest source of water to be re-used, however, it

needs treatments like evaporation, or reverse osmosis; due to its high load of suspended solids, Biochemical Oxygen Demand (BOD) and low pH. (According [5], the total suspended solids in vinasse are around 3966.8 mg/L while the pH is around 4.8). So, in this work, its re-use was not considered, as is usual nowadays.

Leaving aside vinasse´s water, Case III has the higher sources of water to re-use, explained by greater quantities of water of sugarcane available due to the juice concentration in evaporation and in pans section, and less vinasse produced.

The third step is to simulate the closing of water circuits, which conducts to the effective collecting water needed to attend processes. Table 4 shows the losses in the closed circuits.

Table 4. Water Losses of Closed Circuits [10].

Closed Circuits	Water Losses(%)
By Cooling Towers	3%
Bearing Cooling	
Oil of Lubrification Cooling	
Sulfitation Cooling	
Cooling of juice for Fermentation	
Cooling of Fermentation Vats	
Cooling of Turbogenerators	
Cooling of Crystallizers	
Cooling of Solvent	
By Spray Ponds	4%
Barometric Condenser of Evaporation	
Barometric Condensers of Filters	
Barometric Condensers in Pans	
Condenser of Distillation	
Condenser of Rectification	
Condenser of Extractive Column	
Condenser of Recuperation Column	
Treatment Washing Scrubbers Water	5%
Recirculation Boiler Feed Water (blowdown)	5%

For the simulation, it was assumed that water return to spray ponds at 50ºC where it is cooled down to 30º and then used again. For cooling towers it was assumed water inlet at 30ºC and outlet at 25ºC.

The effective collecting of water occurs for the make-up of the closed circuits and also to attend demands of processes where it is added to the streams, as for example imbibition, yeast dilution, preparing of lime, etc.

Table 5 shows the effective collected water needs for processes.

Table 5. Effective Collected Water by Process

Effective Collecting Water	Case I (m^3/h)	Case II (m^3/h)	Case III (m^3/h)
Imbibition	147.2	147.2	147.2
Make-up Bearing Cooling	0.7	0.7	0.7
Make-up Oil Lubrification Cooling	5.9	5.9	5.9
Make-up Sulfitation Cooling	0.0	0.2	0.3
Lime preparing	9.4	9.4	9.4
Filter Cake Washing	34.3	34.3	34.3
Water for centrifugal washing	0.0	9.0	14.4
Water for dilution of poor molasses	0.0	0.7	1.1
Water for dilution of sugar	0.0	2.1	2.9
Water added to pans	0.0	1.2	2.0
Make-up Barometric Condenser of Evaporation	26.1	50.0	76.8
Make-up Vacuum in Filters	3.7	3.7	3.7
Make-up Cooling of juice for fermentation	49.6	24.7	12.6
Make-up Vacuum Pans Circuit	0.0	36.8	58.3
Dilution of milk yeast	66.2	33.5	17.6
Make-up Cooling of fermentation vats	59.3	30.9	14.7
Make-up Condenser of Destilation	49.1	21.8	8.1
Make-up Condenser of Rectification	14.6	8.1	8.4
Make-up Condenser of Extractive Column	12.3	6.4	3.1
Make-up Condenser of Recuperation Column	2.0	2.1	0.8
Make-up Cooling of solvent	1.0	1.0	0.2
Make-up Washing Scrubbers (boiler)	21.5	20.2	21.5
Make-up Boiler feed water	12.3	11.5	12.3
General cleaning	24.5	24.5	24.5
Drinkable uses	14.7	14.7	14.7
Make-up Cooling of Turbogenerators	2.9	2.9	2.9
Make-up Cooling of Crystallizers	0.0	0.4	0.7
Total (m^3/h)	557.3	504.2	499.2
Ratio (m^3/t of sugar cane)	1.14	1.03	1.02

In theory, the water treatment system has to supply these quantities from the water collected in rivers, lakes, etc.

As it is reported in Table 5, just closing circuits water consumption is reduced dramatically, reaching near 1 m^3/t of sugarcane, which is currently almost the average consumption in sugarcane plants [5].

Even decreasing losses in condensers of evaporation circuit, Case I reports the highest effective collecting water due to the increased needs of condensers in distillation (and consequently increased losses) and the higher demand for dilution of yeast *milk*.

If values of total effective collected water are subtracted from these of total water sources, discounting vinasse, we obtain the net effective collecting as 345.2, 128 and -24.2 m^3/h, or in terms of ratio 0.704, 0.261 and -0.049 m^3/t of sugarcane for Case I, Case II and Case III respectively. The negative symbol means that there is a surplus of water in the processes, which means that water content in sugarcane is more than enough to supply all needs in the plant under this production pattern.

It must be remarked that a dry clean system is considered for the simulation, actually most of the sugarcane plants currently keeps the washing sugarcane system, which, after imbibition process, is the major effective water consumer [6].

5. Simulation Steam Demand Results

Processes in sugar and ethanol production plant are very intensive in the use of energy, mainly thermal. On average, thermal consumption of sugarcane plants are around 330 kWh/t of sugarcane (equal to 500 kg of steam per t of sugarcane) [11].

Currently, sugarcane plants are self-sufficient in terms of electromechanical energy and heat for their processes. Bagasse generated in the extraction process is sent to utility plant, where it is burned in boilers. In most cases cogeneration systems used in the sugarcane plants are based on boilers generating steam at 2.1 MPa and backpressure steam turbines (exhaust at 0.25 MPa). However, there are some sugarcane plants operating with high steam parameters (4.2 – 6.6 MPa), generating electricity surplus, which is sold to the distribution grid [4, 11]. Figure 1 shows the configuration considered in the simulation, all steam produced in the boiler is expanded in backpressure steam turbine 1 from 6.7 MPa to 2.2 MPa, part of this steam at 2.2 MPa goes to turbines for mechanical driving represented by turbine 2, the rest of the steam goes to turbine 3 which have an extraction at 0.6 MPa and final expansion at 0.25 MPa to supply thermal demands. Turbine 2 and 3, in this simulation, are backpressure steam turbines.

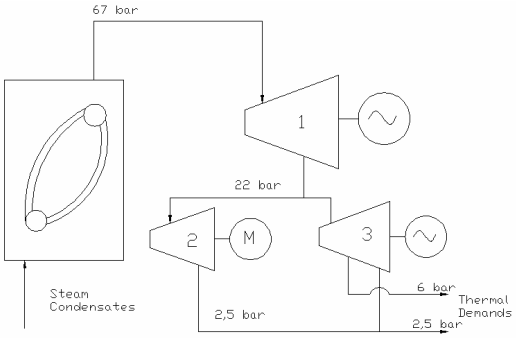

Figure 1. Cogeneration System Considered in Simulation

Steam at 2.2 MPa is extracted for driving sugarcane knives, shredders and tandem mills. Low-pressure exhaust steam is used as thermal source for different processes in the plant. Evaporation process for concentrating sugarcane juice is the major consumer of exhaust steam. Besides that, this process is responsible for supplying heat to diverse process as juice treatment and crystallization.

In the ethanol production process, besides of thermal demands of distillation columns, there is the extractive column where ethanol is dehydrated using MEG (monoethylene glycol), which needs high pressure steam (0.6 MPa) due to bottom temperatures are between 130 and 150ºC. High pressure steam is used also in the sterilization process (130ºC needed).

Table 6. Steam Demands Results

Steam Demands	Case I (t/h)	Case II (t/h)	Case III (t/h)
Steam 6 bar			
Sterilization of must	23.9	11.3	15.3
Dehydration	15.5	9.8	4.2
Steam 2,5 bar			
Evaporation	91.9	155.0	203.5
Distillation	119.9	58.7	26.3
Drying of sugar	0.0	0.5	0.8
Total(t/h)	251.2	235.3	250.1
Ratio (kg/t cana)	512.4	480.0	510.2

Results of steam consumption expressed in kg of steam per t of sugarcane for each production pattern are showed in Table 6.

In Case I, when all juice is dedicated to produce ethanol, distillation becomes the major consumer (47.7%), but it is lowering to second place in Cases II and III, where evaporation has the main demands, 65.8% and 81.38% respectively. There are no great differences in total steam amounts between production patterns, however, Case I have the biggest needs of high pressure steam, besides that, more steam passes through turbines 1 and 3, so, more electricity is produced, however it has the lowest bagasse surplus (see data in Table 1). This bagasse surplus can eventually be burned to produce steam to move a condensation turbine to generate more electricity.

The aim of this study was to analyze working real conditions in production plants, in future work, new improving proposals will be analyzed. Proposal of improvements in steam consumption can be found at the literature. [12, 13, 14, 15]. There are also proposals of more efficient cogeneration systems [16, 17].

6. Conclusions

Having an established sugarcane plant, with the possibility of producing different rates of sugar and ethanol, other parameters such as electricity produced, bagasse surplus, steam demands and water consumption will be affected according the production rates

Changes in production pattern especially affects water needs in the plant, being the exclusive production of ethanol the most intensive water consumer with a ratio 1.14 m^3/t of sugarcane, because great part of water goes out in vinasse form. In this case, and where legislation restricts the withdrawal of water, additional measures must be taken such as concentration of vinasse, in order to recuperate this water lost and supply water needs.

In the other hand it is demonstrated that producing sugar with all juice in sugarcane and ethanol only with molasses allows having water surpluses of 49 liters/t of sugarcane, being the sugarcane plant supplied just with the water content of sugarcane.

Steam demands are not affected in a great amount in each case. Other point to emphasize is that the case of ethanol and sugar production, distributing 50%/50% of TRS, it the most efficient in terms of steam demands.

Acknowledgements

The authors wish to thank to Adriano Ensinas, professor of Federal University of ABC-UFABC, and Marina Dias, researcher of Brazilian Bioethanol Science and Technology-CTBE, by the valuables discussions and suggestions given for the simulation of the plant. To CNPq (Processes 135595/2008-8 and PQ 10 - 307068/2006-4) and CAPES for the master, PhD and researcher fellowships and FINEP (Contract FINEP – FUNCAMP Nr. 01/06/004700) for the financial support.

References

[1] RFA – Renewable Fuels Association. Statistics data. 2008. Available at: http://www.ethanolrfa.org/industry/statistics/# . Accessed on December 2009.

[2] EPE – Empresa de Pesquisa Energética. 2008. Dados Preliminares do Balanço Energético Nacional 2008. Available in: www.epe.gov.br.

[3] Unica, 2010. UNICA Explanations note about exportations. Sugarcane Industry Association. http://www.unica.com.br. Accessed in January 2010.

[4] BNDES and CGEE, 2008, Sugarcane-based bioethanol energy for sustainable development, Rio de Janeiro, BNDES.

[5] Elia Neto, A., 2009, Manual For Water Re-use and Conservation in the Sucroenergetic Industry. Brasilia, ANA. In Portuguese.

[6] Chavez, M.F.R., Ko, L.M., Ensinas, A.V., Nebra, S.A. 2009, Reduction of water consumption in the production of sugar and ethanol from sugarcane. In Proceedings of 20th International Congress of Mechanical Engineering, November 15-20, Gramado, RS, Brazil.

[7] CETESB, 2008, Resolution SMA - 88, of 19-12-2008. www.cetesb.sp.gov.br.

[8] Macedo, I.C., Seabra, J.E.A., Silva, J.E.A.R., 2008, Green house gases emissions in the production and use of ethanol from sugarcane in Brazil: The 2005/2006 averages and a prediction for 2020, Biomass and Bioenergy 32, pp. 582 – 595

[9] Dias, M.O.S., 2008, Simulation of ethanol production processes from sugar and sugarcane bagasse, aiming process integration and maximization of energy and bagasse surplus. Chemical Engineering Faculty, University of Campinas, Sao Paulo, Brazil. (In Portuguese).

[10] Rein, P., 2007, Cane Sugar Engineering. Verlag Dr. Albert Bartens KG – Berlin.

[11] CGEE, 2009, Fuel bioethanol an opportunity to Brazil, Brasilia DF, CGEE. (In Portuguese).

[12] Morandin, M.T., Lazaretto, A., Maréchal, F., Ensinas, A.V., Nebra, S.A., 2009, Synthesis and Parameter Optimization of a Combined Sugar and Ethanol Production Process Integrated with a CHP System – Part 1: Minimization of the Process External Heat Requierement; In Proceedings of ECOS 2009; Foz do Iguaçú, Paraná, Brazil, pp.469 – 478.

[13] Morandin, M., Lazaretto, A., Marechal, F.; Ensinas, A.V., Nebra, S.A., 2009, Synthesis and Parameter Optimization of a Combined Sugar and Ethanol Production Process Integrated with a CHP System – Part 2: Maximization of total site net Power, In Proceedings of ECOS 2009, Foz do Iguaçú, Paraná, Brazil, pp.479 – 490.

[14] Dias, M.O.S., Ensinas, A.V., Modesto, M., Nebra, S.A., Maciel Filho, R., Rossel, C.E.V., 2009, Energy Efficiency in Anhydrous Bioethanol Production From Sugarcane-Part 1: Process Simulation and Thermal Integration, In Proceedings of ECOS 2009; Foz do Iguaçú, Paraná, Brazil, pp. 425 – 436.

[15] Modesto, M., Ensinas, A.V., Dias, M.O.S., Nebra, S.A., Maciel Filho, R., Rossell, C.E.V.; 2009, Energy Efficiency in Anhydrous Bioethanol Production from Sugarcane –Part 2: Cogeneration Systems Technology, In Proceedings of ECOS 2009, Foz do Iguaçú, Paraná, Brazil, pp. 437 – 448.

[16] Ensinas, A.V., Nebra, S.A., Lozano, M.A., Serra, L., 2007, Analysis of process steam demand reduction and electricity generation in sugar and ethanol production from sugarcane, Energy Conversion and Management, 48, pp. 2978 - 2987.

[17] Pellegrini, L.F., Oliveira, S., 2009, Thermo-economic-environmental analysis and optimization applied to the combined production of sugar, ethanol and electricity, In Proceedings of ECOS 2009; Foz do Iguaçú, Paraná, Brazil, pp.501 – 511.

Appendix

In Figure 2 is showed the diagram of the plant simulated for production of ethanol and sugar (working at 50%/50%= showing the streams of exhaust steam, water streams, vapour streams and processes streams.

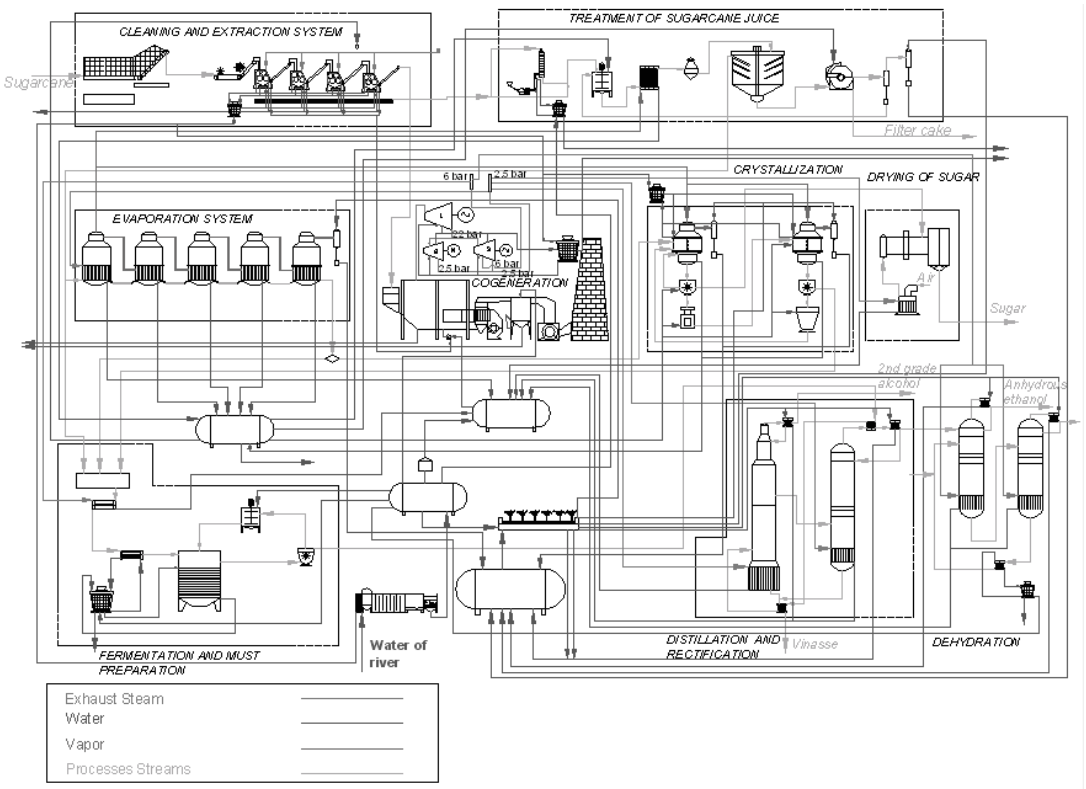

Figure 2. Diagram of the Simulated Plant

Integration of Hybrid Cycles in Bio-Methanol Production

Martin Görling, Mats Westermark

Royal Institute of Technology, School of Chemical Science and Engineering, Energy Processes, Stockholm, Sweden

Abstract: In bio-based methanol production approximately 60% of the biomass energy content is converted into methanol, the remaining part can be recovered as thermal heat. Efficient utilization of the thermal heat is difficult in stand-alone methanol plants. The overall efficiency is to a large extent dependent on the further conversion of power due to the significant quantity of excess heat. Heat can be recovered in a steam cycle but due to poor steam data energy efficiency is low. This paper therefore proposes the integration of a natural gas fired gas turbine. Simulations of the hybrid cycle in methanol production have shown good improvements. The total electrical efficiency is increased by 1.4-2.4 percentage points, depending on the fuel mix. The electrical efficiency for the natural gas used in the hybrid plant is 56-58%, which is in the same range as in large-scale combined cycle plants. A bio-methanol plant with a hybrid power cycle is therefore a competitive production route for both biomass and natural gas.

Keywords: Bio-Methanol, Biomass, Gasification, Hybrid Cycles, Polygeneration

1. Introduction

The power generation and transportation sectors are the two largest emitters of green-house gases. Major developments must take place in these two sectors in order to slow down and stop the anthropogenic green-house effect. Emissions can be decreased by applying more efficient energy utilization and conversion to sustainable energy sources (e.g. biomass). In addition, the use of energy for transportation is predicted to grow by 2% annually [1], which will also need to be met with by green alternatives.

The replacements for today's fossil fuels used for transport are predicted to be liquid and gas fuels from gasification (second generation fuels) and in the future electricity and hydrogen utilized in fuel cells (third generation). There are still various technical difficulties that need to be solved with regard to the transportation and storage of hydrogen, before the "hydrogen economy" can become a reality. The drawbacks of hydrogen utilization; has led to an increased belief in methanol as the fuel of the future. Methanol is easier to handle and better fitted to today's infrastructure [2].

The second generations fuels, which is closest to commercialisation, is able to use waste and non-food crops and will therefore not compete with food production, as opposed to the first generation fuels (fermentation and digestion).

Biofuel plants for second generation fuels are often net users of electricity but produce large amounts of excess heat. To avoid the need to import power, the excess heat can be used in a steam cycle, but in most cases the plant remains a net user of electricity. This report therefore, studies combined bio-methanol production and power production. The unique aspect of this study is the integration of a natural gas fired gas turbine and the surplus heat from a methanol plant into a hybrid cycle. Hybrid cycles have been proven to enhance overall efficiency in other applications such as biomass or municipal waste fired steam cycles [3].

1.1 Aim and scope

The aim of this study is to identify and quantify the potential synergies from integration of natural gas fired gas turbines with bio-based methanol production.

2. Background

A substantial part of the biomass input is converted into chemical reaction heat in the methanol production process. Therefore, a stand-alone plant without efficient heat recovery obtains a rather low overall efficiency. Typically, about 60% of the lower heating value of the biomass input can be converted to lower heating value of the methanol output. To increase efficiency, several studies propose heat recovery in a steam

Corresponding Author: Martin Görling, Email: gorling@kth.se

cycle [4-6]. A number of studies have also examined the possibility to supply district heating, which has also shown an improvement in the overall efficiency and economy [7,8]. A plant located within a district heating grid with a high annual heating demand may lower the cost of methanol by up to 10% [7]. Most biomass to liquid fuel routes demand a substantial portion of electrical energy, mainly for compression and oxygen production which makes the plants net users of power. To increase internal power production, some studies discuss integration of a gas turbine fuelled by non-reacted or pure syngas [4,9]. However, syngas is less suitable than natural gas, for which modern gas turbines are optimized. The composition of the syngas is dependent on the gasification method; usually, the lower heating value is in the range of 5-10MJ/nm^3; corresponding figure for natural gas is 35-40MJ/nm^3. Technical problems with biomass-derived syngas in gas turbines; include combustion stability, pressure drop in the fuel injection system and limitations in mass flow through the turbine [10]. Modifications or use of less advanced turbines are often necessary.

The share of fossil energy that can be replaced by green alternatives is limited by the biomass supply. To avoid these limitations and increase methanol production to achieve economy of scale, some studies discuss the use of coal [11] or natural gas [12] as co-feedstock for methanol production.

Natural gas is therefore used in this study as gas turbine fuel for two reasons: the fact that turbines are optimized for natural gas and limited supply of biomass. Biomass has a rather low energy density, and transportation over long distance is therefore neither economically nor environmentally feasible. A large scale methanol plant (400MW$_{bio}$) would consume most of the available biomass within a suitable transport distance. In a large plant, the biomass transportation cost constitutes a significant portion of the production cost. Meanwhile, there are economies of scale when considering the investment cost. In a study [13] concerning economies of scale; a case study of the possibility for methanol production in Greece showed that an area of 950km^2 (90% of forest) is needed to supply 380MW of biomass. At that plant size, approximately 10% of the methanol production cost would be used for biomass transportation.

2.1. Methanol from biomass

The general production process for bio-methanol is described in *Fig. 1* below. Most of the steps are common for all types of biofuel except for fuel synthesis and purification. Most of the methanol produced today is made from natural gas, which has the last two process steps in common with biomass-based production.

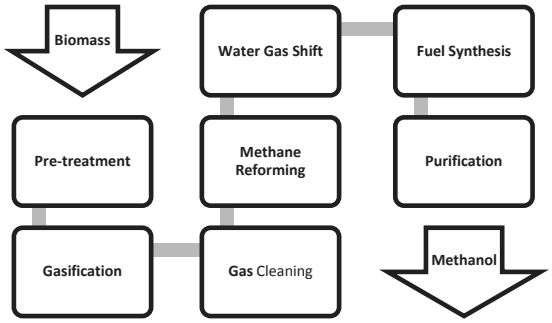

Figure 1: General process scheme for methanol production from biomass.

Before the biomass can be fed to the gasifier it has to be dried and chipped. In the gasification step the biomass is heated and oxidised into syngas, which mainly consists of carbon monoxide, hydrogen and carbon dioxide. The gas cleaned to protect downstream equipment; the most common pollutants being sulphur and alkali metals. A water gas shift is made to achieve the appropriate ratio between hydrogen and carbon monoxide with the purpose of maximizing the fuel synthesis. Both the water gas shift and the fuel synthesis are exothermic processes that produce a great amount of heat at about 300°C. The last step, purification, involves removal of water through distillation. The reaction heat produced widely covers the internal heat demand at high temperatures and can therefore be used for power production in a steam cycle.

2.2. Hybrid cycles

A hybrid cycle is defined as a cycle that uses two types of fuel, often a bottom cycle fired with solid fuel and a top cycle with liquid/gas fuel. Petrov's study [3] of hybrid cycles has shown, among other things, improved efficiency when combining two fuels compared with two single-fuel plants, i.e. one for each fuel. The hybrid configuration has

also been proposed to "repower" old steam power plants with poor steam data.
There are two main configuration opportunities for hybrid combined cycles: serial or parallel. In the serial setup, the flue gas from the gas turbine is fed to the bottom cycle boiler. Using the oxygen surplus in the flue gas from the top cycle for bottom cycle combustion minimizes the flue gas loss. In the parallel configuration, the flue gas from the gas turbine is used separately to raise steam data and high-temperature preheating [3,14]. The hybrid configuration proposed in this study is of the parallel type.
The improved efficiency comes from the fact that both fuels can be used in the most useful way; high quality fuels can be used in the top cycle (gas turbine and internal combustion engines) and solid fuel in the bottom cycle. Since the flue gas from the top cycle (in this case a gas turbine) contains a great amount of oxygen, some supplementary firing in a heat recovery steam generator could be done without any additional flue gas losses [15]. A study [16] evaluating the possibilities of biomass as a fuel in combined cycle power plants concluded that biomass is best used for supplementary firing.
An improvement of efficiency due to the implementation of gas turbines in the production process is not as obvious as it is for steam turbines. The excess heat from the biomass plant has a high temperature; when this heat is used in a steam cycle, a significant amount of steam must be used for preheating. The integration of a top cycle; which can deliver heat for preheating, would therefore improve overall efficiency.

3. Method

This paper evaluates a hybrid cycle with combined power and bio-methanol production. To quantify the effects of a hybrid system a reference case is required. Since the hybrid plant uses two energy sources, waste heat from the production process and natural gas, two reference plants are needed: as a reference case, a bio-methanol plant and a natural gas combined cycle power plant are studied as standalone plants.
Gas turbine performance calculations are performed in the software GTPerform [17] developed by Siemens. The flue gas properties and/or the heat from the methanol plant are used as input data in GateCycle [18] for steam cycle calculations. All simulations are made in cold condensing mode.

Table 1: General parameters for all power production simulations

Parameter:	Value:
Ambient parameters	15°C, 101.3 kPa, 60% RH
Outlet pressure loss GT	3 kPa
Isentropic efficiency ST	0.9
Condenser pressure	6 kPa
Deaerator pressure	0.4 MPa
Exhaust gas temperature	120°C
Economizer ΔT	5°C
Boiler ΔT	10°C

To investigate how the fuel mix (natural gas in GT and excess heat) affects the hybrid performance, a wide range of gas turbines have been tested. The gas turbines tested are Siemens industrial turbines in the range of 5-47MW_{el}.

3.1. Reference case

Two standalone plants serve as the reference case; a bio-methanol plant and a combined cycle power plant.

3.1.1 Stand alone Bio-methanol plant

A study conducted by Katofsky[5] was used as the basis for the methanol process. In the present study, a number of gasifiers were evaluated and the case with an indirect heated gasifier (The Battle-Columbus Laboratory gasifier) is used for its high efficiency and the amount of available heat. The main data for the plant is shown in the table below.

Table 2: Energy and balance for bio-methanol production[5]

Biomass input (MW_{HHV})	384.2
Electricity consumption (MW)	27.4
Waste heat (MW)	83.7
Methanol produced (MW_{HHV})	248.4

A pinch analysis was made from the cooling and heating demand to quantify the surplus of heat available for steam production. A 10°C temperature difference is used to maintain a driving force in the heat exchangers. The analysis shows that 83.7MW of reaction heat is available. However, a fraction of the excess heat may not be recoverable for economic reasons and due to physical distance. The amount of heat available for steam production has therefore been assumed to be 80MW.

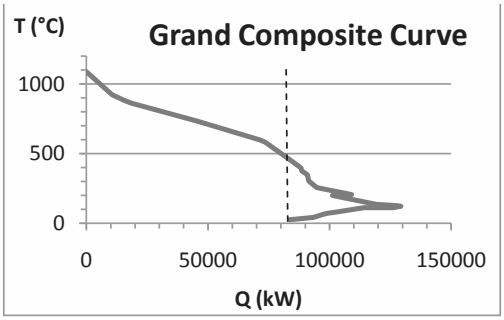

Figure 2: Grand composite curve from pinch analysis of bio-methanol plant.

The grand composite curve shows that the high temperature heat is available for steam production (the left side of the dotted line in *Fig.* 2). The right side of the line represents the heat used to fulfill the internal demand.

The methanol process units that are included in the steam cycle are treated as black boxes, only a heat source. After the pinch analysis, when all the heating demands are fulfilled, the heat sources that remain for steam production are: syngas cooler after the gasifier; the shift reaction cooler and the flue gases from the combustion part of the indirect gasifier. The heat from the syngas cooler is best used for steam production to avoid problems with corrosion in high temperature heat exchangers. The flue gas from the combustion is less corrosive and therefore more suitable for steam superheating.

Table 3: Parameters for the steam cycle in the stand alone bio-methanol reference case.

Parameter:	Value:
Steam turbine inlet	14 MPa, 590°C
Reheat	2.5 MPa, 590°C
Feedwater preheaters	3 + deaerator
Fuel	Waste heat

The input from the methanol plant is the same in all simulations, regardless of the amount of natural gas used.

3.1.2 Natural gas fired combined cycle

The reference case for natural gas is a typical combined cycle with a two-pressure steam cycle. The possibility of duct firing has neither been tested in this reference case nor in the hybrid case. Table 4 shows the general parameters for the combined cycle; the steam temperature depends on the gas turbine model and will therefore vary.

Table 4: Parameters for natural gas fired combined cycle reference case.

Parameter:	Value:
Steam turbine inlet	8 MPa, ≈500°C
Reheat	0.6 MPa, ≈460°C
Feedwater preheaters	3 + deaerator
Fuel	Natural gas

3.2. Hybrid plant

The hybrid plant combines the heat recovery from the methanol production with gas turbine power production. As opposed to the reference case, the heat from the methanol plant and the gas turbine is used in the same steam cycle.

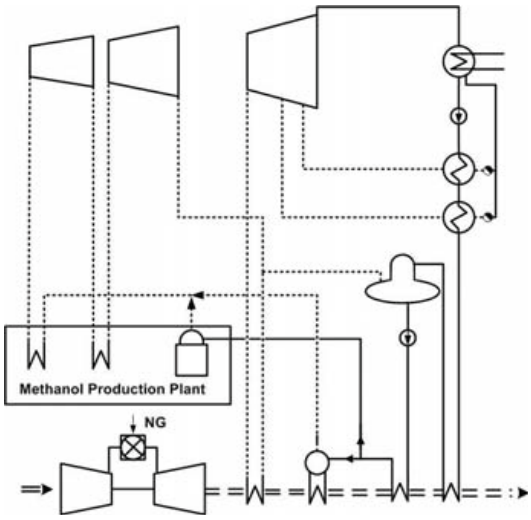

Figure 3: Conceptual flow sheet for the hybrid power cycle.

The flue gas from the gas turbine is primarily used for preheating and the heat from the methanol plant is used for boiling and superheating (see *Fig.* 3).

Table 5: Parameters for hybrid power cycle.

Parameter:	Value:
Steam turbine inlet	14 MPa, 590°C
High pressure reheat	8 MPa, 590°C
Low pressure reheat	0.6 MPa, ≈490°C
Feedwater preheaters	4 + deaerator
Fuel	Waste heat + Natural gas

4. Results

Two reference cases are used to evaluate the performance of the hybrid plant. The total efficiency for the two reference cases is calculated as:

$$\eta_{ref} = \frac{P_{MP} + P_{CC}}{Heat_{MP} + Fuel_{NG}} \quad (1)$$

The same input basis (denominator) is used when calculation the efficiency of the hybrid plant.

The natural gas efficiency (η_{NG}) is calculated by comparing the power output from the hybrid plant and the reference methanol plant, defined as:

$$\eta_{NG} = \frac{P_{Hybrid} - P_{MP}}{Fuel_{NG}} \quad (2)$$

The natural gas efficiency (η_{NG}) for the hybrid plant can be useful when considering the alternative of using the fuel in a large scale combined cycle plant. Only the heat delivered from the methanol plant is included when calculating the proportion of natural gas for power production. The final results from the simulations with the selected gas turbines are presented in the table below.

Table 6: Power production results from simulations.

Turbine	SGT-400	SGT-600	SGT-800
Methanol plant [MW_{el}]	35.2	35.2	35.2
Combined cycle [MW_{el}]	19.1	37.2	67.4
Tot. ref [MW_{el}]	54.3	72.4	102.6
η_{ref} [%]	46.5	47.5	50.3
Hybrid plant [MW_{el}]	55.9	75.7	107.9
η_{hybrid} [%]	47.9	49.7	52.7
η_{NG}[%]	56.4	55.9	58.3
Portion of NG for power production [%]	31.4	47.5	60.9

The simulation results show an increase in power output and efficiency when the natural gas is used in the hybrid plant compared to the reference case. The hybrid plant achieves between 1.4 and 2.4 percentage points higher electrical efficiency in the presented test cases. This increase in efficiency is due to more efficient use of the flue gas from the gas turbine for preheating instead of preheating via steam extraction.

Smaller gas turbines have also been simulated; due to the lower share of natural gas, the effect on overall efficiency is less significant, but still positive. Simulations with Siemens' smallest turbine SGT-100 (5.1 MW_{el}) showed an increase of 0.5 MW_{el} in the hybrid configuration.

Table 7: Total plant performance including methanol production.

	Methanol Plant [5]	Hybrid plant sgt-400	sgt-600	sgt-800
Input [MW]:				
$Biomass_{LHV}$[1]	342.4	342.4	342.4	342.4
NG	0	36.6	72.5	124.6
Portion of NG [%]	0	8.7	17.5	24.5
Output [MW]:				
$Methanol_{LHV}$	218.6	218.6	218.6	218.6
Electricity[3]	7.8	28.5	48.3	80.5
η_{tot}[2] [%]	66.1	65.2	64.3	64.0

[1]The biomass input data has been recalculated to lower heating value as received, 45% moisture content. The input to the gasifier has a 10% moisture content, total 376.6 MW_{LHV}.
[2]The total efficiency is calculated by dividing the total output (methanol and electricity) with the total input (biomass and natural gas).

The table shows a decrease in total efficiency; which is not unexpected since the biomass to methanol efficiency is greater than the efficiency of power production from natural gas. A more remarkable fact is that the share of fossil fuel (natural gas) is modest even with the largest gas turbine.

5. Discussion

One may argue that natural gas would be used most efficiently, in a large combined cycle plant. However, the efficiency for the natural gas used in this hybrid plant (η_{NG} 56-58%) is in the same range as in modern combine cycle plants and a hybrid plant is therefore a competitive route for both fossil and green fuels.

It is possible that the amount of heat from the methanol plant used in steam cycle has been overestimated. The reference study [5] for methanol production has also estimated the potential for power production, but about 30% less than the reference case in the present paper. The main reason for this rather significant difference is

that higher steam turbine inlet pressure and temperature are used. Another, less substantial difference is the temperature differences used in the pinch analysis. This does not, however, affect the conclusions concerning improved efficiency in the hybrid plant.

Despite the fact that only a fraction of the total energy input is natural gas, taxes and environmental policies can be a problem for hybrid plants. Tax reductions and subsidies are of great importance to achieve an economically feasible production of green energy. Increased costs for fossil fuels and CO_2 emissions may steer the plants to use less fossil fuels in the future. Duct firing of the gas turbine with biomass or syngas could be a very efficient way to increase the proportion of green fuel.

The production of biofuel is not only an environmental question but also a matter of security of supply. Oil reserves are concentrated to a few, often politically unstable, countries. The use of biomass would therefore reduce dependency on oil while at the same time lowering emissions. One drawback is that biofuel cost more than fossil fuel, which makes green replacement alternatives dependent on tax systems.

Today's Swedish tax system and subsidies reward avoided CO_2 emissions from green biofuels in the transportation sector more than green power generation [19]. Hybrid plants are well suited for these rules because of their green fuel production and fossil power generation.

A rule of thumb states that approximately 2/3 of the total investment in a combined cycle plant is for the steam cycle. Therefore, integration of the two plants into a hybrid plant would cut the investment cost. The hybrid plant can also be designed for flexibility so that the methanol plant can be used independently of the steam cycle and vice versa.

6. Conclusions

Simulation of the integration of hybrid cycles in methanol production shows good results. The total electrical efficiency is raised by 1.4-2.4 percentage points, depending on the fuel mix. The case with the largest share of natural gas (61%), showed the largest increased in overall efficiency. Smaller gas turbines have also been simulated; due to the lower share of natural gas, the effect on overall efficiency is less significant, but still positive. The electrical efficiency for the natural gas (η_{NG}) used in the hybrid plant is 56-58%, which is in the same range as in large-scale combined cycle plants.

Nomenclature

P	Power output (MW)
Heat	Heat input (from methanol plant) (MW)

Greek symbols

η	efficiency

Subscripts

CC	Combined Cycle
el	Electrical output (generator output)
GT	Gas Turbine
HHV	Higher Heating Value
LHV	Lower Heating Value
MP	Methanol Plant
NG	Natural Gas
RH	Relative Humidity
ST	Steam Turbine

References

[1] Kahn Ribeiro S., et al. 2007, *Transportation and its Infrastructure*, in Climate Change 2007: Mitigation. Contribution of Working Group III to the Fourth Assessment Report of the Intergovernmental Panel on Climate Change, Cambridge University Press, Cambridge.

[2] Olah G.A., Goeppert A., and G.S. Prakash, 2006, *Beyond Oil and Gas: The Methanol Economy*, WILEY-VCH Verlag GmbH & Co.

[3] Petrov M.P., 2003, Biomass and Natural Gas Hybrid Combined Cycles, KTH Licentiate Thesis, TRITA-KRV-2003-02, Stockholm, Sweden.

[4] Hamelinck C.N. and Faaij A.P.C., 2002, Future prospects for production of methanol and hydrogen from biomass, *Journal of Power Sources*, vol. 111, pp. 1-22.

[5] Katofsky R.E., 1993, The Production of Fluid Fuels From Biomass, Center for Energy and Environmental Studies, Princeton University, Princeton.

[6] Ecotraffic R&D AB and Nykomb Synergetics AB, 1997, Feasibility Phase

Project for Biomass-Derived Alcohols for Automotive and Industrial Uses, Technical Report, ALTENER "BAL-Fuels Project", Stockholm, Sweden.

[7] S. Leduc, J. Lundgren, O. Franklin, and E. Dotzauer, 2009, Location of a biomass based methanol production plant: A dynamic problem in northern Sweden, *Applied Energy*, In Press, Corrected Proof.

[8] Ecotraffic R&D AB and Nykomb Synergetics AB, 2000, Planning of Biomass based Methanol energy combine - Trollhättan region, Technical Report, Final report BioMeet-project.

[9] Larson E.D., Williams R.H., and Leal M.R.L., 2001, "A review of biomass integrated-gasifier/gas turbine combined cycle technology and its application in sugarcane industries, with an analysis for Cuba," *Energy for Sustainable Development*, vol. 5, Mar. pp. 54-76.

[10] Consonni S. and Larson E., 1996, "Biomass-Gasifier/aeroderivative Gas Turbine Combined Cycles: Part A - Technologies and Performance Modeling," Journal of Engineering for Gas Turbines and Power, pp. 507-515.

[11] Chmielniak T. and Sciazko M., 2003 "Co-gasification of biomass and coal for methanol synthesis, *Applied Energy*, vol. 74, pp. 393-403.

[12] Borgwardt R.H., 1997, Biomass and natural gas as co-feedstocks for production of fuel for fuel-cell vehicles, *Biomass and Bioenergy*, vol. 12, pp. 333-345.

[13] Sørensen Å.L., 2005, Economies of Scale in Biomass Gasification Systems, Technical Report, International Institute for Applied System Analysis, Laxenburg, Austria.

[14] Westermark M., 1991, Hybridkraftstationer - teknik, ekonomi and potential, Technical Report, Vattenfall Utveckling AB, Utveckling and Miljö, Älvkarleby, Sweden.

[15] Khartchenko N.V., 1998, *Advanced Energy Systems*, Washington, D.C.: Taylor & Francis.

[16] Franco A. and Giannini N., 2005, "Perspectives for the use of biomass as fuel in combined cycle power plants," *International Journal of Thermal Sciences*, vol. 44, pp. 163-177.

[17] GTPerform, Ver. 2.4 Siemens Turbo Machinery, Finspång, Sweden.

[18] GateCycle, 2008, Ver. 6.0.0.3 SP3, GE Energy, Minden, USA.

[19] Lindfeltd E.G. and Westermark M., 2006, The Swedish policy intriments' inconsistent valuation of avoided CO2 emissions, Florence, Italy.

Acknowledgments: The research has been funded by the Swedish Energy Agency, Siemens Industrial Turbomachinery AB and Volvo Aero Corporation through the Swedish research program TURBO POWER, the support of which is gratefully acknowledged.

Modeling the Thermochemical Conversion of Single Wood particle

Márcio F. Martins[a], Marco A. B. Zanoni[a], Emanuel N. Macêdo[b]

[a] *Federal University of Espírito Santo, LFTC, Vitória(ES),Brazil*
[b] *Federal University of Pará, Belém(PA), Brazil*

Abstract: For the optimal design of different reactors using fuel particles, it is necessary to know the effect of moisture and devolatilization rate on solid fuel. These both rates impact directly on the combustion process. Only the drying and pyrolysis module were presented, which integrate a complete thermochemical conversion code for single particles. One-dimensional and transient conservation equations for mass and energy were assumed and written in spherical coordinates. The thermal equilibrium between phases also was considered. The thermochemical conversions that happen during heating, drying and pyrolysis processes were simplified in two-step reactions. By calculating the Damköhler number, it was verified the overlap of drying and pyrolysis process. An external heat transfer controlling regime is established using Biot number and Thiele modulus. The runs were carried out to simulate thermogravimetry experiments in environment temperature range of 573 – 973 K, and for the particles diameters range of 1 – 20 mm. To validate the model, the results were confronted with those numerical models and experimental data proposed by other authors, having satisfactory accuracy and overall agreement when compared. The developed model takes into account variations in the wood particle by means of thermal, physical and chemical properties. The effects of the environment temperature, particle diameter, and initial moisture on the conversion time were evaluated with success.

Keywords: Drying, pyrolysis, overlap reactions, external heat transfer control.

1. Introduction

The thermochemical conversion process of solid fuel particles have been investigated for decades [1, 2]. Especially on wood particles, a lot of experimental and numerical investigation can be found easily, [1]. This is explained due to a variety of wood species found in all part of the world, also because of the understanding of the governing mechanisms, and rates of wood decomposition process are important for designing wood stoves, furnaces, and boilers, and finally, wood is one of the few renewable source of energy available.

All these experimental data allowed the emergence of numerical models. In all of these models the particle size seems to be a very important parameter. For example, fires in buildings involve large wood slabs. Stoves typically use stick wood and small logs. Furnaces and boilers are designed for sawdust, woodchips, or logs. In terms of labs experiments, [1] classified the small sample as the particles having less than 10 mm tick. About the numerical simulation, the term “large particle” has been employed for the particles having between 8 – 22 mm of diameter

In relation to the thermochemical mechanism, the current models allow a *fine* investigation of its various aspects, such as: - chemical structure (drying, pyrolysis and oxidation reaction), [3-7]; - shrinkage particle effect [8-11]; devolatilization regime (if limited by kinetics or by heat transfer), [2, 3, 12]. Each one of these existing numerical models has its advantages and disadvantages, and none has a clear advantage over the others, since all of them require some kind of simplification.

Initially, drying, pyrolysis and char burn processes were modeled as taking place sequentially, [4, 8]. After a new model to compute simultaneous drying and pyrolysis inside a wood and biomass particle was proposed by [3]. The authors report three situations: - for large particles, drying and pyrolysis overlap greatly in combustion rate of devolatilization. The moisture in the fuel can significantly delay devolatilization and reduce its rate; - there is always a small overlap due to the excess temperature of the start of pyrolysis; and - the overlap is insignificant for small particles, due to the kinetics being slower than heat transfer.

Recently, [6] have made a contribution to the study of the temporal relation between drying and devolatilization - this information is useful when one chooses a model -. The authors investigate the influence of Damköhler number (*Dr*). This number

relates the kinetic rate of devolatilization to the rate of evaporation. If the $Dr < 10^{-1}$, drying and devolatilization can be modeled separately; if the Dr is around unity, a more detailed description is needed; if $Dr > 10^{2}$, drying and devolatilization are coupled, as observed by [3].

Concerning physical structure of a solid particle, the importance of the shrinkage effect has been motivated a few number of investigation.

Not long ago, [6] report that wood typically shrinks by 10 vol. % during drying. In this particular example shrinkage has a very small influence on the final result; it reduces the diameter by less than 4% for a sphere and less than 5% for a cylinder. Reference [10] tested three types model: - Uniform of shrinkage model; - Shrinking shell model; - and Shrinking cylinders model. Regarding their results, the models do not significantly differ from each other.

With respect to the devolatilization regime, in other words, the relative velocity between the temperature and reaction fronts, [2] developed in the decade of the 1980's, a new theory to define the parameters controlling the pyrolysis rate of single particles. The devolatilization regime can be estimated whether pyrolysis is limited kinetically or by heat transfer and as of which diameter heat transfer has to be taken into account, by considering two dimensionless, Thiele modulus (Py) and Biot (Bi) number. The Py modulus gives us a measure of the relative importance of the two internal processes – conduction heat transfer and intrinsic pyrolysis reaction. The Bi number gives us a measure of the relative importance of internal temperature gradients. According to their modeling calculations, if $Py>>1$, the reaction proceeds slowly in comparison to the temperature front. If $Py<<1$, the reaction proceeds virtually instantaneously, and the kinetic expression can be; integrated directly at the temperature in question. For $Bi>>1$, internal heat transfer is relatively slow as compared with external heat transfer, and internal temperature gradients will be significant, For $Bi<<1$, internal heat transfer is rapid and the sample temperature can be assumed essentially uniform. How quickly the sample reaches the temperature of the environment will depend on the heat transfer coefficient.

From the question addressed previously, the follow aims were formulated for the present work:

- Present the module of drying and pyrolysis process for single particles;
- Validate the presented module for a large range of cases, found in the literature;
- Evaluate the main non-dimensionless number and to establish the thermochemical regimes;
- To perform a parametric study to evaluate the impact on the conversion time.

2. Description of model

2.1. Chemical reactions and heat transfer processes

Considering a spherical wood particle initially at the environment temperature, T_0, the particle is suddenly exposed to a stagnant and inert atmosphere at the temperature, T_∞.

For the mathematical formulation, we assume here the validity of the following general assumption:

- one-dimensional and transient problem is assumed;
- the principles of the local average volume are used for the development of conservation equations, [13];
- the porous matrix is formed by two distinct phases - solid and fluid, with a perfect contact between then. Thus, the local thermal equilibrium can be adopted;
- the transport mechanisms in the mass conservation equation are neglected, the changes in time are only due to the reaction terms;
- biomass is considered an isotropic porous material where the porosity (φ) depends on the moisture;
- The radiation within the porous matrix, the effects of viscous dissipation and work done by changes in the pressure field are neglected;
- The effectives specific heat and thermal conductivity of biomass depends on the temperature and moisture fields;
- The effects of mass transport by diffusion of moisture and steam water are neglected in the energy equation;
- It is assumed that heat transfer to the solid from the surrounding gas and furnace is made by a combination of convection and radiation;
- the temperature of the gas phase is assumed constant and equal to the furnace wall temperature, T_∞.

Taking a differential control volume, energy and material balances are easily derived; the energy balance becomes:

$$\rho_W C_{P_W}(T)\frac{\partial T}{\partial t} = \frac{1}{r^2}\frac{\partial}{\partial r}\left[r^2\lambda(T)\frac{\partial T}{\partial r}\right] + Q \qquad (1)$$

$$at \ \{0 < r < R_0 \ \ and \ \ t > 0,$$

where ρ, Cp and λ are the solid density, the temperature dependent specific heat capacity and effective thermal conductivity, respectively. T is the local temperature and r is the radial position. Q compute the apparent enthalpy change associated with the set of reactions and physical changes, Table 1.

The pyrolysis reactions are complex and involve both endothermic and exothermic processes. Most solids fuels are chemically and physically heterogeneous and their components have different reactivities and products [11, 14, 15]. Despite this complexity, it should be possible to use simplified models. The most commonly simple model used to describe the chemical kinetics of pyrolysis is the single-step Arrhenius equation, Fig. 1. The process of drying was described by a heterogeneous reaction between liquid water and vapor, [16].

$$H_2O_{(l)} \rightarrow H_2O_{(g)} \qquad \Delta H_e$$

$$wood \rightarrow char + volatiles \qquad \Delta H_p$$

Fig. 1. Reaction scheme for wood decomposition.

Consequently the reaction kinetics is given by (2) and (3).

$$\frac{\partial W}{\partial t} = -\frac{r_e}{\rho_{S0}} \qquad (2)$$

$$\frac{\partial \rho_s}{\partial t} = -r_p \qquad (3)$$

$$at \ \{0 < r < R_0 \ \ and \ \ t > 0,$$

where, the rates of weight loss per unit volume due to evaporation and pyrolysis are represented by $\partial w/\partial t$ and $\partial \rho/\partial t$, respectively, and r_e and r_p are the evaporation and pyrolysis conversion rates, it is assumed to follow first order kinetics, given by (4) and (5):

$$r_e = (\rho_w - \rho_s)A_e Exp\left(-\frac{E_e}{R_g T}\right) \qquad (4)$$

$$r_p = (\rho_s - \rho_c)A_p Exp\left(-\frac{E_p}{R_g T}\right) \qquad (5)$$

with A and E as the apparent kinetic parameters and R as the ideal gas constant. ρ is the density. A constant value for the final char density is assumed. According to [17], density and particle porosity, φ, can be determined as function of the density (S_g) and moisture content (W) by:

$$\rho_W = \rho_s(1+W); \qquad \rho_s = \rho_{H_2O} S_g \qquad (6)$$

$$\varphi = 1 - (0.667 + W)\ S_g \qquad (7)$$

2.2. Initial and boundary conditions

The boundary conditions are assumed that heat transfer to the solid from the surrounding gas and furnace is by a combination of convection and radiation; the temperature of the gas phase is assumed constant and equal to the furnace wall temperature. Thus, at the solid surface (r = R):

$$r = R \ \rightarrow \ k\frac{\partial T}{\partial r} = F(T) \qquad (8)$$

where $F(T)$ compute the heat transfer combination of convection and radiation, Table 1.

Assuming symmetry with respect to the axis of the solid:

$$r = 0 \ \rightarrow \ \frac{\partial T}{\partial r} = 0 \qquad (9)$$

Thus, (10) and (11) form the boundary conditions for (12), (13) and (14). The initial conditions follow from the assumption that at time zero the solid has uniform temperature, T_0, the initial density ρ_0, and the initial moisture content w_0, thus,

$$t = 0 \quad to \quad \begin{cases} T = T_0 \\ W = W_0 \\ \rho_s = \rho_{H_2O} S_g = \rho_{s0} \end{cases} \qquad (15)$$

Table 1 presents the sub-models and data required for heat transfer.

Table 1. List of sub-models used in calculations

Heat transfer	Unit	Ref.
$Q = -[\varphi r_e \Delta H_e + (1-\varphi) r_p \Delta H_p]$	J m^3 s^{-1}	-
$F(T) = h(T_\infty - T) + \varepsilon\sigma(T_\infty^4 - T^4)$	W m^{-2}	-

$A = (0.2 + 0.404W)S + 0.238$	-	[18]
$\lambda = A(0.002T + 0.40368)$	W m^{-1} K^{-1}	[18]
$Cp = \left(\frac{B + 4.19W}{1+W} + C\right)1000$	J kg^{-1} K^{-1}	[18]
$B = 0.1031 + 0.003867T$		[18]
$C = (0.02355T^{-1.32}W^{-6.191})W$		[18]

Note. [10, 12]: σ= 5.67 x 10^{-8} (W m^{-2} K^{-4}) and ε = 0.9, h = 5.0 (W m^{-2} K).

2.3. Dimensionless groups

The set of equations (1-8) can be converted in the dimensionless form by using the following dimensionless quantities:

$$\eta = \frac{r}{R_0}; \phi = \frac{W}{W_0}; \theta = \frac{T}{T_\infty}; Z_0 = \frac{\rho_{W_0}}{\rho_{S0}};$$

$$X = \frac{\rho_s}{\rho_{S0}}; X_c = \frac{\rho_c}{\rho_{S0}}; \tau = \frac{\alpha\, t}{R_0^2};$$

$$\alpha = \frac{\lambda}{\rho_s C_p}; \gamma = \frac{C_p}{C_{p0}}; \beta = \frac{\rho_s}{\rho_{W_0}};$$

$$\vartheta = \beta\, \gamma\ ; \Omega = \frac{Q R_0^2}{\lambda\, T}; \Gamma = \frac{R_0 F(T)}{\lambda\, T};$$

$$\xi = \frac{\varepsilon\, \sigma\, R_0 T_\infty^3}{\lambda}; Bi = \frac{h R_0}{\lambda}; A_e^* = \frac{A_e R_0^2}{\alpha\, W_0}; \qquad (16)$$

$$A_p^* = \frac{A_p R_0^2}{\alpha}; E_e^* = \frac{E_e}{R_g T}; \Delta H_e^* = \frac{\rho_{S0}\alpha\, W_0 \Delta H_e}{\lambda\, T};$$

$$\Delta H_p^* = \frac{\rho_{S0}\alpha\, \Delta H_p}{\lambda\, T}; Dr = \frac{R_p}{R_e};$$

$$R_p = \left(X - X_c\right) A_p^* Exp(-E_p^* / \theta);$$

$$R_e = \left(Z_0 \beta - X\right) A_e^* Exp(-E_e^* / \theta);$$

$$\Gamma(\theta) = Bi\left(1 - \theta\right) + \varphi\left(1 - \theta^4\right) + Q_{rad};$$

$$\Omega = -[\varphi\, R_e \Delta H_e^* + \left(1 - \varphi\right) R_p \Delta H_p^*].$$

Consequently, the differential system equation and its respective initial and boundary conditions become:

$$\begin{cases} \vartheta \dfrac{\partial \theta}{\partial \tau} = \dfrac{\partial}{\partial \eta}\left[\lambda \dfrac{\partial \theta}{\partial \eta}\right] + \dfrac{2}{\eta}\lambda \dfrac{\partial \theta}{\partial \eta} + \Omega \\ \dfrac{\partial \phi}{\partial \tau} = -R_e\ ,\ \dfrac{\partial X}{\partial \tau} = -R_p \end{cases} \qquad (17)$$

$$\begin{cases} \theta = \theta_0 \\ \phi = 1 \qquad \text{at } 0 < \eta < 1,\ \tau = 0 \\ X = 1 \end{cases} \qquad (18)$$

$$\begin{cases} \dfrac{\partial \theta}{\partial \eta} = 0 \qquad \text{at } \eta = 0,\ 0 < \tau \le \tau_0 \\ \lambda \dfrac{\partial \theta}{\partial \eta} = \Gamma(\theta) \qquad \text{at } \eta = 1,\ 0 < \tau \le \tau_0 \end{cases} \qquad (19)$$

2.4. Numerical integration

The conservation equations for the solid domain are solved using second-order accurate finite differencing. The differenced equations developed were implemented in a Fortran-based computer code. In this code was used the subroutine IVPAG from the Fortran IMSL library to solve the system of ODE's, [19]. The number of grid points was chosen to provide good spatial resolution of the steep temperature, moisture and wood density profiles found. The time step was chosen to ensure stability and accuracy of the solution. The time step order was between 0.0125 and 0.05s. The convergence tolerance used was 10^{-4}. The values and correlations used for the physical parameters are presented in Table 2.

3. Results

3.1. Model validation

The model is validated against the numerical models of [12], [7] and [10]. Pyrolysis model are discussed using fuel properties and thermokinetic constants summarized in Table 2.

The biggest uncertainty is related to the coefficients of the pyrolysis model given in the literature. The values of the pre-exponential factor and the activation energy adopted are close to those used by the references cited above. Each one of these authors use a set of heat transfer parameters indicated in the Table 1 footnote.

The code was validated for variations on the particles diameter, moisture content, and the impact for not considering the shrinkage of the particles. Figures 2-4 show the evolution of the

normalized mass loss of particles for every one of these respective variations.

Table 2: Fuel property values and thermokinetic constants.

Property	I. [12]	II. [7]	III [10]
W	33.%	11. – 47. %	0. %
ρ_c (Kg m^{-3})	95.0	147.0	-
S_g (Kg m^{-3})	450.0	650.0	530.0
T_0 (K)	300.0	-	293.15
ΔHp (KJ Kg^{-1})	- 4500	430.	-
ΔHe (KJ Kg^{-1})	2.268	-	-
Ee (KJ Mol^{-1})	24.0	48.22	-
Ep (KJ Mol^{-1})	123.1	137.0	-
Ae (s^{-1})	1.026 x 10^{10}	6.0x10^{5}	-
Ap (s^{-1})	1.35 x 10^{9}	3.5x10^{10}	-

In Fig. 2 is presented mass evolution for different particles diameter. Using configuration I (Table 2) and fixing the temperature T_∞ at 743 K, the developed code in general presented a quite good agreement when compared to simulations of [12] that investigated, among others, the effect of size particles variations on drying and pyrolysis processes.

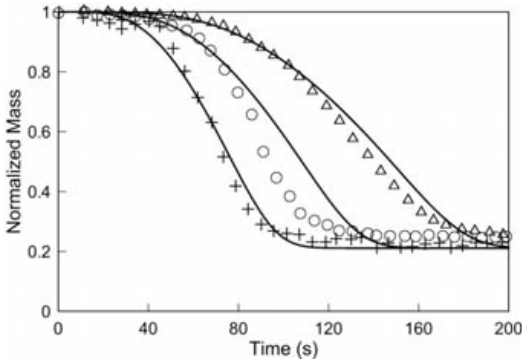

Fig. 2. Solid mass fraction as functions of time as predicted for particle diameter exposed a T_∞ = 743 K. 8mm (+), 12mm (○) and 17mm (Δ) – numerical results reported in [12].Present work simulations, solid line (—).

Concerning the variations of the moisture content in the particle, Fig. 3, the model simulations presented a good agreement with numerical results reported by [5] and [7], at both W values considered, 11 and 47%. For this case, model configuration II was used. The cited works considered wood cylinders of radius 0.02 m submitted to an external heat flux of 49 kW m^{-2}.

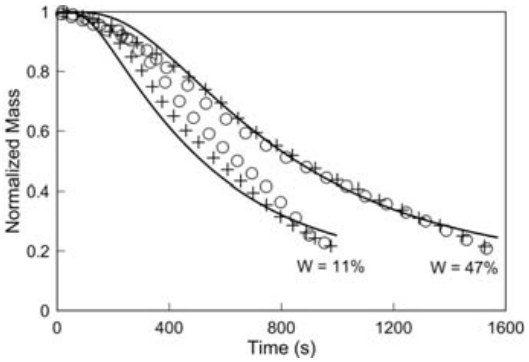

Fig. 3. Solid mass fraction as functions of time as predicted for moisture content of 11% and 47%. Numerical results reported by in [5], (○), and by [7], (+). Present work simulations (—).

The last confrontation was to know if not considering the shrinkage effect of the particle would result in major uncertainty to the model. In this time, the model was run with the configuration III. In [10] are considered two first order reactions, wood → char, and wood → volatiles. Thus, one use the set of Arrhenius parameters adopted by [12] that is equivalent to our reaction scheme, Fig. 1. Figure 4 presents the confrontation of the present model against both the numerical and experimental results of shrinkage undergone by dried particle reported by [10]. At a T_∞ = 873 K, one can see that even that exist a strong volume change, the mass loss is unaffected by the particle shrinkage. Accordingly, the present model shows a quite good agreement.

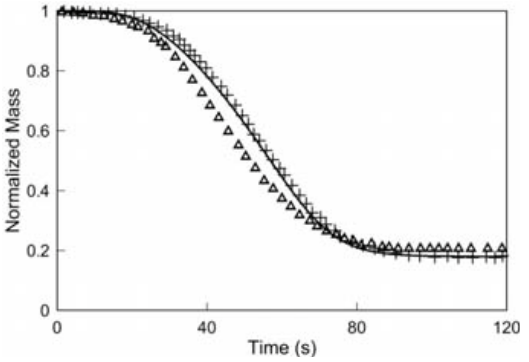

Fig. 4. Solid mass fraction as functions of time. Uniform shrinkage model data reported in [10], (+), as well their experimental results, (Δ). Present work simulation, (—).

3.2. Non-dimensionless number significance

The degree of separation of drying and devolatilization within a fuel particle can be defined whether plotting the conversion rates versus time, Fig. 5, or calculating a *Dr* number that relates the kinetic rate of devolatilization to the rate of evaporation. For the presented model, high values of *Dr* were verified more than 500 meaning an overlap of the processes, [6]. The values of *Dr* were found running all configuration presented at the Table 2, with particles diameter between 10^{-2} and 10^{-3} *m* and T_∞ = 873 K. The main observations are showed in Fig. 5. It was verified that increasing T_∞ increases reaction rates and decreasing the time of conversion. It can also be observed that decreasing in particles diameter leads to total overlap of the processes.

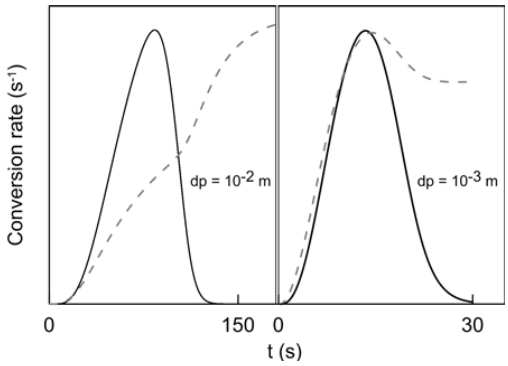

Fig. 5. Characteristic conversion behaviour at high Dr number. The rate of devolatilization (solid line) and the evaporation rate of moisture (dashed line).

Another important parameter in the analysis is the Biot number, *Bi*, which indicates whether internal or external heat transfer controls the process. The relative importance of internal heat transfer can also be found by means of *Py* modulus that gives us the comparison between reaction and temperature fronts velocities. For particle diameter range of 10^{-1} to 10^{-4} m, *Bi* values of 0.7 and 10^{-4} were found. Concerning the *Py* modulus, values about 10^{-3} were found for the referred particle range. According to [2] small values of the *Bi* meaning that internal heat transfer is rapid and the temperature of the particle can be assumed essentially uniform. This information can be established plotting the temperature profile in the particle, Fig. 6. In agreement with [3], the verification of the heat transfer control requires the simultaneous measurement of density and temperature at a point inside a piece of wood. In the Fig. 6, it can be seen that as smaller the particle diameter, the internal temperature gradient becomes not significant. In relation to the small values of *Py* modulus, it means that the reaction occurs virtually instantaneously. As a result of the analysis of these numbers, the process regime cannot be considered controlled by internal heat transfer or kinetics. Thus, the appropriate measure to the control regime is called, external Thiele modulus, *Py**, defined by the product *Bi.Py*. Small values of *Py** correspond to a regime controlled by external heat transfer, [5, 6].

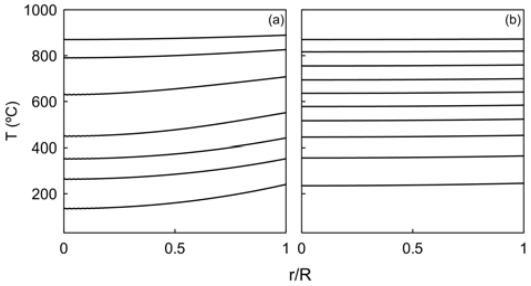

Fig. 6. Temperature profiles inside a 10^{-2} m (a) and 10^{-3} m (b) particle diameters.

3.3. Further discussions

Since the presented model to simulate the pyrolysis of the fuel particles occurs in the external heat transfer regime, it is important to know: what is the impact of the variation in the main parameters on conversion time? It was chosen three parameters for this evaluation: - initial moisture content at 30% and 50%; - environment temperature at 573K and 873K; and finally, - particles diameter between 1mm and 20mm. The results are summarized in the Fig. 7. It was observed that fixing the particle diameter and temperature, and varying the content of the initial moisture, this can significantly delay the conversion time for the large particle, due to reduction in the devolatilization rate. This is also observed earlier by [3]. Increasing the environment temperature, decreases the conversion time of about 1.27 times for all particles diameter and initial moisture content studied. Finally, it was verified that increasing the particle diameter in the range of 1mm to 20mm, increases in 7.25 times the conversion time.

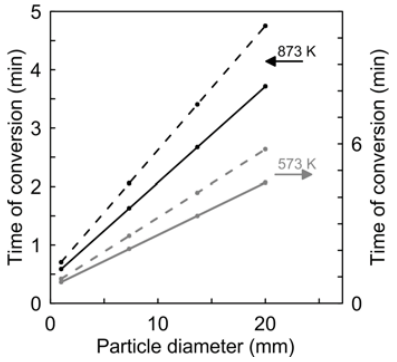

Fig. 7. Time to reach the final process of drying and pyrolysis as function of the particle diameter, for T∞ at 573K, gray line (—), and 873 K, black line(—) with initial moisture content of 30%, dashed line, and 50%, solid line.

3.3. Conclusion

A flexible and stable 1D numerical method to predict thermal decomposition of fuel particles was developed with success. This is an external heat transfer controlling numerical model. It was tested changes on the input conditions as particles diameter, environment temperature, radiative flux, physical properties and sub-models for heat transfer, not causing significant disturbances in the runs. The model is applicable for dry or moist fuel particles which are porous and contains volatile matter and fixed carbon in its composition.

The model was validated face a three different models data found in the literature and showing a quite good agreement. Because it is an external heat transfer controlling regime, high values of Biot number and small values of external Thiele modulus, were found. For this type of regime the internal temperature gradient becomes not significant and the temperature can be assumed as uniform inside the particle.

The overlap of the drying and pyrolysis process was established by means of Damköhler number. It also was observed that decreasing in particles diameter leads to total overlap of the processes.

A parametric study was performed to verify the impact of variations of particles diameter, initial moisture content and environment temperature on the conversion time. Increasing the environment temperature decreases the conversion time of about 1.27 times, and increasing the particle diameter increases in 7.25 times the conversion time.

Finally, the current results found are been used to feed the combustion module, that incorporate a more realistic reaction mechanism for a variety of solid fuel (including bituminous ones).

Nomenclature

A_j	pre-exponential factor of Arrhenius (s^{-1})
b	blowing parameter
C_p	specific heat of biomass (J kg^{-1} K^{-1})
E_j	activation energy (J mol^{-1})
h	convective heat transfer (J m^{-2} s K)
m	mass
q	heat transfer (W m^{-2})
Q	source term (W m^{-2} K^{-1})
r_j	rate of water evaporation or devolatilization
R_g	universal gas constant (J mol^{-1} K^{-1})
R_0	initial radius (m)
S_g	specific gravity
t	time (s)
T	temperature (K)
W	Moisture wood

Main non-dimensionless number

Bi	Biot number
Dr	Damköhler number
Py	Thiele Modulus
$Py*$	External Thiele Modulus

Greek letters

ΔH_j	reaction enthalpy (J kg^{-1})
ε	emissivity
φ	porosity
σ	Stefan-Boltzmann constant
λ	thermal conductivity (W m^{-1} K^{-1})
μ	viscosity (N s m^{-2})
ρ	density (kg m^{-3})

Subscripts

0	initial
c	coal
g	gas
j	components (e, p)

e	evaporation
p	pyrolysis
rad	radiation
s	dry biomass

References

1. Roberts, A.F., *A review of kinetics data for the pyrolysis of wood and related substances*. Combustion and Flame, 1970. **14**(2): p. 261-272.
2. Pyle, D.L. and C.A. Zaror, *Heat transfer and kinetics in the low temperature pyrolysis of solids*. Chemical Engineering Science, 1984. **39**(1): p. 147-158.
3. Saastamoinen, J. and J.-R. Richard, *Simultaneous drying and pyrolysis of solid fuel particles*. Combustion and Flame, 1996. **106**(3): p. 288-300.
4. Macêdo, E.N., R.M. Cotta, and H.R.B. Orlande, *A solution via generalised intergral transform technique for the simultaneous transport processes during combustion of wood cylinders*. International Journal for Numerical Methods in Engineering, 2000. **49**(11): p. 1455-1477.
5. Galgano, A. and C. Di Blasi, *Modeling the propagation of drying and decomposition fronts in wood*. Combustion and Flame, 2004. **139**(1-2): p. 16-27.
6. Thunman, H., K. Davidsson, and B. Leckner, *Separation of drying and devolatilization during conversion of solid fuels*. Combustion and Flame, 2004. **137**(1-2): p. 242-250.
7. Benkoussas, B., et al., *Modelling thermal degradation of woody fuel particles*. International Journal of Thermal Sciences, 2007. **46**(4): p. 319-327.
8. Ouedraogo, A., J.C. Mulligan, and J.G. Cleland, *A Quasi-steady Shrinking Core Analysis of Wood Combustion*. Combustion and Flame, 1998. **114**(1-2): p. 1-12.
9. Babu, B.V. and A.S. Chaurasia, *Heat transfer and kinetics in the pyrolysis of shrinking biomass particle*. Chemical Engineering Science, 2004. **59**(10): p. 1999-2012.
10. Bellais, M., et al., *Pyrolysis of large wood particles: a study of shrinkage importance in simulations[small star, filled]*. Fuel, 2003. **82**(12): p. 1541-1548.
11. Di Blasi, C., *Heat, momentum and mass transport through a shrinking biomass particle exposed to thermal radiation*. Chemical Engineering Science, 1996. **51**(7): p. 1121-1132.
12. Peters, B. and C. Bruch, *Drying and pyrolysis of wood particles: experiments and simulation*. Journal of Analytical and Applied Pyrolysis, 2003. **70**(2): p. 233-250.
13. Whitaker, S., *Simultaneous Heat, Mass, and Momentum Transfer in Porous Media: A Theory of Drying*, in *Advances in Heat Transfer*, P.H. James and Thomas F. Irvine, Jr., Editors. 1977, Elsevier. p. 119-203.
14. Villermaux, J., et al., *A new model for thermal volatilization of solid particles undergoing fast pyrolysis*. Chemical Engineering Science, 1986. **41**(1): p. 151-157.
15. Larfeldt, J., B. Leckner, and M.C. Melaaen, *Modelling and measurements of heat transfer in charcoal from pyrolysis of large wood particles*. Biomass and Bioenergy, 2000. **18**(6): p. 507-514.
16. Chan, W.-C.R., M. Kelbon, and B.B. Krieger, *Modelling and experimental verification of physical and chemical processes during pyrolysis of a large biomass particle*. Fuel, 1985. **64**(11): p. 1505-1513.
17. Siau, J.S., ed. *Transport processes in wood*. Springer series in wood science. 1974, T. E. Timell, Ed. p. 1-34.
18. Borman, G.L., Ragland, K. W. , *Combustion Engineering*. 1998, McGraw-Hill Science/Engineering/Math, 1 Ed.
19. [Anon], *Visual numerics news: IMSL Fortran 90 Library ported to Red Hat Linux*. Computational Statistics & Data Analysis, 2001. **35**(4): p. 503-503.

Fuel-Assisted Solar Thermal Power Plant with supercritical ORC cycle

Fiaschi Daniele [a], Lifshitz Adi[a] , Manfrina Giampaolo [a]

[a] Università degli Studi di Firenze, Dipartimento di Energetica "Sergio Stecco"
Via C. Lombroso 6/17 – 50135 Firenze - Italy

Abstract: In this paper, a 100 kWe reference size solar thermal power plant is considered, having the following features:
- Use of parabolic trough solar collectors with 1-degree of freedom solar tracking
- Double circuit with a liquid heat transfer fluid, connecting the solar field to a supercritical organic vapour generator
- No heat storage; the unavailability of radiation is met by external firing with a suitable fuel, limiting as far as possible the use of this last
- Supercritical ORC system with regenerator, using different possible organic fluids

The operation of the system is considered over the year; the design conditions are assumed at a radiation level I = 700 W/m^2. For lower radiation conditions, external firing is switched on, and the ORC system is operated anyway under design conditions. When radiation is larger, the ORC is operated under off-design conditions, with increased flow rate.
The results confirm that, with a careful choice of the design conditions (type of fluid, pressure, heat exchanger optimization,...) a good performance can be achieved with limited external fuel integration; the performance of the system does not suffer extensively from operation under off-design. An exergy analysis is included examining the contributions of component exergy destructions and system exergy losses over typical daily operations.

Keywords: Solar thermal Energy Conversion, Organic Rankine Cycles, Supercritical, Off-design.

1. Introduction

Solar thermal power plants are an interesting option for power generation from renewables, and can be competitive with photovoltaic energy conversion systems.

The attractiveness of solar thermal power plants is documented by the technical literature, by the operability demonstrated by the first large-scale pilot plants, and by the existence of extensive projects in the near future [1, 2, 3]. As an alternative to building very large solar thermal power plants, equipped with large heat storage systems (e.g. molten salts), a smaller size installation (100 kWe nominal) is proposed, capable of following the availability of solar radiation; when necessary (for low radiation values) the plant is supported by external firing through an auxiliary heater, which substitutes the expensive and inefficient heat storage system. The small-size power plant can be switched off during the night. The typical application considered is for Middle-East desert locations or African Mediterranean countries, which often have considerable land availability as well as favorable radiation conditions.

2. General layout

Figure 1 shows the general layout of the power plant. A typical solar energy generating system (SEGS) arrangement is considered, which has demonstrated durability and availability in large-scale applications [3, 4, 5].

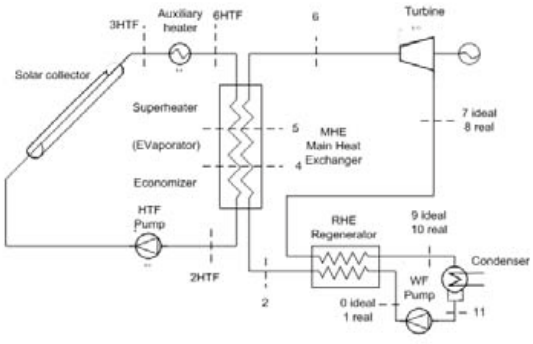

Fig. 1. Solar Thermal Power Plant Layout

The plant uses a dual circuit: in the solar field (primary circuit), a high-temperature oil is used as heat transfer fluid HTF [7]; the main heat exchanger MHE links the primary and the secondary circuit. In the latter, an organic vapor is used in place of steam. This choice allows to use reasonable pressures and size of equipment (turbine, condenser) for a small power plant. As many organic fluids have a limit curve with negative slope, the secondary circuit includes a regenerator RHE, which improves cycle performance and reduces the cooling load at the condenser. The primary circuit includes an auxiliary heater: this is fed using a conventional fuel (natural gas or oil, depending on local availability).

3. Selection of the Working Fluid

The correct selection of the organic working fluid (WF) to be used in the secondary circuit represents a key issue in low-temperature thermal energy conversion processes [6]. The desired features are:

- The WF should be capable of long-term operation at the design temperature level, which is imposed by current SEGS solar collector technology; it must be safe and compatible with materials used within the power plant
- The WF should be operated at reasonable pressure conditions both at steam generator and condenser
- The possibility of building the plant with a supercritical vapor generator is interesting, because it allows an improved matching of heat capacities between the primary and secondary circuit, in comparison with sub-critical vapor cycles.

The main system parameters are :

- The Heat Transfer Fluid's (HTF) maximum temperature is set to T_{M_HTF} = 390 °C (Therminol VP-1; base pressure in the primary circuit p_{HTF} = 1500 kPa; specific heat is c_{pHTF} = 2,32 kJ/(kgK)).
- The temperature at the condenser is set to T_{11} = 35 °C.
- The reference values for ambient temperature and direct irradiation were set at T_{amb} = 25 °C and I_b = 700 W/m² .
- The temperature differences at the MHE hot end DT_{HE} and at the entrance to the evaporator DT_{EE} (in case of sub-critical cycle) were set at 20 °C. In the super-critical case the temperature difference was set at 20°C at the same point (where the critical temperature is reached).
- The RHE effectiveness was set at ε = 0,8 (ε = 0,9 in alternative).
- The pump and turbine isentropic efficiencies were set to η_T = 0,85 ; η_P = 0,85 .

The difference between a sub-critical and a super-critical cycle is shown in Figure 2. In the specific case here considered (Toluene), it is clear that the imposition of a maximum value T_6 = 370 °C for the WF temperature determines exit from the turbine (point 8) in highly-superheated conditions. As the critical pressure for Toluene is 4126 kPa, p_0 = 5000 kPa was chosen for the supercritical cycle.

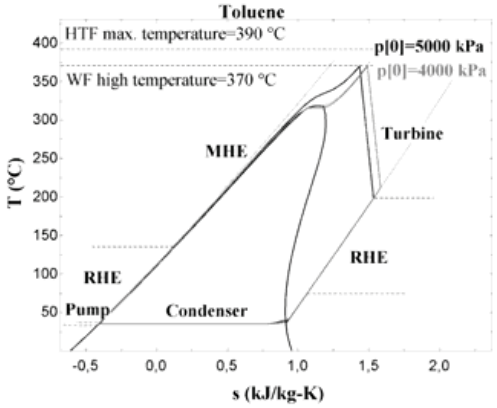

Fig. 2. Example of subcritical and supercritical cycles

The working fluids considered are resumed in Tables 1 and 2.

Table 1. Cycle parameters for different WFs.

Working Fluid	p_0 kPa		DT_{CE} °C	m_{WF} kg/s	m_{HTF} kg/s
Toluene	5000	A	103	0,40	0,81
Cyclohexane	6500	A	53	0,41	0,71
n-dodecane	1000	B	107	0,4	1,44
Ethanol	8000	A	68	0,21	0,51
n-heptane	6000	A	36	0,42	0,70
Ammonia	26000	A	24	0,18	0,422
Steam	1700	B	137	0,09	0,57

A = Supercritical B = Subcritical

The values of η_{TS} reported in Table 2 were determined after a search for possible maximum

efficiency conditions with variable cycle pressure p_0. The trend of η_c in function of p_0 is shown in Figure 3. Results shown in Table 2 and in Figure 3 indicate that a supercritical cycle using Toluene is the most recommendable choice under the considered technical constraints. It is also interesting to notice that Toluene implies a reasonable size of the RHE (with a heat duty limited to 77 kW, much smaller than for other WFs here considered).

Table 2. Cycle performance for different WFs (ε = 0,8)

Working fluid	Q_{MHE} kW	Q_{RHE} kW	Q_C kW	W kW	p_0 MPa	η_{TS}
Toluene	282	77	184	98	5	0,247
Cyclo-hexane	283	116	187	96	6,5	0,242
n-dodecane	278	167	184	94	1	0,237
Ethanol	287	24	196	91	8	0,230
n-heptane	284	153	191	92	6	0,234
Ammonia	289	22	207	82	26	0,207
Steam	286	0	206	80	1,7	0,202

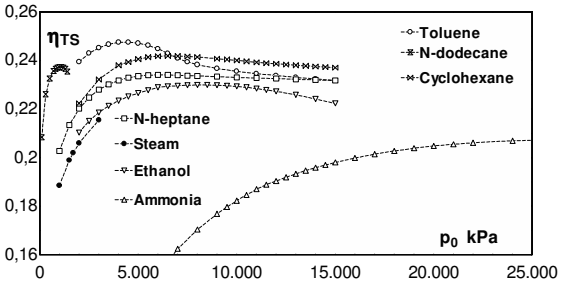

Fig. 3. Calculated cycle performance for different WFs; sensitivity to pressure conditions (p_0)

The performance of the ORC system is very sensitive to the efficiency of the regenerator. In fact, the RHE heat duties are significant as the end of expansion is well inside the superheated region. The effect of improving ε = 0,9 is shown in Table 3.

3. Subcritical vs. supercritical

The advantage of considering a supercritical organic cycle is clear when considering the heat transfer diagram of the MHE. In the subcritical case (Figure 4), it is impossible to improve matching of heat capacities on the hot and cold sides of the MHE: in fact, at least in the evaporator the heat capacity goes to infinity ($c_{p\ WF} = \infty$ with finite flow rate). This determines an uneven temperature profile, with a pinch condition at the end of economizer section (EE), and larger values of DT_{CE} (Table 1); this determines a lower efficiency of the MHE for equal NTU (or surface).

Table 3. Cycle performance for different WFs (ε = 0,9)

Working fluid (*)	Q_{MHE} kW	Q_{RHE} kW	Q_C kW	W kW	p_0 MPa	η_{TS}
Toluene	282	98	180	102	4	0,257
Toluene	282	90	180	101	5	0,256
Cyclohexane	282	145	181	101	5,5	0,255
Cyclohexane	283	137	182	101	6,5	0,255
n-dodecane	278	203	176	102	1	0,256
n-heptane	283	184	183	99	6	0,250

(*) with respect to Table 2, Ammonia and Ethanol were not considered because of the very low regenerated heat.

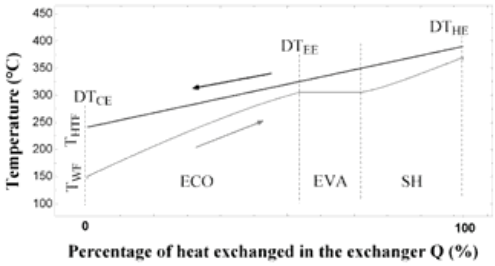

Fig. 4. Heat Transfer diagram of MHE; subcritical case (Toluene, p_0=350 0kPa)

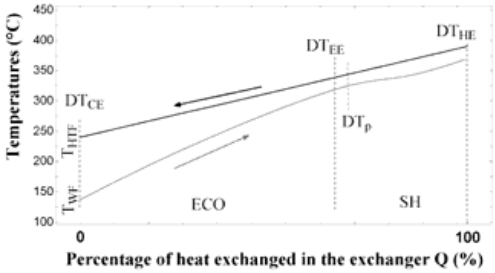

Fig. 5. Heat Transfer diagram of MHE; supercritical case (Toluene)

The situation is much improved in supercritical conditions (Figure 5). In this case, the WF heat capacity varies gradually with temperature, so that

a better matching of the heat transfer curve can be obtained (and consequently, lower values of DT_{CE} result – Table 1). Figure 5 also shows that the pinch condition is not necessarily located at the EE point.

4. Off-design Operation

When radiation is different from the reference conditions (I_b = 700 W/m^2), the system is operating in off-design. In order to limit the deterioration of performance, without recurring to complex heat storage devices, whose transient performance is penalizing, the following guidelines were followed:

A. when radiation I_b < 700 W/m^2, the auxiliary burner is switched on, reaching anyway T_{M_HTF}= 390°C; the design flow rate is circulated both in the primary and secondary circuits. Only the solar collector is operating in off-design. The system operates in a fuel-assisted mode (a Solar Fraction SF is defined)

B. when radiation I_b > 700 W/m^2, the auxiliary burner is off; the condition T_{M_HTF}= 390°C is not exceeded as the flow rate is augmented both in the primary and secondary circuits. Pressure and temperature conditions are not changed. The whole system is operated in off-(over-) design. The performance level is affected, but extra power is produced.

4. 1. Solar collector off-design

The collector performance is modeled through its thermal efficiency curve [5]

$$\eta_{coll} = 0,745 - 0,0065 \cdot X - 0,000339 \cdot I \cdot X^2 \quad (1)$$

Where:

$$X = \frac{T_{abs} - T_{amb}}{I_b} \quad (2)$$

$$T_{abs} = \frac{T_{2HTF} + T_{3HTF}}{2} \quad (3)$$

The collectors are placed horizontally on the ground, with a daily East-West tracking system operating at a nominal rate of 15 degrees per hour.

4. 2. Low-radiation system off-design

Figure 6 summarizes the off-design performance of the collector and the reflected effects on the overall system performance, for case (A), I_b < 700 W/m^2; it can be seen that η_{Coll} is affected by low radiation conditions; the efficiency of the auxiliary heater was assumed constant at η_{aux} = 0,9.

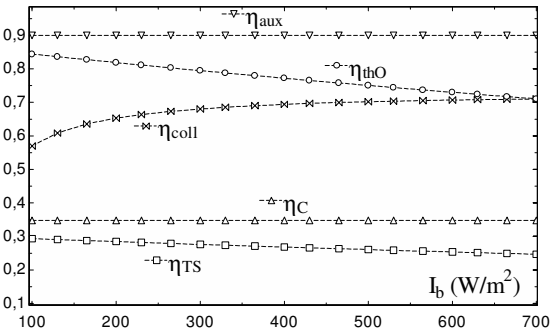

Fig. 6. System efficiencies with variable radiation (I_b < 700 W/m^2)

The overall thermal (collector/auxiliary heater/MHE) system efficiency is defined as the ratio of the heat transferred to the WF in the MHE, divided by the overall heat input to the system:

$$\eta_{thO} = \frac{Q_{MHE}}{Q_{aux} + \frac{A_u \cdot I_b}{1000}} \quad (4)$$

η_{thO} decreases with increasing radiation: in fact, η_{aux} = 0,9 is always much larger than η_{coll}, so that from a purely energetic point of view it is preferable to operate the system on fuel rather than on solar radiation. The power cycle in case (A) is the same as in the 'design' state (pressure, temperature and flow rates in the secondary circuit), and so the power cycle efficiency remains constant for I< 700 W/m^2.

The total system efficiency η_{TS} is the product of the Overall Thermal efficiency η_{thO} and of the conversion efficiency η_c, and so it decreases with increasing radiation and increasing external firing.

4. 3. High-radiation system off-design

When I_b > 700 W/m^2, the auxiliary heater is switched off; the heat transferred in the MHE is equal to that captured by the collector; therefore η_{thO} is equal to η_{coll} - which depends on radiation according to Eqs. 1-3.

The control law for flow rate (primary circuit) maintains the HTF temperature at the outlet of the solar field to its maximum value, T_{M_HTF}= 390°C; the approach value at the hot end of the heat exchanger DT_{HE} was maintained at 20 °C; the WF temperature at turbine inlet is then fixed at T_6 = 370 ºC, and the flow rate in the secondary circuit is consequently adjusted. In order to do that, it is necessary to re-evaluate the performance of heat exchangers (MHE and RHE) under the new, off-design condition with increased flow rates.

The heat balance of the heat exchanger [1] is resumed by the following equations:

$$Q_{MHE} = m_{HTF} \cdot c_{pHTF} \cdot (T_{3HTF} - T_{2HTF}) = m_{WF} \cdot (h_6 - h_2) \quad (5)$$

$$Q_{MHE} = U \cdot A \cdot DT_{LM} \quad (6)$$

$$DT_{LM} = \frac{(T_{3HTF} - T_6) - (T_{2HTF} - T_2)}{\ln \frac{(T_{3HTF} - T_6)}{(T_{2HTF} - T_2)}} \quad (7)$$

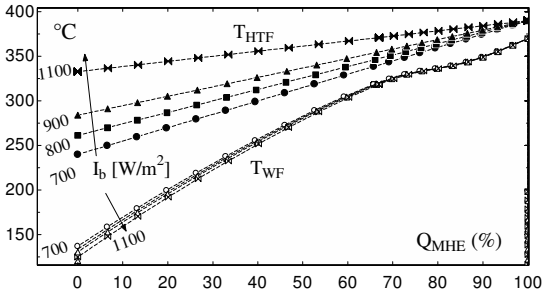

Fig. 7. MHE heat transfer diagram at off-design (I_b > 700 W/m²)

As a first approximation, a constant global heat transfer coefficient U was assumed. This assumption is precautionary since actually U increases as the mass flow rate increases [8]. As A is fixed, the increase in Q_{MHE} is thus directly reflected by an increase in DT_{LM}; as the temperature conditions on the cold side (WF; T_6, T_2) are not changed[2] as well as the condition at collector outlet (T_{3HTF}), this is obtained decreasing the value of T_{2HTF}; in turn, this affects the collector performance (Equation 3); an NTU-ε correlation method (counter-flow heat exchanger) was used to close the system of equations (MHE and RHE) at off-design. The resulting increase in the temperature difference at the cold end is shown in Figure 7.

4. 4. Generalized system off-design

Considering operation over the full range of radiation, the relevant circuit temperatures are shown in Figure 8, and the flow rate values in Figure 9.

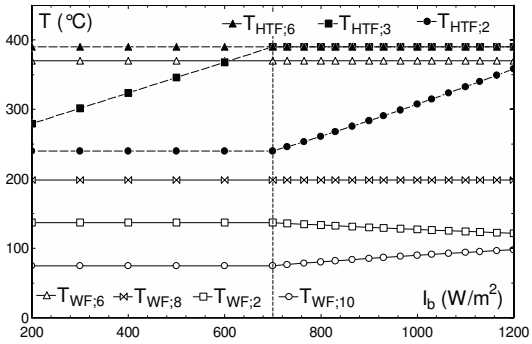

Fig. 8. Circuit temperatures at off-design

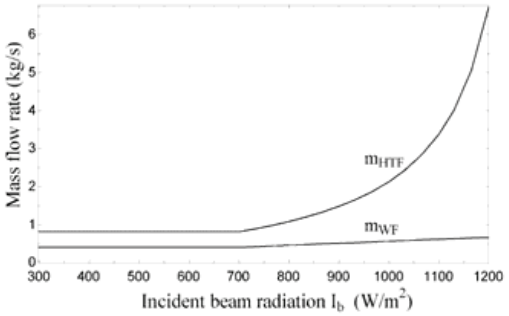

Fig. 9. Circuit flow rates at off-design

The temperature rise of the WF in the MHE remains relatively constant as the radiation increases; accordingly, m_{WF} increases proportionally to Q_{MHE}. On the other hand, the temperature difference of the HTF in the primary side of the MHE decreases greatly due to the increase of the LMTD in the exchanger, as discussed before; this produces an augmented HTF mass flow rate (Figure 9). A too large increase in m_{HTF} is not desirable, since it would produce large

[1] Here, the MHE; a similar procedure is followed for the RHE.

[2] T_2 changes slightly with RHE effectiveness

pressure losses in the solar-field primary circuit. However, it is important to notice that in reality m_{HTF} exceeds 2 kg/s only when I_b >1000 W/m^2, which is a condition very seldom reached even at the desert climate design location.

The augmented mass flow rate m_{WF} for I_b > 700 W/m^2 determines also for the RHE an increase of DT_{ML}; consequently the regenerator's effectiveness is slightly decreased; also Q_{RHE} is decreased with respect to design, and more heat must be rejected to the environment in the condenser. This has a marginally negative effect on the cycle efficiency η_C (Figure 10).

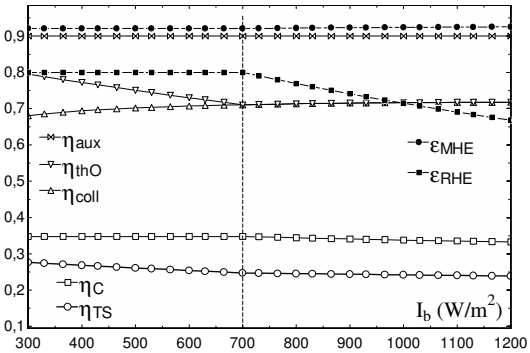

Fig. 10. System efficiencies and RHE effectiveness at off-design

5. Daily and Seasonal Models

Having determined the system settings and performance at design conditions, and developed a simplified model for off-design, it is possible to calculate short- (daily) or long-term (seasonal) performance.

The Solar Fraction of the energy conversion system over a certain time period can be expressed by:

$$SF = \frac{\int_0^T Q_{coll} dt}{\int_0^T Q_{coll} dt + \int_0^T Q_{aux} dt} \quad . \qquad (8)$$

The higher is the value of I_{bD}, the more the system will work with auxiliary heating switched on, resulting in a lower overall SF. A low value of I_{bD}, however, results in the system working for long periods at $I_b > I_{bD}$ "off-design" conditions, hence with a reduced overall conversion efficiency and lower overall energy production. Therefore, the choice of I_{bD} is a compromise between high SF and high system efficiency.

As a first example, the daily operation of the system was simulated on July 8th (a clear sunny day) and 17th (a day with relevant intermittency of solar radiation). The radiation data and the calculated performance are reported in Figures 11 and 12. The Overload is defined as $m_{WF}/m_{WF,D}$*100.

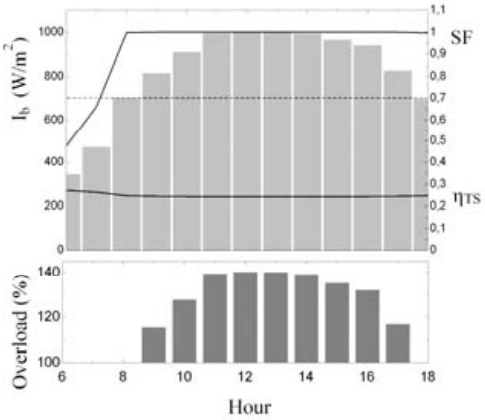

Fig. 11. Daily radiation and ambient temperature (Sede-Boqer, Negev desert; July 8th)

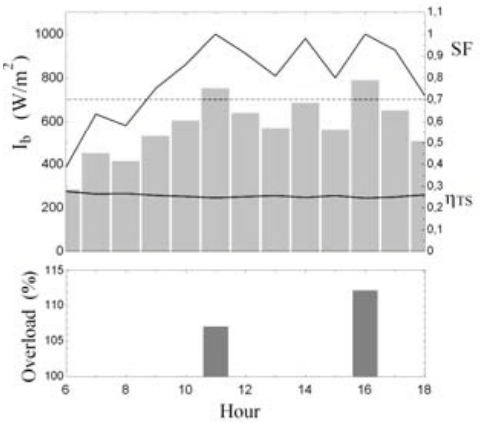

Fig. 12. Daily radiation and calculated performance (Sede-Boqer, Negev desert; July 17th)

In order to show the situation for winter operation, the same data are reported in Figure 13 for January 10th (in this day radiation was always low, so that the plant was run at 100% power using auxiliary firing).

The daily-averaged situation is resumed for some reference days in Table 4. A monthly simulation

was also performed. The results are summarized in Table 5.

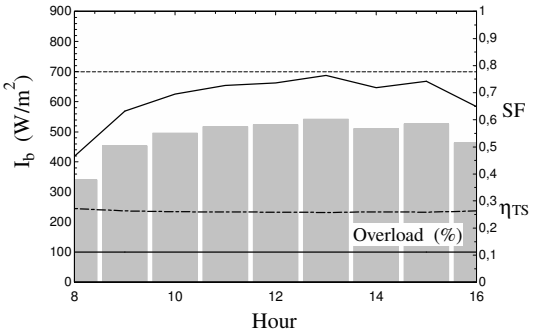

Fig. 13. Daily radiation and calculated performance (Sede-Boqer, Negev desert; January 10th)

Table 4. Daily-averaged system performance for different reference days in (Sede-Boqer, Negev desert, 2007)

Ref. Day	η_{TS}	SF	W, kWh
Jan 10th	0,261	0,681	883
May 19th	0,250	0,902	1375
July 8th	0,247	0,946	1556
July 17th	0,2564	0,800	1294

Table 5. Monthly system performance (Sede-Boqer, Negev desert)

Ref. Day	h	η_{TS}	SF	W, kWh
January	8-16	0,272	0,4748	23541
January	10-15	0,267	0,517	17165
April	7-18	0,272	0,619	36020
April*	7-18	0,252	0,731	28960
July	6-18	0,255	0,800	42630
July	7-17	0,253	0,854	36550

* Shutoff on days no. 2,9,14,15,25,26

6. Exergy analysis

An exergy analysis of the powerplant has been performed, in order to assess the exergy destruction within components and the exergy losses from the system [9], and to understand the main driving mechanisms leading to system optimization.

The calculation approach to exergy balance of power cycle is rather classic and follows traditional literature [10, 11]. The exergy inputs to the system come from (I) sun and (II) auxiliary heater. The exergy from the sun is given by:

$$\dot{E}x_{in,sun} = G_T A_C \left(1 - \frac{T_a}{T_{sun}}\right) \qquad (9)$$

where T_{sun} is taken as 75% of the equivalent black-body sun temperature, in agreement with [12].

The exergy from the auxiliary heater has been taken as equivalent to the heat input (chemical exergy = Lower Calorific Value of the fuel).

The relative exergy destructions (EXD_rs) of power plant components (scaled to the overall exergy input) referred to the daily operation of the system are shown in figure 14 for two days, July 8th and 17th. A higher value of EXD_{r_coll} is evident on 8th July, due to the higher radiation conditions. The opposite behaviour is found for the auxiliary heater, which is turned off for a long time on sunny days.

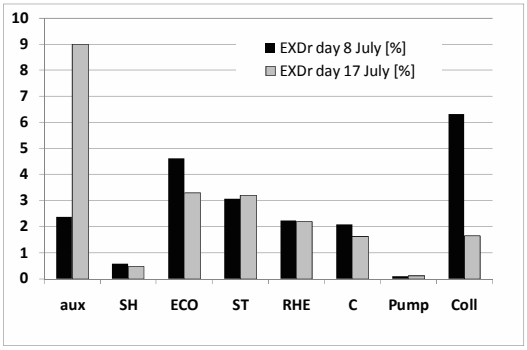

Fig. 14. Daily relative exergy destructions of plant components

The second relevant EXD_r comes from the economiser section (ECO) of the MHE. Its contribution rises from 3.1 to 4.6% of the overall exergy input on the day with higher solar radiation (July 8th), mainly because of larger temperature difference at points 2HTF – 2 (figure 7 and schematic on figure 1). The other relevant EXD_rs (SH, RHE and ST) show a reduced sensitivity to solar radiation conditions.

It is interesting to observe the sum of collector's daily relative EXD and loss EXL on the two investigated days (figure 15) . The Collector Exergy Loss EXL_{r_coll} is due to the collector–environment heat dispersion. The difference between the grey and black bars in Figure 15 corresponds to the EXD_{r_coll} shown on figure 14. The largest fraction of collector's exergy inlet is lost to the environment: on the day with higher irradiation it is about 89%, whereas in the day with lower radiation it rises to 96%, showing that in this day almost all the exergy input is not transferred to the HTF but is lost to the environment.

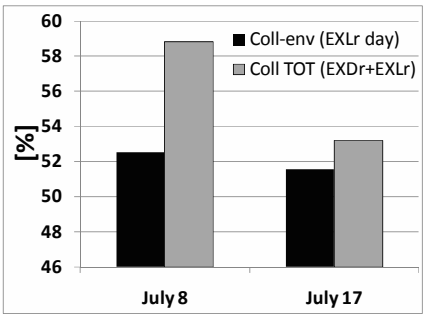

Fig. 15. Daily relative exergy destruction and loss of solar collector

Finally, it is interesting to observe the effect of radiation value on the hourly instantaneous absolute and relative EXDs of the main affected components (ECO, RHE and ST), as a result of off design operation (figure 16). The discussion is referred to July 8th only (a similar behaviour is observed on July 17th). When the radiation is below the design value (I_b < 700 W/m^2), the components EXDs remain unchanged, whereas they increase when I_b > 700 W/m^2 (high-radiation off design). The ECO shows the largest increase, as a result of higher temperature difference (T_{2HTF} – T_2) under off-design.

Also the RHE and ST show a relevant increase in their EXD when I_b > 700 W/m^2, essentially because of the system flow rate control, which provides an increase in m_{HTF} and m_{WF}, and changes significantly the temperature diagrams in the heat exchangers, as discussed at point 4.4 and shown on figure 9.

Conclusions

A complete model for the simulation of a solar thermodynamic energy conversion system has been presented.

The advantage of a supercritical cycle has been confirmed, and the selection of the correct working fluid for the design conditions has been shown to be a key factor.

In order to allow satisfactory operation with low radiation, the system was assisted with a fuel burner. At over-design radiation conditions, the system was operated with increased flow rate and decreased efficiency. The correct selection of the design conditions, in terms of radiation, affects the Solar Fraction and the long-term system performance.

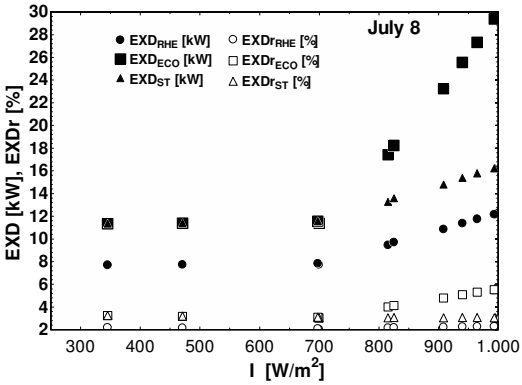

Fig. 16. Absolute and Relative exergy destructions; ECO, RHE, ST; variable radiation (off-design)

Off-design operation included models for the collector efficiency and heat exchanger effectiveness.

The simulations have shown that a high value of solar fraction can be achieved over a long period of the year, and that the situation can be further improved considering plant shutoff on specific days when radiation is clearly inadequate.

The exergy analysis has shown that the highest exergy destructions come from collector, ECO, RHE and ST in days of high radiation; whereas in days of low radiation the auxiliary heater plays a dominant role in the system exergy destruction. Off-design operation at high radiation conditions leads to a consistent increase of the ECO, RHE and ST exergy destructions.

Acknowledgments

Adi Lifshitz performed part of this work during a mobility in the frame of a student cooperation agreement between University of Firenze and Tel Aviv University. The supervision of Prof. A. Kribus and Mr. A. Genani is gratefully acknowledged.

List of symbols

c_p Constant-pressure specific heat, kJ/(kgK)
DT_{CE} Cold End Temp. difference (MHE),°C
DT_{HE} Hot End Temperature difference (MHE),°C
DT_{LM} Log-Mean Temp. difference (MHE),°C
DT_P Pinch Temperature difference (MHE),°C
ECO Economizer
EVA Evaporator
EXD Exergy Destruction
EXL Exergy Loss
I_b Direct radiation incident to collector aperture, W/m^2
m Mass flow rate, kg/s
p Pressure, kPa
Q Heat rate, kW
T Temperature, °C
U Overall heat transfer coefficient, W/(m^2°C)
ε Effectiveness (RHE, MHE)
η Efficiency

Subscripts:

abs absorber
aux auxiliary heater
c cycle
cOpt cycle, optimal (maximum condition)
C Condenser
coll Collector
D Design
day Daily value
EE End of Economizer
HTF Heat Transfer Fluid (primary circuit)
M Maximum
MHE Main Heat Exchanger
r Relative (referred to overall exergy input)
RHE Regenerative Heat Exchanger
SH Super-Heater
ST Steam Turbine
thO Overall Thermal
TS Total System
WF Working Fluid (secondary circuit)

References

[1] Odeh,. S. D., 2003, "Unified model of solar thermal electric generation systems", Renewable Energy, 28, 755-767.

[2] ARCHIMEDE - ENEA Grande Progetto Solare Termodinamico. http://www.enea.it/com/solar/index.html

[3] Mills, D., 2004, Advances in solar thermal electricity technology, Solar Energy, 76, 19-31.

[4] Camacho, E., Berenguel, M., Rubio, F.R., 1997, *Advanced Control of Solar Plants*, Springer-Verlag, London.

[5] http://www.solel.com/products/pgeneration/ls2/

[6] Schuster, A., Karellas, S. Kakaras, E., Spliethoff, H., 2009, Energetic and economic investigation of Organic Rankine Cycle applications, Applied Thermal Engineering, 29, 8-9, 1809-181

[7] http://www.therminol.com/pages/products/vp-1.asp

[8] Cengel, Y.A., Bowles, 2002, Thermodynamics and Heat Transfer, McGraw-Hill.

[9] Bejan, A., Tsatsaronis, G., Moran, M., 1996, *Thermal Design and Optimization*, Wiley Interscience, New York.

[10] A. Bejan, 1982, *Entropy generation through heat and fluid flow*, John Wiley & Sons inc.

[11] Kotas, T.J., 1985, *The Exergy Method of Thermal Plant Analysis*, Butterworths.

[12] S. Farahat, F. Sarhaddi, H. Ajam, 2009, Exergetic optimization of flat plate solar collector, Renewable Energy, 34, 4 1169-1174.

Biomass Thermoelectric Generator as an Electrical Renewable Power Source for Basic Domestic Needs

D. Champier[a], J.P. Bédécarrats[b], T. Kousksou[b], M. Rivaletto[a], F. Strub[c], P. Pignolet[a]

[a] *Laboratoire de Génie Electrique, Université de Pau et des Pays de l'Adour, Pau, France.*
[b] *Laboratoire de Thermique Energétique et Procédés, Université de Pau et des Pays de l'Adour, Pau, France*
[c] *Association Planète Bois, Pau, France*

Abstract: According to the International Energy Agency, 2.5 billion people rely on biomass, such as wood fuel, charcoal, agricultural waste and animal dung, to meet their energy needs for cooking in developing countries. Biomass is too often burnt through open fires or rudimentary stoves. In developed countries, wood is considered as a sustainable fuel source, because the forestry industry currently plants more trees than it chops down. On the contrary, in many developing countries forests are scarce or dwindling and it becomes a necessity to save wood fuel. Open fire stoves are also known to lead to high emissions of health damaging air pollutants and smoke is highly linked to acute respiratory infection (ARI). Replacing traditional open fire stoves, characterized by low efficiency, with improved ones is an important challenge.
The Non Governmental Organisation "Planète Bois" is developing energy-efficient multifunction (cooking and hot water) mud stoves based on traditional stove designs. These stoves need a fan to increase the ratio air to fuel to achieve a complete combustion.
Again 1.6 billion people lack access to electricity and "Planète Bois" has to find an issue for powering the stove's fan. Just giving 10 W to each one will need 16 GW power plants and all the dispatching.
Our laboratories work on a thermoelectric generator using commercial thermoelectric modules (Bismuth Telluride) for powering the electric fan. This thermoelectric generator can also provide electricity for basic needs: radio and light. This generator does not need extra fuel from the stove as the thermoelectric modules convert directly a very small part of the heat moving from the hot gas to the water tank into electricity.
In this paper a review of existing thermoelectric generators for stoves is presented. Then the entire generator set-up is described including the thermal and mechanical part and also the switching electric regulator which converts the fluctuating voltage from the thermoelectric modules to a constant voltage and stores the electrical energy in a battery.

Keywords: thermoelectric power generator, TE module, Seebeck cells, thermoelectricity, biomass stove, thermal energy.

1. Introduction

Open fires or rudimentary stoves are widely used in developing countries by about 2.5 billion people [1]. These traditional stoves or fires are characterized by low efficiency which results in inefficient use of scarce fuel-wood supplies [2]. These rudimentary fire stoves also lead to high emissions of health damaging air pollutants and smoke is highly linked to acute respiratory infection (ARI) [3,4]. Building clean and efficient cook stoves reduces carbon dioxide and methane emissions while providing social and health co benefits through reduced fuel consumption and reduced indoor air pollution. Improved cook stoves also have the potential to reduce significantly black carbon emissions (short-lived non-CO_2 climate warmer) [5].

Again 1.6 billion people lack access to electricity [6] ; providing 10 W to cover basic needs such as lights and radio to these low-income populations living mostly in rural areas, will require more than 16 GW power plants (resistive losses in the conductor grid) and all the dispatching. Individual thermoelectric (TE) generators coupled with cook stoves are an interesting option to provide electricity.

The Non Governmental Organization "Planète Bois" develops energy-efficient multifunction mud stoves based on traditional stove designs. These improved stoves use a smoke extract fan which allows a control of the ratio air to fuel and as a consequence to optimize the combustion. The fan also permits the use of a horizontal pipe avoiding the necessity of long metal pipe and of building chimney in countries where the local workers do

not have the technology to make it go through the roof.

2. Review of existing thermoelectric generators for stoves

2.1. Thermoelectric generators

Thermoelectric generators convert directly a very small part of the heat moving through them into electricity as described in figure 1. They are composed of three parts: two heat exchangers and a TE module.

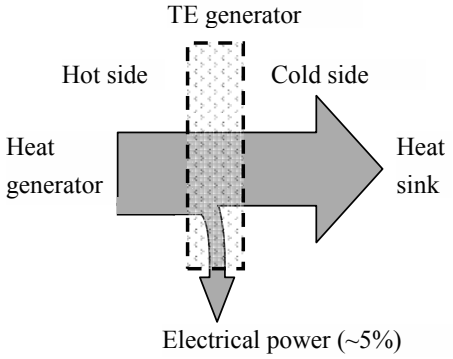

Fig. 1. Basic principle of a TE power generator

TE generators have the advantages of being maintenance free, silent in operation and of involving no moving or complex parts.

The efficiency of the TE module depends on the property of the materials used for the thermocouples. Semiconductors offer the best efficiency for the moment.

The only couple of materials available on the market at a reasonable price is Bismuth Tellurid (Bi_2Te_3). These materials can work at a temperature as high as 260°C continuously and intermittently up to 380°C. Other materials are now being studied for higher temperatures, such as clathrates, skutterudites, alloys Heusler, phases of Chevrel and oxides [7] but are not commercially avaible.

2.2. TE generators for stoves.

In the literature review we have selected the experimental studies. The heat generator is the hot smoke of the stove and all the TE modules are made of bismuth-telluride Bi_2Te_3.

Nuwayhid et al [8] have studied the possibility of using a proportion of the heat from 20–50 kW wood stoves, to provide a continuous 10–100W electric power supply. In a first prototype they used cheap Peltier modules for their TE Generator. The maximum power for a module was very low (1W) mostly because of the limited temperature difference due to the maximum temperature supported by the module and also because of the geometry which is optimized for cooling and not for power generation. In a following prototype [9] their TE generator used 1, 2 or 3 commercially available low-cost power generator modules. The cold side of the TE modules was naturally cooled with the surrounding air. They got a maximum power of 4.2W for one TE module and they showed that the output power per module decreased when increasing the number of TE module in the TE generator. This is a result of the reduction of the temperature difference between the hot and cold surfaces. They also made a TE generator using heat pipes for the heat sink [10]. The maximum power was about 3.4W. Lertsatitthanakorn [11] investigated the same type of prototype and he got a power output of 2.4W. He added an economic analysis indicated that the payback period tends to be very short.

Mastbergen [12] presented at the ETHOS 2005 congress (Engineers in Technical and Humanitarian Opportunities of Service) a prototype of TE generator with a forced air cooling for the cold side with a 1W fan. The net power of 4W generated by the TE generator was sufficient to power an array of high intensity LEDs. Field tests [13] have been made in different countries but results are not available in the literature.

BioLite [14], an industrial lightweight backpacking stove, has been presented at the 2009 ETHOS conference. The TE generator is only used to create clean, efficient cooking with a forced-air draft fan for this gasifier stove.

“Planète Bois” and our laboratories explore water cooling cold heat sink TE generators [15-17]. The multifunction cook stoves of “Planète Bois” produce hot water and the heat flux from the hot gas to the water tank (about 30 liters) can be used to produce electricity without losses of heat. The use of water guarantees that the cold heat sink temperature will always stay under 100°C. The last prototype presented in this paper reaches 9.5W

for one module and produces a charging power of about 8W in the battery under almost matched conditions.

3. Generator set up

Different experimental thermoelectric power generators were made and tested in our laboratory. The first one [15] was used to obtain a simple model of the TE module. The second one TEGBioS [16] was used to improve the thermal contact by adding a compressive load. It showed that a compressive load of about 5 bars is necessary. The current one, TEGBioS II includes an electronic convertor. The thermal part is presented in figure 2 and the electronic regulator is described in part 3.2.

3.1. Thermal and mechanical part

An aluminum heat sink with fins was mounted on the hot side of the TE modules. An aluminum tank (2 liters) filled with water is used as a cold side exchanger. The water in the tank is the cold heat sink for the TE generator and it represents the domestic hot water. A compressive load is applied in the centre of the tank to reduce thermal contact resistance.

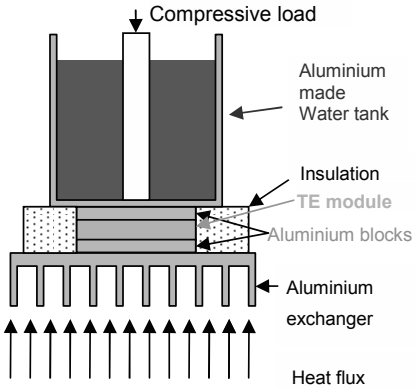

Fig. 2. Schematic of the thermal and mechanical part of the TE generator.

For the experiment it was easier to make measurements with the load applied in the centre but in the final design it will be applied along the edges of the tank. Thermal grease is used for each contact. To reduce thermal contact resistance, we also polish the aluminum surface with a milling machine to get a very good flatness around 25µm (standard deviation of height). A pressure around 5 bars is applied to the TE module. Thermal insulation is used between the two exchangers. For the measurements, we added two aluminium blocks on each side of the TE module.

3.2. Electrical part

At the beginning of the burning, the temperatures are very low and the TE generator does not produce any electricity. A battery is necessary to store the electrical energy from the module. The voltage of the one module TE generator is low and varies as the module temperature difference changes. A power electronic circuit is required to regulate the output voltage and to boost it to the battery level.

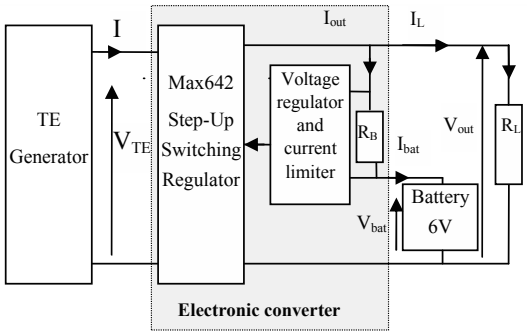

Fig. 3. Schematic of a electronic part of the TE generator with the measurement.

We have developed an electronic converter (figure 3) using a step-up switching regulator MAX642 which works in the 5mW to 10W range with a very good efficiency. Some electronic circuits are added to limit the charging current of the battery. A "6 volts" battery with a steady state voltage of 6.75V is chosen because it is sufficient for the fan and it is very close to the voltage needed by the LEDs.

This electronic converter is tested with a laboratory power supply. Simple tests made on a resistive load showed that the efficiency is in a range of 80% to 85% [16, 17].

3.3. One-dimensional steady-state analysis

Thermoelectric modules are made of n couples of p-type and n-type semiconductor pellets connected

with metal solder. For electrical insulation, two ceramic wafers sandwich the pellets (Fig. 4).

We used the one dimensional model commonly described in literature (1-D heat flow) of a typical TE module made of n thermocouples [18, 19].

These equations are obtained from the study of a single n or p-type element assuming that all connections between the pellets are perfect: no electrical and thermal resistance.

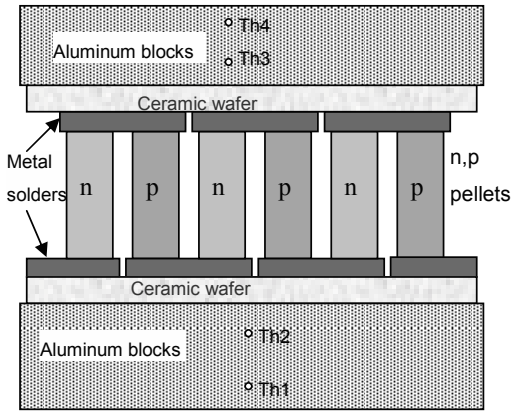

Fig. 4. Schematic of a thermoelectric module

We also assume that there is no conduction, convection and radiation via the ambient which means that the only path for transferring heat from one side of the pellet to the other is through the TE material. These assumptions give the following TE equations for the heat absorbed at the cold side, q_c, the heat released at the hot side, q_h, and for the generated electrical power P_{elec}.

$$q_h = n.\left[\alpha_{pn}.I.T_h - \frac{R_{pn}.I^2}{2} - K_{pn}.(T_c - T_h)\right], \quad (1)$$

$$q_c = n.\left[\alpha_{pn}.I.T_c + \frac{R_{pn}.I^2}{2} - K_{pn}.(T_c - T_h)\right], \quad (2)$$

$$P_{elec} = n.\left[\alpha_{pn}.I.(T_h - T_c) - R_{pn}.I^2\right], \quad (3)$$

where the parallel thermal conductance, K_{pn}, serial electrical resistance, R_{pn}, and Seebeck coefficient, α_{pn} of one thermocouple are :

$$R_{pn} = \frac{\rho_n \times L_n}{S_n} + \frac{\rho_p \times L_p}{S_p}, \quad (4)$$

$$K_{pn} = \frac{\lambda_n \times S_n}{L_n} + \frac{\lambda_p \times S_p}{L_p}, \quad (5)$$

$$\alpha_{pn} = \alpha_p - \alpha_n, \quad (6)$$

$$\lambda_{pn} = \frac{\lambda_p + \lambda_n}{2}, \rho_{pn} = \frac{\rho_p + \rho_n}{2}, \quad (7)$$

L_n, L_p and S_n, S_p are respectively the leg length and cross-sectional area of the pellets.

α_p, α_n, λ_n, λ_p, ρ_n, ρ_p are temperature dependent and are evaluated at the average temperature $T_a = \frac{T_h - T_c}{2}$, the values are taken from CRC Thermoelectric Material Properties n and p-type Bi_2Te_3 [18, 20].

For our particular modules n=126, L_p=L_n=1.4mm, S_n=S_p=6.6mm^2.

For an electric load R_E, the current I can be calculated with

$$I = \frac{Eo}{nR_{pn} + R_E} = \frac{n.\alpha_{pn}.(T_h - T_c)}{nR_{pn} + R_E}, \quad (8)$$

Eo is the open circuit voltage of the TE module.

The maximum output power P_{elec}^{max} will be obtained for a matched load which means nR_{pn}=R_E.

The temperature T_c and T_h can be evaluated by using a thermal resistance model (Fig. 5).

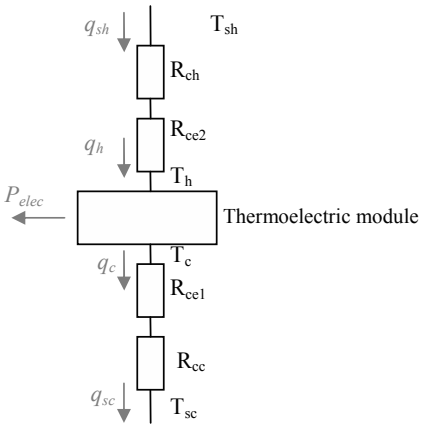

Fig. 5. Thermal resistance model of the thermoelectric module

R_{ce1}, R_{ce2} are the thermal resistances of the ceramic wafers, R_{cc} and R_{ch} are the contact thermal resistances between wafers and aluminum blocks. The thermal resistance of the metal solder is assumed to be negligible. The temperature measurements (T_{h1}, T_{h2}, T_{h3} and T_{h4}) are made with type K thermocouples placed in holes in each of the two aluminum blocks (Fig.6). The temperatures of the hot and cold sides of ceramic wafers of the module T_{sh}, T_{sc} and the temperatures T_h and T_c are calculated with the hypothesis of linearity assuming that the aluminum blocks are well insulated from the ambient : $q_c=q_{sc}$ and $q_h=q_{hc}$.

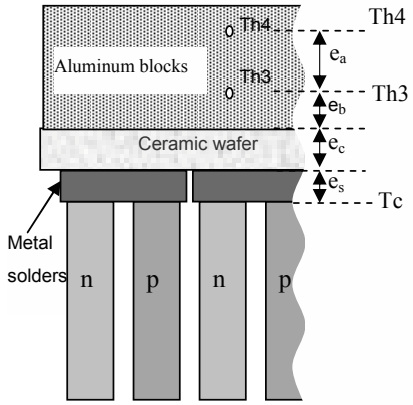

Fig. 6. Details of a thermoelectric module

For example $q_c = \frac{T_{h4} - T_{h3}}{R_{ala}} = \frac{T_{h3} - T_c}{R_{alb} + R}$, (9)

with

$$R_{ala} = \frac{e_a}{\lambda_{al}.S}, R_{alb} = \frac{e_b}{\lambda_{al}.S} \quad (10)$$

$$R = \frac{e_c}{\lambda_{ceram}.S} + \frac{1}{h_{contact}.S} + \frac{e_s}{\lambda_{solder}.S} \quad (11)$$

Where λ_{al} , $\lambda_{ceram,}$ λ_{solder} are the thermal conductivities of respectively the aluminium, the ceramic wafers and the metal solders. $h_{contact}$ is the contact heat transfer coefficient.

According to equation 9 :

$$T_c = T_{h3} + \frac{(R_{alb} + R)}{R_{ala}}(T_{h3} - T_{h4}) \quad (12)$$

$$T_c = T_{h3} + \frac{e_b + e_c\frac{\lambda_{al}}{\lambda_{ceram}} + e_s\frac{\lambda_{al}}{\lambda_{solder}} + x}{e_a}(T_{h3} - T_{h4}) \quad (13)$$

with $x = \frac{\lambda_{ceram}}{h_{contact}}$

The analysis was done with e_a=13.9mm, e_b=3.2mm, e_c=1mm, e_s=0.7mm, $\lambda_{solder} \approx \lambda_{al}$=237W/m.K, λ_{ceram}=25W/m.K and $h_{contact} \approx$20000 W/(m^{2}K) which is quite a good contact.

3.4. Measurements

The temperatures, tensions and currents are recorded by using an Agilent 34970A Data Logger. The measurement system enables us to obtain a precision of 0.01% for the tensions, 0.1% for the currents and 0.5°C for the temperatures. But, because of the difficulty in measuring a temperature accurately, the temperature errors are evaluated to 1°C.

We recorded T_{h1}, T_{h2}, T_{h3}, T_{H4} and also V_{out}, V_{bat}, I_{bat} and I_L.

We calculated the output power from the thermoelectric module $P_{elec} = V_{TE}.I$ and the available power for the end users:

$$P_{av} = V_{out}.I_L + V_{bat}.I_{bat}. \quad (14)$$

For the experiment, the load was a resistor of 12Ω. Fig 7 shows the hot and cold side temperatures and the corresponding electrical power for a half an hour experiment.

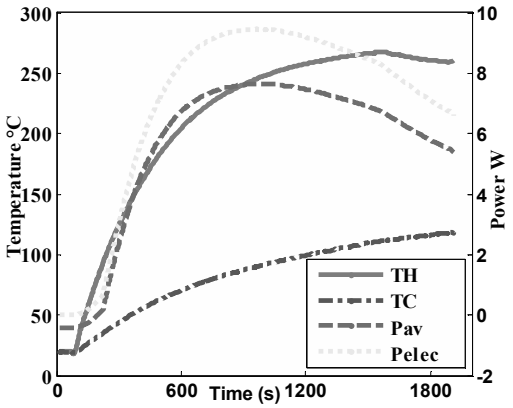

Fig. 7. Cold and hot side temperatures and electrical powers during the experiment

A maximum electrical power of 9.5W was produced by the TE module and because of losses in the electronic convertor a maximum power of 7.6W was available.

The aim of the measurements is to find if we get the maximum available power from our prototype and to understand what could be improved.

The resistor R_E seen by the TE module can be calculated : $R_E = \frac{V_{TE}}{I}$.

This resistor R_E is not matched but it is possible to calculate the maximum power that would be obtained if the electronic convertor matched the load.

As $V_{TE} = E_o \frac{R_E}{R_E + nR_{pn}}$, then P_{elec} can be expressed as :

$$P_{elec} = \left(\frac{E_o . R_E}{R_E + nR_{pn}} \right)^2 . \frac{1}{R_E} \qquad (15)$$

and for a matched load $P_{elec}^{\max} = \frac{E_o^2}{4nR_{pn}}$ (16)

The maximum power (dashed line) on Fig. 8, can be calculated by :

$$P_{elec}^{\max} = P_{elec} \frac{\left(R_E + nR_{pn} \right)^2}{4.nR_{pn}.R_E} \qquad (17)$$

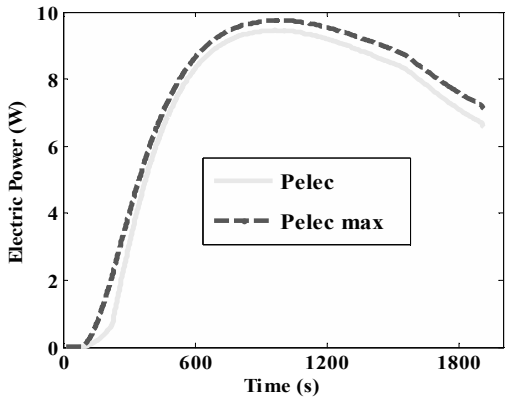

Fig. 8. Measured electrical power and calculated maximum output electrical power.

To analyze these results, we compare this maximum power with the power obtained with the 1D model. Uncertainties are evaluated for a 0.5mm error on the measurements of e_a and e_b.

The results in figure 9, show that in this experiment we have almost reached the maximum power available from such a TE generator. The mechanical and thermal design is optimized.

The point to be improved is the matching between the TE module and the electronic convertor.

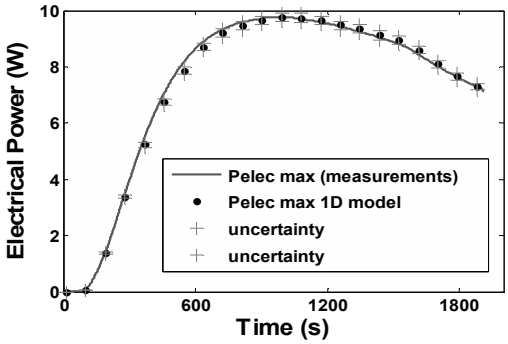

Fig. 9. Comparison between measurements and 1D model of the TE generator.

In our experience the load was chosen to be near the matched load as seen in figure 8 but in different uses the mismatch could be very important and the output power could be much lower than $P_{elec}^{\max}$.

As the output current changes, the working point moves and it will be necessary to use a maximum power point tracking electronic regulator [21]. This can be done by a cheap microcontroller in the electronic circuit. Nowadays microcontrollers have very low power consumption and will not penalize the regulator in comparison with the benefits given by the matching load tracking. Microcontroller could also add some intelligence to control the fan and thus to slow the gas speed in case of an increasing temperature going over the maximum temperature supported by the hot side of the TE module.

4. Conclusion

An experimental TE generator suitable for electricity production in multifunction biomass stoves has been presented. The complete system from the heat source up to the end users electricity production including electronic convertor and

battery charging has been studied. Comparison between the experimental data and the commonly used one dimensional thermoelectric model shows a good agreement. The very reasonable value of the contact resistance validated by the comparison shows that the mechanical design of the generator is almost optimized. In the case of an almost matched load, the TE module has produced up to 9.5W. Due to the fluctuating output, an electronic boost regulator stores this electrical energy in a battery with an around 6.7V stabilised voltage. The maximum power of stabilized electricity available for the end users was around 7.6W.

In case of a mismatched load a maximum power point tracking will be necessary. It will be obtained at a lower cost by ordinary microcontroller in a future work.

Nomenclature

E_o open circuit voltage of TE module,V

e_a, e_b, e_c, e_s distances, m

$h_{contact}$ contact heat transfer coefficient, $W.m^{-2}.K^{-1}$

I current through TE module, A

I_{bat} current through battery, A

I_{out} output current of electronic convertor, A

I_L current in the load, A

K_{pn} thermal conductance of one thermocouple, $W.K^{-1}$

L_n, L_p leg lengthes of the n-type and p-type pellets, m

n number of thermocouple in a module

P_{av} electrical power for end users, W

P_{elec} electrical output power, W

P_{elec}^{max} maximum output power (matched load), W

q_c heat absorbed at the cold side, W

q_h heat released at the hot side, W

q_{sc} , q_{sh} heat flux through ceramic wafers, W

R thermal resistance, $K.W^{-1}$

R_B current sense resistance, Ω

R_{cc}, R_{ch} contact thermal resistances between wafers and aluminum blocks , $K.W^{-1}$

R_{ce1}, R_{ce2} thermal resistances of the ceramic wafers, $K.W^{-1}$

R_E resistance seen by the TE module, Ω

R_{int} internal resistance of TE generator, Ω

R_L load resistance, Ω

R_{pn} electrical resistance of one thermocouple, Ω

S_n, S_p cross-sectional areas of the n-type and p-type pellets, m^2

T_a average temperature, °C

T_C cold-side temperature of TE module, °C

T_H hot-side temperature of TE module ,°C

T_{hi} Temperatures (measurements), °C

T_{sh}, T_{sc} temperatures of the hot and cold sides of ceramic wafers of the module, °C

V_{out} output voltage of electronic convertor, V

V_{bat} battery voltage, V

V_{TE} output voltage of TE module, V

Greek symbols

α_p, α_n, Seebeck coefficients of the n-type and p-type semiconductors, $V.K^{-1}$

α_{pn} Seebeck coefficient of one thermocouple, $V.K^{-1}$

λ_n, λ_p, thermal conductivities, $W.m^{-1}.K^{-1}$

λal , $\lambda ceram$, $\lambda solder$ thermal conductivities of respectively the aluminium, ceramic wafers and metal solders, $W.m^{-1}.K^{-1}$

ρ_n, ρ_p resistivities of the n-type and p-type semiconductors, Ω.m

Abbreviations

TE Thermoelectric

References

[1] International Energy Agency, World Energy Outlook 2006, IEA Publications, France

[2] Anozie A.N., Bakare A.R., Sonibare J.A., Oyebisi T.O., 2007, Evaluation of cooking energy cost, efficiency, impact on air pollution and policy in Nigeria, Energy, 32: 1283–1290

[3] Parikh J., Balakrishnan K., Laxmi V., Biswas H., 2001, Exposure from cooking with biofuels: pollution monitoring and analysis for rural Tamil Nadu, India, Energy , 26: 949–962.

[4] Bhattacharya S.C., Albina D.O., Khaing A.M., 2002, Effects of selected parameters on performance and emission of biomass-fired cookstoves, Biomass & Bioenergy ; 23: 387–395.

[5] Haines A, et al., 2007, Policies for accelerating access to clean energy, improving health, advancing development, and mitigating climate change, The Lancet, Volume 370, Issue 9594, pp1264-1281

[6] www.worldenergyoutlook.org/database_electricity/electricity_access_database.htm

[7] Rowe D.M., 2006, Thermoelectric waste heat recovery as a renewable energy source. International Journal of Innovations in Energy Systems and Power, vol 1, no 1.

[8] Nuwayhid R.Y., Rowe D.M., Min G., 2003, Low cost stove-top thermoelectric generator for regions with unreliable electricity supply, Renewable Energy 28, 205–222

[9] Nuwayhid R.Y., Shihadeh A., Ghaddar N, 2005, Development and testing of a domestic woodstove thermoelectric generator with natural convection cooling, Energy Conversion and Management 46, 1631–1643

[10] Nuwayhid R.Y., Hamade R., 2005, Design and testing of a locally made loop-type thermosyphonic heat sink for stove-top thermoelectric generators, Renewable Energy 30, pp 1101–1116

[11] Lertsatitthanakorn C., 2007, Electrical performance analysis and economic evaluation of combined biomass cook stove thermoelectric (BITE) generator, Bioresource Technology 98, 1670–1674

[12] Mastbergen D., Willson B., 2005, Generating Light from Stoves using a Thermoelectric Generator, Presented at the ETHOS International Stove Research Conference, Seattle, Washington.

[13] Joshi S., Mastbergen D., Willson B., 2007, "Field Testing of Stove-Powered Thermoelectric Generators." Presented at the ETHOS International Stove Research Conference, Kirkland, Washington.

[14] URL: www.biolitestove.com/BioLite.html

[15] Champier D., Bedecarrats J.P., Rivaletto M., Strub F., 2010, Thermoelectric power generation from biomass cook stoves, Energy Volume 35, Issue 2, Pages 935-942

[16] Champier D., Rivaletto M., Strub F., 2009, TEGBioS : a prototype of thermoelectric power generator for biomass stoves, Proc. of ECOS 2009 22nd International Conference on Efficiency, Cost, Optimization, Simulation, and Environmental Impact of Energy Systems, Paraná, Brazil.

[17] Champier D., Rivaletto M., Strub F.,2009, Improving biomass stove with a thermoelectric generator, Proc of SDEWES 5th Dubrovnik Conference on Sustainable Developpement of Energy Water and Environment, Dubrovnik.

[18] Rowe D.M., 1996, CRC Handbook of Thermoelectrics, CRC Press, London

[19] Mitrani D., Salaza J., Turo´ A., Garcıa J.M., Chavez J.A.., 2009, One-dimensional modeling of TE devices considering temperature-dependent parameters using SPICE, Microelectronics Journal, Volume 40, Issue 9, Pages 1398-1405

[20] Rowe D.M., Min G., 1996, Design theory of thermoelectric modules for electrical power generation, IEE Proceedings: Science, Measurement and Technology, vol. 143, no. 6, pp. 351–356.

[21] Eakburanawat J., Boonyaroonate I., 2006, Development of a thermoelectric battery-charger with microcontroller-based maximum power point tracking technique, Applied Energy 83, 687–704

Thermoeconomic Analysis of MicroCHP Thermophotovoltaic (TPV) Systems

Margherita Cadorin, Michele Pinelli, Pier Ruggero Spina and Mirko Morini

Engineering Department in Ferrara, University of Ferrara, Italy

Abstract: Among the various microCHP technologies, systems based on thermophotovoltaic (TPV) generators have received renewed attention. The TPV technique allows the radiation from an artificial emitter to be converted into electricity by using photovoltaic (PV) cells. In this paper, to assess the capability and potential of domestic microCHP TPV systems, a thermoeconomic analysis is performed. Different scenarios are presented and analyzed. The analysis performed allows the assessment of the TPV capability as a domestic microCHP system and the definition of possible configurations and scenarios which may be conveniently applied in the near future.

Keywords: distributed domestic generation, heat-following microCHP, economic profitability, TPV

1. Introduction

MicroCHP for the fulfillment of the energy requirements of residential buildings has received growing attention in recent years, since it can contribute to the reduction of energy consumption compared to the separate generation of heat and power, and, as a consequence, pollutant emissions (in particular greenhouse gases), while securing energy supply by reducing energy imports and conserving energy resources. Among the various microCHP technologies, systems based on thermophotovoltaic (TPV) generators have received renewed attention. The TPV technique allows the radiation from an artificial emitter to be converted into electricity by using photovoltaic (PV) cells [1]. TPV can be seen as a microCHP system particularly suitable for residential users, since it is characterized by high values of the overall CHP efficiency, with thermal energy production, which is predominant with respect to electric energy production. In this paper, a description of the TPV system and its components, and a review of recent literature and the state of the art of this technology is presented. Then, the system analyzed in this paper is introduced. In particular, a gas-fired heating appliance converted to a TPV system is taken into consideration. The main idea is to convert a condensing boiler with a surface porous radiant burner (which is widespread as a domestic boiler) into a TPV system by adding PV cells inside the combustion chamber. To assess the capability and potential of domestic microCHP TPV systems, thermo-economic analysis is then performed. The energy performance is evaluated in terms of Primary Energy Saving (PES) index. Different scenarios are presented and analyzed. The analysis performed allowed the TPV capability to be assessed as a domestic microCHP system and the definition of possible configurations and scenarios, which may be conveniently applied in the near future.

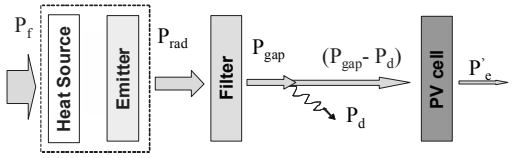

Figure 1. Configuration of a generic TPV system.

2. TPV system description

During TPV energy conversion, PV cells convert part of the thermal radiation emitted by a heated radiator into electricity. A generic TPV system is depicted in Fig. 1. It consists of: (a) source of heat; (b) radiator (emitter), (c) filter to enhance spectral control, (d) photovoltaic cell array (PV).

(a) *The heat source.* The thermal power P_f can come from different sources, such as internal or external combustion systems, concentrated solar radiation, waste heat, nuclear sources, etc. In recent years, great attention has been devoted to combustion-driven TPV systems, which present some notable characteristics:

- radiant intensity which can be very high, much greater than that of the sun; in fact radiant intensity of up 10-20 W/cm^2 (100-200 suns) can be quite easily achieved in these devices;

Corresponding Author: Margherita Cadorin, Email: margherita.cadorin@unife.it

- a number of different fuels can be burned within these devices. This is of great importance, for instance, when renewable fuel is used or when low cost fuel is available but electricity has a higher than average cost (such as in remote communities).

(b) *The radiator*. The radiator (or emitter) is the device which converts the thermal power P_f coming from a heat source into radiation power P_{rad}. The most important requirement of the emitter in a TPV system is that it has to efficiently convert heat into radiation with an emission spectrum adapted to the sensitivity of PV cells. Selective emission is required with the photon energy in a narrow band just above the bandgap of the PV cells. The selectivity of the emission could be obtained by:

- filtering a continuous radiation source (broadband emitters). A broadband radiator emits in the entire radiation spectrum. Hence, the spectral emittance must be as close to unity as possible. The material most commonly to date is silicon carbide (SiC). This has an emittance of about 0.9, and can withstand temperatures up to approximately 1900 K;
- using selective emitters producing radiation mainly in one or several narrow-emission bands (narrow band emitters). In this case, the emitter is made of materials that present particular radiation characteristics, i.e. the radiation emission spectrum is centered on specific wavelength. The materials considered to date are mainly REO (Rare Earth Oxides) materials, which include ytterbia (Yb_2O_3), erbia (Er_2O_3), holmia (Ho_2O_3) and neodymia (Nd_2O_3).

Alternatively, the emitter can be catalogued with respect to its interaction with the combustion system:

- combustion takes place inside a confined domain (shell) and heat is transmitted by heat exchange to the shell itself (emitter), which is brought to incandescence. In this case, since the emitter is an "externally fired" device, any kind of fuel can be used (oils, biomass, biogas, etc.) and the use of advanced combustion systems is feasible;
- the emitter itself is the combustion system, i.e radiant porous burners with surface combustion are used. Since this type of burner is considered in this work, a more detailed description is given below.

(c) *The filter***.** Particularly for broadband radiators, many of the emitted photons have energies that are less than that of the bandgap of the PV cells and are unusable. To ensure higher system efficiency, it is important to return these photons to the radiator, thereby permitting less fuel to be used to achieve a certain radiator temperature. The filter can make a large difference to the efficiency of the system but does not affect the power density, which is only influenced by the use of above-bandgap photons.

(d) *The PV cells*. In TPV applications, incident and output power densities are much larger than solar PV modules. Early work on TPV converters focused mainly on silicon (Si, E_{gap} = 1.11 eV) and germanium (Ge, E_{gap} = 0.8 eV) cells. These cells are commercially available in large quantities but they have a relatively high bandgap for TPV applications. In fact, while the sun mainly radiates in the visible range of wavelengths, a TPV radiator mainly emits in the near-infrared range. This means that semiconductors of much lower bandgaps are required for efficient conversion. Recently, TPV development has been able to exploit the extraordinary progress made in the field of III-V semiconductors and high-efficiency solar cells. Recent research has focused on the use of semiconductors based on gallium (Ga), antimony (Sb), indium (In), arsenic (As) and phosphorus (P), in particular: GaSb (E_{gap} = 0.73 eV), GaInAs (E_{gap} = 0.72 eV) and GaInAsSb (E_{gap} = 0.53 eV). These lower bandgap cells are capable of using more radiation energy but they contain toxic elements (Sb, As) and their production is still expensive. Recently, thin sliver cells have been studied to be used in TPV systems.

3. TPV as a microCHP system

Domestic-level microCHP are units of up to 5 kW of electric power intended for installation in individual homes. These systems should be able to meet both the base-load demand for a family home and the peak requirement. However, connection to the electric grid, either import or export, is always required. It can be noted that, of the total household energy demand approximately 85 % is used for space and water heating (62 % for space and 23 % for water heating), while 10 % is for lights and appliances and 5 % is for cooking. Hence, it is logical to focus on tackling space and water heating (85 %) rather than the remaining 15 % of the total household energy demand [2].

TPV power generation in a fuel-fired heating furnace is particularly suitable as microCHP for domestic application, since thermal power production is predominant with respect to electric power production. Moreover, it would even be attractive when the electric efficiency of the system is low. In fact, a TPV system applied to gas-fired heating appliances is a CHP system where exhaust gases are mainly used for space and/or water heating and where the required electricity share is usually small compared to the thermal load. Hence, the overall efficiency of fuel utilization in such a system can be quite high, usually, higher than 90%, although the electric efficiency of the system is low (approximately 2-5 % of available prototypes). However, it is expected that, with further optimization of cell structure and manufacturing processes, and with the enhancement of the thermal design of TPV CHP systems, the electric efficiency may reach 20 % in the near future.

Qiu and Hayden [3-6] and Qiu *et al.* [7] experimentally studied combustion-driven TPV CHP systems in a variety of configurations. In their papers, they mainly studied the influence of radiant burner configurations [4,5] and the use and optimization of TPV cells [6-8]. They developed very realistic devices and found a maximum η_{TPV} equal to 3.2 %.

Durisch *et al.* [8] developed a small self-powered grid-connected TPV system prototype in order to investigate its feasibility in residential heating systems. An η_{TPV} equal to 2.8 % was achieved by using preheated air. This can be considered a good result for a prototype-scale system (50 W).

Palfinger et al. [9] reported a cost analysis of a residential TPV heating system. They reported costs of the TPV system alone (without boiler) ranging from 340 €/kW_e to 3000 €/kW_e, depending on different scenarios.

Fraas *et al.* [10,11] developed a highly optimized TPV system based on a newly conceived generator designed to replace the residential furnace for household CHP. They reported a η_{TPV} equal to 10.8 % and a forecasting price of 1500 €/kW_e for the TPV system only.

In this paper, household gas-fired heating appliances converted into a TPV CHP system are taken into consideration. The main idea is to convert a condensing boiler with a Porous Radiant Burner (PRB), which is a widespread domestic boiler, into a TPV CHP system, by introducing PV cells inside the combustion chamber. Unlike conventional premixed combustion processes, PRB technology does not operate with a free flame: combustion takes place in the three-dimensional pores of a porous inert medium. In this way, a considerable part of the heat input is converted into radiation power. The system under consideration is sketched in Fig. 2. It consists of a PRB burner fed by a premixed fuel flow of air/natural gas. The burner is surrounded by an array of PV cells, which are capable of converting the radiation emitted by the burner into electricity.

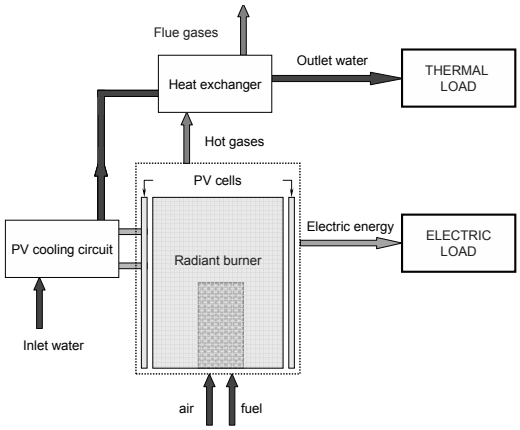

Figure 2. TPV microCHP system.

The thermal energy for space heating and hot water is obtained as in a common household boiler, i.e. by means of a heat exchanger embedded in the boiler itself. Moreover, since the PV cell arrays need a cooling system, the heat subtracted by the cells has to be recuperated by means of a dedicated cooling circuit, which is located on the water path.

4. TPV thermodynamics

The overall efficiency of a TPV systems is the product of four partial efficiencies (see Fig. 1):

$$\eta_{TPV} = \frac{P_e'}{P_f} = \eta_{rad}\,\eta_{sp}\,\eta_{vf}\,\eta_{pv} \qquad (1)$$

In the following, each contribution will be explained separately.

Radiant efficiency η_{rad}. In a combustion-driven TPV system, radiant efficiency represents the ratio between the broadband net radiant power output from the emitter to the fuel energy input and can be written as:

$$\eta_{\mathrm{rad}} = \frac{P_{\mathrm{rad}}}{P_{\mathrm{f}}} = \frac{p_{\mathrm{rad}} A_{\mathrm{rad}}}{m_{\mathrm{f}} LHV_{\mathrm{f}}} \quad (2)$$

where p_{rad} is the net radiant power density from the emitter, A_{rad} is the radiator area, m_{f} is the fuel mass flow rate and LHV_{f} is the fuel lower heating value. The radiation efficiency mainly depends on the type of emitter (porous or non-porous), its material and thickness, the combustion mode, the combustion intensity and the pre-heated air.

Spectral efficiency η_{sp}. The spectral efficiency refers to the ratio of the radiant power output with TPV cell convertible wavelength P_{gap} to the total radiant power emitted by the burner P_{rad}. Hence, it can be written as:

$$\eta_{\mathrm{sp}} = \frac{P_{\mathrm{gap}}}{P_{\mathrm{rad}}} = \frac{\int_{\lambda_0}^{\lambda_{\mathrm{gap}}} W_{\lambda \mathrm{b}}(\lambda, T)\tau(\lambda)\,\mathrm{d}\lambda}{p_{\mathrm{rad}}} \quad (3)$$

where τ is the transmittance of the filter (if present) and $W_{\lambda \mathrm{b}}$ is the radiator spectral distribution of emissive power. The frequency range (λ_0, λ_{gap}) defines the range of the photon energy convertible by the cells. If the emitter can be modeled as a blackbody, $W_{\lambda \mathrm{b}}$ can be evaluated according to Planck law.

View factor efficiency η_{vf}. The view factor efficiency takes into consideration that not all the radiant power output with TPV cell convertible wavelength (P_{gap}) would be incident on the cells, i.e.:

$$\eta_{\mathrm{VF}} = \frac{P_{\mathrm{gap}} - P_{\mathrm{d}}}{P_{\mathrm{gap}}} \quad (4)$$

The dispersed power (P_{d}) is essentially a function of the radiation view factors.

Cell efficiency η_{pv}. The cell efficiency is defined as the ratio of maximum electric power (P'_{e}) to the radiant power output with TPV cell convertible wavelength (P_{gap}), this latter term is reduced by the dispersed power:

$$\eta_{\mathrm{pv}} = \frac{P_{\mathrm{e}}^{'}}{P_{\mathrm{gap}} - P_{\mathrm{d}}} = \frac{p_{\mathrm{e}}^{'}}{p_{\mathrm{gap}} - p_{\mathrm{d}}} \quad (5)$$

This efficiency is a characteristic of the particular cell used and depends on a number of factors (net radiant incoming density power, emitter temperature, PV cell temperature, etc.).

5. Methodology and assumptions

The microCHP control logic defines the basis on which the prime mover is activated, deactivated or turned down. In general there are three types of control: time-led, heat-led, or electricity-led. A hybrid approach may also be adopted.

A TPV-based CHP system is a heat load following device and, thus, should be included in the second family of control logic. Hence, this mode of operation will set the boundary conditions and hypothesis for performance analysis.

The TPV system that will be considered is applied to a typical single household boiler (Fig. 2). A latest generation condensing natural gas boiler is considered herein. The boiler is a 25 kW domestic furnace with a turn-down ratio equal to 4:1 (minimum thermal power equal to 7 kW). Hence, the following hypotheses have been applied:

a) the boiler's nominal working power P_{f} is constant and equal to an annual averaged value $\tilde{P}_{\mathrm{f}}$.
b) all the radiant power emitted by the radiator is received by the cells, i.e. the total cell area is assumed at least equal to the radiator area;
c) since a heat-led domestic device is considered, the total annual thermal E_{t} demand is fixed and it represents the driving quantity which has to be supplied to the utility;
d) the overall TPV efficiency η_{TPV} is independent of the boiler's actual load and equal to an annual constant averaged value $\tilde{\eta}_{\mathrm{TPV}}$. In reality, as outlined above, the TPV efficiency is a function of the load, even though the variation of each term forming the TPV efficiency (Eq. (1)) as a function of the load is not straightforward and, what's more, these terms may even compensate each other;
e) the generated electric energy is self-consumed by the household. This is applicable since the daily generated electric energy is quite low. An electric converter (in this case, an inverter) from DC current (produced by the cells) to AC current has to be taken into account. The efficiency of this converter is considered constant and equal to an annual averaged value $\tilde{\eta}_{\mathrm{e.c.}}$.

Thermal energy. As outlined in the hypothesis, the thermal energy E_{t} is the total annual thermal demand, composed of hot water, space heating demands and general losses. This quantity ranges between the typical figures that can be encountered in practice. In Table 1, some example values for single households are reported.

Table 1 – Thermal demand (kWh/yr).

	Hot Water	Losses	Space heating	Thermal demand E_t
Italy A	1014	100	2240	3354
Italy B	2028	270	10200	12499
Sweden	3110	450	12220	15780
Denmark	3000	518	16201	19700

They refer to a single household in two Italian cases, a Danish case [12] and a Swedish case [13] found in literature. The two Italian cases refer to situations that represent apartments located in different climatic zones.

Electric energy. Recalling hypothesis a) to e), the electric energy E_e produced by the TPV system can be calculated as:

$$E_e = \tilde{\eta}_e \, E_f \tag{6}$$

where the electric efficiency $\tilde{\eta}_e$ is defined as:

$$\tilde{\eta}_e = \tilde{\eta}_{e.c.} \, \tilde{\eta}_{TPV} \tag{7}$$

The produced electric energy E_e can be also calculated as:

$$E_e = \tilde{P}_f \, \tilde{\eta}_e \, t_{op} = \frac{1}{t_{op}} \sum_{j=1}^{n} (P_f)_j (\eta_e)_j \Delta t_j \tag{8}$$

$$t_{op} = \sum_{j=1}^{n} \Delta t_j \tag{9}$$

In Eqs. (8) and (9), index *n* refers to the periods in which the annual load profile is divided in the calculation of the annual average load, i.e. *n* can be on a daily, weekly or monthly basis.

Energy consumption. Since a heat-led scenario is considered, E_t is fixed in order to assure the correct household heat request. Hence, the heat input to produce electricity by means of the TPV device has to provide extra fuel consumption. This extra consumption is readily calculated by considering that all the heat supplied to the PV cell and not used for electric power generation is recuperated. In fact, both the cell cooling water and the heat losses due to non-efficient radiation, spectral and view factor efficiency are used for useful water heating. Hence,

$$\Delta E_f = E_f \, \tilde{\eta}_{TPV} \tag{10}$$

The fuel energy consumption E_f results:

$$E_f = \frac{E_t}{\tilde{\eta}_{HE}} + \Delta E_f = \frac{E_t}{\tilde{\eta}_{HE}} + E_f \, \tilde{\eta}_{TPV} \tag{11}$$

Again, the averaged thermal efficiency of the heat exchanger (boiler) $\tilde{\eta}_{HE}$ can be calculated as

$$\tilde{\eta}_{HE} = \frac{1}{t_{op}} \sum_{j=1}^{n} (\eta_{HE})_j \, \Delta t_j \tag{12}$$

By manipulating Eq. (11), it is readily found that

$$E_f = \frac{E_t}{\tilde{\eta}_{HE}(1 - \tilde{\eta}_{TPV})} \tag{13}$$

In the case considered (a heat-led system), the total TPV CHP system operating hours t_{op} can now be indirectly calculated as the number of operating hours as the TPV system constantly worked through the year at the annual average operating power $\tilde{P}_f$, which corresponds to the energy E_f supplied by the fuel in one year to satisfy the thermal requirement E_t, i.e.

$$t_{op} = \frac{E_f}{\tilde{P}_f} \tag{14}$$

The PES (Primary Energy Saving) inedx is used as an energy performance parameter. The PES index can be written as:

$$PES = 1 - \frac{E_f}{\frac{E_e}{\eta^*_{el}} + \frac{E_t}{\eta^*_{th}}} \tag{15}$$

In [14], the microCHP unit can be considered as a "high efficiency cogeneration unit" when PES > 0. Regarding the reference value for the electric, η^*_e, and thermal, η^*_t, efficiencies, in [15] values are given as a function of the year of construction and type of fuel. Since newly constructed devices fed by natural gas are considered in this work, these values are $\eta^*_e = 0.525$ and $\eta^*_t = 0.90$. Rearranging Eq. (15) for a heat-led TPV system, the PES parameter can be written as

$$PES = 1 - \left[\frac{\tilde{\eta}_e}{\eta^*_e} + \frac{\tilde{\eta}_{HE}}{\eta^*_t} (1 - \tilde{\eta}_{TPV}) \right]^{-1} \tag{16}$$

Two corrections have been applied to the reference electric efficiency η^*_e: (i) a correction factor related to the average climatic situation and (ii) a correction factor for the avoided grid losses. In the first case, a 0.1 %-point efficiency loss/gain is accounted for every degree above/under 15 °C, respectively. In the second case, the correction factor depends on the voltage connection to the grid. In this case, the electricity is consumed on site (Voltage < 0.4 kV) and so the factor is equal to 0.860.

Besides, the PES parameter for energy performance evaluation, the Pay Back Period (PBP) is considered herein for economic evaluation. For the calculation of the discounted cumulative cash flow necessary to calculate the PBP, a discount rate of 5 % has been considered.

Finally, the cost of purchasing the natural gas has been kept constant and equal to 0.514 €/Sm^3, which represents a 2009 Italian residential tariff.

The numerical assumptions for the calculation are reported in Table 2. The reported values resemble a realistic situation.

6. Results and discussion

The energy and economic performances of the TPV system are presented.

For the PES calculation, three climatic scenarios are considered: an average climatic temperature @ 20 °C, @ 15 °C and @ 10 °C. In addition, the avoided grid loss correction factor equal to 0.860 applies (hypothesis (e) described above). Hence, the reference electric efficiency η^*_e values are $(0.447)_{@20\,°C}$, $(0.452)_{@15\,°C}$, $(0.456)_{@10°C}$.

For the PES and the PBP calculation, three different TPV efficiency scenarios are considered. They represent current achievable technology ($\tilde{\eta}_{TPV}$ = 5 %), medium period technology ($\tilde{\eta}_{TPV}$= 10 %) and long period technology ($\tilde{\eta}_{TPV}$ = 20 %).

The results in terms of PES are reported in Tab. 3. As can be seen, the TPV system based on the use of a condensing boiler can always be considered to have good energy performance. It can also be noticed that, since the system is a heat-load device, the PES is almost independent of the climatic zone considered. However, this is not valid for economic evaluation, when the thermal energy request is one of the key factors for TPV profitability, as will be seen in the following.

In Figs. 3 and 4, the economic performances of the TPV system are reported as look-up charts depending on five parameters:

- PBP. Two temporal horizons – 10-year and 20-year – have been considered for the economic profitability of the investment.
- Electric energy cost. This parameter has been varied within a current selling price (0.10 €/kWh) and a highly incentivized selling price (0.50 €/kWh). Between these figures, there is the actual saving due to electric self-consumption found in an Italy scenario (0.185 €/kWh).
- TPV efficiency, referred to the three scenarios described above ($\tilde{\eta}_{TPV}$ = 5 %, 10 % and 20 %).
- TPV specific cost. This cost does not include the cost of the boiler. In fact, a realistic scenario of TPV application is a new installation in substitution of a pre-existing boiler. This implies that the cost of the boiler is already perceived by the customer, while the TPV cost is a possible additional cost. The cost range considered (500 €/kW$_e$ to 4000 €/kW$_e$) can take two limiting cases into account: (i) the cost only includes the purchase of the TPV system alone (lower prices) and (ii) the cost includes the purchase of the inverter (higher prices). The purchase of the TPV system alone can be realistic in a context in which the TPV is installed in a utility where a PV solar system is already present (i.e. the inverter is already in use).
- Thermal energy demand E_t. Since TPV is a heat-led device, this can make a great difference in profitability. In fact, the higher E_t, the higher the yearly operating time t_{op} and, consequently, the production of electricity and saving in cost is also higher. The considered range has been widened to take different situations into account, from small thermal requirements (E_t = 10 MWh/yr) to medium-to-large thermal requirements (E_t = 100 MWh/yr).

By means of the figure reported, a parametric profitability analysis of the TPV system can be performed. For instance, it can be noted that, for the Italy B household reported in Table 1 and by considering current TPV efficiency ($\tilde{\eta}_{TPV}$ = 5 %), as well as the actual cost of electricity in Italy (0.185 €/kWh), a PBP equal to 10 years can be achieved if the TPV specific cost is approximately 680 €/kW$_e$.

Table 2 – Numerical assumptions

Parameter	Value
Yearly average thermal power $\tilde{P}_t$ [kW]	20
Yearly average boiler efficiency $\tilde{\eta}_{HE}$	93 %
Yearly average inverter efficiency $\tilde{\eta}_{e.c.}$	90 %
Discount rate	5 %
Natural gas specific cost [€/Sm^3]	0.514

Table 3 – PES results

	η_{TPV}		
	5 %	10 %	20 %
PES@10 °C	7.4	11.3	18.1
PES@15 °C	7.5	11.5	18.4
PES@20 °C	7.6	11.6	18.6

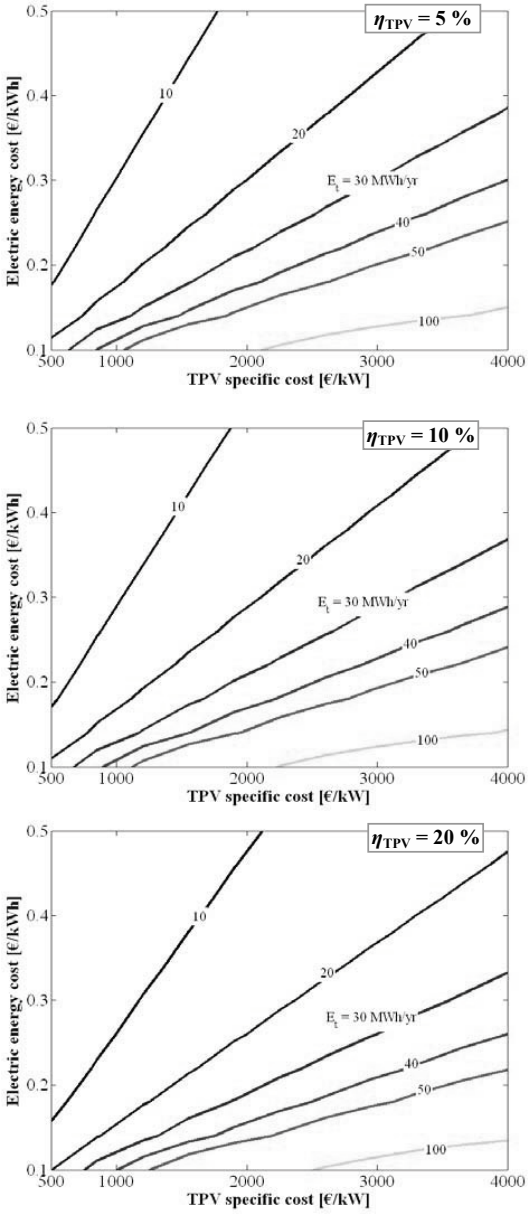

Figure 3. TPV look chart: PBP = 10 year.

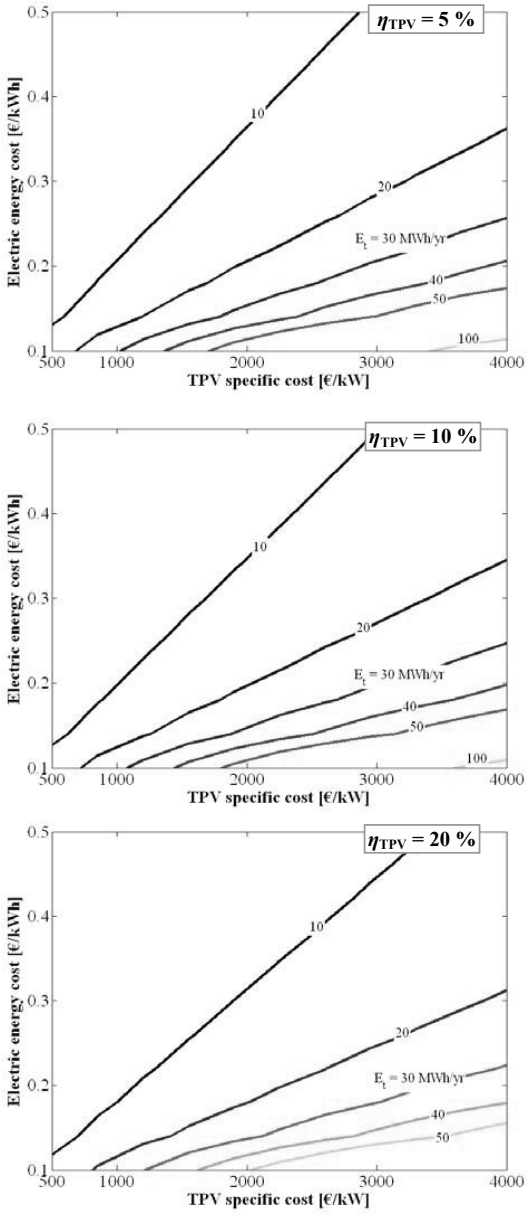

Figure 4. TPV look chart: PBP = 20 year.

On the contrary, with the same assumptions, Italy A household (which is representative of a South region scenario) cannot achieve neither a 10-year PBP performance nor a 20-year PBP with a comparable TPV specific cost.

On the other hand, for a E_t significantly high but still realistic (i.e. 50 MWh/yr), a 10-year profitability can be achieved even if the TPV specific cost is as high as about 2700 €/kW$_e$.

7. Final remarks

MicroCHP innovative technology based on predominant heat production, such as TPV systems, can have great potential as an application in the domestic sector. However, in this paper it is shown that, although energy performance in terms of primary energy saving can be quite easily achieved, economic profitability is difficult to reach, in particular in temperate climate scenarios.

For this reason, if microCHP option is chosen for greenhouse effect mitigation and electric energy provision independence, incentives should be tailored on specific conversion technology, in order to promote the most efficient technology within the specific application (e.g. domestic sector, etc.).

Nomenclature

A	area, cm^2
E	energy, MWh, kWh, eV
LHV	Lower Heating Value, kJ/kg
m	mass flow rate, kg/s
n	number of periods
p	power density kW/cm^2
P	power, kW
t	time, h
W	emissive power, $kW/(m^2\ \mu m)$

Greek symbol

λ	wavelength, μm
η	efficiency, %

Subscripts, superscripts

~	yearly averaged
*	reference value
c	combustion
e.c.	electric converter
HE	Heat Exchanger
d	dispersed
e	electric
f	fuel
gap	gap
op	operating hour
t	thermal
rad	radiation, radiator
sp	spectral
TPV	thermophotovoltaic
vf	view factor

References

[1] Coutts, T.J., 2001, An overview of thermophotovoltaic generation of electricity, Solar Energy Mater. Sol. Cells, 66, pp.443-452.

[2] Peacock, A.D., and Newborough, M., 2005, Impact of micro-CHP systems on domestic sector CO_2 emissions, App. Therm. Eng., 25, pp. 2653-2676.

[3] Qiu K., and Hayden A.C.S, 2007, Thermophotovoltaic power generation systems using natural gas-fired radiant burners, Solar Energy Mater. Sol. Cells, 91, pp. 588-596.

[4] Qiu K., and Hayden A.C.S, 2003, Thermophotovoltaic generation of electricity in a gas fired heater: Influence of radiant burner configurations and combustion processes, Energy Convers. Manage., 44, pp. 2779-2789.

[5] Qiu K., and Hayden A.C.S, 2003, Performance of low bandgap thermophotovoltaic cells in a small cogeneration system, Solar En., 74, pp. 489-495.

[6] Qiu K., and Hayden A.C.S, 2006, Development of a silicon concentrator solar cell based TPV power system, Energy Convers. Manage., 47, pp. 365-376.

[7] Qiu K., et al., 2006, Generation of electricity using InGaAsSb and GaSbTPV cells in combustion-driven radiant sources, Solar Energy Mater. Sol. Cells, 90, pp. 68-81,

[8] Durisch, W., et al., 2003, Small thermophotovoltaic prototype systems, Sol. Energy, 75, pp. 11-15

[9] Palfinger, G., et al., 2003, Cost estimate of electricity produced by TPV, Semicond. Sci. Technol., 18, pp. 254-261.

[10] Fraas, L.M., et al., 2003, TPV generators using the radiant tube burner configuration, *Proc. 17th European Photovoltaic Solar Energy Conf.*

[11] Fraas, L.M., et al., 2003, Thermophotovoltaic furnace–generator for the home using low bandgap GaSb cells, Semicond. Sci. Technol., 18, pp. 247-253

[12] Thur, A., Furbo, S., and Jivan Shah, L., 2006, Energy savings for solar heating systems, Sol. Energy, 80, pp. 1463-1474.

[13] Persson, T., and Ronnelid, M., 2007, Increasing solar gains by using hot water to heat dishwashers and washing machines App. Therm. Eng., 27, pp. 646-657

[14] European Directive 2004/8/EC

[15] Decision 2007/74/EC

Acknowledgments: This paper was carried out within the framework of the 2007 PRIN national research project funded by MIUR.

Exergy Analysis of Single and Double-Flash Geothermal Power Plants

Coviello Marco[a], Manfrida Giampaolo[a]

[a] *Università degli Studi di Firenze, Dipartimento di Energetica "Sergio Stecco"*
Via C. Lombroso 6/17 – 50135 Firenze - Italy

Abstract: A detailed exergy analysis of single-flash and double-flash geothermal power plants is presented. The reasons that lead to optimization of performance in terms of maximum power output are discussed from a second-law perspective. The re-injection of large flow rates of hot drain, and the circulation of large quantities of cooling water at the condenser/cooling tower system represent the most relevant exergy losses. Double-flashing is confirmed as an effective means for performance improvement.

Keywords: Geothermal Power, Single-flash, Double-flash, Exergy.

1. Introduction

Geothermal Power is experiencing a large development in many countries, with an overall worldwide installed capacity of about 10,000 MW_e [1, 2]. Of these, most use pressurized hot water geothermal resources, with about 42% of the power at world level provided by single-flash systems, and 23% by double-flash plants.

The thermodynamic conditions (pressure and temperature) of the geothermal resource determine an upper limit even for reversibly-operating cycle and equipment, which – depending on resource parameters – seldom exceeds 10 % [1, 3]. The real situation is conditioned by the presence of one or more water flashes, by the circulation of extensive water flow rates in the cooling towers/condenser circuits, and by the need for re-injection of large quantities of hot drains: this determines a further decrease of the conversion efficiency of these plants. In order to ensure the best exploitation of the resource, it is important to perform a detailed thermodynamic analysis of the system, and to understand the possible ways of reducing inefficiencies.

2. Single-Flash Plant

The schematic of the reference single-flash plant is shown in Figure 1. A surface condenser is coupled to a cooling tower in order to ensure heat rejection to the environment. The water supply for the tower is ensured by extensive recirculation of the condensed drain from the geothermal fluid at turbine discharge, so that the plant can be considered self-sufficient for cooling water supply.

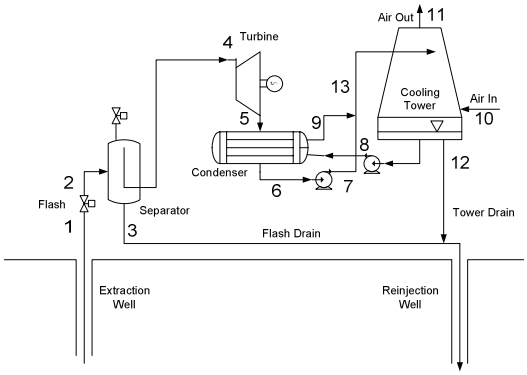

Fig. 1. Single-Flash Power Plant Layout

The operating thermodynamic cycle is shown in Figure 2.

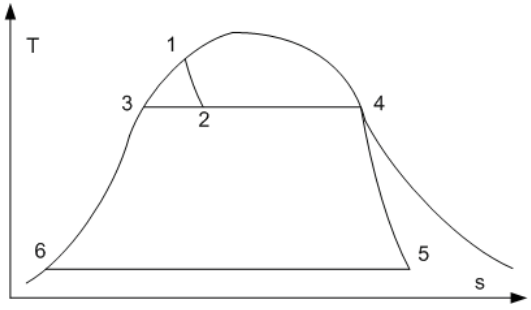

Fig.2. Single-Flash – Thermodynamic Cycle

The flow rate m_1 which can be extracted from the well depends on the well productivity curve, which gives the flow rate vs. the pressure at the separator [1]. The flash process is treated conserving enthalpy:

$$h_2 = h_1 \quad (1)$$

While entropy s_2 is determined at pressure p_2 using equation 1. Point 4 (Turbine inlet) is in saturated steam conditions at $p_4 = p_2$, with a mass flow rate given by:

$$m_4 = m_1 \cdot x_2 \quad (2)$$

The drain is produced at the bottom of the separator in saturated liquid conditions at $p_3 = p_2$, with a mass flow rate given by:

$$m_3 = m_1 \cdot (1 - x_2) \quad (3)$$

The turbine power is given by:

$$W = m_4 (h_4 - h_5) \quad (4)$$

The condenser/cooling tower heat rejection subsystem is solved by a set of equations:

$$Q_c = m_4 \cdot (h_5 - h_6) \quad (5)$$

$$m_8 = \frac{Q_c}{h_9 - h_8} \quad (6)$$

$$h_{13} = \frac{m_4 \cdot h_7 + m_8 \cdot h_9}{m_{13}} \quad (7)$$

$$T_8 = T_{wb} + DT_{Approach} \quad (8)$$

$$T_{13} = T_8 + DT_{Range} \quad (9)$$

$$m_{13} = m_4 + m_8 \quad (10)$$

$$m_a (h_{11} - h_{10}) = m_{13} h_{11} - m_8 h_8 - m_{12} h_{12} \quad (11)$$

$$m_{12} + m_8 = m_{13} - m_a (w_{11} - w_{10}) \quad (12)$$

In the preceding equations, all streams are considered as water/steam, apart of streams 10 and 11 which are humid air streams (10 = ambient conditions, 11 = saturated air at tower outlet). Equation 7 represents the tower/condenser mixing node energy balance; Equation 11 is the cooling tower energy balance. Equation 12 represents the tower water mass balance – accordingly, the tower evaporation make-up is subtracted from the liquid flow rate at point 13 .

After solving the set of equations 1-12, the condenser and cooling tower are preliminarily sized, knowing the condenser coolant flow rate and the air flow rate inside the tower. A simplified model using a mixing-type condenser coupled to the cooling tower was also realized.

The set of preceding equations, together with local property calculation, allows to solve the system and determine the plant performance. Typically, a parametric analysis in function of the separator pressure is run, leading to results shown in Figure 3 a and b, respectively for non-choked and choked well operating conditions[1] [1].

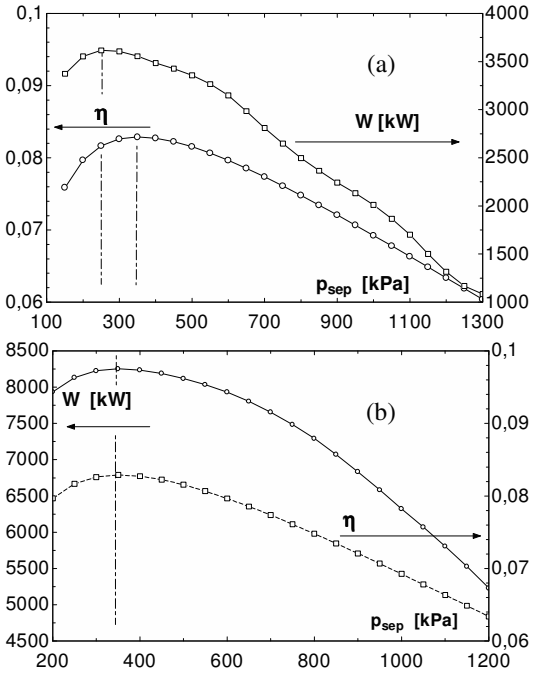

Fig.3. Single-Flash – Power and efficiency vs. p_{sep}; (a) Non-choked well (b) Choked well.

Figure 3 shows that a maximum condition occurs [1], both for work output and efficiency (in the case of the non-choked well, the location of the maximum is significantly different considering either work or efficiency). From an energy analysis point of view, this result is determined by the combined effect of the well productivity curve and of the cycle performance. Exergy analysis [4-

[1] A well is defined as Choked or Non-Choked depending on whether the flash of the pressurized geothermal fluid in liquid conditions – sometimes physically occurring within the well itself – produces respectively a choked or non-choked steam flow rate [1]

9] can help in determining the reasons behind the optimization. The exergy input to the system is:

$$E_{in} = E_1 = m_1 \varepsilon_1 \quad (13)$$

Where the specific exergy ε is calculated for each point as:

$$\varepsilon = (h-h_0) - T_0 (s-s_0) \quad (14)$$

The reference conditions were systematically adjusted to JANAF tables, which is necessary as a part of the system (cooling tower) is working with a humid mixture of air and water vapor. Similarly exergy flows were computed for all calculated points of the cycle (Figure 1). The exergy output is from this plant is the power produced W, so that:

$$\eta_{xD} = \frac{W}{E_{in}} \quad (15)$$

The system is divided into 8 contributions to Exergy Destruction/Loss[2], namely:

EXD_{Flash}, EXD_T, EXD_C, EXL_{Tow}, EXL_{FD}, EXD_{TD}, EXD_{Mix}, EXD_P

All exergy destructions were calculated by differences of exergy fluxes (in-out); exergy losses were accounted as complete loss of the exergy stream to the environment. Once all the 8 exergy destruction/losses are calculated, the indirect exergy efficiency is given by:

$$\eta_{xInd} = 1 - \sum_{i=1}^{8} \frac{EXDL_i}{E_{in}} \quad (15)$$

A typical exergy balance of the system, under optimized conditions for p_C = 12,3 kPa, leading to an optimum for p_{SEP} = 350 kPa (Figure 3) is shown in Figure 4.

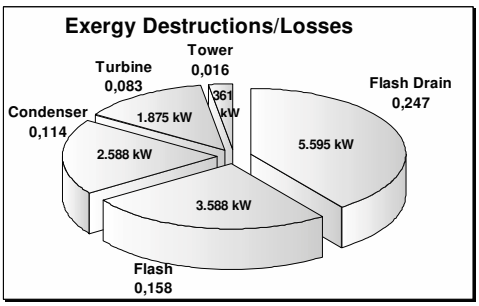

Fig. 4. Single-Flash – Exergy balance. Choked well; p_C = 12,3 Pa; optimized at p_{sep} = 350 kPa; η_x= 0,38.

[2] Throughout this paper the terms Exergy Destruction EXD and Exergy Loss EXL are not a synonym; the reader is directed to Ref. 4 for the different meaning of EXD and EXL.

The reference conditions/parameters assumed are summarized in Table 1. It is clear that the flash EXD [3] and the flash drain EXL [4] connected to reinjection of the hot drain are the most relevant contributions.

It is also interesting to notice that improvement of cycle parameters can influence strongly both the exergy balance and the overall system optimization. As an example, if the condenser pressure is lowered to p_C = 5,5 kPa, the exergy balance is modified as in Figure 5. It is evident that the condenser exergy destruction is much lower than in the case of Figure 4.

Description	Symbol	Value
Well max temperature	T_W	240 °C
Ref./Ambient Temperature	T_0	25°C
Relative Humidity	φ	0,6
Tower approach	DT_{Appr}	5°C
Tower/Condenser Range	DT_R	10°C
Turbine efficiency (dry)	η_T	0,85
Pump efficiency	η_P	0,8

Table 1. Reference conditions/assumed parameters

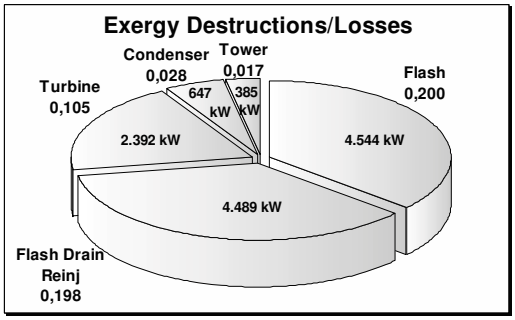

Fig. 5. Single-Flash – Exergy balance. Choked well; p_C = 5,5 kPa ; optimized at p_{sep} = 250 kPa; η_x= 0,45.

3. Double-flash Plant

Multiple flashing is an evident way of improving the utilization of geothermal resources of

[3] That is, the EXD connected to irreversibility in the flash process, which is treated as constant-enthalpy

[4] That is, the EXL connected to release to the environment (re-injection) of the hot stream of drain water

pressurized hot water. The schematic of a double-flash geothermal energy conversion system is shown in Figure 6; the thermodynamic cycle is represented in Figure 7. The governing equations are similar to those introduced for the single-flash thermodynamic model. The flow rate at the second flash (Separator 2) is given by:

$$m_5 = m_3 \cdot (1 - x_{18}) \tag{16}$$

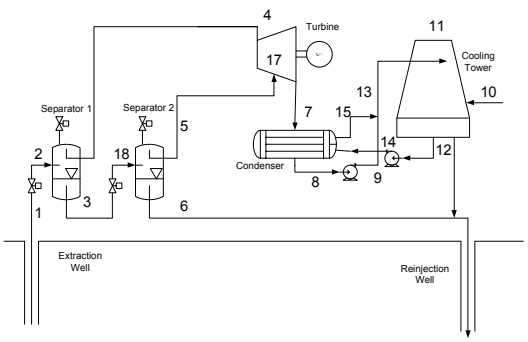

Fig. 6. Double-Flash Power Plant Layout

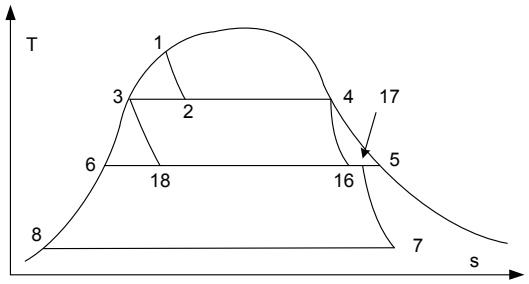

Fig.7. Double-Flash – Thermodynamic Cycle

The low-pressure (LP) turbine power output can be calculated as:

$$W = m_4(h_4 - h_{16}) + m_{17}(h_{17} - h_7) \tag{17}$$

with the LP inlet conditions provided by the mixing energy balance:

$$h_{17} = \frac{(m_4\, h_{16} + m_5\, h_5)}{(m_4 + m_5)} \tag{18}$$

together with the mass balance:

$$m_{17} = m_4 + m_5 \tag{19}$$

The addition of the second flash implies evaluation of two separate exergy destructions for the HP and LP turbines, EXD_{HPT} and EXD_{LPT}; and of two flash exergy destructions, EXD_{Flash1} and EXD_{Flash2}. The methodology is the same as for the single-flash case.

The results of the exergy balance (for the case of choked well) are shown in Figure 8. Figure 9 demonstrates the advantage of lowering the condenser operation pressure (with a larger sizing of condenser and cooling tower).

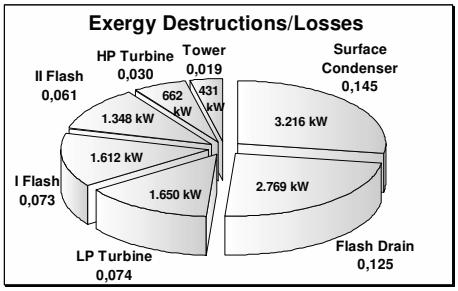

Fig.8. Double-Flash – Exergy balance. Choked well; p_C = 12,3 kPa; optimized η_x= 0,47 at p_{sep1} = 800 kPa; p_{SEP2} = 127 kPa.

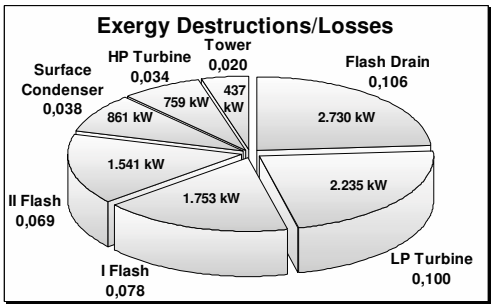

Fig.9. Double-Flash – Exergy balance. Choked well; p_C = 5,5 kPa; optimized η_x= 0,55 at p_{SEP1} = 750 kPa; p_{SEP2} = 102 kPa.

In the case of the double-flash plant, the values of p_{SEP1} and p_{SEP2} are inter-dependent, so that the choice of the second flash pressure must be adjusted to that of the first one (Figure 10); however, one should also consider that the size of equipment (piping, flash drum dimensions, valves) is increased at lower pressures, so that it can be convenient to accept a slightly lower performance if this is compensated by a smaller size of the equipment, which is possible selecting slightly higher well pressures ($p_{SEP1} \cong 850$ kPa, $p_{SEP2} \cong 180$ kPa).

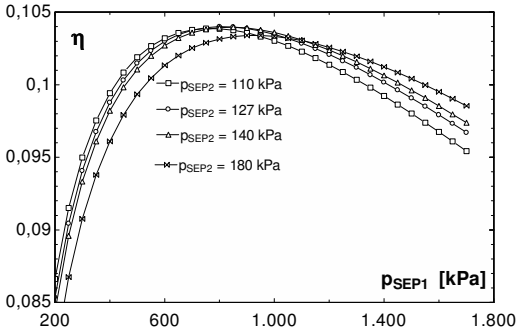

Fig.10. Double-Flash – Cycle efficiency. Choked well; Influence of second flash pressure.

4. Conclusions

Thermodynamic models for single-flash and double-flash geothermal energy conversion systems have been presented. The models include the combined effects of the well productivity curve and of the cycle efficiency.

A detailed exergy analysis, allowing calculation of exergy destructions and losses, has allowed to confirm that the reinjection of the warm drain represents, together with the flash irreversibility, the largest contributions to exergy destruction/loss to the environment. However, the condenser exergy loss must not be disregarded, as it can be noticeably reduced with a larger investment on the condenser/cooling tower subsystem.

Using a double-flash system is an effective way of improving the system performance, which is confirmed both by the increased work output and efficiency, and by the significantly higher achieved exergy efficiency. It is interesting to notice that, even if the overall efficiency is limited on account of the Carnot limit imposed by the use of a low-temperature resource, the exergy efficiency achieves in a double-flash geothermal power plant values in the range of 50%, which can be considered relatively high taking into account the limited complexity of the power plant.

List of symbols

DT Temperature difference,°C
E Exergy, kW
EXDL Exergy Destruction or Loss, kW
h Enthalpy, kJ/(kg K)
m Mass flow rate, kg/s
p Pressure, kPa
Q Heat rate, kW
T Temperature, °C
x Quality of steam
w Specific humidity, kg steam/kg dry air
W Power, kW
ε Specific exergy, kJ/kg
η Efficiency
φ Relative Humidity

Subscripts:

a dry air (cooling tower)
Appr Approach value (cooling tower)
C Condenser
Flash Flash
FD Flash Drain (from separator)
in Inlet
MIX Mixing node, 13-8-9 (condenser/tower)
P Pump
R Range (condenser/cooling tower)
T Turbine
Tow Tower
TD Tower Drain
W Well conditions
0 Reference state

References

[1] Di Pippo, R., 2006, *Geothermal Power Plants: Principles, Applications and Case Studies*. Elsevier Advanced Technology, London, UK.

[2] MIT panel, 2006, The future of Geothermal Energy, http://geothermal.inel.gov

[3] Griggs, J., 2002, A re-evaluation of geopressured geothermal aquifers as an energy resource, MSc Thesis, Louisiana State University.

[4] Bejan, A., Tsatsaronis, G., Moran, M., 1996, *Thermal Design and Optimization*, Wiley Interscience, New York.

[5] Kotas T. J., 1995, *The exergy method of thermal plant analysis*, Krieger, New York.

[6] Szargut, J., Morris, D.R., Stewart, F.R., 1998, Exergy analysis of thermal, chemical and metallurgical processes", Hemisphere.

[7] Moran, M., 1982, *Availability Analysis: A Guide to Efficient Energy Usage*, Prentice-Hall.

[8] Ahern, J. E., 1980, *The* Exergy *Method of Energy System Analysis* , Wiley.

[9] Kanoglu, M., Dincer, I., Rosen, M. A., 2007, Understanding energy and exergy efficiencies for improved energy management in power plants, Energy Policy, 35, 3967–3978

[10] Chase, M.W. (Ed.), 1998, *NIST-JANAF Thermochemical Tables*, Journal of Physical and Chemical Reference Data, Monograph 9.

Experimental investigation of the absorption enhanced reforming of biomass in a 20 kW_{th} dual fluidized bed system

Norman Poboss, Karolina Swiecki, Alexander Charitos, Craig Hawthorne, Anja Schuster, Günter Scheffknecht*

Institute of Combustion and Power Plant Technology (IFK), University of Stuttgart, Germany

Abstract: A gasification product gas with a hydrogen content over 75 vol-%$_{db}$ and a heating value of 15 MJ/m³$_{STP,db}$ has been obtained through the absorption enhanced reforming of biomass. The Absorption Enhanced Reforming (AER) process involves a Dual Fluidized Bed (DFB) system consisting of a gasifier and a regenerator (calciner). In the DFB system, the Ca - looping ratio is an important parameter defined as the ratio of the molar flow rate of regenerated sorbent (F_{Ca}) and carbon (F_c) which enters the gasifier as fuel. A special feature of the 20 kW_{th} DFB test facility at IFK is the Ca - looping rate control through a cone valve. Therefore, the Ca - looping ratio (F_{Ca}/F_C) was varied between a value of 2 and 15 mol_{CaO}/mol_C to investigate its influence on the cold gas efficiency, product gas yield, yield of gas components and gravimetric tar concentration during the AER of biomass. The experiments were carried out with wood pellets and a Greek limestone as CO_2 sorbent. The experimental work shows a clear influence of the Ca - looping ratio on the AER process. It shows also that beyond a certain value of this parameter, the tar and gas composition is stabilized.

Keywords: Steam gasification, Biomass, Tar, Dual fluidized bed gasifier, CO_2 capture, Hydrogen

1. Introduction

1.1. Dual Fluidized Bed Biomass Steam Gasification

The main biomass steam gasification reactions are listed in Table 1. These reactions are mainly endothermic, therefore heat is required to sustain the gasification process. This heat can be provided through two different approaches: by partial fuel oxidation (autothermal gasification), or externally via heat carrier or heat exchanger (allothermal gasification). Absorption enhanced reforming is an allothermal gasification process.

Table 1. Main biomass steam gasification reactions, [1], [2].

Name of reaction	Chemical equation	ΔH^0_{923} kJ/mol	Eq
Biomass reforming	$C_nH_m + nH_2O \rightarrow nCO + \left(\frac{m}{2} + n\right)H_2$	$+\Delta H$	(1)
Water-gas- shift	$CO + H_2O \leftrightarrow CO_2 + H_2$	-41	(2)
Water-gas (i)	$C + H_2O \leftrightarrow CO + H_2$	+131	(3)
Water-gas (ii)	$C + 2H_2O \leftrightarrow CO_2 + 2H_2$	+100	(4)
Boudouard	$C + CO_2 \leftrightarrow 2CO$	+173	(5)
CO methanation	$CO + 3H_2 \leftrightarrow CH_4 + H_2O$	-206	(6)
CO_2 methanation	$CO_2 + 4H_2 \leftrightarrow CH_4 + 2H_2O$	-165	(7)

During allothermal gasification pure steam can be used as the gasification agent leading to a medium calorific value product gas (12-14 MJ/m³$_{STP}$) with a hydrogen content of 40-60 vol-%$_{db}$ [3, 4]. The required heat to the gasifier can be provided by the following steps: (i) transportation of the char generated in the gasifier into a combustion chamber, (ii) combustion of the generated char in the combustion chamber, (iii) transfer of the generated heat from the combustion chamber to the gasifier through solid circulation [5].

This leads to a gasifier system, consisting of a biomass steam gasifier and a char combustion chamber. Additionally, a transport pipe is needed to transfer the heat carrier solids between the reactors. The transport pipe has to ensure gas sealing between the gasifier and the combustor.

Such gasifier systems can be realized by a Dual Fluidized Bed (DFB) system consisting of a Bubbling Fluidized Bed (BFB) as the gasifier and a Circulating Fluidized Bed (CFB) as the combustor. The acronym DFB used to describe these systems, is well established [5].

A 8 MW_{th} DFB steam gasifier with combined heat and power (CHP) has been operating in Güssing since 2002 with Olivine as circulating bed material [6]. Based on this principle a 9 MW_{th} CHP DFB gasifier was constructed in 2009 in Oberwart [7].

Corresponding Author: Norman Poboss, Email: norman.poboss@ifk.uni-stuttgart.de

1.2. Absorption Enhanced Reforming (AER)

The hydrogen concentration of the product gas, during allothermal biomass gasification with pure steam, can be enhanced by using a CO_2 absorbing sorbent, e.g. CaO. Thereby, the CO_2 is captured in situ (8) after it is produced (2). This exothermic removal of the CO_2 leads to a shifting of the water-gas-shift reaction to the product side (2). Therefore, all parallel reforming reactions are influenced, resulting in an enhanced H_2 output.

$$CaO_{(s)} + CO_{2,(g)} \leftrightarrow CaCO_{3,(s)} \quad (8)$$

The CO_2/CaO-equilibrium (8) strongly depends on the process temperature at atmospheric conditions. The CO_2 capture takes place between 450 °C to 750 °C [1]. Above 750 °C, CO_2 can not be captured whereas at a temperature above 800 °C $CaCO_3$ is regenerated to CaO, while CO_2 is released. The gasification temperature should be as high as possible from the view of carbon conversion and tar formation. However, the thermodynamic boundary conditions from the CO_2/CaO-equilibrium for CO_2 capture leads to an operating window between 650 °C and 725 °C.

Additionally, by using CaO, the CO_2 capture releases heat in the gasifier which decreases the need for heat, transported by the circulating bed material [4]. The endothermic regeneration takes place in the combustion chamber at 850 °C to 900 °C. The necessary heat for regeneration is supplied by the combustion of the unconverted char, which is transferred together with the bed material (mixture of CaO, $CaCO_3$ and ash). The principle of the absorption enhanced reforming with circulating Ca - based bed material in a dual reactor system is shown in Fig.1.

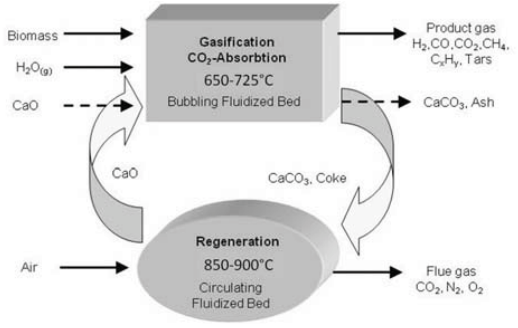

Fig. 1. Principle of the absorption enhanced reforming (AER)

In literature, there are a number of different criteria in order to assess the efficiency of a gasification process. Recommended criteria are carbon conversion and cold gas efficiency (CGE), also found in literature as chemical efficiency [2]. The efficiency of a H_2 - production process via gasification, by calculating the thermal efficiency, was analyzed in [1]. The thermal efficiency is based on the chemical efficiency and is defined as the ratio of the energy output obtained from the H_2 produced (deducting the heat, necessary to drive the reaction process) and the biomass energy input to the system. In addition to the CGE criteria, the gas composition and quality (tar loading and trace pollutants) are necessary to determine the gas cleaning and utilization requirements in order to evaluate the effectiveness of the AER process. In this paper the effectiveness of the AER process is evaluated, based on the CGE, the gas composition (especially H_2 concentration) gas yield and gravimetric tar concentration in the product gas.

The quality of the gas and the efficiency of the process are affected by variation of process parameters, e.g. gasification temperature, biomass and bed composition, steam to biomass-carbon ratio (S/C), weight hourly space velocity (WHSV). Regarding to parameter variation extensive research was conducted in the past. However, this research focused on conventional biomass steam gasification. A summary, regarding 12 variables that influence the effectiveness of the conventional biomass gasifier, was published in [3].

One of the key parameter for the DFB AER process is the Ca - looping rate of the sorbent material between the gasifier and the combustor. The influences of this parameter on the cold gas efficiency (CGE), the product gas composition, product gas yield and the tar concentration are analyzed in [3, 5, 8].

1.3. The Ca - looping Rate and the Role of CaO in the AER Gasifier

As has been shown in many studies, the carbonation reaction is not fully reversible and a sorbent particle exhibits a maximum carbonation conversion (X_{max}) which decays with increasing carbonation-calcination cycles [9]. Moreover, the actual carbonation conversion of a sorbent particle (X_{carb}) during the AER process is always smaller than X_{max}. The difference between the maximum carbonation conversion (X_{max}) and the actual carbonation conversion (X_{carb}) of a sorbent particle

is termed as the free active CaO (f_a) [10]. The f_a has been shown to be the key factor in influencing the carbonation reaction rate and hence CO_2 capture efficiency [10, 11]. It has also been shown, that the Ca - looping ratio is inversely proportional to the actual carbonation conversion (X_{carb}) [11]. This means, that increased Ca - looping ratio leads to higher CO_2 conversion and therefore, in theory, to higher H_2 concentration through the water – gas - shift reaction. Post - combustion CO_2 capture experimentation conducted in the same DFB system as used here, has shown that a minimum molar Ca - looping ratio of $F_{Ca}/F_C = 6$ mol_{CaO}/mol_C is needed to achieve a CO_2 capture efficiency over 80 % [11]. Additionally, unreacted CaO is a catalyst in steam reforming reactions of tar as generally described in (9) [12]. During these reactions different types of tar, which are created at 650 °C (standard AER conditions), are catalytically cracked and steam reformed to H_2 and coke. The created coke covers the surface of the CaO, which leads to a deactivation of the ongoing tar catalysis and prevents CO_2 absorption.

$$tar + H_2O \xrightarrow{CaO} H_2 + CO + coke\ (on\ CaO) \quad (9)$$

Summarizing, the information above suggests that the Ca - looping ratio in a DFB system effects CO_2 capture, H_2 production and tar cracking.

A very important variable is also the turnover time of the bed material. The turnover time τ_{Bed}, shown in (10), is interconnected with the Ca - looping rate G_{CaO} (mass flow of CaO to the gasifier, kg/h) and the total mass of bed material in the gasifier.

$$\tau_{Bed} = \frac{W_{Bed}}{G_{CaO}} \quad (10)$$

A high Ca - looping rate between the beds and therefore a small turnover time could lead to a low residence time of the biomass char in the gasifier. The char and unconverted biomass is transported out of the gasifier together with the bed material. This may result in a low carbon conversion and low CGE. Moreover, a high Ca - looping rate would lead to a high demand of energy in the reactor to heat up the solids to calcination temperature (ca. 850 °C). Therefore, a high amount of char or extra fuel would be needed. The aim of this experimental work is to determine the minimum Ca - looping ratio required to ensure sufficient CO_2 capture for maximum hydrogen yield in the product gas and minimum tar concentration during the AER process in a DFB. The dimensionless calcium looping ratio was therefore varied in this work in the range of 2 to 15 mol_{CaO}/mol_C, resulting in a turnover time of the bed material between 1 and 10 minutes.

2. Experimental

2.1. Description of the 20 kW_{th} DFB Gasifier at IFK

A DFB facility has been built at IFK, consisting of a CFB regenerator with 12.4 m height and 7.0 cm diameter and a BFB gasifier with 3.5 m height and 11.4 cm diameter. The DFB facility is shown schematically in Fig. 2. The design and hydrodynamic suitability of the facility is based on fundamental research, regarding post-combustion CO_2 capture with CaO as the sorbent bed material [13, 14]. Therefore, the reactor design is well transferable to the AER process. The feeding system of biomass and of steam as fluidization agent as well as the measurement techniques had to be adapted. The BFB is used as the gasifier (a) and the riser as the CFB regenerator (b). Both reactors, standpipes and loop seals are electrically heated.

The CaO bed material is transported between the gasifier and combustor-regenerator, allowing for continuous operation of the AER process. The Ca - looping rate is controlled by varying the cone valve (d), opening and the BFB absolute pressure through a pressure control valve (e) in the range of 0 to 100 mbar. By closing the cone valve completely, the bed material is only circulating within the internal loop of the regenerator and no regenerated bed material is provided to the gasifier.

Preheated steam and carrier nitrogen gas from the biomass dosing unit, together with the regenerated CaO, coming from the double exit loop seal (c) through the cone valve (d) enter the BFB gasifier. The maximum height of the bed in the gasifier is limited by an overflow, located 50.0 cm above the BFB distributor (f). The char and partially carbonated CaO exits the gasifier through this overflow, enters the lower standpipe (g) and subsequently the lower loop seal (h), through which the sorbent flow proceeds to the CFB regenerator. The regenerator off gas proceeds to the stack while the riser entrainment is separated in a cyclone (i), proceeds to the upper standpipe (j) and reaches the double exit loop seal (c). The desired Ca - looping rate proceeds to the BFB gasifier and the rest of the flow goes through the

loop seal weir (k) into the internal loop and returns to the regenerator.

The product gas from the gasifier is stripped from particles via a cyclone and candle filter. It is analyzed and afterwards burned.

The upper and lower loop seal are fluidized with nitrogen gas. Nitrogen gas flows in the loop seals as well as the carrier gas in the feeding system leads to a dilution of the product gas. Because of the danger of plugging in the quartz glass standpipe segments (g), it was not possible to perform fluidization of the loop seals with steam. In a commercial DFB the loop seals will be fluidized with steam to avoid this dilution. Moreover, the commercial feeding system is designed as plug screw to avoid back flushing. Therefore, reporting the nitrogen free product gas concentration in this work is appropriate.

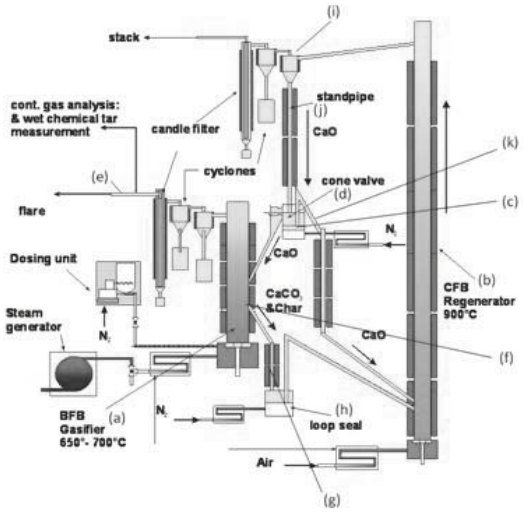

Fig. 2. Scheme of IFK DFB gasifier facility: (a) BFB gasifier, (b) CFB riser regenerator, (c) double exit loop seal, (d) cone valve, (e) pressure control valve, (f) BFB overflow, (g) lower quartz glass standpipe segments, (h) lower loop seal, (i) CFB cyclone, (j) upper standpipe, (k) loop seal weir

2.2. Measurement Technique

All operational and measurement parameters, namely temperature, pressure, opening of the cone valve and gas concentrations are displayed and recorded by a data logging program Labview®. Pressure and temperature are measured at five positions along the gasifier.

A by-pass of the product gas is analyzed, regarding non-condensable and condensable gas components as well as tars. The non-condensable gas compounds CO, CO_2, CH_4, O_2, and H_2 are measured by the online-measurement device Advance Optima of the Swiss company ABB. The non-condensable hydrocarbons (C_1 till C_6) in the product gas can be measured discontinuously by a micro gas chromatograph. The non-condensable gas compounds CO, CO_2, O_2 of the regenerator off gas are measured also by an online-measurement device Advance Optima of the Swiss company ABB.

The total gas flow rate of the product gas is measured via a gas meter for 5 minutes. In this time the condensed water is collected to calculate the steam content in the product gas.

The Ca - looping rate of the bed material between the gasifier and the regenerator is measured manually. Therefore, the fluidization of the lower loop seal has to be interrupted for the measuring period. When the fluidization of the lower loop seal is interrupted, the quartz glass segment of the lower standpipe fills with bed material, exiting the gasifier. The dimensions of the quartz glass segment and the density of the bed material are known. Hence, by measuring the time till the bed material increases to a certain height in the standpipe, the calcium looping rate G_{CaO} between gasifier and regenerator can be calculated.

The European Committee for Standardization (CEN) provides the most suitable analyzing methods for the investigation of tar during biomass gasification. These methods are a guideline to assure a quantitatively and qualitatively high standard of measurement as well as international comparability. The tar sampling method during the experimental work at IFK, presented in this paper, follows the recommendation of this Tar Guideline [15].

2.3. Procedure

The experiment starts with pre-calcination of the bed material in batch mode at 875 °C. Approximately 15 kg of the pre-calcined bed material are filled into the DFB system for start-up. After fluidizing the regenerator with air, the gasifier with steam and the upper and lower loop seals with nitrogen, the Ca - looping rate between the reactors is initiated by opening the cone valve. The Ca - looping rate between the beds is than measured and adjusted. Next, the fuel feeding is

started. A steady-state operation is reached as soon as the product gas composition is constant. Subsequently, the product gas flow rate is measured. Before the tar measurement starts, a gas probe for the GC is taken in a gas probe bag. After tar sampling, the product gas flow rate is measured again. The Ca - looping rate is measured again to verify the existence of constant conditions throughout the experimental phase. After every experimental phase, the fuel dosing is stopped and the bed material is regenerated by burning the char in the gasifier by changing gasifier fluidization from steam and nitrogen to air. This method is important to provide equivalent conditions, in regard to the bed material, for the subsequent experimental phase.

For the final experimental phase the cone valve was totally closed; the bed material was only circulating in the internal loop of the regenerator and no regenerated bed material was provided to the gasifier. In this case, the bed material was continuously laden with CO_2 which leads to a batch mode gasification. Each experimental phase lasted approximately one hour.

2.4. Used Feedstock and Bed Material

To avoid ash accumulation during continuous AER experiments a biomass with very low ash content was used as feedstock. Therefore, the experimental work was carried out with wood pellets as fuel certificated as EN 14961-2. The composition of this feedstock is shown in the following Table 2. The feeding system consists of two dosing screws: (i) a metric screw feeder to control the biomass flow rate, (ii) a rapidly rotating screw feeder, to avoid pyrolysis, which introduces the biomass into the gasifier above the distributor in the lower third of the bed height.

Table 2. Main characteristics of the feedstock

Elemental analysis	Unit	Wood pellets
C	[wt-%$_{a.r.}$]	48.0
H	[wt-%$_{a.r.}$]	5.5
O	[wt-%$_{a.r.}$]	42.6
N	[wt-%$_{a.r.}$]	< 0.3
S	[wt-%$_{a.r.}$]	< 0.3
Ash	[wt-%$_{a.r.}$]	0.2
H_2O	[wt-%$_{a.r.}$]	3.7
LHV	[MJ/kg$_{daf}$]	18.8

As bed material, a limestone from Greece has been used with characteristics shown in Table 3. To ensure the tendencies obtained from the 1st experiment, a 2nd experiment was conducted. The same sorbent type was used for the 2nd experiment, however, the used bed material for the 2nd experiment was originally pre-calcined and re-carbonated in a rotary kiln. This bed material was abbreviated as bed material B.

Table 3. Main characteristics of the bed material A and pre-calcined bed material B

Elemental analysis	Unit	Bed material
CaO	[kg/kg$_{Bed}$]	95.53
MgO	[kg/kg$_{Bed}$]	0.94
SiO	[kg/kg$_{Bed}$]	2.30
ρ_{Solid}	[kg/m³]	1800
dp	[µm]	300-600

2.5. DFB Operating Conditions

The boundary conditions for the gasifier are set to standard AER conditions at 650 °C. The average temperature in the regenerator was approximately 850 °C to ensure complete char combustion and calcination of the bed material. For the experimental phase with bed material A, the Ca - looping ratio was set at seven different levels, as shown in Table 4. Furthermore, Table 4 lists the most important experimental conditions during each experiment, abbreviated as A-1 to A-7.

Table 4. Conditions of the experiments with bed material A

Operational parameter	A-1	A-2	A-3	A-4	A-5	A-6	A-7
Fuel rate (kg$_{a.r.}$/h)	3.3	3.4	3.6	3.9	4.0	4.0	4.1
S/C (mol$_{H2O}$/mo$_{Fuel,C}$)	1.5	1.5	1.4	1.3	1.3	1.3	1.3
WHSV (kg$_{Fuel,a.r.}$h^{-1}/ kg$_{Bed}$)	1.4	1.3	1.5	1.4	1.6	1.7	2.0
TR (kg$_{Fuel,a.r.}$h^{-1}/ m$^2_{Gasifier}$)	326	332	351	379	389	393	397
F_{Ca}/F_c (mol$_{CaO}$/mol$_{Fuel,C}$)	9.7	9.4	2.4	14.7	6.0	3.4	0.0
τ_{Bed} (min)	2.5	2.5	9.3	1.5	3.5	5.0	∞

A problem during these experiments was that the fuel rate increased slightly. This leads to slightly different WHSV and TR as well as S/C-ratio which can influence the CGE, tar and gas composition [3]. The experimental conditions for

the experiments with bed material B are shown in Table 5, abbreviated as B-1 to B-3.

Table 5. Conditions of the experiments with bed material B

Operational parameter	B-1	B-2	B-3
Fuel rate ($kg_{a.r.}/h$)	3.5	3.5	3.5
S/C ($mol_{H2O}/mo_{Fuel,C}$)	1.7	1.7	1.7
WHSV ($kg_{Fuel,a.r.}h^{-1}/kg_{Bed}$)	1.4	1.4	1.4
TR ($kg_{Fuel,a.r.}h^{-1}/ m^2_{Gasifier}$)	342	343	344
F_{Ca}/F_C ($mol_{CaO}/mol_{Fuel,C}$)	8.1	5.5	3.2
τ_{Bed} (min)	3.1	4.5	7.6

3. Results and Discussion

3.1. Effect of the Ca - Looping Ratio on the Gas Composition

Fig. 3 and Fig. 4 show the results of the non-condensable gas composition over the molar Ca - looping ratio (F_{Ca}/F_C) for the experiments with bed material A and B.

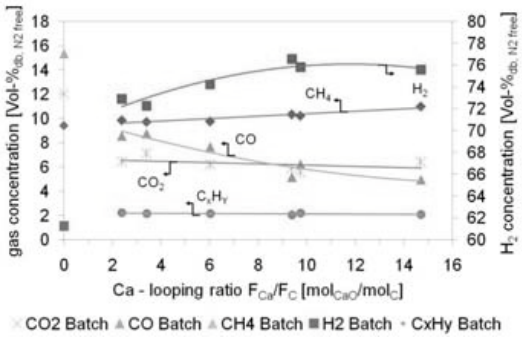

Fig. 3. Gas composition vs. the Ca - looping ratio for experiments with bed material A

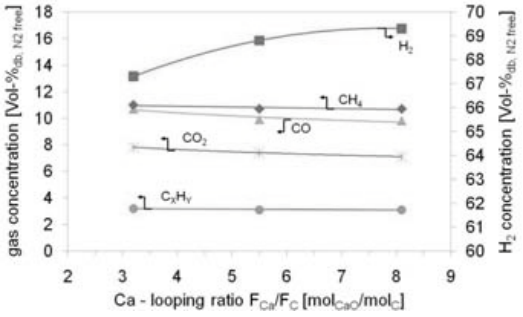

Fig. 4. Gas composition vs. the Ca - looping ratio for experiments with bed material B

The gas concentrations show obvious tendencies as a function of the molar Ca - looping ratio (F_{Ca}/F_C) for both experiments with bed material A and B. Above a Ca - looping ratio value of 6 mol_{CaO}/mol_C, the gas concentrations tend to reach a constant level. A Ca - looping ratio below 4 mol_{CaO}/mol_C leads to a rapid decrease of H_2 and to an increase of CO_2 and CO. This is in accordance with the theoretical analysis, provided in 1.4.

Between the two experiments with bed material A and B a slight difference was noted in regard to H_2, CO_2 and CO concentration. The worse results obtained for the experiments with bed material B, shown in Fig. 4, can be attributed to the sorbent pre-treatment. Due to the pre-treatment, the material is initially in a higher carbonation-calcination cycle while the material of the experiments with bed material A is initially in the first carbonation-calcination cycle. Hence, the "older" bed material of the experiments with bed material B can be responsible for the worse concentrations of Fig. 4 in comparison to those of Fig.3.

3.2. Effect of the Ca - Looping Ratio on the CGE and Gas Yield

The influence of the Ca - looping ratio on the CGE and the product gas yield for both experiments with bed material A and B are shown in Fig. 5. The tendencies for both experiments are similar. With increasing Ca - looping ratio the product gas yield and the CGE are decreasing. This trend can be explained on the basis of the turnover time (τ_{Bed}). With increasing Ca - looping ratio the turnover time becomes less and therefore the time available for biomass conversion is also reduced. As a result, larger quantities of not fully gasified biomass feedstock are transported together with outgoing sorbent flow out of the gasifier.

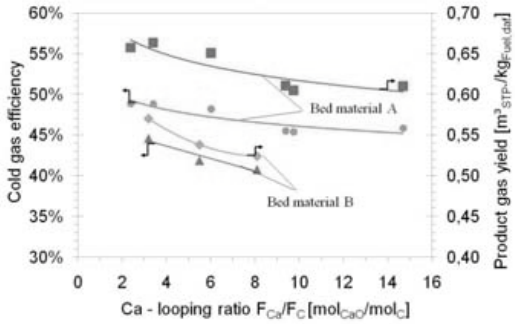

Fig. 5. CGE and product gas yield vs. the Ca - looping ratio for experiments with bed material A and B

The yields for the gas components H_2, CO_2 and CO for the experiments with bed material A are shown in Fig. 6. The tendencies follow the same trends as those in Fig. 3. At a Ca - looping ratio of 10 mol_{CaO}/mol_C the H_2, CO and CO_2 yields reach a nearly constant level. At batch mode conditions (cone valve closed) the H_2 yield is less than at continuous conditions and equal to 0.370 $m^3_{STP}/kg_{Fuel,daf}$. The CO and CO_2 concentrations at batch conditions, shown in Fig.1, are, as expected, much larger than at continuous conditions and the gas yield is equal to $93 \cdot 10^{-3}$ and $73 \cdot 10^{-3}$ $m^3_{STP}/kg_{Fuel,daf}$, respectively. The CO yield decreases faster than the H_2 yield increases with increasing Ca - looping ratio, thus leading to a small decrease of the overall product gas yield, as shown in Fig. 5. The decreasing CO yield leads to a reduction of the CGE because of the higher LHV of CO compared to H_2, as shown in Fig. 5.

At the same gasification conditions, the CGE and the product gas yield are clearly lower than in comparison to the experiments with bed material A. This is an unexpected result which may be caused by a less fuel conversion for the experiments with bed material B compared to the experiments with bed material A.

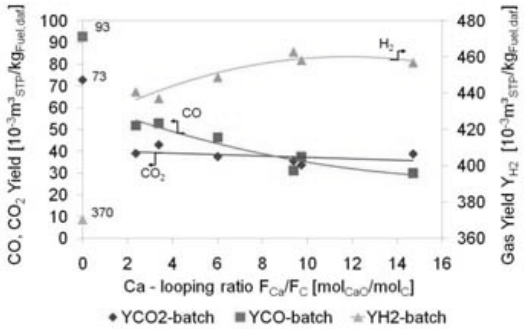

Fig. 6. Yield of H_2, CO, and CO_2 vs. the Ca - looping ratio for experiments with bed material A

3.3. Effect of the Ca - Looping Ratio on the Tar Concentration

The effect of the Ca - looping ratio on the gravimetric tar concentration for both experiments with bed material A and B are shown in Fig. 7. The gravimetric tar concentration decreases significantly with increasing Ca - looping ratio. Because of heat loss in the standpipe, the regenerated bed material is cooled down to 600 to 700 °C before entering the gasifier. Therefore, the tar reduction is not influenced by thermal cracking. Above a Ca - looping ratio of approximately 10 mol_{CaO}/mol_C, the gravimetric tar concentration reaches a constant value. There is a significant difference between the pre-treated sorbent B and the untreated material A with respect to the obtained gravimetric tar concentration. The underlying reason is not fully understood and is subject of further research. However, tar concentrations as low as 13.9 $g/kg_{Fuel,daf}$ and 4.1 $g/kg_{Fuel,daf}$, for the experiments with bed material A and bed material B, were reached, respectively.

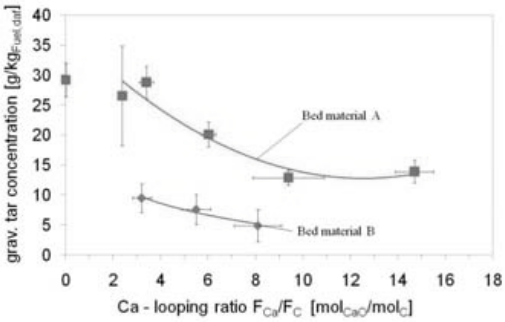

Fig. 7. Gravimetric tar concentration vs. the Ca - looping ratio for experiments with bed material A and B

4. Conclusions

The Ca - looping ratio is identified as a key parameter for DFB biomass steam enhanced reforming with CaO as a CO_2 sorbent. Increasing Ca - looping ratio leads to (i) increasing H_2 concentration and yield, decreasing CO and CO_2 concentration and yield, (ii) decreasing cold gas efficiency (CGE) and overall product gas yield, (iii) decreasing gravimetric tar concentration. Above a molar Ca-looping ratio of 10 mol_{CaO}/mol_C there is no significant influence on the gas composition as well as on the gravimetric tar concentration. However, an increasing Ca - looping ratio leads to a decreasing turnover time of the bed material which results in reduction of the cold gas efficiency and product gas yield. Tar concentrations as low as 13.9 $g/kg_{Fuel,daf}$ and 4.1 $g/kg_{Fuel,daf}$ were measured for the experiments with bed material A and pretreated bed material B, respectively.

Nomenclature

db dry basis

daf dry ash free

a.r. as received

STP Standard Temperature and Pressure (273,15 K 1013hPa)

th Thermal input

CGE Cold Gas Efficiency based on the lower heating value (LHV)

LHV Lower Heating Value

G_{CaO} Calcium looping rate, kg/h

F_{Ca}/F_C Molar circ. ratio, $mol_{CaO}h^{-1}/mol_{Fuel,C}h^{-1}$

WHSV Weight Hourly Space Velocity, $kg_{Fuel,a.r.}h\text{-}1/kg_{Bed}$

TR Throughput, $kg_{Fuel,a.r.}h\text{-}1/ m^2_{Gasifier}$

References

[1] Florin, N. H., Harris, A. T., 2008, Enhanced hydrogen production from biomass with in situ carbon dioxide capture using calcium oxide sorbents, Chemical Engineering Science 63, pp. 287 - 316

[2] Higman, C., van der Burgt, M., 2003, Gasification. Gulf Professional Publishing. United States of America

[3] Corella, J., et. al., 2008, Biomass gasification with pure steam in fluidised bed: 12 variables that affect the effectiveness of the biomass gasifier, Int. J. Oil, Gas and Coal Technology, Volume 1, Number 1-2, pp. 194 – 207

[4] Soukup, G., et. al., 2009, In situ CO_2 capture in a dual fluidized bed biomass steam gasifier: bed material and fuel variation, Chem. Eng. Technol. 32, No.3, pp. 348-354

[5] Corella, J., et. al., 2007, A Review on Dual Fluidized-Bed Biomass Gasifiers, Industrial & Engineering Chemistry Research, American Chemical Society, 46, pp. 6831-6839

[6] Hofbauer, H. et al., 2002, Six Years Experience with the FICFB-Gasification process, 12th European Biomass Conference, Italy, pp. 982-985

[7] Neues Biomassekraftwerk Oberwart, 2009, Optimierte Konzeption der Biomassevergasung aufbauend auf dem DFB-Konzept aus Güssing, Der Reaktor, Vereinszeitung des Vereins der StudentInnen und AbsolventInnen der Verfahrenstechnik an der TU Wien, Jahrgang 19, Ausgabe 88, Nr.4

[8] Pfeifer, C., et. al., 2007, In-Situ CO_2-Absorption in a Dual Fluidized Bed Biomass Steam Gasifier to Produce a Hydrogen Rich Syngas International Journal of Chemical Reactor Engineering, Vol. 5, Article A9

[9] Grasa, G.S., Abanades, J.C., 2006. CO_2 capture capacity in long series of carbonation/ calcination cycles. Ind. Eng. Chem. Res. 45, pp. 8846-8851

[10] Abanades, J.C., et al., 2004, Capture of CO_2 from combustion flue gases in a fluidized bed of CaO, AIChE J. 50 (7), pp. 1614-1622

[11] Charitos, A., et al., 2010, Parametric study of the Calcium Looping process for CO_2 capture in a 10 kWth Dual Fluidized Bed, Int. J. of Greenhouse Gas Control, submitted for publication

[12] Corella, J., et. al., 2006, Steam Gasification of Coal at Low-Medium (600°C~800°C) Temperature with Simultaneous CO_2 Capture in Fluidized Bed at Atmospheric Pressure: The Effect of Inorganic Species. 1. Literature Review and Comments, Industrial & Engineering Chemistry Research, American Chemical Society, 45, pp. 6137-6146

[13] Charitos, A., et al., 2009, Hydrodynamic analysis and design of a 10 kW_{th} Calcium Looping Dual Fluidized Bed for post-combustion CO_2 capture. Powder Technol., accepted for publication.

[14] Hawthorne, C., et al., 2008, Design of a dual fluidized bed system for the post-combustion removal of CO_2 using CaO. Part I: CFB carbonator reactor model, Proceedings of the CFB9 conference, Hamburg; pp. 759-764

[15] Tar Guidline, CEN/BT/TF 143, 2004, Biomass Gasification - Tar and Particles in Product Gases - Sampling and Analysis

Acknowledgments:
This work was carried under the contract AER - Gas II (Contract No. 518309) of the European Union. The authors gratefully acknowledge the financial support by the European Union.

Methodological Aspects in Synthesis of Combined Sugar and Ethanol Production Plant

Andrea Lazzaretto, Matteo Morandin and Andrea Toffolo

Department of Mechanical Engineering, University of Padova, Italy

Abstract:

The synthesis problem, i.e. the definition of type, number and design parameters of system components and their interconnections, is one of the main research topics in the field of chemical and energy systems. The present paper aims at clarifying some methodological aspects for the systematic synthesis of processes by suggesting an organized procedure, which includes some concepts developed in the past by the authors themselves and other concepts taken from the literature. The procedure starts from the definition of a Basic Plant Configuration (BPC) that is built according to the original "concept" of the conversion process (e.g., "transform sugar cane into sugar" or "transform sugar cane into sugar and ethanol"). The BPC comprises the "basic components", i.e. those required to perform the main material and energy conversions, and considers the hot and cold thermal flows only instead of the heat exchangers. A design optimization of this configuration is then to be performed, in which the extreme temperature of the thermal streams are considered among the set of the decision variables. The original BPC is then progressively changed into new BPCs by means of structural modifications including component staging and addition of new material connections or subprocesses. Modifications to the original BPC derive from the interpretation of the process Grand Composite Curve, the ultimate aim being the reduction of the energy bill resulting from plant operation. This procedure is applied here to the synthesis of the sugarcane conversion process. Starting from the original concept of sugar production, process structural developments towards the combined sugar and ethanol production are proposed and discussed in the light of the suggested procedure.

Keywords: Synthesis, Pinch Analysis, HEATSEP

1. Introduction

The present work aims at discussing methodological aspects in the synthesis of energy-intensive industrial processes. We focus the attention particularly on those cases in which the process features several heat sources and sinks and power is a possible additional requirement.

In the field of process integration, heat and power integration is one aspect that can play an important role in reducing the bill for external energy consumption. The idea is matching the demand and availability of energy between subprocesses: usually this leads to reduce the demand of external heat to be provided by fossil fuel combustion.

Different techniques were developed in the past for the design of the heat exchanger network (HEN) that maximizes internal heat recovery possibly at the minimum additional investment costs. Among others, the work by Linhoff *et al.* on Pinch Analysis is important for the definition of a simple and effective methodology for heat and power integration [17, 11]. In particular, when combined heat and power integration is considered for a process, we refer to the possibility of integrating process thermal streams with the thermal streams of other devices, like for instance thermal engines or heat pumps, that are commonly classified as belonging to the set of process utilities. This set includes all the machines that support process operation by supplying its power, heat and refrigeration needs.

The key step of Pinch Analysis is the solution of the process heat cascade, which determines the minimum thermal requirement (MER) of the process for a given minimum temperature difference (ΔT_{min}) and considering that heat can be transferred only from higher temperature levels towards lower temperature levels of the cascade. Moreover, the same methodology suggest heuristic rules for the design of a HEN that complies with process MER.

A subsequent development of this methodology

Corresponding author: Andrea Lazzaretto, Email: andrea.lazzaretto@unipd.it, Tel.: +39 049 8276747

suggests another set of rules to interpret the heat cascade for a more rational identification of integration opportunities. The Grand Composite Curve (GCC), which is the graphical representation of the process heat cascade, is at the basis of the procedure for placing external heat sources (or heat sinks in the case of cooling requirements under environmental temperature) or for the design of the optimum combined heat and power (CHP) system.
Methodological and computational aspects related to the design and the correct placement of external utilities with respect to a given process heat cascade have been extensively discussed in the past. Among others, the contributions by Grossman [7], Kalitvenzeff and Marechal [19, 20] have improved the systematic solution of those problem in which a process has to be integrated with a utility network and combined heat and power technologies. The complexity is an issue that the aforementioned authors have successfully reduced in order to use MILP techniques, whereas the cases in which MINLP is required are less common.

In the design of an industrial process, Pinch Analysis can be applied when thermal streams temperatures and heat loads are known (i.e. they are imposed by process needs), so that the heat cascade problem is completely defined. The result of heat and power integration is a particular result deriving from a unique set of thermal streams, that is for a given layout of process configuration. A more general issue consists in exploring possible process modifications and evaluating their consequences in terms of process productivity improvement and in terms of heat and power integration as well. The changes in process structure and design parameters usually affect temperatures and heat loads, so the results of the heat integration problem will necessarily vary. On the other hand, the same modifications affect the design points and the characteristics of subprocesses, i.e. the overall process productivity.
In principle, in the synthesis of thermal power plants heat and power integration is crucial for achieving high efficiency. In this field some recent works by Lazzaretto and Toffolo [13, 14] were aimed at defining a systematic methodology for design improvement. According to this methodology the synthesis of a thermal power plant starts from the definition of a "Basic Plant Configuration" (BPC) which represents the "basic" design concept of the plant or, in other words, a technical representation of a preliminary idea of the plant. The BPC comprises all the components responsible for chemical or mechanical conversions and their physical connections. Heat exchangers are not considered as part of the BPC and only hot and cold thermal streams appear instead. As a consequence, BPC design parameters can be optimized while the definition of the topology of the HEN for internal heat recovery is left to a separate design step.
In particular, the methodology, also referred as the HEATSEP method ([14]), suggests to explore the cooling or heating of material streams by "cutting" the thermal links between BPC components, so that a material stream that passes from a component to the subsequent one can undergo an intermediate heat exchange. This is done by virtually generating a temperature discontinuity between subsequent components, so for each cut a thermal stream and one additional decision variable (the outlet temperature) are generated. The feasibility of the heat transfer within the system is finally checked by solving the heat cascade problem according to Pinch Analysis rules.
The HEATSEP method has been applied so far to the improvement of heat integration within thermal power plants in order to obtain the maximum exergetic efficiency. When the internal heat recovery associated with these thermal power plant is considered, most of the temperature values deriving from the cuts of thermal links between components can be included in the decision variable set. The complexity of the optimization problem can perhaps be reduced by neglecting some of the thermal cuts for thermodynamic reasons. Conversely, in an industrial process most of the temperature are in general already dictated by process requirements and, therefore, cannot be included in the decision variable set.
The synthesis problem concerns both the definition of the structure, that is the number, the type and connections between components, and the process design parameters. Thus, the initial BPC configuration can be subsequently modified in order to explore possible improved configurations. The synthesis procedure can involve one or more of the following structural modifications:

- component staging;
- change in material connections between the new and the previous components by adding material splits or mixers;

- addition of new components and consequent addition of mixers and splitters.

In more details, while component staging does not alter the basic concept of the BPC, structural changes involving different connections between components and/or addition of new components result in new BPCs, each of which can be optimized according to the proposed procedure.

1.1. A generalized approach for the synthesis of energy intensive industrial processes

While the complexity of the synthesis problem can be possibly reduced by neglecting some trivial structural modifications or some trivial decision variables, the objective of the synthesis is to broaden the analysis towards more interesting configurations starting from an original BPC. Thus, we are looking for a more systematic procedure for process synthesis.

In the field of energy systems and chemical processes important indications about heat and power integration can be obtained from the analysis of the process GCC. The Integrated GCC helps interpret and possibly quantify changes in the original BPC by identifying the relative position of thermal streams of each sub-process in the overall process heat cascade [18].

In the present work we apply the aforementioned elementary structural modifications to an industrial process in order to reduce thermal and possibly power consumption. The effects of these changes in the overall heat and power integration are analyzed by examining the new resulting GCCs. The idea is to extend the heat integration of a preliminary BPC gradually, that is from some sub-processes to the overall process. Among all process parameters, a selection of critical decision variables is considered. The HEATSEP method is followed in order to identify all the possible temperatures to be included in the decision variable set. When the analysis of the proposed BPC shows that there is space for improving heat and power integration, optimization of critical design parameters is performed. Eventually modifications are introduced in the process structure. This is done by interpreting the relative impact of a change in the process GCC (locally in the integrated GCC of a single sub-process).

The effects of modifications in the BPC are analyzed also in terms of the possible improvement in process productivity, being this dependent on the process topology. However this is not the ultimate objective of the proposed procedure which aims at reducing the process energy demand. A more precise assessment of process profitability could be the objective of an extensive thermo-economic analysis which is beyond the scope of this paper.

The procedure is applied here to the synthesis of plants for the conversion of sugar-cane in useful products. The results of process modifications are evaluated in terms of process MER and power consumption along with the number of useful products and their production rates.

2. Production of sugar

In this section we start with the analysis of the conversion of sugarcane into white sugar. According to the proposed procedure, a BPC, which is considered as the base-case scenario for sugar production (Fig. 1), is defined and the relative heat and power consumption along with the sugar production rate are evaluated.

Data found in the literature ([4, 5, 8]) were used for modelling the basic plant sub-processes. The input mass flow rate of sugarcane is set to 138.9 kg/s. Sugar yields and the flow rates of the main material streams along with heat and power requirements of the main sub-processes are shown in Fig. 1.

According to the definition of the BPC, the HEN is omitted, except for the multi-effect evaporator, which is considered here as a “basic” component. The multi-effect evaporator, which appears as a theoretical result of a local heat integration, is in fact already acknowledged in the technical practice as the optimal solution when dealing with concentration of the solid content in a mixture. In particular, in the light of the proposed procedure, this component results from staging the evaporation process into separate units and then optimizing the operating temperatures of each stage. For this sub-system in the base case scenario, a co-current configuration with three effects (1.32 bar, 1.14 bar, 0.81 bar) with equal loads is considered (according to a rule of thumb, equal loads correspond to equal heat transfer surfaces for the same ΔT_{ml}, that is equal sizes of the evaporation units).

As reported at the bottom of Fig. 1, the base case sugarcane conversion plant presents a considerably high heat demand (179 MW). While power demand

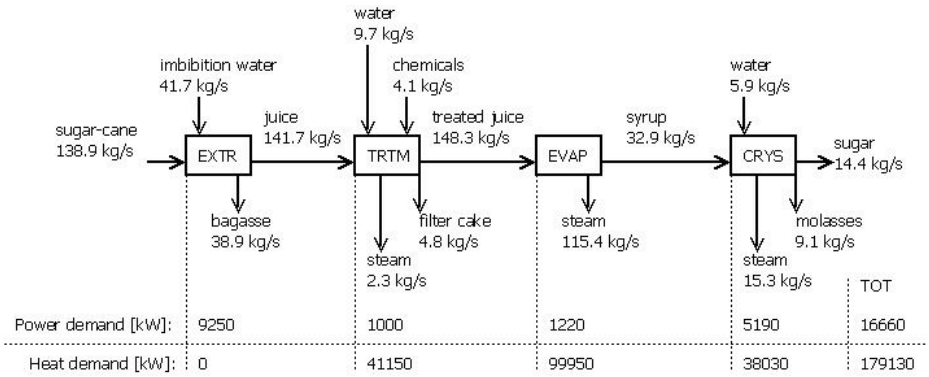

Figure 1: Base case BPC for sugar production

(16.6 *MW*) is proportional to the mass flow rate of the processed materials (sugarcane, juice, syrup and sugar), the heat demand can be potentially reduced by adopting a more heat integrated plant configuration.

2.1. Minimization of the BPC thermal requirement

In agreement with the proposed procedure, we now want to focus on the reduction of the process heat demand. Firstly, all the cold and hot streams in the process are identified. The aim is to maximize step by step the internal heat recovery.

We start from a first set of thermal streams including those of the multi-effect evaporator and those of the crystallization sub-processes. In particular, the previous local heat integration of the multi-effect evaporator is discarded. Conversely the cold stream (juice to be concentrated) and the hot stream (vapor to be condensed and removed) of each unit are left to participate separately to the process heat-cascade problem. In so doing, the total process heat demand evaluated by adding the hot utility demand of the heat-integrated evaporation and crystallization sub-processes to the thermal requirements of the extraction and the juice treatment sub-processes, passes from the 179 *MW* of the base case scenario to 141 *MW*.

The overall process heat integration is finally studied by including all the thermal streams of the other two sub-processes (juice extraction and treatment). The resulting GCC of the process is shown in Fig. 2. The total process heat demand is further reduced to the only heat duty of the first evaporation unit (around 100 *MW*), which corresponds to a reduction of 41 *MW* compared to the previous case in which only the multi-effect evaporator and crystallization were thermally integrated, and of almost 79 *MW* compared to the base case scenario of Fig. 1, in which the sub-processes were considered totally independent from the thermal point of view (no heat integration). Before looking at process structural

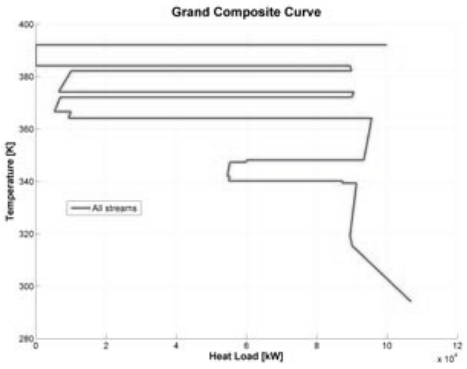

Figure 2: GCC of the base case BPC (sugar production) with total heat integration

modifications, we want to evaluate the possibility of reducing process thermal requirement by optimizing process parameters. In particular, as suggested by the HEATSEP method, we look at the possibility of introducing thermal cuts between the basic components, in order to explore the benefits that intermediate coolings or heatings can bring to the reduction of the process heat demand.

As discussed in section 1., the possibility of introducing thermal cuts in industrial processes is likely to be limited by the feasible temperature ranges of the material streams. As an example, the final temperature of juice heating within the treatment sub-process is constrained to be around 105°C, since

discoloration problems can occur for higher values and juice treatment is less effective for lower temperatures.
Instead, in the multi-effect evaporator, possible thermal cuts can be considered in the juice stream just before the first evaporation unit and between the other units. This allows the temperature of juice entering each unit to vary independently of the actual operating temperature of the unit. Juice pre-heating up to the temperature of the first unit is in fact possible while juice cooling before evaporation appears not to be thermodynamically reasonable. In the base case condition the juice leaves the treatment subprocess at 98 °C while the first effect works at the maximum allowable temperature of 115°C to avoid discoloration. Thus, part of the heat load of the first unit is spent for juice heating rather than for evaporation. Actually, if juice is pre-heated before entering the unit, a thermal stream with an oblique profile from 97°C to 115°C would appear in the process composite curve. The associated thermal load is equal to almost 10 MW, five of which could be possibly covered by other thermal streams in the process at that temperature level.
In addition, when cutting the thermal links of the juice stream between units in a co-current configuration, the juice leaves a unit already at a temperature higher than the evaporation temperature in the subsequent unit. Thus, cooling would be unnecessary while heating would lead to evaporation which is in fact carried out in the subsequent unit.
As a conclusion, the actual benefits that the placement of intermediate heat exchangers and the optimization of their temperatures would bring to the minimization of the process heat demand can be neglected. Other process operating parameters to be optimized at this step of the analysis could be found within the multi-effect evaporator (unit operating pressures and solid content at the outlet of each unit) but, as it appears in Fig. 2, there is not so much space for further improvement in its thermal profile.

2.2. Introducing modifications to the BPC

We want now to introduce some structural changes in the BPC, such as component staging, alternative material connections between components and addition of new components.
Accordingly, we introduce additional stages in the multi-effect evaporator. This structural choice is conceived by looking at the GCC of the overall process in Fig. 2, which shows a heat pocket between the third stage and the crystallization thermal profile big enough to accommodate at least another evaporation stage. Furthermore, it is also possible to fit another stage below the crystallization profile in the heat cascade. As a consequence, we decide to increase the number of units from three to five, still in a co-current configuration. As a preliminary design criterion, we suppose again to split the total evaporation load in five equal parts (1.34 *bar*, 1.21 *bar*, 1.07 *bar*, 0.9 *bar*, 0.53 *bar*). For this new configuration (case S1) heat integration of the total site is studied. The resulting GCC is shown in Fig. 3. This shows that the choice of a thermal cascade including five evaporation effects with almost equal loads is sufficient for further reducing the heat demand to around 62 MW, which corresponds to a reduction of additional 38 MW compared to the case in which three effects are used (Fig. 2). The temperatures (pressures) of the 5 effects were in fact estimated in order to obtain the desired optimum thermal cascade.

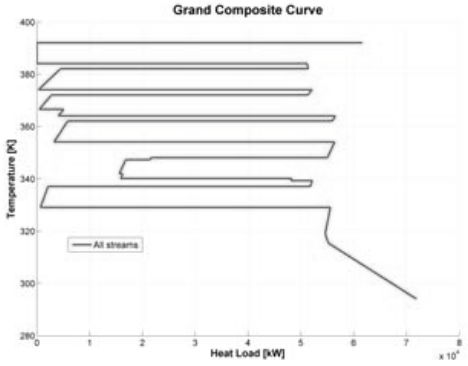

Figure 3: GCC of Case S1 - total heat integration of sugar production plant with 5-effects evaporator

3. Production of ethanol

The production of ethanol is analyzed here starting from the same mass flow rate of sugarcane (138.9 kg/s). After juice extraction and treatment, a possible alternative to sugar production is in fact yeast fermentation of the juice and then ethanol distillation. This corresponds to the introduction of two new sub-processes (fermentation and distillation) and to the exclusion of two others (evaporation and crystallization). These modifications result in the definition of a new BPC, which is the base case scenario for ethanol production (see Fig. 4 including

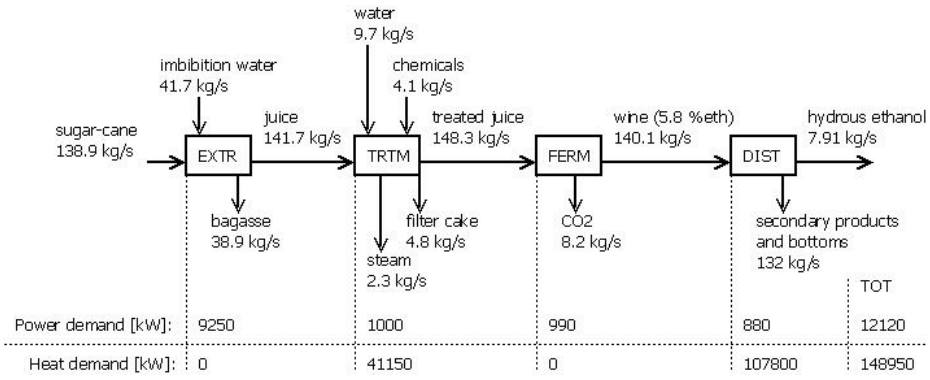

Figure 4: Base case BPC for ethanol production

the figures about ethanol yield and heat and power demands).

Process parameters and characteristics of the conversion sub-processes are based on data taken from the literature [4, 5]. Hydrous ethanol is obtained from distillation, the sub-process in which ethanol is separated from the fermented wine, and water is removed as a bottom (liquid) product. Another possibility, not considered here, would be to remove part of the water in the juice also by means of an upstream evaporation sub-system, as it is done in sugar production (sucrose concentration of the juice is however constrained to be in a range between 10 to 20 % for optimum fermentation conditions). This solution would lead to a higher plant complexity and to an additional sequence of heating (during evaporation) and cooling (before fermentation) processes.

Ethanol production from sucrose-rich vegetables, and especially from sugar-cane is a well-known process and can rely in well-established technologies [12, 10]. Since fermented mashes coming from the fermentation sub-process generally consist in a complex mixture of water and organic compounds, of which ethanol is the most interesting one, distillation products can differ in quality. If part of the heavy organic compounds are removed as bottom products of the distillation, an important part of aldehydes and ethers are still present in the head products of a first stripping column. When high grade ethanol is to be produced these substances need to be removed by an extractive distillation column. Subsequently hydrous azeotropic ethanol can be distilled in a rectifying column. Yet, if motor fuel ethanol is to be produced, aldehydes and ethers are left as part of the product, being these substances easily processed in combustion engines. Ethanol can be distilled up to the azeotropic concentration which for the ethanol-water mixture is 95.6% in mass at 1.032 bar. Anhydrous high grade ethanol or motor fuel can be produced by adding a tertiary compound to the hydrous mixture by means of the so-called tertiary azeotropic distillation.

In the present section, we firstly consider the option of producing motor fuel ethanol from sugar-cane. In the base case scenario, motor fuel ethanol is distilled in a single stripping-rectifying column. Wine is assumed to be an ethanol-water mixture. Main design parameters are: 35 trays and reflux ratio (ratio between the molar flow rate of the recycling stream after the condenser and the distillate stream) equal to 7.

The wine is preheated before entering the distillation column up to 90°C and enters the column in one of the lower trays (an indication about optimal entering stage was evaluated with the McCabe-Thiele approach).

3.1. Minimization of the BPC thermal requirement

In the juice treatment section, juice has to be heated up to discoloration temperature (105°C) while in the subsequent fermentation stage it has to be cooled down to around 28°C. Thus, it is convenient to use a cross heat exchanger. In addition, this stream of juice after treatment is still hot enough to preheat part of the wine before the distillation column.

For the non-integrated plant configuration a total thermal demand of 149 *MW* was evaluated. The slight reduction in total heat demand with respect

to the sugar production is due to the lower specific energy consumption of ethanol distillation from the water-ethanol mixture compared to the pure water evaporation in the case of sugar production.
Fig. 4 shows that the thermal requirement is associated only with juice treatment and ethanol distillation. After cold and hot streams are identified, total site heat integration is studied and resulting GCC is shown in Fig. 5.

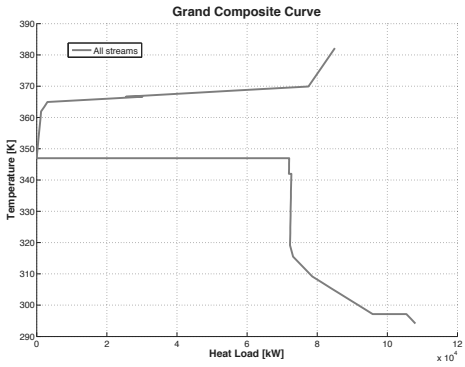

Figure 5: GCC of the base case BPC (ethanol production) with total heat integration

The heat demand potentially decreases from almost 149 MW (BPC without heat integration) to 86 MW. This significant reduction is a paradigmatic example of the benefits deriving from heat integration. In conclusion the proposed base case scenario for ethanol production does not present any important decision variable that can be further adjusted for decreasing process thermal and power demand.

3.2. Introducing modifications to the BPC

In the previous section the heat demand of the plant was shown to be dramatically reduced by integrating the plant thermal streams. The next step of the analysis presented here consists in searching for modifications in the plant configuration that further reduce the thermal requirement while keeping the production of ethanol constant.
As discussed for the case of sugar production in section 2., most of the temperatures are fixed by process requirements with the only exception of the outlet temperature of the wine pre-heater before distillation. Inside the distillation column the wine is heated up to the boiling point for evaporation and this corresponds to an almost isothermal heat requirement at a quite high temperature. Thus, it is reasonable to reduce this heat duty (at reboiler side)

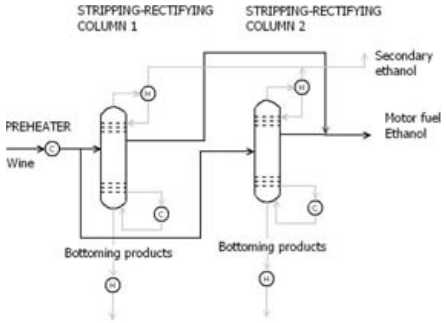

Figure 6: Distillation with parallel of two stripping-rectifying columns

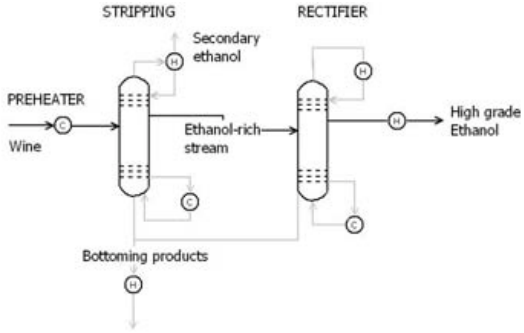

Figure 7: Distillation with sequence of stripping and rectifier

as much as possible (up to the actual evaporation heat load) and pre-heat the wine with other non-isothermal streams coming from other parts of the process (for instance, the hot juice after treatment section). A similar condition was previously shown for the pre-heating before the multi-effect evaporator). So wine is pre-heated approximately up to the re-boiler operating temperature. Since there is no thermodynamic benefit from pre-heating the wine up to a different temperature, we do not include this temperature in the decision variable set. In addition, for the base case BPC, no other significant decision variables are identified in the process.
Thus, we look now for component staging or for changes of component interconnections.

We focus here on possible modifications in the ethanol distillation sub-process, considering the following two possible alternative configurations:

- two columns in parallel, both producing hydrous ethanol: this corresponds to split the wine stream at the outlet of the fermentor into two different portions that are processed in two separate columns (Case E1 in Fig. 6).

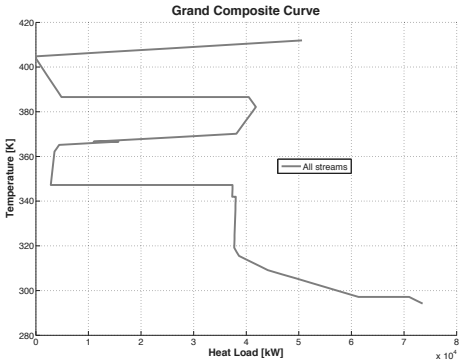

Figure 8: GCC of Case E1 - total heat integration of ethanol production plant with parallel of two stripping-rectifying column

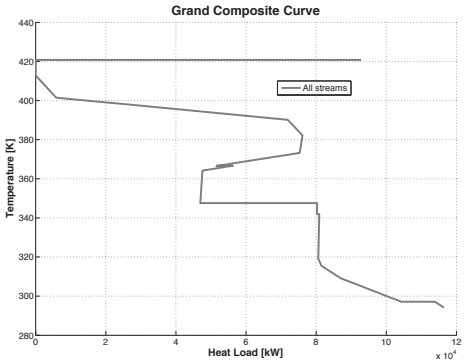

Figure 9: GCC of Case E2 - total heat integration of ethanol production plant with sequence of stripping and rectifier

- a series of a stripping and rectifying column: this corresponds to perform distillation of hydrous ethanol into two stages (Case E2 in Fig. 7).

In addition, we introduce the possibility of operating the columns at different pressures. In fact, in the single column case, the higher the pressure the higher the thermal requirement of the re-boiler. Conversely, when two distillation columns operate at different pressures, a reduction in total heat requirement can be obtained by integrating the thermal streams at different temperature levels.
In case E1 (columns in parallel) it appears that two columns operating with the same design parameters would be justified only by sizing issues, without advantages in thermal matching. In case E2 (series of columns) the overall thermal requirement can easily double the thermal requirement of a single column since, for the same column characteristics (i.e. number of trays and reflux ratio) the fraction of high-boiling substances (modelled as water in this case) to be evaporated and passed to the second column is bigger and, therefore, increases the re-boiler heat duty of the first column.
In technical practice, distillation staging is actually considered when head products from the first stripping column still consists in a mixture of ethanol and undesired compounds that need to be removed in subsequent stages. Thus, case E2 does not refer to the case of motor fuel ethanol production but would rather refer to the case of high grade hydrous ethanol production, where aldehydes and ethers are removed in an intermediate extraction column and the water-ethanol mixture needs to be rectified.

Heat integration of sequence of distillation columns was the objective of several studies in the literature [2][3][9]. When one of the two columns operates at a higher pressure, the temperature levels of both the reboiler and the condenser of that column are shifted up in the total process heat cascade. In so doing, the total heat duty introduced by ethanol distillation can be split into different stages, revealing a high potential for heat integration. Thus, the possibility of integrating the thermal streams of the two columns with those of the rest of the overall plant is also considered.
Both cases (E1 and E2) were modelled in details and simulated in the Aspen environment [1]. In particular, in case E1 (parallel of distillation column) the same parameters of the base case scenario were used for the stripping-rectifier column. According to data found in the literature [4, 5], in case E2 (series of stripping and rectifier) the numbers of trays were set to 25 and 50 and the reflux ratios to 1 and 3.5 for the stripping column and the rectifier, respectively. In order to exploit the heat integration potential of the two columns, the operating pressure was set to 4 bar both for the stripping column in case E2 and for one of the two columns in case E1. For sake of simplicity, in the latter case the juice fraction towards the high pressure column, which would be one of the parameters to be optimized, was fixed at 52%, a value that heuristically leads to a minimum total process hot utility requirement.
The GCC of the overall process (from sugarcane to ethanol) for the two cases are shown in Fig. 8 and 9. The total hot utility requirement in case E1 is equal to 50 MW (36 MW lower than in the base case

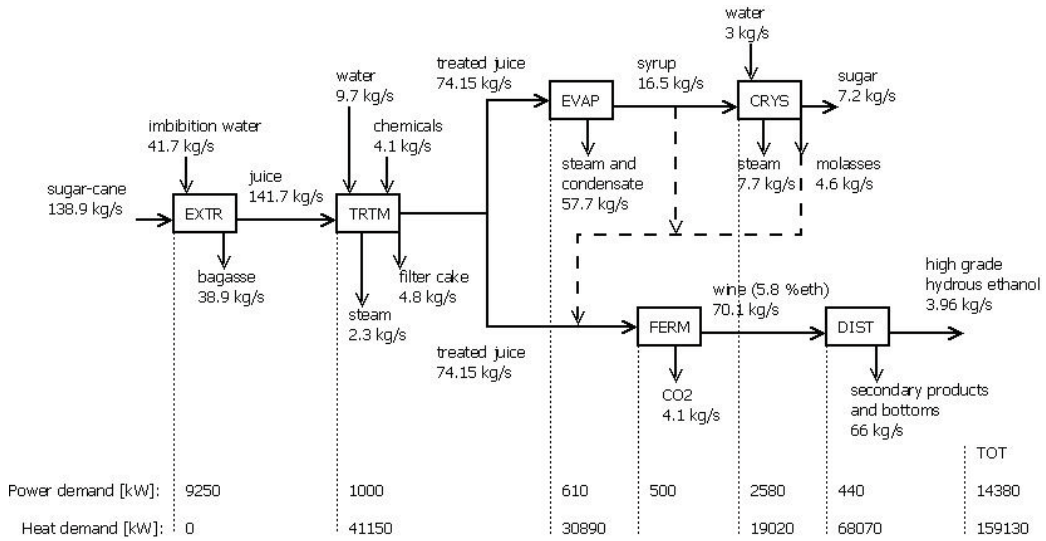

Figure 10: Base case BPC for combined sugar and ethanol production, and possible modifications (dashed lines) for increasing ethanol yield

scenario). A total process hot utility of 93 MW was instead evaluated in case E2, and it actually corresponds to an increase of 7 MW compared to the base case scenario. As expected, the potential reduction in total energy requirement is much lower producing high grade ethanol than motor fuel ethanol. This is due to the more complex, and energy expensive, distillation configuration, which, however, is supposed to be paid off by a higher price of high grade ethanol.

4. Combined sugar and ethanol production

In section 2. and 3., two different BPCs were generated in order to convert a given amount of sugarcane into sugar and ethanol respectively.

We analyze here the possibility of combining the production of ethanol and sugar in a single plant (i.e. in a single BPC). In particular, since juice extraction and treatment sub-processes have the same characteristics in the two cases, only a single instance of these two first sub-processes appear in the BPC. After the juice treatment sub-process, juice is split into two streams, one being processed for sugar production, the other for ethanol production. Actually, juice for ethanol production has to be treated in order to eliminate sulfur in the final product, so some chemicals are usually added to the juice used for sugar production only. However, the estimation of process thermal requirement is not affected by this little difference in juice treatment.

The BPC of the combined sugar and ethanol production is shown in Fig. 10. This BPC assumes that juice is split into two equal parts after the juice treatment section. Five effects are used to concentrate juice into syrup within the evaporation section. In the ethanol distillation section high grade hydrous ethanol is produced, which requires the sequence of stripping and rectifying columns. As a result, almost 4 kg/s of high grade hydrous ethanol and 7.2 kg/s of sugar are obtained, which correspond to half of the production yields of the single-product BPCs, being the yields proportional to the mass flow rates of treated juice diverted to the two separate production sequences. The total heat demand of the process is around 160 MW (31 MW is the local heat demand of the thermal cascade of the 5-effects evaporator), under the assumption that the total evaporation load is equally distributed among the 5 effects and that both the stripping and rectifying columns operate at environmental pressure.

4.1. Minimization of the BPC thermal requirement

Total site heat integration is now considered for the same operating parameters of the various subsystems. The resulting GCC is shown in Fig. 11, in which the zig-zag profile that is typical of the

various steps of water evaporation in the juice concentration (multi-effect evaporator) and ethanol distillation sub-processes can be easily recognized. The overall thermal requirement of this base case scenario is around 83 MW, corresponding to almost half of the total consumption without total heat integration.

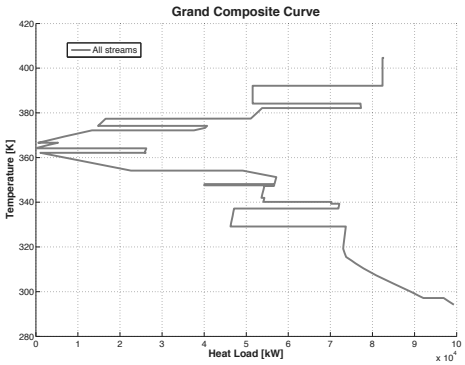

Figure 11: GCC of the base case BPC (combined sugar and ethanol production) with total heat integration

4.2. Introducing modifications to the BPC

As already done for BPCs associated with the separate production of sugar and ethanol, we start from the optimization of the parameters that, according to the previous analysis, significantly affect process thermal requirement.

In particular, as shown in the GCC of Fig. 11, the temperature levels of the distillation plant operating at the environmental pressure and those of the juice evaporation are overlapped. Since the local heat demand of the two sub-processes is quite high, this results in a high thermal demand for the whole process. It appears that a better heat integration between the various evaporation effects and the reboilers and condenser of the distillation columns could be beneficial. So, the operating pressures and evaporation loads (increase in solid content) of the five effects and the operating pressure of the stripping column are optimized in order to reduce total process heat demand. A detailed discussion of the optimization procedure can be found in [21], and similar approaches are suggested in the literature in [22, 15]. The operating pressure of the rectifying column could also be included within the set of the decision variables. However, the rectifier is responsible for the smaller part of local heat demand of the two columns, which can be covered by the thermal stream associated with the condenser of the stripping column if this operates at higher pressure. Optimization results show that the stripping column operating pressure is the parameter that mainly affects total process heat demand. In fact, if the stripping column operates at atmospheric pressure, total process heat demand can be reduced to 68 MW (case CSE1) by optimizing multi-effect evaporator design parameters. When the stripping column is instead operated at 4 bar, total process heat demand can be further reduced to 47 MW (case CSE2). The corresponding GCCs of the two configurations are shown in Fig. 12 and 13. In particular, if distillation is carried out at atmospheric pressure in both columns, the vapour coming from the first evaporation effect can be used to totally cover the distillation heat duty. Thus, it is convenient to evaporate the major part of the water from the juice within the first evaporation unit. Conversely, as soon as stripper operating pressure is increased, it is more convenient to make the major part of the evaporation occur in the subsequent effects.

Molasses, which have a quite high sucrose content

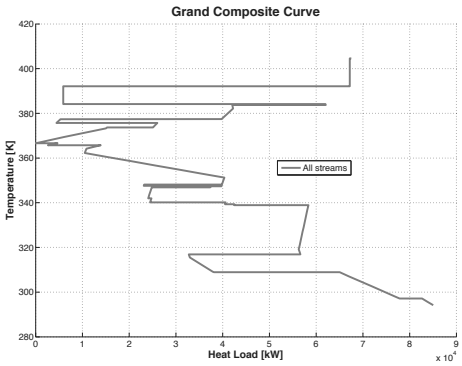

Figure 12: GCC of case CSE1 - total heat integration of the combined sugar and ethanol production plant with atmospheric distillation

(73% of solid content, 58% of which is sucrose), are produced by the crystallization sub-process among other by-products (Fig. 10). This amount of sucrose can be diverted to the must preparation immediately upstream the fermentor, in order to increase the ethanol yield of yeast fermentation. Actually, yeast methabolism can be inhibited by an excess of sucrose content in the must and by an excess of ethanol content in the product [12]. According to data found in [4, 5], we fix this limit at 17.5% that

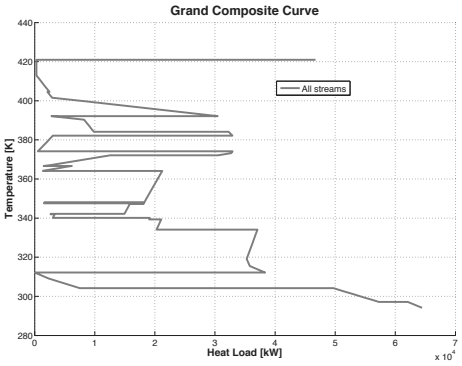

Figure 13: GCC of case CSE2 - total heat integration of the combined sugar and ethanol production plant with stripping column operating at 4 bar

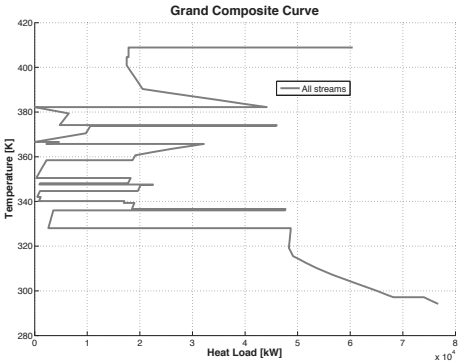

Figure 14: GCC of case CSE3 - total heat integration of the combined sugar and ethanol production plant with recirculation of molasses for ethanol production and stripping column operating at 3 bar

is an optimal value for a given type of yeast. By mixing molasses with the juice coming from the treatment section, the sucrose content is found to be lower than this value, so that some syrup obtained by juice concentration in the multi-effect evaporator has to be added to the must. These new mass interconnections introduce a material mixer upstream the fermentor, and are represented with dashed lines in Fig. 10. As a consequence of the increased sucrose content in the must, yeast fermentation produces wine at 7% vol. of ethanol and the specific energy required by distillation also diminishes slightly as a smaller amount of water has to be removed from the wine.

If the juice is split into two equal parts after the treatment section (as it is done in the base case in Fig. 10), a major part of the syrup has to be added to the juice to obtain the desired sucrose concentration which makes the ethanol production dramatically increase at the expense of a reduction in the sugar yield. Thus, for a fair comparison between the new BPC and the base case scenario in terms of energy consumption and sugar and ethanol yields, sugar production is fixed at 7.2 kg/s and the mass flow rates are adjusted accordingly (38% of the juice and 20% of the syrup are diverted to ethanol production). The new BPC leads to an increase of around 8% in ethanol production (from 3.96 kg/s to 4.27 kg/s).

The operating parameters of the new BPC (pressures and solid content in the 5 evaporation effects and stripping column pressure) are then optimized in order to reduce the overall process heat demand. The GCC of this optimized configuration is shown in Fig. 14. Total process heat demand is around 61 MW when the stripper column operates at about 3 bar.

The increase in total site heat demand compared to the previous case (case CSE2) is due to the fact that more than 60 % of juice is diverted to the multi-effect evaporator and the slight reduction in local heat demand of the ethanol distillation is not sufficient to counterbalance the local heat demand of the first effect of the evaporator. Again, the stripping column pressure appears to be a critical decision variable for the reduction of process MER. In fact, when the stripper operates at environmental pressure, optimization results show that process thermal requirement is about 18 MW higher (79 MW).

5. Conclusions

The objective of the present work was to present an organized procedure for the synthesis of industrial processes towards the systematic generation of alternative plant configurations for more energy efficient industrial processes. An application to the conceptual design of sugarcane conversion processes is presented. Starting from an original idea of a process (in this case sugar production from sugarcane), different configurations for ethanol production and combined sugar and ethanol production are generated and their heat and power consumption and production rates are compared. Total site heat integration is performed without the need of modifying the original BPC because the heat transfer section is seen as a black box enclosing an undefined topology, although the HEN design inside the

black box is likely to be affected. The optimization of the design parameters of the basic plant configuration is firstly discussed. If good values of process parameters cannot defined in advance, optimization is also performed. The next step consists in introducing structural modifications to the BPC by a direct observation of the process GCC aimed at reducing the process thermal requirement. The new BPCs can accommodate component staging that generate more heat sinks and heat sources to be matched in the process heat cascade. In addition, new components and new connections between them can be introduced.

Table 1: Summary of results - (1: Heat Demand; 2: Power Demand; 3: Total Heat Integration of base case BPC; 4: Motor Fuel Ethanol; 5: High Grade Ethanol)

	Figure	H.D.[1] [MW]	P.D.[2] [MW]	Sug. [kg/s]	Eth. [kg/s]
Sugar Production					
Base	1	179	17	14.4	-
T.H.I.[3]	2	100	”	”	-
S1	3	79	”	”	-
Ethanol Production					
Base	4	149	12	-	7.9 (M.F.[4])
T.H.I.[3]	5	86	”	-	”
E1	6	50	”	-	”
E2	7	97	”	-	7.9 (H.G.[5])
Combined Sugar and Ethanol Production					
Base	10	159	14	7.2	3.9 (H.G.[5])
T.H.I.[3]	11	83	”	”	”
CSE1	12	68	”	”	”
CSE2	13	47	”	”	”
CSE3	14	61	”	”	4.3 (H.G.[5])

For the case of the sugarcane conversion, the configurations generated by means of the proposed procedure are compared and a summary of results is presented in table 1.

It is apparent that the real convenience of adopting one of these configurations can be evaluated by taking into account all the economical aspects related to process modifications. For instance, in the case of ethanol production, bigger costs are required by pressurized distillation columns which on the other hand is a key point for the reduction of the energy bill. Nonetheless, the results presented here give a clear picture, in terms of energy consumption, of the benefits deriving from a progressively higher integration of heat and material streams within the processes, which was generated following the proposed organized procedure.

We note that a further increase in plant profitability can be obtained by exploiting the bagasse by-product for combined heat and power generation, but this option is out of the scope of this paper, having been extensively analyzed in a previous work [21].

Nomenclature

BPC Basic Plant Configuration

MER Minimum Energy Requirement

HEN Heat Exchangers Network

GCC Grand Composite Curve

References

[1] ASPEN Plus 11.1. Aspen Technology ©.

[2] R. Agrawal. The Challenges in the Synthesis of Multicomponent Configuration in Chemical Industry. In *The 2006 Annual Meeting*, 2006.

[3] VR Dhole and B. Linnhoff. Distillation column targets. *Computers & chemical engineering*, 17(5-6):549–560, 1993.

[4] A.V. Ensinas. *Integração térmica e otimização termoeconômica aplicadas ao processo industrial de produção de açúcar e etanol a partir da cana-de-açúcar*. PhD thesis, Universidade Estadual de Campinas, Faculdade de Engenharia Mecânica, 2008.

[5] A.V. Ensinas, S.A. Nebra, M.A. Lozano, and L.M. Serra. Analysis of process steam demand reduction and electricity generation in sugar and ethanol production from sugarcane. *Energy Conversion and Management*, 48(11):2978–2987, 2007.

[6] M. Gassner and F. Maréchal. Methodology for the optimal thermo-economic, multiobjective design of thermochemical fuel production from biomass. *Computers and chemical engineering*, 33(3):769–781, 2009.

[7] IE Grossman. Mixed-integer optimization techniques for algorithmic process synthesis. *Process Synthesis*, page 171, 1996.

[8] E. Hugot. *Handbook of cane sugar engineering*. Amsterdam, 1986.

[9] V. Kaiser and JP Gourlia. The ideal column concept: Applying exergy to distillation. *Chem. Eng.(NY)*, 92:45–53, 1985.

[10] R. Katzen, WR Ackley, GD Moon, JR Messick, BF Bruch, and DF Kavpisch. Low energy distillation systems. In *180th National Meeting of the American Chemical Society, Las Vegas, NV*, 1980.

[11] I.C. Kemp. *Pinch analysis and process integration: a user guide on process integration for the efficient use of energy*. Butterworth-Heinemann Ltd, 2007.

[12] N. Kosaric, Z. Duvnjak, A. Farkas, H. Sahm, S. Bringer-Meyer, O. Goebel, and D. Mayer. Ethanol in Ullmann's Encyclopedia of Industrial Chemistry. *Winheim: Wiley-VCH, Revised Edition, Sixth Completely*, 12:463–465, 2003.

[13] A. Lazzaretto and F. Segato. Thermodynamic Optimization of the HAT Cycle Plant Structure-Part I: Optimization of the Basic Plant Configuration. *Journal of Engineering for Gas Turbines and Power*, 123:1, 2001.

[14] A. Lazzaretto and A. Toffolo. A method to separate the problem of heat transfer interactions in the synthesis of thermal systems. *Energy*, 33(2):163–170, 2008.

[15] Z.P. Levasseur, V. Palese, and Marechal F. Energy integration study of a multi-effect evaporator. In *Proceedings of the 11th PRES Conference, Prague, Czech Republic*, pages 1184–1186, 2008.

[16] G. Leyland. *Multi-objective optimisation applied to industrial energy problems*. PhD thesis, Citeseer, 2002.

[17] B. Linnhoff. *A user guide on process integration for the efficient use of energy*. Institution of Chemical Engineers, 1982.

[18] F. Marechal and B. Kalitventzeff. Targeting the minimum cost of energy requirements: a new graphical technique for evaluating the integration of utility systems. *Computers and Chemical Engineering*, 20:225–230, 1996.

[19] F. Marechal and B. Kalitventzeff. Effect modelling and optimization, a new methodology for combined energy and environment synthesis of industrial processes. *Applied thermal engineering*, 17(8-10):981–992, 1997.

[20] F. Marechal and B. Kalitventzeff. Targeting the optimal integration of steam networks: Mathematical tools and methodology. *Computers and Chemical Engineering*, 23:S133–S136, 1999.

[21] M. Morandin, A. Toffolo, A. Lazzaretto, F. Marechal, A.V. Ensinas, and S. Nebra. Synthesis and parameter optimization of a combined sugar and ethanol production process integrated with a chp system - part 1 (base case plant) and part 2 (maximization of total site net power). In *Proceedings of the 22nd ECOS Conference, Foz do Iguaçu, Paraná, Brazil*, pages xx–xx, 2009.

[22] DL Westphalen and M.R.W. Maciel. Pinch analysis of evaporation systems. *Brazilian Journal of Chemical Engineering*, 17:525–538, 2000.

Acknowledgments: Authors gratefully acknowledge professors Francois Marechal and Daniel Favrat for supporting Matteo Morandin's activities at the Industrial Energy System Laboratory (LENI) of the Federal Polytechnic School in Lausanne (Switzerland). Some of the calculations, the results of which are presented in the present work, were performed by using tools developed at LENI (OSMOSE, EASY, MOO [16, 6]). Professors Silvia A. Nebra and Adriano V. Ensinas at the State University in Campinas (Brazil) are also acknowledged for sharing their expertise in ethanol and sugar production processes.

An economic assessment of a power plant under the use of Biomass as a feedstock material for biofuel production

Christos S. Ioakimidis [a] [b], ***Paulo C. Ferrão*** [a] [b],

[a] *MIT|Portugal Program, Lisbon, Portugal*
Sustainable Energy Systems
[b] *IN+, Instituto Superior Técnico, Lisbon, Portugal*

Abstract: Over 80 per cent of the world's primary energy supply is currently derived from fossil fuels. Concerns around energy security, climate change and unstable/increased oil prices are driving the search for cheaper and more environmentally friendly alternatives. However, it is only recently that technological advances and reduced production costs have meant biofuels can fulfill this need. Biofuels have advantages that fossil fuels do not have. Mainly they do not contribute to the climate change since the CO_2 that they release during their use has already been captured during the growth of the plants from which they are produced. Today, biofuels provide about 1% of global transport fuel. In 2003, European Commission issued directives that will govern European biofuels policy through 2010 and target of 5.75% biofuels consumption in the transportation sector by 2010 and 12% by 2020. These include measures to increase biofuels demand and supply and providing tax benefits and exemptions to facilitate growth while the principal goals are improving energy security, boosting rural development, and reducing greenhouse emission. This work presents initially the Biomass potential in the island of São Miguel (Azores) with further work on the possible production in the power, heat and biofuel sectors (the last one under a Fischer Tropsch process). Answers in questions like 'Is this plant large enough to be profitable?' or 'Is waste wood and forest residues a cheap feedstock available for its use in a Fisher-Tropsch (FT) process?' are tried to be given among others.

Keywords: Biomass, Fischer-Tropsch, Biofuels, Economics.

1. Introduction

Transport is responsible for approximately 21% of the EU's greenhouse gas emissions, and recently European Commission directives have made biofuels in transport a regional priority. Biofuels have become a growth industry with worldwide production more than doubling in the last five years. The rapid expansion of ethanol production in the United States and biodiesel production in Germany and other countries in Western Europe has created a biofuels frenzy trend. Many measures have been used to stimulate production and consumption of biofuels, including preferential taxation, subsidies, import tariffs and consumption mandates. Biofuels are currently the most important form of renewable energy in road transportation, but the debate over their environmental and economical impact is ongoing. Not all member states are equally committed to the objectives set by the European Commission, but all are trying to some extent to achieve EU targets. Biodiesel (one of the two main biofuels) accounts for 80% of European biofuels production and ethanol for the remaining 20% [1]. Active market actors and lobbying groups have contributed immensely to the evolution of the market in recent years. The definition of the Biofuel is that is any fuel derived from Biomass - recently living organisms or their metabolic byproducts, e.g., manure from cows. It is a renewable energy source, unlike other natural resources such as petroleum, coal, and nuclear fuels. Since we are already accustomed to use fossil fuels, and fossil fuels are nothing but a geologically processed Biomass the use of the Biomass to produce biofuels would be the easiest way to introduce them as an energy source either in the energy mixture of a country or/and as a transportation fuel. Most biofuels are agrofuels – made from crops and trees grown specifically for that purpose, such as sugar cane, palm oil, soya, jatropha or maize and are characterized as first generation biofuels. Agrofuel expansion means more intensive agriculture and thus more agro-chemicals (including synthetic fertilizers). It also

Corresponding Author: Christos Ioakimidis, Email: christos.ioakimidis@dem.ist.utl.pt

means more destruction of natural ecosystems, which play a vital role in regulating the climate, and the displacement of millions of small farmers, pastoralists and indigenous people. Agricultural products specifically grown for use as biofuels include corn and soybeans, primarily in the United States; flaxseed and rapeseed, primarily in Europe; sugar cane in Brazil and palm oil in South-East Asia. Biodegradable outputs (second generation biofuels) from industry, agriculture, forestry, and households can also be used to produce bioenergy; examples include straw, timber, manure, rice husks, sewage, biodegradable waste, and food leftovers. These feedstocks are converted into biogas through anaerobic digestion. Biomass used as fuel often consists of underutilized types, like chaff and animal waste. In general the idea of using biofuels from renewable sources is attractive as biofuels could help reduce greenhouse gas emissions and our dependency on fossil fuels. However, depending on the type and source of biofuel (first or second generation), the benefits and environmental impacts can vary considerably especially in favor of the second generation biofuels.

2. Second Generation Biofuels and BtL in the transportation sector

Second generation bio-fuels seem to be a more environmentally friend solution. They are already used in the road transportation sector since many years. In Europe there is more experience in bio-diesel than in other bio-fuel types. On the other hand Biomass is the only source of renewable carbon and therewith the most important feedstock for the biofuel production. The preferred production biofuel production routes comprise bioethanol from lingo-cellulose and Fischer-Tropsch (FT) fuel production, respectively, for gasoline and diesel substitution.The latter route is based on conversion of Biomass into syngas followed by Fischer- Tropsch synthesis to yield the high-quality 'designer fuel'. This so-called 'second generation' Biomass-to-Liquids (BtL) biofuel has a much higher environmental efficiency as well as less fuel consumption compared to the first generation fuels like biodiesel [2]. Syngas is the building block to create all chemicals in the petrochemical industry, but the most ultimate and demanding application is its use as a precursor of liquid fuels, in this case BtL fuels. BtL fuels will in future play a significant role for a sustainable transport strategy and for improved security of fuel supply. R&D efforts and interest shown with regard to BtL fuels is already resulting in a multitude of activities and projects demonstrated in Europe & the US. The industry continues to face major challenges as many developers race to find cost effective technologies from cleaning the syngas to converting the clean syngas into liquid products thru the FT line. Another major challenge is the cost of transporting enough Biomass to allow plants to take advantage of economies of scale. Currently most BtL project announced in Europe have partnerships and are co-located near pulp & paper mills. Biomass-to-Liquid (BtL) is a multi-step process to produce liquid biofuels from Biomass: The process uses the whole plant. While biodiesel and bio-ethanol production so far only use parts of a plant, i.e. oil, sugar, etc, BtL production uses the whole plant which is gasified by gasification while improving the CO_2 balance and increasing yield. The result is that for BTL, less land area is required per unit of energy produced compared with biodiesel or bio-ethanol [3]. Generally the catalysts used, for the following reaction, are based on iron and cobalt. The two main catalytic processes for BtL production are Fisher-Tropsch (FT) and the Mobil Process with the first one described more in detail below while is already under use throughout the world in coal-to-liquid and gas-to-liquid plants, and processes which produce methanol at an intermediate stage.

2.1. Fischer-Tropsch (FT)

The FT process is an established technology and is already applied on a large scale from coal or natural gas. Developed in the 1920s in Germany, it was used by both Germany and Japan during World War II and later by South Africa and to a lesser extent in the USA. It is a multi-stage process with a catalyzed chemical reaction in which carbon monoxide and hydrogen are converted into liquid hydrocarbons of various forms. A schematic line-up of the integrated Biomass gasification and FT synthesis (BtL) plant is shown in Fig. 1. It is a process where is used to produce synfuels from gasified Biomass. As is already known Biomass gasification takes Biomass - ideally some sort of waste plant material - and partially burns the material with a controlled amount of oxygen to produce carbon monoxide and hydrogen (synthesis gas, or syngas). Once you have produced syngas,

you can go a number of different directions. You can burn the syngas to produce combined heat and power, produce methanol, ethanol, mixed alcohols, or hydrocarbons like diesel by Catalytic depolymerization using heat and catalysts separating from the hydrocarbon wastes (e.g., Choren Power Plant, next). The diesel they are producing is not biodiesel, but "green diesel".

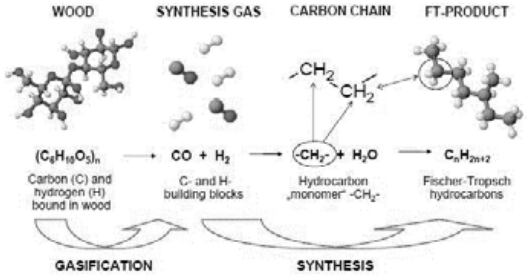

Fig. 1. Scheme of integrated Biomass gasification and Fischer-Tropsch (FT) synthesis (BtL) plan. [4].

2.2. Choren's Process

The Choren process starts off by feeding Biomass into a low-temperature gasifier (about 500°C). The purpose of this step is to remove volatile components that will form tars at higher temperatures. What remains in the gasifier is called char, and is fed into the high temperature gasifier. The volatile components are mixed with oxygen and steam and also fed into the high temperature gasifier where temperatures are around 1400°C.

Table 1. Characteristics of Choren Power Plant [5].

	Choren Plant
Maximum production	~18 million l of BtL p.a (~15,000/year cars), 113,208 bbl/year or 310 bbld
Biomass requirement	~65,000 t of wood (dry matter) p.a.: Forest residue and waste timber
Raw materials	Supply is secure for several years
Investment	~€100 million
Technical details	31.5km pipelines, 57km electrical cables, 5,000 fittings, 5,000 measuring signals, 60 pumps, 181 containers and reactors
Energy production	45MWth output
Partners	SHELL, Daimler and Volkswagen
Synthesis/hydro cracking partner	Shell

Under these conditions, the volatile components are broken down into syngas. The char is first pulverized, and then blown into the bottom of the high-temperature gasifier. The gas that exits the high-temperature gasifier is cooled, generating steam in the process that is used for power generation. The gas is then further treated (filtered and scrubbed), and it is ready for the FT process. The gasification section of the plant has been in operation since 2004, proving the scale up of the design. Since 2005, the FT section of the plant has been under construction and is now mechanically complete. Table 1 presents the characteristics of the Choren plant.

3. Methodology

Implementation of Biomass will influence on local electric power production and fuel consumption, share of emissions reduction available from the electricity generation sector and cost of meeting emissions targets. Therefore a modeling tool to analyze the system has to be precisely chosen to assure application of corresponding data andknowledge of local strategy. Modeling tool TIMES (The Integrated MARKAL-EFOM System) is the latest development of the MARKAL [6] framework maintained by the IEA's Energy Technology System Analysis Programme (ETSAP). TIMES can be described as a dynamic model since results are generated simultaneously over multiple periods. This means that all future periods and events are thus taken into account implying that market players are presumed to have perfect foresight. That is, theyknow what the demand will be in the future and theyknow the attributes (costs, technical data, etc.) of the technologies and energy carriers needed to serve those demands.

3.1. Reference Energy System (RES) in São Miguel

Figure 2 presents a simplified version of the RES used in TIMES energy model. RES represent currently available (blocks of red line) and the possible future energy technologies (blocks of blue line) and energy carriers for this case study. From the RES, the optimization model chooses the least-cost energy system, representing energy technologies and energy flows for a given time horizon and given end use energy demands.

São Miguel presents a large dependence of the primary energy on oil (87%) with the renewables having a respectable 6%. Diversification of the local energy mixture that results in less impact of

the oil imports is very important while the use of the existing high potential of the local renewable energy Biomass source would certainly benefit the present situation. Biomass requires relatively minor change in existing infrastructure and is a good option that has to be studied further and give answer to questions like:

- Is it the existing local Biomass capacity enough to contribute significantly in the energy mixture of the island?
- How can a possible Scenario work with the introduction of a Biomass Power Plant in the short-medium future?
- Is it possible the production of Biofuels by the existing Biomass sources and how much can contribute to the transportation sector?

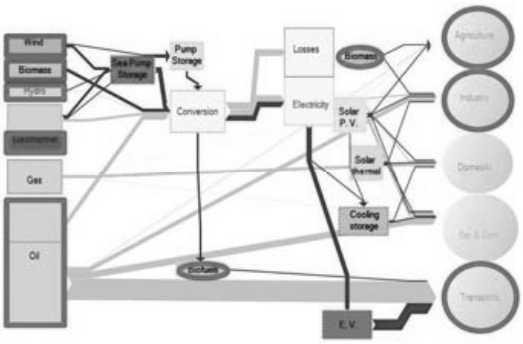

Fig. 2. The Reference Energy System (RES) used in São Miguel (surrounded blocks of red and blue lines represent the sectos used in this study).

3.2. Scenarios and Results

Recent studies [7, 8] have revealed and calculated a possible total Biomass capacity in São Miguel of 468,622 tones/year. From this amount the highest one is for the Industrial residues which correspond to a 35% of the total amount followed by the animal residues (34%), the woody residues (18%) and finally the Municipal Waste Solid (13%). Figure 3 shows a more detail form of the above percentages where in case of the woody residues which is the main Biomass resource that is examined in this study, a 43% corresponds to agricultural and Forrest residues and 57% come from the sawing and the carpentry industry. The Reference Energy Scenario (RES) situation, described in Table 2 as scenario phases contains initially only the production from renewable forms of energy which presently (base year is 2007) are: Geothermal 24MW and Hydro 5MW with a total energy production of 29MW. Then there is also the proposed EDA plan [9] (till year 2013-Phase 2) for the further enhancement and investment of the island in Green Energy while there is the simulation of this plan with further steps proposed by the authors (addition of a 10MW Biomass power plant and a Water Pumped-Storage plant in 2013-Phase 3).

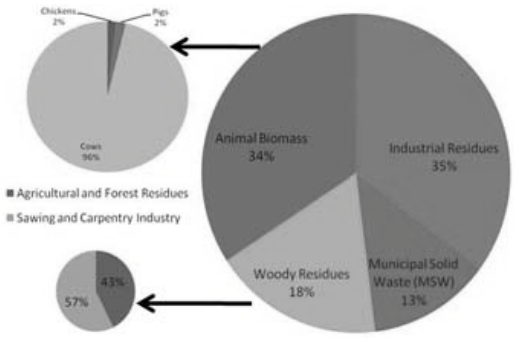

Fig. 3. Sources of Biomass Capacity in São Miguel.

Table 2. Total Primary Energy Production of RES under different scenarios.

Scenarios	Year of Investment				
	2007	2010	2011	2013	2013
BAU	29MW				
+Geo		3MW(1)		10MW(2)	
+Wind			9MW		
+Geo-Wind					
+Biomass					10MW
+Water Pumped Storage					10MW
Total Primary RES	29MW	32MW	41MW	51MW	61MW

The simulation has been performed using a mathematical programming tool based on the load profiles of the energy mixture for the spring period. The intense green area shows the Geothermal load which plus the light blue for the Hydro load results on the baseload of the 29MW are as is the present situation (BAU). In Fig. 4a) there are three main peaks observed which correspond to the highest oil demand, with the first two observed between 10.00-15.00 (~ 60MW) and the third one at 21.00 (~55MW). The weekdays load profile is higher compared to the weekend while it is also observed that the lowest load is on Sundays. When there is the extra penetration of

13MW of geothermal energy and 9MW of wind according to Phase-2 (EDA plan) then the load profile is as seen in Fig. 4b). Now there is a largest percentage of the demand that can be covered as expected by the addition of the geothermal and wind energy thus less oil is needed to cover the needs during the day and the oil use comes to the energy mixture only after 08.30 in the morning (or even later in weekends) till 24.00 as the Fig. 4b) shows that by the less percentage of grey area (corresponding to the use of oil). Even more on Sundays the load profile shows that demand can be covered by RES continuously except a few hours (10.00-17.00 and 21.00-24.00).

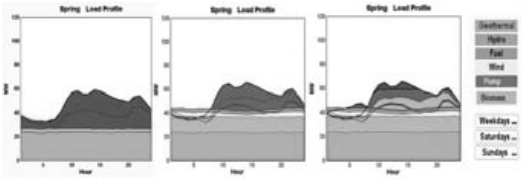

Fig. 4. Spring Load Profile a) Currently-2007, b) Addition of 9MW Wind and 13MW Geothermal - 2013 c) Addition of 10MW Biomass and 10MW of Water Pumped Storage – 2013.

Further addition of baseload energy produced by a Biomass Power plant of 10MW capacity and a Water pumped storage system of the same capacity shows (Fig. 4c) a considerably less use of oil (less grey area). The last one also means that in case of the spring load profile the weekend demand is fully covered by RES while there is an excess in the early morning hours of the energy produced by the RES that flattens the peak (or otherwise valley filling) observed during the afternoon hours. On the electricity sector (Fig. 5), the RES occupy a significant percentage (47%) in the reference energy system (2007) while when it is considered the extension according to the EDA plan then the fuel oil use is reduced by 12%, a not very high number mainly due to the average annual electricity growth rate of 4% which makes the penetration of the wind energy and the geothermal one not to be so significant. In case of the proposed RES penetration of a new Biomass power plant with a water-pumped storage system then it is helped the normalized penetration of the RES in the electricity sector while shifting the renewable production. Then the island reaches an almost ´Green - fully renewable sources state´ since now the percentage of RES is 92% with a very significant decrease of the used oil and further one of the costs related with its use. When we consider the Primary energy then the situation is quite different (Fig. 6) since due to the average annual electricity demand growth and the increase number of vehicles there will be an increase of the primary energy needed which according to the Phase-2 plan (EDA) in 2013 the percentage of reduced use of oil will be only a 3.4% compared to the reference year 2007.

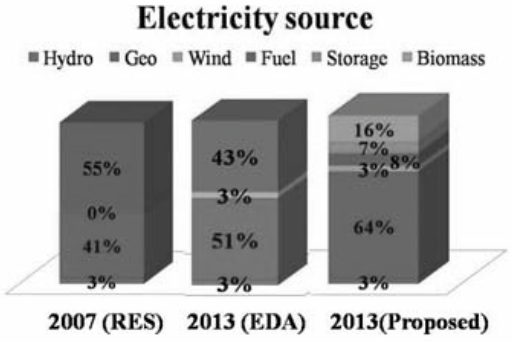

Fig. 5. The electricity source mixture under different Scenarios.

In case of the penetration of the proposed woody Biomass power plant then there is a significant reduction of the oil used which reaches a 14.2% compared to the reference year.

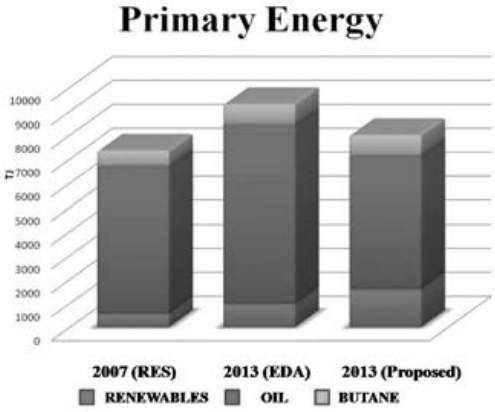

Fig. 6. The primary energy production under different Scenarios.

This reduction is very significant since it corresponds to oil imported for the transportation sector with high costs as is further explained in next paragraphs and Tables. Thus regarding primary energy the transportation sector is the one that consumes the most of the primary oil and it is where a Biomass Power Plant with a conversion via FT would profit directly the local economy on fuel savings in the form of biofuels while completing also environmental issues associated

with the reduce amount of CO_2 emissions. The amount of oil that will be used in 2013 is 6151.9TJ which according to the 2007 data given by the government of Azores corresponds to 47.2% of transportation thus 2900TJ with 75% of it to diesel fuel and 25% to gasoline fuel. In 2013 the number of used oil is reduced to 5574TJ and assuming that the transportation sector still occupies 47.2% of the primary energy then the Diesel oil used is 1970TJ or 52,718,416 l.

4. Economic Assessment

A Biomass Power Plant with a Low Heating Value (LHV) of 12,900kJ/K based on the assumption of a regular seasonal availability of the local woody residues and having an energetic conversion from Biomass to gas of 86% with a Motor Efficiency of ~47% [10] would result in a final available energy through gasification of 433,375MJ/year or a 37.3MW available for primary energy production that can be in fact used to produce a syngas for the partial substitution of the diesel oil used in the IC engines considering that these motors only operate 5,849 h/year. This represents a 52% (or 19.4MW) of Fuel Oil substitution with a reduction of the corresponding import costs of ~€4 millions as can be seen from Table 3 (Oil fuel (kg/year)) or more than the entire Caldeirão Power Plant of 16.8MW (thus responding also to the question of the importance of the existing local Biomass capacity) with a possible investment Plan of ~€31,000,000 on a 5 to 6-years payback period (on a range of Biomass cost of 25-35€/tone). Even more a recent study [11] shows that such a power plant could be able to produce more than 70 jobs, something really important for the local society and the island. Still these are values given in case that the Biomass Power Plant exists and has been constructed in 2007. Since this is something not real then the use of TIMES as an energy mixture tool showed (Fig. 6) that the final primary oil substitution would be 14.2% if such a Power Plant has started, completed and was operating in 2013. Therefore of course the amount of oil fuel reduction would be different as well as that of the cost of the imported oil. In case of using the biofuel (´Green Diesel´) by the BtL power plant then considering as seen in the previous paragraph that the Diesel used in that year for the transportation is 52,718,416 l, the construction would substitute a 34% of Diesel (or 17,924,262 l) used in the transportation sector or a total 14% of transportation fuel which would correspond with a 2.66kg/l of CO_2 for Diesel engines using Diesel fuel to 47,678 tones of CO_2 emissions compared to the 1/3 of it once using biodiesel (0.88kg/l) thus avoiding to have to the atmosphere 31,785 tones of CO_2.

Table3. Characteristics of Caldeirão power plant [11].

Reference Scenario	2007
Power production (MJ)	842,540
Power average demand (MW)	40.01
Hours of operation (h/year)	5,849
Oil fuel (kg/year)	46,807,813
Oil fuel (M€/year)	7.72
Oil fuel cost (€/kg)	0.165
Specific Consumption (kg/MJ)	0.06

Yet, one of the questions of this study was: “what is the cost for a 10MW BtL fuel production under the current Biomass sources”. BtL plants deviate from GTL plants by the feedstock that is used, i.e. solid Biomass instead of natural gas. Based on assessment [12] of the main equipments cost items of a BtL plant, it is concluded that the Total Capital Investment (TCI) for a BtL plant is typically 60% more expensive than a GTL plant with the same capacity, which is caused by the 50% higher ASU capacity, the 50% more expensive gasifier due to the solids handling, and the requirement of a Rectisol unit for bulk gas cleaning. The economy of BtL fuel production is very dependent on the production scale and large-scale facilities are required to benefit from the economy of scale. The reference point for all TCI calculations is the 34,000 bbld ORYX-1 GTL plant of Sasol-QP in Qatar with a TCI of 1,100 million US dollars. From this information the total capital investments (TCI) costs for different scales were calculated using a simple constant scale factor of 0.7 [13]. It is also assumed that commercial FT processes are applied in BtL plants. The relation between the specific TCI of a BtL plant and the plant scale (i.e. production capacity), is described by the relation below, which afford a TCI of 1,800 million US dollars for a 34,000 bbld BtL plant or 52,000$/bbld. However, for smaller scales this results probably in an underestimate of the TCI costs as a smaller scale-factor would be more realistic, i.e. 0.6 or even 0.5 for ‘real’ small GTL plants. A relation

between the TCI [$/bbld] of a BtL plant and the plant scale (i.e., production capacity), which is described by (1) is referred to the Scenario 1 below.

$$SpecificTCI(scaleX) = 52{,}000 \times \left(\frac{34{,}000[bbld]}{scaleX[bbld]} \right)^{(1-0.7)} \quad (1)$$

Available data from the Choren Commercial Power Plant (Table 1) showed that the TCI was ~€100 million ($140 million) thus using (1) while knowing that the scale of the Power Plant is 45MW, we find that for this Power Plant the constant scale factor is 0.55. Therefore we can use the same power factor to other studies since Choren is the only commercial power plant in the world that has been built as a BtL approach and can be used as a real case base comparison. Therefore in case of considering a possible 10MW Biomass (BtL) power plant – one of the main interest of this study - and using the FT process that could be installed in São Miguel, Azores then we can have the TCI of this Small (´Demo´) Power plant. In the oxygen-blown entrained flow gasifier the Biomass is converted into biosyngas with 80% chemical efficiency. The raw biosyngas is cooled, conditioned, and cleaned from the impurities. The on-specification biosyngas is used for FT synthesis to produce C_5+ liquid fuels. Conversion efficiency from biosyngas to FT C_5+ liquids is 71%. All FT liquids products are equally considered as a fuel with the Energy value of FT (C5 + products) 36.3 MJ/l and that of one barrel 159 l.

Scenario 1 (Constant scale factor 0.55 according to CHOREN Power Plant)

$$TCI(ScaleX) = 1{,}800 \times \left(\frac{69[bbld]}{34{,}000[bbld]} \right)^{0.55}$$

= 59.47 [million $] =€42.50 million (2)

$$SpecificTCI(10MW) = 52{,}000 \times \left(\frac{34{,}000[bbld]}{10[bbld]} \right)^{(1-0.55)}$$

= 2,019,151 [$/bbld] (3)

4.1. Pre-treatment, transport and Biomass Logistics

Previous detail study by Boerrigter [12] on the economics of BtL plants including the location logistics; show the cumulative FT fuel production costs for five typical scales from 50 to 8,500MW power plants. Assumptions regarding the pre-treatment, transportation and Biomass logistics are identical to this study. The production costs found were from a high 30€/GJFT for a 50MW plant to just above 15€/GJFT at a scale of 8,500MW. According to the 50MW FT fuel production costs, the two thirds (2/3) corresponded to the Conversion costs or the TCI (CAPEX) while the other one third (1/3) corresponded to the pre-treatment, transport and Biomass costs. A logarithmic extrapolation of the smallest examined power plant (50MW) to our case study of 10MW power plant shows that the FT fuel power production costs are 40€/GJFT with 75% corresponding to the TCI costs of €42.50 million and the other 25% (€14.16 million) corresponding to the pre-treatment, transport and Biomass costs in a total of €56.70 million (or $79.4 million). At the current oil price of ~73$/bbl and once the price of the oil barrel remains on this level for the next years (Scenario A) then the Simple Payback Period of a 10MW BtL Power Plant would be able after 9.6 years. In case of having the oil barrel doubled (Scenario B ~146$/bbl) as it happened in 2008 then the SPP (Simple Payback Period) will be reduced to 6.4 years of this investment. On an extreme Scenario C of ~220$/bbl (mentioned in the oil crisis two years ago by previous USA Government) then as expected this kind of investment would have a very quick SPP (3.2 years). Under Scenario A with the FT fuel power production costs at 40€/GJFT or $1.04/l which corresponds to $166/bbl with the current oil price of ~73$/bbl then the Biomass-based FT fuels are still not directly competitive on this very Small scale of the ´Demo´category. Yet this would change dramatically since the economy of BtL plants is very dependent on the production scale and large-scale facilities are required to benefit from the economy of scale as has been shown by Boerrigter.

5. Discussion

Results show that in the island of São Miguel there are significant woody Biomass sources which in case of being used as a feedstock material on a new Biomass power plant under Gasification for having gas substituting electricity produced by oil engines such as the Caldeirão plant then the penetration of a 10MW power plant would be even more profitable if it is accompanied by a water-pumped storage system. The electrification of the local energy system by renewables can reach an

almost absolute 100% percentage which can characterize even further São Miguel as a truly ´Green Island´. The profits of such an investment would be very important apart from economics - saving the local government from expensive oil imports - also environmentals since a large amount of CO_2 will be avoided due to the further penetration of the RES in the electricity sector while normalizing the demand. A Biomass gasification power plant would certainly benefit also the primary energy production by reducing the use of oil. Capital costs for BtL are still high compared to a gasification Power plant. Yet, on the other hand the difference on the Simple Payback Period of a 10MW Power plant can be profitable under some scenarios especially if the scale of the power plant or/and the oil price increases. Even so, if the power plant could be built, then the economic output in this case is faster in case of having the biofuels substituting the fuels in the transportation sector since the cost of the imported Diesel fuel is more that the cost of oil due to the distillery costs and process while also the environmental benefits are also very significant. As has been shown from this study Biomass can play a very important role in a place especially an islanded one either in the form of power or even more in the form of biofuels. According to my opinion there are a number of Biomass sources that are true waste as in this case the wood residues, and Biomass can be grown sustainably. Biofuels have a great part to play especially if power plants are operational under some scenarios. Yet only an integrated and systematic approach can trully make a place fully sustainable and dependable on its own existing renewable sources.

References

[1] New and Renewable Energy Sources - Directorate J – Energy, 2006, *Biofuels in the European Union*, Technical Report, EUR 22066, European Commission, Directorate-General for Research, Brussels, Belgium.

[2] Baitz, M., et al., 2004, *Comparative Life-Cycle Assessment for SunDiesel (Choren Process) and Conventional Diesel Fuel*, Technical Report, Volkswagen AG and DaimlerChrysler AG, Germany.

[3] Schütte, A. - Fachagentur Nachwachsende Rohstoffe e.V., Welcome Address, 2006, *Proc. 2nd International BtL, Berlin, Germany*.

[4] Hofbauer H., 2007, Thermo-chemical Biomass conversion for the provision of heat, electricity and fuels, *Proc. Fona L2L Conference,* rennet - Renewable Energy Network, Vienna University of Technology, Vienna, Austria.

[5] Kiener C., 2008, Start-up of the first commercial BtL production facility - CHORENs BETA - Plant Freiberg, *Proc. 16th European Biomass Conference & Exhibition*, Valencia, Spain.

[6] Loulou, R., et al., 2005, *Documentation for the TIMES model - PART I,* Energy Technology Systems Analysis Programme.

[7] Direcção Regional do Ambiente, *2007, Plano Estrategico de Gestão de resíduos dos Açores (PEGRA)*, ISBN978-972-99884-3-1, Portugal.

[8] Biomass Centre for Energy, 2004, *Quantificação da Biomassa Florestal e Animal nos Açores, tendo em vista o seu Aproveitamento Energético*, CBE, Portugal.

[9] Amaral J. L., 2008, *Climatic changes: the use of renewable energies in the Azores*, Palma de Mallorca, Spain.

[10] Parente, J. and Macedo, J., 2007, *Analysis of different business opportunities for Transforming Biomass into Energy in S. Miguel, Azores,* Lisbon, Portugal.

[11] Enersilva – *Promoção do uso da Biomassa Florestal para fins energéticos no sudoeste da Europa*, FEDER, 2004 | 2007, Porto, Portugal.

[12] Boerrigter, H., 2006, *Economy of Biomass-to-Liquids (BtL) plants – An Engineering Assessment*, Technical Report, ECN-C--06-019, Energy research Centre of the Netherlands (ECN) – Unit Biomass, Coal & Environmental Research, Petten, the Netherlands.

[13] Peters, M. and Timmerhaus,K., 1980, *Plant Design and Economics for Chemical Engineers*, 3rd ed., McGraw Hill Higher Education, Cambridge, UK.

Acknowledgments: The authors would like to thanks A. Pina and C. Camus and the FCT program for the financial support for the work reported in this paper and performed under the project ´PTDC/SEN/ENR/108440/2008.

Enhanced ethanol production through selective adsorption in bacterial fermentation

R. A. Jones, J. A. Gandier, J. Thibault, F. H. Tezel

Department of Chemical and Biological Engineering, University of Ottawa, 161 Louis-Pasteur, Ottawa, ON, Canada K1N 6N5

Abstract:

To alleviate the ethanol inhibition of *Escherichia coli* KO11 (ATCC 55124), during fermentation, online ethanol sequestration was achieved using F-600 activated carbon. Two separate schemes were tested, one involving direct addition of activated carbon to the fermentation flask for the purpose of in-situ adsorption and a second involving an externally located activated carbon packed bed.

For the in-situ ethanol adsorption experiments, varying amounts of adsorbent were added to the medium, at the start of the fermentation. The addition of the activated carbon in the fermentation broth resulted in increased glucose utilization and ethanol production for all flasks containing activated carbon. For the control flasks, approximately 75% of the available substrate was utilized before the fermentation was inhibited. The entire glucose supply of flasks containing activated carbon was depleted. Ethanol production was also increased from 28 g/L for the control containing no activated carbon to nearly 45 g/L (including the ethanol in the adsorbed phase) for the flasks containing activated carbon.

The implementation of an externally located packed bed adsorber for the purpose of on-line ethanol removal was tested over a number of adsorption cycles to evaluate the performance of the adsorption bed and the ethanol productivity. Results indicate that maintaining ethanol fermentation medium concentrations below 20 to 30 g/L extends and enhances ethanol productivity. After 3 cycles over a period of 180 h, an additional 80% ethanol was produced when compared to the control experiments, despite the suboptimal acidic pH of the medium.

Keywords: Ethanol, adsorption, fermentation

1. Introduction:

Recently, research attention has shifted to the production of ethanol from lignocellulosic biomass due to inherent advantages related to lower crop cost, greater biomass availability across varied climates, and a potential for greater crop utilization and thus ethanol yield per unit of crop.

Despite such advantages, significant challenges must be overcome to render the conversion of lignocellulosic biomass to ethanol economically feasible. Currently, the lower cost of this feedstock is offset by costly feed pre-treatments and waste treatments (Bothast et al., 1999). Unlike starch based feeds, which are easily depolymerised into monomeric glucose, the hydrolysis of lignocellulosic biomass requires greater energy input and results in a complex mixture of hexose and pentose sugars. Traditionally used microorganisms for bioethanol production, such as *Saccharomyces cerevisiae* and *Zymomonas mobilis*, are unable to metabolize pentose sugars (Bothast et al., 1999). Research targeting this step is indispensable in following the path to economical feasibility.

Escherichia coli was recognized early as a "platform organism" in the development of genetically modified biocatalysts and is considered

a potential candidate for the conversion of lignocellulosic feed to fuel grade ethanol (Bothast et al., 1999). Naturally occurring *E. coli* has the ability to metabolize a wide range of substrates, including all those present in lignocellulosic hydrolysate. *E. coli* KO11, has been used in numerous studies with a range of cellulose derived mixed sugar feeds including pine waste (Barbosa et al., 1992), rice hulls (Moniruzzaman and Ingram, 1998), sugar cane bagasse (Takahashi et al., 2000), and corn stover (Kim et al., 2006).

Due to the reported favourable productivity and yield, its environmental robustness, its ability to consume a wide range of mixed sugars, and its commercial availability, *E. coli* KO11 was selected amongst numerous candidates in this investigation to conduct in-situ ethanol recovery via adsorption.

2. Materials and methods

2.1 Microorganism

Escherichia coli KO11 (ATCC 55124) was purchased from the American Type Culture Collection.

2.2 Analytical methods

Cell concentration was determined by measuring the optical density (OD) at a wavelength of 600 nm (Perkin Elmer Lambda 25 UV/Vis). The pH was determined using the Barnant ATC probe and meter. Glucose and ethanol concentrations were determined by high pressure liquid chromatography (HPLC).

2.3 Adsorbent

The adsorbent used for ethanol extraction from the fermentation broth was F-600 activated carbon purchased from Calgon Corporation (Calgon, Mississauga, ON, CA).

2.4 Calcium-alginate encapsulation

Sodium alginate (Fisher scientific, Alginic acid sodium salt from brown algae for the immobilization of microorganisms) was dissolved in water by agitation at 300 rpm in a rotary shaker overnight to achieve a 2% (m/m) solution. Na-alginate solution was then poured into a flask which was then sealed with a foam stopper covered in aluminum foil. A second sealed flask contained a 1% (m/m) calcium chloride solution with a magnetic stir bar. The two flasks were connected using a silicon tube (Tygon, 1 m length x 0.16 cm diameter). One end of the tube was sealed in the Na-alginate containing flask, resting at the bottom of the solution, while the other end was sealed in the $CaCl_2$ containing flask, suspended 12 cm above the surface of the solution. The setup was sterilised by autoclave.

A volume of inoculum was added directly into the sterile alginate solution as to obtain a 2.4 mg/L bacteria/Na-alginate mixture. A peristaltic pump was used to pump the solution into the $CaCl_2$ solution. The Na-alginate formed drops at the end of the tube which fell from a height of 12 cm into the moderately agitated $CaCl_2$ solution. As each drop hit the solution, it gelled and formed an *E. coli* KO11 containing Ca-Alginate bead. The resulting beads were then hardened for 2 hours in the $CaCl_2$ solution.

2.5 Fermentation

Fermentations were carried out in 300 mL Erlenmeyer flasks fitted with rubber stoppers and topped by a wine air-lock. Each flask contained 100 mL fermentation broth consisting of 25 g/L Miller Luria-Bertani (LB) broth, supplemented with glucose as carbon source. Glucose concentration varied between experiments performed in this investigation. A sodium phosphate buffer (79 g NaH_2PO_4/L, 138.6 g Na_2HPO_4/L, pH 7.4) (Sigma Aldrich, Oakville, ON, CA) was also included, unless otherwise stated, to maintain the pH at a relatively constant value. Each flask was inoculated to provide a concentration of 1.2 mg/L of bacteria.

The flasks were kept in a MaxQ 5000 rotary shaker (Geneq Inc., Montreal, QC, CA) and maintained at 30°C. An orbital rotation of 150 rpm was used to agitate the fermentation broth for all experiments.

2.6 Ethanol inhibition experiment

Experiments were conducted under the previously described fermentation conditions. Ethanol was added after 3 h of uninterrupted fermentation in

order to produce a concentration of additional ethanol of 15, 30 and 40 g/L.

2.7 In-situ ethanol adsorption

In the first attempt at ethanol extraction, sterilized activated carbon was added to the fermentation flasks simultaneous with the inoculum in an attempt to recover in-situ a fraction of the ethanol being produced and thereby reducing its inhibitory effect. Four concentrations of activated carbon were tested: 0, 5, 10 and 15 g per 100 mL of initial broth volume. For each experimental condition, three replicate flasks were monitored throughout the duration of the experiment. The ethanol and biomass concentrations were measured along with the pH.

2.8 External extraction experiments

A second extraction scheme was performed with a packed bed adsorption column, located outside of the bioreactor. Plastic columns from Fisher Scientific, 12 cm long and 1.3 cm ID, were used for the external packed bed extraction units. The columns were filled with F-600 adsorbent.

The extraction of ethanol was performed only after ethanol reached levels demonstrated to be inhibitory (25-30 g/L range). The fermentation broth was pumped through the packed bed adsorption column at a low flow rate (1-2 mL/min) until all broth had been treated through the packed bed. Samples were taken immediately prior to and following the extraction and analysed. In order to allow the fermentation to continue, a concentrated substrate solution was added following the extraction in order to replenish the substrate supply.

3. Results and discussion:

3.1 Ethanol tolerance

In this study, the tolerance of ethanol was tested by the sudden addition of anhydrous ethanol, to obtain different ethanol concentrations in the fermentation medium.

In this set of experiments, ethanol was added three hours after seeding the flask to obtain concentrations 15, 30 and 40g/L in the fermentation medium (Figure 1). This was done to allow the bacteria to enter into growth phase before the addition of ethanol. While the addition of exogenous anhydrous ethanol is not perfectly representative of the effect of natural inhibition that occurs due to the slow production of ethanol within the vessel, the technique used, can still provide useful insight into the response and resiliency of the cells in the presence of ethanol.

As for the control where no ethanol was initially present, the substrate was consumed entirely within 24 hours and the ethanol concentration rose to approximately 10 g/L within the same time frame. Cell concentration in the control flasks reached a maximum of concentration of approximately 1.6 g/L.

The experiments with ethanol addition were performed to further explore the impact of ethanol on the bacteria. The fermentation flasks were seeded and ethanol added to each flask after three hours in order to obtain concentrations in the fermentation medium of 15 g/L, 30g/L and 40 g/L.

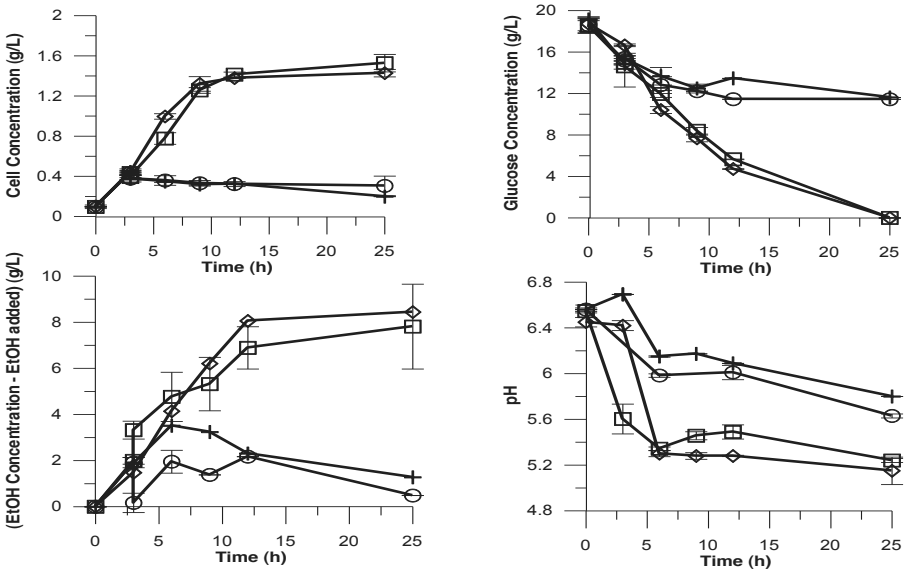

Figure 1: Flask fermentations carried out at 30°C and 150 rpm. Cell concentration, ethanol differential concentration and glucose concentration along with flask pH are plotted vs. time. Diamonds represent the control for which no ethanol was added, for the other runs, ethanol was added at the following loading levels (□: 15, +: 30 and O: 40 g/L) three hours subsequent to seeding.

Figure 1 provides the glucose and cell concentrations, the pH, and the differential ethanol concentration. The differential ethanol concentration corresponds to the amount of ethanol produced by the fermentation. It was determined by subtracting from the total concentration the initial exogenous addition. As demonstrated in Figure 1, the cell concentration for all flasks was approximately the same up until 3 hours, the time at which ethanol was added. Following the addition of different amounts of ethanol, the rate of cell growth differed greatly. For the two highest ethanol concentrations, 30 g/L and 40 g/L, the cell density in the flask did not increase. In fact a slight decrease in the cell density was observed for these trials. For the control fermentation for which no ethanol was added, and for the lowest level of ethanol loading (15 g/L), the cell concentrations were very similar throughout the 24 h run. Both sets of flasks reached a maximum cell concentration of approximately 1.6 g/L. For the substrate concentration, again, the two highest levels of loading showed similar trends with more than 50% of the available substrate going unused as the fermentation shut down at around 10 h fermentation time for both cases. The control flasks along with the low level of ethanol loading followed a similar trend for the substrate concentration. After a period of 24 h, the substrate was completely exhausted in both cases. As for the amount of ethanol produced, the control and the low ethanol loading both reached levels around 8 g/L produced while the 30 g/L and the 40 g/L flasks produced only 1-3 g/L of ethanol. If the differential ethanol concentration is added to the amount of ethanol introduced at 3 h, the total ethanol content in each flask can be determined. For the lowest amount added (15 g/L), a total ethanol concentration of around 23 g/L was present without witnessing any ethanol inhibition. Above 30 g/L, ethanol inhibition is observed as the fermentation shut down despite the ample availability of substrate and the pH was still in the optimal range. These results clearly show that the ethanol tolerance of *E. coli* KO11 is low. Even in

the relatively low ethanol concentration of 30 g/L, inhibition of cell growth and substrate utilization was observed. For this reason, the online extraction of ethanol as it is produced will be extremely important. Although in this study, inhibition was observed earlier than previous work which reported inhibition in the range of 35 to 50 g/L (Ohta et al., 1991; Qureshi et al., 2006), it should be noted that exogenous anhydrous ethanol was added to the flasks in this study while the aforementioned works dealt with ethanol produced through fermentation. Intuitively, the direct addition of ethanol is likely more detrimental to the cells as they may not have sufficient time to acclimate to ethanol and thus the sudden addition of ethanol is a shock to the fermentation system. Nevertheless, the work in this study confirms that ethanol inhibition is still a major restriction when *E. coli* KO11 is used to produce ethanol. The limited ethanol tolerance of *E. coli* KO11 is a major bottleneck for its industrial use.

3.2 In-situ ethanol extraction

Following the ethanol tolerance experiments, a series of experiments were conducted to perform the extraction of ethanol from the fermentation broth using activated carbon added directly into the fermentation flasks. Experiments were performed for three activated carbon loadings: 5, 10 and 15 g/100 mL. A series of control experiments were also conducted in parallel with a number of flasks without the addition of activated carbon. Results of these experiments are presented in Figure 2.

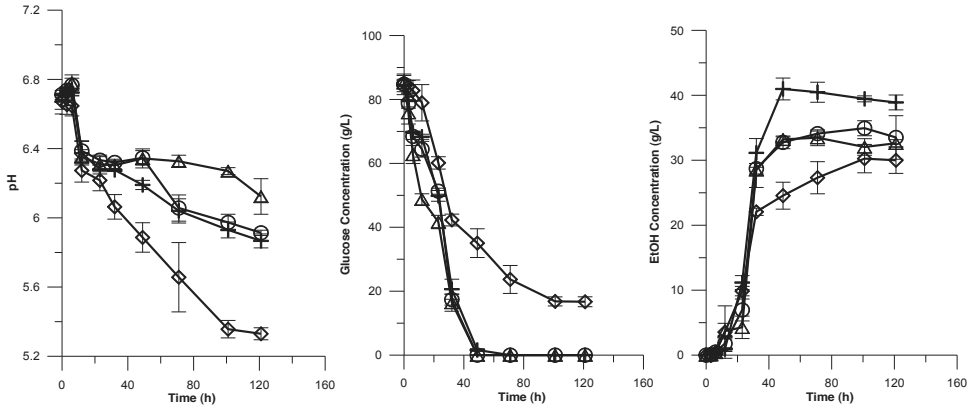

Figure 2: Flask fermentations carried out at 30°C and 150 rpm. Ethanol and glucose concentrations along with pH are plotted vs. time for different amounts of F-600 activated carbon: ◊: 0; +: 5; O: 10; and Δ: 15g of adsorbent/100 mL of solution.

For this set of experiments, all flasks started with nearly identical glucose concentrations of 85 g/L. The results of Figure 2 show that for the flasks containing activated carbon, a rapid drop in the concentration of glucose was observed across all activated carbon loading levels. This depletion of sugar in liquid phase during the first few hours can be attributed to glucose being adsorbed by the activated carbon. Over the same time frame, the control flask shows little change in the glucose level. After 6 h of fermentation, the production of ethanol started for all flasks. For the control flasks, glucose utilization to produce ethanol continued until approximately 100 h where the fermentation appears to be inhibited as a significant portion of the substrate (approximately 20 g/L) still remained unused. The ethanol concentration for the control reached nearly 30 g/L up until that point. It should be noted that the pH of the control flasks was still at a level conducive to ethanol production when the fermentation ceased. Interestingly, the flasks containing activated carbon (across all loading levels) showed complete substrate utilization between 40 and 60 h. The rate of substrate

utilization for flasks containing activated carbon was much greater than the control over the same time period. The activated carbon also had an impact on the pH of the solution. For all levels of activated carbon loading, the pH remained higher when compared to the control despite the fact that more substrate was metabolized for these runs. Fermentation by-products such as lactic and acetic acids that are known to cause the pH to decline are adsorbed by activated carbon (Rao et al., 1991). When monitoring the ethanol concentration for flasks containing activated carbon, the rate of ethanol production was enhanced when the activated carbon was added. Following a period of 40-60 h, the ethanol concentration in the liquid phase was highest for the 5 g/100 mL flask, while the 10 and 15 g/100 mL flasks had similar final liquid phase ethanol compositions.

It should also be noted that the amount of ethanol in the bulk solution is not entirely representative of the total ethanol present in the flask when activated carbon is present. A portion of the ethanol that was produced during the fermentation is bound in the adsorbed phase in equilibrium with the corresponding liquid phase concentration. The amount of ethanol in the adsorbed phase is related to the equilibrium capacity and the total quantity of activated carbon in each flask.

Based on the isotherm model presented by Jones et al. (2010), it is possible to estimate the adsorbed phase ethanol for each experiment. The estimated amount of ethanol adsorbed was combined with the ethanol measured in the liquid to determine the equivalent amount of ethanol that would be in solution if all adsorbed ethanol was unbound. The measured ethanol in the liquid phase, along with the total estimated amount of ethanol is shown in Figure 3.

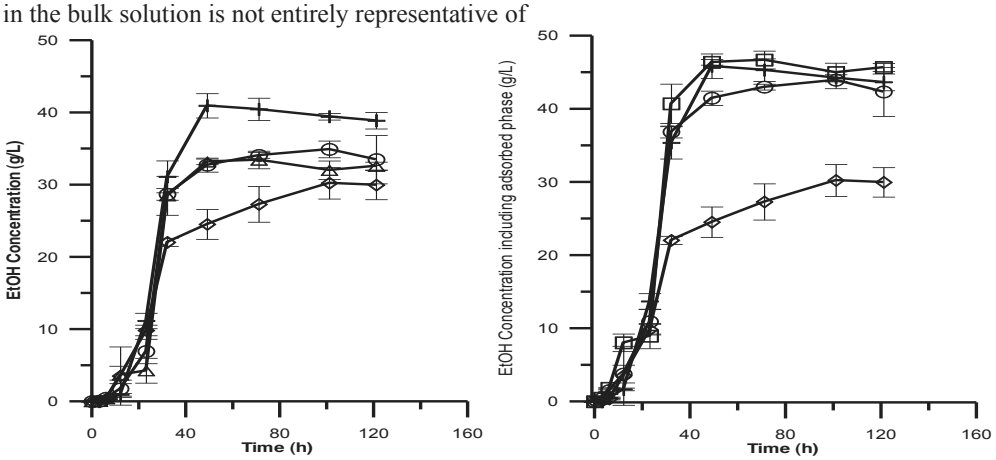

Figure 3: Flask fermentations carried out at 30°C and 150 rpm. On the left, the measured ethanol composition is shown, on the right the total ethanol present in the flask (measured plus the ethanol predicted to be in the adsorbed phase) are plotted vs. time for different amounts of F-600 activated carbon: ◊: 0; +: 5; O: 10; and Δ: 15g of adsorbent/100 mL of solution.

Figure 3 shows that a significantly higher ethanol concentration was achieved through the addition of as little as 5 g of activated carbon per 100 mL of broth. Overall, the flasks with the presence of activated carbon seem to indicate that the loading of the activated carbon (5, 10 or 15 g/100 mL) had little impact on the total amount of ethanol that was produced. In all cases with adsorbent present, the substrate was completely consumed. It should be noted, that the data in the graph on the right hand side of Figure 3 is the result of a combination of the measure liquid composition (on the left) and the isotherm predicted adsorbed phase concentration. Based on this combination, the total ethanol produced is approximately 50% higher for the fermentations where adsorbent was present. The ethanol yield predicted through the combination of the model and experimental data is

in the range of 0.50 to 0.54 g of ethanol per gram of glucose which is close to the theoretical ethanol yield of 0.51g/g.

3.3 External ethanol extraction

In addition to the introduction of activated carbon directly in the fermentation flasks to perform the in-situ partial extraction of ethanol, an alternative method for ethanol extraction was also studied. In this method, rather than adding directly the activated carbon to the flasks, experiments were performed with externally located activated carbon packed beds. Inherently, the in-situ addition of activated carbon has limited potential. One major drawback of this system would be the challenge of recovering the ethanol from the surface of the adsorbent upon saturation. In theory, the activated carbon could be separated from the broth and the ethanol desorption could subsequently be performed. However, this step would require additional solid handling which can be costly. With the activated carbon bed located outside the bioreactor, the solid handling issue is circumvented. The results of the fermentation experiments for the case where the column was located outside the bioreactor are shown in Figure 4.

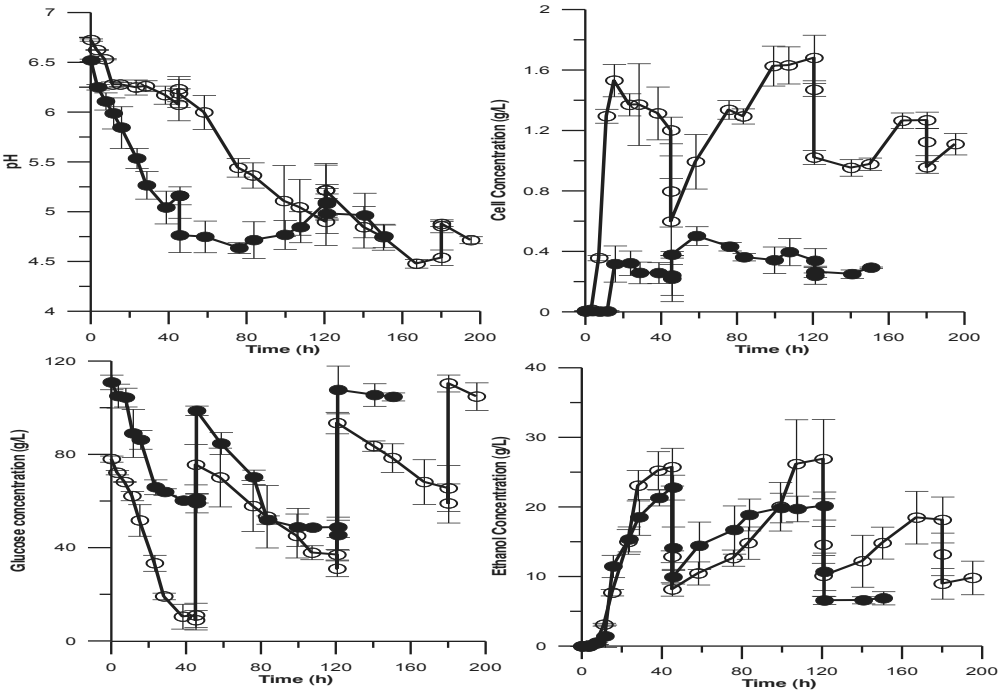

Figure 4: Flask fermentations carried out at 30°C and 150 rpm. Ethanol extractions were performed on the entire fermentation broth at 45, 120.5 for both encapsulated and planktonic bacteria. An additional extraction was performed on the planktonic bacteria at approximately 180 h. Following the extraction, a concentrated substrate solution was added to the fermentation mixture.

Figure 4 depicts the cell, ethanol and glucose concentration along with the pH of the medium for the planktonic and encapsulated fermentations, through three separate extraction cycles over a period of nearly 200 h. Initially starting with a neutral pH, a low cell concentration and a substrate concentration of approximately 80 g/L and 110 g/L glucose (planktonic and encapsulated respectively), the progression of the fermentation was monitored by intermittent sampling of the

bulk solution. The fermentation was allowed to proceed until an ethanol concentration approaching 30 g/L (45 hours) was achieved, at which time the first partial ethanol extraction was performed. A sample was taken prior to the extraction and immediately after the extraction in order to characterize the effects of the passage of the bulk liquid phase through the adsorption unit. A sample was also taken after the introduction of fresh substrate (a pure aqueous glucose solution) in order to evaluate its diluting effect on broth composition.

Within 45 hours, the ethanol concentration had reached approximately 27 g/L with approximately 10 g/L glucose remaining in the planktonic fermentation broth. In the encapsulated fermentation, 23 g/L ethanol and 60 g/L of glucose were present at this time. The rate of glucose consumption had slowed, in both sets, significantly and the concentration of both the glucose and ethanol appeared to be reaching a plateau similar to those observed with the control flasks shown in Figure 3. During the first extraction process, a third of the biomass present in the planktonic fermentation was retained in the adsorbent of the external unit. Due to the sequestration of biomass within the gel beads, this phenomenon was not observed in the encapsulated fermentation. Following the addition of the substrate solution, cell and ethanol concentrations were decreased due to the dilution of the medium. The residual glucose concentrations of the flasks remained relatively constant before and after the first extraction suggesting little glucose was adsorbed by the activated carbon. Nearly half of the ethanol in the plankotonic and encapsulated fermentation medium was adsorbed by the activated carbon of the first extraction. The fermentations were then continued, inhibition caused by the presence of high ethanol concentrations alleviated.

As can be observed in Figure 4, the rate of ethanol production was significantly reduced after the removal of ethanol via adsorption in the planktonic (free) bacterial fermentation. This reduction is correlated to the reduction in biomass concentration also observed post adsorption. As the fermentation broth is passed through the activated carbon bed, a fraction of the biomass is adsorbed along with ethanol. The point at which maximal ethanol production is achieved corresponds to the maximal allowable population represented by the plateau of biomass concentration versus time.

In the case of the encapsulated fermentation, it can be observed in the second adsorption cycle that the rate of ethanol production was maintained higher than that of the planktonic bacteria post adsorption. The sequestration of the bacteria within the beads partially alleviated the decrease in the rate of ethanol production. In order to properly characterize this phenomenon, more work must be conducted.

Additionally, throughout the entire 200 h experiment, a trend of declining pH contributed to the reduced fermentation rate observed with time. The optimal pH is reported to be 6 (Moniruzzaman et al., 1998). After a period of approximately 60 h, the pH of the planktonic fermentation medium remained below this optimal value and reached a final value of 4.5 to 4.75 after nearly 200 h. It can be noted that for each extraction cycle, a small change in pH was observed when comparing the measurement just prior and after the extraction. It is important to note that no buffer was used in the encapsulated fermentation due to its incompatibility with the gel beads. As a result, the pH in the encapsulated fermentation medium attained 4.5 within 40 hours. Fermentation occurs past 40 hours due to the buffering ability of the carboxyl groups present on the residues of the alginate polymer which make up the encapsulation matrix.

Over the second cycle, in both sets of fermentations, an additional 40 g/L of glucose was consumed and approximately 20 g/L of new ethanol was produced.

The third cycle, occurring from 120.5 to 180 hours, with an initial residual ethanol concentration of 10g/L resulted in the consumption of nearly 30 g/L of the glucose in solution and produced an additional 10 g/L of ethanol in the case of the planktonic fermentation. The pH reached a range of 4.5 to 4.7, a level at which inhibition of fermentation is observed, approaching the end of the cycle. No consumption

of glucose or production of ethanol was observed in the encapsulated fermentation during this cycle.

The final extraction, performed at 180 hour on only the planktonic fermentation medium, was less effective in terms of ethanol removal. The likely cause of the diminished ethanol capacity on the adsorbent is the concentration of glucose that remained in solution and the competition for adsorption sites. For the final extraction, the concentration of glucose in solution was approximately 65 g/L prior to the extraction and the ethanol concentration was only 17 g/L. By measuring the composition just before and after the extraction, it was observed that glucose was indeed adsorbed (as much as 6 g/L removed) during this third extraction causing a comparatively lower amount of ethanol to be removed.

Through the cycles performed, a total of approximately 51 g/L of ethanol was produced by the planktonic fermentation with the ethanol production diminishing from cycle to cycle (26, 18 and 8 g/L of new ethanol for the respective cycles). Although a buffer was added to each flask to help regulate the pH initially, pH control by way of NaOH addition or other means may have prolonged the fermentation and enhanced the ethanol production rate. For the flasks having undergone three extraction cycles, 80% more ethanol was produced when compared to the control data shown in Figure 2.

In the case of the encapsulated fermentation, 33 g/L of ethanol was produced ethanol production diminishing from cycle to cycle (23, 10 and 0g/L of new ethanol respectively).

When comparing the extraction schemes tested, the second extraction technique, having an externally located activated carbon packed bed is likely a more practical approach to on-line extraction and recovery of ethanol. Having the adsorbent located externally in a packed column would minimize the solid handling required when performing adsorption and desorption cycles. The external column would allow the extraction to be performed intermittently as ethanol concentration builds up. The adsorption cycle could continue until column saturation. The ethanol could then be recovered from the surface of the activated carbon as a concentrated vapour. The process could then be made cyclical by alternating between ethanol adsorption and column desorption. The adsorption of planktonic bacteria by the activated carbon, resulting in fouling of the adsorbant in addition to a reduced bacterial concentration of the fermentation broth, can be partially alleviated by the encapsulation of the bacteria within macroscopic gel beads.

4. Conclusions:

Ethanol inhibition plays a key role in the conversion of lignocellulosic hydrolysate to ethanol by *E. coli* KO11. By maintaining lower concentrations of this toxic product in the fermentation medium through the recovery of ethanol via adsorption, greater conversions of substrate to ethanol can be achieved. The addition of activated carbon inside the flask was found to increase the rate of substrate consumption and ethanol production. Furthermore, the addition of activated carbon enhanced the total quantity of substrate that was consumed and the total quantity of ethanol produced.

Intermittent ethanol extraction was shown to be effective in prolonging and enhancing the production of ethanol in the fermentation broth. Eighty percent more ethanol was produced during the experiment with externally located activated carbon columns. One problem that remains in the flask experiments was the continually declining pH. In order to best demonstrate the impact of on-line ethanol removal, the pH should be maintained at a level that is conducive to additional ethanol production. This could be achieved through the application of pH control by NaOH addition.

5. References:

1. Alterthum, F., Ingram, L.O., 1989, Efficient Ethanol Production from Glucose, Lactose and Xylose by Recombinant *Escherichia coli*, Appl. Environ. Microbiol., 55 (8), pp. 1943-1948.
2. Barbosa M.F., Beck, M.J., Fein, J. E., Potts, D., Ingram, L.O., 1992, Efficient Fermentation of Pinus sp. Acid Hydrolysates by an Ethanolgenic Strain of *Escherichia coli*, Appl. and Environ. Microbiol., 58 (4), pp. 1382-1384.
3. Bothast R.J., Nichols, N.N., Dien, B.S., 1999, Fermentations with New Recombinant Organisms, Biotechnol. Progr., 15, pp 867-875.
4. Cardona, C.A and Sanchez, O.J., 2007, Fuel Ethanol Production: Process Design Trends and Integration, Biores. Technol., 98 (12), pp. 2415-2457.
5. Jones R.A., Thibault, J., Tezel, F.H., 2010, Simulation and Validation of Ethanol Removal in an Adsorption Packed Bed: Isotherm and Mass Transfer Parameter Determination in Batch Studies, Can. J. Chem. Eng, In-press
6. Kim, T. H., Lee, Y. Y., Sunwoo, C., Kim, J. S., 2006, Pretreatment of Corn Stover by Low-Liquid Ammonia Recycle Percolation Process, Appl. Biochem. Biotechnol., 133, pp. 41-57.
7. Maiorella, B. L., Wilke, C. R., Blanch, H. W., 1981, Alcohol Production and Recovery, Adv. Biochem. Eng., 20, pp. 43.
8. Maiorella, B. L., C. R., and Blanch, H. W., 1984, Economic Evaluation of Alternative Fermentation Processes, Biotechnol. Bioeng., 26, pp. 1003.
9. Moniruzzaman, M., Ingram, L. O., 1998, Ethanol Production From Dilute Acid Hydrolysate of Rice Hulls Using Genetically Engineered *Escherichia coli*, Biotechnol. Lett., 20 (10); pp. 943-947.
10. Moniruzzaman, M., York, S. W., Ingram, L. O., 1998, Effects of Process Errors on the Production of Ethanol by *Escherichia coli KO11*, J. Ind. Microbiol. Biotechnol., 20, pp. 281-286.
11. Ohta K., Beall, D. S., Mejia, J. P., Shanmugam K. T., Ingram, L. O., 1991, Genetic Improvement of *Escherichia coli* for Ethanol Production: Chromosomal Integration of *Zymomonas mobilis* Genes Encoding Pyruvate Decarboxylase and Alcohol Dehydrogenase II, App. Env. Microbiol., 57, (4), pp. 893-900.
12. Qin, Y., 2008, Alginate Fibres: an Overview of the Productions Processes and Applications in Wound Management, Polym. Int., 57, pp. 171-180.
13. Qureshi, N., Dien, B. S., Nichols, N. N., Saha, B. C., Cotta, M. A., 2006, Genetically Engineered *Escherichia coli* for Ethanol Production from Xylose: Substrate and Product Inhibition and Kinetic Parameters, Food and Bioprod. Process., 84, pp. 114-122.
14. Rao, M.B., Sircar, S., Golden T.C., 1991, Equilibrium and Kinetics for Liquid Phase Adsorption of Bulk Acetic Acid from Water on Activated Carbon, Extended abstract and programs, Bienniel Conference on Carbon, pp. 54-55.
15. Smidsrod, O., Skjaok-Br, G., 1990, Alginate as Immobilization Matrix for Cells, Trends in Biotechnol. 8, pp. 71-78.
16. Takahashi, C. M., De Carvalho Lima, K. G., Takahashi, D. F., Alterthum, F., 2000, Fermentation of Sugarcane Bagasse Hemicelluloses Hydrolysate and Sugar Mixtures to Ethanol by Recombinant *Escherichia coli KO11*, World Journal of Microbiol. and Biotechnol., 16, pp. 829-834.
17. Yang, C.Y., Chiu, C.T., Chang, Y.P., Wang, Y.J., 2009, Fabrication of Porous Gelatin Microfibers Using an Aqueous Wet Spinning Process, Artif. Cells, Blood Substitutes, Immobilization Biotechnol. 37 (4), pp. 173-176.

An Analysis of Biogas Reforming Process on Ni/SDC Catalyst

G. Brus[a], Y. Komatsu[b], S. Kimijima[b], J.S. Szmyd[a]

[a] *AGH University of Science and Technology, Krakow, Poland*
[b] *Shibaura Institute of Technology, Tokyo, Japan*

Abstract: The conversion of biogas to electricity presents an attractive niche application for fuel cells. Thus attempts have been made to use biogas as a fuel for high temperature fuel cell systems such as SOFC. Biogas can be converted to hydrogen-rich fuel in a reforming process. For hydrocarbon-based fuel, three types of fuel conversion can be considered in reforming reactions: an external reforming system, an indirect internal reforming system and a direct internal reforming system. High-temperature SOFC eliminates the need for an expensive external reforming system. The possibility of using internal reforming is one of the characteristics of high temperature fuel cells like SOFC. However, for high-temperature operation, thermal management of the SOFC system becomes an important issue. To properly carry out thermal management, both detailed modeling and numerical analyses of the phenomena occurring inside the SOFC system is required. In the present work, the process of reforming biogas on an Ni/SDC catalyst has been numerically and experimentally investigated. Measurements including different thermal boundary conditions, steam-to-carbon ratios and several different fuel compositions were taken. A numerical model containing methane/steam reforming reaction, dry reforming reaction and shift reaction has been proposed to predict the gas mixture composition at the outlet of the reformer. The results of the numerical computation were compared with experimental data and good agreement has been found. The results indicate the importance of combined, numerical and experimental studies in the design of SOFC reformers. The combined approach used leads to the successful prediction of the outlet gas composition for different modelling conditions.

Keywords: Biogas Reforming, Dry Reforming, Ni/SDC catalyst, Methane/Steam Reforming.

1. Introduction

Biomass is of particular interest as a viable energy source. Thus attempts have been made to use biogas produced from the anaerobic digestion of biomass as a fuel for high-temperature fuel cell systems such as SOFC. Biogas, mostly consisting of methane (CH_4) and carbon dioxide (CO_2), is a potentially clean and renewable energy source. The high working temperature of SOFC allows for a wide range of hydrocarbon-based fuels, including biogas, to be fed directly into the system while omitting complex and expensive external reforming. For hydrocarbon-based fuel, two types of internal conversion can be considered in the reforming reactions: direct internal reforming and indirect internal reforming. Because both indirect and direct internal reforming are carried out at high temperatures, thermal management becomes an important issue. However, to do it properly, detailed modeling and numerical analyses of the phenomena occurring inside the reformer are required. The use of biogas in a small tubular SOFC unit was studied in the past [1,2]. High yields of hydrogen from biogas were obtained at relatively low temperatures and low steam-to-carbon ratios. The large carbon dioxide content of biogas enhances hydrogen production, which makes biogas a suitable fuel for fuel-cell power plants [1]. The results by J. Staniforth et al. [2] show that biogas is a suitable fuel for high-temperature fuel cells even when the methane content was below the value at which normal combustion can occur. They also showed that the formation of carbon is a major problem during the biogas reforming process and must be minimised [1, 2]. To do so, both the thermal management and catalyst material must be taken into consideration. They also discovered that by replacing Ni with a noble metal such as Rh, Ru, Pd, Ir and Pt, coke formation could be reduced [3]. Because of the relatively high prices of noble metals, their application is limited. It was reported [4, 5] that Ni supported on Samarium-doped ceria (SDC) is an

Corresponding Author: Janusz S. Szmyd, Email: janusz@agh.edu.pl

effective catalyst material for the suppression of carbon deposition. This benefits the utilisation of methane-rich fuels with a low steam-to carbon ratio. Additionally, ceria oxide based materials exhibit catalytic properties for a number of reactions, including water-gas shift and steam reforming [4,6]. Therefore Ni/SDC catalyst fulfills the requirements as a catalyst material for reforming biofuels, where protecting the catalyst from carbon formation is a key consideration. Due to its use in thermal management, the numerical analysis of biogas reforming was studied in the past [7, 8]. Nishino and Szmyd [7] assumed that a dry reforming reaction can be included in the numerical model indirectly via backward reaction of carbon monoxide with steam (shift reaction). They carried out a numerical study on the thermal and electrochemical characteristics of a tubular solid oxide fuel cell (T-SOFC), employing the steam reforming of biogas in each individual cell unit but indirectly from the anode. It was also shown that for CO_2-rich fuel, temperature gradients within the cell decrease as the proportion of CH_4 in the inlet fuel gas is reduced [7]. This is a promising observation for the future use of biogas-based fuel cell systems. Based on Nishino's work [7], Komatsu et al. [8] conducted a numerical analysis of system performance for a Solid Oxide Fuel Cell (SOFC) - Micro Gas Turbine (MGT) hybrid power system using biogas. It was found that a larger cell active area was required while the CH_4 concentration diluted. The results are promising for the future application of biogas in SOFC–MGT hybrid systems [8]. A system analysis of an SOFC unit run on biogas has been studied by Van Herle [9]. A model for a 100kW class solid oxide fuel cell (SOFC) system running on biogas from a sewage sludge digestion plant was implemented. The analysis showed that an SOFC module run on biogas containing 63% CH_4 and 35% CO_2 can be successfully used for a small heat and power unit. It was indicated that using biogas in the SOFC unit can significantly contribute to a CO_2 reduction strategy [9]. While most of the previous studies on the biogas reforming process focus on experimental or numerical analyses separately, there is a need for research on biogas reforming processes, including a comparison of experimental and numerical simulations. In the present work the reforming process of biogas on Ni/SDC catalyst has been numerically and experimentally investigated.

2. Experimental investigation

2.1. Experimental procedure

A schematic view of the experimental setup is shown in figure 1. A stainless steel reformer was placed in an electrical furnace, which can be heated up to 800°C. The maximum working temperature of pre-heater and post-heater is 400°C; however, for all experimental investigations presented in this paper, the temperature of pre- and post-heater was maintained at 200°C. High purity methane—the fuel used in the experiment—was supplied to the reformer via a flow controller and an evaporator, which was also used as the pre-heater. Water was fed to the system with a pump.

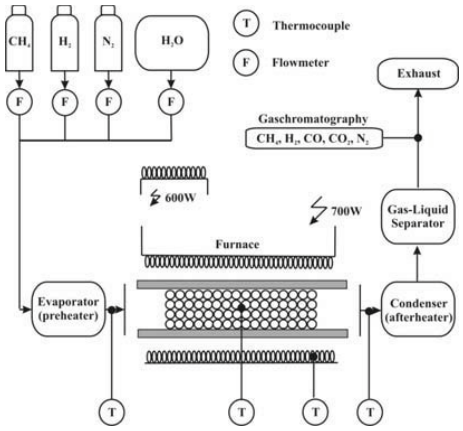

Fig. 1. Schematic view of the experimental set-up.

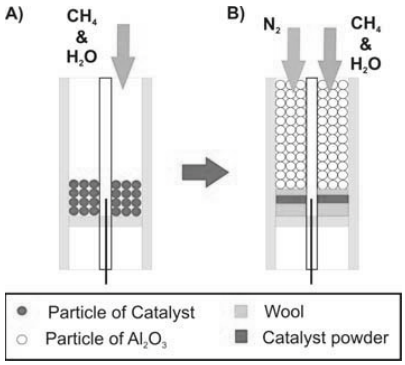

Fig. 2. Schematic view of the reaction tube. A) Typical reaction tube. B) Modified reaction tube.

The gas composition after the reforming process was analysed by gas chromatography prior to which the steam had been separated by cooling down the gas mixture to 2°C. The reforming reaction tube was partially filled with Ni/SDC and

partially with Al_2O_3, (elaboration in subsequent sections). SDC (Samarium-doped ceria) is a new type of catalyst material used for methane/steam reforming reaction. To prevent large temperature gradients in the reformer, modifications of the reaction tube were applied. To avoid a cooling effect of the entering fluid, the reformer was partially filled with Al_2O_3, as shown in figure 2B. In this solution, a mixture of gases before getting to the reaction zone was pre-heated by electric furnace to the reaction temperature. To control thermal conditions of the experiment, four thermocouples were located in the experimental set-up, as shown in figure 1 (marked as "T"). To derive correct kinetics data, the reaction has to occur in the entire volume of catalyst. This can be accomplished by maintaining the reforming conversion rate at a low level. To achieve a low level of methane conversion, the fuel was additionally mixed with nitrogen (see figure 2B). Nitrogen does not have a direct influence on the reforming reaction but the partial pressure of the components changed, which results in a decrease in both the reaction and methane conversion rates.

2.2. Catalyst preparation

The catalyst powder used in the experiment is spherical in shape and has a 0.96-µm diameter with specific surface area 4.4 m^2 per 1 g of catalyst [10]. Catalyst material was treated at the evaluated temperature of ~790^{o}C with a mixture of 150 ml/min nitrogen and 100 ml/min hydrogen due to reduction process of NiO. Figure 3 presents the reduction curve for Ni/SDC catalyst material. ~ 800^{o}C is also the characteristic temperature of cerium oxide reduction. This process is very slow and according to already published data can take over 48 h. Under reducing conditions a large amount of oxygen vacancies within the ceria material can be formed (the ceria ions Ce^{4+} are converted into Ce^{3+} and the oxygen vacancy is formed [11]). Therefore the entire reduction process can be described by the following formulas:

Reduction of nickel oxide

$$NiO \rightarrow Ni + \frac{1}{2}O_2$$

Reduction of Samarium-doped ceria

$$Ce_{0.8}Sm_{0.2}O_{1.9} \rightarrow Ce_{0.8}Sm_{0.2}O_{1.9-\delta} + \frac{\delta}{2}O_2$$

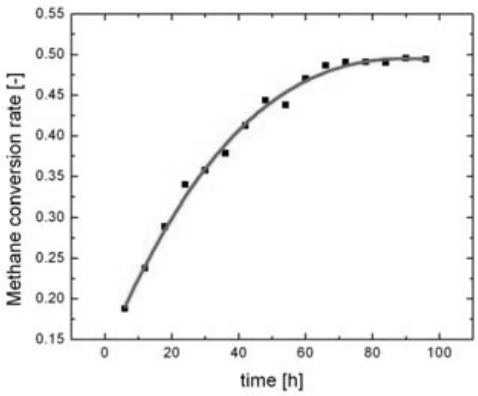

Fig. 3. Reduction curve of Samarium-doped ceria.

2.3. Methane/steam reforming kinetics on Ni/SDC catalyst

The methane/steam reforming process is widely known as a conventional process for producing hydrogen [12, 13]. The main reaction that occurs during such a process can be written:

Methane steam reforming:

$$CH_4 + H_2O \rightarrow 3H_2 + CO \quad (1)$$

Shift reaction:

$$CO + H_2O \leftrightarrow H_2 + CO_2 \quad (2)$$

It follows from the stoichiometry of the steam/methane reforming reaction that the reaction rate expression can be approximated with this equation:

$$r_{st} = k\left(p_{CH_4}\right)^a \left(p_{H_2O}\right)^b \quad (3)$$

where $k=A\exp(-E/RT)$

Where k is the reforming reaction constant, p_{CH4} and p_{H2O} are partial pressures in (Pa) of methane and water, respectively, a and b are the dimensionless coefficients responding to the reaction order, A is the pre-exponential factor (case dependent), E is the activation energy (J/mol), R is the universal gas constant (J/(mol·K)) and T is the reaction temperature, in (K). Figure 4 presents the relationship between the molar flow rate of the methane and the weight of catalyst used. As can be seen for the flow rate of methane, increasing the amount of catalyst results in a decrease in the methane outlet flow rate, which is the effect of the higher conversion rate given the inlet of methane. However, for some amount of catalyst, marked in figure 4 as a 'w_{eq}', no more change occurs in the conversion rate. The equilibrium occurs while the

outlet flow rate stays constant. Therefore, the non-equilibrium reaction for the plug-flow reactor rate can be described as a ratio between the change in the flow rate of methane and the change in the amount of catalyst [14]. Mathematically, this is written

$$r_{st} = -dF_{CH4}/dw_{cat} \quad (4)$$

where $F_{CH4}=F^{in}_{CH4}\cdot(1 - x)$

Where F^{in}_{CH4} is the methane flow rate (mol/s) and x is a dimensionless amount of reacted methane in the reforming reaction, w_{cat} is the weight of catalyst used, in kg.

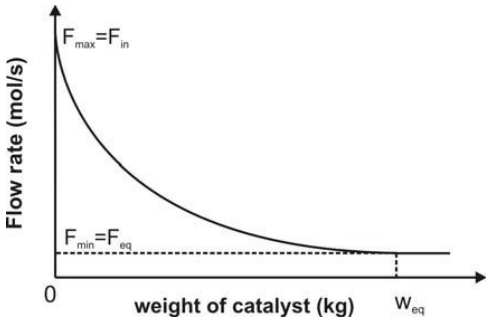

Fig. 4. Methane flow rate as a function of catalyst weight

By combining equations (3) and (4), the following equation was formulated:

$$k = \left(F^{in}_{CH_4} / w_{cat}\right)\cdot \int_0^{x_{out}} \left(1/k\left(p_{CH_4}\right)^a \left(p_{H_2O}\right)^b\right)\cdot dx \quad (5)$$

From the stoichiometry of reactions (1) and (2), the partial pressures can be defined as

$$p_{CH_4} = \left(\frac{n_{CH_4}}{n_{all}}\right)\cdot P = \left[\frac{(1-x)}{(1+SC+NC+2x)}\right]\cdot P \quad (6)$$

$$p_{H_2O} = \left(\frac{n_{H_2O}}{n_{all}}\right)\cdot P = \left[\frac{(SC-x-y)}{(1+SC+NC+2x)}\right]\cdot P \quad (7)$$

where n_{all} is the total amount of product at the outlet of the reaction tube, P is total pressure (Pa), n_{CH4}, n_{H2O} are, respectively, the methane and water fractions at the reformer output, x is a fraction of reacted methane, y is a fraction of reacted carbon monoxide, SC is the steam-to-carbon ratio and NC is the nitrogen-to-carbon ratio. n_{all} was derived from stoichiometry of reactions (1) and (2).

Introducing equations and (7) into equation (5) yields the final form of the equation for the reaction constant:

$$k = \left(\frac{F^{in}_{CH_4}}{w_{cat}}\right)\cdot \int_0^{x_{out}} \left(\frac{(1+SC+NC+2x)^{a+b}}{P^{a+b}(1-x)^a (SC-x-y)^b}\right)\cdot dx \quad (8)$$

where a and b are coefficients related to the reaction order.

Following Itoh et al. [15], the methane conversion rate x is determined by the outlet quantity and can be calculated as

$$x = \left(x_{CO} + x_{CO_2}\right) / \left(x_{CH_4} + x_{CO} + x_{CO_2}\right) \quad (9)$$

The shift reaction occurs very quickly and therefore the conversion rate can be estimated from the equilibrium equation

$$K_{sh}(x-y)(SC-x-y) = y\cdot(3x+y) \quad (10)$$

where: $K_{sh} = \exp\left[-\Delta G/(R\cdot T)\right]$

where ΔG is the change of the standard Gibbs free energy of the shift reaction (J/mol), R is the universal gas constant (J/(mol·K)) and T is the reaction temperature, in (K). Because the reaction constant does not depend on the SC and NC ratios, a and b can be found. k will be constant if a and b are set correctly. The real values of a and b are those that result in the smallest k deviation for different SC and NC ratios. Equation (8) was solved numerically for various values of a and b and for the different SC and NC ratios.

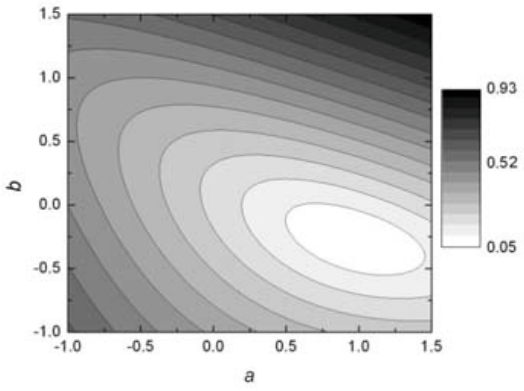

Fig. 5. Relative standard deviation of k

The range from -1.0 to 2.0 was chosen as a common range for reaction order according to previously published data; figure 5 shows the results of computation. The smallest reaction constant deviation was found to be 0.98 and -0.25 for a and b, respectively. To develop a full kinetic model of the reforming reaction on the Ni/SDC

catalyst, the relationship between the reaction temperature and reaction constant was investigated. The effect of the temperature on the reaction was studied by increasing the temperature from 600°C to 750°C. Based on experimentally obtained data, the reaction constant was calculated using equation (8). Following Achenbach and Riensche [16], the experiment was conducted for several different *SC* and *NC* ratios. Reaction kinetics does not depend on *SC* and *NC*, so to obtain more precise results a straight line was fitted to results collected for several different *SC* and *NC* ratios. The results of the experiment are presented as an Arrhenius plot, as shown in figure 6.

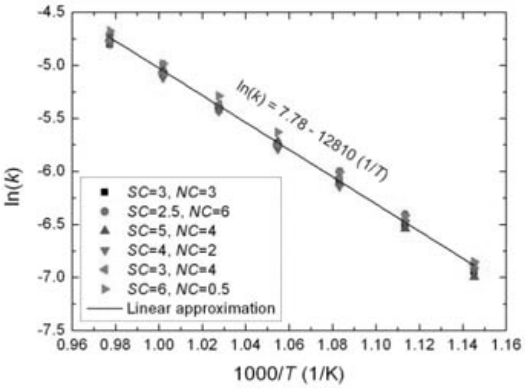

Fig. 6. Arrhenius plot for Ni/SDC

A straight line was fitted to the experimental data as a result of approximation. The equation for the straight line for this experiment takes a form of Arrhenius equation and can be described

$$\ln k = \ln A - (E/R)\cdot(1/T) \quad (11)$$

Where T (K) is the temperature of fuel conversion, R = 8.314472 ((J/(mol·K)) the universal gas constant, A is called the pre-exponential factor and corresponds to the intercept of line at $1/T$=0 and E (J/mol), which is obtained from the slope of the line and provides the activation energy of the steam reforming reaction. Thus the kinetic of the methane/steam reforming reaction can be described by a reforming rate R mol/(min·m^3) based on the experimentally obtained data by following this equation:

$$R_{st} = w'_{cat}\, A \exp\left(-E/(RT)\right)\cdot p_{CH_4}^{a}\cdot p_{CH_4}^{b} \quad (12)$$

Equation (12) is based on experimental data, where w'_{cat} is the catalyst density g/m^3, T K is the temperature of the fuel conversion, R = 8.314472 (J/(mol·K)) is universal gas constant, E=106451 (J/mol) is the activation energy of the fuel reforming reaction [16], A_{st}=2392 is the pre-exponential factor (case dependent) [16], p_{CH4} is the partial pressure of methane (Pa) and p_{H20} is the partial pressure of steam (Pa) and a=0.98 and b=-0.25 are the dimensionless coefficients responding to the reaction order. It was previously reported by [6] that SDC is able to convert methane to synthetic gas; therefore equation (12) describes not only the reaction rate on nickel catalyst but also the reaction rate on co-catalyst SDC. Equation (12) is an effective equation for describing the total reaction rate on bi-catalytic Ni/SDC material.

3. Mathematical model of the biogas reforming process

In the reforming process of biogas, there are three dominant reactions [7]:

Methane/steam reforming reaction

$$CH_4 + H_2O \rightarrow 3H_2 + CO \quad (13)$$

Shift reaction

$$CO + H_2O \leftrightarrow H_2 + CO_2 \quad (14)$$

Dry reforming reaction

$$CH_4 + CO_2 \rightarrow 2H_2 + 2CO \quad (15)$$

The steam reforming reaction described by equation (13) is a slow and highly endothermic one; therefore a kinetic expression is required to calculate the reaction rate. The reaction rate of the methane/steam reforming reaction was described by an empirical equation (12). Wei and Iglesia [17] have suggested that the steam reforming of CH_4 (13) and the dry reforming of CH_4 (15) are mechanistically equivalent to the decomposition reaction of CH_4. It was postulated and confirmed via experiment that a catalytic sequence, which reveals rigorous and intrinsic kinetics and even that the mechanisms are equivalent for reactions (13) and (15). Therefore the effective rate of both dry reforming and methane steam reforming for Ni/SDC catalyst can be described by this equation:

$$R_e = w'_{cat}\cdot A\cdot \exp\left(\frac{-E}{RT}\right)\cdot p_{CH_4}^{a}\left(p_{H_2O} + p_{CO_2}\right)^{b} \quad (16)$$

In the presented study, the separated rates of methane/steam reforming and dry reforming were distinguish by the assumption that rates of dry reforming and methane/steam reforming are

proportional to the partial pressures of steam and carbon dioxide, respectively. The rates of dry and steam reforming can therefore be calculated as

$$R_{\text{dry}} = R_{\text{e}} \frac{p_{\text{CO}_2}}{p_{\text{CO}_2} + p_{\text{H}_2\text{O}}} \tag{17}$$

$$R_{\text{st}} = R_{\text{e}} \frac{p_{\text{H}_2\text{O}}}{p_{\text{CO}_2} + p_{\text{H}_2\text{O}}} \tag{18}$$

The shift reaction (14) is very fast reaction therefore the conversion rate can be estimated from the equilibrium equation:

$$R_{\text{sh}} = K_{\text{sh}}^{+} p_{\text{CO}} p_{\text{H}_2\text{O}} - K_{\text{sh}}^{-} p_{\text{H}_2} p_{\text{CO}_2} \tag{19}$$

where

$$K_{\text{sh}} = \frac{K_{\text{sh}}^{+}}{K_{\text{sh}}^{-}} = \frac{(p_{\text{CO}_2} p_{\text{H}_2})}{(p_{\text{CO}} p_{\text{H}_2\text{O}})} = \exp\left(-\frac{\Delta G_{\text{sh}}^{0}}{RT}\right)$$

From the stoichiometry of reactions (13), (14) and (15), the partial pressures can be defined as follows:

$$p_{\text{H}_2} = \left(\frac{n_{\text{H}_2}}{n_{\text{all}}}\right) \cdot P = \left(\frac{3x + y + 2z}{1 + SC + CC + 2x + 2z}\right) \cdot P \tag{20}$$

$$p_{\text{H}_2\text{O}} = \left(\frac{n_{\text{H}_2\text{O}}}{n_{\text{all}}}\right) \cdot P = \left(\frac{SC - x - y}{1 + SC + CC + 2x + 2z}\right) \cdot P \tag{21}$$

$$p_{\text{CO}_2} = \left(\frac{n_{\text{CO}_2}}{n_{\text{all}}}\right) \cdot P = \left(\frac{CC + y - z}{1 + SC + CC + 2x + 2z}\right) \cdot P \tag{22}$$

$$p_{\text{CO}} = \left(\frac{n_{\text{CO}}}{n_{\text{all}}}\right) \cdot P = \left(\frac{x - y + 2z}{1 + SC + CC + 2x + 2z}\right) \cdot P \tag{23}$$

Introducing equations (20), (21), (22) and (23) into equation (19) yields the shift reaction equilibrium equation in the presence of dry reforming:

$$(x - y + 2z)(SC - x - y) \cdot K_{\text{sh}} = (CC + y - z)(3x + y + 2z)$$

The outlet composition per 1 mole of methane can be calculated from the stoichiometry of reactions (13), (14) and (15). The molar flow rate of each chemical component participating in the fuel reforming process in the reformer can be expressed by assuming x as the conversion rate of methane/steam reforming reaction denoted as y; as the rate of CO consumed by the steam shifting reaction and z as the conversion rate of CH_4 through the dry reforming reaction. Variations of the molar flow rate of carbon monoxide, denoted as $x-y+2z$, are produced by the fuel reforming reaction and dry reforming and consumed by the steam shifting reaction. Thus the mole fraction of each chemical species caused by the methane/steam reforming reaction, dry reforming and shift reaction are calculated as follows:

$$m_{\text{CH}_4} = (1 - x - z) / (1 + SC + CC + 2x + 2z) \tag{24}$$

$$m_{\text{H}_2} = (3x + y + 2z) / (1 + SC + CC + 2x + 2z) \tag{25}$$

$$m_{\text{H}_2\text{O}} = (SC - x - y) / (1 + SC + CC + 2x + 2z) \tag{26}$$

$$m_{\text{CO}} = (x - y + 2z) / (1 + SC + CC + 2x + 2z) \tag{27}$$

$$m_{\text{CO}_2} = (CC + y - z) / (1 + SC + CC + 2x + 2z) \tag{28}$$

Table 1. Changes of chemical components inside the fuel reformer

	inlet	Steam	Shift	Dry	outlet
CH_4	1	$-x$	0	-z	$1-x-z$
H_2O	SC	$-x$	$-y$	0	$SC-x-y$
H_2	0	$3x$	y	$2z$	$3x+y+2z$
CO	0	x	$-y$	$2z$	$x-y+2z$
CO_2	CC	0	y	$-z$	$CC+y-z$

4. Results

Numerical simulation is a useful tool for designing SOFC reformer processes. In the numerical model presented in this paper, gas composition at the outlet of the reformer can be predicted based on the inlet conditions. Examples of numerical results and their comparison with the experimental data are shown in figures 7 and 8. In the present paper, the effect of the temperature on the steam reforming reaction was studied by increasing reaction temperature from 650°C to 750°C. The biogas fed into the reformer was assumed to be composed of CH_4 and CO_2 and the molar percentage of CO_2 contained in the biogas was varied in a range from 10% to 50% (see fig. 7 and fig. 8). It was also assumed that the biogas was fed into the reformer with a steam-to-methane ratio of 3. The data shows the outlet dry gas composition to be a function of reaction temperature. As observed in figures 7 and 8, the amount of carbon monoxide increases along with the reaction temperature. This observation is significant because, in contrast to the low-temperature fuel cell, the carbon monoxide does not poison the high-temperature solid oxide fuel cell anode but can be electrochemically converted as a fuel [16]. The quality of numerical computations can be presented with a correlation plot of the measurements against the numerical model. An example of such a comparison can be seen in figure 9 where the experimental results were set against calculated reforming conversion rates.

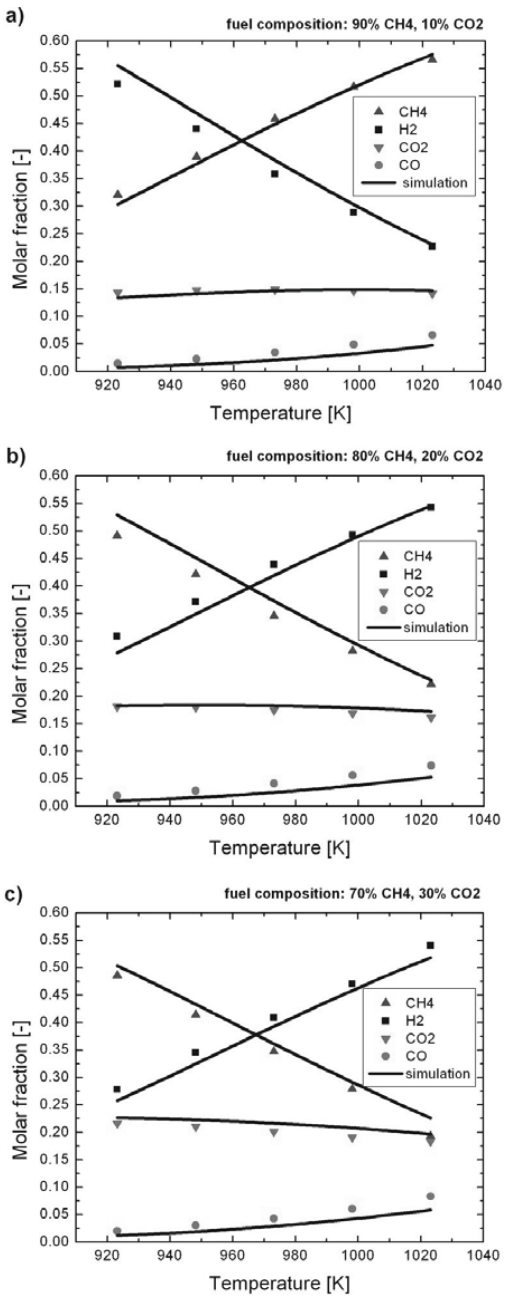

Fig 7. Experimental results compared to numerical simulation for 1.5 g of Ni/SDC. Mole fraction of fuel in the outlet of the reformer as a function of reaction temperature for different fuel composition. a)10% CO_2 90% CH_4 b) 20% CO_2 80% c) CH_4 30% CO_2 70% CH_4

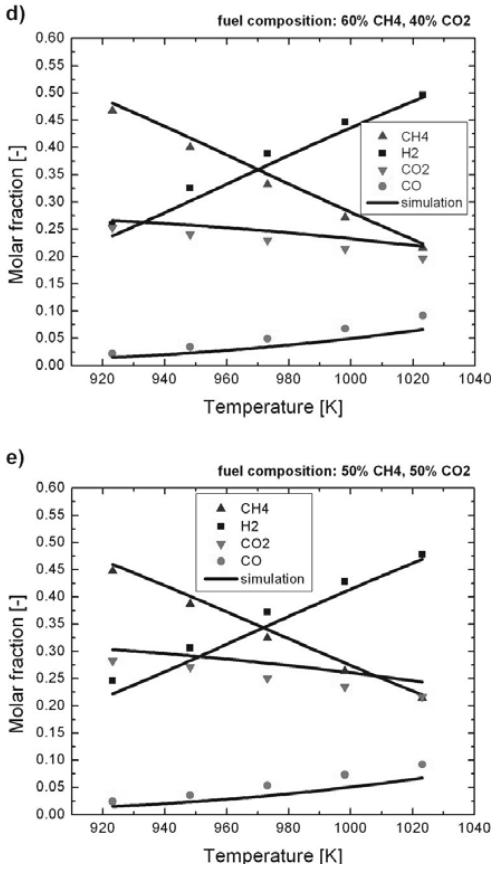

Fig 8. Experimental results compared to numerical simulation for 1.5 g of Ni/SDC. Mole fraction of fuel in the outlet of the reformer as a function of reaction temperature for different fuel composition. d)40% CO_2 60% CH_4 e) 50% CO_2 50% CH_4

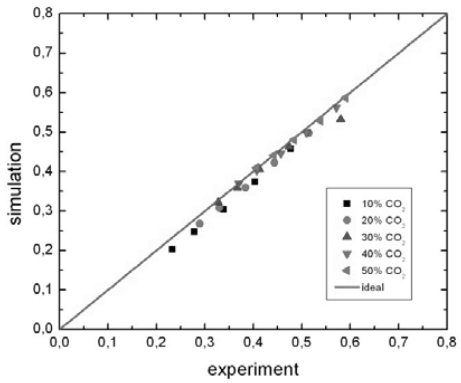

Fig. 9. Correlation plots of the experimental results to calculated reforming conversion rates

The points situated on the line show a perfect fit between experimental and numerical results. Most of the points are located on the line or close to it. The presented correlation plot indicated that the quality of the numerical model is satisfactory and can be used to predict the outlet gas composition for the methane/steam reforming process.

Conclusions

This paper has presented experimental and numerical studies on the fuel reforming process on an Ni/SDC catalyst. The gas mixture composition and the flow rate were measured at the outlet of the reformer to establish the methane reforming rate and kinetics of the reforming reaction. The experimental setup was built to investigate results for different thermal boundary conditions, the fuel flow rate and the steam-to-methane ratios. The reforming rate equation derived from experimental data was used in the mathematical model to predict the synthetic gas composition at the outlet of the reformer for the isothermal fuel reforming process of biogas. It was shown that the results of numerical computations fit the experimental data well. The obtained results show how important parallel, numerical and experimental studies are in the process design of SOFC reformers. It was also shown that applying a combined approach leads to the successful prediction of the outlet gas composition for different modeling conditions.

Nomenclature

a	reaction order
A	pre-exponential factor, (case dependent)
b	reaction order
CC	carbon dioxide to methane ratio
E	activation energy, J/mol
F	molar flow rate, mol/s
G	Gibbs free energy, J/mol
K	equilibrium constant
k	reaction constant, (case dependent)
m	molar fraction
NC	nitrogen to carbon ratio
R	universal gas constants, 8.3144 J/(mol K)
R_i	reaction rate, mol/(s·m^3)
r_i	reaction rate, mol/(s·g)
P	pressure, Pa
SC	steam to carbon ratio
T	temperature, K
u	velocity, m/s
w	weigh of catalyst, g
w'	catalyst mass density, g/m^3
x	fraction of reacted methane in methane/ steam reforming
y	fraction of reacted carbon monoxide
z	fraction of reacted methane in dry reforming

Greek symbols

δ	oxygen non-stoichiometry

Subscripts and superscripts

all	all gases
eq	equilibrium
CH_4	methane
CO	carbon monoxide
CO_2	carbon dioxide
dry	dry reforming
e	effective
f	fluid
H_2	hydrogen
H_2O	steam
max	maximum value
min	minimum value
in	inlet condition
o	ambient
out	outlet condition
sh	shift reaction
st	steam reforming reaction

References

[1] Thyberg N.S. and Carin Myrkn C., 1995, Fuel processing of biogas for small fuel cell power plants, Journal of Power Sources, 56, pp. 45-49.

[2] Staniforth J. and Kendall K., 1998, Biogas powering a small tubular solid oxide fuel cell, Journal of Power Sources, 7, pp. 275-277.

[3] Berman A. et al., 2005, Kinetics of steam reforming of methane on Ru/Al_2O_3 catalyst promoted with Mn oxides, J. Applied Catalysis, 285, pp 73-83.

[4] Brandon N. and Thomas D., 2005, Fuel Cells Compendium, Elsevier, Oxford, UK.

[5] Murray E.P., 1999, A direct-methane fuel cell with a ceria-based anode, Nature, 400, pp. 649-651.

[6] Tsang S.C., 1995, Recent advances in the conversion of methane to synthesis gas, Catalyst Today, 23, pp. 3-15.

[7] Nishino, T. and Szmyd, J.S., 2009, Numerical analysis of a cell-based indirect internal reforming tubular SOFC operating with biogas, Journal of Fuel Cell Science and Technology, In press.

[8] Komatsu Y., et. al., 2009, A Performance Analysis of a Solid Oxide Fuel Cell – Micro Gas Turbine Hybrid System Using Biogas, Solid Oxide Fuel Cells 11 (SOFC-XI), *ECS Transactions,* eds. S. C. Singhal, H. Yokokawa, 25 (2) pp. 1061-1070.

[9] Jan Van herle, et al., 2004, Biogas as a fuel source for SOFC co-generators, Journal of Power Sources 127, pp. 300–312.

[10] AGC SEIMI CHEMICAL CO, 2009, Report - Ni/SDC analysis sheets.

[11] Molenda J., et al., 2007, Functional materials for the IT-SOFC, Journal of Power Sources 173, pp. 657–670.

[12] Xu J. and Froment G.F., 1989, Methane steam reforming; methanation and water-gas shift: I intrinsic kinetics, AIChE Journal, 35, pp. 88-96.

[13] Xu J. and Froment G.F., 1989, Methane steam reforming; II Difusional limitations and reactor simulation, AIChE Journal, 35, pp. 97-103.

[14] Vannice, M.A., 2005, *Kinetics of catalytic reactions*, Springer, New York, USA.

[15] Itoh N., et. al., 2006, Kinetic Analysis on Low-Temperature Steam Reforming of Methane Using a Ruthenium Supported Catalyst, Journal of Japan Institute of Energy, 85, pp. 307-313.

[16] Achenbach E. and Riensche E., 1994, Methane/steam reforming kinetics for solid oxide fuel cells, J. Power Sources, 49, pp 333-348.

[17] Wei J. and Iglesia E., 2004, Isotopic and kinetic assessment of the mechanism of reactions of CH_4 with CO_2 or H_2O to form synthesis gas and carbon on nickel catalysts Journal of Catalyst, 224, pp. 370-383.

Acknowledgments:

This research was partially supported by the European Commission (project *Dev-BIOSOFC*, FP6-042436, MTKD-CT-2006-042436).

Design of a Heat Exchanger for the Coupling between a Thermal Biomass Generator and a Mango Dryer for Burkina Faso

David Beritault[a], Françoise Strub[b], Jean-Pierre Bédécarrats[a], Michel Rivier[c]

[a] *Laboratoire de Thermique, Énergétique et Procédés, Université de Pau et des Pays de l'Adour, Rue Jules Ferry, BP 7511, 64 075 Pau cedex, France.*
[b] *Planète Bois, Technopole Helioparc, 2 avenue Pierre Angot, 64053 Pau Cedex 9, France.*
[c] *CIRAD, Département "Performances des systèmes de production et de transformation tropicaux", UMR 95 Qualisud, TA B-95/15, 73 Rue J.F. Breton, 34398 Montpellier cedex 5, France.*

Abstract: To promote the use of agricultural and forest biomass as a source of sustainable energy to dry food products in developing countries and in our case, the mango in Burkina Faso, an adaptive technology combining a thermal biomass generator and a dryer was proposed. The use and the local legislation forbidding contact between food products and biomass combustion emissions, a heat exchanger was sized up taking into account local constraints. A modelling has enabled us to compare evolutions of the pressure drops and the exchange surfaces for three configurations of the exchanger: air drying in the tubes and smoke outside the tubes, smoke in the tubes and air outside the tubes and finally smoke in the tubes with twisted tapes and air outside the tubes. Examination of the results has allowed us to identify the most efficient configuration: smoke in the tubes with twisted tapes and air outside the tubes.

Keywords: Heat Exchanger, Development of Southern Countries, Local Manufacture, Dryer, Biomass Stove.

1. Introduction

The production of mangoes is important in Western African countries and is increasing in Burkina Faso. Traditional and small scale open air sun-drying has been commonly used to preserve product such as mangoes. These traditional systems do not result in an acceptably uniform quality product and cannot supply the desired quantity for the export of dried mangoes. Thus, a big percentage of fresh products are wasted. In order to reduce the waste of fresh fruit, and to meet the increasing demand in dried mangoes, several more efficient mango dryers have been proposed over the last twenty years particularly with the use of gas or solar energy [1]. To reach the high quantities involved or to meet the quality standards necessary for mango exportation, more research is needed. Models and experimental investigations are carried out in order to design a solar dryer with a higher capacity [2] or a dryer using other energy sources [3, 4].

One disadvantage with solar drying is that the dehydration process is interrupted at night or under low insolation (for example in the rainy season, which is the period corresponding to the production of mangoes). But the main problem concerning solar systems remains the use of the high thermal power, required to obtain the speeds of drying of high water content foodstuffs. The rapid drying avoids deterioration in quality [5].

So far, gas is the energy source most widely used for drying mango in Burkina Faso [6]. A new mango dryer, CSec-T® [7], using gas energy, was developed by the CIRAD, a French Agricultural Research Centre for International Development. Thanks to forced convection and air recycling, the speeds of drying and the energetic efficiencies were notably improved. Moreover, by its specific design, the hot air supplied to the dryer comes from an external system making possible the use of various energy sources.

In West Africa, the initial objective of the grant on the gas was to limit the use of wood and to control the deforestation. However, it generates energy dependence even more burdensome on the economy, given that the price of gas is indexed on oil. It has become urgent for Burkina Faso, as well as for all developing countries which do not produce oil, to manage this energetic problem in a sustainable manner. The use of biomass (agricultural and/or forestry) appears to be a reliable alternative to these conventional energy sources, while accompanying a program of sustainable resource management [8].

Corresponding Author: Jean-Pierre Bédécarrats, Email : jean-pierre.bedecarrats@univ-pau.fr

This use of biomass has numerous advantages. It is above all a neutral energy source, given that the carbon dioxide released into the atmosphere is equal to the carbon dioxide taken out of the atmosphere during the plant's growth. Formerly rejected, cellulose by-products, when they are available on site, are interesting because they contain an important calorific energy, ready to heat great masses of air necessary, for example, for drying [9].

In general, biomass is burnt through open fire stoves. These traditional stoves are characterized by low efficiency which results in an inefficient use of scarce fuel-wood supplies [10]. To save wood fuel and spare rural communities from acute respiratory infections [11], it is important to replace a traditional open fire stove by an improved one.

The Non Governmental Organisation "Planète Bois", specialized in transfer of adapted technology for Southern countries in the Wood-Energy field, is developing energy-efficient mud stove based on traditional stove designs. These improved stoves can be used as energy conversion systems not only for domestic applications but also for industrial needs (electricity, heat, refrigeration, power) through small cogeneration or trigeneration units.

The presented work is integrated in a particular context, specific to Southern Countries. It especially takes into account local manufacturing supplies: availability of materials and the means of production. It consists in carrying out the coupling between the powerful thermal biomass generator, developed by Planète Bois and the mango dryer, developed by the CIRAD. The use of biomass, as a source of energy, forces us either to release the smoke of their toxic compounds, like Polycyclic Aromatic Hydrocarbons in the smoking fish food processing operation, or to integrate an exchange system between the smoke and the air of drying.

Hence, the objective of this original study is to design a specific heat exchanger taking into account the local constraints to permit the use of biomass energy to dry food products. A software is developed to optimize the efficiency of the system analyzed in this article. But this software can be used to assess the coupling of an improved biomass generator with various energy conversion systems (heating process, dryer, electricity generation, power generation…) thanks to a heat exchanger.

2. Specifications of the installation

To ensure the energy exchange between the smoke of the generator and the air of the dryer, it is necessary to know the data concerning the fluids and the possibilities of coupling.

2.1. Drying air

The drying of mangoes breaks up into two phases (phase 1 and phase 2) with quite particular condition of drying for each one (Table 1). They come from studies undertaken by teams of Cirad [12] and knowledge in food science [13-14]. The extraction of "free water" occurs during phase 1 (80% of total water to remove) whereas "bound water" is extracting during phase 2.

Table 1. Data on the air for mango drying (60 kilograms per 10/12 hours of slices of mango to be dried)

Phase	1	2
Approach product temperature [°C]	80	40
Internal Recycling rate [%]	80	95
Air temperature after products before heating system [°C]	60	36
*Flow rate [m^3 h^{-1}]	1500	1500
Heating Power [kW]	8.2	1.8
Time [h]	5/6	5/6

* flow rate imposed by studies [12-14]

2.2. Smoke

The power of the thermal biomass generator is given by starting from the power necessary for the dryer (Table 1). The temperature of the generator's smoke is fixed at 900°C (minimum value measured on a first prototype of an improved biomass fired stove built by Planète Bois). By taking a total generator efficiency of 75% and an exchanger efficiency of 90%, the flow rate and exit temperature of the smoke in the heat exchanger are calculated.

2.3. The choice of coupling

The direct gas combustion, currently used in dryers, consists in mixing with the air drying, the smoke resulting from this combustion. The legislation authorizes it only for gas. The use of biomass, like source of energy, forces us either to release the smoke of their toxic compounds or to integrate an exchange system between the smoke and the air of drying. The second solution was adopted in the shape of an exchanger to transfer calorific energy.

The use of this technology imposes an additional constraint to us. For economic reasons and local manufacture, it was decided to use the fan of the dryer to ensure the air circulation. In our case, this component imposes a pressure drop of maximum 80 Pa for the heat exchanger (value of the total static pressure authorized by

the fan and in which the pressure drop of the dryer is deducted).

Volume available in the dryer being relatively low, the exchanger will be placed in the furnace of the generator. Thus, there will be no risk of smoke's condensation since it will remain in the isolated enclosure of the generator.

The passage from phase 1 to phase 2 implies a reduction in power, which is difficult to obtain with the same exchanger. To ensure a correct operation of the equipment, two heat exchangers are placed in series, each one ensuring the heating of the air for one phase. Two separated dryers are used, one for each phase.

The used configuration is presented in figure 1.

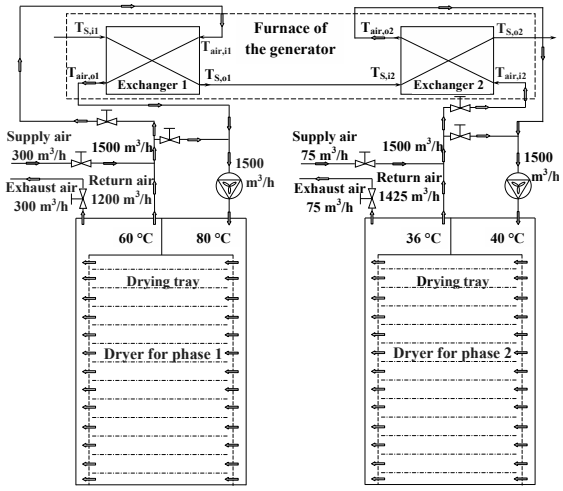

$T_{air,i}$: inlet air temperature ; $T_{air,o}$: outlet air temperature

$T_{S,i}$: inlet smoke temperature ; $T_{S,o}$: outlet smoke temperature

Fig. 1. Scheme of the used solution (with two heat exchangers) for the coupling between the generator and the dryers.

3. Design of the exchanger

The heat exchanger must be able to be manufactured starting from equipments, materials and know-how available locally. The step of design presented hereunder is original since it rests on scientific and technical training applied in a specific context to the Southern Countries.

To satisfy the requirement "being locally manufactured", the solution to import an exchanger was excluded. It was decided to design a tube exchanger: those are available in only one quality (E24 steel) and the most current dimension is one inch (25.4 mm).

For a good efficiency of the air/gas exchanger, we chose a counter current flow with cross flow. The external heat transfer coefficient is improved while placing the tubes in staggered rows and making circulate the external fluid by several passages using baffles (Figure 2).

For a tubular exchanger, two configurations are possible, that is to say:

- the air circulates in the tubes and the smoke around;
- the smoke circulates in the tubes and the air around.

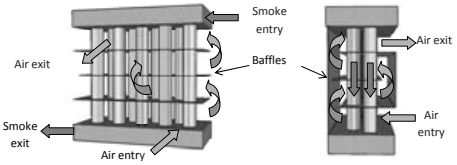

Fig. 2. Geometry of the heat exchanger.

We decided to model the two principles as well as an option for the second configuration: tube with twisted tape inserts (static mixers). This system, represented on figure 3, makes it possible to increase the turbulence of the fluid inside the tubes, for a better exchange coefficient and consequently a weaker necessary surface. Moreover, it makes it possible to carry out a cleaning, following a possible clogging due to the smoke, by rotary scraping of the interior of the tube.

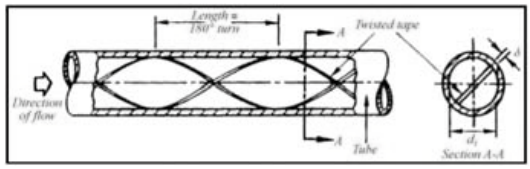

Fig. 3. Function diagram of a turbulator (twisted tape inserts).

3.1. Method of determination of the exchange surface

The method, used for the determination of the exchange surface, is presented in figure 4.

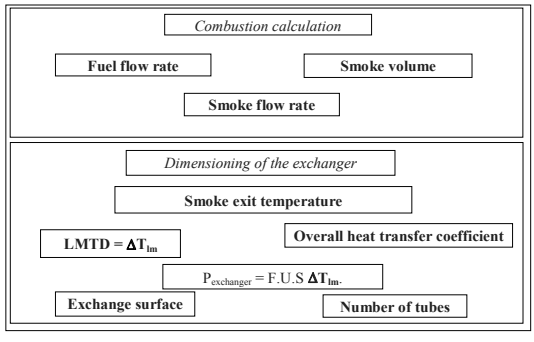

Fig. 4. Calculation Flow charts

We separated the modelling in two parts:

Combustion calculation

The used biomass is wood. The equation of its combustion (Figure 4) enables us to determine the smoke volume. The power necessary at the furnace P_{fur}, to reach the desired air temperature (Table 1), is calculated considering a total furnace efficiency $\eta_{fur} = 75\ \%$ and an exchanger efficiency $\eta_{ex} = 90\ \%$:

$$P_{fur} = \frac{\dot{m}_{air} cp_{air} \left(T_{air,o} - T_{air,i}\right)}{\eta_{fur} \times \eta_{ex}} \quad (1)$$

where $\dot{m}_{air}$ is the air mass flow, cp_{air} its heat capacity, $T_{air,i}$ and $T_{air,o}$ respectively the inlet and outlet air temperatures.

The furnace power value permits to determine the fuel mass flow rate using the low heating value of wood. The smoke volume flow rate is deduced from the smoke volume and the fuel mass flow rate.

Dimensioning of the exchangers

The energy balances, the rate equations and the subsequent analyses are subject to the following idealizations: the heat exchanger operates under steady-state conditions; the specific heats (as well as other fluid properties) of each fluid are constant throughout the exchanger; the individual and overall heat transfer coefficients are constant.

Knowing the volume flow rate of the smoke, its outlet temperature has been calculated from an enthalpy balance of the exchanger:

$$T_{S,o} = T_{S,i} - \frac{\dot{m}_{air} cp_{air} \left(T_{air,o} - T_{air,i}\right)}{\dot{m}_S \times cp_S \times \eta_{ex}} \quad (2)$$

The two fluids of the exchanger are thus characterized. For example for the phase 1, the inlet and outlet temperatures of the smoke are respectively 900 °C and 316 °C and the smoke flow rate is 105 m^3/h.

We use the Log Mean Temperature Difference LMTD method in which the heat transfer rate from the hot fluid (smoke) to the cold fluid (air) in the exchanger is given by:

$$P_{ex} = FUS\Delta T_{lm} \quad (3)$$

Where ΔT_{lm} is the Log Mean Temperature Difference (LMTD) defined for the counterflow arrangement.

F is the correction factor for the LMTD to make it applicable to heat exchangers in which the flow is not entirely counter-current or co-current. F = 0.99 in our case. U is the overall heat transfer coefficient and S the exchange surface.

U is determined according to the properties of the fluids and the configuration of the exchanger using the thermal resistances. If US is defined in terms of external tube side surface, U can be calculated using the following equation:

$$U = \left[\frac{1}{h_i}\left(\frac{d_e}{d_i}\right) + \frac{d_e}{(2\,k)} Ln\left(\frac{d_e}{d_i}\right) + \frac{1}{h_e}\right]^{-1} \quad (4)$$

Where d_i and d_e are respectively the inner and external diameter of the tube and k is the thermal conductivity of the exchanger wall.

Different correlations are used to calculate the internal and external heat transfer coefficients h_i and h_e [15-21].

For the simple tubes, the internal heat transfer coefficient is determined using the different correlations depending on the flow regime (laminar, transient or turbulent) [15].

A simple empirical correlation has been proposed by Seider and Tate [16] to predict the mean Nusselt number Nu for laminar flow in a circular duct : the Reynolds number $Re < 2300$.

The Gnielinski correlation [17] is used in the range $2300 < Re < 1\times10^4$:

$$Nu = \frac{\left(\frac{f}{2}\right)(Re\text{-}1000)\,Pr}{\left[1 + 12.7\left(\frac{f}{2}\right)^{0.5}\left(Pr^{0.66} - 1\right)\right]} \quad (5)$$

$$\text{With : } f = \frac{1}{\left[1.58 \times ln\,(Re) - 3.28\right]^2} \quad (6)$$

the fanning friction factor and Pr the Prandtl number.

For turbulent regime $Re > 1.10^4$, The Bhatti and Shah correlation is used [18] where $0.002 < \frac{\varepsilon}{d_i} < 0.05$ with ε the roughness of the tubes:

$$Nu = \frac{\left(\frac{f}{2}\right) Re\,Pr}{\left(1+\left(\frac{f}{2}\right)^{0.5}\left(4.5\left(Re\left(\frac{\varepsilon}{d_i}\right)\left(\frac{f}{2}\right)^{0.5}\right)^{0.2} Pr^{0.5} - 8.48\right)\right)} \quad (7)$$

Where

$$f = \frac{1}{\left(1.56 \times ln\left(\left(\frac{6.9}{Re}\right) + \left(\frac{\varepsilon}{(d_i \times 3.7)}\right)^{1.11}\right)\right)^2} \quad (8)$$

For the tubes with twisted tape inserts (static mixers), the used correlations are [19-20]:

Nu_{tt} is the Nusselt number for the tube with twisted tape inserts equal to ($h_i\, d_i /k$) and y is the twist ratio defined as

the axial length for a 180° turn of the tape $L(180°)$ divided by the internal diameter of the tube d_i. $y = \frac{L(180°)}{d_i}$.

- laminar flow [19]:

$$Nu_{tt} = 5.172\left(1 + 5.84\,10^{-3}\,Pr^{0.7}\,Re\,y^{-1.25}\right)^{0.5} \quad (9)$$

- turbulent regime (Re> 10^4) [20]:

$$Nu_{tt} = Nu_{\infty}\left(1 + \frac{0.769}{y}\right) \quad (10)$$

Nu_{∞} is the Nusselt number for a straight tape without twist ($y = \infty$):

$$Nu_{\infty} = 0.023\,Re^{0.8}\,Pr^{0.4}\left(\frac{\pi}{\pi - 4\frac{\delta}{d_i}}\right)^{0.8}\left(\frac{\pi + 2 - 2\frac{\delta}{d_i}}{\pi - 4\frac{\delta}{d_i}}\right)^{0.2}\left(\frac{T_m}{T_w}\right)^{0.45} \quad (11)$$

Where δ is the thickness of the tape, T_m is the bulk temperature of the fluid and T_w the wall temperature.

In our case, the thickness tape δ is 0.002 m.

For the external heat transfer coefficient, the correlations developed by Zukauskas [21] are used:

$$100 < Re < 1000 : \; Nu = 0.71\,Re^{0.5}\,Pr^{0.36} \quad (12)$$

$$1000 < Re < 2.10^5 : \; Nu = 0.35\left(\frac{X_t}{X_l}\right)^{0.2} Re^{0.6}\,Pr^{0.36} \quad (13)$$

$$Re > 2.10^5 : \; Nu = 0.031\left(\frac{X_t}{X_l}\right)^{0.2} Re^{0.8}\,Pr^{0.4} \quad (14)$$

With X_t the tube transverse pitch and X_l the tube longitudinal pitch.

We finally determine the exchange surface and the number of necessary tubes respecting the local manufacture imposition. Space available is limited. The tubes length is selected equal to 2 m.

Knowing of the number of tubes enables us to determine thereafter the pressure drop of the exchanger. The calculation of the Darcy–Weisbach friction factor λ ($\lambda = 4f$) is done with an iterative way using the Colebrook formula (15). The pressure drops of the intake and outtake manifolds are calculated using an equivalent length.

$$\frac{1}{\sqrt{\lambda}} = -2\log\left(\frac{2.51}{Re\sqrt{\lambda}} + \frac{\varepsilon}{3.71 d_i}\right) \quad (15)$$

With ε = 0.2 mm is the roughness of the internal tube surface.

When the air circulates outside the tube, the formula (15) is used substituting the inner diameter by the hydraulic diameter D_h.

3.2. Considering the pressure drop constraint

The necessary air flow is high and creates important pressure drop for the exchanger. To decrease it, the solution is to heat a portion of the flow (bypass system in figure 1) at a higher temperature that is determined to get a mixture, after exchanger, at the desired temperature. This solution reduces the pressure drop as well as increases the heat exchanger effectiveness. This will also enable us to be able to regulate the drying air temperature by varying the rate of bypass.

The whole model has been programmed for the three configurations. A sizing tool of the heat exchangers has been developed. Depending on desired flow and temperatures, it is possible to make a comparison of the three configurations and to put up evolutions of surfaces exchanges, number of tubes and head loss.

4. Results and discussion

To determine the optimum configuration, we compared the evolution of the pressure drop and the necessary exchange surfaces as a function of air flow rate in the heat exchangers.

4.1. Phase 1

By looking at the evolution of the exchange surface versus the air flow rate, shown in Figure 5, there is a significant difference between the configurations “Smoke in tubes” and “Smoke in tubes with twisted tape” close to a ratio of two.

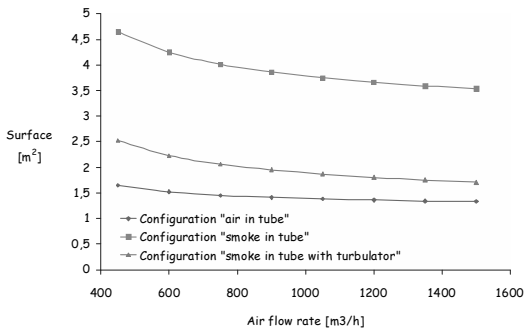

Fig. 5. Evolution of the exchange surface according to the air flow rate through exchanger for each configuration in phase 1. The smoke flow rate is constant.

This is due to an increase in fluid turbulence increasing the heat transfer coefficient; this leads to a better exchange and thus, a lower surface corresponding at a decrease in tube numbers.

For configuration "air in tubes", the heat exchange surface area is smaller than the one expected in the other two configurations. This reduction is due to the higher value of the internal air flow rate compared to that of the smoke flow rate. The high flow rate increases turbulence inside the tubes and heat transfer coefficient.

By analyzing Figure 6, we can see that the pressure drop decreases when the air flow rate decreases. So using the principle of bypass allows to decrease the pressure drop in the heat exchanger. However, we can note that for the configuration "air in tubes", this decrease is not enough to go below the limit of 80 Pa.

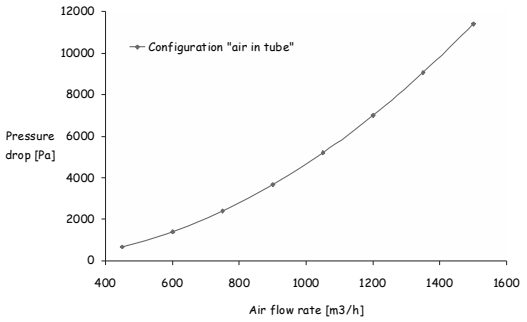

Fig. 6. Evolution of the pressure drop in the exchanger according to the air flow rate in the configuration "air in tubes".

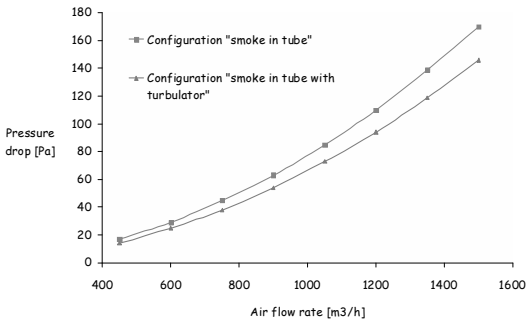

Fig. 7. Evolution of the pressure drop in the exchanger according to the air flow for the configurations "smoke in tubes" with or without turbulators.

For the two other configurations, represented in Figure 7, we can see that their developments are similar and that below 1,000 m^3 h^{-1} in the heat exchanger, pressure drop constraint is respected. So, the choice will be made between these two configurations. We validated the configuration with turbulators (static mixers).

4.2. Phase 2

The evolutions of pressure drops depending on the flow in the heat exchanger for this phase are similar to those of Phase 1 (Figures 6 and 7), they are not presented in this paper. The same conclusion can be made on the configuration "air in tubes" that is to say that it doesn't allow to respect the constraint on the pressure drop, which excludes its use.

For the other two configurations, the difference between the pressure drops is low and below a flow rate of 700 m^3 h^{-1}, the limit of 80 Pa is respected. Therefore, the choice will also be made between these two configurations for this phase.

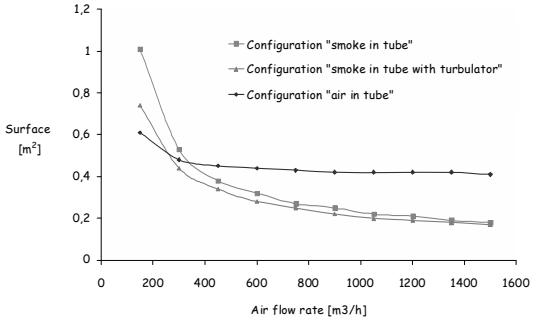

Fig. 8. Evolution of the exchange surface according to the air flow for each configuration in phase 2

By analyzing Figure 8, it is interesting to note that unlike the phase 1, there is a slight difference between the exchange surfaces evolution in configurations "Smoke in tubes" and "Smoke in tubes with twisted tape". This can be explained by the fact that for phase 2, the heat exchange surface area is smaller, and there are fewer tubes than in Phase 1. The smokes flow rate remaining the same, there is a higher internal velocity inducing more turbulence. Using turbulators for this flow regime has very little influence.

However, it seems appropriate to use turbulators, they have an advantage for the cleaning of the heat exchanger. Indeed, it could be done without access to the tubes, but simply by acting on an external control for the rotation of turbulators.

5. Proposed Solution

Only the configuration smoke in tube is retained. The air circulates around the tubes according to the schematic diagram of the exchanger (figure 2). The size that is selected is a function of the flow rate in the heat exchanger. In order to define the exchange area and the number of tubes, we must choose by-pass rates for the two phases of operation.

For phase 1, the maximum air flow rate in the heat exchanger for a pressure drop below than 80 Pa is 1,100 m^3 h^{-1}. We decided to select a by-pass rate of 50% with corresponds to a flow rate of 750 m^3 h^{-1} in the heat exchanger 1, which led to a 38 Pa head loss. This will allow us to be able to adjust the flow rate, while remaining below the 80 Pa. The obtained characteristics are shown in Table 2 for the first exchanger. A similar reasoning permits to obtain the characteristics for the second one (Table 3)

Table 2. Summary of the first exchanger characteristics

By-pass rate [%]	Exchange surface [m²]	Number of tubes	Head loss [Pa]
50	2.06	10	38

Table 3. Summary of the second exchanger characteristics

By-pass rate [%]	Exchange surface [m²]	Number of tubes	Head loss [Pa]
30	0.34	2	35

6. Conclusion

This study enables us to consider several systems adapted to the particular circumstances of Southern countries. This context, reflected in the preliminary phase, led us to eliminate technical solutions certainly more efficient but not applicable. The comparative study of different configurations was made possible by the calculation program designed to size up the exchanger and simulate its operation, and allowed us to propose the most powerful solution: the use of a tubular heat exchanger in the configuration "Smoke in tubes with twisted tape".

The dimensioning tool was also made in order to be able to modify some parameters such as levels of desired temperature and air flow rate. This model will, subsequently, be applied to another food product than mango or to achieve a coupling with several dryers.

Designing an efficient smoke air exchanger permits to develop the use of biomass generators for various applications (heating process, dryer, electricity generation, power generation…).

The project must go through the realization of a prototype. It will, in the first instance, assess the possibility of local manufacturing coupling system and mainly the method for designing turbulators (static mixers). Tests will be conducted to verify its operation, and in particular the principle of regulating the air drying temperature with the airflow.

Nomenclature

Cp heat capacity, J kg^{-1} K^{-1}
d diameter [m]
D_h hydraulic diameter [m]
f fanning friction coefficient
F correction factor for the logarithmic mean temperature difference (LMTD)
h heat transfer Coefficient [W m^{-2} K^{-1}]
k thermal conductivity [W m^{-1} K^{-1}]
L length [m]
$\dot{m}$ mass flow rate [kg s^{-1}]
Nu Nusselt number
p perimeter [m]
P Power [W]
Pr Prandtl number
Re Reynolds number
S exchange surface [m²]
T temperature [°C]
U overall heat transfer Coefficient [W m^{-2} K^{-1}]
X_l tube longitudinal pitch [m]
X_t tube transverse pitch [m]
y twist ratio
ΔT_{lm} Log Mean Temperature Difference [°C]

Greek symbols

ε roughness [m]
δ thickness of the tape [m]
η effectiveness
λ Darcy friction coefficient
μ dynamic viscosity [Pa s]

Subscripts

a Air
air air
e external
ex exchanger
i inlet of the exchanger or inner
fur furnace
m average
o outlet of the exchanger
S smoke

tt twist tape
w wall
∞ straight tape without twist

Subscripts and superscripts

a Air

References

[1] Sharma, A., Chen, C.R., Vu Lan, N, 2009, Solar-energy drying systems: A review. Renewable and Sustainable Energy Reviews; 13, pp. 1185–1210.

[2] Murthy, M.V.R., 2009, A review of new technologies, models and experimental investigations of solar driers. Renewable and Sustainable Energy Reviews, 13, pp 835–844.

[3] Madhlopa, A., Ngwalo, G., 2007, Solar dryer with thermal storage and biomass-backup heater. Solar Energy, 81, pp. 449–462.

[4] Desmorieux, H., Diallo, C, Coulibaly, Y., 2008, Operation simulation of a convective and semi-industrial mango dryer. Journal of Food Engineering, 89, pp. 119–127.

[5] Meot, J.M., 2004, Appui à la structuration de la filière mangues séchées au Burkina Faso. Activités de Recherche et Développement. Compte rendu de mission, CIRAD AMIS DOC n°37/04.

[6] Rivier, M, Niang, A.S., 2006, Appui au développement de la recherche au Burkina Faso. Utilisation d'énergies renouvelables et amélioration de la qualité des produits agroalimentaires séchés au Burkina Faso. Activité 1: Analyse du besoin par filière et type de procédé, CIRAD AMIS DOC n°16/06.

[7] Rivier, M. et al., Le séchage des mangues. Collection Guide Pratique, Editions Quae, ISBN: 978-2-7592-0341-3, 2009

[8] Frombo, F., et al., 2009, Planning woody biomass logistics for energy production: A strategic decision model. Biomass and bioenergy, 33, pp. 372-383.

[9] Demirbas A., 2001, Biomass resource facilities and biomass conversion processing for fuels and chemicals, Energy Conversion and Management, 42, pp. 1357-1378.

[10] Jetter J. J., and Kariher P., 2009, Solid-fuel household cook stoves: Characterization of performance and emissions, Biomass and bioenergy, 33, pp. 294-305.

[11] Bhattacharya, S.C., Albina, D.O., Khaing, A.M., 2002, Effects of selected parameters on performance and emission of biomass-fired cookstoves. Biomass & Bioenergy, 23, pp. 387–395.

[12] Reggad, H, et al., 2004, Appui à la structuration de la filière mangues séchées au Burkina Faso. Activités de Recherche Développement. Rapport final d'étude bibliographique, CIRAD AMIS DOC n°36/04.

[13] Rozis, J.F., 1995, Sécher des produits alimentaires, Techniques, procédés, équipements. Collection Le Point Sur, ISBN: 2-86844-072-X.

[14] Bimbenet, J.J., 1984, Le séchage dans les industries agricoles et alimentaires, Cahier de génie industriel alimentaire, SEPIAC, Paris.

[15] Rohsenow; W.M, Hartnett J.P, Cho Y.I., 1998, Handbook of heat transfer, Third Edition, McGraw-Hill.

[16] Sieder, E.N., and Tate, G.E., 1936, Heat transfer and pressure drop if liquids in tubes. Ind. Eng. Chem., Vol. 28, 1429-1453.

[17] Gnielinski, V., 1976, New equations for heat and mass transfer in turbulent pipe and channel flow, International Chemical Engineering; 16 (2), pp. 359 – 368.

[18] Bhatti, M.S, and Shah R.K., 1987, Turbulent and transition flow convective heat transfer in ducts, in : Kakac¸ S, Shah R.K, Aung W, (Eds). Handbook of Single-phase Convective Heat Transfer, Wiley-Interscience, New York.

[19] Manglik, R.M., and Bergles, A.E., 1993, Heat transfer and pressure drop correlations for twisted-tape inserts in isothermal tubes: Part I – laminar flows, Journal of Heat Transfer; 115(4), pp. 881-889.

[20] Manglik, R.M, and Bergles, A.E., 1993, Heat transfer and pressure drop correlations for twisted-tape inserts in isothermal tubes: Part II – transition and turbulent flows, Journal of Heat Transfer; 115(4), pp. 890-896.

[21] Zukauskas, A., 1987, Heat transfer from tubes in cross Flow, In : T. F. Irvine, Jr. and J. P. Hartnett, editors. Advances in Heat Transfer, volume 18: 87-159. Academic Press, Inc., New York.

Iron oxide-based thermo-chemical cycle for effective hydrogen production using coals and biomasses

N.V. Gnanapragasam[a], B.V. Reddy[a] and M.A. Rosen[a]

[a]*Faculty of Engineering and Applied Science*
University of Ontario Institute of Technology
Oshawa, Ontario, L1H 7K4, Canada

Abstract: Coal and biomass are abundant in supply but contain carbon which, to avoid greenhouse gas emissions, needs to be sequestered after the primary energy conversion. A comparison is reported here of the performance of four different coals and biomass in an iron oxide-based thermo-chemical energy conversion system. This system enables two separate streams; one for hydrogen and one for CO_2. The principal aim is to compare the hydrogen production trends for various coals and biomasses. The impact of fuel blend (mix of coal and biomass) on hydrogen production is compared, and the effect of moisture content of the source fuel on hydrogen production is investigated. Simulation results suggest that low-grade coal can also produce the same amount of hydrogen as high grade coal, but with additional energy requirements. When biomass is blended with 20% coal, 10% additional hydrogen is produced. A 10% moisture content in the source fuel reduces the hydrogen production by 10% for high-grade coal while it eliminates the possibility for low-grade biomass to produce hydrogen within the available energy region.

Keywords: chemical looping combustion, hydrogen, coal, biomass, iron oxide, hydrogen energy system, CO_2 separation, energy, fuel reactor simulation

1. Introduction

Coal is the most significant contributor among fossil fuels to current global electricity generation, accounting for 40% [1]. The most abundant fossil fuel on the planet, global recoverable coal reserves are estimated to range from 216 years to over 500 years at present usage rates [2]. By 2025, it is expected that the US will require over 250 GW of new electrical generation capacity even without considering replacing old plants [3]. Of this new capacity, the International Energy Agency (IEA) estimates that 80 GW will be met through the construction of coal-fired power plants. Worldwide installed capacity of coal-fired plants is expected to increase by over 40% in the next 20 years, exceeding 1400 GW by 2025 [3]. The supply and utilization of other solid fuels are discussed elsewhere [1,4].

Direct chemical looping (DCL) using iron-oxide cycle was proposed recently [5] in which a fuel reactor reduces a metal oxide by directly reacting with coal and some oxygen to produce hydrogen, sequestration-ready CO_2 and a metal stream, similar in design to that shown in Fig. 1. Experimentation, process modelling and simulation suggest that a maximum coal-to-hydrogen conversion efficiency of 80% can be achieved using DCL [5]. Some problems with this process include temperature issues relating to the metal oxide stability and sizing the reactor to control reaction rates [5] and improve mixing. A comparison between DCL and syngas chemical looping (SCL) combustion systems [6] suggests that DCL produces more hydrogen than SCL for lower air inlet conditions. Similar chemical looping combustion processes were investigated for producing hydrogen and electricity from coal [7] and natural gas [8]. The chemical looping based on iron-oxide cycle exhibits greater potential for CO_2 separation [9] compared to membrane separation of CO_2 from syngas after gasification [10].

In this study, four coals and four types of biomass (with values of fixed carbon (FC) and volatile mater (VM) as presented in Table 1) are used in the DCL system for producing hydrogen accompanied with CO_2 separation. Iron oxide is used as the oxygen carrier, and oxygen separated from (using ASU in Fig. 1) air is used for partial combustion to supply energy for the reduction reactions. The principal aim is to compare the hydrogen production trends for various coals and biomasses. The impact of fuel blends (mix of coal and biomass) on hydrogen production is

compared, and the effect of fuel moisture content on hydrogen production is investigated to quantify the need for dry solid fuels when using the DCL system. The potential for coals and biomass in producing hydrogen is discussed. The analysis and results helps in formulating the operating range for an effective design of the fuel reactor within the DCL system.

Table 1. Chemical composition of solid fuels [4] based on proximate and ultimate analyses with corresponding higher heating values (rounded)

No.	Solid Feedstock	Proximate			Ultimate					HHV
		FC	VM	ASH	C	H	O	N	S	(MJ/kg)
		% by wt. dry basis			% by wt. dry basis					
	Coal									
1	Anthracite	85	7	8	84	4	3	1	1	33
2	Coke	91	1	8	89	0	1	1	1	31
3	Lignite	46	49	5	64	5	25	1	0	25
4	Oak char	59	26	15	68	2	14	0	0	25
	Biomass									
5	Douglas Fir	26	73	1	56	6	37	0	0	22
6	Pine	34	66	0	56	6	38	0	0	22
7	Wood Chips	24	76	0	48	6	46	0	0	20
8	Tan Oak	9	91	0	49	6	45	0	0	19

A process simulation of the DCL system is carried out using ASPEN Plus [11], which facilitates a sensitivity analysis for varying air and iron oxide inlets to the fuel reactor, for a fixed amount of the respective solid fuel. The analysis is focussed on the energy requirements of the fuel reactor (Fig. 1) which constitutes a significant step in reducing the metal oxide by direct interaction with coal or biomass. The other two reactors are for reclaiming metal oxide by oxidation and combustion.

2. Direct chemical looping (DCL) combustion system

The DCL system involves the chemical looping combustion concept without gasification [10]. Solid fuels react directly with iron oxide in a fuel reactor (see Fig. 1) in the system. The advantage of using iron oxide (Fe_2O_3) as the oxygen carrier is that it does not involve catalytically dependent reactions [12]. The gaseous products are CO_2 and steam.

The advantages of the DCL system are a reduction in the oxygen consumption thus reducing the energy requirement in the air separation unit [5] (about 2 to 5 % of the system total) and an increase by a factor of 50 in the rates of conversion of the solid fuel [13] thus reducing the solids inventory needed and the reactor size.

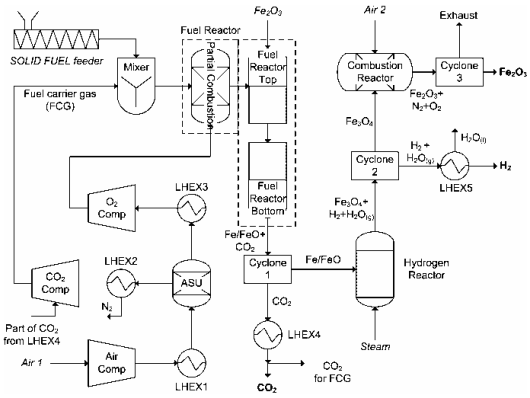

Fig. 1. Schematic of direct chemical looping (DCL) combustion system for H_2 production and CO_2 separation

Recently the minimum requirements for such resources as air, iron oxide and steam for the DCL system were reported [6] as part of a comparison between direct and syngas-based chemical looping systems. The current work extends the DCL system from Gnanapragasam et al. [6] and identifies the maximum hydrogen production for various coals and biomasses.

2.1 Fuel reactor

The fuel reactor is an extended form of a reduction reactor and the series of chemical reactions that occur within this reactor are discussed below. The primary function of the fuel reactor is to reduce iron oxide (Fe_2O_3) to iron using carbon in the feedstock. The fuel reactor is modelled with ASPEN Plus as three separate RGIBBS reactors (rigorous reaction and multiphase equilibrium based on Gibbs free energy minimization) linked together by restricting products from each of the three reactors: partial combustion, fuel reactor top and fuel reactor bottom (see Fig. 1). The reactions and conditions in the fuel reactor, following Fan et al. [5] and Mattison et al. [13], are as follows:

Partial combustion. Solid fuel devolatilisation and partial combustion occur as follows:

$$C_{11}H_{10}O \rightarrow C + CH_4 \qquad (1)$$

$$C + O_2 \rightarrow CO_2,\ \Delta H = -393.5\ \text{kJ/mol} \qquad (2)$$

The formula for the solid fuel used here, $C_{11}H_{10}O$, represents Pittsburgh #8 coal, although a different set of coals and biomass are used in the calculations [5].

Fuel reactor top. Char gasification and iron oxide reduction occur:

$$2C + O_2 \rightarrow 2CO,\ \Delta H = -221\ \text{kJ/mol} \quad (3)$$

$$C + CO_2 \rightarrow 2CO,\ \Delta H = 172.6\ \text{kJ/mol} \quad (4)$$

$$C + H_2O \rightarrow CO + H_2,\ \Delta H = 131.4\ \text{kJ/mol} \quad (5)$$

$$CH_4 + 4Fe_2O_3 \rightarrow CO_2 + 2H_2O + 8FeO,\ \Delta H = 318.5\ \text{kJ/mol} \quad (6)$$

Fuel reactor bottom. Wustite (FeO) reduction occurs:

$$FeO + CO \rightarrow Fe + CO_2,\ \Delta H = -11\ \text{kJ/mol} \quad (7)$$

$$FeO + H_2 \rightarrow Fe + H_2O,\ \Delta H = 30.2\ \text{kJ/mol} \quad (8)$$

The overall chemical reaction within the fuel reactor [5] is

$$C_{11}H_{10}O + 6.44Fe_2O_3 + 3.34O_2 \rightarrow 11CO_2 + 5H_2O + 12.88Fe \quad (9)$$

The residence time for the char in the fuel reactor is between 30 and 90 minutes [5], depending on operating temperature (750-900^{o}C) and pressure (1-30 bar). The reaction in Eq. (6) enables the conversion of methane in the gas-solid stream within the fuel reactor to CO_2 and FeO while reducing iron oxide (Fe_2O_3).

In this work, the range of operation of the fuel reactor is extended below and above that previously reported [9] to assess the impact of a range of air and iron oxide inlet conditions on reactor energy requirements. This approach enables one to identify possible process integrations for a given range of operating temperatures, within the limits imposed by the stability criterion of iron oxide [14] and the thermal limitation of feedstock materials [10].

2.2 Oxidation reactor

In the DCL system, hydrogen is produced in the oxidation reactor, with the use of iron and steam. To obtain the iron necessary for oxidation, the fuel reactor reduces iron oxide using CO obtained from solid fuels. The oxidation reactor operates at 30 bar and 500 to 700^{o}C to oxidize the metal produced in the reduction reactor using steam. The products are 99 % pure hydrogen and magnetite (Fe_3O_4). The reactions follow:

$$Fe + H_2O_{(g)} \rightarrow FeO + H_2 \quad (10)$$

$$3FeO + H_2O_{(g)} \rightarrow Fe_3O_4 + H_2,\ \Delta H = 302.4\ \text{kJ/mol} \quad (11)$$

Both reactions are slightly exothermic and some of the heat may be used for preheating the feed water to make steam.

2.3 Combustion reactor

The magnetite formed in the oxidation reactor enters the combustion reactor where it reacts with oxygen to form the more stable form of iron oxide III (Fe_2O_3). A significant amount of heat is produced during the oxidation of Fe_3O_4 to Fe_2O_3 [5]. The reaction is

$$4Fe_3O_4 + O_2 \rightarrow 6Fe_2O_3,\quad \Delta H = 302.4\ \text{kJ/mol} \quad (12)$$

The gas composition of 'Exhaust' in Fig. 1 is the remaining oxygen after the reaction in Eq. (12) and the corresponding amount of nitrogen.

2.4 System details

Design details and explanations of problems associated with the reduction, oxidation and combustion reactors at the laboratory scale have been reported [5]. The cyclones remove solids (metal oxide) from the gas stream. In the schematic in Fig. 1, only the solid streams are indicated (Fe/FeO, Fe_3O_4 and Fe_2O_3) after each cyclone. The representation of the DCL system in Fig. 1 is for one cycle of operation. The Fe_2O_3 is not recycled, but the setting for the simulation (through cyclones, heat exchangers and bag filters) is such that all Fe_2O_3 is recovered, thereby representing an ideal or maximum-benefit case.

The DCL system is modelled with ASPEN Plus such that all the solids (char and iron oxide) are recovered in each cyclone by adding a bag filter model after cyclone separation. The reason for assuming complete recovery of solids is to focus the analysis on material resource requirements without losses, so the minimum requirement for metal oxide and the corresponding requirements of steam and air are found.

2.5 System operating conditions

The pressure in all the reactors is set at 30 bar. The solid fuel carrier gas (FCG), CO_2 in the current analysis, thus enters the compressor at 15 bar with a 10 kg/s mass flow rate and is compressed to 30 bar before entering a mixer to transport the solid fuel from there to the primary reactor in each of the system. Even though it is also called the 'air' inlet to the fuel reactor, it is actually the oxygen inlet since there is an air separation unit (ASU) in the DCL system as shown in Fig. 1. For all analyses, the simulation performed on the DCL

system involves a full range of operating conditions: air inlet to fuel reactor from 1 to 25 kg/s and iron oxide inlet to fuel reactor from 1 to 30 kg/s. The mass flow rate for coals and biomass is fixed at 5 kg/s for the entire analysis.

2.6 Thermodynamic analysis

A thermodynamic assessment is done on the system in Fig. 1 to determine the energy performance of the proposed system. The following simplifications and assumptions are used:

- Chemical and phase equilibrium based on a Gibbs free energy minimization model [11] are used for the fuel, oxidation and combustion reactors.
- Coal is delivered dry, crushed and chlorine free.
- The following components are not included in the thermodynamic analysis: cyclone, bag filter, mixers, gas separators (ASU).
- Gas property evaluations are based on the Peng-Robinson equation of state with Boston-Mathias modifications [11], with a reference temperature of 298 K at a pressure of 1 bar.

An energy balance for components that involve the mixing of environmental and fuel elements is discussed here for the IGCC system. The energy rate balance considering each component in Fig. 1 as a control volume at steady state is

$$\frac{\dot{Q}_{cv}}{\dot{n}_F} - \frac{\dot{W}_{cv}}{\dot{n}_F} = \sum_P n_e \left(\bar{h}_f^o + \Delta\bar{h} \right)_e - \sum_R n_i \left(\bar{h}_f^o + \Delta\bar{h} \right)_i \quad (13)$$

Here, F denotes fuel (coal for the gasifier and syngas for combustors), i the incoming fuel and air/gas streams and e the exiting combustion products. The enthalpies of reactants (R) and products (P) are evaluated by the Aspen Plus code and the energy balance is evaluated with an Excel spreadsheet.

3. Hydrogen potential for high- and low-grade solid fuels

The four coals and four types of biomass used in this analysis were selected based on having a good variation in fixed carbon, carbon content, oxygen content and HHV. Fixed carbon in solid fuels is the carbon remaining after the volatile matter is removed (Table 1). The heats of reaction for Eqs. (2) to (12) are given to provide a sense of how much energy is provided by certain reactions relative to other reactions, thus creating a situation where the operating conditions dictate the availability or requirement of energy within the fuel reactor. The zero line in Figs. 2 and 3 is the balance of energy available and required when the reactions are at equilibrium.

3.1 Influence of iron oxide consumption on fuel reactor heat duty

The results in Figs. 2 to 7 are shown as colour legends instead of curves for easier distinction. The fuel reactor heat duty mentioned in Figs. 2 and 3 is the thermal energy required or available in completing the set of Eqs. (3) to (6) in obtaining FeO. The wavy (up and down) profile of the values in Fig. 2 is due to simultaneously varying two parameters in the current model: fuel reactor air consumption and iron oxide consumption. The performance of each coal in the DCL system for hydrogen production is shown in Fig. 4 and that of each biomass is shown in Fig. 5.

The parameters in Figs. 2 and 3 are plotted for increasing iron oxide (Fe_2O_3) consumption. The vertical lines in each coal and biomass profile in Figs. 2 and 3 are the range of fuel reactor heat duty for a corresponding increase in iron oxide mass flow rate for a given air flow rate into the fuel reactor.

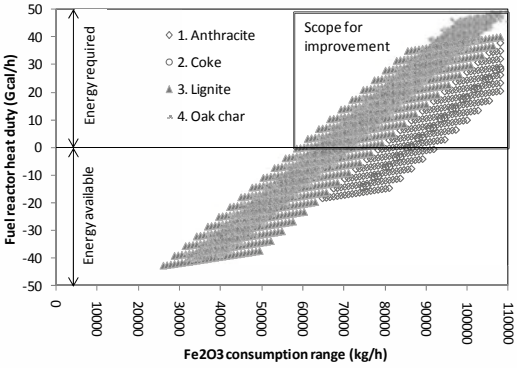

Fig. 2. Fuel reactor heat duty when using four coals for varying Fe_2O_3 consumption

The wavy profiles also provide minimum and maximum conditions for hydrogen production, proportional to each quantity of Fe_2O_3 used. The magnitude of this range (the width of inclined line of points in Figs. 2 and 3) depends on the oxygen content of the solid fuel. For example, biomass has a larger range compared to the coals, corresponding to the higher oxygen content of biomass, as can be observed in the ultimate

analysis in Table 1. Coke has the lowest oxygen content (0.98 % in Table 1), and thus exhibits a small range of Fe_2O_3 intake (less than 1000 kg/h in Fig. 2), while woodchips have the highest oxygen content (45.74 % in Table 1) corresponding with the largest range of Fe_2O_3 intake (about 30000 kg/h in Fig. 3), for the same amount of air. The ranges of Fe_2O_3 intake exhibits a linear relationship with hydrogen production, linking the solid fuel characteristics with the amount of hydrogen produced.

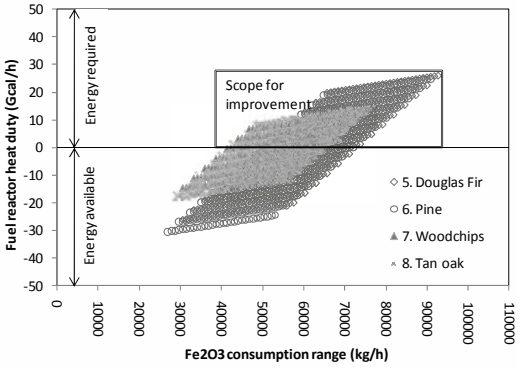

Fig. 3. Fuel reactor heat duty when using four biomasses for varying Fe_2O_3 consumption

When iron oxide is used almost completely, in such cases as lignite and oak char (see Fig. 2), so as to maximize hydrogen production, the energy required for the reactions is large. The iron oxide transport in such cases consumes as much or more energy than that of the air supply. Thus there are two energy penalties for increasing iron oxide consumption in the fuel reactor, while reducing iron oxide to iron.

Note that the iron oxide profile is proportional to the hydrogen profile. Fig. 2 indicates that more iron oxide needs to be reduced in the fuel reactor, so that more hydrogen can be produced. This leaves low grade coals such lignite and oak char with two options: (i) to accept the hydrogen produced from the available energy at 70 % and 65 %, respectively, or (ii) to find means to supply the energy requirement for the additional 20 to 30 % hydrogen. It is unclear if the latter option is worthwhile, since the energy requirement for the additional 20 to 30 % hydrogen output is almost equal to the energy used in producing 70 % hydrogen (say for lignite). This is due to the corresponding decrease in the air consumption when iron oxide consumption is increased, thus reducing the energy available through partial combustion.

Among biomass types, both Douglas fir and pine produce the same amount of hydrogen due to having the same carbon contents (see ultimate analysis in Table 1). Note that in the DCL system, hydrogen production is directly proportional to the carbon (not the fixed carbon) content of the fuel (from Figs. 4 and 5), and the reduction of iron oxide (Eqs. (7) and (8)) is dependent on the amount of CO produced after the first two stages in the fuel reactor (Eqs. (1) to (6)).

Woodchips and tan oak similarly produce the same amount of hydrogen but less than fir and pine. The advantage of having higher oxygen content in biomass is that it enables biomass having higher carbon contents, for example fir and pine, to produce maximum hydrogen at the lowest air and highest iron oxide consumption (Fig. 3).

The comparison of oxygen and carbon contents in solid fuels introduces the limiting factor for high carbon, low oxygen coals. That is, they are able to produce maximum hydrogen only above a certain condition, such as with a considerable amount of air consumption.

3.2 CO_2 separation potential of iron-oxide system

The CO_2 emission for each solid fuel is proportional to its carbon content. Note that the DCL system does not reduce CO_2 emissions, but helps in simple separation of CO_2 for storage and other uses.

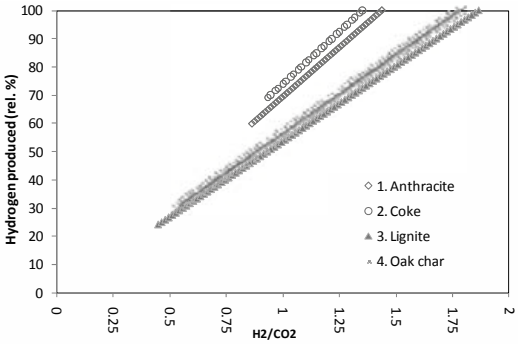

Fig. 4. Comparison of H_2 produced by four coals with H_2/CO_2 ratio

In Figs. 4 to 7, the comparison of hydrogen produced is relative to each solid fuel. 100% is defined by the fuel that produces the maximum hydrogen for a given operating condition. In Fig. 4 the variation of relative hydrogen production with

H_2 to CO_2 ratio is compared for coals and in Fig. 5 for biomasses. With the lowest carbon content (see ultimate analysis in Table 1), lignite produces more hydrogen per CO_2 emission than other coals while coke produces more CO_2 than all the solid fuels considered.

Although it was pointed out earlier that the amount of hydrogen corresponds to the carbon content of the solid fuel, it is evident from Figs. 2 and 4 that anthracite produces more hydrogen and less CO_2 than coke when coke has more carbon than anthracite. Since anthracite has a higher HHV than coke, the energy available for the reactions is more than for coke, thus reducing CO_2 production, in line with the reactions in Eqs. (1) and (6).

Biomass has a better CO_2 profile than the coals and the difference induced by the carbon content is readily visible from the profiles in Fig. 5.

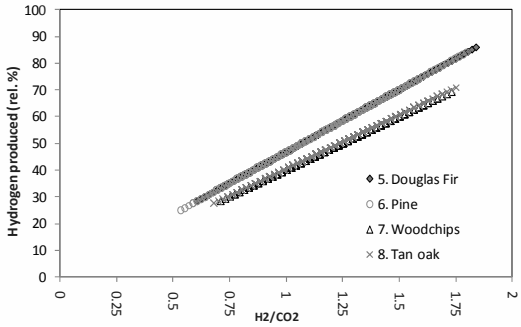

Fig. 5. Comparison of H_2 produced by four biomasses with H_2/CO_2 ratio

4. Scope for improvement

The energy requirement for maximizing hydrogen output to obtain the additional 20 to 30 % for coals ('Energy required' in Fig. 2) and 30 to 40 % for biomasses ('Energy required' in Fig. 3) can be derived from several sources and options. One option is to increase the specific amount of respective fuel used, but again that would also increase the CO_2 emissions except for biomass, owing to its CO_2 neutrality. When considering the specific increase in feedstock as an option, it is advantageous to have two units (with 70 % hydrogen in each when using say lignite) and produce at least 40 % more hydrogen for the same amount of available energy than trying to achieve 100 % hydrogen (only 30 % more on top of 70 % with the same amount of fuel) in a single unit.

Another option is to remain close to the '0' line of the energy spectrum (above the line if additional energy is available) so that losses can be avoided and maintaining the appropriate amount of hydrogen produced from each fuel.

Some of the other options such as blends of low- and high-grade solid fuels, avoiding moisture in the feedstock and using external heat sources are discussed here.

4.1 Blend of coal and biomass

It is assumed that the blending of coal and biomass is performed outside the DCL system and the mixed substance is conveyed to the fuel reactor as a single feedstock. The procedures for pre-treating of feedstock such as drying, crushing and blending are not treated as part of the system in this work, but are assumed done prior to the process simulation. Four blends of anthracite and tan oak (the coal with highest HHV and the biomass with lowest HHV) with different combinations are examined. The quantities of hydrogen produced by blends of anthracite and tan oak (20-80, 50-50, 60-40 and 80-20, on a weight percentage basis) are shown in Fig. 6, as a function of fuel reactor air consumption. The higher the percentage of anthracite, the more hydrogen is produced at higher air consumptions (which suggests the availability of energy) due to the higher HHV of anthracite. When comparing the 20 % anthracite and 80 % tan oak blend in Fig. 6 with 100 % tan oak in Fig. 5, an increase in hydrogen production of about 10 % is realized.

For a blend with 80 % tan oak, the tan oak it contributes to the oxygen demand by producing more hydrogen than at 50 % tan oak with less air consumption. The total range of 80 % tan oak profile is the only one that shows little influence of anthracite.

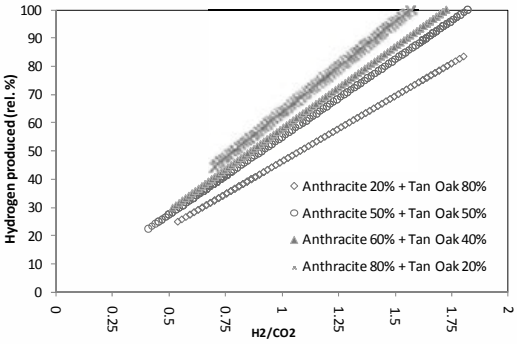

Fig. 6. Comparison of H_2 produced by coal and biomass blend of varying proportions with H_2/CO_2 ratio

Based on the energy availability zone (below the '0' line) a comparison of tan oak and 80% tan oak indicates that only 5 % more hydrogen is produced by adding 20 % anthracite to tan oak. For 50 % tan oak with 50 % anthracite, the increase in hydrogen production is by 15 %, within the energy availability zone. There are three benefits to the 50 % blend: (i) the opportunity for using low-grade tan oak, (ii) the opportunity to reduce usage of high-grade anthracite, and (iii) the opportunity to reduce the CO_2 emission of anthracite.

The CO_2 emissions for the four blends are shown as a function of H_2/CO_2 ratio with respect to hydrogen production in Fig. 6. The CO_2 emission decreases with increasing tan oak contribution to the blend. A comparison of 80 % tan oak and 50 % tan oak blends indicates that the amount CO_2 produced at maximum hydrogen output for both are the same while the 50 % blend produces 15 % more hydrogen.

Using 50 % high-grade coal with 50 % of low-grade biomass is one of the better options for increasing the combined energy availability and the corresponding hydrogen production.

4.2 Moisture in the feedstock

Both coal and biomass contain moisture. The analysis in this work considers all solid fuels on a dry mass basis. The energy spent in drying was not included in the analysis until now. For 10 % fuel moisture content, the corresponding change in hydrogen production is shown Fig. 7 with fuel reactor air consumption. The moisture reduces the HHV of the fuel and the relevant formulation is available in literature [4]. A calculator block is added in the Aspen model to update the moisture information.

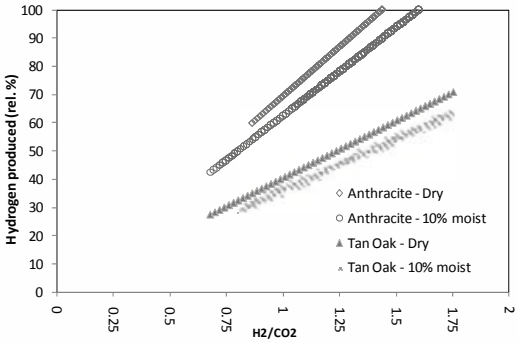

Fig. 7. Comparison of H_2 produced by dry and 10% moist coal and biomass with H_2/CO_2 ratio

With 10 % moisture in anthracite, the hydrogen production decreases by 15 % as shown in Fig. 7. For tan oak the 10 % moisture reduces hydrogen production only by 6 %. The corresponding energy profiles show that, with 10 % moisture in tan oak, there is no energy available for hydrogen production. If tan oak is not delivered dry, it is not a candidate for hydrogen production unless blended with dry coal or another fuel with a better HHV. For anthracite, 10 % moisture reduces the energy availability by 10 %.

Since the moisture reduces hydrogen production, the H_2/CO_2 ratio is increased as shown in Fig. 7 for both anthracite and tan oak. The CO_2 produced is directly proportional to the carbon content (ultimate analysis) in the fuel and thus moisture does not change the CO_2 production unless more fuel is used to meet the hydrogen production criteria.

The advantage of dry solid fuel is realized with higher hydrogen production. Means to dry the fuel may be coupled with waste heat from within the DCL system with proper planning to save resources.

4.3 External thermal sources through process integration

The energy availability in the current analysis is discussed only for the fuel reactor. The oxidation reactor (Eqs. (10) and (11)) requires high-pressure and temperature steam which requires additional energy. The combustion reactor with its exothermic reaction (Eq. (12)) generates some thermal energy which can be used for producing steam. Other energy intensive processes within the DCL system include solid fuel and iron oxide transport, air separation, cyclone separation and heat losses from all relevant processes.

The regions of 'scope for improvement' in the figures discussing energy may be optimized by starting from the '0' line and moving up to a certain level where the percentage of hydrogen produced requires the energy that may be available from say the combustion reactor.

Another possibility is when a DCL system is part of a larger energy conversion facilities such as natural gas combined-cycle power plants, nuclear power generating stations, steal manufacturing plants, oil refineries, etc. The heat from other processes in the larger system may be used for increasing the hydrogen production through the DCL system by externally heating the fuel reactor to maintain higher operating temperature.

5. Conclusions

The direct chemical looping (DCL) system proposed in this work enables the use of various types of coal and biomass ranging from low to high energy contents to produce hydrogen without gasification. The conclusions drawn follow:

- Producing more iron by reducing more iron oxide yields more hydrogen through oxidation by steam.
- In a combustion system involving both oxygen (air) and iron oxide such as the DCL system, it is beneficial to have a solid fuel with higher oxygen content, since it reduces the air intake but increases the iron oxide use, thus providing a greater range for hydrogen production for small fixed air consumption.
- Anthracite produced the maximum hydrogen output of which 90 % was produced within the energy availability of the fuel reactor.
- Lignite produced about 70 % of the maximum capacity within the energy availability zone. To achieve the remaining 30 % hydrogen, an equal amount of additional energy is required. Also, two units with 70 % each can produce 40 % more hydrogen than trying to achieve 100 % within the same unit for the amount of available energy.
- Blending 20 % high-grade coal (anthracite) with 80 % low-grade biomass (tan oak) increases the production of hydrogen from tan oak by 10 %. The 50-50 blend is economic in terms of energy availability and H_2/CO_2 ratio.
- A 10 % moisture content in the anthracite reduces 10 % of the hydrogen production. For tan oak, a 10 % moisture content places the hydrogen production out of the energy availability zone.
- Potential improvements through external heat sources can increase the contribution of low-grade solid fuels.

The results from this work will help in designing the fuel reactor with appropriate control measures when operating under variable conditions.

Acknowledgements

The authors kindly acknowledge the financial support provided by the Natural Sciences and Engineering Research Council of Canada.

References

1. IEA. World Energy Outlook 2008. International Energy Agency, 2008
2. British Petroleum. BP Statistical Review of World Energy, 2003.
3. DOE. Energy Information Agency. International Energy Outlook. U.S. Department of Energy, 2005.
4. Parikh J, Channiwala SA, Ghosal GK. A correlation for calculating HHV from proximate analysis of solid fuels. Fuel 2005;84:487-494.
5. Fan L-S, Li F, Ramkumar S. Utilization of chemical looping strategy in coal gasification processes. Particuology 2008;6:131-142.
6. Gnanapragasam NV, Reddy BV and Rosen MA. Hydrogen production from coal using coal direct chemical looping and syngas chemical looping combustion systems: Assessment of system operation and resource requirements. International Journal of Hydrogen Energy 2009;34:2606-2615.
7. Cleeton JPE, Bohn CD, Müller CR, Dennis JS, Scott SA. Clean hydrogen production and electricity from coal via chemical looping: Identifying a suitable operating regime. International Journal of Hydrogen Energy 2009;34(1):1-12.
8. Rydén M, Lyngfelt A. Using steam reforming to produce hydrogen with carbon dioxide capture by chemical-looping combustion. International Journal of Hydrogen Energy 2006;31(10):1271-1283.
9. Yu J, Corripio AB, Harrison DP, Copeland RJ. Analysis of the sorbent energy transfer system (SETS) for power generation and CO_2 capture. Advances in Environmental Research 2003;7:335-345.
10. Rezaiyan J, Cheremisinoff NP. Gasification Technologies: A Primer for Engineers and Scientists. Taylor and Francis, London, 2005.
11. Aspen Technology Inc. ASPEN Plus 12.1 User Guide, 2006.
12. Gupta P, Velazquez-Vargas LG, Fan L-S. Syngas redox (SGR) process to produce hydrogen from coal derived syngas. Energy & Fuels 2007;21:2900-2908.
13. Mattisson T, Lyngfelt A, Leion H. Chemical-looping with oxygen uncoupling for combustion of solid fuels. International Journal of Greenhouse Gas Control 2009;3(1):11-19.
14. Thurnhofer A, Schachinger M, Winter F, Mali H, Schenk JL. Iron ore reduction in a laboratory-scale fluidized bed reactor – effect of pre-reduction on final reduction degree. ISIJ International 2005;45(2):151-158.

FIRST RESULTS OF THERMAL ANALYSIS ON SULCIS AND SOUTH-AFRICAN COAL INTO GASIFICATION TESTS WITH CO2 AS GASIFICATION AGENTS

Claudia Bassano, Paolo Deiana, Giuseppe Ricci, Elisabetta Veca

ENEA, Italian National Agency for New Technologies, Energy and Sustainable Economic Development, Rome, ITALY

Abstract: Several power plant configurations have been recently studied as an alternative to conventional technologies in the field of energy systems equipped with carbon capture and storage technologies. This is done in order to develop efficient and economically competitive and clean technologies based on coal conversion processes. The use of CO_2 as gasification agent opens new interesting prospects in relation to the gasification of coal or co-gasification of coal and biomasses. The paper proposes an experimental approach to the analysis of coal gasification that uses CO_2 as gasification agent, by thermogravimetric analysis. The aim of the present work is to characterize the kinetics of CO_2 gasification at different reaction temperatures of two different types of chars: low-rank coals Sulcis and high-rank coal South African. The kinetic analysis of coal gasification rate has been implemented by fitting the experimental data with homogeneous kinetic model. The reactivity of the two chars was compared using the Arrhenius kinetic constant and the reactive index. Experimental data obtained for the whole range of experimental conditions explored were satisfactorily described by a single kinetic model showing a 0.99 linear regression fit with greater reactivity achieved by the Sulcis coal.

Keywords: coal gasification, thermogravimetric analysis, CO2, Bouduard reaction.

1. Introduction

The reference frame where this experimental study was carried out is the use of CO_2 as gasification agent

In fact the use of CO_2 as a gasification agent opens new and interesting prospects in relation to the gasification of coal or co-gasification of coal and biomasses.

This technology not only could increase the efficiency of carbon conversion but can also generate a syngas constituted of CO, H_2, CO_2 and water vapour that in the case of oxy-combustion produces carbon dioxide and vapour formation.

This type of combustion gas may then easily be separated by water condensation.

Therefore, this process could be considered an interesting technology to study in the CCT background.

The paper proposes an experimental approach about the analysis of coal gasification that uses CO_2 as a gasification agent as a first step towards commercial application of this technology.

In particular the present work aims to evaluate the reactivity of chars obtained from the pyrolysis of two different coal, Sulcis (from Sardinia, Italy) and South African coal, by thermogravimetric analysis.

The CO_2 gasification of Sulcis char has not been widely studied. This paper contributes to give informations on this coal type and to improve knowledge of its reactivity.

Currently the Sulcis coal is being studied in research Italian sector.

The char reactivity analysis and its comprehension is a first step toward the optimization of gasification reactors.

In fact, the capability of knowing the gasification reaction mechanisms and reactivity is important in terms of gasifier design and operation.

2. Kinetic modelling

In order to predict the behavior of coal during gasification, several models have been proposed with different degrees of complexity. However for practical purposes, simpler models are preferred

Corresponding Author: Claudia Bassano, Email: claudia.bassano@enea.it

for approximate computations in design calculations.

The CO_2 gasification occurs according to the following reaction, defined as Boudouard reaction:

C solid + $CO_2 \leftrightarrow 2CO$ (1)

ΔH_0 (298 K) = + 172.3 kJ/mol [7]

The previous reaction takes place with heat absorption through an endothermic process ($\Delta H_0 > 0$).

Several factors affect char gasification. In fact the solid reactivity depends: on the used gasifying agent, on the operation conditions, such as pressure and temperature, and on other several factors related to the characteristics of char, such the nature and the thermal history of the char. In particular its pore structure, its chemical composition, and its inherent mineral matter, that can play an important role in gasification due to catalytic phenomena.

The kinetic model developed for gas-solid reaction must take into account the various individual step involved in the overall process.

The fundamentals steps may listed as [1]:

- Diffusion of gaseous reactant CO_2 through the film surrounding the particle to the surface of the solid (external mass transfer).
- Penetration and diffusion of CO_2 through the blanket of ash to the surface of the unreacted core (internal mass transfer).
- Reaction of CO2 with solid (reaction step).
- Diffusion of CO gaseous products through the ash back to the exterior surface of the solid. (internal mass transfer).
- Diffusion of CO products through the gas film back into the main body of fluid (external mass transfer).

In some cases we may consider the step with the highest resistance to be rate-controlling.

In the present work a simple model was used.

Moreover, influence of the gasifying agent during the process on chars reactivity was not considered since the CO_2 flow was kept constant in the experimental condition carried out.

Therefore, under the chosen experimental conditions, the mass transfer, the external diffusion, the surface diffusion, and the ash diffusion has only a margin effect on the reaction rate.

In conclusion kinetic analysis of coal gasification rate has been carried out by fitting the experimental data with the homogeneous kinetic model.

In this model the rate of char conversion is expressed using the rate equation given below [2-4]:

$$\frac{dx}{dt} = k(1-x) \quad (2)$$

Where x(t) is the sample conversion expressed on dry ash free basis (daf basis), and defined as:

$$x(t) = \frac{Wo - W(t)}{Wo - Wa} \quad (3)$$

Where:

Wo dry char initial weight

W(t) char weight

Wa ash char weight

k(T), the reaction rate constant is an apparent kinetic parameter.

This model assumes that the reaction take place uniformly throughout the whole volume of the particle and the reaction rate is independent by the particle size.

This model do not consider coal structural changes during reaction and it reduces the heterogeneous gas-solid reaction of coal to an homogeneous reaction.

The conversion may be expressed as follows:

$$x(t) = 1 - e^{-kt} \quad (4)$$

The above rate equation describes the effect of char conversion and temperature on the gasification rate dx/dt. The (2) shows that, as char conversion proceeds initially from x=0 to x=1, the gasification rate slows down.

The model parameter k(T) was evaluated by the fitting between the experimental data and the kinetic model, using the method of least-squares.

k(T) was the slope of the following integrated and linearised model equation [8].

$$-\ln(1-x) = kt \quad (5)$$

Moreover, through the value of the correlation coefficient (r2) it is possible to estimate the fitting goodness and to value the validity of the applied model.

The rate coefficient, k(T), is a function of temperature, assumed to be given by the Arrhenius equation.

$$k(T) = A\,e^{-Ea/RT} \quad (7)$$

Where:

A is a frequency factor, s^{-1}

Ea is activation energy, kJ mol^{-1}

R is the gas constant, K

T is temperature.

The kinetic constant Ea and A, so determined, are valid in the temperature range studied.

3. Experimental study

Thermogravimetric analysis is a technique frequently used for the determination of kinetic parameters of coal.

The experiments were performed in a Mettler-Toledo thermogravimetric analyzer (TGA), where the weight loss of a small fuel sample can be measured as the fuel reacts at atmospheric pressure under controlled gas composition and temperature.

The horizontal furnace design helps minimize possible turbulence caused by thermal buoyancy and by the purge gas. In Fig. 1 [9] is showed the TGA setup.

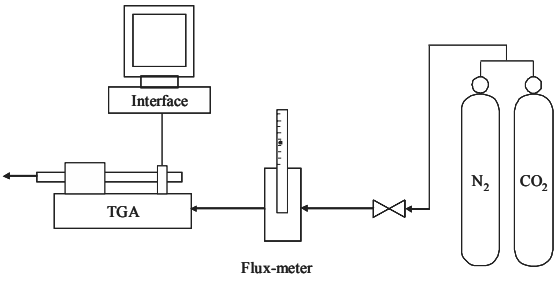

Fig. 1. Thermobalance setup

3.1. Coal samples

The TGA experiments, involved in this study, are CO2 gasification tests of a char obtained by prepyrolysing of two different coals: low rank coal Sulcis and an high rank coal South African.

The proximate analyses of the samples are presented in following table.

Table 1. Sulcis and South African proximate analysis

Sample	Moisture wt %	Volatile matter wt %	Fixed carbon wt %	Ash wt %
Sulcis	7.59	40.37	38.15	14
S. African	3.68	8.52	71.90	16

Coal samples were quartered and grounded until 100% of the mass passed through a 60-mesh sieve (< 250 μm).

3.2. Experimental procedures

The experimental conditions chosen were: low sample mass, small particle size and constant flow of the gasifying agent during the process.

Under such experimental conditions, the resistance due to the stagnant gaseous film around the particle becomes neglectable in relation to the overall resistance of the process.

Therefore, the factors affecting the reactivity were temperature and coal type.

The procedure used for each experiment in the TGA was the following:

1. In an inert atmosphere of pure N_2, the char was heated from ambient temperature to 105°C at a constant rate of 10°C/min.
2. To completely dry out the sample in the inert atmosphere, the temperature was maintained at 105°C for 10 min.
3. In the inert atmosphere of pure N_2, the sample was heated from 105°C to 950°C at a constant rate of 25°C/min.
4. Finally the temperature was maintained at 950°C for 7 min. to completely pyrolyse the sample in the inert atmosphere.
5. The char was cooled from 950°C to the established test temperature at a constant rate of 25°C/min.
6. The char was gasified with the reactive gas (CO_2) at the test temperature until it reached constant weight.

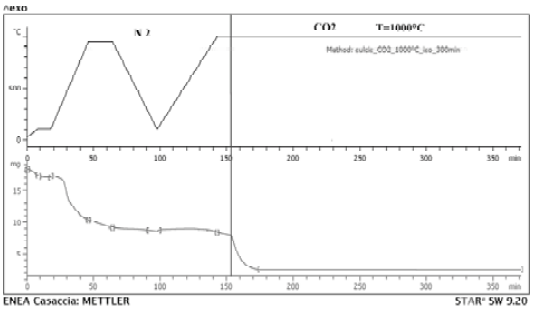

Fig. 2. Mass loss in the time and the temperature program used for Sulcis coal gasified at 1000°C.

The flow of reactant gases and carrier gases chosen were 50 ml/min N2 and 50 ml/min CO2.

In this condition, the factors studied were the gasification temperature (900°C, 1000°C, 1100°C) and the coal type.

An example of obtained data is reported in Fig. 2 and that is related to Sulcis coal sample gasified at 1000°C.

4. Results and discussion

Through the analysis of experimental data a parametric study is carried out to assess the dynamics of the reaction in function on the type of sample used and the temperature.

For this purpose the experimental tests are carried out applying the methodology described above. The samples were maintained under a constant flow of CO2, in isothermal conditions at 900 ° C, 1000 ° C and 1100.

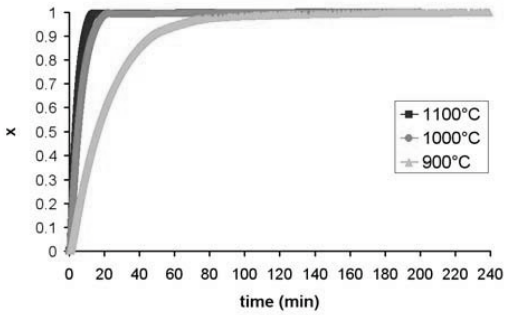

Fig. 3. Sulcis char fixed carbon conversion X(t) versus reaction time

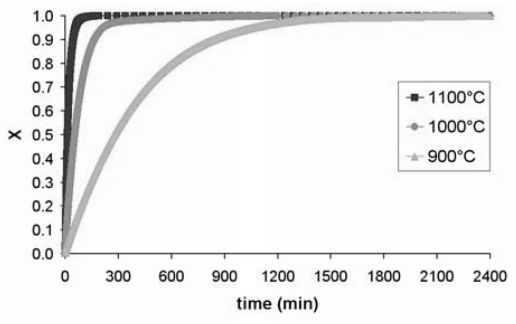

Fig. 4. South African char fixed carbon conversion X(t) versus reaction time

The conversion data obtained for Sulcis and South African coal during CO_2 gasification are plotted against reaction time in Fig. 3 to 4 at each temperature considered.

These graphs show that the gasification rate increases with increasing reaction temperature, evidenced by the conversion curves with steeper slopes.

Moreover, the reaction time necessary to reach the unitary conversion shows a different time scale of 10 times between the two coal.

The experimental data was fitted to the kinetic model using the method of least-squares (5)

Fig. 5 to 6 show the application of the model to the experimental results obtained for the gasification of the two char, at each temperature considered.

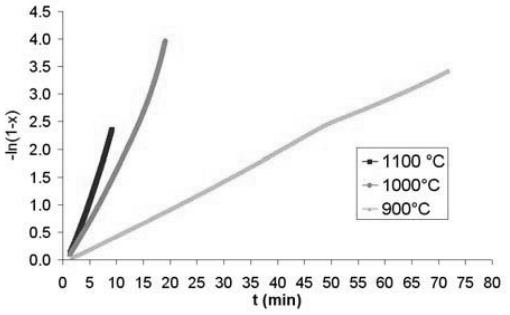

Fig. 5. Experimental data fitted to the kinetic model for Sulcis coal

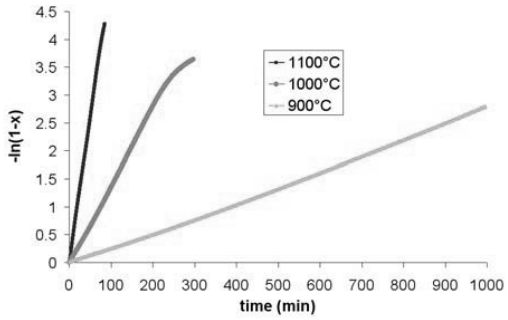

Fig. 6. Experimental data fitted to the kinetic model for South African coal

Table 2 presents the kinetic parameters so evaluated and the value of the correlation coefficient (r2)

Table 2. Kinetic parameters evaluated

Coal type	T/ °C	k(T)/ s^{-1}	r2
Sulcis	900	$8.21*10^{-4}$	0.99
	1000	$2.97*10^{-3}$	0.99
	1100	$5.38*10^{-3}$	0.98
S. African	900	$4.50*10^{-5}$	0.99
	1000	$2.23*10^{-4}$	0.99
	1100	$9.35*10^{-4}$	0.99

A parameter commonly used to compare the gasification reactivity of different fuels is the reactivity index [5]:

$$R_{50} = \frac{0.5}{t_{50}} \qquad (9)$$

Where:

t_{50} is the time (s) required to reach 50% conversion of the fixed carbon.

Fig. 7 shows the R_{50} index for the Sulcis and South African coal. The figure illustrates the different values between the two coals, confirming the higher reactivity of Sulcis coal than the South African coal.

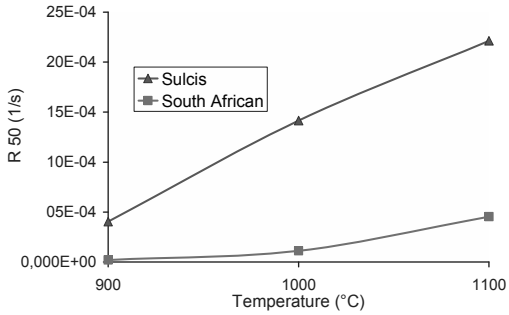

Fig. 7. Reactivity index calculated for Sulcis and South African coal

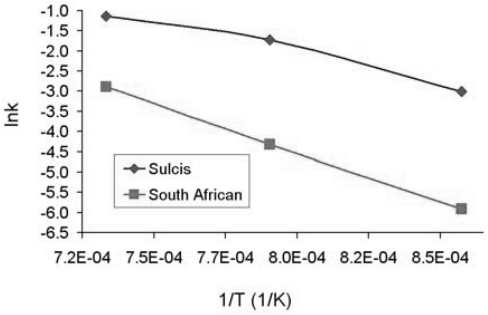

Fig. 8. Arrhenius plot

The data analysis shows a raising process reactivity with the temperature in agreement with the values of reaction rate parameter k(T) obtained and with the values of the reactivity index R_{50}.

The values of parameters A and Ea calculated by Arrhenius analysis are given in Table 3 and shown in Fig. 8 for both coals.

Table 3. Arrhenius constants

Coal type	A/s^{-1}	Ea/kJ mol^{-1}
Sulcis	397	127
S. African	48,829	203

The Arrhenius law for Sulcis and South African are determined using the before values of Ea and A and so written:

for Sulcis coal

$$k(T) = 397\, e^{-127/RT}$$

for South African coal

$$k(T) = 48{,}829\, e^{-203/RT}$$

The Sulcis coal characterized by an activation energy lower than South African needs less energy in order that the Boudouard reaction develops.

The activation energies values deduced for the two char are in good agreement with the results reported by literature for similar coals in similar experimental conditions.

In literature the energies activations values vary between 90 kJ/mol [5] for low rank coal (Sulcis) and 250 kJ/mol [2] for high rank coal (South African).

References in this field it could be the work by D. P. Ye, J. B. Agnew and D. K. Zhang, and the article "Gasification Kinetics of Coal Chars Carbonized Under Rapid and Slow Heating Conditions at Elevated Temperatures" [5] In this work are reported, for a South Australian low-rank coal, experimental gasification studies with carbon dioxide.

In this study, kinetic analysis of coal gasification rate has been carried out by fitting the experimental data with the homogeneous model. The experimental data was obtained in experimental conditions similar to those of our study.

The authors deduced by this work an activation energy of 91 kJ/mol.

For the South African the value of reference in literature comes from the work of Chunhua Luo, Tomokazu Watanabe, Makoto Nakamura, Shigeyuki Uemiya, Toshinori Kojima, with the article "Gasification Kinetics of Coal Chars Carbonized Under Rapid and Slow Heating Conditions at Elevated Temperatures" [2]

In this experimental analysis measurements of CO2 gasification kinetics of coal char were conducted by using a bench-scale fluidized bed reactor.

Samples tested were a medium-volatile bituminous.

In the study the grain model was used to analyze the experimental data.

For coal analyzed the authors founded a m value of 1 and by the Arrhenius analysis carried out an activation energy of 200 kJ/mol.

In conclusion in the present work the reactivity difference between two char coal is expressed by distinct values of Ea and of the reactivity index R_{50}.

This difference is explained, in part, by the variety of coal rank studied; indeed so confirmed in literature [9] coal reactivity decreases as coal rank increases.

Sulcis char is more reactive than South African char since char reactivity depends, in part, on volatile matter content of the coal.

In fact a major volatile matter leads a larger surface area available for the reaction.

The kinetic model used, in the experimental condition and hypothesis considered, can not exactly describes all the experimental data but is limited in the time scale.

In Fig. 9 to 10 is reported the reaction rate dx/dt for Sulcis and South African char versus time.

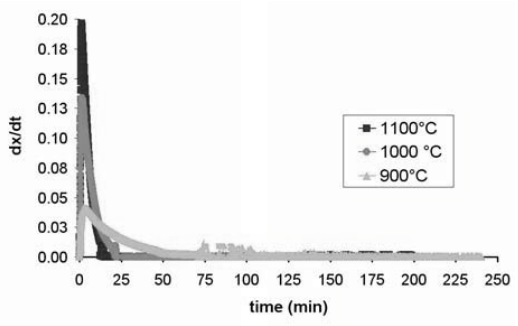

Fig. 9. Reaction rate versus time for Sulcis coal

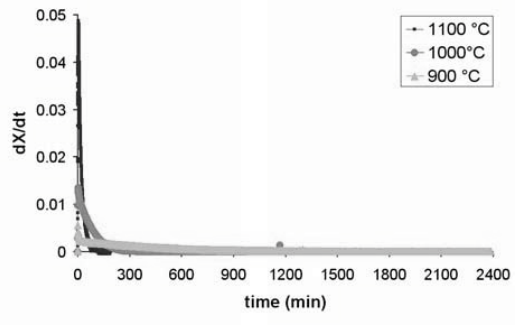

Fig. 10. Reaction rate versus time for South African coal

In this figures are showed that the validity time region of the kinetic model it's until a very short time compared to time of total char conversion for both char.

In fact, after this time the correlation of kinetic model it's not good. The conversion achieved in this first phase is 0.99.

This information is very useful for subsequent process scale up, since greater velocities lead to shorter residence time and as a consequence to reactors smaller dimensions and at the same time leaving only a fraction of char unreacted.

5. Conclusions

A kinetic study of the CO_2 gasification of chars from two different types of coal (low-rank and high-rank), was carried out by TGA at isothermal condition.

In the experimental conditions chosen, we tested the model validity that is able to predict the rate conversion and the two samples reactivity and gives a good experimental data fitting.

The reaction rate depend strongly on temperature and increases with increasing reaction temperature.

The Arrhenius analysis has been carried out, using the reaction rate constants, calculated at each temperature considered, by this way the activation energy (Ea) and the pre-exponential factor (A) were obtained

The activation energies calculated are in good agreement with the results reported by literature for similar coal.

The two experimental determined kinetic equation for CO_2 gasification are:

for Sulcis coal

$$k(T) = 397\, e^{-127/RT}$$

for South African coal

$$k(T) = 48{,}829\, e^{-203/RT}$$

In addition to, the reactivity of the two chars was compared using the Arrhenius kinetic constant and the reactive index R_{50}. Sulcis char is more reactive than South African char since char reactivity depends, in part, on volatile matter content of the coal.

In fact a major volatile matter leads a larger surface area available for the reaction.

Finally, the results of this study will gives us information for further research. In fact, major investigations are on development to valuate the influence of different factors such as particle size, catalytic effect of ash, operating conditions and the possibility to scale up the process.

In conclusion, it should be emphasized, that this activity concerning the characterization of the reaction of CO_2 gasification, is a first study aimed at better understanding of the Boudouard reaction, which is always present in the coal gasification process.

Nomenclature

A	frequency factor, s^{-1}
CCT	Clean Coal Thecnology
daf	dry ash free
Ea	activation energy, kJ mol^{-1}
k	reaction rate constant, s^{-1}
n	reaction order respect to the solid phase
R	universal gas constant, 8.31 $Jmol^{-1}K^{-1}$
R_{50}	reactivity index, s^{-1}
r2	correlation coefficient
t	time, s or min
T	temperature, °C
TGA	thermogravimetric analyzer
Wo	dry char initial weight, kg
W(t)	char weight at time t, kg
Wa	ash char weight, kg
wt	weight, %
x	sample conversion expressed on daf basis

References

[1] Levenspiel, 1999 *Chemical Reaction Engineering* Third Edition Octave John Wiley & Sons

[2] Chunhua Luo, Tomokazu Watanabe, Makoto Nakamura, Shigeyuki Uemiya, Toshinori Kojima, 2001, Gasification Kinetics of Coal Chars Carbonized Under Rapid and Slow Heating Conditions at Elevated Temperatures Journal of Energy Resources Technology by ASME MARCH 2001, Vol. 123 pp 21-26

[3] Raghunathan, K., and Yang, Y. K., 1989 Unification of Coal Gasification Data and Its Applications Ind. Eng. Chem. Res., 28, pp. 518–523

[4] Cozzani V., Reactivity in Oxygen and Carbon Dioxide of Char Formed in the Pyrolysis of Refuse-Derived Fuel Ind. Eng. Chem. Res. 2000, 39, pp. 864-872

[5] D. P. Ye, J. B. Agnew and D. K. Zhang,1998, Gasification of a South Australian low-rank coal with carbon dioxide and steam: kinetics and reactivity studies, Elsevier Fuel Vol. 77, No. 11, pp. 1209-1219

[6] B. Arias, C. Pevida, M. G. Plaza, F. Rubiera, J. J. Pis, J. Fermoso, 2008, Kinetic models comparison for steam gasification of different nature fuel chars Journal of Thermal Analysis and Calorimetry, Vol. 91 3, pp. 779–786

[7] P. Ollero, A. Serrera, R. Arjona, S. Alcantarilla, 2002, Diffusional effects in TGA gasification experiments for kinetic determination Elsevier, Fuel 81 pp. 1989–2000

[8] Molina A. and Fanor Mondrago, 1998, Reactivity of coal gasification with steam and CO2 Fuel Vol. 77, No. 15, pp. 1831–1839

[9] S. Stendardo, A. Calabrò, P.U. Foscolo, 2009, Experimental and numerical investigation on chemical looping carbon capture based on solid particles, Sustainable fossil fuels for future energy 6th-10th July 2009 ROME

Successful conversion of a Kraft pulp mill into a forest biorefinery: energy analysis issues

Mariya Marinova, Enrique Mateos-Espejel, Jean Paris

École Polytechnique de Montréal, Department of Chemical Engineering

Abstract: Pulp and paper mills, in particular Kraft pulp mills, are attractive candidates for conversion into biorefineries. The objective is to produce new value-added products, while maintaining the traditional production of cellulose-based products. However, the sustainability of integrated biorefineries could be jeopardized by additional energy costs. Therefore, it is necessary to analyse the heating and cooling requirements of the biorefinery and of the Kraft process, and to identify potential scenarios that could reduce the overall energy consumption. This work deals with the retrofit integration of a biorefining technology into a Kraft pulp mill. The biorefinery consists of the conversion of hemicellulose hydrolysates collected at several pulp mills into ethanol. The process for ethanol production is simulated using commercial software and the corresponding energy requirements are evaluated. A simulation representing a typical Kraft process is also developed. A Thermal Pinch analysis of the biorefinery and of the receptor pulp mill is performed to identify potential heat sources, currently unused, that could reduce their energy requirements. The synergy between the pulping process and the biorefining technology is analysed and options for improved energy consumption are proposed.

Keywords: Biorefinery, Kraft process, Ethanol, Energy analysis, Sustainability

1. Introduction

In Canada, the pulp and paper industry has been a major contributor to the national economy for a long time. In response to the declined demand for pulp and paper products, the competition from the large and modern mills in South America and Asia and the high energy costs, several mills in Canada have announced temporary or definite shutdowns. These actions represent a clear warning to the industry, which must focus the efforts on making its processes more competitive, sustainable and fossil fuel-free.

The pulp and paper sector is one of the most energy-intensive sectors in Canada, consuming 30% of the industrial energy used. Since energy represents about 25% of the production-costs, the sector has made efforts to reduce its fuel costs by switching to renewable biomass heat sources and implementing energy efficiency measures [1].

Biorefining is the conversion of forestry and agricultural biomass into a large spectrum of products by various extraction and transformation pathways. It has been recognized by the pulp and paper industry as a way to make a better use of the forest resources by producing high-value products such as biofuels, chemicals, polymers, neutraceuticals and pharmaceuticals [2,3]. The main idea of the biorefining is to upgrade several wood components, underutilized in the current pulp and paper making processes. The components that could be valorized are hemicelllose, cellulose, lignin and bark. However, the extraction of hemicellulose or lignin from the line of a Kraft mill will reduce the heating value of the bio-fuel available for internal energy production. Their conversion into value-added products will increase the energy consumption as new process operations will be added to the site. The base process, which will receive the new technology, and the biorefinery, must be optimized and highly integrated from the stand point of energy, to satisfy the modified energy requirements.

Until now, synthesis and process integration applications in the biorefinery field are rare. Few opportunities for computer-aided process engineering on renewable raw material use and conceptual process designs have been discussed in the literature [4]. A synthesis study for the production of lignocellulosic ethanol analyses the variation in energy consumption depending on the process configuration [5]. More recently, the integration between wood gasification processes and electrolysis of hydrogen or methane synthesis

Corresponding Author: Mariya Marinova, Email: m.marinova@polymtl.ca

has been optimized; flowsheets for validation, tools for synthesis and process integration methods have been reported [6]. The biorefining technologies are essentially studied in isolation, without regard to their retrofit integration in existing sites. To compete with conventional processes, biorefineries should achieve maximum efficiency and integration. In addition, their design becomes more complex because the degree of freedom increases with the feedstocks selection, processing technologies and product mixture. Modeling, analysis and optimization will play an essential role in the development of the biorefinery concept to support novelty and innovation.

This work was undertaken to investigate the integration of a hemicellulose-based biorefinery into a Kraft pulping process. The impact of hemicellulose extraction prior to pulping and its conversion into ethanol on the steam produced and consumed by the Kraft mill and the biorefinery has been assessed. This study is also an example which highlights the importance of the energy optimization for the sustainability of the biorefinery.

2. The Kraft process

The Kraft process is the dominating pulping process and a primary candidate to integrate biorefining technologies. A typical Kraft pulp mill uses biomass (wood chips), fuel (hog and/or fossil), chemicals and water to produce market pulp, steam and power. The major components of wood, depending on the type of threes (hardwood from deciduous trees and softwood from coniferous trees) are cellulose (40-47%), hemicellulose (25-35%), lignin (16-31%), and extractives (2-8%) [7]. The core of the Kraft process is the chemical delignification step in which the individual cellulosic fibers are separated from lignin to form the pulp. The delignification agent (white liquor) is a mixture of sodium hydroxide (NaOH) and sodium sulfide (Na_2S). For bleachable grade pulp, 45-65% of the wood mass is dissolved in the pulping liquor during delignification. The dissolved material consists primarily of degraded hemicellulose, lignin, extractives and a small amount of cellulose. After delignification, the fibers are washed, and chemically bleached. Finally, the pulp is drained, pressed, and thermally dried in a pulp machine. The spent delignification liquor (black liquor), separated from the fibers in the washing step, is concentrated and burnt to produce steam and an inorganic smelt. The smelt composed of sodium carbonate (Na_2CO_3) and sodium sulfide is dissolved to form the green liquor, which is reacted with quick lime (CaO) to regenerate the original white liquor. Since the heating value of hemicellulose is only about half that of lignin, removing the hemicellulose from wood chips prior to pulping will provide pulp mills with the opportunity to produce value-added products and offload the recovery boiler capacity. A simplified representation of the Kraft process with a hemicellulose extraction stage is given in Figure 1.

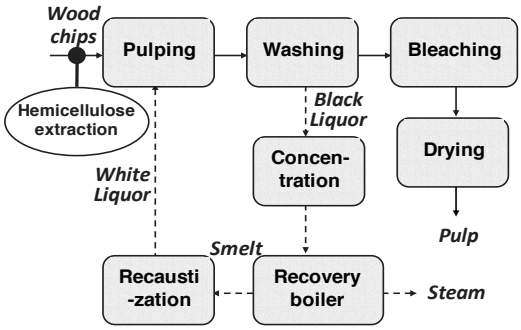

Fig. 1. Simplified diagram of the Kraft process with a hemicellulose extraction stage.

3. Biorefinery opportunities

The biorefinery presents opportunities to generate bio-products at several points in the Kraft process. The following promising technologies have been identified:

- Hemicellulose can be extracted from wood chips using steam, acidic or alkaline solution prior to pulping and then converted into ethanol, furfural, xylitol, organic acids, polymers or chemical intermediates.

- Lignin can be recovered by precipitation from black liquor and used as a feedstock for the production of adhesives, resins, emulsifiers, phenols. An immediate option is to burn lignin within the pulp mill for heat and power generation.

- The wood residues from the manufacturing process, as well as the spent pulping liquor can be gasified; the resulting syngas can be used as a feedstock for hydrogen, methanol, and ethanol production or converted to heat and electric power.

The integration of a prehydrolysis stage in the conventional Kraft pulp mill is an option to provide feedstock for the biorefinery and to

produce a chemical pulp with high cellulose content, known as dissolving pulp. Dissolving pulp is suitable for making rayon, cellulose acetate and cellophane. In addition, the extraction of hemicellulose has important benefits for the pulping process, such as improved delignification rate, decreased alkali consumption, reduced organic and inorganic load to the recovery cycle, and increased pulp production capacity [8].

The conversion of hemicellulose sugars to ethanol by fermentation is a promising option to produce bioethanol from non food crops [9] and has been selected as a biorefining technology for the purpose of this work.

4. Ethanol production from hemicellulose sugars

The ethanol produced from lignocellulosic biomass is a fuel with the potential to match the conventional features of petroleum at low price. An appropriate pre-treatment is required to open the bundles of lignocelluloses and to access the polymer chains of cellulose and hemicellulose. Subsequently, the polymers are hydrolysed to obtain monomer sugar solutions, which in turn are fermented to ethanol by microorganisms. The final step is the separation and purification of ethanol [10]. In this study, the process for ethanol production proposed by the US National Renewable Energy Laboratory [11] has been chosen.

After hydrolysis and phase separation, the liquid stream (hydrolysate) is rich in hemicellulose sugars, while the solid stream contains cellulose and lignin. Downstream ethanol conversion of the hydrolysate will therefore consist of five-carbon sugar fermentation only, or five-and six-carbon sugar fermentation [12]. The NREL process benefits from the conversion of the sugars generated from hemicellulose and cellulose. Because the objective of the pulp mill is to produce pulp, the main difference between the process proposed by the NREL and the process used in this work is that only hemicellulose and a small amount of cellulose degraded during the hydrolysis step are converted into ethanol. A simplified representation of the ethanol production process is given in Figure 2.

4.1. Hydrolysis

In this study, the hydrolysis step is done in batch digesters prior to the pulping process. Steam is used to convert the hemicellulose fraction of the wood into soluble sugars. Under these conditions some of the lignin in the feedstock is also solubilised and acetic acid is released. Furfural, a degradation product from sugars, is also formed.

4.2. Hydrolysate conditioning

During the hydrolysis, various inhibitors are created in addition to the hemicellulose sugars. Before fermentation, detoxification of the hydrolysate is required to remove them. Blow down and ion exchange are used to take out inhibitors. After ion exchange the pH is raised by addition of lime and held at this value for a period of time. Neutralisation and precipitation of gypsum follow the overliming step. Finally, the gypsum is removed via filtration and the purified hydrolysate is sent to fermentation.

4.3. Fermentation

It has been assumed that the fermenting agents used in the fermentation step are purchased from a manufacturer and their production is not considered in this work. Conversion rates of 0.3 gram of ethanol per gram of pentose sugars and 0.5 gram of ethanol per gram of hexose sugars have been used. The resulting ethanol broth is collected and sent to the downstream separation area.

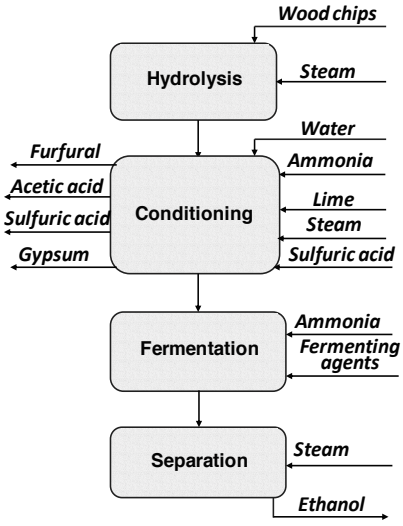

Fig. 2. Simplified diagram of ethanol production from hemicellulose hydrolysate.

4.4. Downstream separation

Distillation and molecular sieve adsorption are used after the fermentation to recover the ethanol

from the fermented beer and to produce almost pure ethanol. Distillation is accomplished in two columns. The first beer column removes the dissolved CO_2 and most of the water, while the second distillation column concentrates the ethanol to near azeotropic composition. Subsequently, the residual water from the azeotropic mixture is removed by vapour phase molecular sieve adsorption.

5. Case study

The pulp mill considered in this study produces 500 t/d of dissolving grade pulp and is located in Canada. The hydrolysis step and the pulping process utilize multiple batch digesters. This mill generates 700 t/d of hemicellulose hydrolysate, which is currently concentrated with the black liquor to approximately 70% and combusted in a recovery boiler to produce high pressure steam. To meet the steam demand of the mill, high pressure steam is also generated in a hog fuel boiler. A computer simulation of the pulp mill, developed on CADSIM Plus® (Aurel Systems Inc.), has been used to supply data for this work.

Considering the difficult situation of the pulp and paper industry, it could be very expensive for one mill to invest alone in the biorefinery initiative. An interesting approach used in this work is the establishments of cooperation between several mills located in the same area. This cooperation will allow them to share investment, operating costs, resources and benefits.

A centralized ethanol plant is located on the site of the studied pulp mill. Hemicellulose hydrolysates collected from several pulp mills are shipped to the ethanol plant. The feedstock for the centralized ethanol plant is 7000 t/d of hardwood hydrolysate generated prior to pulping using steam. The sugars concentration in the hydrolysate is given in Table 1. All heating and cooling demands are provided by utilities. The ethanol production is simulated with Aspen Plus® (Aspen Tech).

Table 1. Hydrolysate composition

Component	Concentration (g/l)
Arabinose	0.24
Galactose	1.6
Glucose	4.9
Xylose	11
Mannose	0.75

6. Energy analysis

Process integration tools such as the thermal composite curves (CC) and the grand composite curve (GCC), which are the core of the Pinch analysis [13], have been used to analyse the energy profile of the Kraft process and the biorefinery. The composite curves are the display in a temperature *vs* enthalpy diagram of all possible heat transfers within a process (heat availability and heat demand) and define the minimum energy requirement (cooling and heating) as well as the pinch point.

The GCC represents the net thermal requirements in successive temperature zones characterized by a specific set of hot and cold streams. In simple cases it can be graphically generated from the composite curves shifted so that they are in contact at the pinch point. The GCC is a plot of the enthalpy difference between the shifted curves as a function of the temperature and it is represented by a straight segment for each temperature zone. The selection of the various utilities available to satisfy the heating and cooling demands of a process is done by means of the GCC.

The strategy for the energy improvement of the processes has been done in two steps:

1. Individual energy analysis of the Kraft process and the hemicellulose biorefinery;

2. Combined analysis of the biorefinery integrated into the Kraft process.

A temperature difference (ΔT_{min}) of 20ºC has been used in the construction of the composite and grand composite curves. This ΔT_{min} is representative of processes with condensing and reboiling duties, and of oil refineries characterized by low heat transfer coefficients and heat exchangers fouling [13]. Additionally, the selected ΔT_{min} value ensures the feasibility of heat exchanges between streams that may be transported from one site to another.

6.1. Data extraction

All operations that use steam or produce hot and warm water, and hot effluents have been taken into account in the analysis. The non-isothermal mixing (NIM) points have also been considered to recover the low temperature energy available within the process [14]. NIM points are direct heat transfers, such as steam injections and mixing of water streams at different temperature levels in accumulation tanks. The elimination of NIMs can

reduce the surface of a retrofit heat exchanger network [15].

6.2. Individual analysis

6.2.1. Base Kraft process

The composite curves of the base Kraft process are shown in Figure 3. The minimum heating (MHR) and cooling requirements (MCR) of the process are 118 MW and 10 MW, respectively and the pinch point is located at 47°C. The current steam production and consumption in the Kraft process is 185 MW.

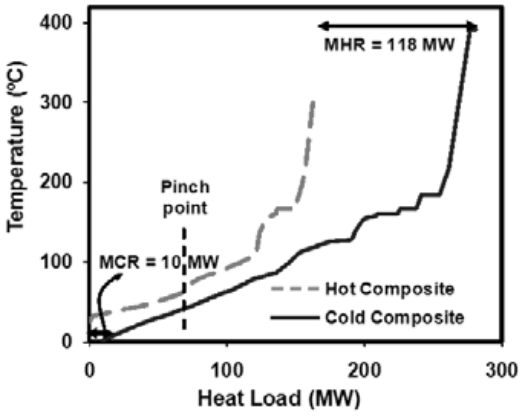

Fig. 3. Composite curves of the Kraft process.

Several energy recovery measures have been identified with the Pinch analysis. The amount of steam consumed for water heating, air-preheating, black liquor concentration and deareation can be reduced using the heat of hot effluents and flue gases. The steam injections required in the process could also be reduced with elimination of NIM points. An example of NIM elimination in the deareator is shown in Figure 4. The current arrangement has two NIM points: the steam injection in the deareator and the mixing of condensate recovered with fresh water (Figure 4a). Fresh water preheating using heat recovered from sources of a lower temperature (40 to 103°C) reduces the steam required in the deareator and eliminates the existing NIM points (Figure 4b). This type of measure ensures the appropriate utilization of the energy available in the process. The maximum steam savings that could be achieved in the Kraft process represent 36% of its current heating requirement.

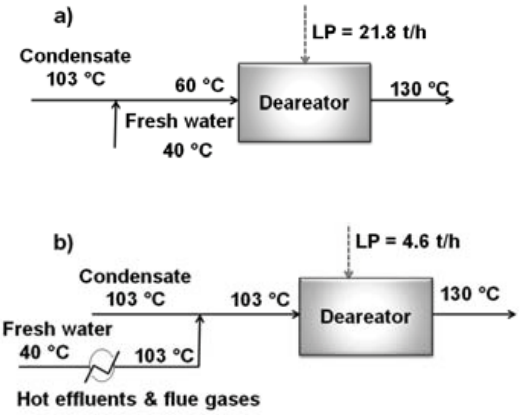

Fig. 4. Elimination of a NIM points in the deareator: a) current arrangement, b) proposed measure.

6.2.2. Hemicellulose biorefinery

The composite curves of the hemicelluose biorefinery using 7000 t/d of hardwood hydrolysate as a feedstock are shown in Figure 5. The minimum heating (MHR) and cooling requirements (MCR) are 17 MW and 21.5 MW respectively and the pinch point is located at 89°C. The ethanol plant requires for its operation 30 MW steam. 5 MW are required in the hydrolysate conditioning stage and 25 MW in the separation stage. From those composite curves energy efficiency measures consisting in heat reutilization around the distillation columns have been identified: the heat from the bottom streams of the two distillation columns is recovered to preheat the feed to the first column and the hydrolysate at the conditioning stage.

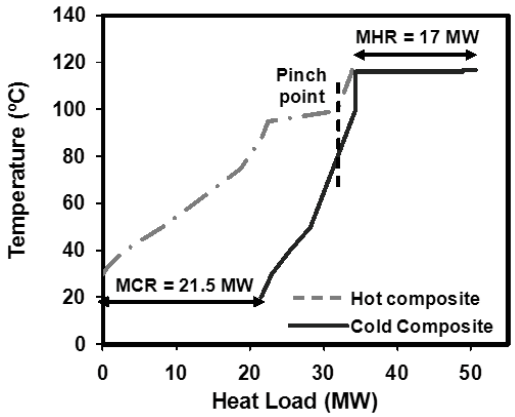

Fig.5. Composite curves of the hemicellulose biorefinery.

6.2.3. Combined analysis

The GCCs of the base Kraft pulping process and the hemicellulose biorefinery have been analysed to identify opportunities for optimal integration of their energy systems (Figure 6). The procedure applied is similar to the one used for the integration of evaporators and dryers in a chemical processes [16,17]. The objective is to identify the temperature levels of heat sources and sinks once the internal heat recovery has been maximized. Furthermore, it is possible to locate the points where the Kraft process and the biorefinery can exchange heat. The flexibility of the hemicellulose biorefinery makes these measures attractive for implementation.

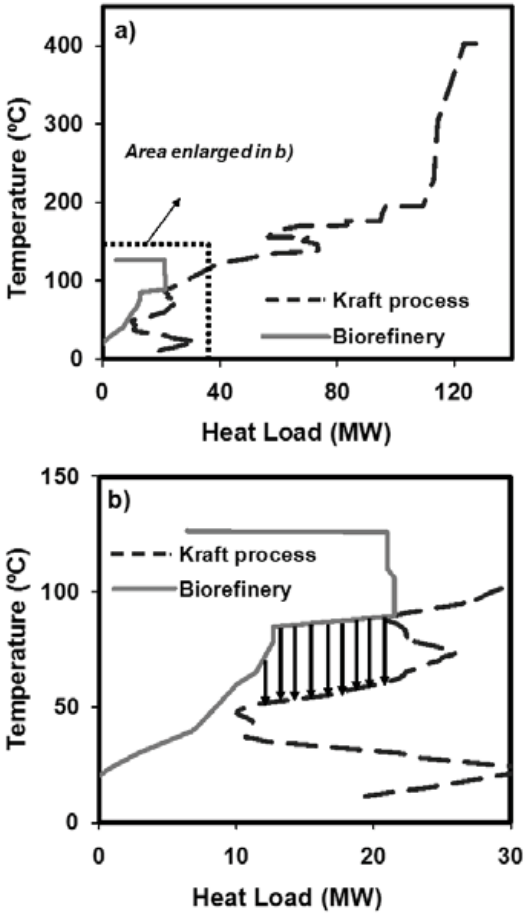

Fig.6. Integration of the base Kraft process and the hemicellulose biorefinery.

The Kraft process has a higher heating demand and a lower cooling requirement than the biorefinery. The heat integration of the two processes is possible because of the big gap between the pinch points (biorefinery = 89°C; Kraft process = 47°C). The energy liberated by the condensers of the two distillation columns (below the biorefinery pinch point) can be recovered by the Kraft process (above the Kraft pinch point) to reduce its energy demand by 11.5 MW.

The total energy required by the integrated site (pulping process and biorefinery) is 123.5 MW. This energy could be supplied by the steam production capacity of the pulp mill and extra steam will still be available for other purposes (cogeneration or export).

However, the amount of heat released by the biorefinery in the distillation column condensers varies with the ethanol production rate. Therefore, three factors in the biorefinery could modify the amount of heat to be recovered by the Kraft process: input flow, hemicellulose content in the wood chips, and, the conversion of xylose and glucose into ethanol. For the conversion rates higher than the rates used in this work [11], the energy savings in the Kraft process would be 13.8 MW.

7. Conclusions

The energy analysis is a fundamental step in development of economically viable and sustainable biorefineries integrated to pulp mills. The opportunities for energy integration between a biorefining technology for ethanol production from hemicellulose derived sugars and a Kraft pulp mill has been studied. Several synergic measures for energy reutilization based on Pinch analysis have been identified. The implementation of the proposed measures reduces the energy costs in the complete site and increases the attractiveness of the project.

The reduction of energy demand that can be achieved in the Kraft process is an important factor for selecting the appropriate feedstock and operations for the biorefinery.

Acknowledgments: This work was supported by a grant from the R&D Cooperative program of the National Science and Engineering Research Council of Canada (CRDPJ 364665 - 07). The industrial partners of this project are gratefully acknowledged.

References

[1] Natural Resources Canada, 2008, Benchmarking energy use in Canadian Pulp

and Paper Mills, Technical Report, Cat. No. M144-121/2006.

[2] Mabee, W.E., et al., 2005, Assessing the emerging biorefinery sector in Canada, Applied Biochemistry and Biotechnology, 121-124, pp. 765-778.

[3] Thorp, B., 2005, Biorefinery offer industry leaders business model for major change, Pulp and Paper, 79(11), pp. 35-39.

[4] Dimian, A.C., 2007, Renewable raw materials: chance and challenge for computer-aided process engineering, Computer Aided Chemical Engineering, 24, pp. 309-318.

[5] Cardona, C.A., and Sanchez, O.J., 2006, Energy consumption analysis of integrated flowsheets for production of fuel ethanol from lignocellulosic biomass, Energy 31 (13), pp. 2447-2459.

[6] Gassner, M., and Maréchal, F., 2009, Methodology for the optimal thermo-economic, multi-objective design of thermochemical fuel production from biomass, Computers & Chemical Engineering, 33 (3), pp. 769-781.

[7] Smook, G., 2002, *Handbook for Pulp and Paper Technologists,* Angus Wilde Publications Inc, Vancouver.

[8] van Heiningen, A., 2006, Converting a Kraft pulp mill into an integrated forest biorefinery, Pulp &Paper Canada, 107(6), pp. 38–43.

[9] Sanchez, O.J., and Cardona, C.A., 2008, Trends in biotechnological production of fuel ethanol from different feedstocks, Bioresource Technology, 99 (13), pp. 5270-5295.

[10] Taherzadeh, M. J., and Karimi, K., 2007, Enzyme-based hydrolysis processes for ethanol from lignocellulosic materials: A review, BioResources, 2(4), pp. 707-738.

[11] Wooley, R., et al., 1999, Lignocellulosic Biomass to Ethanol Process Design and Economics Utilizing Co-Current Dilute Acid Prehydrolysis and Enzymatic Hydrolysis Current and Futuristic Scenarios, Technical Report, NREL/TP-580-26157, National Renewable Energy Laboratory, Golden, CO.

[12] Wyman, C.E., 1996, *Handbook on Bioethanol: Production and Utilization*, Taylor & Francis, Bristol, PA, Chap. 10.

[13] Linnhoff-March, 1998, *Introduction to pinch technology*, Cheshire, UK.

[14] Savulescu, L.E., and Alva-Argaez, A., 2008, Direct heat transfer considerations for improving energy efficiency in pulp and paper Kraft mills, Energy, 33 (10), pp. 1562–1571.

[15] Mateos-Espejel, E., et al.,2009, Systems interactions analysis for the retrofit of a typical Kraft process, Submitted to Energy.

[16] Kemp, I.C., 2007, *Pinch Analysis and Process Integration: A User Guide on Process Integration for the Efficiente Use of Energy*, Elsevier, Oxford,UK.

[17] Marechal, F., and Kalitventzeff, B., 1998, Energy integration of industrial sites: Tools, methodology and application, Applied Thermal Engineering, 18 (11), pp. 921-933.

Exergoenvironmental analysis of methanol production through the thermochemical route as a co-product of an ethanol plant

Maria L. G. Renó[a], Electo E. S. Lora[a], José C.P. Escobar[a], Osvaldo J. Venturini[a], José J. C. S. Santos[b]

[a]*Federal University of Itajubá, Itajubá, Brazil*
[b]*Federal University of Espírito Santo, Vitória-ES, Brazil*

Abstract: Biomass is a promising alternative for the reduction of environmental impacts, as well as long-term a possibility of ensuring energy security and an introduction the socio-economic development of rural regions. Among the technologies under development that uses the biomass detach the thermochemical process of biofuel production from biomass, through gasification route.
In this work is done an exergoenvironmental evaluation of the methanol production process from sugarcane bagasse, considering a methanol plant with a production capacity of 50,000 ton/year. The thermoeconomics and life cycle assessment (applying the Eco-Indicator 99 method) are used. The results allowed determining which stages of methanol production process present the greatest environmental impacts, and the possibilities to minimize these impacts.

Keywords: Methanol, Bagasse, Life Cycle Assessment, Exergoenvironmental.

1. Introduction

1.1. Methanol production

The Methanol can be produced chemically from biomass and fossil fuels. Methanol is suitable as transportation fuel, chemical building block, or as solvent. Another common application of methanol is as a raw material for biodiesel production.

Methanol synthesis via biomass gasification has already been suggested as an environmentally friendly method of biomass utilization. Several biomass-to-methanol demonstration projects have been developed recently, such as the Hynol project in United States, the BioMeet and Bio-Fuels projects in Sweden [1]. In Brazil, there is the Raudi-Methanol project that proposes the methanol production from sugarcane bagasse [2].

The processing steps of methanol from biomass are pretreatment, gasification, gas cleaning, gas conditioning and methanol synthesis that occurs at temperatures of 200 – 300°C and pressures of 5 – 10 MPa [3].

1.2. Exergy analysis and life cycle assessment

Exergy analysis is a thermodynamic analysis technique based on the second law of thermodynamic which provides an alternative and illuminating means of assessing and comparing processes and system rationally. In particular, exergy analysis yields efficiencies which provide a true measure of how nearly actual performance approaches the ideal, and identifies more clearly than energy analysis the causes and locations of thermodynamic losses and the impact of the built environment on the natural environment. Consequently, exergy analysis can assist in improving and optimizing designs [4].

The exergy measures are traditionally applied to assess energy efficiency, regarding the exergy losses in a process system. The exergy loss or destroyed exergy (irreversibility) is a positive quantity for all the actual process and for a steady-state system can be compute by the Equation (1) [5]:

$$\dot{E}_d = \sum_j \left(1 - {T_o}/{T_j}\right)\dot{Q}_j - \dot{W}_{vc} + \sum_i \dot{m}_i e_{fi} - \sum_e \dot{m}_e e_{fe} \quad (1)$$

Where:

$\left(1 - {T_o}/{T_j}\right)\dot{Q}_j$ = It represents the time rate of exergy transfer accompanying heat transfer at the rate $\dot{Q}_j$ occurring at the location on the boundary where the instantaneous temperature is T_j.

$\dot{W}_{vc}$ = This term represents the time rate of energy transfer rate by work

$\dot{m}_i e_{fi}$ = It accounts for the time rate of exergy transfer accompanying mass flow and flow work at inlet *i*.

$\dot{m}_e e_{fe}$ = It accounts for the time rate of exergy transfer accompanying mass flow and flow work at exit *e*.

The irreversibility can be viewed as the wasted work potential or the lost opportunity to do useful work. So this measure manifests itself in environmental degradation and emissions [5] [6].

Decreasing the destroyed exergy of a process means lower primary fuel consumption, thus reducing the operating cost and increasing the process efficiency. This, in turn, will reduce emissions and wasted heat to the environment.

Another tool that can be used for measuring environmental performance is the Life Cycle Assessment (LCA) that is an internationally renowned methodology for evaluating the environmental performance of a product, process or pathway along its partial or whole life cycle, quantifying the potential environmental impacts of them.

In relation the Life Cycle Impact Assessment, many methodologies of human health and environmental risk have been developed. One of these methodologies applied in many LCA works is the Eco-Indicator 99. This method analyzes environmental burden under three impact areas (human health, ecosystem, resources), computing eleven different impact categories like carcinogens, respiratory organics, respiratory inorganic, climate change, radiation, ozone layer, eco-toxicity, acidification, eutrophication, land use, minerals and fossil fuels.

In the inventory, impacts are analyzed by different effect categories then damage assessment has been measured by human health, ecosystem and resource categories. The human health is computed in DALY (Disability Adjusted Life Years) unit, this means that different disabilities caused by diseases are weighted [8]

Ecosystem Quality is measured in PDF*m^{2}yr, where PDF is potentially disappeared fraction of plant species. Finally the resources are measured in MJ surplus energy additional energy requirement to compensate lower future ore grade.

The last step is the weighting that refers to using numerical factors for facility the comparison across impact category indicators. But the weighting remains a controversial element of LCA, mainly because the weighting involves social, political and ethical value choices.

Different works have been applied the exergy analysis and LCA, mainly in energy conversion system [9],[10],[11],[12] . The combination of LCA and exergy analysis is based on the methodological approach of exergoeconomic analysis. But in this case the environmental impacts are assigned to exergy streams of the system. So the method generates information on environmental impacts associated with thermodynamic efficiency (exergy destruction) and environmental impacts related to construction, operation, and maintenance of plant components.

The present work uses this methodology, applying in methanol production from biomass. The methanol plant is annexed to an ethanol autonomous distillery. The thermal and electrical demand of the whole plant is supply by a cogeneration system based in condensing/extraction steam turbines.

The goal of this analysis is appoint which stages from methanol production system present more environmental impacts and which are the possibilities for minimizing them.

2. Methodology and assumptions

This section provides some general information about the case study of the work and the description of the methodology applied.

Some of the definitions used in [9] and [10] are used for the exergoenvironmental analysis.

2.1. Case study parameters

The main parameters of all system analyzed are in Table 1.

Table 1. Main parameters of case study.

COGENERATION SYSTEM	
Equipment performance	
Boiler efficiency (%)	88
Isentropic efficiency of steam turbine (%)	90
Power installed (MW)	78
Steam production (t/h)	600
Fuel (bagasse)	
Sugarcane bagasse – LHV (kJ/kg)	7560
Moisture (%)	50
Milling system	

Steam inlet pressure (MPa)	2
Steam inlet temperature (°C)	320
Steam pressure exhaustion (MPa)	0.17
Percentage of bagasse from sugarcane	28
Milling capacity of sugarcane (t/h)	1351
Environmental conditions	
Atmospheric temperature (°C)	25
Atmospheric pressure (MPa)	0.1013
DISTILLERY AND METHANOL PLANT	
Total consumption of steam (kg/tc)	369
Methanol production (m^3/h)	328
Ethanol production (m^3/h)	2594
Electrical energy demand of distillery (kWh/tc)	12
Electrical energy demand of methanol plant (kWh/kg methanol)	0.25

2.2. Exergoenvironmental analysis

The exergoenvironmental analysis of this work consists mainly of three steps. The first is an exergy analysis of the energy conversion process that contains a methanol plant, an ethanol plant and its cogeneration system for supplying thermal and electrical demand of these plants. Second, it computes the environmental impacts by applying the Eco-Indicator 99 life cycle assessment method. In last step the environmental impact are assigned to the exergy streams in the process, using thermoeconomics tool.

One of results from exergoenvironmental analysis calls specific environmental impact b_j. This represents environmental impact associated with the production of the j stream per exergy unit (mPts/kJ) [9]. Similarly, it computes the environmental impact rate $\dot{B}_j$ (mPts/s) of stream j. This impact is the product of its exergy rate $\dot{E}_j$ and the specific environmental impact b_j, as Equation (2):

$$\dot{B}_j = b_j . \dot{E}_j , \quad (2)$$

Another important variable calculated is the environmental impact of exergy destruction. As work [10], it assumed that exergy destruction is compensated for by higher consumption of fuel to obtain the given amount of product. So, in this case the exergy destruction ($\dot{E}_{D,k}$) is multiplied with specific environmental impact $b_{F,k.}$ associated with the fuel of component. The result is the environmental impact of exergy destruction (Equation (3)).

$$\dot{B}_{D,K} = b_{F,K} \dot{E}_{D,K} , \quad (3)$$

For getting the results, it was necessary formulate mathematical equations, applying the thermoeconomics concept. So, computing the specific environmental impact of all internal flows of exergy (j) through environmental impact balance of the each equipment or sub-system k from thermal system, as it is in Equation (4).

$$\sum (b_j \dot{E}_j) = \dot{Y}_K , \quad (4)$$

Where $\dot{Y}_K$ is the environmental impacts that occur during the life cycle phases of equipment or sub-system k, as example: construction (including manufacturing, transport and installation), operation and maintenance.

These environmental impacts use the Eco-Indicator 99 method for calculation, after it divides the results by lifespan of equipment.

In this study assumed the lifespan of all equipments at 100,000 hours. Only the methanol plant and autonomous distillery it assumed 20 years. The databases (inventory) of equipments and sub-system (Methanol and distillery plants) are from data of SimaPro software version 7 [13] and bibliography references [14], [15], [16], [17].

The thermoeconomic model is a set of cost equations describing all the process of cost formation in the plant, it describes the distribution of the resources in the plant through the components to obtain the final products. To obtain the set of equations, this paper considers the mathematical formalism used in work [18] and [19]. In the exergoenvironmental evaluation the approach of thermoeconomic analysis is modified to deal with an evaluation of the ecological impact instead of an economic problem .The equations are shown in Table 2.

The Fig. 1 represents the physical structure, According to Figure 1 the global plant is compost by a cogeneration system based on condensing/extraction steam turbines, operating with high steam parameters that supplies all the steam and electricity for the autonomous distillery and methanol plant that are included in global plant. The sugarcane bagasse obtained in the milling section is used as fuel for the cogeneration system, as well as raw material for the methanol production, while the sugarcane juice is used for the hydrated ethanol production. In this way the

three systems are integrated producing surplus electricity, hydrated ethanol and methanol.

The Fig. 2 is the productive structure of the case study of this work. The rectangles in Figure 2 are the actual productive units that represent the plant components. The rhombuses and the circles are fictitious productive units called junctions and bifurcation, respectively. The inlet and outlet arrows are productive unit fuels (or resources) and products, respectively. When a productive unit has more than one type of fuel it necessarily incorporates a small junction (e.g., T1+C1, Ethanol plant.). The productive flows are all exergy flows representing: electrical power (E_P), mechanical power (PM) or exergy of sugarcane ($E_{sugarcane}$), bagasse (E_{bag}), juice (E_{juice}) and water/steam (*Ej:k* and *Ej:k`*).For convention it assumed that the exergy of input flow is the negative value, unlike for output flow.

Table 2. Mathematical equations of system

Productive structure	Equation
B3	$b_{bag} \cdot \dot{E}_{bag} + b_{juice} \cdot \dot{E}_{juice} - b_{cane} \cdot \dot{E}_{cane} = 0$
Boiler 1	$b_{16:15} \cdot \dot{E}_{16:15} - b_{bag} \cdot \dot{E}_{bag1} = \dot{Y}_{boiler1}$
B4	$b_{bag} \cdot \dot{E}_{bag1} + b_{bag} \cdot \dot{E}_{bag2} + b_{bag} \cdot \dot{E}_{bag3} + b_{bag} \cdot \dot{E}_{bag4} - b_{bag} \cdot \dot{E}_{bag} = 0$
Boiler 2	$b_{2:1} \cdot \dot{E}_{2:1} - b_{bag} \cdot \dot{E}_{bag2} = \dot{Y}_{boiler2}$
Boiler 3	$b_{4:3} \cdot \dot{E}_{4:3} - b_{bag} \cdot \dot{E}_{bag3} = \dot{Y}_{boiler3}$
Pump 1	$b_{15:18} \cdot \dot{E}_{15:18} - b_{PA} \cdot \dot{E}_{PA} = \dot{Y}_{pump1}$
Pump 2	$b_{1:19a} \cdot \dot{E}_{1:19a} - b_{PB} \cdot \dot{E}_{PB} = \dot{Y}_{pump2}$
Pump 3	$b_{3:19b} \cdot \dot{E}_{3:19b} - b_{PC} \cdot \dot{E}_{PC} = \dot{Y}_{pump3}$
Pump 4	$b_{11:10a} \cdot \dot{E}_{11:10a} - b_{PD} \cdot \dot{E}_{PD} = \dot{Y}_{pump4}$
Pump 5	$b_{12:5a} \cdot \dot{E}_{12:5a} - b_{PE} \cdot \dot{E}_{PE} = \dot{Y}_{pump5}$
Pump 6	$b_{14:10b} \cdot \dot{E}_{14:10b} - b_{PF} \cdot \dot{E}_{PF} = \dot{Y}_{pump6}$
Pump 7	$b_{13:7b} \cdot \dot{E}_{13:7b} - b_{PG} \cdot \dot{E}_{PG} = \dot{Y}_{pump7}$
Pump 8	$b_{17:8b} \cdot \dot{E}_{17:8b} - b_{PH} \cdot \dot{E}_{PH} = \dot{Y}_{pump8}$
T1 + C1	$b_{P1} \cdot \dot{E}_{P1} - b_{20b:5a,b,c,d} \cdot \dot{E}_{20b:5a,b,c,d} - b_{II:I} \cdot E_{II:I} = \dot{Y}_{T1+C1}$
T2 + C2	$b_{P2} \cdot \dot{E}_{P2} - b_{20a:7a,b} \cdot \dot{E}_{20a:7a,b} - b_{IV:III} \cdot E_{IV:III} = \dot{Y}_{T2+C2}$
T3 + C3	$b_{P3} \cdot \dot{E}_{P3} - b_{16:8a,b} \cdot \dot{E}_{16:8a,b} - b_{VI:V} \cdot E_{VI:V} = \dot{Y}_{T3+C3}$
G1	$b_{P4} \cdot \dot{E}_{P4} - b_{P1} \cdot \dot{E}_{P1} = \dot{Y}_{G1}$
G2	$b_{P5} \cdot \dot{E}_{P5} - b_{P2} \cdot \dot{E}_{P2} = \dot{Y}_{G2}$
G3	$b_{P6} \cdot \dot{E}_{P6} - b_{P3} \cdot \dot{E}_{P3} = \dot{Y}_{G3}$
Water Cooler	$b_{VI:V} \cdot \dot{E}_{VI:V} + b_{IV:III} \cdot \dot{E}_{IV:III} + b_{II:I} \cdot \dot{E}_{II:I} - b_{PJ} \cdot \dot{E}_{PJ} = \dot{Y}_{WC}$
J2 + B2	$b_{PA} \cdot \dot{E}_{PA} + b_{PB} \cdot \dot{E}_{PB} + b_{PC} \cdot \dot{E}_{PC} + b_{PD} \cdot \dot{E}_{PD} + b_{PE} \cdot \dot{E}_{PE} + b_{PF} \cdot \dot{E}_{PF} + b_{PG} \cdot \dot{E}_{PG} + b_{PH} \cdot \dot{E}_{PH} + b_{PI} \cdot \dot{E}_{PI} + b_{PJ} \cdot \dot{E}_{PJ} + b_{PK} \cdot \dot{E}_{PK} + b_{EX} \cdot \dot{E}_{EX} - b_{P4} \cdot \dot{E}_{P4} - b_{P5} \cdot \dot{E}_{P5} - b_{P6} \cdot \dot{E}_{P6} = 0$
J1 + B1	$b_{20b:5a,b,c,d} \cdot \dot{E}_{20b:5a,b,c,d} + b_{20a:7a,b} \cdot \dot{E}_{20a:7a,b} + b_{16:8a,b} \cdot \dot{E}_{16:8a,b} + b_{6,7a,8a:10a,b} \cdot \dot{E}_{6,7a,8a:10a,b} + b_{5d:6} \cdot \dot{E}_{5d:6} + b_{5c,d:9a,b} \cdot \dot{E}_{5c,d:9a,b} - b_{16:15} \cdot \dot{E}_{16:15} - b_{2:1} \cdot \dot{E}_{2:1} - b_{4:3} \cdot \dot{E}_{4:3} - b_{15:18} \cdot \dot{E}_{15:18} - b_{1:19a} \cdot \dot{E}_{1:19a} - b_{3:19b} \cdot \dot{E}_{3:19b} - b_{11:10a} \cdot \dot{E}_{11:10a} - b_{12:5a} \cdot \dot{E}_{12:5a} - b_{14:10b} \cdot \dot{E}_{14:10b} - b_{13:7b} \cdot \dot{E}_{13:7b} + b_{17:8b} \cdot \dot{E}_{17:8b} = 0$
Ethanol plant	$b_{ethanol} \cdot \dot{E}_{ethanol} - b_{PK} \cdot \dot{E}_{PK} - b_{6,7a,8a:10a,b} \cdot \dot{E}_{6,7a,8a:10a,b} - b_{juice} \cdot \dot{E}_{juice} = \dot{Y}_{ethanol}$
Milling	$b_{PM} \cdot \dot{E}_{PM} - b_{5d:6} \cdot \dot{E}_{5d:6} = \dot{Y}_{milling}$
Methanol plant	$b_{methanol} \cdot \dot{E}_{methanol} - b_{PI} \cdot \dot{E}_{PI} - b_{5c,b:9a,b} \cdot \dot{E}_{5c,b:9a,b} - b_{bag} \cdot \dot{E}_{bag4} = \dot{Y}_{methanol}$

2.3. Limitations and advantages of exergoenvironmental analysis

The restriction of exergoenvironmental analysis is referred to the LCA method that presents the following typical limitations [11]:

- The nature of choices and assumptions made in LCA (e.g. system boundary setting, selection of data sources and impact categories) may be subjective;
- Models used for inventory analysis or the assess environmental impacts are limited by

their assumptions, and it may not be available for all potential impacts or applications;

- The results of LCA studies focused on global and regional issues, so for local applications it might not be adequately represented;
- The accuracy of LCA studies is limited by accessibility or availability of relevant data, or by data quality;
- The lack of spatial and temporal dimensions in the inventory data used for impact assessment introduces uncertainty in impact results.

According the International Stand on LCA the allocation should be avoided where possible by sub-division or system boundary expansion [20]. However, when the allocation is inevitable, the ISO 14041 recommends that the allocation should reflect the physical relationships between the environmental loads and the functions. Thus, allocation can consider the physical properties of the products, such as mass, volume, energy, because data on the properties are generally available and easily interpreted. The choice and justification of allocation procedures is a major issue for life cycle assessment, especially since it can have a significant influence on subsequent results.

In this way the exergoenvironmental analysis allows to allocate the main environmental loads takes into account the quality of the different kinds of energy.

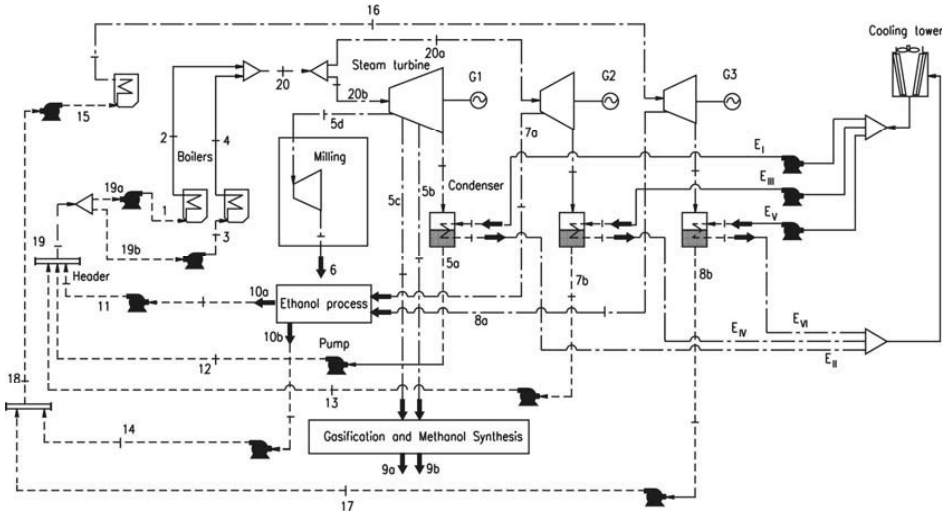

Fig. 1. Physical structure of thermal system

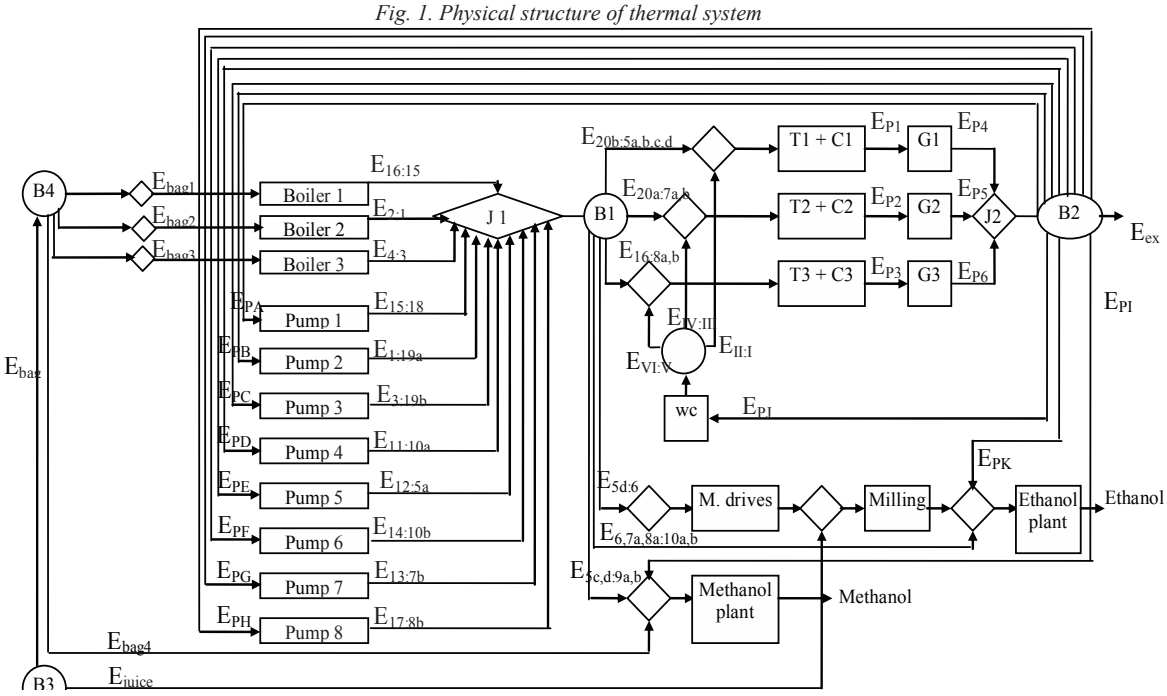

3. Results

Life Cycle Analysis

In Figure 3 and 4 are presented the environmental impacts of all system related the production of 100 m^3 methanol, which is the functional unit of this work. The Figure 3 presents the total environmental impacts (Points/ 100 m^3 methanol), while the Figure 4 presents the environmental impacts divided by impact categories (carcinogens, ecotoxicity, land use, climate change, others).

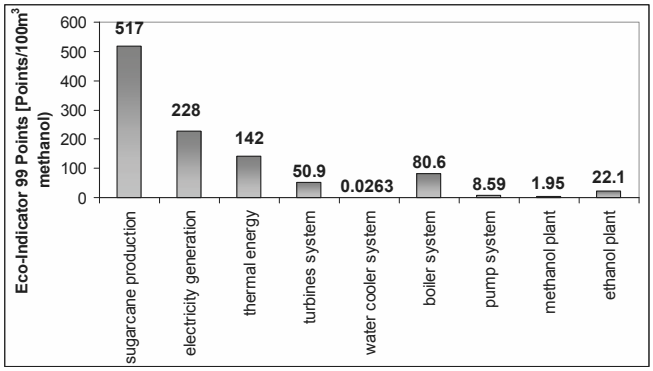

Fig. 3.Total environmental impacts of the system

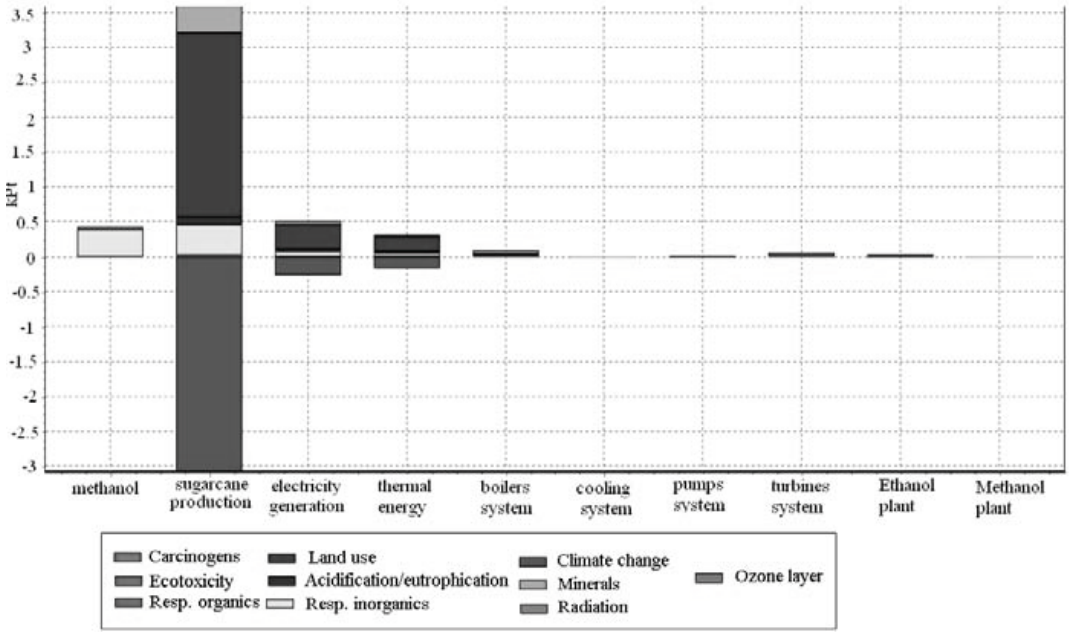

Fig. 4. Environmental impacts of all system by impact categories

The Figure 4 shows that the sugarcane production presents a favorable impact for climate change mitigation, the reason is related the carbon dioxide absorption by the sugarcane during its growth. However, the popular belief is that ethanol production systems release no net CO_2, they actually do because of direct and indirect oil consumption: this system uses external inputs, such as fertilizers, pesticides, transport infrastructure and so on, that demand petroleum in their production, operation and maintenance.

With respect to the system equipments construction, the results from Figure 3 and Figure 4 shows that the environmental impacts from them is relatively low when they are compared with methanol synthesis, sugarcane production, electricity generation and thermal energy.

The life cycle energy efficiency and the fossil energy ratio for this system were determined in [21]. The first ratio refers to the quantity of energy primary necessary to produce 1 kg methanol, the result gotten was 0.20, while the second ratio refers to the fossil energy demand for producing 1 kg of methanol, and the value gotten was 9.4.

Exergy Analysis

The available exergy of sugarcane for the ethanol distillery without and with a methanol plant annexed is presented in the Figures 4 and 5.

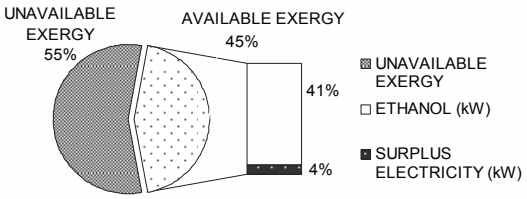

Fig. 4. System without methanol plant annexed

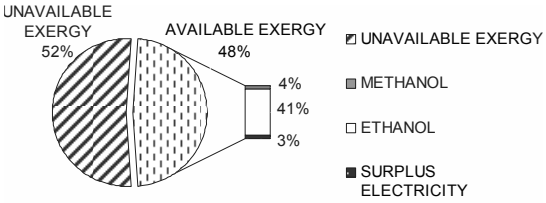

Fig. 5. System with methanol plant annexed

Comparing the Figures 4 and 5, the Figure 5 shows that available exergy of sugarcane is 3% more high in a system that has the methanol plant annexed. So in terms of global exergetic utilization and resources use, the system that produces methanol is more attractiveness and therefore more sustainable.

For the overall energy conversion system, the exergetic efficiency is

$$\eta_{exer} = \frac{E_{Ethanol} + E_{Metanol} + E_{E.exc}}{E_{Sugarcane}} = 48\%$$

Exergoenvironmental Analysis

The solution of linear equations of the Table 2 provides all values of the environmental impact rates within the process (b_j). With this value it is possible compute environmental impact of exergy destruction ($\dot{B}_{D,K}$), as well as, the environmental impact of life cycle phases of system components ($\dot{Y}_K$).The main results are presented in Table 3.

Table 3. Environmental impact of exergy destruction and from system components

Equipment	$\dot{Y}_K$ (mPts/s)	$\dot{B}_{D,K}$ (mPts/s)
Boiler 1	$7.44\ 10^{-5}$	0.0008767
Boiler 2	$7.44\ 10^{-5}$	0.0020797
Boiler 3	$7.44\ 10^{-5}$	0.0020797
Pump system	$2.35\ 10^{-5}$	$7.74\ 10^{-6}$
Water cooler	8.45 10-8	$2.13\ 10^{-5}$
Milling	$2.13\ 10^{-7}$	0.000120
ST1 + C1	$4.71\ 10^{-5}$	0.0002243
ST2 + C2	$4.71\ 10^{-5}$	0.0001009
ST3 + C3	$4.71\ 10^{-5}$	0.0001352
G system	0	$4.038\ 10^{-5}$
Ethanol plant	$7.10\ 10^{-5}$	0.02282
Methanol plant	$6.26\ 10^{-6}$	0.00686

Table 3 shows that the major environmental impacts associated with exergy destruction occur in the components associated to the cogeneration systems (boilers, steam turbines, pumps) and ethanol, the second environmental impacts associated to the exergy destruction occurs in the ethanol plant and the third correspond to the methanol plant. It also shows that the environmental impact caused by exergy destruction ($\dot{B}_{D,K}$) is the main source of environmental impacts when compared with the component-related environmental impact of the system ($\dot{Y}_K$) that were very low.

Some technological alternatives that contributes for decreasing the environmental impacts associated with exergy destruction in the whole systems are: mills electrification, steam consumption reduction in the different process stages of ethanol production through thermal integration or more efficiency technology such as: multipressure-distillation, instead of, atmospheric one, regenerative heat exchangers for juice x stillage, juice x juice and juice x condensate;. Finally in the methanol production process these impacts can be reduced through an adequate controle of the ($H_2 - CO_2/CO+CO_2$) ratio in the

syngas produced by bagasse gasification, having in mind that the necessity of remove more CO2 away and adopt s shift process ($CO + H_2O = CO_2 + H_2$) to adjust H/C, which will cause material and exergy destruction.

4. Conclusion

The exergoenvironmental method shows whether reducing the thermodynamic inefficiencies or reducing consumption of materials during construction or operation of the component can permit to improve the environmental performance of energy conversion system for biofuel production.

The results also prove that the sugarcane exergy is more available and therefore sustainable when increase the quantity of products from sugarcane, in this case: electricity, ethanol and methanol.

References

[1] Ekbom, T., Projekt BioMeeT II – Teknisk Slutrapport, 2003, NYKOMB SYNERGETIC URL: http://www.nykomb-consulting.se

[2] Audi, R., and Fiaschi, A., Project for Renewable Fuels Production and Chemical Products from Biomass, 2005, URL: http://www.int.gov.br

[3] Hamelinck, C. N., and Faaij, A. P. C., 2002, Future Prospects for Production of Methanol and Hydrogen from Biomass, Journal of Power Sources, 111(1), pp. 1-22.

[4] Kanoglu M., et al., 2009, Exergy for Better Environment and Sustainability, Environment, Development and Sustainability, 11(5), pp. 971 – 988.

[5] Moran, M. J., and Shapiro, H. N., 2006, *Fundamentals of Engineering Thermodynamics*, 5th ed., John Wiley & Sons, Inc., UK.

[6] Bösch, M. E., et al., 2007, Applying Cumulative Exergy Demand (CExD) Indicators to the Ecoinvent Database, Int J LCA, 13(3), pp. 181 – 190.

[7] International Organization for Standardization (ISO), 2006, Environmental Management – Life Cycle Assessment, European Standard EN ISO 14040 and 14044, Geneva, Switzerland.

[8] Goedkoop, M., and Spriensma, R., 2000, The Eco-indicator 99: A Damage Oriented Method for Life Cycle Impact Assessment, Methodology Report, PRé Consultants b.v., Amersfoort, The Netherlands.

[9] Meyer L., et al., 2009, Exergoenvironmental Analysis for Evaluation of the Environmental Impact of Energy Conversion Systems, Energy, 34, pp. 75 – 89

[10] Buchgeister, J., et al., 2009, Exergoeconomic and Exergoenvironmental Analysis of Different Optimization Options for Electricity Production using SOFC with Integrated Allothermal Biomass Gasification , *Proc. 22nd International Conference on Efficiency, Cost, Optimization,* Foz de Iguaçu, Brazil.

[11] González, A., et al., 2003, Application Of Thermoeconomics To The Allocation Of Environmental In The Life Cycle Assessment Of Cogeneration Plants, Energy, 28, pp. 557 – 574.

[12] Portha, J., Louret, S., Pons, M., Jaubert, J., 2010, Estimation of the Environmental Impact of a Petrochemical Process using Coupled LCA and Exergy Analysis, Resources, Conservation and Recycling, 54, pp. 291-298.

[13] SimaPro 7, 2006, Software Package, Ver. 7.0, Copyright PRé Consultants, Amersfoort, The Netherlands.

[14] Macedo I.C., et al., Green House Gases Emissions in the Production and use of Ethanol from Sugarcane in Brazil. Biomass and Bioenergy, 32, pp. 582 – 595.

[15] Renouf M.A., et al., 2008, An Environmental Life Cycle Assessment Comparing Australian Sugarcane with US Corn and UK Sugar Beet as Producers of Sugar for Fermentation. Biomass and Bioenergy,32, pp.1144 – 1155.

[16] Rocha J. D., Pretreatment of biomass (Pré-tratamento da biomassa), 2008, URL: http://www.apta.sp.gov.br/cana/anexos/Position_paper_painel1_dilcio.pdf

[17] Baker E. G., et al, 1986, Engineering Analysis of biomass Gasifier Product, Prepared for the Biomass Energy Division – US Department of Energy, Washington.

[18] Santos, J.J.C.S., Application of Neguentropy in Modeling of Thermoeconimcs system, Ph.D. Dissertation, Federal University of Itajubá, Itajubá, Brazil.

[19] Frangopoulos, C. A., 1994, Application of the Thermoeconomic Functional Approach to the

CGAM Problem", Energy, 19 (3), pp. 323 – 342.

[20] Malça, J., and Freire, F., 2006, Renewability and Life-Cycle Energy Efficiency of Bioethanol and Bio-ethyl Tertiary Butyl Ether (BioETBE): Assessing the Implications of Allocation, Energy, 31, pp. 3362-3380.

[21] Renó, M. L.G., Lora, E. S., Escobar, J. C. P., 2009, Life Cycle Assessment Of The Methanol Production From Sugarcane Bagasse, *Proc. 22nd International Conference on Efficiency, Cost, Optimization,* Foz de Iguaçu, Brazil.

Acknowledgments: The authors would like to acknowledge Mr. Jeans Buchgeister (Institute of Technology Assessment and System Analysis), FAPEMIG, CNPq and CAPES for the financial support to perform this study.

Environmental Performance and Thermoeconomic Analysis of Vinasse Treatments

Mauro Francisco Chavez-Rodriguez

Mechanical Engineering Faculty(FEM), State University of Campinas(UNICAMP)

Abstract: For every liter of ethanol from sugarcane is produced in an average 11 liters of vinasse. Vinasse is a highly pollutant effluent and it cannot be discarded to rivers, then currently vinasse is used for fertirrigation; however longer distances make this solution not economical. In this scenario concentration of vinasse could overcome this barrier. The objective of this work is to assess three treatments for vinasse: concentration by evaporation, anaerobic treatment, and ultrafiltration & reverse osmosis using exergetic and thermoeconomical analysis in order to compare in terms of costs and environmental performance, related to exergy, these different treatments. Organic substances responded by the major exergy content in vinasse reflecting its highly pollutant potential. Monetary exergetic costs of products in treatments assessed internalized the reduction or management of this exergy. It is used rational efficiency and environmental exergy efficiency to compare exergetic performances of the treatments; being the second one the most adequate index to asses these kinds of effluent treatment utilities. In thermoeconomical assessment the treatment by ultrafiltration and reverse osmosis reported the highest performance in terms of monetary exergetic costs and the best environmental exergetic efficiency. Based on that, efforts to develop this technology, applied to effluents with higher organic content as vinasse, must be done.

Keywords: Vinasse, Exergetic Costs, Thermoeconomics, Effluents.

1. Introduction

According to UNICA [1], Brazil produced in 2008/2009 around 27.5 billions litres of ethanol from sugarcane, and in 2020 a production of 65 billions of litres is estimated [1]. Considering an average value of 11 litres of vinasse per litre of ethanol produced, in 2008/2009 season, 302.5 billion litres of vinasse were produced, and in 2020, 715 billion litres would be produced if nowadays production patterns continue being used.

Vinasse is a by-product of ethanol production based on sugarcane. It was reported that currently vinasse production is between 7 and 18 litres per litre of ethanol [2]. Because it is a highly pollutant effluent it can not be discarded in courses of water, and due to it is one of the most acid and corrosives substances produced by agro industry it is hardly treated by usual treatment used for other industrial effluents.

However, vinasse goes with a high temperature which can be used to supply heat demands in other processes; moreover it has high quantity of organic matter, high concentration of solids, being re-used as fertilizer for agriculture by their richness in potassium, nitrogen contents and useful micronutrients [2]. Average values for vinasse composition in sugarcane plants in Brazil are showed in Table 1.

Table 1. Physical-chemical characterization of Vinasse [2]

Parameters	Average	Range
pH	4.3	3.5-4.9
Temperature(ºC)	90	65-110.5
BOD (mg/L)	14833	5879-75330
COD(mg/L)	23801	9200-97400
COD/BOD	1.6	1.6-2.8
TS(mg/L)	32788	10780-56780
Nitrogen(mg/L)	433	81-1215
Potassium(mg/L)	2206	814-7612
Calcium (mg/L)	832	39,.4-1451
Magnesium(mg/L)	262	97-1112
Sulphur(mg/L)	1149	92-3364

The so called *fertirrigation* of sugarcane field began with the prohibition of discarding vinasse in water courses (through the Decree Law Nr. 303, February 28, 1967) [3]. Since first studies about effects of vinasse in sugarcane crops, it was proved that vinasse brings higher yields benefits. However, applications at high rates (about 1000 m^3/ha), conducts to negative effects in crop quality, specially, slowing maturation, decreasing

of sucrose content , increasing of ash content and potassium level in sugarcane juice [3].

In this scenario, reduction of production of vinasse using higher alcoholic content along the ethanol production or vinasse concentration to reach higher distances for fertirrigation, or vinasse treatment (when it is not economical to discard) could be solutions for this problem. This work assesses the scenarios of concentration of vinasse and its treatment.

Currently, vinasse is used for fertirrigation, this operation is regulated by the standard P4.231, (Vinasse-Criteria and procedures for application in soil for agriculture) [4], taking care on not exceeding the cationic exchange capacity of the soil and not reaching underground water basins. This practice is giving economical benefits in partial or total substitution of mineral fertilization, improving physical-chemical characteristics of soil, increasing crop yields, and eliminating the possible contaminations of superficial waters basins [2]. However, this solution is not economical when transport along longer distances is necessary. In this scenario, concentration of vinasse could overcome this barrier.

The aim of this work is to compare, in terms of costs and environmental performance, three treatments for vinasse: evaporation, reverse osmosis and anaerobic digestion, using exergetic balances and thermoeconomic as evaluation tools.

2. Base Case

In order to assess the exergetic costs, and the volume of vinasse produced, an "standard" plant is considered, which presents the common characteristics of a sugarcane mill, producing simultaneously sugar and ethanol from juice of sugarcane. It was considered that 50% of sugarcane juice sucrose was used for the production of sugar and 50% for ethanol production. The ethanol production is carried out with the residual molasses from sugar production, besides some amount of syrup and treated juice. The general characteristics of the modeled plant, as also the parameters used for simulation, are described in the Table 2, reporting similar values of averages mills studied in other works [5,6] . These values are considered for all cases presented in this study.

To perform this study, it was considered that 50% of all vinasse produced will be treated, being the other 50% used in fertirrigation along shorter distances.

Table 2. Production Parameters for the Sugar Cane Plant Assessed.

Parameter	Value
Mill Capacity (t cane/year)	2000000
Crushing Rate(t cane/hr)	500
Sugar production (t/day)	780
Hydrated Ethanol production (m3/day)	480
Vinasse Production (L vinasse/L ethanol)	11
Vinasse Produced (m3/d)	5280
Vinasse Treated (m3/d)	2640

3. Exergetic and Thermoeconomic Analysis

The vinasse exergy, considered as a solution, could be divided in thermal, mechanical, chemical, kinetic and potential components. According to Zaleta-Aguilar et al [8] chemical exergy can be divided in: the chemical exergy of water, the chemical exergy of dissolved inorganic substances, and the chemical exergy of organic substances. The chemical exergy of water can be evaluated as a pure substance in a solution by means of its activity a_i:

$$b_{q,i} = x_i(\mu_i - \mu_{i,o}) = x_i RT_o \ln\left(\frac{a_i}{a_{i,o}}\right)\Big|_{i=H_2O} \quad \text{Eq.1}$$

The chemical exergy of the dissolved inorganic substances is determined by the following equation:

$$a_i = \gamma_i m_i \quad \text{Eq.2}$$

Data from Table 1 is considered for inorganic substances. Chemical exergy of inorganic substances are calculated using Eq. 3, which refers to the exergy needed to carry pure substances until equilibrium with the standard environment. Standard chemical exergy of components were based on data reported by [9].

$$\sum_{i=1}^{n} x_i \varepsilon_i^0 \quad \text{Eq.3}$$

Finally the chemical exergy of the dissolved organic substances can be estimated according to the equation suggested by [10,11] :

$$B_{org.mat.} = 13.6\ COD \quad \text{Eq.4}$$

Where COD is the chemical oxygen demand in g/L O_2 . $B_{org.mat.}$ is expressed in kJ.

Physical Exergy of vinasse is determined by the following equation:

$$B_{ph} = (h_1 - h_o) - T_o(s_1 - s_o) \qquad \text{Eq.5}$$

Based on the fact that vinasse is composed by around 96% in mass by water, physical exergy of vinasse was calculated assuming water properties.

The exergy of inorganic substances in vinasse were calculated in other study [12], considering real mixture and 298.15 K as reference temperature. Exergy components of vinasse are presented in Table 3 .

Table 3. Exergy components of vinasse. Source: Chavez-Rodriguez [12]

Exery components of vinasse		kJ/kg
Chemical Exergy	Real Mixture	-1.1
	Inorganic Substances	49.6
	Organic Substances	323.7
Physical Exergy	Thermal Exergy	17.2
	Total	389.4

As it is reported by Table 3, thermal exergy of vinasse at 76ºC [6] is not so significant when compared with chemical exergy of organic substances, which represents 93% of the vinasse exergy. Exergy of mixture has a low value, which is explained by the fact that vinasse is a very diluted solution.

The objective of thermoeconomic analysis is to attribute costs to the exergetic content of energy carriers. When it is applied to a productivity system, an adequate cost function for that system can be obtained [13, 14]. In that sense, thermoeconomics could solve the attributing cost problems in a multi product plant. In Exergetic Cost Theory, effluents are considered without exergetic cost value when they do not have a posterior use, being these costs transferred to products [14]. However, in sugar cane industry (as in many other industries), legislation and technological improvements changed the category of effluents or solid waste, such as vinasse and bagasse, to raw materials for other processes as for instance cattle feeding, biofertilizing [15] or boiler fuelling.

To study alternative proposals, it could be necessary to find monetary values of these by-products, in that way exergetic cost theory, considering by-products with a monetary exergetic cost, is a useful tool. For cost assignment criteria in thermoeconomic assessment of this study, the methodology developed by [14] is used.

4. Treatment Process for Vinasse

Three treatment processes for vinasse are assessed: concentration by evaporation, anaerobic treatment, and ultrafiltration and reverse osmosis, as follows:

4.1. Vinasse Concentration by Evaporation

Vinasse treatment by concentration tries to promote the viability of fertirrigation for farthest areas, avoiding excessive water transport, or attending not continuous areas, where transporting by pipes is not practical. Vinasse concentration technologies by evaporation require stainless steel equipments and considerable quantities of energy in steam form. According [2], evaporation condensates, even when they seem to be "clean", need an additional system for their treatment. Inorganic dissolved solids in evaporation condensates are present in a very low quantity when compared with organic substances, so for this study, their presences in condensates, have not been considered.

4.1.1 Process

For this study, it is considered an evaporator system with four stages, fed in the first stage with 23.76 t /h of exhaust steam from the cogeneration system (127.4ºC and 2.5 bar pressure). Vacuum is made using a barometric condenser. Incondensable gases are extracted using a vacuum pump and properties of these gases are assumed similar to air and quantities of these are estimated based on values presented by [16]. Electricity consume is based on the rate of 3.7 kW/(kg/min) of air handled at 10kPa [16].

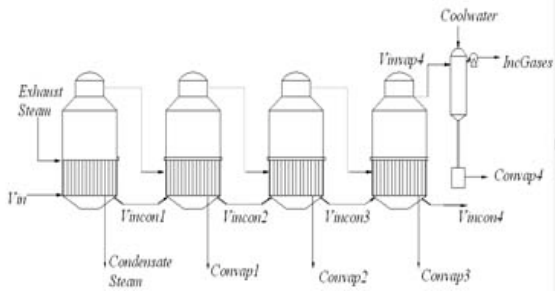

Figure 1. Concentration process by evaporation.

A minimum amount of organic matter is carried by condensates in evaporation, and in order to simplify calculations, all condensates are considered with a same COD (chemical oxygen demand) and inorganic content as phlegmasses, the bottom residues of ethanol rectification [2]. Table 4 shows the streams and operational parameters in evaporation system.

Table 4. Operational Parameters in the Evaporation Process

Stream	COD (mg/NL)	Inorganic (mg/NL)	T (ºC)	P (bar)	Enthalpy (kJ/kg)
Vin	23800	4916	76	6	214
Convap1	1560	51	115.0	1.69	378
Vincon1	27138	5646	115.0	1.69	378
Convap2	1560	51	97.6	0.93	304
Vincon2	32733	6870	97.6	0.93	304
Convap3	1560	51	83.2	0.54	244
Vincon3	41460	9041	83.2	0.54	244
Vincon4	62761	14065	55.3	0.16	127
CoolWater	80	-	30.0	1.01	126
Convap4	130	2	40.0	1.01	209
IncGases	-	-	55.3	1.01	329
Exhaust Steam	-	-	127.4	2.5	2717
Condensate Steam	-	-	127.4	2.5	535
Electrical Energy Input (EEI) Vacuum pump					3.90kW

4.1.2 Costs and Thermoeconomic Results

There is chosen a multi-effect vertical tube evaporator system of 4 effects. Using the software for evaporator design presented by www.sugartech.co.za it is estimated for the first, second, third and fourth evaporator a heat transfer area of 422, 218, 584 and 839 m^2 with a specific evaporation rate of 34.2, 66, 30.8 and 25.8 $kg/m^2/h$ respectively. Evaporator costs were obtained based in data from [17] which gives a cost relation for vertical tube evaporators related to their heat transfer area. Steam condenser cost is based on data from [18]. All costs reported were converted to current dollars (Bureau of Labour Statistics, 2010). Table 5 summarizes plant costs for evaporation plant, considering a life span for equipments of 20 years and an annual tax rate of 10%.

Exergetic costs of incondensable gases were neglected. Water costs were calculated based in the value of 0.54 $cUS\$/m^3$ of water ($0.01R\$/m^3$ collected) [5].

Table 5. Evaporation System Plant Costs

Evaporation Plant Costs	USD$
Fixed Costs	
1st Stage Evaporator	764000
2nd Stage Evaporator	538000
3rd Stage Evaporator	908000
4th Stage Evaporator	1100000
Steam Condenser System	77000
Instrumentation & Piping	331000
Annualized Fixed Costs	436715
O&M	223080
Steam Costs[1]	623757
Electricity Consume*	1397

[1]Exhaust Steam of a Sugar Cane Plant were calculated based on updated to data from [19] to current dollars, which results in an monetary exergetic costs of 35.37 US$/MWh of exhaust steam exergy.

Because cooling water for barometric condenser on vegetal vapor, condensed in the fourth evaporator, have a ratio of 28.8 in mass; exergetic costs of output of the barometric condenser is equaled to cooling water. Also it was assumed that exergetic costs of condensate of exhaust steam are equal to the exhaust steam (35.37 US$/MWh), the other outputs shared the same costs. . Table 6 shows these results.

Table 6. Exergetic Costs for Evaporation streams.

Stream	Flow (kg/s)	ce (10-6 U$/kJ)	Exergy (kJ/kg)	cm (US$/t)
Vin	31.8	15.4	389	6.0
Convap1	4.1	34.65	111	3.8
Convap2	5.0	34.65	95	3.3
Convap3	5.5	34.65	84	2.9
CoolWater	176.2	0.0988	44	0.0044
Convap4	182.3	0.0988	45	0.0044
IncGases	0.018	0	16	0.0
Vincon4	11.0	34.65	922	31.9
Exhaust Steam	6.6	44.71	668	29.9
Condensate Steam	6.6	44.71	111	5.0
EEI total	-	24.86	3.9	-

4.2 Anaerobic Treatment

Anaerobic treatment can be defined biochemically as the conversion of organic compounds into carbon dioxide, methane and microbial cells (sludge) in the absence of free or molecular

oxygen [20]. It has a high capacity of degrading concentrated and resilient substances. It produces very little sludge, requires less energy and can become profitable by cogeneration of useful biogas as well as produce a relatively inoffensive sludge suitable for use as a fertilizer [21].

4.2.1 Process

Raw Vinasse at a temperature of 76ºC is cooled until reach 40ºC and enters into the reactor for 10 days, which is the literature-recommended residence time for anaerobic digestion at 40ºC in a complete mix reactor [22] .

The bacterial culture carried out the conversion of the organic material to a variety of end products including methane (CH_4), carbon dioxide (CO_2), ammonia (NH_3) and cell or bacterial mass. Biogas which is basically composed by CH_4 and CO_2 is considered in the calculations as a by-product. The effluent or digested vinasse withdrawn from the reactor is reduced in organic load (BOD) by 90% [23]. Digested vinasse is basically a mix of water, inorganic and reduced organic substances.

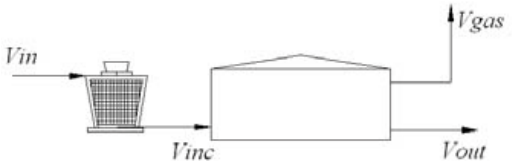

Figure 2. Anaerobic Treatment Process

To project the Anaerobic Digester equations reported by [23] were used, considering an average BOD remove efficiency of 80%.

It was assumed that anaerobic digestion of vinasse takes as little as 10 days, instead of the 30 to 40 days taken by conventional anaerobic digestion. Finally it was assumed that biogas concentration has the composition 60% CH_4, 40%CO_2 as reported in literature [2]. Table 7 shows the results for the anaerobic digestion of vinasse.

It must be remarked that in this kind of treatment only organic matter is degraded, keeping the effluent biodigested basically the same nutritional properties (mainly potassium) and the same potential pollutants for underground water. In that way, biodigested vinasse will have the same application as fertirrigation on the sugar cane field, with lower organic matter [2]. To solve the longer distances economical problems, a posterior concentration treatment must be used.

Table 7. Operational Parameters in the Anaerobic Treatment Process

Stream	T (ºC)	BOD (g/L)	COD (g/L)	Inorganics (mg/L)	Enthalpy (kJ/kg)
Vin	76	14800	23800	4916	213.8
Vinc	40	14800	23800	4916	62.2
Vout	40	2960	4760	4950.9775	49.2
Vgas	40	-	-	-	26

4.2.2 Costs and Thermoeconomic Results

A cooling tower with a thermal load of 4.6 MW is estimated to reach 40ºC. The total reactor volume estimated is 26568 m^3 for a 10 days retention time. As recommended by [24] it is used Upflow Anaerobic Sludge Blanket (UASB) reactors of 2500 m^3 per unit (11 reactors in total), with 26.0 m of diameter and 4.75 m of height. Table 8 summarizes plant costs for producing biogas, considering a life span for equipments of 18 years and an annual tax rate of 10%.

Table 8. Anaerobic Digestion Plant Costs

Anaerobic Digestion Plant	US$
Fixed Cost	
Cooling Tower	30000
UASB reactors[1]	5087500
Instrumentation and Accesories	508750
Annualized Fixed Costs	686010
O&M Costs[2]	97000

[1]Updated Costs based in [25].

[2] Updated Costs based in [26].

It was assumed for both output V_{out} and V_{gas} the same exergetic costs. Results are showed in Table 9.

Table 9. Exergetic Cost for Anaerobic Treatment Streams.

Stream	Flow (kg/s)	ce (10-6 U$/kJ)	Exergy (kJ/kg)	cm (US$/t)
Vin	31.78	15.4	389	5.99
Vout	31.55	31.58	114	3.61
Vgas	0.22	31.58	18885	596.39

The high costs value reported in Table 9 for Biogas produced in the anaerobic treatment is

explained by the high irreversibility in the process transferred to the products.

4.2 Ultrafiltration and Reverse Osmosis

In Ultrafiltrafion (UF) process suspended solids and solutes of high molecular weight are retained, while water and low molecular weight solutes pass through the membrane. Ultrafiltration as a pre-treatment for reverse osmosis is a reliable barrier for microorganisms and particles. Furthermore, it almost completely removes fouling causing substances [27].

The Reverse Osmosis (RO) involves a diffusive mechanism so separation efficiency is dependent on inlet solute concentration, its pressure and water flux rate [28]. According to [23] typical efficiencies of COD % removal for vinasse are found around 99.9%.

4.3.1 Process

In order to minimize membrane fouling, a filtration pretreatment is considered for the removal of suspended matter, bacteria, and perceptible ions. Then, filtrated vinasse is cooled and sent to a high pressure pump, which transport the feed to the spiral wound ultra filtration membrane module at a pressure of 6 bar, after that, permeate obtained from the ultrafiltration process is pumped at a pressure of 20 bar and used as feed for the reverse osmosis module [29].

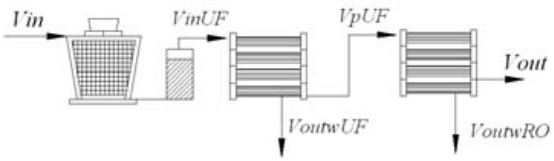

Figure 3. Ultrafiltration and Reverse Osmosis Treatment

For calculations, it is used COD and ions of potassium (K+); remove efficiencies reported by [29] with a Volume Reduction Factor of 5. Potassium (K+) remove efficiency is assumed for removing all the other inorganic substances. Table 10 shows the results for the membranes treatment of vinasse with previous considerations.

Even when rejection stream of Reverse Osmosis have less COD values than rejection stream of Ultra filtration; it presents highest exergy values due to their high load of ions.

Table 10. Operational Parameters in the UF and RO Processes

Stream	T (ºC)	COD (g/L)	Inorganic (mg/L)	Enthalpy (kJ/kg)
Vin	76	23800	4916	214
V_{inUF}	40	23800	4916	62
V_{pUF}	40	12186	3856	63
V_{outwUF}	40	70258	9155	63
V_{final}	40	392	206	64
V_{outwRO}	40	59360	18456	64
Electrical Energy Input UF			23	kW
Electrical Energy Input RO			62	kW

4.3.2 Costs and Thermoeconomic Results

The same cooling system as in anaerobic treatment case is considered, to reach a 40ºC temperature. The purification plant is compounded by 6 modules with a capacity of 660 m^3/d each one using polymeric membranes. Costs are estimated in scale up based in data reported by [30], in O&M costs are included, substitution of membranes based, labour, chemical compounds and maintenance. Table 11 summarizes treatment plant costs, considering a life span for equipments of 10 years and an annual tax rate of 10%.

Table 11. UF and RO Plant Costs

UF and RO Plant	US$
Fixed Costs	
Cooling Tower	30000
Reverse Osmosis Module	1128000
Ultrafiltration Module	564000
Instrumentation & Accesories	169200
Annualized Fixed Costs	307784
O&M	33841
Electricity Consume*	30423

*Based on monetary exergetic costs for electricity produced in a sugar cane cogeneration plant reported by [21] updated to currently dollars (89.5US$/MWh).

All outputs shared the same exergetic cost for the thermoeconomic assessment. Table 12 shows the results.

Table 12. Exergetic cost for UF and RO System

Stream	Flow (kg/s)	ce (10-6 U$/kJ)	Exergy (kJ/kg)	cm (US$/t)
Vin	31.78	15.40	389	6.0
EEI total	-	24.86	85 kW	-
V_{outwUF}	6.36	18.19	1012	18.4
V_{final}	20.34	18.19	49	0.9
V_{outwRO}	5.08	18.19	877.4	16.0

5. Exergy Balances and Environmental Performance

To assess the performance of the different process, it is used the rational efficiency (Ψ), defined as the outputs streams exergy divided by the input streams exergy; additionally it is used the environmental exergy efficiency ($\eta_{env,exergy}$) as proposed by [31] to assess the environmental performance.

The environmental exergy efficiency is defined as the ratio of the final product exergy (or useful effect of a process) to the total exergy of natural and human resources consumed, including all the exergy inputs. Mora and Oliveira [32] applied this index to assessing a wastewater treatment plant enouncing that the environmental exergy efficiency is a suitable indicator for ecological evaluation because it presents a unified thermodynamic measure for objectively evaluating resources utilization, quality of energy conversion processes and environmental impact. The environmental exergy efficiency is calculated according to Eq. (6):

$$\eta_{env,exerg} = \frac{B_{product}}{(B_{Nat,Res} + B_{Prep} + B_{Deact} + B_{Disp})} \quad (6)$$

Where: $B_{product}$=exergy rate of additional natural resources destroyed during waste deactivation; B_{Disp}=exergy rate related to waste disposal of the process; $B_{Nat,Res}$=exergy rate of the natural resources consumed by the process ; B_{Prep}=exergy rate required for extraction and preparation of the natural resources; B_{Prod}=exergy rate of the useful effect of a process.

$B_{product}$ are considered, in all processes evaluated, every output streams exergies with the exception of incondensable gases in evaporation case that they are not used. B_{Disp}=0 in all cases, incondensable gases does not need disposal and there is no other stream considered as waste (condensates could be recycled in sugarcane plant; biogas could be burned in the plant boiler, etc.). $B_{Nat,Res}$=exergy rates of vinasse flows. To estimate the $B_{Prep,}$ it is used the coefficient exergetic factors reported by [21] for a sugarcane cogeneration plant being considered for electricity 5.02 and for steam 4.34. This means for instance, to supply the 85 kW of exergy needed for the UF and RO processes it was used 426.7 kW of exergy (as input and destroyed).

In Table 13 they are summarized the values of input, output, destroyed exergy flowrate/rate for the studied Treatment Processes, and the efficiencies indexes used.

Table 13. Values of the input, output and destroyed exergy flows, rational and environmental efficiencies.

Process	Exergy rate/flow rate			Ψ	$\eta_{env,exergy}$
	Input (kW)	Output (kW)	Destroyed (kW)		
Concentration by Evaporation	24601	10332	14269	0.42	0.24
Anaerobic Treatment	12355	7846	4509	0.64	0.64
Ultrafiltration and Reverse Osmose	12440	11886	555	0.96	0.92

6. Results Discussions and Conclusions

Thermoeconomic assessment based on exergetic theory costs usually have been applied to assess thermal plants, however it is a useful tool to assign costs in multiproduct processes as in the cases studied in this paper. However, there are distortions that must be recognized; as for example in the concentration by evaporation case, the condensate water, which is a treated boiler water, have less costs in mass basis than a condensate of vegetal vapor from vinasse, as consequence of having a lower exergy content .

Chemical Oxygen Demand (COD), reflecting the organic substances, responds for the major exergy content and the pollution potential of vinasse. Exergetic monetary costs of products in the treatments assessed internalized the reduction or management of this exergy, caused by the COD. For instance in evaporation and UF-RO processes the initial stream was separated in streams with a

higher COD content, and streams with characteristics of water. In the case of anaerobic treatment, the reduced COD content stream and the biogas produced carry the costs to destroy the pollutant potential of raw vinasse, reflected in the exergy destroyed.

Besides of that, thermoeconomics allowed to compare the different costs of treatment processes, resulting the Ultrafiltration and Reverse Osmosis as the treatment with higher economies in terms of costs, based on this, efforts to develop this technology, applied to effluents with higher organic content as vinasse, must be done.

Concentration by evaporation results in high steam needs, and high variable costs, being higher even than capital costs. This process reported a great amount of exergy destroyed being not explained through the reduction of COD as in the Anaerobic Treatment, but for the exergy losses in heat fluxes.

Rational efficiency was not an appropriate index for the assessment of these treatment plants, giving the lowest efficiency for the anaerobic treatment, contrasted with the environmental exergy efficiency, which results in the lowest value for the concentration by evaporation; this is because this index penalized the exergy used as input and destroyed to produce the steam needs for the processes.

Nomenclature

BOD Biochemical Oxygen Demand, mg/L

COD Chemical Oxygen Demand mg/L

TS Total Solids mg/L

x_i Molar fraction

a_i Activity

ε_i Chemical Standard Exergy kJ/kg

h Enthalpy kJ/kg

s Entropy kJ/(kg K)

ce Specific Monetary Exergetic Cost

cm Specific Cost

T temperature, °C

References

[1] UNICA, Sugar Cane Industry Association. Ethanol Production in Brazil. www.unica.com.br Acessed in January 2010.

[2] Elia Neto Andrea. Manual For Water Re-use and Conservation in the Sucroenergetic Industry. Brasilia, ANA 2009. In Portuguese.

[3] Pinto, Claudia Piaza. 1999. “Technology of anaerobic digestion of vinasse and sustainable development.

[4] CETESB, 2006. Standard P4.231, (Vinasse-Criteria and procedure for application in soil for agriculture) . www.cetesb.sp.gov.br

[5] Chavez-Rodriguez M. F.; Ensinas A.V.; Nebra A. S.. Reduction of Water Consumption in the Production of Sugar and Ethanol from Sugar Cane. In: International Congress of Mechanical Engineering, COBEM 2009. Gramado-RS,Brazil.

[6] Ensinas, A. V. 2008. “Thermal Integration and Thermoeconomic Optimization applied to the industrial process of sugar and ethanol production from the sugar cane”. Doctoral Thesis. University of Campinas.

[7] Jørgensen. S.E. Parameters, ecological constraints and exergy. Ecol Model 1992;62:163–70.

[8] Zaleta-Aguilar, A., Ranz, L., Valero, A., 1998. Towards a unified measure of renewable resources availability: the exergy method applied to the water of a river. Energy Conversion Manag. 39, 1911–1917.

[9] Szargut J., Morris D. R., Steward F. R., 1988, “Exergy Analysis of Thermal, Chemical, and Metallurgical Processes”,Hemisphere, New York, USA, 332 p.

[10] Hellstörm, D., 1997. An exergy analysis for a wastewatertreatment plant—an estimation of the consumption of physical resources. Water Environ. Res. 69, 44–51.

[11] Hellstörm, D., 2003. Exergy analysis of nutrient recovery processes. Water Sci. Technol. 48 (1), 27–36.

[12] Chavez-Rodriguez, M. F., Ensinas A.V.,Nebra S.A. . “Allocating monetary costs for sugar cane plants residues based on Exergetic Cost Theory”. Internal Document, Faculty of Mechanical Engineering. State University of Campinas.

[13] Valero, A.,Lozano M.A., Muthos, M.A. General Theory of Exergy Saving. PartI. On the Exergetic Cost. Part II. On the Thermoeconomics. Part III. Exergy Saving and Thermoeconomics. In Computer-Aided

Engineering Energy Systems, vol 3 Second Law Analysis and Modelling, R.A. Gaggioli, ed. ASME, New York,1986.

[14] Lozano, M.A., Valero A. Theory of the Exergetic Cost. Energy, Vol. 1, No.9, pp. 939-960, 1993.

[15] CGEE, Center for Strategic Studies and Management in Science, Technology and Innovation Studies. Sugarcane-Based Bioethanol Energy for Sustainable Development. 271p. 2008.

[16] Rein, Peter. (2007) "Cane Sugar Engineering". Verlag Dr. Albert Bartens KG – Berlin 2007.

[17] Sinnot RK, Coulson & Richardson's Chemical cngineering; Vol. 6: Chemical Engineering Design, 3th edition, Butterworth Heinemann, Oxford, 1999

[18] Eijsberg, Richard. Ethanol Production: The current situation – Technical design and economic evaluation of modern ethanol factory located in Brazil. Master Thesis. Technical University of Delft (TUD), Holland.

[19] Barreda del Campo, E.R.; Araújo da Gama Cerqueira, S.A . and Nebra, S.A . ; "Termoeconomic Analysis of a Cuban Sugar Cane Mill", Energy Conversion & Management, 1998, Vol. 39, Iss 16-18, pp 1773-1780

[20] Corbitt, R.A. Standard handbook of environmental engineering. 1989. McGraw-Hill Inc., New York.

[21] Mohana Sarayu, Acharya Bhavik, Madamwar Datta. Distillery spent wash: Treatment technologies and potential applications. Journal of Hazardous Materials 163 (2009) 12–25.

[22] Metcalf & Eddy, Inc., Wastewater Engineering, treatment, disposal and reuse, 3rd Edition.1991, McGraw-Hill, Inc., New York.

[23] Smith Baez, 2006. Anaerobic Digestion of Vinasse for the Production of Methane in the Sugar Cane Distillery.www.smithbaez.com. Accessed in January 2010.

[24] Granato, Eder Fonzar. Electrical Generation by Anaerobic Digestion of Vinasse. Master Thesis, Universidade Estadual Paulista-UESP, Bauru,SP, Brazil. Abril 2003. In Portuguese.

[25] Collazos, C.J, Cala, J.M. WWTW "Rio Frio", aplication of the UASB technology for the treatment of municipal wastewater in Bucaramanga. Risk Management Office for Prevention and Attention to Disasters.Colombia 1985. http://www.sigpad.gov.co Accessed in January 2010.

[26] Salomon K.R.,Lora E.E.S., Monroy E.F.C. Biogas cost coming from vinasse biodigestion and its utilization. In: 8º Iberoamerican Congress in Mechanical Engineering. Cusco, October 2007. In Portuguese.

[27] Inge AG. 2002. Ultrafiltration Technical Manual. Greifenberg, Germany.www.aquamarine.co.za. Accessed in January 2010.

[28] Crittenden, John; Trussell, Rhodes; Hand, David; Howe, Kerry and Tchobanoglous, George. Water Treatment Principles and Design, Edition 2. John Wiley and Sons. New Jersey. 2005

[29] Murthy Z.V.P e Chaudhari L.B. 2009. Treatment of Distllery Spent Wash by Combined UF and RO Processes Global NEST Journal. http://www.gnest.org. Accessed in August, 2009.

[30] Simões Cristine L. Ribeiro de Sena Maria E., Campos Renato. Economical Analysis about vinasse concentration using reverse osmosis. In: XXIV National Production Engineering Congress. SC, Brazil, 2004.

[31] Mora B. C. H., Oliveira Jr. S., 2004, "Exergy Efficiency as a Measure of the Environmental Impact of Energy Conversion Processes", In: Proceedings of ECOS 2004, Vol.1, Guanajuato, Mexico, pp. 423-431

[32] Mora-Bejarano Carlos Humberto, Oliveira Jr Silvio. Exergoenvironmental Evaluation of Wastewater Treatment Processes.In Proceedings of ECOS 2009, Foz do Iguaçu, Parana, Brazil.

Environomic optimization of SNG production from lignocellulosic biomass using Life Cycle Assessment

Leda Gerber [a], *Martin Gassner* [a] *and Francois Marechal* [a]

[a] *Industrial Energy Systems Laboratory, Ecole Polytechnique Federale de Lausanne, Lausanne, Switzerland*

Abstract: This paper discusses strategies for the environomic optimization of renewable energy conversion technologies that are at the conceptual process design stage and produce multiple energy services, using Life Cycle Assessment (LCA). It is illustrated by an application to the thermo-chemical production of Synthetic Natural Gas (SNG) from lignocellulosic biomass, producing both SNG and electricity. The MJ of wood at the inlet of the process is selected as the functional unit. In a first time, the effects of process scale on environmental impacts are investigated using three different impact assessment methods. This is done by performing multi-objective optimization with the SNG production costs and the cumulated environmental impacts of each impact assessment method as the two objectives. The process size is included in the decision variables. The identified optimal size range varies depending on the impact assessment method. For all methods, the impacts increase with the process size in this optimal range. This is due to a joint effect of the biomass logistics and of the scaling of the gasifier, which leads to an increased resource consumption per unit of volume with an increasing size. In a second time, multi-objective optimization is conducted at fixed process size, using three objectives. The two first objectives are the SNG output and the electricity output, and the third one is either one of the three environmental indicators or the SNG production costs. Results show that the choice of the impact assessment method and of the hypothesis for electricity substitution have an important influence on the results, and favor either the production of SNG or of electricity. In all cases, process efficiency is one of the most important aspects for impact reduction.

Keywords: Life cycle assessment, multi-objective optimization, environomic optimization, biofuels, synthetic natural gas, optimal process scale, process design, renewable energy conversion systems

1. Introduction

Environmental impacts of emerging technologies such as the production of biofuels have become an important concern. To assess these impacts, life cycle assessment (LCA) is a widely used and well-established method, standardized in [1, 2]. Several LCAs surveys have been conducted to highlight the environmental impacts generated by the production of fuels from biomass, like the study of Zah et al [3] on the Swiss level, or the study of von-Blottnitz and Curran [4] on the international level. However, in such studies the life cycle inventory (LCI) is established using average technologies and data from different sources that are not necessarily consistent. With this conventional approach, the changes in process design, the effects of process integration and scaling, and the possible technology evolutions are not considered. Therefore, it is not possible for engineers to integrate LCA at the conceptual process design stage to target simultaneously not only the economic performance but also the environmental impacts. In a former article [5], the authors proposed a methodology to integrate the LCA in a computer aided process design platform that allows for the optimal thermo-economic design of production processes, and demonstrated its application to the design of thermochemical production of synthetic natural gas (SNG) from lignocellulosic biomass, using the model described in Gassner and Marechal [6]. The authors did however not present the application in an optimization framework.

Several authors have conducted studies on the environomic optimization for the identification of optimal process design for energy conversion systems, which refers to the simultaneous optimization of economic, thermodynamic and environmental aspects. Von Spakovsky and Frangopoulos [7] introduced the concept of environomic for energy systems by taking into account not only the total costs as performance indicators, but also the exergy and

Corresponding author: Leda Gerber, Email: leda.gerber@epfl.ch

some environmental aspects, such as direct emissions and resource consumption. Later, Li et al included also environmental criteria in the multi-objective optimization (MOO) framework of district heating systems [8] and of combined cycle power plants including CO2 separation options [9]. Lazzaretto and Toffolo [10] also conducted work on the thermo-environomic optimization and published the results of a MOO considering the three aspects of economy, exergy and environment, calculating the corresponding Pareto surface for a cogeneration plant. However, all of the above studies do not consider the use of LCA, and focus only on the emissions or the resource consumption to represent the indicator of environmental impacts. Regarding the integration of LCA in the optimization procedure, Bernier et al [11] use process integration techniques and thermo-economic analysis in combination with LCA for the design of natural gas combined cycle power plants including CO2 separation options, and perform an environomic optimization. They yet focus only on global warming potential, which is relevant in the case of fossil energy systems, but may not be the case for renewable energy systems.

In the present paper, we propose a strategy for the environomic optimization using LCA applied to the conceptual process design of renewable energy conversion systems producing multiple energy services and integrating the biomass supply chain aspects. It is illustrated by an application to the thermochemical production of SNG from lignocellulosic biomass. The important aspects specific to the application of LCA to process design by multi-objective optimization are as well highlighted.

2. Methodology

The thermo-economic design approach described in [12] is repeated in figure 1. It is based on a computational platform which creates interfaces between different models required for the energy system design. In a first step, the energy flow model based on given operating conditions is calculated to obtain the mass and energy flows in the process, as well as the corresponding thermodynamic states. These results are used to generate the energy integration model, which optimizes the heat recovery and the combined heat and power production in the system by minimizing the total exergy depletion or the operating cost under the heat cascade constraints. The results of the energy-flow and the energy integration models are used to size the equipments, estimate the cost and evaluate the performance of the process configuration, including the environmental impacts calculated by life cycle impact assessment (LCIA). The performance indicators are then further used in a MOO framework, in which an evolutionary genetic algorithm is used.

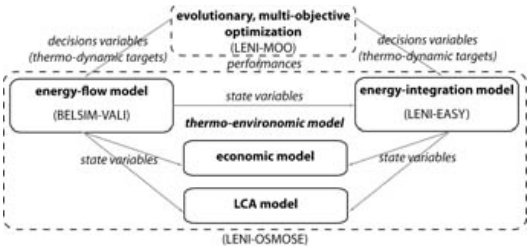

Figure 1: Overall computation sequence including the LCA model

2.1. LCA model

The methodology used to develop the LCA model, based on the ISO-norms [1], and to link the LCI flows with process design and scale is described in [5], and the same application example of the SNG production process from [6] is taken here as an illustrative example.

2.1.1. Goal and scope definition

The goal and scope of the study, and therefore the functional unit (FU) and system boundaries are first defined [1]. From the LCA perspective, the goal and scope of the study can be defined as the identification of the process configurations for SNG production that minimize the environmental impacts generated by the conversion of lignocellulosic biomass into useful energy services. Unlike for the example case presented in [5], which uses the MJ of produced SNG as FU, the MJ of input wood is chosen here. Indeed, the process can, under certain conditions, simultaneously produce both SNG and electricity as energy services, and the present study becomes therefore a resource allocation problem. Moreover, this choice of FU allows to fix as constant the impacts per MJin due to wood production at forest, on which the design of the process has no influence. The impacts per MJin due to wood supply chain from the forest to the plant and back, wood conversion to SNG, and the beneficial impacts due to the substitution of the produced energy services will remain variable.

2.1.2. Life Cycle Inventory

The second step is the establishment of the LCI and its linking with the flows of the thermo-economic model. The LCI database ecoinvent [13] is used to find equivalences for each process flow and equipment. The LCI of the process was established in [5] and is illustrated in Figure 2. Same systems boundaries and LCA model are kept in the present study. To account for the benefit of the produced energy services in the optimization procedure, the electricity produced by the process is assumed to substitute the Swiss mix including the imports, and the SNG is assumed to substitute the extraction and transport of fossil natural gas, as well as to avoid fossil CO_2 emissions from fossil natural gas combustion.

2.1.3. Life Cycle Impact Assessment

The third step is the choice of the impact assessment methods used in the LCIA phase, which are used as indicators for the environmental performance of the system configuration. The general equation to aggregate the emissions and extractions of the LCI in more general indicators by the mean of an impact assessment method is described by Equation 1.

$$\begin{bmatrix} F_{1,1} & \dots & F_{1,n} \\ \dots & \dots & \dots \\ F_{m,1} & \dots & F_{m,n} \end{bmatrix} * \begin{bmatrix} E_1 \\ \dots \\ E_n \end{bmatrix} = \begin{bmatrix} I_1 \\ \dots \\ I_m \end{bmatrix} \quad (1)$$

where, $F_{i,j}$ is the weighting factor to convert the LCI emission i into the impact category j, E_i is the emission or extraction i calculated at the LCI, and I_j is the impact category j of the impact assessment method. Since the weightings vary among the different impact assessment methods, it is necessary here to use more than one of them. Three different impact assessment methods are chosen: Ecoscarcity06 [14], Ecoindicator99-(h,a) [15], and the Global Warming Potential at 100 years (GWP,100a) of the Intergovernmental Panel on Climate Change [16]. The first one is based on the scientifically supported goals of the Swiss environmental policy, the second one uses a damage oriented-approach, and the third one specifically targets the global warming issue using a problem-oriented approach. The different endpoint impact categories of these three methods are summarized in Table 1.

Table 1: Impact assessment methods used

Method	Impact category	Units
Ecoscarcity06	Air emissions	pts
	Surface water emissions	pts
	Groundwater emissions	pts
	Top soil emissions	pts
	Energy resources	pts
	Natural resources	pts
	Deposited waste	pts
Ecoindicator99-(h,a)	Human health	pts
	Ecosystem quality	pts
	Resources	pts
IPCC	Global warming pot., 100a	$kgCO_2$-eq

3. Process optimization

Multi-objective optimization is performed to calculate the trade-offs between the environmental performance indicators and the thermo-economic performance indicators of the system, such as the SNG production costs and the energy efficiency, and to identify the optimal process configurations.

Although the chosen impact assessment methods allow for a detailed analysis of the different impact categories in the case of Ecoscarcity06 and Ecoindicator99-(h,a), it seems more appropriate to use a single synthetic indicator for each impact assessment method representing the overall environmental performance. Indeed, although the use of an evolutionary algorithm allows easily for multi-objective optimization and thus for the use of several environmental indicators at the same time, this makes the results interpretation difficult, especially when the goal is to calculate the trade-offs between environmental objectives and other objectives (economic). The maximal number of objectives is then preferably limited to three, in which at least one is economic, and the single score is therefore chosen as the representative optimization objective with respect to environmental performance. It is calculated by the weighted sum of the normalized impact categories:

$$I_{tot} = \sum_{i=1}^{m} I_i * w_i \quad (2)$$

where w_i is a factor used for the normalization and weighting of the different impact categories.

3.1. Optimal process scale

3.1.1. Optimization strategy

Considering the biomass supply chain, the optimal process scale can be calculated, considering economic and environmental objectives. Indeed, while

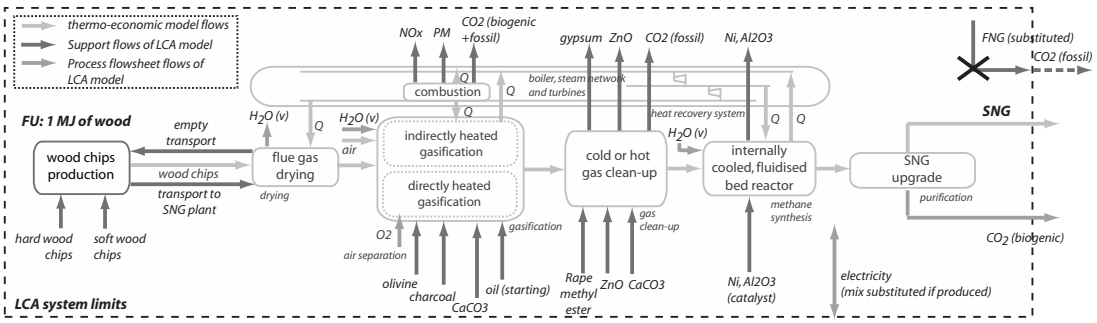

Figure 2: Flows of environmental concern included in the LCI

the impacts due to the biomass logistics should increase with process scale because of increased transportation distance, the impacts due to the process equipment and to the increase in process efficiency should be decreasing with process scale. Therefore, there should be an optimal trade-off with respect to process scale. This is calculated by simultaneously minimizing the single score of a selected impact assessment method, and by minimizing the SNG production costs per MWh.

The chosen technology for this scenario is the indirect gasification at atmospheric pressure using steam drying and membranes for CO_2 removal. This scenario is chosen over the more evolved technologies described in [17], since it uses larger process equipment and more resources during gasification than the other scenarios. The optimization is more likely to identify if the variations in process design allow for a significant impact reduction due to these contributions. For the optimization, the same decision variables and ranges are used than in [17]. The process size is given as an additional decision variable of the optimization problem, and is expressed as the thermal capacity in terms of biomass input, in the range of 5 to 50 MW_{th}. Three optimizations are performed, one for each impact assessment method.

3.1.2. Results

The results obtained by the successive use of the three impact assessment methods show that there is a trade-off between SNG production costs and environmental impacts. This is shown in Figure 3 for the method of Ecoscarcity06, and in Figure 4 for the method of Ecoindicator99-(h,a). Results obtained with the GWP,100a are not displayed here, but show a similar trend to the results obtained with

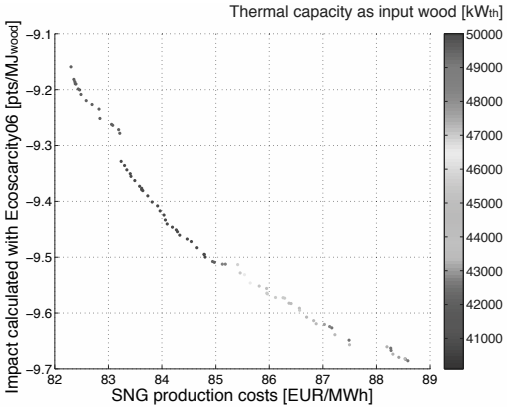

Figure 3: Pareto curve for Ecoscarcity06 and SNG production costs with varying process size

Ecoindicator99-(h,a). However, the range of process sizes concerned by this trade-off varies among both impact assessment methods. While in the case of Ecoindicator99-(h,a), the whole range of process sizes is represented in the optimal process configurations, in the case of Ecoscarcity06, the range of selected sizes considers rather large scales, and goes from 42 to 50 MW_{th}. In both cases, a larger process size within the optimal range tends to lead to higher environmental impacts and lower SNG production costs.

The different results produced by the impact assessment methods are explained by the different weightings attributed in the impact assessment methods, which give more importance to one energy service produced or another. By its high weight attributed to nuclear electricity, the solutions proposed by the Ecoscarcity06 objective favor the production of electricity substituting the Swiss mix. As the coproduced electricity is sold for the market price, this reduces the SNG production costs. Ecoindicator99-

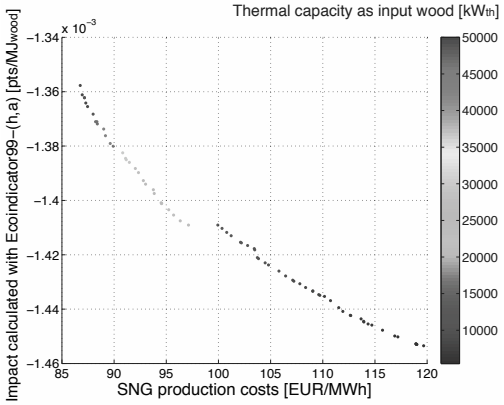

Figure 4: Pareto curve for Ecoindicator99-(h,a) and SNG production costs with varying process size

(h,a) and the GWP,100a give on the contrary a higher weighting to the fossil energy resources emitting high amounts of CO_2. The solutions obtained with this indicator therefore favor the substitution of fossil natural gas with lower level of electricity production.

Small process sizes have the effect to penalize the cogeneration of electricity, which decreases the avoided impacts from electricity substitution and increase the investment costs that are accounted in the SNG production costs. This has the effect that small-scale processes are not considered as optimal. For Ecoindicator99-(h,a) and the GWP,100a , the SNG production is favored over the production of electricity. However, specific SNG production varies to a less extent with process scale, unlike the cogeneration of electricity. This is shown in Table 2 that compares the specific electricity and SNG production per unit of wood for two extreme points of the Pareto curve shown in Figure 4. However, the impacts from wood transport and from specific resource consumption by the gasification are increasing with process scale. For the biomass logistics, this is due to the increase of the average distance from forest to SNG plant. For resource consumption by gasification, it is an effect of the gasifier sizing which affects the consumption of olivine, charcoal, starting oil, solid waste generated and transport of these different materials. The increase of the cumulated impacts of these different processes with process scale is stronger than the benefit from the increased electricity production for Ecoindicator99-(h,a) and GWP,100a, and explains why these impact assessment methods rather favor small-scale processes.

Table 2: Detailed energy service production for two points of the Pareto curve calculated with Ecoindicator99-(h,a)

	Point 1	Point 2
Thermal capacity [MW_{th}]	5	50
SNG [MW/MW_{wood}]	0.704	0.701
Electricity [kW/MW_{wood}]	0.9946	5.606

In the case of Ecoscarcity06, the joint effect of the biomass logistics and of the specific resource consumption by gasification is only visible after the specific electricity production does not increase significantly with size anymore, in the upper range of the potential process sizes.

It should be noted that the impact contribution of the process equipment is decreasing with process scale. However, unlike for the SNG production costs which are affected in an important way by the investment, it does not affect the optimal process configurations with respect to the impact, since this effect is not significant compared to the effect of electricity cogeneration, biomass logistics and specific resource consumption by gasification.

3.2. Environomic design

3.2.1. Optimization strategy

Fixed-scale process environomic optimizations are conducted, with respect to three objectives: the SNG output, the electricity output, and either the SNG production costs or one of the environmental indicators. Using both the SNG output and the electricity output as optimization objectives instead of the single objective of energy efficiency allows one to clearly identify the trade-offs between the environmental impacts and the production of one of these services. A process size of 20 MW_{th} of input wood thermal capacity has been assumed, and the technological scenario considered is the same than for the varying size optimization.

3.2.2. Results

The results for the optimization of SNG production costs, SNG output and electricity output are shown in Figure 5.

A trade-off between the minimization of SNG production costs and electricity and SNG maximization is observed. As it can be seen, minimization of the costs prefers slightly the SNG over the electricity

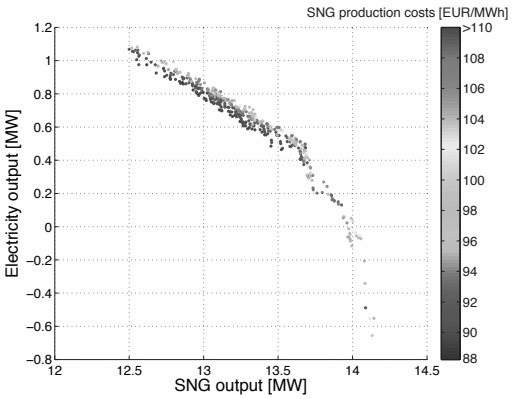

Figure 5: Pareto curve for SNG output, electricity output, and specific SNG production costs

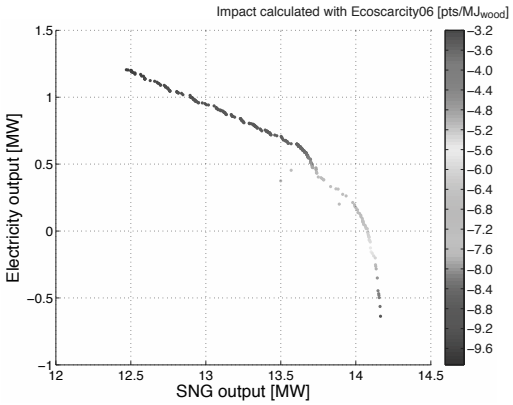

Figure 6: Pareto curve for SNG output, electricity output, and single score of Ecoscarcity06

output, but it could however be shown that there exist solutions with similar SNG production costs for both trends. This indicates also that the selection will be based on other criteria or could be adapted to account for the market prices of energy. Furthermore, the most efficient solutions are not necessarily the most economic ones since the investment cost becomes dominant.

The results for the optimization of environmental impacts, SNG output and electricity output are shown in Figure 6 and 7. Results for the optimization of the GWP,100a are not displayed here, since they show the same trend than the results obtained with Ecoindicator99-(h,a).

The optimization shows different trends in the impact assessment when one use one or the other environmental indicator, Ecoscarcity06 favoring electricity cogeneration while Ecoindicator99-(h,a) favors SNG production. It is shown that increased substitution of a single service is more important than the potential impact reduction of any other contribution. It means that in the case of a similar renewable energy conversion system producing only one single energy service, it might be possible to assimilate the environmental impact reduction to the maximization of the process efficiency. However, the results show clearly that this can not be assumed here, in the case the process produces multiple energy services. Indeed, the optimizer may environmentally favor one or the other energy service which leads to the higher avoided impacts. Here, the results differ completely depending on the used impact assessment method, and this demonstrates the necessity to use different impact assessment methods giving different weightings to the produced energy services, which may lead otherwise to mistaken conclusions and affect the decision making. This further demonstrates the importance of the hypothesis made regarding the electricity mix substitution, which may thus be questioned, since it greatly influences the configurations that will be evaluated. This is an issue that has to be studied in detail in further work.

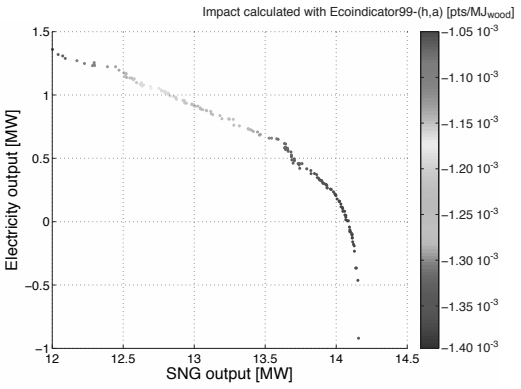

Figure 7: Pareto curve for SNG output, electricity output, and single score of Ecoindicator99-(h,a)

In the case where a trade-off is observed between an economic objective and an environmental objective, like it is the case here for the Ecoscarcity06 and the SNG production costs that do not favor the same energy service, it is possible to conduct further optimizations to calculate the optimal configurations. This is done by a 3-objective optimization with the SNG production costs, the environmental impacts, and the energy efficiency of the process expressed as SNG equivalent, which replaces the two objec-

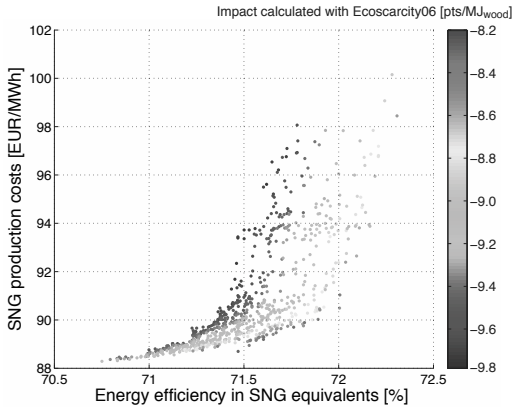

Figure 8: Pareto curve for chemical energy efficiency, specific SNG production costs and single score of Ecoscarcity06

tives of SNG output and electricity output. The results of this optimization are shown in Figure 8. The trade-off between energy efficiency, environmental impact and SNG production costs, are explained by the higher avoided impacts by the electricity production, but which leads to a lower SNG production and overall efficiency.

4. Conclusions

A strategy for the multi-objective environomic optimization of energy conversion systems that produce multiple energy services using LCA has been proposed. It was illustrated by an application to the thermochemical production of SNG from lignocellulosic biomass with power cogeneration.

The optimal process scale has been first investigated with respect to SNG production costs and environmental impacts. In any case, minimization of SNG production costs favors large processes. For the minimization of the environmental impacts, however, the optimal process scale varies depending on the impact assessment method that is used. The impact contributions that increase with process scale are the biomass logistics and the specific resource consumption from gasification. The impact contributions that decrease with process scale are the electricity substitution and the process equipment, though this last one has generally a minor effect. Therefore, if electricity substitution is weighted more strongly, the impact assessment method will favor large processes, since at small scale, electricity cogeneration decreases while SNG production remains constant. If this is not the case, the joint effect of the biomass logistics and of the specific resource consumption from gasification become more important, and small scale processes are favored to minimize the environmental impacts.

For a fixed scale process, the environomic optimization demonstrated that the impact reduction potential lies primarily in the increase in process efficiency. This leads to a higher avoided impact from substitution, before any other design consideration which is likely to reduce the consumption of resources or the size of the equipment. However, in the case of a conversion process producing multiple energy services, it is not possible to replace the objective of impact reduction by the objective of energy efficiency, since environmentally more favorable energy service may depend on the weightings considered in the impact assessment methods. In case where the assumption on the substitution of one or more of the energy services is questionable, like it is the case for the electricity mix, this may influence the process configurations in the final solution.

Nomenclature

FU	Functional Unit
GWP	Global Warming Potential
LCA	Life Cycle Assessment
LCI	Life Cycle Inventory
LCIA	Life Cycle Impact Assessment
MOO	Multi-Objective Optimization
SNG	Synthetic Natural Gas

References

[1] ISO. Environmental management - Life Cycle Assessment - Principles and framework. International Standard, ISO 14'040., 2006.

[2] ISO. Environmental management - Life Cycle Assessment - Requirements and guidelines. International Standard, ISO 14'044., 2006.

[3] R. Zah et al. Oekobilanz von Energieprodukten: okologisches Bewertung von Biotreibstoffen. Technical report, Swiss Federal Laboratories for Materials Testing and Research (Empa), St. Gallen, Switzerland, 2007.

[4] H. von Blottnitz and M.A. Curran. A review of assessments conducted on bio-ethanol as a

transportation fuel from a net energy, greenhouse gas, and environmental life cycle perspective. *Journal of Cleaner Production*, 15: 607–619, 2007.

[5] L. Gerber et al. Integration of LCA in a thermo-economic model for multi-objective process optimization of SNG production from woody biomass. In J. Jezowski and J. Thullie, editors, *Proc. 19th European symposium on CAPE*, volume 1, pages 1405–1410, Amsterdam, 2009. Elsevier.

[6] M. Gassner and F. Marechal. Thermo-economic process model for thermochemical production of Synthetic Natural Gas (SNG) from lignocellulosic biomass. *Biomass and Bioenergy*, 33:1587–1604, 2009.

[7] M.R. Von Spakovsky and C.A. Frangopoulos. A global environomic approach for energy systems analysis and optimization (Part II). In *Proc. Energy Systems and Ecology 93*, pages 133–144, 1993.

[8] H. Li et al. Green heating system: characteristics and illustration with multi-criteria optimization of an integrated energy system. *Energy*, 29:225–244, 2004.

[9] H. Li et al. Multi-objective optimization of an advanced combined cycle power plant including CO2 separation systems. *Energy*, 31: 3117–3134, 2006.

[10] A. Lazzaretto and A. Toffolo. Energy, economy and environment as objectives in multi-criterion optimization of thermal systems design. *Energy*, 29:1139–1157, 2004.

[11] E. Bernier et al. Multi-objective design optimization of a natural gas-combined cycle with carbon dioxide capture in a life cycle perspective. *Energy*, 35:1121–1128, 2009.

[12] M. Gassner and F. Marechal. Methodology for the optimal thermo-economic, multi-objective design of thermochemical fuel production from biomass. *Computers & Chemical Engineering*, 33:769–781, 2009.

[13] R. Frischknecht et al. The ecoinvent database: Overview and methodological framework. *International Journal of Life Cycle Assessment*, 10:3–9, 2005.

[14] G. Brand et al. Bewertung in Oekobilanzen mit der Methode des oekologischen Knappheit Oekofaktoren 1997. Technical report, Swiss Federal Office of Environment, Bern, Switzerland, 1998.

[15] M. Goedkoop and R. Spriensma. The Eco-Indicator 99: A damage oriented method for life cycle impact assessment. Technical report, PRe Consultants, Amersfoort, The Netherlands, 2000.

[16] Intergovernmental Panel on Climate Change. IPCC(2001) Climate Change 2001: The Scientific Basis. In: Third Assessment Report of the Intergovernmental Panel on Climate Change (2001). Technical report, IPCC, 2001.

[17] M. Gassner. *Process design methodology for thermochemical production of fuels from biomass. Application to the production of Synthetic Natural Gas from lignocellulosic resources.* Ph.D. Thesis, Ecole Polytechnique Federale de Lausanne, Lausanne, Switzerland, 2010.

Energetic and exergetic analysis of energy generation system with integrated gasification of RDF

S. Karellas[a], K. D. Panopoulos[b] , G. Panousis[a] , E. Kakaras[a], I. Boukis[c]

[a] *Laboratory of Steam Boilers and Thermal Plants, National Technical University of Athens, Heroon Polytechniou 9, 15780 Athens, Greece*

[b] *Institute for Solid Fuels Technology and Applications, Centre for Research and Technology Hellas, 4th km N.R. Ptolemais-Kozani, P.O. Box 95, 50200 Ptolemais, Greece*

[c] *HELECTOR S.A. 25 Ermou str., N. Kifissia, Greece*

Abstract: The efficient use of solid recovered fuels (SRF) or refuse-derived fuels (RDF) produced from mechanical and biological treatment of municipal solid wastes (MSW) is a very promising approach concerning their treatment. Gasification is advantageous in comparison with direct combustion, as gaseous fuel can be used in high efficient systems (Gas engines, Gas turbines) or even in conventional generation systems (Steam boilers) with easier gas cleaning effort since only the fuel volume has to be cleaned and not the entire flue gas volume.

This paper presents the results from simulations of energy generation system based on Rankine cycle under 1MWe, integrated to an autothermal , air blown gasifier that utilizes the solid recover fuel under the registered sign Stabilat®. This recovered fuel is formed by the remaining organic waste fraction of MSW treatment and its calorific value is 15-18 MJ/kg. The simulation of the gasification process was based on a chemical equilibrium model with corrections for methane formation. Finally an exergetic analysis of the above system was implemented in order to be calculated the overall exergetic efficiency of the process as well as the irreversibilities in systems elements.

Keywords: RDF, autothermal gasification, Rankine cycle.

1. Introduction

Nowadays there is an increasing trend to treat efficiently municipal solid wastes (MSW). Solid fuels that derived from MSW treatment can be used for energy generation through their combustion with electrical efficiencies around 20%. [1,2]. An alternative technique is the gasification where the gaseous fuel can be cleaned before its combustion, thus can be used in high efficiency generation systems. The cost of cleaning equipment in that case is significantly lower as only the gaseous fuel has to be treated rather than the exhaust flue gas [2]. Gas cleaning system depends on the application of the gas [3]. Engines and gas turbines requirements for power generation are highly demanding with upper limits on tars, alkalis, ammonia and particulates.

This work presents an investigation on the combination of an air blown gasifier with CHP system less than 1 MW_{el}, based on Rankine cycle. The autothermal gasification is operated in temperature around 850 °C. The analysis is performed in process simulation software for all the integrated unit operations. Finally an exergetic analysis was implemented in order to calculate the exergetic efficiency of all processes as well as the exergy destruction in system's units.

2. System description and modeling aspects

The selected configuration for a combined heat and power system is shown in Figure 1. An air blown autothermal gasifier produces the gaseous fuel that is utilized in a Rankine cycle. The other components apart from gasifier that comprise the system are the steam boiler, heat exchangers (HX1, HX2) for gasification air and feed water preheating, two small power output steam turbines in tandem configuration, condenser, feed pump, condensate pump and a heat consumer heat exchanger. The total air stream, that provides air for the Stabilat gasification and for syngas combustion is preheated up to 100 °C in HX2 from

*Corresponding Author: Sotirios Karellas, e-mail: sotokar@mail.ntua.gr

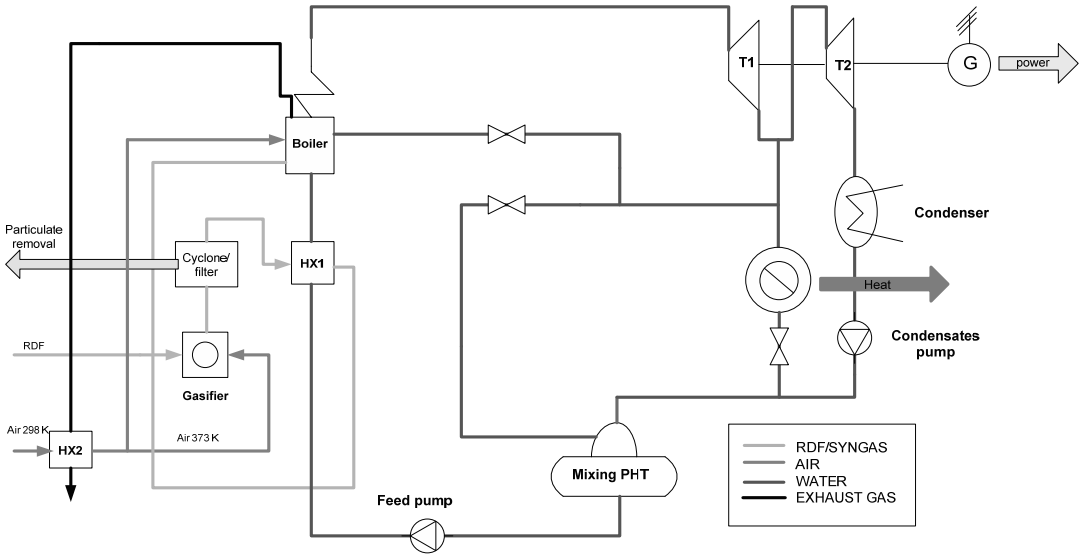

Figure 1. Energy generation system using extraction steam turbine

the exhaust gas stream exiting the boiler. Syngas leaves gasifier in high temperature of 850 °C. Part of the syngas sensible heat is used to preheat feed water in HX 1 before is fed into the boiler. Syngas exits HX 1 in temperature around 450 °C to avoid tar condensation [4].

3. Exergetic analysis

Exergy is the maximum work that can be produced when a heat or material stream is brought to equilibrium in relation to a reference environment, which is kept at reference conditions (p_o=1.013 bar ,T_o=298 K) and consisting from reference components. The exergy of a material stream is given as the sum of molar physical and chemical exergies:

$$E = N\left(\varepsilon_{ph} + \varepsilon_{ch}\right)\ (\mathrm{W}) \qquad (1)$$

where N $(\mathrm{mol \cdot s^{-1}})$ is the molar flow. Potential, kinetic exergies etc were neglected in this work. The molar physical exergy of a material stream is calculated using the data on physical properties, temperature (T), pressure (p), enthalpy (h), entropy (s) and its properties in the reference environmental conditions using the following expression:

$$\varepsilon_{ph} = \left(h - h_o\right) - T_o\left(s - s_o\right)\left(\mathrm{J \cdot mol^{-1}}\right) \qquad (2)$$

Molar flows, molar fractions, and molar enthalpy and entropy were calculated for its stream from the simulation program IPSEpro. Chemical exergy is the exergy component associated with the departure of the chemical composition of a system from that of the environment. The molar chemical exergy is obtained when the components of the energy carrier are first converted to reference compounds and then diffuse into the environment, which is in reference state. For a gaseous stream, the molar chemical exergy is given by the following expression:

$$\varepsilon_{ch,gas} = \sum x_i \cdot e_i^{ch} + R \cdot \sum x_i \cdot \ln x_i \ \left(\mathrm{J \cdot mol^{-1}}\right) \qquad (3)$$

where x_i is the mole fraction of stream's compounds and e_i^{ch} $(\mathrm{J \cdot mol^{-1}})$ the standard chemical exergy for each compound i ,assuming a reference atmospheric composition given by Kotas [5] and R is the ideal gas constant (8314 $\mathrm{J \cdot mol^{-1} \cdot K}$). The chemical exergy of RDF was calculated with the help of the statistical β correlation, proposed by Szargut [6]:

$$E_{ch,RDF} = \left(LHV_{RDF} + w \cdot h_{fg}\right) \cdot \beta + \left(\varepsilon_s + H_{us}\right) \cdot S \quad (4)$$

Table 1 presents the ultimate analysis of RDF.

Table 1. RDF composition

RDF data	
Ultimate analysis (% ww, dry basis)	
C	42.81
H	5.54
N	1.30
O	21.54
S	0.29
Cl	1.12
Ash	27.40
Moisture	15.20

RDF heating value is 15 MJ/kg in wet basis. The exergy of a heat stream is given with the help of Carnot factor:

$$E_T{}^{Q} = Q \cdot \left(1 - {}^{T_o}\!/_{T}\right) \quad (5)$$

where T is the temperature at which Q is available. Finally the exergy rate of a power output E^W, equals the power itself. Exergy losses due to mechanical and electrical inefficiencies were taken into account but heat losses of the different units that comprise the systems were neglected. Both exergy losses and exergy destruction have been summed under the term of "irreversibilities", *IR*. In a control volume the exergy balance can be expressed as:

$$\sum E_{i,in} = \sum E_{i,out} + \sum E_{losses} + IR \quad (\mathrm{W}) \quad (6)$$

Exergetic efficiency is defined as:

$$\eta_{ex} = \frac{\sum E_{i,out}}{\sum E_{i,in}} \quad (7)$$

$\sum E_{i,\mathrm{in}}$ and $\sum E_{i,\mathrm{out}}$ are defined properly for each system to describe exactly the amount of exergy that the system consume to produce useful products [7].

4. Modeling of CHP

4.1 Modeling of RDF air gasification

Gasification can be described from the general gasification equation:

$$CH_XO_YN_Z + wH_2O + m\left(O_2 + 3.76N_2\right) \rightarrow n_1H_2 + n_2CO + n_3CO_2 + n_4H_2O + n_5CH_4 + \left(\frac{z}{2} + 3.76m\right)N_2$$

Gibbs free energy minimization method for the C-H-O blend of the RDF and the oxidant mixture was applied for predicting the thermodynamic equilibrium of the product gas major components: H_2, CO, CH_4, H_2O, N_2, as well as char, which was considered as solid graphite (Cs). The thermodynamic prediction underestimates methane and unreacted char amounts in RDF gasification [8]. Therefore non equilibrium correlations were taken into account to bring these products closer to experimental values. The unreacted char was assumed to consist only of carbon and to be 1% of the total fuel carbon content. This amount did not participate in thermodynamic equilibrium calculations. Similarly the CH_4 content (mainly deriving from the decomposition/pyrolysis of RDF) was assumed to reach 3% v/v in the final product gas.

The gasifier operating temperature is determined from the oxidizing agent throughput. Gasifier heat losses were assumed to be 3% of the total gasifier's LHV input. The air ratio (λ) is expressed considering the amount of the required air for RDF stoichiometric combustion :

$$\lambda = \frac{\text{Air input } \left(\mathrm{kg \cdot s^{-1}}\right)}{\text{Stoichiometric air } \left(\mathrm{kg \cdot s^{-1}}\right)} \quad (8)$$

The gasification cold gas efficiency neglects the sensible heat of the product gas and char produced and is defined as

$$\eta_{cg} = \frac{\dot{m}_G \cdot LHV_G}{\dot{m}_{RDF} \cdot LHV_{RDF}} \quad (9)$$

Based on the general definition of the degree of perfection for a process by Szargut [6], the exergetic efficiency of air gasification is

$$\eta_{ex,gas} = \frac{E_{gas} + E_{char}}{E_{RDF} + E^{Q}{}_{T} + E_{air}} \quad (10)$$

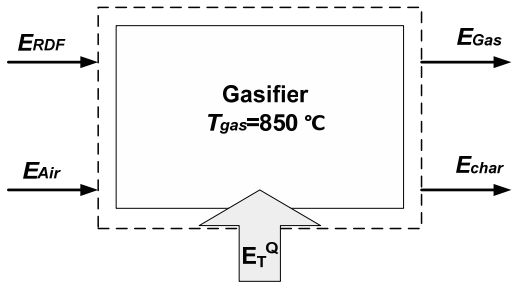

Figure 2. Gasifier control volume for exergy analysis

Here, E_{gas} includes the sensible heat of the product gas. The gasifier operates autothermally, therefore $E_T{}^{Q}$ is zero. Since in this application, the physical

and chemical exergy of char is of no use, is not included in the above equation.

4.2 Modeling of Rankine-Cycle

The electrical power that is generated is calculated from :

$$P_{el} = \eta_m \cdot \eta_{el} \left(\dot{m}_{T1} \cdot \left(h_{T1in} - h_{T1out} \right) + \dot{m}_{T2} \cdot \left(h_{T2in} - h_{T2out} \right) \right) \quad (11)$$

Net electrical power occurs when the electrical consumptions of pumps motors are subtracted from the total power. Cycle's efficiency is given from :

$$\eta_{cycle} = \frac{P_{net} + Q_H}{\dot{m}_G \cdot LHV_G} \quad (12)$$

Heat generation was modeled by a water current heated up to 70 °C. Feedstock consumption was chosen to be 760 kg/hr, which is a real plant production. The main parameters that describe system operation are shown in Table 2.

Table 2. System modelling parameters

Heat exchangers			
	Hot stream	Cold stream	
	In/out (°C)	In/out (°C)	
HX 1	850/450	102.9/190.7	
HX 2	175.8/115.6	25/100	
Turbines			
	η_{is} %	In (°C/bar)	Out(°C/bar)
	70	300/30	60/0.2
Boiler			
	η_b %	pressure drop (bar)	
	90	5	
Generator			
	η_{el} %		
	95		

5. Results and discussion

5.1 Gasifier analysis results

In Fig.3, it can be seen that autothermal operation for a specific temperature (850 °C), taking into account heat losses 3% of fuel LHV, is achieved for λ>0.38. In this λ area, it is ensured maximum carbon conversion (Fig.3 c). Moreover a parametric analysis of the gasification process for different operating temperatures and air preheating temperatures was done, being always in autothermal operation. Product gas composition is shown in Fig.4. Fig.5 shows the calculated air ratio λ and the cold gas efficiency of the air gasification vs. gasification temperatures for different air preheating temperatures. It can be seen that λ increases for higher gasification temperatures as greater amount of air is needed to rise gasifier temperature. For higher air preheating temperature gasifier requires less air to achieve its operating temperature, thus λ is lower than before. Fig.6 shows exergetic efficiency the air gasification process vs. gasification temperature. Increasing the gasifier's operating temperature, therefore λ, has a negative effect on the exergetic

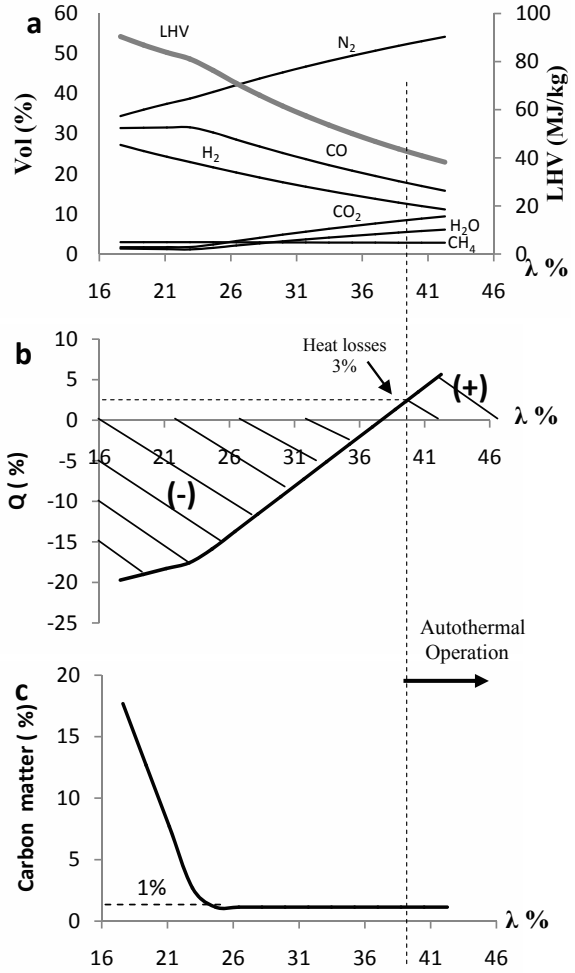

Figure 3. a) Product gas composition and LHV, b) Process excess/shortage heat as percentage of LHV, c) Percentage of total fuel carbon that remains in ash vs. Air ratio.

efficiency because major chemical exergy carrier components i.e. combustible products, are minimized. Moreover higher air preheating temperature favours exergetic efficiency.

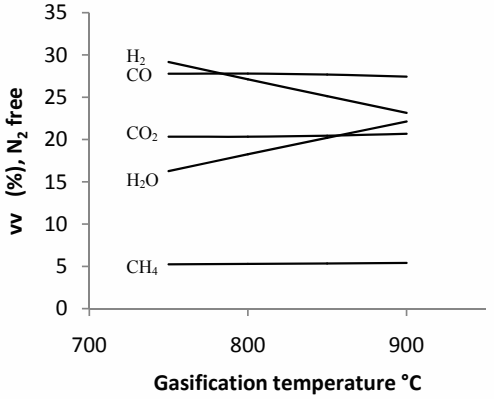

Figure 4. Syngas composition (N_2 free) vs. gasification temperature

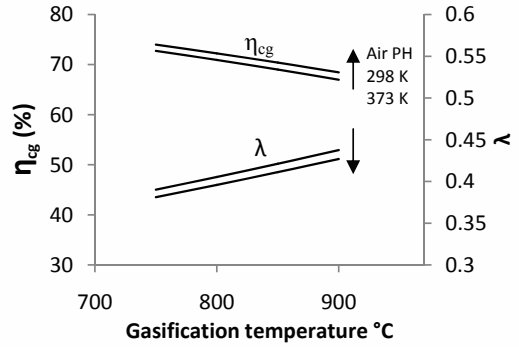

Figure 5. Gasifier cold gas efficiency and air ratio λ. for different air preheating temperatures vs. gasification temperature

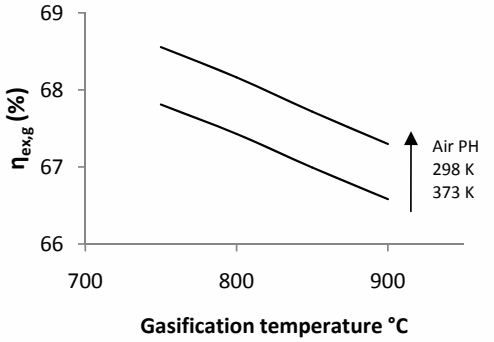

Figure 6. Gasifier exergetic efficiency vs. gasification temperature.

5.2 Rankine cycle analysis results

For the system simulation it was chosen gasification temperature 850 °C and air preheating temperature 100 °C, while 1% carbon loss was assumed. Choosing these parameters air ratio λ is determined, thus the gasification air mass flow. Product gas composition and its lower heating value are shown in Table 3.

Table 3. Product gas composition

Product gas composition (vol%)	
H_2	12.5
CO	13.8
CO_2	10.2
CH_4	2.7
H_2O	10.1
N_2	50.2
LHV (MJ/kg)	3.66

Table 4. System exergy balance and components exergetic efficiencies

	ζ %	IR/E_{RDF}(%)
Gasifier	67.71	31.718
Boiler	37.90	37.110
HX 1	45.06	3.360
HX 2	48.17	0.380
Turbine 1	72.28	2.660
Turbine 2	68.66	2.750
Condenser	23.48	3.810
Condensates pump	57.88	0.002
Feed pump	60.48	0.060
Mixing PHT	70.47	0.270
Consumers HX	39.42	0.590
Valves	-	0.680
Exergy losses		
Flue gas		2.750
Cooling water		1.170
Useful products		
Power E^P		12.31
Heat E_T^Q		0.38
Total		100

5.3 CHP system analysis results

The electrical efficiency of the system is:

$$n_{el} = \frac{P_G - P_{pumps}}{\dot{m}_{RDF} \cdot LHV_{RDF}} \quad (13)$$

while the power and thermal energetic efficiency of the system is

$$n_{CHP} = \frac{P_G - P_{pumps} + Q_{useful}}{\dot{m}_{RDF} \cdot LHV_{RDF}} \quad (14)$$

The CHP system exergetic efficiency is

$$n_{ex,CHP} = \frac{E^{P_G} - E^{P_{pumps}} + E^{Q}{}_{useful}}{E_{RDF} + E_{air}} \quad (15)$$

Overall CHP system performance is summarized in Table 5.

Table 5. Overall system results

CHP system results		
RDF throughput	760	kg/hr
Energetic/exergetic	3150/3555	kW
RDF throughput		
Total air throughput	4104	kg/hr
Net power	440	kW
Useful heat	130	kW
η_{CHP}	18.1	%
$\eta_{ex,CHP}$	12.6	%

6. Conclusions

In this work the combination of solid recovered fuel air gasification with a rankine cycle was evaluated. The gasification process was studied for different gasification temperatures and different air preheating temperatures. Higher air preheating temperatures increase gasifier cold gas efficiency as well as its exergetic efficiency. Regarding the whole CHP system, the total energetic efficiency is considerably low as in that scale of power generation there are limitations concerning steam maximum pressure and temperature as well as turbines isentropic efficiencies. Moreover total exergetic efficiency is low. The results showed that the gasifier and the boiler of the system have the highest irreversibilities. The gasification process cannot be improved significantly concerning its exergy destruction. Therefore, the boiler is the system's component that is mainly responsible for the low total exergetic efficiency. Such a system may seem inappropriate for utilizing this recovered fuel, but an important factor is that requires a less demanding gas cleaning system. In a future work this system should be evaluated through economic and exergoeconomic analysis and be compared with other possible configurations taking into account the appropriate gas cleaning system.

Nomenclature

E	Total exergy of material stream (W)
E_T^Q	Exergy of heat stream available in temperature T (W)
E^W	Work of power output (W)
h	Enthalpy of stream (J kg^{-1})
h_o	Standard enthalpy at environmental conditions (J kg^{-1})
H_{us}	Sulphur lower heating value (9259 kJ/kg)
IR	Irreversibilities of process (W)
LHV	Fuel lower heating value (kJ/kg)
m	Mass flow of a stream (kg s^{-1})
N	Mole flow rate (mole s^{-1})
P_G	Power from generator (W)
Q	Heat stream (W)
R	Universal gas constant (8.314 J kg^{-1} K^{-1})
s	Entropy of stream
s_o	Standard entropy at environmental conditions
T	Temperature (K)
T_o	Standard temperature (K)
x_i	Mole fraction of component i

Subscripts/superscripts

cg	Cold gas
CHP	Combined heat and power system
el	Electrical
ex	Exergetic
g	Gasification
G	Product gas
m	Mechanical
RDF	Fuel feedstock
T1	Turbine 1
T2	Turbine 2
IN	Input
OUT	Output

Greek symbols

β	Statistical correlation for solid fuel exergy calculation
ε_{ph}	Specific physical exergy of material stream (J ·mol^{-1})
ε_{ch}	Specific chemical exergy of material stream (J· mol^{-1})

ε_S Chemical exergy of sulphur (18676 kJ/kg)

λ Air ratio

η Efficiency

References

[1] Granatstein. D, 2003, Case Study on Waste-Fuelled Gasification Project Greve in Chianti, Italy, Natural Recourses Canada/CANMET Energy Technology Centre (CETC).

[2] Morris. M, Waldheim. L, 1998, Energy Recovery from Solid Waste Fuels Using Advanced Gasification Technology, Waste management 18, 557-564.

[3] Waldheim. L, 1992, Heat and Power Production via Gasification in the Range 5-50 MWe. Advances in Thermochemical Biomass conversion, Interlaken, Switzerland.

[4] Karellas. S, Online analysis of the composition of biogenous gases and their effect on microturbine and fuel cell systems, VDI Verlag GmbH, Düsseldorf (2006).

[5] Kotas. T.J, 1995, *The Exergy Method of Thermal Plant Analysis*. Malabar (FL): Krieger Publishing Company.

[6] Szargut J, Morris. D, Steward. F, 1988, *Exergy Analysis of Thermal, Chemical, and Metallurgical Processes*. Taylor & Francis Inc.

[7] Bejan. A, Tsatsaronis. G, Moran. M, 1996, *Thermal Design and Optimization* , John Wiley & Sons, Inc

[8] Hingman. C, Van Der Burgt. M, 2003, *Gasification*, Gulf Publishing.

Operability Challenges of Renewable Energy Utilisation

Petar Sabev Varbanov, Jiří Jaromír Klemeš, Zsófia Fodor

EC Marie Curie Chair (EXC), Centre for Process Integration and Intensification - CPI², Research Institute for Chemical and Process Engineering, Faculty of IT, University of Pannonia, Hungary

Abstract: The majority of the energy systems are dominated by fossil energy sources. They are equipped with internal combustion engines, boilers, steam turbines, and water heaters. The challenge to increase the share of renewables in the primary energy mix could be met by integrating solar, wind, biomass and waste with the fossil fuels. This work analyses some challenges imposed by the integration of renewable sources, with their variable availability and provides an overview of the techniques to measure and quantify the operability of the energy systems employing renewables.

Keywords: Heat Exchanger Networks, Process integration, Renewables, Varying supply & demand.

1. Introduction

Renewable resources are usually distributed over an area. Their availability varies with time and location mainly due to changing weather and geographic conditions. The energy demands (heating, cooling and power) vary with time of the day and period of the year. Some renewable supplies are changing in regular time intervals – as day and night, summer and winter for solar energy. However, the availability of the wind-generated energy is less predictable. Therefore, the design of energy conversion systems using renewable resources is more complex compared with fossil fuels due to the need to account for the variability on both the demand and supply sides.

2. Demand and supply properties

Fluctuating energy demands require specific approach and have been studied by various researchers. As en example can serve a study investigating the variation of energy consumption for residential heating, electricity and hot water [1].

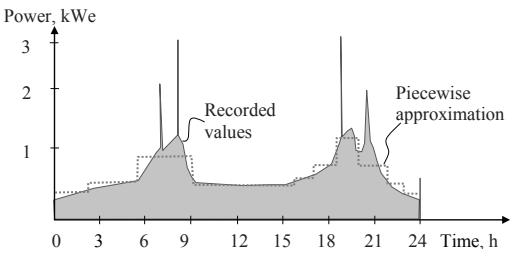

Fig. 1. Typical residential electricity demands for a 24-hour cycle after [1]

The results show two types of trends – hourly variations during each day (Fig. 1) and seasonal variations during the year.

The availability of renewable energy sources varies too. For instance, biomass supply varies by year seasons, while for wind and solar the variations are faster – in hours and minutes. These variations present an integration challenge with diverse time horizons of the changes. The main issues are the system operability and the appropriate performance targeting procedures. Targeting has been investigated and some results have been published [2]. The operability challenges imposed by the variations in the renewables supply and the demands also need attention. As energy efficiency implementation deals with heat exchange and recovery, the synthesis and operational analysis of Heat Exchanger Networks (HENs) is of key importance. HENs have been subject to intensive research since the 1970s [3], and new refinements are regularly published. One example is the contribution by Gassner and Maréchal [4] employing HENs for improving the performance of fuel production from biomass.

The focus of the current work is on the operability of (HENs) to enable the use of these analyses for renewable integration.

For thermal energy demands mainly the load varies. Usually the required heating or cooling temperatures remain the same and are determined by considerations such as human comfort – e.g. room temperature 20-25 °C, or quality of an activity – e.g. 40-45 °C for domestic hot water.

Corresponding Author: Petar Sabev Varbanov, Email: varbanov@cpi.uni-pannon.hu

The variations in the parameters of the renewable energy supply usually concern both the loads and the temperatures. E.g. for solar collectors it depends on the weather and time of the day. As a consequence both the load and the temperature of the captured solar heat could vary.

3. Operability of HENs

The operability of a process system includes the flexible operation and system control properties.

3.1. Basic definitions

Parameter variations can be classified into long-term (gradual) – changing the steady states, and transient (true dynamic) process conditions. A HEN is feasible if it satisfies the process heating and the cooling demands and complies with the minimum allowed temperature difference (ΔT_{min}).

A HEN is flexible if it remains steady-state feasible a given set of desired operating points. A HEN is termed controllable [5, 6, 7] if its topology and heat transfer equipment allow the selection of an adequate control configuration capable of satisfying control objectives. A HEN is operable if it is simultaneously flexible, controllable, and with sufficiently high availability.

3.2. Flexibility analysis of HENs

3.2.1. Representing flexibility

The set of operating points, over which the network has to be flexible, can be defined in two ways. One is a list of discrete operating points, if the operating conditions can be predicted or approximated with some certainty [8]. Another way is to define a nominal operating point and add the variation intervals of each disturbance – process stream flow-rates and their inlet temperatures [9].

Flexible operation can be ensured by specifying the operating points and feasibility constraints. This is useful for applying cost or profit as the objective function. Another approach is to maximise the operability or multi-criteria optimisation using quantitative flexibility indicators.

An important flexibility indicator is the Flexibility Index (FI) [11]. Another one, specific for HENs is the Resilience Index (RI) [12]. Both provide approximate measures of the size of the feasibility region around the nominal operating point.

The FI is defined as the largest scaled range of variation of uncertain parameters, normalised to a scale factor (usually the expected parameter variation range) and varying in the interval [0...1]. If the inlet temperature of a hot solar stream and its load are allowed to vary, the resulting network may define a feasible space as in Fig. 2.

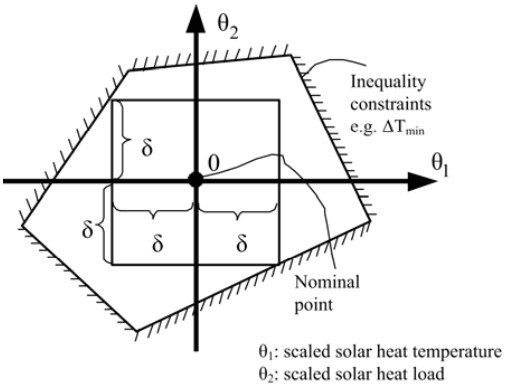

Fig. 2. Geometrical Interpretation of Flexibility Index

The RI had been defined specifically for HENs. It is based on the scaled disturbance loads for the network in question [12]. The variations of the process stream inlet or outlet temperatures result in disturbance loads as follows:

$$L_i = w_i \cdot \Delta T_i \tag{1}$$

where "**i**" is the current process stream, "$\mathbf{w_i}$" is the heat capacity flow-rate and "$\mathbf{\Delta T_i}$" the temperature deviation from the nominal. The disturbance loads are further scaled to represent values between -1, 0 and +1:

$$l_i = \frac{L_i}{L^*}; \quad L^* = \max_i \left(L_i\right) \tag{2}$$

The RI is defined as the largest scaled disturbance load independent of its direction, which the HEN is able to tolerate remaining feasible. Geometrically (Fig. 3), the disturbance space is searched starting from the nominal operating point, along the axes defining the disturbances. The points of intersection of these axes with the boundaries of the feasibility region are identified. The smallest one among them is the RI of the network.

The FI is more general, since it is defined for any process system. It is also clearer and easier to apply. However, its computation is generally complex. The RI is less versatile, but is easier to compute.

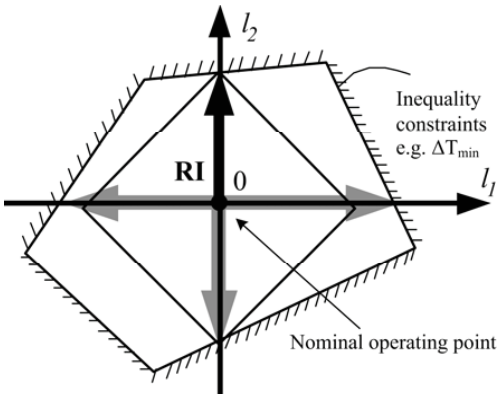

Fig. 3. Geometrical Interpretation of Resilience Index

The flexibility indicators can be used to perform different tasks – including assessing the flexibility of existing HENs, synthesis of new flexible HENs, or retrofit of HENs accounting for flexibility.

3.2.2. Synthesis of flexible HENs

There are several possible approaches to the synthesis of flexible HENs.

Multiperiod operation. A list of desired discrete operating points is assigned to periods in an operating cycle of e.g. one year. The procedure then synthesises a HEN with the minimum total cost, which is steady-state feasible for all operating points. However, processes rarely operate at fixed points, and it is difficult to predict them precisely. The computational difficulty imposed by the optimisation of the resulting superstructures is significant, combining combinatorial complexity and non-convexity.

Ranges of variation. Specifying uncertainty ranges allows more realistic representation of the uncertainty of the parameter variations. This makes it impossible to estimate the energy-capital cost trade-offs, but it is still possible to synthesise minimum utility use/cost HENs.

A hybrid method is also possible [10]. It has been developed by using Pinch methodology [13]. Initially a HEN for a specified set of operating points ensuring minimum utility cost and minimum number of units is obtained. Then the HEN's FI is compared with the variation ranges on the uncertain temperatures and flowrates. If the network meets the flexibility target, the procedure is completed. If not, the operating point limiting the flexibility is added to the list of operating points and the procedure is repeated.

The synthesis of flexible HENs using directly the specified ranges of variation for the uncertain parameters is tackled in several stages [9]:

(a) Computation of the various Pinch [13] locations and utility targets, accounting for the variations in the parameter values.
(b) Partitioning the overall temperature span of the process streams into blocks.
(c) Synthesis of sub-networks within each block, featuring a minimum number of HE matches, using the superstructure approach.
(d) The resulting HE matches are further assigned to actual exchangers and sized.

A methodology following this approach has been developed in three papers [9,14,15]. They introduce the concepts of permanent and transient process streams. Heat cascades comprising permanent and transient stream components are constructed, following a hierarchy of three heat recovery priorities:

(i) Permanent-permanent heat recovery target. Maximise the heat exchanged between permanent hot and permanent cold streams.

(ii) Permanent-transient heat recovery target. Maximise both the heat transferred from transient hot streams to permanent cold streams and the heat transferred from permanent hot streams to transient cold streams.

(iii) Transient-transient heat recovery target. Maximise the heat exchanged between transient hot and transient cold streams.

This defines the sub-networks for the heat recovery system synthesis, based on the concept of the dominant pinch points. Next the synthesis procedure constructs a superstructure for every sub-network and optimises the combination of these to find a topology with minimum number of units and maximum energy recovery. The matches in each sub-network are sized based on the worst operating conditions within the range of variation of the uncertain parameters.

3.2.3. Structural flexibility analysis of HENs

Another analysis of HEN flexibility has been developed by Calandranis [5]. It is based on the representation of parameter variations by "disturbance loads". The procedure attempts to eliminate the latter by shifting them through paths in the HEN to existing heaters or coolers. Such shifts alter the loads and the temperature driving forces of the process to process heat exchangers

involved in the shift paths. The advantage is the uniform representation of temperature and flow-rate variations. An important requirement is that the disturbance load shift paths cannot cross a pinch in the network, resulting from a stipulation for maximum energy recovery. The non-convexity associated with pinch jumps is considered from a point of the structure of the existing network. The procedure assumes that the pinch jump is discovered and defines several theorems stating the conditions under which the HEN becomes infeasible and would regain or not feasibility.

This flexibility analysis can be applied to synthesis or retrofit of HENs. One option is the procedure for evolutionary HEN synthesis under flexibility requirements [5]:

- Obtain or synthesize an initial HEN topology, with maximum energy recovery for the nominal operating conditions. The heat integration can be used for this task [13].
- Impose the required parameter variations and generate the necessary disturbance loads.
- Analyse the network for feasibility by trying to shift the disturbance loads to existing utility exchangers. If the network is feasible the design is finished. Otherwise, structural modifications are necessary.
- The topology modifications suggested include mainly compliance with the pinch design rules [13] for the so called 'essential matches'. They ensure feasibility of the HEs around the pinch points existing at nominal conditions as well as at any other pinch points taking place by continuous pinch displacement or pinch jumps.

3.3. Controllability of HENs

Georgiou and Floudas [16] use the generic rank of the system's structural matrix for analysis and synthesis of feasible control structures for large-scale systems. The proposed procedures use mixed-integer linear programming (MILP) problems.

Daoutidis and Kravaris [17] proposed the relative order as a main analysis tool for evaluation of alternative control configurations. Based on graph theory, they have shown that the calculation of the relative orders of the system outputs with regard to manipulated inlets and disturbances requires only structural information about the process. They presented the concept of relative order as a measure of sluggishness of the response. A matrix of relative orders of input/output pairs leads to a characterisation of structural coupling among input and output process variables.

Huang and Fan [18] presented a knowledge-engineering approach incorporating the controllability into HEN synthesis, based on disturbances propagation. They have shown that the integration of the process and control systems design is of critical importance. Just the sequencing of the process system and its control system designs gives rise to a time consuming and tedious procedure requiring extensive iteration, and does not guarantee a good final decision.

Mathisen et al. [19] investigated the effects of bypass placement on HENs behaviour. They formulate several optimisation problems taking controllability into account and adding constraints to ensure flexibility.

Westphalen et al. [20], using a previous work [21], formulated a controllability index for HENs, based on the condition number of the HEN gain matrix.

From the above mentioned literature sources, [17] and [20] are considered in more detail next.

For HEN synthesis, the system controllability has to be estimated and managed based on incomplete data. To fully estimate and characterise HEN dynamics, the certain details are required – beside topology, equipment design details are needed – including areas and internal flow arrangements.

The potential disturbances include process stream inlet temperatures and flow-rates, heating/cooling demand loads, as well as the loads and temperatures of the captured renewable energy. The controlled variables include the temperatures of the heating and cooling demands. The possible manipulated variables are the loads of the various recovery heat exchangers, splitter ratios, and the duties of the utilities based on fossil fuels. In the view of the demands variations, the control tasks will be both servo and regulatory tasks.

From all of these data, at the stage of topology synthesis, only the basic stream data together with the disturbances and the controlled variables are known. All the other are obtained as a result of the synthesis and the following detailed design. According to the definition of controllability, the existence of at least one feasible control configuration qualifies the HEN as controllable, meaning that for steady-state the manipulated inputs have sufficient capacity to cause the desired steady state changes of the controlled outputs for

servo tasks or to neutralise the steady state effects of the disturbances for regulatory tasks. Regarding the process dynamics, the controlled variables have to be affected faster by the manipulated inputs than by the disturbances. This gives rise to static and dynamic controllability indicators, linked to the steady-state gain and the transition durations.

3.3.1. The dynamic aspect of controllability

Relative order and relative order matrix. Regarding HEN dynamic behaviour, the dynamic responses of individual HEs have been modelled [20]. Daoutidis and Kravaris [17] proposed controllability evaluation of the complete HENs using topological information based on the sluggishness of the response of the controlled outputs towards manipulated inputs and disturbances.

Control configuration synthesis consists of generation of all feasible control configurations, followed by selection of the optimal one. The proposed intuitive tool is based on the concept of the "relative order" [17]. There are two types of relative order. The first type of the relative order $\mathbf{r_{ij}}$ is defined between a controlled output $\mathbf{y_i}$ and an individual manipulated input $\mathbf{u_j}$. This reflects the number of integration steps that the input $\mathbf{u_j}$ has to go through before it affects the output $\mathbf{y_i}$. This metric represents the number of the heat exchangers or other operating units in the path from a manipulated input (e.g. utility flowrate) to a controlled output (e.g. temperature of a heating or a cooling demand). Similarly, the individual relative order $\boldsymbol{\rho_{ik}}$ of the controlled output with respect to disturbance $\mathbf{d_k}$ is defined. This reflects the physical closeness between system inputs (e.g. process stream inlet temperatures and flow-rates) and control outputs.

The calculation of the individual relative orders is done using only structural information from the system digraph. Let $\mathbf{L_{ij}}$ and $\mathbf{L_{ik}}$ denote the lengths of the shortest paths connecting the manipulated input $\mathbf{u_j}$ with the controlled output $\mathbf{y_i}$ and the disturbance $\mathbf{d_k}$ with the controlled output $\mathbf{y_i}$ respectively. Then, if there is a path from the input signal to the output, the relative orders can be calculated using the following expressions:

$$r_{ij} = L_{ij} - 1 \quad (3)$$

$$\rho_{ik} = L_{ik} - 1 \quad (4)$$

If no such path exists, the relative orders are assigned infinity (∞).

The relative order can be used to partially represent the time-dependent characteristics of the synthesised process system and eventual control configurations. The relative orders $\mathbf{r_{ij}}$/$\boldsymbol{\rho_{ik}}$ are structural indicators of how sluggish the responses of the output $\mathbf{y_i}$ are to step changes in the manipulated input $\mathbf{u_j}$ and the disturbance $\mathbf{d_k}$. The larger the relative order, the more sluggish the response is. An illustration of this relationship is shown in Fig. 4. The curves representing transitions for relative orders larger than one (i.e. r = 2 and r = 3), can be approximated by a first-order curve with dead-time before it.

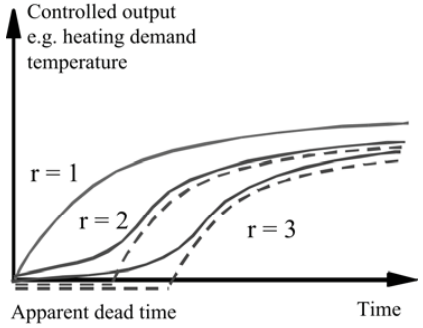

Fig. 4. Relative order as a measure of sluggishness

Using the above approximation allows estimating the feasibility and the quality of alternative control configurations. For a control configuration to have high probability of being feasible from a dynamic point of view, for each controlled output $\mathbf{y_i}$ the relative order $\mathbf{r_{ij}}$ of the control pairs with the corresponding manipulated input $\mathbf{u_j}$ has to be smaller than any of the relative orders $\boldsymbol{\rho_{ik}}$ of the same controlled output $\mathbf{y_i}$ with respect to any of the disturbances $\mathbf{d_k}$. Also, a control configuration is better if it features lower-order response characteristics in terms of the relative orders of the control pairs.

To evaluate entire control configurations the relative order matrix [17] is used. Its elements are the individual relative orders for the control pairs $\mathbf{u_j}$-$\mathbf{y_i}$ and the disturbance pairs $\mathbf{d_k}$-$\mathbf{y_i}$ (Fig. 5). Each column of the matrix corresponds to a manipulated input and contains the relative orders of all controlled outputs with respect to the current manipulated input. Similarly, each row corresponds to a controlled output and contains the relative orders of the current controlled output

with respect to each of the manipulated inputs. Finally, the main diagonal of the matrix corresponds to the selected control pairs in the control configuration.

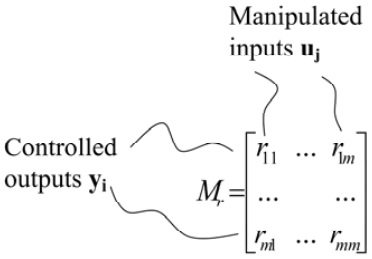

Fig. 5. Relative order matrix - definition

The relative order matrix allows evaluation of how suitable a control configuration is for a given process system.

3.3.2. The static aspect of the controllability

Evaluating the static aspect of controllability involves calculation of the steady-state gains for given sets of controlled outputs and the manipulated inputs. One way is to use of the condition number of the process gain matrix, applied to HENs [23], further obtaining the corresponding Relative Gain Array (RGA).

The Process Gain Matrix (PGM). For a given HEN (and any process system), a separate process gain matrix exists for every control configuration. For the controlled outputs $\mathbf{y_i}$, **i = 1..N** and the manipulated inputs $\mathbf{u_j}$, **j = 1..N**, the process gain matrix is a **N×N** array of sensitivity coefficients, similar to the Sensitivity Tables for HENs [24]. Each matrix element $\mathbf{k_{ij}}$ represents the relative sensitivity of controlled output "**i**" to manipulated input "**j**":

$$k_{ij} = \frac{\Delta y_i}{\Delta u_j} \tag{5}$$

where $\mathbf{\Delta y_i}$ is the change in the value of the controlled output "**i**" as a result of the change $\mathbf{\Delta u_j}$ in the manipulated input "**j**". The calculation of the elements $\mathbf{k_{ij}}$ is performed by starting from the nominal operation point, changing the steady state value of the relevant manipulated input and re-calculating the network. Each such operation yields one column in the process gain matrix.

The condition number of the PGM. Condition number of a matrix is the ratio of the largest to the smallest singular value of that matrix. For computing, a singular value decomposition of the PGM has to be performed and the singular values to be retrieved. The significance of the condition number is that if it is infinite, then the PGM is singular meaning that one or more of the controlled outputs are not sensitive towards the manipulated inputs paired with them, rendering the corresponding control configuration infeasible. The PGMs and condition numbers calculated in this way represent the system sensitivity relative to the nominal operating parameters of the network.

Degrees of freedom and control variables. The usual choices of manipulated inputs in a HEN are the duties of the utilities; the stream split fractions, and bypasses fractions. Westphalen et al. [23] discussed that using stream split fractions as manipulated inputs may not affect the downstream controlled outputs monotonically. For this reason it is advisable to avoid this practice.

For faster responsiveness, the best choice to control an outlet temperature is always the nearest upstream utility exchanger. For instance, to control the outlet temperature of a hot stream, the best case would be to have a cooler immediately before the stream leaves the HEN. This requirement is in a trade-off with the very purpose of HENs – saving energy. Therefore, utility exchangers are not usually placed on all streams and when placed, they may not be even located at the end of the trains for the particular streams.

Another possibility is to place bypasses around some of the exchangers. Increasing the bypass fraction effectively lowers the duty of the corresponding heat exchanger, leading to the following properties:

- Placing bypasses on both streams involved in a heat exchanger is excessive and would not lead to better control than a bypass on only one of the sides. Which of the two possible bypass locations to choose is a meaningful question.
- The actual manipulated variable in the case of bypass usage is the heat exchanger duty. Therefore in the HEN synthesis, instead of estimating the controllability of the system with regard to all particular bypass fractions, it is computationally much more efficient to estimate it with regard to the duties of the corresponding heat exchangers.

Controllability index (based on steady-state gains). The condition number of the PGM can be

used as an approximate measure of how sensitive the controlled outputs (e.g. the stream outlet temperatures) are to a particular ordered set of manipulated inputs (control configuration). A different gain matrix exists for each control configuration. This potential multiplicity raises the question: Which of the condition numbers to use as a controllability measure? This could be the smallest of all condition numbers, the largest, or even some weighted combination of them. The controllability has been defined as representing the control properties of the HEN only. As many control configurations may be possible for a HEN, the Controllability Index (CI) is defined as the smallest of condition number that can be calculated among all control configurations.

The smaller the value of the CI, the better is the controllability. The HEN would be controllable only if the CI has a finite value, while infinite values indicate lack of feasible control configurations.

4. Summary

The field of HEN operability has been under development. A number of works deserves attention. Among them Aaltola [25] and Ma et al. [26] who published synthesis methods for flexible HENs, employing the multi-period paradigm, where [26] considers multistream heat exchangers.

In synthesising flexible HENs, multiperiod operation and ranges of variation representations, some of them overviewed in this paper, can be used and also combined. Flexibility of HENs can be represented by the direct sets of desired parameter variations plus the relevant process constraints and thus used in optimisation studies directly. It is also possible to express the flexibility quantitatively through the Flexibility Index or the Resilience Index. These two measures are scaled representations of the size of the feasible region for parameter variation.

Controllability is used mainly as a quantitative measure intended to integrate the control considerations into the synthesis of process systems and HENs in particular. The controllability aspect has also received attention [27] employing reliability theory. Two different measures of controllability have been considered. The Relative order is biased towards the dynamics of the system response. The Controllability index is based exclusively on the calculation of the process steady-state gain matrix.

From the methods for evaluating the flexibility of the considered energy systems, the FI is more appropriate. The RI is specific only to HENs, while the energy systems integrating renewables also involve other equipment types beside heat exchangers – e.g. boilers, steam turbines, Stirling engines, etc.

With regard to evaluating the controllability of energy systems, the available tools are quite broad, but need further development mainly to reduce their computational demands while preserving the validity of the controllability estimates.

The main challenges imposed by the variations of the renewables supply and thermal energy demands involve both servo tasks – for handling transitions between steady states defined by the changing demands, and regulatory tasks – for maintaining the demand temperatures under the conditions of varying temperatures and loads of the renewable supplies. This field has been developing and deserves continuing attention.

References

[1] Bance, P., 2008, Residential-Scale Fuel Cell CHP: A Better Match for Domestic Loads, *Cogeneration & On-Site Power Production*, vol. 9, no. 3 <www.cospp.com/display_article/330132/122/CRTIS/none/none/1/Residential-scale-fuel-cell-CHP-a-better-match-for-domestic-loads> [accessed on 06.07.2009].

[2] Varbanov, P. S., Klemeš, J. J., 2010, Total Sites Integrating Renewables With Extended Heat Transfer and Recovery, *Heat Transfer Engineering*, 31(9), pp. 733–741.

[3] Linnhoff, B., Hindmarsh,E., 1983, The Pinch Design Method for Heat Exchanger Networks, *Chem. Eng. Sci.*, 38, pp.745-763.

[4] Gassner, M., Marechal, F., 2009, Methodology for the optimal thermo-economic, multi-objective design of thermochemical fuel production from biomass. *Computers Chem. Engng.*, 33(3), pp. 769-781.

[5] Calandranis, J. C., 1988, Operability Studies in Heat Exchanger Networks: Analysis, Control and Synthesis, PhD Thesis, Massachusetts Institute of Technology, US.

[6] Skogestad, S., Postlethwaite, I., 1996, *Multivariable Feedback Control - Analysis and Design*, John Wiley & Sons, New York.

[7] Oliveira,S., G., Liporace, F. S., Araújo, O. Q. F., Queiroz, E. M., 2001, The Importance of Control Considerations for Heat Exchanger Network Synthesis: A Case Study., *Braz. J. Chem. Eng.*, 18, p.195.

[8] Floudas, C. A., Grossmann, I. E., 1986, Synthesis of Flexible Heat Exchanger Networks for Multiperiod Operation, *Computers Chem. Engng.*, 10(2), pp. 153-168.

[9] Cerda, J., Galli, M. R., Camussi, N., Isla, M. A., 1990, Synthesis of Flexible Heat Exchanger Networks - I. Convex Networks, *Computers Chem. Engng.*, 14, pp. 197-211.

[10] Floudas, C. A., Grossmann, I. E., 1987, Synthesis of Flexible Heat Exchanger Networks With Uncertain Flowrates and Temperatures, *Computers Chem. Engng.*, 11(4), pp. 319-336.

[11] Swaney, R. E., Grossmann, I. E., 1985, An Index for Operational Flexibility in Chemical Process Design – I . Formulations and Theory and II. Computational Algorithms, *AIChE Journal*, 31, pp.621 -630; 631 – 641.

[12] Saboo, A. K., Morari, M., 1984, Design of Resilient Processing Plants - IV. Some New Results on Heat Exchanger Network Synthesis, *Chem. Eng. Sci.*, 39, pp.579-592.

[13] Klemeš, J., Friedler, F., Bulatov, I., Varbanov, P., 2010. Sustainability in the Process Industry: Integration and Optimization. McGraw Hill Professional, 400 ps.

[14] Cerda, J., Galli, M. R., 1990, Synthesis of Flexible Heat Exchanger Networks - II. Nonconvex Networks with Large Temperature Variations, *Computers Chem. Engng.*, 14, pp. 213-225.

[15] Galli, M. R., Cerda, J., 1991, Synthesis of Flexible Heat Exchanger Networks - III. Temperature and Flowrate Variations, *Computers Chem. Engng.*, 15, pp.7-24.

[16] Georgiou, A., Floudas, C. A., 1989 Structural analysis and synthesis of feasible control systems - theory and applications, *Chem. Eng. Res. Des.*, 67(6), pp.600-18.

[17] Daoutidis, P., Kravaris, C., 1992, Structural Evaluation of Control Configurations for Multivariable Nonlinear Processes, *Chem. Eng. Sci.*, 47(5), pp.1091-1107.

[18] Huang, Y. L., Fan, L. T., 1992, Distributed Strategy for Integration of Process Design and Control. A Knowledge Engineering Approach to the Incorporation of Controllability into Exchanger Network Synthesis, *Computers Chem. Engng.*, 16, pp.497-522.

[19] Mathisen,K. W., Skogestad, S., Wolff, E.A., 1992, Bypass Selection for Control of Heat Exchanger Networks, 1st European Symposium on CAPE – ESCAPE 1, Elsinore, Denmark.

[20] Westphalen, D. L., Young, B. R., Svrcek, W. Y., 2003, A Controllability Index for Heat Exchanger Networks, *Ind. Eng. Chem. Res.*, 42, pp.4659-4667.

[21] Ogunnaike, B. A., Ray, W. H., 1994 *Process Dynamics, Modeling and Control*, Oxford University Press, New York.

[22] Mathisen,K. W., Morari, M., Skogestad, S., 1994, Dynamic Models for Heat Exchangers and Heat Exchanger Networks. *Computers Chem. Engng.*, 18, pp.S459-S463.

[23] Westphalen, D. L., Young, B. R., Svrcek, W. Y., 2003, A Controllability Index for Heat Exchanger Networks, *Ind. Eng. Chem. Res.*, 42, pp.4659-4667.

[24] Kotjabasakis, E., Linnhoff, B., 1986, Sensitivity Tables for the Design of Flexible Processes. (1) How Much Contingency in Heat Exchanger Networks is Cost-Effective? *Chem. Eng. Res. Des.*, 64, pp.199.

[25] Aaltola, J., 2002, Simultaneous synthesis of flexible heat exchanger network, *Applied Thermal Engineering*, 22, pp. 907–918.

[26] Ma, X., Yao, P., Luo, X., Roetzel W., 2008, Synthesis of multi-stream heat exchanger network for multi-period operation with genetic/simulated annealing algorithms, *Applied Thermal Engineering*, 28, pp. 809–823.

[27] Tellez, R., Svrcek, W., Ross, T. J., Young, B. R., 2006, Heat exchanger network process modifications for controllability using design reliability theory, *Computers Chem. Engng* 30, pp. 730–743.

Acknowledgments: The financial support from the EC Marie Curie Chair (EXC) FP6-042618 "INEMAGLOW Integrated Waste to Energy Management to Prevent Global Warming" and PIAP-GA-2008-230659 "DECADE Development of Efficient and Robust Controllers for Advanced Energy Systems" is gratefully acknowledged.

Model Validation and Simulation of a Biomass Gasifier Integrated in a 6 MWe Engine Cogeneration Plant of an Alcohol Distillery

Maria Puig-Arnavat, Joan Carles Bruno, Alberto Coronas

University Rovira i Virgili, Department of Mechanical Engineering, Tarragona, Spain

Abstract: Interest in the use of biomass as an energy resource is increasing, and specially its use in gasification. For this reason, it is important to have a model capable to simulate the operation of a biomass gasifier. Several different types of models have been developed for gasification systems. Equilibrium models are less computationally intensive than kinetic models and they are a useful tool for preliminary comparison, however they cannot give highly accurate results for all cases. A thermodynamic equilibrium model has been developed and validated with other models and experimental data from other authors with good results. This model has also been applied to reproduce the operation of a real gasifier in an alcohol distillery in Spain.

Keywords: Biomass gasification, Cogeneration, Modeling.

1. Introduction and objectives

The use of biomass as an alternative to fossil fuels has stimulated substantial research and development. It has been attracting great attention these days due to the declining fossil fuel reserves and the ever-increasing greenhouse effects produced through fossil fuel utilization. Biomass is a renewable resource and considered to be CO_2 neutral. The potential for biomass to supply much larger amounts of useful energy with reduced environmental impacts, compared to fossil fuels, and its wide spread availability has been widely recognized [1].

Biomass can be converted to commercial products via either biological or thermochemical processes [2-4]. Biological conversion of low-value lignocellulosic biomass still faces challenges in low economy and efficiency [2]. Combustion, pyrolysis and gasification are the three main thermochemical conversion methods. Biomass is traditionally combusted to supply heat and power in the process industry. The net efficiency for electricity generation from biomass combustion is usually very low, ranging from 20% to 40% [3]. Biomass cofired in existing combustors is usually limited to 5–10% of the total feedstock due to the concern about plugging of existing coal feed systems [4]. Pyrolysis converts biomass to bio-oil in the absence of oxygen (O_2). Limited uses and difficulty in downstream processing of bio-oil have restricted the wide application of biomass pyrolysis technology [5]. Gasification converts biomass through partial oxidation into a gaseous mixture, small quantities of char and condensable compounds. It is considered one of the most efficient ways to convert the energy embedded in the biomass and it is becoming one of the best alternatives for waste solids reuse.

The efficient operation of a biomass gasifier is dependent on a number of complex chemical reactions, including fast pyrolysis, partial oxidation of pyrolysis products, gasification of the resulting char, conversion of tar and lower hydrocarbons, and the water-gas shift reaction. These complicated processes, coupled with the sensitivity of the product distribution to the rate of heating and residence time in the reactor, called for the development of mathematical models. Their main goal is the study of the thermochemical processes during the gasification of the biomass, evaluating the influence of the main input variables, such as moisture content and air/fuel ratio, the producer gas composition and its calorific value

The objective of the present paper is to study and compare the models proposed by different authors as well as to develop a simple model that will be validated with other models and with experimental published data. This model will also be applied to a case study in a gasification plant of an alcohol distillery.

Corresponding Author: Maria Puig-Arnavat, Email: maria.puig@urv.cat

In the next section, a brief description of the fundamentals and technologies of biomass gasification are presented. Later, different developed models are analyzed and a simple model, based on the thermodynamic equilibrium, is proposed and validated with other models and experimental published data. Finally, a case study for a 6 MWe gasification plant, in an alcohol distillery, using the developed model is described.

2. Fundamentals and technologies of biomass gasification

Gasification is a partial thermal oxidation, which results in a high proportion of gaseous products (carbon dioxide, water, carbon monoxide, hydrogen and gaseous hydrocarbons), small quantities of char (solid product), ash and condensable compounds (tars and oils). Steam, air or oxygen, are supplied to the reaction as oxidising agents. Usually, the term equivalence ratio (ER) is used in gasification as the ratio between the actual air fuel ratio and the air fuel ratio for complete combustion. The gas produced can be standardised in its quality and is easier and more versatile to use than the original biomass e.g. it can be used to power gas engines and gas turbines, or used as a chemical feedstock to produce liquid fuels. Gasification adds value to low or negative-value feedstock by converting them to marketable fuels and products.

The chemistry of biomass gasification is quite complex. However, on a broad basis, the following four stages are involved in the gasification process [6-8]:

- Drying: The moisture content of the biomass is reduced. Typically, the moisture content of biomass is in the range 5-35%. Drying occurs at about 100-200ºC with reduction in moisture content of biomass <5%.
- Devolatilization (pyrolysis): This is essentially thermal decomposition of biomass in absence of oxygen or air. In this process, the volatile matter in the biomass is reduced. This results in release of hydrocarbon gases from biomass due to which the biomass is reduced to solid charcoal. The hydrocarbon gases can condense at sufficiently low temperature to generate liquid tars.
- Oxidation: This is a reaction between solid carbonised biomass and oxygen in the air resulting in formation of CO_2. Hydrogen present in the biomass is also oxidized to generate water. Large amount of heat is released with the oxidation of carbon and hydrogen. If oxygen is present in substoichiometric quantities, partial oxidation of carbon may occur resulting in generation of carbon monoxide.
- Reduction: In absence (or substoichiometric presence) of oxygen, several reduction reactions occur in the temperature range 800-1000ºC. These reactions are mostly endothermic. The major reactions in this category are as follows:

  Water-gas reaction:

  $C + H_2O \rightarrow CO + H_2 - 131.4$ kJ/mol (1)

  Boudouard reaction:

  $C + CO_2 \leftrightarrow 2CO - 172.6$ kJ/mol (2)

  Water shift reaction:

  $CO_2 + H_2 \leftrightarrow CO + H_2O - 42$ kJ/mol (3)

  Methane reaction:

  $C + 2H_2 \leftrightarrow CH_4 + 75$ kJ/mol (4)

  Several authors [9-11] have stated that the Boudouard reaction and the water-gas reaction can be combined to give the water-gas shift reaction:

  $CO + H_2O \leftrightarrow CO_2 + H_2$ (5)

Gasification reactor designs have been investigated for more than a century, which resulted in the availability of several designs at small and large scale. They can be classified in different ways [12]:

- According to the gasification agent: Air-blown gasifiers, oxygen gasifiers and steam gasifiers.
- According to heat for gasification: Auto-thermal or direct gasifiers (heat is provided by partial combustion of biomass) and allo-thermal or indirect gasifiers (heat is supplied from an external source through heat exchanger or indirect process).
- According to pressure in the gasifier: Atmospheric and pressurised.
- According to the design of the reactor: Fixed bed (updraft, downdraft, cross-draft and open-core), fluidized bed (bubbling, circulating and twin bed), entrained flow, stage gasification with physical separation of pyrolysis, oxidation and/or reduction zones.

3. Biomass gasification modeling

Biomass gasification is rather complex and many researchers have focused on modeling, in order to better understand the gasification process and carry out design, simulation and optimization of gasifiers and perform process analysis.

The models could be divided into kinetic rate models, thermodynamic equilibrium models and neural network models. Some models use the process simulator Aspen Plus combining thermodynamic and kinetic rate models.

Kinetic models provide essential information on kinetic mechanisms to describe the conversion during biomass gasification, which is crucial in designing the gasifiers, evaluation and improvement. These rate models are accurate and detailed but are computationally intensive [13]. However, several researchers focused extensively on kinetic models of biomass gasification [13-15]. Kinetic models describe the char reduction process using kinetic rate expressions obtained from experiments and permit better simulation of the experimental data where the residence time of gas and biomass is relatively short.

Thermodynamic equilibrium models have the ability to predict the maximum possible conversion of biomass during gasification and the theoretical efficiency. They are also important in the optimization of the operating conditions at the equilibrium state and also being a simple tool to estimate the gasification performance for preliminary techno-economic analysis of the whole process. There are two approaches for thermodynamic equilibrium modeling: stoichiometric approach, based on stoichiometric reactions, and non-stoichiometric approach, based on minimizing the total Gibbs free energy in the system. Some recent efforts with thermodynamic equilibrium models include the work done by several authors [9-10, 16-19].

3.1. Description of the developed model

Based on the previously mentioned works of other authors, a thermodynamic equilibrium model is developed. The objective is to have a simple model that can simulate the operation in a gasification plant and used to analyse the effect of changing the operating conditions as well as the biomass to be gasified in the producer gas. This model aims to be used in preliminary and viability studies.

The formula considered in this model to describe biomass composition is $CH_xO_yN_zS_r$. It can be calculated from the ultimate analysis of the biomass and the mass fractions of the carbon, hydrogen, oxygen, nitrogen and sulphur.

The algorithm that estimates the composition of the producer gas is based on chemical equilibrium between the different species, the global reaction can be written as:

$$CH_xO_yN_zS_r + wH_2O + m(O_2+3.76N_2) \rightarrow n_{CO}\,CO + n_{CO2}\,CO_2 + n_{H2}\,H_2 + n_{CH4}\,CH_4 + n_{H2O}\,H_2O + ((z/2)+3.76m)\,N_2 + n_{SO2}\,SO_2 \quad (6)$$

The variable *m* corresponds to the molar quantity of air used during the gasifying process. To find the six unknown species of the producer gas, six equations are required. Those equations are generated using mass balance and equilibrium constant relationships. Considering the global gasification reaction, the first four equations are formulated by balancing each chemical element (carbon, hydrogen, oxygen and sulphur). For the model in this study, the thermodynamic equilibrium is assumed for all chemical reactions in the gasification zone. All gases are assumed to be ideal and all reactions form at atmospheric pressure. Therefore, the equilibrium constants, which are functions of temperature for the water-gas shift reaction (K_1) and the methane reaction (K_2) are used for the remaining two equations. The equilibrium constants can be calculated using the expressions of [9] or the procedure described in [10].

The temperature of the gasification zone needs to be calculated in order to obtain the equilibrium constants. For this reason, energy balance is performed for the gasification process. According to the first thermodynamic principle, the enthalpy of the products at the reaction temperature is equal to the sensible and formation enthalpy of the biomass, the moisture and the air, incremented with heat inputs (preheating, $Q_{in} > 0$) and the heat outputs (heat loss, $Q_{out} < 0$). The energy balance can be formulated as it appears in [18].

Since gasifiers are different in designs, the producer gases generated by them are also different in composition. To increase the results'

accuracy, some authors developed models that can be modified for a specific gasifier.

Gumz [20] stated that a modified equilibrium constant can be defined as the true equilibrium constant multiplied by the degree of approach to equilibrium. In calibrating the model of [21], the amount of methane predicted was adjusted in such a way that it was equal to the amount of methane measured in the product gas. Reference [10], using experimental data from other authors, calculated two coefficients for correcting the equilibrium constant of water-gas shift reaction and methane reaction that improved the accuracy. The coefficients were obtained from the average value of the ratio of experimental data and calculated data from their model, for CH_4 and CO. Other authors like [16] applied empirical parameters in order to modify the carbon conversion.

In the present model, when it is validated using different experimental data from the literature, the adjustment will be carried out by means of coefficients to correct the equilibrium constants or estimating a reasonable value for overall heat losses.

3.2. Comparison of the developed model with other models and experimental data

The model developed in this study was first compared with another similar model developed by [9]. These authors developed an equilibrium model to predict the gasification process in a downdraft gasifier. The effects of initial moisture content in wood chips on the producer gas composition at 800ºC gasification process have been compared using both models as it is plotted in Fig. 1.

Using both models (Fig. 1) it can be observed that the composition of the inert nitrogen is almost constant with moisture content. The composition of the methane produced is almost constant at a very low percentage (0.7-1.6%). The percentage of hydrogen in the fuel gas increases continuously with the moisture content from about 20% to 25% for an increase in moisture content from 0% to 40%. A similar trend is also observed for the carbon dioxide; however the increase is from about 5% to 15%. The percentage of carbon monoxide reduces from about 28% to 15% for the same variation of moisture content. From these results, it can be concluded that the model developed by [9] and the present one predict similar results for the same gasification conditions with a difference less than 5%.

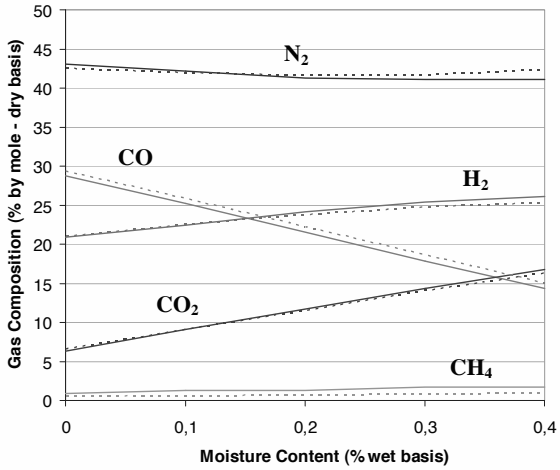

Fig. 1. Comparison of the effect of moisture content in wood chips on gas composition at 800ºC using Zainal's model [1] and the model developed in the present study. Solid lines are for Zainal's model [1] and dotted lines are for the present model.

Reference [18] proposed a thermochemical equilibrium model for downdraft gasifiers and compared it with experimentally obtained producer gas composition from pine wood gasification. The proposed model in this study has also been compared with this model and experimental data. The results are shown in Fig.2. For this case, the developed model has been modified to adjust it to the other model and to the experimental data. It has been necessary to multiply the equilibrium constant K_2 with a coefficient of 50 and it has also been necessary to consider an overall heat loss of 5% of the HHV of the biomass to be gasified. Reference [18] modified their equilibirum model correcting the O_2 content in the producer gas. This adjustment was not possible on the present model because no information about the O_2 content in the producer gas is given in the authors' paper.

In Fig. 2 solid lines are the predictions of the present modified model and the ones with symbols are the predictions of [18]. Similar predictions can be found for CO_2 and CO percentages for both models. For H_2 and CH_4 the predictions are slightly different. At a normal gasifying relative fuel/air ratio (F_{rg}= 3-4) the modified model

predicts with accuracy the values of the measured producer gas composition and for H_2 the predictions are even better that the ones of [18].

The predictions of the developed model have also been compared with experimental data reported by other authors like [22] (Table 1 and Table 2) and [21] (Table 3 and Table 4).

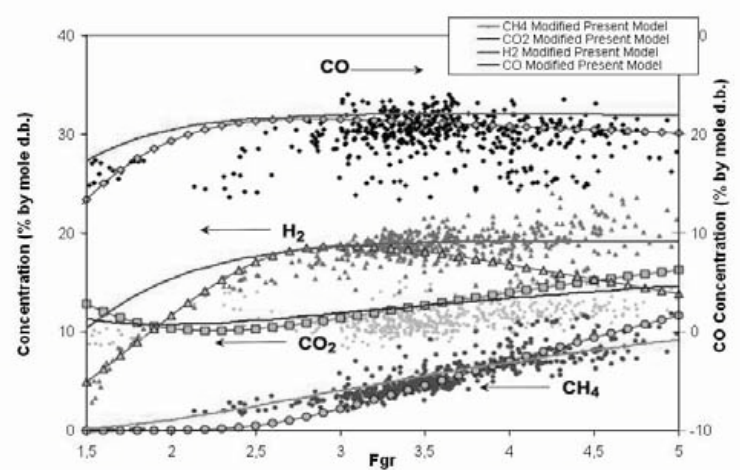

Fig. 2. Comparison of the predicted (Melgar et al, 2007 and present modified model) and experimentally obtained producer gas composition for pine wood with 18% moisture where F_{gr} is the relative fuel/air ratio. Solid lines represent the present modified model and lines with symbols are Melgar et al (2007) model predictions.

Table 1. Experimental results from [22] for biomass (Dalbergia sisoo *wood waste) with different moisture content and different equivalence ratio (ER). All percentages are in dry basis.*

Moisture Content (%)	ER	CH_4 (%)	CO (%)	CO_2 (%)	H_2 (%)	N_2 (%)
11.45	0.2533	0.008	16.05	7.79	7.03	68.32
4.37	0.1791	0.002	16.97	6.72	12.53	63.89
4.37	0.1673	0.008	21.86	5.20	-	60.07
4.37	0.1992	0.000	21.86	4.43	13.45	59.91
7.3	0.2054	0.000	20.33	5.20	9.32	64.96
10	0.3546	0.000	15.59	6.57	10.85	66.64

From Table 1 and Table 2 it can be seen that the values predicted by the modified model adjust correctly with the experimental ones. Only for N_2 and CO a slight deviation can be found.

Different authors [10, 18] have used data from [21] to validate their models. For this reason, these experimental data have also been used to validate the present model. The experimental data from [21] for rubber wood gasification in a downdraft gasifier can be seen in Table 3 and the predicted values, using the present model, for the same operating conditions can be seen in Table 4.

From Table 3 and Table 4 it can be seen that the gas compositions predicted by the gasification developed model are in good agreement with the experimental data obtained by [21].

Table 2. Predicted results with developed model for the same operating conditions than [22].. To increase the accuracy of the model, K_1 and K_2 have been multiplied by two coefficients, 0.403 and 0.0402 respectively.

Moisture Content (%)	ER	CH_4 (%)	CO (%)	CO_2 (%)	H_2 (%)	N_2 (%)
11.45	0.2533	0.00008154	21.02	8.66	6.73	63.59
4.37	0.1791	0.0007191	26.59	6.19	12.10	55.11
4.37	0.1673	0.001151	27.23	6.02	13.32	53.44
4.37	0.1992	0.0003436	25.42	6.58	10.22	57.78
7.3	0.2054	0.0003156	24.65	7.00	9.97	58.38
10	0.3546	3.813E-06	13.33	12.59	2.22	71.86

Table 3. Experimental data form [21] for biomass gasification with different moisture content and air to fuel ratio. All percentages are in dry basis.

Moisture Content (%)	Air/Fuel (Nm^3/kg)	CH_4 (%)	CO (%)	CO_2 (%)	H_2 (%)	N_2 (%)
18.5	2.03	1.40	19.6	9.9	17.2	51.9
16	2.2	1.10	20.2	9.7	18.3	50.7
14.7	2.37	1.10	19.4	9.7	17.2	52.6
16	1.96	1.30	18.4	10.6	17	52.7
15.2	2.12	1.30	19.7	10.8	13.2	55
14	2.29	1.20	18.9	8.5	12.5	59.1
14.7	1.86	1.10	19.1	11.4	15.5	52.9
13.8	2.04	1.30	22.1	10.5	12.7	53.4
12.5	2.36	1.20	19.1	10.7	13	56

Table 4. Predicted results with developed model for the same operating conditions than [21].. To increase the accuracy of the model, K_1 and K_2 have been multiplied by two coefficients, 1.04 and 11.76, respectively.

Moisture Content (%)	Air/Fuel (Nm^3/kg)	CH_4 (%)	CO (%)	CO_2 (%)	H_2 (%)	N_2 (%)
18.5	2.03	1.80	17.85	12.34	16.62	51.4
16	2.2	1.11	18.42	11.48	15.69	53.29
14.7	2.37	0.67	18.45	11.06	14.61	55.21
16	1.96	2.00	18.53	12.01	16.65	50.81
15.2	2.12	1.34	18.7	11.47	16	52.49
14	2.29	0.82	18.77	11.01	15.03	54.38
14.7	1.86	2.43	18.88	12.03	16.8	49.87
13.8	2.04	1.58	19.12	11.36	16.21	51.73
12.5	2.36	0.64	18.96	10.7	14.46	55.24

3.3. Case study of a 6 MWe cogeneration plant of an alcohol distillery

The presented model, which has been validated with other models and experimental data from other authors in the section above, has also been used to estimate the producer gas composition that can be obtained in a gasification plant of an alcohol distillery in Spain. This plant, with an estimated electrical output of 5.9 MW has 4 bubbling fluidised bed gasifiers that can gasify 1000 kg/h of waste bagasse from an alcohol factory or other biomass each one and allows total elimination of the liquid bagasse and effluent of the factory. Three Jenbacher producer gas engines are used for electricity generation. A set of gasifier operating conditions is used as input parameters for the developed gasifier model. The biomass gasified is grape marc that includes waste stems, seeds and skins of grape. Table 5 shows the proximate and ultimate analysis of this grape residue.

Table 5. Proximate and ultimate analysis of grape marc.

Parameter	Dry basis
HHV (MJ/kg)	21.3
Proximate analysis (wt%)	
Moisture	14
Ash	5.5
Ultimate analysis (wt%)	
C	58.40
H	7.5
O	31.62
N	2.45
S	0.16
Cl	0.03

The producer gas composition obtained using the present model for the gasification of 1000 kg/h of this biomass at 800ºC is detailed and compared with experimental data in Table 6. A factor of 19 to correct the constant equilibrium K_2 and a factor of 0.87 to correct the constant equilibrium K_1 have been applied.

Table 6. Experimental data of producer gas composition and estimated results for the gasification of grape marc using the present model adjusted.

Parameter	Experimental data	Present model
N_2	52.07%	60.64%
H_2	10.24%	10.45%
CO_2	12.87%	12.75%
CO	16.12%	12.9%
CH_4	3.80%	3.25%
LHV MJ/Nm^3	4.50	3.54

As it can be seen in Table 6, the model is capable to reproduce the operation of this gasifier with

reasonable good agreement. However, the LHV found is lower mainly due to the under prediction of CO composition.

If this producer gas is used in a cogeneration module and, according to the manufacturer's data, 1459 kWe of electricity and 1756 kWth of useful heat could be produced. The electrical efficiency would be about 35.5%.

More operating data sets will be collected in the future in order to adjust the model to the operation conditions of the plant. However, as an example of its potential application, this adjusted model has been used to calculate the influence of moisture content in the biomass on the producer gas composition and LHV (Fig. 3) and also on the electrical efficiency and electrical and thermal output of the cogeneration module (Fig. 4). The thermal output is divided into two values: the waste heat recovered from the engine exhaust gases and the waste heat recovered from the engine cooling hotwater.

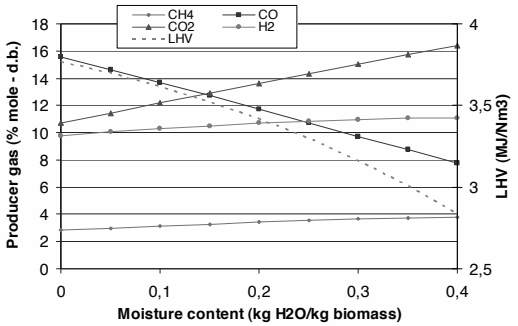

Fig. 3. Estimated producer gas composition and LHV using the developed model vs moisture content of biomass.

It can be observed that the tendency in producer gas composition of the different components is in good agreement with the tendency observed by other authors [9, 10]. The inert nitrogen is almost constant with moisture content. The composition of the methane produced is almost constant at a percentage around 3%. The percentage of hydrogen in the fuel gas increases continuously with the moisture content from about 9.8% to 11%. A similar trend is observed for the carbon dioxide increasing from about 10.7% to 16.5%. The percentage of carbon monoxide reduces from about 15.5% to 7.5%. In Fig. 4 it can be observed that the electrical efficiency as well as the electrical and thermal power output decrease when the moisture content of biomass increases. Althought their impact is quite low with respect to the electrical efficiency, about 1% for the whole range of moisture content.

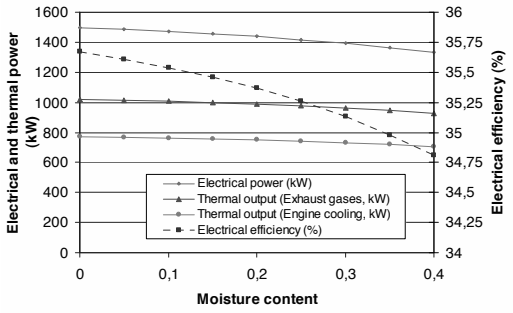

Fig. 4. Estimated electrical efficiency and electrical and thermal output of a cogeneration modules vs moisture content of biomass.

4. Conclusions

Interest in the use of biomass as an energy resource is increasing, and specially its use in gasification. For this reason, it is important to have a model capable to simulate the operation of a biomass gasifier. Several different types of models have been developed for gasification systems – kinetic, equilibrium, and artificial neural networks. Unlike kinetic models that predict the progress and product composition at different positions along a reactor, an equilibrium model predicts the maximum achievable yield of a desired product from a reacting system. It also provides a useful design aid in evaluating the limiting possible behaviour of a complex reacting system which is difficult or unsafe to reproduce experimentally or in commercial operation. Equilibrium models are less computationally intensive than kinetic models and they are a useful tool for preliminary comparison, however they cannot give highly accurate results for all cases.

A thermodynamic equilibrium model has been developed and validated with other models and experimental data from other authors with good results. This model has also been applied to reproduce the operation of a real gasifier in an alcohol distillery in Spain. More experimental data sets will be collected in the future in order to achieve a better adjustment of the model.

References

[1] Maniatis, K., Guiu, G., Riesgo, J., 2002, The european commission perspective in biomass and waste thermochemical conversion. In A. V. Bridgwater, editor, Pyrolysis and Gasification of Biomass and Waste. Proceedings of an Expert Meeting, pp. 1 – 18, Newbury, October 2002. CPL Press.

[2] Lin, Y., Tanaka S., 2006, Ethanol fermentation from biomass resources: current state and prospects, Applied Microbiology and Biotechnology, 69, pp. 627–42.

[3] Caputo, A.C., Palumbo, M., Pelagagge, P.M., Scacchia, F., 2005, Economics of biomass energy utilization in combustion and gasification plants: effects of logistic variables, Biomass & Bioenergy, 28, pp.35–51.

[4] Yoshioka, T., et al, 2005, Biomass resources and conversion in Japan: the current situation and projections to 2010 and 2050, Biomass & Bioenergy, 29, pp. 336–46.

[5] Faaij, A.P.C., 2006, Bio-energy in Europe: changing technology choices, Energy Policy, 34, pp. 322–42.

[6] McKendry, P., 2002, Energy production from biomass (part 2): Conversion Technologies, Bioresource Technology, 83, pp. 47-54

[7] McKendry, P., 2002, Energy production from biomass (part 3): Gasification technologies, Bioresource Technology, 83, pp. 55-63

[8] Li, X., 2002, Biomass gasification in circulating fluidized bed. PhD dissertation. Vancouver, Canada: University of British Columbia.

[9] Zainal, Z.A., Ali, R., Lean, C.H., Seetharamu, K.N., 2001, Prediction of performance of a downdraft gasifier using equilibrium modeling for different biomass materials, Energy Conversión and Management, 42, pp. 1499-1515

[10] Jarungthammachote, S., Dutta, A., 2007, Thermodynamic equilibrium model and second law analysis of a downdraft waste gasifier, Energy, 32, pp. 1660-69

[11] Highman, C., Van der Burgt, M., 2008, Gasification, 2nd Edition, Elselvier, USA

[12] Rauch, R., 2003, Biomass gasification to produce synthesis gas for fuels and chemicals, report made for IEA Bioenergy Agreement, Task 33: Thermal Gasification of Biomass

[13] Sharma, A.Kr., 2008, Equilibrium and kinetic modelling of char reduction reactions in a downdraft biomass gasifier: A comparison. Solar Energy, 52, pp. 918-28.

[14] Wang, Y., Kinoshita, C.M., 1993, Kinetic model of biomass gasification, Solar Energy, 51, pp. 19-25

[15] Giltrap, D.L., McKibbin, R., Barnes, G.R.G., 2003, A steady state model of gas–char reactions in a downdraft gasifier, Solar Energy, 74, pp. 85–91.

[16] Li, X., et al., 2001, Equilibrium modeling of gasification: a free energy minimization approach and its application to circulating fluidized bed coal gasifier, Fuel, 80, pp. 195-207

[17] Li, X., et al, 2004, Biomass gasification in a circulating fluidized bed, Biomass Bioenergy, 26, pp. 171-93

[18] Melgar, A., Pérez, J.F., Laget, H., Hornillo, A., 2007, Thermochemical equilibrium modelling of gasifying process, Energy Conversion and Management, 48, pp. 59-67

[19] Jarungthammachote, S., Dutta, A., 2008, Equilibrium modeling of gasification: Gibbs free energy minimisation approach and its application to spouted bed and spout-fluid bed gasifiers. Energy Conversion and Management, 49, pp. 1345-56

[20] Gumz, W., 1950, Gas producers and blast furnaces, Wiley, New York

[21] Jayah, T.H., Aye, L., Fuller, R.J., Stewart, D.F., 2003, Computer simulation of a downdraft wood gasifier for tea drying. Biomass and Bioenergy, 25, 459-69

[22] Sheth, P.N., Babu, B.V., 2009, Experimental studies on producer gas generation from wood waste in a downdrat biomass gasifier, Bioresource Technology, 100, pp. 3127-33.

Synthesis/Design Optimization of Organic Rankine Cycles for Low Temperature Geothermal Sources with the HEATSEP Method

Andrea Toffolo[a], Andrea Lazzaretto[a], Giovanni Manente[a] and Nicola Rossi[b]

[a] *University of Padova, Padua, Italy*
[b] *ENEL Ingegneria e Innovazione, Pisa, Italy*

Abstract: Organic Rankine cycles are now a mature technology for the conversion of low temperature geothermal sources into electricity. In this paper a synthesis/design optimization of binary cycle power plants with a pure thermodynamic objective is discussed. According to the HEATSEP method, a "basic" plant configuration is first defined including all the components that are strictly needed to realize the "concept" of the plant itself and are different from heat exchangers, while different matching between hot and cold thermal streams within the plant are allowed for the same conditions at the boundary of the heat transfer section. Different structural options for the heat transfer section can then be obtained using the same basic plant model. Two organic fluids (isobutane and R134a) and different brine input temperatures are considered here and both super- and subcritical solutions are taken into account. Although the optimization problem is quite simple, the results show that the objective function (exergy recovery efficiency) is a non-smooth surface due to the feasibility constraint applied to the undefined heat transfer section. This surface is drawn to show not only the optimum solutions but also the sub-optimal ones, which could be of interest for further evaluations with objectives of different nature.

Keywords: geothermal sources, synthesis/design optimization, organic Rankine cycles.

1. Introduction

The conversion of thermal energy at low temperatures is a widely studied issue in the field of energy systems. Such kind of heat is made available by many industrial processes, and valuable efforts have been devoted to recover it internally although in most cases it is rejected to the environment as is. The renewable energy field also deals with this kind of heat when natural or artificial low temperature geothermal resources are exploited and when solar energy is collected by means of low-to-medium temperature devices.

Power generationfrom low temperature heat is affected by the low thermal efficiency dictated by Carnot limit. Organic Rankine cycles (ORCs) are a suitable way to perform this energy conversion, as they provide the highest thermal efficiencies in that temperature range. The maximization of the performance of these cycles has been investigated in the literature from the thermodynamic point of view, but technological and economical aspects are involved as well. The choice of the organic fluid operating the cycle also plays a key role.

Thermal efficiency has been initially considered as the pure thermodynamic objective to be maximized at different heat source temperatures. Badr, Probert and O'Callaghan [1] present some thermo-physical requirements that the fluid should fulfil. Hung, Shai and Wang [2] distinguish among three categories of fluids (dry, wet and isentropic) according to the slope of the saturated vapor curve in the T-s diagram and show that isentropic fluids are the most suitable. Maizza and Maizza [3] underline the relationship among the critical temperature of the operating fluids, the evaporating temperature and cycle efficiency. In these early studies the nature of the available heat source in terms of both mass flow rate and temperature is not considered. A sensitivity analysis on vaporization temperature is made for a single pressure level saturated vapor cycle, superheating being allowed only when the critical temperature of the operating fluid is too low. This approach is sound [4] when the heat source has an infinite heat capacity or when it is continuously regenerated in a closed loop, as it happens in thermodynamic solar systems [5]. However, in many cases the low temperature heat source consists of sensible heat and must be cooled as much as possible in order to completely exploit its thermal energy. Thus, power rather than efficiency has to be considered as an objective [6].

Corresponding Author: Andrea Lazzaretto, Email: andrea.lazzaretto@unipd.it

Liu, Chen and Wang [7] explain the difference between maximum cycle efficiency and maximum exploitation of the heat source as objectives. Thermal efficiency is not able to describe the best coupling between the heat source and the cycle operated by the organic fluid, because the ultimate aim is obtaining the maximum power output from a given heat source. Consequently, the choice of cycle design parameters and of the organic fluid should be based on "total heat recovery efficiency", which is the ratio between cycle power and the overall available heat (and not only the fraction that is actually exploited). As pointed out by Wei et al. [8], the energy conversion is strongly affected by the exergy destruction in the evaporator. The methods proposed to decrease the irreversibilities in the evaporation phase are:

- the use of supercritical pressures [9,10] (but the higher the pressure, the higher the power absorbed by the feed pumps)
- the use of mixtures [11], the glide of which reduces the distance between the two temperature profiles in the evaporator. However, the benefits are not so high, because the temperature profile in the condensation is not horizontal as well, and this forces the increase of turbine discharge pressure.

Other options involve more complex cycles, in which the evaporation is split into two pressure levels [12], or in which the compositions of the operating fluid in the evaporator and in the condenser are kept different by means of a distillation column as in Kalina cycles [13].

Component technology also affects the choice of cycle design parameters and of the organic fluid:

- *Expander*. On one hand, the use of steam would require multi-stage turbines [1], as the enthalpy drops across the expander are high even with moderate temperature differences, and erosion of turbine blades may occur if a sufficient level of superheating cannot be obtained. On the other hand, the organic fluids with molecular weights higher than water can be expanded in single stage turbines and erosion problems are avoided because of the different slope of the saturated vapour curve. In addition, the higher operating fluid mass flow rate makes the full admission condition possible at turbine inlet for small power outputs as well [1].
- *Pumps*. In general, operating fluids having a high density of the liquid phase are preferred to reduce the load absorbed by feed pumps, which is a relatively high percentage of the expander power output
- *Heat exchangers*. Fluids with too low pressures in the condenser and/or too high pressures in the evaporator are usually avoided. Fluids are searched with thermophysical properties yielding high heat transfer coefficients both in the evaporator and condenser in order to reduce heat transfer areas and costs (in [16] the ratio of the total heat exchanger area to net power output is used as objective function to be minimized).

A special attention is to be addressed also to the thermal stability of the organic working fluid, as it could limit the maximum temperature of the cycle.

These considerations show the strong correlation existing among thermodynamic, economic and technological issues and justify the increased interest towards ORCs even for higher temperature levels, e.g. biomass applications [14] and other small-scale integrated plants, such as the innovative solar desalination systems [15] that combine ORCs with an efficient utilization of the energy produced.

In this work, the heat source is a low temperature geothermal source (pressurized hot water, the so-called "brine") having a finite mass flow rate and a given input temperature. Moreover, the brine must not be cooled below 70°C because it is re-injected into the well. The energy conversion is performed by a plant based on a single pressure level ORC, the structure and the parameters of which have to be optimized. The thermodynamic objective to be maximized is the exergy recovery efficiency or, equivalently, the net electrical power generated by the plant. A sensitivity analysis is performed by considering six inlet temperatures for the brine (130°C to 180°C at steps of 10°C) and two organic fluids operating the cycle, isobutane and R134a.

The HEATSEP method [17,18] is applied to the synthesis/design optimization of the ORC cycle, so that the design of the heat transfer section within the plant is considered separately from the design optimization of the basic plant components, and different options about its configuration can then be defined for the same temperatures and mass flow rates of the thermal streams involved. Sub-optimal solutions are taken into account as well, and the optimal response surface as a function of cycle maximum pressure and temperature is

explored. In fact, the problem is deceptively simple, mainly because of the way in which the heat transfer feasibility constraint (HTFC) affects the optimum response surface, generating sharp edges that correspond to the (de)activation of pinch points.

2. Methodology

2.1. The application of the HEATSEP method

The HEATSEP method simplifies the problem of the synthesis/design optimization of complex energy systems by separating the choices about the configurations of the heat transfer section from those about the rest of the system. The main problem is therefore divided into two subproblems:

- The first is about the configuration and the design parameters of the "basic" components of the system, i.e. those components that are not involved in the heat transfer. They are called "basic" considering that they are strictly needed to realize "the concept" behind the plant. As shown in [17], in order to simplify the definition of this "basic" system configuration, basic components can be organized according to elementary thermodynamic cycles (this is, however, out of the scope of this paper). In this subproblem, the section of the system in which heat transfers occur is seen as an undefined "black-box";
- The second is about the configuration of the heat transfer section only, that is the configuration of the heat exchanger network inside the black-box. The thermodynamic conditions at the boundary of this black-box are those of the thermal streams involved in the heat transfer and have already been evaluated in the previous subproblem.

So, the preliminary concept about the energy conversion system is first translated into a basic plant configuration, which is defined by the essential components and their links. These links are then cut from the thermal point of view only, that is the temperature at the inlet of a basic component is made independent from that at the outlet of the preceding component. In this way, the heat transfer section of the system is isolated from the basic plant configuration, and the potential thermal streams (hot and cold) that interact within the black-box are generated. Of course, the additional degrees of freedom introduced by these thermal cuts correspond to new decision variables in the design optimization of the basic plant configuration.

In this work, the considered single pressure level ORC has a very simple basic plant configuration (Fig. 1), which is the only possible one and is made of two basic components only (the feed pump and the turbine) and three thermal cuts. In the first thermal cut the brine is cooled from its initial temperature down to 70°C (both these temperatures are given, so no additional degree of freedom is generated by this cut), in the second one the operating fluid is heated from pump outlet temperature up to turbine inlet temperature (i.e. cycle maximum temperature, which has to be considered as a the decision variables of the design optimization problem), and, finally, in the third one the operating fluid is cooled from turbine outlet temperature down to pump inlet temperature (this temperature is strictly related to condensation pressure, so the latter quantity is included in the set of the decision variables instead of the former).

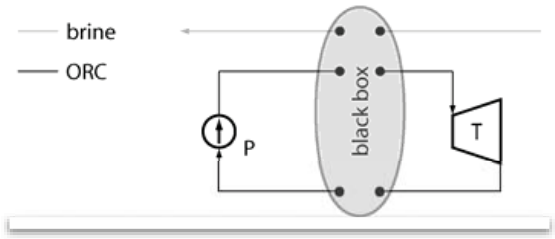

Fig. 1. Basic plant configuration of the single pressure level ORC.

As mentioned before, the configuration of the heat transfer section is not included in the basic plant configuration, so that the search space of the possible basic plant configurations and the associated design variables can be explored more freely, provided that the feasibility of the heat transfer within the black-box has to be checked. This is one of the main advantages of the HEATSEP method: the design optimization of the basic plant configuration is not performed using a model that takes into account all the possible configurations of the heat transfer section, or embeds them in a superstructure (this would then require mixed-integer programming techniques to select the units to be included in the plant configuration).

In the considered single pressure level ORC, significant alternatives must be considered in the

definition of the heat transfer section although the black-box encloses three thermal streams only:

- The heat transfer between the brine and the organic fluid can be operated by means of one, two or three devices according to cycle maximum pressure and temperature (just one heat exchanger if the cycle is supercritical, two or three if the cycle is subcritical and saturated or superheated vapor enters the turbine, respectively);
- A regenerator is required when the thermal energy that is needed to heat the operating fluid between pump outlet and turbine inlet is greater than the thermal energy made available by the geothermal source.

Thanks to the HEATSEP method, the design optimization of the ORC cycle can leave aside these alternatives and concentrate on the most significant cycle parameters, as illustrated in the following section. The correct (or the most convenient) alternative will then be determined according to the results of the design optimization itself.

2.2. The optimization problem

A single pressure level ORC is used to generate power from a low-temperature geothermal source of given characteristics. The brine has a reference mass flow rate of 100kg/s, a pressure of 15bar and its input temperature is varied in the range between 130°C and 180°C at steps of 10°C. Brine heat can be exploited until a minimum temperature (70°C) is reached: below that limit the brine must be re-injected into the well to avoid silica precipitation. Two operating fluids are considered, isobutane and R134a, which provide a suitable matching of the temperature profiles in that range. The efficiencies of the turbomachinery are fixed (η_P=0.70, η_T=0.85), and so is the efficiency of the generator (η_{gen}=0.96). Ambient air at 20°C is used as cold utility in an air cooled condenser (ACC). Air outlet temperature is imposed to be 5°C below the condensation temperature of the organic fluid, and the air mass flow rate is obtained from this condition. The power absorbed by ACC fans is assumed to be proportional to the air mass flow rate that is needed for condensation (0.15kW per kg/s of air).

Four decision variables are required to evaluate all the remaining dependent quantities of the model:

- the condensation pressure (p_{cond});
- the mass flow rate of the organic fluid (W_{ORC});
- cycle maximum pressure (p_{max});
- the degree of superheating, measured in terms of entropy (Δs_{sup}). This quantity has been preferred to cycle maximum temperature so that super- and subcritical cycles can be treated in the same way. The degree of superheating is measured from the entropy of the point on saturated vapor curve for subcritical cycles and from the entropy of the critical point for supercritical cycles.

The objective function to be maximized is the exergy recovery efficiency ζ_{rec} (1), that is the ratio between the net power generated by the plant (the power generated in the generator minus the power absorbed by the feed pump and ACC fans) and the exergy flow rate made available by the brine from its initial temperature down to 70°C: since the denominator of the ratio is constant, this is equivalent to the maximization of the net power generated by the plant.

$$\zeta_{rec} = \frac{P_{gen} - P_P - P_{ACC}}{\dot{E}_b(T_{b,in}) - \dot{E}_b(T = 70°C)} \quad (1)$$

For each set of values assigned to the four decision variables during the optimization process, heat transfer feasibility within the black-box is checked by building the Pinch Analysis Problem Table [19], with a minimum allowed temperature difference equal to 10°C. The hot composite curve (HCC, shown in red in Fig. 2) combines two of the three thermal streams generated by the cut of the thermal links (see Fig. 1), that is the brine cooled from its input temperature down to 70°C and the organic fluid cooled from turbine outlet to pump inlet. The cold composite curve (CCC, shown in blue in Fig. 2) simply consists of the third thermal stream, that is the organic fluid heated from pump outlet to turbine inlet. Since the specific heat at constant pressure radically changes during the transformation, the profile of this curve is discretized with eight points connected by linear segments (if the cycle is subcritical the 4th and the 5th point represent the beginning and the end of the evaporation, respectively).

The HCC comprises the only heat source in the system (brine), and other external hot utilities are not available: the HCC starts from the abscissa corresponding to the maximum temperature of the CCC in the temperature-thermal power diagram (Fig. 2) and must cover the entire load required by

the CCC. The thermal power in excess is released to a cold utility (the air flow in the ACC). The HTFC requires that the cumulated balance of thermal power has no deficit at any temperature level [19], that is the heat made available by the hot streams is always larger that the heat requested by the cold streams. The possible pinch points of the heat transfer process (i.e. the points in which the cumulated heat made available is strictly equal to the heat requested) are indicated in Fig. 2 with numbers from 1 to 8: note that these are also the points that are used to discretize the heating process of the organic fluid.

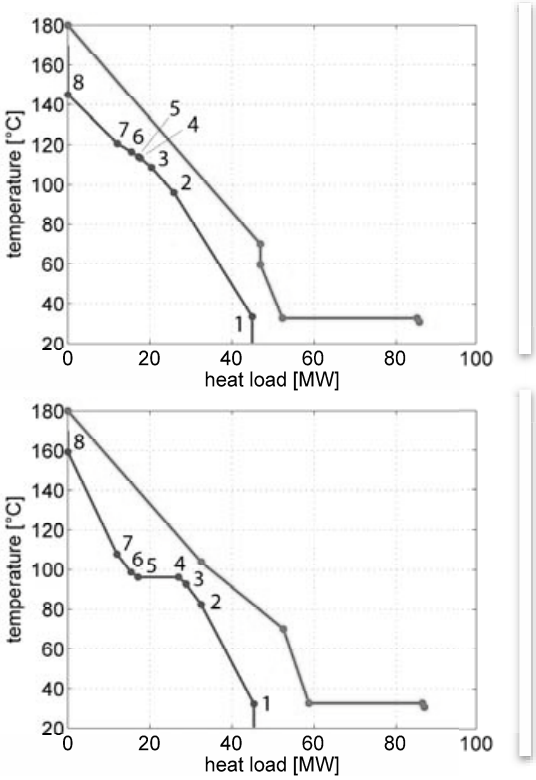

Fig. 2. Composite curve and discretization of the organic fluid heating in the supercritical (above) and subcritical (below) case.

The (de)activation of these possible pinch points generates non-smooth features on the optimum response surface (ORS) of the optimization problem, that is the surface that results from the mapping from a selected set of significant degrees of freedom (in this case, cycle maximum pressure and temperature) to the corresponding optimal objective function values. In fact, the feasibility region of the search space is enclosed by portions of different hypersurfaces that correspond to a particular active set of the inequalities that are used to express the HTFC, and when the frontier of the feasibility region is projected to the optimum response surface, its non-smooth features are transformed as well. Thus, in addition to the optimal solution, we consider here also the sub-optimal solutions in the neighbourhood in order to investigate how the HTFC acts on the objective function and see what happens to the composite curves when departing from the optimum.

2.3. Optimization tools

The model of the basic plant configuration was built in the MATLAB/Simulink environment (Fig. 3). The block diagram of the Simulink model is a straightforward translation of the scheme given in Fig. 1: the blocks named “pump” and “turbine” represent the basic components, whereas those named “brine cooler”, “ORC heater” and “ORC cooler” represent the three thermal cuts. The blocks of the latter group can be considered as cold or hot sides of heat exchangers, but the source of the absorbed heat or the destination of the released heat remains undefined. Organic fluid properties are evaluated by custom routines that interpolate the thermodynamic data provided by the NIST database [20]. Since the temperature profile of the organic fluid heating is discretized in linear segments, the model is able to deal with both super- and subcritical cycles.

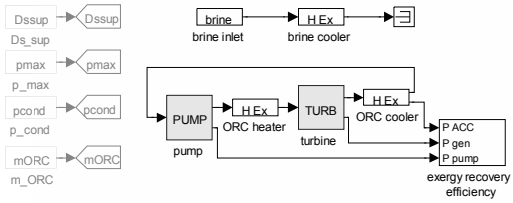

Fig. 3. The Simulink model of the basic plant configuration.

The optimization problem is solved with the sequential quadratic programming routines implemented in the MATLAB Optimization Toolbox. The optimization algorithm actually operates on p_{cond}, p_{max} and Δs_{sup}, while the fourth decision variable (W_{ORC}) is evaluated in order to maximize ζ_{rec} while satisfying the HTFC. This strategy avoids the evaluation of non-feasible solutions, because W_{ORC} is a variable that acts a linear transformation of the abscissas of the whole CCC in the temperature-heat load diagram.

3. Results

The optimal design parameters obtained at different brine inlet temperatures are summarized in Tables 1 and 2 for isobutane and R134a, respectively. Comparing the results obtained with the two different organic fluids it appears that the exergy recovery efficiency is always higher in R134a cycles, in particular at the lowest temperature of the geothermal source. R134a cycles are all supercritical (except for the case with 130°C brine) while most of the isobutane ones are saturated vapour subcritical cycles (in the case with 170°C brine the subcritical vapour is superheated and the cycle with 180°C brine is supercritical). Thanks to the thermophysical properties of the R134a and the better coupling of the thermal streams, in the supercritical cycles the higher power absorbed by the pump is largely compensated by the higher power generation.

Table 1. Optimal design parameters of the basic plant configuration using isobutane as ORC fluid.

isobutane						
$T_{b,in}$ [C°]	130	140	150	160	170	180
p_{cond} [bar]	4.375	4.345	4.376	4.376	4.396	4.381
p_{max} [bar]	14.27	15.16	18.85	23.11	35.24	44.19
$T_{T,in}$ [°C]	84.4	87.4	98.5	109.4	135.1	152.0
W_{ORC} [kg/s]	62.4	76.0	81.8	91.6	105.6	114.5
net power [kW]	1814	2344	2995	3792	5078	6045
ζ_{rec}	0.337	0.356	0.381	0.411	0.476	0.496
sub/supercritical	sub	sub	sub	sub	sub	super
superheated?	no	no	no	no	yes	-
regenerator?	no	yes	no	no	yes	yes
pinch point(s)	4	4	4	4	1,2,3	1,2

Table 2. Optimal design parameters of the basic plant configuration using R134a as ORC fluid.

R134a						
$T_{b,in}$ [C°]	130	140	150	160	170	180
p_{cond} [bar]	8.475	8.454	8.323	8.319	8.308	8.286
p_{max} [bar]	40.47	45.21	47.97	52.57	58.64	66.70
$T_{T,in}$ [°C]	104.4	118.5	129.4	139.4	149.3	159.3
W_{ORC} [kg/s]	138.2	145.0	159.5	177.4	195.0	212.1
net power [kW]	2090	2738	3498	4310	5165	6063
ζ_{rec}	0.388	0.416	0.445	0.467	0.484	0.498
sub/supercritical	sub	super	super	super	super	super
superheated?	yes	-	-	-	-	-
regenerator?	no	no	yes	yes	yes	yes
Pinch point(s)	1,2,3	1,2,3	1,2,3	1,2,3	1,2,3	1,2,3

Figures 4 and 5 show the ORS of the optimization problem as a function of pressure and specific enthalpy of the organic fluid at turbine inlet in two representative cases in which the input temperature of the brine is 150°C and isobutane (subcritical) or R134a (supercritical) are considered, respectively. In these figures, the maximum of the exergy recovery efficiency, that is the result of the optimization process, is shown as a white circle, the saturation curves that enclose the two-phase zone are represented with a thick red curve at the base of the diagram and a thick black isothermal curve at base of diagram indicates the upper limit to the heating of the organic fluid (if this line were passed, the difference between brine inlet temperature and organic fluid maximum temperature would be less than 10°C, violating the HTFC). The diagrams also show in which portions of the ORS the possible pinch points related to the HTFC are active: the numbers that identify ORS portions refer to the points used to discretize the CCC (see Fig. 2).

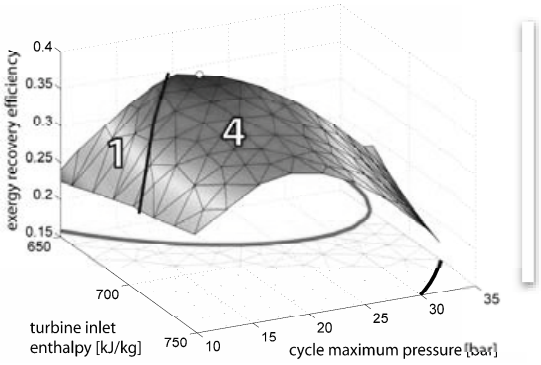

Fig. 4. ORS obtained with subcritical cycles (isobutane, brine input temperature 150°C).

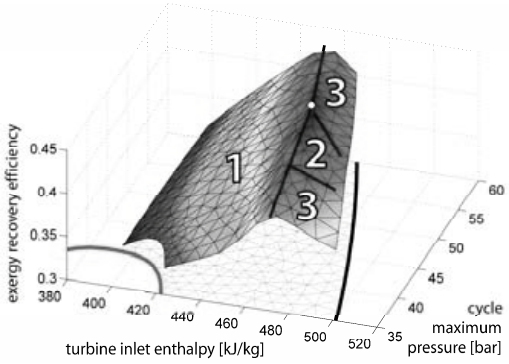

Fig. 5. ORS obtained with supercritical cycles (R134a, brine input temperature 150°C).

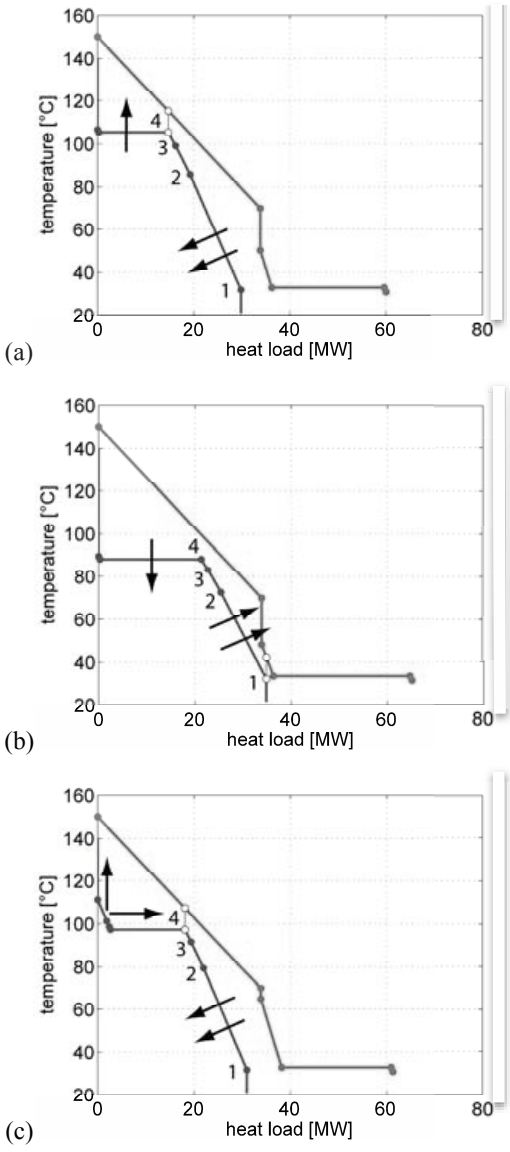

Fig. 6. Transformations of the composite curves in the neighborhood of the optimal solution (isobutane, brine input temperature 150°C).

On the sharp edges shared by two or more portions, drawn with continuous black lines, two or more pinch points are simultaneously active. For instance, in the subcritical case (Fig. 4), on the edge shared by the zones "1" and "4" two pinch points are simultaneously active at pump outlet and at the beginning of the evaporation. On the other hand, in the supercritical case (Fig. 5), the vertices shared by the zones "1", "2" and "3" correspond to three pinch points that are simultaneously active, one at pump outlet and two along the heating curve (this effect is obviously due to the discretization of the heating curve with a series of linear segments).

What happens in the neighbourhood of the optimal solution strongly depends on cycle maximum pressure. In the case shown in Fig. 4, which is representative of subcritcal cycles, the shape of the ORS can be explained by the following facts:

- The maximum ζ_{rec} is obtained for saturated vapour conditions at turbine inlet and the only active pinch point is at the beginning of the evaporation (point 4).
- If p_{max} is increased (Fig. 6a), the resulting increase of the evaporation temperature causes a decrease of the organic fluid mass flow rate to avoid a deficit of available heat at that temperature level. The heat made available by the geothermal source is only partially exploited and, in spite of the higher temperature at turbine inlet, a lower net power is generated.
- If p_{max} is decreased (Fig. 6b), the pinch point at the beginning of the evaporation is deactivated and the one at regenerator inlet is activated instead (point 1). ORC mass flow rate can be increased but the decrease of evaporation temperature results in a decrease of the exergy content of the organic fluid and in a reduction of net power generation.
- In case of superheating (Fig. 6c), the specific exergy of the organic fluid at turbine inlet increases, but the shift of the isothermal segment of the CCC towards the HCC imposes a reduction of ORC mass flow rate, which in turn results in a partial usage of the geothermal source and a consequent reduction of the exergy recovery efficiency.

In the case shown in Fig. 5, which is representative of supercritcal cycles, the shape of the ORS can be explained by the following facts:

- If cycle maximum temperature is lowered while p_{max} is kept constant (Fig. 7a), the CCC "rotates" counter-clockwise in the temperature-heat load diagram so that ORC mass flow rate can be increased, the active pinch point being still at pump outlet (point 1). Although the heat transferred to organic fluid increases, the exergy content of the organic fluid at turbine inlet diminishes because of the lower temperature, and the exergy recovery coefficient is lower.

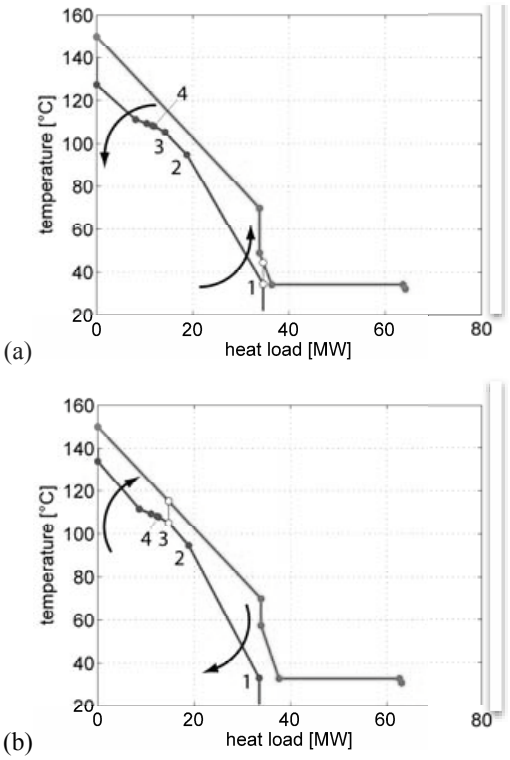

Fig. 7. Transformations of the composite curves in the neighborhood of the optimal solution (R134a, brine input temperature 150°C).

- On the contrary, if cycle maximum temperature is raised while p_{max} is kept constant (Fig. 7b), the CCC "rotates" clockwise so that ORC mass flow rate has to decrease and the active pinch point is found along the heating profile (points 2 and/or 3). In spite of the higher specific exergy of the fluid at turbine inlet, the lower mass flow rate makes the exergy recovery coefficient decrease.
- Along the edge shared by zones "1" and "2" or "1" and "3" in Fig. 5 (where two corresponding pinch points are simultaneously active) the exergy recovery efficiency is not very sensitive to the variation of p_{max}. This is due to the substantial equilibrium between the differences in the power absorbed by the pumps and those in the power generated by the turbine.

4. Conclusions

The HEATSEP Method allows the designer to draw the configuration of the heat transfer section independently of the configuration of the rest of the system (that is called "basic" plant configuration). The paper shows that:

- Even if the basic plant configuration is extremely simple, (here a Rankine cycle including two "basic" components only: a pump and a turbine), various design options exist for the heat transfer section, which may include a regenerator, a superheater, subcritical or supercritical evaporation. However, according to the HEATSEP method all these options are considered using the only plant model associated with the basic plant configuration (in which the thermal interactions appear in terms of heat and cold thermal streams only) with considerable saving in terms of calculation time.
- This plant model allowed us to generated easily the complete exergy recovery coefficient Optimum Response Surface (ORS) for different values of the brine input temperature, which shows not only the optima but also sub-optimal points. These points become of high interest when economic evaluations are performed which may suggest minor thermodynamic penalties at the advantage of important economic savings.
- The use of R134a results in higher exergy recovery coefficients for all the brine input temperatures considered in this analysis (130°C-180°C). R134a optimal cycles are all supercritical except for the lowest brine input temperature (130°C), while most of the isobutane ones are saturated vapour subcritical cycles (when brine input temperature is 170°C the subcritical vapour is superheated, whereas the optimal cycle becomes supercritical when this temperature is 180°C).

Nomenclature

$\dot{E}$	exergy flow rate, kW
p	pressure, bar
P	power, kW
s	specific entropy, kJ/(kg K)
T	temperature, °C
W	mass flow rate, kg/s

Greek symbols

η	efficiency
ζ_{rec}	exergy recovery coefficient

Subscripts and superscripts

ACC	air cooled condenser

b brine
cond condensation
gen generator
in inlet
max cycle maximum
net net
ORC organic Rankine cycle
P pump
sup superheating
T turbine

References

[1] Badr, O., Probert, S. D., and O'Callaghan, P. W., 1985, Selecting a Working Fluid for a Rankine-Cycle Engine, Applied Energy, 21(1), pp. 1-42.

[2] Hung, T. C., Shai, T. Y., and Wang S. K., 1997, A Review of Organic Rankine Cycles (ORCs) for the Recovery of Low-Grade Waste Heat, Energy, 22(7), pp. 661-667.

[3] Maizza, V., and Maizza, A., 2001, Unconventional Working Fluids in Organic Rankine Cycles for Waste Energy Recovery Systems, Applied Thermal Engineering, 21, pp. 381-390.

[4] Salehl, B., et al., 2007, Working Fluids for Low-Temperature Organic Rankine Cycles, Energy, 32, pp. 1210-1221.

[5] Tchance, B. F., 2009, Fluid Selection for a Low-Temperature Solar Organic Rankine Cycle, Applied Thermal Engineering, 29, pp. 2468–2476.

[6] Borsukiewicz-Gozdur, A., and Nowak, W., 2007, Comparative Analysis of Natural and Synthetic Refrigerants in Application to Low Temperature Clausius–Rankine Cycle, Energy, 32, pp. 344-352.

[7] Liu, B.-T., Chen, K.-H., and Wang, C.-C., 2004, Effect of Working Fluids on Organic Rankine Cycle for Waste Heat Recovery, Energy, 29, pp.1207-1217.

[8] Wei, D., et al., 2007, Performance Analysis and Optimization of Organic Rankine Cycle (ORC) for Waste Heat Recovery, Energy Conversion and Management, 48, pp. 1113–1119.

[9] Schuster, A., Karellas, S., and Aumann, R., 2010, Efficiency Optimization Potential in Supercritical Organic Rankine Cycles, Energy, 35, pp. 1033-1039.

[10] Chen, Y., et al., 2006, A Comparative Study of the Carbon Dioxide Transcritical Power Cycle Compared with an Organic Rankine Cycle with R123 as Working fluid in Waste Heat Recovery, Applied Thermal Engineering, 26, pp. 2142–2147.

[11] Angelino, G., and Colonna di Paliano, P., 1998, Multicomponent Working Fluids for Organic Rankine Cycles (ORCs), Energy, 23, pp. 449-463.

[12] DiPippo, R., 2005, *Geothermal Power Plants: Principles, Application and Case Studies*, Elsevier, New York.

[13] Kalina, A. I., 1984, Combined Cycle System with Novel Bottoming Cycle, Journal of Engineering for Gas Turbines and Power, 106(4), pp.737-742.

[14] Drescher, U., and Bruggemann, D., 2007, Fluid Selection for the Organic Rankine Cycle (ORC) in Biomass Power and Heat Plants, Applied Thermal Engineering, 27, pp. 223–228.

[15] Schuster, A., et al., 2009, Energetic and Economic Investigation of Organic Rankine Cycle Applications, Applied Thermal Engineering, 29, pp. 1809–1817.

[16] Madhawa Hettiarachchia, H. D., et al., 2007, Optimum Design Criteria for an Organic Rankine Cycle Using Low-Temperature Geothermal Heat Sources, Energy, 32, pp. 1698-1706.

[17] Lazzaretto, A., and Toffolo, A., 2008, A Method to Separate the Problem of Heat Transfer Interactions in the Synthesis of Thermal System, Energy, 33, pp. 163-170.

[18] Toffolo, A., Lazzaretto, A., and Morandin, M., 2009, The HEATSEP Method for the Synthesis of Thermal Systems: an Application to the S-Graz Cycle, Energy, In press.

[19] Kemp, I. C., 2007, *Pinch analysis and process integration* (2nd ed.), Butterworth-Heinemann, London.

[20] http://webbook.nist.gov/chemistry/fluid/.

Process Design and Life Cycle Analysis of a Lignocellulosic Bioethanol Process: Comparing Pretreatment Options

Anne-Laure Cuvilliez [a], Jeremy S. Luterbacher [b], Martin Gassner [a], François Maréchal [a] and Larry P. Walker [b]

[a] *Industrial Energy Systems Laboratory, Ecole Polytechnique Fédérale de Lausanne, Switzerland*
[b] *Biofuels Reasearch Laboratory, Cornell University, Ithaca,NY, USA*

Abstract: During the conversion of biomass to ethanol, the pretreatment step is crucial for allowing cellulose accessibility to hydrolytic enzymes by partially deconstructing hemicellulose and lignin. This step is an important bottleneck in the ethanol production system: it can have high energy or chemical inputs, degrade sugars and produce fermentation inhibitors. All these issues are linked, directly or indirectly, to safety and environmental concerns and should be investigated from a life cycle perspective.
The environmental impacts of systems using dilute acid, hot water, steam explosion, AFEX and biphasic CO2-water pretreatment are calculated and compared using life cycle assessment tools. Pretreatment processes have been modeled using Belsim Vali® modeling software. Energy integration is performed for the five models using software developed in the LENI laboratory (École Polytechnique Fédérale de Lausanne, Switzerland). A Matlab LCA interface is used to assess environmental impacts using the Ecoinvent® database and the Impact 2002+ aggregation method. This allows us to compare the influence of pretreatment choices on the life cycle performance of a lignocellulosic biorefinery. Initial results show that the process parameters having the most influence on environmental impacts are: the use of chemical products and biomass dilution during pretreatment, enzymatic hydrolysis and fermentation. These results justify and guide the experimental development of a high pressure CO2-H2O pretreatment technology developed at Cornell University, which can offer high yields using no additional chemicals and high solid contents.

Keywords: Biofuel, Life Cycle Analysis, Lignocellulosic Ethanol, Pretreatment.

Nomenclature

Q volumetric flow, m^3/s
μ growth factor, /s
μ_m maximum growth factor, /s
S substrate concentration, g/L
P product concentration, g/L
P_m maximum product concentration, g/L
K_s saturation constant, g/L
K_i inhibition constant, g/L

1. Introduction

During the last century, the extensive use of fossil resources has led to concerns about oil reserve depletion [1] and increased extraction costs [2]. In addition, the threat of global warming linked to the burning of fossil fuel and its associated greenhouse gas emission has created a demand for sustainable fuels. [3].

Second generation biofuels, such as ethanol, are interesting since they allow the use of lignocellulosic plants that are not destined for food production [4]. Moreover, any CO_2 emitted during combustion had been previously removed from the atmosphere during growth [5]. Hence, no net amount of carbon is emitted to the atmosphere.

However, the pretreatment step of the process of converting lignocellulosic biomass to ethanol has been identified as one of the process's bottlenecks, since it can dramatically affect the rest of the process [6]. Several alternative technologies are currently being studied and optimized to maximize the efficiency of pretreatment [7-14].

Life Cycle Analysis (LCA) is increasingly used to compare different technological scenarios and assess their environmental impact [15]. Many LCA studies have assessed the sustainability of biofuel productions methods [16-18] and pretreatment technologies [19]. However, energy efficiency is critical in processes that use high

Corresponding Author: Larry Walker, Email: lpw1@Cornell.edu

temperature and pressure, but is often ignored in such studies.

This study presents and applies a methodology that combines the use of energy integration and LCA. Energy integration methods have been developed at the LENI (Industrial Energy Systems Laboratory) Laboratory, EPFL, Switzerland, which allow the computation of the process's minimum energy requirement [20]. This methodology is used to compare hot water, dilute acid, catalyzed and uncatalyzed steam explosion, AFEX and biphasic CO_2-Water pretreatment technologies in the context of ethanol production from lignocellulosic biomass.

2. Methodology

2.1. Flow sheet modeling

The processes are modeled using the Belsim-Vali® flowsheet modeling software [21]. Known temperatures, pressures and mass flows are entered as parameters.

The software performs mass and energy balances for all the flows going through the system. It also gives access to technical parameters such as volumetric flows or mechanical energy that allow for equipment sizing.

Reaction kinetics are not taken into account in the flow sheet modelling. Only the extent of the reaction through the conversion is modelled.

2.2. System Integration

A method described by Gassner et al. [22] and Luterbacher et al. [23] is applied for modeling and system integration. All process heat requirements are extracted from the flow sheet model and are fed into the energy-integration software, which computes the optimal heat and power production using heat cascade constraints and optimal utility integration calculation [20].

2.3. Life Cycle Analysis

Data extracted from the system model forms the core of a larger life cycle inventory model built in a Matlab® environment [24]. The Ecoinvent® database [25] is used to provide inventory data for all the system inputs, emissions and equipments. The equipment impacts vary in function of its size, through correlations, which have been defined by Gerber et al. [26].

Two methods are used for impact analysis: Impact 2002+ for human health and CML2001 for the GWP100a. Impact 2002+ method links all types of life cycle inventory results via 14 midpoint categories (expressed in a reference substance equivalent quantity) to four damage categories: human health, resources, climate change and ecosystems quality, expressed in points [27]. CML 2001 method only aggregates emissions in midpoints, which are classified in 3 groups of impact categories (baseline, study-specific, and other impact categories) [28].

3. Modeling

3.1. Life cycle Assessment of the non-pretreatment model

The ethanol conversion process and its associated energy integration models were based on a previous study by Zhang et al. [29].

The modeled reactions are cellulose (1) and hemicellulose (2) hydrolysis, glucose (3) and xylose fermentation (4) and pretreatment liquor neutralization (5).

$$C_6H_{10}O_5 + H_2O = C_6H_{12}O_6 \quad (1)$$

$$C_5H_{10}O_4 + H_2O + A^{2+} = C_5H_{10}O_5 + A + 2H^+ \quad (2)$$

$$C_6H_{12}O_6 = 2C_2H_5OH + 2CO_2 \quad (3)$$

$$3C_5H_{10}O_5 = 5C_2H_5OH + 3CO_2 \quad (4)$$

$$CaO + H^+ = Ca^{2+} + OH^- \quad (5)$$

The modifications performed on this model are listed below:

- The double dilute acid hydrolysis had been replaced by an enzymatic hydrolysis at 323.15 K.
- The enzymatic conversion reactors modeled in [29] were conserved but the temperature and conversion were changed accordingly to the performance of each pretreatment.

An evaluation of the impact of enzyme fabrication was based on Nielsen et al. [30] since no data was available in the Ecoinvent database.

All reactors and equipments are sized in order to account for the environmental impact of their constitutive materials.

The sizing of the enzymatic reactors is based on the residence time of 48 hr, on estimate. The sizing of fermentation reactors is based on the following equations [31]:

$$V = \frac{Q}{\mu} = Q\left\{\frac{\mu_m S}{K_S + S + \frac{S^2}{K_i}\left(1 - \left(\frac{P}{P_m}\right)^{\beta}\right)}\right\}^{-1}$$

The separators sizing was based on Perry's Chemical Engineers' Handbook [32] and manufacturer's data. Columns diameters were calculated using the method described by Copigneaux. [33].

The impact of hardwood harvesting and transport in Switzerland was modeled using the method described by Gerber et al. [26]. Wood harvesting and forest management is assumed not to deplete the forest carbon stock. Corn stover was considered to be a co-product of corn grain production, and the harvest was considered to be simultaneous with corn grain harvest. All the impacts of corn stover production were allocated to corn grain production, because we consider that the produced corn quantity is uncorrelated with corn stover demand. The storage impacts were neglected. Hence, the only impact modeled is corn stover transport to the plant.

3.2. Lignin treatment model

The model described by Zhang et al. in [29] used lignin drying and subsequent combustion to meet the process heat requirements, and producing SNG through lignin gasification.

In this study, catalytic hydrothermal gasification is used to produce Synthetic Natural Gas (SNG) from lignin [34], which was previously modeled and assessed through life cycle analysis by Luterbacher et al. [23].

3.3. Pretreatment stage modeling

In order to compare the pretreatment systems, models of pretreatment technologies have been included in a superstructure that included the following technologies.

3.3.1. Flow sheet modeling

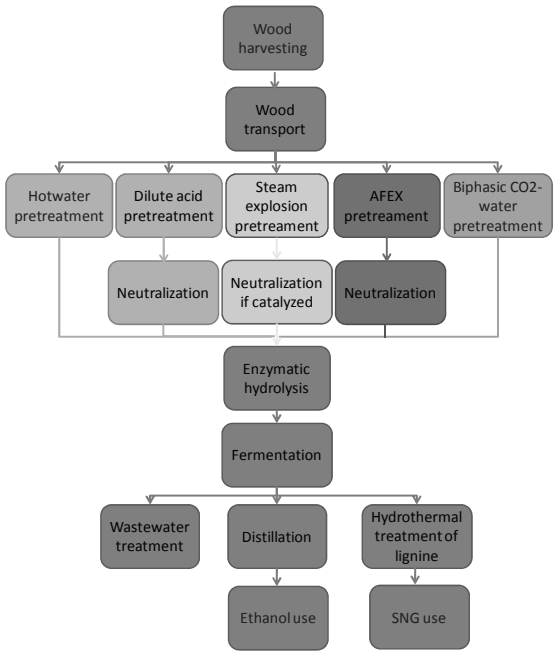

Fig.1 Flowsheet of the modelled process

The following pretreatments have been modeled:

- dilute acid [7-8] : biomass is mixed with water and sulfuric acid at high temperature (160-190°C, 7-13 bar, 1.96%-2% H_2SO_4) for a residence time of 1.1 to 20 minutes.
- hotwater [9-10]: biomass is mixed with water at high temperature and pressure is used to maintain water liquid (190-200°C, 13-16 bar) for a residence time of 10 to 15 minutes.
- catalyzed and uncatalyzed steam explosion[9,11]: biomass is heated by high pressure steam (mixed with a catalyzer if catalysed) at high temperature and pressure for a residence time of 5 minutes followed by an explosive decompression.(190°C, 12.6 bar, 0%-3% SO_2)
- AFEX [9,12-13] : a 1:1 water ammonia solution is mixed with biomass at high temperature and high pressure (90-180°C,

15-47 bar) for a residence time of 5 minutes.

- Biphasic CO_2-Water [14]: biomass is mixed with CO_2 and Water at high temperature and pressure (160-170°C, 200 bar, 250% CO_2) for a residence time of 1 hour.

3.3.2. Energy Integration

Energy integration mainly affects heat recovery and utility integration. Integration of the ethanol conversion and hydrothermal processes was performed with the pretreatment process.

Two energy recycling options were explored. The first uses heat pumps to recover low-grade heat from certain parts of the process to produce electricity, while the second does not.

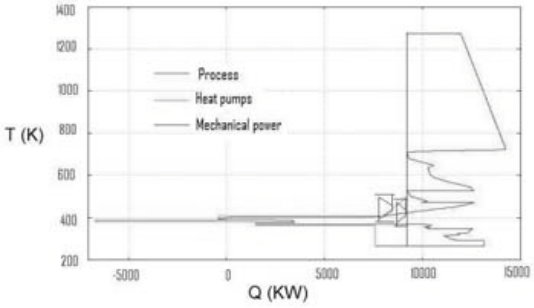

Fig.2 Example of Composite Curve

Fig. 2 shows the utility integrated composite curve for option 1. The red curve represents the requirements of the integrated process. For example the COP of the heat pump integrated in Fig. 2 would be around 4.5. The exergy analysis is not the most important analysis at this stage of the study, the analysis of the process integration [29] is in fact the next step of the analysis. An energy balance, as shown on Fig. 3, can also be produced.

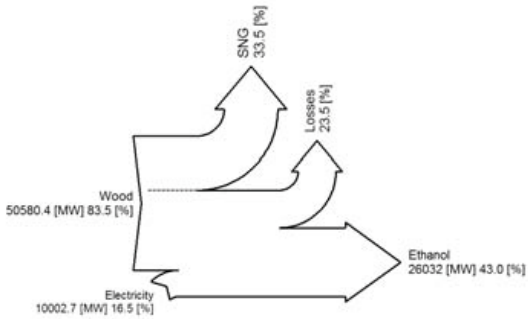

Fig.3 Example of energy balance [35]

3.3.3. Life Cycle Analysis

The Functional unit is a km-driven by a van <3.5 tons defined in Ecoinvent database [25]. Utilization phase of SNG is also considered.

The pretreatment reactor volumes are calculated based on their entering mass flow and the residence time. Since the dimension of the reactor was less than 60 m^3, only one reactor was considered for the pretreatment stage. Shape of the reactor can also be critical in term of material requirements. However, this parameter was not taken into account, since the experimental apparatus described in the literature would be very different from the one implemented in reality. Hence, the reactor shape was assumed to be cylindrical, with the height equal to three times the diameter.

Impacts of chemicals used during pretreatment are also considered. The quantities required were found in the literature cited above for each relevant pretreatment technology.

Neutralization of acids used in the different processes (H_2SO_4, SO_2) was taken in account. However, buffering of enzymatic hydrolysis was neglected in each pretreatment model.

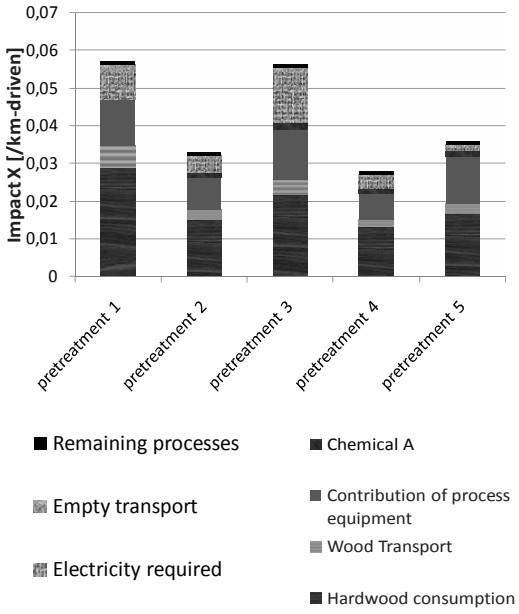

Fig.4 Example of graphic of impacts obtained by the use of method described above

4. Conclusion

Process parameters controlled by the pretreatment stage can have an important influence on the environmental impact of the whole system. Most importantly, dilution and the use of chemicals during pretreatment, hydrolysis and fermentation hugely affect our results.

Therefore pretreatment is a critical step of lignocellulosic ethanol production. In order to achieve sustainable and economically viable pretreatment technologies, tools must be developed to compare them on a common basis. Life cycle analysis allows this type of comparison and offers a design tool that highlights the critical parameters of each pretreatment technology. These parameters can be chosen as degrees of freedom in a further process optimization. In parallel, the use of energy integration is essential in order to study a process with systematically optimized heat and power production.

References

[1] Bentley, R.W., 2002, Global oil & gas depletion: an overview, Energy Policy, 30(3) : pp. 189-205

[2] EIA, (Energy Information Administration), 2009, Petroleum basic Statistics updated in February 2009, Department of Energy, Washington, D.C.

[3] Croezen H. and Kampman, B., 2009, Energy Policy, 37(12), pp. 5226-5238

[4] Naik, S.N. et al., 2010, Production of first and second generation biofuels: A comprehensive review, Renewable and Sustainable Energy Reviews, 14(2), pp. 578-597

[5] Osamu, K. , et al.,1989, Biomass Handbook, Gordon Breach Science Publisher

[6] Zhua, J.Y. , and Pan, X.J., 2009, Woody biomass pretreatment for cellulosic ethanol production: Technology and energy consumption evaluation, Bioresource Technology, In Press

[7] Luterbacher,J.S., Tester, J.W., and Walker, L.P., High-solids biphasic CO2-H2O pretreatment of lignocellulosic biomass, Biotechnology & Bioengineering, Submitted

[8] Todd A. Lloyd and Charles E. Wyman, 2005, Combined sugar yields for dilute sulfuric acid pretreatment of corn stover followed by enzymatic hydrolysis of the remaining solids, Bioresource Technology, 96(18), pp. 1967-1977

[9] Kumar, R., et al.,2009, Physical and chemical characterizations of corn stover and poplar solids resulting from leading pretreatment technologies, Bioresource Technology, 100(17), pp. 3948-3962

[10] Mosier, N., et al., 2005, Features of promising technologies for pretreatment of lignocellulosic biomass, Bioresource Technology, 96(6), pp. 673-686

[11] Kim, Y., 2008, Enzyme hydrolysis and ethanol fermentation of liquid hot water and AFEX pretreated distillers' grains at high-solids loadings, Bioresource Technology, 99(12), August 2008, Pages 5206-5215

[12] Bura, R., Chandra , R., Saddler, J., 2009, Influence of xylan on the enzymatic hydrolysis of steam-pretreated corn stover and hybrid poplar, Biotechnology Progress, 25(2), pp. 315 – 322

[13] Teymouri, F., 2005, Optimization of the ammonia fiber explosion (AFEX) treatment parameters for enzymatic hydrolysis of corn stover, Bioresource Technology, 96(18), pp. 2014-2018

[14] da Costa Sousa, L., 2009, 'Cradle-to-grave' assessment of existing lignocellulose pretreatment technologies, Current Opinion in Biotechnology, 20(3), pp. 339-347

[15] Lund, C. and Biswas, W., 2008, A Review of the Application of Lifecycle Analysis to Renewable Energy Systems, Bulletin of Science Technology Society, 28, pp. 200-209

[16] Reinhardt,G., et al., 2004, Comparison of well-to-wheel analyses of biofuels for transportation, Proceedings from: world conference and technology exhibition on biomass for energy, industry and climate protection Rome, Italy (2004).

[17] Kim, S., and Dale, B.E., 2005, Life cycle assessment of various cropping systems utilized for producing biofuels: bioethanol and biodiesel, *Biomass Bioenergy* 29, pp. 426–439.

[18] Gnansounou, E., 2009, Life cycle assessment of biofuels: Energy and greenhouse gas

balances, Bioresource Technology,100(21), pp. 4919-4930

[19] MacLean, H. and Spatari, S., 2008, The contribution of enzymes and process chemicals to the life cycle of ethanol, Environmental Research Letter, 4(10)

[20] Maréchal, F.; Kalitventzeff, B., 1996, Targeting the minimum cost of energy requirements: A new graphical technique for evaluating the integration of utility systems, Comput. Chem. Eng.

[21] Belsim, 2004, ValiModeller version 4.4.0.1, Belsim SA, Awans, Belgium

[22] Gassner, M., Maréchal, F., 2008, Thermo-economic optimization of the integration of electrolysis in synthetic natural gas production from wood, Energy, 33(2), pp. 189-198

[23] Luterbacher, JS, 2009, Hydrothermal Gasification of Waste Biomass: Process Design and Life Cycle Assessment , Environ. Sci. Techno, 43 (5), pp. 1578–1583

[24] Matlab, 2009, version 7.9.0.529, Mathworks Inc., Natick, MA,USA

[25] Frischknecht, R., et al., 2007, Overview and Methodology. Final report ecoinvent data v2.0, No. 1. Swiss Centre for Life Cycle Inventories, Dübendorf, CH.

[26] Gerber, L., Gassner, M., Maréchal, F., 2009, Integration of LCA in a thermo-economic model for multi-objective process optimization of SNG production from woody biomass In: Proceedings of the 19th European Symposium on Computer Aided Process Engineering, Cracow, June 14-17, 2009.

[27] Jolliet, O., et al., 2003, IMPACT 2002+: A new life cycle impact assessment methodology, The International Journal of Life Cycle Assessment, 8(6), pp. 324-330

[28] Guinée, JB, et al., 2001, Life Cycle Assessment; An Operational Guide to the ISO Standards; Final Report, May 2001, Ministry of Housing, Spatial Planning and Environment (VROM) and Centrum voor Milieukunde (CML), Rijksuniversiteit Den Haag and Leiden

[29] Zhang, S., et al., 2009, Process Modeling and Integration of Fuel Ethanol Production from Lignocellulosic Biomass Based on Double Acid Hydrolysis. Energy & Fuels, 23(3): pp. 1759-1765

[30] Nielsen, P., Oxenbøll, K., and Wenzel, H., 2007, Cradle-to-gate environmental assessment of enzyme products produced industrially in Denmark by Novozymes A/S, The International Journal of Life Cycle Assessment, 12(6), pp. 432-438.

[31] Krishnan, M., Ho, N., and Tsao, G., 1999, Fermentation kinetics of ethanol production from glucose and xylose by recombinant Saccharomyces 1400(pLNH33), Applied Biochemistry and Biotechnology, 78, pp. 373-388

[32] Perry, R.H., Perry's Chemical Engineers' Handbook 7th ed. 1997: McGraw-Hill

[33] Copigneaux, P.,2001, Distillation. Absorption - Colonnes garnies, Techniques de l'ingénieur Vol. 2J2610, pp. 1-20.

[34] Vogel, F., et al., 2007, Synthetic natural gas from biomass by catalytic conversion in supercritical water, Green Chem., 9(6), pp. 616-619

[35] DrawSankey,Matlab, Current Version: 02.11.2009 , developed by: James Spelling, KTH-EGI-EKV

Statistical Wind Data Analysis and Energy Prediction of Onshore Wind Farms in Greece

Eleni Ioannou[a], Christos Chourpouliadis[a], Vassiliki Katsirou[a],

Andreas Koras[b] and Anestis I. Kalfas[a]

[a]*Department of Mechanical Engineering, Aristotle University of Thessaloniki, GR 54124 Thessaloniki, Greece*
[b]*Hellenic Air Force Academy, Dekeleia, GR 1010 Athens, Greece*

Abstract: This paper presents the study of wind data analysis in Greece for power generation, coupled with the large interconnected network, as a result of the recent global request for clean energy as well as the rapid increase of the wind energy total capacity in the European Union. Since the energy production of a wind farm depends on wind flow, which is intermittent, the study presents the meteorological potential in two different locations in Greece and concentrates on the problem of the annual variability of wind speed. Numerical prediction tools are used, which are designed to facilitate accurate predictions of wind farm energy production, using the WAsP model. Furthermore, the Weibull distribution is used to describe wind speed distributions, estimating the shape (k) and scale factor (c), which represents the average wind speed. Finally, via the simulation of the operation of two wind farms using actual wind input data by the regions of interest, emerged the important points of the operation, which are the wind speed frequency and direction, the turbulence intensity, the annual energy production including the wake losses, as well as the wind parks' capacity factors.

Keywords: Wind energy, Weibull distribution, WAsP model, Energy prediction.

1. Introduction

The use of clean energy technologies has increased greatly over the past several decades. Clean energy technologies consist of renewable energy technologies which reduce the use of "conventional" sources, such as fossil fuels. This increasing interest reflects a growing awareness of the environmental, economic and social benefits that these technologies offer [1]. Wind energy is an important cornerstone of a non-polluting and sustainable electricity supply. Due to favorable regulatory frameworks, this renewable energy source has experienced a tremendous growth in recent years, resulting in substantial shares of electricity produced by wind farms in the national energy mix of a number of countries [2]. For example, in the leading countries, until the end of 2004, Denmark meets 19% of its national electricity demand from wind power, while in Spain and Germany the percentages are 6 and 5%, respectively [3].

Europe has to invest in new capacity to replace ageing plants and meet future demand. In the period 2005-2030, the EU needs to install 862 GW of new electricity capacity [4]. 427 GW of generating capacity will be retired in the EU and an additional 435 GW will be needed to satisfy the growing demand for power. The required capacity exceeds the total capacity operating in Europe (723 GW). The re-emergence of the wind as a significant source of the world's energy must rank as one of the significant development of the 20th century [5]. The politics and economics of wind energy have played an important role in the development of the industry and contributed to its present success [6]. Wind energy delivers the energy security benefits of avoided fuel costs, long term fuel price risk as well as economic and supply risks that emerge from imported fuels and political dependence on other countries.

The EU continues to be the world's strongest market for wind energy development, with over 8,500 GW of new installed capacity in 2007 [7]. At present, much of the development of the wind power in Europe and elsewhere, takes place in complex and mountainous terrain, such as the landscapes found in certain parts of Greece, Portugal, Spain and United Kingdom. These sites

Corresponding Author: Eleni Ioannou, Email: ioannoueleni@hotmail.com

in elevated terrain often favor high wind resources because of the enhancement of the flow by the terrain features. [8] The mainland power supply system in Greece has a total installed conventional power capacity of 112,343.3 MW with a low wind power contribution (549.21 MW at the end of 2006) [9]. However, Greece has a large potential for wind power, with a unique geographical character. Surrounded by mountains, creates a regular airflow, while the location between the colder European and the warmer African systems causes a wide variety of temperature and climate difference.

In practice, the integration of wind energy into the existing electricity supply system is a real challenge, as one major disadvantage of wind energy is that its availability mainly depends on meteorological conditions. The power output of wind farms is determined by the prevailing wind speed and cannot be adjusted as conveniently as the electricity production of conventional power plants. Knowledge of the statistical properties of the wind speed is essential for predicting the energy output of a wind energy conversion system. Because of high variability in direction and time of wind energy, it is important to verify that the method of analysis being used on the measured wind data will yield the estimated energy collected that is close to the actual energy collected.

The numerous studies in different locations of the world have shown that the Weibull, two-parameters, distribution gives an excellent fit to the wind speed distribution. In Izmir (Turkey), Ozerdem and Turkeli found Weibull approximation very good [10], while in Sicily (Italy), Binova, Burlon and Leone, using the Weibull distribution exhibit the high variability of wind energy [11]. Also, in Japan, in Thessaloniki (Greece), in India and in Cyprus, the wind speed distribution is represented by the typical two-parameter Weibull function, showing the high variability of the wind energy in each location, [12-15], while in some specific locations the use of this widely recommended method leads to incorrect results, such as the case of La Ventosa in Mexico, where the frequency of the wind speed shows a bimodal distribution [16].

This study utilizes full-scale wind data from three meteorological masts in Greece, in order to carry out a statistical analysis of this data, for two different regions. A WAsP method uses the wind data and within the model, the measured directional wind speed distributions are described by Weibull function. Moreover, the average wind speed and the turbulence intensity are presented. Finally, the design of a wind farm in each region is studied, as well as the annual energy production and the capacity factors are estimated.

2. Measurements

Initially, the regions of wind interest are identified, based mainly on the wind map, which illustrates the wind potential at a local level (Fig.1). The wind and topographical data were collected from two Diplomatic Theses [17,18]. The first two meteorological masts, Mast 1 and Mast 2, are located in the mountains of Aitoloakarnania (Region A), in central Greece, while the third mast, Mast 3, is located in the mountainous area of Serres (Region B). The reference areas where identified and considered to be suitable because of there are no large town centres near these regions, while these locations are not characterized as wildlife and landscape protected areas by Natura Network.

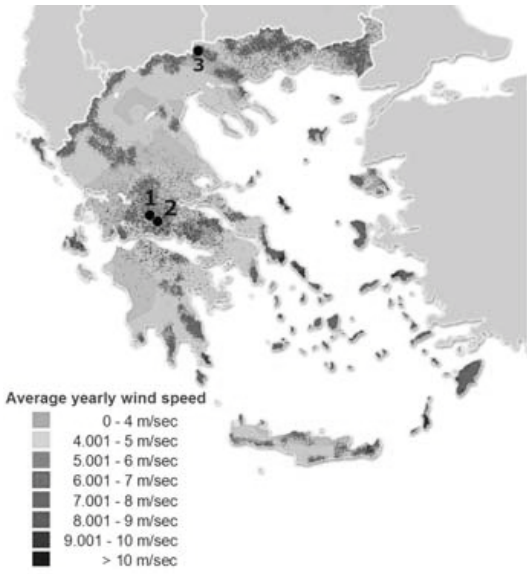

Fig 1. Wind map of Greece and meteorological stations 1, 2 and 3, where data collected

Table 1 shows the details of the three meteorological masts. The measurements were collected 20 m above ground level from Mast 1, 10 m above ground level from Mast 2 and 30 m above ground level from Mast 3. A data logger

was connected with each sensor on the masts to collect data in time series. The data were collected between 5/3/2007 and 4/15/2008 from Mast 1, between 6/15/2006 and 9/30/2007 from Mast 2, while for Mast 3, between 9/29/2008 and 5/31/2009, using 10 min time intervals. The collected data included date and time stamp, wind direction, maximum, minimum, average and deviation values of wind speeds at 20, 10 and 30 m heights for each mast respectively.

Table 1. Meteorological stations-Location description.

Meteorological Mast	1	2	3
Measurement Height Above Ground Level [m]	20	10	30
Measurement Height Above Sea Level [m]	1000	946	500
Data Collection Period	5/3/2007-4/15/2008	6/15/2006-9/30/2007	9/29/2008-5/31/2009
Characteristics of Site	Hilltop	Hilltop	Hilltop

3. Models

3.1. WAsP model

The Wind Atlas Analysis and Application Program (WAsP), is the standard method for wind resource predictions of candidate sites in rugged, complex terrain, such as the landscapes found in certain parts of Greece, Portugal, Spain and United Kingdom. It has been used recently to develop the European Wind Atlas and validated extensively for land conditions. WAsP is a PC program which can generalize long-term meteorological data series at a (reference) site which may then be used to estimate conditions at other (predicted) sites.

WAsP model gets to vertical extrapolation of wind data taking into account obstacles, surface roughness changes and terrain height variations. First, a set of wind data measurements is taken at a reference site. WAsP model is used to predict the wind resource for the prediction site from the wind data at the reference site assuming that there is a unique speed-up factor between the two sites for each wind direction sector [19,20]. The output consists of predictions of Weibull wind speed distribution in 12 or 16 directional sectors.

3.2. Weibull distribution

Within the WAsP method, the measured directional wind speed distributions are described by a statistical model, usually Weibull functions. Statistical models are used for describing the wind speed frequency distribution which may be used for predicting the energy output of a wind energy production system. Weibull distribution is the most universal among normal, lognormal and exponential distributions. It is applied mostly for wind speeds and can follow the experimental frequency even at a low speed part [19,20]. This distribution gives a good fit to experimental data, as indicated by Henessey [21], who compared Weibull and Rayleigh distribution. Petersen also proved the excellent fit of Weibull distribution in wind data in Denmark [22], while in India, 12 stations were studied for Weibull fit and the results were satisfactory [23].

Determination of the Weibull probability density function requires knowledge of two parameters, k and c [12,13]. Both these parameters are a function of the mean wind speed. The analytical expression of Weibull distribution is given by the equation:

$$f(U)=\frac{k}{c}\left(\frac{U}{c}\right)^{k-1}\exp\left[-\left(\frac{U}{c}\right)^{k}\right]. \quad (1)$$

The Weibull scale factor is closely related to the mean wind speed while the shape factor is a measurement of the width of the distribution parameter.

The cumulative distribution function is given by:

$$F(U)=1-\exp\left[-\left(\frac{U}{c}\right)^{k}\right], \quad (2)$$

while, the mean of the distribution, i.e. the mean wind speed or expected value EV is given by:

$$EV = A\Gamma\left(1+\frac{1}{k}\right), \quad (3)$$

where Γ is the gamma function.

3.3. Wake model

The wake model chosen for the energy calculations of WindPRO is the N.O. Jensen model which is a simple single wake model [24]. It is based on the assumption of a linearly expanding wake diameter, determined by the wake decay factor k and calculates the normalized velocity deficit. When calculating the velocity

deficit, the reduced wind speed, V, downwind of the turbine is derived from:

$$1-V/U=\frac{1-\sqrt{1-C_T}}{\left(1+\frac{2kx}{D}\right)^2}, \quad (4)$$

The thrust coefficient varies with wind speed and is defined as:

$$C_T=\frac{F}{\frac{1}{2}\rho \mathrm{U}^2 A}, \quad (5)$$

The wake decay factor k is defined as follows:

$$k=0.5/\log(h/z_0), \quad (6)$$

The wake decay factor increases with increasing level of ambient turbulence.

3.4. Capacity factor

The capacity factor is a very significant index of the productivity of a wind turbine, since the annual energy production of a park is directly proportional to this factor. It corresponds with the percentage of hours in a year that the wind turbine would need to operate at rated capacity, to obtain the same production as calculated [24]. Dividing the annual production by wind turbine's rated capacity, results in the calculation of the number of hours that the turbine needs to operate in rated capacity. Thus, the division of this number with the total number of hours of one year leads to the percentage of the capacity factor.

4. Results

4.1. Statistics

This section provides the results of the statistical analysis of the collected wind data.

4.1.1. Weibull distribution and wind speed analysis of monthly mean speed

The wind speed distribution at hub height as well as the relative Weibull curve is shown in Figs 2-4 for each meteorological station.

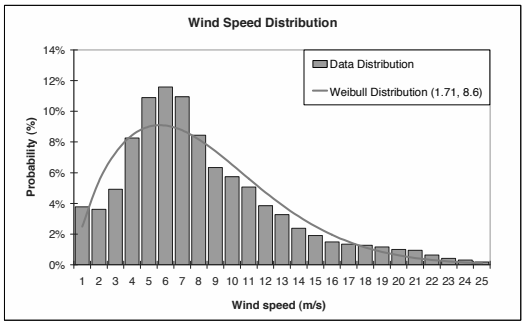

Fig. 2. Weibull distribution for the full data set by Mast 1 in Region A.

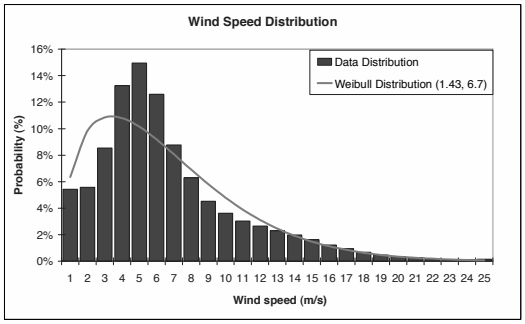

Fig. 3. Weibull distribution for the full data set by Mast 2 in Region A.

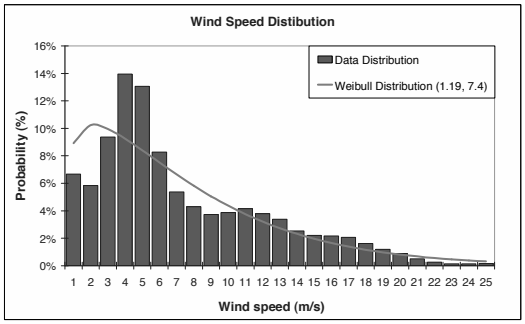

Fig. 4. Weibull distribution for the full data set by Mast 3 in Region B.

Using software WindRose, an add-in program to Microsoft Excel 2000/XP/2003/2007 for wind data analysis and correlation [25], we need two basic sets of data in order to estimate the annual energy production of a wind turbine. These sets are the turbine's power curve and the wind speed distribution.

The power curve describes the electric power output from a specific wind turbine versus the wind speed at hub height. The turbine chosen is Vestas V-80, 2 MW, with a hub height of 78 m. The wind speed distribution describes the probability of a specific value of wind speed versus the wind speed. The mathematical two-parameter Weibull distribution is often used to describe the wind speed distribution. Figures 2 and 3 present the measured distributions from the two masts in Region A, as well as the corresponding Weibull curves. In Fig. 2, for Mast 1 in Region A, the values of k and c are 1.71 and 8.6 m/s, respectively. In Fig. 3, for the same Region but for Mast 2, the same values are 1.43 and 6.7 m/s, respectively, while, for Mast 3 in Region B, k is 1.19 and c is 7.4 m/s.

The Weibull parameters k and c emerged from each meteorological station. In Station 3, the data collected from Mast 3 were not full-length probably because of icing and operational conditions of the instrumentation which limited the data acquisition capabilities.

4.1.2. Wind speed frequency and direction analysis

The wind rose provides information about the occurrence of number of hours during which wind remained in a certain wind speed bin in a particular wind direction. By using the measurements of the three masts, in WindRose, we obtain the polar diagrams that are illustrated in Figs 5-7. For each sector the wind is considered separately. The length of the time that the wind comes from this sector is shown by the length of the spoke and the speed is shown by the thickness of the spoke. The directions can be specified as ordinal number of the axis counted. The labels on the axis is by default short forms of the compass directions, for example, "E", "N", "W", "S".

For each meteorological station the statistical analysis leads to polar diagrams, which provide important information for wind turbine's siting. In Figs 5 and 6, the diagrams give quite the same results, as the distance between the two stations is quite close and the topography has no significant differences between the two masts.

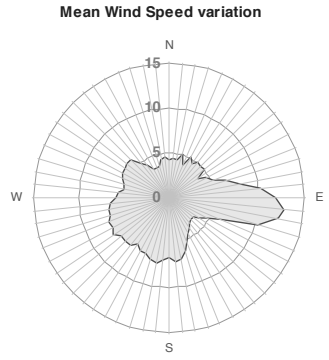

Fig. 5. Wind rose polar diagram of the Mast 1.

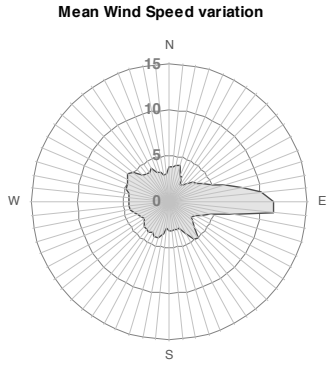

Fig. 6. Wind rose polar diagram of the Mast 1.

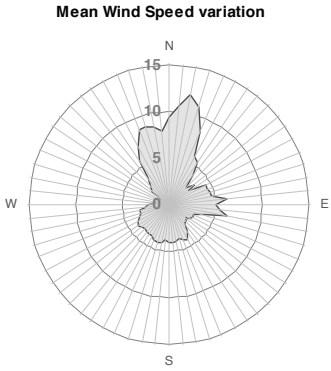

Fig. 7. Wind rose polar diagram of the Mast 3.

Consequently, according to the polar diagrams of Figs 5-7, the main direction of the wind seems to be Eastern for Region A, while for Region B, the

main direction is Northern. For Region A, the highest time distribution is in East direction, by 31.75% in Station 1 and 37.59% in Station 2. Thus, as a large share of wind comes from a particular direction for each location, the wind turbines should be put against this direction in order to achieve the maximum energy production.

4.1.3. Variation in turbulence intensity

When setting the conditions for the park simulation in these locations, it is necessary to estimate the turbulence intensity on the inlets. For this reason, the statistical analysis of the wind data from Masts 1, 2 and 3 leads to the estimation of turbulence intensity for each meteorological station. In Fig.8 the percentage of the turbulence intensity that emerged from the measurements of the three meteorological stations is presented for every wind direction sector and for constant wind speed. It is obvious that the turbulence intensity depends strictly on the inland terrain roughness and large-scale topography. Also, the measurement height is different for the three stations, so the contradictory results are not unexpected.

For Station 1, the maximum value of turbulence intensity, in SSE direction, is 23.7%, while for Station 2, in WSW direction, the value is 32.29%. For Station 1, where the measurement height is 20 m, we expect lower turbulence intensity, because of at Station 2, in 10 m, the surface roughness influence is more intensive. Finally, in spite of the fact that the mast of the Station 3 is at higher height (30 m), the maximum percentage of turbulence intensity, which is 35.87% in ESE direction, is bigger than the respective percentage of the other two stations. The possible reason is the different orography of the Region B.

The turbulence intensity, for the main direction for each station, presents a lower value as the wind speed increases. The thermal variation in inland areas, such are these three stations, is significant. In lower wind speed the thermal effects grow stronger and the wind is affected by them while blowing over inland roughness.

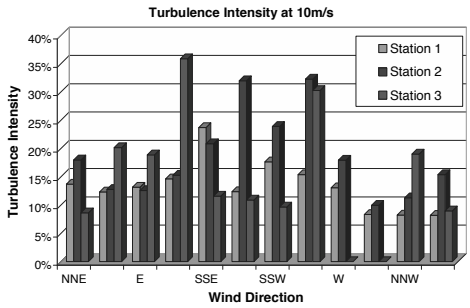

Fig. 8. Variations in wind's turbulence intensity at 10m/s for the three meteorological stations.

4.2. Energy prediction

WindPRO is a Windows 2000/XP/Vista based software suite for the design, development and assessment of wind energy projects. Using the wind data measurements from Station 1, 2 and 3 and entering the wind turbines via maps which include the contours, we estimate the complete annual energy production from the two parks, Park 1 and Park 2. The parks' turbines, which are 13 and 42 for Park 1 and Park 2 respectively, are the same wind turbines we used for the statistics of wind data. The roughness length scale of the potential sites, which is a characteristic value of its orography, is assumed to be 0.13. This value results from the combination of practical experience and existent data [25].

The results that emerged from the wind data analysis of the two parks are illustrated in Figs 9 and 10 respectively.

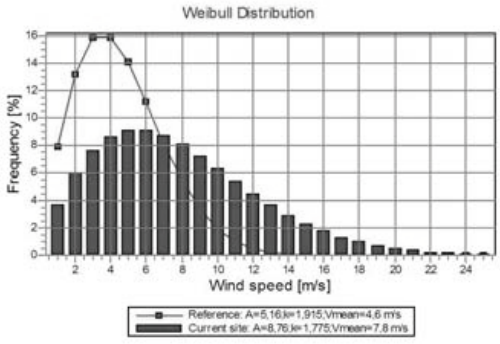

Fig. 9. Weibull distribution for the full data set for Park 1 in Region A.

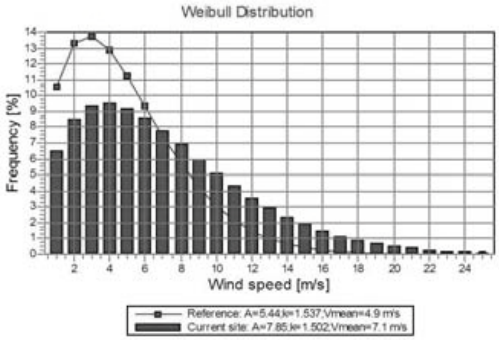

Fig. 10. Weibull distribution for the full data set for Park 2 in Region B.

In Figs 9 and 10, the wind data of the designed wind farms are compared with a reference site, which is associated with a flat terrain and a roughness length scale of 0.03. This theoretical reference site is chosen because is the best onshore condition and thereby the effects of a coastline near the site or a hilly terrain can be clearly seen. For both sites we consider that the installation of a wind farm benefits from the orography as the results give much more energy than a site with a flat terrain.

The results of the annual wind energy production of the parks are presented in Fig 11 for each wind direction sector. The calculation of the energy production accrued via the N.O Jensen wake model.

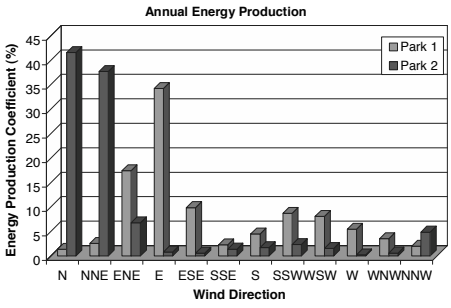

Fig. 11. Annual energy production per wind direction sector for the two wind parks.

Figure 11 presents the percentage of the wind energy production coefficient versus the sectors of wind direction. Wind energy production coefficient emerges by dividing the energy production of each sector by the total annual energy production. The results show that for Park 1 the maximum percentage of the wind energy production coefficient, which is 34.22%, corresponds to East direction, while, for Park 2, with a respective percentage of 41.55%, is in North direction.

Table 2 presents the main results for the turbine's hub height of 78 m above the ground level, with regards to the measurements of the three meteorological stations. The annual mean wind energy is related to the wind energy density, which indicates how much energy is available at the site for conversion by a wind turbine. Thus, mean wind energy is a substantial parameter of a wind energy project, while mean wind speed affects the total energy production, since the energy production of a wind turbine is proportional to the cube of the wind speed.

Wind energy density is measured in watts per square meter. Dividing the annual mean wind energy, which is given in KWh/m^2, by the total number of hours in a year and converting the kilowatts into watts, yields the wind energy density of the meteorological stations. The results for the three stations are 580, 384 and 524 W/m^2. Considering the relevant heights of measurements, the wind energy classes of the two wind-parks range between the values of 6 and 7, according to the base principles of wind resource evaluation.

Moreover, it seems that despite the fact that the first two stations are closely sited, the results indicate significant differences, since the mean wind energy is 5,078 and 3,362 KWh/m^2 for the first and the second station respectively. The possible reason is the different measurement height of the two masts.

Table 2. Main results for height 78.0 m above ground level for the tree meteorological stations.

	Mean Wind Energy [KWh/m^2]	Mean Wind Speed [m/s]
Station 1	5,078	8.1
Station 2	3,362	6.7
Station 3	4,589	7.2

The complete calculation of the wind parks' energy production is included in Table 3, which presents the annual energy production, the mean wind turbine's energy production, as well as the capacity factors of the two wind parks.

Table 3. Annual energy production results for the two wind parks.

		Park 1	Park 2
Annual Energy Production [MWh]	Result	59,524.2	134,433.0
	Result-10%	53,571.8	120,989.7
Mean Wind Turbine's Energy [MWh]		4,578.8	3,200.8
Capacity Factor	Result	26.1	18.3
	Result-10%	23.5	16.4

The results of the annual energy production and the capacity factors are shown with and without the losses, which are represented as a percentage of 10% of total energy production. The annual energy production for each park is expected to be 59,524.2 MWh for Park 1 and 134,433 MWh for Park 2 without considering the losses. These values drop down to 53,571.8 and 120,989.7 MWh, respectively deducting a 10% of losses. Considering that the acceptable values of the capacity factor are between 25 and 30% in order to characterize a wind park as effective, the capacity factor of the first wind park, which is 23.5 and 26.1 with and without the losses, respectively, is acceptable. On the contrary, the capacity factor of the second park, which is 16.4 and 18.3 respectively, can be considered as low. The possible reason for that is the large amount of missing data during the period of measurements, as well as the lower mean wind speed with regards to the first wind park.

5. Conclusions

This paper concentrates on the problem of the annual variability of wind speed due to the fact that the energy production of a wind farm depends on the non-constant of the wind flow. Via the simulation of the operation of two wind farms in two different regions, emerged the substantial parameters which were further analyzed in order to define the effectiveness of each wind project. The conclusions that accrued from the results can be summarized as follows:

- The main direction in points of measurement, appear to be Eastern for the first region and Northern for the second region. This element is decisive for the future planning of the park and concerns the arrangement of wind turbines in each region.
- The wind data collected from the first two meteorological stations during the one year of measurements was full length, in contrast with the third station, wherein, during the eight month period of measurements, the record data system provided results only for six months. The possible reasons include icing and operational conditions of the instrumentation, which limited the data acquisition capabilities.
- The statistical analysis of the wind data showed that the wind turbulence intensity in the points of measurement influences the distribution of wind speed. Furthermore, increased turbulence affects the associated losses in the turbine wings. These losses may reduce the total energy production of the turbines as well as their life expectancy.
- Considering the results of the energy prediction, it seems that the first wind park has a capacity factor within the acceptable range. This fact indicates a satisfactory effectiveness. On the other hand, despite the large size of the second wind park project, its total capacity factor is quite low, probably because of the significant amount of missing data during the period of wind measurements.
- The total annual energy production as well as the capacity factor of the wind parks are substantial parameters, since they can affect the cost effectiveness of the venture and as a result, the economic viability of the project. The relative results of the first park indicate that the investment could be characterized as profitable, while, for the second park, it seems that additional measurements and relevant analysis are required in order to reduce the investment risks.
- Based on the Weibull distribution of the energy calculation for the two wind parks, the installation of those seems that benefits from the orography as the results give much more energy than a flat terrain.
- The wind energy density of the wind parks that emerged from the results of the annual energy production calculation, indicate that the wind energy classes of the potential sites are ranged between the values of 6 and 7. Considering that wind energy class of 4 or higher are satisfactory for large-scale wind plants, it is obvious that the two regions are excellent potential sites for wind park installation.

Nomenclature

A rotor swept area, m
c Weibull scale factor
C_T thrust coefficient
D rotor diameter, m
F axial thrust
h hub height, m
k Weibull shape factor,
wake decay factor
U wind speed, m/s
z_0 roughness length

Greek symbols

ρ air density

References

[1] RETScreen International, Clean Energy Decision Support Centre, Introduction to Clean Energy Project Analysis, Minister of Natural Resources Canada 2001 – 2005.

[2] Lange, M., and Focken, U., 2005, Physical Approach to Short-Term Wind Power Prediction, Published by the Met Office.

[3] Global Win Energy Council, 2005, Wind Force 12, A Blueprint to Achieve 12% of the World's Electricity from Wind Power by 2020.

[4] The European Wind Energy Association (EWEA), 2008, Pure Power, Wind Energy Scenarios up to 2030.

[5] Manwell, J.F., et al., 2002, *Wind Energy Explained, Theory Design and Application,* Copyright © 2002 John Wiley & Sons Ltd.

[6] Gardner, P., et al., 1999, *Wind Energy - The Facts*, The European Wind Energy Association, Brussels, Belgium.

[7] Zervos, A., et al., 2008, *Global Wind Energy Outlook 2008*, Global Wind Energy Council, Brussels, Belgium.

[8] Mortensen, N.G., and Petersen, E.L., 1998, Influence of Topographical Input Data on the Accuracy of Wind Flow Modelling in Complex Terrain, *Proc. 1997 European Wind Energy Conference & Exhibition*, Dublin, Ireland, October 6-9, 317-320.

[9] Caralis, G., et al., 2008, On the Effect of Spatial Dispersion of Wind Power Plants on the Wind Energy Capacity Credit in Greece, Environmental Research Letters 3 015003 (13 pp).

[10] Ozerdem, B., and Turkeli, M., 2003, An Investigation of Wind Characteristics on the Campus of Izmir Institute of Technology, Turkey, Renewable Energy 28, 1013-1027.

[11] Binova, S., et al., 2003, Hourly Wind Speed Analysis in Sicily, Renewable Energy 28, 1371-1385.

[12] Shoji, T., 2006, Statistical and Geostatistical Analysis of Wind: A Case Study of Direction Statistics, Computer and Geosciences 32, 1025-1039.

[13] Viogiatzis, N., et al., 2004, Analysis of Wind Potential and Characteristics in North Aegean, Greece, Renewable Energy 29, 1193-1208.

[14] Gupta, B.K., 1986, Weibull Parameters for Annual and Monthly Wind Speed Distributions for Five Locations in India, Solar Energy 37(6), pp. 469-471.

[15] Pashardes, S., and Christofides, C., 1995, Statistical Analysis of Wind Speed and Direction in Cyprus, Solar Energy 55(5), pp 405-414.

[16] Jaramillo, O.A., Borja, M.A., 2004, Wind Speed Analysis in La Ventosa, Mexico: A Bimodal Probability Distribution Case, Renewable Energy 29, 1613-1630.

[17] Ioannou, E., 2009, Applications and Analysis of Installation of Wind Turbines, Diploma Thesis, Aristotle University of Thessaloniki, Thessaloniki, Greece.

[18] Chourpouliadis, C., 2010, Estimation of Energy Production and Noise Emission of Wind Turbine Installations, Diploma Thesis, Aristotle University of Thessaloniki, Thessaloniki, Greece.

[19] Bowen, A.J., and Mortensen, N.G., 1996, Exploring the Limits of WAsP-The Wind Atlas Analysis and Application Program', *Proc. European Union Wind Energy Conference*, Sweden, P. O. 15.2.

[20] Lange, B., and Hojstrup, J., 2001, Evaluation of the Wind-Resource Estimation Program WAsP for Offshore Applications, Journal of Wind Engineering and Industrial Aerodynamics 89, 271-291.

[21] Hennessey Jr., J.P., 1978, A comparison of Weibull and Rayleigh distribution for estimating wind power potential, Wind Eng. 2, 156-164.

[22] Petersen, E.L., et al., 1981, Wind Atlas for Denmark, RISO, Denmark.

[23] Mani, A., and Mooley, D.A., 1983, Wind Energy Data for India, Allied, India.

[24] Nielsen, P., 2008, WindPRO 2.6 User Guide, 1st Edition, EMD International A/S.

[25] Wind Data Analysis Program, WindRose, Handbook, Handbook Edition: 6.5, Excel COM+ Add In Edition: 3.5.

Acknowledgments: The authors would like to acknowledge the help and support of EOLFI Wind Hellas SA. and their kind permission to use the data presented.

Wind Speed Dynamics in Scenario Generation for Energy Systems Modelling

Kiti Suomalainen [a,b], *Carlos Silva* [a,c] *Stephen Connors* [a,d] *and Paulo Ferrão* [a,b]

[a] *MIT-Portugal Program, Lisbon, Portugal*
[b] *IN+, Instituto Superior Técnico, Lisbon, Portugal*
[c] *IDMEC, Instituto Superior Técnico, Lisbon, Portugal*
[d] *Massachusetts Institute of Technology, Cambridge, USA*

Abstract: Modelling an energy system with high ratios of renewable sources is challenging due to the natural and often unpredictable variations of the resources and how their characteristics may change in the long term. As the models' time-steps become smaller and renewables' penetration larger, renewable energy resource dynamics is no longer negligible in energy planning. The proposed methodology characterises the wind resource's variability by studying diurnal, monthly and annual patterns and constructing scenarios that reflect the various possible outcomes based on historical statistical analysis. The result is not a prediction of the wind speed at a given hour, but a simulation of a possible chain of events. In this new approach it is assumed that a sum of sinusoidal waves may be used to define a set of 24-hour wind speed profiles. Each profile has a different probability of occurrence, depending on both the season and on the profile of the previous day. It is shown that the sum of two sin-waves is sufficient to describe the most relevant wind profiles, i.e. both the lower, synoptic frequency (passing weather systems) and daily peaks.

Keywords: Renewable resource variability, Wind scenario generation, 24-hours wind speed profile.

1. Introduction

The intermittency of the wind resource has been widely studied and many methods for its prediction have been developed [1]-[4]. Most of these methods focus on statistical, numerical or physical models to predict hourly wind speeds for up to a few days.
What makes the study of diurnal patterns relevant is the match or mismatch with demand patterns. As demand follows a relatively predictable repetitive daily pattern, the 24h period becomes relevant for renewable energy resource characterisation as well. The fact that the wind resource also seems to have diurnal patterns caused by the "breeze effect" leads to the possibility of better evaluating the resource availability and better dimensioning the system to match overall supply with demand.
The research presented in this paper aims at characterizing the wind resource in a manner that allows realistic scenario generation of hourly wind speeds for several years or even decades.
The proposed methodology builds on characterising the wind resources by its variability by studying diurnal, monthly and eventually inter-annual patterns, including relevant stochastic effects, and constructing scenarios that reflect the various possible outcomes based on historical statistical analysis. If climatologists foresee, for example, windier winters and calmer summers for the future, corresponding changes can be made in the probability distributions and new scenarios generated accounting for this new information.
This paper presents a methodology for characterising the daily variability of the wind on a coastal location on Terceira island in the Azores archipelago. First, a methodology for identifying the critical parameters that characterise the shape of diurnal wind patterns is presented, followed by a demonstration of how a set of such patterns, or profiles, each with its own probability distribution, can be used to generate scenarios with realistic variability for energy modelling purposes.

2. Methodology

The presented methodology is a combination of curvefitting, determining probability distributions, and sampling hourly wind speeds in order to create one or several years of synthetic hourly wind data.

Corresponding author: Kiti Suomalainen, Email: kiti.suomalainen@dem.ist.utl.pt

2.1. Background

According to the Wind Energy Handbook [5] the long-term variations of the wind at a given location, i.e. variations from one year to the next, or even larger scale variations over periods of decades or more, are not well understood and may make it difficult to make accurate predictions of the total energy production of particular wind installations. On shorter time-scales of minutes down to second or less, wind speed variations known as turbulence can have significant effect on the design and performance of individual wind turbines, as well as on the quality of power delivered to the network. Seasonal variations, i.e. 3-month average wind speeds, are much more predictable, whereas shorter time-scale variations, from day to day or hour to hour, are often not very predictable more than a few days ahead. Depending on the location, there may be significant diurnal variations and in these time-scales the predictability of the wind is important for integrating large amounts of wind power into the electricity grid, in order to allow other generating plants to prepare accordingly. Therefore, including diurnal, seasonal and inter-annual variations into energy planning scenarios with large wind installations becomes relevant for cost-effective dimensioning of supply side technologies.

In [6] a wind speed spectrum generated from long- and short-term records at Brookhaven, New York, shows clear peaks corresponding to synoptic (passing weather systems), diurnal and turbulent variations. There is a significant "spectral gap" between the diurnal and turbulent peaks, indicating that the synoptic and diurnal variations can be treated as distinct from the higher-frequency variations of turbulence. These higher-frequency variations are left outside the scope of the current research since they mostly affect turbine design and power quality, and to less degree the overall system dimensioning and planning.

A similar study was presented in [7], computing the power spectrum for Bushland, Texas, and it was found that although the general shape of the curve is similar to the Van der Hoven spectrum [6], few of his peaks were found in the Bushland. It is argued that although the Van der Hoven spectrum from 1957 is often used as a reference in papers and publications on wind turbulence, it is of little use to the wind turbine industry because it was measured too high above the ground and at different elevations, was of low resolution, and represented the high frequency end of the spectrum recorded at a time with unusually gusty, high wind speed data. It is not applicable to all wind farm sites or heights above the ground. As an example of such a difference, they conclude, the Bushland confirms some of the shape found by Van der Hoven, but few of his peaks. The Bushland data shows a very pronounced daily peak in wind speeds.

2.2. Curve fitting

The hypothesis studied in this paper is that a sum of sinusoidal waves may be used to define a set of 24 hour profiles, that represent various types of wind patterns. Each profile has a different probability of occurring, depending on both the season, or the month, and on the profile of the previous day(s). It is assumed that the sum of two sin-waves and a constant, giving a total of seven parameters, is sufficient to capture all relevant wind profiles, i.e. both the synoptic frequency and daily peaks as described by the function 1.

$$f(x) = a_1 * sin(b_1 * x + c_1) + a_2 * sin(b_2 * x + c_2) + a_3 \quad (1)$$

$x \in \{1, 2, .., 24\}$, corresponds to the 24 hours of a day, and a_1, b_1, c_1, a_2, b_2, c_2 and a_3 are the seven parameters used to define the curve. The first sin-wave represents the low frequency, i.e. the synoptic frequency, component of the profile describing the overall tendency of the wind speed that day, for example if the wind decreases throughout the day. Thus a_1 and b_1 determine the amplitude and frequency of the curve and c_1 determines in which phase the curve best represents the profile. The second sine-wave captures local peaks along the day; the frequency, b_2, depending on the number of peaks, the amplitude, b_2, giving the deviation from the general tendency of the day (the low-frequency sine-wave) and c_2 influencing the placement of the peaks. This however assumes that the amplitude of the peaks along the day is the same and that they are equally spaced along the day. This is not the case with the wind and it is clearly an aspect that needs further consideration, although it is assumed to be an acceptable simplification here for testing this new methodology. Finally, a_3 adjusts the curve vertically to the level of the wind speed.

2.3. Parameter analysis

To test this methodology, the function is fit to two years (731 days) of hourly wind data. Daily profiles are identified by looking at the distributions of the parameters and subgrouping certain combinations of parameters that result in a similar overall daily profile. Similar profiles can be reached by different combinations of parameters and therefore they will be grouped in the end to a finite number of daily profiles. The range of each parameter is defined in Table 1. The amplitude of the first sine, a_1, is allowed to go to 30 to guarantee that maximum wind speeds fit well within these limits. The amplitude of the second sine, a_2, is only allowed to go up to 15 because it reflects a change in wind speed over the period defined by b_2, which is eight hours or more, and the wind speed is not expected to change more than 15 m/s in four hours, excluding extreme weather conditions. The parameters b_1 and b_2 have the same constraints, zero and $2\pi/8$, corresponding to a period of eight hours. The upper limit exists to avoid fitting to capture hourly fluctuations and instead capture the trend over the day (first sine) and frequencies that are slower than hourly dynamics during the day (second sine). The phases, c_1 and c_2, and constrained between $-\pi$ and π, allowing the peak to shift to any hour of the day. The constant a_3 is limited by -30 and 30, which allows the curve to shift vertically. In certain cases, e.g. when the wind speed is zero for several hours, the curve fitting may result in negative values with these constraints. In this case any negative values are assigned the value zero.

Table 1: Parameters Table

Parameter	Min	Max
a_1	0	30
b_1	0	$2\pi/8$
c_1	$-\pi$	π
a_2	0	15
b_2	0	$2\pi/8$
c_2	$-\pi$	π
a_3	-30	30

To enable comparison of wind energy availability with periods of electricity demand, five profile types are defined by dividing the day in to 4 periods of six hours and determining during which of those periods most of the wind energy that day is produced:

1. No significant variability along the day,
2. Most energy produced between 00:00 and 06:00,
3. Most energy produced between 06:00 and 12:00,
4. Most energy produced between 12:00 and 18:00,
5. Most energy produced between 18:00 and 24:00.

The parameter analysis is started by looking at a few combinations of parameters that are expected to give profiles that can be directly slotted to the profiles listed above. Looking at the distributions of the seven parameters it can be seen which values are more common than others for each parameter, and those ”clusters” can be analysed as a group. For example, if both a_1 and b_1 are small, or, if $a_1 \times b_1$ is small, then the first sine is quite flat and the variability during the day is mainly defined by a_2 and b_2. So, if a_2 is also small, then all the cases with these characteristics can be slotted in to the first profile group. Or, if b_1 is approximately $2 \cdot \pi/48$, i.e. fitting approximately half a cycle in a day, *and* b_2 is small, then c_1 will mainly define the profile of the day. This logic is continued until all cases are slotted to the categories above.

2.4. Scenario generation

It is assumed that the average daily wind speed depends on the average wind speed of the month (to include seasonality) and the average wind speed of the previous day (to include passing weather systems that typically take 2-10 days [5]). The occurrence of a certain profile is assumed to depend on the average wind speed of that day but not on the profile of the previous day, since the average wind speed already includes that dependency. Given the set of daily wind profiles and average wind speeds, the probability distribution for the average wind speed and profile is obtained and a process for generating scenarios for energy modelling is developed. From the historical data several probability matrices can be constructed corresponding to for example a ”normal” year, ”windy” year, a ”low wind” year, or just a windy season , keeping the rest of the year ”typical”. These scenarios can be used to include uncertainty analysis in energy planning scenarios or, for example, with reasonable assumptions on how the wind characteristics may change in future

decades, scenarios reflecting the impact of climate change on wind power can be studied.

3. Results

The methodology is tested and improved by application to a case study, starting with the a two-year data set from a coastal location and with the prospect of comparing various locations as the research proceeds.

3.1. Application: Green Islands case study

This research is part of the Green Islands project [8] which aims at designing pathways towards more sustainable energy systems for the Azores islands in the mid-Atlantic. The methodology is applied to two years of wind data from Terceira island, recorded at the airport. Plotting this hourly data (Fig. 1) by hour (horizontal axis) and day (vertical axis) shows a general tendency for afternoon winds in spring, summer and fall.

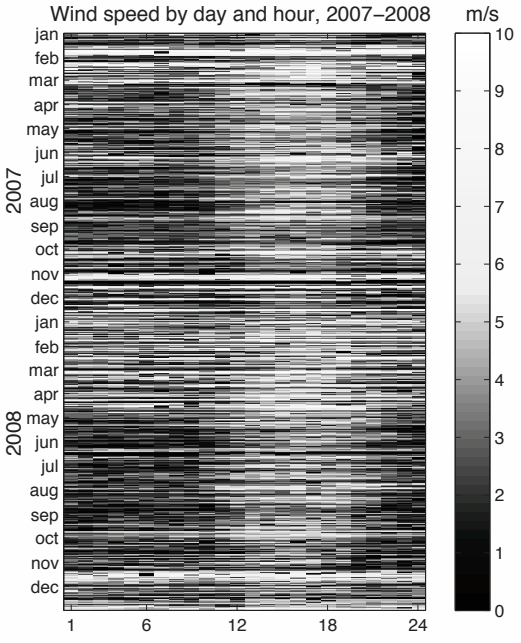

Figure 1: A graphic of hourly wind data for two years, 2007 and 2008, shows higher wind speeds in the afternoons in spring, summer and fall.

3.2. Curve fitting

In most cases the curve fitting resulted in a good approximation of the wind speed along the day. However, 10 percent of the cases were omitted from parameter analysis due to bad fits. These cases were manually observed and slotted to the corresponding categories. The parameter distributions for the remaining cases are given in Fig. 2. The parameter analysis resulted in a total of 32 subgroups. All subgroups describe one of the five categories but with different combinations of parameters. For example a day with little variability can result from a combination of small values for a_1, b_1 and a_2 or in a case where a_1 and a_2 are approximately equal, b_1 and b_2 are approximately equal and c_1 and c_2 differ by π or $-\pi$. The subgroups were regrouped to the five categories shown by box plots in Fig. 3. The box plots show the variation within each group, the rectangle indicating the lower quartile, median and upper quartile values and the whiskers showing the adjacent values within the range of 1.5 times the lower and upper quartile values and '+' signs indicate outliers, values beyond the whiskers. The sixth subplot gives the probability distribution of the profiles in the order as they are plotted. As expected, the profile describing afternoon winds is most frequent, followed by stable, low winds of around 2-4 m/s.

The probability distribution of the average wind speed of day n, depending on the average wind speed of day $n-1$, based on the two years of data, is shown in Fig. 4. The distributions show some inconsistensies, which can be expected from a data set of just two years, but generally the most probable average wind speed for the next day is somewhere between the average wind speed of the day and the annual average wind speed which is approximately

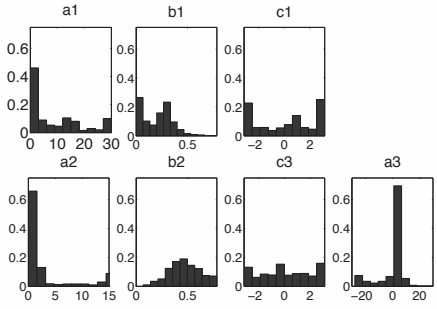

Figure 2: The distribution of values for the seven parameters.

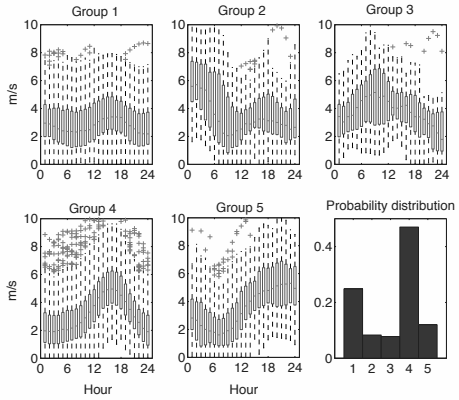

Figure 3: All possible combinations of the seven parameters reduced to five groups of profiles shown in box plots. The rectangle, whiskers and '+' signs indicate the lower quartile, median, and upper quartile values, adjacent values within the range of 1.5 times the lower and upper quartile values and outliers, respectively. The histogram shows the probability of each profile category.

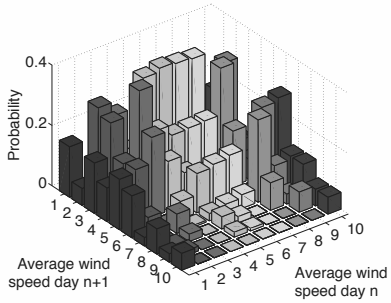

Figure 4: Average wind speed distribution for day $n+1$, depending on the average wind speed of day n. Results based on two years of wind data.

3.5 m/s.

The probability of each profile, given the average wind speed for that day, is shown in Fig. 5 As the box plot shows, unvarying wind profiles are most common at low daily averages. Otherwise, stronger afternoon winds (12:00-18:00) prevail in all average wind speed bins. On days with high average wind speeds, also evening (18:00-24:00) and night (00:00-06:00) winds are common.

3.3. Scenario generation

Beginning with the original data set's average wind speed for January, and the probability distributions given above, a data set of 365 days was generated by sampling from the discrete distributions.

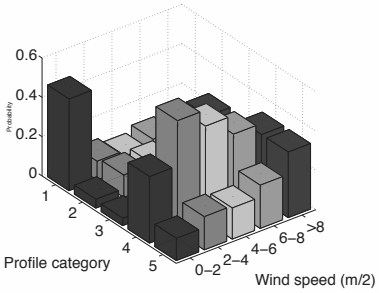

Figure 5: Probability of occurrence of a profile given the average daily wind speed.

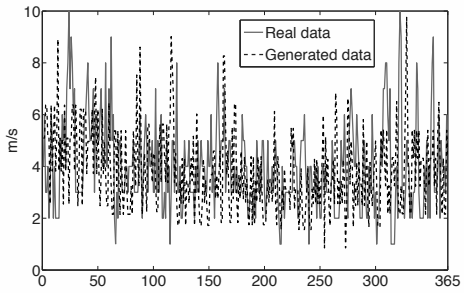

Figure 6: The generated sequence of average daily wind speeds (discontinuous line) agrees well with the original data (continuous line), the average daily wind speeds for 2007.

From the original data set the monthly average wind speeds were calculated and this seasonal variation was added to the generated data set. The results are shown in Fig. 6. The generated set of daily averages agree well with real data with regard to seasonal variability, and the frequency of high or low values. Adding a sequence of daily profiles for each day of the year and scaling the normalized profiles with the generated sequence of average daily wind speeds gives an hourly data set for the whole year. Each individual daily profile was obtained by discrete sampling hour by hour from the distributions that Fig. 3 is based on.

3.4. Power spectrum analysis

The goodness of the generated data set was evaluated by comparing the hourly wind speed distributions and the power spectrum densities of the original and the generated data set. The hourly wind speed distributions show a Weibull distribution as is typical for wind (Fig. 7). The generated data set has fewer values close to zero and more around the an-

nual average wind speed than the original data set. For higher values there is good agreement. The results of power spectrum analysis, Fig. 8, compare the power spectrum densities of the original data set to the generated data. This graph includes the frequencies with a period of one hour or more. It does not capture dynamics at higher frequencies than this due to the lack of data with a higher temporal resolution. The original data set's (continuous line in Fig. 8 first local peak, at 0.041 cycles per hour, corresponds to approximately one cycle per day, and the second peak, at 0.083 cycles per hour, corresponds to approximately two cycles per day. The so called synoptic peak, a slower dynamic (every 2-10 days) is shown more vaguely as the shoulder to the left of the first peak. This is represented by the first term in Eq. 1. The second term in Eq. 1 captures upto three peaks per day, set as the limit of b_2. The results from the generated data agree well with the frequencies of the two main peaks of the original data with clear peaks at both 0.041 and 0.083.

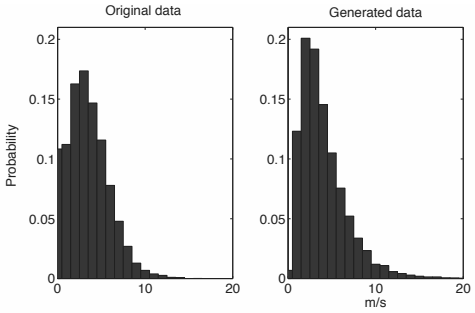

Figure 7: Comparison of the real data and the generated data by their hourly wind speed distribution over one year.

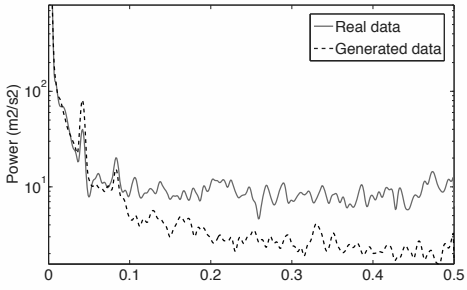

Figure 8: Comparison of the power spectrum density of the real data and the generated data. The two main peaks at 0.041 and 0.083 cycles per hour, i.e. approximately one and two cycles per day, are reproduced accurately by the generated data.

4. Discussion and conclusions

With the results of the current research in identifying daily patterns in wind speed it can be concluded that there are locations where the wind shows clear tendencies along the day. The studied location shows frequent afternoon winds especially in spring, summer and fall. The presented methodology identifies a set of profiles that can be used to generate realistic hourly data sets for the whole year, taking into account seasonal variations and the probability distribution of daily average wind speeds and corresponding profiles. The results for daily averages agree well with the original data set for daily averages. Sampling to generate hourly wind speeds resulted in a fairly good resemblance with the original data set, although this methodology shifted a significant number of hours of low wind speeds to average wind speeds as seen in the compared Weibul distributions in Fig. 7. The methodology can still be improved in this aspect. However, if these deviations are near or below the cut-in speed for wind generation, the energy production error will be low.

This methodology seems plausible for generating scenarios where the occurence of certain uncertain events at realistic frequencies is of importance, e.g. the occurence of afternoon winds in energy modelling. A next step in research will include a modified application to solar data to study the effect of e.g. afternoon rains on solar heating.

References

[1] F. Castellanos and V. I. Ramesar,2006 , Charasterization and Estimation of Wind Energy Resources Using Autoregressive Modelling and Probability Density Functions, *Wind Engineering Volume*, Vol. 30, No. 1, pp. 1-14.

[2] R. Billington et al., 1996, A sequential Simuation Technique for Adequacy Evaluation of Generating Systems Including Wind Energy, *IEEE Transactions on Energy Conversion*, Vol. 11, No. 4.

[3] F. Castro Sayas and R. N. Allan, 1996, Generation availability assessment of wind farms, *IEEE Proc.-Gener. Transm. Distrib.*, Vol. 143, No. 5.

[4] R. D. Prasad and others, 2008, Some of the design and methodology considerations in

wind resource assessment, *IET Renew. Power Gener.*, Vol.3, No. 1, pp. 53-64.

[5] T. Burton et al., 2001, *Wind Energy Handbook*, John Wiley & Sons, Ltd, Chichester, England.

[6] I. Van der Hoven, 1957, Power Spectrum of Horizontal Wind Speed in the Frequency Range from 0.0007 to 900 cycles per hour, *Journal of Meteorology*, Vol. 14, pp. 160-164.

[7] E. D. Eggleston and R. N. Clark, 2000, Wind Speed power Spectrum Analysis for Bushland Texas, USA, *Wind Engineering*, Vol. 24, No. 1, pp. 49-52.

[8] C. Silva et al., 2009, A Systems Modeling Approach to Project Management: The Green Islands Project example, Second International Symposium on Engineering Systems. http://esd.mit.edu/staging/symp09/submitted-papers/silva-carlos-paper.pdf

Acknowledgments: The Portuguese national science and technology foundation, Fundação para Ciências e Tecnologia, is gratefully acknowledged for the support of this research (SFRH/BD/35331/2007) within the MIT-Portugal Program.

An Integrated Energy Storage Scheme for a Dispatchable Solar and Wind Powered Energy System

Jared Garrison[a], *Michael Webber*[a]

[a] *The University of Texas at Austin, Austin, USA*

Abstract: The goal of this research is to analyze an integrated energy system that includes a novel configuration of wind and solar coupled with two storage methods to make both wind and solar sources dispatchable during peak demand, thereby enabling their broader use. Named DSWiSS for Dispatchable Solar and Wind Storage System, the proposed system utilizes compressed air energy storage (CAES) that is driven from wind energy and thermal storage supplied by concentrating solar thermal power (CSP) in order to achieve this desired dispatchability. Although DSWiSS mimics the operation of a typical CAES facility, the replacement of energy derived from fossil fuels with energy generated from renewable resources makes this system unique. Through a thermodynamic and a levelized lifetime cost analysis the power system performance and the cost of energy are estimated for this integrated wind-solar-storage system. We calculate that the combination of these components performs with an efficiency of 46% for the main power block, and the overall system cost is only slightly more expensive per unit of electricity generated than the current technologies employed today.

Keywords: Energy storage, Renewable energy, Dispatchable power, Compressed air energy storage, Thermal energy storage.

1. Introduction

As concerns about global warming, carbon costs, and energy security converge, the power sector is seeking to implement carbon-free renewable energy systems that can be fuelled by a countries domestic resources. Two promising technologies are wind and solar. Currently, these technologies only generate 1.28% and 0.02% of electricity demand in the U.S., respectively [1]. However, both technologies have seen growth recently. For instance, the state of Texas has increased its installed wind capacity by more than a factor of 7 during the past 5 years with installations totalling over 9400 MW [2, 3]. However, the growth of these two technologies is hindered by the inherent variability of the wind and solar resources, a key issue that this research attempts to address.

In their current form, both wind and solar energy are subject to diurnal (daily) variation, seasonal variation, and weather conditions, such that both require backup/reserve generation facilities as firming power in case of daily or seasonal outage. As seen in Figure 1, wind in West Texas is out of phase with demand in the load centers of Texas over a typical one-day period in the summer. When demand is highest in the afternoon, wind is at its weakest and when demand is lowest at night wind energy reaches its peak [4, 5]. Figure 1 also shows how solar radiation in West Texas increases along with demand in the afternoon, but as evening approaches it quickly drops off while demand is still high [4, 6].

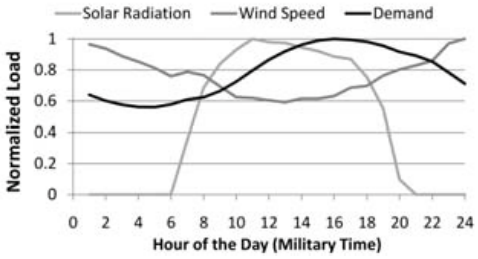

Fig. 1. The profiles of typical wind velocities, solar radiation, and ERCOT load in West Texas have important differences. Wind is out of phase with demand, while solar availability tracks demand more closely.

One way to overcome the issues with the inherent variability of wind and solar resources and their mismatch with demand is to incorporate energy storage so that they can then be used on a dispatchable, load-balancing basis much like natural gas plants.

2. Compressed air energy storage and thermal energy storage

As of today, there are only three practical and deployable industrial scale energy storage methods: compressed air energy storage (CAES), thermal storage, and pumped hydroelectric energy storage (PHS), only the latter of which is currently in wide use. However, major obstacles for PHS include the need for specific terrain requirements and water, which are not available in the regions of the USA where solar resources are strongest.

2.1. Description of CAES

Currently, there are two CAES facilities in the world, the first in Huntorf, Germany and the second in McIntosh, Alabama, that operate by using off-peak electricity to compress air that is stored in an underground cavern (see Figure 2). Both CAES plants use natural gas-fired combustors to heat the compressed air before expansion in order to generate electricity during times of peak demand. It is convenient to think of these facilities as similar to a conventional gas turbine power plant but with one important difference: the compressors are powered by cheap off-peak grid electricity so that all the power created by the turbines can be used to produce electricity in the generator [7]. In effect, this pre-compression step significantly increases the amount of produced electrical power per unit of heat required by the combustors (note: by standard convention, no fuel use is associated with the consumed grid electricity).

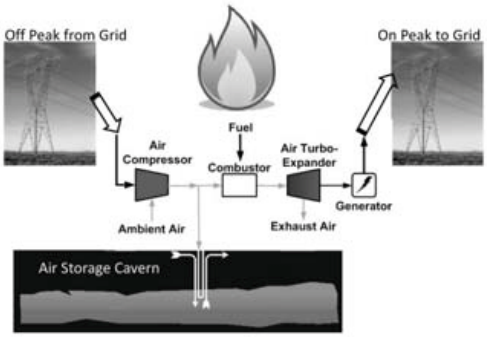

Fig. 2. CAES mimics a typical natural gas power cycle with the addition of an air storage cavern and the decoupling of the compressor and turbine.

In the case of a typical natural gas plant, the compression ratios are in the range of 15:1, which is much less than the 70:1 ratio of a CAES facility. With much more energy input from the compressors to reach such a high compression ratio, it could be anticipated that the CAES plant may not need to heat the air before entering the expansion turbine. However, because the heat removed from the air during compression in a series of intercoolers is not recovered, the air exits the storage cavern at a temperature of around 311 Kelvin. So, in order to increase the energy content and avoid freezing during the expansion process, the existing CAES facilities add heat by using a natural gas combustor [8].

2.2. Description of thermal storage

There are a few types of thermal storage technologies currently used in the industrial market, including high pressure steam, molten salt, and hot oil. Thermal storage, though less mature than PHS, is already under development in industrial applications. NREL demonstrated one of the first thermal storage systems in the Solar Two project in the mid 1990's. Solar Two was able to achieve a capacity factor of around 65% which is remarkable when compared to the typical 25% capacity factor of solar technologies that do not incorporate thermal storage [9].

The analysis detailed in this report does not include research or selection on the different types of thermal storage to be used, but rather just considers its total output. Later work will include this topic as well as analysis necessary to design and size the particular solar thermal and thermal storage components.

3. Description of the integrated system

The purpose of the proposed DSWiSS system is to combine wind and solar energy with both compressed air and thermal storage techniques in a way that couples excess night-time wind capacity with peak solar output. In essence this design mimics the CAES plants previously described but replaces the natural gas combustor with concentrating solar power and thermal storage and will draw power to operate the compressors from excess off-peak wind energy instead of off-peak grid electricity. These key changes ① eliminate all fossil fuel consumption of the CAES plant and ② maintain the system's dispatchability. A detailed block diagram of the proposed energy system can be seen below in Figure 3.

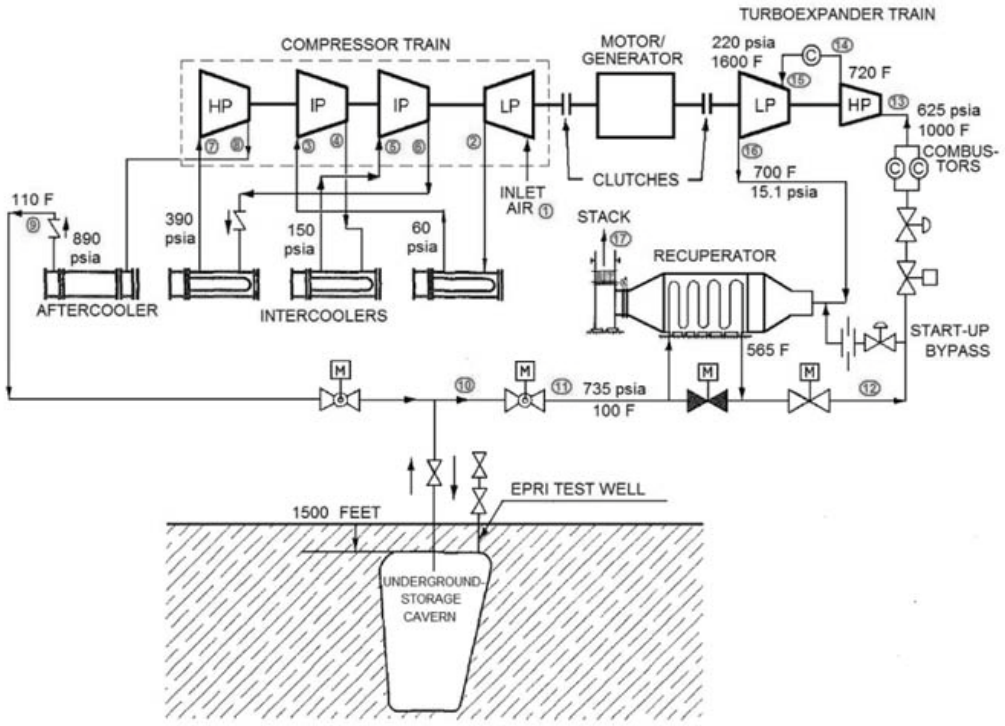

Fig 3: A solar thermal and thermal storage system replaces the natural gas combustor © and electricity is supplied by wind turbines in order to turn the typical CAES plant into DSWiSS (LP = low pressure, IP = intermediate pressure, HP = high pressure). States 1 through 17 are indicated [10].

In this system electricity from wind power drives the compression of air, which is then stored in underground caverns. Then, whenever the operator decides, the air is released from the cavern to be heated by the solar thermal system and expanded through the turbine-generator. Thermal storage is also incorporated here in order to ensure that the turbine-generator system can run into the early evening hours when the price for electricity is still high, or continue to run during off peak hours as a form of firming power. Using this combination of technologies, the energy system should be able to operate on demand during afternoon and early evening hours. The duration of the system's operation into the evening is dependent on the size of the solar thermal and thermal storage system. These two components could be sized large enough to ensure twenty-four hour operation.

It is illustrated in this diagram that the compression and expansion processes will actually be accomplished by multistage units that utilize intercooling and reheat respectively, all of which are modelled in the subsequent thermodynamic analysis. The compressor train modelled herein consists of four stages of compressors with three intercoolers and an aftercooler in order to minimize the required compression work. The turbine system consists of a two-stage turbine with a reheater supplied by the solar thermal system. By utilizing reheat, the second stage turbine will operate at conditions identical to that of a typical gas turbine. Also shown on the diagram is a recuperator that preheats the air exiting the cavern by using the hot exhaust air from the turbine. This form of waste heat recovery will reduce the amount of heat the solar thermal system will need to provide. This turbomachinery system is identical to that located in the McIntosh CAES facility and was designed by Dresser Rand [10].

The operation of such a combination of technologies will not be restricted to a single

method. Based on real time variables like energy price and solar availability, the operator will be able to choose the mode of operation in order to maximize profits. For instance, at any point in time, the operator may choose to sell the wind-generated electricity directly to the grid. This scenario might occur in the middle of the day when the price for electricity is highest. Once these types of decisions have been optimized, it is expected that the generation operation will be run only for a period of time when electricity price is high. Future research will include optimizing the operation of the system in an effort to increase efficiency and maximize profit.

4. Thermodynamic Analysis

A thermodynamic model was created for analyzing the performance of the DSWiSS power generation equipment. This detailed simulation uses first and second law concepts in order to estimate the required energy inputs per unit energy output. Figure 4 illustrates that the wind and solar components are not yet included in this model, rather, they are considered inputs. From this analysis the power system efficiency and required cooling loads will be calculated.

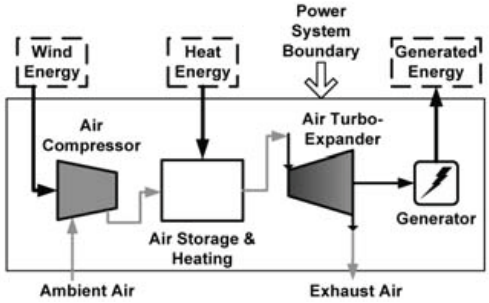

Fig 4: The power system energy inflows and outflows (marked on this diagram) are needed to calculate the power generation efficiency.

4.1. McIntosh CAES facility data and assumptions

Since the DSWiSS facility will operate similarly to a typical CAES facility, it was decided that the power generation equipment would be modelled after the turbomachinery at the McIntosh CAES plant. Table 1 lists the data used directly from the McIntosh plant as well as values that are calculated from McIntosh plant data.

Table 1. These data, taken from the McIntosh CAES facility, are used for the thermodynamic simulation of DSWiSS [10].

McIntosh Parameter	Value	Unit
Inlet Temperature to Cavern	316	K
Inlet Temperature to Recuperator	311	K
Inlet Temperature to Turbine 1	811	K
Inlet Temperature to Turbine 2	1144	K
Installed Generator Capacity	100	MW
Air Storage Cavern Maximum Pressure	7.928	MPa
Air Storage Cavern Minimum Pressure	5.171	MPa
Calculated Parameter	**Value**	**Unit**
Pressure Ratio – Compressor 1	4.16	--
Pressure Ratio – Compressor 2	2.55	--
Pressure Ratio – Compressor 3	2.65	--
Pressure Ratio – Compressor 4	2.33	--
Pressure Ratio – Turbine 1	2.48	--
Pressure Ratio – Turbine 2	14.57	--
Turbine 1 Isentropic Efficiency	89.1	%
Turbine 2 Isentropic Efficiency	87.39	%
Recuperator Effectiveness	76.99	%
Recuperator Pressure Losses	2.65	%
Heat Exchanger Pressure Losses	12.65	%

In addition to these data, some basic and detailed assumptions had to be made in order to complete the thermodynamic model. First, the four basic assumptions are: ① kinetic and potential energy effects are negligible, ② all components are well insulated (Adiabatic), ③ air behaves as an ideal gas, and ④ inlet dry air molal composition is made up of oxygen, nitrogen, carbon dioxide, argon, and helium in mole fraction percentages of 20.95, 78.08, 0.03, 0.93, 0.01, respectively. In addition to these, Table 2 lists some specific assumptions that are made regarding particular components of the power generation equipment.

Table 2. These specific assumptions are necessary for the simulation of the power system and were not available from McIntosh data.

Parameter	Value	Unit
Ambient Air Temperature	295	K
Ambient Air Pressure	101.3	kPa
Compressor Isentropic Efficiencies	80	%
Cooler Pressure Losses	2	%
Cooler Effectiveness	85	%
Heat Exchanger Effectiveness	85	%
Generator Electrical Efficiency	90	%
Motor Electrical Efficiency	90	%
Water Coolant Inlet Temperature	295	K

These parameters make up all the user specified data required to run a complete thermodynamic simulation of the power generation system.

4.2. Creation of a thermodynamic property calculator

A thermodynamic property calculator was created for air. The calculator, for any specified temperature, pressure, and molal composition of oxygen, nitrogen, carbon dioxide, water vapor, argon, and helium, will determine the following properties: mixture molecular weight, mixture ideal gas constant, mass fraction of air mixture components, specific heats, mixture enthalpy, mixture internal energy, and mixture entropy.

At the heart of this property calculator is a 7^{th} order polynomial function that calculates the specific heat at constant pressure (C_p) for each constituent based on temperature [11]. From the C_p values, the air enthalpy, internal energy, entropy, and all other values can be calculated by using appropriate reference values and the definition of each property.

4.3. Component details

The following sections describe in detail the multistage configuration that is modelled in the thermodynamic simulation. Note that all enthalpies expressed in the following sections are in units of kJ/kg.

4.3.1. Compression subsystem

This subsystem consists of a four-stage train of compressors that utilize intercooling and aftercooling between stages, as seen in Figure 3, in order to minimize the required compression work. Through this sequence, outside ambient air is compressed and cooled before being sent to an underground air storage cavern. States 1 through 9 are noted on the Figure.

Using First Law analysis and the previously listed data, the compression system can be analyzed. For each compressor, the exit enthalpy can be calculated based on the inlet enthalpy and compressor efficiency. For each cooler the air-side exit enthalpy can be determined from the air and coolant side inlet enthalpies and the cooler effectiveness, which is defined as the ratio of the actual amount of heat removed versus the maximum amount that could be removed [12].

Using these calculations, in addition to the compression ratios and pressure losses through the coolers, the temperature and pressure at each state can be determined thereby setting all states 1 through 9. Once all temperatures and pressures have been found, the required energy per unit mass flow for each compressor can be found and the compressor train's total specific work can be calculated by simply summing the specific work of all four compressors. Additionally, the cooling load can be found by summing the cooling load of all four coolers [12].

4.3.2. Turbine generator subsystem

This subsystem, seen in Figure 3, consists of a two-stage turbine, primary heater, reheater, recuperator, and generator. As air first exits the cavern it passes through a throttling valve, is heated first by the turbine exhaust in the recuperator and then by the primary heater. Next, after the first turbine stage a reheater increases the air temperature before the second stage turbine. Both the primary heater and reheater are supplied by the solar thermal system. For this model it is assumed that all necessary heat is available in order for the turbine inlet temperatures to be met.

The exit enthalpy of the air for each turbine can be calculated based on the inlet enthalpy and turbine isentropic efficiency. For the recuperator, the cold and hot side exit enthalpies can be calculated using the known inlet air temperature and the recuperator effectiveness. Based on these calculations as well as using the turbine pressure ratios and pressure losses through the recuperator, heater, and reheater, the temperature and pressure for each state can be determined, thereby setting the thermodynamic states 11 through 17. Next, the specific energy output for each turbine can be calculated and summed in order to calculate the total specific electrical power output from the generator. Additionally, the total required heat load for the solar thermal and thermal storage subsystem can be calculated from the combination of the heat loads of the heater and reheater. Knowing this heat load will help when determining the size of the solar thermal and thermal storage subsystems [12].

4.3.3. Air Storage Cavern

The air storage cavern is inherently an unsteady device that requires a separate model to accurately determine thermodynamic conditions during the filling and emptying processes. However, the simple assumption that the earth acts as an infinite heat sink and an infinite heat source allows for the assumption that whether filling or emptying, the

air in the cavern will be at a constant temperature equal to that of the ground temperature. Also of interest is the total volume required for the air storage cavern, which can be calculated using the ideal gas law at the charged and discharged states when the cavern pressure is at its maximum and minimum allowable limits.

4.3.4. Solar thermal and thermal storage subsystem

This analysis assumes that all the necessary heat input needed from the concentrating solar thermal power (CSP) and thermal storage system is adequately supplied. At this time, the analysis focuses on calculating the amount of heat required per unit air mass flow and estimating the sizes of the CSP and thermal storage units based on an assumed generation time window, which will be discussed more in section 4.5. It is expected that almost any CSP design could be used.

4.3.5. Component summary and state table

Table 3 below gives a summary of the equipment in the power system and the thermodynamic states associated with the inlet and outlet of each piece of equipment. Additionally, the 1st Law equation that governs each component is also shown.

Table 3. Summary of power system components inlet and outlet states and associated equations. (ω = specific work, q = specific heat transfer)

System Component	State In	State Out	Equation
Compressor 1	1	2	$\omega_{C1} = h_2 - h_1$
Compressor 2	3	4	$\omega_{C2} = h_4 - h_3$
Compressor 3	5	6	$\omega_{C3} = h_6 - h_5$
Compressor 4	7	8	$\omega_{C4} = h_8 - h_7$
Intercooler 1	2	3	$q_{removed1} = h_2 - h_3$
Intercooler 2	4	5	$q_{removed2} = h_4 - h_5$
Intercooler 3	6	7	$q_{removed3} = h_6 - h_7$
Aftercooler	8	9	$q_{removed4} = h_8 - h_9$
Turbine 1	13	14	$\omega_{T1} = h_{13} - h_{14}$
Turbine 2	15	16	$\omega_{T2} = h_{15} - h_{16}$
Heater	12	13	$q_{added1} = h_{13} - h_{12}$
Reheater	14	15	$q_{added2} = h_{15} - h_{14}$
Recuperator (hot side)	11	12	$q_{exchange} = h_{12} - h_{11}$
Recuperator (cold side)	16	17	$q_{exchange} = h_{16} - h_{17}$

4.4. Cycle analysis

By following the methodology and calculations detailed in the previous section, performance parameters that will be used to evaluate the DSWiSS concept, such as thermal efficiency, can be estimated. All calculations done to this point are on a per unit air mass flow basis, which is useful, but will be expanded upon in the next section. Every thermodynamic state of the power system in DSWiSS has been set based on the compression train and turbine train analysis already described. Now, using the calculated values for total specific compression work, total specific turbine work, and total specific heat input requirement of the heater and reheater, the thermodynamic efficiency, total specific energy input, and energy inputs per unit energy output of the DSWiSS power system can be calculated. Table 4 lists the results.

Table 4. The results show that DSWiSS must use both wind and solar resources.

Cycle Analysis Output Parameters	
Turbine Total Specific Work output (kJ/kg)	724.0
Generator Specific Work output (kJ/kg)	651.6
Heater Total Specific heat Input Req (kJ/kg)	803.4
Compressor Total Specific Work Req (kJ/kg)	545.0
Motor Specific Work Req (kJ/kg)	605.6
Coolers total Specific heat removed (kJ/kg)	525.4
Energy Input Total (kJ/kg)	1409.0
Energy Input Fraction Wind	0.43
Energy Input Fraction Solar	0.57
Power System Efficiency	0.46
Electricity Input per unit Energy Output	0.93
Heat Input per unit Energy Output	1.23

Note that the power system efficiency is the efficiency of the power system only and does not include the efficiency of the wind turbines or solar thermal system.

In addition to these power and efficiency calculations, the power system process was sketched on *T-s* diagram, seen in Figure 5.

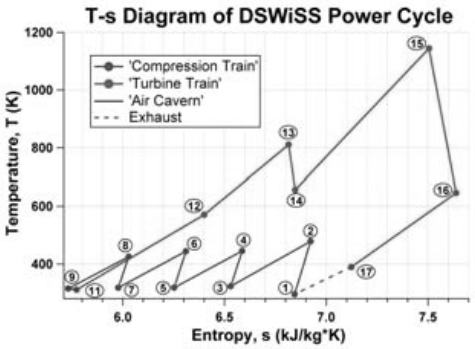

Fig 5. Conceptual T-s diagram of the DSWiSS cycle illustrates the complexity of the turbomachinery.

4.5. Assuming rated output capacity and generation time window

Ideally, determining how the DSWiSS plant will operate over a typical day is one of the goals. Therefore, calculating values such as the steady state air flow rate through the turbine or compressor trains, the steady state electrical energy and heat energy input required, the total daily air mass flow, and the air storage cavern size is useful. However, in order to calculate these values, two important assumptions must be made:

- For this simulation, the rated capacity is assumed to be 100 MW, which is consistent with the McIntosh CAES facility.
- To calculate daily values, the time period when generation and compression takes place must be set. This simulation uses a generation time window of four hours during the peak time period of the day when electricity price is highest. During the generation time period, since compression cannot be occurring, the electricity generated from the wind turbines could also be sold to the grid to increase profits.

Based on the specified rated power output and four-hour generation time window a number of important parameters including the total daily air mass flow through the turbine and compressor train can be calculated. These results can be seen in Table 5.

Table 5. Steady state and daily output parameters.

Important Output Parameters	
Motor Steady State Work Req (MW)	18.6
Motor Daily Work Req (MWh)	371.7
Generator Steady State Work output (MW)	100.0
Heaters Steady State heat Input Req (MW)	123.3
Heaters Daily heat Input Req (MWh)	493.2
Total Daily Air Flow (kg)	2,210,000
Cavern Volume (m^3)	500,000

5. Economic Analysis of the DSWiSS Power System

In order to be utilized in today's electricity market, this renewable energy system will have to compete from an economic standpoint with coal, nuclear, and natural gas power plants. In order to make this economic comparison a levelized lifetime cost approach was adopted. This method takes into account all capital, operation and maintenance, and fuel costs. For DSWiSS, the levelized cost of electricity (*LCOE*), must be estimated for each individual subsystem (wind, solar/thermal storage, and CAES), then combined to equal the total *LCOE*. In order to calculate the *LCOE* for each subsystem, all that is needed is an estimate of the capital expenditures (*CAPEX*) and the operational and maintenance expenditures (*OPEX*), along with appropriate values for the discount rate (d), technical lifetime (N), and plant capacity factor (CF). With these values, both the *CAPEX* and *OPEX* can be calculated on a dollar per MWh generated basis.

In most references, the *OPEX* is already listed in dollar per MWh generated form. However, the *CAPEX* is nearly always given in the form dollar per kW, which is dollars per kW installed capacity. This value must then be annualized over the technical lifetime of the plant using the already specified discount rate, then converted from a per kW installed capacity value to a per MWh generated annually value by using two conversion factors (kW per MW and hr per yr) and the plant's capacity factor. Table 6 lists the *CAPEX* and *OPEX* values found in literature as well as the calculated *LCOE*.

Table 6. Selecting the CAPEX and OPEX costs allows for the calculation of the LCOE [13-16].

Subsystem	CAPEX [$/kW]	OPEX [$/MWh]	LCOE [$/MWh]
Wind	1604	10.5	55.0
Solar Parabolic Trough	4000	16.3	32.6
Solar Power Tower	4000	13.9	26.3
CAES	770	2.38	10.5

It must be pointed out that the *LCOE* values for the two solar technologies have been adjusted to incorporate the efficiency of a solar plant in converting the heat energy to electrical energy. Additionally, all solar costs have incorporated thermal energy storage and the CAES costs have incorporated any necessary equipment including all compressors, turbines, generators, recuperators, and storage caverns.

Each *LCOE* is given in dollars per MWh, but these do not refer to the same MWh. The wind system is in dollars per MWh of electricity supplied from the wind turbines. The solar thermal systems are in dollars per MWh of heat supplied to the air before entering the turbine. And the CAES system is in dollars per MWh of electricity sent to the grid from the DSWiSS facility.

The last step before calculating the entire system's *LCOE* is to incorporate the energy requirement ratios for the wind and solar subsystems. Shown previously in Table 4, incorporating these values allows the conversion of each subsystems cost to a basis of dollars per MWh of generator output; note that the *LCOE* for the CAES system is already in terms of dollars per MWh of generator output.

Seen in Table 7 are two complete system *LCOE* values based on the different solar thermal technologies.

Table 7. Estimated LCOE for the DSWiSS using two different solar thermal technologies.

DSWiSS Plant Design	LCOE [$/MWh]
DSWiSS with Power Tower	94.1
DSWiSS with Parabolic Trough	101.8

5.5. Comparison to other generation technologies

In the U.S., coal, natural gas and nuclear plants are the majority providers of electricity. In 2007 these three combined to generate over 88% of all electricity consumed in the U.S. [1]. Based on data from the Electric Power Research Institute (EPRI), Figure 6 illustrates the relationship of the *LCOE* for all these types of facilities as well as a stand-alone wind farm and solar thermal trough facility to that of DSWiSS [17].

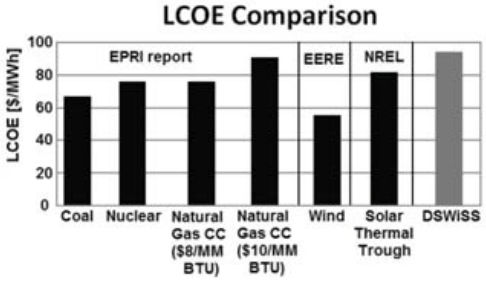

Fig 6. LCOE for DSWiSS is competitive with that of current generation technologies [13, 14, 17]. However, this LCOE does not include any of the available tax credits or any carbon costs.

6. Conclusions

Through this analysis, the thermodynamic performance and cost of energy production from an integrated system consisting of wind and solar energy systems coupled to compressed air and thermal energy storage have been estimated. The combination of these components yielded a power system efficiency of over 46%. A better understanding of the size of the wind and solar components has been gained through the assumption of a rated generation capacity and generation time period. Additionally, the system has been shown to use both wind and solar resources fairly equally in order to generate dispatchable power.

The integrated system is also found to be slightly more expensive on a dollar per MWh generated basis than some of the current technologies employed around the world today but competitive with others such as stand-alone solar facilities and natural gas facilities at a high fuel price. Even though the DSWiSS system was found to have higher expenses, there are many cost externalities that were not taken into account. These include rising fuel costs, fuel cost volatility, global warming, energy independence, national security, resource depletion, and the uncertainty over the future cost of emissions. Furthermore, the production tax credit (PTC), investment tax credit (ITC), and renewable energy credit (REC), all of which are available in the U.S., were not included in this economic analysis. Additionally, the DSWiSS facility will be dispatchable and able to quickly ramp up or down to provide valuable load-balancing power, a claim that only natural gas and hydroelectric power plants can currently make.

This analysis is the beginning of a much more detailed thermo-economic investigation of this energy system's performance and profitability. For future work, real time data will be incorporated including area specific wind velocity along with wind turbine power profiles, local solar radiation, real time electricity pricing, and local daily temperature variation. It is evident that system optimization will be needed in order to determine the operation scenario of maximum profit. Optimization parameters such as time interval of energy production, wind turbine energy split between compression versus direct selling, and time duration of thermal storage heating will all need to be considered in order to determine the most profitable design.

References

[1] EIA, "Annual Energy Review 2008," U.S. Department of Energy, Energy Information Administration, Washington D.C. DOE/EIA-0384(2008), 2009.

[2] AWEA, "U.S. Wind Energy Projects - Texas."
[3] Comptroller, "The Energy Report 2008," Office of the Texas Comptroller, , Austin, TX 2008.
[4] M. Kapner, "Dispatchable Hybrid Wind / Solar Power Plant," Austin Energy, Austin.
[5] AEI, "Wind Data for Tall Tower South (Sweetwater)," Alternative Energy Institute - West Texas A&M University, 2007.
[6] G. Vliet, "Texas Solar Radiation Database," The University of Texas at Austin.
[7] BINE, "Compressed Air Energy Storage Power Plants," 2007.
[8] R. B. Schainker and M. Nakhamkin, "Compressed Air Energy Storage (CAES): Overview, Performance and Cost Data For 25MW to 220MW Plants," IEEE Power Engineering Society 1985.
[9] EERE, "Concentrating Solar Power: Energy from Mirrors," U.S. Department of Energy 2001.
[10] M. Nakhamkin, L. Andersson, E. Swensen, J. Howard, R. Meyer, R. Schainker, R. Pollak, and B. Mehta, "AEC 110 MW CAES Plant: Status of Project," *Journal of Engineering for Gas Turbines and Power,* vol. 114, pp. 695-700, 1992.
[11] P. P. Walsh and P. Fletcher, *Gas Turbine Performance*: Blackwell Science Ltd and ASME, 2004.
[12] P. S. Schmidt, O. A. Ezekoye, J. R. Howell, and D. K. Baker, *Thermodynamics An Integrated Learning System*: John Wiley & Sons, 2006.
[13] EERE, "Annual Report on U.S. Wind Power Installation, Cost, and Performance Trends: 2007," U.S. Department of Energy, Washington D.C. 2008.
[14] Sargent and Lundy, "Assessment of Parabolic Trough and Power Tower Solar Technology Cost and Performance Forecasts," National Renewable Energy Laboratory, Sargent and Lundy LLC Consulting Group, Chicago, IL NREL/SR-550-34440, 2003.
[15] Ridge, "The Economic Impact of CAES on Wind in TX, OK, and NM," Texas State Energy Conservation Office, Ridge Energy Storage & Grid Services, Houston, TX June 27 2005.
[16] LCRA, "Study of Electric Transmission in Conjunction with Energy Storage Technology," Texas State Energy Conservation Office, Lower Colorado River Authority, Austin, TX August 21, 2003 2003.
[17] EPRI, "Program on Technology Innovation: Integrated Generation Technology Options," Electric Power Research Institute, Palo Alto, CA 2008.

Acknowledgments: The report was prepared with the assistance and support of both Mark Kapner from Austin Energy and the Department of Mechanical Engineering and Center for International Energy and Energy Policy at the University of Texas at Austin.

Thermo-economic Optimisation of the Heliostat Field of Solar Tower Thermal Power Plants

Germain Augsburger[a], *Daniel Favrat*[a]

[a] *Industrial Energy Systems Laboratory, École Polytechnique Fédérale de Lausanne, Switzerland*

Abstract: A method of optimising the thermodynamic and economic performance of a heliostat field within a solar tower thermal power plant has been developed. The method includes the generation of a heliostat field given a set of design variables, the assessment of its thermodynamic and economic performance, a sensitivity analysis of chosen key design variables, and a multi-objective optimisation using an evolutionary algorithm. Parameters of the former *Solar One* power plant in California are set as reference to illustrate the method throughout the article and to highlight potential setup improvements as well as optimal solutions under given constraints.

Keywords: thermo-economic optimisation, heliostat field, solar tower thermal power plants.

1. Introduction

As more and more solar thermal power plants are being built and/or planned in sunny places such as South Spain and North Africa, the assessment and the optimisation of their economic performance in parallel with their energy performance are required. Among concentrating solar power technologies – mainly trough, Fresnel and dish collectors – solar tower thermal power plants are expected to reach levelised electricity costs below 10 USct/kWh$_{el}$ [13] as their high source temperature level allows annual solar-to-electricity efficiencies exceeding 20 % thanks to combined cycles [15].

Among previous works, thermo-economic modelling and optimisation methods have been applied to parabolic trough systems by Allani [1] and later by Kane [6] for an Integrated Solar Combined Cycle System (ISCCS) in a Tunisian project. In the absence of subsidies a predicted solar power cost lower than 13 USct/kWh$_{el}$ were quoted for a solar share close to 25 %. Kane [7] then performed a multi-criteria optimisation of a small hybrid solar power system, including aspects such as energy performance, economic and financial analysis, and environmental aspects. Regarding solar tower thermal plants, Pelet [12] introduced a multi-objective approach for designing their concentrator field, and Zhang [18] extended this work with a simplification of the model with the aim of facilitating the identification of the heliostat fields with the lowest specific energy cost.

Keeping the methodological concept of a multi-objective thermo-economic optimisation this paper presents a more complete model including the receiver's heat flux distribution and coupling a thermal conversion cycle to assess the overall plant performance.

2. Evaluation of one heliostat field

In the following, a method of evaluating one heliostat field is presented and illustrated with the *Solar One* case (*SO*) [10, 15, 16].

2.1. Field design input variables

2.1.1. Heliostats, field layout, tower and receiver

The generation of one heliostat field requires the definition of a set of design variables (Table 1) which has been broken down into three subsets: heliostat variables, field layout variables, and tower and receiver variables:

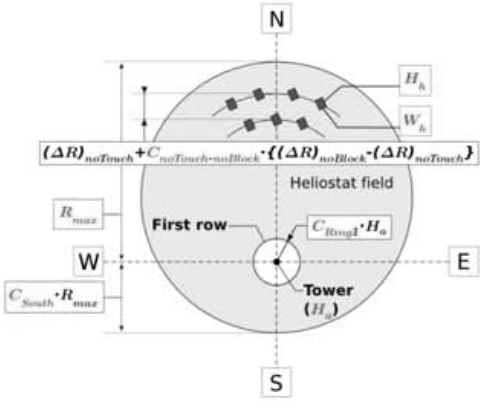

Fig. 1. Geometrical layout design variables defined to generate heliostat fields in lenisolar [9].

Corresponding Author: Germain Augsburger, Email: germain.augsburger@epfl.ch

- Heliostat variables include heliostat dimensions and optical properties. Heliostat dimensions are the width and height that correspond to the heliostat total area, and the ratio of reflective surface to total surface is taken into consideration, as well as the heliostat base. Optical properties are the heliostat mirror reflectivity, and its slope and tracking error deviations [4]. Heliostat variables are summarised in Table 1 in the case of *SO*.
- Field layout variables comprise the number of heliostats, the geometrical layout variables and some terrain properties. Geometrical layout variables are (Fig. 1): the ratio of the field's first ring of heliostats to the tower height, the coefficient of radial spacing between rings, and the ratio of the south furthest ring to the north furthest ring. Two terrain properties are available: the slope of the field (from south to north) and the distance from the tower feet where this slope starts.
- Tower and receiver variables are their dimensions as well as the receiver type and orientation (Table 1).

Based on this set of design variables a first heliostat field can be generated [14] as a default field.

2.1.2. Location, plant, costing and financing

The assessment of the thermodynamic and economic performance then requires the definition of location variables, of simple plant parameters, and costing and financing parameters:

- Location variables consist of longitude, latitude and sun shape standard error deviation [1].
- Parameters of a simple steam-based power plant allow the estimation of the yearly electricity yield: the nominal and the yearly cycle efficiencies of a reference [17] power conversion unit (PCU) as well as its solar multiple [7].
- Costing parameters concern the terrain, heliostats, the tower, the receiver and the power conversion unit, while financing parameters comprise operation and maintenance costs [13], the plant lifetime, interest rate and local electricity tariff for solar thermal power plants (STPP) such as the Spanish feed-in tariff (Real Decreto 661/2007).

Table 1. Field design input variables – Solar One.

Heliostats		
Width	6.24	(m)
Height	6.6	(m)
Base	0.2	(m)
Reflectivity	0.9417	(-)
Slope error	2.6	(mrad)
Tracking error	2.1	(mrad)
Field layout		
Number of heliostats	1818	(#)
First ring to tower ratio	unk.	(-)
Radial spacing coefficient	unk.	(-)
South to north ratio	unk.	(-)
Field slope	0	(°)
Field slope start	none	(m)
Tower and receiver		
Aim point height	83.95	(m)
Receiver type	cyl.	(-)
Receiver radius	3.5	(m)
Receiver height	13.7	(m)
Receiver tilt angle	0	(°)
Location		
Longitude	117.02	(°)
Latitude	34.89	(°)
Sun shape error	2.24	(mrad)
Plant		
Solar multiple	1.45	(-)
Nominal cycle efficiency	0.307	(-)
Yearly cycle efficiency	0.2418	(-)
Costing and financing		
Operation and maintenance	3	(USct/kWh$_{el}$)
Plant lifetime	25	(y)
Interest rate	9	(%)
STPP electricity tariff	34	(USct/kWh$_{el}$)

2.2. Field thermo-economic performance

Once field design input variables are defined, the field's performance is evaluated with *lenisolar* [9] (whose computation details are not addressed in this paper): according to longitude and latitude a link is established with a solar radiation online database, and the heliostat field performance is evaluated over 4 perfect solstices and equinoxes on an hourly basis (about 50 time points). This allows the estimation of the field efficiency over an entire year as an interpolated function of sun azimuth and elevation angles (about 4000 time points).

In the following, key output figures are defined to assess the field energy and economic performance.

2.2.1. Energy performance

Field energy performance is given by its efficiency, its maximum thermal power incident on the receiver, the incident heat flux peak, and the yearly electrical energy yield:

- The field energy efficiency is given by the ratio of thermal energy incident on the receiver, to the solar irradiance incident on heliostats (*Direct Normal Irradiance* Wh/m^2 × *Number of heliostats* × *Heliostat reflective area* m^2).
- The maximum thermal power incident on the receiver and the incident heat flux peak are given by the highest values achieved over a year.
- The yearly electrical energy yield is the yearly sum of hourly outputs calculated with the plant parameters mentioned here above.

2.2.2. Costing and financing performance

Field costing and financing performance is assessed by the total investment cost, costs breakdown, levelised electricity cost (LEC), payback period and net present value (NPV) [3].

- The total investment cost sums up field and plant costs, while costs breakdown shows the spread of costs between receiver, heliostats, terrain and tower.
- Levelised electricity cost is defined as the minimum required sale price per unit of electricity such that the power plant is economically viable.
- The payback period is given by the time point when the plant starts being profitable and the net present value is the balance of expense and income annuities over lifetime.

Table 2 shows results in the case of *SO* - like variables.

Table 2. Field thermo-economic performance – SO, estimated with lenisolar [lenisolar].

Energy performance		
Yearly field efficiency	0.6644	(-)
Max. incident power	54.98	(MW_{th})
Incident heat flux peak	1048.3	(kW_{th}/m^2)
Yearly energy yield	22.056	(GWh_{el})
Costing and financing		
Total investment cost	56.5	(milUSD)
Levelised electricity cost	29.08	($USct/kWh_{el}$)
Payback period	15.8	(y)
Net present value	10.67	(milUSD)

3. Improvement of one heliostat field

A sensitivity analysis of design variables such as dimensions or geometrical layout variables is ran to study their influence on the heliostat field thermodynamic and economic performance, i.e. on thermal peak power, yearly thermal energy yield or levelised electricity cost. According to this influence one already suggests some modifications leading to quantifiable improvements.

3.1. Sensitivity of aim point height

Without changing any other design variable, the aim height of *SO* tower undergoes a step-by-step linear variation in a range from 60 m to 140 m.

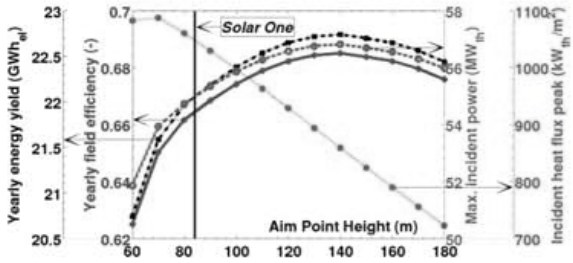

Fig. 2. Sensitivity of aim point height on SO: energy performance indicators .

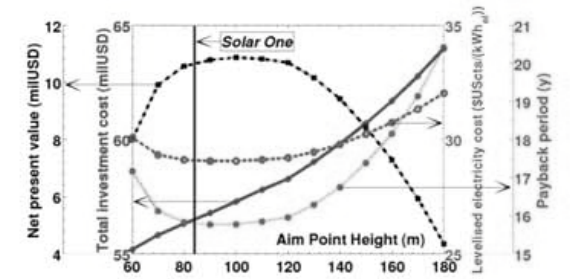

Fig. 3. Sensitivity of aim point height on SO: economic performance indicators.

As a result (Fig. 2), field energy efficiency first increases by 6 points from 60 m to 140 m, reaches a maximum of 68.5 %, and drops by 1 point from 140 m to 180 m. This obviously shows the presence of an optimum aim point height, which *SO* is fairly below but with 97 % of the maximum efficiency. Aim point height has a similar influence on other performance indicators: maximum thermal power incident on the receiver follows a similar trend as well as yearly electrical energy yield. Minimum levelised electricity cost of 29.05 $USct/kWh_{el}$ and minimum payback period

are achieved with 90 m, while 100 m results in maximum net present value.

3.2. Sensitivity of heliostat dimensions

Heliostat total area is varied linearly from 20 m^2 to 100 m^2 keeping constant the *SO* width-to-length ratio and *SO* field layout is kept exactly the same.

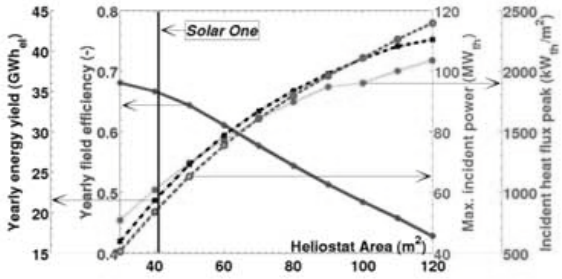

Fig. 4. Sensitivity of heliostat area on SO: energy performance indicators .

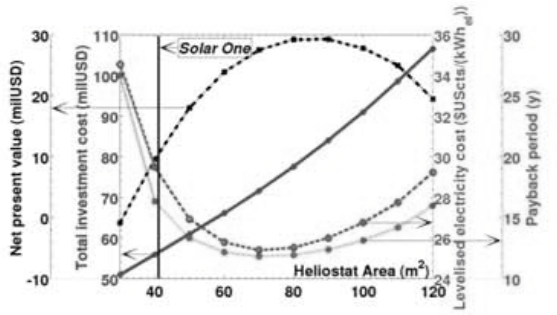

Fig. 5. Sensitivity of heliostat area on SO: economic performance indicators .

Results (Fig. 4) show that doubling the mirror surface causes a 40 % rise in maximum thermal power incident on the receiver, but also a 20 % drop in energy efficiency because of higher blocking and shadowing losses.

At the economic level, a minimum LEC appears on Fig. 5 with a 70 m^2 area.

3.3. Sensitivity of receiver dimensions

In a similar way, receiver area now follows a linear variation around *SO*-values, from 200 m^2 to 700 m^2 with the receiver diameter-to-height ratio kept constant.

As a result, yearly field efficiency rises but reaches a plateau around 68.5 % and the price of this 2 points efficiency gain is high given the strong influence of the receiver area on investment costs (+34.7 %). On the other side, minimum levelised electricity cost, minimum payback period and maximum net present value are achieved with a 150 m^2 area.

Thus the sensitivity of receiver dimensions on both energy and economic indicators emphasizes in this case the trade-off to decide between efficiency and levelised cost: *SO* is a fair one, with a –3 % relative efficiency difference from the plateau and a +8.7 % relative LEC difference from the minimum.

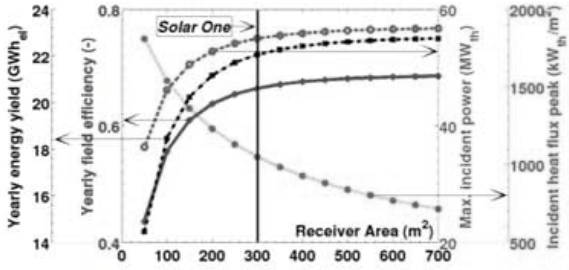

Fig. 6. Sensitivity of receiver area on SO: energy performance indicators .

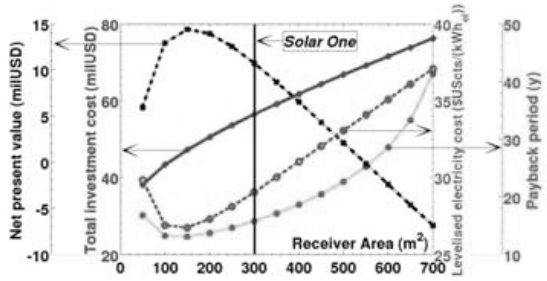

Fig. 7. Sensitivity of receiver area on SO: economic performance indicators .

3.4. Sensitivity of field slope

A field slope is envisaged when the terrain allows it (smooth hills). Here field slope is varied from 0° to 20°, which makes an optimum field slope appear of 6° according to performance indicators: field energy efficiency achieves a maximum of 66.83 % and a maximum thermal power incident on the receiver of 55.17 MW_{th}, which is a much too slight improvement according to original *SO*.

When both plain and hill are available, a combination between a flat and a sloping field sector separated by a west-east breaking line is also envisaged. Thus the y-coordinate (South-North dir.) of this breaking line is added among variables, and a combined sensitivity ("slope" and "slope start") is run through a variation of slope start from 0 m to 400 m: a tiny 0.003 % gain in

efficiency is observed with the best combination, i.e. slope 6° and start at 100 m. Despite these insignificant enhancements, field slope and slope start should not be put aside once and for all, as some fields different from *SO*-case might still benefit from their introduction.

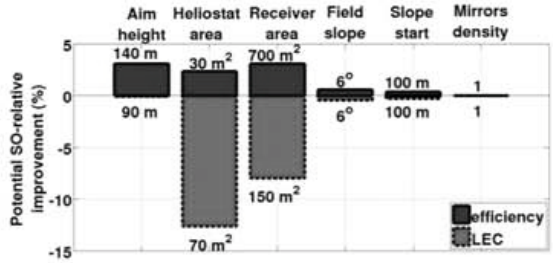

Fig. 8. Summary of efficiency and LEC potential enhancements through design variations.

Additional sensitivity analysis is performed on mirrors density through down and up scaling of *SO*-heliostat coordinates, which turns out to be already optimal. Fig. 8 sums up how field design variables potentially have an influence on performance indicators with *SO* as reference (since sensitivity analyses here above are uncoupled, these potential improvements are not cumulative).

4. Thermo-economic optimisation of heliostat fields

Evolutionary multi-objective optimisation needs the definition of a set of decision variables, of 2 contradictory objectives, and of constraints. Constraints are the accepted variation range of both the decision variables and the objectives, but also of auxiliary outputs such as e.g. heat flux peak on the receiver. By choosing the total investment cost and levelised electricity cost as objectives, a Pareto front of the best trade-offs is obtained in order to select an appropriate solution for the given location.

4.1. Field decision variables

The main field design input variables are selected as decision variables (Table 3): heliostat width and height, geometrical layout variables and terrain properties, tower and receiver dimensions. The number of decision variables indirectly determines the minimum number of evaluations needed by the evolutionary multi-objective optimiser *Q-MOO* [10] to achieve Pareto front stability: from experience based on our model, with 7 decision variables and 2 objectives the number of evaluations required roughly is 4000.

4.2. Contradictory objectives

Contradictory objectives proposed here are the yearly electrical energy yield and the field energy efficiency. These two energy performance indicators are directly linked with two economic performance indicators: total investment cost and levelised electricity cost are contradictory too.

Table 3. Decision variables, objectives and constraints of the thermo-economic optimisation.

Decision variables	Range	
Heliostats		
Width	1 – 15	(m)
Height	1 – 15	(m)
Field layout		
Number of heliostats	50 – 15000	(#)
First ring to tower ratio	0.2 – 2	(-)
Radial spacing coefficient	0 – 1	(-)
South to north ratio	0 – 1	(-)
Tower and receiver		
Aim point height	20 -300	(m)
Objectives		
Yearly field efficiency	max	(-)
Levelised electricity cost	min	(USct/kWh$_{el}$)
Constraints		
Max. incident power	> 30	(MW$_{th}$)

4.3. Constraints

Constraints may be applied to decision variables as well as to any performance indicator (Table 3): the values of field design input variables do not exceed the given lower and upper limits, while maximum incident power is kept above 30 MW$_{th}$.

4.4. Pareto front of optimal fields

The *Q-MOO* evolutionary algorithm first generates an initial population (Fig. 9) by randomly picking values of decision variables within the limits given in Table 3, and by evaluating corresponding objectives. Crossing over is performed between individuals and objectives are evaluated again: best individuals according to a temporary theoretical Pareto front are kept alive whereas worst ones are killed. The process is run iteratively till completion of the maximum number of evaluations defined previously.

The resulting Pareto front provides the limit between feasible and unfeasible solutions, and illustrates the set of trade-offs of field energy efficiency against levelised electricity cost.

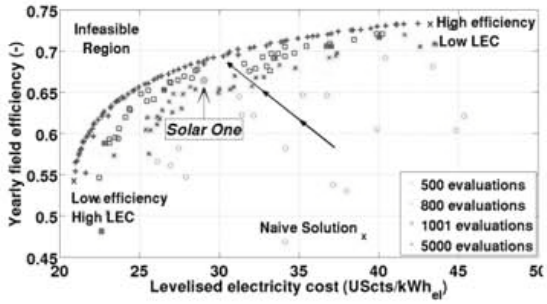

Fig. 9. Pareto front (trade-off curve) after optimisation of efficiency vs. LEC, on SO-basis.

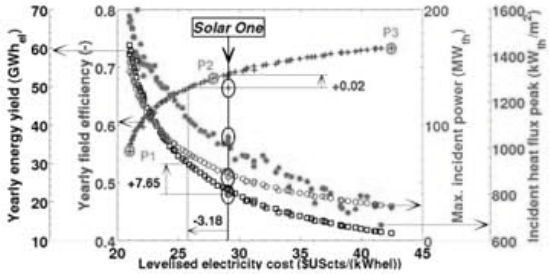

Fig. 10. Energy performance indicators on the Pareto front (trade-off curve).

The comparison of points on the Pareto front with *SO*-values (Fig. 10) gives a 0.02 potential gain in efficiency at an equivalent LEC. At an equivalent efficiency, a 3.18 UScts/kWh$_{el}$ drop in LEC is achievable as well as a significant 7.65 GWh$_{el}$ rise in yearly energy yield (+19.6 MW$_{th}$ in thermal power) with a still reasonable 74.91 kW$_{th}$/m^2 increase in heat flux peak.

4.5. Three solutions on the Pareto front

Three points on the Pareto front are selected (see Fig. 10) and presented in detail - two extreme points: low efficiency and low levelised electricity cost (P1), high efficiency and high levelised electricity cost (P3); one trade-off between efficiency and levelised electricity cost (P2).

Setup *P1* points out how a 2.05 m increase in heliostat height combined with a 54.3 m higher tower, with a large number of heliostats, with a rather low radial spacing coefficient and a high south-to-north ratio, leads to a low 21 USct/kWh$_{el}$ LEC in relation to *SO*. Nevertheless, consequences on efficiency are not negligible: it drops to 55.5 %.

On the other side, *P3* reaches a fairly high 73.3% efficiency with smaller heliostats and tower, with a high 0.84 radial spacing coefficient and a lower south coverage. But LEC is so high that the plant net present value turns negative and thus makes this setup unreasonable.

Table 4. Selected points on the Pareto front (trade-off curve).

Decision variables	*P1*	*P2*	*P3*	
Heliostats				
Width	6.27	5.62	5.11	(m)
Height	8.65	7.16	5.30	(m)
Field layout				
Number of heliostats	4532	2061	1344	(#)
First ring to tower ratio	0.31	0.36	0.24	(-)
Radial spacing coef.	0.21	0.74	0.84	(-)
South to north ratio	0.91	0.62	0.48	(-)
Tower and receiver				
Aim point height	138.2	127.1	117.1	(m)
Performance ind.				
Energy performance				
Yearly field efficiency	0.555	0.681	0.733	(-)
Max. incident power	154.4	63.6	30.0	(MW$_{th}$)
Incident heat flux peak	1544	1061	742	(kW$_{th}$/m^2)
Yearly energy yield	68.9	25.2	11.9	(GWh$_{el}$)
Costing and financing				
Total investment cost	107.5	61.6	46.2	(milUSD)
LEC	21.0	27.9	42.5	(USct/kWh$_{el}$)
Payback period	8.3	14.3	24.1	(y)
Net present value	77.8	15.2	-10.0	(milUSD)

P2 is similar to *SO* except a lower heliostat width-to-length ratio and a 43.2 m higher tower. This results in better efficiency and LEC.

4. Conclusion

A method of optimising heliostat fields of solar tower thermal power plants both at the energy level and the economic level has been presented. The main field design input variables have been identified and illustrated with the Californian *Solar One*-case, and have allowed a first single field thermo-economic evaluation based on chosen energy, costing and financing performance indicators. Subsequently, six sensitivity analyses have been performed separately around selected *SO*-parameters to identify potential performance improvements: mainly aim height, heliostat area and receiver area variations have turned out to lead to significant efficiency increases and LEC decreases. Decision variables of optimisation have thus been chosen among field design variables, likewise two contradictory objectives – field efficiency and LEC – have been selected among energy and economic performance indicators. Constraints have been set on decision variables in

the form of limiting intervals and on receiver thermal power as an inequality to avoid fields below 30 MW_{th}. Thanks to an evolutionary multi-objective optimiser a Pareto-front (trade-off curve) has been obtained, which describes the achievable compromises between efficient fields and less costly fields. As a result, optimised solutions have highlighted a feasible 2 points rise in efficiency when keeping *SO*-LEC, as well as a 3.18 $USct/kWh_{el}$ drop in LEC when keeping *SO*-efficiency. On the other side, detailing two extreme Pareto-points shows that with different variables combinations, a given field setup may reach a 73.3 % yearly field efficiency while another one may reach a 21-$USct/kWh_{el}$ LEC with an *SO*-like non-improved steam-based conversion cycle. Unfortunately, available literature on *SO* does not allow assessing the relevance of this optimum value, but here should be reminded that receiver dimensions are kept *SO*-like throughout the optimisation and that receiver cost correlations [8] have a tremendous influence on LEC estimation.

Given its flexibility and its relevance in the current decision-making process on solar thermal power plants, the presented method for thermo-economic optimisation of heliostat fields aims at suitability for designing new plants, and is to be extended to multi-tower configurations, to enhanced conversion cycle and to the evaluation of geographical locations.

Nomenclature

C coefficient, -

H height, m

R radius, m

Subscripts and superscripts

a	Aim point
h	Heliostat
max	Maximum
noBlock	No blocking between heliostats
noTouch	No touching between heliostats
Ring1	Relating to first ring of heliostats
South	Relating to South

References

[1] Allani, Y., et al., 1997, CO2 Mitigation through the Use of Hybrid Solar-Combined Cycles, Energy Conversion and Management, 38(SUPPL. 1), pp. S661-S667.

[2] Biggs, F., and Vittitoe, C. N., 1979, The HELIOS Model for the Optical Behavior of Reflecting Solar Concentrators, Technical Report, SAND76-0347, Sandia Laboratories, Albuquerque, NM.

[3] Bossaerts, P., and Ødegaard, B. A., 2006, *Lectures on Corporate Finance*, 2nd ed., World Scientific, Singapore, Chap. 6.

[4] Collado, F. J., et al., 1986, An Analytic Function for the Flux Density due to Sunlight Reflected from a Heliostat, Solar Energy, 37(3), pp. 215-234.

[5] Fernandez, V., 2006, PS10: a 11.0-MWe Solar Tower Power Plant with Saturated Steam Receiver, *Solúcar report presentation*, URL:http://www.upcomillas.es/catedras/crm/report05/Comunicaciones

[6] Kane, M., Favrat, D., 2000, Thermo-economic Analysis of Advanced Solar-Fossil Combined Power Plants, International Journal of Applied Thermodynamics, 3(4), pp. 191-198.

[7] Kane, M., Favrat, D., 2002, Multi-criteria Optimisation of Small Hybrid Solar Power System, *Proc. Eurosun 2002*, Bologne.

[8] Kistler, B. L., 1986, A User's Manual for DESOL3: A computer Code for Calculating the Optical Performance and Optimal System Design for Solar Thermal Central Receiver Plants, Technical Report, SAND86-8018, Sandia Laboratories, Albuquerque, NM.

[9] Lenisolar, Thermo-economic Optimisation of Heliostat Fields, 2009, Ver. 1.0, Industrial Energy Systems Laboratory, Lausanne, CH.

[10] Molyneaux, A., et al., 2008, Environomic multi-objective optimisation of a district heating network considering centralized and decentralized heat pumps, Energy, 35(2), pp. 751-758.

[11] Pacheco, J. E., 2002, Final Test and Evaluation Results from the Solar Two Project, Technical Report, SAND2002-0120, Sandia National Laboratories, Albuquerque, NM.

[12] Pelet, X., et al., 2006, Design of Heliostat Fields Using a Multi-objective Evolutionary Algorithm, *Proc. 13th International Symposium on Concentrated Solar Power and Chemical Energy Technologies – SolarPACES 2006* [CD ROM], Seville, pp. A7-S1.

[13] Price, H., et al., 2003, Assessment of Parabolic Trough and Power Tower Solar Technology Cost and Performance Forecasts, Subcontractor Report, NREL/SR-550-34440, National Renewable Energy Laboratory, Golden, CO.

[14] Siala, F. M. F., and Elayeb, M. E., 2001, Mathematical Formulation of a Graphical Method for a No-Blocking Heliostat Field Layout, Renewable Energy, 23(1), pp. 77-92.

[15] Spelling, J., et al., 2009, Evaluation of a Combined Cycle Setup for Solar Tower Power Plants, *Proc. SolarPACES 2009* [USB-stick], Deutsches Zentrum für Luft- und Raumfahrt e.V. (DLR), Stuttgart.

[16] Stine, W. B., and Harrigan, R., W., 1985, *Solar Energy Systems Design*, John Wiley and Sons, Hoboken, Chap. 10.

[17] Stoke, W., 1999, Solar Two Central Receiver, Consultant Report, P600-00-017, California Energy Commission, Rosemead, CA.

[18] Zhang, H., et al., 2007, Multi-objective Thermo-economic Optimisation of the Design of Heliostat Field of Solar Tower Power Plants, *Proc. Engineering for Sustainable Energy in Developing Countries 2007*, Rio de Janeiro.

Acknowledgments: The authors are definitely in dept of Marco Simiano, Raffaele Bolliger and Martin Gassner for their contribution.

Thermo-Economic Optimisation of Solar Tower Thermal Power Plants

James Spelling[a,b], *Daniel Favrat*[a], *Andrew Martin*[b] *and Germain Augsburger*[a]

[a] *Industrial Energy Systems Laboratory, Ecole Polytechnique Fédérale, 1015 Lausanne, Switzerland*
[b] *Department of Energy Technology, KTH Royal Institute of Technology, 100 44 Stockholm, Sweden*

Abstract: A dynamic model of a pure-solar combined cycle power plant has been developed in order to allow determination of the thermodynamic and economic performance of the plant for a variety of operating conditions and superstructure layouts. The model was then used for multi-objective thermo-economic optimisation of both the power plant performance and cost, using a population-based algorithm. In order to examine the trade-offs that must be made, two, conflicting, objectives will be considered, namely minimal investment costs and minimal levelised energy costs. It was shown that efficiencies lie in the region of 18-24% accompanied by levelised electricity costs in the region of 12-24 UScts/kWh$_e$.

Keywords: solar, thermal, combined-cycle, multi-objective optimisation, thermo-economics

1. Introduction

All existing commercial solar thermal power plants focus on the use of Rankine cycles, which are limited in the efficiencies they can achieve by the relatively low temperatures at the receiver. However, recent developments in the field of high temperature volumetric receivers [1] along with rock-based packed-bed storage systems have opened up an interesting possibility. High temperature receivers allow the use of higher-efficiency combined-cycle setups, whereas packed-bed units offer the possibility of cheap storage.

In order to maximise use of the Sun's energy, as well as minimise the levelised cost of the electricity produced, a dynamic model of a central receiver solar thermal power plant was developed in a form suitable for multi-objective optimisation. The model was then used for thermo-economic optimisation of both the power plant performance and cost, in order to examine the trade-offs that must be made.

2. Dynamic Models of Solar Power Plant Components

In order to simplify the process of dynamic simulation of the power plant, the models have been coded using object-oriented techniques. Under this approach, each power plant component is represented by an object, which encapsulates all the equations required for the resolution of the model, as well as links to upstream and downstream components, allowing automatic communication of thermodynamic states and other variables between components.

Once all the models are assembled and designed, the simulation can proceed. Though the individual models have been coded using implicit techniques, the simulation itself is explicit. As a result of this, the timesteps involved cannot be too large, with values of above 180 seconds showing instability in the calculations due to numerical energy conservation losses. A timestep of 30 seconds was chosen for the simulations performed as part of this project, as this ensures the conservation of energy to within 0.2%.

2.1. Modelling the Volumetric Receiver

To be able to determine the temperature and mass flow that can be obtained from the volumetric receiver for a given radiant flux and inlet air temperature, a mathematical model of the heat and mass transfer that takes place within the porous structure was developed.

The coolant air returning from the power generation cycle is blown around and between the receiver modules. As the coolant air exits at the front of the receiver it mixes with a certain amount of atmospheric air, governed by the air return ratio of the receiver. This mixture of air is then drawn back through the receiver structure, where it is heated by contact with the solid phase. This is shown schematically in Fig. 1.

Corresponding Author: James Spelling, Email: spelling@kth.se

Energy balances were performed on both the solid *s* and fluid *f* phases within the porous foam, as well as on the coolant fluid *c* to give a set of partial differential equations for the temperature profiles T_s, T_f, T_c:

$$C\frac{\partial T_i}{\partial t} + M\frac{\partial T_i}{\partial x} + \sum_j H_j\left(T_i - T_j\right) = q_i + D\frac{\partial^2 T_i}{\partial x^2} \quad (1)$$

where C is the capacitive term, M the advective term, D the diffusive term, H_j the heat-transfer term between phase i and j and q_i the local heat source. These must be determined individually for each phase based on its material characteristics and geometric configuration.

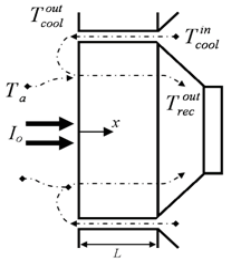

Fig. 1. Schematic View of the Volumetric Receiver

The solid-fluid heat transfer coefficient in the porous media is evaluated using the Wakao and Kaguei correlation [2], and the solid-coolant heat transfer coefficient is evaluated using the Kern correlation [3]. The surface-area to volume ratio of the porous medium is determined from Duffie and Beckman [4].

The solar radiation is assumed to be absorbed only by the solid phase, and the local heat source can be determined assuming a geometric reduction in flux intensity through the receiver and applies only to the solid phase.

In addition to the temperature profiles, the pressure drop across the receiver is calculated using the McCorquodale correlation [4], in order to allow evaluation of the power consumption of the air control blowers.

Given the complexity and number of equations involved, no analytical solution exists for the temperature and pressure profiles and the solution is thus obtained using an implicit finite-difference approach.

2.2 Modelling the Storage Unit

The storage unit is a volumetric packed-bed unit, with air as the heat transfer fluid, and rock as the solid phase storage medium. A mathematical model for the heat and mass transfer within the unit was developed by applying energy balances to the solid and fluid phases to give a set of differential equations in a similar manner as for the receiver, see (1).

The volumetric heat transfer coefficient is given by the Löf and Hawley correlation [4] and the model solved using an implicit finite-difference approach.

2.3 Modelling the Turbomachinery

In order to take into account the off-design operation of the turbomachinery units, a set of characteristic curves is used for each unit to update the efficiency of the device based on the current operating conditions.

In order to represent the increase in efficiency of the turbomachinery units as their power rating increases, the nominal efficiency of each device will be selected based either on their nominal power (gas turbine/compressor) or their nominal volumetric flow rate (steam turbine). Based on the work of Pelster [5], the curves shown in Fig. 2 can be used to determine the efficiencies during the power-plant design phase of the model.

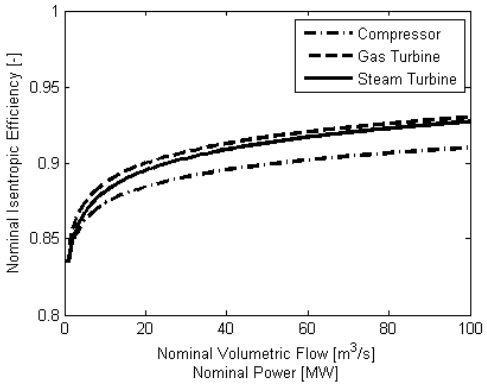

Fig. 2. Evolution of the Isentropic Efficiency as a Function of the Nominal Power or Flowrate

2.4 Modelling the Heat Exchangers

The heat exchangers are designed and modelled using the technique proposed by Staine [3], which selects the geometry of a heat exchanger based on standard values of minimum approach temperature and heat transfer coefficient. In this way, the number of parameters to be selected is kept to a minimum whilst still allowing each heat exchanger

to be individually designed for the heat load and flow rates under which it must operate.

Once the geometry of the exchanger has been selected, the exchanger efficiency and pressure drop can be calculated for all flow conditions encountered during simulation using the NTU-effectiveness method [10] and standard heat exchanger pressure drop correlations.

2.5 Modelling the Heliostat Field

The heliostat field is not directly modelled in this simulation. Based on the work of Augsburger [6], a number of correlations have been established for optimal field layouts at the latitude selected for the plant (44°N) which enable determination of the field costs based on the peak thermal power Q_{th} at the receiver.

$$c_{helio} = 2.7 \cdot 10^6 + 0.17 \cdot \dot{Q}_{th}^{peak} \quad (2)$$

The height (and thus cost) of the central tower is determined based on the work of Augsburger [6] and Kistler [7], and is a function of the peak thermal power of the receiver

3. Optimisation Specifications

3.1. Solar Irradiation Profiles

The four solar irradiation profiles chosen for this study are shown in Fig. 3. The data for the days in question were obtained from the SoDa Service [8], which is based on the HelioClim-3 satellite data, for a power-plant location chosen at 44°N in the region of Aix-en-Provence, France.

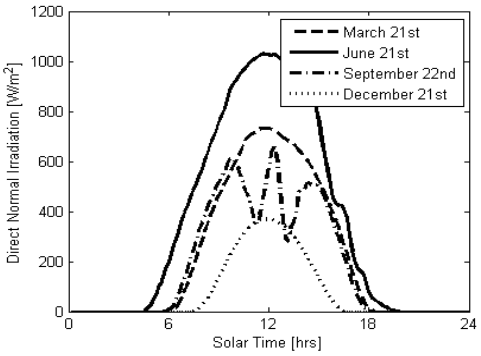

Fig. 3. Selected Solar Irradiation Profiles

3.2 Decision Variables

Before any optimisation calculations can be performed, it is necessary to determine the design parameters that the optimisation procedure is able to modify. Both the number of parameters and the manner in which their values are interpreted will have an effect on the speed of convergence of the optimisation routine. Parameters that will have a large impact on the performance should be preferentially chosen. Those selected for this study are shown in Table 1.

Table 1. Optimisation Decision Variables

Variable	Lower	Upper	Unit
Receiver Temperature	750	1250	°C
Receiver Surface Area	10	300	m^2
Storage Tanks	0	20	#
GT Nominal Flowrate	5	250	kg/s
GT Pressure Ratio	5	25	-
HP Steam Level	0.05	0.95	-
LP Steam Level	0.05	0.95	-
Condenser Temperature	45	200	°C

In order to prevent conflicts occurring between the values chosen for the three Rankine cycle parameters, the pressure levels in the waste heat boiler are not chosen directly. Rather, a dimensionless parameter is used to fix the value between two limits fixed by the other decision variables. In this way the optimiser does not waste time dealing with impossible combinations of parameters and can better focus on correct exploration of the decision space.

The high pressure steam design pressure is chosen between the limits fixed by the condensation pressure (determined as a function of the condensation temperature) and the critical pressure of water:

$$P_{st}^{HP} = P_{cond} + f_{HP} \cdot \left(P_{crit} - P_{cond}\right) \quad (3)$$

where P_{cond} is the condensation pressure, P_{crit} the critical pressure of water and f_{HP} the steam pressure level. In this way, the choice of a live steam pressure below that chosen for the condenser is avoided. The low pressure steam design pressure is chosen in a similar manner between the condensation pressure and the high pressure steam design pressure P^{HP} determined using (4) and is therefore given by:

$$P_{st}^{LP} = P_{cond} + f_{LP} \cdot \left(P_{st}^{HP} - P_{cond}\right) \quad (4)$$

where P_{cond} is the condensation pressure and f_{LP} the steam pressure level defined in Table 1. In this way, the pressure value for the low pressure steam can never be higher than that chosen for the high

pressure steam, ensuring coherence of the parameters.

3.3 Superstructure Options

In addition to the decision variables, representing physical quantities, two integer variables are used to select between different technology options. In this way, the optimiser can adjust the superstructure of the power-plant in order to improve its performance and allow analysis of the trade-off between performance and cost. Based on the values chosen for the decision variables in Table 1, the different superstructure options will be more or less effective and the results of the optimisation will therefore allow selection of the appropriate technology for a given setup.

The technology options for the Brayton cycle are shown in Table 2. The option to include compressor intercooling and/or turbine reheating is specified by an additional decision variable, and allows the units to better approach the idealised isothermal compression/expansion of the Carnot cycle, thereby improving the efficiency of the power block.

Table 2. Brayton-Cycle Superstructure Options

Value	Compressor	Turbine
0	no intercooling	no reheat
1	no intercooling	with reheat
2	with intercooling	no reheat
3	with intercooling	with reheat

The technology options for the Rankine cycle are shown in Table 3. The option to increase the number of evaporation pressure levels to two is included, as well as to remove the bottoming Rankine cycle entirely. The use of multiple evaporation levels within the waste heat boiler allows for a greater degree of recuperation of the energy contained in the hot exhaust gases of the Brayton cycle [9].

Table 3. Rankine-Cycle Superstructure Options

Value	Signification
0	no Rankine cycle
1	single pressure level in waste heat boiler
2	two pressure levels in waste heat boiler

A flow sheet for the solar thermal power plant with the full range of superstructure options selected is shown in Fig. 4.

Three subsections can be identified, based on the different working fluids. The receiver and storage unit operate together using atmospheric air, the Brayton cycle uses a separate, high-pressure air loop and the Rankine cycle is the standard water-based variety.

This complete flow sheet can later be compared with the options selected by the optimiser.

3.4 Objective Functions

The two objectives selected for the optimisation of the power plant are the initial total investment cost and the levelised electricity cost, representative of the trade-off between upfront costs and potential profits.

The investment cost is determined using cost functions based on a number of corporate communications and on the work of Pelster [5], taking into account the investment in power plant equipment and power electronics, purchasing of land, as well as civil engineering costs.

$$c_{inv} = \sum c_{equip} + c_{land} + c_{civil} \tag{5}$$

The levelised electricity cost *LEC* is determined using equation (6). The value of the annuities payment A calculated for a 15 year payback time at 8% interest.

$$LEC = \frac{A}{\frac{365}{n_{day}} \sum_{day=1}^{n_{day}} \int_{day} \dot{E}^{-}_{net} dt} + c_{O\&M} \tag{6}$$

As only four days are simulated, the total power output for the year has to be determined by extrapolation of the daily evolution of the net power E_{net}. Each of the four days is representative of a season and as such can be assumed to have an equal weight in the interpolation. The specific O&M cost $c_{O\&M}$ is set to 0.03 USD/kWh$_e$ [10].

4. Multi-Objective Optimisation

The majority of cases of energy system optimisation will require the consideration of multiple objectives. Usually it is desirable that a power plant be the most efficient possible, whilst at the same time producing electricity as cheaply as possible. Often, the two objectives will be conflicting; a cheap power plant will most likely have a low efficiency, whereas a more efficient

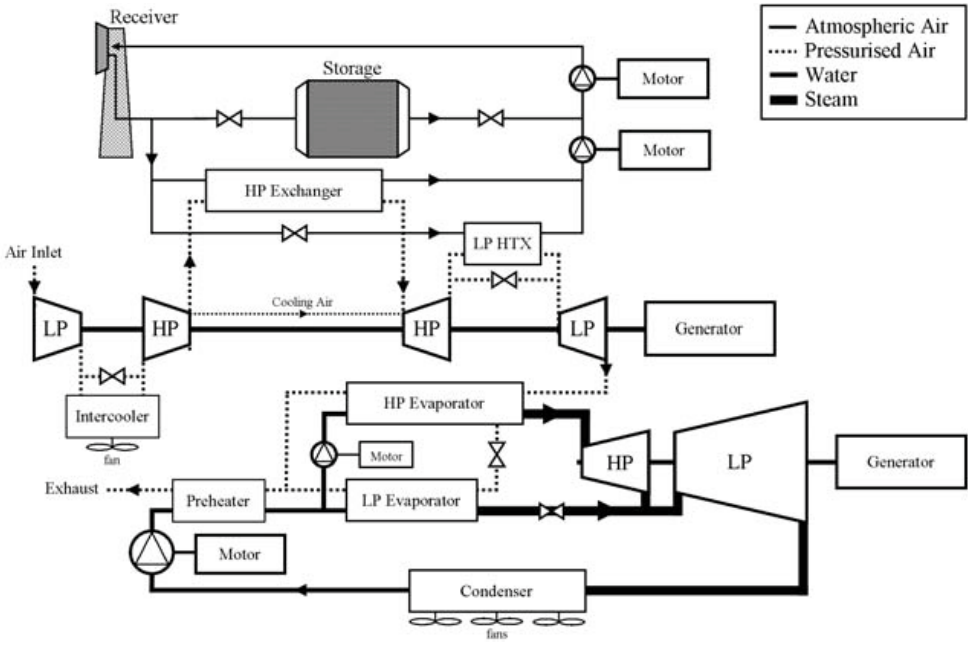

Fig. 4. Solar Thermal Power Plant Complete Flow-Sheet

plant will cost more. As such, no single optimum can be found for both objectives.

Numerous techniques exist for converting multiple objective problems to single objective problems, such as the environomic approach adopted by Pelster [5]. However, such techniques are usually based on the use of a number of poorly-defined weighting or cost factors upon which the result of the optimisation depends heavily.

A more useful approach is to attempt to determine the trade-off curve that exists between the different objectives. In this way, a range of solutions is presented to the decision maker, who can choose the desired compromise between the objectives. The optimal trade-off curve is given [11] by the points on the Pareto-optimal front.

4.1 Convergence

The optimisation of the solar thermal power plant was performed using the QMOO program, written at the LENI, with calculations performed on the Pleiades2 Cluster, using a total of 20 processors for a period of 5 days. A major advantage of evolutionary algorithms is that they are very well adapted to being solved using parallel computing resources.

The evolution of the 'population' of points during the optimisation process is shown in Fig. 5. It can be seen that starting from an initial population of 'mediocre' points, the algorithm progresses through a series of points that are better in both objectives, before arriving at a well defined Pareto frontier after 8600 evaluations.

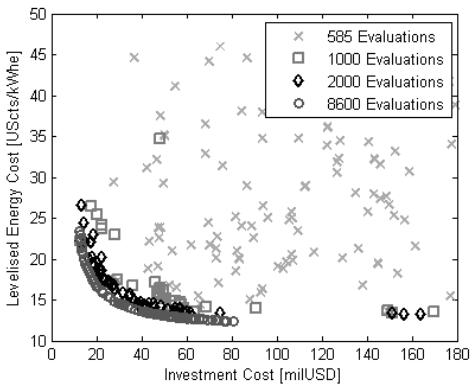

Fig. 5. Evolutionary Algorithm Convergence

4.2 Pareto-Optimal Trade-Off Curve

The curve of Pareto-optimal points is shown in Fig. 6. It can be seen that the trade-off between the two objectives is both smooth and continuous.

Table 4. Characteristics of Selected Points on the Pareto Optimal Front after 8600 Evaluations

Characteristic	Point 1	Point 2	Point 3	Point 4	Unit
Total Plant Investment Cost	12.6	22.2	47.1	81.2	milUSD
Levelised Electricity Cost	23.4	16.1	13.2	12.4	UScts/kWh$_e$
Nominal Power Output	0.98	2.74	7.84	17.2	MW$_e$
Exergy Efficiency	18.4	22.1	23.2	22.9	%
Specific Investment Cost	12'900	8'100	6'000	4700	USD/kW$_e$
Annual Net Electricity Production	4.3	11.9	32.3	66.8	GWh$_e$
Capacity Factor	50.1	49.2	47.1	44.2	%
Receiver Temperature	802	937	983	962	°C
Receiver Surface Area	10.0	22.1	59.2	124.3	m^2
Storage Tank Volume	302	603	1359	3020	m^3
Brayton Mass Flow Rate	5.0	9.3	23.1	53.7	kg/s
Brayton Pressure Ratio	5.0	7.9	9.5	10.5	-
Live Steam Pressure	66.6	79.7	63.6	52.0	bar

After the 8600 iterations performed, the minimum possible levelised electricity cost was found to be 12.4 UScts/kWh$_e$, for an investment cost of 81.2 million USD.

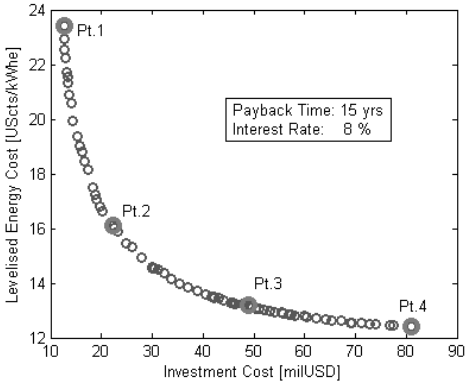

Fig. 6. Pareto Optimal Front after 8600 Evaluations

It can clearly be seen in Fig. 6 that reducing the levelised electricity cost requires an increase in the total investment cost, but that the relative reduction in levelised cost decreases rapidly as the amount investment increases.

In order to analysis in more detail the effect of the different design variables on the optimisation objectives, a number of objective curves will be considered in §5.2.

4.3 Pareto Point Analysis

In order to further understand the trends resulting from the optimisation process, the details of four specific points on the Pareto-optimal curve are presented.

The points chosen are shown on Fig. 6 with the data presented in Table 4. The two extreme points, i.e. lowest levelised cost and lowest investment cost, have been chosen, along with two intermediary points.

4.4 Objective Curves

The evolution of both the levelised energy cost and the total investment cost as a function of the nominal power output of the power plant is shown in Fig. 7.

It can be seen that the levelised energy cost falls as the size of the power plant increases, due to the reduction in specific investment cost when purchasing equipment with a larger power rating. However, the total plant investment cost increases as, despite the reduction in specific costs, the overall cost of both the power block and the solar components increases with plant size.

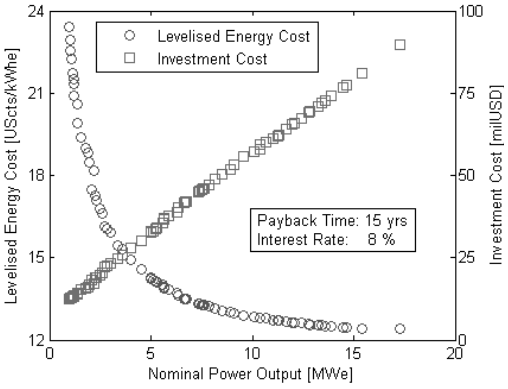

Fig. 7. Objectives vs. Nominal Power Output

The evolution of both the total investment cost and the levelised energy cost as a function of the annual total electricity produced by the power plant is shown in Fig. 8. It can be seen that as the total electricity production increases, the levelised electricity cost decreases, approaching the lower limit of 12.4 UScts/kWh$_e$ for a total production above 50 GWh$_e$ per year.

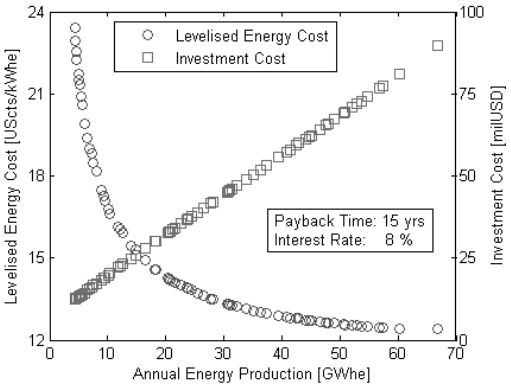

Fig. 8. Objectives vs. Annual Energy Production

It can also in Fig. 8 be seen that the annual production is a linear function of the total amount invested in the construction of the power plant; the more that is invested in the plant, the greater its total production. This curve can be used to predict the total investment cost required for the construction of a solar thermal power plant with a specified annual electricity production.

5 Power Plant Configuration Results

5.1 Power Plant Parameter Selection

In order to be able to draw conclusions about optimal superstructure configurations for solar thermal power plants, the distributions of certain decision variables are presented. In this way the range of values that provide the best solutions can be studied.

The distribution of the Brayton and Rankine cycle technology options chosen by the optimiser is shown in Fig. 9.

For the Brayton cycle, all the solutions retained by the algorithm make use only of the intercooling option; the reheat option is never selected. This is due to the fact that the introduction of a reheat results in an unmatched set of heat-load curves in the main cycle exchanger which introduces an additional exergy loss that is not compensated for elsewhere in the cycle.

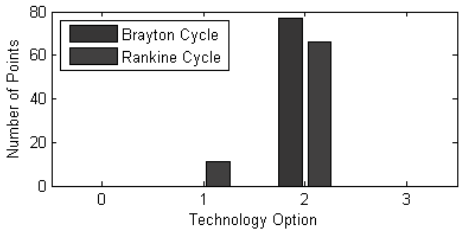

Fig. 9. Superstructure Selection

For the Rankine cycle, it can be seen that the vast majority of the solutions retained make use of a dual-pressure level boiler. The increase in output of the power generation cycle can therefore be assumed to outweigh the additional cost for a large fraction of the point. It can be shown that the small number of points that do not select the dual pressure levels are points with a low nominal turbine power for which the additional investment cost is proportionally larger and thus not justifiable.

In a similar a manner to the analysis performed for the superstructure, the distribution of the receiver operating temperature is plotted in Fig. 10.

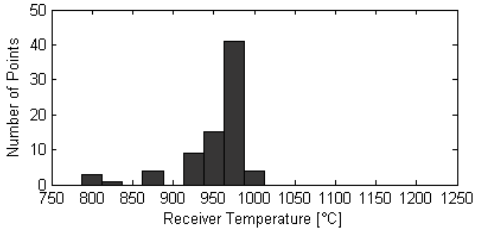

Fig. 10. Receiver Temperature Selection

It can be seen that no values exceeding 1000°C are chosen by the algorithm. As was shown by the analysis of the Sankey diagrams presented in Spelling *et al.* [12], the receiver is the major source of exergy loss in solar thermal power plants using open volumetric receivers. It is the rapidly increasing radiation losses from the receiver that render the use of higher temperatures uninteresting when open volumetric designs are considered, as well as the increasing cost of the high temperature heat exchangers. The cost and operation of the power generation equipment is not yet a limiting factor, as the temperatures involved remain well below those routinely encountered in gas-fired combined-cycle plants [13].

5.2 Power Plant Design Curves

Using the points located on the Pareto curve, a number of design curves can be established, which present the relationships between the decision variables themselves. These graphs can then be used to select combinations of power plant parameters than work 'well' together. As the points considered lie on the Pareto-frontier, the relationships obtained can be assumed to be truly representative of the choices possible for the design, as they have been obtained by considering variation of not one, nor two, but all of the decision variables.

The relationship between the nominal power output of the power plant, the receiver surface area and the storage capacity is shown in Fig. 11. The receiver surface area can be directly linked to the peak thermal power given to the plant. As the global exergy efficiency of the plant is relatively constant (at least for the larger values of nominal power output as shown in Fig. 12), the relationship between nominal power output and receiver surface area is linear.

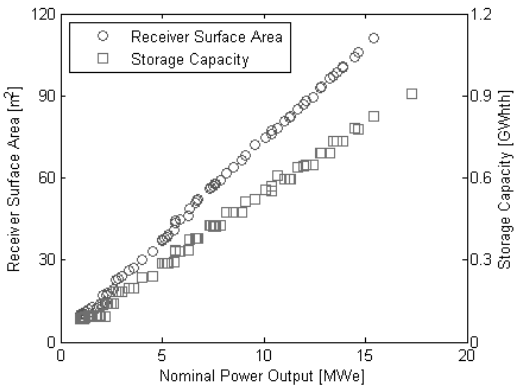

Fig. 11. Receiver Surface Area and Storage Capacity as a function of the Nominal Power Output

The storage capacity also increases with the nominal power output (and thus the receiver surface area) due to the fact that as the receiver area increases, the mass flow that can be achieved is greater, and a greater volume of storage material will therefore be required to store the larger volumes of air produced.

The evolution of the specific power plant investment cost as a function of the nominal power output of the plant can be evaluated, and is shown in Fig. 13. It can be seen that as the plant size increases, the specific energy cost drops, due to the reduction in specific cost of the power plant components as well as the overall increase in efficiency of the plant.

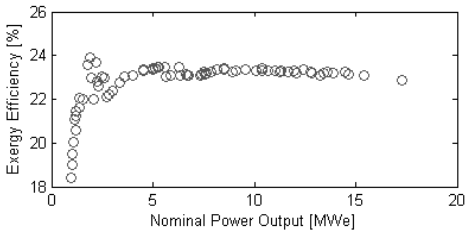

Fig. 12. Exergy Efficiency vs. Nominal Power Output

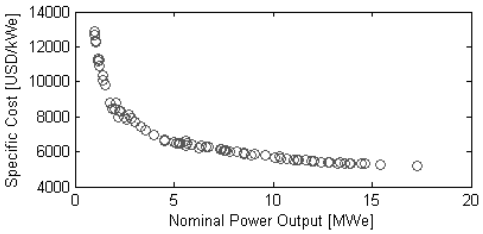

Fig. 13. Specific Investment Cost as a function of the Nominal Power Output

The variation in the plant capacity factor as a function of the nominal power output is shown in Fig. 14 below.

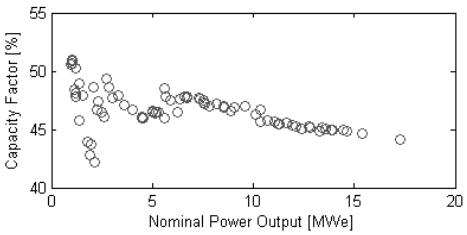

Fig. 14. Plant Capacity Factor as a function of the Nominal Power Output

It can be seen that the capacity factor decreases with increasing nominal power output of the plant, due to the fact that maintaining a higher capacity rating requires a proportionally larger receiver and storage unit, both of which are costly. The proportion of investment in solar equipment (receiver, storage, heliostats) increases with power plant size, meaning that the cost and efficiencies of these units begin to dominate the overall optimisation.

6. Conclusion

A multi-objective, thermo-economic optimisation of both the power plant superstructure and operating conditions was performed using the new, dynamic models. Using an evolutionary algorithm [11], a family of Pareto-optimal points were obtained, representing the trade-off between lower power plant investment costs, and lower levelised energy costs.

Through use of optimisation, it was shown that efficiencies in the region of 18-24% can be achieved, and this for levelised electricity costs in the region of 12-24 UScts/kWh$_e$. The nominal power outputs of the configurations selected by the optimiser were relatively low however, being the region of 3-18 MW

Additionally, based on the design options made available in this study, optimal superstructure options were identified for the solar thermal power plant, as well as a number of design and parametric curves that can be used in future studies of such systems.

It can be concluded that, when properly designed, solar thermal power plants based on combined cycles are both economically and thermo-dynamically promising.

By raising the efficiency of the plant, the size of the solar collector field is diminished, increasing the otherwise low energy densities of solar power systems. This also contributes to reducing the investment required in the solar components (receiver, heliostat field) which dominate the total cost of the power plant.

By reducing the levelised electricity costs, solar thermal power plants become more economically viable, accelerating their construction and thus, hopefully, reducing our dependence on fossil-fuels.

Nomenclature

A annuities payment, USD/yr

c cost, USD

E power, W

P pressure, Pa

T temperature, K

x axial position, m

References

[1] Hoffschmidt B., Tellez F., Fernandez J., 2003, *Performance Evaluation of the 200kWth HiTRec-11 Open Volumetric Receiver*, Solar Energy Engineering, 125, pp. 87-97

[2] Kaviany M., 1995, *Principles of Heat Transfer in Porous Media*, Springer-Verlag, New York

[3] Staine F., 1995, *Intégration Energétique des Procédés Industriels Etendue aux Facteurs Exergétiques*, Ph.D. Dissertation, Ecole Polytechnique Fédérale de Lausanne, Switzerland

[4] Duffie J., Beckman W., 2006, *Solar Engineering of Thermal Processes*, Third Edition, John Wiley & Sons, New Jersey

[5] Pelster S., 1998, *Environomic Modeling and Optimisation of Advanced Combined Cycle Power Plants*, Ph.D. Dissertation, Ecole Polytechnique Fédérale de Lausanne, Switzerland

[6] Augsburger G., 2008, *Simulation and Optimisation of Heliostat Fields for the Design of a 300MW$_{th}$ Central Receiver*, Master Thesis, Ecole Polytechnique Fédérale de Lausanne, Switzerland

[7] Kistler B., 1986, *A User's Manual for DELSOL3*, Sandia National Laboratories, Albuquerque

[8] www.soda-is.com, 2005 Sample, HelioClim-3 Satellite Data

[9] Borel L., Favrat D., 2009, *Thermodynamics and Energy Systems Analysis*, EPFL Press, Lausanne

[10] Price H., Mehos M., Jones S., 2003, *Assessment of Parabolic Trough and Power Tower Solar Technology Cost*, National Renewable Energy Laboratory, Golden

[11] Leyland G., 2002, *Multi-Objective Optimisation applied to Industrial Energy Problems*, Ph.D. Dissertation, Ecole Polytechnique Fédérale de Lausanne, Switzerland

[12] Spelling J., Augsburger G., Favrat D., 2009, *Evaluation of a Combined-Cycle Setup for Solar Tower Power Plants*, SolarPACES2009 Conference Proceedings [USB Drive], Deutsches Zentrum für Luft- und Raumfahrt

[13] Bölcs A., 1995, *Turbomachines Thermiques*, Volume I, EPFL-LTT, Lausanne

Exergy Evaluation and Design of Advanced Solar Tower Power Plant

*Chuanqiang Zhang[a, b], Hui Hong, [a,] *, Hongguang Jin [a]*

[a] *Institute of Engineering Thermophysics, Chinese Academy of Sciences, Beijing, China*
[b] *Graduate University of the Chinese Academy of Sciences, Beijing, China*

Abstract: In this paper, an 11MW solar tower power plant is analyzed by graphical exergy methodology based on energy-utilization diagram (EUDs). The exergetic performance is evaluated and the key features of energy conversion processes are clarified. As a result, the largest exergy destruction takes place in the solar collector, amounting up to about 60-70% based on the input solar exergy. The potential of reducing the irreversibility for enhancing performance is identified. By comparing the improved system with the current 11 MW solar tower power system, the rated solar-to-electric efficiency of the improved system would be expected to increase by about 3-5 percent points. In addition, the principle of energy level match is applied in the design of the cascade utilization of solar thermal energy, and several suggestions are pointed out for further research.

Keywords: Graphical exergy analysis, Concentrated Solar Thermal Power Plant, Tower Receiver.

1. Introduction

In the latest years, the concentrated solar tower thermal power plant is considered as an important candidate for providing a major share of renewable bulk electricity production. At present, several solar tower power plants between 0.5 and 10 MW have been demonstrated in test platforms and pilot plants. The typical plants include Solar one (America, 1982-1988), Solar two (America, 1996-1999), PHOEBUS-TSA (Spain, 1992-). These plants have been demonstrated operation with water-steam, molten salt, and atmospheric air as heat transfer fluids (HTF).

The Spanish 11MW PS10 plant, as the first commercial solar tower power plant in the world, has been demonstrated. It was built by Abengoa Solar and began operation on March 30th, 2007 [1]. During nearly three years of operation, it can produce the grid-connected electricity under a purely commercial approach, and its solar-to-electric efficiency is 21.7% at rated load and 16.3% at annual level.

At present, with the development of technology progresses of solar tower power plants, the efficiencies of 23% at design point and 20% annual by 2030 is expected to reach [2]. However, such lower efficiency will further hinder the wide and scale application in the future. It is due to the fact that in the solar-only power plants, the concentrated solar radiation energy usually transforms to thermal energy of working fluid which is converted into electricity power through the steam cycle (i.e. Rankine cycle). However, steam with higher pressure and higher temperature can hardly be obtained in the receiver due to the limitation of material caused by the great instability of temperature variation. Consequently, the advanced supercritical steam turbine technology cannot be applied in the solar tower power plants.

To overcome this problem, several penetration strategies have been proposed. For example, the hybridization with high-temperature gas turbine cycle is developed to improve the solar-to-electric

* Corresponding author: Hong Hui, Email: honghui@mail.etp.ac.cn

efficiency. Several novel receivers are designed such as open or closed loop volumetric air receiver or super-heated steam technology. However, for engineering and system design, the integration of steam cycle is the main power producers in the state-of-the-art solar tower power technologies. Thus, the researchers need to look for methods to improve the power output and thermal efficiency of already installed solar tower power plants.

The objective of this paper is to clarify the fundamental features of recently demonstrated solar tower power systems by using graphical exergy analysis, and to identify key factors for improvements of existing advanced PS10 commercial plant, to propose the improved scheme, and finally to provide useful guidance for further design.

2. Power plants description

2.1. PS10 Plant

PS10 solar tower is located in Sevilla, Spain. Fig.1 illustrates the schematic flow diagram. The receiver is designed to absorb about 55 MW thermal power from the concentrated solar radiation with peak flux of 650 kW/m^2 and produce saturated steam at 40 bar, 250 ºC [3]. The steam generated by the receiver is sent to a saturated turbine to produce mechanical work and electricity. Between high and low turbine pressure bodies, a humidity separator (HS) is fixed to increase the quality of steam. A water-cooled condenser working at 0.06 bar is used for cooling the outlet of the turbine. First pre-heater and deaerator are fed with 0.8 bar and 16 bar turbine extraction respectively. The third and last pre-heater is fed with steam from the receiver and increases feed water temperature to 245 ºC. After mixed with returned water from the drum, temperature of feed water to the receiver is increased to 247 ºC [3].

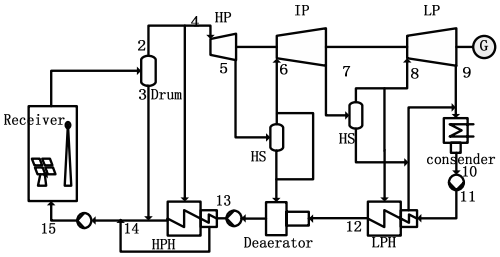

Fig. 1 Schematic flow sheet of PS10 plant

2.2. Proposed Scheme

In order to increase the solar-to-electric efficiency, we proposed the improved system using receiver with both saturated steam and molten salt as heat transfer fluids. Fig. 2 shows the proposed scheme flow diagram.

Different from PS10 plant, the receiver of the proposed system consists of two parts: one is a saturated steam section (SSR), and the other is a molten salt section (MSR). In the saturated receiver, the saturated steam is first generated at 102 bar, 312 ºC, while the second part heats molten salt from 330 ºC to 565 ºC. Then, the produced saturated steam is flowed into a molten salt exchanger (HX) and superheated to 515 ºC. After that, the superheated steam is introduced into the steam turbine to produce electricity.

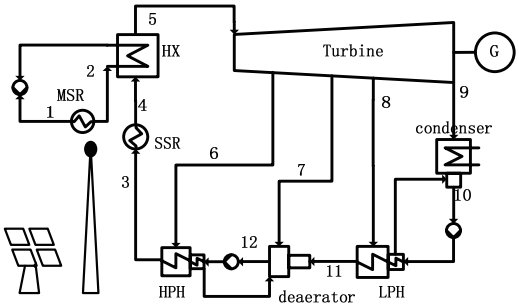

Fig. 2 Schematic flow sheet of proposed scheme

Compared with the PS10 plant, the combination of water and molten salt as heat transfer fluid is applied in the receiver. In this manner, the average temperature of heat absorption can be raised. For the proposed scheme, the higher temperature of the solar collector may cause the decrease of the receiver efficiency, while it is desired for the higher efficiency of the thermal cycle. Here, according to the reference [1], the receiver efficiency of the proposed scheme would be expected to achieve in the range of between 88% and 92%, with a bit lower than that of PS10.

In this paper, this kind of receiver is similar to the dual receiver reforming of PHOEBUS addressed by Buck, etc. [4], in which both water and air are used as HTF in solar absorption receiver, and could show a 27% higher efficiency than that with only atmospheric air as HTF. This dual receiver has two advantages: i) increasing the quality of working fluid enthalpy transferred from the concentrated solar radiation for enhancing the potential of work output; ii) avoiding the risk of producing superheated steam in the receiver.

3. System performance

3.1. Operating conditions

The overall performance of the demonstration PS10 plant and the proposed scheme was predicted using the commercial Aspen Plus code. To simplify the simulation, it was assumed that the system operated at a steady state. According to the design condition of PS10 plant, the input solar energy of the proposed scheme was set at 50264 kW without the consideration of the thermal storage. The direct normal solar intensity was assumed as 981W/m^2 and efficiencies of optic and solar receiver were 77% and 92% for PS10 plant, while 77% and 90% for the proposed scheme. The salt used was composed of 60% $NaNO_3$ and 40% KNO_3. STEAM-TA and ELECNRTL were chosen for simulating the property of steam and molten slat respectively. The isentropic efficiencies of steam turbine and pumps were assumed to be 0.80 and 0.75 respectively. A pinch-point of 10ºC in the heat exchangers was taken into account. The most relevant parameters are summarized in Tables 1 and 2 respectively.

Table 1. Stream parameters of PS10 simulation

State points	G (kg/hr)	T (℃)	P (bar)	Steam quality
1	106914	250.4	40	0.69
2	73914	250.4	40	1.00
3	33000	250.4	40	0.00
4	64357	250.4	40	1.00
5	49211	201.38	16.00	0.93
6	49211	201.08	15.90	1.00
7	49211	93.50	0.80	0.88
8	38970	93.50	0.80	1.00
9	38970	36.18	0.06	0.92
10	49211	35.00	0.06	0.00
11	49211	35.12	11.00	0.00
12	49211	85.00	6.00	0.00
13	64357	189.39	45.00	0.00
14	97357	246.83	40.00	0.00
15	106914	247.20	40.00	0.00

Table 2. Stream parameters of proposed scheme simulation

Flow points	G (kg/hr)	T (℃)	P (bar)
1	129943	330.00	1
2	129943	565.00	5
3	52227	256.82	104
4	52227	312.43	102
5	52227	515.00	101
6	8879	387.62	40
7	1733	236.76	10
8	7075	155.31	4
9	34540	36.18	0.06
10	41614	35.00	0.06
11	41614	138.47	15
12	52227	161.93	10

1-2: molten salt; 3-12: water, saturated/superheated steam.

3.2. Performance evaluation

Exergy efficiency is more appropriate than thermal efficiency for performance evaluation of energy systems. For the PS10 and the improved system, exergy destructions of the main components were analyzed. Table 3 compares the exergy destruction in the various processes among two kinds of systems.

Table 3. Comparisons of cycle performance and exergy destruction

Parameters	PS10		Proposed scheme	
	Exergy (kW)	Ratio (%)	Exergy (kW)	Ratio (%)
Input exergy				
Solar thermal exergy	47802	100.00	47802	100.00
Exergy destruction				
Solar collector	32480	67.95	29562	61.85
Steam turbine	2248	4.70	2448	5.12
Exchangers	975	2.04	1164	2.44
Condenser	930	1.94	783	1.63
Others	150	0.31	193	0.40
Output exergy				
Net power	11019	23.05	13356	27.94

It was obviously seen that the largest exergy destruction happens in the solar collector where solar radiation is transformed to thermal energy and absorbed by the HTF, amounting up to 67.95% for PS10 and 61.63% for proposed scheme based on the input solar exergy. Attractively, the irreversibility in the solar collector of the proposed scheme is less than that of PS10. In addition, the output work and the exergy efficiency of the proposed scheme could be advantageous over that of PS10, with efficiency of about 5 percentage points higher. At an optical efficiency of 77% and absorption efficiency of 90%, the overall solar-to-electric efficiency is about 26.57% under design conditions, approximately 15.30% higher than that of PS10.

4. Exergy assessments with the EUD methodology

4.1. Exergy presentation on EUDs

With the development of solar thermal cycles, several researchers have paid close attention to the exergy principle for analysis, optimization, and synthesis of the solar thermal power plants. The EUD methodology we used in this paper focuses graphically on the energy level difference in a pair of energy donor and energy acceptor. It was first proposed by professor Ishida [5]. Both the variation of energy level (A) and energy quantity (ΔH) are graphically shown with A- ΔH co-ordinates. Here, the energy level A is a dimensionless criterion ($A = 1\text{-}T_0 \Delta S/\Delta H$, a ratio of exergy change to energy change). In this way, the exergy destructions of thermal or chemical processes may be presented by using clearly graphical method.

It has three specific features: i) the energy level degradation in each process, instead of only magnitudes of exergy destructions obtained from the exergy value difference between the output and input of units; ii) the variation of driving force by dividing the whole process into infinitive processes; iii) the relationships between the first law and the second law of thermodynamics presented on the global graph. Hence, the EUD methodology may provide the information on the feasibility of process, driving force, defect points, and potential of improvement from intuitive and global viewpoints.

4.2. Collector subsystem

For the solar collector subsystem, the solar radiation is concentrated and transformed to the thermal energy of the working fluids in the reciever. It is involved with two energy conversion processes. Figs. 3 and 4 illustrate the solar collector subsystems of the PS10 power plant and the proposed scheme, separately.

For simple consideration, we here assumed the solar radiation as a high-temperature heat source at a constant temperature of 5777 K, i.e. the surface temperature of the sun (T_{sun}). Thus, the energy level of the solar radiation may be represented as the Carnot cycle efficiency between solar surface temperature (T_{sun}=5777K) and atmospheric temperature (T_0=298K) given as equation 1 according to ([5], [6]), and its value is 0.95.

$$A = 1 - \frac{T_0}{T_{sun}} \qquad (1)$$

In Fig. 3, the width of curve A_{ed} is identical to the heat released by the solar radiation. The heights of curves in areas 1 and 2 indicate the energy level degradation due to transformation of solar heat into the thermal energy associated with saturated steam. Area 3 between $A_{ed,sol}$ and $A_{ea,eva}$ refers to the exergy destruction caused by larger energy-level difference between the solar heat and the saturated steam. At a temperature of 250℃, the level of thermal energy is 0.42, much lower than that of solar thermal energy (0.95). The exergy destruction of the solar collector is 32480 kW and is about 67.95% based on the input solar exergy.

For the proposed scheme, Fig. 4 shows the three processes in the solar collector subsystem. Area 3 represents the preheating water by solar radiation in which the curve of $A_{ea,pre}$ shows the energy level variation of preheating water by solar heat. Area 4 between $A_{ed,sol}$ and $A_{ea,eva}$ illustrates the process of saturation for steam. The area on the right shows the molten salt heated by the solar radiation where its energy level is increased from 0.49 to 0.62.

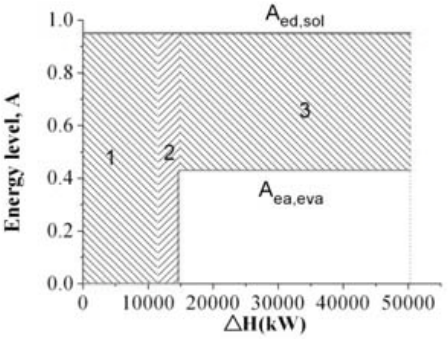

Fig. 3 Collector subsystem of PS10

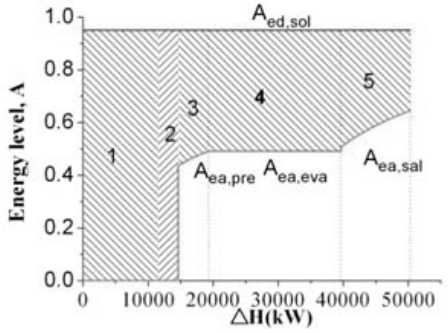

Fig. 4 Collector subsystem of proposed scheme

Compared with Fig. 3, it can be clearly seen that, for the proposed scheme, the energy-level difference between the solar heat and the working fluid is relatively smaller than that of PS10 power plant. It is due to the fact that as the water and molten salt being simultaneously applied in the receiver, the average energy-level of energy acceptor can be raised and the energy-level degradation from solar energy to working fluid can be decreased, lowering the process irreversibility in the receiver. Thus, the exergy destruction in the solar collector subsystem can be reduced by

approximately 6 percent points, compared to that of PS10 plant based on the input solar heat. It indicates that from the exergy viewpoint, the addition of molten salt as the heat transfer fluid in the receiver is superior to the only saturated steam due to less exergy destruction, and a profit of enhancing plant performance could be obtained.

4.3. Heat exchange subsystem

Figs 5 and 6 show the degradation of energy-level in the heat exchangers in the steam cycle and the exergy waste of the condenser to the environment for PS10 and the proposed scheme, separately. In Fig. 5, the energy donor A_{ed} is the extracted steam of the turbine, while the energy acceptor A_{ea} is the feeding water. It can be seen that the area between A_{ed} and A_{ea} is relatively smaller. It means that the energy-level matches between the extracted saturated steam and the water is satisfied, resulting in the less exergy destruction (975 kW) with the value of 2.04% based on the input of solar thermal exergy. In addition, the left rectangle area illustrates the exergy loss of the condenser and about 1.94% is caused.

On the contrary, for the proposed scheme, an additional heat exchanger is added where the molten salt is utilized to produce superheated steam, as shown in Fig. 6. Here, A_{ed5} represents the released heat by molten salt. Although this approach may bring about more exergy destruction, it can offer an option of producing superheated steam without in the receiver directly. The exergy destruction and the exergy loss in the heat exchanger subsystem for the proposed scheme are 1164 kW, relatively higher than that of PS10.

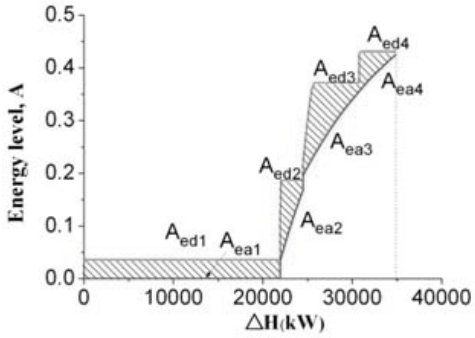

Fig. 5 Heat exchange subsystem of PS10

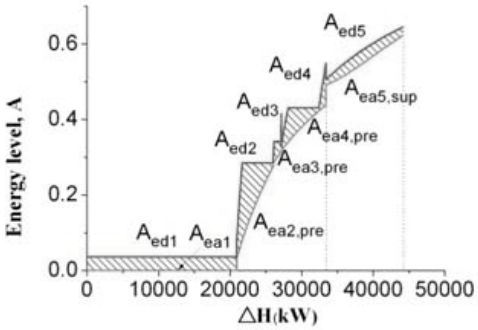

Fig. 6 Heat exchange subsystem of proposed scheme

4.4. Power subsystem

Fig. 7 depicts the exergy destruction in the power subsystem of PS10, mainly caused by the turbine. The exergy destruction in the turbine corresponds to the area between the curve of A_{ed} in Fig. 7 and the unity (identical to work). The exergy destruction caused by the turbine is 2248 kW. The power output from the turbine is 11019 kW. Comparatively, the exergy destruction in power subsystem for the proposed scheme is 2448 kW, shown in Fig. 8, caused by inefficiency of the turbine. Obviously, we can identify the fact that there is an important difference of the power output between the two power subsystems. This primarily relies on that superheated steam is provided to produce electricity in the new cycle.

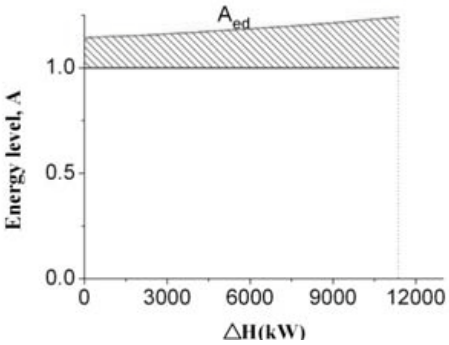

Fig. 7 Power subsystem of PS10

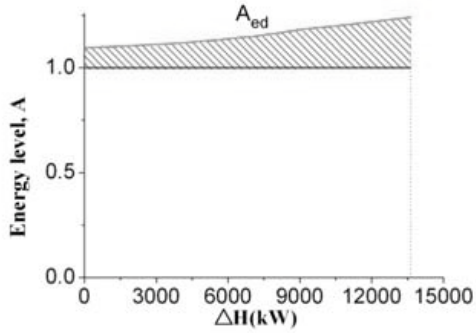

Fig. 8 Power subsystem of proposed scheme

5. Further considerations in the design

From the preceding analysis, the graphical exergy presentation on EUD is able to illustrate the distribution of exergy destruction of various processes. It can tell us how to perform system synthesis and how to determine the optimal system in the design. In the solar tower power plant, the exergy destruction of the solar collector subsystem with the concentrator and receiver is the largest one among all sections. One of the methods is to increase the energy-level of the heat-accepting through the rise of the inlet temperature for the working fluid.

For example, in the proposed scheme, molten salt receiver replaces part of the saturated steam receiver of PS10, and high temperature molten salt at 565 ℃ can be obtained. Thus the exergy destruction is reduced by 6 percentage points. Furthermore, reheating the extracted steam from the turbine in the receiver may be another approach of enhancing the energy-level of the working fluid. If the option is applied in the proposed scheme, exergy destruction of the receiver will be decreased by about 2 percent points. It means that at a given work output of the power plant, the efficiency of the solar collector is gained and the heliostat field will be smaller than that of PS10. This achieved additional benefit in the design will reduce the cost of the investment of power tower plant, although critical issue of this kind of dual receiver is the increased complexity compared to the separate receiver subsystems.

On the other hand, the current design also focuses on the improvement of the system efficiency. It not only takes into account the efficiencies of the different components, but also pays much more attention on the evaluation of integration with the thermodynamic cycle. Today, the technologies of solar tower power plants have achieved several maturity and reliability; however, the basic design methods for system integration are currently under development. The EUD methodology may become one of the candidates for designing the cost and effective system integration/synthesis. In addition, due to the instantaneity of solar energy, the dynamic analysis of solar thermal power system, involving part load performance and reliability, is also important for the design of solar tower thermal power plant having the satisfied performance.

6. Conclusions

Recently advanced solar tower thermal power system of PS10 has been analyzed by applying the EUD methodology. Since the exergy destructions and features of the systems may be described by using diagrams. Through the graphical exergy analysis based on EUD methodology, problems and potentials for substantial improvements have been revealed. The improved system with dual receiver by using saturated steam and molten salt has been proposed. The net solar-to-electric efficiency of the improved system would be expected to be increased by about 5 percent points. It is clear that the tendency of decreasing the energy–level mismatch between the concentrated solar heat and the working fluid will lead to the new generation of solar thermal power systems.

Nomenclature

A Energy level

G Mass flow rate, kg/hr

H Enthalpy, kW

P Pressure, bar

T Temperature, ℃

Subscripts and superscripts

ea Energy acceptor

ed Energy donor

eva Evaporate

pre Preheat

sal Salt

sol Solar energy

sup Superheat

References

[1] Robert Pitz-Paal, Jürgen Dersch, Barbara Milow, 2005, European concentrated solar thermal road-mapping, Technical Report, SES6-CT-2003-502578, DLR, Germany.

[2] Manuel Romero, Reiner Buck, James E. Pacheco, 2002, An Update on Solar Central Receiver Systems, Projects, and Technologies. ASME Trans. Journal of Solar Energy Engineering, Vol. 124, pp. 98-108.

[3] Solúcar et al., 2006, 10 MW Solar Thermal Power Plant for Southern Spain, Technical Report, NNE5-1999-356.

[4] Reiner Buck, et al., 2006, Dual-receiver concept for solar towers， Solar energy, Vol. 80, pp. 1249-1254.

[5] Hongguang Jin, and Masaru Ishida, 1993, Graphical exergy analysis of complex cycles, Energy-the international Journal, Vol.18. No 6, pp. 615-625.

[6] Hui Hong, Hongguang Jin, Jun Ji, et al., 2005, Solar thermal power cycle with integration of methanol decomposition and middle-temperature solar thermal energy , Solar Energy, Vol.78, pp. 49-58.

[7] Hongguang Jin, M. Ishida, M Kobayashi et al., 1997, Exergy evaluation of two current advanced power plants: supercritical steam turbine and combined cycle. ASME Trans Journal of Energy Resources Technology, Vol.119, pp. 250-256.

Acknowledgments

The authors gratefully acknowledge the support of the Natural Scientific Foundation of China (No.50976114, 50836005), and the National High Technology Research and Development Program (No. 2010CB227104).

Modelling and Control of the Rankine Cycle of a Small Solar Thermal Power Plant

D. Bohn, R. Krewinkel, V. Nolte

Institute of Steam and Gas Turbines, RWTH Aachen University, Aachen, Germany

Abstract: In 2009, a solar tower demonstration plant with an open volumetric receiver concept started operation in Jülich, Germany. A research collaboration (vICERP) was founded with the goal of creating detailed physics-based models of this plant that are lean enough for online optimisation. The open-source Modelica language is used for this purpose. The focus of this paper is on the Rankine cycle. The modules for the turbine and the cold end of this cycle are briefly outlined, but the emphasis lies on the plant's fire-tube boiler as the most important delay element in the control strategy. The models incorporated in the fire-tube boiler module are therefore discussed in detail and some simulation results are presented. The control strategy is also briefly specified.

Keywords: Fire-Tube Boiler, Modelica, Rankine Cycle, Solar Thermal Power Plant

1. Introduction

Most of today's operational solar thermal power plants as well as those that are under construction make use of the parabolic trough solar field with oil as a heat transfer fluid. The known limitations of this technology, especially when it comes to efficiency, ask for improved concepts for the future solar electricity market. Therefore other technologies are pursued parallel to the construction activities in parabolic trough plants. A number of direct steam generation solar tower concepts like PS 10 and PS 20 near Sevilla are for example already in operation, others are in their demonstration phase. The open volumetric receiver system [1] is another promising technology. It is based on the use of air at ambient pressure as a heat transfer medium in combination with a Rankine cycle. This approach allows high steam parameters in the Rankine cycle and heat storage in solid materials.

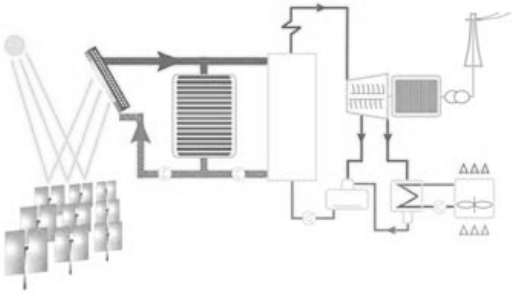

Fig. 1. Schematics of the Jülich Demonstration Plant

The demonstration plant "Solar Tower Jülich" in Germany (see Fig 1) uses this technology on a relatively small scale: it has started grid operation with a nominal power output of 1.5 MW_{el} [2]. Apart from the obvious goal of producing electricity for the German power grid, the demonstration plant offers for the first time the possibility to study the behaviour of the integrated power plant system under real conditions.

To further speed up market introduction of the technology used in Jülich by means of scientific support and project development activities, the virtual Institute of Central Receiver Power Plants (vICERP) was founded [3]. The virtual Institute puts the emphasis of its activities on creating detailed physics-based models that are lean enough for online optimisation. These should help to solve important questions with regard to the optimal operational strategy of the entire plant, especially during transient states. The Institute of Steam and Gas Turbines (IDG) performs the modelling of the Rankine cycle within this research collaboration.

The underlying principle of the open volumetric receiver technology used is the solar heating of air to temperatures in the region of 973 K. The receiver is open since the heat transfer medium air is taken from the atmosphere just in front of it and is released to the atmosphere again at the end of the cycle. The receiver is volumetric since the concentrated solar irradiation that hits the receiver is absorbed within a three-dimensional porous

structure. This principle reduces heat losses to the surroundings since the highest temperatures are reached at the inside and not on the outer surface of the receiver.

An inherent advantage of the technology is the possibility to integrate a robust heat storage technology based on solid materials. The storage operates similar to a regenerator, i.e. while charging hot air flows through the storage, heating up its ceramic tiles. While discharging, cold air flows through the storage in reverse direction and is thus heated up. This enables the operation of the plant after sunset (or before sunrise) and during periods of reduced solar input. But as the storage capacity is limited to ca. 2 hours at full-load, highly transient dynamic behaviour cannot be excluded altogether.

The open volumetric concept of the plant also enables the application of a conventional Rankine cycle. The live steam parameters reached in Jülich are for example 693 K at 2.6 MPa. The thermal energy of the hot air at ambient pressure is transferred to the Rankine cycle in a heat exchanger similar to those used in chemical plants or, for the planned upscaled version of the Jülich Tower, to that in combined cycle power plants. Due to the steam paramaters that can thus be reached, a conventional (and comparatively cheap) small industrial steam turbine can be used.

The cold end consists of a condenser and an air-cooled heat exchanger for the secondary cooling cycle. The cold end determines the back-pressure for the turbine and thereby the overall plant efficiency. The fans in the heat exchanger of the secondary cooling cycle also are the largest consumers of electricity within the plant by far. As the solar tower will be applied in areas where water is scarce, the use of an air-cooled heat exchanger is imperative, though.

2. Modelling of Components from the Rankine Cycle

The most important components of the Rankine cycle are the turbine, the cold end and the steam generator. These components are discussed in the following subchapters. The pump is of the utmost importance for the control of the plant but is no modelling challenge and will therefore not be discussed here.

All fluid models are taken from the Modelica Library developed by [4] for compressible flows. This library also includes the complete steam tables and is therefore suited for the modelling of evaporation and condensation.

A validation of the models will be carried out as soon as operational data from the Jülich plant becomes available in the summer of 2010.

2.1. Turbine

The modelling of the turbine is based on the experience gained in the development of another in-house code at the IDG, called Aix-PAT [5]. The expansion through the turbine is calculated using Zweifel's method. This enables the calculation of the polytropic efficiency, or, if the efficiency is known, the outlet parameters. Equation (1) gives Stodola's steam cone law [6] that is used to calculate the mass flow through the turbine for a given pressure difference over the turbine during start-up.

$$\frac{\dot{m}}{\dot{m}_0} = \frac{\mu}{\mu_0}\sqrt{\frac{n/(n-1)}{n_0/(n_0-1)}}\sqrt{\frac{p_{in,0}v_{in,0}}{p_{in}v_{in}}}\frac{p_{in}}{p_{in,0}}\sqrt{\frac{1-\left(\frac{p_{out}}{p_{in}}\right)^{n+1/n}}{1-\left(\frac{p_{out,0}}{p_{in,0}}\right)^{n_0+1/n_0}}} \quad (1)$$

As even the last high pressure stages of the turbine already operate in the wet steam region, a Baumann factor, defined as:

$$\eta = \eta_0\left[1-\alpha(1-x)\right] \quad (2)$$

has to be included in the model as well. This empirical factor encompasses all losses due to wetness in the last turbine stages [7]. As can be seen from Fig. 2, the difference in the calculated polytropic efficiency with and without the incorporation of the Baumann factor can be significant. In this particular example, the inlet temperature and initialised polytropic efficiency were kept constant, whereas the pressure was increased linearly from 1.3 to 2.6 MPa. The enthalpy at the turbine outlet changes accordingly, i.e. the lower efficiency leads to higher values for the outlet enthalpy.

The turbine module is provided with the inlet conditions from the pump (pressure) and HRSG (temperature), respectively. The outlet pressure is prescribed by the cold end, the wetness and temperature are a result of the turbine calculation.

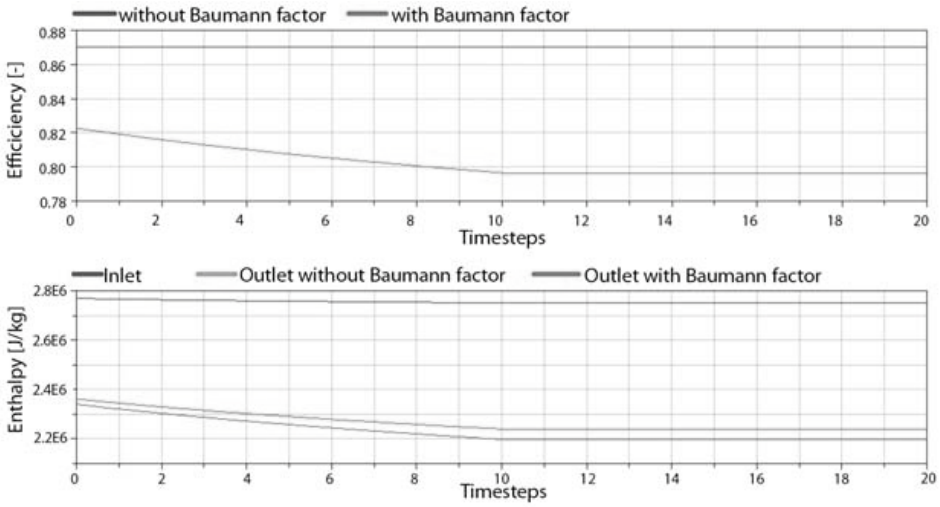

Fig. 2. Results of the Turbine Calculation

2.2. Cold End

Since the cold end determines the back-pressure of the turbine it also greatly contributes to the overall efficiency of the plant. Natural draft cooling towers provide the lowest cooling water temperature and therewith the lowest back-pressure. Air cooling, though, is typical for plants the size of (future) solar-thermal power plants [8]. Most of these plants will be built in regions where water is scarce and a cooling tower is therefore not an option. It should furthermore not be forgotten that the fans of the air-cooled heat exchanger are the largest consumers of electricity in the plant by far. Therefore the demonstration plant in Jülich is also equipped with an air-cooled secondary cooling cycle. This enables a good estimation of the impact the fans have on the efficiency of (future) solar thermal power plants.

For the optimisation of the plant under changing ambient conditions accurate models of these components have been developed. The model adopted for the condenser that of a horizontal shell-and-tube condenser is based on [9]. The future application of the model, online optimisation, requires some simplifications. The most important is the separate balancing of water and steam, i.e. there is only a thermodynamic equilibrium on the phase boundary. The model consists of the space within the condenser (in which condensation takes place), the walls of the tubes and the tubes' inner space. The latter is taken from the standard Modelica Library [10], the condenser space and the tube walls have been developed at the IDG in the framework of the vICERP.

The cooler for the secondary cooling cycle is divided into the same components as the condenser. The model itself is based on the conservation of mass on both the air and coolant side, as well as the equality of the heat flux into and out of both flows. The correlation between electricity consumption and air mass flow, which is of considerable importance for the correct simulation of the plant in transient and part-load conditions, will be provided by the manufacturer when the test phase of the plant is finished.

2.3. Heat Recovery Steam Generator (HRSG)

The heat exchanger is both the most complex component to model and, with regard to control, the most important delay element in the power plant cycle. The modelling of heat exchangers for power plants has hitherto mainly focussed on the large water tube boilers in general and drum boilers in particular [11]. These are applied in conventional and nuclear power plants, but in the framework of the vICERP smaller applications are looked at, for which it is common to use a fire-tube boiler. In this type of boilers the exhaust gas or, in this case, heated air, flows on the inside of the tubes that are situated within a water-filled pressurised drum. The lower part of the drum is

filled with water, whereas the upper part is filled with steam.

Although models for steam drums exist, these have to be expanded with additional source terms in the form of the heated fire-tubes. The heat transfer around these tubes is also of the utmost importance. Not only do these differ significantly from the phase-change in water-tube boilers, they also determine the amount of evaporated water and therewith the mass flow to the turbine.

The economiser and superheater, where no phase change occurs, are modelled using elements from the standard Modelica Library [10] and will not be discussed here.

The implemented dynamic model of the boiler is based on the physical models of [12]. Both the steam and the water are modelled as a lumped volume. This means that it is assumed that the pressure is constant, i.e. the losses that occur when the flow enters the volume cannot be calculated. The pressure loss due to the flow through the pipes in the boiler is, of course, calculated.

A non-equilibrium model for the energy and mass balances of water and steam is implemented in the boiler module. This means that separate balances are formulated for both phases and the liquid volume can be under-cooled, saturated or can consist of a water-/steam mixture with low gas content. The gas volume can also be saturated or superheated. If the volume is a water-/steam mixture it always has a high gas content [12]. Mass transfer can take place between the liquid and gaseous phases (condensation or evaporation). The drum wall is also modelled and therefore heat fluxes from the drum to the environment and from the water and steam to the wall can be calculated as well. Equations (3) – (7) describe the mass and energy balances in the boiler.

$$\frac{dM_v}{dt} = m_{ev} - m_v - m_C - m_{cs} \tag{3}$$

$$\frac{dM_l}{dt} = m_f + m_c + m_{cs} - m_b - m_{ev} \tag{4}$$

$$\frac{dE_v}{dt} = m_{ev}h_{vs} - m_v h_v - m_c h_{ls} - m_{cs}h_{vs} + Q_{wv} - Q_{vl} - p\frac{dV_l}{dt} \tag{5}$$

$$\frac{dE_l}{dt} = m_f h_f + m_c h_{ls} - m_{cs}h_{vs} - m_{ev}h_{vs} + Q_{wl} + Q_{vl} + Q_H - p\frac{dV_l}{dt} \tag{6}$$

$$\frac{dE_w}{dt} = -Q_{wl} - Q_{wv} - Q_{we} \tag{7}$$

These equations are slightly modified from [12]. The terms w_c, w_{cs}, w_{cv} and Q_{vl} are also calculated using the algebraic equations provided by [12] but with the time constants appropriate for a fire-tube boiler. The model of the different heat fluxes and mass flows in the boiler is depicted in Fig. 3.

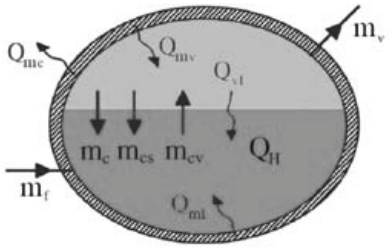

Fig. 3. Schematics of the Boiler Model in Modelica after [12]

The modelling of the boiler section poses a considerable challenge since the phase change takes place here. The semi-empirical models implemented here are based on [13]. It is known that, depending on the heat flux, different kinds of boiling can occur and accordingly more or less steam is generated. It should be noted that only the most relevant type of boiling, i.e. saturated pool boiling, will be discussed here. Under-cooled pool boiling is implemented, but it can be assumed that the high inertia of the boiler ensures this type of boiling will seldom occur. Therefore the presented results were all generated using the former model. Pool boiling starts with convective boiling, followed by nucleate boiling and partial film boiling. The amount of evaporated water decreases sharply in this last regime, since a film of evaporated water around the tubes diminishes the heat transfer. Only when the heat flux is increased further, film boiling ensues and the heat transfer increases again, mainly due to steam convection within the film around the tubes and radiation. The accurate modelling of these boiling regimes is of the utmost importance for the prediction of the steam mass flow during disturbances or controlled transients like start-up.

3. Simulation Results of the HRSG

As mentioned above, the solar power plant in Jülich is operated in a climate in which the solar irradiation is far from constant. The storage, be it relatively large, cannot mitigate all transients and disturbances. Therefore two typical disturbances, a change in heat input and a change in pressure, have been modelled to estimate their effect on the Rankine cycle. Especially their effect on the water level in the boiler has to be taken into account. Data for a typical start-up sequence will be part of the information provided by the Solar Tower to the virtual Institute in the summer of 2010. This sequence will be simulated when the data is available.

For now, the control strategy and some disturbances will be discussed. The first sub-section is concerned with the control strategy. The results of the pressure and heat flux disturbances on the boiler will be presented in the second sub-section as their behaviour is amongst others determined by the chosen control strategy.

3.1. Control Strategy

The control of the air side of the solar thermal power plant as discussed in [14] is mostly detached from the control of the Rankine cycle. A simplified sketch of the latter is presented in Fig. 4. The most important control variable in the Rankine cycle is the water level in the drum. This should under no circumstance come below the level of the heating tubes. This would cause the tubes to overheat, with considerable damage to the plant as a result. Any short-term control of the cycle is therefore based on increasing the mass flow through the pump. If the water level deviates from its prescribed value, the pump speed increases (or indeed decreases if the water level should rise) in accordance with implemented pump characteristics that correlate mass flow and pump speed. A simple P/I controller is used for this purpose.

If the level in the feed water storage tank should be too low or the water level in the drum does not rise quickly enough the control of the Rankine cycle intervenes in the control of the entire power plant and decreases the air mass flow through the HRSG.

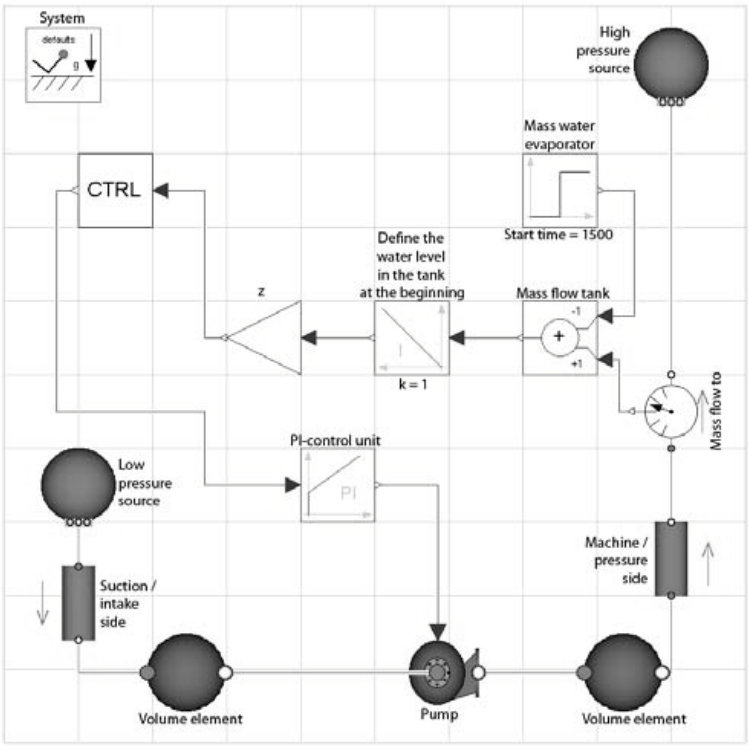

Fig. 4. Visualisation of the Control Strategy for the Rankine Cycle of the Solar Thermal Power Plant

3.2. Pressure and Heat Flux Disturbance

The pressure disturbance was chosen of all possible disturbances in the plant since it has particular significance for the steam phase. The effects of this disturbance are shown in Fig. 5.

One can see that after the first couple of iterations the steam phase within the liquid, generated by the tubes in the water volume, remains constant. At $t = 100$ the pressure in the drum volume is decreased by 0.1 MPa. In reality this may happen when steam valves are opened in the cycle. The saturation temperature falls with the pressure drop, which leads (for a constant heat flux) to an increase of the steam phase within the liquid volume. After a while, the amount of steam drops off slightly since a new equilibrium is reached within the volume.

The wall temperatures are also affected by the pressure drop. The heat stored in the drum walls heats up the steam volume, superheating it slightly. This is a feature of the non-equilibrium model that does not require saturated steam conditions in the control volume. The delay in the superheating of the steam is caused by the instantaneous character of the pressure drop. This forces, in accordance with the conservation of impulse, additional steam out of the control volume (the drum) to the turbine. The pump compensates immediately for this by supplying additional water to the drum, but this needs to be heated up to its evaporation temperature first. Only when this is reached the steam is superheated.

Another possible disturbance is a sudden increase in the heat flux at constant pressure (see Fig. 6). This can be caused for example by an increase in the solar irradiance when a cloud stops blocking the sun. Again, the system requires a number of iterations before it reaches a stable condition. In this particular case, a jump in the heat flux of 100 kJ at $t = 100$ was simulated once the stable condition was reached.

As was the case for the pressure disturbance, the steam content in the liquid volume increases if the heat flux is increased. This leads, of course, to an increased steam mass flow to the turbine. At the same time the specific volume of the liquid volume increases with increasing steam generation. In other words, a lesser amount of water takes up a (relatively) larger volume. These two effects counteract one another and lead to a very mild disturbance of the water level in the drum. In this case, the pump speed is only decreased slightly because the disturbance of the water level is well within the defined limits.

The simulations show that the developed model for the fire-tube boiler can simulate the delay times between disturbances and changes of the steam mass flow to the turbine. The corresponding changes in the water level in the drum are calculated as well.

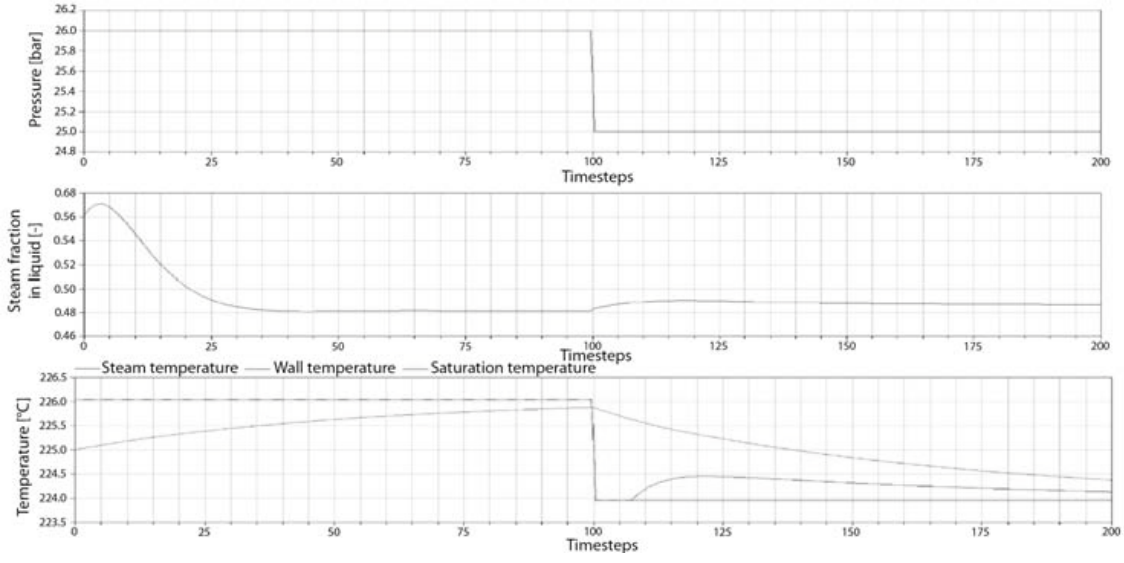

Fig. 5. Reaction of the System to a Pressure Disturbance

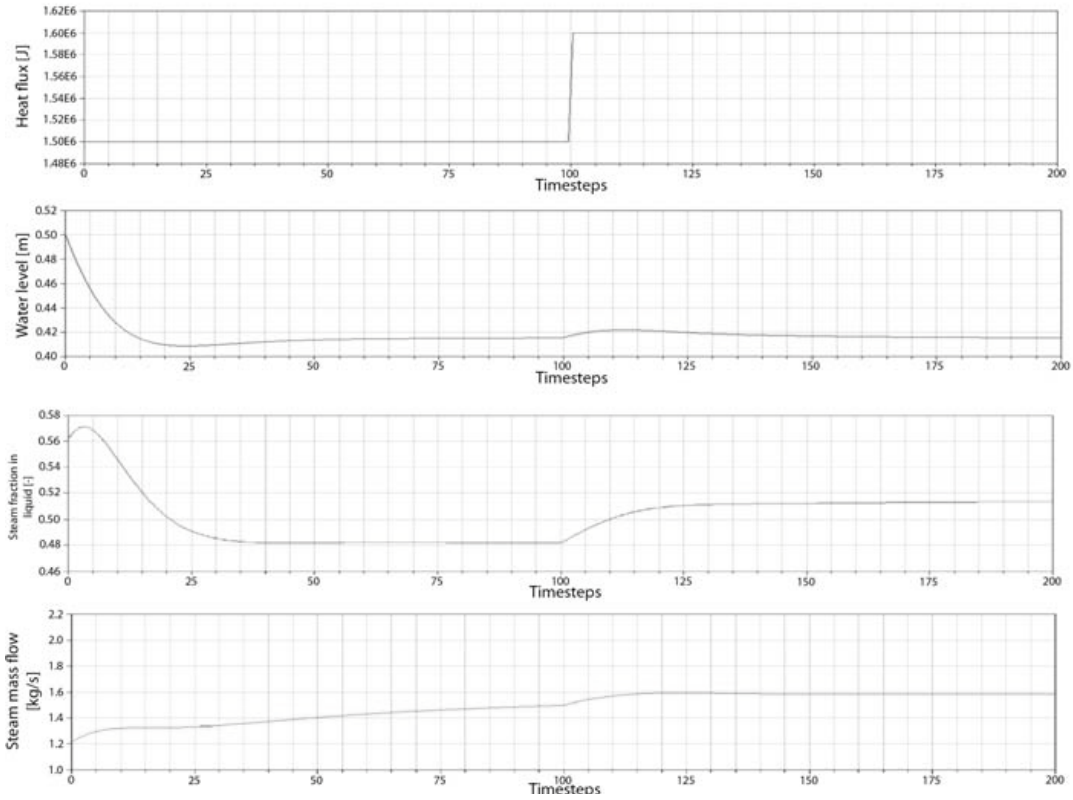

Fig. 6. Reaction of the System to a Heat Flux Disturbance

4. Summary and Conclusion

A demonstration plant for open-volumetric solar thermal power plants has been built in Jülich, Germany. A research collaboration of different institutes was founded to develop software that can model the plant with high accuracy and is yet lean enough to allow online real-time predictions of the plant behaviour.

A model for the Rankine cycle of small solar tower power plants was developed in the Modelica language. Within this cycle, the HRSG is the most important component when it comes to control and delay times in the system, and therefore this component was the focus of this study.

It was shown that it is possible to keep the water level in the fire-tube boilers within the safe limits with a relatively simple control strategy. The model predicts the physical phenomena and delay times in the boiler qualitatively well.

The validation data for a quantitative evaluation are as yet lacking, but will be provided by the plant's operator in the summer of 2010. Further future work includes establishing a connection between the control of the air cycle and that of the Rankine cycle as well as numerical optimisation of the presented models for online calculations.

Nomenclature

c	velocity, m/s
h	enthalpy, J/kg
$\dot{m}$	mass flow rate, kg/s
n	polytropic exponent
p	pressure, MPa
v	specific volume, m³/kg
t	time, s
x	wetness fraction
y	specific flow work, J/kg
E	internal energy, J

Q	heat flux, W
M	mass, kg
T	temperature, K
V	volume, m³

Greek symbols

α	Baumann factor
η	efficiency
μ	choke parameter, $\mu = \frac{c_m}{\sqrt{2\lvert y\rvert}}$

Subscripts and superscripts

0	design point
c	condensation
cs	superficial condensation
f	feed
in	inlet
l	liquid
m	meridional direction
out	outlet
v	vapour
vl	vapour-to-liquid
w	wall
we	wall-to-environment
wl	wall-to-liquid
wv	wall-to-vapour

References

[1] Ahlbrink, N., Belhomme, B. and Pitz-Paal, R., 2009, Modeling and Simulation of a Solar Tower Power Plant with Open Volumetric Receiver, *Proc. 7th Modelica Conf.*, Como, Italy, pp. 685-693.

[2] Abel, D. *et al.*, 2009, The Virtual Institute for Central Receiver Power Plants - vICERP, *Proc. SolarPACES 2009 Conf.*, Berlin.

[3] www.vicerp.de

[4] Casella, F. *et al.*, 2006, The Modelica Fluid and Media Library for Modeling of Incompressible and Compressible Thermo-Fluid Pipe Networks, *Proc. 4th Modelica Conf.*, Vienna, pp. 631-640.

[5] Bohn, D., Krewinkel, R. and Rakut, Chr., 2008, Proposing a Novel Approach in Plant Design: The Combined Calculation of Power Plant Processes and Component Stress, *Proc. 12th ISROMAC*, Honolulu, U.S.A., Paper 20008.

[6] Traupel, W., 1962, *Thermische Turbomaschinen, Band 1*, Springer Verlag, Berlin.

[7] Baumann, K., 1921, Some Recent Developments in Large Steam Turbine Practice, Engineer, 111, pp. 435-458.

[8] Witte, R., 1997, Optimierung des kalten Endes von Kraftwerken, BWK, 49 (11/12), pp. 56-61.

[9] Botsch, T.W., 1997, *Modelle zur Beschreibung des stationären und des dynamischen Verhaltens von Rohrbündelkondensatoren*, VDI Fortschrittsberichte 101, VDI Verlag, Düsseldorf, Germany.

[10] Modelica – A Unified Object-Oriented Language for Pysical Systems Modeling, 2009, Language Specifications Version 3.1: Standard Fluid Library, The Modelica Association.

[11] Aström, K.J. and Bell, R.D., 1999, Drum-Boiler Dynamics, Automatica 36, pp. 363-378.

[12] Casella, F. and Leva, A., 2003, Modelica Open Library for Power Plant Simulation: Design and Experimental Validation, *Proc. 3rd Intl. Modelica Conf.*, pp. 41-50.

[13] Gorenflo, D., Behältersieden (Sieden bei freier Konvektion), In: N.N., 2002, VDI-Wärmeatlas, Springer Verlag, Berlin.

[14] Gall, J. *et al.*, 2010, Simulation and Control of Solar Thermal Power Plants, *Proc. ICREPQ'10*, Granada, Spain.

Acknowledgments: The authors would like to thank the Initiative and Networking Fund of the Helmholtz Association, the Ministry of Innovation, Science, Research and Technology of the State of North Rhine-Westphalia and the European Union/European regional development fund for their financial support to the vICERP. The responsibility for the content of this publication lies solely with the authors.

First Test Results of a Small Joule Cycle Ericsson Engine Prototype for Solar Energy Conversion or for Micro-CHP Application

Abdou Touré, Pascal Stouffs

Laboratoire de Thermique, Energétique et Procédés, LaTEP, Université de Pau et des Pays de l'Adour, Pau, France

Abstract: An Ericsson engine is an external heat supply engine working according to a Joule thermodynamic cycle. Such engines are specially interesting for low power solar energy conversion and micro-CHP from conventional fossil fuels or from biomass. A first prototype of an open cycle Ericsson engine with air as the working fluid has been designed. The 'hot' part of this prototype has been built and tested. Experimental results are presented such as pressure evolutions, indicated diagrams, mechanical efficiency.

Keywords: Joule cycle engine, Ericsson engine, hot air engine, solar energy conversion, external heat supply reciprocating engine, micro-cogeneration, experimental results.

1. Introduction

A special family of thermal engines can be identified from the following features: reciprocating engines, external heat supply, separate compression and expansion cylinders, regenerator or recuperator, monophasic gaseous working fluid [1]. These engines are sometimes called 'hot air engines' [2], even if the air used in the XIXth century engines has been replaced by high pressure hydrogen or helium in a lot of modern engines. Hot air engines have known commercial success during the XIXth century [3], but, since the beginning of the XXth century, they have been discarded and replaced by internal combustion engines or electric motors. The family of hot air engines is divided in two subgroups: the Stirling engines, invented in 1816, have no valves (Fig. 1) whereas Ericsson engines, invented in 1833 (Fig. 2) have valves in order to isolate the cylinders.

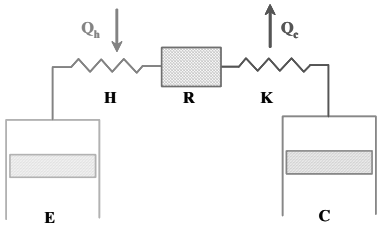

Fig. 1. Principle of the Stirling engine.

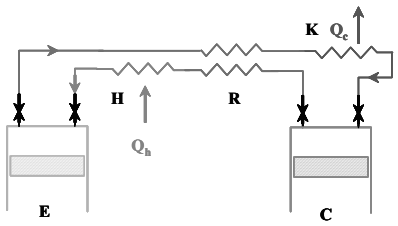

Fig. 2. Principle of the Ericsson engine.

Since the pioneer work of the Philips company, around the second world war, the attention has been drawn on Stirling engines and lots of research and developments have been carried out. However, up to now, not many studies are dedicated to Ericsson engines. While some works are devoted to internal combustion Joule cycle Ericsson engine from fossil fuel [4,5], other studies deal with external heat supply Joule cycle Ericsson engine [6,7].

The Ericsson configuration, with valves, shows several advantages compared to the Stirling configuration [8]. Amongst them, it is worth to note that the Ericsson engine heat exchangers are not dead volumes, whereas the Stirling engine heat exchangers designer has to face a difficult compromise between as large heat transfer areas as possible, but as small heat exchanger volumes as possible.

The theoretical Ericsson cycle is made up of two isothermal processes and two isobaric processes. Unfortunately it is not suitable to describe an ideal Ericsson engine. Indeed due to the lack of heat exchange surface in the cylinder, the heat transfers between the working fluid and the hot and cold sources take place in external heat exchangers adjacent to the cylinders instead of through the cylinders wall. So, the cycle made up of two isentropic and two isobaric processes, usually called the Brayton or Joule cycle, seems more suitable to describe the Ericsson engine.

2. Ericsson engine applications

As for Stirling engines, Ericsson engines are specially interesting for thermodynamic solar energy conversion and for micro-cogeneration. However, in both fields, Ericsson engines can have some specific advantages on Stirling engines.

2.1. Micro-cogeneration

Unlike internal combustion engines, hot air engines generate low noise and do not need frequent maintenance. Therefore they are particularly suited for low-power combined heat and power (CHP), for residential applications for instance. Up to now, several Stirling engines have been designed for micro-cogeneration [9,10]. However it has been shown that a natural gas CHP system based on an open cycle Ericsson engine could be interesting and profitable [6].

Furthermore there is a great interest for micro-cogeneration systems based on wood energy. The only commercially available system up to now is based on a Stirling engine fuelled by wood pellets [11]. Other tests have been carried out by coupling a Stirling engine in a conventional wood boiler. One of the main problem consists in the fouling of the Stirling heater and the difficulty to clean its surface due to its compactness [12,13]. For this application the Ericsson engine is interesting since the heater does not need to be compact and may be designed according to heat transfer and fouling consideration only.

2.2. Low power solar energy conversion

Most current existing systems for low power thermodynamic solar energy conversion are based on the 'Dish/Stirling' technology [14,15], which relies on high temperature Stirling engines and requires a high solar energy concentration ratio. This technology holds the world record for efficiency in converting solar energy into grid-quality electricity since a instantaneous global solar to electric energy conversion efficiency higher than 30% has been measured on the SES dish/Stirling system.

However it is clear that these systems are quite heavy, leading to high costs. Especially the parabolic 'dish' concentrator, the sun tracking system and the engine fixation at the concentrator focus are quite expensive. Also the high pressure high temperature engine requires an expensive technology.

Due to the need to minimize the heater volume, solar energy conversion by means of a Stirling engine implies to focus solar beams on a point, that means to use an expensive parabolic dish. Using an Ericsson engine allows large heater thus linear solar concentrator such as parabolic trough. Modelling results have shown that the coupling of a parabolic trough with an open cycle Ericsson engine could lead to a yearly global efficiency higher than 10 % while using a low tech and cheap system [7,16].

3. Description of the prototype

It has thus been decided to build and test a first Ericsson engine prototype. The prototype built up to now is not a complete engine but only the most difficult part to design, that is the 'hot' part of the reciprocating Joule-cycle Ericsson engine. It comprises not only the 'hot' valves, but also the whole expansion cylinder, the double contrarotating crankshaft and the camshaft. By comparison with a complete Ericsson engine, only the compression cylinder is missing. However, as soon as the 'hot' prototype is validated, it will be easy to add a compression cylinder in order to obtain a complete engine. It has been thought that the decoupling between the expansion and the compression cylinder was interesting for the first experimental phase, in order to avoid the problem of compressor-expander matching during the tests of the 'hot' part. The 'modularity' of the Ericsson engine allows to design and develop each component of the engine separately whereas a Striling engine has to be designed and tested as a whole.

According to the modelling results [16], the prototype is designed to work with air in open cycle as the working fluid and to withstand compressed air supply at a pressure of 300 kPa and a maximum temperature of 650 °C. The prototype expansion cylinder capacity is 0.65 dm^3. The

expansion cylinder bore is 80 mm, the piston stroke is 129 mm and the maximum rotation speed is 950 rpm. This leads to an expected air mass flowrate of 5 10^{-3} kg, an indicated expansion cylinder power of 1140 W and an expected mechanical power of about 1 kW. Eventually an expansion cylinder of 257 mm bore and a compression cylinder of 163 mm bore will be fitted to the prototype instead of the actual 80 mm bore expansion cylinder leading to an expected net mechanical power of 3.8 kW at 950 rpm suited for solar application [16]. Fig. 3 presents a picture of the prototype.

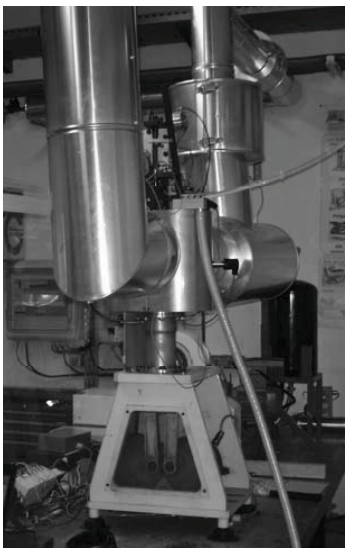

Fig. 3. The prototype of the 'hot 'part of the Ericsson engine.

For low pressure ratio reciprocating engine, achieving a very good mechanical efficiency is of utmost importance. Therefore, it has been thought that the best lay-out for a complete Ericsson engine should be to have the expansion cylinder piston and the compression cylinder piston on the same rod. So the kinematic link between the work producing piston in the expansion space, and the work consuming piston in the compression space is as short as possible and the power supplied to the crankshaft is only the net useful mechanical power. It can be seen on Fig. 3 that the link between the expansion cylinder piston of the prototype on the upper part of the engine and the crankshaft on the lower part can easily be dismantled in order to insert the compression cylinder in the future.

Also, Fig. 3 shows that the technology of Lancaster crankshaft (double contrarotating crankshaft) has been chosen. The main reason is that this kinematics allows a very good mechanical balancing of the moving parts, thus a good mechanical efficiency.

The lower part of the expansion cylinder is water-cooled while the upper part of the cylinder is insulated and is maintained at high temperature. A high thermal resistance is realized between both parts of the cylinder.

The 'hot' valves are the most difficult part of the prototype. The valves have to ensure opening and shutting of the inlet and outlet ports at a constant and uniform temperature of 650 °C. They have to work with sufficient airtightness and durability conditions. Commercial automotive valves are used. But the valves rods are linked to extension rods which are cooled by internal water circulation. So thermal conduction towards the rocker arm and the cam is reduced.

Fig. 4 presents a view of the exhaust valve cam, rocker arm and valve spring. The flexible pipes for the valve rod water cooling are clearly shown. Also it can be seen that the cam is made up of two superimposed half-cams whose angular position can be adjusted on the camshaft. By this way the opening angle and duration of the valve can be manually varied. A similar design has been adopted for the inlet valve cam.

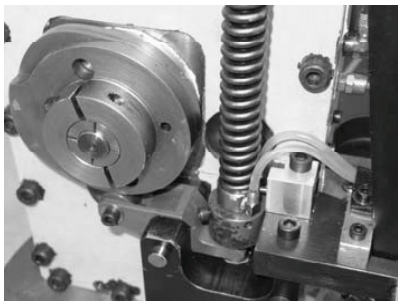

Fig. 4. Exhaust valve cam, rocker arm, valve spring and valve rod water cooling pipes.

4. The test bench

4.1. General description

Fig. 5 presents a general view of the test bench. In order to have an autonomous and stable air supply for the prototype, the compressed air is delivered by a dedicated air compressor not shown on Fig. 5.

The compressed air is dried by refrigeration in order to avoid damage of some delicate transducers such as the mass flowmeter. The air dryer is also equipped with a pre-filter and a submicronic filter.

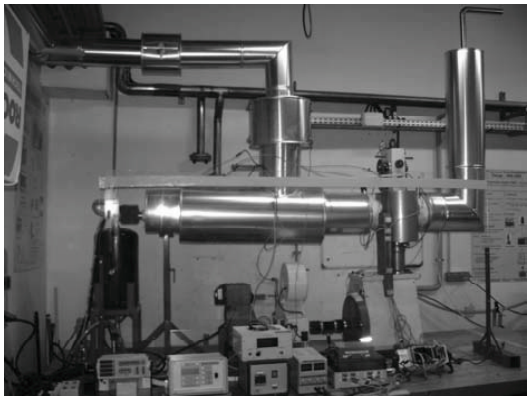

Fig. 5. The test bench of the 'hot 'part of the Ericsson engine prototype.

The air pressure is then regulated up to a maximum pressure of 300 kPa and the mass flowrate is measured. A first 'cold' buffer tank is inserted between the mass flowmeter and the heater (black cylindrical tank on Fig. 5). The compressed air is then heated by means of an electric heater up to the setting point temperature, limited to 650 °C. The maximum heating power is 8 kW. A stainless steel 'hot' buffer space of a capacity of about 8 liters is inserted in the delivery line in order to avoid pulsating flow in the mass flowmeter, the thermocouple for the temperature regulation and the heater, due to the cyclic opening and closing of the prototype inlet valve. The prototype is connected to an exhaust line. The maximum expanded air temperature at the exhaust is about 200 °C. A crank angle transducer is mounted on the prototype crankshaft. Finally, the prototype is coupled to a powder brake. The prototype shaft torque is measured by means of a transducer inserted between the prototype and the brake.

Moreover, several temperature and pressure transducers are implemented in different locations of the circuit. The data acquisition system is driven by the crank angle transducer which delivers an impulsion every degree of rotation of the crankshaft.

4.2. Measurements calibration and reliability

Prior to implementation on the test bench, the four pressure transducers have been mounted on a small test vessel in order to calibrate them. The pressure range for the calibration in the vessel extended from 10^5 Pa up to 8 10^5 Pa. The pressure transducers have been calibrated by comparison with the value given by the transducer eventually implemented in the cylinder head. The calibrations obtained by this method are in very good agreement with those given by the calibration chart supplied with each transducers.

The calibration of the torquemeter has been checked by a static device realized in our Laboratory. Again, the result is in close agreement with the calibration data given by the torquemeter supplier.

For the temperature measurements, the standard correlation for the type K thermocouple signal conversion has been used.

For the TDC calibration, two devices have been used. A geometrical reference has been constructively marked on the crankshaft, allowing accurate TDC calibration of the crank angle transducer. Moreover a Hall effect transducer has been placed on the inertia wheel in order to check the TDC. It is estimated that the crankshaft angle is measured with an absolute accuracy of ±1°.

For the mass flowmeter, the calibration given by the supplier has been used.

When the prototype is in steady state operation, a very high repeatability of all instantaneous measurements has been observed from one to another cycle. The results presented hereafter are obtained from phase average on 165 cycles.

It has been observed that it is difficult to reproduce strictly identical operating conditions from one test to the other, due to the fact that the absolute positions of each of the four half-cams are difficult to reproduce with a high accuracy. Also the manual pressure relief valve in the inlet line does not allow a very fine adjustment.

The total period for the tests extended over 8 months. From the beginning to the end of the period, a small variation in the global performance of the prototype has been observed due to a weak degradation of the mechanical efficiency.

5. Experimental results

Extended tests have been carried out in a wide range of rotational speed and inlet temperature. However due to insufficient cooling of the cylinder liner, the maximum temperature has been limited to 550 °C instead of 650 °C in order to avoid any damage to the piston ring.

5.1. Pressure evolutions

Fig. 6 presents the pressure evolutions recorded upstream from the heater, in the prototype inlet pipe and in the cylinder head for an air temperature of 518 °C in the inlet pipe.

It can be observed that the pressure difference between the inlet pipe and the cylinder head is very low during the admission phase, that is from about the top dead center TDC = 0 ° up to 90 ° crankshaft. This shows that the pressure loss due to the inlet valve is very weak. This pressure loss through the inlet valve is logically higher when the rotational speed increases, but it is always lower than 0.1 10^5 Pa even at 900 rpm. A similar result has been obtained for the outlet valve.

Fig. 6 shows important pressure oscillations in the inlet pipe and in the cylinder during the admission phase. These pressure oscillations are due to acoustic phenomena in the inlet line. It can be observed that the pressure oscillations amplitude gets higher as the rotational speed increases. The frequency of the pressure oscillations is constant, the number of pressure maxima being inversely proportional to the rotational speed. This parasitic acoustic effect is due to the upstream buffer space which includes several rough section variations.

Finally it can be observed on Fig. 6 that in spite of two important buffer spaces upstream from the inlet pipe, the pressure in the inlet pipe decreases during the admission phase, while the pressure upstream the heater remains constant. The increase of the inlet pipe pressure up to the inlet heater pressure is logically slower (in term of crankshaft angle) when the rotational speed gets higher.

5.2. Indicated diagram

Fig. 7 presents the indicated diagrams corresponding to the three rotational speeds of Fig. 6.

The three diagrams are not perfectly superimposed on one another for each rotational speed because the inlet pressure and the inlet and outlet cam adjustments have not been reproduced exactly identically in the three tests. It is however observed that the shape of the diagrams is globally independent of the rotational speed as expected.

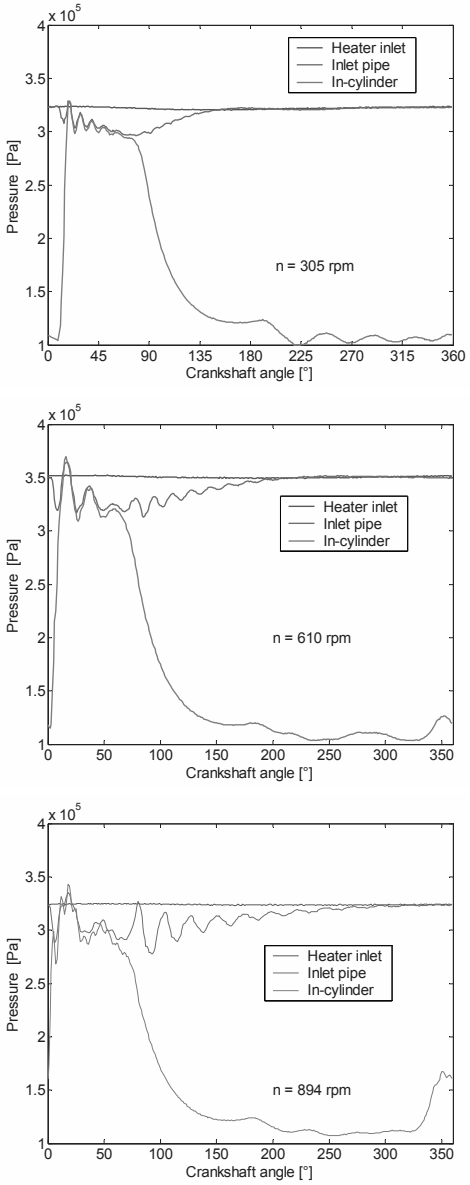

Fig. 6. Pressure evolutions for an inlet temperature of 518 °C and for three rotational speeds.

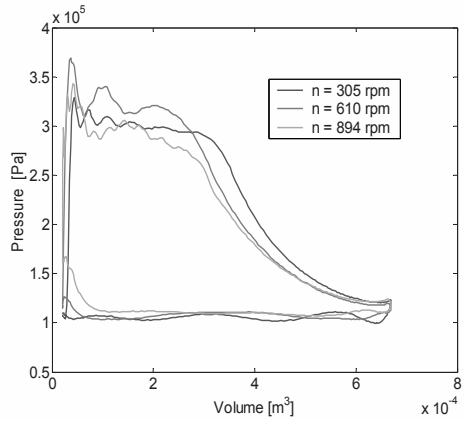

Fig. 7. Indicated diagrams for an inlet temperature of 518 °C and for three rotational speeds.

5.3. Outlet temperature

Table 1 presents experimental averaged temperatures measured in the inlet pipe, on the external wall of the cylinder head and in the outlet pipe for three different inlet temperatures. The cylinder head wall temperature is always comprised between the inlet and the outlet temperature. It is close to the mean temperature between inlet and outlet for a low inlet temperature but it gets closer to the outlet temperature when the inlet temperature gets higher.

Table 1. Experimental averaged temperatures and calculated adiabatic temperature.

Temperature	[°C]	[°C]	[°C]
Inlet	314	405	494
Wall	260	295	362
Outlet	212	258	318
Adiabatic	145	211	282
Δ(Out – adiab.)	67	47	36

The experimental outlet temperature is systematically higher than the temperature calculated from the reversible adiabatic expansion assumption. The difference between experimental and adiabatic outlet temperature gets lower when the inlet temperature increases. Experimental results also show that this difference slightly decreases when the rotational speed increases.

Several explanations can be found to this temperature difference. First the expansion is not adiabatic as the in-cylinder air exchanges heat with the wall and is heated by the wall at the end of the expansion process. Secondly it has been observed that the inlet and outlet valves leak. So it can be thought that, during expansion, the inlet valve let hot air enter the cylinder and that the outlet valve let hot air go out of the cylinder. New tests have to be carried out with no valves leakage in order to have an accurate evaluation of the wall to air heat transfer effect.

5.4. Indicated power

Fig. 8 shows the experimental indicated power for three inlet temperatures as a function of the rotational speed. It can be seen that there is no influence of the inlet temperature on the indicated power.

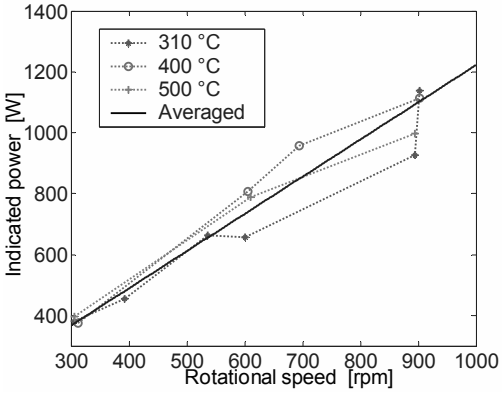

Fig. 8. Indicated power for three inlet temperatures as a function of the rotational speeds.

Superimposed is the indicated power calculated from a constant value of the indicated work. The averaged indicated work calculated from all the experimental results is 73.3 J/cycle. The indicated power calculated from this constant indicated work fits the experimental results, meaning that there is no influence from the temperature nor from the rotational speed on the indicated work, as expected.

The indicated power obtained for a rotational speed of 950 rpm is 1160 W. This result perfectly fits the value of 1142 W expected from the modeling results.

5.5. Shaft power

Fig. 9 presents the experimental shaft power for three inlet temperatures as a function of the rotational speed. Here also it can be seen that there is no influence of the inlet temperature on the shaft

power. An averaged mechanical efficiency has been computed from all the experimental results. The averaged experimental mechanical efficiency value is 0.87, very close to the mechanical efficiency of 0.90 considered in the modeling work.

On Fig. 9 the averaged shaft power calculated from a constant indicated work of 73.3 J/cycle and a constant mechanical efficiency of 87 % is superimposed on the experimental shaft power results. It can bee seen that the average shaft power fits very well the experimental results confirming that the mechanical efficiency as well as the indicated work does not depend on the inlet temperature nor on the rotational speed.

For a rotational speed of 950 rpm the shaft power is 1003 W. This value is to be compared to the expected value of 1028 W.

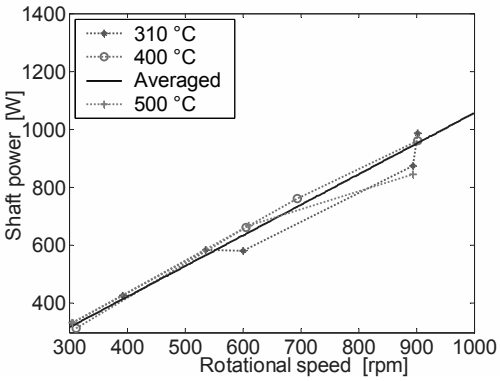

Fig. 9. Shaft power for three inlet temperatures as a function of the rotational speeds.

5.6. Volumetric effectiveness

Fig. 10 presents the volumetric effectiveness for three different inlet temperatures as a function of the rotational speed. The volumetric effectiveness is defined as the ratio of the measured mass flowrate to the mass flowrate which would have been obtained if the cylinder is filled with the working fluid at the inlet pipe thermodynamic conditions at the time of the inlet valve closure.

It can be seen that the volumetric effectiveness does not seem to depend on the inlet temperature but it decreases when the rotational speed increases. The experimental results for the volumetric effectiveness are much higher than expected. This is probably due to the important leaks through the inlet valve as well as through the outlet valve as already mentioned earlier. These leaks have been observed when the prototype is not running, both valves closed, and the inlet line is pressurized.

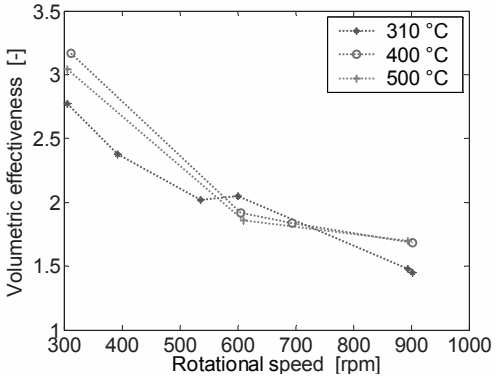

Fig. 10. Volumetric effectiveness for three inlet temperatures as a function of the rotational speeds.

These leaks are due to a bad manufacturing of the valve seats. These seats are made of refractory stainless steel which is hard to machine.

When the prototype is dismantled in order to add the compression piston, the actual expansion cylinder valve seats will be replaced. It is thought that this problem of leaks through the expansion cylinder valve will be easy to solve.

6. Conclusion

A prototype of an expansion cylinder for an Ericsson engine has been designed, built and tested. At the end of the first tests the following conclusions can be drawn:

- The prototype has run correctly during all the tests.
- Tests have not been carried out up to the maximal temperature of 650 °C because of a lack of effectiveness of the water cooling of the cylinder liner. Tests up to 550 °C have not shown any problems. The improvement of the liner cooling will be easy to realize and it is thought that no problem will be met in the future with an inlet temperature of 650 °C.
- The mass flowrate through the prototype is larger than expected. This is probably due to leaks between the valves and their seats. New improved seats will be manufactured.

- Experimental results are perfectly in agreement with modeling results and assumptions for the indicated power, the shaft power and the mechanical power.
- As it was expected, the indicated work and the mechanical efficiency do not depend on the inlet temperature nor the rotational speed.

The tests results have been very encouraging. Therefore it has been decided to dismantle the prototype in order to add the compression piston to allow the test of a complete Ericsson engine.

References

[1] Stouffs, P., 2002, Le moteur Ericsson, un moyen de valorisation de l'énergie thermique à réhabiliter ?, Entropie, 241, pp 26-32.

[2] Finkelstein, Th., and Organ A.J., 2001, *Air engines*, Professional Engineering Publishing Ltd, London.

[3] Kolin, I., 1991, *Stirling motor*, Zagreb Univ. Publications Ltd, Zagreb.

[4] Moss R.W., Roskilly A.P., Nanda S.K., 2005, Reciprocating Joule-cycle engine for domestic CHP systems, Applied Energy, 80, pp. 169-185.

[5] Bell, M. A., and Partridge, T., 2003, Thermodynamic design of a reciprocating Joule cycle engine, Proc. Instn Mech. Engrs, Vol. 217, Part A: J. Power and Energy, pp. 239-246.

[6] Bonnet, S., Alaphilippe, M., Stouffs, P., 2005, Energy, exergy and cost analysis of a micro-cogeneration system based on an Ericsson engine, Int. J. Therm. Sci., 44(12), pp. 1161-1168.

[7] Alaphilippe, M., Stouffs, P., 2008, Instantaneous and yearly electric production of a low power thermodynamic solar energy conversion system: modeling results, *Proceedings of the 21st ECOS*, A. Ziebik, Z. Kolenda, W. Stanek, eds, Cracow-Gliwice, Poland, 3, pp. 1161-1168.

[8] Stouffs, P., 2002, Does the Ericsson engine deserve more consideration than the Stirling engine?, *Proc. European Stirling Forum 2002*, ECOS GmbH, Osnabrück, Germany.

[9] Pehnt, M., et al., 2006, *Micro Cogeneration: Towards Decentralized Energy Systems*, Springer-Verlag Berlin Heidelberg, Germany.

[10] Onovwiona, H.I., and Ugursal, V.I., 2006, Residential cogeneration systems: review of the current technology, Renewable and Sustainable Energy Reviews, 10, pp 389–431.

[11] Thiers, S., Aoun, B., Peuportier, B., 2010, Experimental characterization, modeling and simulation of a wood pellet micro-combined heat and power unit used as a heat source for a residential building, Energy and Buildings, Elsevier, in Press.

[12] Kammerich, B., 2008, Heat and Electricity based on Wood: Short report of a field test with a micro-Stirling engine and a log boiler, *Proc. International Stirling Forum, ISF 2008*, ECOS GmbH, Osnabrück, Germany.

[13] Sicre B., Schüle K., Wapler J., Maurath T., 2008, Development of a wood-fired micro-CHP-system with Stirling engine for residential applications, *International Stirling Forum, ISF 2008*, ECOS GmbH, Osnabrück, Germany.

[14] Stine W.B., Diver R.B., 1994, A Compendium of Solar Dish/Stirling Technology, Rapport SAND93-7026 UC-236, Sandia National Laboratories, Albuquerque; updated versions available at www.grc.nasa.gov.

[15] Bancha Kongtragool, Somchai Wongwises, 2003, A review of solar-powered Stirling engines and low temperature differential Stirling engines, Renewable and Sustainable Energy Reviews, 7, pp.131-134.

[16] Alaphilippe, M., 2007, Recherche d'un nouveau procédé de conversion thermodynamique de l'énergie solaire, en vue de son application à la cogénération de petite puissance, Ph.D. Dissertation, Université de Pau et des Pays de l'Adour, Pau, France.

Acknowledgments: The mechanical design and the manufacturing of the prototype have been realized by Luc DANDO, Consulting Engineer. The authors acknowledge the financial support of France Télécom, the Aquitaine Regional Council and the CNRS (Scientific Research National Council).

Study of Integration of Wind Power with Coal-derived Synthetic Natural Gas System

Jie Feng[a], Jianyun Zhang[a], Weidou Ni[a], Zhen Chen[a] and Zheng Li[a]

[a] *State Key Lab of Power Systems, Department of Thermal Engineering, Tsinghua-BP Clean Energy Center, Tsinghua University, Beijing, China*

Abstract: A new integrated system which combines the coal-derived synthetic natural gas system with off-grid wind power is presented in this paper. In this system, wind power is used to electrolyze water to produce H_2 and O_2. The O_2 is fed to the gasifier as gasification agent. The H_2 is mixed with the syngas to adjust the H_2/CO ratio for methane synthesis. In comparison with the conventional system, the integrated system makes use of off-grid wind power, avoiding impacts to grids and reduces the water-gas shift process, which brings both advantages in the utilization of all raw materials and mitigation of CO_2 emission. Taking a coal-derived synthetic natural gas project and a typical wind power farm in Inner Mongolia for demonstration, the integrated system was designed and analyzed for technical feasibility. The integration improves energy efficiency and decreases CO_2 emission. One key issue is the scale and proportion of H_2 from water electrolysis by wind power and the instability of wind power should not interrupt the chemical process. Results show that 90% of H_2 needed to adjust the H_2/CO ratio should be produced by the conventional process and another 10% of H_2 should be generated from water electrolysis.

Keywords: Coal-derived synthetic natural gas, Off-grid wind power, Water electrolysis, Stability.

1. Introduction

1.1. Demand and problems of synthetic natural gas

The demand of clean energy has increased greatly with the rapid social and economic development in China. Natural gas is becoming more and more important for China's primary energy supply as a kind of cleaner energy compared with coal and oil. The proportion of natural gas in primary energy consumption structure has also risen up obviously in recent years. However, because of the limited domestic conventional natural gas resource and the backward exploration of natural gas, the contradiction between the supply and demand of natural gas is becoming apparent. China's demand for natural gas is estimated to reach 100 billion m^3 in 2010 and the gap between supply and demand will be about 10 billion m^3. By 2020, the demand will exceed 200 billion m^3 and the gap will be 50 billion m^3 [1].

China's coal resource is relatively abundant and the development of modern coal chemical industry has enabled the feasibility of a large-scale production of synthetic natural gas (SNG) from coal. Coal-derived synthetic natural gas (coal-to-SNG) has become an important consideration to fill the gap between the natural gas supply and demand. There are several advantages associated with the coal-to-SNG technical pathway. For example, coal-to-SNG can utilize coal of poor quality such as lignite and SNG could be a major driver for energy security. SNG could diversify energy options and reduce natural gas imports, thus helping to stabilize natural gas prices. SNG can be transported and distributed using existing natural gas infrastructure [2-3]. In summary, coal-to-SNG could be a potential way of comprehensive utilization of China's coal, especially for the coal resource in the remote areas. However, coal-to-SNG also takes the disadvantages of coal chemical industry. It will consume a large amount of coal and water. Moreover, coal-to-SNG emits a significant amount of CO_2 due to the water-gas shift process to adjust H_2/CO ratio. The reason for the CO_2 emission is the lack of H in the coal feedstock compared to a full conversion to CH_4. These problems make coal-to-SNG less competitive in future low-carbon economy. Therefore, the reduction of coal and water consumptions and CO_2 emission is a great issue for the future development of coal-to-SNG.

1.2. Problems of wind power utilization

Renewable energy technologies exhibit a significant growth nowadays in power systems due

Corresponding Author: Weidou Ni, Email: niwd@mail.tsinghua.edu.cn

to limited availability of fossil fuels, ever-increasing fuel prices and growing environmental concerns. Annual installed capacity of wind power increases at a rate of more than 100% in recent years and wind power development has already reached a relatively mature stage compared with other renewable energy technologies [4]. The cost of a wind turbine generator has declined by approximately 90% since the early 1980s. Meanwhile, the cumulative installed capacity of wind power in China is about 12.1 GW by 2008, ranking the fourth largest in the world [5]. More capacity is expected to be added in the near to mid-term future with the strong governmental support in terms of policy and other financial means. For instance, new wind power "Three Gorges" projects, the capacity of each project being about 10 GW, have already been launched in Xinjiang, Inner Mongolia, Gansu and Jiangsu Provinces.

However, the intermittency and power quality of wind power is becoming a major obstacle with the development of concentrated and large-scale wind power for on-grid use. Wind power will cause stability problems to the grids due to the attributes of instability and volatility [6-9]. Figure 1 shows the normalized on-grid electricity of the wind farm in Chifeng of Inner Mongolia in 2008. Compared with the average of 1.0 in the whole year, the peak is more than 3.0 and the trough is less than 0.2. There is a deviation of about 20-30 times from the maximum to the minimum.

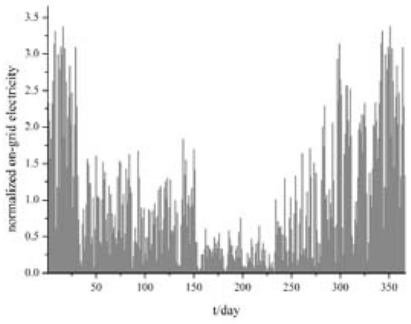

Fig. 1. Wind power in Chifeng, Inner Mongolia, 2008.

In addition, areas with rich wind resources are usually in remote regions in China. The local grid load is usually small and grid structure is relatively weak. Grid connection to large-scale wind power could lead to severe instability problems. These issues greatly increase the difficulties of effective utilization of wind power in China. Moreover, additional spare capacity of fossil power is also required to compensate for the instability caused by the intermittent supply of wind power, leading to higher investment costs [10]. Therefore, the off-grid utilization of wind power is one of the potential ways for future development of wind energy.

1.3. Integration of wind power and the coal-derived synthetic natural gas system

The principle of developing a sustainable energy system is "to put the right things in the right place", making integrated use of various energy resources to construct an optimized energy system according to their specific characteristics [6]. The strategic position of different types of renewable energy in the whole energy system should be carefully defined based on their features and locations. Renewable energy is developing very fast as a substitution for fossil fuels. However, renewable energy cannot take on a large share in primary energy mix at the current stage of development due to technological and economic bottlenecks. It is difficult to solve these problems separately within their specific systems, whilst systems integration provides great potential to tackle these challenges in a systematic way. Considering these facts, one solution is to create systems to utilize primary renewable energy in combination with conventional fossil fuels and integrate advantages of both.

Fortunately, the abundant reserves of coal and wind energy geographically coincide in China, which provides the beneficial conditions for the integration of renewable energy and fossil fuels. Based on the similar ideas with what [6] demonstrated, a new integrated system (the coal-to-SNG system integrated with off-grid wind power) was presented in this paper as an example of energy system integration. The main ideas of the integrated system are as follows: wind power is applied to electrolyze water to produce H_2 and O_2 for the coal-to-SNG system. The H_2 can be mixed with syngas of the coal-to-SNG system to adjust the H_2/CO ratio to an appropriate value for methane synthesis. The addition of H_2 from electrolysis decreases the lack of H_2 in the coal feedstock and thus the CO_2 emission. The O_2 is fed

to the gasifier as gasification agent. The scale of the air separation unit (ASU) can also be reduced.

This paper proposed the conceptual design of the integrated system. Based on a case study in Inner Mongolia, several integrated systems with different scales and proportions of H_2 from water electrolysis were designed and compared with the conventional coal-to-SNG system for coal and water consumptions and CO_2 emission to analyze the effects of different integration parameters on the integrated systems design and performances. Moreover, other related issues which might influence the performance of the integrated system were also studied.

2. Conceptual design of the integrated system

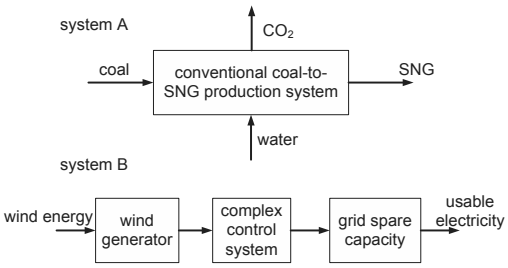

Fig. 2. Conventional coal-to-SNG and wind power systems.

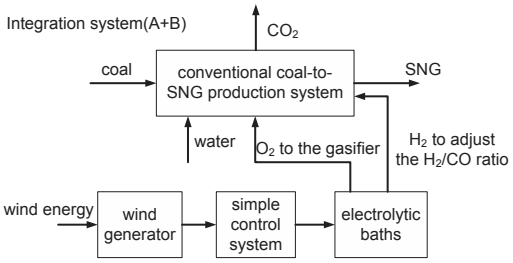

Fig. 3. The integrated system to utilize wind power with coal-to-SNG.

Figure 2 shows the conventional coal-to-SNG system and on-grid wind power system. The integrated system in which wind power is utilized in combination with coal-to-SNG production is shown in Fig. 3. Off-grid wind power can operate with simpler control system and grid spare capacity is not necessary compared with the conventional on-grid wind power.

More details about the conventional coal-to-SNG system are shown in Fig. 4. In the conventional system, only a proportion of carbon in the coal is used for SNG production because the water-gas shift process converts CO and H_2O to H_2 and CO_2 to adjust H_2/CO ratio in the syngas. Much carbon is emitted into the atmosphere in the form of CO_2 consequently. Not all carbon in the coal feedstock is effectively used to produce SNG. The main source of CO_2 emission is the CO_2 separation unit after the shift process.

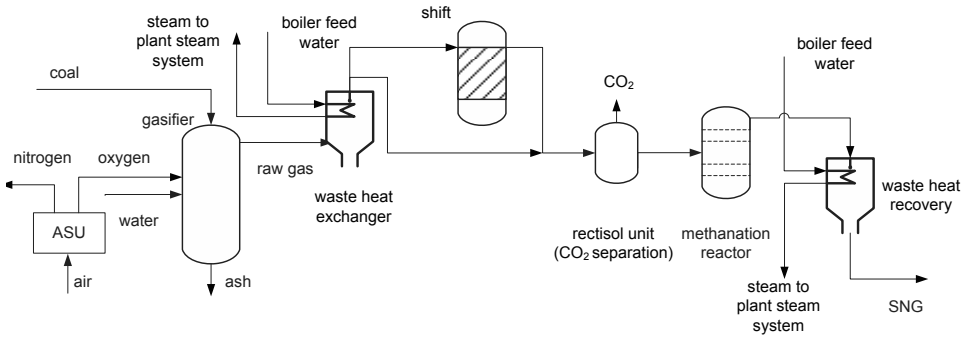

Fig. 4. Schematic representation of the stand-alone coal-to-SNG system.

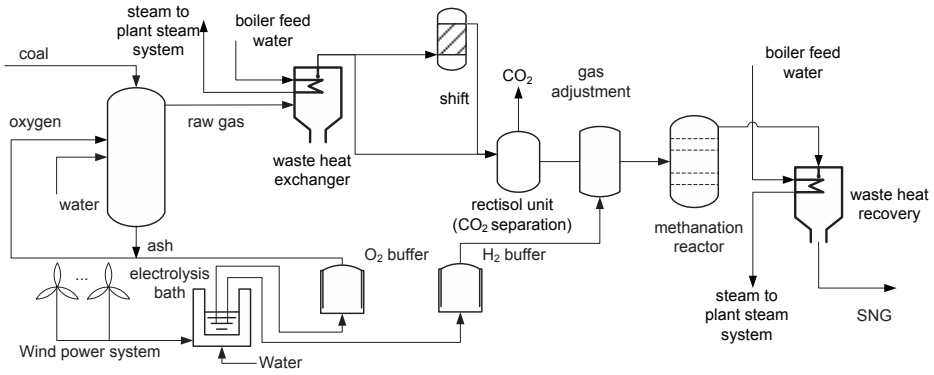

Fig. 5. Schematic representation of the integrated system.

However, in the integrated system shown in Fig. 5, the H_2 from the water electrolysis using wind power is mixed with the syngas to adjust the H_2/CO ratio, which reduces the scale of water-gas shift unit and large CO_2 separation unit. More CO in the syngas is utilized for methane synthesis instead of CO_2 emission. Therefore, more carbon the coal feedstock is converted into SNG and CO_2 emission is reduced, which means that the conversion efficiency of coal-to-SNG is increased. In addition, the O_2 from the water electrolysis can be utilized as gasification agent, so ASU could be partly omitted if there is enough O_2. Because of the instability of wind power, O_2 and H_2 buffers might be needed to balance the intermittency and ensure the relatively stable SNG production.

In comparison with conventional coal-to-SNG system, the proposed system makes use of off-grid wind power, avoiding impacts to grids, and reduces CO_2 emission due to the reduction of the water-gas shift process. This system will be very attractive in the regions of China which have abundant wind and coal resources.

3. Analysis of the integrated system by a case study

Taking a coal-to-SNG project and a typical wind power farm in Inner Mongolia for demonstration, the integrated system was designed and analyzed for technical feasibility. The actual project applies the pressurized fixed-bed gasification of Lurgi as the coal gasification technique.

The integrated system needs a wind power farm and an electrolysis unit. The average of annual operation time of wind generators is 2300 h/a according to the local collecting data. The average power consumption of water electrolysis is 4.5 kWh/Nm^3 H_2 in China. O_2 and H_2 buffers are also designed to balance the fluctuations of wind power using data collected in Chifeng.

One key issue of system design is the scale and proportion of H_2 from water electrolysis by wind power and the integration should not interrupt the production of the chemical process because of the instability of wind power. The H_2/CO ratio in the syngas must be increased to at least 3 for a full conversion of CH_4 before entering the methanation reactor. If all the H_2 produced by the shift process in the conventional system is provided by water electrolysis and the water-gas shift unit is completely omitted, the intermittency of wind power will easily influence the stable operation of the integrated system. When the electrolysis unit cannot provide enough H_2 due to wind power fluctuations, the process for SNG production will be interrupted. For example, during August when wind power supply is very low, H_2 generated by water electrolysis might not be sufficient to adjust the H_2/CO ratio for methane synthesis and the production is hindered. Therefore, the reasonable design would be intermediate choices that water electrolysis only generates a relatively small proportion of H_2 needed to adjust H_2/CO ratio while the left is from the conventional process. The integrated system combines H_2 from the electrolysis and H_2 from the water-gas shift reaction to provide the necessary amount of H_2. For example, 20% of H_2 needed for methane synthesis is from water electrolysis when another 80% is produced by water-gas shift process. Calculation will be carried out in a wide range of

proportions to make a comparison among different integrated systems. Moreover, if there is enough O_2 from electrolysis for gasification, the integrated system will not need ASU for O_2 production. Nevertheless, according to the calculation results, the generated H_2 will greatly exceed the system consumption in such a situation. Considering the difficulties and safety of storing a large quantity of H_2, the modelling and calculations will only concentrate on designs that can use up all H_2 produced from water electrolysis.

Table 1 lists the main material and energy flows for different cases in which the same kind of lignite is used. "Integrated level" is defined as the proportion of H_2 produced by the new integrated system. For example, integrated level of Case 2 is 30%, which means that 30% of H_2 needed is produced by water electrolysis with wind power and 70% of H_2 needed is generated from the conventional process. Case 1 is the results of the stand-alone coal-to-SNG system, while Cases 2, 3 and 4 are integrated systems with different integrated levels.

Table 1. Main material and energy flows of the stand-alone coal-to-SNG system and different integrated systems with the same SNG yield.

Case	1	2	3	4
System	A	A+B	A+B	A+B
Integrated level (%)	0	30	20	10
Proportion of O_2 from electrolysis with respect to total O_2 demand for gasification (%)	0	20.03	13.34	6.67
SNG production (10^9 Nm^3/a)	4.0	4.0	4.0	4.0
Coal consumption (10^9 kg/a)	21.70	20.50	20.89	21.29
Water consumption (10^9 kg/a)	22.81	21.56	21.97	22.38
CO_2 emission (10^9 kg/a)	11.07	10.03	10.36	10.71
Wind power consumption (TWh/a)	0	4.15	2.77	1.39
Energy production of SNG (10^{17} J/a)	1.38	1.38	1.38	1.38
Energy consumption of coal (10^{17} J/a)	3.12	2.95	3.01	3.07
Conversion energy efficiency (%)	44.23	46.78	45.85	44.95

For the same SNG yield of 4.0×10^9 Nm^3/a, the coal consumption of the integrated system decreases by $0.41\sim1.20\times10^9$ kg/a and the water consumption drops by $0.43\sim1.25\times10^9$ kg/a. Compared with the stand-alone system, the CO_2 emission of the integrated system reduces by $0.36\sim1.04\times10^9$ kg/a. The share of O_2 from electrolysis with respect to total O_2 demand for gasification is 6.67~20.03%, thus the scale and investment of ASU are reduced.

The conversion energy efficiency is defined as the ratio of the energy consumption of coal to the energy production of SNG. As listed in Table 1, the energy efficiency of the integrated system increases with the integration while the CO_2 emission goes down. For example, the conversion energy efficiency increases by 2.55% when the integrated level is 30%. The results show that the integration helps to improve the conversion energy efficiency.

The coal and water consumptions decrease as the integrated level increases. CO_2 emission also decreases with the integrated level. Higher integrated level means larger proportion of H_2 from water electrolysis, thus less syngas would go through the shift process to adjust the H_2/CO ratio. As more carbon is used for production and less water vapor is needed for the shift process, the integrated system consumes less coal and water when integrated level is higher. The CO_2 emission could be reduced more obviously with higher integrated level. However, high integrated level could allow the intermittency of wind power to easily influence the operation of the integrated system, so the integrated level should be limited to ensure stability of the integrated system. Further consideration would be discussed in the next section.

According to the modelling and calculations listed in Table 1, the reduction of coal and water consumption is not so obvious and CO_2 emission only decreases by about 3~10% compared with the stand-alone coal-to-SNG system. It is because the H_2/CO ratio is relatively high in the raw gas produced by the Lurgi gasfiers used in the cases and the integrated level is low. If other gasification technology for SNG is applied, such as Gaskombiant Schwarze Pumpe (GSP) gasifiers which can be applied to lignite as well, the reduction of energy consumption and CO_2 emission will be much remarkable. Suppose that

GSP gasfiers were used in the system, the coal and water consumption for the same SNG yield could decrease by 31.2% and 20.4%, respectively when the integrated level is 20%. Furthermore, CO_2 emission can be reduced by 19.8% in the integrated system compared with the stand-alone coal-to-SNG system.

In addition, the integrated system comprehensively utilizes large-scale and off-grid wind power effectively to avoid problems of impacts to grids. One of the most important values for the integration system is that the integration can support the development of wind power in China. The integration system has showed the integration advantages not only in energy utilization and environmental impact but also in a comprehensive way of using wind power.

4. Further discussion of the system integration

4.1. Feasibility of using wind power for water electrolysis and integration

According to the investigations into the manufacturer of electrolytic baths and the results of [7], the operation of electrolytic baths does not require a stable electricity supply. Variations of the current density in a wide range have almost no effect on the current efficiency and the voltage fluctuations in production process only influence the productivity, not the quality of the product or the regular facility operation. The electrolysis technology and wind power supply could match perfectly. Even if large fluctuations occur, the controlling system of electrolytic baths can operate in time and ensure the operating security. Therefore, wind power can be utilized to generate H_2 in a large scale through water electrolysis.

Furthermore, the outlet pressure of the H_2 and O_2 from water electrolysis can be easily controlled to coordinate with that of downstream. The outlet purities of gases are 99.8% for H_2 and 99.3% for O_2 while the impurities are mainly water vapour. Because the syngas is a kind of mixed gas with water vapour, the mixture of the H_2 from electrolysis and the syngas is feasible.

4.2. Stability of the integrated system

The operation stability is a great issue in the integrated system due to the instability of wind power. The intermittency of wind power should be balanced well in the integrated system. When the wind power cannot provide sufficient electricity for electrolysis, using the grid electricity to compensate for the wind power is possible but not so wise because such a choice might greatly bring down the system economics due to the cost for purchasing electricity from the grids. Another method, as proposed above, would be the application of tanks as buffers. Table 2 shows results of unit changes of the stand-alone system and different integrated system if buffers are applied.

Table 2. Unit changes of the stand-alone coal-to-SNG system and different integrated systems.

Case	1	2	3	4
System	A	A+B	A+B	A+B
Integrated level (%)	0	30	20	10
Total scale of electrolytic baths (10^4 Nm^3 H_2/h)	0	11.54	7.70	3.85
Total area of electrolytic baths (10^3 m^2)	0	88.17	58.83	29.41
Total scale of H_2 buffers (10^4 Nm^3)	0	252.9	168.8	84.31
Total scale of O_2 buffers (10^4 Nm^3)	0	126.5	84.38	42.16
Installed capacity of wind power (GW)	0	1.807	1.201	0.602

The total scale of H_2 and O_2 buffers is very large as listed in Table 2. Such a huge store of H_2 is very dangerous and expensive, thus the safety and economics of the integrated system may not be guaranteed. The recommended ways to ensure the stability of SNG production are to control the integrated level and enlarge the design load of water-gas shift unit. To control the integrated level means that the proportion of H_2 from water electrolysis should be limited and most of H_2 is still produced by the conventional process. Considering that coal chemical system can work properly when the load is 90~110% of normal capacity, 10% of H_2 generated by water electrolysis is acceptable theoretically. If the integrated level is 10%, the integrated system can operate continuously in the range of 90~110% of normal capacity even without any wind power supply. More optimization work is needed to decide the integrated level considering not only the whole system but also different units. Another suggestion is to enlarge the design load of water-

gas shift unit. When the amount of H_2 from electrolysis is not enough, the shift unit can operate in a larger load to produce enough H_2 to adjust the H_2/CO ratio. The proportion of O_2 from electrolysis with respect to total O_2 demand for gasification is only 6.67% when the integrated level is 10% as listed in Table 1 and the design load of ASU decreases little. Considering that ASU can also operate continuously in the range of 90~110% of normal capacity, O_2 buffers are not needed when the integrated level is 10%.

4.3. Arrangement of the electrolysis unit

In the case study, there are about several hundred kilometers between the wind farm and the coal-to-SNG plant. The electrolytic baths can be built near the wind farm or near the coal-to-SNG plant. The pipelines for gas (H_2 and O_2) transportation will be very complex and a long distance for transportation of H_2 is also quite expensive and dangerous. Therefore, a better choice would be that electrolytic baths are built near the coal-to-SNG plant and electricity from the wind farm is transmitted. The electricity wires are relatively easy to be set and electricity transmission helps to avoid the transportation of H_2. The electrolysis unit should be arranged near the wind farm to guarantee the safety and economic of the integrated system.

4.4. Preliminary economic analysis

Whether a new system can be accepted and applied in practice in the future mostly relies on whether the system can bring economic benefit. On-grid wind power units must have more complicated control systems and the optimized kinetic characteristics of wind turbines must be sacrificed as well. According to estimation, off-grid wind power application can simplify the equipments and reduce the cost of wind power units by 20~30% [10]. Furthermore, the size of ASU and the water gas shift unit could be reduced to some extent. However, an electrolysis unit should be added in the integrated system.

The integrated system yields SNG and other relevant byproducts such as sulfur and naphtha. The analyses show that the integrated system with 10% integrated level is the most reliable. The data of equipment investment is from [11-12]. The sensitivity of the SNG cost with the coal price is shown in Fig. 6.

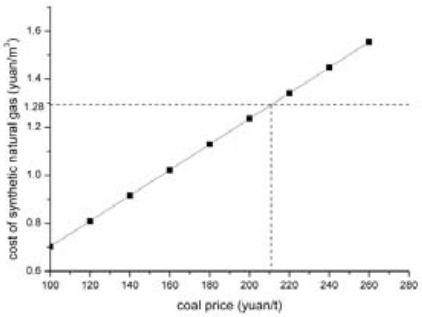

Fig. 6. Sensitivity of the SNG cost with the coal price.

The cost of SNG decreases significantly with the price of lignite. The present city-gate price of natural gas is 1.28 yuan/m^3 in Beijing and the annual average price of lignite in 2009 was about 170~180 yuan/t in China. Therefore, the integrated system is economic beneficial at present and it is still competitive even if the price of lignite reaches 200 yuan/t.

5. Conclusions

1) As renewable energy is developing rapidly in China, their strategic position in the sustainable energy system should be carefully considered and defined according to different features and locations. The utilization of renewable energy in combination with fossil fuels is one of the potential ways. The integrated system presented in the paper is a remarkable example that could be applied in remote areas where the abundant reserves of coal and wind geographically coincide. In this way, the integration can provide “win-win” condition for both wind power and coal chemical industry.

2) The integrated system successfully uses a large scale of wind power in an off-gird way and makes wind power more competitive because the investment of off-grid wind generator is reduced.

3) Most of the carbon in the coal, including the H_2 and O_2 from water electrolysis, are converted into SNG, thus the influence on the environment would be minimal. The coal and water consumptions decrease due to effective utilization of all raw materials. Most of the technologies in this integrated system are mature and have been widely used in the industry.

4) Considering the technical feasibility, especially the instability of wind power, the results

show that 10% integration is the most rational for stable operation of chemical process. That is, about 90% of H_2 needed to adjust the H_2/CO ratio should be produced by the conventional process and 10% of H_2 needed should be generated from water electrolysis using wind power. The integrated system is also economically competitive currently.

References

[1] Liu, Z. G., et al., 2009, SNG Development in China, Coal Chemical Industry, 2(4), pp. 1-5.

[2] Bu, X. P., et al., 2007, Analysis of Coal Gasification/Poly-generation to Produce Substitute Natural Gas (SNG), Coal Chemical Industry, 6, pp. 1-7.

[3] Zhao, G. W., et al., 2009, Analysis and Discussion of Process Coal Based Synthetic Natural Gas and the Factors Effecting the Catalysts, Ceramics, 11, pp. 21-25

[4] European Wind Energy Conference, *Wind Power 12: Blueprint for Wind Power Sharing 12% of Total Worldwide Power by 2020*, China Environment Press, Beijing, China.

[5] Recknagel, P., 2004, Wind Power in China 2008: an Analysis of the Status Quo and Perspectives for Development. Ph.D. Dissertation, University of Applied Sciences Konstanz, Konstanz, Germany.

[6] Ni, W. D., et al., 2009, How to Make the Production of Methanol/DME "GREENER", Frontiers of Energy and Power Engineering in China, 3(1), pp. 94-98.

[7] Burton, T., et al., 2005, *Wind Energy Handbook*, John Wiley & Sons Ltd, New Jersey, US.

[8] Thakur, D. and Mithulananthan, N., 2009, Influence of Constant Speed Wind Turbine Generator on Power System Oscillation, Electric Power Components and Systems, 37(5), pp. 478-494.

[9] Faried, S., et al., 2009, Probabilistic Evaluation of Transient Stability of a Wind Farm, IEEE Transactions on Energy Conversion, 24(3), pp. 733-739.

[10] Gu, W. D., 2006, *New Strategy for the Development of the Wind Power Industry in China and the Wind Power Non-grid-connection Theory*. Chemical Industry Press, Beijing, China.

[11] Deng, Y., 1987, *Pressured Gasification of Coal*. China Architecture Press, Beijing, China.

[12] Wang, M. H., et al., 2008, Technical and Economic Analysis on Pithead Coal to Substitute Natural Gas System and Its Developing Routine in China, Modern Chemical Industry, 28(3), pp. 13-16.

Risks Associated with Increasing the Harvest Area for the Production of Brazilian Ethanol Fuel

Cristina Mariaca[a] *and Noam Lior*[b]

[a] *The Joseph H. Lauder Institute of Management & International Studies*
University of Pennsylvania, Philadelphia, USA
[b] *Department of Mechanical Engineering and Applied Mechanics*
University of Pennsylvania, Philadelphia, USA

Abstract: This analysis aims to evaluate the environmental and economic risks associated with the Brazilian government's commitment to support tripling ethanol exports by 2014 and fostering growth in the industry. The study finds that growth in Brazilian ethanol production is very likely to result in the growth of the land area used for sugarcane harvest. We identify three significant risks that can be expected as a result, and that would be highly counter-productive to Brazil's sustainable development. First, land used for sugarcane harvest for ethanol production in the Amazon grew 5% between the 06/07 and 07/08 harvests, and continued growth could lead to a direct negative impact on the rainforest. Second, an evaluation of the growth in harvested land for Brazil's ten key food crops shows that the land used for all food crops except those used for fuel is decreasing, while the land used for fuel crops is increasing. This indicates that fuel crops may be displacing food crops, which could lead to a decrease in the food supply and increase in prices. Third, several studies have linked the change of land-use to severe environmental impacts. While the government argues that there are more than 100 million hectares of degraded pastures that are currently unused and could be utilized for sugarcane, research suggests that the change in land-use causes erosion of up to 30 tons of soil per hectare per year, a loss of soil organic carbon and high levels of GHG emissions. Based on these findings, we recommend changes in policy that focus on two objectives: 1) better management of land use, and 2) better support for other renewable sources. For the first point, a sustainability analysis is needed in order to identify the regions where sugarcane harvest area should or should not increase. Legislation should deter growth in those areas where conversion to sugarcane is not sustainable, and to minimize harmful environmental effects in the areas where land would be converted for sugarcane harvest. On the second point, policy should be centered on providing continuous incentives for diversification in the country's fuel supply, fomenting growth in more innovative methods to generate power, and partnering with other countries to continue to promote a steep learning curve in the field of biofuels.

Keywords: Ethanol; Sugarcane; Biofuels.

1. Introduction

This analysis aims to evaluate the environmental risks associated with the Brazilian government's commitment to supporting growth in ethanol supply and tripling ethanol exports by 2014. We conducted an analysis of Brazilian government data and academic research and found three environmental threats that could result from a further increase in the land area used for sugarcane harvest. First, land used for sugarcane harvest for ethanol production in the Amazon region has been growing at a rate of 5%, as evidenced by government data on the 06/07 and 07/08 harvests. Continued growth could lead to a direct negative impact on the rainforest. Second, an evaluation of the growth in harvested land for Brazil's ten key food crops shows that the land area for all food crops except those used for fuel is decreasing (Table 6), while the land area for fuel crops is increasing. This indicates that fuel crops may be displacing food crops, which could lead to a decrease in the food supply and increase in prices. Furthermore, growth in land used for sugarcane creates an indirect threat to the rainforest, since there is an incentive to use that land to raise cattle or harvest crops that would have alternatively been harvested in land used for sugarcane. Third, we present several studies that have linked the change of land-use to severe environmental impacts. While the government argues that there are more than 100 million hectares of degraded pastures that are currently unused and could be utilized for sugarcane, research suggests that land-use change causes erosion of up to 30 tons of soil per hectare per year, a significant loss of soil organic carbon and high levels of GHG emissions that last over several decades.

Based on these findings, this study concludes that current aggressive growth targets for ethanol production could be detrimental to the environment and the food supply.

2. Brazilian Ethanol Export Forecast

Brazilian President Luiz Inacio Lula da Silva has consistently promoted the country's ethanol industry since taking office in 2003, and has recently supported trade agreements with Asia and Europe to foment ethanol exports [1-2]. In 2007, Brazil's Agriculture Minister Luis Carlos Guedes Pinto announced the government's objective of raising investments of $13.4 billion to boost the country's current ethanol output and triple ethanol exports by 2014 [3]. During the first meeting between President Lula and President Obama in March 2009, their conversation turned to the topic of ethanol trade between the two countries [2]. President Obama acknowledged that the US$0.54 tariff per gallon of Brazilian ethanol levied by the US is a "source of tension" [2] between the two countries, while President Lula expressed a great interest in increasing Brazilian ethanol exports to the US as a lever for the country's and the ethanol industry's development.

Furthermore, several countries have recently expressed interest in biofuel conversion. In 2005, the EU started to require that gasoline be blended with 2% of ethanol, with the blend increasing to 5.75% by 2010 [4]. Sweden, which has been importing Brazilian ethanol for years, now offers consumers a 20% tax break in the purchase of FlexFuel cars, as well as other incentives such as parking privileges for environmentally friendly vehicles [4]. In Japan, new laws will require a 3% ethanol blend in fuels and the country has been negotiating a trade deal to boost imports of Brazilian ethanol during much of the past decade [4]. China, where E10 blends are mandated in some provinces [5-6], has also been negotiating ethanol trade with Brazil [4]. Though the country is starting to develop its own ethanol production facilities, growth is very much controlled by the government. Government subsidies maintain gas prices low, and there is a general fear of the impact on food prices that would result from high levels of production of biofuels, and thus Chinese domestic production of ethanol is still very low [7].

In the following tables, we present data collected from [8] in an effort to present the tons of sugarcane produced by the top 20 sugar markets in the world, as well as the harvested area and tons of sugarcane produced per hectare in each market. From the data in Table 1 we see that Brazil yields almost twice as much sugar as the second largest producer, or about 36% of the production by the top 20 supplying countries.

Table 1. Sugarcane Producers, 2006.

	2006 Production Quatity (tons)	2006 Area Harvested (ha)	Tons/ha
1 Brazil	457,245,516	6,144,286	74
2 India	281,171,800	4,201,100	67
3 China	100,435,041	1,215,300	83
4 Mexico	50,675,820	679,936	75
5 Thailand	47,658,097	965,333	49
6 Pakistan	44,665,500	907,300	49
7 Colombia	39,000,000	420,000	93
8 Australia	38,169,000	415,000	92
9 United States	27,033,200	367,780	74
10 Indonesia	25,200,000	350,000	72
11 Philippines	24,345,106	392,280	62
12 South Africa	20,275,430	420,000	48
13 Argentina	19,000,000	285,000	67
14 Guatemala	18,721,415	233,334	80
15 Egypt	16,000,000	135,000	119
16 Viet Nam	15,678,600	285,100	55
17 Cuba	11,060,000	397,100	28
18 Venezuela	9,322,937	123,470	76
19 Sudan	7,500,000	72,000	104
20 Myanmar	7,300,000	140,000	52

Source: Authors; data extracted from [8]

Table 2. Ethanol Producers, 2006.

Country or Area	2006 Production (1000 Metric tons)	2006 Imports (1000 Metric tons)	2006 Exports (1000 Metric tons)
United States	15,077	2,192	0
Brazil	14,229	0	2,760
Germany	870	15	4
Sweden	349	0	0
France incl. Monaco	235	0	0
Colombia	196	0	0
Canada	184	40	21
Spain	179	0	0
Poland	119	2	33
Netherlands	106	342	0
Austria	73	0	0
Cuba	58	0	0
Australia	41	0	0
Belgium	33	33	0
Hungary	19	0	0
Lithuania	10	3	4
Bulgaria	9	0	0
Paraguay	7	0	0
Latvia	5	0	3
Ireland	3	0	0

Source: Authors; data extracted from [8]

Table 2 presents the top 20 countries that produce ethanol, as well as their exports and imports. As shown, Brazil and the US are the only two

countries that produce significant amounts of ethanol. Furthermore, while all of the US production is consumed domestically, the country also imports additional ethanol (from Brazil) to meet its needs. Brazil, on the other hand, is the only country that is exporting significant amounts of ethanol. As other countries that lack the resources to produce biofuels establish regulation to foment the use of ethanol, there is an incentive for Brazil to increase its ethanol exports.

Given thus that Brazil will now face a strong incentive to increase its ethanol production capacity, it is important to note that growth in supply can be achieved in two ways: use of more land to harvest more sugarcane, or increase in efficiency of production per hectare of land.

Table 3 presents historical growth rates for ethanol production in Brazil. From 1990 to 2005, the compounded annual growth rate (CAGR) in ethanol (alcohol) production was 2.2%, most of which came through the use of more land area to harvest more sugar (2.1% CAGR for harvested land versus 0.1% CAGR for productivity in terms of metric tons per hectare). As will be further presented in Section 3.1 and Table 4, between the 06/07 and 07/08 sugarcane harvests in Brazil, the increase in sugarcane harvest area was 7.4%. Even though, as shown in Table 3, there have been productivity improvements in terms of metric tons of sugarcane per hectare of harvest land, growth in ethanol supply has always been derived from an increase in the area of sugarcane harvest land.

The high interest from other countries in importing Brazilian ethanol and the Brazilian government's commitment to support high growth in supply, provide a clear incentive for Brazilian farmers and ethanol producers to maintain high production objectives. As the key industry players face high incentives to increase production, there will be pressure to continue to increase the area of land used for harvesting sugarcane for ethanol production. In Section 3 we evaluate current trends in the use of ethanol land area and attempt to quantify the three key threats associated with increasing the land area used for sugarcane harvest: 1) deforestation in the Amazon, 2) displacement of food crops, and 3) erosion of soil. Our objective is to bring awareness to these threats in an effort to encourage policy-makers to enforce legislation that will curtail growth in sugarcane land area and foster safe agriculture.

Table 3. Ethanol Productivity in Brazil, 1990-2005.

	Historical Ethanol Productivity				
	1990	2000	2005	*90-05 CAGR*	*00-05 CAGR*
Tot Area (mill ha)	845.9	845.9	845.9		
Area for Arable and Permanent Crops (mill ha)	57.4	65.2	66.6		
Ethanol Area Harvested (mill Ha)	4.3	4.8	5.8	*2.1%*	*3.7%*
% Ethanol Area Harvested / Tot Arable	*7.4%*	*7.4%*	*8.7%*		
Alcohol - production (metric tons, mill)	9.3	8.6	12.8	*2.2%*	*8.4%*
Metric Ton / Ha	2.2	1.8	2.2	*0.1%*	*4.6%*
Density ethanol (g/mL) (1)	0.8				
L / Ha	2,759.6	2,237.5	2,800.8		
Liters per year (billion)	11.8	10.8	16.3	*2.2%*	*8.4%*

Notes: CAGR refers to Compounded Annual Growth Rate; Tot refers to total; mill ha refers to millions of hectares.
Sources:
Authors, except where noted. Data extracted from [8].
(1) [10]

3. Environmental Risks

The Brazilian government's commitment to ethanol production could be met under two scenarios: 1) productivity would increase at an annual rate of 9.3% from 2005 to 2018; or 2) Brazil's sugarcane harvested land area would increase, either in unused land or in land that could

otherwise be used for other crops, cattle-raising, rain forests, or reforestation. As discussed in Section 2, the underlying productivity improvement assumptions in the government's supply commitment is aggressive if compared to historical productivity improvement rates. For the supply target to be met, more harvest land would probably be needed. This section will quantify the environmental threat of expansion in the sugarcane harvested land area in an effort to raise awareness to this issue.

According to Brazil's President Lula, the Brazilian Sugarcane Association [12] and the former Minister of Agriculture Roberto Rodrigues [5-6], sugarcane expansion in Brazil is taking place in degraded pastures in the Center-South of the country and the use of this land does not displace other crops because it is land that is not currently being used. Reference [5-6] argues that, of the approximately 850 million hectares of land in Brazil, about 106 million hectares of land are not being exploited and thus concludes that sugarcane, which currently uses about 6 million hectares of land [8], still has plenty of room for growth.

As will be explained in detail in this section, data from the Brazilian government shows that there are irregularities in these arguments for three reasons:

1. The area used for growing sugarcane in the Amazon is increasing, and this will be quantified in section 3.1;
2. Sugarcane is replacing other crops and growing in territory once used for the agriculture of important food crops, as will be quantified in detail in section 3.2; and
3. There are negative environmental impacts of harvesting sugarcane, such as a deterioration of soil and water supplies and higher GHG emissions. Even if growth were to be concentrated in the unused lands referred to by [5-6], using more land for sugarcane agriculture could threaten the environment. This point will be analyzed in section 3.3.

3.1 Sugarcane in the Amazon

Folha de São Paulo, one of Brazil's largest newspapers, has reported that large ethanol conglomerates have been lobbying the government to allow them to buy large areas of land around the Pantanal, a biologically diverse area of tropical wetlands in western Brazil [9]. In the Amazon region, growth in land area used for ethanol production is already a reality. To quantify this threat, we evaluated sugarcane harvest data from the Brazilian government, part of a frequent series of surveys conducted by CONAB (National Supply Company), a public entity linked to the Ministry of Agriculture, Livestock and Supply and part of Brazil's federal government [14]. In its first survey on the 2007/2008 harvest, conducted between April 29th, 2007 and May 12th, 2007, 40 CONAB employees visited 398 businesses related to sugar production and ethanol distillation across all of Brazil, which include all of the businesses related to ethanol production in the country [14]. Each of these businesses completed a survey and provided key production metrics.

The CONAB data shows that in the 2007/2008 sugarcane harvest there were almost 21 thousand hectares of land within the Amazon basin (i.e., within the North region of Brazil) used for sugarcane agriculture, an increase of 5% compared to the 2006/2007 harvest. Furthermore, during the 2007/2008 harvest there were 271 thousand acres of land dedicated to sugarcane agriculture within the states of Maranhão and Mato Grosso, where large areas of rainforest exist, an increase of over 8% compared to the 2006/2007 harvest. The growth within these two states is larger than the national average growth of 7.4% and the growth in the state of São Paulo (+5%), where most sugarcane agriculture takes place.

Within the presented tables, we calculated the share of total land used for sugarcane agriculture within each of the selected states. While the land area used for sugarcane in the Amazon basin is still small, it is growing. It now adds up to more than 0.3% of the total harvested land in the country.

Below the Harvest Area table, we also present tables on Production (in thousands tons of sugarcane) and Productivity (kg of sugarcane per hectare). The key takeaway from this part of the analysis is that productivity levels in the North are low (56,000-70,000 kg/ha vs. national average of 77,000 kg/ha) and improving only slowly (0-2% improvement across the North vs. 3.5% average). The land used in the Amazon basin is being used inefficiently, and it could be used for better purposes such as for planting food crops to nourish the region.

Table 4. Historical trend in land allocation and ethanol production in selected states of Brazil, 1990-2007.

			Harvested area (1000 ha)				
Region	State	Abbrev.	06/07 Harvest	*06/07 %/TOT.*	07/08 Harvest	*07/08 %/TOT.*	*Y/Y VAR.%*
	Amazonia	AM	4.8	*0.1%*	5.2	*0.1%*	*8.3%*
	Pará	PA	10.5	*0.2%*	10.5	*0.2%*	*0.0%*
	Tocantins	TO	4.5	*0.1%*	5.1	*0.1%*	*13.3%*
NORTH			**19.8**	*0.3%*	**20.8**	*0.3%*	*5.1%*
	Maranhão	MA	40.3	*0.7%*	40.3	*0.6%*	*0.0%*
NORTHEAST			**1,123.4**	*18.2%*	**1,138.3**	*17.2%*	*1.3%*
	Mato Grosso	MT	209.7	*3.4%*	230.7	*3.5%*	*10.0%*
CENTRAL WEST			**604.5**	*9.8%*	**698.9**	*10.6%*	*15.6%*
	São Paulo	SP	3,288.2	*53.4%*	3,452.6	*52.2%*	*5.0%*
SOUTHEAST			**3,928.2**	*63.7%*	**4,164.5**	*62.9%*	*6.0%*
SOUTH			**487.3**	*7.9%*	**597.6**	*9.0%*	*22.6%*
BRAZIL			**6,163.2**	*100.0%*	**6,620.1**	*100.0%*	*7.4%*

			Production (1000 tonnes)					Productivity (kg/ha)			
Region	State	Abbrev.	06/07 Harvest	*06/07 %/TOT.*	07/08 Harvest	*07/08 %/TOT.*	*Y/Y VAR.%*	06/07 Harvest	07/08 Harvest	*Y/Y VAR.%*	*% Ethanol/ TOT Sugarcane*
	Amazonia	AM	273.1	*0.1%*	303.0	*0.1%*	*10.9%*	56,900.0	58,500.0	*2.8%*	*45.0%*
	Pará	PA	736.7	*0.2%*	736.7	*0.1%*	*0.0%*	70,160.0	70,160.0	*0.0%*	*57.1%*
	Tocantins	TO	252.1	*0.1%*	291.1	*0.1%*	*15.5%*	56,030.0	57,200.0	*2.1%*	*100.0%*
NORTH			**1,261.9**	*0.3%*	**1,330.8**	*0.3%*	*5.5%*	**63,732.0**	**64,073.0**	*0.5%*	***63.3%***
	Maranhão	MA	2,341.4	*0.5%*	2,341.4	*0.4%*	*0.0%*	58,100.0	58,100.0	*0.0%*	*92.2%*
NORTHEAST			**62,860.3**	*13.2%*	**65,011.4**	*12.3%*	*3.4%*	**55,954.0**	**57,112.0**	*2.1%*	***41.5%***
	Mato Grosso	MT	14,073.6	*3.0%*	15,642.1	*3.0%*	*11.1%*	67,100.0	67,800.0	*1.0%*	*76.3%*
CENTRAL WEST			**45,473.0**	*9.6%*	**53,544.2**	*10.1%*	*17.7%*	**75,219.0**	**76,610.0**	*1.8%*	***70.2%***
	São Paulo	SP	284,825.6	*60.0%*	309,010.4	*58.5%*	*8.5%*	86,620.0	89,500.0	*3.3%*	*57.7%*
SOUTHEAST			**329,204.2**	*69.3%*	**360,948.2**	*68.4%*	*9.6%*	**83,806.0**	**86,673.0**	*3.4%*	***57.4%***
SOUTH			**36,001.0**	*7.6%*	**47,142.0**	*8.9%*	*30.9%*	**73,879.0**	**78,886.0**	*6.8%*	***56.3%***
BRAZIL			**474,800.4**	*100.0%*	**527,976.6**	*100.0%*	*11.2%*	**77,038.0**	**79,754.0**	*3.5%*	***56.9%***

Source: Authors; 06/07 and 07/08 data extracted from [14].

Also shown in the Tables, in the bottom right column, is our calculation of the share of tons of sugarcane production that is used to supply sugar specifically to the ethanol industry. Not all growth in the sugarcane harvested area is due to growing demand for ethanol but, as the data shows, harvests in the Amazon basin are mainly supplying sugar for ethanol production. This data was also extracted from [14], but from a different survey. This data was presented in the third survey carried out and pertains to information solely on the 2008 harvest. This recent survey does not provide productivity or harvested area information, but does break down production tons into those used for sugar versus ethanol. It is interesting to note that many surveys, such as those from UNICA, state that about 50% of Brazilian sugar is used by the ethanol industry [11-13], while this recent survey from CONAB presents a significantly higher share of 56%. Furthermore, the average in the North region is even higher at 63%; the state of Maranhão is at 92% and Mato Grosso at 76%. Clearly, it is the ethanol industry that is driving the growing use of the Amazon for sugarcane harvest.

It is important to note that the tables following the map present data only for selected states of Brazil to highlight those in the Amazon basin as well as the state with the highest production of ethanol (São Paulo). Other states are not included in the table, but are included in the totals provided for each region of Brazil. Therefore, the sum of each region cannot be obtained by summing the few states presented. Information for all states can be found in the CONAB 2008 report.

There are important caveats regarding this data. Since the data collected by CONAB is provided by the ethanol manufacturers, there is always a doubt as to the validity of the data.

Furthermore, one could argue that the growth in sugarcane harvested area in the Amazon is not causing deforestation, because it could be taking place in land that had already been cleared for other agriculture or for raising livestock. As a counterargument, though it would be much harder

to prove, is the fact that if more and more land that had already been cleared is being used for sugarcane, then it is limiting the use of that land for other resources. Indirectly, this could eventually lead to further deforestation.

We do not suggest that sugarcane and ethanol growth in the Amazon is high, but to show that it is significant. The few inefficient sugarcane plants in the Amazon should be monitored by regulators to deter further growth. Not only would further growth result in deforestation in areas of rich biodiversity, but also reduce earth's carbon dioxide absorption capacity as the forest is replaced by other crops.

It is important to compare at this point the harvested land area growth rate of 7.4% reported by [14]. This growth rate reinforces the assumption we make in Section 2 that growth in ethanol supply will come from growth in the area of land used for sugarcane harvest, and not only from productivity improvements. The Brazilian government's commitments to triple ethanol exports by 2014 and support high growth in production will lead to further growth in the area of land used for sugarcane harvest. In Section 3.2 we continue to quantify the risks of growth in land area used for ethanol production.

3.2 Land displacement

Data from [8] presented in Table 5 shows that growth in sugarcane harvested land is a highly-threatening issue at the national level. The authors collected data from [8] on harvested land area for forests, all food crops, and total arable land. As shown, from 1990 to 2005 the proportion of Brazilian land covered by forest has fallen from 61% to 56%, or more than 42 million hectares. During this same time period, there was a growth in the area for arable and permanent crops of about 9 million hectares, meaning that land that was previously used for other purposes (forests, cattle, etc) is now being used for harvesting crops.

In further analysis of this data from [8], we discovered that even though there was an increase in the country's total arable land, the land area used for almost every one of Brazil's key food crops decreased. The only three food crops for which harvested area increased were the three crops related to biofuel production – soybean, sugarcane, and maize.

Table 5. Historical trend in land allocation in Brazil, 1990-2007.

	1990	2000	2005	2006	2007	2005/1990 CAGR%
Land Area (1000 ha)	845,942	845,942	845,942	845,942	845,942	
Land covered by forest (1000 ha)	520,027	493,213	477,698	n.a.	n.a.	*-0.6%*
% Forest / Land area	*61%*	*58%*	*56%*	*n.a.*	*n.a.*	
Area for Arable and Permanent Crops (1000 ha)	57,408	65,200	66,600	n.a.	n.a.	***1.0%***
% Arable and crop / Land area	*7%*	*8%*	*8%*	*n.a.*	*n.a.*	
Soybeans area harvested (1000 ha)	11,487	13,640	22,949	22,047	20,638	***4.7%***
% Soybean / arable and crop area	*20%*	*21%*	*34%*	*n.a.*	*n.a.*	
Sugarcane area harvested (1000 ha)	4,273	4,846	5,806	6,144	6,712	***2.1%***
% Sugarcane / arable and crop area	*7%*	*7%*	*9%*	*n.a.*	*n.a.*	
Maize area harvested (1000 ha)	11,394	11,615	11,549	12,613	13,828	***0.1%***
% Maize / arable and crop area	*20%*	*18%*	*17%*	*n.a.*	*n.a.*	
Beans, dry area harvested (1000 ha)	4,680	4,332	3,749	4,034	3,907	*-1.5%*
% Beans / arable and crop area	*8%*	*7%*	*6%*	*n.a.*	*n.a.*	
Rice, paddy area harvested (1000 ha)	3,947	3,655	3,916	2,971	2,901	*-0.1%*
% Rice / arable and crop area	*7%*	*6%*	*6%*	*n.a.*	*n.a.*	
Coffee, green area harvested (1000 ha)	2,909	2,268	2,326	2,312	2,284	*-1.5%*
% Coffee / arable and crop area	*5%*	*3%*	*3%*	*n.a.*	*n.a.*	
Cassava area harvested (1000 ha)	1,938	1,722	1,902	1,897	1,945	*-0.1%*
% Cassava / arable and crop area	*3%*	*3%*	*3%*	*n.a.*	*n.a.*	
Wheat area harvested (1000 ha)	2,681	1,066	2,361	1,560	1,818	*-0.8%*
% Wheat / arable and crop area	*5%*	*2%*	*4%*	*n.a.*	*n.a.*	
Seed cotton area harvested (1000 ha)	1,904	802	1,263	899	1,110	*-2.7%*
% Cotton / arable and crop area	*3%*	*1%*	*2%*	*n.a.*	*n.a.*	
Oranges area harvested (1000 ha)	913	856	806	806	799	*-0.8%*
% Oranges / arable and crop area	*2%*	*1%*	*1%*	*n.a.*	*n.a.*	

Source: Authors, based on data extracted from [8].

While harvested land for soybeans, maize and sugarcane increases, Brazil is losing land that used to be covered by forest or for the production of essential foods. Based on the data from [8], the area used for harvesting sugarcane has been increasing at an increasing rate since 2000 (from 1% compounded annual growth from 1990-2000 to 9% growth from 2006-2007). That growth has been necessary to supply the growing demand for sugarcane, of which production grew 12% from 2006 to 2007, and the growing demand for ethanol, of which production grew 11% from 2005 to 2006. Even though the efficiency of sugarcane production has improved, as shown by the improvement in tons of sugarcane produced per hectare of harvested land from 73 to 77 tons/ha, the need for more hectares of harvested land has outweighed those improvements in efficiency. The data implies that fuel crops are displacing land used for Brazil's key food crops. Figure 1 presents graphically these quantities from the previous table in an effort to clarify this point. We use the total land for arable and permanent crops present by FAO as a proxy for the total harvestable area of Brazil. In blue, green and yellow, we have indicated the proportion of total arable land used by fuel crops in 1990, 2000, and 2005. As shown, that proportion is increasing rapidly, at the expense of food crop land. It seems that there are incentives for farmers to use more land for harvesting fuel crops, while there seem to be weak incentives for increase of food crop land.

Eight-percent of the area used for arable land and harvested crops in Brazil is already used for sugarcane production, and only about 50% of the motor vehicle combustion fuel market is being met by ethanol. The aggressive growth forecasts that would need to be met to meet expected domestic and international demand would require a substantial improvement in efficiency or a substantial increase in land harvested, or both. Unless there are policy incentives to control this growth, then there would be an incentive to continue extending sugarcane harvest over land previously used by other food crops or forests.

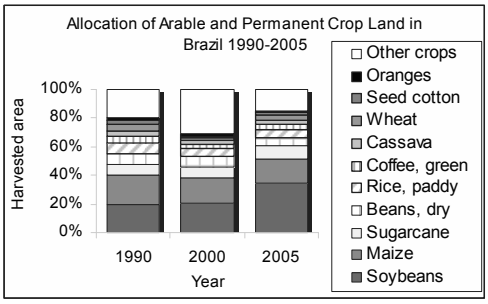

Fig. 1. Brazilian allocation of arable land.
Source: Authors, with data extracted from [8].

If the displacement of food crops continues, there could be a reduction in the food supply and an increase in prices. Though supporters of ethanol point out that food production has not fallen over the past few years because the efficiency of agriculture has improved and productivity per acre has increased (this has been confirmed by the authors using FAO 2009), there is a threat that the demand for more land for sugarcane agriculture will result in a decrease in the harvested land used for food crops. It is important to note that, according to FAO 2009, there has been no increase in food imports into Brazil since 1990. If food crop harvesting decreases and imports do not increase, then the general food supply would fall and prices would rise.

Though it is out of the scope of this paper, since we have chosen to focus on ethanol rather than all types of biofuels, it is important to note the high amount of land used in Brazil for soybeans, the food crop used for biodiesel production. The same risks that exist with growth in ethanol production as presented in this study exist with growth in the biodiesel industry in Brazil.

3.3 Soil and Water Deterioration

References [5-6] defend growth in the ethanol industry by using the data shown here in Table 6.

Table 6. Unused Available Land in Brazil, 2007.

	Million Hectares
Total area of Brazil	851
Amazon	345
Grazing fields	220
Protected area	55
Cities, lakes and roads	20
Cultivated forests	5
Other used land	38
Arable Crops	47
Permanent Crops	15
Unexplored land, available for harvest	**106**

Source: [5-6].

According to [5-6], while all of the harvested land (arable and permanent crops in Table 6) in Brazil amounts to about 62 million hectares, there are an additional 106 million hectares of land currently available for harvest. During the past five to ten years, the government has been using calculations presented by [5-6] to defend the idea that ethanol growth has not displaced other crops or forests and has much more room for growth in unused land. Even though we have shown in Section 3.1 that sugarcane land area is in fact growing in the Amazon and in Section 3.2 that it is growing in land area previously used for other food crops, we will present in Section 3.3 the potential threats of conversion of unused land for sugarcane harvesting. They relate to three categories: 1) the deterioration of land, 2) the deterioration of the water supply, and 3) higher GHG emissions.

Regarding the deterioration of land, [15-17] report that there is ample evidence that sugarcane fields suffer from high soil erosion. Reference [15] mentions that in São Paulo state, with the highest concentration of sugar plantations, it is estimated that erosion is up to 30 tons of soil per hectare per year (or up to 3 mm/year). Soil erosion is a result of having extensive areas of bare soil that are exposed to wind and rain, which occurs in the initial preparation of a field for sugarcane planting, during the period between harvesting and re-growth, and also when sugarcane stalks are replaced every 5-6 years [16]. Another negative impact on the soil is that of compaction, which can occur as a result of the constant traffic of heavy machinery over the soil. Contraction destroys soil porosity and density, decreases water infiltration, and further increases soil erosion. Reference [18] states that erosion conditions are severe or extremely severe in areas of land where sugarcane cultivation has taken place for many decades.

Soil erosion and degradation can lead to further deterioration in the surrounding water systems, because erosion can loosen sediments that are transported by wind or rain into nearby rivers, streams, or wetlands. Reference [19] presents the example of a sugarcane field that was planted near Piracicaba, in the State of São Paulo, near a reservoir. Twenty years after the first sugarcane harvest, the nearby reservoir could no longer be used as a water supply due to heavy sugarcane sedimentation in the water. Accelerated erosion can also result in sugarcane organic matter being transported to nearby water streams, which can severely impact the quality of the water.

Furthermore, there are two indirect factors that should be considered when estimating the impact of growth in ethanol production on the world's fresh water supply. First, 24% of sugarcane crops do require irrigation, and the area of those crops is increasing at 2.1% per year [8]. Second, increased deforestation may reduce rainfall in the region. A reduction in rainfall would lead to an increase in water use to irrigate the other 76% of sugarcane crops that are currently produced under rain-fed conditions [8].

Not only can sugarcane harvest have a negative impact on the quality of soil and nearby water, but it can also increase GHG emissions. Reference [20] points out that there is a significant loss of soil organic carbon and high levels of GHG emissions when degraded pasture land is converted to sugarcane cropland. Reference [21] quantifies these higher levels of GHG emissions and found that when there is a land-use change from grasslands or forests to agriculture of corn for the production of corn-based ethanol, the GHG emissions in the area nearly double over 30 years and these increases last for 167 years after the land conversion. It is important to note, as did [20], that these findings are based on several assumptions that are difficult to measure and define. It would be difficult to measure the exact impact of land conversion on the GHG balance of Brazil if unused degraded pasture land were to be replaced with sugarcane crops, but the findings of these studies certainly can be used as indications of the potential negative impact and justify the concern over land-use change in Brazil.

Though it is difficult to quantify the negative environmental impact that could occur from further growth in sugarcane harvest land area, it is important to discourage the premise that Brazil has an abundance of harmlessly available land for sugarcane growth. Brazil does have an abundance of available land, but converting that land to sugarcane fields could result in many indirect threats to the country's environment.

Though it is out of the scope of this paper, it is important to note that, in addition to the environmental risks associated with growth in the land area used for ethanol, there are social and economic risks. For example, in [20] it is noted that there is an industry trend in sugarcane agriculture of charging high fees from farm workers to pay for their transportation and lodging. This makes net real wages for labourers substantially lower than the national average. Furthermore, cane-cutting is an arduous job that imposes health risks and [22] states that, between 2002 and 2005, 312 sugar and ethanol workers died on the job and almost 83,000 suffered job-related accidents. Labourer workload has doubled in the last 30 years, as workers are now expected to cut 12 tons of cane per day vs. 6 tons per day in the 1970s [22]. Furthermore, productivity improvements could lead to an increase in unemployment in sugarcane harvest regions as the need for manual labour decreases.

4. Conclusions and recommendations

Our study presents three reasons that should discourage Brazilian policy-makers from pursuing their current plans for growth extent and rate of ethanol production. First, sugarcane harvest land area is growing in the Amazon Basin, which, as mentioned in Section 3.1, results in deforestation in a region of rich biodiversity and a decrease of earth's carbon dioxide absorption capacity. About 20,000 hectares are used in the region to harvest sugarcane, and that land area has recently increased by 5%. Second, sugarcane harvest seems to be replacing the harvest of important food staples. From 1990 to 2005, three out of the ten largest crops in Brazil were food products used in fuel production: soybean (biodiesel), sugarcane (ethanol) and maize (ethanol). The land area used for the agriculture of these fuel crops increased. The land area used for harvesting all of the other key food crops in Brazil – including rice and beans – decreased year per year from 1990 to 2005. The total amount of arable land in the country has not increased by the same amount, so within the total harvested land there is a displacement from food to energy crops. The third reason is that the Brazilian government defends growth in sugarcane ethanol by suggesting that there are over 106 million hectares of land of degraded pastures that could be made available for sugarcane. Several studies point to the environmental impacts of converting this land, including a deterioration of the soil and the nearby fresh water supplies, and a significant long term increase in the GHG emissions resulting from the land-use change.

In an effort to avoid further land displacement, reduction in food supply, increase in food prices, and deterioration of the environment, all of which are highly counter-productive to Brazil's sustainable development, Brazil's policies for the ethanol industry must be re-evaluated, applying rigorous sustainability analysis that analyzes carefully all of the economic, environmental and social aspects. Two obvious specific policy foci should be: 1) better management of land use, and 2) better support for other renewable sources, and, of hybrid and plug-n electric cars, which seems to be the current worldwide consensus direction for vehicular transportation, and not just focused on ethanol. For the first point, policy should focus on fomenting further improvements in productivity, managing land use and displacement, maintaining a closer relationship between government, farmers, and key industry players through regulation, and encouraging the export of processes rather than just of ethanol. Legislation should impose strict controls on which areas can be used for sugarcane harvest and where growth can take place, as well as enforce controls on land conversion procedures so that erosion can be minimized. On the second point, policy should be centered on providing continuous incentives for the diversification of renewable sources in the country's fuel supply, fomenting growth in the use of bagasse and more innovative methods to generate power, and partnering with other countries to continue to promote a steep learning curve in the field of biofuels. Furthermore, legislation should address labourers and ensure that working conditions are safe and fairly-compensated, as well as stimulate education and training of sugarcane workers so that they may develop skills that will sustain their development.

References

[1] Lula da Silva, L. I., 2007, *Our Biofuels Partnership*, Op Ed to The Washington Post, published on 03/30/07, p. A17.

[2] Mason, J., 2009, *Obama Reassures China on Bonds*., Reuters, published 03/14/09, [online], URL:http://www.reuters.com/article/idUSTRE52D0DH20090314.

[3] Sato, S., and Forster, H., 2007, *Brazil Plans to Triple Ethanol Exports in 7 Years*, Bloomberg, published 03/14/07, [online], URL: http://www.bloomberg.com/apps/news?pid=20601086&sid=a1aRbSp18ly0.

[4] Martines-Filho, J.; Burnquist, H.; and Vian, C., 2006, *Bioenergy and the Rise of Sugarcane-Based Ethanol in Brazil*. CHOICES 2nd quarter 2006, issue 21(2).

[5] Rodrigues, R., 2008, *Facing Energy Security in the Americas through Agroenergy Sources*, XXX Lecture of the OAS Lecture Series of the Americas, 10/28/08.

[6] Rodrigues, R., 2007, *AgroEnergia*, Montevideo Capital Rural Energy Conference, 10/05/07.

[7] China Chemical Reporter, 2008, *Fuel Ethanol vs. Security of the Food Supply*, published 08/26/08, p.11.

[8] FAOSTAT Food and Agriculture Organization of the United Nations. Production Statistics Online Databases. Accessed on 03 Mar 2009 and 16 Mar 2009, [online], URL: http://faostat.fao.org/site/567/DesktopDefault.aspx?PageID=567#ancor.

[9] Salomon, M., 2009, *Lula estuda liberar plantio de cana na borda do Pantanal.* A Folha de São Paulo, published on 04/11/2009.

[10] Whitten et al., 1996, *General chemistry*. Saunders College Pub., 1996, p.28.

[11] ÚNICA, 2007, *Venda de automóveis e vehiculos leves no Brasil*, [online], URL: http://www.unica.com.br/dadosCotacao/estatistica/

[12] UNICA, 2008, Sustainability Report, [online],URL: http://www.unica.com.br/dadosCotacao/estatistica/

[13] UNICA, 2009, Brazilian Sugarcane Map, [online],URL: http://www.unica.com.br/dadosCotacao/estatistica/

[14] CONAB (National Supply Company). Follow Up of Brazilian Harvests: 2007 1st Survey, May 2007; 2007 3rd Survey, Nov 2007; 2008 1st Survey, Apr 2008; 2008 3rd Survey, Dec 2008 (Online). Accessed on 16 Apr 2009. http://www.conab.gov.br/conabweb/index.php?PAG=133.

[15] Martinelli, L. A.; Filoso, S., 2007, *Polluting Effects of Brazil's Sugar-Ethanol Industry*. Nature 445/364, Published online 01/24/07.

[16] Martinelli, L. A.; Filoso, S., 2008, *Expansion Of Sugarcane Ethanol Production In Brazil: Environmental And Social Challenges*, Ecological Applications, 18(4), pp. 885–898.

[17] Martinelli, Luiz; Camara, Gilberto; Nobre, Carlos; Ometto, Jean Pierre. Biofuels in Brazil: Impact on Land Change. 4th IGBP Congress, Session D6: Land System Change: Competing for Food, Energy and Environmental Services. Cape Town, South Africa, 8 May 2008.

[18] Politano, W., Pissarra, T., 2005, *Evaluation of Areas of Different States of Accelerated Erosion of Soil in Sugar Cane Plantations and Citrus Orchards Utilizing Photointerpretation Techniques*. Engenharia Agrícola, vol.25, n.1, pp. 242-252.

[19] Fiorio, P., Dematte, J., and Sparovek, G., 2000, *Cronology and environmental impact of land use on Ceveiro Microbasin in Piracicaba region, Brazil.* Pesquisa agropecuaria brasileira., vol.35, n.4, pp. 671-679.

[20] Smeets, E., et al, 2008, *The sustainability of Brazilian ethanol: An assessment of the possibilities of certified production*. Biomass and Bioenergy 32.8, 781-813.

[21] Searchinger, T., et al, 2008, *Use of U.S. Croplands for Biofuels Increases Greenhouse Gases Through Emissions from Land-Use Change*. Science Express.

[22] Smith, M., Caminada, C. 2007, *Brazil Ethanol Boom Belied by Diseased Lungs Among Cane Workers*, Bloomberg, [online], URL: http://www.bloomberg.com/apps/news?pid=20601082&sid=acyvyWb1Sk0Y.

Optimization of the Operation Management of an Organic Rankine Cycle Fed by Biomass Serving a District Heating Grid

Anna Stoppato and Andrea Cisotto

Department of Mechanical Engineering, University of Padova, Padova, Italy

Abstract: In these last years, many actions have been taken to decrease the consumption of fossil fuels and the impact on the environment of the human activity. Among these actions, a special attention is paid to the use of renewable energy sources to substitute the more traditional fossil fuels. This paper describes a new plant sited in Asiago (Italy). It is arranged by 2 boilers fed by the wastes from a sawmill: one of them directly supplies hot water to a district heating grid, while the other provides for the heat a cogenerative Organic Rankine Cycle (ORC). The ORC plant has a nominal electric power of 1.25 MW and can produce 5.3 MW of heat. The plant is connected to the electric grid. For different operation strategies, the results of the energy analysis as well as those of the economic one will be described. A special attention will be paid to the influence of the incentives on the results of the economic analysis. The emissions will be also evaluated and compared with those of the pre-existing solution, where each user produced heat by domestic boilers fed by natural gas or diesel oil.

Keywords: Biomass, Cogeneration, Influence of incentives, Organic Rankine Cycle.

1. Introduction

The increased awareness of European and Italian governments about the importance of environment defence has brought to a series of actions for energy saving and reducing the impact of energy systems. This seems to be a winning strategy also from an economic point of view, especially for nations, as Italy, strongly dependent from abroad for fossil fuels. In addition, the potentiality of developing and improving a national productive sector related to the energetic efficiency can support the drive to a new energetic strategy.

The promotion of the use of renewable resources is considered one of the main points to reach the target in the reduction of greenhouse emissions: the 20-20-20 Climate action and renewable energy package by the European Union [1] states to reach a 20% of production by renewables by 2020. To get this target, many directives have been promulgated and incentives and facilitations introduced. The most important in Italy are:

- The Italian law 79/99 [2] and its modifications, entertaining the European Directive 96/92/CE [3] introducing the requirement for electric producers and importers of electricity from not renewable sources to put into the grid a quota of electricity by renewable fonts. For 2010, this quota is 6.05% of their production by fossil fuels. It is also possible to fulfil the renewable quota obligation by purchasing Green Certificates (GC) which have been issued in respect of certified renewable electricity (RES-E) generated by other parties. One Green Certificate is worth 1 MWh of electricity. The electricity generated by RES plants commissioned or repowered after 1 January 2008 is certified as RES-E for the first 15 years of operation of the plants.
- The law on the promotion of the electric energy produced by renewable sources, defining the characteristics, the benefits and the incentives for the plants using renewable energy sources [4].

A special attention is paid to small plants and distributed generation, whose promotion contributes to reduce the transmission losses on the grid and the grid congestion problems and permits the use of low density distributed renewable sources (biomass, wind, solar, minihydro) [5]:

- Simplified procedures for the connection to the grid are contemplated.

Corresponding Author: Anna Stoppato, Email: anna.stoppato@unipd.it

- Small plants (P<10MVA) can opt for indirect sale through the Italian Energetic Services Manager (Gestore Servizi Energetici, GSE), instead of direct sale in the market profit. For plants having P>1MW the sellback prizes are the market ones, while smaller plants have minimum granted prizes for the first 2 billions kWh.
- Very small plants (P<1MW) can also choose the all-inclusive feed-in tariff, comprehensive of the Green Certificates, which gives granted sellback prizes for the whole production.
- Finally, the net metering service is granted for electricity generated by RES plants of up to 200 kW.

These facilitations have promoted the growth in Italy of distributed (P<10MVA) and small (P<1MW) generation. In 2006, 13.5TWh of electric energy were produced by these plants, about 4.3% of the Italian production, with an increase of 0.4 TWh (3%) with respect to 2005. Among them, about 70% of energy is produced by renewable fonts, of which about 15% using biomass.

For applications using biomass the employ of Organic Rankine Cycles (ORC) is a good solution [6-7]. Among other technologies, they present high efficiency for low temperature applications, high availability and simple management. The combustion takes place in boilers of proven and simple operation, where diathermic oil is heated and so the use of water steam with its management problems is avoided. Then this oil provides heat to the organic fluid, which evaporates and expands in a turbine. ORC plants seem to be particularly interesting for low temperature cogenerative applications.

Since the end of 2009, an ORC plant has been working in Asiago, Italy, using the wastes of a sawmill. It produces electricity, sold to the grid, and heat for the local district heating grid.

In this paper, different operation management for this plant will be analysed both from energetic and economic viewpoint. Special attention will be paid on the influence of the incentives on the results of the analysis. This aspect is particularly interesting for this plant whose size, 1255 kW_{el}, gives the possibility to choose among different options of incentives. The paper will also present the analysis of the emissions of the plant, comparing them with the pre-existing situation, where each user produced heat by domestic boilers fed by natural gas or diesel oil.

2. Description of the plant

The plant is sited in Asiago, Italy, a town of about 6500 residents at 1000 m over s.l. of altitude, which is a winter and summer holiday site, and so in some periods the population can double.

The plant has been built very close to a big sawmill, whose wastes (wood shavings, bark, sawing, chips) are directly sent to the bunker of the boilers by a conveyor belt.

The thermal section is arranged by two moving grate furnace boilers fed by biomass:

- The first directly produces hot water for the district heating grid and is sized 3.5 MW.
- The second heats diathermic oil and is sized 6.8 MW.

They have both a design efficiency of about 85%.

A supplementary boiler (5.8 MW sized) fed by rape seed oil is present only for integrative purposes.

The cogenerative section of the plant is an ORC unit T1100 by Turboden s.r.l. [8]

Its main design characteristics are summarized in Table 1. Note that the efficiencies are calculated with respect to the thermal power supplied by the diathermic oil to the organic fluid, which is a siliconic oil, and so do not consider the boiler efficiency.

Table 1. Main characteristics of T1100 unit.

Diathermic Oil	
Temperature (in/out) high temperature loop	310/250 °C
Thermal power high temperature loop	6130 kW
Temperature (in/out) low temperature loop	250/130 °C
Thermal power low temperature loop	585 kW
Total thermal power	6715 kW
Water (for thermal use)	
Temperature (in/out)	60/80 °C
Thermal power to water	5350 kW
Performances	
Gross active electric power	1317 kW
Gross electric efficiency	0.196
Captive Power Consumption	62 kW
Net active electric power	1255 kW
Net electric efficiency	0.186
Total efficiency	0.98
Electrical generator	asynchronous triphase L.V. 400 V

T1100 is a cogeneration unit with **split**: as can be seen in Fig.1, after the feed pump the fluid is splitted into two streams: the first goes, as in

standard ORC cycles, to a regenerative exchanger, while the other is heated by the diathermic oil in a supplementary preheater. Then the two streams are remixed together before the evaporator. Note also that there are two economizers between exhaust gases and oil and a last economizer between flue gases and hot water. These devices permit to maximize the electric power and to grow the net electric efficiency of the group up to 18.6%. In the condenser the organic fluid supplies with heat the water of the heating grid. Two heat dissipaters permit to work also with the thermal requirement by the users lower (down to 0) than the heat supplied in the condenser.

Fig. 2 shows the thermodynamic cycle of the unit.

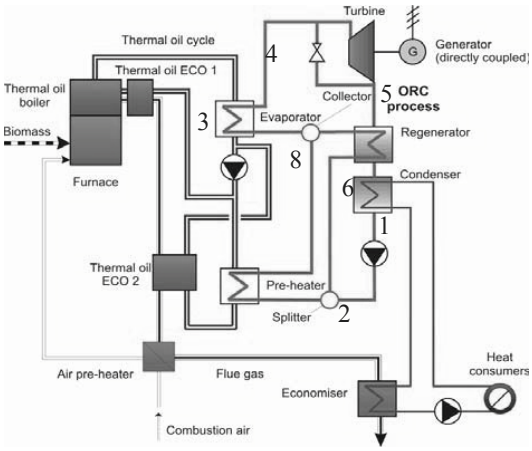

Fig. 1 . Scheme of the ORC cogenerative unit.

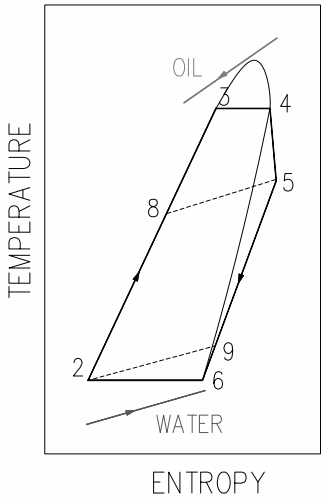

Fig.2 Thermodynamic cycle of the ORC unit.

2.1. The users

At present, 43 thermal users are connected to the grid, among them a hospital, some schools and hotels. Globally, their installed thermal power is 9234 kW, while the peak request is 2550 kW. The annual requirement is 8237 MWh: considering a 10% of losses in the grid, the plant must yearly supply 9061 MWh. Table 2 and Fig 3 summarize the load trends during the year. They have been obtained combining data registered in the first months of work of the grid and data from literature [9], considering the annual temperature trend of Asiago. Note that at present the users' requirement is much lower than the plant potentiality.

Table 2. Monthly thermal requirement.

	Heating requirement [kWh]	Hot water requirement [kWh]	Total for the plant [kWh]
January	1 007 979	190 860	1 318 723
February	965 329	172 390	1 251 491
March	721 708	190 860	1 003 825
April	599 682	184 703	862 824
May	118 903	190 860	340 739
June	0	184 703	203 174
July	0	190 860	209 946
August	0	190 860	209 946
September	349 061	184 703	587 140
October	638 132	190 860	911 891
November	703 291	184 703	976 794
December	885 953	190 860	1 184 494
Total	5 990 037	2 247 223	9 060 986

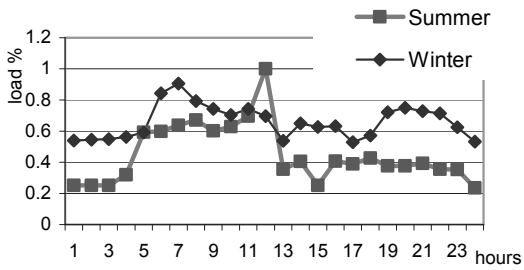

Fig 3. Hourly electric request in typical winter and summer days, %

3. Analysis

The size of the plant permits three different choices for electricity remuneration:

- Declaring as sale capacity the nominal power (1250 kW), it is convenient to opt for the sale to GSE while the plant production can also issue Green Certificates.

- Declaring as sale capacity a limited power (990 kW) and taking advantage of Green Certificates: minimum prizes are granted for the first 2 billion kWh.
- Declaring as sale capacity a limited power (990 kW) and choosing the all-inclusive feed-in tariff: prizes are granted for all the production.

For each of the previous choices, two different operation strategies can be adopted:

- Maximize the electric production and dissipate the exceeding thermal power.
- Follow the thermal load and accordingly vary the electric production.

They both satisfy the grid thermal request, but supply different quantities of electricity, burn different quantities of biomass and have different emissions and so have different effects on energetic, economic and environmental aspects.

3.1. Energetic analysis

To maximize the electric production, the plant works at nominal power for 6500 hours/year, considering about three months of stop for the maintenance during the summer when the thermal request will be satisfy by the 3.5 MW boiler. If the ORC follows the thermal requirement, the electric power varies during the operation. In this case, the plant will be stopped both during the period of maintenance and when the load results lower than 10% of its design power, which is the minimum for the plant. Since under these hypotheses the maximum electric power results 550 kW, there is not any difference between scenario 3 and 4, i.e. with a sale capacity power of 1250 or 990kW.

Table 3 summarizes the results of the energetic analysis for the four scenarios [10].

As can be seen, in the first two scenarios a great amount of the heat produced must be wasted, with in addition a consumption of electricity in the dissipaters of about 5% of net production. In the last two scenarios the ORC operation hours are about half than in scenarios 1 and 2, but it satisfies 67% of thermal requirement. The differences of electric and thermal efficiencies among the different scenarios are related to the operation average load more or less close to the design one. But the most significant parameter is the efficiency calculated only on the useful thermal energy: it is clear that the best use of biomass is done when the

Table 3. Results of the energetic analysis for different operation strategy

	Maximum electric production		**Thermal load search**	
	SCENARIO 1	SCENARIO 2	SCENARIO 3	SCENARIO 4
Sale power, kW	1250	990	1250	990
ORC				
Annual operation hours	6500	6500	3776	3776
Annual electric production, kWh	8 125 000	6 435 000	936056	936056
Electric efficiency	0.158	0.155	0.095	0.095
Thermal energy production, kWh	34 636 454	27 432 072	6 087 637	6 087 637
Average thermal efficiency	0.674	0.661	0.62	0.62
Total efficiency	0.832	0.815	0.715	0.715
Primary energy consumption, kWh	51 387 241	41 529 280	9 817 401	9 817 401
Useful thermal energy, kWh	8 437 921	8 437 921	6 087 637	6 087 637
Total efficiency considering only useful thermal energy	0.322	0.358	0.712	0.712
BOILER				
Useful thermal energy, kWh	623 065	623 065	2 973 349	2 973 349
Average thermal efficiency	0.788	0.788	0.788	0.788
Primary energy consumption, kWh	791 174	791 174	3 775 585	3 775 585
Annual operation hours	2260	2260	4984	4984
TOTAL				
Thermal energy requirement, kWh	9 060 986	9 060 986	9 060 986	9 060 986
Biomass consumption, tons	22 588	18 321	5884	5884
Thermal energy wasted, kWh	26 198 533	18 994 151	0	0
Dissipaters consumption, kWh	388 126	281 395	0	0
Other plant auto consumption, kWh	325 000	300 000	231 000	231 000
Annual net electric production, kWh	7 411 874	5 853 605	705 056	705 056
Global net efficiency	**0.316**	**0.352**	**0.718**	**0.718**

ORC follows the thermal load even if it must work far from its design operation point.

3.2. Economic optimization

For the economic analysis, the following aspects have been considered:

Purchase of biomass: a prize of 45 €/ton has been assumed, while the amount of biomass depends on the operation strategy, as seen in Table 3. At present, the sawmill is bind by contract to supply all the needed biomass.

Plant management has been assumed as 309000€/year for all the scenarios, considering assistance, maintenance, insurance, staff salaries,…

Sale of thermal energy. The average sale price is 0.1 €/kWh, and so the income is 826583€/year for all the scenarios.

Sale of electric energy, which depends on operation strategy:

- For scenarios 1 and 3, where the sale power is 1250 kW, a price of 90.6 €/MWh has been considered, which is the average value of 2008 North Italian market prices for medium-voltage electricity (comprehensive of transmission, measurement and administrative charge). It was considered preferable do not consider the prices of 2009 (about 60 €/MWh), because their low value was considered strictly related to the present Italian economic crisis and not significant as reference. The Green Certificates in the last year had an average price of 85.5 €/MWh. For production using biomass, Italian law assign a multiplicative coefficient of 1.8, and so that price can be recalculated as 153.9 €/MWh. This value has been used in the following.
- For Scenarios 2a and 4a, when sale power is 990 kW and Green Certificates are issued, for the first 500000 kWh a price of 101.1 €/MWh is granted, between 500000 and 1000000 kWh it is 85.2 €/MWh, and between 1000000 and 2000000 it is 74.5€/MWh. The remaining production is sold at market prices. Green Certificates are evaluated as in Scenarios 1 and 3.
- For scenarios 2b and 4b, when sale power is 990 kW and the all-inclusive feed-in tariff is chosen, a price of 280€/MWh is granted for all the production.

Table 4 summarizes the results of the economic analysis. They show that, whatever the electricity remuneration choice, the highest net profit is reached if the electric production is maximized. This result is in contrast with that of the energetic analysis (Table 3) and so the conclusion is that for this plant the prices policy promotes the dissipation of energy.

Table 4. Main results of the economic analysis.

	Maximum electric production			**Thermal load search**		
	SCENARIO 1	**SCENARIO 2a**	**SCENARIO 2b**	**SCENARIO 3**	**SCENARIO 4a**	**SCENARIO 4b**
	GC	**GC**	**All-incl. tariff**	**GC**	**GC**	**All-incl. tariff**
Sale power, kW	**1250**	**990**	**990**	**1250**	**990**	**990**
ANNUAL PROFITS						
Electric energy, €	1 812 348	1 423 391	1 639 009	172 281	178 372	197 416
Thermal energy, €	826 583	826 583	826 583	826 583	826 583	826 583
Total profit, €	2 638 931	2 249 974	2 465 593	998 864	1 004 955	1 023 999
ANNUAL COSTS						
Biomass, €	-1 016 463	- 824 424	- 824 424	-264 798	-264 798	-264 798
Other costs, €	-309 000	-309 000	-309 000	-309 000	-309 000	-309 000
Total cost, €	-1 325 463	-1 133 424	-1 133 424	-573 798	-573 798	-573 798
NET PROFIT	**1 313 469**	**1 116 550**	**1 332 168**	**425 065**	**431 157**	**450 200**
Thermal production cost, €/kWh	0.03	0.03	0.03	0.03	0.03	0.03
Electric production cost, €/kWh	0.14	0.14	0.14	0.27	0.27	0.27
Thermal income for biomass unit, €/ton	146	145	145	140	140	140
Electric income for biomass unit, €/ton	81	79	91	41	43	47

Table 5 Sensitivity analysis on the net profits of scenario 1 respect to scenario 2b for different values of Green Certificates and market energy prize (dotted cells represent 2009 conditions, grey cells negative values, the bold number is near that of this work. The values represent the difference of net profits is in €/year.

	Energy market price [€/MWh]									
GC [€/MWh]	50	55	60	65	70	75	80	85	90	100
75	-460 108	-423 048	-385 989	-348 930	-311 870	-274 811	-237 751	-200 692	-163 633	-89 514
80	-393 401	-356 341	-319 282	-282 223	-245 163	-208 104	-171 045	-133 985	-96 926	-22 807
85	-326 694	-289 635	-252 575	-215 516	-178 456	-141 397	-104 338	-67 278	**-30 219**	43 900
90	-259 987	-222 928	-185 868	-148 809	-111 750	-74 690	-37 631	-572	36 488	110 607
95	-193 280	-156 221	-119 162	-82 102	-45 043	-7 983	29 076	66 135	103 195	177 313
100	-126 573	-89 514	-52 455	-15 395	21 664	58 723	95 783	132 842	169 902	244 020
105	-59 867	-22 807	14 252	51 312	88 371	125 430	162 490	199 549	236 608	310 727

Indeed, as shown in the last raw of Table 4 each ton of biomass permits to earn 80 - 90 € for electricity sale while its cost is 45 €, so also the operation in non-cogenerative mode is always convenient. Note that the sale of thermal energy permits a greater net profit, but it is related to a requirement by a user, while electricity can always be sold to the grid.

Scenarios 1 and 2b seem to be the best solutions, with a small difference of annual income. While the prizes in Scenario 2b are granted, in Scenario 1 they depend on the market. So a sensitivity analysis on the effects of the prizes of Green Certificates and of electric energy has been performed. Table 5 summarizes the results. The combinations where the all-inclusive tariff is convenient are represented in gray. The dotted cells represent the 2009 conditions; the bolded value is near to that considered in this paper. Considering also the historical values of the prices of electricity and Green Certificates, it seems that the all-in tariff will be probably also in the near future more convenient.

In any case, these results are strongly connected to the presence of incentives. Table 6 shows the most significant results of the economic analysis without incentives. If the sale capacity is 1250 kW, electricity is sold at market prices, if the sale capacity is 990kW the electricity is sold to GSE; there are not GC, nor the all-inclusive tariff. As can be seen, the best strategy is now that which follows thermal requirement. It can be noted that each ton of biomass permits to earn for electricity less than its cost, so the only sale of electricity can not cover the cost of the fuel. Note that the incentives will end after 15 years of plant operation, and so these results suggest that after this period it will be convenient to change the management strategy [2].

All these results depend on the thermal requirement by the users which is much lower

Table 6. Main results of the economic analysis without incentives

	Maximum electric production		**Thermal load search**	
	SCENARIO 1	**SCENARIO 2**	**SCENARIO 3**	**SCENARIO 4**
Sale power, kW	**1250**	**990**	**1250**	**990**
Electric energy, €	671 885	516 787	63 878	68 021
Thermal energy, €	826 583	826 583	826 583	826 583
Biomass, €	-1 016 463	- 824 424	-264 798	-264 798
Other costs, €	-309 000	-309 000	-309 000	-309 000
NET PROFIT	172640	209 925	316 680	320 824
Thermal production cost, €/kWh	0.03	0.03	0.03	0.03
Electric production cost, €/kWh	0.14	0.14	0.27	0.27
Thermal income for biomass unit, €/ton	146	145	140	140
Electric income for biomass unit, €/ton	30	29	15	17

than the plant potentiality.

An analysis performed by the Authors [10] under the hypothesis of a doubling of the demand, which is expected by the grid managers, brings to higher income, but to the same considerations about the best operation strategy, even though the difference of income between the two operation strategies decreases. This brings to state that, with a bigger thermal demand, the need to maximize electrical production become less important.

3.3. Emissions analysis

The flue gas treatment section presents an electrostatic precipitator and a condenser to eliminate the plume from chimney. Table 7 gives the maximum granted concentration of pollutant in the flue gas. Table 8 summarizes the annual plant emissions.

Table 7 Maximum granted plant emissions.

NOx	200	mg/Nm3
PM	20	mg/Nm3
CO	100	mg/Nm3

Table 8 Annual plant emissions.

	SCENARIO 1	SCENARIO 2	SCENARIOS 3 AND 4
Boiler design flow rate, Nm3/h	9540	9540	9540
ORC boiler design flow rate, Nm3/h	18 803	18 803	18 803
ORC boiler annual emissions, Nm3	120 210 913	95 207 043	21 128 040
Boiler annual emissions, Nm3	1 698 297	1 698 297	8 104 500
Total emissions, Nm3	121 909 210	96 905 340	29 232 540

The plant substitutes the boilers of the users. It has been calculated that in the previous conditions were burnt 289064 kg of diesel oil and 398670 Nm^3 of natural gas. Considering the usual emission factors of these fuels, the results reported in Fig.4 have been obtained.

As presumed, the maximization of electric production is more pollutant, and the new plant produces more emission than the previous boilers, excluding the production SOx which is lower.

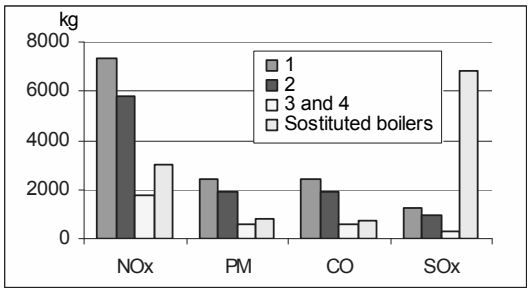

Fig. 4. Pollutant emissions for the different strategy scenarios.

The advantage is that these emissions are farer from buildings. It could be more interesting considering also the emissions avoided from the thermoelectric power plants due to the electric production of this plant fed by renewable source. Considering the average emission factors of Italian plants [11] the results reported in Fig. 5 are obtained which show the environmental convenience of this plant. It is important to underline that while the effects of CO2 are at global scale, the emissions of CO, NOx, PM and SOx have local effects and this aspect must be considered in a critical analysis.

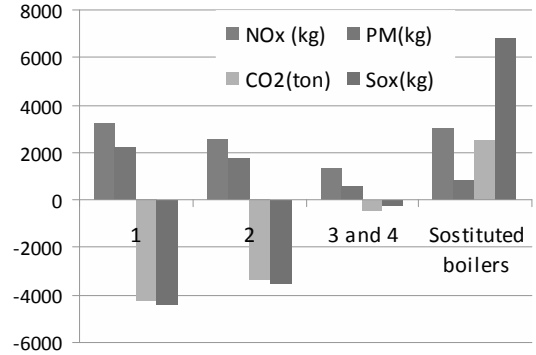

Fig. 5. Pollutant emissions for the different strategy scenarios considering the avoided emissions from thermoelectric power plants.

Conclusions

The analysis of an ORC cogenerative plant fed by biomass has been performed. The analysis has shown that the present incentives prize to a not rational use of energy since it is convenient to maximize electric production, with a total efficiency of about 15%, instead of cogenerate heat and electricity, with a total efficiency of about

80%.The optimization of the operation strategy shows that at present the all inclusive tariff is the most convenient, but that different conditions in the market can bring to a different solution.

References

[1] European Union, 2008, *Climate action and renewable energy package*, December 17th, European directive, www.europarl.europa.eu.

[2] Decreto legislativo 79, 1999, *Attuazione della direttiva 96/92/CE recante norme comuni per il mercato interno dell'energia elettrica*" (in Italian).

[3] Directive 96/92/EC *concerning common rules for the internal market in electricity*.

[4] EU directive 2009/28, O*n the promotion of the use of energy from renewable sources* and amending and subsequently repealing Directives 2001/77/EC and 2003/30/EC

[5] Autorità per l'energia elettrica e il gas, 2009, *Testo Unico della Produzione elettrica* (in Italian).

[6] Moratza Yari, 2008, *A comparative study on the performance of the Organic Rankine Cycles*, Proc. of ECOS 2009, Cracow-Gliwice, Poland, June 24-27.

[7] Orbernberger, I., Carlsen. H., Biedermann, F., 2003, *State of the art and future developments regarding small-scale biomass CHP systems with a special focus on ORC and Stirling engine technologies*. Proceeding of the International Nordic Bioenergy 2003 conference.

[8] Turboden, 2009, Technical data Sheet-standard cogeneration units with split, from http://www.turboden.eu/en/public/downloads/Turboden_datasheet_CHP_08A05269_e.pdf

[9] Macchi, E., Campanari, S., Silva, P., 2006, *La microcogenerazione a gas naturale (Microcogeneration with natural gas)*, Polipres, Milano.(in Italian)

[10] Cisotto, A., 2009, *Ottimizzazione della gestione dell'impianto di teleriscaldamento cogenerativo a ciclo Rankine a fluido organico alimentato a biomassa di Asiago*, University of Padova, Italy (In Italian)

[11] http://www.isprambiente.it/site/en-GB/default.html

Acknowledgments: The authors gratefully acknowledge Dr. Simone Micheletto of Vi.Energy for the help provided during the work.

Optically filtered and concentrated solar energy for PV conversion

C. Firat[a], A. Beyene[b]

[a] *Istanbul Technical University, Energy Institute, Istanbul, Turkey*
[b] *San Diego State University, College of Engineering, San Diego, USA*

Abstract: Various configurations of Photovoltaic (PV) energy conversion systems were investigated and their performances compared to direct solar PV conversion. The systems involved use of fiber optic, lens, filter, and PV with and without concentrator. The use of Plastic Optical Fiber (POF) bundle for light transmission proved to be the most efficient, but also the most expensive. However, a fresnel concentrator with an infrared heat removal filter was the most affordable. The current price of fiber optic for light transport, though interesting, renders them economically not viable for energy conversion.

Keywords: Solar energy conversion, optical fibers, concentrated PV systems, cost reduction

1. Introduction

Optical light transfer is used in various applications such as PV driven power generation [1] as well as providing direct illumination in single or hybrid solar lighting [2]. These conventional applications cover areas such as communication links [3], sensing platforms [4], and other specialized collection of optical systems [5]. However, application of optical light transfer to producing electricity through the use of PV has been modest. Optical light transfer offers flexibility and expanded functionality to applications of solar energy.

In conjunction with simple light transfer, optical fibers may also serve as concentrators, reducing capital cost as a result of lesser foot-print of solar energy collectors, i.e., PV cells, which are more expensive than an equal area of concentrators. This reduction in surface area as a result of concentrating the input energy enables the use of high efficiency cells, otherwise deemed too expensive for flat plate module application. However, the concentrator module collects a higher rate of solar incident flux at elevated temperature, adding to the system intricacy and cost [6]. The only feasible cost reduction of tracking systems comes through high production volume, or possibly if coupled with filtering systems.

Filtering: Solar energy reaches the earth in the form of electromagnetic waves at wide range of wave lengths measuring from 10^{-3} nm or even lower up to 10^{9} nm or higher. The energy that arrives with wave lengths between about 1 nm and 10^{6} nm is considered to be light. This light range has three major components:

- Ultraviolet (UV) light with wavelengths between about 1 nm and 390 nm,
- Visible light with wavelengths between 390 nm and 760 nm,
- Infrared radiation (IR) with wavelengths exceeding 760 nm but shorter than 10^{6} nm.

Average direct sunlight is about 93 lumens per watt of radiant flux. Infrared is about 47% of the spectrum, visible is about 46%, and ultraviolet about 7%. These numbers can vary significantly depending on altitude, Earth's position relative to the sun, and environmental conditions.

Filtering for PV applications is essentially removal of infrared radiation much of which causes passive heating of the cell, thereby increasing the cell temperature which in turn drops cell energy conversion efficiency, and also reducing the life of the cell. These negative effects can be much more pronounced in desert and very high altitude environments. High temperature impacts can be minimized with the use of appropriate filters, dichroic materials that block or limit infrared

Corresponding Author: Asfaw Beyene, Email:abeyene@rohan.sdsu.edu

radiation and heat transfer but allow maximum visible radiation transfer, [7].

Concentrated fiber-optic transfer of light for PV driven electrical power can also be channeled through filters to exclude interferences and disturbances [8]. In fact concentrators may also serve as filters. Such filtering and also the longer exposition time of the PV cells as a result of solar tracking may more than compensate for the added cost of tracking and filtering systems. Most concentrators cause significant temperature rise necessitating external cooling. Fresnel lens has been proposed as a concentrator because it offers low mass density without significant increase in temperature; hence it is considered more economical than other concentrators such as "hot glasses" [9].

Filters such as "hot mirrors" transmit more than 93% of the visible light and reflect more than 95% of the infrared range. Unfortunately such mirrors can be fairly expensive. On the other hand, optical fiber may, in addition to serving as a filter, also offer more heat insulation because it attenuates the illumination more rapidly than glass. This attenuation increases sharply in the infrared as well as the ultraviolet ends of the radiation spectrum. In this study, various configurations of solar PV energy conversion systems using concentration and filtering are assessed.

2. Factors affecting output of a PV solar cell

One common loss takes place during intrinsic or extrinsic fiber attenuation in a fiber optic integrated PV system. At the fiber input, there are losses due to reflections at the light-fiber interface, known as Fresnel losses, which occur at both the entrance and exit ends of the fibers. During the passage through the fibers, transmission and absorption losses take place. These losses may become dominant over longer lines, compounded by losses due to connectors and splices when present. Other losses may originate as a result of mismatch of coupled fiber ends, [10]. In a straight optical fiber, the power decreases exponentially with the distance L, [11]:

$$P_{tr} = P_{\text{into}} 10^{-\alpha L/10} \tag{1}$$

where α is the attenuation of fiber optic cable and P_{into} is the power inputted into the fiber cable. The magnitude of the Fresnel loss depends on the difference in refractive index of air and the transporter core. Multimode optical fibers only propagate light that enters the fiber within a certain cone, known as the acceptance cone of the fiber. The half-angle of this cone is called the acceptance angle, θ_A. For step-index multimode fiber, the acceptance angle is determined using the indices of refraction where n_{fo} is the refractive index of the fiber core, and n_2 is the refractive index of the cladding. The numerical aperture (NA) is an important performance indicator, a dimensionless number that characterizes the range of angles over which the system can accept or emit light. NA of any type of fiber is [12]:

$$NA = \sqrt{n_{fo}^2 - n_2^2} \tag{2}$$

where n_{fo} is the refractive index along the central axis of the fiber and n_2 is the refractive index of the fiber clad.

2.1. Effect of temperature on solar cells

For a typical commercial PV module operating at its maximum power output, 10 to 15% of the incident sunlight is converted into electricity, with much of the remainder converted into heat [13]. The power output is strongly impacted by ambient temperature. Conversion equation is given by [14],

$$C.(1-\eta_{nom})E_{pv}.\mu_i = k.S_{pv}.(T_{pv} - T_a) + 2.S_{pv}.\sigma.(T_{pv}^4 - T_a^4) \tag{3}$$

where C is geometric concentration ratio of the lens, η_{nom} is the nominal efficiency of the PV cell, E_{pv} is energy density on the PV cell in W/m^2, μ_i is the portion of whole solar spectrum (0.46, 0.07 and 0.47 for visible, ultraviolet and infrared portion respectively), k is the convective heat transfer coefficient of the process (~33 W/m^{2}K for air), S_{pv} surface area of the PV cell, T_{pv} is the temperature of PV cell at E_{pv}, T_a is ambient temperature in K, σ is Stephan-Boltzmann constant. The efficiency of a solar cell as a function of the irradiance E_{pv} and temperature T_{pv} is given as [15],

$$\eta_{pv} = \eta_{\text{nom}}\left[1+\beta\left(T_{pv}-25\right)+\gamma\log_{10}\left(\frac{E_{pv}}{1000}\right)\right] \quad (4)$$

where β and γ are the temperature and solar irradiance coefficients for the PV cell respectively. Hence the power output of the cell at maximum point for a given power density E_{pv} is [16],

$$P_{out} = P_{M,E_{pv}} = P_M^{STC}\frac{E_{pv}}{1000}\left[1+\beta\left(T_{pv}-25\right)\right] = \eta_{pv}P_{in} \quad (5)$$

where $P_{M,E_{pv}}$ is maximum power point at E_{pv}, P_M^{STC} is the maximum power point at standard test conditions, and $P_{in}=\eta_{pv}$. E_{pv} is the input power onto the PV cell.

In addition to losses due to increases in temperature, cells are also exposed to dust that block some of the sunlight and reduce power output. For California, generally, a typical annual power reduction factor due to dust of about 7% is assumed. The maximum power output of the total PV array is always less than the sum of the maximum output of the individual modules. This mismatch loss is at least 2%. Another 3% or more of power is also lost to resistance within the system wiring. Additional losses of 8-12% are imminent in the inverter when converting the DC power generated by the solar module into common household AC power. In this study, losses common to all the investigated configurations are ignored.

2.2. A single PV cell under direct sunlight (DPV)

Fig. 1: An a-Si PV cell

For a 10 cm diameter amorphous silicon (a-Si) PV solar cell, Fig. 1, subjected to $H_s=E_{pv}$=1000 W/m^2 solar radiation, the typical electrical parameters under standard test conditions (STC) of AM1.5, E_{STC}=1000 W/m2, T_a=25 ^{o}C [17] are given by manufacturer as [18]:

Short circuit current $I_{sc}^{STC}\approx 1.5\,\text{A}$, open circuit voltage $V_{oc}^{STC}=0.887\,\text{V}$, nominal operating cell temperature T_{nom}=50 ^{o}C, fill factor FF=0.741, and nominal efficiency of the cell η_{nom}=13%.

Thus the maximum power at STC is $P_M^{STC}=FF.I_{sc}^{STC}.V_{oc}^{STC}=1.021\,\text{W}$.

The power on the PV cell can be estimated as,

$$P_{in}=H_sS_{pv}\approx 6.3\,\text{W} \quad (6)$$

Instant operating temperature of the PV cell under the assumed irradiance is calculated using equation (3), which yields T_{pv}=44 ^{o}C. The efficiency and output power of the PV cell at these operating conditions are calculated using equations (4) and (5) as η_{pv}=10.8% and P_{out}=0.85 W respectively. Fig. 2 shows efficiency and output power of PV cell as a function of the irradiance.

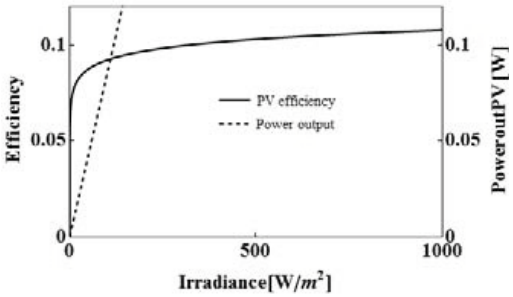

Fig. 2: The efficiency and output power of PV cell versus irradiance.

3. Photon transmission through fiber optics

Typically, optical fiber for communication purposes uses glass fiber with very small core diameters. On the other hand, more recent development work has concentrated on improving the light-propagating properties of larger core diameter fiber, made of plastic [19]. Large-core multimode fiber has the benefit of reducing the power density within the fiber. For high values of power density, nonlinear effects could increase the

attenuation losses, and therefore decrease the power-transmission efficiency [20].

In this study, it is assumed that the sunlight is transmitted as a mix of visible and UV light onto a PV solar cell by plastic optical fiber or fiber bundles after filtering light to minimize the IR radiation. The portion of the both visible and UV lights is about 55% of the total solar radiation. Heat removal filter transmittance for visible light is given as τ_{IR}=0.92 (425-675 nm at zero angle of incidence) [21]. The attenuation of the Plastic Optical Fiber (POF) is α=0.2 dB/m at λ=650 nm and in this study transmission of the POF at the visible range is chosen as τ_{fb}=1. The acceptance angle of fiber optics is θ_A=20° and thus the numerical aperture is $NA=n_{fb}.\sin\theta_A$ =0.5.

For more detailed analyses below, we consider various combinations with and without concentrators, filters, and fiber optics.

3.1. Use of a POF bundle

In this case study, direct sun light is transmitted on a PV cell by passing through a POF bundle of L=1 m in length. A fused fiber optics bundle, Fig.3, (r_{fb}=5 cm) carries the sunlight onto an r_{pv}=5 cm radius PV cell. The radius of the fiber cable is greater than the cable core. The fiber diameter is about 1.02 times the core radius. Thus, the surface area of the POF core is,

$$S_{fo} = \pi\, r_{fo}^2 \approx 8\times10^{-3}\,\mathrm{m}^2 \tag{7}$$

Incident light power on the fiber is,

$$P_{fo} = H_s \times S_{fo} \approx 7.85\ \mathrm{W} \tag{8}$$

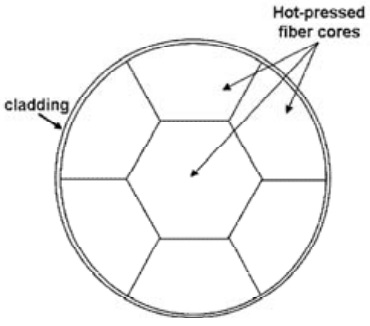

Fig. 3: A fused POF bundle [22]

The refractive index of the fiber core and the air are n_{fo}=1.49 and n_{air}=1.003 respectively [21]. Fresnel losses also occur at both the entrance and exit ends of the fibers. But in this study, the fiber bundle is assumed to be glued to the PV cell, and therefore the exit loss is ignored. Thus the light reflection is only on the entrance of the fiber cable. Then the reflection coefficient is,

$$R_{loss} = \left(\frac{n_{fo} - n_{air}}{n_{fo} + n_{air}}\right)^2 \approx 3.82\,\% \tag{9}$$

Power into the POF bundle is,

$$P_{\mathrm{into}} = (1 - R_{loss}) \times P_{fo}(\mathrm{W}) \approx 7.55\ \mathrm{W}\,. \tag{10}$$

The power transmitted to the end face of the POF is,

$$P_{\mathrm{tr}} = P_{\mathrm{into}} 10^{-a_{dB}L/10} \approx 7.21\,\mathrm{W}\,. \tag{11}$$

This value is the input power to the PV cell at the same time, P_{in} = 7.21 W. Efficiency of the fiber optic is calculated as,

$$\eta_{fo} = P_{tr} / P_{fo} \approx 92\,\%\,. \tag{12}$$

The power density on the PV cell is calculated as,

$$E_{pv} = P_{\mathrm{tr}} / S_{pv} \approx 918.6\ \mathrm{W/m^2}\,. \tag{13}$$

The working temperature of the PV cell is calculated as T_{pv} = 42 °C by using equation (3). The efficiency and output power of the PV cell at this operating condition are calculated as $\eta_{pv} \approx 11\,\%$ and $P_{out} \approx 0.79\,\mathrm{W}$ using equations (4) and (5). Thus, the overall system efficiency is,

$$\eta = \eta_{fo}\eta_{pv} \approx 10.1\ \% \tag{14}$$

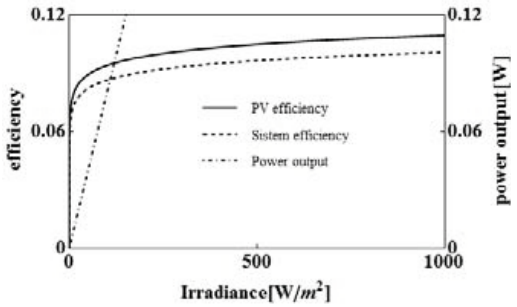

Fig.4: PV system performance.

Fig. 4 shows power output and efficiencies of PV cell for this case. Fig. 4 is determined using equations (4), (5), and (14).

3.2. Transmission of filtered light onto PV cell using a POF bundle

In this case it is assumed that the direct sunlight is filtered by an IR filter which has the same radius of fiber. Transmittance of IR filter is τ_{IR}=0.85 (480-680 nm) and its maximum operating temperature is 250 ^{o}C [21]. Incident light power on the filter is,

$$P_{IR} = H_s \times S_{IR} \approx 7.85 \text{ W} \quad (15)$$

The refractive index of the IR filter and the air are n_{IR}=1.472 and n_{air}=1.003 respectively [21]. In this study, fiber bundle is assumed to be glued on the IR filter and the PV cell. Therefore, Fresnel losses are ignored.

The power on the POF bundle is calculated as,

$$P_{\text{into}} = 0.55 \times \tau_{IR} \times (1 - R_{loss}) P_{IR} (\text{W}) \approx 3.54 \text{ W} \quad (16)$$

Below, steps involving equation (11) through equation (14) are employed and the efficiency and output power of the PV cell at the operating condition are determined using equations (4) and (5) as η_{pv}=11.5% and P_{out}=0.41 W, at T_{pv}=33 ^{o}C. Thus, the overall system efficiency is,

$$\eta = \tau_{IR} \eta_{fo} \eta_{pv} \approx 9.3 \ \% \quad (17)$$

4. Concentrated transmission

The primary goal of using concentrators in a PV-driven energy conversion is to focus sunlight on a small receiver, thus is to reduce the cell area by the concentration ratio (Fig.5). This allows replacement of cell surface by roughly an equivalent of the concentrator surface.

Fiber optic solar energy concentration complemented with some level of filtering could offer more progressive and economically feasible ways of taking the advantages of concentrating solar energy without predicaments of high temperature that accompany such concentration. The high flux solar energy transmission by a flexible fiber optic bundle, the possibility of filtering and excluding the undesired radiation range, and the research on the associated materials will surely expand and benefit solar energy conversion. Various types and technologies of solar collectors have been developed to operate both at low and high temperature ranges. Optical concentration systems have been investigated with the aim of reducing the cost of PV-driven solar energy conversion.

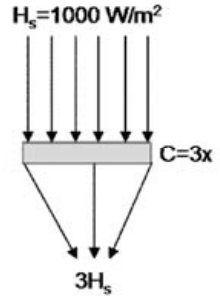

Fig.5: Concentration of Solar light.

4.1. Transmission of concentrated light onto PV cell using a POF bundle

Fresnel lenses are optical devices for solar radiation concentration, used in conjunction with thermal collectors and PVs. Acrylic Fresnel lenses in particular possess attractive features such as low volume and weight, smaller focal length, and lower cost compared to other lenses. Natural cooling of these lenses is sufficient to avoid harmful temperature range, [9]. The maximum operating temperature of a Fresnel lens is about 80 ^{o}C.

In this case, a fused bundle is considered to transmit the light, which is concentrated by an acrylic Fresnel lens. The Fresnel lens has τ_l=0.92 optical efficiency, which is transmission of the lens and the refraction index of Fresnel lens is n_l=1.49 [21].

The geometric concentration ratio of the lens is given as,

$$\text{C} = \frac{S_l}{S_{fo}} = \left(\frac{r_l}{r_{fo}} \right)^2 = 3 \times \quad (18)$$

where S_l and S_{fo} are the surface areas and r_l and r_{fo} are the radius of the Fresnel lens and the fiber

bundle respectively. It is assumed that the lens can magnify the light by three factor, which equals the geometric concentration ratio. Therefore, if the radius of a fiber optic bundle is 5cm, then the radius of the lens has to be r_l = 8.7cm. The surface area of the lens is about S_l=0.024 m^2.

In a similar fashion as for the previous cases, equations (6) through (11) are used to determine the input power to PV cell, yielding P_{in} = 19.3 W, E_{pv} = 2461 W/m^2 (~2.5 suns), and η_{fb} = 0.95. The working temperature of the PV cell is T_{pv} = 70 ^{o}C. The efficiency and output power of the PV cell at this operating condition are calculated using equations (4) and (5) as η_{pv} = 8.3%, P_{out} = 1.5 W. The overall system efficiency is then, $\eta = \tau_l \eta_{fb} \eta_{pv}$ = 7.3%.

4.2. Using concentrated and filtered light through a POF bundle

In this case, a concentrated and then filtered solar light is transmitted onto a PV cell using a POF bundle. For non-fused bundles, Fig. 6, the interstitial light leakage area accounts for about 10.3% of the total facet area. For this reason non-fused bundles are less preferred [22]. The efficiency and output power of the PV cell at T_{pv} = 46 ^{o}C is calculated using equations (4) and (5). This offered η_{pv} = 10.6%, P_{out} = 0.95 W, and a system efficiency of η = 7.9%.

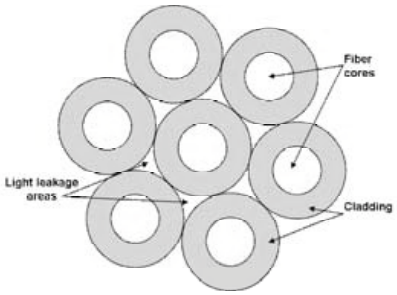

Fig. 6: A non-fused (mechanical) bundle of POF [22].

5. PV conversion without POF

In these cases, the scenarios without using plastic optical fibers (POF) are investigated by means of solar PV conversion.

5.1. Transmission of filtered light

For this scenario, the direct solar radiation is transferred after filtering by using IR filter. The efficiency and output power of the PV cell at this operating condition is calculated using equations (4) and (5). This offered η_{pv} = 11.4%, P_{out} = 0.42 W, and a system efficiency of η = 9.7% at T_{pv} = 34 ^{o}C.

5.2. Transmission of concentrated light

For this scenario, the direct solar radiation is transferred after concentration using a Fresnel lens. As above, the efficiency and output power of the PV cell at this operating condition are calculated using equations (4) and (5). This gave η_{pv} = 8.0%, P_{out} = 1.54 W, and a system efficiency of η = 7.4% at T_{pv}=73 ^{o}C.

5.3. Using concentrated, filtered light

For this scenario, the direct solar radiation is transferred after concentrating and filtering, using a Fresnel lens and a IR filter respectively. The efficiency and output power of the PV cell at this operating condition is calculated using equations (4) and (5). This resulted in η_{pv} = 10.5%, P_{out} = 0.98 W, and a system efficiency of η = 8.2% at T_{pv} = 47 ^{o}C.

Material selection: The price of a 1-mm diameter solar fiber is about $0.58 /m [23]. It has been argued that the optical fiber temperature will reach a critical point at the fiber inlet unless some type of IR filtering is used. Tekelioglu [24] evaluated a number of different filtering and cooling methods and concluded that two techniques could be economical and effective. For cost calculations the component prices are assumed to be: Fresnel lens $65/m^2, IR cut off filter $23/m^2, POF $0.58/m and PV cell (panel) $520/m^2.

Results and conclusion

Simulated results are shown in Table 1, and cost data for PV system components are presented in Table 2.

In Table 1, PV temperature differences and % power changes are calculated using the formulas $\Delta T_{pv} = T_{pv} - T_{pv}(DPV)$ and $\%P_{out} = \frac{P_{out} - P_{out}(DPV)}{P_{out}(DPV)}$ respectively, where DPV refers the direct PV results.

Below we summarize results for seven scenarios listed as case studies 1 through 7:

1. Transmission of light onto PV cell using a POF bundle,
2. Transmission of filtered light onto PV cell using a POF bundle,
3. Transmission of concentrated light onto PV cell using a POF bundle,
4. Transmission of concentrated and filtered light onto PV cell using a POF bundle,
5. Transmission of filtered light onto PV cell,
6. Transmission of concentrated light onto PV cell,
7. Transmission of concentrated and filtered light onto PV cell.

Table 1: Simulated results of all scenarios

Case #	P_{out} (W)	η_{pv} (%)	η (%)	T_{pv} (^oC)	ΔT_{pv} (^oC)	% P_{out} change
DPV	0.85	10.8	10.8	44	0	0
1	0.79	11	10.1	42	-2	-7.1
2	0.41	11.5	9.3	33	-11	-51.8
3	1.5	8.3	7.3	70	26	76.5
4	0.95	10.6	7.9	46	2	11.8
5	0.42	11.4	9.7	34	-10	-50.6
6	1.54	8.0	7.4	73	29	81.2
7	0.98	10.5	8.2	47	3	15.3

Table 2: Cost data

Case #	Con.	Filter	Fiber	PV	Total ($/W)
DPV	-	-	-	✓	4.89
1	-	-	✓	✓	1840.71
2	-	✓	✓	✓	3547.18
3	✓	-	✓	✓	970.52
4	✓	✓	✓	✓	1532.60
5	-	✓	-	✓	10.34
6	✓	-	-	✓	3.76
7	✓	✓	-	✓	6.09

It is concluded that a PV system using optically filtered solar energy is more efficient than direct or concentrated PV systems. But a concentrated PV system is more cost effective than the other systems.

Under the sun's ray, solar panels degrade over time as a result of ultraviolet and infrared waves. Solar panels are also exposed to the ambient weather which may affect their lifetime and performances. Lifetime may not be a serious problem - solar power systems have typically a design lifespan of about 30 years. In fact crystalline and thin film modules are typically under warranty for 20-25 years. These are based on manufacturers' statements, and more field data are required to substantiate these claims. Many factors such as degradation effects, wind, dust, breakdown of a module's encapsulant, gradual obscurations between the modules are ignored in this study.

References

[1] Schlegel, G. O., Burkholder, F. W., Klein, S. A., Beckman, W.A., Wood, B.D., and Muhs, J. D., 2004, Analysis of a full spectrum hybrid lighting system, Solar Energy, 76, 359-368.

[2] Sansoni, P., Francini, F., Fontani, D., Mercatelli, L., and Jafrancesco ,D., 2008, Indoor illumination by solar light collectors, Lighting Res.Technol., 40, 323-332.

[3] Savovic, S., and Djordjevich, A., 2008, Calculation of the coupling coefficient in strained step index plastic optical fibers, Appl. Optics, 47:27, 4935-4939.

[4] Cao, H., Chen, Y., Zhou, Z., and Zhang, G., 2005, General models of optical-fiber-bundle displacement sensors, Microwave and Optical Tech. Lett., 47:5, 494-497.

[5] DiBerardino, D., Rafac, R. J., Boone, S., Gerginov, V. P., and Tanner, C. E., 2002, Construction of fiber-optic bundle light-collection systems and calculations efficiency, Optics Comm., 210, 233-243.

[6] Segal, A., Epstein, M., and Yogev, A., 2004, Hybrid concentrated photovoltaic and thermal power conversion at different spectral bands, Solar Energy, 76, 591-601.

[7] Rahman, F., Farmer, C. D., Schmidt, C., Pfaff, G., and Stanley, C. R., 2008, Heat blocking gallium arsenide solar cells, Appl.Phys. A, 90, 231-236.

[8] Toivola, M., Ferenets, M., Lund, P., and Harlin, A., 2009, Photovoltaic fiber, Thin Solid Films, 517, 2799-2802.

[9] Ferriere, A., Rodriguez, G. P., and Sobrino, J. A., 2004, Flux distribution delivered by a Fresnel lens

used for concentrating solar energy, Trans. of the ASME, 126, 654-660.

[10] Pedrotti, F. L. S. J., and Pedrotti, L. S., 1997 Introduction to optics, 2nd Ed., Prentice-Hall International, Inc., NJ.

[11] Zubia, J., and Arrue, J., 2001, Plastic Optical Fibers: An Introduction to Their Technological Processes and Applications, Optical Fiber Technology 7, 101-140.

[12] Ziemann, O., Krauser, J., Zamzow, P. E., and Daum, W., 2008, POF Handbook Optical Short Range Transmission Systems, Springer-Verlag Berlin.

[13] Martinelli, G., and Stefancich, M. at Luque, A., and Andreev, V., 2007, Concentrator Photovoltaics, Springer, Berlin.

[14] Min, C., Nuofu, C., Xiaoli, Y., Yu, W., Yiming, B. and Xingwang, Z., 2009, Thermal analysis and test for single concentrator solar cells, J.Semiconductors, 30,4,044011(1-4).

[15] Notton, V., Cristofari, C., Mattei, M., and Poggi, P., 2005, Modelling of a double-glass photovoltaic module using finite differences, Applied Thermal Engineering, 25,2854-2877.

[16] Rosell, J. I., and Ibanez, M., 2006, Modelling power output in photovoltaic modules for outdoor operating conditions, Energy Conversion and Management, 47, 2424–2430.

[17] Würfel, P. 2005, Physics of Solar Cells, Wiley-VCH Verlag GmbH&Co.KGaA, Weinheim.

[18] Green, A. M., and Emery, K., 1994, Solar Efficiency Tables (Version 3), Prog.in PVs:Research and Applications, 2, 27-34.

[19] Grise, W., and Patrick, C., 2003, Passive solar lighting using fiber optics, J. Industrial Tech., 19:1,1-7.

[20] Pena, R., Algora, C., Matias, I. R., and Lopez-Amo, M., 1999, Fiber-based 205-mV (27% efficiency) power-delivery system for an all-fiber network with optoelectronic sensor units, Appl. Optics, 38:12, 2463-2466.

[21] http://www.edmundoptics.com, (02.17.2010).

[22] Anton, I., Silva, D., Sala, G., Bett, A. W., Siefer, G., Luque-Heredia, I., and Trebst, T., 2007, The PV-FIBRE concentrator: A system for indoor operation of 1000X MJ solar cells, Prog. in Photovoltaics:Research and Apllications, 15, 431-447.

[23] Kribus, A., Zik, O., and Karni, J., 2000, Optical fibers and solar power generation, Solar Energy, 68:5, 405-416.

[24] Tekelioglu, M., and Wood, B. D., 2007, Thermal management for a poly (methyl acrylate) optical fiber in solar lighting, J Thermal Analysis and Calorimetry, 87:2, 529-537.

A new thermal-hydraulic process for solar cooling

Matthieu Martins[a,b], Sylvain Mauran[a,b], Driss Stitou[a]

[a.] *PROMES Laboratory, UPR CNRS 8521, Rambla de la Thermodynamique, Tecnosud, 66100 Perpignan Cedex, France.*

[b.] University of Perpignan UPVD, 52 avenue Paul Alduy, 66860 Perpignan cedex 9

Abstract: Air conditioning is usually realized by electricity-powered mechanical vapor compression cycles. However, during the summer the demand for electricity increases drastically because of the extensive use of these systems. This paper presents a novel and innovative solar cooling process (so-called CHV3T) for air-conditioning for individual buildings using common flat plate collectors. The principle of the process is based on an original coupling between two dithermal thermodynamic cycles. The engine cycle and the reverse cycle, which are respectively a Rankine-like cycle and a reverse Rankine cycle, use their own working fluid (HFC's) and their performances are close to Carnot cycles. The coupling of these dithermal cycles allows obtaining a global tri-thermal system with an internal work transfer realized by an inert liquid LT which plays the role of a liquid piston. This new system appears as an attractive alternative for solar cooling technologies due to its ability to use low temperature driving heat source. Several versions of the thermo-hydraulic system has been investigated in order to obtain the best cost-effective compromise for an individual building application. A modelling of a solar process coupled with 20 m² of flat plate solar collectors and providing 5 kW cooling capacity is developed by using the concept of Equivalent Gibbs Systems. This method, issued from thermodynamics of irreversible processes is applied here to describe the dynamic behaviour of all the components of the system. This model allows determining the performances of the machine on the stationary and non-stationary regimes. The pressure, temperature and thermal powers evolutions are observed during the cyclic operating in all the components of the system. The performances seem to be very competitive with existing solar cooling systems. A 5 kW cooling capacity prototype is under construction and will be in operation during the next summer.

Keywords: *Solar cooling, Thermo-hydraulic process, Gibbs systems dynamics.*

1. Introduction

In recent times, efforts were made in developing environmental-friendly technologies. Indeed, in Europe, the services buildings represent 40% of primary energy consumption [1]. During the last years the energy consumption for air-conditioning has increased drastically in industrialized countries. Solar cooling systems are one of the most apparent applications of renewable energy to reduce this increasing energy demand and moreover to reduce the peak loads for electricity utilities [2]. Furthermore the use of solar thermal energy for cooling allows synchronization between cooling needs and solar energy availability.

There are many different ways to convert solar energy into cooling process. The dominating type of thermally driven cooling technology is the sorption-type system [3-4]. However, this technology is cost-effective for high cooling capacity. There are very few available systems in the low cooling power range, i.e. below 10 kW. This paper presents a novel solar cooling process (so-called CHV3T) using common flat plate collectors. A 5 kW cooling capacity process coupled to 20 m² of flat plate solar collectors is studied here. This new equipment in this power range will open up a new market opportunity for solar cooling technology in domestic area.

First the study describes the principle of the thermal-hydraulic process and the different versions in order to optimize the process performances. A dynamic modelling is established with the intention of demonstrating the feasibility of such an innovative process. This dynamic modelling uses the concept of Equivalent Gibbs systems which has been developed recently [5] for highly unstationnary processes simulations.

2. Process

2.1. Principle

The principle of the process is based on an original coupling between two thermodynamic cycles: an engine cycle M that produces the work W from the

Corresponding Author : Martins Matthieu, Email : matthieu.martins@univ-perp.fr

heat supplied by flat plate collectors and a reverse cycle R that consumes this work enabling thus a cooling production. The work transfer is originally realized by an inert liquid LT which plays the role of a liquid piston. So, the two cycles are associated by a hydraulic coupling. The coupling of the two dithermal cycles allows obtaining a global tri-thermal system with an internal work transfer. The system exchanges heat with the environment at three temperature levels : a high temperature ($T_h \approx 70°C$) delivered by solar collectors, an intermediate temperature ($T_m \approx 32°C$) that corresponds to the outdoor temperature and a low temperature ($T_b \approx 12°C$) at which is produced the cooling effect. A schematic diagram in Fig. 1 represents this original coupling between the two dithermal machines.

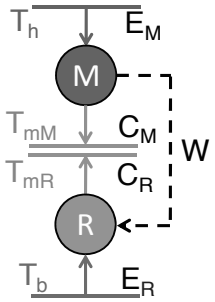

Fig. 1. Schematic diagram of the coupling between two dithermal machines.

Each machine (M or R) is composed of classical components of thermodynamic cycles: a condenser C, an evaporator E, a separating receiver BS and a "transfer cylinder" CT. Fig. 2 shows the schematic diagram of the coupled system. The liquid also called "liquid of transfer" LT, contained in the two transfer cylinders, flows alternatively from one cylinder to the other. It acts like a liquid piston and allows the work transfer.

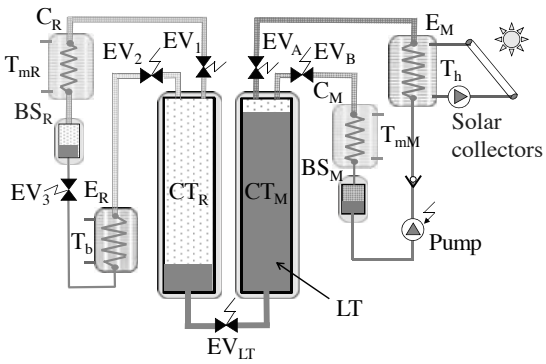

Fig. 2. Schematic diagram of the system CHV3T

2.2. The CHV3T cycle

The engine cycle and the reverse cycle, which are respectively a Rankine-like cycle and a reverse Rankine cycle use their own working fluid (HFC's) and their performances are close to Carnot cycles. The work transfer occurs at a constant pressure (at P_h or P_b) between the two machines M and R during the isothermal phases of two cycles, a description of these operations is given on a Ln(P)-h diagram in Fig. 3.

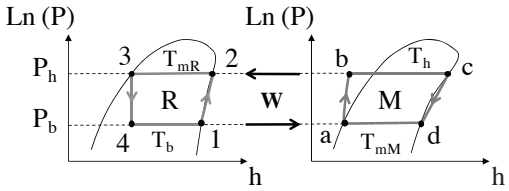

Fig. 3. Drawing of engine cycle (M) and reverse cycle (R) in the (Ln(P)- h) diagram

- Phase 1→2: At the opening of the valve EV_1, there is a communication between the cylinder CT_R, the condenser C_R and the receiver BS_R in which the fluid R is at high pressure P_h. Then, the pressure in the cylinder CT_R is quickly imposed by the liquid-vapor equilibrium of the fluid R in the bottle BS_R. The heat necessary for the evaporation of the fluid in BS_R is supplied at ambient temperature T_{mR}. During this short phase the condenser C_R acts as an evaporator.

- Phase 2→3 and a→b→c: The fluid M contained in the bottle BS_M in liquid state is drained off and compressed by a circulator, and brought into the evaporator E_M in which the pressure is P_h. The fluid M is heated and then evaporates at T_h by the heat supplied by the solar collectors Q_h. As the saturated vapour occupies a larger volume than the liquid state, the liquid LT in the cylinder CT_M is pushed down to the other cylinder CT_R when the valve EV_A is opened. The work of expansion during this evaporation phase is then transferred to the reverse cycle at a constant pressure P_h .

As the liquid LT in the cylinder CT_R is pushed forward, the saturated vapour of the fluid R condenses in C_R and the condensate accumulates in BS_R. The heat of condensation Q_{mR} of fluid R is released at the outdoor temperature T_{mR}, Fig. 4a.

- Phase c→d: The valve EV_A is closed and the valve EV_B is opened. The pressure of the working fluid in the cylinder CT_M that was previously equal to P_h, decreases rapidly to the value imposed by the

liquid-vapor equilibrium in the condenser C_M. The heat of condensation is evacuated outwards at T_{mM} and the condensate of the fluid M accumulates in the bottle BS_M.

- Phase 3→4→1 and d→a: The working liquid of reverse cycle R contained in the bottle BS_R at the pressure P_h flows though a throttling device EV_3 from the receiver BS_R to evaporator E_R at low pressure P_b. The liquid is then evaporated in E_R producing the cooling effect Q_b at T_b. The produced saturated vapor of the fluid R push down the liquid LT in the cylinder CT_R to the cylinder CT_M. The expansion work produced by this evaporation phase is transferred to the engine cycle at constant pressure P_b.

As the liquid LT in the cylinder CT_M is pushed forward, saturated vapor of fluid M condenses in C_M and the condensate are accumulated in BS_M. The heat of condensation Q_{mM} of fluid M is released at the outdoor temperature T_{mM}, Fig. 4b.

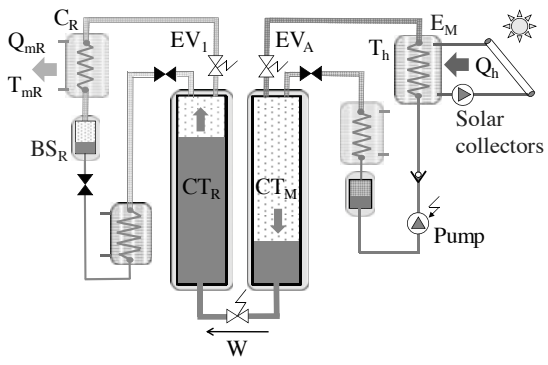

Fig. 4a : Representation of the work transfer at P_h

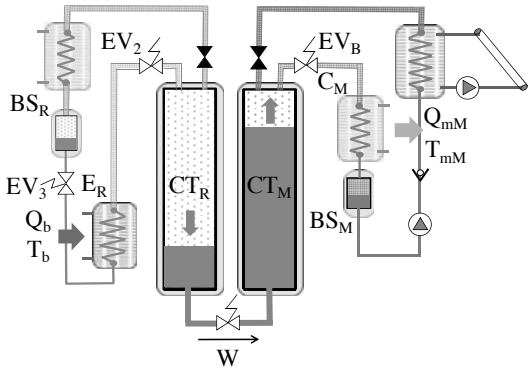

Fig. 4b : Representation of the work transfer at P_b

2.3. Optimization by an internal work recovery

An other version called "CHV3T-WL"of the system CHV3T has been studied. In this new configuration, there are two additional cylinders $CT_{M'}$ and $CT_{R'}$, and additional solenoid valves in order to make the machine operate with two cycles in phase opposition. When a cycle execute a work transfer from the engine cycle to the reverse cycle at the high pressure P_h, in the same time the other cycle in phase opposition perform a work transfer from the reverse cycle to the engine cycle at the low pressure P_b. In this way, evaporators and condensers are in continuous operation. The cooling effect is almost produced continuously. Moreover, the CHV3T's cycle include a new phase allowing users to implement an internal work recovery during the pressurization / depressurization steps of cycles. This step occurrs just after the work transfer at the high pressure P_h. During this new phase the valves $EV_{M'}$, EV_I and EV_R are opened. This connection enables to recover some work during the phase 1→2 in the reverse cycle thanks to an equalization of the pressure between the cylinder $CT_{M'}$ at the pressure P_h and the cylinder CT_R at the pressure P_b. This CHV3T-WL configuration is shown in the Fig. .

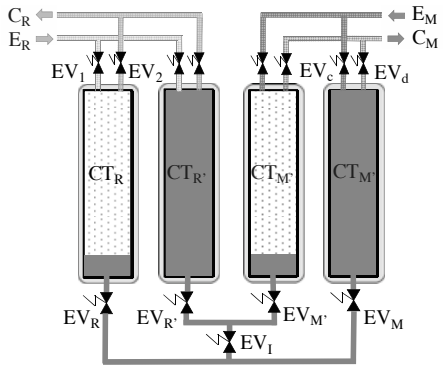

Fig. 5. A part of schematic diagram of the system CHV3T – WL

The heat of condensation rejected to the ambient during the phase c→d is in this version partially recovered by the receiver cycle as show in the Fig. .

attenuation losses, and therefore decrease the power-transmission efficiency [20].

In this study, it is assumed that the sunlight is transmitted as a mix of visible and UV light onto a PV solar cell by plastic optical fiber or fiber bundles after filtering light to minimize the IR radiation. The portion of the both visible and UV lights is about 55% of the total solar radiation. Heat removal filter transmittance for visible light is given as τ_{IR}=0.92 (425-675 nm at zero angle of incidence) [21]. The attenuation of the Plastic Optical Fiber (POF) is α=0.2 dB/m at λ=650 nm and in this study transmission of the POF at the visible range is chosen as τ_{fb}=1. The acceptance angle of fiber optics is θ_A=20° and thus the numerical aperture is $NA=n_{fb}.\sin\theta_A$ =0.5.

For more detailed analyses below, we consider various combinations with and without concentrators, filters, and fiber optics.

3.1. Use of a POF bundle

In this case study, direct sun light is transmitted on a PV cell by passing through a POF bundle of L=1 m in length. A fused fiber optics bundle, Fig.3, (r_{fb}=5 cm) carries the sunlight onto an r_{pv}=5 cm radius PV cell. The radius of the fiber cable is greater than the cable core. The fiber diameter is about 1.02 times the core radius. Thus, the surface area of the POF core is,

$$S_{fo} = \pi\, r_{fo}^2 \approx 8\times10^{-3}\,\mathrm{m}^2 \tag{7}$$

Incident light power on the fiber is,

$$P_{fo} = H_s \times S_{fo} \approx 7.85\ \mathrm{W} \tag{8}$$

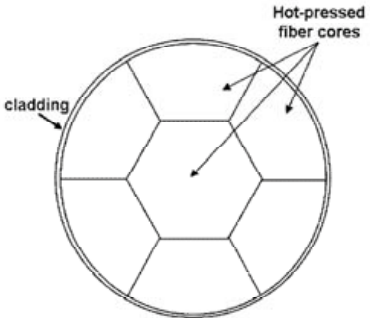

Fig. 3: A fused POF bundle [22]

The refractive index of the fiber core and the air are n_{fo}=1.49 and n_{air}=1.003 respectively [21]. Fresnel losses also occur at both the entrance and exit ends of the fibers. But in this study, the fiber bundle is assumed to be glued to the PV cell, and therefore the exit loss is ignored. Thus the light reflection is only on the entrance of the fiber cable. Then the reflection coefficient is,

$$R_{loss} = \left(\frac{n_{fo} - n_{air}}{n_{fo} + n_{air}}\right)^2 \approx 3.82\,\% \tag{9}$$

Power into the POF bundle is,

$$P_{\mathrm{into}} = (1 - R_{loss}) \times P_{fo}(\mathrm{W}) \approx 7.55\ \mathrm{W}\,. \tag{10}$$

The power transmitted to the end face of the POF is,

$$P_{\mathrm{tr}} = P_{\mathrm{into}} 10^{-a_{dB}L/10} \approx 7.21\,\mathrm{W}\,. \tag{11}$$

This value is the input power to the PV cell at the same time, P_{in} = 7.21 W. Efficiency of the fiber optic is calculated as,

$$\eta_{fo} = P_{tr} / P_{fo} \approx 92\,\%\,. \tag{12}$$

The power density on the PV cell is calculated as,

$$E_{pv} = P_{\mathrm{tr}} / S_{pv} \approx 918.6\ \mathrm{W/m^2}\,. \tag{13}$$

The working temperature of the PV cell is calculated as T_{pv} = 42 °C by using equation (3). The efficiency and output power of the PV cell at this operating condition are calculated as $\eta_{pv} \approx 11\,\%$ and $P_{out} \approx 0.79\,\mathrm{W}$ using equations (4) and (5). Thus, the overall system efficiency is,

$$\eta = \eta_{fo}\eta_{pv} \approx 10.1\ \% \tag{14}$$

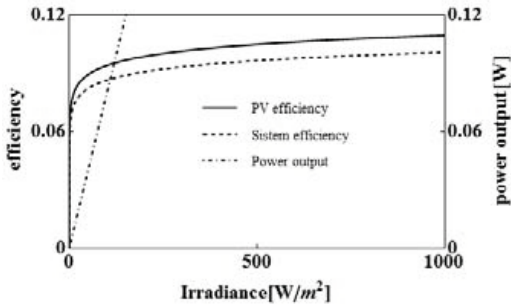

Fig.4: PV system performance.

Fig. 4 shows power output and efficiencies of PV cell for this case. Fig. 4 is determined using equations (4), (5), and (14).

3.2. Transmission of filtered light onto PV cell using a POF bundle

In this case it is assumed that the direct sunlight is filtered by an IR filter which has the same radius of fiber. Transmittance of IR filter is τ_{IR}=0.85 (480-680 nm) and its maximum operating temperature is 250 ^{o}C [21]. Incident light power on the filter is,

$$P_{IR} = H_s \times S_{IR} \approx 7.85 \text{ W} \quad (15)$$

The refractive index of the IR filter and the air are n_{IR}=1.472 and n_{air}=1.003 respectively [21]. In this study, fiber bundle is assumed to be glued on the IR filter and the PV cell. Therefore, Fresnel losses are ignored.

The power on the POF bundle is calculated as,

$$P_{\text{into}} = 0.55 \times \tau_{IR} \times (1 - R_{loss}) P_{IR} (\text{W}) \approx 3.54 \text{ W} \quad (16)$$

Below, steps involving equation (11) through equation (14) are employed and the efficiency and output power of the PV cell at the operating condition are determined using equations (4) and (5) as η_{pv}=11.5% and P_{out}=0.41 W, at T_{pv}=33 ^{o}C. Thus, the overall system efficiency is,

$$\eta = \tau_{IR} \eta_{fo} \eta_{pv} \approx 9.3 \ \% \quad (17)$$

4. Concentrated transmission

The primary goal of using concentrators in a PV-driven energy conversion is to focus sunlight on a small receiver, thus is to reduce the cell area by the concentration ratio (Fig.5). This allows replacement of cell surface by roughly an equivalent of the concentrator surface.

Fiber optic solar energy concentration complemented with some level of filtering could offer more progressive and economically feasible ways of taking the advantages of concentrating solar energy without predicaments of high temperature that accompany such concentration. The high flux solar energy transmission by a flexible fiber optic bundle, the possibility of filtering and excluding the undesired radiation range, and the research on the associated materials will surely expand and benefit solar energy conversion. Various types and technologies of solar collectors have been developed to operate both at low and high temperature ranges. Optical concentration systems have been investigated with the aim of reducing the cost of PV-driven solar energy conversion.

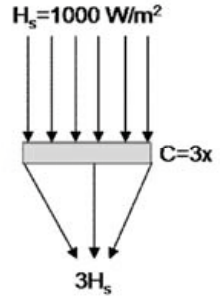

Fig.5: Concentration of Solar light.

4.1. Transmission of concentrated light onto PV cell using a POF bundle

Fresnel lenses are optical devices for solar radiation concentration, used in conjunction with thermal collectors and PVs. Acrylic Fresnel lenses in particular possess attractive features such as low volume and weight, smaller focal length, and lower cost compared to other lenses. Natural cooling of these lenses is sufficient to avoid harmful temperature range, [9]. The maximum operating temperature of a Fresnel lens is about 80 ^{o}C.

In this case, a fused bundle is considered to transmit the light, which is concentrated by an acrylic Fresnel lens. The Fresnel lens has τ_l=0.92 optical efficiency, which is transmission of the lens and the refraction index of Fresnel lens is n_l=1.49 [21].

The geometric concentration ratio of the lens is given as,

$$\text{C} = \frac{S_l}{S_{fo}} = \left(\frac{r_l}{r_{fo}} \right)^2 = 3 \times \quad (18)$$

where S_l and S_{fo} are the surface areas and r_l and r_{fo} are the radius of the Fresnel lens and the fiber

bundle respectively. It is assumed that the lens can magnify the light by three factor, which equals the geometric concentration ratio. Therefore, if the radius of a fiber optic bundle is 5cm, then the radius of the lens has to be r_l = 8.7cm. The surface area of the lens is about S_l=0.024 m^2.

In a similar fashion as for the previous cases, equations (6) through (11) are used to determine the input power to PV cell, yielding P_{in} = 19.3 W, E_{pv} = 2461 W/m^2 (~2.5 suns), and η_{fb} = 0.95. The working temperature of the PV cell is T_{pv} = 70 ^{o}C. The efficiency and output power of the PV cell at this operating condition are calculated using equations (4) and (5) as η_{pv} = 8.3%, P_{out} = 1.5 W. The overall system efficiency is then, $\eta = \tau_l \eta_{fb} \eta_{pv}$ = 7.3%.

4.2. Using concentrated and filtered light through a POF bundle

In this case, a concentrated and then filtered solar light is transmitted onto a PV cell using a POF bundle. For non-fused bundles, Fig. 6, the interstitial light leakage area accounts for about 10.3% of the total facet area. For this reason non-fused bundles are less preferred [22]. The efficiency and output power of the PV cell at T_{pv} = 46 ^{o}C is calculated using equations (4) and (5). This offered η_{pv} = 10.6%, P_{out} = 0.95 W, and a system efficiency of η = 7.9%.

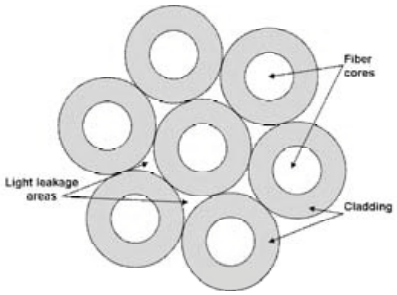

Fig. 6: A non-fused (mechanical) bundle of POF [22].

5. PV conversion without POF

In these cases, the scenarios without using plastic optical fibers (POF) are investigated by means of solar PV conversion.

5.1. Transmission of filtered light

For this scenario, the direct solar radiation is transferred after filtering by using IR filter. The efficiency and output power of the PV cell at this operating condition is calculated using equations (4) and (5). This offered η_{pv} = 11.4%, P_{out} = 0.42 W, and a system efficiency of η = 9.7% at T_{pv} = 34 ^{o}C.

5.2. Transmission of concentrated light

For this scenario, the direct solar radiation is transferred after concentration using a Fresnel lens. As above, the efficiency and output power of the PV cell at this operating condition are calculated using equations (4) and (5). This gave η_{pv} = 8.0%, P_{out} = 1.54 W, and a system efficiency of η = 7.4% at T_{pv}=73 ^{o}C.

5.3. Using concentrated, filtered light

For this scenario, the direct solar radiation is transferred after concentrating and filtering, using a Fresnel lens and a IR filter respectively. The efficiency and output power of the PV cell at this operating condition is calculated using equations (4) and (5). This resulted in η_{pv} = 10.5%, P_{out} = 0.98 W, and a system efficiency of η = 8.2% at T_{pv} = 47 ^{o}C.

Material selection: The price of a 1-mm diameter solar fiber is about $0.58 /m [23]. It has been argued that the optical fiber temperature will reach a critical point at the fiber inlet unless some type of IR filtering is used. Tekelioglu [24] evaluated a number of different filtering and cooling methods and concluded that two techniques could be economical and effective. For cost calculations the component prices are assumed to be: Fresnel lens $65/m^2, IR cut off filter $23/m^2, POF $0.58/m and PV cell (panel) $520/m^2.

Results and conclusion

Simulated results are shown in Table 1, and cost data for PV system components are presented in Table 2.

In Table 1, PV temperature differences and % power changes are calculated using the formulas $\Delta T_{pv} = T_{pv} - T_{pv}(DPV)$ and $\%P_{out} = \frac{P_{out} - P_{out}(DPV)}{P_{out}(DPV)}$ respectively, where DPV refers the direct PV results.

Below we summarize results for seven scenarios listed as case studies 1 through 7:

1. Transmission of light onto PV cell using a POF bundle,
2. Transmission of filtered light onto PV cell using a POF bundle,
3. Transmission of concentrated light onto PV cell using a POF bundle,
4. Transmission of concentrated and filtered light onto PV cell using a POF bundle,
5. Transmission of filtered light onto PV cell,
6. Transmission of concentrated light onto PV cell,
7. Transmission of concentrated and filtered light onto PV cell.

Table 1: Simulated results of all scenarios

Case #	P_{out} (W)	η_{pv} (%)	η (%)	T_{pv} (^oC)	ΔT_{pv} (^oC)	% P_{out} change
DPV	0.85	10.8	10.8	44	0	0
1	0.79	11	10.1	42	-2	-7.1
2	0.41	11.5	9.3	33	-11	-51.8
3	1.5	8.3	7.3	70	26	76.5
4	0.95	10.6	7.9	46	2	11.8
5	0.42	11.4	9.7	34	-10	-50.6
6	1.54	8.0	7.4	73	29	81.2
7	0.98	10.5	8.2	47	3	15.3

Table 2: Cost data

Case #	Con.	Filter	Fiber	PV	Total ($/W)
DPV	-	-	-	✓	4.89
1	-	-	✓	✓	1840.71
2	-	✓	✓	✓	3547.18
3	✓	-	✓	✓	970.52
4	✓	✓	✓	✓	1532.60
5	-	✓	-	✓	10.34
6	✓	-	-	✓	3.76
7	✓	✓	-	✓	6.09

It is concluded that a PV system using optically filtered solar energy is more efficient than direct or concentrated PV systems. But a concentrated PV system is more cost effective than the other systems.

Under the sun's ray, solar panels degrade over time as a result of ultraviolet and infrared waves. Solar panels are also exposed to the ambient weather which may affect their lifetime and performances. Lifetime may not be a serious problem - solar power systems have typically a design lifespan of about 30 years. In fact crystalline and thin film modules are typically under warranty for 20-25 years. These are based on manufacturers' statements, and more field data are required to substantiate these claims. Many factors such as degradation effects, wind, dust, breakdown of a module's encapsulant, gradual obscurations between the modules are ignored in this study.

References

[1] Schlegel, G. O., Burkholder, F. W., Klein, S. A., Beckman, W.A., Wood, B.D., and Muhs, J. D., 2004, Analysis of a full spectrum hybrid lighting system, Solar Energy, 76, 359-368.

[2] Sansoni, P., Francini, F., Fontani, D., Mercatelli, L., and Jafrancesco ,D., 2008, Indoor illumination by solar light collectors, Lighting Res.Technol., 40, 323-332.

[3] Savovic, S., and Djordjevich, A., 2008, Calculation of the coupling coefficient in strained step index plastic optical fibers, Appl. Optics, 47:27, 4935-4939.

[4] Cao, H., Chen, Y., Zhou, Z., and Zhang, G., 2005, General models of optical-fiber-bundle displacement sensors, Microwave and Optical Tech. Lett., 47:5, 494-497.

[5] DiBerardino, D., Rafac, R. J., Boone, S., Gerginov, V. P., and Tanner, C. E., 2002, Construction of fiber-optic bundle light-collection systems and calculations efficiency, Optics Comm., 210, 233-243.

[6] Segal, A., Epstein, M., and Yogev, A., 2004, Hybrid concentrated photovoltaic and thermal power conversion at different spectral bands, Solar Energy, 76, 591-601.

[7] Rahman, F., Farmer, C. D., Schmidt, C., Pfaff, G., and Stanley, C. R., 2008, Heat blocking gallium arsenide solar cells, Appl.Phys. A, 90, 231-236.

[8] Toivola, M., Ferenets, M., Lund, P., and Harlin, A., 2009, Photovoltaic fiber, Thin Solid Films, 517, 2799-2802.

[9] Ferriere, A., Rodriguez, G. P., and Sobrino, J. A., 2004, Flux distribution delivered by a Fresnel lens

used for concentrating solar energy, Trans. of the ASME, 126, 654-660.

[10] Pedrotti, F. L. S. J., and Pedrotti, L. S., 1997 Introduction to optics, 2nd Ed., Prentice-Hall International, Inc., NJ.

[11] Zubia, J., and Arrue, J., 2001, Plastic Optical Fibers: An Introduction to Their Technological Processes and Applications, Optical Fiber Technology 7, 101-140.

[12] Ziemann, O., Krauser, J., Zamzow, P. E., and Daum, W., 2008, POF Handbook Optical Short Range Transmission Systems, Springer-Verlag Berlin.

[13] Martinelli, G., and Stefancich, M. at Luque, A., and Andreev, V., 2007, Concentrator Photovoltaics, Springer, Berlin.

[14] Min, C., Nuofu, C., Xiaoli, Y., Yu, W., Yiming, B. and Xingwang, Z., 2009, Thermal analysis and test for single concentrator solar cells, J.Semiconductors, 30,4,044011(1-4).

[15] Notton, V., Cristofari, C., Mattei, M., and Poggi, P., 2005, Modelling of a double-glass photovoltaic module using finite differences, Applied Thermal Engineering, 25,2854-2877.

[16] Rosell, J. I., and Ibanez, M., 2006, Modelling power output in photovoltaic modules for outdoor operating conditions, Energy Conversion and Management, 47, 2424–2430.

[17] Würfel, P. 2005, Physics of Solar Cells, Wiley-VCH Verlag GmbH&Co.KGaA, Weinheim.

[18] Green, A. M., and Emery, K., 1994, Solar Efficiency Tables (Version 3), Prog.in PVs:Research and Applications, 2, 27-34.

[19] Grise, W., and Patrick, C., 2003, Passive solar lighting using fiber optics, J. Industrial Tech., 19:1,1-7.

[20] Pena, R., Algora, C., Matias, I. R., and Lopez-Amo, M., 1999, Fiber-based 205-mV (27% efficiency) power-delivery system for an all-fiber network with optoelectronic sensor units, Appl. Optics, 38:12, 2463-2466.

[21] http://www.edmundoptics.com, (02.17.2010).

[22] Anton, I., Silva, D., Sala, G., Bett, A. W., Siefer, G., Luque-Heredia, I., and Trebst, T., 2007, The PV-FIBRE concentrator: A system for indoor operation of 1000X MJ solar cells, Prog. in Photovoltaics:Research and Apllications, 15, 431-447.

[23] Kribus, A., Zik, O., and Karni, J., 2000, Optical fibers and solar power generation, Solar Energy, 68:5, 405-416.

[24] Tekelioglu, M., and Wood, B. D., 2007, Thermal management for a poly (methyl acrylate) optical fiber in solar lighting, J Thermal Analysis and Calorimetry, 87:2, 529-537.

A new thermal-hydraulic process for solar cooling

Matthieu Martins[a,b], Sylvain Mauran[a,b], Driss Stitou[a]

[a.] *PROMES Laboratory, UPR CNRS 8521, Rambla de la Thermodynamique, Tecnosud, 66100 Perpignan Cedex, France.*

[b.] University of Perpignan UPVD, 52 avenue Paul Alduy, 66860 Perpignan cedex 9

Abstract: Air conditioning is usually realized by electricity-powered mechanical vapor compression cycles. However, during the summer the demand for electricity increases drastically because of the extensive use of these systems. This paper presents a novel and innovative solar cooling process (so-called CHV3T) for air-conditioning for individual buildings using common flat plate collectors. The principle of the process is based on an original coupling between two dithermal thermodynamic cycles. The engine cycle and the reverse cycle, which are respectively a Rankine-like cycle and a reverse Rankine cycle, use their own working fluid (HFC's) and their performances are close to Carnot cycles. The coupling of these dithermal cycles allows obtaining a global tri-thermal system with an internal work transfer realized by an inert liquid LT which plays the role of a liquid piston. This new system appears as an attractive alternative for solar cooling technologies due to its ability to use low temperature driving heat source. Several versions of the thermo-hydraulic system has been investigated in order to obtain the best cost-effective compromise for an individual building application. A modelling of a solar process coupled with 20 m² of flat plate solar collectors and providing 5 kW cooling capacity is developed by using the concept of Equivalent Gibbs Systems. This method, issued from thermodynamics of irreversible processes is applied here to describe the dynamic behaviour of all the components of the system. This model allows determining the performances of the machine on the stationary and non-stationary regimes. The pressure, temperature and thermal powers evolutions are observed during the cyclic operating in all the components of the system. The performances seem to be very competitive with existing solar cooling systems. A 5 kW cooling capacity prototype is under construction and will be in operation during the next summer.

Keywords: *Solar cooling, Thermo-hydraulic process, Gibbs systems dynamics.*

1. Introduction

In recent times, efforts were made in developing environmental-friendly technologies. Indeed, in Europe, the services buildings represent 40% of primary energy consumption [1]. During the last years the energy consumption for air-conditioning has increased drastically in industrialized countries. Solar cooling systems are one of the most apparent applications of renewable energy to reduce this increasing energy demand and moreover to reduce the peak loads for electricity utilities [2]. Furthermore the use of solar thermal energy for cooling allows synchronization between cooling needs and solar energy availability.

There are many different ways to convert solar energy into cooling process. The dominating type of thermally driven cooling technology is the sorption-type system [3-4]. However, this technology is cost-effective for high cooling capacity. There are very few available systems in the low cooling power range, i.e. below 10 kW. This paper presents a novel solar cooling process (so-called CHV3T) using common flat plate collectors. A 5 kW cooling capacity process coupled to 20 m² of flat plate solar collectors is studied here. This new equipment in this power range will open up a new market opportunity for solar cooling technology in domestic area.

First the study describes the principle of the thermal-hydraulic process and the different versions in order to optimize the process performances. A dynamic modelling is established with the intention of demonstrating the feasibility of such an innovative process. This dynamic modelling uses the concept of Equivalent Gibbs systems which has been developed recently [5] for highly unstationnary processes simulations.

2. Process

2.1. Principle

The principle of the process is based on an original coupling between two thermodynamic cycles: an engine cycle M that produces the work W from the

Corresponding Author : Martins Matthieu, Email : matthieu.martins@univ-perp.fr

heat supplied by flat plate collectors and a reverse cycle R that consumes this work enabling thus a cooling production. The work transfer is originally realized by an inert liquid LT which plays the role of a liquid piston. So, the two cycles are associated by a hydraulic coupling. The coupling of the two dithermal cycles allows obtaining a global tri-thermal system with an internal work transfer. The system exchanges heat with the environment at three temperature levels : a high temperature ($T_h \approx 70°C$) delivered by solar collectors, an intermediate temperature ($T_m \approx 32°C$) that corresponds to the outdoor temperature and a low temperature ($T_b \approx 12°C$) at which is produced the cooling effect. A schematic diagram in Fig. 1 represents this original coupling between the two dithermal machines.

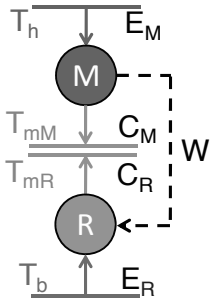

Fig. 1. Schematic diagram of the coupling between two dithermal machines.

Each machine (M or R) is composed of classical components of thermodynamic cycles: a condenser C, an evaporator E, a separating receiver BS and a "transfer cylinder" CT. Fig. 2 shows the schematic diagram of the coupled system. The liquid also called "liquid of transfer" LT, contained in the two transfer cylinders, flows alternatively from one cylinder to the other. It acts like a liquid piston and allows the work transfer.

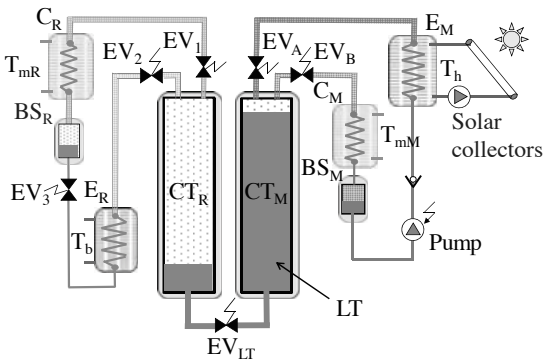

Fig. 2. Schematic diagram of the system CHV3T

2.2. The CHV3T cycle

The engine cycle and the reverse cycle, which are respectively a Rankine-like cycle and a reverse Rankine cycle use their own working fluid (HFC's) and their performances are close to Carnot cycles. The work transfer occurs at a constant pressure (at P_h or P_b) between the two machines M and R during the isothermal phases of two cycles, a description of these operations is given on a Ln(P)-h diagram in Fig. 3.

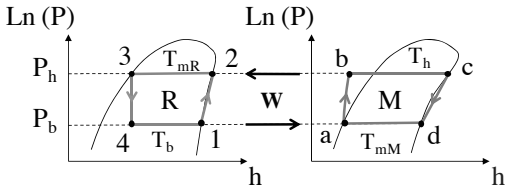

Fig. 3. Drawing of engine cycle (M) and reverse cycle (R) in the (Ln(P)- h) diagram

- Phase 1→2: At the opening of the valve EV_1, there is a communication between the cylinder CT_R, the condenser C_R and the receiver BS_R in which the fluid R is at high pressure P_h. Then, the pressure in the cylinder CT_R is quickly imposed by the liquid-vapor equilibrium of the fluid R in the bottle BS_R. The heat necessary for the evaporation of the fluid in BS_R is supplied at ambient temperature T_{mR}. During this short phase the condenser C_R acts as an evaporator.

- Phase 2→3 and a→b→c: The fluid M contained in the bottle BS_M in liquid state is drained off and compressed by a circulator, and brought into the evaporator E_M in which the pressure is P_h. The fluid M is heated and then evaporates at T_h by the heat supplied by the solar collectors Q_h. As the saturated vapour occupies a larger volume than the liquid state, the liquid LT in the cylinder CT_M is pushed down to the other cylinder CT_R when the valve EV_A is opened. The work of expansion during this evaporation phase is then transferred to the reverse cycle at a constant pressure P_h .

As the liquid LT in the cylinder CT_R is pushed forward, the saturated vapour of the fluid R condenses in C_R and the condensate accumulates in BS_R. The heat of condensation Q_{mR} of fluid R is released at the outdoor temperature T_{mR}, Fig. 4a.

- Phase c→d: The valve EV_A is closed and the valve EV_B is opened. The pressure of the working fluid in the cylinder CT_M that was previously equal to P_h, decreases rapidly to the value imposed by the

liquid-vapor equilibrium in the condenser C_M. The heat of condensation is evacuated outwards at T_{mM} and the condensate of the fluid M accumulates in the bottle BS_M.

- Phase 3→4→1 and d→a: The working liquid of reverse cycle R contained in the bottle BS_R at the pressure P_h flows though a throttling device EV_3 from the receiver BS_R to evaporator E_R at low pressure P_b. The liquid is then evaporated in E_R producing the cooling effect Q_b at T_b. The produced saturated vapor of the fluid R push down the liquid LT in the cylinder CT_R to the cylinder CT_M. The expansion work produced by this evaporation phase is transferred to the engine cycle at constant pressure P_b.

As the liquid LT in the cylinder CT_M is pushed forward, saturated vapor of fluid M condenses in C_M and the condensate are accumulated in BS_M. The heat of condensation Q_{mM} of fluid M is released at the outdoor temperature T_{mM}, Fig. 4b.

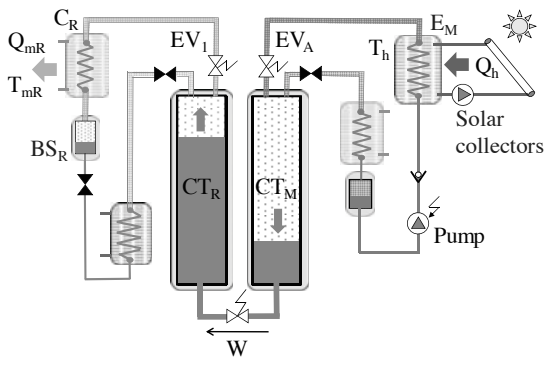

Fig. 4a : Representation of the work transfer at P_h

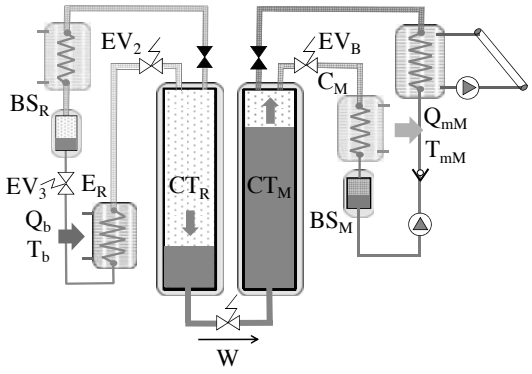

Fig. 4b : Representation of the work transfer at P_b

2.3. Optimization by an internal work recovery

An other version called "CHV3T-WL"of the system CHV3T has been studied. In this new configuration, there are two additional cylinders $CT_{M'}$ and $CT_{R'}$, and additional solenoid valves in order to make the machine operate with two cycles in phase opposition. When a cycle execute a work transfer from the engine cycle to the reverse cycle at the high pressure P_h, in the same time the other cycle in phase opposition perform a work transfer from the reverse cycle to the engine cycle at the low pressure P_b. In this way, evaporators and condensers are in continuous operation. The cooling effect is almost produced continuously. Moreover, the CHV3T's cycle include a new phase allowing users to implement an internal work recovery during the pressurization / depressurization steps of cycles. This step occurrs just after the work transfer at the high pressure P_h. During this new phase the valves $EV_{M'}$, EV_I and EV_R are opened. This connection enables to recover some work during the phase 1→2 in the reverse cycle thanks to an equalization of the pressure between the cylinder $CT_{M'}$ at the pressure P_h and the cylinder CT_R at the pressure P_b. This CHV3T-WL configuration is shown in the Fig. .

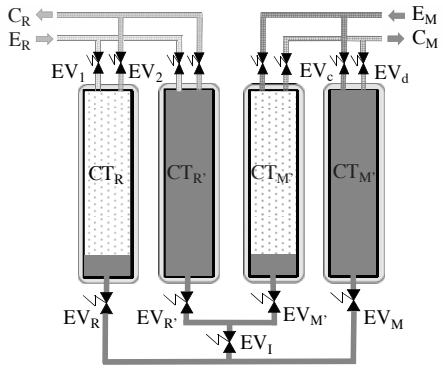

Fig. 5. A part of schematic diagram of the system CHV3T – WL

The heat of condensation rejected to the ambient during the phase c→d is in this version partially recovered by the receiver cycle as show in the Fig. .

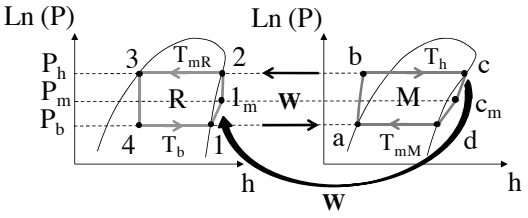

Fig. 6. Schematic internal work recovery between the engine cycle (M) and the reverse cycle (R) in the CHV3T – WL configuration

3. Dynamic process modeling

3.1. Gibbs systems dynamics

The concept of equivalent Gibbs systems, issued from thermodynamics of irreversible processes is applied here to describe the dynamic behavior of all the components of the system. The method consists in dividing the whole process in sub-systems and associate each real components with an equivalent Gibbs system supposed at uniform pressure and temperature.

This equivalent Gibbs system is defined by the two following considerations:

- At the thermodynamical equilibrium, the real and the equivalent component have the same extensive values (internal energy U, entropy S and mass m).
- For a given operating condition (usually the design point), the real and the equivalent Gibbs sub-system leads to the same entropy production.

For example, let us consider an evaporator or a condenser, which is composed of two phases of a pure substance, Fig. 7.

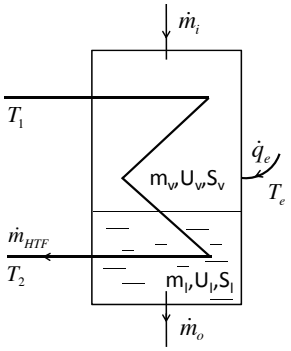

Fig. 7. A schematic equivalent Gibbs system

The equivalence conditions are expressed as:

$$\begin{aligned} U(T,p,m_l,m_v) &= U(T^*,p^*,m_l^*,m_v^*) = U^* \\ S(T,p,m_l,m_v) &= S(T^*,p^*,m_l^*,m_v^*) = S^* \\ \sigma_{irr} &= \sigma^*_{irr} \end{aligned} \quad \textbf{(1)}$$

where superscript (*) refers to the equivalent system, m_l is the mass of condensed liquid (kg) and m_v is the mass of vapor (kg).

The mass balance for liquid and vapor phases and the first and second laws are applied in this method:

$$\begin{cases} \dfrac{dm_l}{dt} = \dfrac{dm_l^*}{dt} = \dot{m}_i \cdot (1-x_i) + \dot{m}_o \cdot (1-x_o) + \dfrac{dm_x}{dt} \\ \dfrac{dm_v}{dt} = \dfrac{dm_v^*}{dt} = \dot{m}_i \cdot x_i + \dot{m}_o \cdot x_o + \dfrac{dm_x}{dt} \\ \dfrac{dU}{dt} = \dfrac{dU^*}{dt} = \dot{q}_e + \dot{m}_i \cdot h_i + \dot{m}_o \cdot h_o + \dot{m}_{HFT} \cdot (h_1 - h_2) \\ \dfrac{dS}{dt} = \dfrac{dS^*}{dt} = \dfrac{\dot{q}_e}{T_e} + \dot{m}_i \cdot s_i + \dot{m}_o \cdot s_o + \dot{m}_{HFT} \cdot (s_1 - s_2) + \dot{\sigma}_{irr} \end{cases} \quad (2)$$

with

$$\begin{aligned} \dot{\sigma}_{irr} &= \dot{q}_e \cdot \left(\frac{1}{T^*} - \frac{1}{T_e} \right) + \dot{m}_i \cdot \mu_i + \dot{m}_o \cdot \mu_o + \frac{A^*}{T^*} \cdot \frac{dm_x}{dt} \\ &+ \dot{q}_{HTF} \cdot \left(\frac{1}{T^*} - \frac{1}{\widetilde{T}_{12}} \right) + \dot{q}_i \cdot \left(\frac{1}{T^*} - \frac{1}{\widetilde{T}_i} \right) + \dot{q}_o \cdot \left(\frac{1}{T^*} - \frac{1}{\widetilde{T}_o} \right) \end{aligned} \quad (3)$$

where $\dot{m}$ is mass flow rate of the substance (kg/s)

$\dot{q}$: heat flow (W)

h : specific enthalpy ($J.kg^{-1}$)

s : specific entropy ($J.kg^{-1}.K^{-1}$)

$\dot{\sigma}_{irr}$: entropy generation ($W.K^{-1}$)

From the entropy production (3) that has always a positive value, one can deduce some linear phenomenological laws:

$$\dot{q}_e = L_e \cdot \left(\frac{1}{T^*} - \frac{1}{T_e} \right) \quad (4)$$

$$\dot{m}_i = L_{mi} \cdot \mu_i \quad (5)$$

$$\dot{m}_o = L_{mo} \cdot \mu_o \quad (6)$$

$$\frac{dm_x}{dt} = L_{vap} \cdot \frac{A^*}{T^*} \quad (7)$$

$$\dot{q}_{HTF} = L_{HTF} \cdot \left(\frac{1}{T^*} - \frac{1}{\widetilde{T}_{12}} \right) \quad (8)$$

$$\dot{q}_i = L_i \cdot \left(\frac{1}{T^*} - \frac{1}{\widetilde{T}_i} \right) \quad (9)$$

$$\dot{q}_o = L_o \cdot \left(\frac{1}{T^*} - \frac{1}{\widetilde{T}_o} \right) \quad (10)$$

The phenomenological coefficients L can be determined from a given operating point of the real component (i.e. the design point). They could also be calculated from common engineering correlations.

3.2. Modeling the process

This method is applied to all components of the CHV3T process. Dynamic behavior of the sub-systems is described by the set of equations (2) coupled with the phenomenological laws, equations (4) to (10).

The dynamic behavior of the whole machine is calculated following the steps described in Fig 8.

One can notice that only 3 equations of the set (2) (and therefore three extensive variables) should be required to describe each sub-system, for example m_l, m_v and U. However, due to the non linear form of fluid state properties equations, the fourth (entropy S) could be used as supplementary constraint for the intensive state calculation.

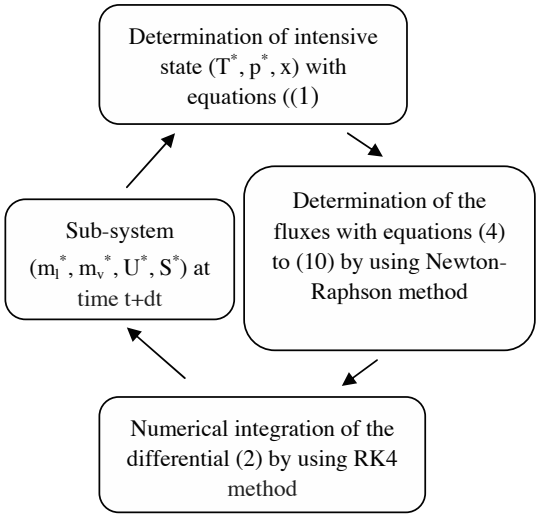

Fig. 8. Dynamic model of the whole process

4. Results

The performances of the different versions of the CHV3T process have been numerically evaluated through out the model. The variant CHV3T-WL seems to lead to the best cost-effective compromise for a domestic building application. The following results were achieved with simulations using the CHV3T-WL's cycle.

A static design point was defined for the process with the following working fluids: R134a for the reverse cycle and R236fa for the engine cycle. Some working fluids have been investigated with the different versions. The favourable properties of zero flammability and low toxicity displayed by most hydro-fluorocarbons (HFC), make them suitable fluids for this specific application. Furthermore, they have zero ozone depletion potential (ODP). The working pressures and temperatures are describes on the table 1.

Table 1. Working pressure and temperature for the two promising working fluids suitable for domestic solar-cooling application

R134a		R236fa	
P_h	8.69 bar	P_h	8.69 bar
P_b	4.43 bar	P_b	4.43 bar
T_{mR}	34.3°C	T_h	65°C
T_b	12°C	T_{mM}	40.3°C

A series of extensive simulations was used to study and optimize all the system components. This model allows determining the performances of the machine on the stationary and non-stationary regimes. The pressure and temperature evolutions are observed during the cyclic operating in all the components of the system.

The temperature and pressure evolutions on stationary regime for the four evaporators and condensers are represented in the Fig. .

The stationary regime is defined by:

- A solar irradiation of 950 W/m². The process is coupled to 20 m² of flat plate solar collectors.
- The inlet temperatures of the heat transfer fluid of the condensers C_M and C_R is fixed at 30°C.
- The inlet temperature of the heat transfer fluid of the evaporator E_R is fixed at 19°C.

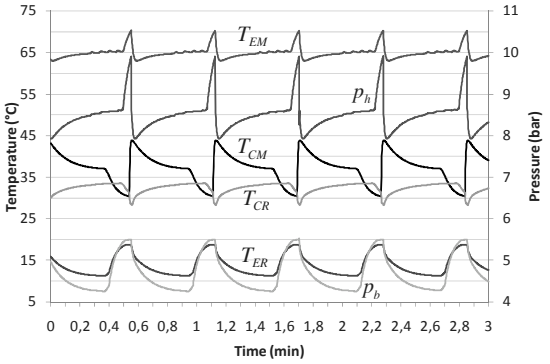

Fig. 9. Temperatures and pressures on the stationary regime

The CHV3T cycle operating in phase opposition is represented in Fig. . One can notice cyclic variations of the temperature and pressure in the evaporators and condensers. The evaporator E_M and the condenser C_R are coupled by the transfer cylinders at the high pressure during the work transfer phase. Inversely, the evaporator E_R and the condenser C_M are coupled by the transfer cylinders at low pressure during the other work transfer phase. The average temperatures of the four components correspond practically to the static design point. Indeed the average temperature of the evaporators E_M and E_R are respectively 65°C and 13.5°C, and for the condensers C_M and C_R, 37.2°C and 32.5°C. During the internal work recovery phase the evaporators and condensers are separated off from the other components of the system and their temperatures reach progressively the inlet temperature of the heat transfer fluid. The solar collector field operates at an average temperature of 74°C.

The evolution of thermal powers of the evaporators and condensers on the stationary regime were represented in the Fig. . These heat fluxes fluctuate in the same way as the temperatures and pressures. As a result, the powers are alternating with a cycle duration of about 1 minute. The average cooling power $\dot{q}_{ER}$ provided at 10°C is approximately of 5.8 kW for an average driving heat power $\dot{q}_{EM}$ of 10.6 kW supplied at the high temperature by the flat plate collectors. The condensation powers are approximately 9.7 kW for the condenser C_M ($\dot{q}_{CM}$) and 5.9 kW for the condenser C_R ($\dot{q}_{CR}$). The heat losses of the machine represent 0.8 kW.

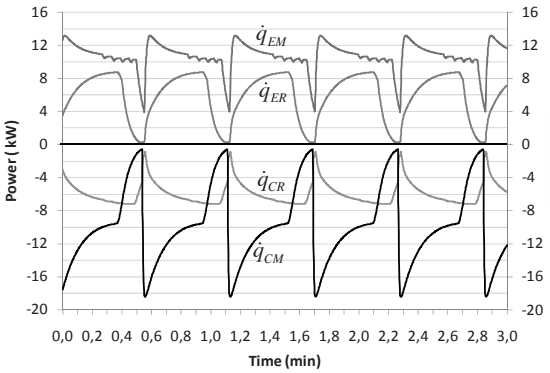

Fig. 10. Power of condensers (C_M, C_R) and evaporators (E_M, E_R) on the stationary regime

The Coefficient of Performance, COP, that characterise the energy performance of a refrigeration machine, is defined as the ratio between the cooling power provided at low temperature to the driving heat supplied at the high temperature level:

$$COP = \frac{\dot{q}_{low}}{\dot{q}_{high}} \quad \textbf{(11)}$$

In the stationary regime, the COP of the process is 0.55.

The COP is compared to the Carnot COP_C that defines the ideal performance for a trithermal machine.

$$COP_C = \frac{T_b\left(T_h - T_{mM}\right)}{T_h\left(T_{mR} - T_b\right)} \quad \textbf{(12)}$$

$$COP_C = 1.24$$

$$\frac{COP}{COP_C} = 44.3\%$$

The specific collector area, which defined as the collector area installed per kW of cooling capacity is equal for this process to 3.4 m²/kW cooling.

4. Conclusion

An innovative solar cooling process of a thermo-hydraulic system has been presented in this paper. The vapor hydraulic compression machine is composed of two dithermal machine coupled with a liquid piston. The coupling of these two dithermal cycles allows obtaining a global tri-thermal system with an internal work transfer realized by this liquid piston. Several versions of the thermo-hydraulic system has been investigated in order to obtain the best cost-effective compromise for an individual building application.

A modeling of the whole process is developed by using the concept of Equivalent Gibbs systems. Dynamic models based on this concept offer several advantages:

- Thermodynamic consistency, required for a reliable exergy analysis,
- Numerical stability, required for short computer time and simple algorithm.
- Generalized concept, allowing to simulate a large number of processes on same thermodynamics basics.

Moreover, this methodology is mainly based on the standard engineering knowledge, and this could facilitate its expansion for engineer community.

The performances obtained for this innovative cooling process seem to be very competitive with existing solar cooling systems [3-4]. Indeed a COP value of 0.55 can be achieved for a cooling production at an average temperature of 13.5°C. This new system has a strong potential for significant primary energy savings. Moreover it appears as an attractive alternative for solar cooling technologies due to its ability to use low temperature driving heat source (65°C).

A 5 kW cooling capacity prototype coupled to 20 m² of flat plate solar collectors is under construction and will be in operation during the next summer.

Nomenclature

BS	Separating Bottle
CT	Transfer Cylinder
C	Condenser
COP	Coefficient of performance
dm_x/dt	Vaporization rate, kg/s
E	Evaporator
EV	Solenoid Valve
h	Specific enthalpy, J/kg
HFC	HydroFluoroCarbons
LT	Liquid of Transfer
M	Engine cycle
m	Mass, kg
$\dot{m}$	Mass flow, kg/s
p	Pressure, Pa
Q	Heat, J
$\dot{q}$	Heat flow, W
R	Reverse cycle
S	Entropy, J/K
s	Specific entropy, J/(Kg K)
T	Temperature, K
$\tilde{T}$	Mean Entropic temperature, K
U	Internal energy, J
x	Vapor quality
W	Work, W

Greek symbols

μ	Chemical potential, J/kg
$\dot{\sigma}_{irr}$	Entropy generation, W/K

Subscripts and superscripts

b	Low
e	Environment
h	High
HTF	Heat Transfer Fluid
i	Refrigerant inlet
l	Liquid
m	mean
o	Refrigerant outlet
v	Vapor
1	Heat transfer fluid inlet
2	Heat transfer fluid outlet
*	Gibbs equivalent system

References

- Journals:

[1] Commission of European Communities, 2001, Green Paper – Towards a European strategy for the security of energy supply. Brussels/Belgium.

[2] Papadopoulos, A. M., Oxizidis, S., Kyriakis, N., 2003, Perspectives of solar cooling in view of the developments in the air-conditioning sector, Renewable and Sustainable Energy Reviews, 7(2003), pp.419-438.

[3] Henning, H-M., 2006, Solar assisted air conditioning of buildings – an overview, Applied Thermal Engineering, 27(2007), pp. 1734-1749.

[4] Balaras, C. A., et al., 2005, Solar air conditioning in Europe – an overview, Renewable and Sustainable Energy Reviews, 11(2007), pp.299-314.

- Conference Proceedings and Electronic publications:

[5] Neveu, P., and Mazet, N., 2002, Gibbs systems dynamics: a simple but powerful tool for process analysis, design and optimization, Proc. IMECE2002, ISBN 0-7918-1693-1, New Orleans, USA.

Acknowledgments: This study is financed by Vaillant Group – Saunier Duval society.

THE SRB EVACUATED FLAT SOLAR PANEL

Cristoforo Benvenuti[a], *Vladimir Ruzinov*[a]

[a] *SRB Energy Research SARL, c/o CERN, CH-1211 Genève 23, Switzerland*

Abstract: This report describes the Evacuated Flat Solar Panel developed at CERN and presently produced industrially by SRB in Spain (Almussafes, close to Valencia).
The distinctive feature of this panel is the very high temperature it may reach by simple exposure to solar light (over 300°C for 1000W/m^2 of incident power). Even higher temperatures may be obtained making use of non focusing mirrors, which allow also diffuse light to be collected. With different mirror configurations this panel may be used for all possible solar thermal and thermodynamic applications at temperatures ranging from 60°C to 390°C.
The panel contains a Getter pump driven by sun and dimensioned so as to maintain the panel internal pressure lower than 10^{-4}Torr for the specified panel life. The daily and seasonal pressure variations are presented and discussed.

Keywords: Solar thermal panel, vacuum, getter pumping .

1. Introduction

It is commonly accepted that thermal solar panels may reach high temperatures only when making use of light focusing or concentration mirrors. The distinctive advantage of the SRB evacuated solar panel is that it reaches temperatures higher than 300°C without the help of mirrors, so as to collect also the diffuse component of the solar light which cannot be focused. This feature is particularly important in central Europe, where diffuse light easily exceeds 50%, but it is also relevant for the best solar areas, where at least 25% of the light is diffuse.

High temperatures are feasible thanks to a drastic reduction of the panel thermal losses due to both gas conduction/convection and infrared radiation emission. The panel is evacuated and its operating pressure is maintained to below 10^{-4}Torr by an incorporated getter pump, while the IR radiation emission is minimized by coating the light absorbers with a highly selective chromium black film of proprietary recipe.

2. Panel design

The standard panel consists of a metal frame to which two glass windows, facing each other, are tightly joined by soft soldering.

The evacuation of the panel brings about the need of supporting the glass windows against atmospheric pressure i.e. an applied force of 10 tons per m^2. For this purpose longitudinal steel spacers are interposed between the two glasses. The adopted spacers inter distance is 15cm for a glass thickness of 5mm.

In order to minimize glass loss in the panel manufacturing process, the adopted glass window dimensions are integer submultiples of the glass panes produced by Industry (6m x 3.21m). Our choice is a width of 64cm and a length of either 3m or 2m.

Over such lengths the long sides of the frame would bend if not sustained against atmospheric pressure. Therefore transverse spacers are welded on the inside of the two long frame sides, at a distance of about 50cm from each other. These spacers, which are not in contact with the glass windows, also help centering and holding the cooling pipes welded to the black absorbers. The overall panel thickness is 42mm.

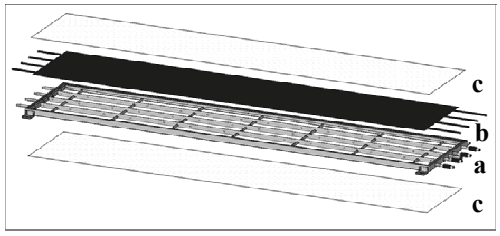

Figure 1: Global view of the panel a: frame with spacers; b: absorbers with cooling pipes; c: glass windows

A schematic global view of the panel is shown in fig.1, while the spacer structure is shown in fig.2.

Corresponding Author: Cristoforo Benvenuti, Email: cbenvenuti@srbenergy.com

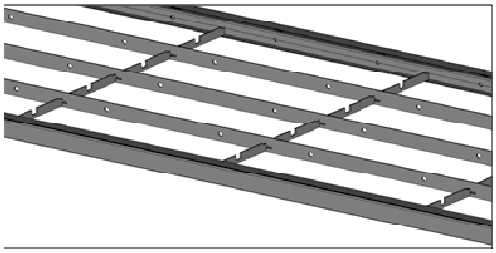

Figure 2: Spacer structure

The absorbers, blackened on both sides and made of copper, extend over the whole length of the panel, with a final clearance of 10/15 mm to accommodate the thermal expansion at the maximum panel temperature.

Four stainless steel cooling pipes are welded individually to the four absorbers and to the short sides of the frame at both extremities. A bellows is interposed at one side to accommodate the thermal expansion of the pipe (see fig.3a and 3b). This straight pipe configuration will be adopted for power plant use, where a high fluid flow rate is desired to maximize the length of the panel rows.

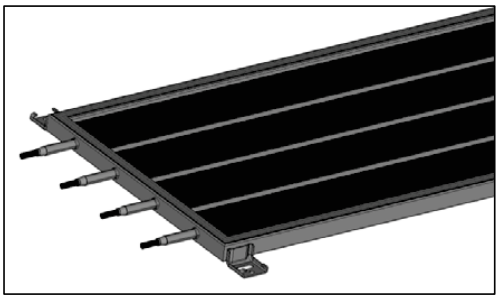

*Figure 3**a:** Fixed point connection of the cooling pipe to the frame*

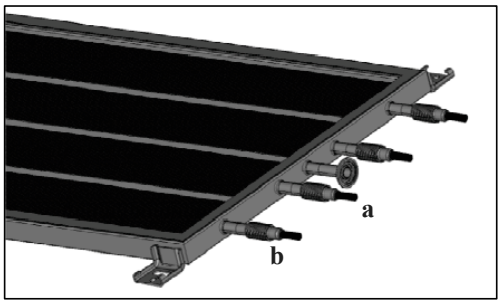

Figure 3b: a: The pumping port and b: the bellows

Whenever a small size application is being considered, another configuration is preferable because it is simpler and provides lower thermal losses. In this case two hair-pin shaped pipes are welded each on two absorbers. The four inlet and outlet connections of these pipes are located on the same short side of the frame, so as to avoid the need of bellows.

3. Vacuum considerations

The evacuation of the panel is mandatory to achieve high temperature. The influence of the pressure on the stagnation temperature is shown in fig.4 for a sample exposed to solar light of 1000W/m^2 intensity.

Fig 4 indicates that below 10^{-4}Torr the thermal losses due to gas conduction become negligible.

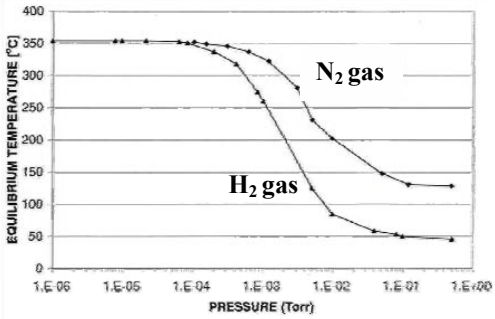

Figure 4: Variations of the absorber temperature as a function of the panel pressure and gas nature. The measurements are carried out on a sample suspended inside a vacuum vessel and exposed to 1000W/m^2 solar power.

However, the vacuum is beneficial not only for reducing the thermal losses, but also to protect the panel internal surfaces against contamination and corrosion, and to extend the life of the absorber selective coating.

To maintain the vacuum over the life span of the panel (at least 20 years) a Non Evaporable Getter (NEG) is used. This approach provides the major advantage of removing the need of external pumps and vacuum piping, but imposes severe constraints on the panel design.

NEGs have a finite pumping capacity; therefore the total gas load must be minimized by reducing as much as possible the pressure before NEG activation as well as the degassing of the panel components. The panel is initially pumped by a turbomolecular pumping station and baked at about 120°C to remove the adsorbed water vapor.

All organic materials are proscribed because of their excessive degassing, and all internal surfaces must be cleaned according to UHV standards.

NEGs do not pump rare gases, like Argon, present in the atmospheric air, and possibly entering the panel through leaks. In order to avoid an accumulation of argon which would results in appreciable thermal losses over of 20 years, a maximum leak rate of ~10^{-8}(Torr.L)/s is tolerable.

During room temperature operation the NEG surfaces are saturated by the pumped gas molecules and the pumping action is lost. To avoid this inconvenience the NEG must be heated (either continuously or intermittently) to diffuse the pumped gas from the surface into the getter bulk. A traditional way to achieve this goal is to heat resistively the NEG using an external power supply via an electric vacuum feedthrough. In the present case a simpler solution was adopted, making use of the freely available solar power.

4. Optical requirements

Although vacuum is essential to provide an adequate thermal insulation, in order to achieve high temperatures the panel absorbers must provide a high absorption of the solar light and a low emission in the IR range.

Fig.5 shows the influence of the absortivity (α) and emissivity (ε) ratio on the panel stagnation peak temperature (1000W m^{-2}, normal incidence power, glass temperature 30°C). Since the two sides of the absorber emit, the sum of their emissivities appears in the plot. Selective coatings always present higher emissivity values as compared to bare copper or aluminum, therefore only one face of the absorber is usually coated in traditional flat panel solar collectors. In our case, the panel may be exposed to sun on both sides (see par. 5 of this report), therefore if both absorber sides are coated $\varepsilon = 2 \cdot \varepsilon_1$, while if only one side is coated $\varepsilon = \varepsilon_1 + \varepsilon_2$.

The lesson which may be extracted from fig.5 is that achieving temperatures higher than 300°C requires ratios higher than about 7, i.e. that for α=0.9, ε should not exceed 0.14, a value not so easily obtained for absorbers blackened on both sides. For one side blackening ε=0.10 could be achieved.

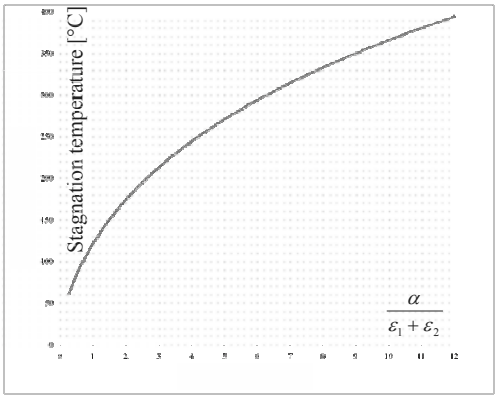

Figure 5: Calculated variation of the peak stagnation temperature as a function of the $\frac{\alpha}{\varepsilon_1 + \varepsilon_2}$ *ratio. For simplicity the IR radiation reflection by the glass was neglected in the calculation.*

5. Mirrors

The unique feature of this panel is that it may cover the whole temperature range of solar applications, from domestic water heating, to production of industrial heat and air conditioning at intermediate temperatures, up to the high temperatures required for the production of electricity.

However, in order to improve the panel cost effectiveness and/or its efficiency at high temperatures, non focusing mirrors may be added.

The chosen configurations are shown in fig 6.

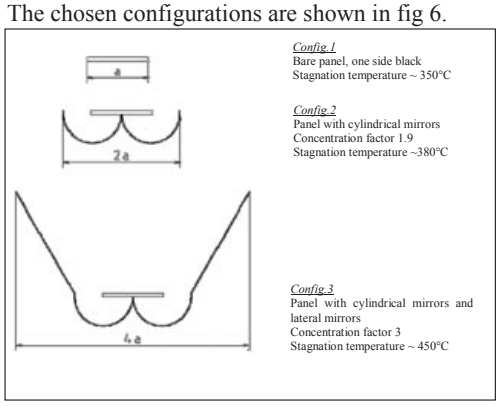

Figure 6: Different panel configurations

While the cylindrical mirrors transmit to the panel the direct and the diffuse light with equal

efficiency, a fraction of the diffuse light reflected by the lateral mirrors in configuration 3 is lost. Therefore the concentration factor of 3, given in fig.6 for this mirror configuration, depends on the light conditions and may be worse in cloudy days

It should be noticed that configuration 3 is just one amongst the many possible mirrors choices under study, of which some are characterized by a higher concentration factor.

For instance, a tracking system which provides a concentration factor of 7 was developed at Almussafes (see fig 7) and its evaluation is under way.

Bare panel mounting may be adopted for applications up to 200°C whenever the space to accommodate the cylindrical mirrors is not available, as for instance for roof mounting. Since the mirrors are cheaper than the panel, the configuration 2 is preferable for any temperature up to about 250°C. For electric power plants to be feasible a mirror configuration providing a concentration factor not lower than 3 is mandatory to allow an operating temperature higher than 300°C to be adopted.

Figure 7: Tracking system

6. Thermal performance

The stagnation temperatures of the best and worst absorbers of a panel prototype without mirrors are shown in fig.8 as a function of the incident solar power. Since the radiation emission increases with the fourth power of the absorber temperature expressed in K, the linearity of T^4 versus the available solar power indicates that only radiation losses are present, and that the selective coating emissivity undergoes little, if any, variation up to temperatures higher than 300°C. In this case only one side of the absorber was blackened.

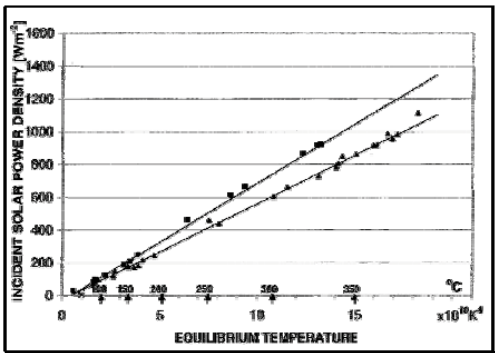

Figure 8: Stagnation temperatures of the best and worse absorber of a panel prototype exposed to various solar power densities as indicated on the vertical axis.

The efficiencies of the solar panel in three different mirror configurations, i.e. no mirrors, cylindrical mirrors and cylindrical and lateral mirrors, are given in figs 9, 10, 11 respectively. In these figures the efficiency is plotted against the operating temperature, for different values of the incident solar power.

The reported curves are calculated for a glass light transmission of 0.9, α= 0.9, ε=0.17 for two sides blackening and ε=0.10 for single side blackening (quite conservative values), a black absorber covering 0.84 of the total panel aperture, and taking into account the measured thermal impedance between the absorber and the circulating cooling fluid (oil in this case). The mirrors efficiency is measured. Small differences between panels may occur due to the spread of the absorbers optical quality.

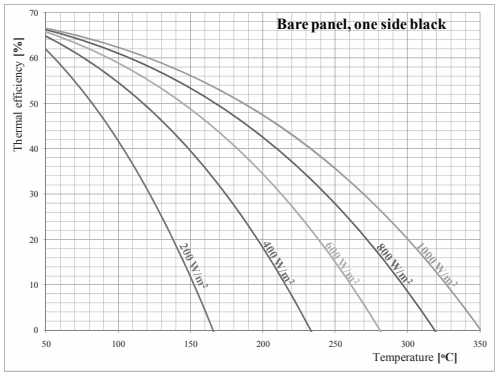

Figure 9: Efficiency of bare panel. One side of absorber is blackened, ε =0.10.

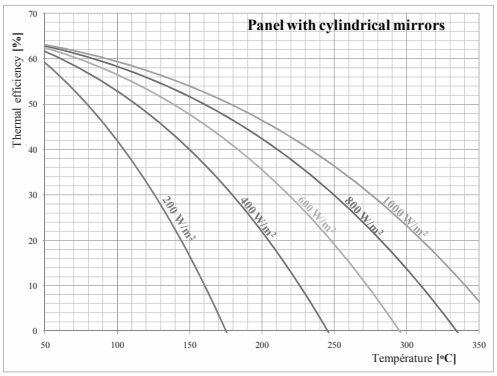

Figure 10: Efficiency of the panel with cylindrical mirrors.

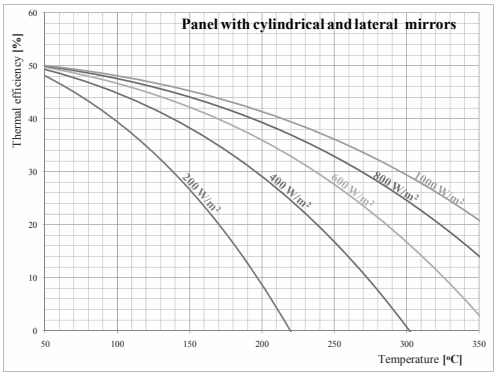

Figure 11: Efficiency of the panel with cylindrical and lateral mirrors.

7. Vacuum performance

After panel baking and seal-off, the pressure is typically in the 10^{-6}Torr range. During the panel life, the pressure undergoes daily variations consequent to the variation of the absorbers temperature, with a superimposed long term drift resulting from the competing actions of the decrease of the panel degassing and NEG pumping speed. If the NEG pump is properly dimensioned, the panel degassing rate decreases faster than the NEG pumping speed does, therefore in the absence of leaks the pressure decreases steadily.

A typical pressure variation during the first months of panel life ranges from 10^{-8}Torr at room temperature, to 10^{-6}Torr above 300°C. During cold winter nights pressures below 3.10^{-9}Torr were reached. The data recorded on a 2m long prototype are given in Fig. 12.

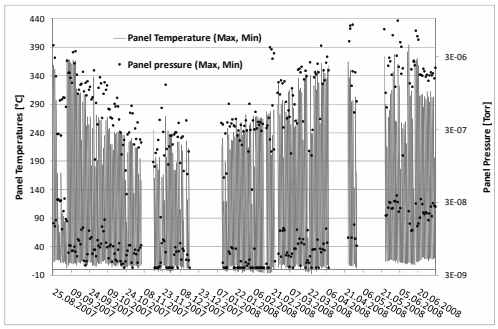

Figure 12: Time evolution of the panel pressure for various absorber temperature conditions. The vertical red lines indicate the maximum and minimum temperatures of each day, while the dots represent the corresponding maximum and minimum pressures inside the panel.

8. Applications

The described panel is very polyvalent: it may be used to produce heat at temperature required by any solar energy application, from the domestic water heating to the production of electricity.

Obviously, in sunny hot countries, less sophisticated solar panels may be used preferably for domestic water heating, but in cold countries the good thermal insulation provided by vacuum represents a competitive advantage even for this application, and even more so if district heating is adopted.

At the other temperature extreme, as required for the production of electricity, parabolic trough mirrors provide higher concentration factors but they cannot make use of diffuse light, a feature which imposes severe restrictions on the choice of the plant location. These restrictions do not apply in our case because some of the possible mirror configurations we intend to adopt are very effective for diffuse light. For this reason the SRB panel is ideally suited to complement biomass/fossil fuel thermal power plants in Central Europe.

More generally, the SRB panel represents the best possible choice to provide heat for industrial processes (120°C to 250°C), particularly in continental climate regions where most of the industrial production takes place.

9. Conclusions

The SRB panel fills a gap in the temperature range of the thermal solar applications, corresponding to the needs of industrial processes and electricity (co)generation, particularly for continental climate regions.

Since summer 2009 a production plant is operational at Almussafes (close to Valencia, Spain). Presently the production rate of the panel is of the order of 10 to 50 units/day, i.e. quite small if compared to the potential market needs. Accordingly, a panel cost is not yet standardized, but it is rather defined case by case on the ground of the size of the installation and of its interests for SRB. Some installations have already been equipped with this panel and many others are planned for 2010.

Nomenclature

[IR]: Infra Red

[UHV]: Ultra High Vacuum

[NEG]: Non Evaporable Getter

[(Torr.L)/s]: Flow rate

References

[1] Evacuable Flat Panel Solar Collector.
PCT/EP 2004/000503 (18/08/2005).
Inventor: C.Benvenuti.
Applicant: CERN,
1211 Geneva23 (Switzerland).

Pumped storage : a compulsory stage in securing the future energy supply

Eric Wuilloud[a],

[a]*Alpiq SA, Martigny, Switzerland*

Abstract: Irrespective of the scenario that is envisaged, the future energy supply will require an increase in electrification. In order to ensure a balance between electricity production - which will become increasingly uncertain - and consumption, with its great power fluctuations, pumped storage proves to be the most suitable tool. The example of the Nant de Drance pumped storage project is described briefly.

Keywords: primary, final and useful energy, pumped storage, Nant de Drance project

1. The current energy situation

Energy in all its forms is a good without which it would be impossible to live on our planet. To describe the current energy situation, it is useful to recall the concepts of primary energy, final energy and useful energy.

Primary energy corresponds to the resources that are available to us on earth. These come mainly from fossil fuels (oil, gas), the atom (nuclear energy), water (hydroelectric power), wind and the sun. Currently, global consumption is dominated by fossil fuels with oil, coal and natural gas. Hydropower accounts for only 5% of resources and nuclear energy for 6%.

Before being distributed to consumers, a part of the primary energy is transformed into a usable form. It then has to be transported to the point of consumption. This gives the final energy, which consists of more than 70% fossil fuel, 24% electrical energy and the balance of energy in other forms (heat, ...). The conversion and transportation of primary energy into final energy at the point of consumption produces losses that are of the order of 30%. The electrical energy comes mainly from hydroelectric and nuclear power and from a portion of fossil fuels.

When the final energy is consumed, the losses again amount to over 40%. They come, for example, from heat losses in vehicles or from the heat lost in light bulbs. Finally, the useful energy for the consumer is about 45% of primary energy. The rest is lost forever.

Figure 1 shows the energy situation for Switzerland in 2008. We find that compared to the global situation, the proportion of useful energy is 50%.

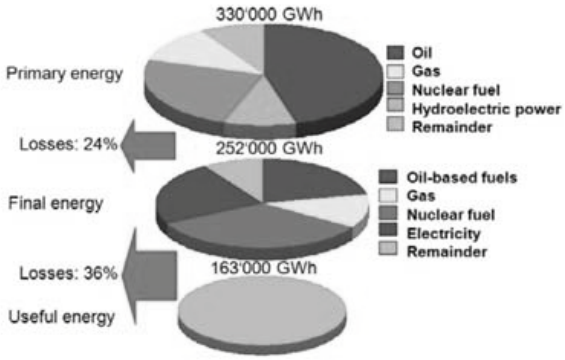

Fig. 1. Energy situation in Switzerland in 2008 (Sources: SFOE).

In Switzerland, primary energy amounts to 1,176,230 TJ, which corresponds to 330,000 GWh. Final energy amounts to 252,000 GWh, of which 23.5% or **60,000 GWh correspond to electricity consumption**. Only 163,000 GWh will be useful for consumers.

With its 7.5 million inhabitants, the average annual consumption per person is 44,000 kWh. Assuming that energy is supplied continuously and constantly, this is equivalent to a power range of more than 5,000 watts per person. So we are very far from the "2000-watt society" proposed by the Swiss Federal Institute of Technology in Zürich.

2. The future energy supply

The current energy situation can no longer evolve as it did in the past. The main reason is the growing scarcity and eventual disappearance of fossil fuels. Although the prospects for nuclear fuel resources are better, it is highly unlikely that they can be maintained in the very long term.

The following possibilities are available to react to this situation:

First of all, the requirements must be reduced. There is great potential, especially in the thermal area, by improving insulation.

Increasing the efficiency of energy systems is also very promising. For example, the use of ambient heat to heat buildings with heat pumps, or electrification of transport, allows natural resources to be used much more rationally. A prerequisite for these improvements is an increase in the use of electricity, which is easily transportable and can be readily converted into light, heat or force, but which has to go through another medium to be stored.

To compensate for this scarcity in fossil and nuclear energy, renewable energies including hydroelectric power must be developed.

What will the energy situation be like in a distant future? Although it is impossible to answer this question precisely, we propose a scenario which could be plausible, especially in the long term and based on two assumptions:

First assumption: In the year 2100, the "2000-watt society" will be a reality. The result of this for Switzerland, whose population will have increased to 10 million inhabitants, will be that primary energy will be 175,000 GWh, which is the same order of magnitude as current useful energy.

Second assumption: In year 2100, the fossil fuel resources will have completely disappeared and the nuclear energy resources will be abandoned. To replace these energies, use will be made of new renewable energies, hydroelectric power and the biomass.

It is not our aim here to predict the manner in which the transition will take place between the present energy situation and the long-term energy situation. All that is certain is that it is a change that will take several generations.

Figure 2 shows a scenario with primary energy distributed as follows: 76,000 GWh come from new renewable energies, 45,000 GWh from hydroelectric power and 53,000 GWh from biomass. The energy losses between primary and secondary energy will remain identical, because of the inexorable laws of thermodynamics. Thus in 2100, 133,000 GWh will be distributed to consumers, and owing to increased electrification, it is reasonable to think that more than half, that is, 75,000 GWh will be distributed in the form of electricity and 43,000 GWh in the form of biomass to produce mainly heat.

Other scenarios could be envisaged, but irrespective of the one used, we will always reach the same conclusion: as fossil fuels are depleted, the quantity of electrical energy will increase. **The disappearance of fossil fuels and the reduction of requirements call for electrification of the energy system**.

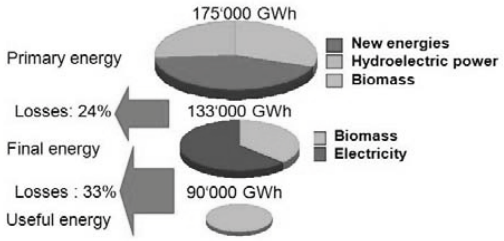

Fig. 2. Energy situation in Switzerland in 2100 (according to assumptions in the text).

3. Electrification increases storage requirements

In addition to the increase in electrification, it will be necessary in future to increase the energy storage capacities. Two reasons explain this situation:

On one hand, the share of new renewable energies used to generate electricity will increase. This means that electricity production will become more and more uncertain and will not be correlated with the energy used by consumers but will depend mainly on the weather situation (wind, sunlight). In windy conditions, a wind farm produces electricity; but when the wind drops, production is zero. Figure 3 shows the changes in the wind speed over five days in Sion.

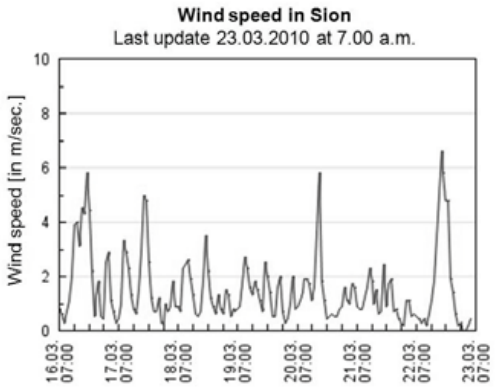

Fig. 3. Changes in wind speed between March 16 and 23, 2010 in Sion.

On the other hand, in the future, consumers will want to maintain or even improve the quality of life available to them through electrification. This means that over a day variations in power will increase significantly. Figure 4 shows the consumption in Switzerland for the year 2008, hour-by-hour and day-by-day. This curve shows that between the off-peak hours (for example, at night in summer) and peak hours (between 10:00 a.m. and 12:00 noon), the power demand can double.

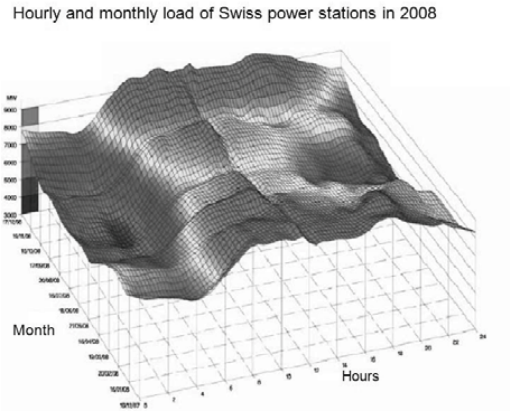

Fig. 4. Electrical energy consumption in Switzerland in 2008.

Therefore, to maintain a power grid, it is necessary to ensure a permanent balance between electricity generated and electricity consumed. If the development of generating facilities is compared with the trend in consumption, it will be seen that regulation will become increasingly important in future. Since electrical energy cannot be stored as such, other means of storage have to be used. **To ensure a constant balance, the need to store energy very quickly in order to be able to recover it as quickly as possible will become an essential operation in the future**.

4. Pumped storage: a necessary tool

A detailed analysis of the systems available for storage and recovery of energy shows that pumped storage is the most suitable tool.

Figure 5 shows the operating principle: when demand for electricity is high, the water from the upper reservoir is channelled through turbine generators to the lower reservoir to produce electricity. When demand is low, water is pumped from the lower reservoir to the upper reservoir. The switch from the pumping mode to the turbine mode and vice versa can be achieved in a very short time. The efficiency of such a facility is over 80%, which is currently the best available battery.

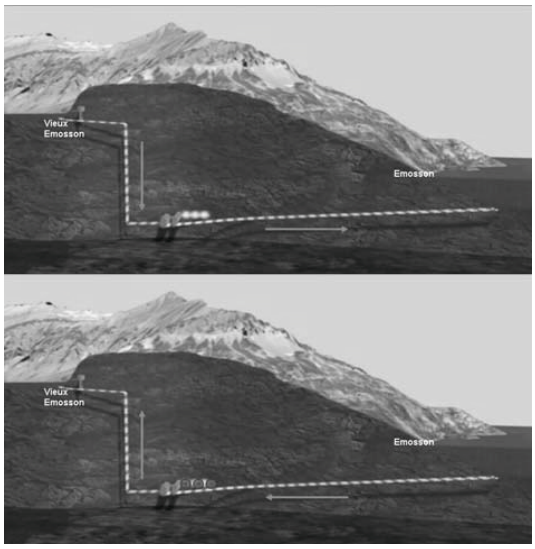

Fig. 5. Principle of pumped storage

Systems such as the flywheel, super capacities, vanadium batteries and fuel cells have interesting characteristics, but never reach the performance of a pump-turbine facility.

A pumped storage power plant can store 10 GWh in a few hours, and recover them again

very quickly. The efficiency of such a facility is over 80%.

5. The Nant de Drance pump-turbine project

The Nant de Drance project perfectly satisfies the criteria mentioned above. This project is part of a series of relatively complex hydroelectric plants operated by two different companies and which straddles two countries. The facility is situated on the road from Martigny in Switzerland to Chamonix, France, in the municipality of Finhaut (Figure 6).

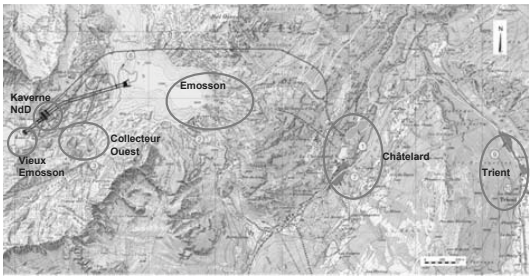

Fig. 6. Location of the pumped storage project

Currently, the waters from the two dams, originating from various regions of France and Switzerland, are operated by two companies: the Swiss Federal Railways (CFF) and Emosson SA (ESA).

Feasibility studies conducted in the early 2000s showed that the site was technically and economically appropriate to build a pumped storage facility. The project provides for construction of a completely underground plant, which reduces the environmental impact to a minimum.

The application for the concession and building permit was filed by the CFF at the Federal Office of Energy (SFOE) on March 12, 2007. A procedure at the federal level was necessary because the new concession affects international treaties with France.

On August 25, 2008, the Federal Department of the Environment, Transport, Energy and Communications (DETEC) awarded the concession and the building permit for the pumped storage power station. On November 7, 2008 the project partners established the company Nant de Drance SA (NdD), with registered office in the municipality of Finhaut. The same day the CFF and NdD signed an agreement governing the transfer of the concession being upgraded in the Nant de Drance hydroelectric plant.

Since that date, the concession and the construction of the facility have been the responsibility of NdD. The shareholder structure of NdD is as follows: Alpiq: 54%, CFF: 36%, 10% FMV.

Work began in September 2008 as soon as the time-limit for appeals had expired. It began with deforestation, establishment of the on-site installations and construction of the main access roads.

As the diagram of figure 7 shows, the hydroelectric system and the machines cavern form the heart of the project. It is made up of the following elements:

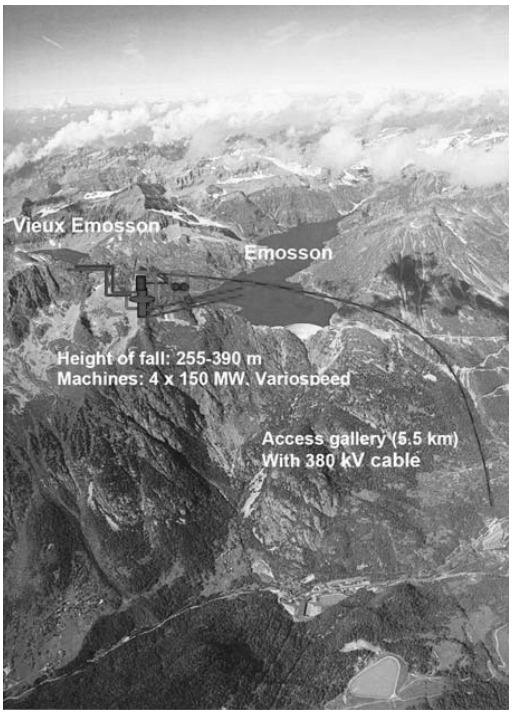

Fig. 7. Description of the pumped storage project

- The existing Lake Vieux-Emosson, which is the upper reservoir and has a service capacity of 11.2 mill. m3.

- 2 independent parallel upper hydroelectric galleries, containing 2 vertical shafts of 434 m, dimensioned for a flow of 120 m^3/s per tube.
- Machines cavern (L = 138 m, W = 32 m, H = 52 m) equipped with four 150 MW Francis turbine pumps, and a spherical valve upstream and downstream of each turbine.
- 2 parallel lower hydroelectric galleries.
- The existing Lake Emosson, which is the lower reservoir with a capacity of 225 mill. m^3.

Access to the machines cavern is provided by a bridge over the river Eau Noire at Châtelard, a 510-metre tunnel and through the main gallery of 5500 m with a slope of 11.5%, excavated by means of the 9.45-metre diameter tunnelling machine (figure 8).

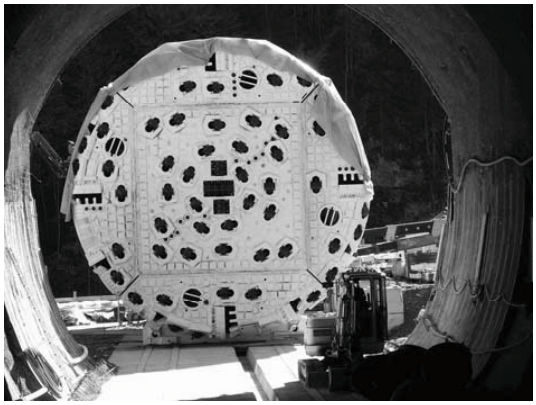

Fig. 8. Head of the tunnelling machine for boring the main gallery leading to the caverns

Other galleries will link the machines cavern to the upper and lower valve chambers.

When the works are completed, all that will be visible next to the gateways is a definitive warehouse with a volume of 1,600,000 m^3.

In October 2009 NdD announced its intention to analyze the possibility of improving the flexibility of the plant by increasing the power from 600 to 900 MW and by raising the upper dam by 20 metres to double its capacity. The surveys for this project (NdD+) and the authorization procedures are currently being launched. A final decision is expected by the end of 2010.

The rock, which is composed mainly of granite, orthogneiss, metagraywacke and migmatitic gneiss, is considered to be of good-to-very-good quality, with the exception of some Carboniferous shales which are very heterogeneous.

The schedule of works is as follows:

September 2008: Preliminary work started

December 2008: Excavations began on the Châtelard access tunnel

March 2009: Excavation work began on the gateway of the main access gallery

April 2009: The preliminary works began at Emosson, together with surveys for the water intakes at the bottom of the lake

May 2009: Boring of the Châtelard access tunnel

August 2009: Assembly of the tunnelling machine began, blasting work began on the upper galleries at Emosson

January 2010: Excavation of the main tunnel began with the tunnelling machine

Summer 2011: Excavations on the access galleries ends, excavation of the main cavern begins

Spring 2012: Excavation work begins on the hydroelectric galleries

Summer 2012: First shoring works

Summer 2013: Concreting of the main cavern begins

Winter 2015: Assembly of the first turbine begins

Spring 2016: The first two machines will be commissioned

Spring 2017: The next two machines will be commissioned.

Such a hydroelectric project in the Alpine environment involves numerous challenges. They require a substantial commitment on the part of the project team and the contractor and appropriate risk management.

Owing to snow and the risk of avalanches, the Emosson site is closed from December to April. Safety is monitored by mountain guides, who keep a watch on the access roads and construction sites until the snow melts. The guides have the power to suspend work in the event of danger. To reduce the risk of avalanches during construction work, explosive devices are used in the Emosson sector throughout the winter.

The areas where there is a risk of falling rocks are also the subject of monitoring and seasonal purges.

Works are only possible in Lake Emosson in April and May. The aim is to avoid emptying a large part of Lake Emosson in summer, which would cause a substantial financial loss to the operator of the dam.

A concept of enhanced surveillance of the two dams has been established. The potentially water-bearing areas have been identified by geologists. Reconnaissance boreholes, which are destroyed as work progresses, are planned in these sectors. Management of water intrusions during excavation will be of paramount importance. Injection scenarios were developed in order to be able to safely cross a possible water-bearing area. Springs will be the subject of enhanced surveillance during the works. Water intrusions will be reduced by injections, if necessary.

The excavation of a very large cavern and two very high shafts (434 m) are also challenges for the contractor and the planners. The great distance between the gateways and the large excavations requires careful planning of logistics and safety.

Fig. 9. View of the two existing reservoirs

6. Conclusion

As fossil fuels are gradually depleted, electrification will become more widely used and electricity storage requirements will increase.

Pumped storage is a particularly favourable form of storage from the environmental, technical and economic points of view.

The Alps, with installations already in place (figure 9), are an ideal site for the construction of pumped storage facilities.

The Nant de Drance project forms part of this perspective and marks the beginning of a new era in the construction of large hydroelectric projects. In Switzerland, it is the age of pumped-storage power stations, facilities that re-use the water of the existing reservoirs, allowing electricity supply security to be increased significantly without having a major impact on the environment. They are the future of the energy production of Switzerland and the other Alpine countries.

Exergy Efficient Application of LNG Cold

Lydia Stougie[a] and Hedzer J. van der Kooi[a]

[a] *Delft University of Technology, Delft, The Netherlands*

Abstract: The worldwide demand for Liquefied Natural Gas (LNG) is growing, which results in numerous LNG import terminals being under construction. In the interest of sustainable development, it is important to decide carefully upon which technology to apply for evaporating the LNG to natural gas. Three options for the evaporation of LNG have been investigated and analysed: a system that uses the waste heat from a coal-fired power plant to evaporate LNG, an integrated system consisting of LNG evaporation, air separation and a coal-fired oxy-fuel power plant, and a system in which LNG evaporation is combined with electricity production through a thermodynamic cycle. The oxy-fuel option appeared to be preferable with regard to the results of the exergy analysis, but it is not yet sure whether this option is the most sustainable of the three options. A more detailed analysis is needed before conclusions can be drawn upon the effects of involving exergy analysis in the choice between the three options for LNG evaporation.

Keywords: Electricity production, Exergy, LNG evaporation, Sustainability.

1. Introduction

The import of LNG, Liquefied Natural Gas, is one of the ways to fulfil the growing demand for energy carriers and the desire to diversify the origin of these energy carriers, especially for countries without or with limited natural resources of energy carriers. Worldwide, numerous LNG import terminals are under construction. One of the issues that has to be dealt with when realizing a new LNG import terminal, is the heat required for evaporation, also called 'regasification', of the LNG from minus 162 °C to about plus 2 °C. Several options exist, varying from heating with seawater in 'open rack vaporizers' and using the waste heat from a power plant, to integrating the LNG terminal with an air separation unit or combining the evaporation process with an Organic Rankine Cycle (ORC) to produce electricity. Some options are currently being applied in practice, while other options have been mentioned in literature only.

In the interest of sustainable development it is important to decide carefully upon which technology to apply for the evaporation of LNG; the amount of LNG and the corresponding heat requirement is usually large. However, it is difficult to compare the several options with respect to the many issues that play a role. Examples of issues to be taken into account are environmental impact, investment costs and the consequences of integration with other technologies, like availability, reliability and interdependency. According to literature, e.g. [1], a relation exists between sustainability and exergy.

In this research three options for the evaporation of LNG have been analysed. These options are a system that uses the waste heat from a coal-fired power plant to evaporate LNG, an integrated system consisting of LNG evaporation, air separation and a coal-fired oxy-fuel power plant, and a system in which LNG evaporation is combined with electricity production through a thermodynamic cycle. The consequences of involving exergy in choosing between the various options have been investigated with respect to making LNG evaporation more sustainable.

2. The exergy of LNG cold

Exergy is called a measure for the quality of energy. It can be defined as the maximum amount of work that can be obtained when a substance, mass flow or other amount of energy, is brought into total equilibrium with the (reference) environment.

Nowadays many people are focused on energy saving, but it is the work potential – the exergy amount – that we need to carry out the things we want to do. Every process is accompanied with exergy losses, losses that cannot be made visible with energy analyses because energy cannot be lost nor created according to the first law of thermodynamics.

Corresponding Author: Lydia Stougie, Email: l.stougie@tudelft.nl

2.1. Calculation of exergy values

The exergy value of electricity is by definition equal to the energy amount (1):

$$Ex_{\mathrm{W}} = W\,. \tag{1}$$

The exergy value of heat at a constant temperature T can be calculated by multiplying the amount of heat with the Carnot factor as depicted in (2):

$$Ex_{\mathrm{Q}} = Q\left(1 - \frac{T_0}{T}\right), \tag{2}$$

when T is higher than T_0.

The physical component of the exergy value of a mass flow is calculated from the enthalpy and entropy values, as in (3):

$$Ex_{\mathrm{m,ph}} = \dot{m}\left[\left(H - H_0\right) - T_0\left(S - S_0\right)\right]. \tag{3}$$

In this study T_0 is assumed to be 10 °C.

2.2. Exergy potential of LNG

LNG is transported overseas at about 1 bar and minus 162 °C and stored in large import terminals, e.g. in Rotterdam, The Netherlands. When natural gas is needed, the LNG is compressed and subsequently evaporated to meet the conditions of the gas in the Dutch pipelines for gas transport, which are about 70 bars and 2 °C. By applying (3) the theoretical amount of work that can be obtained from this transition can be calculated (4,5):

$$W_{\max} = Ex_{\mathrm{m,ph,LNG,in}} - Ex_{\mathrm{m,ph,NG,out}}\,, \tag{4}$$

$$W_{\max} = \dot{m}\left[\left(H_{\mathrm{in}} - H_{\mathrm{out}}\right) - T_0\left(S_{\mathrm{in}} - S_{\mathrm{out}}\right)\right]. \tag{5}$$

Assuming that LNG consists of pure methane, the theoretical amount of work can be calculated from the enthalpy and entropy values tabulated in [2]. In theory about 383 kJ/kg LNG can be obtained from the transition of LNG at 1 bar and -162 °C to natural gas at 70 bars and 2 °C. When a lower pressure of the resulting natural gas is needed, even more work can be obtained from this transition.

3. Brief description of options for the evaporation of LNG

Worldwide, several options exist for evaporating LNG to natural gas. Most applied are so-called 'open rack vaporizers' and 'submerged combustion vaporizers' [3]. In some countries, e.g. Japan, the LNG cold is used in power generation, air separation etcetera [4]. Many advanced options for LNG evaporation in combination with power generation can be found in literature [5-9].

The three options that are compared in this paper are expected to be appropriate for the situation in Rotterdam, The Netherlands. To comply with the composition of the natural gas in the Dutch gas transport system, so called G(roningen)-gas, after evaporation of the LNG an amount of nitrogen is added resulting in a gas mixture of about 95 vol.% methane and 5 vol.% nitrogen.

3.1. Use of waste heat from a coal-fired power plant

In the Rotterdam port area, The Netherlands, two LNG import terminals and a coal-fired power plant are under construction. In this ultra-supercritical power plant the conditions of the steam are about 300 bars and 600 °C, resulting in an electrical efficiency of about 47 percent [10]. In accordance with the current plans for Rotterdam, the waste heat (i.e. cooling water) from the power plant will be used for evaporating the LNG, see Fig. 1.

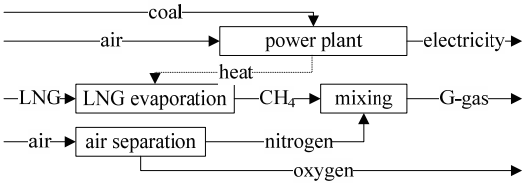

Fig. 1. Use of waste heat from a power plant.

3.2. Integration with air separation and a coal-fired oxy-fuel power plant

In this option LNG evaporation is integrated with an air separation unit and a coal-fired oxy-fuel power plant as described in [10,11], see Fig. 2.

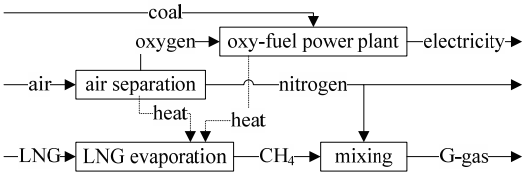

Fig. 2. Integration with air separation and an oxy-fuel power plant.

The power plant is based upon the 30 MWe pilot plant in Schwarze Pumpe (Germany) and has an electrical efficiency of about 45 percent [10]. In contrast to [10,11] the carbon dioxide is captured but not compressed.

3.3. Electricity production through an Organic Rankine Cycle.

In the third option, see Fig. 3, the LNG cold is used for electricity production through an ORC like presented in [5,6]. After performing calculations with several working fluids (nitrogen, methane, ethylene and ethane), ethane appeared to be the most suitable working fluid for the ORC. In this option the LNG is first compressed to 39 bars and subsequently evaporated and compressed to 72 bars. Seawater acts as the 'high' temperature heat source (10 °C).

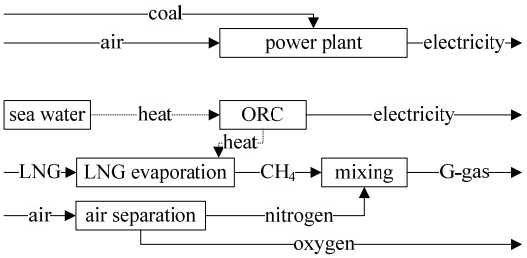

Fig. 3. Combination with electricity production through an ORC.

4. Analysis and results

4.1. Starting points

The data used for the analysis originate from the literature mentioned in paragraph 3, completed with calculations and estimates made by the authors.

To be able to make a fair comparison of the three options, the overall products and feedstocks are the same for each option. The analysed overall system is depicted in Fig. 4. On a yearly basis each option delivers 27 PJ of electricity, based on a 1000 MWe coal-fired power plant, and 12 Mtons of G-gas. The 27 PJ of electricity is the net amount of electricity produced; the electricity consumption of processes like LNG compression and air separation has been accounted for. In each option the carbon dioxide is captured for reasons of comparability of the three options. The carbon dioxide is not compressed.

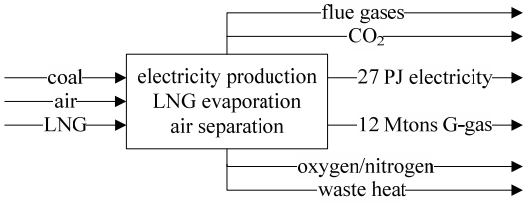

Fig. 4. Analysed overall system with a net electricity production of 27 PJ.

With regard to the economic comparison it is assumed that the nitrogen needed in the first and last options is bought from another company instead of taking into account the investment costs involved with building a new air separation unit.

4.2. Consequences of integration

In general, integration of installations and processes results in lower costs and higher efficiencies, but has the disadvantage of inter-dependency of the installations. One of the issues that has to be dealt with is the continuous operation of the power plant and the discontinuity in the send-out of the LNG terminal. It is expected that the LNG terminal will send out natural gas about 60 percent of the time, depending on the weather conditions. Apart from the discontinuous operation of the LNG terminal, the integrated facilities will need back-up installations to overcome an (unexpected) shut-down of a connected installation.

Of the three options, the oxy-fuel option is clearly the most vulnerable with regard to the dependency between the (sub)installations. The option in which LNG cold is used for electricity production through an ORC is considered to be the most independent. The other option, in which waste heat of the power plant is used for LNG evaporation, comes in between with regard to the inter-dependency.

It is unknown which option is preferred with regard to the availability and reliability of the options.

4.3. Environmental impact

The environmental impact of the three options is presented in Table 1. Of every option the coal use, the emissions of carbon dioxide, nitrogen and sulphur oxides and the excess amount of waste heat are presented. With the 'excess amount of waste heat' the cooling water originating from the power plant is meant that is not applied for heating

purposes elsewhere in the analysed option. The temperature of the emitted waste heat is about 17.5 °C. Other kinds of environmental impact, like noise, have not yet been taken into account.

Table 1. Environmental impact of the three options.

Per year	Waste heat	Oxy-fuel	ORC
Coal [Mtons]	2.9	2.6	2.7
CO_2 [Mtons]	1.0	0.3	0.9
NO_x [tons]	1.4	0	1.3
SO_x [tons]	11	0	11
Waste heat [PJ]	22	21	29

Apart from the environmental impact presented in Table 1, each option results in approximately 5.6 Mtons of carbon dioxide being captured as well as 0.3 Mtons of ash.

From an environmental point of view the oxy-fuel option is preferred. The ORC option seems to have a lower environmental impact than the waste heat option, with exception of the amount of wastewater produced.

4.4. Financial aspects

The capital and operational costs have been estimated from the data in [3,10,12-14]. The costs of the back-up installations as mentioned in paragraph 4.2 have not been accounted for. The same holds for the costs and revenues related to the purchase of LNG and sale of the resulting natural gas respectively.

It is assumed that the costs and revenues related to the purchase and sale of nitrogen and oxygen and the costs related to carbon dioxide emissions are negligible compared to the other operational costs.

Figure 5 gives an overview of the indicative capital and operational costs, with price level of about 2006.

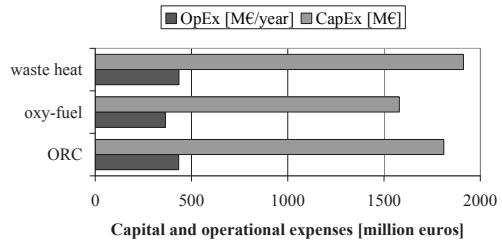

Fig. 5. Financial aspects (indicative numbers) without taking into account the costs of back-up installations.

According to Fig. 5, the oxy-fuel option is preferred to the other two options when the costs of back-up installations are neglected.

4.5. Exergy analysis

Figure 6 presents the results of the exergy analysis of the three options investigated. The overall exergy loss is defined as the exergy amount of the feedstocks minus the exergy amount of the products. In this case the exergy amount of the feedstocks is equal to the exergy value of the coal used plus the physical exergy value of the LNG. The exergy amount of the products is equal to the net amount of electricity produced plus the physical exergy value of the G-gas that is produced.

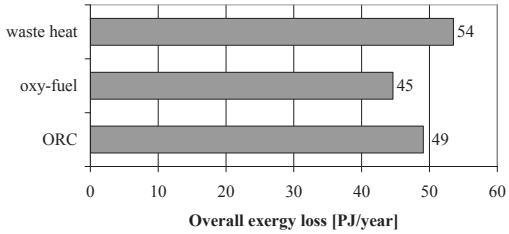

Fig. 6. Results of the exergy analysis.

Figure 6 makes clear that the oxy-fuel option is preferred, followed by the ORC option. The waste heat option is the least favourable option.

5. Conclusions

According to the exergy analysis, the oxy-fuel option is preferred, followed by the ORC option. The oxy-fuel option is the option with the lowest environmental impact as well. With regard to the interdependency between the various (sub)installations, the oxy-fuel option is the most vulnerable. The oxy-fuel option seems to be less expensive than the other two options when the costs of back-up installations are neglected.

Apart from the vulnerability with regard to the dependency between the (sub)installations, a careful conclusion could be drawn that the option that causes the lowest exergy loss, is the most sustainable option as well. However, because of the uncertainty in mainly the capital and operational costs, a more detailed analysis is needed before definite conclusions can be drawn upon the effects of involving exergy analysis in

the choice between the three options for LNG evaporation.

6. Future Research

In the future, a more detailed investigation and analysis will be carried out of options for the evaporation of LNG. LNG is one of the case studies in a more general research after the consequences of involving exergy analysis in decisions regarding future energy supply with respect to the environmental, economical and social aspects of the sustainability of this energy supply.

Nomenclature

Ex	exergy flow, J/s
H	enthalpy, J/mol
$\dot{m}$	mass flow rate, kg/s
Q	heat flow rate, J/s
S	entropy, J/(mol K)
T	temperature [K]
W	work, J/s

Subscripts and superscripts

0	at reference conditions (1 bar, 10 °C)
max	theoretical amount
ph	physical

References

[1] Dincer, I. and Rosen, M., 2007, *Exergy: energy, environment and sustainable development*, Elsevier, Oxford, UK.

[2] Zagoruchenko, V. and Zhuravlev, A., 1970, *Thermophysical properties of gaseous and liquid methane*, Israel Program for Scientific Translations Ltd, Jerusalem.

[3] Tarakad, R.R., 2003, *LNG receiving and regasification terminals*, Revised edition, Zeus Development Corporation, Houston.

[4] Sugiyama, M., The Utilization of LNG Cryogenic Energy, *Energy and Information Technology Journal* [online journal], EIT No. 32, URL: http://www.eit.or.jp/magazine/pdf/eit32e.pdf.

[5] Tsatsaronis, G. and Morosuk, T., 2010, Advanced exergetic analysis of a novel system for generating electricity and vaporizing liquefied natural gas, Energy, 35(2), pp. 820-829.

[6] Szargut, J. and Szczygiel, I., 2009, Utilization of the cryogenic exergy of liquid natural gas (LNG) for the production of electricity, Energy, 34(7), pp. 827-837.

[7] Liu, M., et al., 2009, Thermoeconomic analysis of a novel zero-CO2-emission high-efficiency power cycle using LNG coldness, Energy Conversion and Management, 50(11), pp. 2768-2781.

[8] Lu, T. and Wang, K., 2009, Analysis and optimization of a cascading power cycle with liquefied natural gas (LNG) cold energy recovery, Applied Thermal Engineering, 29(8-9), pp. 1478-1484.

[9] Deng, S., et al., 2004, Novel cogeneration power system with liquefied natural gas (LNG) cryogenic exergy utilization, Energy, 29(4), pp. 497-512.

[10] Buck, A. de, Croezen, H. and Rensma, K., 2008, The 'oxy-fuel' route (in Dutch), Technical Report, 08.3509.09, CE, Delft, The Netherlands.

[11] Anonymous, 2008, The LNG/oxyfuel route for new coal plants – Environmental benefits *plus* cost savings?, Brochure, 2MJAF0801, SenterNovem, Utrecht, The Netherlands.

[12] Anonymous, 2004, LNG vaporizer options study for ConocoPhillips, Technical Report, Exhibit G, Foster Wheeler USA Corp., USA.

[13] Coulson, J.M. and Richardson, J.F., 1983, *An Introduction to Chemical Engineering Design*, 1st ed., Pergamon Press, Oxford, UK.

[14] Anonymous, 2006, *DACE price booklet*, 25th ed., Reed Business Information bv, Doetinchem, The Netherlands.

Exergy Analysis of Propane Pre-cooled Mixed Refrigerant Process Used in LNG Plants

Amirali Dolatshahi[a], *Majid Amidpour*[b]

[a] *Mapna Group, Tehran, Iran*
[b] *K.N.T. University of Technology , Tehran, Iran*

Abstract: This paper provides an exergy analysis for propane precooled mixed refrigerant Process Used in LNG Plants. The equation of exergy destruction and exergetic efficiency for the main system components such as heat exchangers, compressors and expansion valves are developed. The relations for total exergy destruction in the system and the system overall exergetic efficiency are obtained. Also, combine pinch and exergy analysis based method; has been used to improve the overall exegetic efficiency of the refrigeration system through decreasing the temperature difference between the process and refrigerant streams in heat exchangers. It can help to determine which part of the process has the most lost work. Hence, it will be easily identify which sources of system should be optimized. The results show that the minimum work depends only on the properties of incoming and outgoing process streams cooled or heated with refrigeration system and the ambient temperature.

Keywords: LNG, Exergy Analysis, C3Mr, Combine pinch and Exergy Analysis.

1. Introduction

Increasing global demand for natural gas is supporting the rapid growth of worldwide liquefied natural gas (LNG) production capacity. The liquefaction reduces its volume 600- times and thus makes long distance transportation convenient, which has a final temperature of about -162 ◦C approximately atmospheric pressure. The process of cooling and condensing the natural gas requires large amounts of energy, therefore it is necessary to optimize the process and find a suitable way to implement the optimal operation at steady state. There are several processes for liquefying natural gas based on the different refrigerant cycles used, capacity and ambient conditions.

The Propane pre-cooled mixed refrigerant Process (C3/MR) was evaluated in this paper. This process is the most commercial process was used in last decade. In this cycle the natural gas is first pre-cooled with propane, and then cooled further with a mixture of light hydrocarbons (MR means Mixed Refrigerant). The used MR is regenerated by first compressing it and cooling with water, and then cooling it with propane, too. This means both MR and natural gas are cooled with propane.

LNG plant is interesting for pinch and exergy analysis since spends exergy (fuel, electricity) to remove energy (heat) from the substances. Exergy analysis is a powerful tool for designing, optimizing, and performance evaluation of energy systems. Moreover, pinch analysis relies on a process grand composite curve, which is a result of separation process design and By combining pinch analysis and exergy analysis in such a manner, it is possible to predict the shaft work requirement for refrigeration systems with a certain accuracy.

In this paper, the operation C3MR cycle is described first. Then, the exergy equations have been developed for each component of refrigeration system. The next step is applying the exergy analysis to calculate exergetic efficiency and exergy destruction for each component in the system and also on the entire of system. Pinch and exergy analysis that have been studied in this paper, it can help to determine which part of the process has the most lost work. Hence, it will be easily to identify which sources of system should be optimized. The objective of this paper includes the, suggestions for increasing efficiencies, along with the discussion about the reasons for deviation from reversible process.

2. Cycle Operation

The liquefaction of C3MR cycle is analyzed in this study. After a pre-treatment, where the condensate (light oil), carbon dioxide, heavier

Corresponding Author: Amirali Dolatshahi, Email: dolatshahi_a@mapna.com

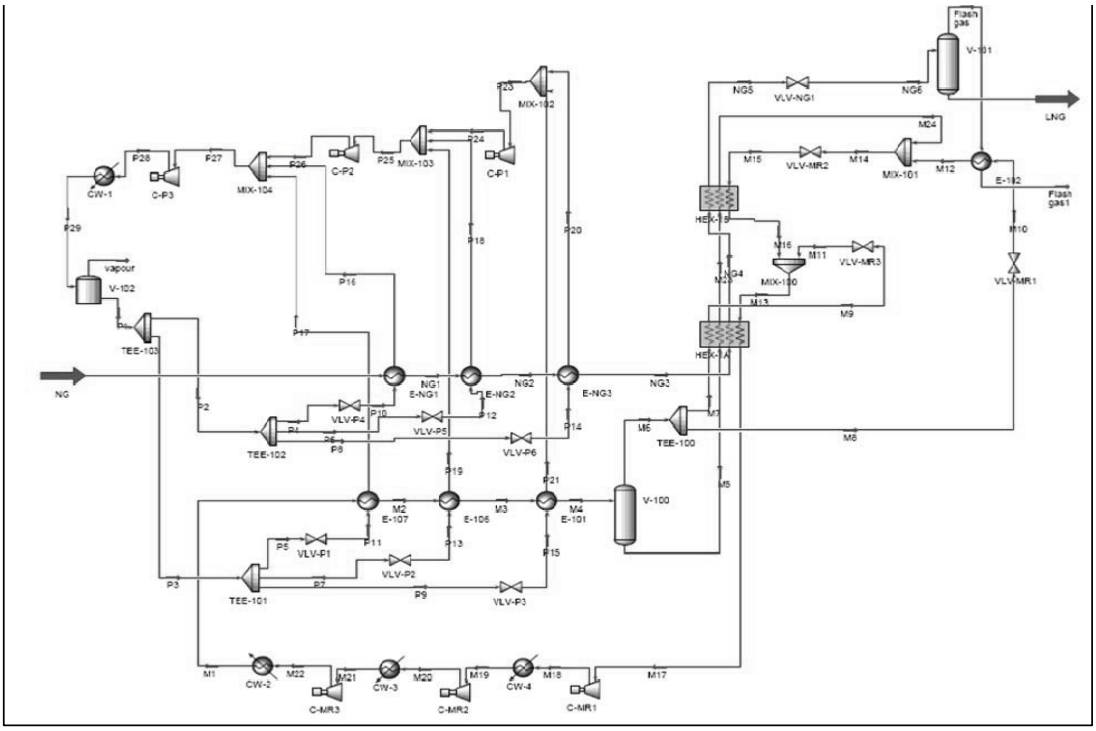

Fig. 1 : C3MR Flow Diagram

hydrocarbons, glycol/water (MEG) and mercury are separated out, the natural gas (NG Stream) is fed to C3MR process. It is cooled down to -162 °C by passing through two main refrigerant cycles, the pre-cooling cycle uses pure component propane. The liquefaction and sub cooling cycle uses a mixed refrigerant made up of nitrogen, methane, ethane and propane.(see Fig.1

Under nominal conditions the properties of the natural gas (NG Stream) and the liquefied natural gas (LNG) leaving the C3MR process are given in table 1.

Table 1. Physical properties of the natural Stream (NG) and LNG stream leaving C3MR

Description	NG	LNG
Flow (m^3gas-(ton)/day)	9.26E+04	8.03E+04
Temperature(°C)	25	-162.9
Pressure (kpa)	5500	117
Methane (Mol-%)	89.70%	91.34%
Ethane (Mol-%)	5.50%	5.76%
Propane (Mol-%)	1.80%	1.71%
i-Butane (Mol-%)	0.20%	0.15%
Nitrogen (Mol-%)	2.80%	1.04%

The pre-cooling cycle uses propane at three pressure levels and can cool the process gas down to -36˚c.In the MR the partially liquefied refrigerant is separated into vapour and liquid streams that are used to liquefy and sub cool the process stream from typically -36˚c to -162˚c .this carried out in proprietary spiral wound exchanger, the main cryogenic heat exchanger (MCHE). (In modelling the MCHE was replaced by shell-and-tube heat exchangers where the cold refrigerant stream was divided in two, upper part of MCHE) and Three, lower and middle parts).

Propane (C3) loop For each pressure level there are two vaporizers: One for cooling natural gas, one for cooling the MR. This gives a total of six propane vaporizers.(HEX:E-NG1 to E-NG3 and E-MR1 to E-MR3)

The propane vapor leaving each vaporizer goes to the corresponding compressor stage. Thus the propane compressor has three stages. Before each vaporizer there is a choke valve that reduces pressure and temperature.

The propane loop contains liquid receivers. For safety reasons it will typically have a suction drum

before each compressor, this is because the feed stream to a gas compressor should never contain liquid as this could damage the compressor.

When the mixed refrigerant (abbreviated MR) leaves the MCHE it should be 100 % vapour. It is compressed from the low pressure at which it leaves the MCHE to a pressure well above 40 bar, in three compressor stages with water coolers between them. (Compressors: C-MR1, 2&3). Then the high pressure MR is cooled with vaporizing propane to about the same temperature as the natural gas. It enters a gas-liquid separator tank. The liquid is fed to the bottom bundle of the MCHE and travels through the bottom and middle bundles. It leaves the middle bundle at about the same temperature as the natural gas leaving the same bundle, and is flashed to a lower pressure before entering the shell side of the MCHE.

The gas fraction from the MR gas-liquid separator is split in two streams. The larger stream enters the bottom bundle of the MCHE and travels through all three bundles of the exchanger, leaving on the top. It is then expanded in a valve and enters the shell side of the MCHE. The other stream is used to heat the fuel gas from the LNG separator tank (HEX: E102), after the exchanger it is expanded in a valve and enters the shell side of the MCHE together with the other stream.

The MR pours down over the tube bundles of the MCHE, and leaves the bottom of the exchanger completely vaporized before entering the first compressor stage, closing the loop.

3. Exergy Analysis

Exergy analysis is useful for evaluating and improving the efficiency of process cycles. It can identify the impact of the efficiency of individual equipment on the overall process and highlight areas in which improvements will produce the most benefits. Exergy is defined as the maximum work obtainable while the system communicates with environment reversibility [1],[2]

$$e = h - h_0 - T_0(s - s_0), \quad (1)$$

Where h is enthalpy, s is entropy, and T_0 is the absolute temperature of the heat rejection sink. For LNG processes, T_0 is the temperature of the ambient air or cooling water since this is the ultimate heat sink for the process.

Multiplying the specific flow exergy by the mass flow rate gives the exergy rate:

$$\dot{E} = \dot{m}\, e, \quad (2)$$

The reversible work as a fluid goes from an inlet state to an exit state is given by the exergy change between these two states. That is:

$$e_2 - e_1 = h_2 - h_1 - T_0(s_2 - s_1), \quad (3)$$

3.1. Compressors

There are six compressors in this cycle. The total work consumed in the refrigeration system is the sum of work inputs to these equipments. There will be no exergy destruction in a compressor if irreversibilities can be totally eliminated. This results in a minimum work input for the compressor. In reality, there will be irreversibilities due to friction, heat loss, and other dissipative effects. The exergy destruction in mixed refrigerant compressors (C-P1toP3 & C-MR1toMR3) can be expressed, respectively, as

$$\dot{I}_c = \dot{E}_{in} - \dot{E}_{out} = \sum (\dot{m}e)_{in} + \dot{W}_{in} - \sum (\dot{m}e)_{out}, \quad (4)$$

Where W_{in} is the actual power inputs to the refrigerant compressors, The exergetic efficiency of the compressor can be defined as the ratio of the minimum work input to the actual work input. The minimum work is simply the exergy difference between the actual inlet and exit states. Applying this definition compressor, respectively, we find :

$$\varepsilon_0 = \frac{\sum (\dot{m}e)_{in} - \sum (\dot{m}e)_{out}}{\dot{W}_{in}}, \quad (5)$$

3.2. Heat exchangers

There are three categories of heat exchangers in the refrigeration system, analyzed in this work. The first and second categories are the multi-steam heat exchanger (HEX-1 A&B) and evaporators (E-NG1 to E-NG3 and E-MR1 to E-MR3) the third category is the cooling water condensers of refrigerant cycle (CW 1-4).

There is negligible heat transfer with the surrounding from above mentioned heat exchangers. Therefore, exergy destruction by undesired heat is zero. An exergy balance written on the first and second categories heat exchangers should express the exergy destroyed in the system

as the difference of exergies of incoming and outgoing streams. That is: [3]

$$\dot{I}_{HEX} = \dot{E}_{in} - \dot{E}_{out} = [\sum (\dot{m}e)_{in}] - [\sum (\dot{m}e)_{out}], \quad (6)$$

The exergetic efficiency of heat exchangers can be defined as the ratio of increase in the exergy of cold fluids to the decrease in the exergy of hot fluids. Applying this definition to the first and second categories of heat exchangers, we obtain:

$$\varepsilon_{HEX} = \frac{\sum [\dot{m}e_{in} - \dot{m}e_{out}]_{hot-stream}}{\sum [\dot{m}e_{in} - \dot{m}e_{out}]_{cold-stream}}, \quad (7)$$

For the third category (CW-1 to 4), in some references exergy analysis for this kind of heat exchangers those use infinite resource as heat sink is not done,[1] but if we define exergetic efficiency as the ratio of increase in the exergy of cold fluids to the decrease in exergy of hot fluids, we obtain:

$$\varepsilon_{CW} = \frac{(\dot{m}_f e_f)_{in} - \dot{m}_f e_f)_{out}}{(\dot{m}_w e_w)_{out} - (\dot{m}_w e_w)_{in}}, \quad (8)$$

Where f refers to flow and w refers to cooling water.

3.3. Expansion valve

There are ten expansion valves in the refrigeration system. Expansion valves are essentially isenthalpic devices with no work interaction and negligible heat transfer with the surroundings. From an exergy balance, we express the exergy destruction for expansion valves of process, respectively, as

$$\dot{I}_c = \dot{E}_{in} - \dot{E}_{out} = (\dot{m}e)_{in} + (\dot{m}e)_{out}, \quad (9)$$

The exergetic efficiency of expansion valves can be defined as the ratio of the total exergy output to the total exergy input. Applying this to all expansion valves with the same order, we obtain:

$$\varepsilon_{CW} = \frac{(\dot{m}e)_{out}}{(\dot{m}e)_{in}}, \quad (10)$$

The total exergy destruction of the entire process shortens by the sum of exergy destruction in heat exchangers, compressors, pumps, and expansion valves.

The total exergy destruction of the entire process shortens by the sum of exergy destruction in heat exchangers, compressors, pumps, and expansion valves.

Using Eqs. (1)-(10), exergy destruction and exergetic efficiency for all compartments in refrigeration system can be listed, and then by comparison of both efficiency and destruction values it will be possible to find the sources of the plant operate in low performance of energy with a large amount of exergy destruction. After finding these weak sources, we can suggest some practical ways like changing the process operation conditions or changing the type of equipments.

4. Simulation results and discussions

The exergy analysis of propane pre-cooled mixed refrigerant process was carried out in the present study to evaluate the magnitude of exergy destruction and exergetic efficiency in each component. The results are summarized in Figs. 2

Actual work input required for a C3MR process depends mainly on cooled or heated process streams, ambient conditions and on compressor efficiency (The actual work input term is the sum of the work inputs to the compressors and pumps).

The obtained results reveal that the main site of exergy destruction in the C3MR process is the compression system. Therefore, any improvement in the exergetic efficiency of the compressors will automatically yield lower input for the system and increase the exergetic efficiency of the overall refrigeration system. The temperature difference and heat exchange load in heat transfer contribute to the exergy destruction, so large temperature difference and heat exchange load are the primary reasons of the exergy destruction in cooling water heat exchangers. Although the lowest efficiencies is in the refrigeration system belong to the evaporators heat exchangers (E-NG1).

In this case we can improve the exegetic efficiency of the overall refrigeration system by decreasing the temperature difference between the process and refrigerant streams in the heat exchangers or by changing the type and configuration of heat exchangers for cooling water system.

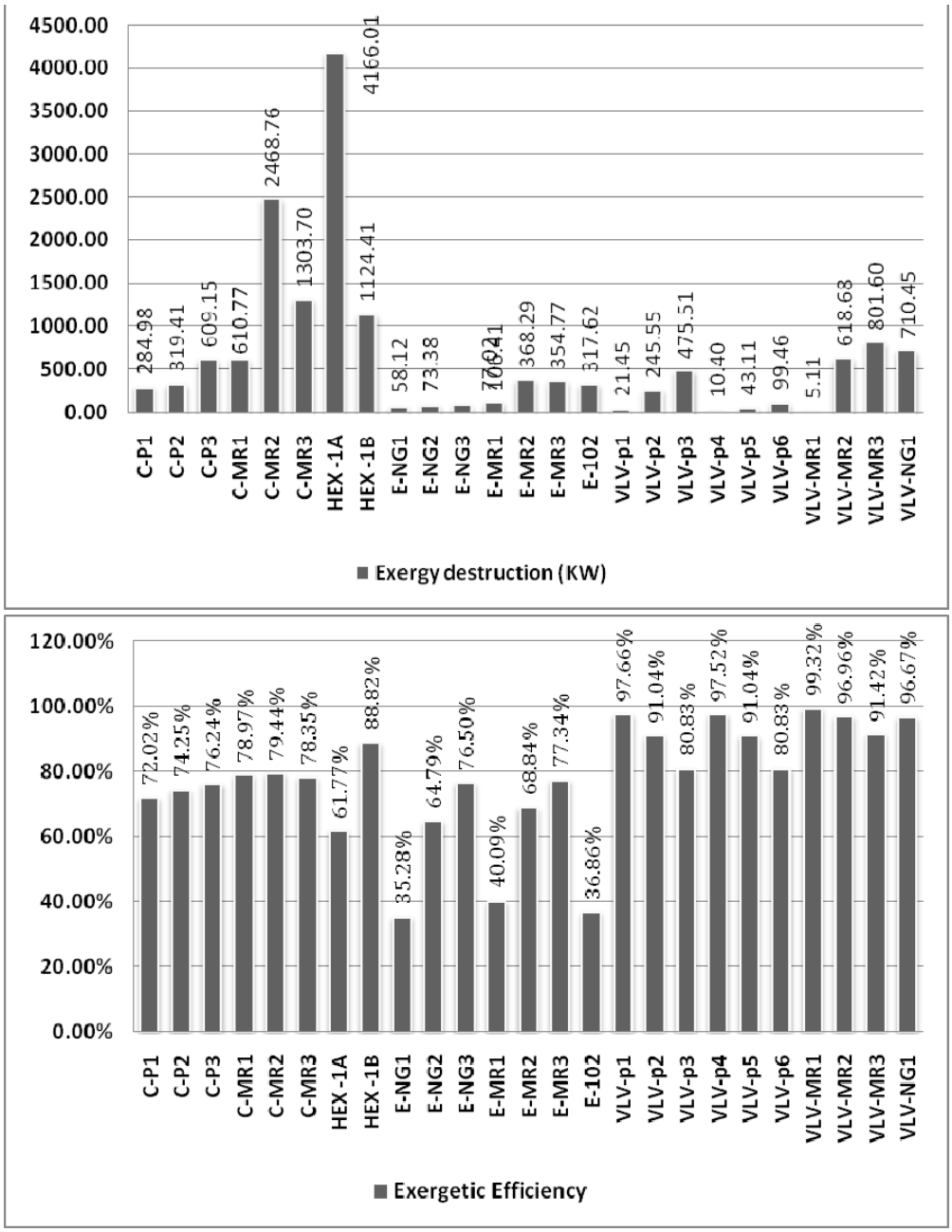

Fig. 2 Exergy Destruction and Exergetic Efficiency of C3MR components.

5. Shaft work targeting through combined pinch and exergy analysis

Exergy Composite curves (ECC) and& Exergy Grand composite curve (EGCC) [5] of the main heat exchanger (HEX-1A&B), C3MR process of LNG plant studied in this work is shown in Fig. 3and.[5]

Minimum temperature approach $\Delta T = 2°C$ min is used. The GCC provides the overall source and sink temperature profiles of a process. It allows setting the refrigeration load at any temperature level continuously. Another benefit of using GCC

is that it considers the integration among the process, heat exchanger network and refrigeration cycle simultaneously.

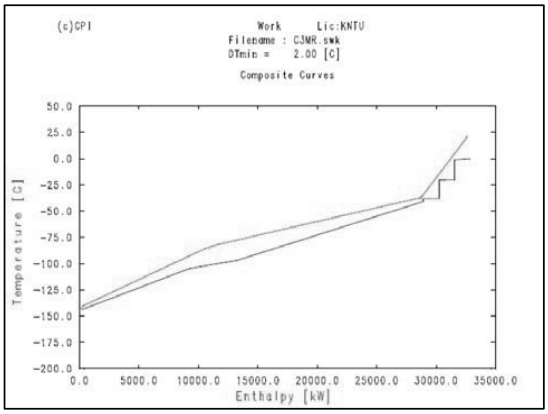

Fig. 3 Exergy Composite curves(ECC)[4]

Due to the complicated interactions amongst refrigeration systems, processes and Heat Exchanger network (HEN) it is impractical to use rigorous simulation tools to check the impacts on refrigeration systems every time there are design changes in processes. Linnhoff and Dhole introduced an exergy-based procedure for estimating shaftwork. It estimates shaftwork directly from the process stream data without going through detailed refrigeration calculations. The temperature axis of the GCC is converted to Carnot Factor ($\Omega = 1- T_0 /T$) to generate Exergy Grand Composite Curve (EGCC) as illustrated in Figs. 5[5]

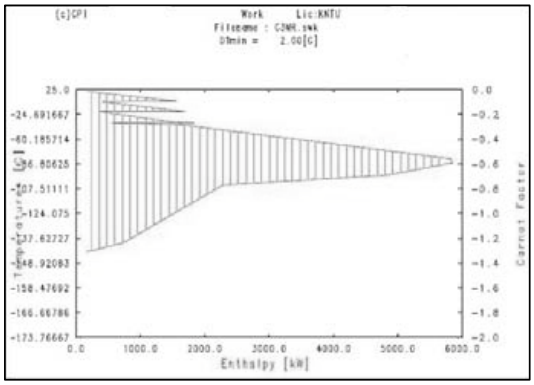

Fig. 5 Exergy Grand composite curve(EGCC)[4]

It shows the process grand composite curve plotted in Carnot axis. The below ambient exergy loss is highlighted by the shaded regions. Knowing this target value significantly aids the process optimization problem by providing an ultimate goal with which possible process improvements can be compared.

6. Conclusion

An exergy analysis of the propane pre-cooled mixed refrigerant process of LNG plant is performed. The equations of exergy efficiency and exergy destruction for each component of refrigeration system are developed. The exergy analysis results on the refrigeration cycle indicate that the major irreversibilities in the process due to losses within the compression system, driving forces across the cooling water heat exchangers, and losses due to refrigerant letdown, and it shows changing the type and configuration of heat exchangers for cooling water system can improve the exegetic efficiency of the overall refrigeration system by decreasing the temperature difference between the process and refrigerant streams in the heat exchangers. In the end ECC and EGCC for main heat exchangers show The below ambient exergy loss regions .

Acknowledgments

We appreciate Iran power plant projects management company (MAPNA) for supporting this work.

References

[1] Bejan A. Advanced Engineering Thermodynamics. New York: John Wiley & Sons, 1997.

[2] Kotas TJ. The Exergy Method of Thermal Plant Analysis. London: Butterworths. 1995.

[3] M. Mafi, S.M. Mousavi Naeynian, M. Amidpour. Exergy analysis of multistage cascade low temperature refrigeration systems used in olefin plants International Journal of Refrigeration 2008.

[4] CPI software Umist (university of Manchester) .

[5] Linnhoff B, Dhole VR. Shaftwork targets for low temperature process design. Chemical Engineering Science. 1992.

[6] Smith R. Chemical Process Design and Integration. New York: John Wiley & Sons. 2004.

Effect of DSM in Cold Storage on Product Properties and Electricity Usage

Chutchawan Tantakitti[a] *and Preecha Sriprapakhan*[a]

[a] *Faculty of Engineering, Chiangmai University, Chiangmai 50200, Thailand*

Abstract: Frozen packages of shrimp and bean are stored in a cold room where temperature is set at -20 °C during on-peak and switched to -40 °C during off-peak period to reduce energy demands. In this study, effects on frozen products properties and electricity requirement were investigated. Temperature at various positions in the cold room as well as core and surface temperature of products and electricity requirement are monitored. All measurements have been undertaken and recorded every 6 minutes for at least 9 months. Products are sampled at 0, 1, 3, 6 and 9 month to evaluate physical and chemical properties, and against both control and international food standards. Preliminary results show that significant electrical peak reduction of about 54 % can be achieved while frozen products quality remained acceptable, in accordance to international standard.

Keywords: Frozen shrimp, Bean, DSM, Thermal storage.

1. Introduction

By December 2008, Thailand has 29,139.5 MW installed electric production capacity. The Electricity Generating Authority of Thailand (EGAT) is responsible for 49% and another 51% has been taken care by a private sector. On April 2009, the usage peak is 22,886 MW therefore only 22.4 % is left for reserve. However, the reserved capacity will continuously decrease due to higher electricity consumption from the economic growth, high ambient temperature, maintenance shut down, and accidents of NPG supply to the power plants. To catch up with this demand, more power plants are required. However, this approach takes much longer time because of the probable conflicts with local residents around the intended area of construction. Therefore, alternative ways to reduce the electricity demand should be improved concurrently with building new power plants. For many years, the thermal storage technique has been implemented to reduce peak in most buildings but has never been applied to the refrigerated cold storage due to a lack of research on the economics of the refrigeration system as well as changes of product qualities.

In the study by [1], the electrical demand reduction in refrigerated warehouses by using thermal storage for frozen products was modeled. From his model, full demand shifting offered the greatest saving but required the largest amount of installed refrigeration capacity. This strategy involved a complete shutdown of the refrigeration equipment during On-Peak period. The temperature fluctuated between -12.5 °F and -2.5 °F. The electrical saving was 53 % and a simple return on investment was approximately 83 %. Nonetheless, the effect of temperature fluctuation on quality of frozen products was not tested.

Reference [2] investigated the qualities of freeze/thaw cycle of cauliflower, sealed in polyethylene bag, with the temperature ranges between -8 °F and 39 °F for a period of 10 days. They found a 35% loss of Vitamin C over the controlled samples. No color change. However, the loss of flavor and softened products were observed.

Another study [3] investigated the qualities of frozen strawberry and blackberry in 10 lb moisture-proof bags inside corrugated boxes, raspberry in 3 lb metal can, and peach in 1 lb waxed cartoons. The temperature was controlled ranging between -20 °F to 0 °F and 0 °F to 10 °F for 12 months. The results showed that color, flavor and aroma of all products under low temperature cycle were slightly less pleasing than those kept at constant temperature of –10 °F. For high temperature cycle, the results were worse.

A similar study [4] examined frozen snap beans, corn, peas, strawberry, raspberry and cantaloupe with unidentified packing. The temperature is set ranging between -20 ^{o}F and 0 ^{o}F for 6 months. No differences on appearance or palatability occurred as compared with the constant temperature one.

Reference [5] studied frozen roast pork wrapped in cellophane. The product was kept under 0 ^{o}F for 6 days and followed by additional 6 days under 20 ^{o}F; this cycle went on for 1 year. They reported the quality changes to be equivalent to the control food that was kept under a constant temperature of 10 ^{o}F.

In Thailand, there are 549 refrigeration plants that have installed 165 MW electricity power [6]. 205 plants (with 66 MW power) are cold storages which keep frozen products. These frozen products can be used as the cold storage media, similar to ice storage in a building system. The reduction of the electrical peak is possible, but the physical and chemical properties of the products also have to be within the acceptable range.

Fig.1. Frozen Japanese bean and shrimp.

This study was conducted on frozen Japanese bean (vegetable) and shrimp (meat), as shown in Fig. 1, the two most exported products of Thailand. The temperature was controlled fluctuation between -40 ^{o}C during the Off-Peak (21.00 PM to 8.00 AM.) and -20 ^{o}C during the On-Peak (8.00 AM. to 21.00 PM.), everyday for 9 months. The samples at the month of 0th, 1th, 3th, 6th and 9th were taken for the physical and chemical tests for qualities by comparing with the controlled products of that month.

2. Experimental setup

In determining physical and chemical qualities of the products, frozen beans were packed at 1kg each in a polyethylene bag; 3 bags were put in one corrugated box to the total of 72 boxes (216 kg). Frozen shrimps were stored 1.5 kg each in a waterproof box; 6 boxes were in one corrugated box to the total of 24 corrugated boxes (216 kg). The typical forced-air cooling cold storage, 2.4 x 2.4 x 2.4 m^3 (outside dimension) with 200 mm. thick of sandwich polystyrene panel as shown in Fig. 2, were built to store those products. The concrete blocks were laid on the floor to imitate the concrete floor as in a typical cold room. The piping and instrument of refrigeration system (Fig. 3) was designed to cool down the room to -40 ^{o}C.

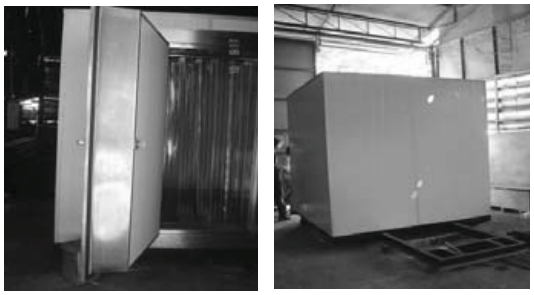

Fig. 2. A 2.4 x 2.4 x 2.4 m^3 cold storage room.

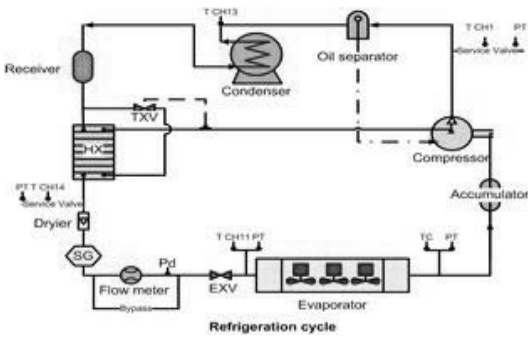

Fig. 3. Piping and instrument of refrigeration system.

The 2.1 kW refrigeration load was calculated. The condensing unit "Emerson" Model ZX1060e TFD 450 and the evaporator "ECO" Model CTE065L8 ED, which a cooling capacity of 3.8 kW. (-40 ^{o}C evaporating temperature and +38 ^{o}C condensing temperature), were selected due to minimum available and installed; R404a was used as a refrigerant. The room thermostat was set to cut-in and cut-out at 2 ^{o}C. The data logger was connected to record the pressure, temperature and refrigerant's flow-rate of the refrigeration system as well as room temperature, surface and core temperatures of product, electric usage, and power peak every 6 minutes for 9 months. Physical and chemical properties of the products from this room

were tested and compared with the controlled products.

3. Results and discussion

3.1. Product qualities

The qualities of shrimp, gross weight and net weight slightly increased with time due to the ice flake that occurred and became larger. This also increased the shearing force (before thawing). Larger ice crystal may had destroyed shrimp cells, so after thawing, the solid inside the cells were drained out with water. With lesser solid components, the shearing force was lower. The color of frozen shrimp had a small change to blue which corresponded to the quality drop in color aspect. However, the quality of a microorganism tended to decrease as occurred in controlled products.

For beans, the shearing force dropped starting at the 0th month because the cells of bean were destroyed by ice flakes and the enzyme "Peroxidase" which was used in a blanching process. The quality of microorganism tended to drop as it also appeared in the controlled products.

Tables 1 and 2 show the average physical and chemical properties of both products as well as the controlled ones. All properties passed the export standards and the international frozen food standards.

Table 1. Physical Properties.

Physical Qualities	Frozen shrimp		Frozen bean	
	Sample	Control	Sample	Control
Gross weight (kg)	1.97^{ns}	2.00^{ns}	1.02^{ns}	1.02^{ns}
Net weight (kg)	1.96^{ns}	1.97^{ns}	1.00^{ns}	1.01^{ns}
Drain weight (kg)	1.51^{ns}	1.49^{ns}	1.01^{ns}	1.00^{ns}
L (Lightness)	46.35^{ns}	46.96^{ns}	55.59^{ns}	55.34^{ns}
a (Greenness - Redness)	$0.44-^{ns}$	$0.49-^{ns}$	$17.46-^{ns}$	$16.90-^{ns}$
b (Yellowness - Blueness)	4.33^{ns}	4.04^{ns}	22.39^{ns}	22.01^{ns}
Shear force (N) before thawing	124.96^{ns}	111.98^{ns}	-	-
Shear force (N) after thawing	124.96^{ns}	111.98^{ns}	12.93^{ns}	12.83^{ns}

Table 2. Chemical Properties.

Chemical Qualities	Frozen shrimp		Frozen bean	
	sample	Control	Sample	Control
Total soluble solid (°Brix)	16.88^{ns}	17.25^{ns}	8.59^{ns}	8.77^{ns}
pH	7.12^{ns}	7.06^{ns}	6.31^{ns}	6.27^{ns}
Salt (%)	0.34^{ns}	0.33^{ns}	1.19^{ns}	1.19^{ns}
Aw	0.81^{ns}	0.82^{ns}	0.82^{ns}	0.84^{ns}
Microorganism Qualities				
Total plate count (cfu/g)x10^{-3}	22.3^{ns}	17.9^{ns}	13.8^{ns}	9.3^{ns}
Yeast and mold (cfu/g)	53.08^{ns}	114.58^{ns}	92.91^{ns}	41.38^{ns}
Total coliform (cfu/g)	171.08^{ns}	177.08^{ns}	280.25^{ns}	255.50^{ns}
E. coli (cfu/g)	0	0	0	0
Enterobacteriaceae (cfu/g)	720.98^{ns}	446.67^{ns}	368.81^{ns}	518.92^{ns}
Salmonella	none	none	none	none
S. aureus (cfu/g)	0	0	0	0

Table 2. Chemical Properties (cont.)

Sensitivity	Frozen shrimp		Frozen bean	
	Sample	Control	Sample	Control
Color (non-cooked)	6.93^{ns}	6.96^{ns}	-	-
Flavor (non-cooked)	7.01^{ns}	7.04^{ns}	-	-
Color (cooked)	7.15^{ns}	7.20^{ns}	7.36^{ns}	7.14^{ns}
Flavor (cooked)	7.25^{ns}	7.33^{ns}	7.05^{ns}	7.09^{ns}
Taste (cooked)	7.26^{ns}	7.56^{ns}	7.21^{ns}	7.26^{ns}
Firmness (cooked)	7.42^{ns}	7.49^{ns}	7.12^{ns}	7.16^{ns}
Overall acceptability (cooked)	7.36^{ns}	7.54^{ns}	7.35^{ns}	7.18^{ns}

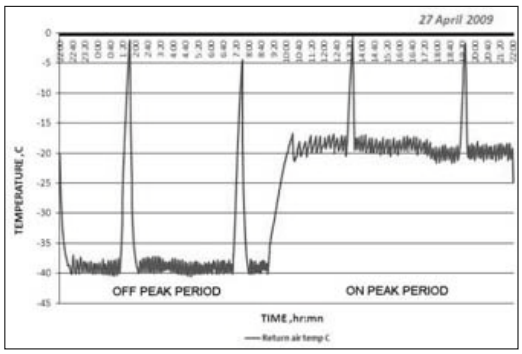

Fig. 4. Daily room temperature.

3.2. Room temperature

Fig. 4 illustrated the room temperature over time during Off–Peak and On-Peak periods on April 27th, 2009, the recorded hottest day. At 22:00 PM, the refrigeration system started to cool the room down to -40 °C which took approximately 40 to 60 minutes depending on the ambient temperature. Then, the refrigeration system was run approximately under a cycle of 5 minutes ON and 10 minutes OFF. The system worked only 20 minutes per hour because the installed

refrigeration capacity was greater than the designed valve. The spikes of the room temperature occurred at the defrosting period (every 6 hours). The electric defrost was used instead of the typical hot-gas defrost. At 9:00 AM, the room thermostat was reset to -20 °C. It took approximately one hour to raise the room temperature up to this setting point because the cooling energy, stored in the products, was released out in the room. The compressor runtime during this On-Peak period was longer than the Off-Peak due to a higher ambient temperature. However, the refrigeration capacity was still too large.

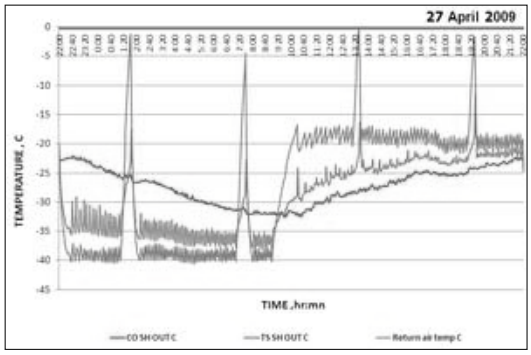

Fig. 5. Daily core and surface temperature of shrimp.

3.3. Surface and core temperature of products

Fig. 5 shows the core (CO SH IN C) and surface (TS SH IN C) temperature of frozen shrimp on April 27th, 2009. The core temperature started to drop from -22.6 °C to -32.1 °C during Off-Peak period while the surface temperature decreased with a faster rate to the final temperature close to the room temperature. The rate of stored energy was 0.73 °C/hr. During On-Peak period, the surface temperature rose quickly to the room temperature; the core temperature rose with the similar trend to -22.8 °C at the end of On-Peak period. The rate of released cooling energy was 0.85 °C/hr. The rate of released energy was greater than the stored energy because the compressor runtime during On-Peak was longer than during Off-Peak. Fig. 6 shows the similar changes of temperature for frozen beans. However, the rate of stored energy in beans was 1.04 °C/hr and the rate of released energy was 1.24 °C/hr. Both rates were higher than in shrimp because beans have higher surface area per weight than shrimp does; the energy could be stored and released faster.

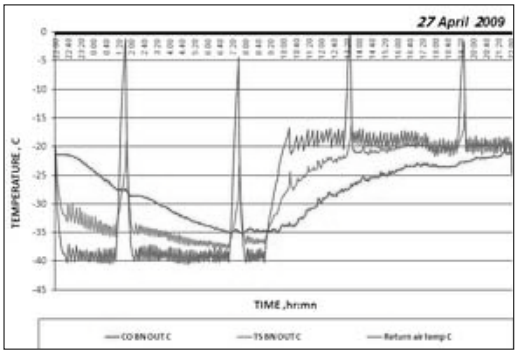

Fig. 6. Daily core and surface temperature of bean.

3.3. Partial storage system

In this experiment, the partial storage was achieved. The refrigeration system was on during On-Peak period because the room temperature was raised up to the set temperature, when the core temperature of the products was below -20 °C. If the measured room temperature was equal to a core temperature, the refrigeration system would not be turned on; a full storage would be necessary. In practice, a room thermostat will be placed at the return air of evaporator and close to the exterior wall as similar to this experiment. In this case, there may be heat gain from outside which will affect a thermostat. Further study is required to study this effect.

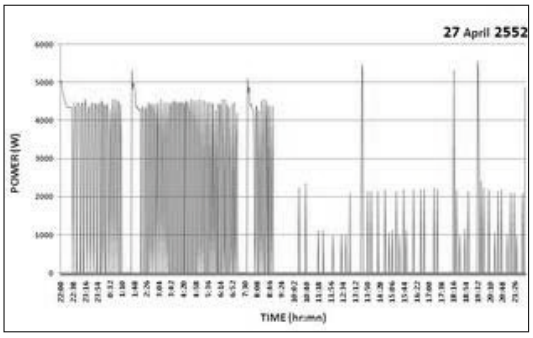

Fig. 7. Daily total power profile for a thermal storage.

3.4. Electric power of refrigeration system

Fig. 7 illustrated total electric power consumption of refrigeration system on April 27th, 2009. The power consumption during Off-Peak was approximately 4.5 kW which was higher than

during On-Peak which was about 2.28 kW. This was due to the refrigeration system was operated at lower evaporating temperature and higher cooling load during Off-Peak than On-Peak. Moreover, the flow of refrigerant in the compressor could be varied. During defrosting period, the power peak was dominant by the electric heater. Fig. 8 demonstrated that the electricity usage and rate during Off-Peak were higher than during On-Peak period.

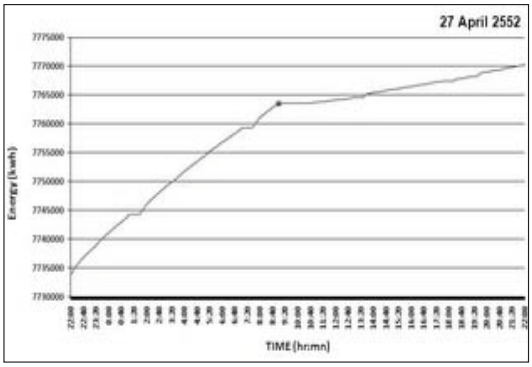

Fig. 8. Electric energy consumption profile.

Table 3 illustrated total electric consumption of each month which was separated into On-Peak and Off-peak periods. The electricity usage during Off-Peak was 274 % higher than during On-Peak.

Table 3. Monthly electricity consumption.

	Energy (kWh)			Peak
Month	Total	On peak	Off peak	(kW)
October	1,042.90	198.8	844.1	2.06
November	990.1	222.62	767.48	2.11
December	968.4	202.15	766.25	2.07
January	938.3	187.8	750.5	2.01
February	854.6	191.08	663.52	2.07
March	1,075.60	235.44	840.16	2.18
April	1,141.60	226.05	915.55	2.28
May	1,128.20	245.9	882.3	2.31
June	1,092.30	239.38	852.92	2.14
Total	9,232	1,949.22	7,282.88	

3.5. Peak reduction

Since most large cold storage plant would have the hot-gas defrost, or even an electric defrost, the peak would not dominant from both of these. But this study only measured the peak from the refrigeration system so the power from the electric defrost would be a major peak as shown in Fig. 7. To be able to study the peak reduction due to a thermal storage, the power due to the electric defrost were neglect. So, the electricity peak with a thermal storage was approximately at 2.28 kW, This cold room had also been operated at a constant -20 ^{o}C room temperature, as shown in Fig. 9, the peak was close to 4.8 kW; 2.52 kW greater than the peak with a thermal storage (2.28 kW). So the electricity peak reduction was 53.8 % which was close to the result of [1].

If this figure was used to predict for the entire country, the potential peak saving was estimated to be 36.3 MW.

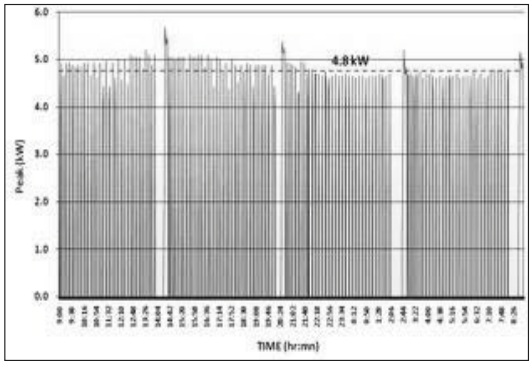

Fig. 9. Power profile for -20 ^{o}C constant room temperature.

4. Conclusion

The fluctuation of storage temperature in the cold room has small effect on both physical and chemical qualities of frozen products for a long storage period. All properties passed the export standards and the international frozen food standards. Frozen products can be used as a thermal storage media. Partial storage is achieved. The electricity usage and rate during Off-Peak were higher than during On-Peak period. The electricity peak reduction was 53.8 %.

Further detailed study and verification on the refrigeration system and control, frost formation, and rates of stored and released heat from the products will be done. The computer simulation will be developed; the calculated results will be compared with the experimental data so the program can be applied for future DSM prediction without additional experimental runs.

References

[1] Altwies, J.E., 1998, Electrical Demand Reduction in Refrigerated Warehouses, M.Sc. Theses, University of Wisconsin-Madison, Madison, WI .

[2] Aparicio-Cuesta, M.P. & Garcia-Moreno, C. 1988, Quality of Frozen Cauliflower during Storage, Journal of Food Science, 53.2 (1988), pp. 491-493.

[3] Woodroof, J.G., & Shelor, E., 1947, Effect of Freezing Storage on Strawberries, Blackberries, Raspberries and Peaches, Food Freezing, pp 206-209, 223.

[4] Hustrulid, E. & Winter, J.D., 1943, The Effect of Fluctuating Storage Temperature on Frozen Fruits and Vegetables, Agricultural Engineering, 24(12), pp. 416.

[5] Gortner, W.A., et al., 1948, Effect of Fluctuating Storage Temperatures on Quality of Frozen Foods, Industrial Engineering and Chemistry, 40 (8), pp. 1423-1426.

[6] Department of Industrial Works, Cold Storage Factory Databases, Group 92, 1993.

Acknowledgments: The authors would like to thank the Electricity Generating Authority of Thailand for funding this research.

Integrated Thermo-economic Modeling of Geothermal Resources for Optimal Exploitation Scheme Identification

Michael Hoban[a], Léda Gerber[b], and François Maréchal[b]

[a] *RES | The School for Renewable Energy Science, Akureyri, Iceland*
[b] *Industrial Energy Systems Laboratory, Ecole Polytechnique Federale de Lausanne, Lausanne, Switzerland*

Abstract: This paper details the development of a systematic methodology using thermo-economic modeling that can be used to identify the optimal exploitation schemes of geothermal resources. A multi-period approach is used, integrating the superstructure of exploitable resources with the superstructure of conversion technologies and multiple demand profiles. In the example case, exploitable resources include an enhanced geothermal system, a deep aquifer, and a shallow aquifer. Power generating systems considered are organic Rankine cycles and both single and double flash steam cycles, which can be used for combined heat and power production. Heat pumps are also considered, as well as back up systems in case geothermal resources alone cannot fully satisfy demand. Periods considered for the demand profiles of district heating and cooling are summer, winter, inter-seasonal, and extreme winter and summer conditions. These are based on the city of Nyon, Switzerland for the example case. In the next step, process integration techniques are then used to design the overall geothermal system. The economic and thermodynamic performance of the system is then calculated. Finally, an evolutionary algorithm is employed to determine the optimal exploitation schemes and system configuration across the multiple periods, with exergy efficiency and annual profit as objectives.

Keywords: Energy systems, Geothermal, Multi-objective optimization, Multi-period, Process design, Renewable energy conversion, and Simulation

1. Introduction

There has been recent interest in the use of geothermal resources to deliver utility scale electricity and district heating and cooling [1]. The first step developing a geothermal system is the identification of the resource. Geothermal resources can exist in a variety of forms, the majority of which fall into natural hydrothermal systems, geopressured systems, enhanced geothermal systems (or hot dry rock), magma, and ultra low-grade systems [1].

Next, there must be a determination of the service that the geothermal resource would provide. This must take into account nearby cities and their respective demand for electricity, heating, and cooling. As the demand for these services changes throughout the year, it is useful to consider the system for all the periods for which it is used.

Finally, it must be decided what is the best way to convert the geothermal source into the useful service to be delivered. Conversion technologies can include a number of power cycles including flash systems and organic Rankine cycles. Furthermore, a wide range of configurations for each of these conversion systems exists, including options for meeting a district heating demand. This includes the type of conversion and distribution system and in what ways the geothermal source is utilized (heat extraction, injection, or storage) and at what depth these actions are to take place [2].

For each of these configurations of the above-mentioned factors, there will be a set of associated thermodynamic and economic performance indicators. The need for a tool to evaluate the various resources, conversion technologies, and demand combinations using these performance indicators is readily apparent in order to identify the optimal configurations of the system. This can be achieved by the use and optimization of a model that can simulate the configurations and their associated performance within the multiple demand profiles throughout the year.

Girardin and Marechal (2007) [3] have applied pinch analysis methods for the optimal integration of the geothermal conversion system. This required modeling of the major geothermal conversion systems and their multi-objective optimization. However, this study does not take

into account geothermal resource parameters, but solely the conversion technology parameters. Analysis of the multi-period problem has been explored by studies [4] and [5], but none pertain specifically to geothermal systems and the specific challenges they present.

This paper presents a systematic methodology for optimizing energy conversion system design and to identify the optimal exploitation scenarios of geothermal systems within the multi-period framework.

2. Methodology

The methodology is developed using a computational platform that creates interfaces between different models that represent the energy system design. The resolution of the system follows the diagram in Fig. 1. If the results of only a single set of decision variables are desired, the system optimization step is not performed.

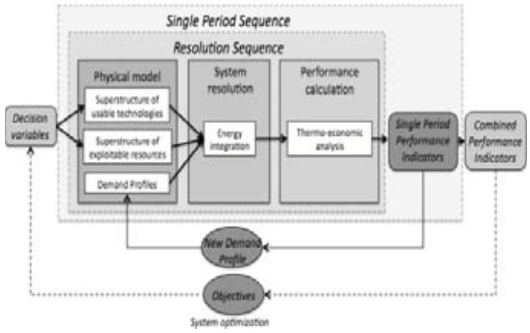

Fig. 1. Resolution Sequence

The multi-period aspect of the system specifically affects the demand profiles and as such, the system performs the resolution sequence for each demand period. The physical model stage includes the superstructures of usable technologies, exploitable resources, and demand profiles. System resolution uses process integration techniques to optimize heat exchange and to size various system components. A thermo-economic analysis is then performed to evaluate the performance of the system configuration. Iterations of the sequence can be performed in order to run an optimization while varying selected decision variables.

2.1. Physical model development

Physical models in this system are represented using process flow diagrams in the flowsheeting software Belsim-Vali. A separate model is created for each resource and conversion technology. This allows for calculating the operating conditions and thermodynamic states associated with a given set of input parameters. Demand profiles are implemented within the system resolution.

2.1.1 Resource Models

For the application of the methodology, three hypothetical geothermal resources are considered in the resource superstructure. They are an enhanced geothermal system (EGS), a deep aquifer (DA), and a shallow aquifer (SA). For each one, the geothermal fluid is assimilated to pure water. The table below contains the default parameters of these resources, where T1 and T2 refer to the production and injection temperatures, respectively.

Table 1. Resource Parameters

	EGS	DA	SA
T1 [K]	473.15	363.15	285.15
T2 [K]	373.15	318.15	283.15
Flow [kg/s]	50	20	20

The EGS model is based on the work done by Haring [6] in his paper on deep heat mining of an enhanced geothermal system in Basel, Switzerland. The DA and SA systems modeled in this study refer to a natural hydrothermal system that can produce fluid spontaneously. For the DA, the model is based on an existing system in Riehen, Switzerland, which is used to provide district heating [7]. All models use reinjection of the geothermal fluid. The amount of available heat is determined from the resource models. Additionally, the drilling depth is calculated using an assumed thermal gradient of 4°C for every 100 meters of drilling depth [6].

2.1.2 Conversion Technologies

Ten separate ways to convert energy from the geothermal resources are considered for the application of the methodology (see Fig. 2).

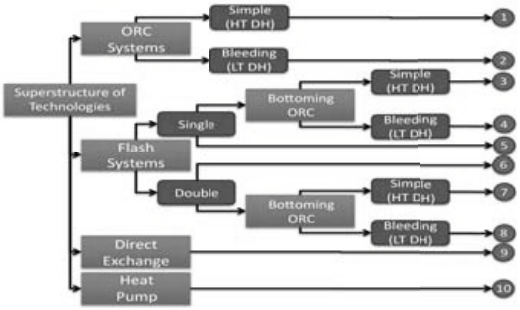

Fig. 2. Geothermal Conversion Technologies

In Fig. 2, ORC refers to an organic Rankine cycle. The ORC with bleeding is a cycle that includes intermediate bleeding in the turbine. HT DH and LT DH stand for high temperature district heating and low temperature district heating, respectively. LT DH uses intermediate bleeding in the turbine. The default working fluid in the ORC is iso-butane and the heat pump model uses ammonia as the working fluid. Direct exchange between the geothermal fluids and cooling stream with the district heating and district cooling streams is also considered. A boiler is included as a back up option in case the geothermal system is unable to meet the district heating demand alone.

2.1.3 Demand Profiles

Finally, it is necessary to consider the demand for the energy services and how this changes throughout the year. These periods and their associated demand profiles can be viewed in Table 2 below. DH and DC stand for district heating and district cooling, respectively.

Table 2: Demand Profiles

	DH (MW)	DC (MW)	Hours	Ambient (°C)
Extreme Cold	30.0	0.0	40	-6.0
Winter	20.0	0.0	2900	1.0
Inter-Seasonal	10.0	7.0	2700	10.0
Summer	5.0	10.0	400	14.0
Extreme Hot	1.0	10.0	20	17.0

For the application, the demand profiles are based on data for the city of Nyon, Switzerland. The data are derived from a statistical demand calculation of the number and type of buildings. Factors affecting the individual building consumption include construction period and utilization. Geographical data including building position and area are also taken into account [8]. Demand for electricity is not included within the demand profiles. It is assumed that the geothermal system will be providing services for a grid connected region and as such, shortcomings in electricity generation will be met from other sources on the grid.

2.2. System Resolution

System resolution refers to the determination of the various heat loads and the relevant equipment sizing and integration. At this stage, the energy flows (the hot and cold streams of the system) calculated by the physical model are provided as inputs to perform the energy integration. This aims to determine the optimal integration of the energy conversion system to satisfy the demand of the current period using the available resources. The demand period heavily influences this as it affects the size of the district heating and district cooling streams. Process integration techniques are then used, whose methodology is defined in [9]. After this step, it is possible to determine the design of the heat exchanger network. This includes the minimum number of heat exchangers, the total heat exchanger area, and the sizing of any variable hot or cold streams and the units they belong.

2.3 Performance Indicators

After the completion of energy integration, the thermodynamic conditions of the system are defined and the necessary equipment identified and sized. Thermodynamic and economic performance indicators are now computed to evaluate the performance of the system configuration.

2.3.1 Thermodynamic Performance Indicators

Of interest to this study is how efficiently the conversion systems utilize the geothermal resources to deliver useful services. As such, energy efficiency, exergy efficiency, and electrical efficiency are calculated. Exergy efficiency is particularly relevant in the case of geothermal systems, as it allows for a better evaluation of the system in terms of electricity and district heating and cooling production [10]. Although other thermodynamic indicators are defined, this analysis will focus on exergy. Exergy efficiency will be defined as shown in (1).

$$ex_{eff} = \frac{\dot{E}_{Net\_Electric} + \dot{E}x_{Heating} + \dot{E}x_{Cooing}}{\dot{E}x_{EGS} + \dot{E}x_{DA} + \dot{E}x_{SA} + \dot{E}x_{Cool} + \dot{E}x_{Boiler}}, \quad (1)$$

Note that if the net electricity is negative, the term will be made positive and divided by an assumed exergetic electrical generation of 0.35 and added to the denominator. This creates a significant penalty for a system that imports electricity. Since all exergy terms besides the net electricity are related to thermal streams, each one will be defined as seen in (2).

$$\dot{E}x = \dot{Q} \cdot (1 - \frac{T_a}{T_{lm}}), \quad (2)$$

$\dot{Q}$ is the heat load of the stream and T_a is the ambient temperature. T_{lm} is the log mean temperature difference and is defined in (3).

$$T_{lm} = \frac{T_{in} - T_{out}}{\ln(T_{in}/T_{out})}, \quad (3)$$

Each thermodynamic indicator is computed for each demand period. Combined indicators are found taking a weighted average considering the operating hours of the period, as shown in (4).

$$ex_{total\_eff} = \frac{\sum_{i=1}^{6} ex_{eff,i} \cdot period_i}{8760}, \quad (4)$$

2.3.2 Economic Performance Indicators

Costs were estimated for the relevant capital, operations and maintenance, and fixed costs. The equipment cost is calculated using the data from [11] and [12]. The Marshall and Swift index is used to actualize these costs. Drilling costs were based on data from the WellCost Lite model as outlined in [13]. Equation (5) shows the general formulation, based on drilling depth, in million USD.

$$CI_{drilling}(D) = 3 \times 10^{-8} \cdot D^2 + 0.0019D - 1.3958, \quad (5)$$

Drilling at shallow depths is assumed to costs approximately 100USD per meter of drilling depth. The cost of the district heating network was based on data from the Riehen system in northwest Switzerland [7].

$$CI_{DH\_Network} = 38.7 \cdot DH_{load}, \quad (6)$$

Here, the maximum district heating load (usually extreme winter) will be used to size the system.

Cooling tower costs are based on actual cooling tower costs and then scaled based on size as recommended by [14].

$$CI_{Cooling} = 154179 \cdot (Q_{Cooling}/5193)^{0.93} \quad (7)$$

Other direct and indirect costs were estimated using relationships between the total purchased equipment costs and total direct costs [14]. The total capital investment was annualized using an interest rate of 0.06 and an assumed project lifetime of 15 years. The total operating costs are comprised of import costs, export costs, maintenance costs, and man power costs. It is assumed that there are no import costs associated with the extraction of the geothermal fluid. However, any purchased electricity or fuel for the back up boiler is considered here. Export costs are actually the profits produced by the system: electricity, district heating, and district cooling sold.

Maintenance costs will vary depending on the system used. For the flash systems, it is assumed to be \$100/kW/year [15]. ORC maintenance costs will be much lower, and are estimated to be \$10/kW/year. Employment or the specific manpower costs for all systems are estimated to be \$68/kW/year. This is assuming that 1.7 jobs per MW of capacity and each job is compensated \$40,000 [16]. The fixed cost, F, is assumed to be \$613/kW/year, independent of the type of system [13]. Operating costs are calculated for each period and then summed. Note that equipment costs are based on the maximum needed over the multi-period problem. The total annual cost of the system is therefore seen in (8).

$$C_{Annual} = CI_{Annual} + \sum_{p=1}^{6} OPEX(p) + F \quad (8)$$

A negative total annual cost signifies a net profit. This will also be referred to as total annual profit.

3. Validation and Optimization

With the completion of the model development and identification of the demand profiles, it is necessary to validate the methodology used. This is accomplished using a set of single runs of the model and a multi-objective optimization.

3.1. Single Run

Four separate scenarios were selected for the model validation. These can be seen in Table 3.

Table 3: Single Run Scenarios

Heat and Power		District Heating	
Flash	ORC	DA Cold	DA Hot
EGS on	EGS on	EGS off	EGS off
DA on	DA on	DA(LT)	DA(HT)
SA on	SA on	SA on	SA on
Flash on	ORC on	HP on	HP off

The first two scenarios focus specifically on combined heat and power production and the choice between the flash and ORC system. The deep and shallow aquifers are options that can be selected at energy integration if needed. In these situations, the temperature of the deep aquifer is sufficient to meet the district heating demand without a heat pump. The last two scenarios focus

on the district heating capacity of the system and the choice of the temperature of the resource. The EGS is not considered here. DA(LT) is the first available deep aquifer, but with a temperature too low to provide direct district heating, therefore obligating the use of the heat pump. DA(HT) is a second available deeper aquifer (the same used in the combined heat and power scenarios), with a production temperature high enough to provide direct district heating but with an increased drilling depth.

3.1.1 Results for Combined Heat and Power

The combined indicators for the multi-period combined heat and power scenarios are seen in Table 4. Note that the revenue does not include operating costs, capital costs, and fixed costs.

Table 4: Combined Heat and Power Results

Indicator	Flash	ORC
Net Electricity [MWh]	7627	24716
Net DH [MWh]	115220	115220
Net DC [MWh]	42000	42000
Total energy efficiency	0.62	0.46
Total exergy efficiency	0.46	0.54
Revenue [M*USD/yr]	5.19	9.18
Investment [M*USD]	77.02	71.19

Of the two scenarios, the simple ORC scenario was shown to have the higher profitability and exergy efficiency. In this system, the performance is strong with relatively high exergy efficiency. Total investment is high, but the system is nonetheless profitable. In comparison, the flash system had higher total costs and lower energy and exergy efficiencies. As a result, the system is not profitable.

The variability of the economic and thermodynamic performance across the six demand profiles can be seen for the ORC scenarios in Fig. 3.

It is apparent that the profitability of the system corresponds to the combined district heating and cooling demand of the system. This is because electricity production is fixed across the demand periods and there are relatively small increases in operating costs associated with an increase in district heating or cooling delivery. Exergy efficiency approaches 60% during the inter-seasonal periods.

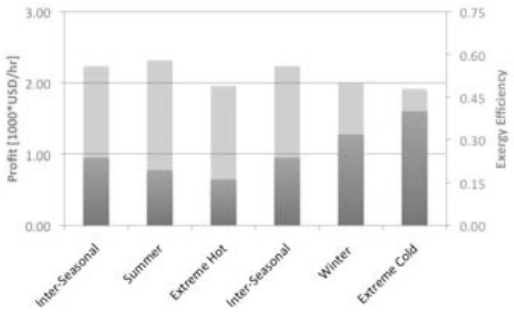

Fig. 3. Profit and Exergy Efficiency of the ORC

During this period, the system is fairly well optimized as seen in the results of the energy integration (Fig. 4). Compared with the worst performing period (the extreme cold period seen in Fig. 5), it is clear that the increase in the district heating usage creates some exergy losses. This is the result of increased usage of the DA for direct exchange with the district heating.

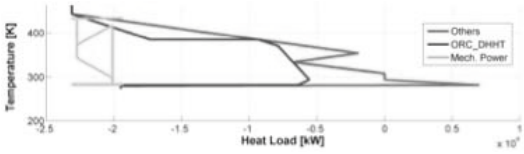

Fig. 4. Integrated Composite Curce of ORC for Inter-Seasonal period

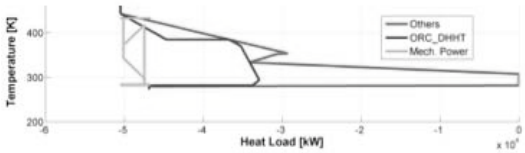

Fig. 5. Integrated Composite Curve of ORC for Extreme Cold Period

Overall, there is a net annual profit for this system. This makes the ORC system an attractive option economically, as long as reliable heat sources are available to meet the district heating demand. If the deep aquifer is not readily available or the extraction rate is limited, the results may differ significantly. Improvements for this scenario might include increasing the size of the ORC system within the feasible constraints of the EGS. The increase in power would be beneficial economically, and the increase in residual heat would be useful in helping to meet the district heating demand during colder operating periods.

3.1.2 Results for District Heating and Cooling

The last two simulations deal directly with variation in the production temperature of the deep aquifer. In the first, the production temperature of the deep aquifer is not of sufficient temperature to meet the district heating specifications. Therefore, drilling depth costs are reduced, but the heat pump must be used. The results of the two scenarios can be seen below.

Table 5: District Heating Combined Results

Indicator	DA(LT)	DA(HT)
Net Electricity [MWh]	-47843	0
Net DH [MWh]	115220	115220
Net DC [MWh]	42000	42000
Total energy efficiency	0.65	0.53
Total exergy efficiency	0.16	0.44
Revenue [M*USD/yr]	-6.72	3.66
Investment [M*USD]	221.25	21.46

Most striking about the results for the low temperature DA are the very high investment costs and negative yearly profit. Fig. 6 shows the profitability and exergy efficiency across the demand periods. Here, the profitability is shown to be negative for each period.

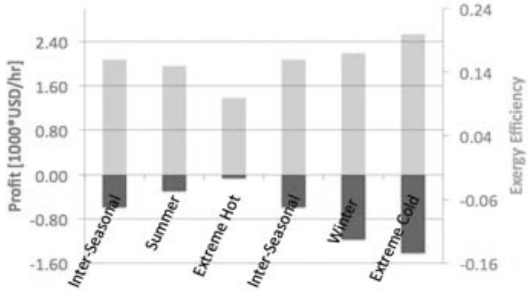

Fig. 6. Profit and Exergy Efficiency of the Heat Pump

The reason for this is that the ratio of the cost of imported electricity to the selling price of the district heating is higher than the coefficient of performance of the heat pump used to provide the heat for the district heating. Furthermore, the investment costs of the system with the low temperature district aquifer are an order of magnitude higher than that of the system with the high temperature deep aquifer. This can be explained by looking at the integrated composite curve for the extreme winter conditions (Fig. 7). During this demand period, the district heating demand exceeds that which can be provided by the shallow aquifer and heat pump. This is due to limitations placed on heat pump of 3.5 times the nominal size. This also represents a potential production limitation of the shallow aquifer.

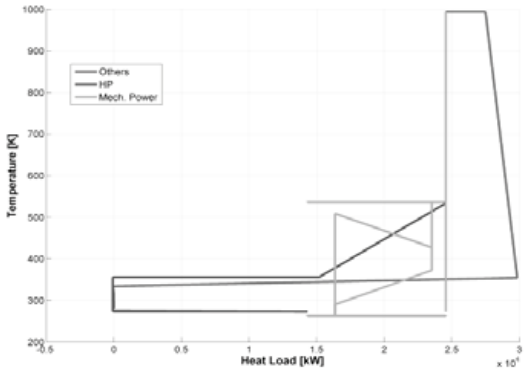

Fig. 7. Integrated Composite Curve of the Heat Pump for Extreme Cold Period

As a result, this system must purchase a large heat pump and a boiler, even though these components are used to their full potential for only 40 hours of the year. The low exergy efficiency of the system is the result of the penalty that occurs from the import of electricity from the grid. In contrast, the results from the scenario with high temperature DA show that a system, which increases the drilling depth, thereby avoiding the need for the heat pump, has lower investment costs and is profitable across all six demand periods. Therefore, the optimal exploitation scheme under these conditions is the use of the higher temperature aquifer. Although the drilling costs are higher, avoidance of the heat pump and boiler purchase is beneficial exergetically and economically.

3.2. Multi-Objective Optimization

Analyses of single run scenarios alone are limiting, as they do not allow for the methodical variation of decision variables and the identification of their optimal ranges. Moreover, it is necessary to account for the interactions between the different decision variables, and to calculate the trade-offs between conflicting objectives represented by the performance indicators. For these reasons a multi-objective optimization (MOO) is needed. An evolutionary genetic algorithm is used for this, and the two objectives are the total exergy efficiency to be maximized and the annual profit to be minimized.

3.2.1 Moo Using the ORC

From the single run results seen previously, it is apparent that usage of the ORC may be a promising approach to the utilization of the default geothermal resource. As such, a multi-objective optimization of the geothermal system in the multi-period framework will be performed, varying the decision variables as shown in Table 6. Integer decision variables are those that can only be integer values.

Table 6: Moo Decision Variables

Decision Variable	Type	Range	Unit
DA	Integer	[0,1]	-
SA	Integer	[0,1]	-
ORC	Integer	[1,2]	-
Simple ORC, Max Pressure	Variable	[10,30]	bar
ORC w/ bleeding, Max Pressure	Variable	[10,30]	bar
Simple ORC, Min Temp Diff	Variable	[1,5]	K
Split fraction of flow to second turbine	Variable	[0,1]	-
ORC w/ bleeding, min temp diff: condenser 1	Variable	[1,5]	K
ORC w/ bleeding, min temp diff: condenser 2	Variable	[1,5]	K

Here, the use of the EGS system is obligatory. Usage of the deep and shallow aquifer is either on (1) or off (0), and usage of the ORC is either a simple ORC (1), or an ORC with bleeding (2). Other variables concern the conversion system design. The results of this optimization are shown in Fig. 8. All of the final configurations make use of the deep aquifer to provide district heating and none use the shallow aquifer. A trend exists between decreased annual profit and increased exergy efficiency. Configurations with the lowest efficiency but highest profitability are those with the simple ORC selected and the high-pressure region of the cycle from 11.5 to 13.5 bars. The minimum temperature difference is in the range of 1.1 to 2.1 °C. Upon close inspection of Fig. 8., it is apparent that two distinct trend lines exist in the more profitable regions corresponding to the clusters of the MOO. For two configurations of the same exergetic performance, the more profitable configuration has a lower maximum pressure and a lower minimum temperature difference.

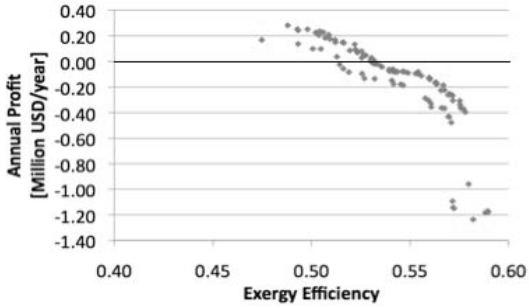

Fig. 8. Annual Profit vs. Exergy Efficiency

The most exergetically efficient configurations have high maximum pressures, approaching 30 bars. Four of the top fifteen best performing systems in terms of exergy efficiency utilize the ORC system with bleeding. However these configurations are not economical due to the high investment cost of the system.

As both objective functions within a demand profile depend strongly on the period duration, the MOO results will favor performance in those periods. However, configurations that avoid capital-intensive consequences in the extreme periods are also maintained, highlighting the importance of consideration of extreme conditions.

4. Conclusions

The development of a methodology for the thermo-economic evaluations of geothermal systems within the multi-period framework has been completed. Validation of this methodology was accomplished with the use of single run results and multi-objective optimizations using an evolutionary genetic algorithm.

Single run results clarified the importance of the multi-period approach. For the assumed conditions, the ORC system performed better than the single flash. The amount of DH, DC, and electrical production is important for the annual profit and exergy efficiency. In the case where no electricity is produced, results suggest that the use of deeper resources with higher production temperatures is the best approach, as it does not require the investment of a large heat pump for extreme conditions. The multi-period approach is

specifically relevant as there are large variations in system performance over the different periods. Some periods have significant potential of improvement if the seasonal storage of heat is considered, especially in summer.

Multi-objective optimizations were successful in demonstrating the ability of the system to select between integer decision variables, such as the selection of a conversion technology or resource, as well as specific parameters for a given configuration across the different periods. The optimization within the multi-period approach favors the inter-seasonal demand profiles as the demand periods are the longest and therefore have the greatest effect on the combined performance indicators. However, extreme conditions have an important influence on investment costs, as they change the maximum size of some capital-intensive components.

Future work includes more intensive multi-objective optimizations considering additional scenarios and conversion technologies. Furthermore, additional development of the model is required, especially for the inclusion of an option for heat storage in the aquifer, which will allow for an assessment of the potential of seasonal heat storage to increase the overall system performance.

References

[1] Tester, J,. et al., 2005 *Sustainable Energy – Choosing Among Options*. MIT Press, Cambridge.

[2] Poppei, J., Seibt, P., and Fischer, D., 1998. Recent examples for the utilisation of geothermal aquifers for heat or cold storage or improvement of the reservoir conditions by heat injection. 23rd workshop on Geothermal Reservoir Engineering, January 26-28

[3] Girardin, L and Marechal, F, 2007. Energy conversion processes for the use of geothermal heat, report: Methodology for the optimal integration of energy conversion system in geothermal power plants. Swiss Federal Office of Energy

[4] Marechal, F. and Kalitventzeff, B., 2003, Targeting the integration of multi-period utility systems for site scale process integration, *Applied Thermal Engineering*, 23(4), pp. 1763-1784

[5] Tveit, T. and Fogelholm, C., 2006, Multi-period steam turbine network optimisation. Part II: Development of a multi-period MINLP model of a utility system, *Applied Thermal Engineering* 26(14-15), pp. 1730-1736

[6] Haring, M., n.d. Deep Heat Mining: Development of a cogeneration power plant from an enhanced geothermal system in Basel, Switzerland. Geothermal Explorers.

[7] Grass, R, Schädle, KH, and Siddiqi, G., 2008. 15 Years of Direct Use–District Heating Riehen, Canton Basle-City, NW Switzerland. IEA Sustainability Workshop, Taupo

[8] Girardin, L., et al., 2008. 'A geographical information based system for the evaluation of integrated energy conversion systems in urban areas' *ENERGY, The International Journal*. 26 November 2008

[9] Maréchal F., Kalitventzeff B., Process integration: Selection of the optimal utility system, *Computers and Chemical Engineering* 22(1), pp. S149-S156

[10] R. DiPippo, 2004, Second Law assessment of binary plants generating power from low-temperature geothermal fluids, *Geothermics* 33(5), pp. 565-586

[11] Turton, R., et al., 2008. *Analysis, Synthesis, and Design of Chemical Processes*, 2nd edn. Prentice Hall PTR, New Jersey

[12] Ulrich GD 1984. *A Guide to Chemical Engineering Process Design and Economics*. John Wiley and Sons, New York

[13] Tester, J., et al., 2006 *The future of geothermal energy - impact of Enhanced Geothermal Systems (EGS) on the United States in the 21st century*. MIT

[14] Bejan, A., Tsatsaronis, G., and Moran, M., 1996. *Thermal Design and Optimization*. Wiley and Sons, INC. New York

[15] Kutscher, C., 2000. The Status and Future of Geothermal Electric Power. American Solar Energy Society (ASES) Conference. Madison, Wisconsin. 16-21 June

[16] Kagel, A., 2006. A Handbook on the Externalities, Employment, and Economics of Geothermal Energy. Geothermal Energy Association

Key Technology of Solar Energy Restaurant Waste Biomass Power Generation and Waste Heat Utilization

SHAO Youyuan[a*], YANG Minlin[a], YANG Xiaoxi[a], SUI Jun[b], JIN Hongguang[b]

a. Key Laboratory of Distributed Energy Resources System of Guangdong Province, Dongguan University of Technology, Gongguan City, Guangdong Province, 523808, China;

b. Institute of Engineering Thermophysics, Chinese Academy of Sciences, Beijing 100080, China

Abstract : In this work, the technological processes of the solar energy restaurant waste biomass power generation and waste heat utilization was introduced. The process parameters, key unit technology and benefits were analyzed. The temperature in fermentation tank was compensated by solar energy in order to meet the optimal fermentation temperature. Restaurant waste was used as a main fermentation material. Biogas was pretreated for dehumidification, desulfurization and ammonia gas removal, etc. The pure methane fueled for electricity generation. That is that high energy level biomass was used power generation. Low energy level from generator set such as flue gas heat and hot-water waste heat was used as refrigeration. The waste liquid and solid were used as organic fertilizer. It is to achieve the goal that makes full use of energy and material resources. It indicated that the process was practicable to solve pollution of restaurant waste and realize comprehensive utilization of domestic waste. It will bring about good economic and social benefits.

Key words: Solar energy, Biomass power generation, Restaurant waste, Waste heat utilization

1. Introduction

In developing countries, electricity generation is achieved through fossil fuel consumption or hydroelectric dams, both of which have a high environmental impact, including greenhouse gas emissions and ecosystem alteration. In many developing countries, the price of electricity is relatively high, making it inaccessible to portions of the population. In China, the average household electricity price is \$0.10 kwh^{-1} China is one of countries of the fastest economic development in the world. At the same time, China is also the serious country of energy shortage. As the word economics develops faster and faster, challenges from environment pollution and energy crisis become more and more serious. Biogas power generation technology turns the biogas produced in garbage such as food waste and restaurant waste disposal into energy, which decreases the charges of garbage disposal and produces clean and highly efficient energy [1, 2].

Biogas electricity generation is an effective way to provide the clean energy and the solution of environment problem [3]. Biogas technology has been known about for a long time, but in recent years the interest in it has significantly increased, especially due to the higher costs and the rapid depletion of fossil fuels as well as their environmental considerations [4, 5].

With the development of catering industry, the pollution caused by the more and more kitchen wastes is a problem to be solved urgently. Biomass power generation with biogas production using kitchen waste can provide us with multiple value-added, renewable energy products. These products can meet heating and power needs or serve as transportation fuels. The primary objective of this work is to present the technological process of solar energy restaurant waste biomass power generation and waste heat utilization. Biogas

residues after biogas fermentation produce bio-fertilizer. Waste water uses for agricultural irrigation in this technology.

2. Process route of Methane Power Generation

2.1. Basic state

Methane power generation demonstration project located in Dongguan, Guangdong province. The main fermentation material is the kitchen waste from dining hall of Dongguan university of technology and greening garbage from the campus. Daily output kitchen waste reaches about 1t in the three dining halls of Dongguan university of technology. The anaerobic batch digestion was carried on for biogas production at the loading rate $35gL^{-1}$.

2.2. Process flow

Three 5 m^3 fermentors were applied in this process. The loading rate is 35 gL^{-1}. The fermentation period is 35d. The biogas yield was measured by a downward drainage method. The methane content was determined by gas chromatography. The process flow is the following as Fig.1.

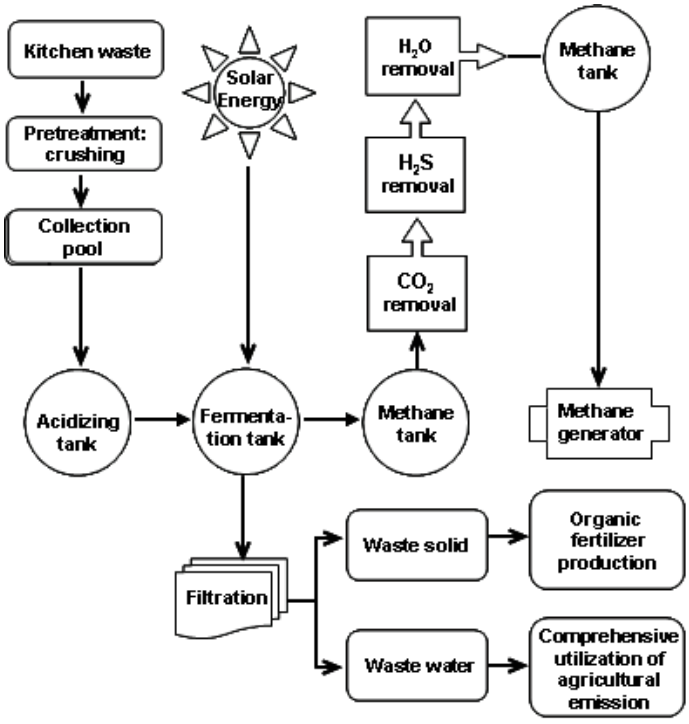

Fig.1 System of solar energy kitchen waste biomass power generation

2.2.1. Material collected Pool

The equipment used to collect and blend the kitchen waste and greening garbage includes two parts of separation equipment and collection pool. The separation equipment applied in the removal of animal bone, fishbone, napkin and other sundries. The collection pool is used in the collection of kitchen waste and greening garbage after removal as the material of temporary store. And then, it was pumped into acidizing tank with the volume of 5 m^3. 2 kW agitator and 2 kw diving pump were installed in the tank. The main task of agitator is to make the raw uniform in the size. The diving pump is used for pumping the uniform material into the

acidizing tank.

2.2.2. Acidizing Tank

5 m^3 acidizing tank with cylinder was applied in acidizing the raw, which is difficult to biodegrade organic matter such as greening garbage. The raw of kitchen waste and greening garbage was acidized in the acidizing tank to provide high quality material for the later methane fermentation. It could speed up the process of methane fermentation. A set of 2kw agitator and liquid-level controlling unit were designed in the tank. A sampling tube was set on the tank wall. Feeding screw pump and Ultrasonic Flowmeter were designed out of the collection pool. The raw was pumped into the collection pool by diving pump. The fermentation material was pumped punctualy and quantitatively into the fermentation tank by the screw pump.

2.2.3. Fermentor

Three 5 m^3 globular fermentors were applied in this process. A set of stirring system and high position overfall equipment were designed in the fermentor. The mixing of material in the tank was implemented though methane gas presses reflux. A sampling tube was designed on the tank wall. The safe water seal and defoaming device were fixed on the fermentor roof. The temperature compensation system with solar energy was designed for the fermentor.

2.2.4. Biological Desulfurization Tower

Biological Desulfurization Tower was designed to an above-ground, cylinder, 0.5 m^3. The spherical support particle was filled in the tower. The liquid level gauge was deigned on the tower wall. The inlet and outlet pipe of methane were installed on the top and at the bottom of the tower, respectively. The air and water return pipe line and reflux pump were set in the middle and at the bottom of the column.

Biological desulfurization was developed in 1980's, considered as an alternative to physicochemical methods, in which sulfide was converted into elemental sulfur by microorganism community, moreover elemental sulfur could be recovered. In the biotechnological desulfurization process, first of all, the pollutant containing sulfur of oxidation state was changed into sulfide or H_2S as a result of biological reduction, and then could be removed after being converted into elemental sulfur by biological oxidation.

2.2.5. Generator Unit

The generator unit is a special methane generator (FSDTYQ5K/H). Its rated power is 6 kw. The actual work power is 5 kw. The inlet pressure is demanded for 2~ 3kPa. The demand for the content of CH_4 is more than 60%. There is mortal relativity between the actual power and inlet pressure or the content of methane.

2.2.6. Biogas Storage Tank

Biogas storage tank is a wet air tank which was designed to an above-ground, cylinder bell shaped, 6m^3. Auto-exhaustion and manual-exhaustion were designed on the top of tank. It may play a role of protection in the safe of gas storage tank.

3. Key Technological Units and Technical Parameters

3.1 Waste Heat Utilization

The main waste heat of methane generator is the waste heat of flue gas. There may be two kinds of mode to utilize the waste heat.

Hot Water Style The waste heat of flue gas heated the water to 90 ^{0}C or higher. The style is particularly suitable for north area need to space heating in China.

Flue Gas Style The cooling source loading was provided by LiBr absorption type refrigerating machine through using the flue gas waste heat.

3.2. Fermentor Heat Preservation with Solar Energy

SOLAR ENERGY HEAT COLLECTOR: By using of QB—AL-N / AI-37 / 47-1500 evacuated collector tube, 38 heat collectors, 9 groups with total area of 50.4m^2.The warm water tank with stainless steel inner liner could storage warm water 2 t. The fermentor was heated by warm water from solar energy heat collector through warm water was directly added into the fermentor holding temperature of 35 ℃ in the process. It could increase biogas yield by 30%.

3.3. Conversion of Biogas to Electric Energy

The calorific value is 23-27 MJ at per cubic meter methane (0.1MPa, 0 centigrade) in theory [6]. It could make the Internal Combustion Engine of 1kw work for 1.8~2.3h. It could generate energy 1.25~1.5kwh (equivalent to 0.6~0.8kg standard coal).

3.4. Experiment of Biogas Production Performance

The batch experiment of biogas production was carried on in a 5L airtight jar using waste food under the volumetric pollution loading 35 gL^{-1}. The figure 1 showed that there were three small peaks of biogas yield. The biogas production was steady from 2d to 30d except for a lot of CO_2 production on the first day. The average daily output could be 1.75~2.65L. The biogas yield was higher in the first 10d, and gradually decreased after 25d. The biogas production almost cease on the 35d. Results in Fig.2 showed that the cumulative biogas production kept elevating with the level of 62.30L. The biogas production reached 363 mlg^{-1}. The results in figure 3 showed that methane content was less 40% in the first 3 d, kept elevating and tended to be stable thereafter. The highest content of methane was up to 83%. The biogas cumulative production was 45.43 L. The average methane content was 54.5%. The yield of methane was 220mlg^{-1}.

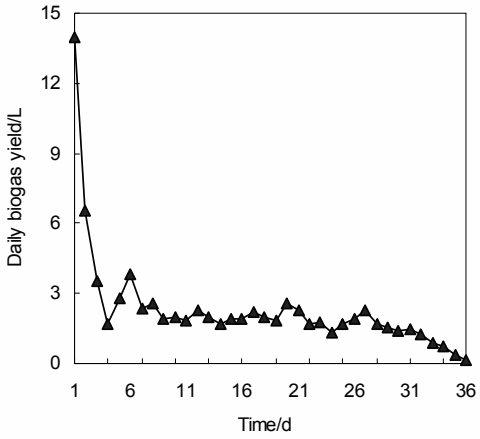

Fig.2 The change of daily biogas production at 35gL^{-1}

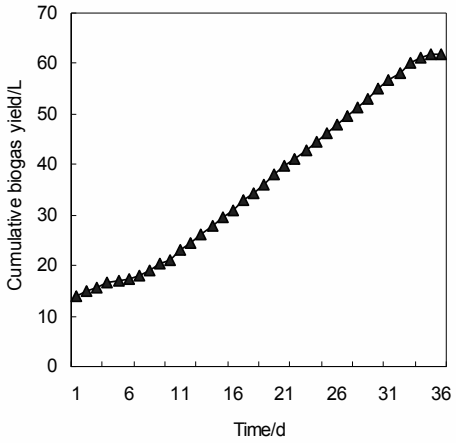

Fig.3 The change of cumulative biogas production at 35gL^{-1}

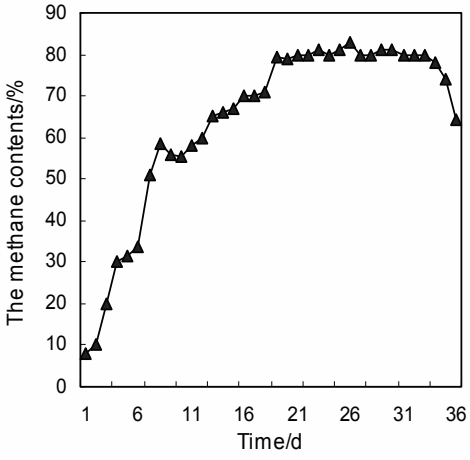

Fig.4 The methane content in biogas

4. Conclusions

Based on this investigation of anaerobic batch digestion using kitchen waste, the results indicated that there is a good potentiality of biogas production at a mesophilic temperature of 35 ^{0}C. The value of pH has little change in the process. The system performance is comparatively stable. Therefore, biomass power generation is an effective approach of kitchen waste resource recovery. It also provides a theoretical basis for its future research and applications.

Solar energy is available way used for the thermal insulation of fermentor. It is also worth generalizing in the biogas power generation. It can ensure the optimal operation of anaerobic sludge digester.

The result showed that 600~700m^3 of biogas and 1 t of bio—fertilizer could be produced from 1 m^3 of kitchen waste. And 1200~1400 kwh of electricity could be generated with the biogas produced. Combined with the available successful experience in biogas power generation in China, it is pointed out that the comprehensive utilization of kitchen waste through anaerobic digestion and biogas power generation has better development prospects.

Acknowledgements

The project supported by National Key Basic Research Program of China (973) (2010CB227306) and NSFC（50836005）

Reference

[1] Li M., Zhang X.Q. , 2006, Application demonstration of small Methane power plant, **China Biogas**, 24(3), pp.51-57.

[2] Yang Z.Y., Liu X.F., Zhang Y., Yuan Y.X., 2009, An Analysis on UNIDO Demonstration Biogas Project Treating Sisal Waste in Tanzani, **China Biogas**, 26(4), pp.27-30.

[3] Ran G.W., Zhang R.K., Feng A.G., 2006, The Analysis of Present Situation of M ethane Electricity Generation and its Discussion of Developing Direction, **Agricultural Mechanization Research**, 3, pp.189-192.

[4] Keri B., Cantrell, Thomas Ducey, Kyoung S. Ro, Patrick G. Hunt., 2008, Livestock waste-to-bioenergy generation opportunities, **Bioresource Technology**, 99, pp.7941–7953.

[5] Joaquin Viquez, Stephanie Lansing and Helen Martine., 2008, Low-tech digesters alleviate environmental degradation and produce high-quality biogas,but technological improvements are needed, **Biocycle**, 2, pp.51-55

[6] Zhang H.B., Li J.R., Chen Z.M., 2008, Benefit Analysis of Methane Electricity Generation in Breeding Pig Farm, **Acta Ecologiae Animalis Domastici**, 29(4), pp.109-112.

Energy and Exergy Analysis of Biorefinery Processes

Araceli García, María González Alriols, José Antonio Quijera, Rodrigo Llano-Ponte, Jalel Labidi

Department of Chemical and Environmental Engineering,University of the Basque Country, Donostia-San Sebastián, Spain

Abstract: In this work, the energy and exergy yields of the fractionation processes of lignocellulosic biomass into cellulose, hemicelluloses and lignin has been determined by using process simulation tools. The folowsheet of the organosolv process based on experimental data has been developed and different treatment steeps (reaction, solvents recovery) have been optimized in order to maximize the exploitation of the lignocellulosic material. Aspen Plus® software has been used to simulate the process and to establish the energy and exergy balances at the different stage of the organosolv process with the purpose to evaluate its energy efficiency.

Keywords: Process Simulation, Energy, Exergy, Organosolv, Lignocellulosic biomass.

1. Introduction

The scarcity of fossil resources, instability of oil prices and the environmental concerns associated with CO_2 emissions are impelling the development of alternative ways to produce energy, heat, electricity, fuels, materials and chemicals. An option that is generating considerable expectations is the replacement of petroleum-based processes with biomass [1].

Lignocellulose is a world wide available, versatile, abundant and relatively cheap type of biomass that is obtained as a by-product or residue in several applications as forest management, food and feed industries and agricultural activities. Lignocellulosic materials comprise a wide range of plants that are generally classified as wood and non-wood materials. In the last type raw materials as grass, straw and shrub are included. The main components of lignocellulosic biomass, cellulose, hemicelluloses and lignin can be extracted, separated and purified to obtain different chemicals, fuels and materials [2,3].

Biomass presents a complex chemical composition and varied functionality, contrary to crude oil products, that have to be functionalized by reaction processes. Therefore, synthesizing functional chemical products from biomass would require lower energy requirements than the petroleum based routes. This way, biomass biorefinery technologies focussed on using the biomass structure for the production of chemicals and materials are more efficient and interesting than the generation of fuels or energy alone [4].

In order to be economically efficient, biorefinery production routes need to be integrated into current processes and facilities of actual technologies (petrochemical platform, pulp and paper technology) as it is the existing way to obtain chemicals and other products. The simulation of biorefinery processes is a useful tool to analyze their energy efficiency in order to design competitive routes [8-13].

Exergy analysis (based on a thermodynamic second law analysis) has proved to be a powerful tool in the study of energy systems [6], because it allows analyze the impact on the environment of energy use, evaluate the existing inefficiencies in the process, locate and quantify losses of energy quality of the process, and improving the efficiency of energy use [7]. In this way, exergy concept allows to estimate requirements for energy and material in a process that interacts with the environment. Exergy can be also a useful tool for determining reactivity and quality of products.

In this work, the energy and exergy yields of the fractionation processes of lignocellulosic biomass into cellulose, hemicelluloses and lignin has been determined. Aspen Plus® software has been used to simulate the process and to establish the energy and exergy balances.

Corresponding author: Jalel Labidi, Email: jalel.labidi@ehu.es

2. Biorefinery process

2.1. Organosolv process description

The elected organosolv fractionation process consists in the treatment of a non-wood raw material with a mixture of ethanol and water.

In Fig. 1 a diagram of the studied organosolv process is showed. The different inputs and outputs of the process are represented. Four main stages can be distinguished:

- the reaction stage, where raw material is fractionated with a solvent at appropriate temperature, pressure and time conditions,
- the cellulosic solid fraction processing (washing),
- liquid fraction ultrafiltration, where lignin fractions with narrow molecular weight distributions are obtained by using membrane technology,
- solvents recovery stage, which includes distillation and concentration processes.

More details about the used process are reported in previous work [5].

The raw material (biomass) is mixed with the solvent (ethanol-water, 60/40 w/w) in a pressurized reactor (160ºC, 10 bar, 90 min, liquid/solid ratio: 6/1 w/w). Once reaction time is finished, the reactor content is depressurized to 1 bar, and a flashed stream composed by ethanol and water, is obtained from the item F1, condensed in HEX1 and reused in the process. Two fractions are obtained from the reaction stage: the liquid and the solid fractions. The resulting solid fraction, mainly constituted by cellulose, is washed with the mixture of ethanol and water and filtrated. The rejected a liquid fraction, containing dissolved hemicelluloses, lignin and remaining solvent, is mixed with the liquid fraction from the reactor and treated together to recover by-products and solvents. This stream is ultrafiltrated (by using ceramic membranes) in order to obtain different liquid fractions, which contain lignin with specific molecular weight distribution. Remaining liquid fraction after lignin precipitation is sent to the distillation unit, where a mixture of ethanol-water is obtained as distillate and recycled to the reaction unit. The residue, composed by water and co-products, mainly hemicellulosic sugars, is treated by heating in a flash unit (items HEX2 and F2) to obtain a clean water stream, which is sent back to the lignin precipitation unit, and a concentrated stream with the remaining process by-products for subsequent treatment and use.

2.2. Simulation methodology

2.2.1. Organosolv process approach

Aspen Plus was used to design and simulate organosolv process on the basis of experimental results [5]. Lignin, cellulose and hemicelluloses were defined by their chemical structure and physical properties which were obtained from the National Renewable Energy Laboratory (NREL) database (NREL/MP-425-20685; task number

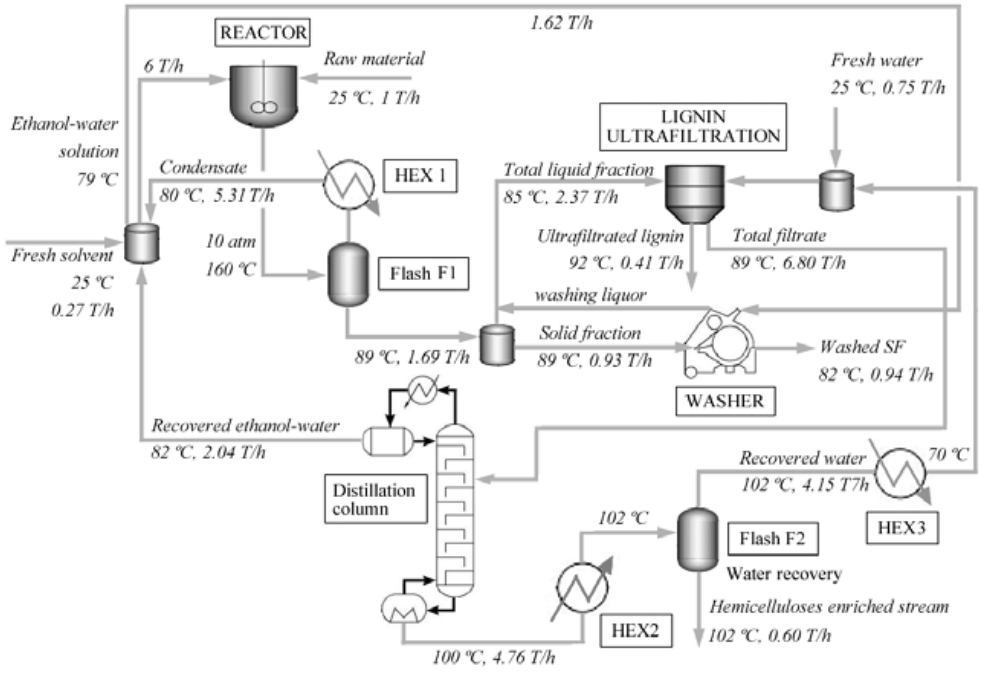

Fig.1. Diagram of the studied organosolv-ethanol process.

BF521004), whereas other conventional components were selected from the ASPEN PLUS data bank. NRTL-RK model (Non-Random, Two Liquids - Redlich Kwong) was used to simulate the thermodynamic properties of solutions. These routes include the NRTL equation, obtained by Renon and Prausnitz, for the liquids activity coefficients calculation, Henry's law for the dissolved gases and, in the second case, RKS (Redlich-Kwong-Soave) equation of state for the vapour phase.

The simulation process was developed using the following inlet streams to the reactor: 1000 kg/h of dry raw material and 6000 kg/h of solvent (ethanol-water 60% w/w) which corresponded to a liquid/solid ratio (w/w) of 6.

Raw material composition was defined as a typical lignocellulosic non-wood material composition: 45% cellulose, 28% hemicelluloses, 25% lignin, 2% inorganic compounds (% on a dry weight basis).

2.2.2. Energy and exergy balances

Many authors have applied first and second thermodynamic laws to establish energy and exergy balances of a process. The energy and exergy balances of a process may be expressed as:

Energy inputs = energy output+ energy loss (1)

Exergy inputs = exergy outputs + exergy destruction (2)

Energy or exergy efficiency of equipments or processes may be defined as follows:

$$\eta = \frac{\sum \text{energy in products}}{\sum \text{energy inputs}} \quad (3)$$

Exergy expresses the loss of available energy due to the creation of entropy in irreversible processes [6]. This way, for a process stream [14], exergy is determined by the physical exergy and the molar flow rate of the stream:

$$\overline{E} = N\,\overline{e}_{ph} \quad (4)$$

Physical exergy of a material stream is expressed as:

$$\overline{e}_{ph} = (h - h_0) - T_0(s - s_0) \quad (5)$$

and takes into account the enthalpy and entropy of the stream at reference conditions (T_0=298.15 K, P_0=1.013 bar).

For process equipments, general energy and exergy balances are defined by (1) and (2). In reactors and exchangers the energy balance takes into account the energy flow of inputs or reactants, of outputs or products and the consumption of energy due heat transference or reaction processes. In this way energy balance is described by:

$$\sum E_{in} + \sum Q = \sum E_{out} \quad (6)$$

and the exergy balance by:

$$\sum \overline{E}_{in} + \sum Q\theta = \sum \overline{E}_{out} + \overline{E}_{dest} \quad (7)$$

The Carnot factor is calculated as:

$$\theta = 1 - \frac{T_0}{T} \quad (8)$$

where T is the process temperature (of reaction or associated outlet stream) and T_0 the reference temperature.

The simulation software Aspen Plus® allows obtaining the enthalpies of the process streams, so energy balances for simulated equipments can be easily determined. For exergy balances, the enthalpy and entropy at reference conditions (298.15 K, 1.013 bar) for the process streams were also determined.

3. Results and discussion

3.1. Mass and energy balances

In Table 1 the simulation results for the main process streams are showed. Mass and energy flows, temperature and composition of the main streams components are presented. It can be seen that the fractionation process allows obtaining a solid fraction with high cellulose content, and about 50 % of the lignin present in the raw material as a high value product.

In Table 2 energy flows of de simulated equipments are showed. According to the results and taking into account the energy of the products (i.e. washed solid fraction, ultrafiltrated lignin and the hemicelluloses enriched liquid) and energy inputs (i.e. raw material, fresh water, fresh solvent and the energy requirement of the process) the simulation process presents a total energy efficiency of 0.43, similar value to those reported in other studies for different processes [10,11]. However, there is still not taken into account energy requirements of auxiliary equipment (such as pumps and filtration equipment).

Table 1. Simulation results for the main streams of the simulated organosolv process

Stream	Mass (T/h)	Compositions (% w/w)					T (ºC)	Energy (MW)
		Cellulose	Hemicelluloses	Lignin	Ethanol	Water		
Raw material	1.00	42.39	23.55	26.38	0.00	5.80	25	2.36
Fresh solvent	0.27	0.00	0.00	0.00	92.59	7.41	25	0.51
Fresh water	0.75	0.00	0.00	0.00	0.00	100.00	25	3.30
Washed solid fraction	-0.94	37.09	9.45	11.46	21.76	17.24	82	-2.21
Ultrafiltrated lignin	-0.41	0.00	0.00	27.62	9.85	61.87	92	-1.49
Hemicelluloses enriched liquid	-0.60	0.00	39.06	3.56	0.00	57.37	102	-2.17

Table 2. Energy and exergy balances for some equipments involved in the studied process

Equipment	Energy Required (MW)	Exergy Balanced (MW)	Temper. (K)	Carnot Factor	Exergy Destroyed (MW)
REACTOR	1.940	0.550	433.15	0.312	0.055
FLASH F1	0.000	-0.230	-	-	0.230
HEX1	-1.990	-0.321	353.35	0.156	0.010
ULTRAFILTRATION	0.000	0.523	-	-	0.523
DISTILLATION	0.001	-2.90			0.119
Condenser	-2.900	-	355.15	0.160	
Boiler	2.920	-	372.95	0.201	
HEX2	2.620	0.527	375.15	0.205	0.011
HEX3	- 2.760	-0.550	343.15	0.131	0.188

3.2. Exergy balance

The exergy destruction due to the irreversibility's of the different process operation has been determined. Energy requirements, balanced exergy, operation temperature, Carnot factor and exergy destruction are reported in Table 2. For other equipment that doesn't perform heat transference processes (e.g. ultrafiltration or flash units), the second term of (7) is null, and only the input and output of exergy due process streams are considered. Fig. 2 shows the results of this analysis.

The total exergy destruction in the simulated process resulted to be 1.136 MW. Moderate exergy destruction was observed in the reactor, where raw material is fractionated into its main components using solvents and heat. Distillation column operated with a moderate value of exergy [11], so it confirms that the solvents recovery process requires better design and integration to improve to energy use.

Heat exchangers showed different exergy losses according to several factors like the temperature

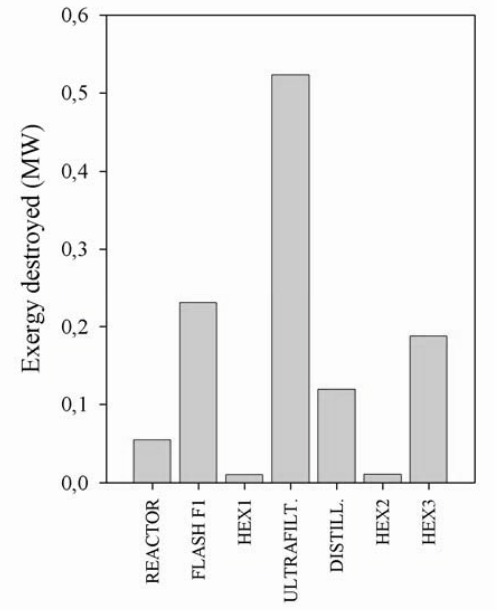

Fig. 2. Exergy destruction (MW) for different process equipment

difference or the amount of material heated or cooled. In this way, in the exchanger HEX3 significant exergy destruction can be observed, since it condensates considerable amount of vapor (more than 4.1 tons per hour) but also cools this condensate. HEX1 and HEX2 heat exchangers, where a phase change is done, showed slight destruction of exergy (about 0.01 MW).

A simple process element (FLASH F1) that doesn't require heating or cooling processes shows high destruction of exergy. This could be explained by the fact that not only heat transference process show exergy losses, but also the processes associated with streams mixing, phase change and pressure change [11]. This also can be observed for the ultrafiltration unit, which shows the highest exergy destruction.

4. Conclusions

In this work process simulation tools have been used to analyze the energy effectiveness of an organosolv biorefining process. Energy requirements have been determined, showing low value of the process energy efficiency (0.43). The exergy balance applied to process equipment has showed high irreversibilities in the reactor, associated to raw material fractionation, but also a loss of available energy in the process, that could be solved with the application of optimization tools and energy integration.

Acknowledgments: Authors would like to thank the Department of Agriculture, Fishing and Food of the Basque Country (scholarship of young researchers training), and the Diputación Foral de Guipúzcoa (project OF 94/2008) for supporting financially this work.

Nomenclature

E energy flow of a stream, W

$\bar{E}$ exergy flow of a stream, W

$\bar{e}$ exergy, J/mol

h enthalpy of a stream, J/mol

Q energy requirement of a process, W

N molar flow, mol/s

s entropy of a stream, J/mol K

T temperature, K

Greek symbols

η energy efficiency

θ Carnot factor

Subscripts and superscripts

0 standard conditions (298.15 K, 1.013 bar)

B boiler

C condenser

D distillate

$dest$ destroyed

F feed

in input flow

out output flow

ph physical (exergy)

W waste

References

[1] Clark, J.H. et al., 2009, The Integration of Green Chemistry into Future Biorefineries, Biofuels, Bioproducts and Biorefining, 3, pp. 72-90.

[2] Huang, H.J. et al., 2008, A Review of Separation Technologies in Current and Future Biorefineries, Separation and Purification Technology, 62, pp. 1-21.

[3] González Alriols, M. et al., 2009, Agricultural Palm Oil Tree Residues as Raw Material for Cellulose, Lignin and Hemicelluloses Production by Ethylene Glycol Pulping Process, Chemical Engineering Journal, 148, pp. 106-114.

[4] Alvarado-Morales, M. et al., 2009, Biorefining. Computer Aided Tools for Sustainable Design and Analysis of Bioethanol Production, Chemical Engineering Research and Design, 87(9), pp. 1171-1183.

[5] González Alriols, M. et al., 2009, Combined Organosolv and Ultrafiltration Lignocellulosic Biorefinery Process, Chemical Engineering Journal, In Press

[6] Hepbasli, A., 2008, A Key Review on Exergetic Analysis and Assessment of Renewable Energy Resources for a Sustainable Future, Renewable and Sustainable Energy Reviews, 12, pp.593-661.

[7] Nilsson, D., 1997, Energy, Exergy and Emergy Analysis of Using Straw as Fuel in District Heating Plants, Biomass and Bioenergy, 13(1-2), pp. 63-73.

[8] Bram, S. and De Ruyck, J., 1997, Exergy Analysis Tools for Aspen Applied to Evaporative Cycle Design, Energy Conversion and Management, 38(15-17), pp. 1613-1624.

[9] Harvey, S. and Kane, N., 1997, Analysis of a Reheat Gas Turbine Cycle with Chemical Recuperation Using Aspen, Energy Conversion and Management, 38(15-17), pp. 1671-1679.

[10] Ojeda, K. and Kafarov, V., 2009, Exergy Analysis of Enzymatic Hydrolysis Reactors for Transformation of Lignocellulosic Biomass to Bioethanol, Chemical Engineering Journal, In Press.

[11] Ptasinski, K.J. et al., 2002, Exergy Analysis of Methanol from the Sewage Sludge Process, Energy Conversion and Management, 43, pp. 1445-1457.

[12] Talens, L., Villalba, G. and Gabarrell, X., 2007, Exergy Analysis Applied to Biodiesel Production, Resources, Conservation and Recycling, 51, pp. 397-407.

[13] Karamarkovic, R. and Karamarkovic, V., 2009, Energy and Exergy Analysis of Biomass Gasification at Different Temperatures, Energy, In Press.

[14] Panopoulos, K.D. et al., 2006, High Temperature Solid Oxide Fuel Cell Integrated with Novel Allothermal Biomass Gasification. Part II: Exergy Analysis, Journal of Power Sources, 159, pp. 586-594.

Optimal Operating Temperature of Solar Collectors at Maximal Exergy Output

Driss STITOU, Sylvain MAURAN and Matthieu MARTINS

Laboratory PROMES-CNRS (PROcédés, Matériaux et Energie Solaire), Rambla de la Thermodynamique, Tecnosud, 66100 Perpignan, France

Abstract: This paper aims to establish the optimal operating parameters of a solar collector in order to perform a maximum exergy output during the collection of solar energy. The optimal collector operating temperature and mass flow rate of the heat transfer fluid are investigated under given solar irradiation and for a given solar collector characterized according to EN 12975-2 standards.

Keywords: Solar collector, Optimal temperature, Exergy maximization.

1. Introduction

Solar collectors are now widely used for industry and domestic use. The use of solar energy is of considerable interest for two reasons: firstly, it leads to a diminution of fossil fuels consumption and secondly, solar energy is a non-polluting source of energy.

The fundamental operational problem with solar collectors is the collection and the delivery of solar energy to users with minimum losses. The optimum solar collector operating temperature has been studied by many researchers and can be investigated using different analysis approach [1-11].

When a solar collector is used as a heat input source of a power generation process, one of the design objectives is to optimize the overall system performance. In general, the collector works best at low temperatures and its energy efficiency decreases with increasing operating temperature T_c.

On the other hand, a power generation process is more efficient with increasing temperature of the driving heat source Q_c. If the power generation process is considered as an idealized Carnot engine, then maximizing the exergy output of the solar collector leads to a maximization of the overall work production:

$$W_{id} = Q_c\left(1 - \frac{T_o}{T_c}\right) \quad (1)$$

In this paper, we develop a simple method to determine the optimal operating temperature that maximizes the exergy output of a real solar collector characterized according to the European standards.

2- Collector performance

Under steady-state conditions and considering the heat losses from the solar collector to the surroundings, the net solar heat absorbed by the absorber plate, is given by:

$$Q_c = A_c\, F_R\left[\tau\alpha\Phi - K\left(T_f - T_o\right)\right] \quad (2)$$

where K is a heat loss coefficient, F_R is a correction factor for heat transmission between the absorber surface and the heat transfer fluid circulating in the collector, T_f is the mean temperature of heat transfer fluid defined as:

$$T_f = \frac{1}{2}\left(T_{fo} + T_{fi}\right) \quad (3)$$

Moreover, the useful heat delivered by the solar collector corresponds to the energy transferred to a heat transfer fluid which is in direct contact with the absorber surface:

$$Q_c = q_m c_p\left(T_{fo} - T_{fi}\right) \quad (4)$$

where T_{fo} and T_{fi} are the temperature of the working fluid at the inlet and outlet of the solar collector.

Corresponding Author: Driss STITOU, Email: stitou@univ-perp.fr

The classical approach assumes the linearity of the overall heat loss term. At low and intermediate temperatures, heat losses are dominated by convection and/or conduction. The radiation losses are generally linearized and included in the heat loss term. Thus, the instantaneous thermal power provided by a solar collector depends on the global irradiance arriving to the absorber surface as well as on the collector thermal losses, which varies according to operating conditions (ambient temperature T_o, mean temperature of the thermal fluid T_f, wind speed,…).

In reality the heat losses from the solar collector that are a combination of convective and radiative heat losses are highly not linear. Thus, the heat loss coefficient K is not constant but varies in first approximation, linearly with the temperature difference of the collector with its surroundings:

$$F_R K = k_1 + k_2\left(T_f - T_o\right) \quad (5)$$

In this expression, k_1 is a coefficient for conductive and convective heat losses and k_2 a coefficient that takes into account the temperature dependence of radiative heat losses, that are linearized in this expression. All these parameters include the correction factor F_R for heat transmission between the absorber surface and the heat transfer fluid for a given solar collector.

The collector instantaneous efficiency is then defined as the ratio between the useful heat Q_c delivered per collector area A_c and the global irradiance Φ:

$$\eta = \frac{Q_c}{A_c \Phi} \quad (6)$$

According to the standard certification of solar collectors EN 12975-2, the efficiency curve is described by a second order expression that fits the measured efficiency points obtained during stationary tests. This efficiency curve follows the relation:

$$\eta = \eta_o - k_1\left(\frac{T_f - T_o}{\Phi}\right) - k_2\Phi\left(\frac{T_f - T_o}{\Phi}\right)^2 \quad (7)$$

Where η_o is the optical efficiency (also known as the corrected absorbance-transmittance product ($F_R\tau\alpha$) for flate plate collectors), k_1 and k_2 are the negative heat loss coefficients of first and second order. Typical values for these coefficients are given in table 1 for different technologies of solar collectors and their impact on the collector efficiency is shown in Fig. 1.

Consequently, for any thermal solar collector, the efficiency η decreases as the collector operating temperature is increased. This efficiency equals zero for the maximum collector temperature T_{max}, also known as the stagnation temperature T_{st} of the collector. For this stagnation temperature obtained under no-flow conditions, the entire collected solar irradiation is lost to the ambient at T_o.

Table 1 : Typical values of efficiency parameters for different collector technologies

Type of solar collector	η_o	k_1	k_2
Uncovered collector (U.C)	*0.85*	*15*	*0.05*
Simple glazed collector (SGC)	*0.78*	*3.5*	*0.01*
Double glazed collector (DGC)	*0.70*	*2.0*	*0.01*
vacuum-tube collector (VTC)	*0.65*	*1.3*	*0.005*
Parabolic through collector (PTC)	*0.63*	*0.1*	*0.0005*

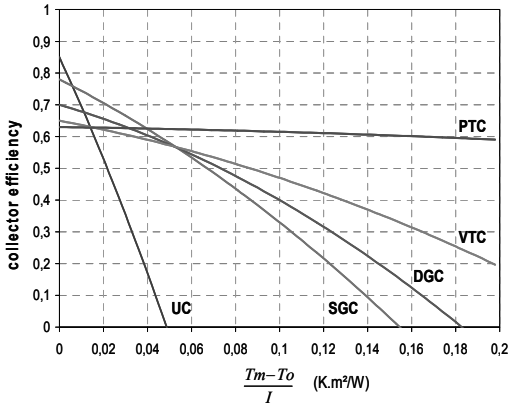

Fig. 1 : Solar collector efficiency according to their design and for a standard solar irradiation of 1000 W/m²

The stagnation temperature T_{st} is given by solving the second order equation:

$$\eta\Phi = \eta_o\Phi - k_1\left(T_{st} - T_o\right) - k_2\left(T_{st} - T_o\right)^2 = 0 \quad (8)$$

One finally obtains:

$$T_{st} = T_{\max} = T_o - \frac{k_1}{2k_2} + \sqrt{\left(\frac{k_1}{2k_2}\right)^2 + \frac{\eta_o\Phi}{k_2}} \quad (9)$$

This stagnation temperature is a function of the irradiation and is generally given by the constructor for the standard solar irradiation of 1000 W/m² and an ambient temperature of 30°C (EN 12975-2 standards).

The second solution T_{min} that cancels the solar collector efficiency is a virtual temperature, since it is negative:

$$T_{\min} = T_o - \frac{k_1}{2k_2} - \sqrt{\left(\frac{k_1}{2k_2}\right)^2 + \frac{\eta_o \Phi}{k_2}} \qquad (10)$$

Then, the heat collected per m², Q_c, can be rewritten as a function of these two temperatures, considering that the collector temperature T_c is at the mean fluid temperature T_f :

$$Q_c = \eta\Phi = k_2(T_c - T_{\min})(T_{\max} - T_c) \qquad (11)$$

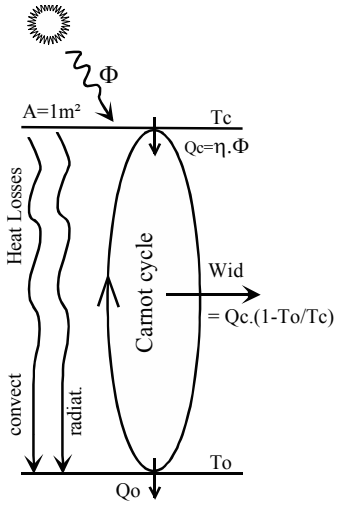

Fig 2 : Exergy analysis of a solar collector

3. Exergy output of a solar collector

Exergy analysis is based on the second law of thermodynamics. The exergy characterises the maximum amount of work that can be produced by an ideal Carnot engine cycle from a given amount of driving heat Q_c available at a temperature level T_c (Fig. 2). It can be expressed as the product of the Carnot factor θ_c calculated at collector temperature T_c by the amount of heat Q_c collected by the heat transfer fluid :

$$Ex_c = Q_c\left(1 - \frac{T_o}{T_c}\right) = Q_c.\theta_c \qquad (12)$$

where T_o is the temperature of heat rejected by the Carnot cycle, which is generally the ambient temperature.

In this way, the exergy output of a 1 m² solar collector can be expressed as :

$$Ex_c = k_2(T_c - T_{\min})(T_{\max} - T_c)\left(1 - \frac{T_o}{T_c}\right) \qquad (13)$$

Since the solar collector efficiency decreases and the Carnot factor increases with increasing collector temperature T_c, there is an optimum operating temperature T_{opt} that maximizes the exergy output of the solar collector (Fig 3).

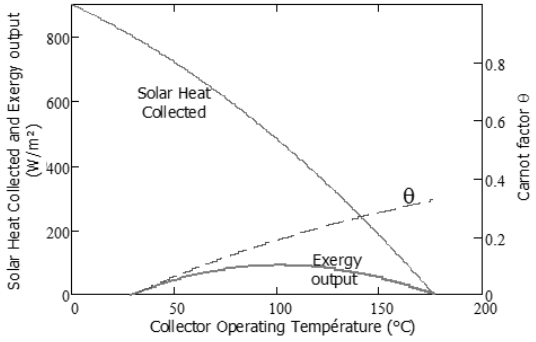

Fig. 3 : Temperature dependence of collector efficiency and collector exergy output

4- Optimal operating temperature of a given collector

The optimal operating temperature of a given collector, which is characterized according to the EN 12975 standard, is obtained by taking the derivative of the exergy output corresponding to the heat collected Qc by the heat transfer fluid, and setting it equal to zero:

$$\frac{dEx_c}{dT_c} = 0 \qquad (14)$$

This derivation leads to the resolution of a third order equation:

$$2T_c^3 - S.T_c^2 - P = 0 \quad (15)$$

Where the terms S and minus P are respectively de sum and the product of T_o, T_{min} and T_{max} :

$$S = T_o + T_{\max} + T_{\min}$$

$$P = -T_o.T_{\max}.T_{\min}$$

The resolution of this third order equation is carried out by the Cardan's method, which finally gives the optimal operating temperature T_c^*:

$$T_c^* = U + \frac{S}{6}\left(1 + \frac{S}{6U}\right) \quad (16)$$

where :

$$U = \frac{1}{2}\left(\sqrt{P} + \sqrt{V}\right)^{\frac{2}{3}}$$

with $$V = P + \left(\frac{S}{3}\right)^3$$

As T_{min} and T_{max} are function of the irradiance, then the terms S, P, U and V are also function of the irradiance.

The optimal operating temperature T_c^* can be approximated with high accuracy as the mean temperature of the ambient temperature T_o and the stagnation temperature $T_{st}=T_{max}$:

$$\tilde{T}_c^* = \frac{T_o + T_{st}}{2} \quad (17)$$

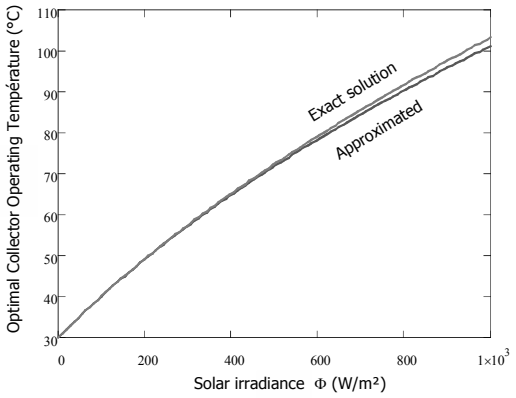

Fig 4: Comparison of the exact and approximated optimal operating temperature of a given collector (η_o=0.8; k_1=3.7 and k_2=0.012)

As it can be shown in Fig. 4, the difference between the exact solution of eq.15 and the approximated solution defined by eq.17 is lower than 3°C for a high irradiance of 1000 W/m².

5- Mass flow optimization of a solar collector

The optimal mass flow rate (per m² of solar collector) of the heat transfer fluid circulating in the solar collector is then given by:

$$q_{m_{opt}} = \frac{(\eta\,\Phi)_{opt}}{c_p\left(T_{fo} - T_{fi}\right)} \quad (18)$$

Where $(\eta.\Phi)_{opt}$ is the heat output from the solar collector operating at its optimal temperature T_c^*. Considering the relation in eq. (3), the optimal temperature outlet of the heat transfer fluid is defined as:

$$T_{fo}^* = 2.T_c^* - T_{fi} \quad (19)$$

Then :

$$q_{m_{opt}} = \frac{(\eta\,\Phi)_{opt}}{2\,c_p\,(T_c^* - T_{fi})} \quad (20)$$

As the optimal operating temperature is only function of the irradiance Φ, then it will be also the case for the optimal mass flow rate for a given inlet temperature T_{fi} of the heat transfer fluid (Fig. 5):

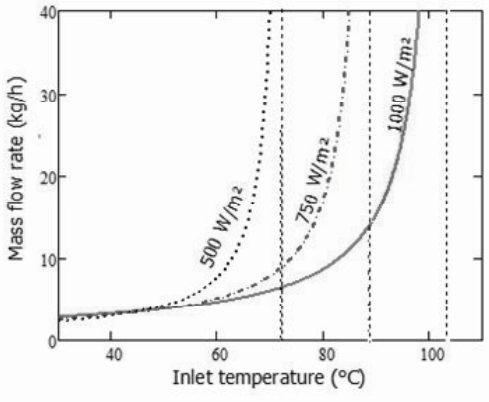

Fig. 5 : Evolution of the optimal mass flow of the heat transfer fluid as a function of the irradiance and the inlet temperature of a solar collector

One can notice that the mass flow rate increases with inlet temperature, and tends to an infinite value when the temperature becomes close the optimal operating temperature corresponding to a given solar irradiation.

6- Conclusions

The determination of the optimal operating temperature and the corresponding solar efficiency is of considerable theoretical and practical interest. This optimal temperature can be easily calculated at a given irradiance for any solar collector by determining the stagnation temperature. This result provides a guideline for designing an optimal solar thermal system and for the performance comparison of existing solar systems.

Nomenclature

c_p	specific heat, J/(kg K)
Q_c	solar Heat , W
A	area, m²
q_m	mass flow rate, kg/s
T	temperature, °C
Ex	exergy, W
K	thermal loss coefficient
k_1, k_2	thermal losses coefficients
W_{id}	ideal work, W

Greek symbols

η	solar efficiency
η_o	optical efficiency
τ, α	optical transmittance and absorbance,
Fr	correction factor
Φ	solar irradiance (W/m²)

Subscripts and superscripts

opt,*	optimal
c	collector
st	stagnation
o	ambient
f	heat transfer fluid
fo	fluid outlet
fi	fluid inlet

References

[1] E. Torres-Reyes, J.G. Cervantes, B.A. Ibarra-Salazar, M. Picon-Nuñez "A design method of flat-plate solar collectors based on minimum entropy generation", Exergy Int. J. 1(1) (2001) 46–52

[2] Kandpal, T. C., Singhal, A. K. and Mathur, S. S. (1983). "Optimum power from a solar thermal power plant using solar concentrators", Energy Convers. Mgmt., 23, p 103-106.

[3] Bejan, A., Kearney, D. W. and Kreith, F. (1981). "Second law analysis and synthesis of solar collector systems", J. Sol. Energy Engng., 103, 23-28.

[4] Yan, Z. and Chen, J. (1994). "The maximum overall coefficient of performance of a solar-driven heat pump system", J. Appl. Phys., 76, 8129-8134.

[5] S. Farahat, F. Sarhaddi, H. Ajam, "Exergetic optimization of flat plate solar collectors", Renewable Energy, Volume 34, Issue 4, April 2009, 1169-1174

[6] S. Kalogirou, "Solar thermal collectors and applications", Progress in Energy and Combustion Science, Vol 30, Issue 3, 231-295

[7] V. Badescu, Optimal control of flow in solar collectors for maximum exergy extraction" International Journal of Heat and Mass Transfer, Vol. 50, Issues 21-22, 4311-4322.

[8] A. K. Kar, "Optimal operation of solar collectors", Applied Energy, Vol 32, Issue 4, 287-294.

[9] M. Kovarik, "Optimal solar energy collector system", Solar Energy, Vol 17, issue 2, 91-95

[10] M. Kovarik and P.F. Lesse, "Optimal control of flow in low temperature solar heat collectors", Solar Energy, Vol **18** (5), 431–435.

[11] K. Altfeld, W. Leiner and M. Fiebig , "Second law optimization of flat-plate solar air heaters. Part 2: results of optimization and analysis of sensibility to variations of operating conditions", Solar Energy, Vol **41**, 309–317.

Environmental impact assessment of Grid connected Photovoltaic plants with and without two-axes tracking systems

Angel A. Bayod-Rujula[a], Ana M. Lorente-Lafuente[b], Fernando Cirez-Oto[c]

[a] *Electrical Engineering Department/CIRCE, University of Zaragoza, Spain*
[b] *Area of Research, Development & Technological Services, Instituto Tecnológico de Aragón (ITA), Spain*
[c] *CIRCE, University of Zaragoza, Spain*

Abstract: Photovoltaics are called to play a fundamental role in the embedded generation of electricity from renewable sources. The continuous development and advances in the PV sector facilitate new solutions for the solar radiation conversion, giving rise to less costly production rates. In some countries, Spain for instance, the use of two axes tracking systems has been widely implemented, but the reduction of PV modules cost makes the economic advantage of these tracking systems not so evident. This has aroused the interest of analysing them, not only from an economic, but also from an functional (efficiency or energy performance) and environmental point of view. In this paper, a Life cycle analysis of these two types of installations (with and without solar tracking) in the same geographic location is presented. This methodology, based on recognized international standards, provides the best framework for assessing the most relevant factors in the product environmental impacts and gives relevant information for further product improvements. The results also allow the calculation of the Energy and Environmental Payback time of both configurations.

Keywords: Grid connected, Photovoltaics, Life cycle Analysis, Payback time, Sun Tracking System.

1. Introduction

The life cycle analysis methodology is considered as one of the most complete and efficient tools to quantify the environmental effects of a product throughout its whole life cycle, starting from the raw materials extraction and processing, the manufacturing processes employed for the production, product transport, use and maintenance until its final recycle or management as waste. This methodology is very widely used in the solar photovoltaic sector for the assessment and comparison of the different technological alternatives available in the market.

As solar energy is a renewable energy, its generation has a very little impact in the environment, in contrast with the impact of the manufacturing phase of the components due to the amount of energy and resources needed (for example, in the cell production). This is the reason why most of the research activities are oriented to the production of less energy consuming or more efficient cells, which can lead to a better payback time.

In the case of a solar photovoltaic (PV) installation (in a building or on the ground), where different solutions are possible, it is necessary to count with the right information regarding the economical figures and efficiency of the electricity generation, already in the design phase, so as to make the best decision with a long term approach. This is only possible if a life cycle study is carried out, and the economic and environmental impacts associated to the product are determined.

Most of the existing LCA studies [1], [2], [3], [4], [5], [6], [7], [8], [9], [10] related to Photovoltaic systems are focused in the comparison of the technologies used for mono-crystalline, multi-crystalline or amorphous silicon, as well as for thin film cell production (some reports include also the module assembly), but there is little information regarding the environmental impact caused by the installation of the solar photovoltaic plant. In the majority of the cases, the results are expressed in

Corresponding Author: Ana M. Lorente Lafuente, e-mail address: alorente@ita.es

terms of CO_2 emissions, Energy yield or Cumulative Energy Demand.

In this paper, the Life cycle analysis methodology has been applied to assess the environmental impact of two possible configurations of Grid connected PV plant, with sun trackers and without them, producing different energy yield, to calculate the time necessary to pay back the CO_2 Emissions and Energy consumption in all the cases. The results have also been expressed in the units of the eco-indicator-99 commonly used in the industry.

2. Methodology

The LCA methodology is described in the Standards ISO 14040 [11] and ISO 14044 [12]. According to those standards, a Life Cycle Analysis has to be carried out in four distinct phases, as is described in the next sections.

2.1. Goal and scope definition

In this phase, the goal and scope of the study has to be defined in relation to the intended use or application of the results. The object of study is described in terms of a so-called *functional unit.* The functional unit is a key element of the LCA which has to be clearly defined, as it is a measure of the function of the system under analysis and provides a reference to which the inputs and outputs can be related. This enables comparison of two essential different systems.

Apart from describing the functional unit, the overall approach used to establish the system boundaries must be clarified, as this system boundary determines which shall be the unit processes included. This phase shall also include a description of the method applied for assessing the potential environmental impacts and which are the impact categories that are included. Finally, mention shall be made to the quality required to the data.

2.2. Life Cycle Inventory analysis, LCI

During this phase, the data on inputs and outputs for all the processes constituting the product system shall be collected. These data can be classified as energy, raw- or auxiliary material, other physical inputs, products, co-products, waste, and emissions to the air, water or soil.

2.3. Life Cycle Impact Assessment, LCIA ,

Once the inventory has been completed, the inputs and outputs are translated into indicators to express the environmental impact of the product system classified by the selected impact categories.

2.4. Interpretation

In this phase, the results of the LCI and LCIA are interpreted according to the goal of the study so as to identify the most significant aspects of the product system, which after an integrity, sensitivity and uncertainty analysis make it possible to reach conclusions and make recommendations.

3. Case Study

As mentioned in the previous sections, the purpose of the this study is to compare two different configurations of solar Grid connected PV Plants located in Sádaba (province of Zaragoza, Spain), whose UTM coordinates are: X=64439, Y= 4680651, Altitude = 454 m and Time zone= 30 and Geographical coordinates the following; Latitude: 42.264 N = 42° 15' 53 " N, Longitude: 1.249 W = 1° 14' 57 W and Altitude = 454 m.

The first one is a PV Plant with a two axes tracking system for 147 modules of 180 Wp polycrystalline silicon and 13.1% efficiency, being the generator field peak power 26.46 kWp, the Inverter Nominal Power 25 kW and the electrical connexion 7 strings in parallel (21 modules/string).

The second PV plant consist of 147 fix panels of 180 W polycrystalline silicon with 13.1% efficiency, and 26.46 kWp arranged in 7 strings in parallel separated a distance of 4.25 m and with an inclination of 32º, perfectly south oriented. The Nominal Power of the installation is 25 kW.

Since the LCA goal is the comparison of two technologies, the product system considered and the boundaries shall be the same for both. Due to the fact that the elements producing energy are identical, the assessment shall be made over the complete installation and must cover all major environmental aspects. Further, the definition of the functional unit (the object of the assessment) is extremely important in order to keep the

Corresponding Author: Ana M. Lorente Lafuente, e-mail address: alorente@ita.es

comparison fair, as the key parameters will be related to it.

In the case of a Solar Grid connected PV plant devoted to energy production for sale, the profitability is usually measured in terms of energy produced by Euro spent. In the same way, the environmental impact of the installation has to make reference to the environmental impact of the installation per energy unit produced. In this case study, the work has been structured as explained below.

3.1 Definition of the Product system and Boundaries.

The first step has been the definition of the Product system and its Boundaries, as well as the identification of products and processes that are equal for both technologies; this has helped to set the cut off criteria for the simplification.

The product system considered is the complete solar photovoltaic plant, including, solar PV modules, mechanical structures that support them, materials for the shallow foundation, electrical components and motors.

The full life cycle of both plants has been evaluated, ranging from the production of the different components that constitute the PV plant, to their end of life.

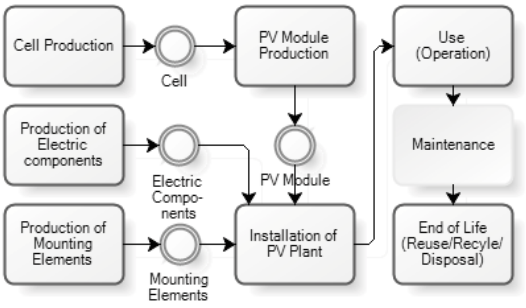

Fig. 1. Life cycle of a Grid connected PV Plant.

The maintenance works, such as cleaning of the modules, preventive maintenance for the solar trackers and Inverter reparation or replacement, (every 5 and 10 years respectively [8], have not been taken into consideration).

The effect of this simplification does not distort the result of the comparison, since both Plants have similar inverter ratings and the weight of their environmental impact in percentage is very similar. The impact of the cleaning operations of solar modules as well as the trackers maintenance have a reduced environmental relevance.

The End of Life scenario has been modelled according to ITA procedures, with data from the Environmental statistics.

Table 1. End of Life Scenario considered.

Treatment of waste material	(%)
Recycling of Steel and Iron	57,5
Recycling of Paper	62,5
Recycling of Glass	45
Recycling of Aluminium	85
Recycling of electric and electronic mat. and other materials	0
Treatment of waste after separation	**(%)**
Incineration	11,5
Landfill	88,5

Although most of the literature available does not include information about the impact caused by this phase of the product life cycle of Photovoltaics, this can be relevant depending on the eco-indicator used for the assessment (0,8 % for the PV Plant with sun trackers and 1,2% for the one with fixed panels if we look at the CO2 emissions, 0,25 and 0,35% respectively in energy consumption and about 4,5% and 2,5% in the case of the Eco-indicator 99).

3.2 Definition of the functional unit.

The functional unit considered is 1kWh of energy produced by the PV plant, being the lifetime of the PV plant estimated in 25 years. This allows a comparison of the environmental impact of the two different PV plant configurations.

3.3 Software used and Data Sources.

The environmental impact of the PV plant has been calculated using the Software Simapro [13]. The data corresponding to the environmental impact of the commercial components are background data available in the Simapro libraries and databases (the energy mix considered in the manufacturing processes has not been modified, since it represents the average of the sector). The information regarding the rest of the materials or components not available in these libraries, as well

Corresponding Author: Ana M. Lorente Lafuente, e-mail address: alorente@ita.es

as the impact of the energy mix considered have been taken from ITA databases (traceable to the library data) or created ad hoc for this study using information from the literature.

3.4 Allocation procedures.

The allocation procedures for the manufacturing processes of the different components are described in the library data.

3.5 Environmental Impact Assessment Methodology.

As explained below, the methodology chosen for the assessment of this case study is the life cycle analysis, because it covers all the factors of relevance. The results of the environmental impact of the Plants will be expressed in three different eco-indicators explained below:

3.5.1 Direct global warming potential (GWP):

This eco-indicator estimates the relative contribution to the global warming, due to atmospheric emission of a kg of a particular greenhouse gas compared to the emission of a kg of carbon dioxide. For this calculation, these figures have been taken from the Intergovernmental Panel on Climate Change (IPCC). The effects of the atmospheric lifetime of the different gases, has been estimated within a time horizon of 100 years.

3.5.2 Cumulative energy demand (CED):

This is also a widely used indicator for environmental impacts. It investigates the direct and indirect (for example due to the use of raw materials) consumption of energy necessary to obtain a product or service. The values obtained in the assessments can be therefore used to compare the results of a detailed LCA study to others where only primary energy demand is reported. Furthermore, this methodology makes it easy for the user to detect whether or not major errors have been made, as the results are very easily understandable.

The way to determine the primary energy requirement can vary depending, for example, on the heating value of primary energy carriers considered (the lower or the upper). Apart from that, the energy requirements of renewable and non-renewable resources can be distinguished. At present, there is no standardized way for this type of assessment method.

The CED-indicator considered in this work is divided into eight categories:

Non-renewable resources:

1. Fossil (hard coal, lignite, crude oil, natural gas, etc)
2. Nuclear (Uranium)
3. Wood and Biomass from primary forests

Renewable resources:

4. biomass (other sources of wood, food, biomass from agriculture, etc.)
5. wind
6. solar
7. geothermal
8. water (hydro power)

For each category, the intrinsic value is determined by the amount of energy withdrawn from nature by the energy carriers, expressed in MJ-equivalents.

Although this kind of analysis constitutes a life cycle thinking approach, it is not as precise as methods like Eco-indicator 99 [10] or ecological scarcity, whose results are much more reliable. Therefore, CED cannot be considered alone, but in combination with other methods.

3.5.3 Eco-Indicator 99:

This eco-indicator has been developed by Pré Consultants and is one of the most commonly used in the Industry.

It is a damage oriented method which classifies the environmental impact categories in three types depending on their damage to:

Human health: Number and duration of diseases (years lived disabled) and life years lost due to environmental effects such as climate change, ozone layer depletion, carcinogenic effects, respiratory effects and ionising radiation. These are combined as Disability adjusted life years (DALYs)

Ecosystem Quality: where the effects that ecotoxicity, acidification, eutrophication and land-use have on the species diversity is accounted, and expressed as the loss of species over a certain area, during a certain time.

Corresponding Author: Ana M. Lorente Lafuente, e-mail address: alorente@ita.es

Resources: surplus energy needed in the future to extract mineral and fossils of lower quality and depletion of agricultural and bulk resources due to the land use.

The results in this case are expressed in dimensionless figures (points or milipoints), which allow comparison between products or components. The value of 1 point is representative for one thousand of the yearly environmental load of one average European inhabitant.For decision making, the differences will be quantified in the standard expressions used by the PV sector, which are Energy- and CO2 Payback time.

3.6 Inventory analysis and assumptions.

For the analysis, the Grid connected Power plants have been inventoried as follows:

Materials:

PV Plant with Sun Trackers (P.P. with S.T):

1. Brackets: 2 Units, made of Galvanized steel, with a total weight of 1575 kg.
2. Wiring: 358,2 m weighting 373 kg.
3. Hydraulic Damper: One unit (18 kg). Including hydraulic oil.
4. Grid for the modules support: of galvanized steel (3854 kg).
5. Column: Consisting of the column structure, two geared motors and a bearing for the Grid orientation.
6. One 25 kW Inverter, weighting 280 kg.
7. 147 Modules of polycrystalline silicon with a surface of 1,38 m2 Units weighting a total of 2500 kg.
8. Shallow Foundation made of concrete, plus nuts, rods, clamps and corrugated steel bars. The plastic elements for the water and wiring conduction have not been considered, as their weight is not significant. Total weight is of the Shallow Foundation is 1126,4 kg.

Data obtained from a sun tracker manufacturer.

PV Plant with fixed modules. (P.P. with F.M):

1. Wiring: 376 m of wire (weighting 391 kg).
2. Concrete: 2,6 m^3 of concrete (6065 kg).
3. Inverter: two 7,6 kW units and one 10 kW unit weighting all together 190 Kg.
4. 147 Units of PV modules of the same class as in the other plant.
5. A galvanized steel structure of 2610 kg weight to support the PV modules.

Transport:

Transport of components to the PV plant: The average distance of the components' suppliers from the PV plant is estimated as 300 km except for the supplier of the inverters (200 km), PV modules (450 km) and Concrete (150 km). Road transportation in 20-28 ton lorries is assumed.

Energy consumption during the Use phase:

The yearly energy consumption of the Installation with Sun trackers is 200kWh, This value has been estimated according to the characteristics of the motor and hydraulic damper provided by the manufacturers. The fix modules do not consume energy during the use phase.

Energy Output:

The electrical energy generated by the PV Plants, has been calculated using the Software package PVSyst [14], developed by the University of Geneva (Switzerland) for the study, sizing, simulation and data analysis of complete PV systems. It is suitable for grid connected, stand alone, pumping and DC-grid (public transport) systems, and offers an extensive meteorological and PV components database. PVSyst has become reference software in the sector. The climatological data corresponding to the geographic area of analysis have been obtained from Global Meteorological Database Metereonorm [15], which generates a data file exportable to PVSyst.

Table 2. Solar Radiation of the PV Plant with Sun trackers.

	with Sun trackers		**fixed modules**	
	Wh/(m^2.day)		Wh/(m^2.day)	
Month	PVGIS	METEONORM	PVGIS	METEONORM
Jan	3390	N/A	2660	2480
Feb	4230	N/A	3380	3670
Mar	6000	N/A	4710	5180
Apr	6370	N/A	4970	5470
May	7340	N/A	5510	5750
Jun	8360	N/A	5980	6240
Jul	8620	N/A	6160	6450
Aug	7910	N/A	5890	6150

Corresponding Author: Ana M. Lorente Lafuente, e-mail address: alorente@ita.es

Sep	7140	N/A	5470	5290
Oct	5360	N/A	4200	3900
Nov	3780	N/A	2970	2740
Dec	3110	N/A	2410	2110
Yearly average	**5980**	N/A	**4530**	**4619**

The calculations give a value of 46.239 kWh /year generated by the Power Plant with Sun trackers. 35% higher than the Energy production of the fix panels, which amounts to 34.166 kWh.

3.7 Impact Assessment

The list of materials and transport data have been introduced in the Software Simapro, the above described end of life scenario defined, and the environmental impact of the two solar plants has been calculated. The results in % of the environmental impact attributable to each of the PV components are shown in tables 2 & 3:

At this point, it must be reminded again that the maintenance phase has not been considered and therefore the replacement of components due to malfunction or break down is not accounted. The effect of this simplification reduces the environmental impact of the component. For example, if the inverter is changed once during the life of the plant, its impact shall be multiplied by two.

Table 3. Environmental impact of the PV plant with Sun trackers:

	IPCC GWP 2007 in CO2 eq.(%)	CED in kWh eq. (%)	Eco-Indicator 99 (%)
Brackets	8%	7%	9%
Wiring	2%	3%	10%
Hydraulic Damper	1%	1%	2%
Column	4%	4%	6%
Inverter	3%	3%	5%
PV Modules	51%	56%	39%
Grid	19%	18%	22%
Shallow Foundation	8%	4%	4%
Transport	4%	4%	4%

Table 4. Environmental impact of the PV plant with fixed Panels:

	IPCC GWP 2007 in CO_2 eq. (%)	CED in kWh eq. (%)	Eco-Indicator 99 (%)
Wiring	3%	4%	15%
Shallow foundation	1%	0,5%	0,3%
Inverter	4%	4%	7,7%
Modules	72%	74,5%	55%
Structure	18%	16%	21%
Transport	1%	1%	2%

The results obtained show that the use of just one eco-indicator for assessing the importance of each of the components of the PV plan can lead to inaccurate conclusions, because depending on the product and the manufacturing processes involved, the damage to the environment occurs differently. Each eco-indicator focuses the attention in different impact categories (in this case in Global warming potential, primary energy consumption and damage to the health, ecosystem quality and resources respectively). Therefore the use of more than one eco-indicator in the assessment is very convenient.

As it can be noticed, the environmental impact of the use phase for the PV plant with sun trackers has not been accounted. Instead, this energy consumption is subtracted from the value of the electrical energy generated. Then we get:

Net Energy supplied to the Grid by the PV Plant with sun trackers: 46.039 kWh /year

Net Energy supplied to the Grid by the PV Plant with fixed modules: 34.166 kWh /year.

The difference results to be 11.873kWh.

3.8 EPBT, CO_2 Payback time and ERF calculation

The comparison of the two plants will be made by means of the following ratios (most of them usual in the Photovoltaics sector [16] and [17]).

Energy payback time (EPBT), defined as the ratio of the total energy input during the system life cycle to the yearly energy generation during the system operation.

$$EPBT = \frac{Energy_{input}}{Yearly\_Energy_{generated}}$$

A more exact formulation of the EPBT [3] looks at all energy inputs in the complete PV System life cycle and calculates inputs and outputs back to their equivalent Primary energy value, which is

Corresponding Author: Ana M. Lorente Lafuente, e-mail address: alorente@ita.es

also known as Cumulative Energy Demand (CED).

$$EPBT_{Primary\ Energy} = \frac{CED_{input}}{Yearly\_CED_{avoided}}$$

CO_2 payback time (CO_2PBT), defined as the ratio of the total CO_2 emissions produced during the system life cycle to the emissions avoided by replacing the energy mix by Solar PV renewable energy.

$$CO_2PBT = \frac{CO_{2input}}{CO_{2avoided}}$$

The Energy return factor (ERF) time is defined as the ratio of the total energy input during the system life cycle to the yearly energy generation during the system operation.

$$ERF = \frac{Yearly\_Energy_{generated} \times L}{Energy_{input}} = \frac{L}{EPBT}$$

In the case of the $EPBT_{,Primary\ Energy}$ and the CO_2 Payback time, the impact avoided due to the replacement of the energy mix has been calculated for two different energy mix in Spain, (year 2006 and year 2009), so as to see the effect of the gradual introduction of cleaner energies in the mix of a Country.

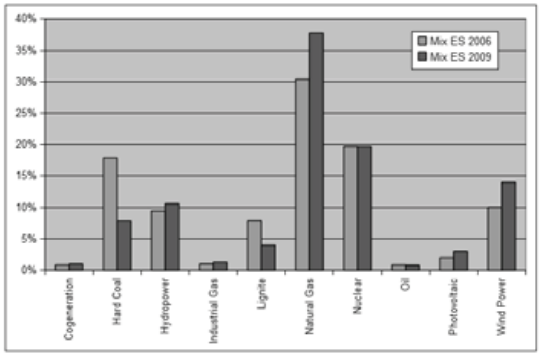

Fig. 3. Evolution of the Spanish Energy mix (2006-2009).

In table 4, we show all these figures for the case study. "Difference" corresponds to the environmental impact of all the elements that are not equal in both PV plants (including not only the manufacture, but also their transport and final disposal).

Table 5. Ratio Indicators for the different components

	$EPBT_{Primary\ Energy}$	CO_2PBT	ERF (L=25 years)
Difference (Mix 2006)	3	4,2	8,3
Difference (Mix 2009)	3,2	5,6	7,8

3.9 Sensitivity Analysis

To end the study, a review of the factors influencing the results has been carried out to check the sensitivity of the analysis.

Location: The climatic conditions of the PV plant location are crucial for the payback time. The higher the solar radiation, and the lower the temperature, the more energy will be produced, thus increasing the Plant profitability from all points of view.

Structure supporting the Modules: Again, the wind conditions on site will determine the loads applied to the structure and will determine the design parameters of the grid, column and shallow foundation. Additionally, there are many different sun trackers models and manufacturers in the market and their particular characteristics will determine the final results. From an energy point of view, the optimisation of the sun tracker design is of utmost interest.

Distance from the components suppliers: The components of the PV plant with solar trackers are much heavier than the ones of the plant with fixed modules. Any reduction in the distance travelled by the components will be of advantage for the environment and can even alter the decision about the best performing configuration, since the impact caused during the transport phase in the case of the tracking system is significant.

Energy Mix considered: The cleaner the energy mix, the longer will be the payback time.

Life of the Plant: A longer life will increase the Energy Return Factor

Although in this case, a general End of Life scenario has been defined for the purpose of checking the impact of the plant components disposal, it is sure that in 25 years time, the plant dismantling will be subject to strict environmental regulations and much more advanced recycling technologies will be available for the sector, making it possible to reuse and recycle more materials than today. This will reduce the impact

Corresponding Author: Ana M. Lorente Lafuente, e-mail address: alorente@ita.es

of the disposal phase and the payback times will get better. With view to the future dismantling the shallow foundation is in clear disadvantage with respect to metallic structures that could partially perform the same function, so this could be a potential improvement for study.

Finally, the completion of a Life Cycle analysis, with exact data of all the mechanical components and real data regarding the transport media used and real distances travelled could improve the accuracy of this assessment.

4. Conclusions

The Life cycle analysis has shown to be an adequate tool not only for the comparison of different PV technologies, but also for different plant configurations, since it allows evaluating the importance of every single material, component, consumable or energy used at every stage of the product Life Cycle.

In the case study, the environmental impact caused by the components that differ in the two PV plants, with and without sun tracking systems, show energy payback times in line with the values available in the literature. The CO_2 payback time is higher than the $EPBT_{PrimaryEnergy}$ and both ratios increase if we calculate them with the data of the Spanish energy mix in 2009, as the CO_2 emissions and CED were reduced a 25% and 5% respectively with respect to the values of year 2006.

However, the sensitivity analysis carried out shows that many relevant factors affect the results, and hence, conclusions can only be obtained after a deep, complete and particularized.

Acknowledgments: The authors would like to thank the people from the Materials and Mechatronic Product Design departments of Instituto Tecnológico de Aragón for their contribution to this work with their data and support regarding the mechanical components.

References

1. Varun, Bhat, I.K. and Prakash R., 2009, LCA of Renewable Energy for Electricity Generation Systems-A review, Renewable and Sustainable Energy Reviews 13 (2009), pp. 1067-1073.
2. Nieuwlaar, E., Alsema, E., van Engelenburg, B., 1996, Using Life-Cycle Assessments for the Environmental Evaluation of Greenhouse Gas Mitigation Options, Energy Convers. Mgmt Vol. 37, Nos 6-8, pp 831-836.
3. Alsema, E., Energy Requirements of Thin-Film Solar Cell Modules-a Review, Sustainable Energy Reviews 2, pp. 387-415.
4. de Wild-Scholten, M., Alsema, E., 1998, Towards Cleaner Solar PV, Refocus, September/October 2004, pp 46-49.
5. Alsema, E.A, Nieuwlaar, E., 2000, Energy Viability of Photovoltaic Systems, Energy Policy 28, pp 999-1010.
6. Battisti, R., Corrado, A., 2005, Evaluation of Technical Improvements of Photovoltaic Systems through Life Cycle Assessment Methodology, Energy 30, pp. 952-967.
7. Stoppato, A., 2008, Life Cycle Assessment of Photovoltaic Electricity Generation, Energy 33, pp. 224-232.
8. Gürzenich, D., Wagner, H.-J., 2004, Cumulative Energy Demand and Cumulative Emissions of Photovoltaics Production in Europe, Energy 29, pp. 2297-2303.
9. Gürzenich, D., et al., 1999, Cumulative Energy Demand for Selected Renewable Energy Technologies, The International Journal of Life Cycle Assessment 4 (3), pp. 143-149.
10. Goedkoop, M. and Sprensma, R. 2000, The Eco-indicator 99. A damage oriented method for life cycle assessment, 3rd ed., Pré Consultants B.V.
11. ISO 14040:2006 Environmental management - Life cycle assessment - Principles and framework
12. 14044:2006, Environmental management - Life cycle assessment - Requirements and guidelines.
13. Simapro, Software for Life Cycle Analysis, Ver. 7.1, Pré Consultants B.V.
14. PVSYST, Study of Photovoltaic Systems, 2009 Software Package, Ver. 5,05, University of Geneva, Switzerland.

Corresponding Author: Ana M. Lorente Lafuente, e-mail address: alorente@ita.es

15. METEONORM, Global Meteorological Database for Engineers, Planners and Education, Edition 2009, Ver. 6.1, Meteotest.
16. Evans, A., Strezov, V. and Evans, T. J., 2009, Assessment of Sustainability Indicators for Renewable Energy Technologies, Renewable and Sustainable Energy Reviews 13. pp. 1082-1088.
17. Wagner, H.-J., Pick, E., 2004, Energy Yield Ratio and Cumulative Energy Demand for Wind Energy Converters, Energy 29, pp. 2289-229.

Corresponding Author: Ana M. Lorente Lafuente, e-mail address: alorente@ita.es

Bitumen heating up to 180°C by the SRB solar panel

C.Benvenuti[a], M.Maranzana[b], S.Pauletta[a].

[a] *SRB Energy Research SARL, c/o CERN, CH-1211 Genève 23, Switzerland*

[b] *COLAS Suisse SA, 20, route de Berne - CH-1010 Lausanne, Switzerland*

Abstract: The bitumen used for road coating is stored at temperatures ranging from 160°C to 180°C to improve its pumpability. COLAS Suisse SA has decided to make use of solar energy for this task, with the aim of totally or partially replacing fossil fuel. The chosen solar panels are produced by Corp. SRB Energy close to Valencia (Spain). These solar panels are evacuated at pressures lower than 10-4 Torr (0.01 Pa), reducing the thermal losses and increasing the efficiency at high temperatures. To further enhance the high temperature efficiency, the panels are equipped with non focusing cylindrical mirrors. To achieve this, a solar field of 80 m^2 will be installed on the roof of a metallic warehouse. Given the building orientation and constraints, the panels will be oriented 45° West with no tilt on the horizontal plane. The details of the installation design and performance estimation are presented and discussed.

Keywords: Solar thermal panel, process heat, bitumen, storage tanks.

1. Introduction

With more than 70000 collaborators and a turnover exceeding 11 billions €, COLAS Group, world leader in road construction, has developed deep interest in renewable solutions to reduce the carbon footprint and the fossil fuel price exposure of its several process plants and refineries. To enforce this strategic goals, and in the framework of an agreement with the Swiss AENEC *("Agence de l'Energie pour l'Economie")*, one of its subsidiaries, COLAS Suisse, is equipping its bitumen process plant in Geneva with solar thermal collectors featuring Ultra High Vacuum and capable of providing the needed process heat at temperatures in the range from 150 to 190°C.

Replacing fossil fuel by solar energy could not be done until now in high temperature applications, because of the lack of technical solutions capable of providing efficiently solar heat. The widely used flat solar panels may hardly reach these temperatures, while solar systems based on light focusing, which may provide higher temperatures, cannot collect the diffuse component of the solar light, and for this reason are not very efficient at our latitudes (central Europe).

The situation has changed recently with the industrial production of a new flat plate solar thermal panel by Corp SRB Energy S.A., at Almussafes, close to Valencia, Spain. This panel, commercially available since summer 2009, and based on a patent by CERN (the European Organization for Nuclear Research close to Geneva, Switzerland), makes use of vacuum and optical selectivity to drastically reduce the thermal losses. Thanks to the very low thermal losses, this panel may reach a stagnation temperature higher than 300°C without mirrors, and close to 400°C when equipped with cylindrical mirrors, which convey both the direct and the diffuse light to the back of the panel with equal efficiency.

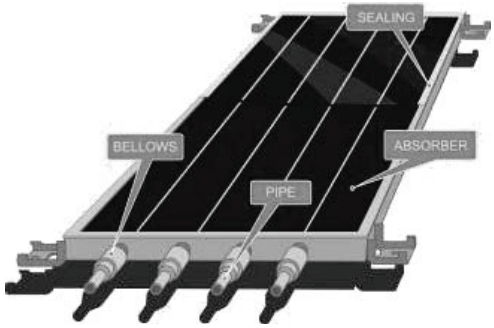

Fig. 1. Schematic view of the SRB solar collector (70 cm wide, 4.5 cm thick, 3 m long).

In the next paragraph the main characteristics of the SRB panel are summarized, followed by a short description of the process plant for bitumen treatment. Further in the document the solar field is described in its layout and simulation results are presented.

Corresponding Author: Stefano Pauletta, Email: spauletta@srbenergy.com

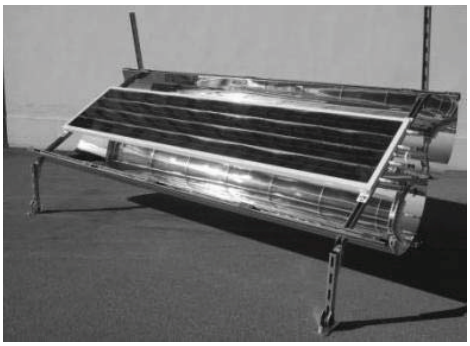

Fig. 2. SRB "serpentina" collector equipped with cylindrical mirrors (aperture area: 3.9 m^2; gross area: 4.17 m^2).

2. The SRB solar panel

The SRB panel is shown schematically in Fig.1. Its standard dimensions are width 70 cm, thickness 4.5 cm, length 2 or 3 m [1].

It is produced in two different versions, one with cooling pipes crossing the panel frame from one short side to the other ("*straight*" panel), the second with cooling pipes bent at 180° so as to have both the inlet and the outlet on the same short side of the frame ("*serpentina*" panel).

After the initial pump-down and bake out, the vacuum is maintained by a built in getter pump powered by sun. The light absorbers are coated with a galvanic layer of Cr black which provides an absorption coefficient of about 0.9 and an emissivity lower than 0.07 at 300°C.

The SRB panel may be equipped with mirrors of different configuration, depending on the chosen application. In the present case cylindrical mirrors were chosen, combined with "*serpentina*" panels

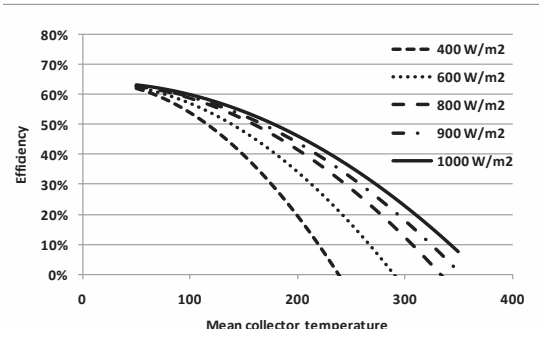

Fig. 3. SRB collector efficiency as a function of the mean operating temperature for several values of solar irradiance.

Table 1. Main thermal properties of the bitumen at 160°C and main features of the storage tanks.

Bitumen properties		
Density @ 160°C	919	kg/m^3
Specific heat @ 160°C	2.05	kJ/kg/K
Dynamic viscosity@ 160°C	24	mPa*s
Tank		
Height	9	m
Diameter	3.4	m
Volume	82	m^3
Insulation Thickness	200	mm
Thermal resistance	0.023	K/W
Tank Inner Heat Exchanger		
Area	25	m^2
N. of Pipes	64	
Pipes diameter	18	mm
Inlet/outlet diameter	32	mm

(see Fig.2), featuring an aperture and gross areas of 3.9 and 4.17 m^2 respectively.

The thermal efficiency for different light intensities is given in Fig.3 as a function of the panel mean operating temperature.

3. The industrial process

With more than 650 collaborators, COLAS Suisse Holding SA is a corporation of fifteen firms involved in road construction and civil engineering. At their Geneva site, bitumen is stored for process purposes in six large, thermally insulated vessels of about 80000 lt, at temperatures higher than 160°C (see Fig.4). From the storage tanks, the bitumen is transferred on trucks for delivery, or it is used in a process plant for asphalt production.

Fig. 4. Insulated tanks used to store bitumen at COLAS premises in Geneva.

A 700kW fossil fuel heater provides the plant with the heat needed to keep the stored bitumen at a viscosity acceptable for pumping and to balance the heat losses of the bitumen distribution network. Heat transfer oil is used to supply energy to the tanks (i.e., via an inner coil heat exchanger) and to the bitumen distribution network (i.e., via twin tracing-lines installed below bitumen main circuit). Table 1 shows the main features of the bitumen storage tank and the values of the main thermal properties of bitumen at 160°C [2].

4. The solar plant

A field made with SRB Energy thermal collectors has been designed to satisfy part of the heating needs of COLAS process at its Geneva premises by solar energy. Four parallel loops of five solar collectors connected in series are installed in parallel with the main fuel heater of the bitumen circuit.

Fig. 5 shows the solar field made of 20 SRB solar thermal collectors installed at COLAS premises, while Fig.6 shows a schematic diagram presenting the solar plant integration into the process circuit, simplified for the sake of clarity.

Referring to Fig.6, the heat transfer fluid is heated from 170 up to 180-190°C and it is circulated back to the bitumen storage tanks circuit. When possible or profitable, oil is extracted from the main loop to be heated by the solar collectors up to about 190°C and reinserted into the main circuit branch to heat the storage tanks at about 160°C, decreasing the need of fossil fuel in the heater. At start-up, to avoid using fossil fuel energy to warm up the oil content of the solar field, the solar plant is run in pre-heating loop until the oil reaches

Fig. 5. The solar field made of 20 SRB solar thermal collectors installed at COLAS premises.

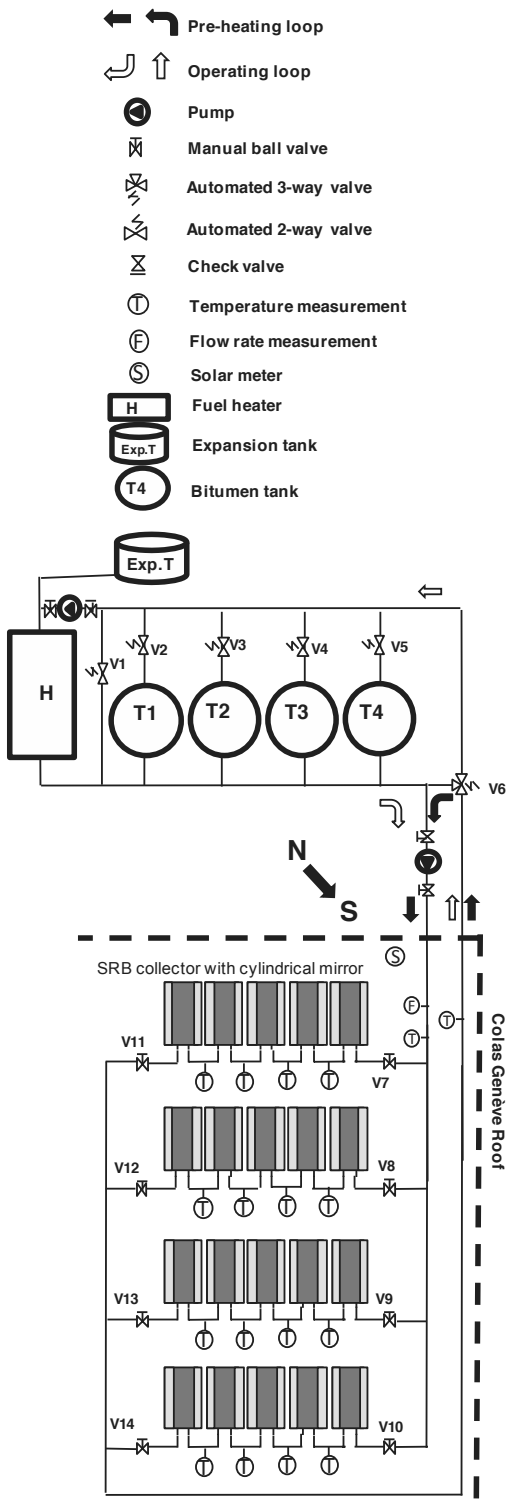

Fig. 6. Simplified process flow diagram of the solar field and bitumen heating plant at COLAS premises in Geneva.

$$\eta = \eta_0 \left(\frac{G_b}{G} IAM(\vartheta) + k_{\vartheta dA} \frac{G_d}{G}\right) - a_1 T_{red} - a_2 G T_{red}^2$$

$$IAM(\vartheta) = 1 - \psi\left(\frac{1}{\cos(\vartheta)} - 1\right)$$

G_b : direct impinging irradiance $\left[\frac{W}{m^2}\right]$

G_b : diffused impinging irradiance $\left[\frac{W}{m^2}\right]$

$$T_{red} = \frac{\left(\langle T_{cll,mean} \rangle - T_{amb}\right)}{G} \left[\frac{Km^2}{W}\right]$$

$\eta_0 = 0.6389$

$a_1 = 0.1162 \left[\frac{W}{m^2 K}\right]$

$a_2 = 0.0048 \left[\frac{W}{m^2 K^2}\right]$

$\psi = 0.09$

$k_{\vartheta dA} = 1.008$

Fig. 8. Collector model in use. IAM: Incident Angle Modifier; G: impinging global irradiance (direct G_b; diffused G_d); $T_{cll,mean}$: mean temperature in collector; T_{amb}: ambient temperature; η_0, a_1, a_2, ψ and $\kappa_{\vartheta dA}$ are empirical coefficients.

170°C.

The solar field is installed on the roof of a metallic structure warehouse with 45° West orientation (see Fig. 7). The collectors have been given 5° tilt to facilitate rain-water drainage (5°), to simplify their installation on the warehouse roof and to optimize the economic return of the solar plant. Given the peculiarity of the chosen building, in fact, the adoption of an optimized tilted structure would have increased the project cost by about 25%.

Table 2. Solar data for Geneva during year 2005 (Source: Soda Solar Services [3])

Period	DNI [kWh/m2]	Horizontal Diffused [kWh/m2]
January	28	25
February	38	33
March	101	52
April	101	57
May	152	63
June	209	63
July	175	70
August	141	65
September	110	51
October	76	39
November	41	28
December	15	20
Year	1188	566

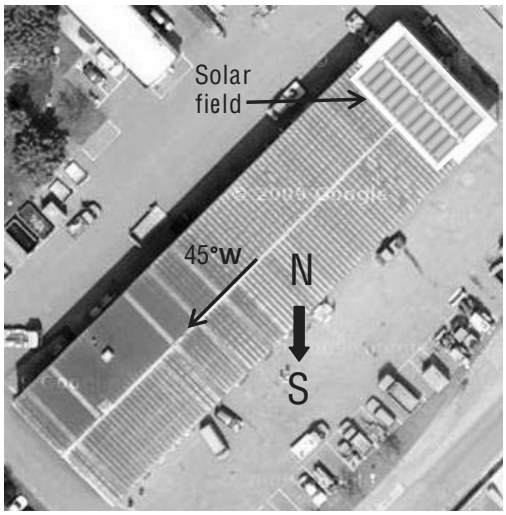

Fig. 7. The metallic structure warehouse where the SRB collectors are installed.

5. Calculated thermal performance

Hourly based simulations have been performed to estimate the expected annual solar energy yield and to quantify the economic viability of the project. Table 2 shows the irradiation data for Geneva for the reference year 2005. Hourly values of the direct normal irradiance (DNI) and of the diffuse horizontal irradiance [3] have been used through simulations together with the standardized collector model shown in Fig.8 [4]. This latter is referred to the aperture area of the panel equipped with cylindrical mirrors.

The process plant in which the solar field has been integrated features energy needs for bitumen heating which are extremely large in comparison to the solar field output (e.g., about 160MWh/year needed for tank thermal losses only). For this reason, the oil temperature at the solar field inlet is constantly assumed at about 170°C during plant operations. And, as a consequence, the net solar yield of the solar plant is directly computed from impinging radiation and piping thermal losses.

In the case of larger solar fields, it has been estimated that the temperature at which bitumen is stored (160°C) is low enough to allow storing the excess solar energy as bitumen sensible heat at temperatures up to its stability limits (~190°C).

Table 3. Features adopted to model the thermal losses of the solar field piping

	Insulation thickness [mm]	Total length [m]	Thermal resistance [K/W]
Solar field piping	30	39	0.12
Inlet/outlet distributors	50	27	0.15

The solar field has been installed with 5° tilt and following the orientation of the supporting building to decrease the building adaptation costs, improving the economical impact of the project. Fig.9 shows the comparison between the gross solar energy yield for the real tilt and orientation (45° West oriented with 0° tilt) and that of the other two options available: a South oriented field with 34° tilt, and a 45° West oriented field with 33° tilt. The gross annual solar yield is about 35 MWh/y in the optimal case, and it lowers to 33 and 30 MWh/y for the 45° West oriented cases with 34° and 0° tilt, respectively.

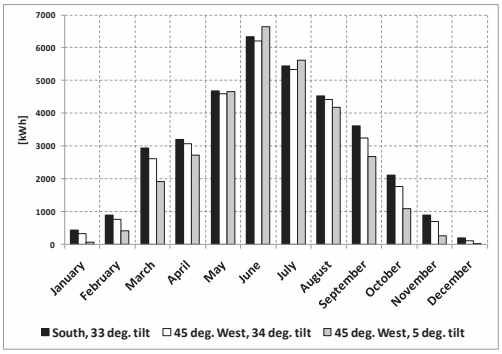

Fig. 9. Estimated gross energy yield of the solar field for each month of the reference year 2005.

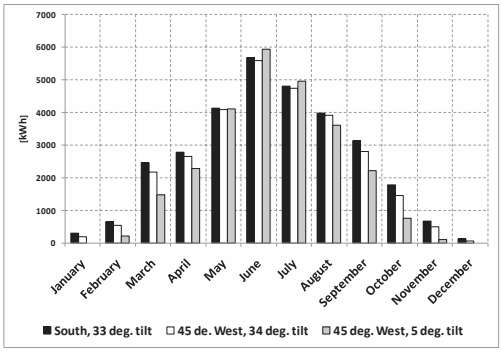

Fig. 10. Estimated net energy yield of the solar field for each month of the reference year 2005.

Fig.10 shows the same comparison for the solar field net production, where piping thermal losses have been estimated according to the features listed in Table 3. As a result, the net annual solar yield is about 30 MWh/y in the optimal case, and it lowers to 29 and 26 MWh/y for the 45° West oriented cases with 34° and 0° tilt, respectively.

Referring to the net yield, the relative difference is quite significant since the solar plant under installation will produce on an annual base 16% less than if it were installed in optimal conditions and 10% less than if it were installed 45° West-oriented with 33° tilt. Nevertheless, these amounts are inferior to the increase of cost to adapt the installation building to receive a tilted structure (about 25%). Industrial metallic buildings, in fact, are usually designed to be structurally optimized for their original purpose and it is rare that they are able to withstand the off-axis loads typical of large tilted solar fields without needing major interventions. For this reason, and in view of future installations, SRB Energy is developing a simplified structure for tilted solar collectors adapted to SRB collectors provided with mirror concentrator which will be able to decrease the constraints transmitted to the supporting building, lowering the adaptation costs and decreasing the amount of time needed for installation.

6. Results

The solar plant manufactured by SRB Energy Corp. for installation at COLAS Suisse premises has been conceived to provide the process plant

Table 4. Estimated values of CO2 emission reduction and fossil fuel substitution corresponding to the net annual energy yield of the solar plant under construction

Net Solar Energy Yield	26	MWh/y
Heating oil equivalence	2.2	Ton
	2.6	m^3
CO2 emission reduction	7.1	Ton

with part of the energy needs for bitumen heating.

As shown in Table 4, when simulations are run based on hourly values of solar irradiance in Geneva (Switzerland) during year 2005, the solar plant is estimated to produce about 26 MWh/y of net process heat at over 170°C. This corresponds to the substitution with solar energy of about 2200 lt/y of heating oil and to a reduction of CO_2 emission by about 7100 kg/y (based on heating oil power value of 11.48 kWh/kg [5], and CO_2 emission factor of 3.128 TonCO_2/TEP [6]).

7. Conclusions

The SRB solar thermal panel provides high temperatures with high efficiencies even in countries characterized by a large diffuse light component, such as in Central Europe.

A solar field equipped with SRB solar collectors has been installed at COLAS Suisse premises in Geneva, Switzerland. The solar plant will provide about 26 MWh/y process heat for bitumen storage and treatment in the temperature range 170-190°C. Substituting about 2200 lt of heating oil, it will reduce CO_2 emission by about 7.1 tons.

The experience gathered with such pilot plant will be transferred to other process plants and refineries of COLAS Group for applications requiring heat at temperatures ranging from 160 to 200°C, presently out of the reach of other existing solar thermal collectors.

9. References

[1] Benvenuti, C., and Ruzinov, V., 2010, The SRB Evacuated Solar Panel, ECOS 2010, In press.

[2] Whiteoak, D., and Read, J., 2003, The Shell Bitumen Handbook, Thomas Telford Ltd., Chaps. 12, 389.

[3] SoDa Solar Radiation Data, Mines Paristech – Armines, http://www.soda-is.com/

[4] EN 12975-2, Thermal solar systems and components. Solar collectors. Test methods

[5] UNI 10389-1, Heat generators – Flue gases Analysis and Measurement on Site of Combustion Efficiency.

[6] EIA, Documentation for Emissions of Greenhouse Gases in the United States 2005, DOE/EIA-0638 (2005), 2007, Tables 6-1, 6-2, 6-4, and 6-5.

8. Acknowledgments

The energy policy of the State of Geneva is based on the long term vision of a sustainable society without nuclear energy where the energy consumption is entirely covered by renewable resources. The availability of solar heat over a temperature range extending above 200°C opens up new perspectives, justifying the important financial support reserved to the evaluation of this new technology.

This project has been made possible thanks to the support from several institutions. We gratefully acknowledge the funding granted by the *Etat de Genève*, *ScanE* (*Service cantonal de l'énergie*), *DSPE* (*Département de la Sécurité, de la Police et de l'Environnement*), in the framework of its renewable energy promotion program., by the *Swiss Federal Office of Energy*, in the framework of its Solar Heating R&D program, by the *Service Industriels de Genève* (*SIG*), and their fund for renewable energies *COGENER*. In particular, we thank Dr. Jacobus Van der Maas of *ScanE* for his support and suggestions during all phases of the project.

LED Solar Spectrum Simulator

Marta Maria Nogueira Assad[a], *Paulo Celso Xavier Assad*[b]

[a] *Universidade de Taubaté, Taubaté, Brazil*
[b] *Robota Engenharia, Taubaté, Brazil*

Abstract: This paper is intended to report a solar spectrum simulator based on high power LED (Light-Emitting Diode) as the source of radiation for the tests and trials of systems that otherwise would depend on the natural solar radiation. Among the devices that would benefit from this simulator for testing are solar thermal collectors and photovoltaic cells. Traditionally, solar simulators employ metal halide, xenon or tungsten halogen lamps, which consume much more power than Leds and have a shorter life, around 1000 hours. Furthermore, these simulators only approximate the spectral characteristics of natural sunlight because of the mismatch between the spectrum of radiation generated and the natural solar spectrum. The light-emitting diodes are recognized for their low power consumption and its small dimensions. Recent advances in led technology have provided high power and high efficiency devices. Leds with power levels of radiation in the order of 100 mW and reduced dimensions are now available. Moreover the power radiated can vary from 0 to 100% by controlling the current flowing through the leds. This makes it possible to reproduce the solar spectrum with high fidelity.

Keywords: Solar simulator, LED, Solar radiation spectrum.

1. Introduction

The search for renewable energy sources has caused an increasingly demand for solar photovoltaic cells (PV) and solar thermal collectors (STC). Solar energy is abundant and free and produces no greenhouse substances or other environmental impact. To use this exceptional energy source, however, efficient photovoltaic and thermal collectors systems must be developed. In order to achieve this premise, solar simulation systems play an important role to guarantee the quality of the tests as in the development phases as in the production and deployment phases.

At present, solar simulation systems are largely based on halogen, xenon or metal-halide lamps. Besides the high cost, huge amount of electric power wasted and short life of the lamps that this technology exhibits, solar simulation based on lamps is far from matching the solar spectrum, spatial uniformity of irradiance and temporal stability demanded by the test systems of PV and STC. These three characteristics of a solar simulation system are mandatory to ensure measurement uniformity that allows results comparability and traceability.

An LED solar simulator has been proposed [1, 2, 3] to measure the spectral response (SR) and current-voltage (I-V) characteristics of monocrystalline silicon solar cells. Light intensity of the LEDs in this arrangement is in the range of 10 mW/cm^2. The characteristics of spectrum and irradiance of the LEDs used in this approach are different from the reference solar spectrum. A method is proposed [4] to calculate the cell's I-V characteristics under the standard test condition (STC).

This paper is intended to report the design and construction of a solar spectrum simulator based on high power LEDs. Solar simulation means not only choosing a lighting source with a suitable spectrum. The foundation behind artificial solar simulation is to reproduce, as precisely as possible, the effects of sunlight on products such as PV and STC. ASTM G173-03 and IEC 60904-3 international standards compute the solar radiation energy level across the spectrum from 280nm to 4000nm. For classification of solar simulation systems, this spectrum is restricted to the wavelengths from 400nm to 1,100nm. This spectral bandwidth is defined in reference IEC 60904-9 and ASTM E927-05. The spectral match of a simulation system is classified with respect to these standards.

Air Mass (AM) is the measure of how far light travels through the Earth's atmosphere. One air mass, or AM1, is the thickness of the Earth's atmosphere. Air mass zero (AM0) describes solar irradiance in space, where it is unaffected by the atmosphere. The power density of AM1.5 light is about 1,000W/m2 (1 SUN).

The solar simulation system described in this paper is a unit capable of illuminating an area 10cm x 10cm, or 100cm^2, with a power density of AM1.5 (1,000W/m^2) and a spectrum of wavelengths distributed in 5 ranges, approximately from 400nm to 1100nm.

2. LED Solar Spectrum Simulator

The LED solar simulator makes use of semiconductor technology for generation of light. LEDs are recognized by their low energy consumption and reduced size. Furthermore, its life expectancy of 50,000 to 100,000 hours is unparalleled by those of the conventional simulators based on lamp technology. By controlling the current flowing into the leds in each range of wavelengths, it is possible to control precisely the shape of the simulator spectral output to mimic that of the natural solar spectrum. Also by controlling the current from 0% to 100% one can control the insolation from 0 SUN to 1 SUN, compared to 75% to 100% achieved by the conventional (lamp) simulators. It is useful to simulate all levels of a cloudy sky.

LEDs with a radiated power in the order of 100mW and wavelength from 340nm to 1550nm are now commercially available at reasonable prices. This implementation uses five different leds in order to cover the spectral range from 400nm to 1100nm, as defined by IEC 904-9 as the ideal spectral range to test photovoltaic devices. The LEDs used are:

- LED1: 400nm - 750nm, white LED;
- LED2: 500nm – 560nm, green LED;
- LED3: 725nm – 795nm, red LED;
- LED4: 790nm – 910nm, infrared LED;
- LED5: 850nm – 1030nm, infrared LED.

IEC standards define the spectral match of a solar simulator as a percentage of the integrated intensity in 6 spectral ranges, listed in Table 1. Any deviation from the specified percentages must then lie within a range that determines the class of the simulator. For a Class A simulator, this range is 0.75 to 1.25 times the ideal percentage.

Table 1. Spectral Match Defined by IEC Standard

Spectral Range (nm)	Ideal %
(1) 400 – 500	18.5
(2) 500 – 600	20.1
(3) 600 – 700	18.3
(4) 700 – 800	14.8
(5) 800 - 900	12.2
(6) 900 - 1100	16.1

An observation to LED1 (the white LED) is that it has a spectral power distribution from 400nm to 750nm with a valley in the 500nm region, as shown in Fig. 1. This valley is somewhat compensated by LED2 (500nm – 560nm).

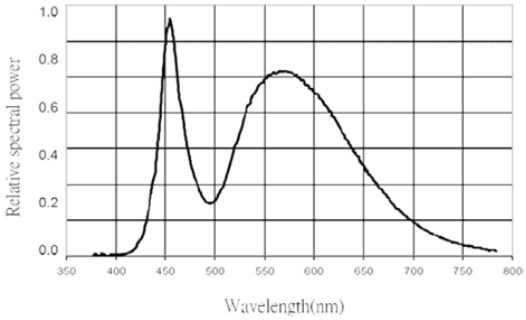

Fig.1. Relative spectral power distribution of LED1

To illuminate the proposed square area of 100cm^2 the total incident power should be 10W, as per AM1.5. According to the data in Table 1 and Fig. 1, LED1 covers the ranges (1) and (3), so it is responsible for 36.8% of the incident power. LED2, LED3, LED4 and LED5 are responsible for 20.1%, 14.8%, 12.2% and 16.1%, respectively, accumulating 100% of the total incident power.

2.1. Construction details

To illuminate a square area of 100cm^2 it is necessary to project a circumscriptive circular area of 157cm^2. This is so because LEDs emit light as a cone of circular base. So the total incident power in this circular area should be 0.0157 m^2 X 1kW/m^2, or 15.7W. In order to compensate for attenuations and to have enough power to simulate an 1.25 SUN, a 50% increase in power has been done. Then, the total power radiated by all the LEDs in this solar simulator is 15.7W X 1.50, or 23,5W.

According to the percentages specified in Table 1, the LEDs of type LED1 must irradiate 36.6% of 23.5W which equates 8.6W. Correspondingly, the other four LED types must irradiate 4.7W, 3.5W, 2.9W and 3.8W respectively.

The types LED1 and LED2 are parts from company Brightek, coded 1ZKW37FWOMAZ1 and 1ZKG77DCKMAZ1. Each of these parts produces 120mW of radiated power. In this way it is necessary 72 LEDs of type LED1 to achieve 8.6W and 39 LEDs of type LED2 to achieve 4.7W. All the other three LEDs are from company Epitex. LED3 is coded SMB760-1100-01 and radiates 84mW. It is necessary 42 LEDs of this type. LED4 is coded SMB850D-1100-01 and radiates 138mW. It is necessary 21 LEDs of this type. LED5 is coded SMB940-1100-01 and radiates 170mW. It is necessary 23 LEDs of this type. The total number of LEDs is 197. As there are five types of LEDs they are accounted in excess, the total number were rounded to 200 LEDs and distributed as 70 of type LED1, 40 of types LED2 and LED3 and 25 of

types LED4 and LED5. These 200 LEDs are distributed in five modules each containing 14 of type LED1, 8 of LED2 and LED3 and 5 of LED4 and LED5. Fig. 2 illustrates one of such module, showing the LEDs, the printed circuit board (the green board) and the heat sink (in gray), necessary to dissipate the heat generated by the LEDs.

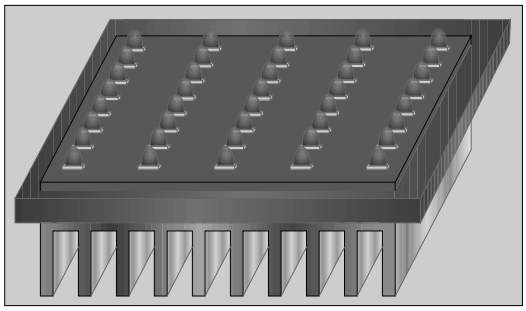

Fig.2. Basic LED module

All the LEDs are constructed with an integral lens that focuses the radiated light in a 14° viewing angle. It can be demonstrated that at a distance of 57cm each module illuminates a circular area of 157 cm^2 which in turn circumscribes a 100cm^2 square area.

The five modules are assembled in a conveniently curved frame, the shape of a spherical cap. This is so to concentrate the light irradiated by all five modules in the same 157 cm^2 circular area.

Each group of LEDs has its own power supply. So this simulator uses five independent power supplies. Each power supply is remotely controlled by means of a 4 – 20 mA control port. In this way the trial and test sessions can be recorded and precisely repeated any time. By varying the current fed to each group of LEDs it is possible to shape the spectral power distribution.

2.2. Results

The experimental solar simulator was assembled and tested to verify the validity of the assumptions. LED1 and LED2 groups were fed with a 350mA current. This is its nominal current. LED3 and LED4 were fed with 200mA. Their nominal maximum current can reach up to 600mA. LED5 was fed with 600mA, its nominal current. With these current levels the solar simulator produced a total radiated power of 17.7W measured at a distance of 57cm with a Photodyne #500 optical power meter. This result correspond to 1.125 SUN, a little lower than the intended 1.25 SUN. However, it is enough to saturate any test to screen the photovoltaic cell.

As for the spectral characteristics, Fig. 3 shows the radiation spectrum of the LED solar simulator.

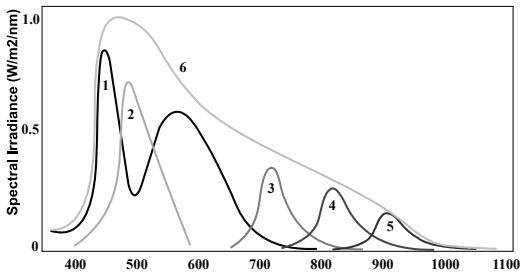

Fig.3. LED solar simulator radiation spectrum

The curves 1, 2, 3, 4 and 5 in Fig. 3 correspond to the radiation spectrum of LEDs of groups LED1, LED2, LED3, LED4 and LED5 respectively. Curve 6 is the total radiation spectrum of the simulator and corresponds to the integrated effect of all LEDs.

For comparison Fig. 4 shows the natural solar radiation spectrum contrasting, in red, the radiation at sea level. It can be seen that the radiation spectrum of the LED solar simulator has a good match with the natural radiation spectrum.

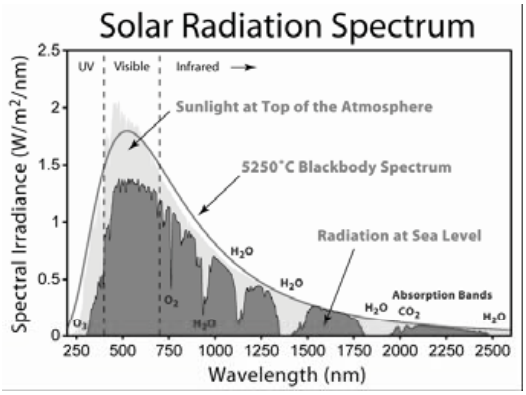

Fig 4.Natural solar radiation spectrum

3. Conclusion

The LED solar spectrum simulator described in this paper uses 200 LEDs and is capable to produce a total power of 17.7W in a 157cm^2 area, which correspond to a power density of 1,125 W/m2, or 1.125 SUN. Several modules similar to the one described in this paper could be assembled together to achieve a simulator capable of testing solar thermal collectors, with the same quality of solar spectrum matching, spatial uniformity of irradiance and temporal stability. As the power high power LED technology evolves to produce more powerful devices, and as the price lowers, the solid state lighting devices will be the natural choice over the

traditional lamps in the construction of solar spectrum simulators.

References

[1] Koyanagi, J., and Kurokawa, K., 2006, A Fundamental Experiment of Solar Cell's I-V Characteristics Measurement Using LED Solar Simulator, Renewable Energy Proceedings, pp. 270-273.

[2] Kohraku, S., and Kurokawa, K. 2004, A Fundamental Experiment for Discrete-Wavelength LED Solar Simulator, 14th International Photovoltaic Science and Engineering Conference.

[3] Hishikawa, Y., Imura, Y., and Oshiro, T. 2000, Irradiance-Dependence and Translation of the I-V Characteristics of Crystalline Silicon Solar Cells, Japan Journal of Applied Physics. Part2, 39-7A, L6.

[4] Kohraku, S., and Kurokawa, K., 2003, New Method for Solar Cells Measurement by LED Solar Simulator, WCPEC – 3rd

Forest Biomass Gasification Integrated to a Kraft Pulping Mill: Technology Options

PVKK Varma[a], J.Chaouki[a], J.M.Lavoie[b] and J.Paris[a].*

a. Ecole Polytechnique de Montreal, Department of Chemical Engineering, Montreal, Canada.
b. Universite de Sherbrooke, Départment de genie chimique et genie biotechnologique, Sherbrooke, Canada

Abstract: The pulp and paper industry in industrial countries is undergoing a very serious crisis because, among other reasons, competition from emerging producing countries in tropical regions, the increasing energy costs and the drop in demand in commodity products such as newsprints. This situation has arisen, despite large investment in research and innovation during the last decades to find alternative routes to meet the energy and added value products requirements. The conversion of pulp and paper mills into biorefineries while maintaining the production of their core traditional product has been identified as an approach to restore the industry profitability. Kraft processes are particularly well suited for such conversion because wood components such as hemicelluloses and lignin can be readily separated and used as precursors of a broad spectrum of "green molecules". Appropriate gasifier design and operating conditions for the production of a high quality syngas suitable for conversion to energy in the form of electricity and into biofuels, like methanol and dimethylether as an example have been identified. This combined biorefinery approach could provide combined heat and power (CHP) for the upgrade of pulp and paper mills. This paper discusses the implementation of biorefinery options in pulp and paper industry. It presents in details the general characteristics of gasification and defines the wood residue and black liquor gasification process flow sheets. It also gives guidelines on how to integrate a gasifier in a kraft mill by replacing the recovery boiler for the steam and electricity production.

1. Introduction

The pulp and paper industry is the largest producer and user of biomass-related energy and nearly all of it is derived from sustainably grown trees. Renewable resources used at pulp mills include bark, wood wastes, and black liquor, the lignin-rich by-product of cellulose-fiber isolation. Additionally, there are substantial volumes of wood residues (around 40 - 50%) that remain behind after harvesting trees for the production of pulping grade wood chips. Perlack and co-workers (Perlack et al., 2005) estimated that there are plenty of unused wood resources (logging residues, fire-prevention thinnings, mill residues, and urban wood waste) that could be recovered on a sustainable basis at present. While most pulp and paper manufacturing facilities in North America today do not export electricity and none export transportation fuels, their established infrastructure for collecting and processing biomass resources provides a strong foundation for future gasification-based bio-refineries that could produce biofuels, electricity, and chemicals in conjunction with pulp and paper products. If the biomass resources from which energy carriers are produced in such biorefineries are sustainably grown and harvested, there would be few net emissions of CO_2 associated with biorefineries and their products. These environmental issues coupled with the potential to address national energy security and global warming concerns is the looming need which can catalyze capital investments in the pulp and paper industry to replace the aging fleet of Tomlinson recovery boilers used today to recover energy and pulping chemicals from black liquor.

The high cost of new Tomlinson recovery boilers provides an unusual window of economic opportunity for their replacement by black liquor gasifiers. Concerted efforts are ongoing in North America and Sweden to develop commercial black liquor gasification (BLG) technologies (Consonni et al., 2009). The biorefinery concept pursued in this study comprises two different types of gasifiers: one that handles the black liquor and the other for woody biomass. A combination of both

Corresponding Author: PVKK Varma, Email: kanthi.penmetsa@polymtl.ca

should meet the thermal energy needs of the mill as well as to produce added value chemicals.

The conversion of biomass to biofuels has gained substantial interest recently because of the rising cost of fossil fuels, increasing concerns about greenhouse gas emissions and global warming. As world energy demand is likely to continue to increase, there is a need for alternative sources of renewable energy. In Canada, lignocellulosic biomass is an attractive renewable energy source, because it is abundant and does not compete with food crops for available land. Following gasification, it could be used to produce liquid and gaseous bio-fuels such as, DME, FT-diesel, SNG and hydrogen via specific catalysis. Although the process has shown net advantages, gasification of forest residues at commercial scale is still in development. The challenges and benefits of the implementation of two specific gasification technologies, wood biomass gasification and black liquor gasification into Kraft pulping mills.

Gasification technologies enable low-quality solid or liquid fuels like wood residues and black liquor respectively to be converted into a fuel gas (synthesis gas or "syngas") consisting largely of H_2 and CO and CO_2. After adequate cleaning, this syngas can be burned cleanly and efficiently in a gas turbine to generate electricity, or passed over appropriate catalysts to synthesize "green" liquid transportation fuels or chemicals. The biorefinery designs assumed (Consonni et al., 2009) that gasification technologies have successfully moved beyond the development stage now in progress and that the risks involved with installing gasification systems are comparable to those of installing a new Tomlinson-based power/recovery system. If the BLG experiences currently being pursued meet their promise (Lindblom and Landälv, 2007) and pressurized biomass gasification technology (Evans et al., 1987; Lau et al., 2003) overcomes the hurdles encountered in past demonstrations, this condition of commercial reliability could be reached within a decade. All of the equipment for downstream processing of the synthesis gas from the gasifiers, including for sulphur capture and for catalytic synthesis of at least two of the liquid fuels of interest (methanol and DME), is already commercially available.

The present manuscript discusses the benefits of implementing gasification technologies in pulp and paper mill, the necessary considerations for selecting feed and the end uses. The possible biorefinery options to implement in pulp and paper industry are also presented.

2. Gasification general characteristics

2.1 Feedstock pre-treatment

The degree of pre-treatment of the feedstock is dependent on the gasification technology used. The main problem areas are (McKendy, 2002):

(a) Drying: The biomass moisture content should be below 10–15 % before gasification.
(b) Particle size: In most gasifiers, gas has to pass through the biomass and the feed has to have sufficient compressive strength to withstand the weight of the feed above. Feed particle sizes in the range 20–80 mm are typical.
(c) Fractionation: The nitrogen and alkali contents of the biomass are critical, as they are partially carried over into the gas-stream. Small particles tend to contain less nitrogen and alkalis, so fractionation into fine and coarse particles helps to produce a gas with fewer impurities.
(d) Leaching: The nitrogen and alkali contents of the biomass can be reduced by prior leaching with water.

Drying wood from 50% to 60% (as-felled) or using air-dried wood with a moisture content of 20%, to the required level of 10–15% moisture requires the use of driers. The dryers can be directly heated rotary dryers using the flue gas or indirectly heated fluidized bed dryers using steam to heat the feed material. The vapors emitted during drying contain a number of volatile organic

compounds (VOCs), which require appropriate air pollution control systems.

2.2. Feedstock properties

The characteristics of the biomass feedstock have a significant effect on the performance of the gasifier, especially the following characteristics.

2.2.1. Moisture content

Fuel with moisture content above about 30% makes ignition difficult and reduces the calorific value of the product gas due to the need to evaporate the additional moisture before combustion/gasification can occur. High moisture content reduces the temperature reached in the oxidation zone, resulting in the incomplete cracking of the hydrocarbons released from the pyrolysis zone. Increased levels of moisture and the presence of CO produce H_2 by the water gas shift reaction and in turn, the increased H_2 content of the gas produces more CH_4 by direct hydrogenation. The gain in H_2 and CH_4 of the product gas does not, however, compensate for the loss of energy due to the reduced CO content of the gas and therefore gives a product gas with a lower CV. It should be taken care that the feedstock has low moisture content before feeding it to the gasifier (Stamford Consulting Gp., 1994).

2.2.2. Ash content

High mineral content can make gasification impossible. The oxidation temperature is often above the melting point of the biomass ash, leading to clinkering and slagging problems in the hearth and subsequent feed blockages. Clinker is a problem for ash contents above 5 %, especially if the ash is high in alkali oxides and salts which produces eutectic mixtures with low melting points.

2.2.3. Volatile compounds

The gasifier must be designed to reduce as much as possible the formation of tar and of heavy hydrocarbons released during the pyrolysis stage of the gasification process.

2.2.4. Particle size

The particle size of the feedstock material depends on the hearth dimensions but is typically 10–20% of the hearth diameter. Larger particles can form bridges which prevent the feed moving down, while smaller particles tend to clog the available air voidage, leading to a high pressure drop and the subsequent shutdown of the gasifier.

2. 3. Gasification processes

Gasifiers are of two main types, fixed bed and fluidized bed, with variations within each type (Rampling, 1993; Rampling and Gill, 1993). A third type, the entrained suspension gasifier, has been developed for coal gasification but the need for a finely divided feed material (<0.1–0.4 mm) presents problems for fibrous materials such as wood, which make the process largely unsuitable for most lignocellulosic materials.

Process summary

The advantages and disadvantages of the various generic types of gasifying reactor are summarized in Table 1. The selection of the gasifier type and its design will be dependent upon a number of factors (including the process attributes identified in Table 1) such as the influence of the properties of the feedstock (both chemical and physical), the characteristics of the required product gas and the various operational variables involved. Listed below are key criteria that need to be addressed when selecting a gasifier type:

• Investment costs of the gasifier and product gas cleaning unit should be as low as possible,
• Operation and maintenance costs should be low,
• the gasifier should be robust, ideally without moving parts,
• feedstock preparation, such as separation, size reduction or pelletisation should be avoided as much as possible to reduce the costs.

In comparison to fluidized bed (FB), the fixed bed gasifier appears the most practicable option for the production of gas for use in small-scale power generation unit. It is simple to construct, robust and has no or few moving parts (Ragnar, 2000). Whereas with FB gasifier its complex in design and operation. Proper consideration should be

given to the feed input, where it requires the particle size of the biomass feedstock to be reduced in size which produces fines that are not suitable for fluidization, and the product gas has high tar content requiring external gas cleaning.

Table 1: Properties of gasification reactor types (Rampling, 1993 and McKendry, 2002*)*

Advantages	Disadvantages
Fixed/moving bed, updraft	Large tar production
Simple, inexpensive process	Potential channeling
Exit gas temperature about 250 ^{o}C	Potential bridging
Operates satisfactorily under pressure	Small feed size
High carbon conversion efficiency	Potential clinkering
Low dust levels in gas	
High thermal efficiency	
Fixed/moving bed, downdraft	Minimum feed size
Simple process	Limited ash content allowable in feed
Only traces of tar in product gas	Limits to scale up capacity
	Potential for bridging and clinkering
Fluidised bed	
Flexible feed rate and composition	Operating temperature limited by ash clinkering
High ash fuels acceptable	High product gas temperature
High CH_4 in product gas	High tar and fines content in gas
High volumetric capacity	Possibility of high C content in fly ash
Easy temperature control	
Circulating fluidised bed	
Flexible process	Corrosion and attrition problems
Up to 850^{o}C operating temperature	Poor operational control using biomass
Double fluidised bed	
High CH_4 due to low bed temperature	More tar due to lower bed temperature
Temperature limit in the oxidiser	Difficult to operate under pressure
Entrained bed	Low in CH_4
Very low in tar and CO_2	Extreme feedstock size reduction required
Flexible to feedstock	Complex operational control
Exit gas temperature	Carbon loss with ash
	Ash slagging

3. Gasification of Wood Residue

The use of biomass to provide energy has been fundamental to the development of civilization. In recent times pressures on the global environment have led to calls for an increased use of renewable energy sources, in lieu of fossil fuels. Wood biomass is one potential source of renewable energy and the conversion of plant material into a suitable form of energy, usually electricity or as a fuel for an internal combustion engine.

The burning of biomass in air i.e. combustion, is used over a wide range of outputs to convert the chemical energy stored in biomass into heat, mechanical power, or electricity using various equipment, e.g. stoves, furnaces, boilers, steam turbines, turbo-generators, etc. Combustion of biomass produces hot gases at temperatures around 800–1000 ^{o}C. It is possible to burn any type of biomass but in practice combustion is feasible only for biomass with moisture content <50%, unless the biomass is pre-dried. High moisture content biomass is better suited to biological conversion processes. Net bio-energy conversion efficiencies for biomass combustion power plants range from 20% to 40%. The higher efficiencies are obtained with systems over 100 MWe or when the biomass is co-combusted in coal-fired power plants. Combustion process was not considered in this study, as it does not produce any product gases either to produce fuel suitable for use or in a gas turbine. Apart from that it has the major environmental constraints of GHG

emissions. So the alternative for energy generation from biomass is gasification (McKendry 2002).

Gasification is the conversion of biomass to a gaseous fuel by heating it at temperatures ranging from 800 – 1000 ^{o}C in an oxidizing medium such as air, oxygen or steam. Unlike combustion where oxidation is substantially completed in one process, gasification converts the intrinsic chemical energy of the carbon in the biomass into a combustible gas in two stages. Quality of the produced gas can be standardized which makes it easier and more versatile to use than the original biomass e.g. it can be used to power gas engines and gas turbines, or used as a chemical feedstock to produce liquid fuels. The gas should be pretreated well before passing to gas turbine for low levels of contaminants primarily tar, alkali metals, sulfur and chlorine compounds. The extent of gas cleaning is also effects the net electrical output from gas turbine (Bridgwater, 1994a).

4. Black liquor gasification

A number of concepts for black liquor gasification (BLG) have been proposed in the past (Consonni et al., 2003). In numerous reported investigations on the subject, a pressurized, oxygen-blown, high-temperature design being developed by Chemrec (Whitty and Nilsson, 2001; Marklund et al., 2006) for black liquor gasification is used. The Chemrec design is characterized by the majority of the inorganic material from the BLS leaving the reactor as a smelt due to the high reactor temperature (950–1000 ◦C). In the late 1990's, the Weyerhaeuser company installed the world's first commercial Chemrec gasifier, an atmospheric-pressure, air-blown unit designed to process 300 metric t/d BLS at a mill in North Carolina to increase the chemical recovery capacity of the existing Tomlinson boiler. A pilot-plant pressurized Chemrec gasifier (30 bar pressure and capacity to process up to 20 t/d BLS with oxygen firing) has been operating under a test program at a pulp mill in Piteå, Sweden, since mid-2006. As of early 2008, feasibility studies were being done for commercial-scale installations at the Smurfit Kappa Kraftliner mill in Piteå, Sweden and the New Page pulp and paper mill in Escanaba, Michigan. With gasification (unlike with a Tomlinson boiler), there is a natural partitioning of sulfur (mainly as hydrogen sulfide, H_2S) to the gas phase and sodium to the condensed phase. This split represents an important potential benefit to a pulp mill, since it can facilitate the implementation of alternative pulping chemistries (e.g., polysulfide) that can lead to increased pulp yield per unit of wood consumed (Lindstrom et al., 2002). With the high-temperature gasifier design adopted, slightly more than half of the sulfur goes to the gas phase. To take advantage of the natural separation of sulfur (S) and sodium (Na), it is necessary to recover H_2S from the gas in a form suitable for the preparation of modified pulping liquors. Another reason that H_2S must be removed from the syngas is to avoid poisoning of downstream fuel synthesis catalysts. Capture of acid gases like H_2S is routinely practiced in other industries (e.g., petroleum refining) using patented physical or chemical absorption processes such as Selexol® or Rectisol®. A negative consequence of the S/Na split in a gasifier is a higher causticizing load, i.e., larger required lime kiln capacity and lime kiln fuel consumption per unit of BLS processed compared to processing in a Tomlinson boiler (Larson et al., 2003).

5. Biorefinery Design

Considering various designs from those suggested by Consonni et al., (2009), it was decided to consider possible biorefinery options for implementing in pulp and paper industry in the present study. One each for the biomass gasification and black liquor gasification. The major emphasis of the biorefinery options is to gasify the biomass to produce syngas for the production of electricity using gas turbine and resale the syngas for the production of biofuels like methanol or dimethyl ether. The process designs include five basic equipments: (i) black liquor gasification, (ii) biomass gasification (or, in one case, a hog fuel boiler), (iii) syngas heat recovery and syngas clean-up, (iv) fuel synthesis,

and (v) power. The designs proposed by Cansonni et. al., gives great change and advantages to the pulp and paper industry in terms of economy and valuable products. But all the designs have two gasifiers one each for biomass and black liquor. From these designs the only point of concern was that installing two gasifiers is an expensive proposition in the present economical situations.

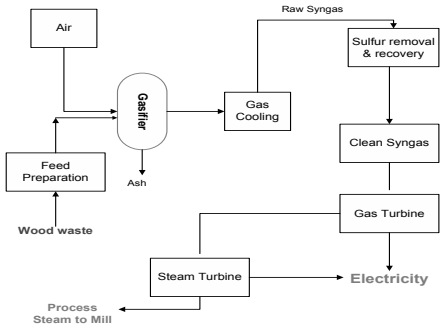

Figure 1: Flow sheet for wood biomass gasification process

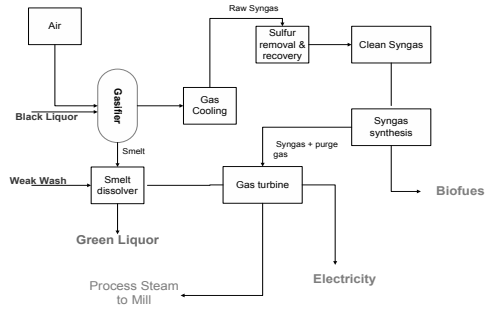

Figure 2: Flow sheet for black liquor gasification

From various designs in recently published articles, it was decided to consider two separate biorefinery options for gasification of wood and black liquor. The black liquor and biomass gasification are essentially the same except for the size of the biomass gasifier, which changes very significantly from one case to another. Wood gasification as shown in Figure 1 is considered as one of the best possible options that could be implemented with the kraft process to replace the power boilers due to availability of enough feed stock in the form of wood biomass for the electricity production. Such an approach should meet the energy requirements and supply steam for the whole process. Black liquor gasification should also be considered as one shown in Figure 2. The design of black liquor gasification is different from the wood gasification due to the production of smelt apart from steam and electricity production. The smelt produced from the gasifier need to be dissolved with weak wash and treat to produce green liquor. The syngas produced also needed to be treated well due to the presence of more impurities in black liquor in comparison with wood biomass. But the costs can be offset due to the production of value added products and electricity from syngas. A more detailed study need to be carried out for all the process options necessary for cleaning syngas to remove all the impurities for the production of biofuels. The advantages of all the process in comparison with having the regular boilers is that there is a drastic reduction of green house gas emissions and at the end and have product syngas which can be resold or can be further treated for the purification and synthesis to produce biofuels.

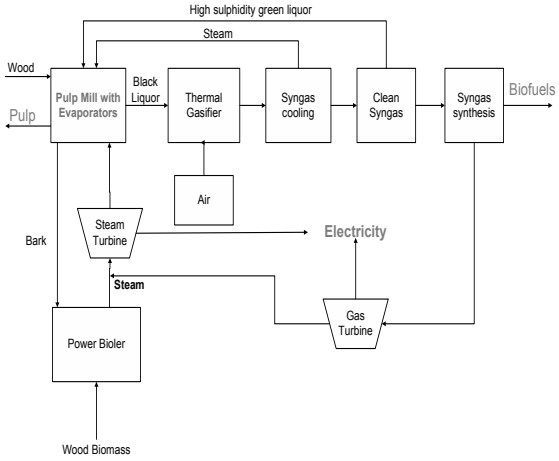

Figure 3: Flow sheet for the proposed biorefinery design for black liquor gasification

From the above assumptions, integrating gasifier in a kraft mill by replacing recovery boiler for the steam and electricity generation has been considered. A systematic flow sheet with major input and output process options is shown in figure

3. Air is supplied as a gasifying medium to the thermal gasifier. The high temperature gasifier enables high contents of H_2 and CO in the synthesis gas (Larson et al., 2006). The green liquor from the gasifier is cooled and sent back to the pulp mill for cooking in digestion unit. The heat of high temperature synthesis gas is recovered in gas cooling unit and to produce medium and low pressure steam. Part of treated syngas with very low level of impurities is also supplied to gas turbine for the steam and electricity production. The synthesis gas can be further treated for sulfur removal and other impurities to synthesize for biofuel production or can resale it. It must be underscored that for all the above processes, the syngas produced and cleaned for low levels of impurities can be primarily used to generate electricity using gas turbines and can be further extended to synthesize syngas for biofuels production depending on the economical feasibilities.

6. Conclusions

Gasification-based pulp mill biorefinery technologies have major advantages in generating electricity and production of value added products and can help in revitalize of the pulp and paper industry. They also offer the potential for important contributions toward petroleum savings, GHG emissions reductions, improved energy security, and rural economic development. These potential private and public benefits arise, fundamentally, because of the integration of biorefining with pulp and paper production, such that the biorefinery is providing chemical recovery services, process steam in addition to exporting liquid fuels and perhaps some electricity. Integration can effectively enable more efficient use of biomass resources for electricity generation and liquid biofuel production. Integration also can effectively reduce the capital investment required per unit of biofuel production to levels comparable to investments needed for coal-to-liquids facilities that are more than an order of magnitude larger than prospective pulp mill biorefineries.

7. References

1. R.D. Perlack, L.L. Wright, A. Turhollow, R.L. Graham, B. Stokes and D.C. Erback, Biomass as feedstocks for a bioenergy and bioproducts industry: The technical feasibility of a billion-ton annual supply, ORNL/TM-2005/66 for USDA and USDOE, April (2005).
2. Stefano Consonni, Ryan E. Katofsky, Eric D. Larson. A gasification based biorefinery for pulp and paper industry. Chemical engineering research and design 87 (2009) 1293–1317.
3. Lindblom, M. and Landälv, I., Chemrec's atmospheric & pressurized BLG (Black Liquor Gasification) technology—Status and future plans, In *Proceedings of the International Chemical Recovery Conference 2007* Quebec City (Canada), 29 May–June 1, 2007, (Part 1. Printed by Pulp and Paper Technical Association of Canada (PAPTAC), Montreal, Canada), pp. 51–57.
4. Evans, R.J., Knight, R.A., Onischak, M. and Babu, S.P., Process performance and environmental assessment of the renugas process, in Energy from Biomass and Wastes X, Klass, D.L. (ed) (Elsevier Applied Science (London) and Institute of Gas Technology (Chicago)), pp. 677–694 (1987).
5. F.S. Lau, D.A. Bowen, R. Dihu, S. Doong, E.E. Hughes, R. Remick, R. Slimane, S.Q. Turn and R. Zabransky, Techno-economic analysis of hydrogen production by gasification of biomass, final technical report for the period 15 September 2001–14 September 2002, contract DE-FC36-01GO11089 for US Dept. of Energy, Gas Technology Inst., Des Plaines, IL, June,145 pp (2003).
6. Peter McKendry., Energy production from biomass (part 2): conversion technologies, Bioresource Technology 83 (2002) 47-54.
7. Peter McKendry., Energy production from biomass (part 3): gasification technologies, Bioresource Technology 83 (2002) 55-63.
8. Whitty, K. and Nilsson, A., Experience from a high temperature, pressurized black liquor gasification pilot plant, In *Proceedings of the Tappi Chemical International Recovery*

Conference (pp. 655–662). (Tappi Press, Atlanta Stamford Consulting Gp., 1994. Coppice Wood Drying in a Gasifier Power Plant. ETSU B/M3/00388/08 (2001).

9. Ragnar Warnecke., Gasification of Biomass: comparison of fixed bed and fluidized bed gasifier. Biomass and Bioenergy, 18 (2000), 489-497.

10. Rampling, T., 1993. Fundamental research on the thermal treatment of wastes and biomass: literature review of part research on thermal treatment of biomass and waste. ETSU B/T1/00208/Rep/1.

11. Rampling, T., Gill, P., Fundamental research on the thermal treatment of wastes and biomass: thermal treatment characteristics of biomass. ETSU B/T1/00208/Rep/2 (1993).

12. E.D. Larson, S. Consonni and R.E. Katofsky, A cost–benefit assessment of biomass gasification power generation in the pulp and paper industry, final report, Princeton Environmental Institute, Princeton, NJ (2003).

13. M. Marklund, R. Gebart and R. Tegman, Scale-up method for high temperature black liquor gasification in pressurized entrained flow gasifiers, Presented at the 7th International Colloquium on Black Liquor Combustion and Gasification, Jyvaskyla, Finland, 2 August (2006).

14. Bridgwater, A.V., The technical and economic feasibility of biomass gasification for power generation. Fuel 74 (5), (1994b) 631–653.

Experimental studies of biomass gasification installation consisting of a new gasifier and gas cleaning system

Janusz Kotowicz[a], Aleksander Sobolewski[b], Tomasz Iluk[a,b], Katarzyna Matuszek[b]

[a] *Institute of Power Engineering and Turbomachinery Silesian University of Technology, Gliwice, Poland*
[b] *Institute for Chemical Processing of Coal, Zabrze, Poland*

Abstract: The article presents the issues related to the possibility of using biomass for energy purposes. Particular attention is given to the gasification process of one of the key renewable energy sources in Poland, which is the biomass. An experimental research installation for biomass gasification is presented. The installation consisting of reactor, gas purification installation and auxiliary devices is described. The installation was designed and built in the Institute for Chemical Processing of Coal in Zabrze (Poland). Construction of a new gas generator GAZELA, developed by the Institute for Chemical Processing of Coal was described in details. It is a 3-zonal moving-bed reactor working in overpressure. Gasifier is a vertical, cylindrical reactor, inside which in the axis of the apparatus there is a tube for discharging of the generated gas. The operational experiences from the conducted technological tests are presented. Fuels used for test are characterized. Producer gas cleaning installation is presented. Temperatures occurring in the characteristic points of the installation with particular emphasis on temperature inside the reactor are shown. The composition of the gas obtained during the tests, together with dust and organic impurities is presented. Exemplary timelines of temperature and gas composition variations are shown

Keywords: biomass, gasification, gasifier, investigatory installation.

1. Introduction

Poland, by joining the European Union structures, obliged to comply with the energy policy of the Community. One of the main assumptions of the accepted in Brussels on 8÷9 March 2007 document "Presidency Conclusions" is to increase the share of the renewable energy in primary energy balance up to 20%, in relation to the year 1990 [1]. Simultaneously, also polish legislative authorities introduce legal acts that are aiming to increase the share of renewable sources in the overall balance of the fuels used, e.g. the Order of the Minister of the Economy from 14th August 2008 [2]. This document regulates the problems connected, among others, to the certificates of the origin, substitutive charges and purchase of electricity and heat coming from renewable sources. According to the order [2] to the renewable energy sources are classified first of all:

- hydroelectric power stations and wind power stations,
- sources producing the energy from biomass and biogas,
- solar photovoltaic panels and solar collectors for heat production and geothermal sources.

In the day of the obligation of the sale of energy from renewable sources (certificates of origin), rational use of biomass can bring not only ecologic benefits but also economic ones. It is estimated that in 2030 potential biomass resources will amount to around 814 PJ, what will stand for around 13.4÷16.2% of the primary energy need [3,4]. The indication of the biomass as one of the main sources of the electricity and heat production, besides coal, lignite and natural gas, is connected to the relatively well known technology of the conversion of biomass chemical energy into thermal energy. For energy purposes the biomass is mainly used for the following applications:

- combustion,
- gasification.

Due to the increase of the biomass price and logistical constraints, as well as to the increasing difficulties connected to obtaining of its large amounts for centralized power units, it is becoming reasonable to use biomass in dissipated energy sector. Particularly attractive can be small and medium-sized cogeneration systems that produce electricity and heat based on the gasification technology. Produced in a reactor gas

after purification supplies a gas engine or gas turbine, coupled with a generator, used for electricity production. Heat recovered from the exhausts and cooling systems (e.g. piston engine) is used for heating water and/or the production of steam in the heat recovery steam generator.

An important advantage of such systems is the possibility of the use of waste fuels, such as waste from forestry or agricultural industry, where acquisition costs are equal to zero or are very low. One possible fuel source for such systems can also be the dedicated energy plantations.

2. Test installation

Gasification is a series of termochemical processes proceeding in the presence of gasifying factor (air, oxygen, water vapour) aiming at obtaining of process gas. The main components of the gas is carbon monoxide, carbon dioxide, hydrogen, methane and nitrogen. Apart from flammable gas, some solid residues, in the form of coke, ash or slag, and fluid residues, e.g. tars and moisture are also obtained.

The essentials problem connected to the gasification process is pollution of the process gas by tar substances and by dust. It causes a need of gas purification before its further use, e.g. in gas engine or gas turbine. The biggest difficulties are met during the removal of organic impurities.

Minimisation of tar and ash impurities contained in the process gas was one of the premises for creating of a new type of biomass gasification reactor. In the Institute for Chemical Processing of Coal in Zabrze, a new conception of three-zonal fixed-bed reactor was created [5]. Common cooperation of the Institute and SYNGAZ company led to the construction and starting of a new fixed-bed generator.

2.1. Three-zonal generator GazEla

GazEla reactor combines the advantages of co-current and counter-current reactor and gives the opportunity of the use of different fuels of different granulations and increased moisture content. Collecting of the process gas directly from gasyfing zone, thus from the place with high temperatures causing decomposition of tar substances, allows for reducing of the amount of highly-aromatic substances that are formed.

Scheme and a picture of gas generator is presented in Fig. 1 and Fig. 2. It is a vertical cylindrical reactor with internal diameter 400 mm and technical high around 900 mm.

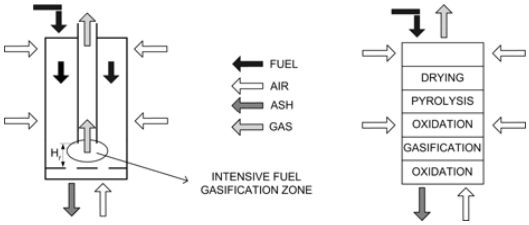

Fig.1. Scheme of the gasifier

In the axis of the device there is a riser tube with variable level of reception, that serves for gas collecting. Proper selection of the height H_r (the distance between air distributor and the inlet to the raiser tube) allows for receiving gas with lower amount of tar impurities and of higher temperature.

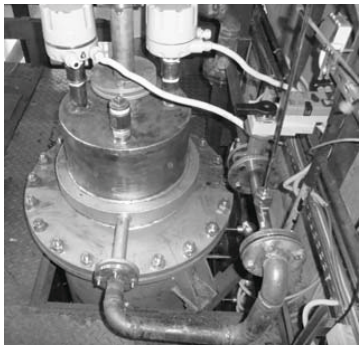

Fig.2. Gasifier GazEla

Humid fuel supplied by means of a screw worm to the upper part of the reactor is moving down and is subjected to the following thermal process: drying, pyrolysis, combustion and gasification. As a gasyfing factor air is used, supplied by axial fan in 3 points of reactor: under the grate, in the middle part and above the fuel bed. Reactors operate at slight overpressure. In the drying and pyrolysis zone fuel and air are moving in co-current flow, while combustion process occurs in counter-current. Capacity of the reactor and load of particular process zones are regulated by means of the amount of air supplied to particular air nozzles of the device. The generator is characterised by thermal power at 60 kW_t.

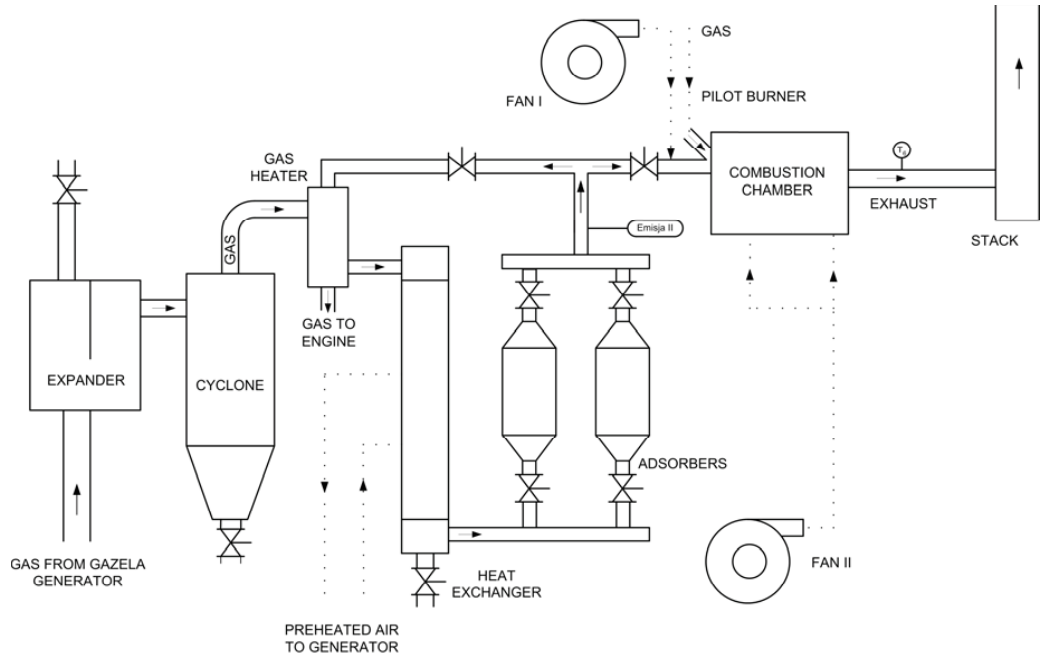

Fig.3. Diagram of the installation for gas purification

2.2. Gas cleaning system

Generated in the reactor process gas is directed to gas cleaning system in order to meet the requirements of gas engines producers.

The first element of the gas is cylindrical expander, owing to receiving of the excess amount of moisture contained in the process gas and bigger ash fractions due to speed lowering. Than, in order to remove dust, gas is directed to the inertial precipitator. Pre-purified gas is passed to the counter-current cylindrical heat exchanger in order to condensate remaining in the gas moisture and tar pollutants. In this heat exchanger gas is giving up the heat to the gasifying factor, which is directed to GazEla generator. Successively, process gas flows through adsorber filled with filtration bed. One adsorber is operating while the other one serves as a reserve. Change of the adsorber takes place after increase of pressure difference before and after the device. During first conducted tests as a filtration agent washed coke was used, with granulation of 10÷20 mm. In further experimental tests it is planned to use different adsorbers. A scheme of the gas cleaning process is shown in Fig. 3. At present cleaned gas is directed to the combustion chamber where it is combusted and successively transported to atmosphere through a stack. After obtaining required gas purity it is planned to mount and start gas engine in order to produce heat and electricity in cogeneration.

3. Results

In order to confirm the applicability of various types of biomass and to assess their influence on the work of the reactor different types of fuels were used, i.e.: pellets from dust wood, pellets from straw, chip wood of the fibrous (denoted “II” in Table 2) or cut structure (denoted “I”). Detailed physicochemical analysis of used fuels is presented in [6]. In the Table 1 properties of chip woods used for gasification is presented.

The influence of the type of tested fuel on reactor operation was small. Composition of produced gas was stable, temperatures in particular zones similar. In Table 2 composition of the gas obtained during the tests with various types of biomass is compared. Only in the case of gasifying of straw pellets a problem of slagging of the tube collecting process gas and of occurring of ash sinters in lower part of reactor (in the carbonate combustion zone above the grate) occurred. When different fuel was gasified, such problem occurred sporadically. Slagging problem was a consequence of exceeding of ash softening, melting and flowing

temperatures, what was confirmed by laboratory analyses. For the pellets used in the test, softening temperature was equal to $t_{A(O)}$ =870°C, while ash melting temperature was equal to $t_{B(O)}$ =1220°C. In the case of chip woods these temperatures were equal to $t_{A(O)}$ =850°C, $t_{B(O)}$=1530°C. Slagging problem should be eliminated by keeping lower temperatures in combustion zone, which should be much lower for straw pellets than chip woods. Conducted test of gasyfing alder chips at maximal temperature inside the reactor around t_{max} =1050°C showed lack of any ash sinters. A picture of ash sinter obtained during gasification of straw pellets is shown in Fig. 4.

Table 1. Properties of biomass used for gasification

DENOTATION	SYMBOL	UNIT	CHIP WOOD II
Moisture content Q/ZK/P/15/05/A:2002	W_t^r	%	14.6
Ash content Q/ZK/P/15/06/A:2005	A^a	%	0.5
Volatile matter content Q/ZK/P/15/07/A:2002	V^a	%	78.97
Sulphur content Q/ZK/P/15/08/A:2002	S_t^a	%	0.02
Carbon content Q/ZK/P/15/09/A:2002	C_t^a	%	48.5
Hydrogen content Q/ZK/P/15/09/A:2002	H_t^a	%	5.75
Nitrogen content Q/ZK/P/15/09/A:2002	N^a	%	0.19
Oxygen content (calculated)	O_d^a	%	40.15
Higher heating value Q/ZK/P/15/12/A:2005	Q_s^a	J/g	19084
Lower heating value Q/ZK/P/15/12/A:2005	Q_i^r	J/g	15654

Table 2. Comparison of gas composition obtained from different types of biomass gasification (vol.)

GAS	CHIP WOOD I	CHIP WOOD II	PELLET WOOD	PELLET STRAW
H_2, %	7.5	6.1	7.0	8.0
O_2, %	0	0	0	0
N_2, %	55.9	59.3	57.5	57.2
CO, %	25	20.3	24.0	24.0
CH_4, %	2.1	3	1.6	1.3
CO_2, %	9.5	11.3	9.9	9.5
LHV, MJ/m^3_n	4.7	4.3	4.4	4.4

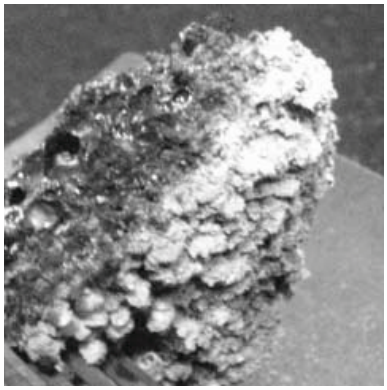

Fig.4. Ash sinter obtained in the straw pellets gasification test

Exemplary fragment of the time course of temperature variations inside the reactor and the temperature of gas leaving the generator is shown in Fig. 5 (denotations as in Fig. 3). Temperature course is stable, observed small fluctuations are normal for such type of devices. The average gas temperature T_s leaving the reactor was equal to around 650ºC. An important fact is stability of this temperature in the context of further use of produced gas, e.g. for preheating of the process water or for heating of the cleaned process gas before entering gas engine. An exemplary time course of gas composition variations of such components as CO, CO_2, H_2, CH_4 at the outlet of generator is shown in Fig. 6. Gas composition is stable.

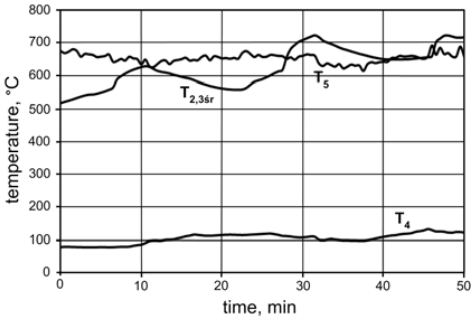

Fig.5. Time course of temperature variations inside the reactor bed and the temperature of gas leaving the generator for chip woods (T_4- fuel inlet, $T_{2,3śr}$- temp. inside reactor, T_5-gas outlet)

The average values of the share of particular components of the process gas, devoid of moisture, from that period equals to: CO=20.3%, CO_2=11.3%, H_2=6.1%, CH_4=3%, O_2=0%. The rest

of the producer gas is N_2. Low content of H_2 in gas results from low temperature in gasification zone. Variations of gas composition that can be observed are normal in this type of devices and are connected with periodical fuel supply to the reactor, however bigger changes in gas composition were caused by temporary pressure increase in generator, as the effect of plugging of gas collecting spot.

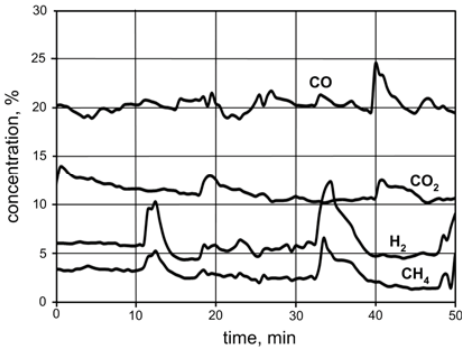

Fig.6. Time course of concentration variation of CO, CO_2, H_2, CH_4 in the process gas for chip woods

The analysis of 16 higher aromatic hydrocarbons, including B(a)P obtained during biomass gasification test is shown in Fig. 7. For determination of the amount of impurities in the process gas a gravimetric method was used. The sum of 16 higher aromatic hydrocarbons, including Benzo(a)Pyrene, received during the test, amounted to 156.4 mg/m^3_n, while the total amount of organic impurities equaled to 12000 mg/m^3_n. Ash content in the gas was determined at the level 600 mg/m^3_n.

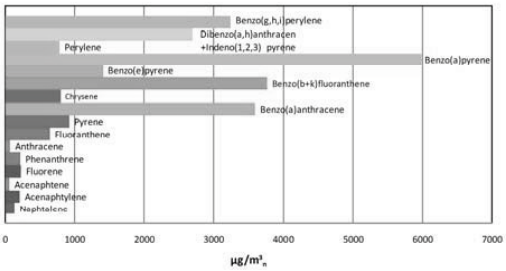

Fig.7. PAH(s) including B(a)P according to IChPW procedures [7]

Sankey chart, which illustrates the flow of particular mass streams supplied to GazEla generator, is shown in Fig. 8, counting on 100 kg of wet biomass. Nominal stream of supplied fuel (chip woods) during the test equaled to around 15 kg/h.

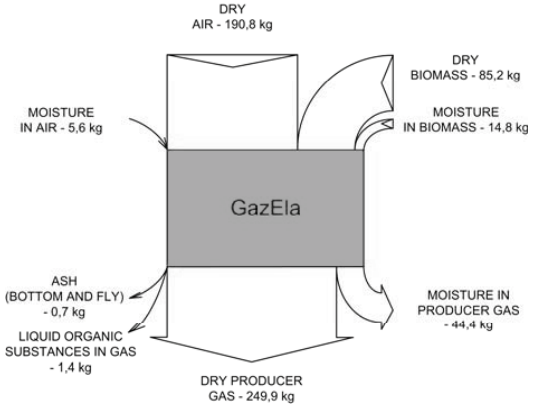

Fig.8. Sankey graph of biomass gasification (for 100 kg of wet biomass)

4. Summary

The conducted so far technological tests of biomass gasification confirmed the correctness of operation of generator GazEla itself as well as a whole installation. The tests allowed for determination of the main working parameters of the system and for initial optimization of reactor settings, mainly in order to minimize tar impurities in process gas.

Information obtained in the test allowed for determination of assumptions for gas cleaning installation. In the year 2010 technological tests of the cleaning installation will be conducted aiming for reaching of the gas purity required by the gas engines producers.

In the same time technological tests of GazEla generator will be continued in order to optimise operation of generator from the point of view of minimization of impurities (organic and dust). It is also important to obtain gas with optimal share of particular components in order to its further use in gas engine.

References

[1] Commission of the European Communities. Communication from the Commission to the European Council and the European Parliament. An Energy Policy for Europe. Brussels. COM(2007), 843.

[2] Decree of the Minister of Economy from 14 August 2008 on the detailed scope of duties to obtain and submit to the cancellation of certificates of origin, the replacement fee, purchase of electricity and heat produced in renewable energy sources and the obligation of confirmation of the data concerning the amount of electricity produced in renewable energy source. Act Nr 156. Poz. 969. s. 8372-8377. (in polish)

[3] Chmielniak T.: Energy Techonologies – new horizons. Inaugural Lecture of the academic year 2007/2008 in the Silesian University of Technology. Gliwice 2007. (in polish)

[4] Ericsson K., Nilsson L.J.: Assessment of the potential biomass a supply in Europe using a resource - focused approach. Biomass and Bioenergy 30, 2006, 1-15.

[5] Patent application P383541. Fixe bed gasifier. Ściążko M., Sobolewski A., Billig P.

[6] Sobolewski A., Kotowicz J., Iluk T, Matuszek K.: The influence of the biomass type on the operation parameters of a fixed bed gasifier. Energy Market 3, 2009, p. 53-58. (in polish)

[7] Determination of the content of aromatic hydrocarbons, including benzo(a)pyrene in exhaust gases. Test procedure no Q/ZF/P/15/05/B:1999.

COMPARISON OF BIOMASS GASIFICATION UNDER ATMOSPHERIC AND PRESSURIZED CONDITIONS

Amauri Menezes Leal Junior, Roger Riehl

Vale Soluções em Energia, Energy Technological Center, São José dos Campos, SP, Brazil.

Abstract: Modern agriculture is an energy intensive process and there has been a trend towards the use of alternative energy sources because of the recent price rise of fossil fuels. However these energy resources have not been able to provide an economically viable solution for agricultural applications. One biomass energy based system, which has been proven reliable, is biomass gasification. Biomass gasification means the incomplete combustion of biomass (thermochemical process) resulting in the production of combustible gases consisting of carbon monoxide, hydrogen and traces of methane. This mixture is often called synthesis gas or syngas and can be converted into mechanical energy or electricity by using an internal combustion engine, for example. This paper presents a comparison of biomass gasification under atmospheric and high pressure conditions using a fluidized bed gasifier. Air was used as the oxidant and two cases of operation were studied. The first case study the equipment at atmospheric pressure while the second study the equipment pressurized at 2 MPa. In both cases, the biomass used has 50% of humidity and the results show the temperature behavior when the equipment works under atmospheric pressure (0.101 MPa) and pressurized (2 MPa) conditions. Under atmospheric conditions, the temperature showed a peak on the top of the bed. On the other hand, under pressurized condition, the temperature exhibited a linear profile.

Keywords: Gasification, Biomass, Syngas production, Simulation.

1. Introduction

Currently, direct gasification systems have been demonstrated at both elevated and atmospheric pressures. Both of the gasifier working operations have its drawbacks. Gasifier operating pressure affects not only equipment cost and size, but also the interfaces to the rest of the power plant including the necessary cleanup systems.

Gabra et al. [1] and Dasappa et al. [2], discuss the gasification when the conversion of solid fuel to gaseous fuel occurs by thermochemical reactions of a fuel with oxidizer under sub-stoichiometric conditions to get combustible gases (CO, CH_4 and H_2). At the mechanism of gasification the combustible fraction of a solid fuel can be divided into volatile and non-volatile fractions. The overall rate of the gasification into individual rates of the processes involved, i.e. drying, release of the combustible volatiles, mixing of the volatiles vapors and the oxidant, combustion of the volatiles and the gasification of non-volatile combustibles. The rates of these individual processes depend upon the size of a fuel particle, the heat transfer with surroundings and the gas composition in the vicinity of the particle. Another important aspect is regarded to residence time which will be different in different types of gasifiers. After introducing the fuel in the bed, the particles start drying and are pyrolysed. Consequently, a self-sustaining exothermic reaction takes place and devolatilisation starts. During this process, the size of the particles is only slightly reduced but the particle density is decreased. The result is a residual solid (char) and a gas mixture composed primarily of carbon dioxide, carbon monoxide, hydrogen, water vapor, nitrogen and pyrolysis products including tar and hydrocarbons. Key operating parameters include: l) the gasification temperature, 2) operating pressure, 3) steam input, 4) type of feedstock, 5) biomass moisture content and limiting feed rate and 6) residence time.

This paper presents a simulation of fluidized bed gasifier and compares two situations of biomass gasification. The first simulation of the process is conducted under atmospheric conditions and the second is conducted under high pressure (2 MPa) while air is used as the oxidant. These simulations used the software CFSBMI® (Comprehensive Simulator for Fluidized and Moving Bed Equipment).

2. Simulation conditions and data

The CFSBMI® program simulates different conditions with different fuels at the same device. In this context, the worse scenario was proposed, which is the simulation of a biomass with 50% of moisture. This situation can be found in distillery, for example. For this simulation, it was considered a fluidized bed gasifier and air as the oxidant. Table 1 shows the input data and proximate and ultimate biomass analysis.

Table 1. Input and proximate and ultimate analysis data.

Ultimate Analysis Data (Dry basis)	
Carbon	49.66%
Hydrogen	5.71%
Nitrogen	0.21%
Oxygen	41.08%
Sulfur	0.03%
Silica	3.31%
Proximate Analysis Data	
Moisture	50%
Volatile	40.8%
Fixed Carbon	7.6%
Ash	1.7%
Input Data (atmospheric pressure)	
Carbonaceous particle (kg/s)	0.71
Temperature biomass (K)	293
Air temperature (K)	300
Input Data (pressurized: 2 MPa)	
Carbonaceous particle (kg/s)	14.00
Temperature biomass (K)	293
Air temperature (K)	300

3. Mathematical Model

According to Souza-Santos [3], the mathematical model considers one-dimensional approach. The basic assumptions of the model are: (a) two main phases in the bed (emulsion and bubble. The bubbles are free of particles); (b) steady-state regime for the equipment and plug-flow regime for the gas streams (emulsion, bubble phase, and freeboard); (c) transport equations with no second-order terms; (d) homogeneous composition for the solid particles throughout the bed; (e) gas-solid reactions described by unexposed and exposed core model; (f) radiative heat transfer in gas phases neglected; and (g) fluidization dynamics neglected in the momentum equations.

The governing equations for the conservation of mass in the emulsion gas phase and in the bubble phase are, respectively [3]:

$$\frac{dF_{GE,j}}{dz} = \sum_{m=1}^{3}\left(R_{m,j}^{se}\frac{dA_{GE,m}}{dz}\right) + R_j^{GE}\frac{dV_{GE}}{dz} + G_j^{GE}\frac{dA_B}{dz} \qquad 1 \le j \le 500 \tag{1}$$

$$\frac{dF_{GB,j}}{dz} = R_j^{GB}\frac{dV_B}{dz} - G_j^{GE}\frac{dA_B}{dz} \quad 1 \le j \le 500 \tag{2}$$

The energy balance for the emulsion phase and for the bubble phase is described by, respectively [3]:

$$dF_{GE}C_{GE}\frac{dT_{GE}}{dz} = \frac{dV_{GE}}{dz}\left[-R_{QGE} + \sum_{m=1}^{3}\left(R_{GE,m}^{cs} + R_{GE,m}^{hs}\right) + \left(R_{GE}^{cGB} + R_{GE}^{hGB}\right)\frac{dV_{GB}/dz}{dV_{GE}/dz} - R_{GE,t}^{c} - R_{GE,d}^{w}\right] \tag{3}$$

$$F_{GB}C_{GB}\frac{dT_{GB}}{dz} = \frac{dV_{GB}}{dz}\left[-R_{GB} + R_{GE}^{cGB} + R_{GE}^{hGB} - R_{GB,t}^{c}\right] \tag{4}$$

The mass and energy balances in the freeboard are, respectively [3]:

$$\frac{dF_{F,j}}{dz} = \sum_{m=1}^{3}\left(R_{m,j}^{sf}\frac{dA_{PF,m}}{dz}\right) + R_j^{GF}\frac{dV_{GF}}{dz} \tag{5}$$

$$F_{GF}C_{GF}\frac{dT_{GF}}{dz} = \frac{dV_{GF}}{dz}\left[-R_{GF} + \sum_{m=1}^{3}\left(R_{GF,m}^{csf} + R_{GF,m}^{hsf}\right) - R_{GF,t}^{c} - R_{GF}^{w}\right] \tag{6}$$

For $1 \le j \le 1000$. The energy balances for the solids in the freeboard are [3]:

$$F_{SF,m}C_{SF,m}\frac{dT_{SF,m}}{dz} = \frac{dV_{SF,m}}{dz}\left[-R_{QSF,m} - \left(R_{GF,m}^{csf} + R_{GF,m}^{hsf}\right)\frac{dV_{GF}/dz}{dV_{SF,m}/dz} - R_{SFt,m}^{r} - \sum_{n=1}^{3}\left(R_{SF,m,n}^{r}\right)\right] \quad 1 \le m \le 3 \tag{7}$$

The sets of differential equations (1 – 7) should be solved from the surface of distributor ($z = 0$) to the top of the bed ($z = z_D$) and at the freeboard from the top of the bed ($z = z_D$) to the top of the freeboard ($z = z_F$).

The conditions of the gas stream injected through the distributor ($z = 0$) are known, the total gas flow rate (F_G), its composition ($W_{G,j}$), and temperature (T_G) are set.

4. Results and discussions

Figure 1 shows the temperature behavior from the bed and Figure 2 from the freeboard, both working under atmospheric pressure (0.101 MPa) and

pressurized (2 MPa). During the gasification process the material formed on the surface of the carbonaceous particle is detached and disintegrated into very small particles. Therefore, the core is always exposed to the gas environment. As the particles move downward and approach the combustion region the temperature increase due to the exothermic reaction between oxygen molecules from air and carbonaceous particle. Higman and van der Burgt [4] exhibit that very high temperatures can cause increase in oxygen consumption and reduction in the gasification process efficiency. On the other hand, the softening-ash point works as an indicator to control the temperature process.

Figure 2 draws attention when the temperature profile from the freeboard is higher than the average bed temperature. It occurs due the bubbles, during the trip towards the top of the bed, acquire velocity. The bubble's momentum implies a pressure difference between the top and the lower part of each bubble. This phenomenon drags small particles of solid fuel, and after bursting, the gas inside bubbles reacting oxidizes the particles and the temperature increases [3].

Chemical equilibrium is strongly affected by the temperature because there is equilibrium constant for each reaction. Given sufficient time, the concentration of these gases will reach their equilibrium concentrations [5]. The temperature dependency of these equilibrium constants can be derived from fundamental data, but is usually expressed by Eq. (8) as a correlation of the type [4]:

$$\ln\left(K_{p,T}\right) = \ln\left(K_{p,T_0}\right) + f(T) \qquad (8)$$

A pressurized product gas is advantageous to overcome pressure drops of downstream gas processing units, piping, and flow control stations, and it is necessary for efficient combined cycle power generation schemes in addition to reducing the equipment size, for example. On the other hand, the equipment should be robust to operate at high pressures (over atmospheric). The pressure in a gasifier is generally selected in accordance with the requirements of the process or equipment upstream or downstream of the gasifier. The syngas yield and its heating value are somewhat different at two gasification pressures. The gas composition changes with pressure, and promote a methanation according to [4]:

$$CO + 3H_2 \rightarrow CH_4 + H_2O \qquad (9)$$

Figure 3 displays the molar fractions of the components under atmospheric and pressurized conditions versus temperature of the equipment. It is related to Eq. (9), which considered the thermodynamic equilibrium among species only for illustration since the gasification process does not occur in equilibrium.

Figure 3 exhibits that the increased pressure favors the methane production. Hydrogen production has a peak in higher temperature for the pressurized conditions. Results of the gasification process simulated in the CSFMB® software and applying the equilibrium equations is given in Table 2. According with the results in Table 2, some divergences between equilibrium and the CSFMB software confirm that the gasification process is not in equilibrium. However, for a first approximation, the equilibrium results can be used.

Table 2. Results of the gasification process (CSFMB® software and equilibrium).

	CSFMB		**Equilibrium**	
Species	**2 MPa**	**0.101 MPa**	**2 MPa**	**0.101 MPa**
H_2/CO	3.6683	4.9984	3,2731	5.0034
H_2/CO_2	0.9747	0.8961	0,8645	0.8913
CO/ CO_2	0.2657	0.1793	0,2641	0.1781
H_2/H_2O	0.4925	0.4573	0,4121	0.4541
CO/H_2O	0.1343	0.0915	0,1259	0.0908
CH_4/H_2	0.0334	0.0067	0,0810	0.0086
CH_4/CO	0.1227	0.0337	0,2651	0.0430

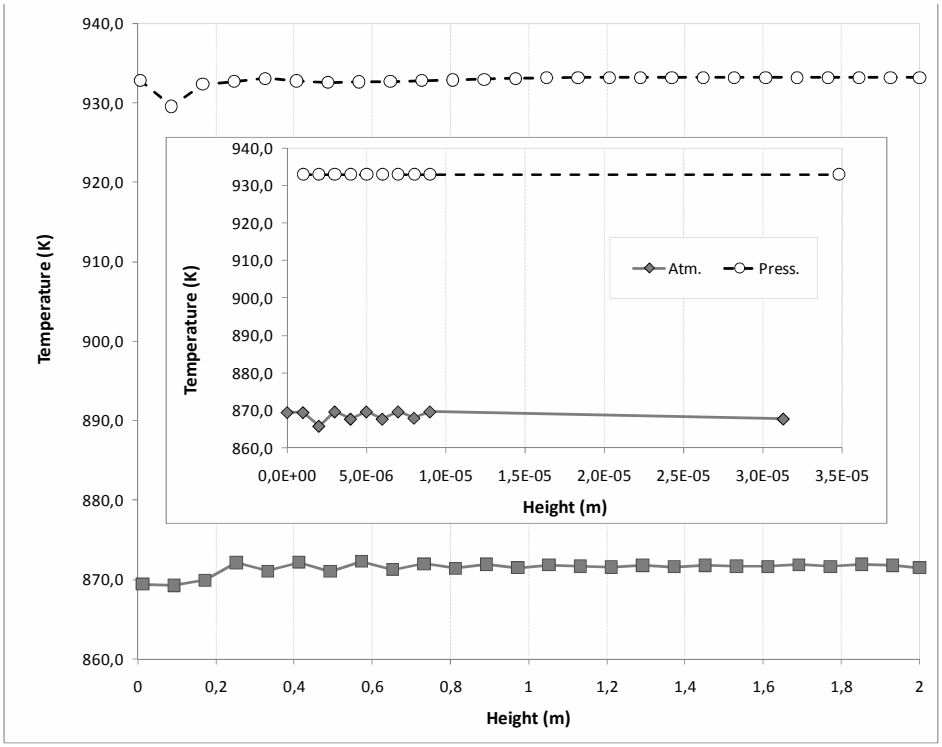

Figure 1. Results of the bed temperature profile.

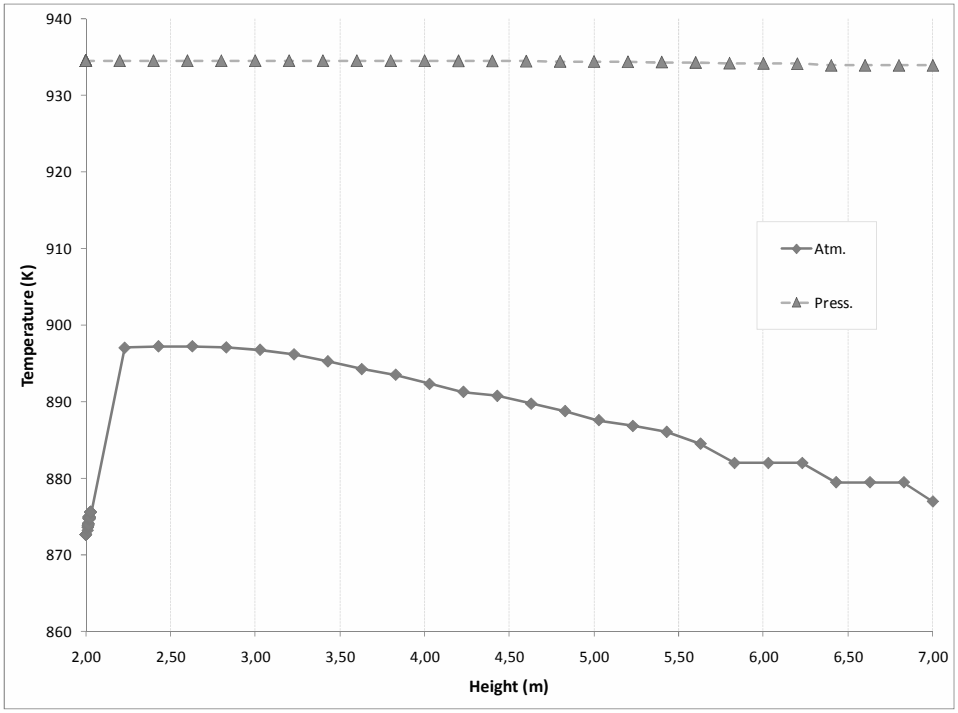

Figure 2. Results of the freeboard temperature profile.

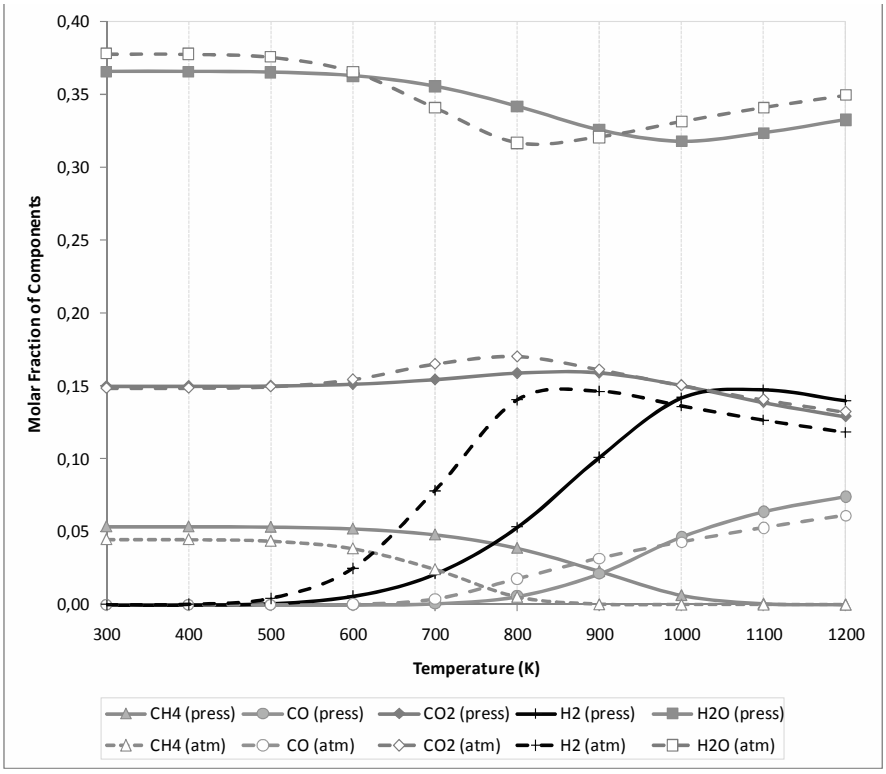

Figure 3. Results of the Molar fraction of the components.

10. Conclusions

Direct gasification systems have been demonstrated at both elevated and atmospheric pressures. Gasifier operating pressure affects not only equipment cost and size, but also the interfaces to the rest of the power plant including the necessary cleanup systems.

This paper presented a simulation of fluidized bed gasifier and compared two situations of biomass gasification.

The results showed the temperature behavior from the bed and from the freeboard, both working under atmospheric pressure (0.101 MPa) and pressurized (2 MPa). It showed a linear behavior in the bed for the pressurized system which was not observed in the atmospheric one. At the freeboard, the behavior of the temperature under pressurized condition was linear but under atmospheric pressure had a peak on the top of the bed.

The next step of this research is the study of different kinds of biomass, under different conditions (temperature and pressure), and the process optimization. Also, it is envisioned an exergetic analysis of the process.

Nomenclature

F_{GE} mass flow in the emulsion gas [kg.s^{-1}].

$R^{se}_{m,j}$ rate of production (or consumption if negative) of gas component j by gas-solid or heterogeneous reactions [kg.m^{-3}.s^{-1}].

$A_{GE,m}$ area of gas solid interface (m^2)

R^{GE}_j rate of production (or consumption if negative) of gas-gas homogeneous reactions [kg.m^{-3}.s^{-1}].

V_{GE} volume occupied by the gas in the emulsion [m^3]

G^{GE}_j mass flux of component j between bubble and emulsion phase [kg.m^{-2}.s^{-1}]

A_B area in the interface between bubble and emulsion (m^2)

j chemical component

F_{GB} mass flow in the bubble gas [kg.s^{-1}]

z coordenate

R_j^{GB} rate of production (or consumption if negative) of gas-gas homogeneous reactions in the bubble phase [kg.m^{-3}.s^{-1}].

V_B volume occupied by the gas in the bubble phase [m^3].

C_{GE} specific heat at constant pressure in the emulsion phase [kJ.kg^{-1}.K^{-1}].

T_{GE} temperature at the emulsion phase [K].

R_{QGE} rate of energy generation (or consumption, if negative) due to gas-gas chemical reactions [W.m^{-3}].

R_{GE}^{cs} rate of convective heat transfer between each solid species m and the emulsion gas [W.m^{-3}].

R_{GE}^{hs} rate of energy transfer to (or from, if negative) the emulsion phase due to mass transfer between phases [W.m^{-3}].

R_{GE}^{cGB} rate of heat transfer by convection between the emulsion gas and the bubbles [W.m^{-3}].

R_{GE}^{hGB} rate of energy carried from the emulsion gas to the bubbles (or vice versa) due the mass exchange between these phases [W.m^{-3}].

V_{GB} volume occupied by the gas in the bubble [m^3].

$R_{GE,t}^{c}$ rate of energy transfer by convection between the emulsion gas and the tubes immersed in the bed [W.m^{-3}].

$R_{GE,d}^{w}$ rate of energy transfer between emulsion gas and the bed wall [W.m^{-3}].

C_{GB} specific heat at constant pressure in the bubble phase [kJ.kg^{-1}.K^{-1}].

T_{GB} temperature at the bubble phase [K].

R_{GB} rate of energy generation (or consumption, if negative) due to homogeneous reactions occurring in the bubble phase [W.m^{-3}].

$R_{GB,t}^{c}$ rate of heat transfer by convection between bubbles and tubes eventually immersed in the bed [W.m^{-3}].

F_F net mass flow in the upward direction [kg.s^{-1}].

$R_{m,j}^{sf}$ rate of production (or consumption if negative) of solid-phase component j in the specie m [kg.m^{-3}.s^{-1}].

m refers to the particular solid phase (1 = carbonaceous solid, 2 = limestone, and 3 = inert).

References

[1] Gabra, M., Pettersson, E., Backman, R., Kjellström, B. Evaluation of cyclone gasi_er performance for gasification of sugar cane residue—Part 1: gasification of bagasse. Biomass and Bioenergy v. 21, p. 351–369, 2001.

[2] Dasappa, S., Paul, P. J., Mukunda, H. S., Rajan, N. K. S., Sridhar, G., and Sridhar, H. V. Biomass gasification technology – a route to meet energy needs. CURRENT SCIENCE, V. 87, No. 7, 2004.

[3] Souza-Santos, M. L. Solid Fuels Combustion and Gasification – Modeling Simulation and Equipment Operation, Marcel Dekker, 2004.

[4] Higman, C., van der Burgt, M. Gasification, Elsevier, Second Edition, 2008.

[5] Basu, P., Combustion and Gasification in Fluidized Beds, Taylor & Francis Group, LLC, 2006.

Theoretical Study of the Transesterification of Triglycerides to Biodiesel Fuel under Various Conditions

Yusuke Asakuma [a], Osamu Kawanami [a], Kouji Maeda [a], Hidetoshi Kuramochi [b] and Keisuke Fukui [a]

[a] *University of Hyogo, Himeji, Japan*
[b] *National Institute of Environmental Study, Tsukuba, Japan*

Abstract: The transesterification of triglycerides under various conditions was considered in terms of the activation energy obtained from molecular orbital method. The transesterification reaction is completed via a transition state, in which ring formation consisting of the carbon of the carboxyl and alcohol groups appears. Moreover, reaction pathway was shown by an activation energy analysis and electrostatic potential distribution.

Keywords: Biodiesel fuel, transesterification reaction, electrostatic potential

1. Introduction

Biodiesel is becoming increasingly important as an alternative fuel for diesel engines due to diminishing petroleum reserves and as part of the effort to save the global environment. Biodiesel is made from renewable biological sources such as vegetable oils and animal fats consisting of the simple alkyl esters of fatty acids, and is considered to contribute much less to global warming than fossil fuels [1].

Transesterification is a process of reacting a triglyceride such as vegetable oil with an alcohol, usually methanol, in the presence of acidic or alkaline catalyst to produce fatty acid esters and glycerol. An alkaline-catalyzed transesterification process is normally adopted for biodiesel production because alkaline metal alkoxides (methoxide) and hydroxides are more effective than acid catalysts. On the other hand, in the case of usage of acid catalyst, the reaction rate is slower than the rate of alkaline condition [2]. Moreover, biodiesel fuel is made from fatty acid in subcritical and supercritical methanol or water at the catalyst free condition [3, 4]. In this case, high energy is required to proceed with this hydrolysis process due to the low reactivity of water molecule.

A number of researchers have demonstrated the importance of variables such as reaction rate and selectivity of catalyst to the transesterification. Generally, the properties of the biodiesel fuel are strongly influenced by not only the structure and concentration of the fatty acid esters, which depend on the source, such as palm, soybean, corn or sunflower, but also reaction condition such as temperature and catalyst. Therefore, we have studied the solubility properties of a mixture of triglyceride and methanol in a vapor-liquid-liquid three phases equilibrium to improve reaction rate [5] and analyzed decomposition mechanism by molecular orbital method [6].

Normally, a typical transesterification of ester bond of a triglyceride is shown in Fig. 1 (a) (b), consisting of consecutive reversible reactions under acidic or basic condition. The triglyceride is converted stepwise to a diglyceride, a monoglyceride and finally, to glycerol by removal of an alkyl in each step, as shown in Fig. 2, where R^1, R^2 and R^3 represent long chain alkyl groups [7-10]. Accordingly, we thought that systematic theoretical estimations of the transesterification would be essential to clarify the transesterification pathways and the complex transesterification mechanism by acid or basic catalyst. Our interest in this study was focused on the transesterification and hydrolysis mechanism. Molecular orbital method was used to analyze the mechanism in a first attempt. In this study, various types of behavior such as the effect of reaction process of hydrolysis and transesterification under acidic or basic condition on the reactivity, and the pathway from triglyceride to diglyceride and monoglyceride, were considered by means of activation energy and electrostatic potential (ESP) distribution obtained from molecular orbital

Corresponding Author: Yusuke Asakuma, Email: asakuma@eng.u-hyogo.ac.jp

method.

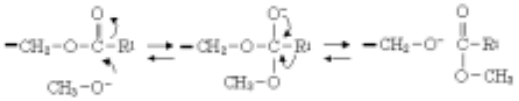

(a)

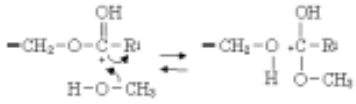

(b)

Fig. 1. Triglyceride transesterification mechanism: (a) Basic condition, (b) Acidic condition.

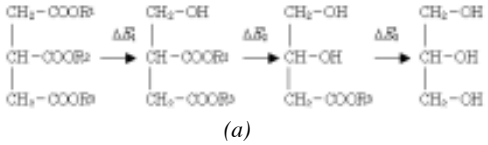

(a)

(b)

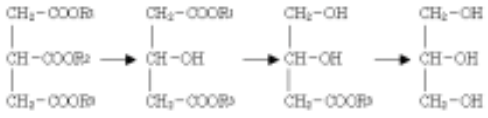

(C)

Fig. 2 Three different pathways of transesterification: a) 1 -> 2 -> 3 , b)1 -> 3 -> 2, (c) 2 -> 1 -> 3

2. Calculation

Figure 1 shows the transesterification reaction of a triglyceride such as vegetable oil or animal fat. The meaning of the numbers 1, 2, and 3 in Fig. 2 is the position of the carboxyl group, either in the center (2) or on the outside (1 and 3). The triglyceride is split into its components via transesterification catalyzed by the addition of an acid or a base. Alkaline-catalized transesterification is the process of exchanging the alkoxy group of an ester compound for another alokoxy group of a different alcohol such as methanol as shown in Fig. 1(a). The fatty acid monoalkyl ester can be used as biodiesel fuel (BDF) in diesel engines. After the ester linkage of triglyceride is cut by an alkoxy group under basic condition, three fatty acid esters and glycerol (glycerin) are produced via a transesterification reaction. When the carbonyl is attacked by the alkoxy group, this reaction proceeds through a tetrahedral intermediate or transition state [11]. Transesterification by acid catalyst is similarly completed as shown in Fig. 1(b). On the other hand, in the case of hydrolysis reaction, methoxide and methanol as a reactant are displaced to hydroxide ion and water, respectively. The characteristics of these reactions are best considered by evaluation of the activation energy [11, 12].

It is first necessary to calculate the optimised size of the ground state and transition state for the transesterification because each state has different energy. In this study, ab-initio molecular orbital was chosen because semi-empirical calculation [13] might be insufficient for evaluation of electronic structure. The quantum data of each state is derived using Gaussian software (Gaussian R 03W Ver. 6, Gaussian, Inc.) [11, 12]. The structures of ground state molecules (triglyceride, alkoxyl group and fatty acid ester) and the transition state of the transesterification reaction were simulated. The activation energy of the transesterification reaction was obtained from optimized structures calculated under minimum energy configurations from the initial approximate coordinates of the atoms. The basis set used in this calculation was HF/STO-3G [6].

The reactivity of transesterification and hydrolysis under acidic and basic conditions are considered. In this case, methanol and water molecule are used for transesterification and hydrolysis as the reactant, respectively. Finally, the main reaction pathway is predicted. The triglyceride has three ester bonds which are transesterified one by one as shown in Fig. 2. The activation energy obtained from this calculation can show which ester bonds are easier to transesterify initially, and which are main pathways.

3. Results and Discussion

Every transesterification and hydrolysis proceeds via the transition state. Oxygen atom of reactant attacks the carbon of the carboxyl group, and a polygonal ring with a tetrahedral intermediate carbon and an alkoxy group is formed

[11, 12]. Transesterification by alkoxy group under basic condition has been shown in reference and Fig. 3(a), the shape of ring is pentagonal [6]. In this study, reaction of acidic condition is shown as follows. First, proton is attached on atom of carboxyl oxygen under acidic condition. Additionally, methanol attacked on carbonyl carbon, square ring is formed simultaneously as shown in Fig. 3(b) [2].

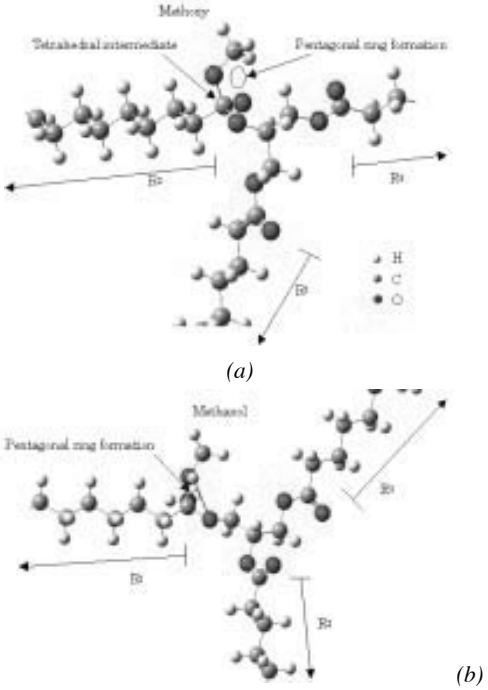

Fig. 3 Ring formation involving methanol at the transition state in transesterification: a) Basic condition, b) Acidic condition

Figure 4 (a) and (b) show the electrostatic potential (ESP) distribution around the ester bond of the triglyceride. Electrons of the carboxyl carbon are pulled by the neighbor oxygen atoms because of their higher electronegativity. ESP distribution of acidic condition shows higher than basic condition because proton is attached on carbonyl oxygen as shown in Fig. 1(b). ESP values of the carbonyl carbon becomes the highest in the triglyceride molecule. In the same way, ESP near oxygen atoms shows the lowest value and so ESP values of oxygen and carboxyl carbon of the triglyceride become negative and positive, respectively. On the other hands, negative ESP distribution of the methoxy and methanol oxygen concentrates around the oxygen atom as shown in Fig. 4 (c)(d). Accordingly, the polygonal (pentagonal and square) ring is formed by two forces, electrostatic force between the oxygen atom of the methanol and the carboxyl carbon, hydrogen bond between the hydrogen atom of the methanol and the carbonyl oxygen. This ring appeared in every calculation of the optimum structure, and this tetrahedral structure is therefore defined as a transition state. The importance of the ring formation in the transition state was reported for another transesterification reaction [11, 12].

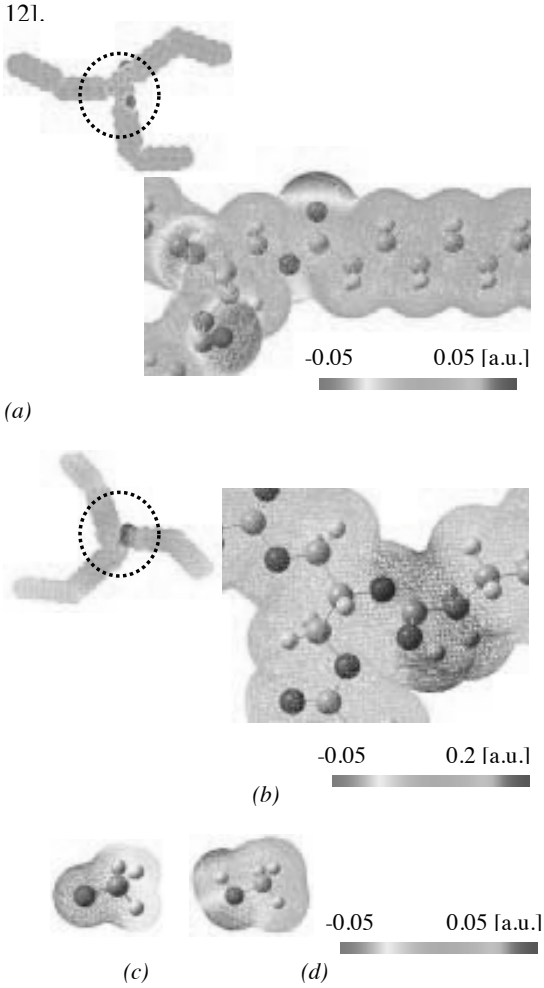

Fig. 4 Electrostatic potential distribution : a) Triglyceride under basic condition, b) Triglyceride under acidic condition, c) Methoxy, d) Methanol

3.1. Pathway of transesterification and hydrolysis under basic condition

Figure 5 shows the activation energy of each of the three stages of transesterification and hydrolysis. According to the activation energy values, pathway (c) is ideal because the total activation energy of pathway (c) is lower than the others. This means that transesterification and hydrolysis of a center ester bond is performed in preference to outside ester bonds. Moreover, transesterification reactions of diglycerides and monoglycerides (ΔE_2 and ΔE_3), which have larger activation energies, are more difficult than for triglycerides (ΔE_1). This behavior corresponds to experimental data wherein transesterification is incomplete, and a small portion of monoglyceride and diglyceride remains in the end [9, 10]. On the other hand, hydrolysis shows higher activation energy than transesterification by methoxy. It is caused by ring size of transition state. In other word, square ring of hydrolysis is more unstable than pentagonal of transesterification. This behavior accords with that high energy is required at severe environment such as subcritical condition to complete hydrolysis reaction [3, 4].

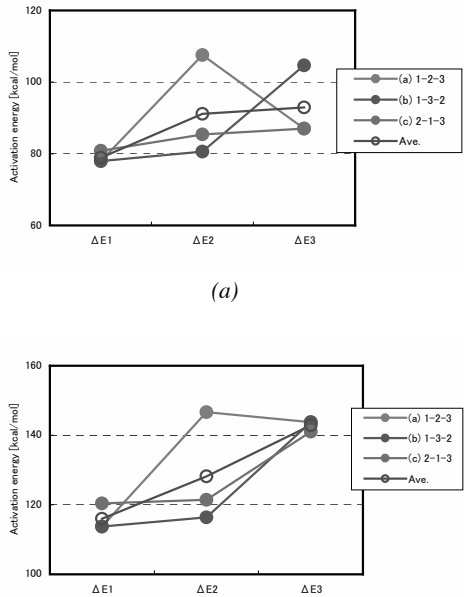

Fig. 5 Activation energy of the transesterification pathway under basic condition a) Transesterification, b) Hydrolysis

3.2. Pathway of transesterification and hydrolysis under acidic condition.

The activation energy of each of the three stages of hydrolysis and transesterification under acidic condition is shown in Fig. 6. Same tendency with basic condition was obtained. The energy of acidic condition shows lower values than the base although the acid-catalyzed reaction is slower in general [2]. The reason can be explained by optimized structure of the transition state. In the case of acid-catalyzed transeterifiation and hydrolysis, intramolecular bond between centar and side carboxyl bonds is formed as heptagonal ring as shown in Fig. 7. This ring includes the ester linkage which is cut by methanol and hydroxide at transesterification reaction. Accordingly, Appearace of the larger ring at transition state causes difficulty of ring opening reaction which completes transesterification and hydrolysis. This stable strucure with larger ring mainly happens when center carboxyl bond is attacked by methanol and water molecule. Moreover, geometrical position of reactant affects on formation of larger ring.

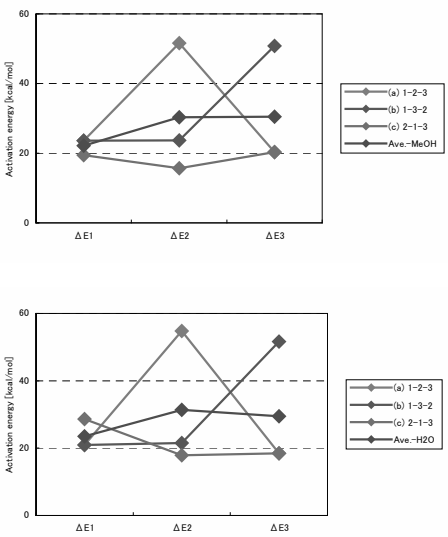

Fig. 5 Activation energy of the transesterification pathway under acidic condition a) Transesterification, b) Hydrolysis

4. Conclusions

The activation energies of transesterification and hydrolysis reactions of triglycerides under acidic and basic condition were calculated by Gaussian software to clarify the mechanism. The values show that the difference of the reactivity for transesterification and hydrolysis. Moreover, formation of the fatty acid alkyl ester by the addition of an alkoxy group was considered by the activation energy. Ring formation involving the carbon of the carboxyl group and the reactant at the transition state is essential for the transesterification and hydrolysis reactions. Finally, the transesterification reaction under acidic condition was analyzed in detail by activation energy and ESP obtained from molecular orbital method. Reactivity of triglyceride, monoglycerides and diglycerides, and pathway center and outside ester bonds are analyzed, acid-catalyzed reaction becomes more difficult than basic condition due to the stabilized transition state formed with larger ring by reactant.

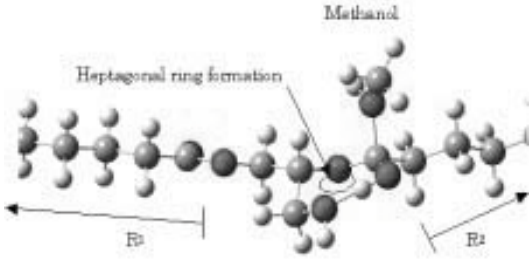

Fig. 7 Heptagonal ring formation at the transition state in transesterification

References

[1] Demirbas A., 2007, Progress and recent trends in biofuels, Progress in Energy Combustion Science, 33, pp.1-18.

[2] Sharma, Y.C., Singh, B., Upadhyay S.N., *2008,* Advancements in development and characterization of biodiesel: A review, Fuel, 87, pp.2355-2373.

[3] Minami E., Saka S., 2006, Kinetics of hydrolysis and methyl esterification for biodiesel production in two-step supercritical methanol process, Fuel, 85, pp.2479-2483.

[4] Alenezi R., Leeke, G.A., Santos R.C.D., Khan A.R., *2009,* Hydrolysis kinetics of sunflower oil under subcritical water conditions, Chemical Engineering Research and Design, 87, pp.867-873.

[5] Maeda K. et al., 2008, Phase equilibrium of biodiesel compounds for the triolein-palmitic acid-methanol system with dimethyl ether as cosolvent, Chemical Engineering data, 53, pp.973-977.

[6] Asakuma Y., Maeda K., Kuramochi H., Fukui, K., 2009, Theoretical study of the transesterification of triglycerides to biodiesel fuel, Fuel, 88, pp. 786-791.

[7] Jin F. et al., 2007, NMR spectroscopic study on methanolysis reaction of vegetable oil, Fuel, 86, pp.1201-1207.

[8] Demirbas A., 2008, Comparison of transesterification methods for production of biodiesel from vegetable oils and fats, Energy Conversion Management, 49, pp.125-130.

[9] Barakos N., Pasias S. and Papayannakos N., 2008, Transesterification of triglycerides in high and low quality oil feeds over an HT2 hydrotalcite catalyst**,** Bioresource Technology, 99, pp.5037-5042.

[10] Boocock D.G.B., Konar S.K., Mao V., Lee C., Buligan S, 1998, Fast Formation of High-Purity Methyl Esters from Vegetable Oils, JAOCS, 75, pp.1167-1172.

[11] Hori K., Hashitani Y., Kaku Y. and Ohkubo K., 1999, The role of water for the exchange reaction**,** Journal of Molecular Structure THEOCHEM, 461-462, pp.589-596.

[12] Hori K. et al., 2007, Theoretical study on the reaction mechanism for the hydrolysis of esters and amides under acidic conditions, Tetrahedron, 63, pp.1264-1269.

[13] Neyda C. et al., 2008, Transesterification of Jatropha curcas oil glycerides, Theoretical and experimental studies of biodiesel reaction. Fuel, 87, pp.2286-2295.

AUTHOR'S INDEX

KEYWORD'S INDEX

ecos 2010

SPONSORS

ÉCOLE POLYTECHNIQUE FÉDÉRALE DE LAUSANNE

Schweizerische Eidgenossenschaft
Confédération suisse
Confederazione Svizzera
Confederaziun svizra

Office fédéral de l'énergie OFEN

INSTITUTIONAL PARTNERS

Lausanne

canton de vaud
LIBERTÉ ET PATRIE

TECHNICAL PARTNERS

ALPIQ

ecleer

HOLDI GAZ

BG
Ingénieurs Conseils
Ingenieure & Berater
Consulting Engineers

SUPPORTING ORGANIZATION

ASME
SETTING THE STANDARD

International centre for applied thermodynamics
ICAT
1997